

PROCEEDINGS OF SPIE



SPIE—The International Society for Optical Engineering

Design, Fabrication, and Characterization of Photonic Devices

Marek Osinski
Soo Jin Chua
Shigefusa F. Chichibu
Chairs/Editors

30 November–3 December 1999
Singapore

DISTRIBUTION STATEMENT A
Approved for Public Release
Distribution Unlimited

Sponsored by
SPIE—The International Society for Optical Engineering
Nanyang Technological University, Singapore

Cosponsored by
SPIE Singapore Chapter
Institute of Physics, Singapore
United States Air Force Asian Office of Aerospace Research
and Development (AFOSR/AOARD)
United States Army Research Office-Far East (ARO-FE)



20000526 113

Volume 3896

REPORT DOCUMENTATION PAGE

Form Approved
OMB No. 0704-0188

The public reporting burden for this collection of information is estimated to average 1 hour per response, including the time for reviewing instructions, searching existing data sources, gathering and maintaining the data needed, and completing and reviewing the collection of information. Send comments regarding this burden estimate or any other aspect of this collection of information, including suggestions for reducing the burden, to Department of Defense, Washington Headquarters Services, Directorate for Information Operations and Reports (0704-0188), 1215 Jefferson Davis Highway, Suite 1204, Arlington, VA 22202-4302. Respondents should be aware that notwithstanding any other provision of law, no person shall be subject to any penalty for failing to comply with a collection of information if it does not display a currently valid OMB control number.

PLEASE DO NOT RETURN YOUR FORM TO THE ABOVE ADDRESS.

1. REPORT DATE (DD-MM-YYYY) 19-05-2000			2. REPORT TYPE Conference Proceedings		3. DATES COVERED (From - To) 30 Nov 99 - 3 Dec 99	
4. TITLE AND SUBTITLE International Symposium on Photonics and Applications (ISPA'99), held 30 Nov 99 - 3 Dec 99, in Singapore					5a. CONTRACT NUMBER F6256200M9015	
					5b. GRANT NUMBER	
					5c. PROGRAM ELEMENT NUMBER	
6. AUTHOR(S) Conference Committee					5d. PROJECT NUMBER	
					5e. TASK NUMBER	
					5f. WORK UNIT NUMBER	
7. PERFORMING ORGANIZATION NAME(S) AND ADDRESS(ES) Division of Microelectronics, School of EEE Block S-2, Nanyang Technological University Singapore 639798 Singapore					8. PERFORMING ORGANIZATION REPORT NUMBER N/A	
9. SPONSORING/MONITORING AGENCY NAME(S) AND ADDRESS(ES) AOARD UNIT 45002 APO AP 96337-5002					10. SPONSOR/MONITOR'S ACRONYM(S) AOARD	
					11. SPONSOR/MONITOR'S REPORT NUMBER(S) CSP-991014	
12. DISTRIBUTION/AVAILABILITY STATEMENT Approved for public release; distribution is unlimited.						
13. SUPPLEMENTARY NOTES						
14. ABSTRACT Conference Proceedings provided in 3 Volumes: Volume 3896, "Design, Fabrication, and Characterization of Photonic Devices" (Pages: 772) Volume 3897, "Advanced Photonic Sensors and Applications" (Pages: 776) Volume 3899, "Photonics Technology Into the 21 st Century: Semiconductors, Microstructures, and Nanostructures" (Pages: 552)						
15. SUBJECT TERMS Photonics, Optoelectronic materials, Optoelectronic components, Optoelectronic applications						
16. SECURITY CLASSIFICATION OF:			17. LIMITATION OF ABSTRACT	18. NUMBE OF PAGES 2,100	19a. NAME OF RESPONSIBLE PERSON Joanne H. Maurice	
a. REPORT U	b. ABSTRACT U	c. THIS PAGE U			19b. TELEPHONE NUMBER (Include area code) +81-3-5410-4409	



PROCEEDINGS OF SPIE
SPIE—The International Society for Optical Engineering

Design, Fabrication, and Characterization of Photonic Devices

Marek Osiński
Soo Jin Chua
Shigefusa F. Chichibu
Chairs/Editors

30 November–3 December 1999
Singapore

Sponsored by
SPIE—The International Society for Optical Engineering
Nanyang Technological University, Singapore

Cosponsored by
SPIE Singapore Chapter
Institute of Physics, Singapore
United States Air Force Asian Office of Aerospace Research
and Development (AFOSR/AOARD)
United States Army Research Office-Far East (ARO-FE)

Cooperating Organizations
National University of Singapore
SPIE Hong Kong Chapter
SPIE India Chapter
SPIE Japan Chapter
SPIE Korea Chapter
SPIE Taiwan Chapter

Published by
SPIE—The International Society for Optical Engineering



Volume 3896

SPIE is an international technical society dedicated to advancing engineering and scientific applications of optical, photonic, imaging, electronic, and optoelectronic technologies.



The papers appearing in this book comprise the proceedings of the meeting mentioned on the cover and title page. They reflect the authors' opinions and are published as presented and without change, in the interests of timely dissemination. Their inclusion in this publication does not necessarily constitute endorsement by the editors or by SPIE.

Please use the following format to cite material from this book:

Author(s), "Title of paper," in *Design, Fabrication, and Characterization of Photonic Devices*, Marek Osinski, Soo Jin Chua, Shigefusa F. Chichibu, Editors, Proceedings of SPIE Vol. 3896, page numbers (1999).

ISSN 0277-786X
ISBN 0-8194-3498-1

Published by
SPIE—The International Society for Optical Engineering
P.O. Box 10, Bellingham, Washington 98227-0010 USA
Telephone 360/676-3290 (Pacific Time) • Fax 360/647-1445

Copyright ©1999, The Society of Photo-Optical Instrumentation Engineers.

Copying of material in this book for internal or personal use, or for the internal or personal use of specific clients, beyond the fair use provisions granted by the U.S. Copyright Law is authorized by SPIE subject to payment of copying fees. The Transactional Reporting Service base fee for this volume is \$10.00 per article (or portion thereof), which should be paid directly to the Copyright Clearance Center (CCC), 222 Rosewood Drive, Danvers, MA 01923. Payment may also be made electronically through CCC Online at <http://www.directory.net/copyright/>. Other copying for republication, resale, advertising or promotion, or any form of systematic or multiple reproduction of any material in this book is prohibited except with permission in writing from the publisher. The CCC fee code is 0277-786X/99/\$10.00.

Printed in the United States of America.

Contents

xiii Conference Committee

PLENARY SESSION I

- 2 **Future technology and business opportunities in photonics: a view from the Optoelectronics Industry Development Association (OIDA) [3896-201]**
A. A. Bergh, Optoelectronics Industry Development Association (USA)
- 12 **Oxide-confined vertical-cavity surface-emitting lasers, quantum dots, and the Purcell effect: can scaling the mode size improve laser performance? [3896-202]**
D. G. Deppe, D. L. Huffaker, H. Huang, L. A. Graham, Univ. of Texas/Austin (USA)

PLENARY SESSION II

- 24 **Optical nonlinearities in semiconductors [3896-203]**
S. W. Koch, T. Meier, Philipps-Univ./Marburg (Germany)
- 36 **Advances in missile technology: impact of photonics [3896-204]**
A. S. Pillai, Defence Research and Development Organisation (India)

KEYNOTE PAPER

- 46 **Recent progress of photonic device research [3896-01]**
K. Kobayashi, NEC Corp. (Japan)

SESSION 1 HIGH-POWER SEMICONDUCTOR LASERS

- 56 **Measurement of mounting-induced strain in high-power laser diode arrays (Invited Paper) [3896-02]**
J. W. Tomm, R. Müller, A. Bärwolff, Max-Born-Institut für Nichtlineare Optik und Kurzzeitspektroskopie (Germany); D. Lorenzen, Jenoptik Laserdiode GmbH (Germany)
- 65 **Fabrication and characterization of high-power diode lasers [3896-03]**
J. Jandeleit, N. Wiedmann, A. Ostlender, W. Brandenburg, P. Loosen, R. Poprawe, Fraunhofer-Institut für Lasertechnik (Germany)

SESSION 2 WIDE-BANDGAP MATERIALS

- 72 **Stimulated emission and pump-probe studies of wide-gap nitrides for UV-blue photonic applications (Invited Paper) [3896-04]**
J.-J. Song, S. Bidnyk, Oklahoma State Univ. (USA); T. J. Schmidt, Williams Communications (USA)

- 86 **Optical properties of InGaN grown by MOCVD on sapphire and on bulk GaN [3896-05]**
M. Osiński, Ctr. for High Technology Materials/Univ. of New Mexico (USA); P. G. Eliseev, Ctr. for High Technology Materials/Univ. of New Mexico (USA) and P.N. Lebedev Physical Institute (Russia); J. Lee, V. A. Smagley, Ctr. for High Technology Materials/Univ. of New Mexico (USA); T. Sugahara, S. Sakai, Univ. of Tokushima (Japan)
- 98 **Comparison of optical properties in GaN and InGaN quantum well structures [3896-06]**
S. F. Chichibu, Univ. of Tsukuba (Japan); A. Shikanai, T. Deguchi, Waseda Univ. (Japan); A. Setoguchi, R. Nakai, Univ. of Tsukuba (Japan); K. Wada, Massachusetts Institute of Technology (USA); S. P. DenBaars, Univ. of California/Santa Barbara (USA); T. Sota, Waseda Univ. (Japan); T. Mukai, S. Nakamura, Nichia Chemical Industries, Ltd. (Japan)
- 107 **Low-cost synthesis of ZnCdSe semiconducting thin films for optoelectronic applications [3896-07]**
R. Chandramohan, Sree Sevugan Annamalai College (India); T. Mahalingam, Alagappa Univ. (India)

SESSION 3 SEMICONDUCTOR LIGHT EMITTERS

- 116 **Shot-noise-limited VCSELs for high-speed fiber optic data transmission (Invited Paper) [3896-08]**
R. Jäger, D. Wiedenmann, M. Grabherr, C. Jung, M. Kicherer, R. King, F. Mederer, M. Miller, P. Schnitzer, K. J. Ebeling, Univ. of Ulm (Germany)
- 133 **Manufacturing of lasers for DWDM systems (Invited Paper) [3896-09]**
K. T. Campbell, A. Robertson, S. J. Wetzell, Lucent Technologies/Bell Labs. (USA)
- 143 **Integrated thermal-electrical-optical simulator of vertical-cavity surface-emitting lasers [3896-10]**
M. Osiński, G. A. Smolyakov, Ctr. for High Technology Materials/Univ. of New Mexico (USA)
- 155 **Analysis and design of AlGaInP single-quantum-well LED [3896-11]**
L. P. Lee, S. J. Chua, National Univ. of Singapore
- 163 **Intracavity piezoelectric InGaAs/GaAs laser modulator [3896-12]**
J. P. R. David, E. A. Khoo, A. S. Pabla, J. Woodhead, R. Grey, G. J. Rees, Univ. of Sheffield (UK)

SESSION 4 SEMICONDUCTOR DEVICE PROCESSING

- 172 **Quantum well intermixing: from visible to far-IR wavelength applications (Invited Paper) [3896-13]**
E. H. Li, Univ. of Hong Kong
- 184 **Quantum well intermixing of GaAs/AlGaAs laser structure using one-step rapid thermal oxidation of AlAs [3896-14]**
S. L. Ng, O. Gunawan, B. S. Ooi, Y. L. Lam, Y. Zhou, Y. C. Chan, Nanyang Technological Univ. (Singapore)
- 191 **Multiwavelength lasers fabricated by a novel impurity-free quantum-well intermixing technology [3896-15]**
J. H. Teng, S. J. Chua, Y. H. Huang, Z. H. Zhang, G. Li, National Univ. of Singapore; A. Saher Helmy, J. H. Marsh, Univ. of Glasgow (UK)

- 199 **Dry plasma etching of GaAs vias using BCl_3/Ar and Cl_2/Ar plasmas** [3896-16]
Y. W. Chen, B. S. Ooi, G. I. Ng, C. L. Tan, Y. C. Chan, Nanyang Technological Univ. (Singapore)
- 207 **Effect of etch pit density of InP substrate on the stability of InGaAs/InGaAsP quantum well laser materials** [3896-17]
H. S. Lim, T. K. Ong, B. S. Ooi, Y. L. Lam, Y. C. Chan, Y. Zhou, Nanyang Technological Univ. (Singapore)

SESSION 5 POLYMERIC MATERIALS AND DEVICES

- 214 **Highly scattering optical transmission polymers for liquid crystal display (Invited Paper)** [3896-18]
A. Tagaya, Y. Koike, Keio Univ. (Japan) and Kanagawa Academy of Science and Technology (Japan)
- 223 **Development of metal-containing polymers for optoelectronic applications** [3896-19]
W. K. Chan, S. Hou, P. K. Ng, C. T. Wong, S. C. Yu, Univ. of Hong Kong
- 231 **Polymer light-emitting diodes based on novel soluble poly(p-phenylene vinylene)** [3896-20]
H. Jiang, Y. Zhou, Nanyang Technological Univ. (Singapore); J. Huang, Jilin Univ. (China); B. S. Ooi, Y. L. Lam, Y. C. Chan, Nanyang Technological Univ. (Singapore)
- 237 **Optical properties and waveguiding in films of a nonlinear polymer: difluorophenyl-polydiphenylenevinylene (DFP-PDPV)** [3896-21]
A. Samoc, B. Luther-Davies, M. Samoc, Australian National Univ.; H. Liebegott, R. Stockmann, H. H. Hoerhold, Friedrich-Schiller-Univ. Jena (Germany)

SESSION 6 POLYMERIC DEVICES AND OPTICAL LINKS

- 250 **High-speed plastic optical fibers and amplifiers (Invited Paper)** [3896-22]
Y. Koike, Keio Univ. (Japan) and Kanagawa Academy of Science and Technology (Japan)
- 265 **Development of microlens arrays for integration with optoelectronic devices** [3896-24]
C. Wang, Y. C. Chan, Y. L. Lam, B. S. Ooi, Nanyang Technological Univ. (Singapore)
- 273 **Multigigabit/s perfluorinated graded-index plastic-optical-fiber data links with butt-coupled single-mode InGaAs VCSEL** [3896-25]
F. Mederer, R. Jäger, P. Schnitzer, H. J. Unold, M. Kicherer, K. J. Ebeling, Univ. of Ulm (Germany); M. Naritomi, R. Yoshida, Asahi Glass Co., Ltd. (Japan)
- 281 **Monolithically integrated detector/receiver in standard CMOS operating at 250 Mbit/s for low-cost plastic optical fiber data links** [3896-26]
M. Kuijk, D. Coppée, R. A. Vounckx, Free Univ. of Brussels (Belgium)

SESSION 7 FIBER LASERS AND AMPLIFIERS

- 290 **Passive mode locking in erbium-ytterbium fiber lasers** [3896-29]
S. Thai, M. J. Hayduk, Air Force Research Lab. (USA)

- 298 **Spectroscopy of Nd³⁺, Tm³⁺, and Er³⁺ ions in tellurite glasses and fibers for broadband optical fiber amplifiers in the 1350- to 1600-nm range [3896-30]**
M. Nafataly, S. Shen, A. Jha, Univ. of Leeds (UK)

SESSION 8 MEASUREMENT TECHNIQUES FOR OPTOELECTRONICS

- 308 **Metrology for optoelectronics (Invited Paper) [3896-31]**
G. W. Day, National Institute of Standards and Technology (USA)
- 313 **Imaging the evanescent intensity gradients of an optical waveguide using a tapping-mode near-field scanning optical microscope [3896-32]**
C. W. Yang, National Chung Cheng Univ. (Taiwan); D. P. Tsai, National Taiwan Univ.; H. E. Jackson, Univ. of Cincinnati (USA)
- 319 **Effective index measurement of propagated modes in planar waveguide [3896-33]**
J. E. Batubara, H. R. Yulianto, Univ. of Pelita Harapan (Indonesia); H. P. Uranus, Univ. of Pelita Harapan (Indonesia) and Univ. of Indonesia; Muljono, Univ. of Pelita Harapan (Indonesia)
- 328 **Determination of white and 1/f FM noise components of semiconductor laser spectrum by a delayed self-heterodyne interferometer using short delay fiber [3896-34]**
M. N. Islam, Bangladesh Univ. of Engineering and Technology; T. Nomura, Toshiba Corp. (Japan); M. M. Imai, Muroran Institute of Technology (Japan); Md. Q. Huda, Bangladesh Univ. of Engineering and Technology

SESSION 9 PLANAR WAVEGUIDES AND DEVICES

- 334 **Reconstruction of refractive index profile of planar waveguide using inverse WKB method [3896-35]**
A. Supit, Univ. of Pelita Harapan (Indonesia); H. P. Uranus, Univ. of Pelita Harapan (Indonesia) and Univ. of Indonesia; Muljono, J. E. Batubara, Univ. of Pelita Harapan (Indonesia)
- 342 **Planar add/drop two-wavelength filter employing a blazed Bragg grating and a 3 × 3 asymmetric coupler [3896-36]**
K. W. Gaff, Optical Sciences Ctr./Australian National Univ.; F. J. Ladouceur, Virtual Photonics Inc. (Germany); J. D. Love, Optical Sciences Ctr./Australian National Univ.
- 352 **3C(β)-SiC-on-insulator waveguide structures for modulators and sensor systems [3896-37]**
A. Vonsovici, G. T. Reed, Univ. of Surrey (UK); M. R. Josey, P. R. Routley, A. G. R. Evans, Univ. of Southampton (UK); F. Namavar, Spire Corp. (USA)
- 360 **Blazed-grating couplers in unbonded SOI [3896-38]**
T. W. Ang, G. T. Reed, A. Vonsovici, Univ. of Surrey (UK); A. G. R. Evans, P. R. Routley, M. R. Josey, Univ. of Southampton (UK)
- 369 **Effective index method with built-in perturbation correction for the design of polarization-insensitive optical waveguide directional couplers [3896-39]**
K. S. Chiang, C. H. Kwan, City Univ. of Hong Kong

SESSION 10 WDM AND OPTICAL LINK COMPONENTS

- 380 **Arbitrary-response gain-flattening filters with low amplitude and phase noise and in-built ASE suppression [3896-40]**
M. Janos, B. Smith, S. B. Poole, JDS Uniphase Pty Ltd. (Australia)
- 385 **Avalanche multiplication in $\text{Al}_x\text{Ga}_{1-x}\text{As}/\text{GaAs}$ multilayer structures [3896-41]**
C. K. Chia, Univ. Sains Malaysia; J. P. R. David, G. J. Rees, S. A. Plimmer, R. Grey, Univ. of Sheffield (UK)
- 395 **Quantum mechanical analysis of a Muller effect plasma wave optical modulator/switch [3896-42]**
S. Khorasani, A. Nojeh, B. Rashidian, Sharif Univ. of Technology (Iran)
- 403 **Integrated acousto-optic tunable filter, equalizer, and switch in WDM communication system [3896-43]**
E. Dai, D. Wu, A. Xu, Peking Univ. (China)

SESSION 11 SOL-GEL PROCESSING

- 412 **Fabrication of gratings and design of diffractive optical elements embossed on sol-gel films [3896-44]**
G. Tan, Y. C. Chan, J. Liu, C. Y. Liaw, Y. L. Lam, Y. Zhou, Nanyang Technological Univ. (Singapore)
- 417 **Deposition of sol-gel-derived inorganic and composite material films on InP for integrated optics [3896-45]**
J. Liu, Y. L. Lam, Y. C. Chan, Y. Zhou, W. Que, G. Tan, B. S. Ooi, Nanyang Technological Univ. (Singapore)
- 425 **Deposition of potassium lithium niobate films by sol-gel method [3896-46]**
H. X. Zhang, Y. Zhou, C. H. Kam, X. Q. Han, S. D. Cheng, B. S. Ooi, Y. L. Lam, Y. C. Chan, Z. Sun, M. B. Yu, X. Shi, S. F. Yoon, Nanyang Technological Univ. (Singapore)
- 433 **Influence of Al/Nd ratio on light-emitting properties of Nd-doped glass prepared by sol-gel process [3896-47]**
Q. Xiang, Y. Zhou, Y. L. Lam, B. S. Ooi, Y. C. Chan, C. H. Kam, Nanyang Technological Univ. (Singapore)
- 438 **Characterization of reactive ion etching of sol-gel SiO_2 using Taguchi optimization method [3896-48]**
T. C. L. Wee, B. S. Ooi, Y. Zhou, Y. C. Chan, Y. L. Lam, Nanyang Technological Univ. (Singapore)

SESSION 12 SOL-GEL DEVICES

- 446 **$\text{TiO}_2/\text{SiO}_2/\text{ORMOSIL}$ hybrid material planar waveguides prepared at low temperature by sol-gel processing [3896-49]**
W. Que, Y. Zhou, Y. L. Lam, Y. C. Chan, S. D. Cheng, H. Li, J. Liu, C. H. Kam, Nanyang Technological Univ. (Singapore)

- 453 **Light-emitting properties of sol-gel-derived Er³⁺-doped Yb³⁺-codoped SiO₂-TiO₂-Al₂O₃ planar waveguide [3896-50]**
Q. Xiang, Y. Zhou, Y. L. Lam, Y. C. Chan, C. H. Kam, Nanyang Technological Univ. (Singapore)
- 459 **Temperature-dependent luminescence and energy transfer in Europium and rare-earth-codoped nanostructured sol-gel SiO₂ glasses [3896-51]**
S. Buddhudu, Nanyang Technological Univ. (Singapore); M. Morita, Seikei Univ. (Japan); H. X. Zhang, C. H. Kam, Y. L. Lam, Y. Zhou, T. K. S. Wong, Y. C. Chan, B. S. Ooi, S. L. Ng, W. Que, Nanyang Technological Univ. (Singapore)
- 466 **Structural, electrical, and optical properties of sol-gel-processed thin films of BaTiO₃ on ITO glass [3896-52]**
C. H. Kam, S. D. Cheng, Y. Zhou, Nanyang Technological Univ. (Singapore); K. Pita, Singapore Productivity and Standards Board; X. Q. Han, W. Que, H. X. Zhang, Y. L. Lam, Y. C. Chan, Nanyang Technological Univ. (Singapore); W. S. Gan, Acoustical Technologies Singapore Pte Ltd.; Z. Sun, X. Shi, Nanyang Technological Univ. (Singapore)

SESSION 13 SOLAR CELLS

- 474 **Electrochemical synthesis of SnS thin films for photoelectrochemical cells [3896-53]**
B. Subramanian, Jayaram College of Engineering and Technology (India); C. Sanjeeviraja, Alagappa Univ. (India); M. Jayachandran, M. J. Chockalingam, Central Electrochemical Research Institute (India)

SESSION 14 UNCONVENTIONAL PHOTONIC DEVICES

- 484 **Influence of the hole-carrier layer controlled by electrochemical method on electroluminescence [3896-57]**
G. Wang, X. Hu, T. K. S. Wong, Nanyang Technological Univ. (Singapore)

SESSION 15 POSTER SESSION

- 494 **Polarization-sensitive performance of strained-quantum-well semiconductor optical amplifiers [3896-61]**
D. Liu, W. Xu, Z. Duan, D. Huang, Huazhong Univ. of Science and Technology (China)
- 499 **Phase calculation of (100) oriented InGaAsSb grown with liquid phase epitaxy [3896-62]**
X. Mao, Y. C. Chan, Y. L. Lam, Nanyang Technological Univ. (Singapore)
- 507 **Fabrication of infrared LEDs/LDs at wavelength of 1.5 μ m using LPE-grown wafer [3896-63]**
D. Bayuwati, M. R. T. Siregar, T. B. Waluyo, Indonesia Institute of Sciences
- 515 **Development of a laser holographic interference lithography system [3896-65]**
O. Gunawan, L. W. Hoe, B. S. Ooi, Y. C. Chan, Y. L. Lam, Y. Zhou, Nanyang Technological Univ. (Singapore)
- 523 **Electrodeposited polycrystalline GaAs films and their characteristics [3896-66]**
C. Yang, Z. Zhang, W. Xu, A. Han, Harbin Institute of Technology (China)

- 528 **Solute redistribution during the accelerated crucible rotation Bridgman growth of $\text{Hg}_{1-x}\text{Mn}_x\text{Te}$** [3896-67]
W. Jie, Y. Li, X. Liu, Northwestern Polytechnical Univ. (China)
- 534 **Simple theory of steam oxidation of AlAs** [3896-68]
M. Osiński, T. Svimonishvili, G. A. Smolyakov, V. A. Smagley, Ctr. for High Technology Materials/Univ. of New Mexico (USA); P. Maćkowiak, W. Nakwaski, Technical Univ. of Łódź (Poland)
- 547 **Dual-wavelength response in double-barrier quantum well infrared photodetectors** [3896-69]
T. Osotchan, D. H. Zhang, W. Shi, Nanyang Technological Univ. (Singapore)
- 557 **Novel method for stabilization in harmonically mode-locked erbium-doped fiber laser with external optical modulation by laser diode** [3896-70]
V. H. Pham, D. T. Vu, National Ctr. for Science and Technology of Vietnam; Q. V. Tran, Vietnam Post and Telecommunication Inc.; C.-J. Yuon, Y. C. Chung, Korea Advanced Institute of Science and Technology
- 562 **Tunable long-period fiber gratings for EDFA gain equalization** [3896-71]
K. S. Chiang, Z. Chen, M. K. Pandit, City Univ. of Hong Kong
- 570 **Efficient white-light-emitting organic/polymeric electroluminescent device** [3896-72]
J. Huang, K. Yang, Z. Xie, C. Li, Y. Zhao, S. Liu, Y. Wang, F. Wu, Y. Li, J. Shen, Jilin Univ. (China)
- 576 **Applications of FFT and digital filtering in reconstruction of refractive index profile of surface channel waveguides from near-field intensity pattern** [3896-73]
H. Susanto, Univ. of Pelita Harapan (Indonesia); H. P. Uranus, Univ. of Pelita Harapan (Indonesia) and Univ. of Indonesia; Muljono, J. E. Batubara, Univ. of Pelita Harapan (Indonesia)
- 585 **Numerical study of beam propagation in multilayer planar waveguide with optically nonlinear medium** [3896-74]
H. Harsoyono, Institut Teknologi Bandung (Indonesia); R. E. Siregar, Univ. Padjadjaran (Indonesia); A. Soehiani, M. O. Tjia, Institut Teknologi Bandung (Indonesia)
- 594 **Mode theory and analysis of planar array waveguides** [3896-75]
H. Lei, H. Ou, Q. Yang, X. Hu, Q. Wang, Institute of Semiconductors (China)
- 602 **Energy approach to the propagation of light waves in anisotropic crystals** [3896-76]
S. Khorasani, B. Rashidian, Sharif Univ. of Technology (Iran)
- 608 **Optical damage in Zn:Ga:LiNbO_3 waveguide substrates** [3896-77]
Y. Zhao, W. Xu, H. Zhang, Y. Xu, Harbin Institute of Technology (China); J. Wang, Shandong Univ. (China)
- 614 **Novel U-groove channel for self-alignment of optical fibers with optical quality end-polished silicon rib waveguides using wet chemical micromachining techniques** [3896-78]
N. Q. Ngo, Griffith Univ. (Australia); M. A. Rosa, Xerox Palo Alto Research Ctr. (USA); D. R. Sweatman, S. Dimitrijević, H. B. Harrison, A. Titmarsh, Griffith Univ. (Australia)

- 624 **Crossover photonic switching network with CMOS/SEED smart pixel device and 2D optical fiber bundle array [3896-80]**
F. Luo, M. Cao, Q. Hu, A. Wan, J. Xu, C. Deng, D. Liu, Huazhong Univ. of Science and Technology (China)
- 631 **Photo-, electro-, and cathodoluminescence of porous silicon [3896-81]**
L. S. Monastyrskii, I. B. Olenych, V. P. Savchyn, Ivan Franko National Univ. of Lviv (Ukraine)
- 637 **Radiative transitions in porous silicon [3896-82]**
H. Bui, H. B. Phi, T. C. Dao, V. H. Pham, D. T. Vu, National Ctr. for Science and Technology of Vietnam
- 642 **Optoelectronic properties of new amorphous silicon photoreceptor [3896-83]**
J.-C. Chou, H.-Y. Yang, National Yunlin Univ. of Science and Technology (Taiwan)
- 653 **Temperature-dependent luminescence characteristics of Sm³⁺-doped silicate glass [3896-86]**
K. Annapurna, R. N. Dwivedi, Central Glass and Ceramic Research Institute (India); S. Buddhudu, Sri Venkateswara Univ. (India)
- 658 **Energy transfer luminescence in (Eu³⁺, Nd³⁺)-doped tellurite glass [3896-87]**
K. Annapurna, R. N. Dwivedi, Central Glass and Ceramic Research Institute (India); S. Buddhudu, Sri Venkateswara Univ. (India)
- 663 **Temperature-dependent luminescence in (Eu³⁺, Dy³⁺)-doped tellurite glass [3896-88]**
K. Annapurna, R. N. Dwivedi, Central Glass and Ceramic Research Institute (India); S. Buddhudu, Sri Venkateswara Univ. (India)
- 667 **Comparison of Er-doped sol-gel glasses with various hosts [3896-89]**
Q. Xiang, Y. Zhou, Y. L. Lam, B. S. Ooi, Y. C. Chan, C. H. Kam, Nanyang Technological Univ. (Singapore)
- 673 **Preparation and properties of organically modified sol-gel silica/titania optical waveguides [3896-90]**
W. Que, Y. Zhou, Y. L. Lam, S. D. Cheng, Y. C. Chan, C. H. Kam, L. P. Zhao, S. Buddhudu, Nanyang Technological Univ. (Singapore)
- 680 **Dependence of cracking behavior of sol-gel films on symmetries of substrates [3896-91]**
S. D. Cheng, Y. Zhou, C. H. Kam, W. Que, Y. L. Lam, Y. C. Chan, Nanyang Technological Univ. (Singapore); W. S. Gan, Acoustical Technologies Singapore Pte Ltd.
- 687 **Characteristics of sol-gel-derived (Pb,Ca)TiO₃ pyroelectric thin films [3896-93]**
C.-M. Wang, Y.-C. Chen, Y.-T. Huang, M.-C. Kao, National Sun Yat-Sen Univ. (Taiwan)
- 697 **Fabrication of planar waveguides of poly(N-vinylcarbazole) [3896-94]**
F. Fitrilawati, Institut Teknologi Bandung (Indonesia) and Univ. Padjadjaran (Indonesia); M. O. Tjia, Institut Teknologi Bandung (Indonesia); J. Ziegler, C. Bubeck, Max-Planck-Institute for Polymer Research (Germany)
- 705 **Electro-optical properties of an epoxy-based polymer-dispersed liquid crystal [3896-97]**
P. Mormile, Istituto di Cibernetica (Italy); L. Petti, Istituto di Cibernetica (Italy) and Trinity College (Ireland); M. Abbate, P. Musto, G. Ragosta, Istituto di Ricerca e Tecnologia delle Materie Plastiche (Italy); W. J. Blau, Trinity College (Ireland)

- 712 **Crystal growth and morphology investigation with 3D luminance of photonic organic DAST thin film [3896-98]**
T.-J. Sheu, C.-Y. Yui Whei, S.-S. Lin, Chung Yuan Christian Univ. (Taiwan); F.-Y. Tsai, Y.-K. Tu, Chunghwa Telecom Co., Ltd. (Taiwan)
- 720 **Optical refractive synchronization: linewidth coherency analysis and measurement [3896-100]**
J. R. Palmer, SilkRoad, Inc. (USA)
- 733 **Stark effect modulation with Doppler broadening at 10.784 μm [3896-101]**
D. Zhu, Univ. of Electronic Science and Technology (China); Z. Wan, Southwest Institute of Technical Physics (China); Z. Zhang, Univ. of Electronic Science and Technology (China)
- 741 **Theoretical comparison of 0.78% tensile strained InGaAs/InAlGaAs and InGaAs/InGaAsP quantum well lasers emitting at 1.55 μm [3896-105]**
H. K. Khoo, S. J. Chua, National Univ. of Singapore
- 751 **Imaging the near-field intensity gradients of a low-power semiconductor laser [3896-106]**
N. H. Lu, Sze-hai Institute of Technology and Commerce (Taiwan); D. P. Tsai, National Taiwan University; W. C. Lin, H. J. Huang, National Chung Cheng Univ. (Taiwan)
- 756 **Influence of pulse reversal on the characteristics of CdSe films [3896-85]**
K. R. Murali, V. Swaminathan, Central Electrochemical Research Institute (India)

ADDITIONAL PAPER FROM SESSION 7

- 762 **Fiber distributed feedback lasers and dispersion compensators (Invited Paper) [3896-28]**
M. N. Zervas, M. Ibsen, M. K. Durkin, Univ. of Southampton (UK); L. Chao, Nanyang Technological Univ. (Singapore); M. J. Cole, Qtera Corp. (USA); R. I. Laming, Kymata Ltd. (UK); D. N. Payne, Univ. of Southampton (UK)
- 770 *Author Index*

Conference Committee

Conference Chairs

Marek Osinski, Center for High Technology Materials/University of New Mexico (USA)
Soo Jin Chua, National University of Singapore
Shigefusa F. Chichibu, University of Tsukuba (Japan)

Program Committee

Gordon W. Day, National Institute of Standards and Technology (USA)
Karl Joachim Ebeling, University of Ulm (Germany)
Richard H. Friend, University of Cambridge (UK)
Waguih S. Ishak, Hewlett-Packard Laboratories (USA)
Kohroh Kobayashi, NEC Corporation (Japan)
Yasuhiro Koike, Keio University (Japan)
E. Herbert Li, University of Hong Kong
John D. Love, Australian National University
Shuji Nakamura, Nichia Chemical Industries, Ltd. (Japan)
David N. Payne, Southampton University (UK)
Simon B. Poole, JDS Uniphase Pty Ltd. (Australia)
Wenxiu Que, Nanyang Technological University (Singapore)
Mark G. Sceats, Australian Photonics Cooperative Research Center
Jin-Joo Song, Oklahoma State University (USA)
Jeff Y. Tsao, Sandia National Laboratories (USA)
John M. Zavada, U.S. Army European Research Office/London (UK)

Session Chairs

Plenary Session I
Chan-Hin Kam, Nanyang Technological Univ. (Singapore)

Plenary Session II
Anath Dodabalapur, Lucent Technologies/Bell Laboratories (USA)

- 1 High-Power Semiconductor Lasers
Marek Osinski, Center for High Technology Materials/University of New Mexico (USA)
- 2 Wide-Bandgap Materials
Soo Jin Chua, National University of Singapore
- 3 Semiconductor Light Emitters
Shigefusa F. Chichibu, University of Tsukuba (Japan)

- 4 Semiconductor Device Processing
Kevin T. Campbell, Lucent Technologies/Bell Laboratories (USA)
- 5 Polymeric Materials and Devices
Roland Jäger, University of Ulm (Germany)
- 6 Polymeric Devices and Optical Links
Akihiro Tagaya, Keio University (Japan) and Kanagawa Academy of Science and Technology (Japan)
- 7 Fiber Lasers and Amplifiers
Simon B. Poole, JDS Uniphase Pty Ltd. (Australia)
- 8 Measurement Techniques for Optoelectronics
Jin-Joo Song, Oklahoma State University (USA)
- 9 Planar Waveguides and Devices
Gordon W. Day, National Institute of Standards and Technology (USA)
- 10 WDM and Optical Link Components
Mark G. Sceats, Australian Photonics Cooperative Research Center
- 11 Sol-Gel Processing
Yasuhiro Koike, Keio University (Japan)
- 12 Sol-Gel Devices
John D. Love, Australian National University
- 13 Solar Cells
E. Herbert Li, University of Hong Kong
- 14 Unconventional Photonic Devices
Wenxiu Que, Nanyang Technological University (Singapore)

SPIE and Nanyang Technological University wish to thank the following for their contribution to the success of this conference:

- United States Air Force Asian Office of Aerospace Research and Development (AFOSR/AOARD)
- United States Army Research Office-Far East (ARO-FE)

Plenary Session I

Future Technology and Business Opportunities in Photonics: A View from the Optoelectronics Industry Development Association (OIDA) *

Dr. Arpad A. Bergh

Optoelectronics Industry Development Association, 2010 Massachusetts Avenue, NW, Suite 200,
Washington, DC 20036, P:202-785-4426, F: 202-785-4428, email: aboida@osa.org

ABSTRACT

The "optoelectronics industry" is a collection of six or more distinct industries that all depend on OE technology. The major markets are in communication, imaging, storage and displays. This paper gives a brief overview of the anticipated paradigm shifts, the potential markets and the promising new technologies in various OE markets.

Keywords: optoelectronics industry, optical communications, imaging, optical storage

1. INTRODUCTION

The dictionary defines Optoelectronics as "a branch of electronics that deals with electronic devices for emitting, modulating, transmitting, and sensing light".

Today Optoelectronics has a broader meaning. It also incorporates Electro-optics, a branch of physics that deals with the effects of an electric field on light transversing it (e.g. gas and solid state lasers), and Photonics, a branch of physics that deals with the properties and applications of photons, especially as a medium for transmitting information. It also increasingly overlaps with many facets of Optics, a science that deals with light, its genesis and propagation.

This relatively new branch of science and engineering interchangeably deploys electrons and photons, to take advantage of their best attributes. It has already laid the foundation of the technology that enables the information age. Optoelectronics enables all functions of the information industry. It is essential in gathering the information (imaging), as well as in transporting and displaying it. It also has a role, along with other technologies, in storing and processing information. Due to their increasingly important role optoelectronics components already represent a substantial worldwide market exceeding by a factor of three the market for traditional optics, Fig 1.

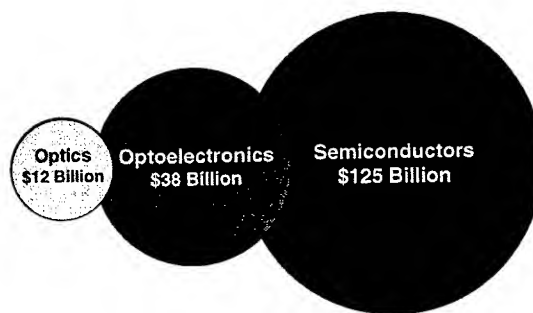


Figure 1. Worldwide Component Markets 1998

This is indeed remarkable when we consider that these elementary particles were only discovered in this Century.

Discovery of the electron:

It was in 1887, when J. J. Thomson working in the Cavendish laboratory at Cambridge measured the ratio of the charge e of an electron to its mass m by observing its deflection in both electric and magnetic fields. The discovery of electron is usually said to date from this historic experiment.

*Also published in *Proc. of SPIE* Vols. 3897, 3898, and 3899

Discovery of the Photon.

The discovery of the photon dates back to Planck's experiments in 1900 on the energy of photo-electronics leading to h , the Planck constant, 6.6254×10^{-27} erg sec. This was followed in 1905 by the famous Planck-Einstein equation:

$$E = h\nu,$$

Where h is the Planck constant and E is the energy of a quantum of light (called photon by others at a later date).

Some of the major attributes of the two particles explain their application domains and are compared in the following table:

Attributes	Electrons	Photons
wavelength	3 cm – 30 m	500 nm
Frequency	10 MHz – 10 GHz	500 THz
Energy	40 neV – 40 μ eV	2 eV
Propagation loss	High (in copper wire)	Low (in optical fiber)
Particle interaction	High	None

There are certain functions that can be uniquely provided by optoelectronics. In other areas OE competes with other technologies or assumes a supporting role as shown in the following table.

The Role of Optoelectronics in the Information Age Technologies

Dominant Enabling Technology	Competing with Other Technologies (Market Share)	Supporting Role Dominated by Electronics
Transmission	Sensors	Logic functions
Display	Storage	Processing
Imaging	Lighting	

2. OPTOELECTRONICS INDUSTRY

There is no single optoelectronics industry. It is, in fact, a combination of several industries supported by common technology and common infrastructure as shown in Fig. 2

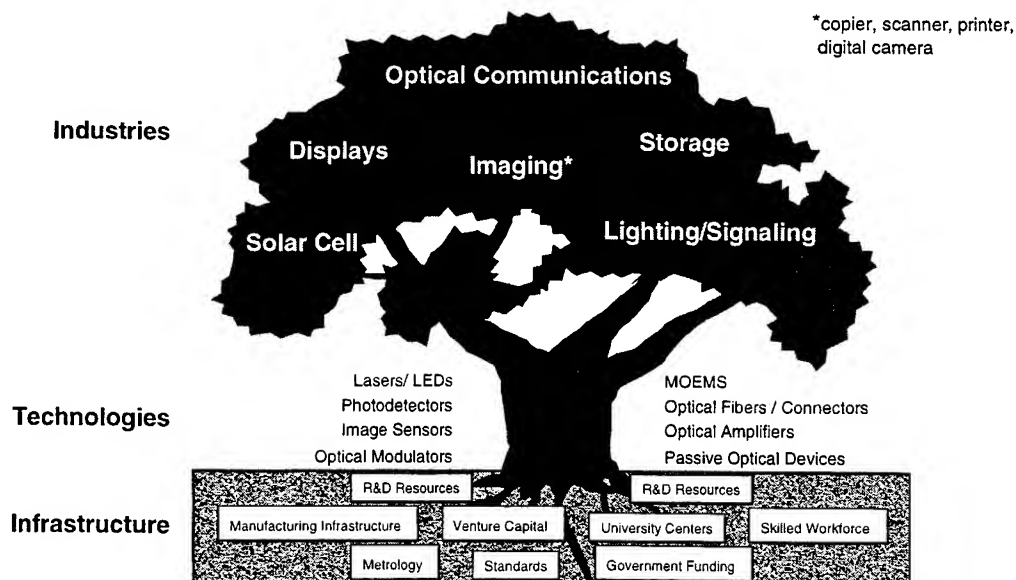


Figure 2. Optoelectronics Industries

Of the industry segments depicted in this figure communications, imaging, storage and displays have a large worldwide market, Fig 3 Emerging markets in optoelectronics are energy related and will have an increasingly important role as the world's known energy sources are depleted. Solar cells produce environmentally clean energy and solid state lighting has the promise of providing more efficient and environmentally benign replacement for the currently used incandescent and fluorescent light sources.

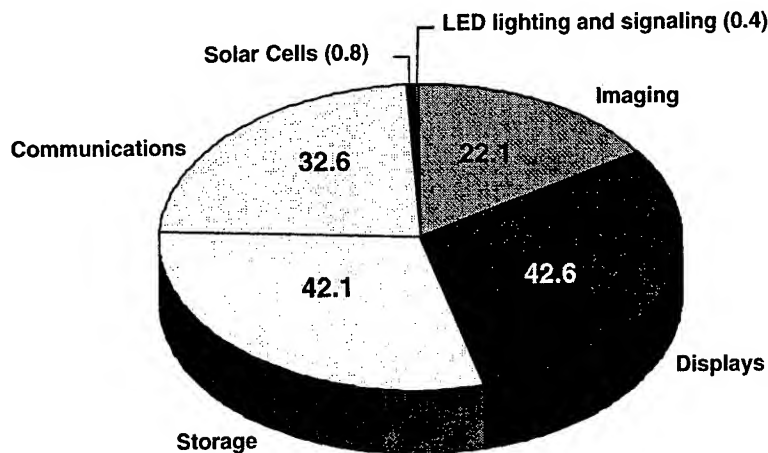


Figure 3. World OE Production (\$B) 1998 (Total: \$140.6 B, North America Estimate: \$42.8B)

This paper gives a brief overview of the anticipated paradigm shifts, the potential markets and the promising new technologies in various OE markets.

3. OPTICAL COMMUNICATION

Driven by Internet and data services, the evolution of information networks continues at an unprecedented pace. The traditional telephone architecture is rapidly changing:

- Transmission is moving to all-digital before the end of the next decade
- Voice services are increasingly augmented by multi media (incl. imaging)
- Voice, relative to data, becomes insignificant part of transmission bandwidth
- Intelligence is moving from the central office to the perimeter of the network
- The stationary telephone is replaced by the mobile telephone
- Telecom and datacom networks converge.

All these changes are made possible by the evolution of the electronic and optoelectronic technologies. Multi-Gb/s SONET/SDH and WDM transmission, resulting in capacities in excess of one Terabit/sec on a single fiber meet the explosive demand for bandwidth. Simultaneously, the increasing dominance of Internet, Web and data services is causing a conversion from voice- to data-centric networks, with a need for high-speed and broadband transmission at the lowest-possible cost.

In addition to the ongoing research and development at universities and industry the government has also played a significant role in this evolution. Some of the fruits of DARPA sponsored technologies are being implemented commercially and are changing the communications landscape. On the service level there is the Internet, on the system level WDM is reaching all segments of the network and on the device level VCSELs promise to lower costs, facilitate the integration of electronic and photonic components and render optical networks more affordable. Simultaneously the 1996 Telecommunication Act is unleashing competition among service providers and the consumer is left with a bewildering array of options. The streets of major cities are under attack from competing carriers laying new cable, and mobile phones are spreading faster than before.

OIDA's roadmapping in optical communication started in 1992. The most recent studies took place in 1998 and 1999. The 1998 study concentrated on the anticipated demand on communication systems that can deliver the required services. The predicted growth rate of the various communication services is shown in Fig 4.

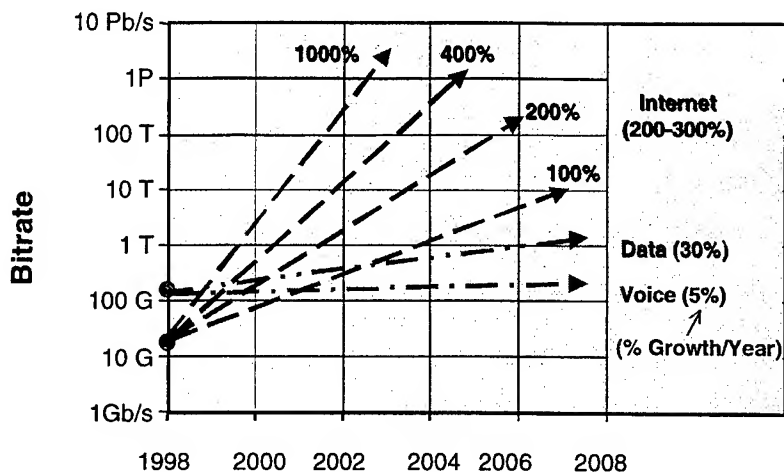


Figure 4. Growth Rate of Communication Services

This amazing growth rate is fueled by the evolution of the communication bandwidth which got a major boost in the mid-nineties from the commercial implementation of wavelength division multiplexing (WDM). To keep up with this growth and to deploy all the technology that has been demonstrated to date many practical and commercial issues must be addressed. The migration of the optical technology from the high performance backbone networks toward the high volume access network requires a drastic cost reduction of the OE components. The relentless cost reduction in the transmission network expressed in bit-km is shown in Fig 5.

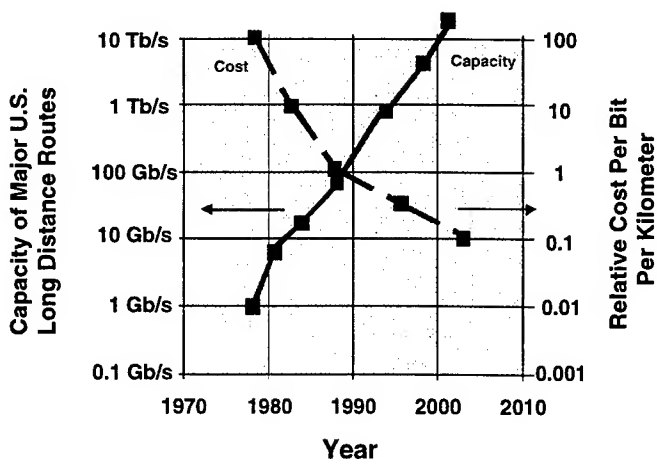


Figure 5. Transmission Cost Erosion, Ref. Yanming Liu, Corning

When the study was initiated two years ago it was obvious that communication would expand exponentially. It was also obvious that communication is segmented into several markets with sometimes overlapping and other times with divergent requirements.

The main areas of applications of the key OE components are:

- Long-Distance,

- Metro/Interoffice,
- Enterprise and Metro/Access,
- Local Area Network/Wide Area Network,
- Local Access Networks, and
- Backplane/Building Wiring.

In developing a roadmap estimates are made of the potential market volumes of the components in these various network segments, along with the key performance parameters and price targets as function of time. It is, however, exceedingly difficult to make predictions on the growth of the market volume of specific optoelectronic components. Nevertheless, using trend curves, latest technology developments and input from industry sources and analysts, a roadmap is constructed with the proviso that the predictions must be updated as data on actual equipment deployments and network applications become available.

The 1999 OIDA Roadmap Report delineated the OE components that require major industry efforts for their commercial realization. The following is a sample of key components required for optical networks with significant near term (1 to 4 years) market potential:

- Optical Crossconnects
- Optical Switches
- Optical Add-Drop Multiplexers
- Tunable Lasers
- Optical Amplifiers
- Optical Transceivers

An overriding requirement of these products is the simultaneous improvement in performance and ongoing cost reduction. The cost of components on the other hand depends on the volume of production. It is difficult to build high volumes when there is a proliferation of products for a given function. Optical switching for instance is one of the most desired functions but there are at least nine different approaches in which this can be accomplished. It will take several years and several generations of equipment before commonality is reached and standards are developed. In the meantime one can expect a steady increase in component performance with ongoing price erosion as shown in the next OIDA roadmap chart, Fig 6.

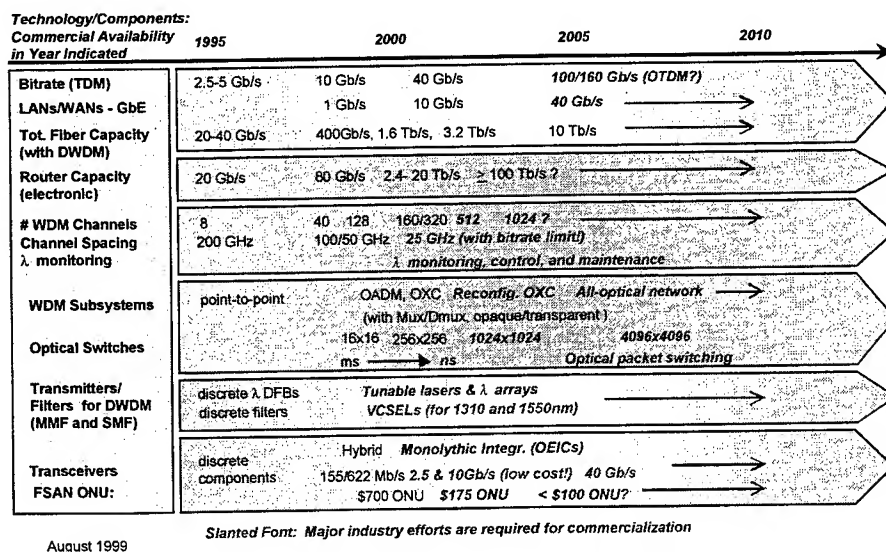


Figure 6. OIDA Communications Roadmap – 1999

All this activity will fuel the growth of the optoelectronic communications market, which in 1997 has already reached \$ 30 billion worldwide. As indicated in Fig 7 this market is expected to double by 2001 with no saturation in site for many years to come.

1997 Communications Market \$30.

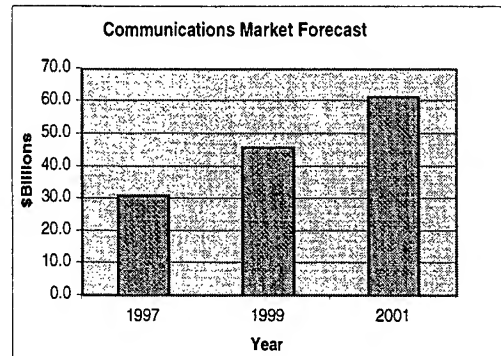
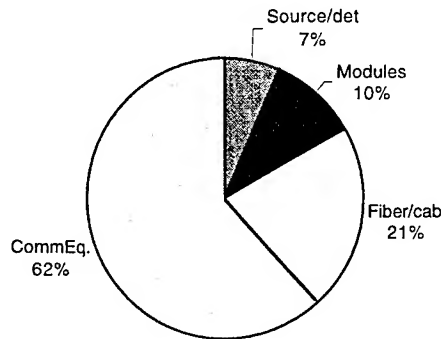


Figure 7. Optoelectronic Communications Market

4. IMAGING

Growth in the market value of the imaging industry has significantly lagged other technology sectors of the economy over the last five years as evidenced by the aggregate stock performance of imaging companies compared to the performance of the S&P 500 index. The Salomon Smith Barney Imaging Composite (SSIC), a weighted index of 50 imaging companies, widely used to track industry trends was up only 12%, versus more than 25% for the S&P 500 index.

The SSIC is composed of 5 sectors with Diversified Imaging/Photo and Document Processing companies representing 90% of the value of the composite. This Sector actually declined 4% last year, since many products in this sector are "mature" and experienced rapid price declines and decelerating volumes. Companies in this sector are looking to Advanced Imaging Applications as key growth drivers for future earnings.

Imaging companies are looking to Advanced Imaging Applications as key growth drivers for future earnings.

Advanced Imaging refers to the extension of conventional imaging products such as photographic film and cameras, video, copiers etc. as well as enabling entirely new capabilities through the application of digital technology. In the image capture area for example, electronic still cameras are replacing instant photography for scientific, insurance and real estate applications. Last year in Japan digital camcorders outsold both 8mm and VHS analog models. Worldwide digital camcorder sales totaled over \$3B. In 1998, it is estimated that 1.1 million digital cameras were sold in the U.S., up from 740,000 the prior year. Those figures should expand rapidly as PC based imaging becomes more user friendly and photo-realistic digital printers are able to interface directly to digital cameras.

Also, digitization is expected to provide significant growth for traditional film-based imaging companies and photofinishers. Digitization refers to high-resolution scanning and digital printing of film images and photographs. While commercial labs and motion picture special effects houses have transitioned to a digital infrastructure over the last 10 years, minilabs and wholesale photofinishers are just now beginning to install equipment that allows in line digitization of film with minimal impact on workflow.

When this digital infrastructure is in place and broadband internet access is widely available, it will enable a wide range of internet based imaging products and services. Also, new partnerships and joint ventures between film companies, internet companies and chip manufacturers are expected to increase growth. Many advanced imaging applications will be enabled by the wide spread access of broadband communication to the internet, greater microprocessor performance and highly integrated optoelectronic components.

Once optical networks enable broadband access to the internet, a major beneficiary will be imaging with many opportunities for instant transfer of still and motion picture images.

While the potential market for military and industrial imaging applications at \$3 to \$5 billion is much smaller than digital photo-finishing and networked imaging services (\$15 to \$20 billion), the technology demands will be an important driver for advanced imaging capabilities. Current market forecasts are based on extrapolations and are probably too conservative.

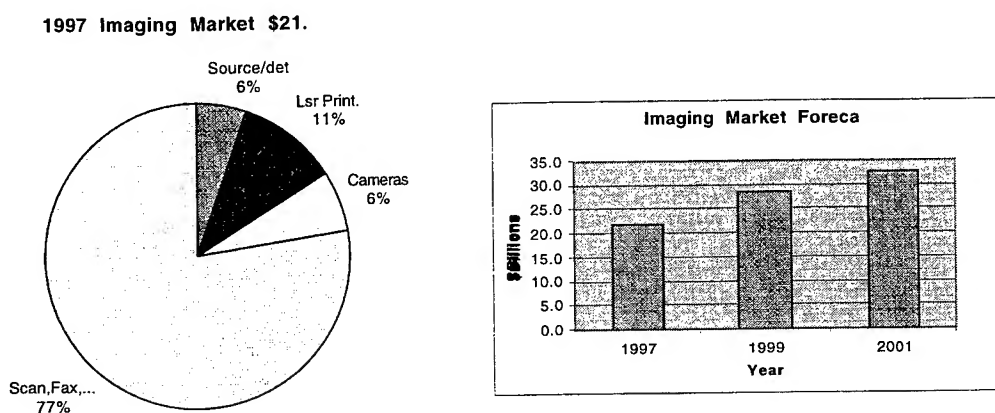


Figure 8. Optoelectronics Imaging Market

Typical areas of growth in imaging will benefit from

- Digital image format
- Digital signal processing with a great latitude of manipulating images
- Intelligent image capture/tracking
- Improved image sensor technology expanding the spectral and spatial resolution at an affordable cost
- Miniaturization, increasing portability and lowering power
- Fiber to the home, and
- Increased Small Office – Home Office use of imaging equipment.

Expanded Vision refers to the ability to outperform human vision.

Expanded Vision Characteristics are:

- Wider Field of View
- Broader Spectral Range (Uncooled detector)
- Increased Spatial Resolution
- Increased depth of field

These attributes are achieved by using advanced image sensors and by electronically processing the gathered information, such as in image fusion. In the future images acquired from multiple detectors will be combined using image fusion algorithms with integrated optoelectronics hardware systems to provide enhanced performance over a much broader spectral range than products are currently capable of delivering.

Night Vision Products

Night vision products have a long history dating back to the '60s. Refined military applications developed in the last two decades leading to many advanced products.

Currently military and law enforcement applications represent the largest segment of the night vision equipment market. In 1998 the market size for this segment exceeded \$3B. However, in the 2003 –2005 time frame, automotive, surveillance and home security applications are expected to approach the size of the current military /law enforcement segment. Optoelectronic products are estimated to be roughly 1/3 the total market size for these applications.

Miniaturization in Imaging – “The Micro Camera”

Many of the applications for micro cameras are similar to those identified for digital cameras, which are currently enjoying double digit growth in the marketplace. The acceptance of digital cameras as solutions for advanced imaging applications has been paced by the ability of the technology to meet market needs better than existing technology i.e. traditional photography. Micro camera characteristics include:

- Significantly Smaller Size
- Higher Spatial Resolution (In Color!)
- Lower Power

Today, micro cameras are used largely by law enforcement, military and private security agencies for surveillance and home security applications. In total these represent a market size of \$1B/yr. As digital cameras become a common peripheral for desktop and notebook PCs, demand for micro cameras for notebooks PDAs and other portable appliances will drive significant demand. In the 2003 –2005 time frame, these applications will represent the largest market segment followed by surveillance and inspection systems. In the table below, the optoelectronic products are estimated to be about 20% of the total market.

Intelligent Image Capture

The intelligent image capture system addresses the technology associated with the integration of a complex imaging system capable of automatically recognizing, isolating and tracking a target or object of interest in a scene in real time. Imaging applications identified for intelligent image capture also drive significant demand for digital image processing hardware as system complexity increases. The required image processing speeds for future systems might outpace Moore's Law.

Although many of the key enabling technologies for Intelligent Image Capture are algorithm based, the integrated systems designed for most applications drive significant demand for optoelectronic components.

Market Potential for Tracking Systems

Application	Estimated Total Market for Application in 2003	Estimated Market Size for OE Products
Weapons/Guidance Target Tracking	\$5B	\$1B
Surveillance / Security	\$100M	\$20M
Automotive	\$1B	\$200M
Consumer Web Camera	\$500M	\$100M

5. OPTICAL STORAGE

Data storage is an area where the optical approach competes with other technologies, such as magnetic hard disc, magnetic tape, semiconductor memory, etc.

Optical storage offers a reliable and removable storage medium with excellent archival lifetime at a low cost. Both optical recording and readout can be performed with a head positioned relatively far from the storage medium, unlike magnetic hard drive heads. This allows the medium to be reliable and removable, but the heavier head also leads to slower access time compared to hard disk drives. Consequently optical storage is limited to applications requiring reliability and removability, such as archival storage, software distribution, medical imaging, storing digital photographs, etc.

The market for disc storage exceeded \$60 B/year in 1996 with a small fraction attributed to optical storage as shown in Fig 9

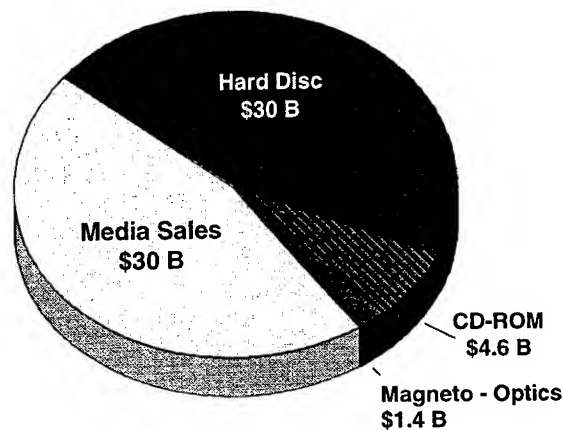


Figure 9. Worldwide Storage Market - 1996

With the rapid expansion of the Internet, server-based applications will emerge. Electronic commerce, medical imaging, libraries and corporate networks require modest access time (<10 ms) but very large storage capacities and reasonable transfer rates. These applications might give a further boost to the optical disc market. Optical disk market is also expected to grow for computer applications with the new DVD format gaining market share as shown in Fig 10

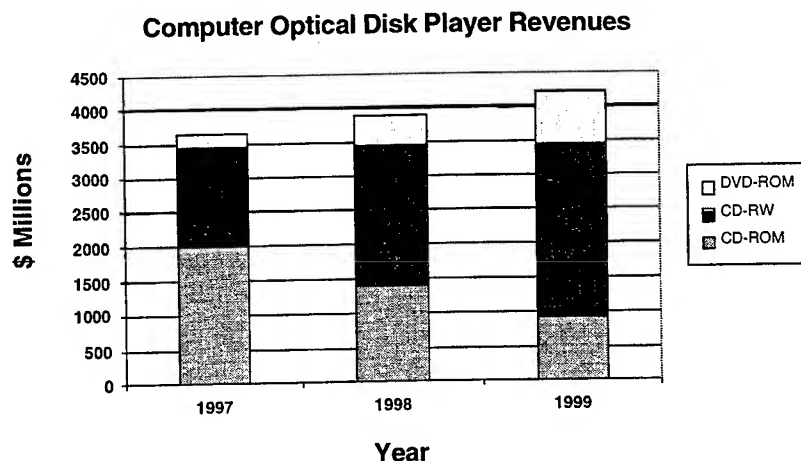


Figure 10. Optical Storage for Computers, Source: OITDA

It should be noted that storage technology is facing the same cost reduction pressure than all other market segments. Similar to the charts shown for communication, storage has a history of steady improvement in performance with a decline in unit price. For optical storage to maintain its position and increase its market share it must outperform competing technologies on both counts.

6. FUTURE TRENDS IN OPTOELECTRONICS

Future opportunities in optoelectronics will come in three areas:

- Improvements in technology – new breakthroughs
- Low cost, high volume manufacturing, and
- Integration with other technologies.

The first two items require no explanation. Integration requires the vertical integration of traditional academic disciplines. It should be a natural extension of optoelectronics which itself was created from the integration of optics and electronics. Future opportunities will rise from the integration with electronics, electronic processing (including software), micromechanics, etc as depicted in Fig 11

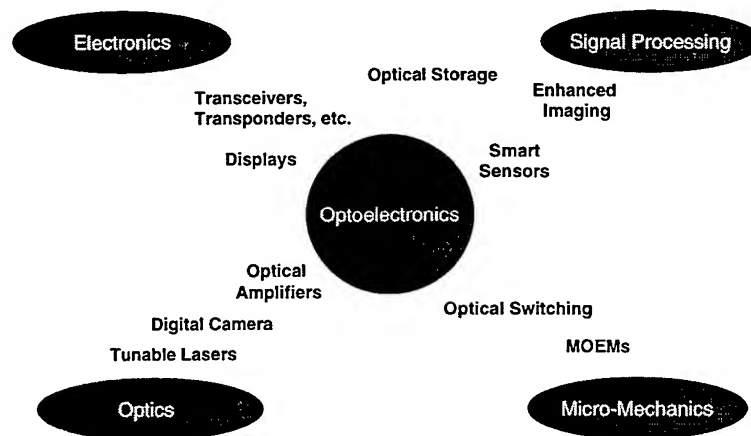


Figure 11. OE Centered Technology Integration

These are exciting times to be in optoelectronics. Our research and products will have major impact in many application areas from communication to transportation, medicine, biotechnology, electronic commerce, entertainment, etc. It will also support the leading technologies of the 21st Century, Fig 12.

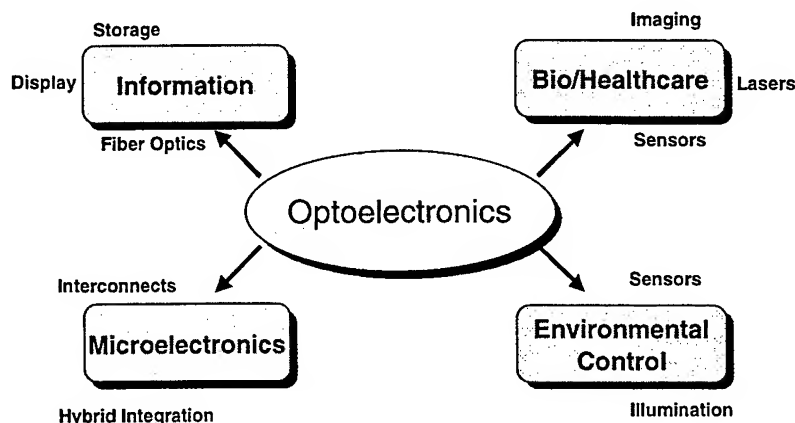


Figure 12. Leading Technologies for the 21st Century

Oxide-Confined Vertical-Cavity Surface-Emitting Lasers, Quantum Dots, and the Purcell Effect: Can Scaling the Mode Size Improve Laser Performance? *

D.G. Deppe, D.L. Huffaker, H. Huang, and L.A. Graham

Microelectronics Research Center
Department of Electrical and Computer Engineering
The University of Texas at Austin, Austin, Texas 78712-1084

ABSTRACT

The development of vertical-cavity surface-emitting lasers (VCSELs) has led to new types of low power, high efficiency light sources for data communication. The small size, low power, and surface-normal emission of VCSELs has enabled relatively dense two-dimensional arrays for highly parallel data communication and optical signal processing. In this paper we examine the issues of device scaling on VCSEL performance. We look specifically at what benefits may be derived from continued scaling of the active volume down to minimum sized dimensions, and what device schemes may be required to obtain the scaling. Laser rate equations are used to show that when the VCSEL mode volume is reduced to wavelength cubed dimensions, a significant improvement in modulation speed is predicted based on the radiative lifetime change due to the Purcell effect. However, several parasitic effects must be controlled in order to realize these benefits. Most important are control of the optical loss due to diffraction or scattering, and control of the electronic losses due to carrier diffusion and surface effects. Novel optical confinement schemes based on oxide-apertures, photonic bandgaps, and/or closely coupled two-dimensional arrays may be useful for controlling optical loss, while self-assembled quantum dots are attractive for controlling electronic diffusion to dimensions within the minimum optical mode volume.

Keywords: Semiconductor lasers, VCSELs, microcavities, cavity design, quantum dots, controlled spontaneous emission, high speed modulation.

1. INTRODUCTION

Vertical-cavity surface-emitting lasers (VCSELs) have emerged as one of the most important semiconductor lasers for low power optical interconnects.¹ Most commercial VCSELs are presently based on proton implantation to control the current injection into a small area of the optical cavity.² The optical mode volume is then defined by gain-guiding. This fabrication scheme has numerous proven advantages for manufacturing VCSELs including photolithographic patterning of the active area, planar processing, high device reliability, and high yield. On the other hand, in many ways devices based on gain-guiding have inferior performance to index-confined VCSELs, especially oxide-confined VCSELs.³ For gain-guided VCSELs, diffraction loss from the optical mode limits scaling the active volume to very small sizes, and can lead to instabilities in the VCSEL threshold and operating characteristics due to thermally induced index-guiding. Because of this there is a wide-spread industrial research effort in developing commercial VCSELs based on oxide confinement, for which these thermal effects are reduced or eliminated by the built-in index guide of an oxide-aperture. As compared to proton implanted VCSELs, oxide-confined VCSELs have low threshold currents and lower threshold current densities,³⁻⁹ higher wall-plug efficiency,¹⁰⁻¹² higher modulation speed,^{13,14} and improved mode characteristics for both multi-mode and single-mode operation.^{15,16} The lower power operation is crucial for two-dimensional arrays for reducing thermal cross-talk and increasing the VCSEL packing density. Oxide-confined VCSELs also have greatly improved scaling behavior. While gain-guided VCSELs that operate at 0.85 μm or 0.98 μm begin to show diffraction loss effects when the optical mode is reduced below $\sim 10 \mu\text{m}$ diameter, oxide-confined VCSELs show good scaling behavior down to $\sim 3 \mu\text{m}$ diameter. The improved scaling behavior is due to control of the diffraction loss by the oxide aperture.^{17,18}

In this paper we examine the impact of scaling the VCSEL optical mode to even smaller sizes than that presently achieved, ultimately to volumes approaching a cubic wavelength. If such small optical modes can be achieved new VCSEL characteristics are predicted, especially for the modulation response. Simply scaling the active volume to small size can greatly reduce the lasing threshold current, since fewer electronic states must be inverted to achieve optical gain. This may be of interest for realizing extremely low threshold VCSELs for new ultralow power operations, such as for optical interconnects for dense focal plane arrays.¹⁹ As we discuss below, though, a potentially more interesting result is the decreased radiative

*Also published in *Proc. of SPIE* Vols. 3897, 3898, and 3899

lifetime that results due to the Purcell effect, which can lead to high speed VCSEL operation even for bias levels at or below lasing threshold. High speed bias-free operation may then be possible, greatly improving VCSEL array performance and further reducing power consumption. Although the maximum power from such a small optical mode is reduced over today's commercial VCSELs, this power limitation can in principle be eliminated by using microarrays of Purcell enhanced VCSELs.

At present there are two serious device constraints that prevent the scaling of VCSELs to small optical modes. The first is optical loss. Depending on the mode confinement scheme, either diffraction or scattering loss usually accompanies a reduction in the optical mode size, and this is a major scaling limitation in today's VCSELs. In principle diffraction or scattering loss may be eliminated through lateral confinement using either very short cavities along with oxide apertures or photonic bandgaps for lateral confinement, or perhaps more simply by diffractively coupling the elements of a microarray. However, if optical loss is not controlled the gain required for lasing threshold in the small mode volume can exceed the maximum available from the active material. The second constraint is in the electronic confinement. Planar quantum well active regions can lead to lateral carrier diffusion lengths of several microns at room temperature, while electrons and holes must effectively be confined to the optical mode volume in order to realize the Purcell effect. Actually, the Purcell effect can reduce the diffusion length by shortening the recombination time, but it would be more effective to achieve tight lateral electronic confinement to sub-micron optical mode sizes. This can be obtained using quantum dot (QD) light emitters, for which lateral electronic confinement is "built-in" due to the self-organization of highly strained epitaxial films. The recent advances in QD lasers,²⁰⁻²⁴ including QD VCSELs,²⁵⁻²⁹ shows that this approach appears viable. Note that the diffusion problem is not of such a concern for infrared lasers, for which the optical wavelengths are a few microns within the semiconductor material.

Below we discuss the Purcell effect in oxide-confined VCSELs in detail. Experimental results on QD and planar quantum well microcavity light emitters and lasers aimed at characterizing the Purcell effect are described. Rate equations are used to predict the impact of the Purcell effect on VCSELs, both for lasing threshold and modulation response.

2. PURCELL EFFECT IN AN APERTURED-MICROCAVITY

It is well-known that an emitter's spontaneous emission rate is controlled by the volume and Q (loss rate) of the optical modes to which it's coupled.^{30,31} Recently it was shown that the spontaneous lifetime can be controlled in apertured-microcavities³²⁻³⁴ similar to those used for very low threshold VCSELs. Although Purcell's original arguments were brief and based on an ideal single mode cavity,³⁰ the VCSEL cavity typically contains many optical modes that exist within the emitters optical bandwidth. However, despite the existence of many optical modes, aperture confinement (or an etched pillar) can lead to one or two highly confined optical modes with sufficient Q to dominate the microcavity emission characteristics. This is illustrated in Fig. 1 for a VCSEL-type cavity based on distributed Bragg reflectors (DBRs). Each high index layer of the microcavity forms waveguide modes propagating in the plane of the layer, while apertured modes also exist that propagate back and forth vertically to the mirrors.

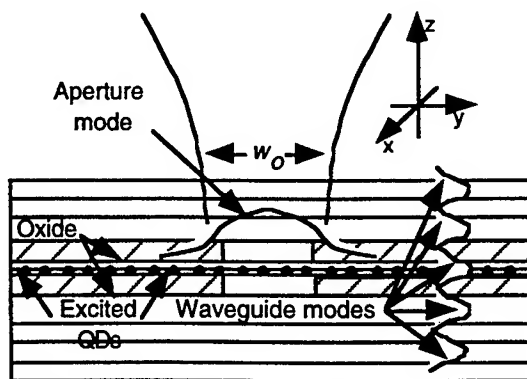


Fig. 1 Schematic illustration of an oxide-apertured microcavity based on QD light emitters and DBRs. Resonant optical modes exist due to the high index layers of mirrors and due to the double oxide apertures. However, for very small apertures the combined effects of Q and mode volume can lead to nearly 100% of the spontaneous emission being coupled into the aperture modes. (After Ref. [34])

When QD light emitters are used within the microcavity their coupling to the electromagnetic field depend on their positions within the cavity. Those QD emitters lying within the oxide-aperture interact with both the waveguide modes and the apertured-modes, while those QD emitters that lie outside the aperture interact with only the waveguide modes. We model the

QD light emitters as two-level systems. When only spontaneous emission is important for QD level decay, the total spontaneous from an emitter depends on the summation over all optical modes as given by

$$\frac{dN_2}{dt} = -\frac{2q^2\omega_d^2}{\hbar^2} \sum_m |\mathbf{d} \cdot \mathbf{A}_m(\mathbf{r}_d)|^2 \frac{(\gamma_d + \frac{\omega_m}{2Q_m})}{(\omega_d - \omega_m)^2 + (\gamma_d + \frac{\omega_m}{2Q_m})^2} N_2(t). \quad (1)$$

In Eq. (1), N_2 is the upper level population, m labels each cavity mode, q is the electronic charge, ω_d is the resonant frequency of the 2-level emitter, ω_m is the resonant frequency of mode m , V is the normalization volume of the cavity, \mathbf{d} is the dipole vector strength, $\mathbf{A}_m(\mathbf{r}_d)$ is the normalized vector strength of the cavity field at the QD position, $\frac{\omega_m}{2Q_m}$ is the photon loss rate from mode m , and γ_d is the QD dephasing rate. The vector strength of the cavity field is normalized such that $\int_V d^3r \epsilon(\mathbf{r}) |\mathbf{A}_m(\mathbf{r})|^2 = \hbar/(2\omega_m)$, where $\epsilon(\mathbf{r})$ is the material permittivity at \mathbf{r} .

The collection of the cavity emission can be restricted to the apertured-modes using the spectral dependence of the emission from the cavity. These apertured-modes have frequencies that increase with the transverse mode number. By making very small apertures, higher order transverse modes can be eliminated from the bandwidth of the QD emitters, so that only the two lowest order transverse modes collect significant emission. The spontaneous photon number in these lower-order modes satisfy the rate equation

$$\frac{dn_o}{dt} = -\frac{\omega_o}{Q} n_o + \sum_{n=1}^{N_{ap}} \frac{2q^2\omega_n^2}{\hbar^2} |\mathbf{d}_n \cdot \mathbf{A}_o(\mathbf{r}_n)|^2 \frac{(\gamma_n + \frac{\omega_o}{2Q}) N_{2,n}(t)}{(\omega_n - \omega_o)^2 + (\gamma_n + \frac{\omega_o}{2Q})^2} \quad (2)$$

where the subscript n labels each emitter. We approximate the apertured-modes as Gaussian, and the QD emitters as having randomly oriented dipole moments. The coupling strength for these modes [Eqs. (1) or (2)] then becomes

$$|\mathbf{d}_n \cdot \mathbf{A}_o(\mathbf{r}_n)|^2 = \frac{|\mathbf{d}|^2 \hbar e^{-(x_n^2 + y_n^2)/w_o^2}}{3\epsilon\omega_o\pi w_o^2 L_z}, \text{ with a mode volume given by } V = \pi w_o^2 L_z \text{ where } w_o \text{ is the mode radius and } L_z \text{ is an}$$

effective cavity length. It has previously been estimated that when an oxide-apertures is not present, 80 to 90% of the spontaneous emission is coupled to waveguide modes (see Fig. 1), and this emission is approximately independent of the aperture. In terms of the dipole moment, the spontaneous emission rate of the QD embedded in bulk material is

$$\frac{1}{\tau_{sp,o}} = \frac{q^2\omega_n^3 n^3 |\mathbf{d}|^2}{3\pi\epsilon\hbar c^3}, \text{ where } n \text{ is the refractive index and } c \text{ is the speed of light in vacuum. This means that for frequencies}$$

close to that of the lowest order apertured-mode, the position dependent summation over emitter positions given from Eq. (1) can be expressed by

$$\frac{1}{\tau_{sp}(x_n, y_n, \omega_n)} \approx \frac{1}{\tau_{sp,o}} + \frac{1}{\tau_{sp,o}} \frac{4c^3/n^3}{\omega_o\omega_n w_o^2 L_z} \frac{(\gamma_n + \frac{\omega_o}{2Q}) e^{-(x_n^2 + y_n^2)/w_o^2}}{(\omega_n - \omega_o)^2 + (\gamma_n + \frac{\omega_o}{2Q})^2}, \quad (3)$$

where the first term on the right in Eq. (3) reflects the fact that the summation over the waveguide modes leads to a spontaneous emission rate nearly independent of the cavity, and the second term is due to the Purcell enhancement by the apertured modes. For large apertures the fraction of spontaneous emission actually captured by the apertured modes is negligible, while for small apertures the enhancement into the apertured modes can dominate the spontaneous lifetime. On

resonance the second term in brackets becomes $\frac{(\lambda_o^3/n^3)Q}{\pi^2(\pi w_o^2 L_z)}$ which is very nearly the mathematical form of the enhancement

described by Purcell for a single mode cavity.³⁰ Aside from constant factors, the cavity field intensity decay measured at frequency ω_n after a short-pulse excitation is given by

$$\frac{\omega_o}{Q} n_o(\omega_n, t) \propto \int_0^\infty d\rho_n \rho_n \frac{(\gamma_n + \frac{\omega_o}{2Q}) e^{-\rho_n^2/w_o^2} e^{-\frac{t-t_o}{\tau_{sp}(\rho_n, \omega_n)}}}{(\omega_n - \omega_o)^2 + (\gamma_n + \frac{\omega_o}{2Q})^2}. \quad (4)$$

The QD heterostructure has been used to characterize the Purcell effect for a micron sized oxide-apertured microcavity consisting of an 18 pair GaAs/AlAs DBR, an AlGaAs $\lambda/2$ cavity spacer, and a single upper $\lambda/4$ GaAs layer. The cavity spacer is $\text{Al}_{0.97}\text{Ga}_{0.03}\text{As}$ at the center of which is grown a single $\text{In}_{0.50}\text{Ga}_{0.33}\text{Al}_{0.17}\text{As}$ QD active region, with 100 Å GaAs layers and 135 Å grading layers immediately adjacent on either side. The apertured-microcavity is fabricated by patterning 5 μm squares in photoresist and reactive ion etching to a depth of 2900 Å to form mesas exposing both $\text{Al}_{0.97}\text{Ga}_{0.03}\text{As}$ layers of the cavity spacer. Lateral oxidation³⁵ is performed at 450 °C, after which a 5 pair ZnSe/MgF₂ DBR is deposited to complete the microcavity. The microcavity is measured at 10 K, for which the QD ground state emission wavelength is ~ 9700 Å with a spectral width of ~ 600 Å. Time resolved measurements are performed using a mode-locked Ti-Sapphire laser beam (pulse rate reduced to 5 MHz) focused with a microscope objective to a 5 μm diameter spot on the microcavity. Photoluminescence is collected through the same objective and time resolved using a grating spectrometer and photon counting module with rise and fall times of ~ 300 ps. The InGaAlAs/GaAs QDs have radiative lifetimes of ~ 2 ns and are conveniently used to obtain high sensitivity in the photodetection. Larger InGaAs/GaAs QDs that emit at longer wavelengths ranging from ~ 1.2 to ~ 1.3 μm at room temperature show shorter radiative lifetimes ranging from ~ 400 psec to ~ 800 psec. The longer wavelengths and shorter spontaneous lifetimes make these larger QDs of interest for fast VCSELs. The longer lifetimes and shorter wavelengths of the InGaAlAs/GaAs QDs make them convenient for characterizing the cavity effects.

Figure 2 shows photoluminescence decay for wavelengths around resonance for the 1 μm diameter apertured-microcavity. Curves (a) and (c) show off-resonance decays taken at 9800 and 9950 Å, while curve (b) shows the on-resonance decay for the lowest order mode at 9860 Å. There is a factor of ~ 2.3 increase in the emission rate at 9860 Å as compared to off-resonance wavelengths. The fact that wavelengths both shorter and longer than resonance show similar slower decays is clearly indicates that the increased rate at resonance is due to the microcavity. Considering the first 2 ns of decay, the on-resonance lifetime [curve (b) in Fig. 1] is 0.9 ns, compared with the off-resonance lifetimes of 2.2 ns at 9950 Å and 1.9 ns at 9800 Å. The off-resonance lifetimes are close to the 2.1 ns lifetime measured for the epitaxial sample before processing. Therefore, the spontaneous emission rate is increased for the spatially averaged emitter positions by a factor of ~ 2.3 , with little inhibition off-resonance. Figure 3 shows spontaneous spectra and decay rates plotted versus wavelength for the 1 μm apertured-microcavity. The inset shows the emission over a greater wavelength range. The longer wavelength spectral peaks at 9860 Å

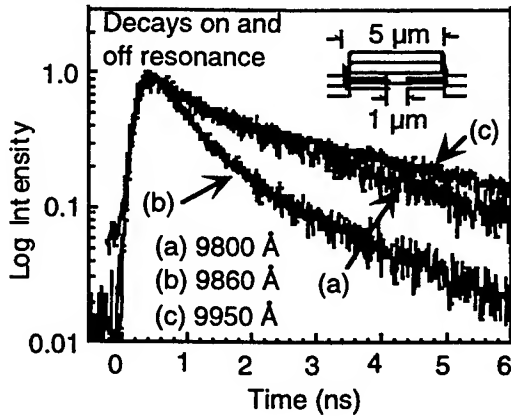


Fig. 2 Measured decay curves for a 1 μm apertured microcavity containing QD light emitters. Curve (a) for 9800 Å is for a wavelength shorter than resonance, curve (b) for 9860 Å is for a wavelength at resonance, and curve (c) for 9950 Å is for a wavelength longer than resonance.

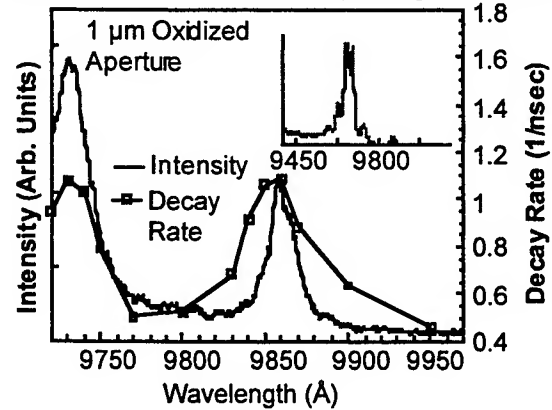


Fig. 3 Plot of measured decay rates versus wavelength and intensity versus wavelength for the 1 μm apertured microcavity.

and 9730 Å correspond to apertured-microcavity modes. The larger emission peaks starting at 9687 Å and visible to 9600 Å are due to emission from the oxide region (blue-shifted as compared to apertured modes) within the 5 μm mesa (see Fig. 1). Figure 3 shows that the spontaneous decay rate is enhanced at the lowest and next lowest order apertured-mode wavelengths of 9860 Å and 9730 Å. The spectral separation between the lowest and next lowest order modes depends on the mode area. The aperture-mode frequencies are approximately set by $\omega_m = (c/n)\sqrt{(\zeta_m/w_o)^2 + k_z^2}$, where the wavevector component k_z is

fixed by the mirrors. Bessel function modes satisfy the cylindrical symmetry of the cavity, so that we take $\zeta_0 = 4.810$ and $\zeta_1 = 7.664$ for Bessel functions of the first kind. From Figs. 2 and 3, $\omega_0 = 1.912 \times 10^{15}$ rad/s and $\omega_1 = 1.937 \times 10^{15}$ rad/s, and the mode diameter is estimated to be $w_0 = (c/n) \sqrt{(\zeta_1^2 - \zeta_0^2)/(\omega_1^2 - \omega_0^2)} \approx 1.8 \mu\text{m}$. The linewidth of the lowest order mode under continuous wave excitation is $\Delta\lambda = 15 \text{ \AA}$ which gives a $Q = \lambda_0 / \Delta\lambda = \omega_0 / (2\gamma_0) \approx 650$. Measurements to date suggest that electronic dephasing rates in the QDs can be $< 10^{11} \text{ s}^{-1}$, and we assume $\gamma_d < \frac{\omega_0}{Q}$ is satisfied.

From Eq. (4) we can also calculate the mode size required to achieve the spontaneous emission enhancement of 2.3 for the on-resonance wavelength. $\frac{\lambda_0^3 Q}{\pi^3 n^3 w_0^2 L_z} \approx 3.1$ provides a good match with the experimental data in Figs. 2 and 3. Given $\lambda_0 =$

$0.986 \mu\text{m}$, $Q = 650$, an assumed value of $n = 2.95$ for the refractive index of the cavity spacer, and an effective cavity length of $L_z = 0.75 \mu\text{m}$, the estimated mode size is $w_0 = 0.7 \mu\text{m}$. This Gaussian mode diameter of $2w_0 = 1.4 \mu\text{m}$ is in rough agreement with the $1.8 \mu\text{m}$ diameter estimated from the spectral separation of the transverse modes assuming Bessel functions. From the calculations, the spontaneous emission rate enhancement for emitters placed at the center of the optical mode is then a factor of 3.1 compared to the factor of 2 for the emission rate averaged over emitter positions. This dependence on the emitter position can lead to spatial hole burning of the QD emitters at the mode center. It was noted in the introduction that diffraction loss can decrease the mode Q for very small optical modes. For the experimental data of Figs. 2 and 3 we expect that a larger enhancement of the emission rate can be obtained with an increased Q, but only slightly higher Q's have been achieved in similar cavities with more DBR pairs.

Although the scaling behavior of selectively oxidized VCSELs with planar quantum well active regions has been studied extensively and gives some information on the cavity loss rate for small apertures, the actual optical loss dependence on mode size can be difficult to extract from the experiment. Generally, the threshold current density increases as the oxide aperture is decreased and can prevent lasing for very small apertures. However, the increase in threshold current density is not only due to a reduction in the mode Q, electronic losses can also play a role. Even a relatively small diffusion coefficient of $10 \text{ cm}^2/\text{sec}$ will lead to a diffusion length of $\sim 1.7 \mu\text{m}$. Ideally, if optical loss does not increase for the small aperture then neither should the threshold carrier density. On the other hand, the entire pumped area must be supplied through the small aperture, so that the current density through the aperture must increase to maintain the same carrier density. In addition, electronic losses often increase under and around the oxide aperture due to nonradiative recombination. These electronic effects due to diffusion make it difficult to clearly separate optical losses from electronic losses. However, a general trend is that the threshold current density is not so dependent on the aperture size as it is on the optical mode size. This is consistent with both the optical loss and electronic losses depending on the optical mode size, and for small apertures the larger optical mode both decreases the diffraction loss and increases the optical overlap with the injected carriers that suffer diffusion.

A more straightforward way to directly measure the optical loss dependence due to aperture and mode size is to measure the spontaneous linewidth dependence on the optical mode size. Care must also be taken using this approach to avoid stimulated emission or absorption effects that narrow or broaden the "cold-cavity" linewidth. We have made such measurements for oxide-apertured VCSEL-type cavities that contain either QD or planar quantum well active regions. The measured results are shown in Fig. 4. The number of upper MgF/ZnSe DBR pairs are either five or seven. The QD cavities are undoped and measured in photoluminescence, while the cavities containing planar quantum wells are lightly doped and excited with current injection. An interesting trend is that the Q's for similar type cavities depend on the type of active region used. This suggests that absorption intrinsic to the planar quantum well active region may in fact limit the Q for high reflectivity. In Fig. 4 the measured Qs for the QD cavity with seven MgF/ZnSe DBR pairs exceeds 5000 for aperture sizes greater than $4 \mu\text{m}$ diameter, while it is only ~ 2000 for the planar quantum well active region. A similar reduction from ~ 3000 to ~ 1200 is found for five pairs. For each of the cavity types the Q drops significantly for aperture sizes smaller than $3 \mu\text{m}$ in diameter. The $3 \mu\text{m}$ diameter is also the size for which VCSEL threshold current densities begin to sharply rise with reducing aperture size. This shows that diffraction loss must indeed be considered for small apertures, but also shows that the VCSEL Q may contain subtleties that we do not yet understand.

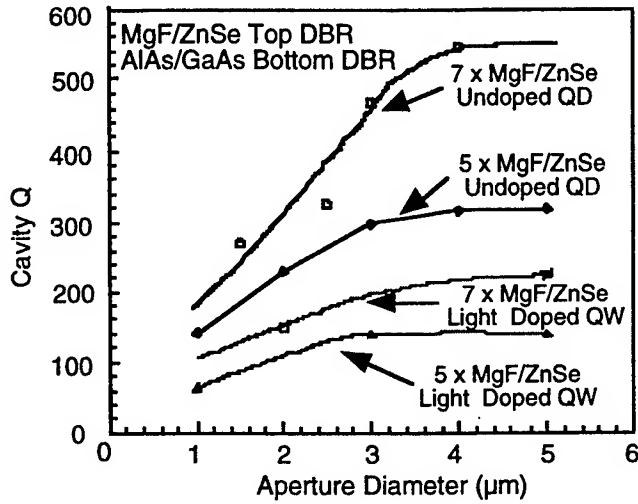


Fig. 4 Plot of Q versus aperture diameter for oxide-confined microcavities containing either QD or planar quantum well light emitters.

3. PURCELL EFFECT AND VCSEL CHARACTERISTICS

There has been a great deal of speculation about how laser thresholds will scale when the optical mode size is reduced due to microcavity confinement, with predictions that "zero-threshold" lasing will be obtained. However, the basis for some of these predictions are that the light versus current curve from the source can ideally be linear with 100% slope efficiency. This in itself is not the basis for a laser. A perfect "integrating sphere" would presumably give 100% spontaneous coupling efficiency from an emitter to a detector coupled through an emitting port, but this would not necessarily constitute a zero-threshold laser. The same is true for an ideal microcavity that can provide 100% spontaneous coupling efficiency to a detector, but with a Q that is insufficient to obtain lasing. Under extreme conditions the oxide-apertured microcavity that also uses strong QD electronic confinement such as shown in Fig. 1 can lead to nearly 100% spontaneous coupling efficiency. However, this microcavity emitter may not be a laser at all.

On the other hand, the increase in the spontaneous emission rate due to an oxide-apertured VCSEL-type cavity with a small enough volume to cause the Purcell effect can greatly improve the modulation rate of either a microcavity light emitting diode or a VCSEL. An interesting modification to the threshold also occurs, but the threshold current density is actually increased due to the increase in the spontaneous emission rate. Still the threshold current for very small optical modes and ideal electronic confinement such as provided by QDs can be very low, reaching sub-microamps. The very low threshold current is due to the small transparency current of the QD active region, while the optical gain can exceed that of a planar quantum well if inhomogeneous broadening is eliminated. The homogeneous linewidth from a QD emitter is measured to be $\leq 100 \mu\text{eV}$ at cryogenic temperatures, and is predicted to be ~ 2 to 3 meV or less at room temperature. While scaling the mode size has been studied for VCSELs, the impact on laser performance of changing the spontaneous emission rate by using a small mode volume has not yet been addressed. One reason is that experimentally, diffraction loss in part limits performance in single element VCSELs and is in itself an important scaling issue. Another reason though is that the VCSEL rate equations have not been put in a form that accurately accounts for the spontaneous lifetime dependence on the optical mode size.

A QD VCSEL microarray can be used to obtain milliwatt output powers typical of today's commercial VCSELs. Diffraction loss may also then be controlled through inter-element coupling. Below though we consider that the optical scattering losses are eliminated through strong lateral optical confinement, and consider the emission characteristics of a single element. From Fig. 1 we assume that the Gaussian optical mode has a free space wavelength $\lambda_o = 1.3 \mu\text{m}$, an effective mode area of πw_o^2 , an effective length of L_z , and a photon loss rate of ω_o/Q . To maintain resonance L_z must depend on w_o with $L_z(w_o) = L_z(\infty) / \sqrt{1 - \lambda_o^2 / (\pi^2 n^2 w_o^2)}$, and we take $L_z(\infty) = 0.59 \mu\text{m}$ and the cavity's average refractive index as $n = 3.3$. We hold $\omega_o/Q = 2 \times 10^{11} \text{ sec}^{-1}$ to isolate the effect of enhanced emission on laser performance.

The emitters are assumed to have a Gaussian density distribution with an effective area πw_{QD}^2 and a peak density $n_{QD} = 1.5 \times 10^{10} \text{ cm}^{-2}$. The spontaneous emission rate $1/\tau_{sp,o}$ is that which would occur without the cavity and for unity state

occupation by electrons and holes. $1/\tau_{sp,o} = 2.5 \times 10^9 \text{ sec}^{-1}$ is consistent with the radiative lifetime recently measured for 1.3 μm QDs.³⁷ The average population inversion of QD states is given by $2\sqrt{x} - 1$ with the upper state excitation given by x , where $0 \leq x \leq 1$. The \sqrt{x} dependence assumes equal probabilities of electron and hole occupation in the QD ground state levels with random capture. We consider that ideally the QD emitters will be homogeneously broadened with a linewidth of $2\gamma_d$ due to dephasing. The QD VCSEL will likely require high Q, so that the adiabatic approximation $\gamma_d \gg \omega_o/Q$ will be valid. For this case the QD spontaneous emission rate depends on the mode volume, dipole dephasing rate, and QD position within the mode, but not on the mode Q. Averaging over the emitter positions and retaining only leading terms gives the lasing mode's photon number rate equation as

$$\frac{dn}{dt} = -\left[\frac{\omega_o}{Q} - \frac{2\pi w_{QD}^2 w_o^2 n_{QD}}{w_{QD}^2 + w_o^2} \frac{\Omega^2}{\gamma_d} (2\sqrt{x} - 1)n\right] + \frac{2\pi w_{QD}^2 w_o^2 n_{QD}}{w_{QD}^2 + w_o^2} \frac{\Omega^2}{\gamma_d} x \quad (5)$$

with the emitter population x driven by a current source $\frac{I}{q}$ given as

$$\frac{I}{q} = 2\pi w_{QD}^2 n_{QD} \frac{dx}{dt} + \left(\frac{2\pi w_{QD}^2 w_o^2 n_{QD}}{\tau_{sp,o}} + \frac{4\pi w_o^2 w_{QD}^2 n_{QD}}{w_{QD}^2 + w_o^2} \frac{\Omega^2}{\gamma_d}\right)x + \frac{2\pi w_o^2 w_{QD}^2 n_{QD}}{w_{QD}^2 + w_o^2} \frac{\Omega^2}{\gamma_d} (2\sqrt{x} - 1)n \quad (6)$$

and

$$\Omega = \sqrt{\frac{c\lambda_o^2}{2\pi n^3 \tau_{sp,o} \pi w_o^2 L_z}} \quad (7)$$

We assume that the elements are designed so that $w_{QD}^2 = w_o^2$. The two spontaneous emission terms in Eq. (7) (in parenthesis and multiplying x) account separately for emission radiated into waveguide modes and into the aperture, just as above in Eq.

(3). A modified Purcell effect (with $\gamma_d \gg \omega_o/Q$) doubles the total spontaneous emission rate when $w_o = \frac{(\lambda_o/n)}{2\pi} \sqrt{\frac{(c/n)}{\gamma_d L_z}}$.

The threshold characteristics and the modulation response are calculated for a range of values of the mode diameter $2w_o$ and two different values of γ_d . We assume that the QD emitters are limited in linewidth only by homogeneous broadening, so that the spontaneous full-width at half-maximum energy spread is $2\hbar\gamma_d$ with $2\hbar\gamma_d = 6.6 \text{ meV}$ or $2\hbar\gamma_d = 1.3 \text{ meV}$. Figure 5 shows the calculated thresholds for mode diameters ranging from $5 \mu\text{m} \geq 2w_o \geq 0.6 \mu\text{m}$, and for the two different values of $2\hbar\gamma_d$. Threshold is taken as the pump rate needed to obtain a stimulated emission rate equal to the photon loss rate. Curves

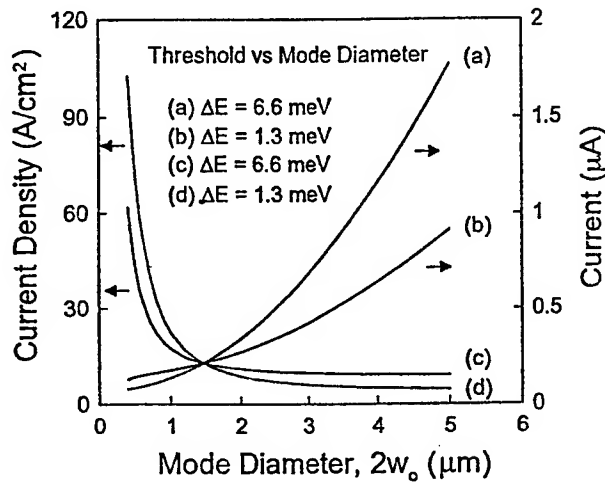


Fig. 5 Calculated threshold current and current density versus mode size for the QD VCSEL. The threshold currents versus mode diameter, $2w_o$, are shown in curve (a) for $\Delta E = 6.6 \text{ meV}$ and (b) for $\Delta E = 1.3 \text{ meV}$, and the current density versus mode diameter is shown in curve (c) for $\Delta E = 6.6 \text{ meV}$, and (d) for $\Delta E = 1.3 \text{ meV}$. The other laser parameters held fixed are $\omega_o/Q = 2 \times 10^{11} / \text{sec}$, $\tau_{sp,o} = 400 \text{ psec}$, $n_{QD} = 1.5 \times 10^{10} / \text{cm}^2$, $\lambda_o = 1.3 \mu\text{m}$, $n = 3.3$, $L_z = 0.59 \mu\text{m}$, and $w_{QD}^2/(w_o^2 + w_{QD}^2) = 0.5$.

(a) and (c) are the threshold current and current density for $2\hbar\gamma_d = 6.6 \text{ meV}$, and (b) and (d) are for $2\hbar\gamma_d = 1.3 \text{ meV}$. For modes with $2w_o < 2 \mu\text{m}$ the threshold current density increases as the mode size decreases due to the increased spontaneous

emission rate. For our parameter values, the mode sizes for which $2w_o = \frac{(\lambda_o/n)}{\pi} \sqrt{\frac{c/n}{\gamma_d L_z}}$ are $0.7 \mu\text{m}$ for $2\hbar\gamma_d = 6.6 \text{ meV}$, and $1.6 \mu\text{m}$ for $2\hbar\gamma_d = 1.3 \text{ meV}$. Curves (c) and (d) show that for mode diameters $2w_o > 1.5 \mu\text{m}$ the threshold is less for $2\hbar\gamma_d = 1.3 \text{ meV}$, but for $2w_o < 1.5 \mu\text{m}$ the threshold is less for the larger linewidth of $2\hbar\gamma_d = 6.6 \text{ meV}$. The transition occurs because the current density required for a fixed population inversion increases as the spontaneous emission rate increases. Since the spontaneous rate enhancement increases as the spontaneous linewidth decreases, the threshold for a given population inversion increases. For $2w_o = 5 \mu\text{m}$ the calculated threshold current densities are 9.0 A/cm^2 for $2\hbar\gamma_d = 1.3 \text{ meV}$, (c), and 4.7 A/cm^2 for $2\hbar\gamma_d = 6.6 \text{ meV}$, (d). These are close to the experimental values for $1.3 \mu\text{m}$ QD edge-emitting lasers.³⁶

The calculated small signal modulation responses from Eqs. (5) and (6) for different mode diameters at a bias level of twice threshold are shown in Fig. 6. The response curves in Fig. 3 are for $2w_o = 5 \mu\text{m}$, $2 \mu\text{m}$, or $0.6 \mu\text{m}$. The spontaneous linewidth in (a) is $2\hbar\gamma_d = 6.6 \text{ meV}$, and in (b) it is $2\hbar\gamma_d = 1.3 \text{ meV}$. Both the mode volume and linewidth impact the VCSEL's modulation response through the cavity coupling Ω^2/γ_d . As $2w_o$ is reduced the relaxation oscillation peak is reduced in amplitude and the 3 dB bandwidth increases. Decreasing the spontaneous linewidth also decreases the relaxation oscillation amplitude and increases the 3 dB bandwidth.

Calculated bias-free pulse responses are shown in Fig. 7. The responses are for current pulses of unit step functions 500 psec long with amplitudes of either the steady-state transparency current value ($x = 0.25$) or twice the steady-state threshold value,

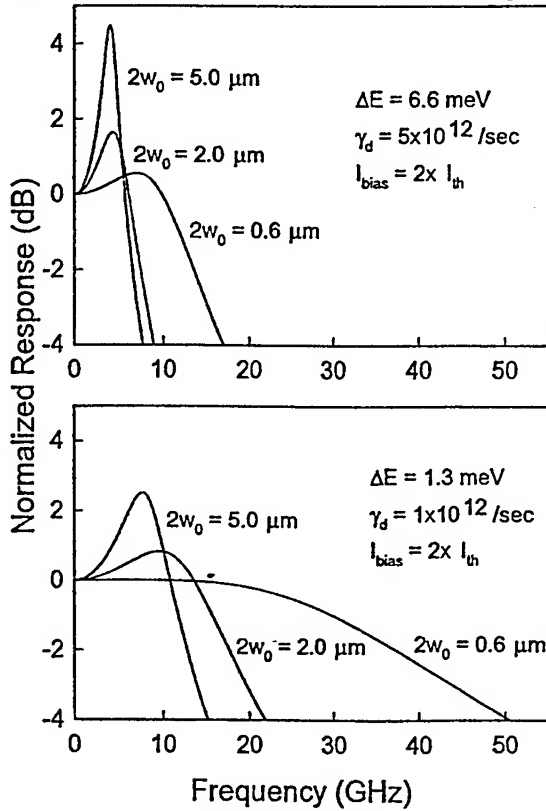


Fig. 6 Calculated small signal modulation responses for three different mode sizes of $2w_o = 5.0 \mu\text{m}$, $2.0 \mu\text{m}$, and $0.6 \mu\text{m}$. (a) shows the responses for $\Delta E = 6.6 \text{ meV}$, and (b) shows the responses for $\Delta E = 1.3 \text{ meV}$. The other laser parameters are given in the Fig. 2 caption.

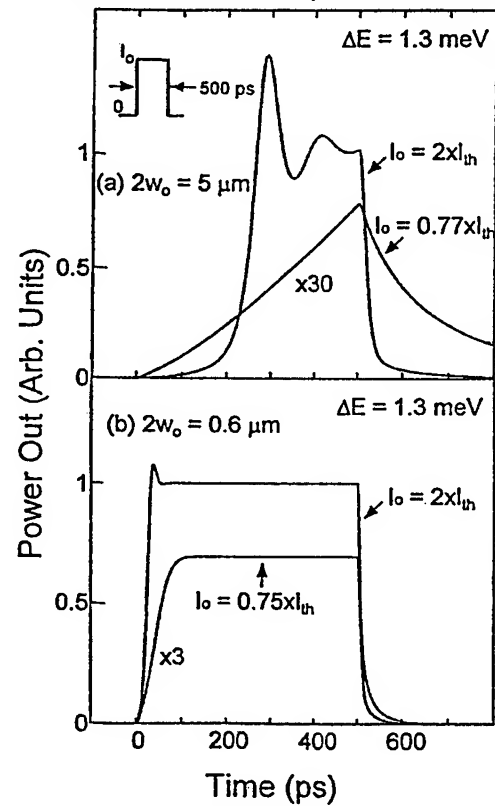


Fig. 7 Calculated bias-free responses for a 500 psec long current excitation pulse and $\Delta E = 1.3 \text{ meV}$, with the current amplitude equal to either transparency or twice the threshold current. (a) shows the responses for $2w_o = 5.0 \mu\text{m}$, and (b) shows the responses for $2w_o = 0.6 \mu\text{m}$. The other laser parameters are given in the Fig. 2 caption.

and two different mode sizes with $2w_o$ equal to either (a) 5 μm or (b) 0.6 μm . The spontaneous linewidths are held equal at $2\hbar\gamma_d = 1.3$ meV to study only those effects due to mode size changes. From Fig. 7 (a) and (b) we see that for current pulses of $\sim 0.7I_{th}$ (transparency) the smaller mode size of $2w_o = 0.6$ μm greatly improves the spontaneous pulse response, even allowing multi-gigabit data transmission. For current pulses of twice threshold the turn-on delay of ~ 250 psec for $2w_o = 5$ μm in (a) is reduced to ~ 31 psec for $2w_o = 0.6$ μm in (b). It's clear that the Purcell effect can have a major impact on the modulation response for microcavity QD VCSELs, especially around at bias levels around threshold.

4. SUMMARY

Scaling of the optical mode size has been examined for VCSELs. In order to take full advantage of the cavity effects strong lateral confinement must be achieved for both photons and electrons. The strong lateral confinement can be achieved using etched-pillars or oxide-apertures, but scattering and diffraction losses must be controlled to obtain high Q for micron-sized optical modes. Quantum dots are attractive for obtaining electronic confinement, but inhomogeneous broadening should be eliminated to take full advantage of cavity effects. For small sized QD VCSELs, the Purcell effect can greatly improve the modulation characteristics, perhaps even allowing high speed bias-free operation. Similar improvements in the modulation speed can be obtained using photonic bandgap cavities, but in many cases the microcavity QD VCSEL can be a direct replacement for today's commercial VCSELs.

ACKNOWLEDGMENTS

Various aspects of this work have been supported by the DARPA/Ultraphotonics program monitored by the AFOSR, and the DARPA supported Univ. of New Mexico OptoCenter.

REFERENCES

1. K. Iga, F. Koyama, and S. Kinoshita, "Surface emitting semiconductor lasers," *IEEE J. Quant. Electron.* **24**, pp. 1845-1855, 1988.
2. Y.H. Lee, B. Tell, K. Brown-Goebeler, J.L. Jewell, C.A. Burrus, J.M. Van Hove, "Characteristics of top-surface-emitting GaAs quantum-well lasers," *IEEE Phot. Tech. Lett.* **2**, pp. 686-688, 1990.
3. D.L. Huffaker, D.G. Deppe, K. Kumar, and T.J. Rogers, "Native-oxide defined ring contact for low threshold vertical-cavity lasers," *Appl. Phys. Lett.* **65**, pp. 97-99, 1994.
4. D.G. Deppe, D.L. Huffaker, T.-H. Oh, H. Deng, and Q. Deng, "Low-threshold vertical-cavity surface-emitting lasers based on oxide-confinement and high contrast distributed Bragg reflectors," *IEEE J. Quant. Electron.* **3**, pp. 893-904, 1997.
5. K.D. Choquette, R.P. Schneider, Jr., K.L. Lear, and K.M. Geib, "Low threshold voltage vertical-cavity lasers fabricated by selective oxidation," *Electron. Lett.* **30**, pp. 2043-2044, 1994.
6. Y. Hayashi, T. Mukaiyama, N. Hatori, N. Ohnoki, A. Matsutani, F. Koyama, and K. Iga, "A record low threshold index-confined InGaAs/GaAlAs vertical-cavity surface-emitting laser with a native oxide confinement structure," *Electron. Lett.* **31**, pp. 560-561, 1995.
7. G.M. Yang, M.H. MacDougall, and P.D. Dapkus, "Ultralow threshold current vertical-cavity surface-emitting lasers obtained with selective oxidation," *Electron. Lett.* **31**, pp. 886-887, 1995.
8. B.J. Thibeault, E.R. Hegblom, P.D. Floyd, R. Naone, Y. Akulova, and L.A. Coldren, "Reduced optical scattering loss in vertical-cavity lasers using a thin (300Å) oxide aperture," *IEEE Phot. Tech. Lett.* **8**, pp. 593-595, 1996.
9. E.R. Hegblom, D.I. Babic, B.J. Thibeault, and L.A. Coldren, "Scattering losses from dielectric apertures in vertical-cavity lasers," *IEEE J. Sel. Top. Quant. Electron.* **3**, pp. 379-389, 1997.
10. K.L. Lear, K.D. Choquette, R.P. Schneider, Jr., S.P. Kilcoyne, and K.M. Geib, "Selectively oxidized vertical cavity surface emitting lasers with 50% power conversion efficiency," *Electron. Lett.*, vol. 31, 208 (1995).
11. R. Jager, M. Grabherr, C. Jung, R. Michalzik, G. Reiner, B. Wieg, and K. Ebeling, "57 % wallplug efficiency oxide-confined 850 nm wavelength GaAs VCSELs," *Electron. Lett.* **33**, pp. 330-331, 1997.
12. B. Wieg, M. Grabherr, G. Reiner, and K.J. Ebeling, "High efficiency selectively oxidized MBE grown vertical-cavity surface-emitting lasers," *Electron. Lett.* **32**, pp. 557-558, 1996.
13. K.L. Lear, A. Mar, K.D. Choquette, S.P. Kilcoyne, R.P. Schneider, Jr., and K.M. Geib, "High-frequency modulation of oxide-confined vertical-cavity surface-emitting laser," *Electron. Lett.* **32**, pp. 457-458, 1996.
14. B.J. Thibeault, K. Bertilsson, E.R. Hegblom, E. Strzelecka, P.D. Floyd, R. Naone, and L.A. Coldren, "High-speed characteristics of low-optical loss oxide-apertured vertical-cavity lasers," *IEEE Phot. Tech. Lett.* **9**, pp. 11-13, 1997.
15. B. Wieg, M. Grabherr, R. Michalzik, G. Reiner, and K.J. Ebeling, "High power single-mode selectively oxidized vertical-cavity surface-emitting lasers," *IEEE Phot. Tech. Lett.* **8**, pp. 971-973, 1996.

16. M. Grabherr, R. Hager, R. Michalzick, B. Weigl, G. Reiner, and K.J. Ebeling, "Efficiency single-mode oxide-confined GaAs VCSEL's emitting in the 850 nm wavelength regime," *IEEE Phot. Tech. Lett.* **9**, pp. 1304-1306, 1997.
17. G. R. Hadley, "Effective index model for vertical-cavity surface-emitting lasers", *Opt. Lett.* **20**, pp. 1483-1485, 1995.
18. D.G. Deppe, T.-H. Oh, and D.L. Huffaker, "Eigenmode confinement in the dielectrically apertured Fabry-Perot microcavity," *IEEE Phot. Tech. Lett.* **9**, 713-715, 1997.
19. W.B. Veldkamp, "Wireless focal planes 'On the road to amacronic sensors'," *IEEE J. Quant. Electron.* **29**, pp. 801 - 813, 1993.
20. N. Kirkstaedter, N. Ledentsov, M. Grundmann, D. Bimberg, V. Ustinov, S. Ruvimov, M. Maximov, P. Kop'ev, Zh. Alferov, "Low threshold, large To injection laser emission from (InGa)As quantum dots," *Electron. Lett.* **30**, pp. 1416-1417, 1994.
21. K. Kamath, P. Bhattacharya, T. Sosnowski, T. Norris, and J. Phillips, "Room temperature operation of In_{0.4}Ga_{0.6}As/GaAs self-organized quantum dot lasers," *Electron. Lett.* **32**, pp. 1374-1375, 1996.
22. H. Shoji, Y. Nakata, K. Mukai, Y. Sugiyama, M. Suagawara, N. Yokoyama, and H. Ishikawa, "Room temperature CW operation at the ground state of self-formed quantum dot lasers with multi-stacked dot layer," *Electron. Lett.* **32**, pp. 2023-2024, 1996.
23. R. Mirin, A. Gossard, and J. Bowers, "Room temperature lasing from InGaAs quantum dots," *Electron. Lett.* **32**, pp. 1732-1733, 1996.
24. Q. Xie, A. Kalburge, P. Chen, and A. Madhukar, "Observation of lasing from vertically self-organized InAs three-dimensional island quantum boxes on GaAs (001)," *IEEE Phot. Tech. Lett.* **8**, pp. 965-967, 1996.
25. H. Saito, K. Nishi, I. Ogura, S. Sugov, and Y. Sugimoto, "Room-temperature lasing operation of a quantum-dot vertical-cavity surface-emitting laser," *Appl. Phys. Lett.* **69**, pp. 3140-3142, 1996.
26. D.L. Huffaker, O. Baklenov, L.A. Graham, B.G. Streetman, and D.G. Deppe, "Quantum dot vertical-cavity surface-emitting laser with a dielectric aperture," *Appl. Phys. Lett.* **70**, pp. 2356-2358, 1997.
27. J.A. Lott, N.N. Ledentsov, V.M. Ustinov, A.Yu. Egorov, A.E. Zhukov, P.S. Kop'ev, Zh.I. Alferov, and D. Bimberg, "Vertical cavity lasers based on vertically coupled quantum dots," *Electron. Lett.* **33**, pp. 1150-1151, 1997.
28. D.L. Huffaker, H. Deng, and D.G. Deppe, "1.15 μm Wavelength Oxide-Confined Quantum Dot Vertical-Cavity Surface-Emitting Laser," *IEEE Phot. Tech. Lett.* **10**, pp. 185-187, 1998.
29. Z. Zou, D.L. Huffaker, S. Csutak, and D.G. Deppe, "Ground State Lasing From a Quantum Dot Oxide-Confined Vertical-Cavity Surface-Emitting Laser," *Appl. Phys. Lett.* **75**, pp. 22-25, 1999.
30. E.M. Purcell, "Spontaneous emission probabilities at radio frequencies," *Phys. Rev.* **69**, p. 681, 1946.
31. K.H. Drexhage, "Interaction of light with monomolecular dye layers," in *Progress in Optics*, edited by E. Wolf (North-Holland, Amsterdam, 1974), Vol. XII, Chap. IV.
32. Q. Deng and D.G. Deppe, "Spontaneous lifetime change in a dielectrically-apertured Fabry-Perot microcavity," *Optics Express* **2**, pp. 157-162, 1998.
33. L.A. Graham, D.L. Huffaker, S.M. Csutak, Q. Deng, and D.G. Deppe, "Spontaneous lifetime control of quantum dot emitters in apertured microcavities," *J. Appl. Phys.* **85**, pp. 3383-3385, 1999.
34. L.A. Graham, D.L. Huffaker, and D.G. Deppe, "Spontaneous lifetime control in a native-oxide-apertured-microcavity," *Appl. Phys. Lett.* **74**, pp. 2408-2410, 1999.
35. J.M. Dallesasse, N. Holonyak, Jr., A.R. Sugg, T.A. Richard, and N. El-Zein, "Hydrolization oxidation of AlGaAs-AlAs-GaAs quantum well heterostructures," *Appl. Phys. Lett.* **57**, pp. 2844-2846, 1990.
36. L. Zhang, T.F. Boggess, D.G. Deppe, D.L. Huffaker, O.B. Shchekin, and C. Cao, "Dynamic response of 1.3 μm wavelength InGaAs/GaAs quantum dots," unpublished.
37. G. Park, D.L. Huffaker, Z. Zou, O.B. Shchekin, and D.G. Deppe, "Temperature Dependence of Lasing Characteristics for Long-Wavelength (1.3 μm) Quantum Dot Lasers," *IEEE Phot. Tech. Lett.* **11**, pp. 301-303, 1999.

Plenary Session II

Optical Nonlinearities in Semiconductors*

S. W. Koch and T. Meier

Department of Physics and Material Sciences Center,
Philipps University, Renthof 5, D-35032 Marburg, Germany

ABSTRACT

A microscopic many-body theory for the nonlinear optical response of semiconductors is reviewed. The importance of Coulomb interaction induced carrier correlations is demonstrated in excitonic pump-probe spectra. The influence of excitonic and biexcitonic contributions to coherent pump-induced absorption changes at the exciton frequency are discussed. Absorption changes induced by incoherent exciton and unbound electron-hole populations are studied.

Keywords: optical nonlinearities, many-body theory, Coulomb correlations, excitonic pump-probe

1. INTRODUCTION

The study of optical nonlinearities in semiconductors and semiconductor heterostructures is a field of active theoretical and experimental research. Microscopic theoretical descriptions of optical nonlinearities in semiconductors generally have to deal with the different relevant quasiparticles and their interactions. In this paper we mainly focus on the important influence of the many-body Coulomb interaction on near-bandgap optical nonlinearities in semiconductors.

One subject of particular interest that has been investigated intensively already in the 1980s and is still receiving considerable attention are nonlinear absorption and refractive index changes induced by the presence of an electron-hole plasma. In the theoretical description of such nonlinearities many-body effects were included microscopically on a non-perturbative level.¹⁻⁵ This approach gives a good basic understanding of the weakening (bleaching) of excitonic absorption with increasing plasma density, the appearance of optical gain (negative absorption), as well as the corresponding dispersive nonlinearities caused by the presence of uncorrelated electron-hole pairs. These nonlinear population-induced absorption changes can be attributed to the effects of Pauli blocking (also called phase-space filling), as well as genuine many-body effects such as band-gap renormalization (electronic self energies) and screening of the Coulomb interaction potential.

Typically in optically excited semiconductors the quasi-particle scattering processes which govern the dephasing of optical excitations can be characterized by typical interaction times in the picosecond to sub-picosecond range. Hence, investigations of the coherent nonlinear optical response of semiconductors, which requires laser pulses shorter than the dephasing time, became generally possible only after the development of femtosecond laser sources in the late 1980s.

In the early ultrafast coherent pump and probe experiments particular attention was paid to the dynamical optical Stark effect of excitons in semiconductors.⁶⁻⁸ To investigate this Stark effect, a strong pump pulse is tuned below the lowest excitonic transition and the resulting absorption changes are monitored by a weak probe pulse.⁵ Analogous to atomic systems the experiments revealed that for large detuning the pump pulse leads to a blueshift of the excitonic resonance.⁶⁻⁸ In a two-band semiconductor model and for relatively large detuning below the exciton, the experimentally observed blueshift could be well described on the basis of the semiconductor Bloch equations (SBE) in the time-dependent Hartree-Fock (TDHF) approximation.^{4,5,9,10}

Generally, the TDHF-SBE are surprisingly successful in the analysis of coherent nonlinear optical effects in semiconductors and semiconductor nanostructures. With improved sample quality and experimental techniques, however, it became evident that many-body Coulomb correlations, i.e. many-body effects beyond the TDHF approximation, can lead to characteristic signatures in semiconductor nonlinearities that cannot be described with the TDHF-SBE.

Further author information: (Send correspondence to S. W. Koch)
S. W. Koch: E-mail: Stephan.W.Koch@physik.uni-marburg.de
T. Meier: E-mail: Torsten.Meier@physik.uni-marburg.de

*Also published in *Proc. of SPIE* Vols. 3897, 3898, and 3899

For example, the relevance of such correlations was clearly shown by analyzing the dependence of the measured signatures on the polarization directions of the incident pulses. Such experiments provided evidence for excitation-induced dephasing processes¹¹ and two-exciton (biexciton) contributions.^{12–16}

To calculate the nonlinear optical response of semiconductors including two-exciton resonances it is necessary to include not only two-point functions, but also higher-order correlation functions in the theoretical description. For arbitrary excitation conditions this would mean that due to the many-body Coulomb interaction an infinite hierarchy of equations of motion has to be solved. One way to restrict this hierarchy to a finite number of correlation functions is to limit the theoretical analysis to a finite order in the optical field. Hence, only a finite number of interactions between the semiconductor and the light field takes place and thus only a finite number of electron-hole pairs is generated.^{17,18}

In order to describe four-wave mixing and pump-probe experiments one needs to consider at least processes up to the third-order in the light field ($\chi^{(3)}$). In the coherent limit, where interaction with other quasiparticles, for example phonons, are neglected, it is sufficient to consider just two quantities (density matrices). These two are the single-exciton amplitude p and the two-exciton amplitude B , which describes the evolution of two interacting electron-hole pairs.^{17,18} Nevertheless, solutions of the full coherent $\chi^{(3)}$ -equations are computationally quite demanding since effectively a quantum mechanical four-body problem has to be solved. Thus, one often restricts the numerical analysis to one-dimensional model systems,^{19–22} where however the parameters are chosen to represent realistic quantum-well configurations. Fully two-dimensional calculations are possible,¹⁵ however, they require rather involved computational analysis and cannot conveniently be used for extended model studies in which dependencies of the results on large numbers of system parameters are investigated. In the coherent $\chi^{(3)}$ -limit for excitation at and below the exciton resonance, the one- and two-dimensional results predict qualitatively similar absorption changes at the exciton which are in good agreement with experiments.¹⁵

Beyond the coherent limit additional occupation-type dynamical variables need to be considered. Up to third-order one then has to deal with four relevant variables, i.e. besides the coherences p and B also the pair occupation N and the exciton to two-exciton transition Z contribute.¹⁹ Since Z is a six point function, solutions of the coupled equations for these four density matrices are numerically even more demanding, such that up to now only few such calculations have been reported. In Ref. 20 it has been shown that in the presence of low-density incoherent occupations N also the six point function Z is significant in order to describe exciton bleaching and to account for transitions from incoherent single- to two-exciton states.

In this paper we review some of our recent results made towards the understanding of nonlinear optical processes in semiconductors including many-body correlations, see Refs. 15 and 20–24. After a brief description of the theoretical approach in Section 2, we focus on the discussion of numerical results on excitonic absorption changes in different situations. Resonant and off-resonant excitation are discussed in Sections 3 and 4, respectively. In both cases we find distinct signatures induced by many-body correlations. In Section 5 absorption changes induced by incoherent populations are analyzed and a brief summary is presented in Section 6.

2. THEORY

To theoretically model correlation effects relevant in coherent two pulse experiments such as pump-probe and four-wave mixing spectroscopy, see Fig. 1(a), we compute the nonlinear optical response in the coherent $\chi^{(3)}$ -limit.^{14,17,18} This is done by numerically solving the relevant equations of motion for the single-exciton amplitude p and the correlated part of the two-exciton amplitude \bar{B} , see Ref. 21. Omitting the various sums and indices the basic structure of the equations of motion is given by

$$\frac{\partial}{\partial t} p = i [\omega_p p + \mu E (1 - 2p^* p) + V p^* p p + V p^* \bar{B}], \quad (1)$$

$$\frac{\partial}{\partial t} \bar{B} = i [\omega_B \bar{B} + V p p]. \quad (2)$$

Here, ω_p and ω_B are energies of a single- and a two-exciton state, respectively, μ is the transition dipole, E the external laser field, and V the Coulomb interaction potential. In Refs. 15 and 21 we have numerically solved the microscopic versions of Eqs. (1) and (2), both for a fully two-dimensional model of the quantum-well structure²⁵ and for a simplified, quasi one-dimensional system. As shown in Ref. 15 the spectra obtained for both models are in good

qualitative agreement and explain correlation-induced signatures in the experimental differential absorption of high quality quantum wells.

Within our model we include the two spin-degenerate electron and heavy-hole bands using the circularly-polarized dipole matrix elements describing the optical interband transitions.^{13,16} Besides the heavy holes also light-hole transitions can be incorporated.²³ The monopole-monopole Coulomb interactions between particles at sites i and j are given by V_{ij} . In our one-dimensional model,^{15,21} the spatial variation is given by a regularized potential: $V_{ij} = U_0 d / (|i - j|d + a_0)$, where d is the distance between the sites and U_0 and a_0 are parameters characterizing the strength of the interaction and the spatial variation taken as $U_0 = 8meV$ and $a_0/d = 0.5$, respectively. In our numerical study we use a tight-binding model with electron and heavy-hole couplings of $J_e = 8meV$ and $J_{hh} = 0.8meV$ between neighboring sites. These system parameters result in an exciton binding energy of $8meV$ and a biexciton binding energy of $1.4meV$.¹⁵

The theory allows us to identify three types of optical nonlinearities.^{15,21} The total differential absorption signal is the sum of a *Pauli-blocking term* ($\propto \mu E p^* p$ in Eq. (1)) and *Coulomb-induced many-body nonlinearities*, which can further be separated into a first-order term ($\propto V p^* p p$ in Eq. (1)) and higher-order correlations ($\propto V p^* B$ in Eq. (1)), see Refs. 15 and 21. Thus the total differential absorption $\delta\alpha$ can be written as the sum of three contributions^{15,21}

$$\delta\alpha(\omega) = \delta\alpha_{pb}(\omega) + \delta\alpha_{CI,1st}(\omega) + \delta\alpha_{CI,corr}(\omega), \quad (3)$$

where pb denotes the optical nonlinearity induced by Pauli-blocking. The terms denoted with CI are Coulomb-interaction-induced nonlinearities. $CI,1st$ is the first-order (Hartree-Fock) term, and $CI,corr$ the higher-order correlation contribution. The lineshape is different for each of the three terms in Eq. (3) which therefore introduce distinct signatures in the differential absorption spectra.^{15,21}

Besides the coherent response, we also analyze the importance of Coulomb correlations in situations where incoherent occupations are present. We focus on the fully incoherent situation and analyze absorption changes induced by incoherent occupations \bar{N} . Omitting the various sums and indices, which can be found in Ref. 20, the basic structure of the equations relevant in this case is given by

$$\frac{\partial}{\partial t} p = i [\omega_p p + \mu E (1 - 2\bar{N}) + V p \bar{N} + V \bar{Z}], \quad (4)$$

$$\frac{\partial}{\partial t} \bar{Z} = i [(\omega_B - \omega_p) \bar{Z} + V p \bar{N}]. \quad (5)$$

As before, we can also here distinguish between the different types of optical nonlinearities. Therefore the absorption changes induced by incoherent occupations \bar{N} are given by the sum of a *Pauli-blocking term* ($\propto \mu E \bar{N}$ in Eq. (4)) and *Coulomb-induced many-body nonlinearities*, which can again further be separated into a first-order term ($\propto V p \bar{N}$ in Eq. (4)) and higher-order correlations ($\propto V \bar{Z}$ in Eq. (4)), see Ref. 20. This allows us to write the total differential absorption $\delta\alpha$ as the sum over the three contributions as given by Eq. (3).

3. RESONANT EXCITATION

The differential absorption spectrum for resonant excitation at the exciton resonance with co-circularly polarized pump and probe pulses ($\sigma^+ \sigma^+$) with a time delay of $\tau = 2ps$ is shown in Fig. 1(b). The differential absorption $\delta\alpha(\omega)$ is strictly negative in the vicinity of the exciton resonance corresponding to a pump-pulse-induced bleaching of the exciton resonance. Positive contributions to $\delta\alpha(\omega)$ appearing well above the exciton are related to excited state absorption induced by exciting unbound two-exciton states. Besides the total signal, Fig. 1(b) also displays the three optical nonlinearities according to Eq. (3) separately. It is shown that $\delta\alpha_{pb}$ is weak and corresponds purely to a bleaching of the exciton resonance. $\delta\alpha_{CI,1st}$ is very strong and is antisymmetric around the exciton resonance. The dispersive shape of the differential absorption corresponds to a blueshift of the exciton. $\delta\alpha_{CI,corr}$ is also mainly dispersive around the exciton resonance, but with opposite sign compared to $\delta\alpha_{CI,1st}$, i.e. this term yields a redshift. Besides contributions with resonances at the exciton energy, $\delta\alpha_{CI,corr}$ also includes terms having resonances at the transition energies to unbound two-exciton states. Therefore it is not completely antisymmetric around the exciton resonance. Including all three contributions to obtain the total signal via Eq. (3), strong cancellations occur between $\delta\alpha_{CI,1st}$ and $\delta\alpha_{CI,corr}$ and the resulting differential absorption shows a predominantly absorptive spectral shape around the exciton resonance. It can be inferred from Fig. 1(b) that the bleaching at the exciton resonance is dominated by Coulomb-induced nonlinearities $\delta\alpha_{CI,1st} + \delta\alpha_{CI,corr}$ and only weakly enhanced by $\delta\alpha_{pb}$.

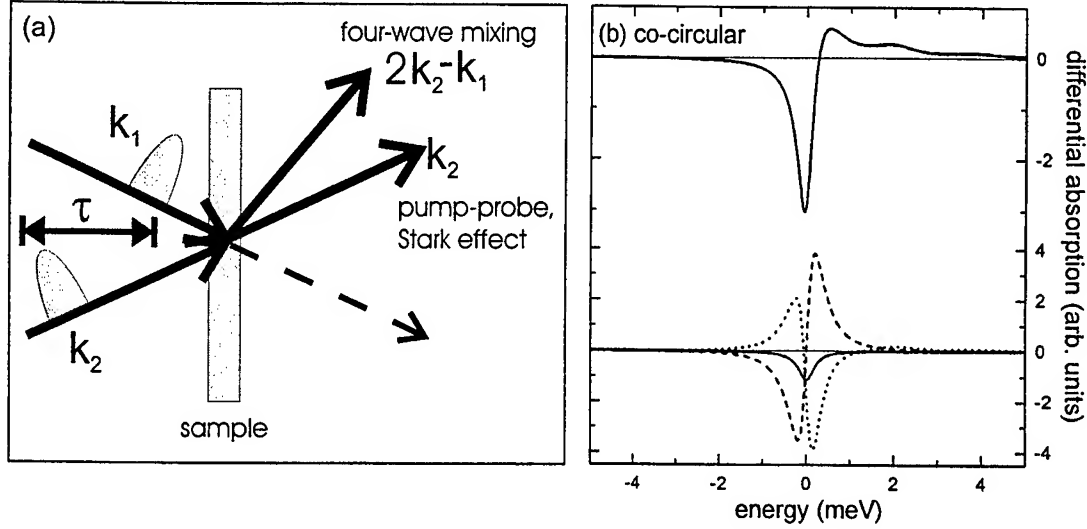


Figure 1. (a) Schematic illustration of nonlinear optical four-wave mixing and pump-probe experiments performed by excitation with two optical laser pulses having a time delay τ . (b) Total differential absorption spectrum $\delta\alpha(\omega)$ for resonant excitation at the exciton resonance and a time delay of $\tau = 2ps$ for co-circularly polarized pump (σ^+) and probe (σ^+) pulses. Also displayed in the lower part are $\delta\alpha_{pb}$ (solid), $\delta\alpha_{CI,1st}$ (dashed), and $\delta\alpha_{CI,corr}$ (dotted). The zero of the energy scale is chosen to coincide with the 1s-exciton resonance. The pump pulse has a duration of 1.18ps (full width at half maximum of pulse intensity). For further parameters see text.

Differential absorption spectra for time delays of $\tau = 2ps$, $0ps$, and $-2ps$ are displayed in Fig. 2 for both co-circularly ($\sigma^+\sigma^+$) and opposite-circularly ($\sigma^+\sigma^-$) polarized pump and probe pulses. As is shown in Ref. 21, for $\sigma^+\sigma^+$ excitation similar compensations among the Coulombic nonlinearities as displayed in Fig. 1(b) arise for all time delays. Within the coherent limit the signal amplitude is strongest for small delays and decreases with both increasing positive and negative delay, see Fig. 2. Apart from the change in strength, for $\sigma^+\sigma^+$ excitation the lineshapes are very similar for 0 and 2ps delay. The main visible difference between these two cases is that for $\tau = 0ps$ there is weak induced absorption appearing energetically below the exciton. This feature is reminiscent of the coherent spectral oscillations,⁴ which dominate the spectra for negative delays, see dotted line in Fig. 2(a) for $\tau = -2ps$. For negative time delays the probe arrives before the pump pulse. With calculations performed in the limit of ultrashort pulses it can be shown that in this case the differential polarization $\delta P(\omega, \tau)$ which determines the absorption changes is multiplied by the phase factor $\exp(i(\omega_p - \omega)\tau)$, where ω_p is the exciton frequency. Since the differential absorption $\delta\alpha(\omega, \tau)$ is determined by the imaginary part of $\delta P(\omega, \tau)$ the phase factor introduces $\sin((\omega_p - \omega)\tau)/(\omega_p - \omega)$ -like spectral oscillations of $\delta\alpha(\omega, \tau)$ around ω_p .^{4,21}

If only heavy-hole transitions are important, $\sigma^+\sigma^-$ polarized excitation makes it possible to analyze pure correlations effects.^{15,21,23} This is due to the fact, that for this geometry $\delta\alpha_{pb}$ vanishes, and also $\delta\alpha_{CI,1st}$ vanishes as long as the system is homogeneous, since neither of these contributions introduces any coupling between the subspaces of different spin states.^{21,22} Differential absorption spectra for $\tau = 2ps$, $0ps$, and $-2ps$ and $\sigma^+\sigma^-$ excitation are displayed in Fig. 2(b). For zero and positive time delays also in this configuration the spectra show bleaching at and some excited state absorption above the exciton resonance. Since with opposite-circularly polarized pump and probe pulses also a bound biexciton is excited, we see in Fig. 2(b) additional strong induced absorption below the exciton resonance. The energetic difference between the maximum of this induced absorption and the bleaching is just the biexciton binding energy. For negative delays also in this polarization configuration which is entirely induced by Coulombic correlations the spectra are characterized by coherent spectral oscillations.²¹ The presence of the oscillations in the correlation terms is in agreement with simplified analytical calculations presented in Ref. 21.

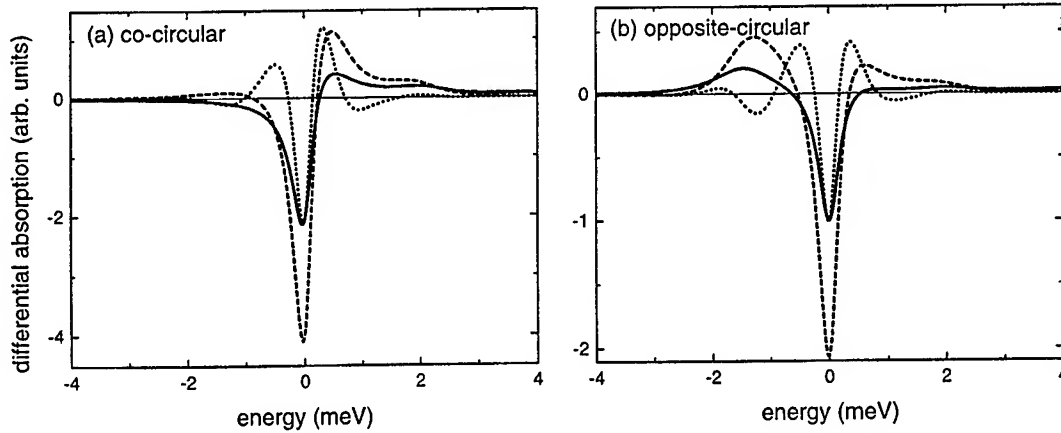


Figure 2. Total differential absorption spectra $\delta\alpha(\omega)$ for resonant excitation at the exciton resonance and a time delay of $\tau = 2ps$ (solid), $0ps$ (dashed), and $-2ps$ (dotted). (a) for co-circularly polarized ($\sigma^+\sigma^+$) and (b) for opposite-circularly polarized ($\sigma^+\sigma^-$) pump and probe pulses.

4. OFF-RESONANT EXCITATION

Here we investigate the influence of correlations on the excitonic optical Stark effect by tuning the pump pulse below the exciton resonance. Fig. 3 shows the resulting differential absorption spectra for co-circularly polarized excitation and various detunings of the central pump-pulse frequency below the exciton energy. The higher detunings ($5meV$ and $7.5meV$) exceed both the spectral width of the pump pulse and the homogeneous width of the exciton resonance. The solid line gives the full $\delta\alpha$, whereas the dashed line gives the result within TDHF where correlations are neglected, i.e. $\delta\alpha_{HF} = \delta\alpha_{pb} + \delta\alpha_{CI,1st}$. With increasing detuning the amplitude of the signal decreases and the bleaching at the exciton resonance develops into a dispersive shape corresponding to a blue-shift.^{4,21} Fig. 3 directly shows that the importance of the carrier correlations diminishes rapidly with increasing detuning. We thus conclude that the time-dependent Hartree-Fock approximation provides a good description for this polarization configuration as long as off-resonant excitation is considered.

An interesting effect induced by the dynamics of Coulomb correlations is found by analyzing for a fixed detuning the polarization-dependence of the Stark effect. We choose the detuning of the pump pulse as $4.5meV$ below the exciton resonance and investigate the absorption changes for the various polarization configurations. Fig. 4(a)-(d) displays the theoretical results for $\sigma^+\sigma^+$, xx , xy , and $\sigma^+\sigma^-$ excitation. Whereas for the three cases (a), (b), and (c) the differential absorption corresponds to a blueshift, for $\sigma^+\sigma^-$ clearly a redshift appears. Since for $\sigma^+\sigma^-$ excitation both the Pauli blocking and the first-order Coulomb-induced nonlinearities, i.e. the Hartree-Fock contribution, vanish identically, the redshift of the differential absorption is purely induced by Coulomb correlations.¹⁵

The physical origin of the redshift can be analyzed in more detail by looking at the individual contributions to the signal, as displayed on the right panels in Fig. 4. For $\sigma^+\sigma^+$, xx , and xy polarization both the Pauli blocking and the first-order Coulomb terms always induce a blueshift, whereas the Coulomb correlations always correspond to a redshift, see Fig. 4(a)-(c). The fact that also for $\sigma^+\sigma^+$ excitation, where no bound biexcitons are excited, the correlation term alone corresponds to a redshift indicates that the correlation-induced reversal of the direction of the shift is not directly related to the existence of a *bound* biexciton. For $\sigma^+\sigma^+$, xx , and xy polarization, however, the influence of correlations is rather small and its redshift is always overcompensated by the Pauli blocking and the first-order Coulomb terms resulting in a net blueshift.¹⁵

To substantiate the claim that the existence of a bound biexciton is not necessary to obtain a correlation-induced redshift, we have performed additional calculations of the differential absorption spectra for $\sigma^+\sigma^-$ configuration. As discussed in Ref. 15, the bound biexciton contribution has been eliminated by artificially dropping the six terms containing the attractive and repulsive Coulomb terms between the two electrons and two holes appearing in the homogeneous part of the equation of motion for the two-exciton amplitude \bar{B} . In this case, also for $\sigma^+\sigma^-$ excitation no bound biexcitons exist. The approximation of neglecting the Coulomb terms that lead to the formation of bound

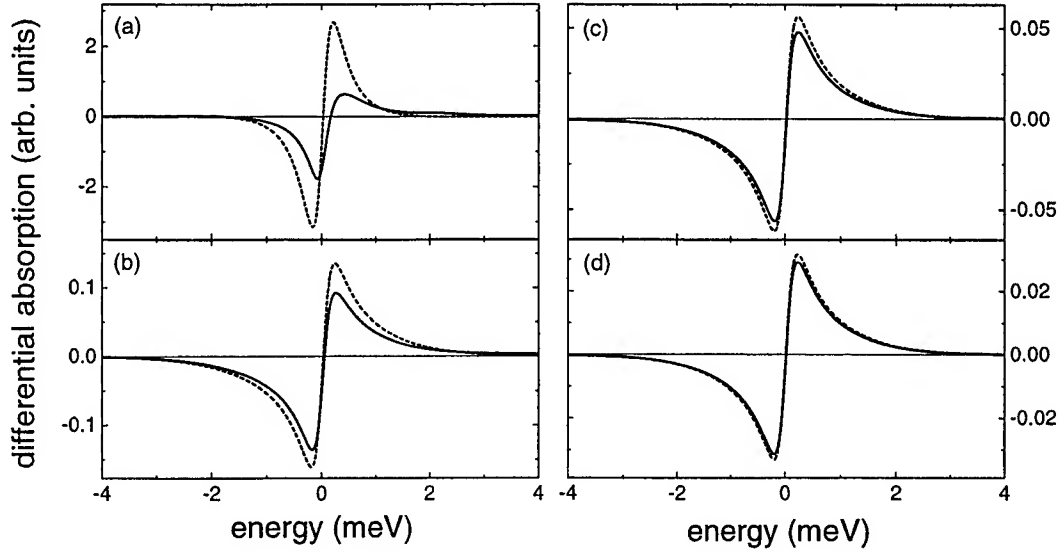


Figure 3. Differential absorption spectra for various detunings of the pump pulse below the exciton resonance with co-circularly polarized pump and probe pulses for time delay $\tau = 0ps$. The central frequency of the pump pulse is chosen (a) $1meV$, (b) $3meV$, (c) $5meV$, and (d) $7.5meV$ below the energy of the $1s$ -exciton. The solid line gives the full $\delta\alpha$, and the dashed line the result of a Hartree-Fock calculation ($\delta\alpha_{pb} + \delta\alpha_{CI,1st}$) neglecting correlations ($\delta\alpha_{CI,corr}$).

two-exciton states is identical to the second Born-approximation (SBA), since only terms up to second-order in the Coulomb interaction are retained in the signal.^{25,26} By solving a dynamic equation for \bar{B} , Coulomb memory effects are still included on this level.¹⁵ The resulting spectrum displayed in Ref. 15 shows that in the SBA the signal amplitude is somewhat reduced, however, the redshift clearly persists. Further calculations performed for the SBA in Markov approximation did not reproduce the redshift. This allows us to conclude that it is clearly the *dynamics* of Coulomb correlations that is responsible for the presence of a redshift.¹⁵ Our numerical results on the polarization-dependence of the optical Stark effect are in good agreement with experiments performed on high-quality InGaAs quantum wells with spectrally very narrow exciton linewidth, see Ref. 15.

In order to show that the redshift depends crucially on the energetic separation between heavy- and light-hole excitons and on the detuning we now extend our model to include both types of valence bands using the typical selection rules and the three to one ratio of the oscillator strengths.²³ The in-plane dispersion of the valence band structure in quantum wells is modeled by considering heavy- and light-hole masses according to the Luttinger-Hamiltonian. For GaAs parameters we get $m_{hh} = m_0/(\gamma_1 + \gamma_2) = 0.112m_0$ and $m_{lh} = m_0/(\gamma_1 - \gamma_2) = 0.211m_0$. Further band-mixing effects are neglected here for simplicity. For the conduction band electrons we use $m_e = 0.0665m_0$ and take the same coupling of $J_e = 8meV$ as used above. The valence band masses then enter into the model by taking the nearest-neighbor coupling to be inversely proportional to the mass, which yields $J_{hh} = J_e m_e / m_{hh} = 4.75meV$ and $J_{lh} = J_e m_e / m_{lh} = 2.52meV$. The site energies for the light-holes are chosen relative to the heavy-holes to have an adjustable splitting between the heavy- and light-hole excitons. Within our model the heavy- and light-hole transitions are coupled by sharing a common electronic state and via the Coulomb coupling.

Fig. 5 shows calculated differential absorption spectra for co-circularly and opposite-circularly excitation for various splittings between the heavy- and light-holes excitons (a) and (b), as well as for various detunings (c) and (d). Considering a detuning of $4.5meV$ below the $1s$ heavy-hole exciton and a splitting of $15meV$ between the heavy- and light-hole excitons (which is the splitting present in the InGaAs quantum well sample investigated in Ref. 15) we reproduce the blueshift for $\sigma^+\sigma^+$ and the redshift for $\sigma^+\sigma^-$ excitation, see Fig. 5(a) and (b). For reduced heavy-light splitting the blueshift for $\sigma^+\sigma^+$ excitation remains unchanged. However, for $\sigma^+\sigma^-$ excitation the amplitude of the redshift strongly decreases with decreasing splitting. For a splitting of $1meV$ and less the redshift even changes

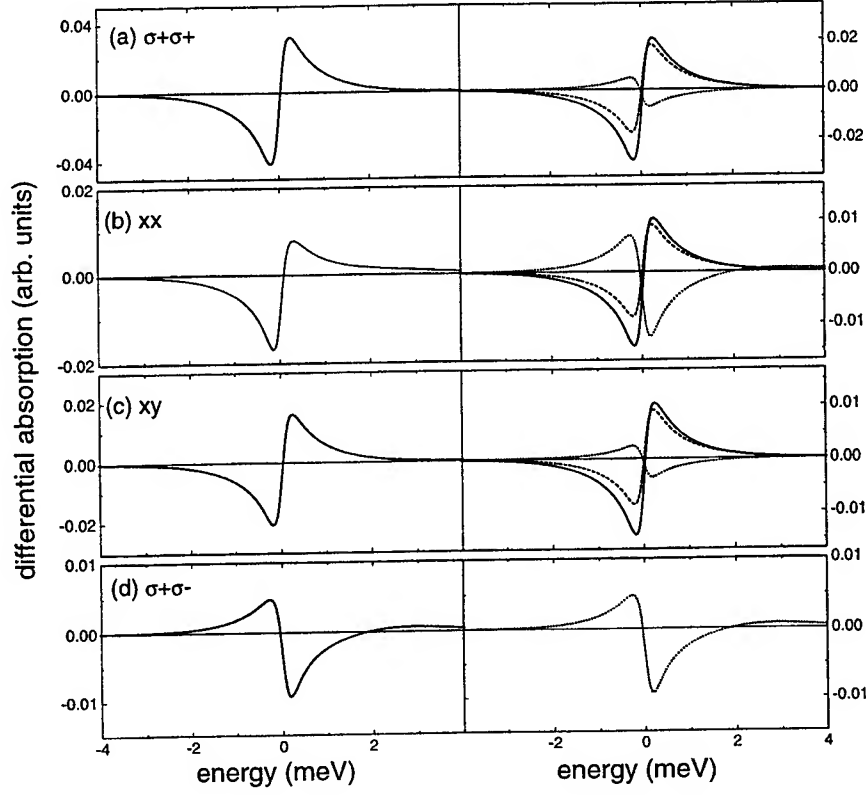


Figure 4. Differential absorption spectra for excitation 4.5 meV below the exciton and time delay $\tau = 0\text{ ps}$. (a) Co-circularly ($\sigma^+\sigma^+$), (b) linear parallel (xx), (c) linear perpendicular (xy), and (d) opposite-circularly ($\sigma^+\sigma^-$) polarized pump and probe pulses. The left panels show the full results, whereas the right panels show the three contributions to the signal: Pauli blocking (solid), first-order Coulomb (dashed), and Coulomb correlations (dotted).

into a blueshift. We thus conclude that the redshift should be well pronounced only in samples with a significant heavy-light splitting. For small splittings the coupling between heavy- and light-hole excitons leads to a blueshift which overcompensates the correlation-induced redshift of the heavy-hole exciton alone.

For a fixed heavy-light splitting taken as 15 meV in Fig. 5(c) and (d) the differential absorption spectra depend strongly on the detuning. For co-circularly excitation the blueshift present for a detuning of 4.5 meV survives also for larger detunings and is only reduced in amplitude with increased detuning. For opposite-circular excitation, however, besides a strong reduction in amplitude also the direction of the shift changes with increasing detuning. For very large detuning we again obtain a switch over from red- to blueshift. The reason for this behavior is that for very large detuning, heavy- and light-hole excitons are both off-resonant and we enter the regime of complete adiabatic following where the frequency dependent optical response decays only weakly with increasing resonance frequency.²⁷ Thus with increasing detuning the *relative* weight of the light-hole exciton increases, which then due to heavy-hole light-hole coupling induces the blueshift at the heavy-hole exciton.

The results presented in Fig. 5 clearly demonstrate that the Coulomb memory induced redshift for opposite-circularly polarized excitation is very sensitive to both the heavy-hole light-hole splitting and the pump detuning. Thus it should only be observable in samples with sufficiently large exciton splittings and only in a certain detuning range,²³ as was the case in the experiments presented in Ref. 15. The exact detuning and splitting ranges that allow to observe the redshift depend on the heavy- and light-hole masses and on the ratio of their oscillator strengths.

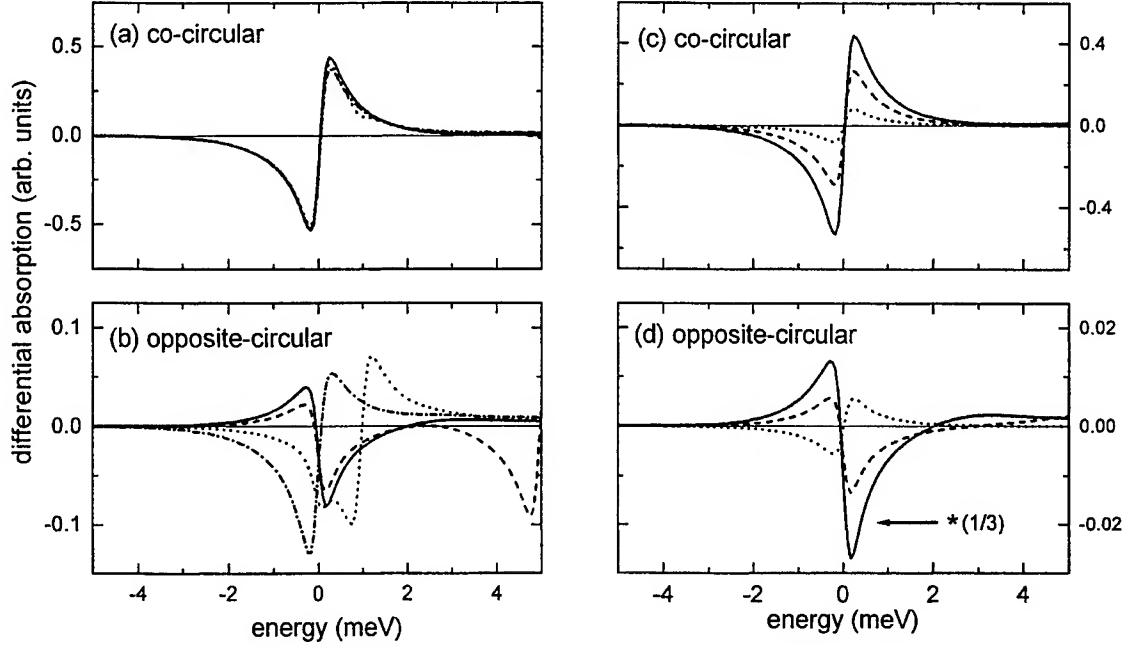


Figure 5. Differential absorption spectra including heavy- and light-holes for time delay $\tau = 0$ ps. (a) Co-circularly and (b) opposite-circularly polarized pump and probe pulses, respectively, for a fixed detuning of 4.5 meV below the $1s$ hh-exciton resonance and various splittings between the heavy- and light-hole excitons: 15 meV (solid), 5 meV (dashed), 1 meV (dotted), and 0 meV (dashed-dotted). (c) Co-circularly and (d) opposite-circularly polarized pump and probe pulses, respectively, for a fixed splitting between the heavy- and light-hole excitons of 15 meV and various detunings below the heavy-hole exciton resonance. 4.5 meV (solid), 6.75 meV (dashed), and 18 meV (dotted).

5. ABSORPTION CHANGES DUE TO INCOHERENT OCCUPATIONS

Numerical results on the absorption changes induced by incoherent exciton as well as electron-hole pair populations \bar{N} have been presented in Ref. 20, where the full Eqs. (4) and (5) have been solved numerically for our model. The homogeneous part of the equation of motion of \bar{N} contains the difference of energies of two single excitons. Thus \bar{N} describes pair occupations and coherences.^{19,28} As outlined in Ref. 20, the pair occupation can be expanded using the complete set of excitonic eigenstates Ψ_α , which are the eigenstates of the homogeneous part of the equation of p . For low-densities (non-degenerate limit) and in thermal equilibrium we assume that \bar{N} is given by a summation over thermally populated exciton states, i.e. schematically

$$\bar{N} = \sum_{\alpha} \frac{\exp(-\epsilon_{\alpha}/k_B T)}{A} \Psi_{\alpha}^* \Psi_{\alpha} \quad , \quad (6)$$

with

$$n = \frac{1}{L} \sum_{\alpha} \frac{\exp(-\epsilon_{\alpha}/k_B T)}{A} \quad , \quad (7)$$

where ϵ_{α} is the energy of Ψ_{α} , L the length of the system, and A is a constant determining the total density n .²⁰ In Eq. (6) we have assumed that no coherences between different exciton states are present and that excitons of both optically coupled pairs of degenerate electron and heavy-hole subbands are equally populated.

Besides assuming that initially thermally populated excitons are present, we can also consider the situation where unbound electron-hole states are populated. To model this situation we simply replace the exciton wavefunctions Ψ_{α} in Eq. (6) by the complete set of single-particle eigenstates Φ_{α} with energies $\tilde{\epsilon}_{\alpha}$, which are the eigenstates of the homogeneous part of the equation of p if the electron-hole Coulomb attraction V is neglected. For generating the thermal electron-hole-pair occupation \bar{N} we then use Eq. (6), where Ψ_{α} is replaced by Φ_{α} and ϵ_{α} by $\tilde{\epsilon}_{\alpha}$.²⁰

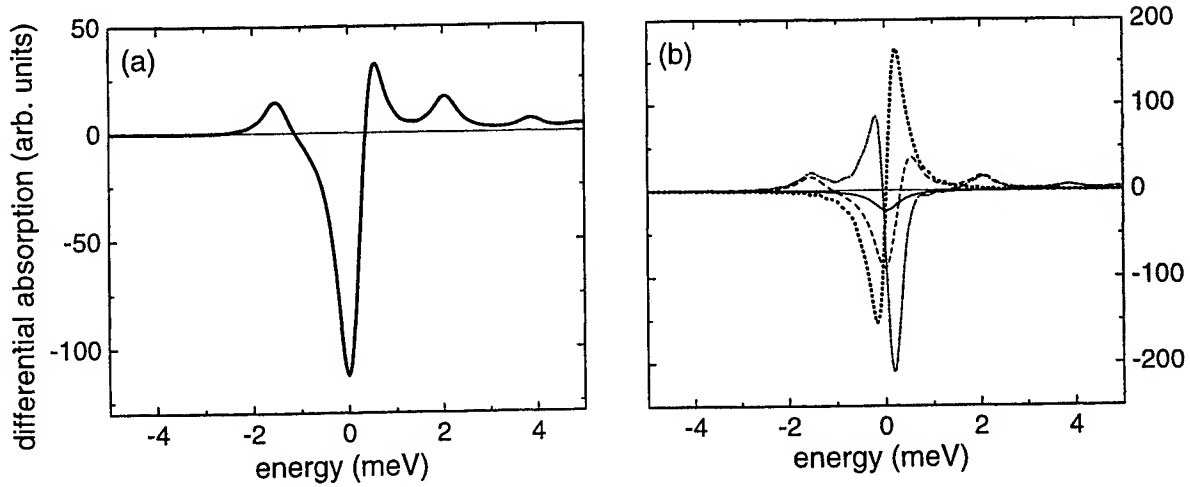


Figure 6. Differential absorption spectra induced by an incoherent occupation of the lowest exciton state. (a) total signal and (b) Pauli blocking (solid), first-order Coulomb terms (dotted), higher-order Coulomb-correlations (dashed-dotted), and sum of the two Coulomb terms (dashed). Dephasing times of $2ps$ for p and \bar{Z} have been considered.

We start our numerical analysis with the low temperature limit. At $T = 0K$ only the energetically lowest exciton state, i.e. the optically active $1s$ -exciton, is initially populated, and we calculate the differential absorption induced by an incoherent occupation \bar{N} of this exciton viewed by a circularly polarized probe pulse. Fig. 6 show the numerically calculated differential absorption spectra at $T = 0K$. Besides the total signal displayed in Fig. 6(a) also the three contributions due to Pauli blocking and first- and higher-order Coulomb-interactions, as well as the sum of the two Coulomb terms are shown separately in Fig. 6(b). We see that Pauli blocking induces a pure and rather small bleaching of the exciton, whereas the first-order Coulomb-term has a dispersive shape at the exciton corresponding to the well-known blueshift.^{10,29} As for the resonant coherent excitation, this blueshift is strongly compensated by the higher-order Coulomb-term ($\propto V\bar{Z}$), which besides excited-state absorption induced by exciton- to two-exciton transitions shows a redshift at the exciton resonance,²⁰ see Fig. 6(b). Adding the contributions we find that the total signal shows no net shift but bleaching of the exciton resonance, see Fig. 6(a). This bleaching of the exciton is mainly induced by the strong Coulomb-interaction-induced terms, and the Pauli blocking introduces only weak additional bleaching. Furthermore, we obtain excited state absorption above and below the exciton which is induced by unbound and bound biexcitonic two-exciton states, respectively. The results displayed in Fig. 6 clearly demonstrate that for a proper description of both exciton bleaching and excited-state absorption higher-order Coulomb correlations represented by the six-particle density matrix \bar{Z} are important and should not be neglected.²⁰ The Pauli blocking- and Coulomb-interaction-induced signatures in the differential absorption including strong cancellation between the first- and higher-order Coulomb-terms and the dominance of the Coulomb-terms over the Pauli blocking in the presence of incoherent occupations²⁰ are very similar to the signatures obtained in the analysis of coherent pump-induced differential absorption changes, see Refs. 15 and 21.

Fig. 7 displays the differential absorption induced by (a) thermalized excitons and (b) thermalized electron-hole pairs for two temperatures of $T = 2K$ and $100K$. As shown in Ref. 20, also at elevated temperatures for both excitons and electron-hole pairs the different signatures of the three nonlinearities as discussed above remains. Fig. 7(b) shows that with raising the temperature of an occupation of unbound electron-hole pairs both the bleaching of the exciton as well as the amplitude of the excited state absorption decrease. The result obtained for thermalized exciton occupations, Fig. 7(a), looks similar. At very low temperatures, where only the lowest exciton is populated, one sees clear signatures of the individual two-exciton states. These positive contributions become less structured at elevated temperatures due to the fact that for increased temperatures also energetically higher excitons are populated. Their transitions to two-exciton states, which occur at different frequencies, are added to the signal induced by the lowest exciton. The tail of the excited state absorption towards low energies appearing for elevated temperatures in the

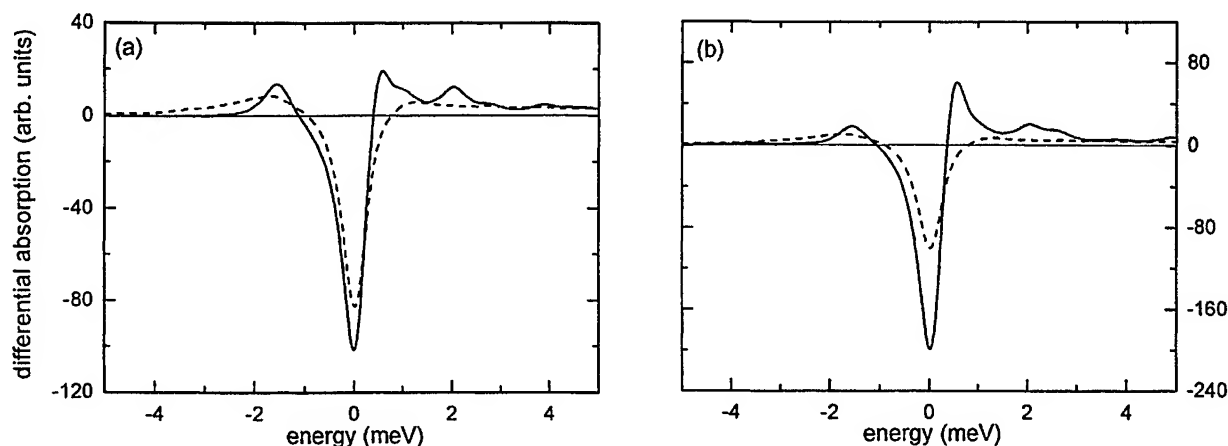


Figure 7. Differential absorption spectra for $T = 2K$ (solid) and $100K$ (dotted) induced by (a) thermally occupied excitons and (d) thermally occupied electron-hole states.

excited state absorption below the exciton directly shows that also energetically higher excitons are Coulombically-coupled to two-exciton states. Comparing the cases of unbound excitons and electron-hole pairs, Fig. 7(a) and (b), we note that for a fixed temperature the lineshapes of the differential absorption are quite similar. However, for thermalized electron-hole pairs the bleaching of the exciton resonance is stronger than for excitons. This stronger bleaching induced by electron-hole pairs compared to excitons means that there is stronger nonlinear coupling of low-energy electron-hole pairs to the $1s$ -exciton compared to the nonlinear coupling among the excitons themselves. For the Pauli-blocking these differences can be analyzed simply by using the exciton and electron-hole wavefunctions, as described in Ref. 29. If Coulomb-correlations are included in the description, on the other hand, due to the relevance of six particle correlations no such simple explanation is possible, since also two-exciton states (which can not be calculated analytically) are relevant. The temperature dependence of the bleaching induced by thermalized excitons and unbound electron and hole pairs obtained within our model has been investigated in detail in Ref. 20.

The dominance of the unbound electron-hole pair over the exciton contributions to the resonance bleaching is most likely the reason for the success of electron-hole plasma theories explaining experimentally observed exciton saturation at low temperatures.^{1,3,5,29} This trend is expected to be even more pronounced in systems with dimensionalities greater than one because of the reduction of the Coulomb-correlation effects with increasing dimensionality.

6. SUMMARY

A microscopic theory capable of describing coherent excitation effects in semiconductors including many-body Coulomb-induced carrier correlations is reviewed. The theory is applied to analyze polarization-dependent ultra-fast absorption changes at the $1s$ exciton resonance. For two-band semiconductors it is shown that the optical Stark effect may change from a blueshift for co-circularly polarized pump and probe pulses to a redshift for opposite-circularly excitation conditions. A theoretical analysis including heavy and light holes shows that the occurrence of the redshift for opposite-circularly polarized excitation depends sensitively on both the splitting between the heavy- and light-hole excitons and the pump detuning.

The theory is also applied to an incoherent situation. Whereas one could expect that correlations might not be important in this situation, strong correlation effects on the differential absorption induced by incoherent thermalized excitons and free electron-hole pairs are found. For low temperatures it is shown that populated free electron-hole pairs induce stronger bleaching at the exciton resonance than populated excitons of the same density.

In Ref. 21 the approach has been generalized to treat also effects of energetic disorder. Furthermore, the theory has been applied to excitons in microcavities,²¹ yielding numerical results on reflection changes that are in good qualitative agreement with recent experiments.³⁰ The theoretical approach has further been extended to include effects of higher intensities (coherent $\chi^{(5)}$ -limit) where it yields results on the excitonic differential absorption in good

agreement with experimental results.³¹ In addition, the theoretical approach has been used to clarify the relevance of a new coherent technique called "coherent excitation spectroscopy" which is based on partly nondegenerate four-wave mixing.²⁴ Work is in progress dealing with the analysis of disorder-induced dephasing in four-wave mixing spectroscopy, which can only be understood properly if both disorder and correlations are treated microscopically.²²

ACKNOWLEDGMENTS

We thank P. Thomas and our co-workers C. Sieh, F. Jahnke, and A. Knorr for many collaborations and valuable discussions. This work is supported by the Deutsche Forschungsgemeinschaft (DFG) through the Sonderforschungsbereich 383 and the Leibniz prize, and by the John von Neumann Institut für Computing (NIC), Forschungszentrum Jülich, Germany, through grants for extended CPU time on their supercomputer systems.

REFERENCES

1. H. Haug and S. Schmitt-Rink, "Electron theory of the optical properties of laser excited semiconductors," *Prog. in Quant. Electron.* **9**, pp. 3–100, 1984.
2. S. Schmitt-Rink, D. A. B. Miller, and D. S. Chemla, "Linear and nonlinear optical properties of semiconductor quantum wells," *Adv. in Phys.* **38**, pp. 89–188, 1989.
3. L. Bányai and S. W. Koch, "A simple theory for the effects of plasma screening on the optical spectra of highly excited semiconductors," *Z. Phys. B* **63**, pp. 283–291, 1986.
4. S. W. Koch, N. Peyghambarian, and M. Lindberg, "Transient and steady-state optical non-linearities in semiconductors," *J. Phys. C* **21**, pp. 5229–5249, 1988.
5. H. Haug and S. W. Koch, *Quantum Theory of the Optical and Electronic Properties of Semiconductors*, World Scientific, Singapore, 1994.
6. D. Fröhlich, A. Nöthe, and H. Reiman, "Observation of the resonant optical stark effect in a semiconductor," *Phys. Rev. Lett.* **55**, pp. 1335–1337, 1985.
7. A. Mysyrowicz, D. Hulin, A. Antonetti, A. Migus, W. T. Masselink, and H. Morkoc, "'Dressed excitons" in a multiple-quantum-well structure: Evidence for an optical stark effect with femtosecond response time," *Phys. Rev. Lett.* **56**, pp. 2748–2751, 1986.
8. A. V. Lehmen, D. S. Chemla, J. E. Zucker, and J. P. Heritage, "Optical stark effect on excitons in GaAs quantum wells," *Opt. Lett.* **11**, pp. 609–611, 1986.
9. S. Schmitt-Rink and D. S. Chemla, "Collective excitations and the dynamical stark effect in a coherently driven exciton system," *Phys. Rev. Lett.* **57**, pp. 2752–2755, 1986.
10. R. Binder, S. W. Koch, M. Lindberg, W. Schäfer, and F. Jahnke, "Transient many-body effects in the semiconductor optical stark effect: A numerical study," *Phys. Rev. B* **43**, pp. 6520–6529, 1991.
11. H. Wang, K. B. Ferrio, D. G. Steel, Y. Z. Hu, R. Binder, and S. W. Koch, "Transient nonlinear optical response from excitation induced dephasing in GaAs," *Phys. Rev. Lett.* **71**, pp. 1261–1264, 1993.
12. B. F. Feuerbacher, J. Kuhl, and K. Ploog, "Biexcitonic contribution to the degenerate-four-wave-mixing signal from a GaAs/Al_xGa_{1-x}As quantum well," *Phys. Rev. B* **43**, pp. 2439–2441, 1991.
13. K. Bott, O. Heller, D. Bennhardt, S. T. Cundiff, P. Thomas, E. J. Mayer, G. O. Smith, R. Eccleston, J. Kuhl, and K. Ploog, "Influence of exciton-exciton interactions on the coherent optical response in GaAs quantum wells," *Phys. Rev. B* **48**, pp. 17418–17426, 1993.
14. V. M. Axt and A. Stahl, "The role of the biexciton in a dynamic density matrix theory of the semiconductor band edge," *Z. Phys. B* **93**, pp. 205–211, 1994.
15. C. Sieh, T. Meier, F. Jahnke, A. Knorr, S. W. Koch, P. Brick, M. Hübner, C. Ell, J. Prineas, G. Khitrova, and H. M. Gibbs, "Coulomb memory signatures in the excitonic optical stark effect," *Phys. Rev. Lett.* **82**, pp. 3112–3115, 1999.
16. W. Schäfer, D. S. Kim, J. Shah, T. C. Damen, J. E. Cunningham, K. W. Goosen, L. N. Pfeiffer, and K. Köhler, "Femtosecond coherent fields induced by many-particle correlations in transient four-wave mixing," *Phys. Rev. B* **53**, pp. 16429–16443, 1996.
17. M. Lindberg, Y. Z. Hu, R. Binder, and S. W. Koch, " $\chi^{(3)}$ formalism in optically excited semiconductors and its applications in four-wave-mixing spectroscopy," *Phys. Rev. B* **50**, pp. 18060–18072, 1994.
18. V. M. Axt and A. Stahl, "A dynamics-controlled truncation scheme for the hierarchy of density matrices in semiconductor optics," *Z. Phys. B* **93**, pp. 195–204, 1994.

19. V. M. Axt, K. Victor, and A. Stahl, "Influence of a phonon bath on the hierarchy of electronic densities in an optically excited semiconductor," *Phys. Rev. B* **53**, pp. 7244–7258, 1996.
20. T. Meier and S. W. Koch, "Excitons versus unbound electron-hole pairs and their influence on exciton bleaching: A model study," *Phys. Rev. B* **59**, pp. 13202–13208, 1999.
21. C. Sieh, T. Meier, F. Jahnke, A. Knorr, F. Jahnke, P. Thomas, and S. W. Koch, "Influence of carrier correlations on the excitonic optical response including disorder and microcavity effects," *Europ. Phys. J. B*, in press.
22. S. Weiser, T. Meier, J. Möbius, A. Euteneuer, E. J. Mayer, W. Stolz, M. Hofmann, W. W. Rühle, P. Thomas, and S. W. Koch, "Disorder-induced dephasing in semiconductors," submitted.
23. S. W. Koch, C. Sieh, T. Meier, F. Jahnke, A. Knorr, P. Brick, M. Hübner, C. Ell, J. Prineas, G. Khitrova, and H. M. Gibbs, "Theory of coherent effects in semiconductors," *J. Lumin.*, in press.
24. A. Euteneuer, E. Finger, M. Hofmann, W. Stolz, T. Meier, P. Thomas, S. W. Koch, W. W. Rühle, R. Hey, and K. Ploog, "Coherent excitation spectroscopy on inhomogeneous exciton ensembles," *Phys. Rev. Lett.*, in press.
25. F. Jahnke, M. Kira, S. W. Koch, G. Khitrova, E. K. Lindmark, T. R. Nelson, D. V. Wick, J. D. Berger, O. Lynnes, H. M. Gibbs, and K. Tai, "Excitonic nonlinearities of semiconductor microcavities in the nonperturbative regime," *Phys. Rev. Lett.* **77**, pp. 5257–5260, 1996.
26. F. Jahnke, M. Kira, and S. W. Koch, "Linear and nonlinear optical properties of excitons in semiconductor quantum wells and microcavities," *Z. Phys. B* **104**, pp. 559–572, 1997.
27. R. Binder, S. W. Koch, M. Lindberg, N. Peyghambarian, and W. Schäfer, "Ultrafast adiabatic following in semiconductors," *Phys. Rev. Lett.* **65**, pp. 899–902, 1990.
28. G. Bartels, G. C. Cho, T. Dekorsy, H. Kurz, A. Stahl, and K. Köhler, "Coherent signature of differential transmission signals in semiconductors: Theory and experiment," *Phys. Rev. B* **55**, pp. 16404–16413, 1997.
29. S. Schmitt-Rink, D. S. Chemla, and D. A. B. Miller, "Theory of transient excitonic optical nonlinearities in semiconductor quantum-well structures," *Phys. Rev. B* **32**, pp. 6601–6609, 1985.
30. X. Fan, H. Wang, H. Q. Hou, and B. E. Hammons, "Biexcitonic effects in the nonperturbative regime of semiconductor microcavities," *Phys. Rev. B* **57**, pp. 9451–9454, 1998.
31. P. Brick et al., unpublished.

Advances in Missile Technology - Impact of Photonics*

Dr. A. Sivathanu Pillai

Chief Controller R&D, Defence Research and Development Organisation
B Wing, Sena Bhavan, New Delhi - 110 011

ABSTRACT

This paper discusses the role and impact of advancements in Photonics Technology on the performance enhancement of guided missile weapon systems with specific reference to the development of Indian guided missiles programme. India is emerging as a technologically strong nation with core competence in Space, Missile and Nuclear technologies, advanced computing including supercomputers and software. Based on the realisation of the fact that high technology strength is the key to economic prosperity and military strength, India is progressing several high technology areas that help in attaining the global competitiveness. Photonics is identified as one of the important areas in this direction and hence high priority has been accorded for Research & Development in Photonics. This paper reviews the current trends and developments in missile technology and highlights some of the important developments in Photonics that have a force multiplying effect on the performance enhancement of guided missile systems.

Key words: High technology in India, Guided Missiles Technology, Photonics

1. INTRODUCTION

A study of the evolution of war weaponry reveals that, over the years, guided missiles have evolved as a weapon of choice for the modern warfare. During the early days of warfare, the wars were fought using human and animal strength and the role of weapons were mainly to augment this physical strength. At that time the theatre of war was confined only to the land and sea. This trend continued up to the 18th century till the invention of gunpowder changed the nature of warfare. Rocketry made its beginning during the last quarter of the 18th century. A major milestone in the history of Rocketry occurred in 1792 AD, when the world's first war rocket was used by Tippu Sultan, Prince of Mysore, India, to defeat the British cavalry attack at Srirangapatnam, near Mysore in India. This has triggered the development of rocket as a war weapon. However, the real transformation happened almost 150 years later, towards the end of World War II, with the development of world's first guided missile - V2, by Germany. That was the beginning of revolutionary changes in the warfare that resulted in the development and use of a wide spectrum of guided missiles launched from multiple platforms and aided by variety of sensors. Gradually the theatre of war had extended to encompass the deep sea and outer space. High technology devices and intelligent and autonomous systems have emerged as the dominating features of the modern warfare. As a result of the transformation of the nature of warfare from being a human & animal warfare to weapon warfare to ultimately the high technology warfare, guided missile systems are at the core of this high technological warfare. There has been a continuous performance enhancement in every aspect of the guided missiles, as a result of the advancement of technologies in various fields. Photonics is one such area having significant impact on the performance enhancement of the guided missile weapon systems. This paper highlights some of the important developments in Photonics that have a force multiplying effect on the performance enhancement of guided missile systems.

*Also published in *Proc. of SPIE* Vols. 3897, 3898, and 3899

This paper is organised into three parts in the following sequence:

- A brief review of high technology growth in India, strength and core competence
- Integrated Guided Missile Development Programme, Missions, Technologies, and Global assessment
- Advances in Photonics and their impact on the performance enhancement of guided missile systems

2. TECHNOLOGY LEADERSHIP AND CORE COMPETENCE

A Nation is strong and gets its rightful place only if it has economic prosperity and comprehensive security. Realising that this can be achieved through technology, India has progressed several technological areas that helped the country to emerge as a technologically strong nation. During the last five decades, India has made an all round technological progress with many accomplishments. The green revolution and the operation flood made the country self sufficient in food production, milk, vegetables, fruits, cereals and other essential areas. The technology related to healthcare has resulted in increase of life expectancy. The quest for tapping natural resources for generating power has given new impetus to the power sector. The nuclear tests in 1974 and in 1998 made India a nuclear weapon state, and India mastered harnessing of nuclear power to meet the growing demand for electricity. 500 MW fast breeder development and the target of 3000 MW power generation by 2000 are the immediate goals. By 2020 the nation is targeting 20000 MW nuclear power generation. India already has a 2 GFLOP super computer, which will reach 8 GFLOP by 2000 and teraflop speed by 2020. The nation is passing through a communication revolution towards reaching 20 million lines and soon to 100 million lines. With the established strength in computing systems, software and communication, large pool of talented software specialists, together, India is emerging as a strong nation in the area of information technology. India's current software export has already reached 1 billion US dollars.

The guided missiles Agni and Prithvi have demonstrated India's capability to develop high technology strategic systems without any help from outside. India made spectacular achievements in building its own launch vehicles, SLV-3, ASLV, and PSLV, and the GSLV which is getting ready will give India the capability to inject satellites into the geo-stationary orbit. The Indian satellites INSAT and IRS with 6 m resolution are among the best in the world. Recently PSLV launched German and Korean satellites providing cost effective launch services to the world. India is self-sufficient in space systems and their applications. In the area of aeronautics, the Indigenous light combat aircraft will take off very soon. India is dreaming of launching a reusable missile, deep penetration strike aircraft, and multipurpose aerospace vehicle - Hyperplane, harnessing the technological base established in aeronautics, space and missiles.

India is self-sufficient in production of all raw materials, special alloys, armour materials, electronic components and devices, computing systems and software for meeting the demands of the nation. Both public and private sector industries have been well knitted with R&D and academy to meet the demands. The Indian Defence R&D organisation, DRDO, achieved technology breakthrough in certain devices and computing systems, ASICs and MMICs, both Silicon and Gallium Arsenide based, PACE+ super computer, ANUPAMA microprocessor with state-of-the-art architecture to meet the requirements of strategic programmes. DRDO has developed core competence in many critical areas of armaments, combat vehicles, electronics and communications, aeronautics, missiles, life supporting systems and computing systems. This core competence is being used to develop state-of-the-art high technology systems for the armed forces.

India is blessed with abundance of manpower, natural resources and good value system. The R&D development cost varies from $1/10^{\text{th}}$ to $1/3^{\text{rd}}$ of the advanced nations depending on the type of programme. Also through various programmes, Indian specialists have learnt to work together with academic institutions and industries as partners, sharing each others strength to design, develop, and produce high technology systems in the country without any dependence from abroad.

3. INTEGRATED GUIDED MISSILE DEVELOPMENT

3.1 Mission & Technologies

The Integrated Guided Missile Development Programme (IGMDP) commenced in 1983 with an objective of design, development and leading to production of four types of missile systems namely, Prithvi, Trishul, Akash and Nag and technology demonstrator for long range system - Agni. Prithvi is a short range battlefield Surface to Surface missile launched from a mobile transporter. Prithvi uses liquid propellant rocket engines, light weight airframe, high accuracy strapdown inertial guidance system and electro-hydraulic control system. Trishul is a low level quick reaction surface to air missile system designed to defend the moving armoured columns from attacking aircraft and helicopters. The Naval version of Trishul is designed to defend the ships from the incoming sea-skimming missiles. Akash is a medium range surface to air missile with multi-target handling capability and ECCM features. Nag is a 3rd generation anti tank guided missile with a fire and forget and top attack capabilities. Nag has two state-of-the-art guidance systems, one using an Imaging Infra Red seeker and the other using a Millimetric wave active radar seeker. Agni is an Intermediate Range Ballistic Missile, which uses a specially developed carbon-carbon re-entry vehicle structure and re-entry guidance and control.

The technological goal of the IGMDP is to ensure that the systems are contemporary at the time of their induction into the Services. As a result, the technologies have been forecast 10 to 15 years in advance, concurrently developed, and channelled into the missile systems. The programme used several innovative management practices including the multi-institutional partnership, consortium, collaboration, technology empowerment, and developed all the critical technologies required for the programmes within the country using a network of R&D laboratories, academic institutions, public and private sector industries. The systems developed are of multi-user and multi-role in nature with contemporary performance.

3.2 Global Assessment

With a high supersonic manoeuvrable trajectory, high lethality, multiple field interchangeable warheads, and high accuracy, Prithvi is among the best in its class. With a quick reaction time of 6 sec, jamming proof Ka-band guidance, and anti-sea skimming missile capabilities, Trishul has contemporary performance in its class. The performance of Trishul is comparable to ADATS, CROTALE and BARAK. With multi-target engagement capability and modern homing guidance, Akash is state-of-the-art and comparable in performance to the PATRIOT. Nag is aiming to be the first of its kind in the world with fire & forget and top attack capabilities and a Tandem warhead capable of defeating composite and reactive armour.

3.3 Further advancements

Based on the above strength, India is working on several next generation technologies to enhance the performance of its guided missiles. The general directions of improvements include:

- (a) Faster speeds towards hypersonic missiles
- (b) Improved precision towards zero CEP
- (c) Intelligent systems like the Terminally Guided Sub-munitions
- (d) Capability of launching from multiple platforms
- (e) Enhanced stealth
- (f) Better ECM / ECCM capabilities

The above directions of improvement requires major technology advancements in the subsystems towards:

- (a) Lower weight
- (b) Less volume (Miniaturisation)
- (c) Lower power consumption

- (d) Better performance in terms of the processing efficiency, minimum errors, greater sensitivity and greater precision
- (e) Minimum aerodynamic interference and better integration with missile
- (f) Lower cost

It is interesting to note that many developments in Photonics could help in realising the above objectives. Some of them are discussed below.

4. ADVANCEMENTS IN PHOTONICS AND THEIR IMPACT ON PERFORMANCE ENHANCEMENT OF GUIDED MISSILES

4.1 Current applications of Photonics in Guided Missiles

Photonics has always been one of the important technologies used in various aspects of guided missiles. Some of the important areas where Photonics and related technologies play a crucial role in guided missiles include:

- (a) Missile guidance applications
 - Missile tracking sensors for command guidance
(Ex : IR plume trackers used in 2nd generation anti tank guided missiles and IR imaging sensors used in surface to air missiles)
 - Target tracking sensors for homing guidance
(Ex : IR homing seekers for air to air missiles, IR imaging sensors for 3rd generation anti tank guided missiles)
 - Inertial sensors for navigation systems used in surface to surface missiles and number of other applications
(Ex: Fibre optic gyros, ring laser gyros)
 - Imaging sensors for mid course guidance and terminal homing for long range missiles
(Ex : Imaging sensors for terrain contour matching and terminal guidance)
 - Illuminating source and homing sensors for semi-active homing applications, and range finders used in certain class of missiles
- (b) Proximity sensors for initiating warhead detonation
(Ex: IR Proximity fuzes used in anti sea skimmer missiles, altitude sensors used in surface to surface missiles)
- (c) Surveillance, target detection and target acquisition applications
 - Thermal sights for target acquisition in 3rd generation anti-tank guided missiles
 - Infra red search & tracking systems for naval applications
 - Space based sensors for detection of missile launch point for Ballistic Missile Defence Systems
 - Laser radars for precision tracking
- (d) Equipment for command, control & communications
 - Fibre optic communications
 - Display systems
- (e) Electro-optic counter measures & counter counter measure

- (f) Design aids for missile subsystems
(Ex: Experimental stress analysis tools, Laser anemometers used in wind tunnel testing applications)
- (g) Test & evaluation instrumentation for guided missiles
(Ex : Electro-optic tracking instruments used in missiles test ranges)
- (h) Manufacturing of precision missile components and quality control
(Ex : Laser welding, equipment for inspection and measurement, holography for NDT)

The above list indicates that Photonics is important at every phase of the guided missiles lifecycle. Therefore any development in this technology has a wide ranging impact on the missile systems performance.

4.2 Advancements in Photonics and their impact on guided missiles

4.2.1 Some of the important developments in Photonics and related technologies with potential applications for guided missile systems include:

- (a) Uncooled Imaging technology
- (b) Focal plane array technology
- (c) Conformal optics
- (d) Adaptive optics
- (e) Fiber optics technology
- (f) Micro-Opto-Electro -Mechanical Systems (MOEMS)
- (g) Optical Correlators
- (h) Multi-Spectral fusion (fusion of 3-5 μ and 8-12 μ images)
- (i) Multi-sensor Fusion (fusion of 3-5 μ and 8-12 μ images of IR and MM wave images)
- (j) Real-time Image Processing

4.2.2 Uncooled Imaging

Uncooled thermal imaging systems are very important for missile systems as these system offer significant operational advantages and saving of weight, space as well as cost associated with the cooling system. Towards this the resistive microbolometer technology, ferro-electric bolometer technology, uncooled thermo electric linear arrays are becoming more important. The research effort in uncooled infrared technology is directed towards several other military applications including reconnaissance, surveillance and weapon sighting capabilities as well as for precision munitions and dispenser system applications and anti armour submunition programmes.

4.2.3 Focal Plane Array Technology

Focal Plane Arrays technology is crucial for missile seekers and other imaging sensors. The focus is on developing larger size arrays, higher resolution and higher sensitivity focal planes. The current research is also focused on reducing the pixel size and increasing pixel sensitivity using advanced materials and micro electromechanical device structures. The advancement in FPA technology has a direct impact on the guided missile systems. For example, target detection and lock on range of a 3rd generation anti tank guided missiles can be significantly increased by enhancing the performance of the FPA.

4.2.4 Conformal optics

Conformal optics minimises the aerodynamic interference of the missile IR domes and windows by shaping the optics to minimise the aerodynamic drag coefficient. This will increase the aerodynamic efficiency of the missile and thus increase its range. However, the design, manufacturing and testing of the conformal optics and development of techniques & methods for dynamic aberration correction is a great challenge that is being addresses by the current research.

4.2.5 Adaptive optics

Adaptive optics compensates for the turbulence induced phase distortions of optical waves propagating through the atmosphere. Adaptive optic systems typically consist of a wavefront phase sensor, focusing optics, a spatial light modulator (SLM) for correcting phase errors, imaging sensors, and the control and processing electronics. These systems improve the image quality by reducing the phase aberrations introduced when the wavefront travels through turbulent atmosphere or aberrations introduced by the optical system itself. Adaptive optic system is a growing area of interest for the guided missiles. Advanced technologies are now becoming available to make these systems lightweight, low power, and compact. The technologies that are making this possible include highly integrated low power electronics, and new processing architectures for error sensing and control, flexible high density packaging, and Micro-Opto-Electro-Mechanical Systems.

4.2.6 Fibre optic technology

The advancement in Fibre optic technology has multiple implications for guided missile systems. The most beneficial development is the enhanced communication abilities of the fibre optics, which are important for command, control and communication applications. Fibre optic guided missile and track via missile systems are some of the important developments in this direction.

Another major application of fibre optic technology is in the area of sensors. Fibre optic gyro used in the inertial navigation units of missiles is an example for this. The Fibre Bragg grating sensors also called "Smart sensors" represent an exciting development in fibre-sensor technology. Fibre Bragg grating sensors can monitor the manufacture of a product or the condition of a structure in use by providing the real-time feedback by reflecting different wavelengths depending on the condition of the structure. Writing a periodic series of gratings (refractive-index modulations in the core of a single-mode fibre) using an ultraviolet beam generates a low-loss, highly reflective, wavelength-sensitive filter system. This non invasive process does not change the fibre's strength, electromagnetic-interference immunity or dielectric properties. Bragg grating sensors, when fabricated and annealed properly, have proven to be permanent, easily reproducible reflectors that can withstand high temperatures. The gratings respond to changes in temperature, compression and strain by changing the wavelength that they reflect, and their performance is not amplitude or intensity dependent. The sensors are small and can easily attached to surfaces to provide information on the structure's integrity. These sensors are very useful for monitoring the structural conditions during flight testing of guided missiles.

4.2.7 Micro- Opto-Electro-Mechanical Systems (MOEMS)

These systems represent another exciting development for missile and space applications. The saving in the weight, volume and power requirements are of great importance for the applications such as the terminally guided sub-munitions. Micro mirrors are the crucial enabling technology for these systems. Design techniques and fabrication processes for both individual micro mirrors as well as the arrays of micro mirrors are the focus of the current research efforts.

4.2.8 Optical correlators

Optical correlators relies on the Fourier transform property of a lens and a hologram of the Fourier transform of an object as viewed from a particular perspective, to establish a matching correlation coefficient. Optical correlators can be effectively used for automatic target recognition, missile guidance and tracking of the target scenes which do not have prominent features or high contrast with the background. The speed and innate parallel-processing capability of optics enable the correlator to simultaneously recognize and locate all objects in a scene almost instantaneously. These systems are very important for the missile guidance applications, especially the mid course and terminal guidance of long range surface to surface missiles.

4.2.9 Multi-Spectral fusion & Multi-Sensor fusion

The Multi-Spectral fusion methods greatly improve the detection and identification of low observable and camouflaged targets. Hence these methods are becoming more and more common for future applications. Missile seekers with two color detectors are already in operation. However for a battle field application, Multi-sensor fusion is emerging as a major technique to overcome limitations of IR and radar seekers, especially in a dense electronic / electro-optic counter measures environment. Dual mode missile seekers with both IR and radar imaging seekers are becoming important for future applications. Hence this is an important area for missile technology.

4.2.10. Real-time Image Processing

Due to the limitations imposed by the electronic processors for the real-time solutions to critical military application such as automatic target recognition, clutter rejection in infrared search and track (IRST) applications, vision-assisted piloting tasks in unmanned robotic vehicles (e.g., Remotely Piloted Vehicles, Unmanned Aerial Vehicles, or Unmanned Underwater Vehicles), and imaging Identification Friend of Foe, real-time image processing is an important technology. The intrinsic parallelism of optics is expected to circumvent these limitations in future. Towards this, the optronics processor holds a great promise for future real time applications for guided missiles.

4.2.11 The Indian scenario

India has already developed thermal Imagers based on 60 & 100 element linear arrays and 288x4 FPAs for MBT-FCS and Nag missile respectively. It is working on IRST system for Naval applications. A wide technology base exists within the country and also enough skilled manpower available in this field. Keeping in view the technology trends and the requirements of the country, DRDO is working in the development of several state-of-the-art systems including; Night Vision Devices based on Optical Amplification, Intelligent Search & Track system for Airborne platforms, High performance Thermal Imagers using staring FPAs/IR CCDs, Dual-bank/Bi-spectral 3-5 μm and 8-12 μm imagers, Thermal Imagers using uncooled detectors, Real time (on-line) image processing. Laser Instrumentation including Laser Designator/Range Finders using Laser diode pumped Nd:YAG laser, Eye-safe laser systems, Laser Range gated imaging, Laser proximity fuses, Blue-green lasers for underwater imaging, Coherent laser imaging, Sensors for smart ammunitions. Integrated Multi-spectral laser and Radar Warning systems and Autonomous EO Missile jammers with programmed auto-controls. Servo Control Systems will include LOS stabilization to an accuracy of 10 μ rad. Photonics includes EO tracking/guidance system based on optical correlation techniques, Helmet mounted display using wave-guide HOE, EO sensor using IO chips, Real-time imaging system through turbulent media. Optical Designs include design of light weight optical systems using GRIN/Binary optics. Special attention is being given to the development of non-linear materials, lasers, IR transmitting materials, thermal sensors, electro-optical devices and transducers, within the country.

Some of the identified focal areas for R&D include :

(a) Photonic Devices

- Optical amplifiers for night vision communication.
- Associated memory devices using neural network for recognition of targets.
- Correlator, convolver, pulse compressor and tuneable filters for signal processing.
- Gallium Arsenide based integrated optical components such as phase-shifters, modulators.
- A to D converter for optical computing applications.
- Distortion free optical recognition.

(b) Photonic Materials

- Laser host materials such as Nd, YAG, Er YAG, CNGG, Alexandrite, Ti Sapphire, Nd Glass.
- Laser non-linear materials such as Lithium Nichate, KTP, BBO, LBO for parametric devices, BSO, BGO and KNB for OPC applications.
- Organic and polymer materials such as Urea, MNA, POM, etc. for SHG applications, MNA/PMMA for guided wave applications, organic dyes for Q-switching and mode locking applications.
- Semiconductor materials such as GaAs, CdTe, CdZnTe, MCT, etc.
- IR materials such as ZnS, ZnSe and Chalcogenide glasses for IR optical components.

(c) Photonic Technologies

- OPC techniques
- Diode laser pumping for solid state lasers
- Optical parametric oscillator
- Er doped passive fibre optical amplifiers
- Real-time optical processing
- Integrated optical waveguide technology
- Holographic optical elements

(d) Sensors

- Optical & IR sensors and thermal imagers for IR detection and thermal imaging.
- Fiber optic sensors , Fiber Optic gyros (FOGs) and Ring-Laser gyros (RLG)
- Multi-spectral and multi-mode homing seekers

5. CONCLUSION

Advances in Photonics technology holds great promise for the performance enhancement of guided missile systems. Realising this potential, the Indian Defence R&D identified Photonics as one of the high priority areas for the research and development. In this context, this paper discussed the various important developments in Photonics and highlighted some areas related to guided missiles. It is clear from the above discussions that Photonics is a great force multiplier for guided missile technology. This paper also briefly outlined the Indian scenario in the area of Photonics and the thrust areas for R&D. With an established core competence in space, missile and nuclear technologies, and information technology, India is poised for greater technological advancement through the synergistic growth of Photonics and guided missile technology.

ACKNOWLEDGEMENT

The author gratefully acknowledges the contributions of several specialists from various DRDO laboratories, projects and partner organisations for their help in evolving the technology vision 2010 for DRDO, identifying the thrust areas in many critical technological areas including Photonics. This paper draws upon those inputs and highlighted some of these areas relevant to the guided missiles.

REFERENCES

1. *Technology Vision 2020*, Technology Information, Forecasting and Assessment Council (TIFAC), New Delhi
2. *Technology Vision 2010 for DRDO*, internal report of Defence Research & Development Organisation, New Delhi
3. R.S. Balcerak, "Uncooled IR imaging: technology for the next generation", *Infrared Technology and Applications XXV*, Proceedings of SPIE, Vol. 3698, USA, 1999
4. R.R. Shannon, "Overview of conformal optics", *Window and Dome Technologies and Materials VI*, Proceedings of SPIE, Vol. 3705, USA, 1999
5. Jeffrey A. Sloan and Donald W. Small, "Design and fabrication of a miniaturized optical correlator", *Optical Engineering*, , Vol. 32, No.12, pp. 3307-3315, 1993
6. Keith E. Drundin, "Fiber Optic Sensors: Smart Technology for Safety", *Photonics*, pp. 106-107, January 1996.
7. Deborah Jackson, *A Structural Approach to the Photonic Processor*, RAND Note N-3399-RC

Keynote Paper

Recent progress of photonic device research

Kohroh Kobayashi

Research and Development Group, NEC Corporation

4-1-1, Miyazaki, Miyamae-ku, Kawasaki, 216-8555 Japan

ABSTRACT

Application of optoelectronics technologies to communication has come to a transition from point-to-point transmission to photonic backbone networks. This paper reviews recent progress of photonic device research with emphasis on the key technologies concerning this transition. Among them are multi-channel WDM and photonic switching. Photonic integration is coming a reality on monolithic as well as hybrid scheme.

Keyword: photonic device, photonic backbone networks, photonic integration, WDM, photonic switching

1. INTRODUCTION

The history of optical communication technologies can be recognized as a history to meet the demand for the higher traffic capacity and longer transmission distances in global communication networks. In recent ten years, the tendency has become much clearer with the explosion of internet, intranet and/or IP-based data communication. Research and development activities started with technologies for higher data speed, longer repeater spacing in trunk transmission lines in early 1970's. They have been continuing over 30 years. The efforts are now turning toward more efficient, flexible and reliable photonic backbone networks. Photonic device research has supported and sometimes guided their progress. This paper reviews recent progress of photonic device research with emphasis on their contribution to communication networks and future network backbones.

2. PROGRESS OF OPTICAL COMMUNICATION TECHNOLOGY

As a measure to indicate the progress of optical transmission performance, products of the transmission bit-rate and the repeater-less transmission distance are plotted against time(year)¹ in Fig. 1. The bit-rate distance products are classified by the key technologies by which the most excellent performance has been achieved in each time frame. This chart clearly shows that the performance saturation has overcome by new technologies. Such situations have kept throughout the time since the optical fiber communication systems have appeared at least experimental results are concerned.

Since the advent of Erbium-doped fiber amplifiers, the repeater-less transmission distance has expanded drastically. In addition to the remarkable increase of the repeater-less transmission distance by EDFA, multi-channel wavelength division multiplexing (WDM) has come into existence in 1990's. The channel number in experiments have increased from few to 50- over 100²⁻⁵. The bit-rate for each channel has also increased to 10-100Gb/s, which pushed forward further the bit-rate distance products toward over 10⁶ Gb/s km. For the bit-rate beyond around 40Gb/s, all optical signal processing such as optical multiplexing and demultiplexing becomes necessary.

With the use of the high speed and multi-channel WDM technologies, point-to-point transmission throughput has reached to terabit-per-second level. Research targets have moved toward the use of photonic technologies in the network nodes in order to build efficient, flexible and reliable networks. Figure.2 shows a rough image of photonic networks, where photonic technologies are applied to both transmission and node functions. Photonic devices have supported and sometime guided such a progress of photonic networks. Important functions of the nodes and main photonic devices are described in Fig.2. Optical cross connects (OXC) are expected to secure the network reliability by rerouting and reconnecting the transmission

Correspondence: Email: kobayasi@rdg.cl.nec.co.jp, Telephone: +81-44-856-2004; Fax: +81-44-856-2049

line in case of breakdown or failure of transmission. These functions are extremely important for networks with ultra high throughput. In the network nodes in a big city, a huge amount of information signals are coming down from and going up to the network transmission lines. Optical add-drop multiplexing (OADM) is expected to make the signal handling easier in the high speed region beyond the pure electronics can treat.

At the transition from 1.5 μm single mode fiber (SMF) systems to 1.5 μm EDFA optical fiber amplifier systems(Fig.1), the device research has moved from simple isolated devices to integrated devices. The integration includes monolithic and hybrid schemes.

3. PHOTONIC INTEGRATION

A term "integration" will easily induce us an image of silicon microelectronics, where huge number of transistors, capacitors and resistors are integrated on a single chip. Photonic integrated devices are still in a preliminary stage and just began to be used in practical systems. The situation of silicon microelectronics is far beyond that of optoelectronics from the view point of integration scales. We, working in the field of photonic device research, can study many things from the history of microelectronics. Under this understanding, comparison is made on the progress between microelectronics and optoelectronics. Important events for both electronics regions are depicted in Fig. 3. In microelectronics, thirty years after the birth of transistors has enabled the full popular use of silicon integrated circuits. On the other hand, thirty years after the birth of semiconductor lasers does not produce such a large scale integration. The situation is partly because that optoelectronics has been developed mainly for signal transmission, while microelectronics has been developed mainly for signal processing and storing.

For photonic integration, integrated element number may not be a unique importance. There are two key directions for photonic integration, i.e., integration of functions and integration of many elements (integrations of "numbers"). Main photonic integrated devices are mapped in Fig.4. For comparison, the typical IC's in microelectronics are also described near each axis, i.e., CPU/MPU for function axis and DRAM for number axis. Integration of function in photonic devices means to realize higher performance and higher functionality by integrating elements with a different function. The typical examples are modulator integrated light sources, spotsizer converter integrated light sources, and photonic terminal devices or photonic network unit devices where a lightwave transmitter and receiver are integrated. The element number for this direction is very small, i.e. two to ten. The most important advantage of the photonic integration in this direction will be reduction of connection point number, which results in the fabrication cost reduction and reliability increase. For example, in case of a combination of light source and an external modulator, optical connection numbers are reduced from three to one by photonic integration as shown in Fig. 5.

4. MONOLITHIC PHOTONIC INTEGRATION

4.1. Selective MOVPE Crystal Growth

For monolithic photonic integration, crystal growth is required to fabricate semiconductor structures with layers with a desired bandgap energy or a desired refractive index in the desired position on a semiconductor wafer. So far, "cut and paste" method has been applied to make monolithic photonic integration. Complicated processes with many number of crystal growth is likely to meet a severe problem of device yield. As a new crystal growth method for monolithic integration, a narrow stripe selective MOVPE method has been developed⁶. In the selective MOVPE technique, growth enhancement occurs in between the patterned masks as shown in Fig. 6. The growth rate and compositional ratio between In and Ga varies with the mask width. They are predominantly attributed to lateral gas phase diffusion of metalorganic species. By changing the mask width from 4 to 30 μm , the grown InGaAsP stripe layer's composition changes from 1.28 μm to 1.54 μm in photo-luminescence peak wavelength. Thickness enhancement phenomena can be effectively applied to grow a tapered stripe structure by changing the mask width gradually.

4.2. Modulator Integrated Light Sources

A most important application of bandgap energy control in selective MOVPE technique is to monolithically integrate an external modulator with a single frequency DFB laser diode(LD). Such a combination is a key light source for high speed and long distance optical fiber transmission. A structure of a modulator integrated DFB LD for 10-Gb/s systems is shown in Fig. 7⁷. In order to increase the bandgap energy of the modulator part by about 70nm in wavelength, the patterned mask width for the modulator part was set narrower by about 12 μm than that for DFB laser diode part. To reduce the unwanted capacitance, semi-insulating InP doped with iron was overgrown on the active and modulator stripe. The chip was packaged with a GaAs heterojunction FET driving IC. A receiver module was also developed by installing a superlattice avalanche

photodiode (APD)⁸ and a GaAs pre-amplifier IC in a single package, as shown in Fig.8. Transmission experiments have been done using the transmitter and the receiver modules. A receiver sensitivity as high as -26.2 dBm was observed at 10 Gb/s. The sensitivity degradation penalty after 80km transmission was 1.7dB⁹.

4.3. Spot-size Converter Integrated LD/OSA

High coupling efficiency between an LD and an optical fiber or an optical waveguide without lens or without precise adjustment are indispensable for low cost module fabrication. This is extremely important to make full use of optoelectronics not only to trunk networks but to access networks or to interconnections. By applying the attractive feature of thickness taper formation of selective MOVPE technique, it is fairly easy to integrate spot-size converter (SSC) in a laser diode. Fig. 9 shows a structure of SSC-LD¹⁰. The mask width is narrowed from 50 μm for LD part to 5 μm for SSC. The narrower mask width leads to less growth enhancement in the stripe window in between the masks. An output beam with a circular cross-section was obtained and lens-free coupling efficiency of -2.8 dB was observed. Due to the smooth transition from LD to SSC achieved by selective MOVPE technique, high performance was realized comparable to that of LD without SSC.

The same technique was applied to semiconductor optical amplifier (SOA)¹¹. SOA is a key element for a gate switch for optical matrix switch. The required features are high gain, high saturation power, high extinction ratio and ease of coupling with a waveguide or a fiber. Low reflectivity at the facet is necessary for the high performance. SSC integration will solve the coupling issue. Three types of SSC-SOA gates were developed¹². Their active and SSC stripe configurations are shown in Fig. 10. The S-shaped (b) and angled facet (c) waveguide structure provide a higher gain and a higher extinction ratio compared with those of straight waveguide structure(a). A fiber-to-fiber gain of as high as 20 dB and an extinction ratio as high as 70 dB were obtained. These gate chips were integrated with planar lightwave circuits (PLC's)¹² in a hybrid fashion, as shown later.

4.4. Multi-wavelength Light Sources

A configuration of transmitter for multi-channel dense WDM systems is shown in Fig. 11. Among the elements depicted in Fig. 11, many possibility can be considered to integrate. However, state-of-the-art technology does not allow to integrate such elements on a single chip to realize a high performance WDM transmitter. At present, many modulator integrated single frequency light sources with a different wavelength connected through a fiber to a WDM multiplexer and wire-connected to an electronic driving circuit will be most promising. Bandgap energy control by selective MOVPE technique was effectively applied to fabricate such a light source. By designing the mask pattern properly, forty modulator integrated DFB LDs with a wavelength ranging from 1526nm to 1594nm were fabricated on a single 2 inch wafer¹³. The wavelength region covered almost all of the expanded erbium-doped fiber amplifier gain bandwidth. These results demonstrate the possibility of low cost fabrication of dense WDM light sources and to open the future integrated WDM light sources. An array of LDs with a different wavelength will be attractive as a stand-by light source for dense WDM systems or as a wavelength tunable light source for wavelength selective add-drop multiplexing systems. Densely arrayed LDs with individually controlled lasing wavelengths were developed by applying again selective MOVPE technique. Multi-wavelength microarray LD¹⁴ showed the possibility of realizing wavelength selective light sources with wavelength range of larger than 100 nm in a very limited space.

5. HYBRID PHOTONIC INTEGRATION

A combination of semiconductor active elements and passive waveguide circuits have attracted a great interest from view points of large scale integration. Planar lightwave circuits provide a good platform to make an optical functional devices such as optical matrix switches, optical transmitter receiver, optical add-drop multiplexers and many other photonic devices. When compared with a semiconductor waveguide, a glass waveguide has advantages on transmission loss, fabrication cost and large circuit size. Hybrid integration technologies are attractive to realize a fairly large scale photonic devices/circuits.

5.1. Optical Matrix Switches

Among many photonic functional devices are optical matrix switches which can cope with the node functions such as switching and rerouting. SOAs have advantages over other switching elements on their high extinction ratio, high switching speed and high optical gain. In Fig. 12, a schematic of the hybrid 4x4 optical matrix switch module structure is shown¹⁵. Four 4-ch SOA gate arrays fabricated by selective MOVPE technique are installed on a PLC platform in which 4:1 combiners and 1:4 splitters are formed by CVD method. The SOAs have a monolithically integrated spot-size converter, which expanded significantly the alignment tolerance. They were mounted and self-assembled by flip-chip manner using

surface tension of a solder bump. Input and output fibers were also self-aligned and fixed in V-grooves made on a Si-substrate. The fiber-to-fiber insertion loss, its polarization dependence, and extinction ratio were 5-9 dB, 0.5 dB, and 40 dB, respectively. High speed switching performance was confirmed through 10-Gb/s photonic cell switching demonstration.

5.2. Optical Network Units

Hybrid integration scheme was also applied to optical network units in ultra-wideband access systems, called Gigabit-To-The-Home(GTTH)¹⁶. Integration is expected to realize a compact transmitter/receiver module. It is also expected to achieve high-volume fabrication with low cost if required. A prototype network units with 2.5-Gb/s (@1.5 μ m) up-link and 156-Mb/s (@1.3 μ m) down-link capability was realized by combining a PLC platform with a Y-branch splitter, a 1.3 μ m Fabry-Perot LD for a up-link transmitter, a super-lattice APD for a down-link receiver and one-chip Si receiver IC in a single module¹⁷ as shown in Fig. 13. When combined with a high power LD for 2.5-Gb/s downlink transmission, the developed PLC module enables a 30 dB link loss budget. This module can be applied to ultra-broadband optical access systems.

6. PHOTONIC DEVICE RESEARCH TOWARD NEXT GENERATION NETWORK

Next generation information network has a photonic backbone, which will be constructed on the basis of multi-channel WDM. The photonic backbone will handle a huge amount of information traffic, beyond tera-bit-per-second, and will deliver mega-bit to giga-bit-per-second information to homes or offices. Photonic integrated devices/circuits described above will play an important role to realize such a photonic backbone. Further extensive effort is expected to photonic device research for both transmission and network nodes.

For more flexible and efficient network nodes, add-drop functions are desired to be realized by photonics. Optical add-drop multiplexers (OADMs) were developed by integrating monolithically arrayed waveguide gratings (AWGs) and optical switches in a PLC platform. An A WG-optical switch combination will have a possibility of realizing a variety of functions on WDM based photonic backbones. In addition to glass/Si material systems widely used in PLCs, semiconductors as well as optoelectronic non-linear crystals such as LiNbO₃ will also be very attractive for photonic integrated functional devices. Photonic approach will allow us to go beyond the speed limit of electronics. This provides a good opportunity to increase the channel capacity per wavelength over 40-Gb/s. Demultiplexing of 40-Gb/s signals into 10-Gb/s signals was successfully demonstrated using mode-locked semiconductor lasers in which a saturable absorber was integrated monolithically¹⁸. All-optical switches were developed using symmetric Mach-Zehnder and polarization discriminating symmetric Mach-Zehnder configurations¹⁹. Possibility of demultiplexing Tb/s signal by these all-optical switches were shown in preliminary experiments.

Photonic device research will continue their efforts to explore the wide bandwidth of lightwave. Photonic integration technologies will be a key to make their full use a reality.

ACKNOWLEDGEMENTS

The author would like to thank Drs. I.Mito, K.Emura, S.Sugo, T.Torikai and M.Fujiwara and their colleagues for providing the latest results.

REFERENCES

1. R.Linke, OFC'88, Tutorial, TuE1, 1988. His chart was modified and added additional data after 1988 by the author.
2. H.Onaka, H.Miyata, G.Ishikawa, K.Otsuka, H.Ooi, Y.Kai, S.Kinoshita, M.Seino, H.Nishimoto, and T.Chikama, OFC'96, PD19 (1996)
3. A.H.Gunack, A.R.Chraplyvy, R.W.Tkach, J.L.Zyshind, J.W.Sulhoff, A.J.Lecero, Y.Sun, R.M.Jopson, F.Forghieri, R.M.Derosier, C.Wolf, and A.R.McComic, OFC'96, PD-20(1996)
4. T.Morioka, H.Takara, S.Kawanichi, O.Kamatani, K.Tagiguchi, K.Uchiyama, M.Saruwatari, H.Takahashi, M.Yamad, T.Kanamori, and H.Ono, OFC'96, PD-21(1996)
5. Y.Yano, T.ono, K.Fukuchi, T.Ito, H.Yamzaki, M.Yamaguchi, and K.Emura, ECOC'96, ThB3.1 (1996)
6. T.Sasaki, M.Kltamura, and I.Mito, "Selective metalorganic vapor phase epitaxial growth of InGaAsP/InP layers with bandgap energy control in InGaAs/InGaAsP multiple-quantum well structures," J.Crystal Growth, 132, pp.435-443, 1993
7. Y.Furushima, K.Kudo, Y.Muroya, Y.Sakata, Y.Inomoto, K.Fukuchi, M.Ishizaka, and M.Yamaguchi, OFC/IOOC'99, WH2-1, pp.131-133, 1999

8. K.Taguchi, K.Makita, I.Watanabe, M.Tsuji, M.Hayashi, and T.Nakata, "Superlattice avalanche photodiodes for optical communications", *Optical and Quantum Electronics*, **30**, pp.219-238, 1998
9. I.Watanabe, M.Ishizaka, N.Yoshida, M.MORie, M.Fujii, S.Wada, K.Numata, K.Fukushima, J.Shimizu, T.Maeda and M.Yamaguchi, "1--Gb/s High Performance Transmitter and Receiver Modules Using Modulator-Integrated DFB-LD, Superlattice-APD, and GaAs HJFET-ICs," to be presented at APCC/OECC'99 at Beijing, 1999
10. Y.Furushima, Y.Sakata, Y.Sasaki, H.Yamazaki, K.Kudo, Y.Inomoto and T.Sasaki, *Electron. Lett.*, "1.3 μ m spot-size converter integrated ASM-BH LDs with low operating current and high coupling efficiency," **34**, pp.767-768, 1998
11. T.Tamanuki, S.Kitamura, H.Hatakeyama, T.Sasaki, and M.Yamaguchi, *IEICE Trans. Electron.*, "Spot-size-Converter Integrated Semiconductor Optical Amplifiers for Optical Switching Systems," **E82-C**, pp.379-386, 1999
12. M.Kawachi, *Optical and Quantum Electronics*, **22**, pp.391-416(1990)
13. K.Kudo, M.Ishizaka, T.Sasaki, H.Yamazaki, and M.Yamaguchi, *IEEE Photonics Tech. Lett.*, "1.52-1.59- μ m Range Different-Wavelength Modulator-Integrated DFB-LD's Fabricated on aSingle Wafer," **10**, pp.929-931, 1998
14. K.Kudo, Y.Furushima, T.Nakazaki, and M.Yamaguchi, "Multiwavelength microarray semiconductor lasers", *Electron. Lett.*, **34**, pp.1-2, 1998
15. T.Kato, J.Sasaki, T.Shimoda, H.Hatakeyama, T.Tamanuki, S.Kitamura, M.Yamguchi, T.Sasaki, K.Komatsu, M.Kitamura, and M.Itoh, *IEICE Trans.Electron.*, "Hybrid Integrated 4x4 Optical Matrix Switch Module on Silica Based Planar Waveguide Platform," **E82-C**, pp.305-312, 1999
16. M.Shibutani et. al., *OECC*, pp.314-315, 1998
17. S.Shioir, M.Soda, A.Goto, N.Kitamura, I.Watanabe, and M.Shibutani, *OFC/IOOC'99*, ThN1-1, 1999
18. H.Kurita, I.Ogura, and H.Yokoyama, *IEICE Trans. Electron.*, "Ultrafast All-Optical Signal Processing with Mode-Locked Semiconductor Lasers," **E81-C**, pp.129-139, 1998
19. S.Nakamura, Y.Ueno, and K.Tajima, *IEICE Trans. Electron.*, "Femtosecond Operation of a Polarization-Deiscriminating Symmetric Mach-Zhender All-Optical Switch and Improvement in Its High-Repetition Operation," **E82-C**, pp.327-334, 1999

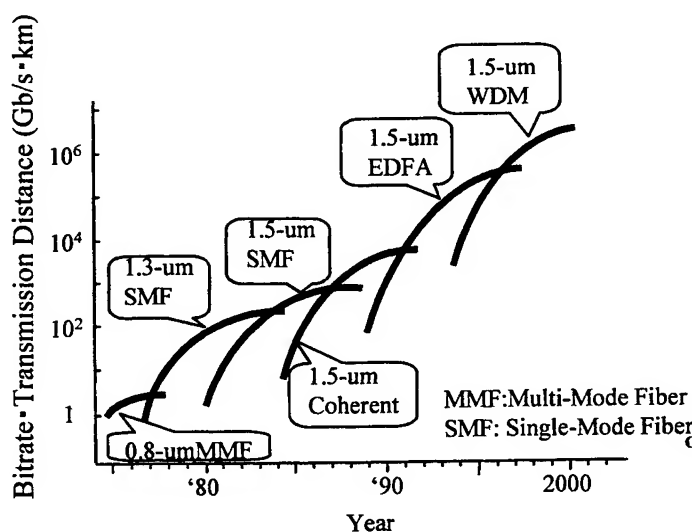


Fig.1 Progress of optical communication systems

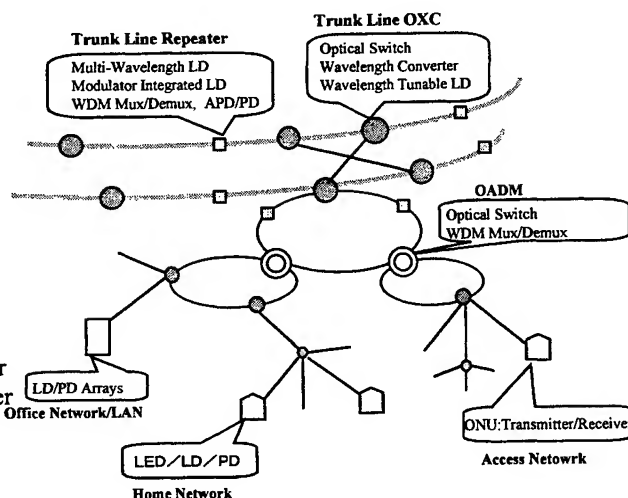


Fig. 2 Photonic backbone networks

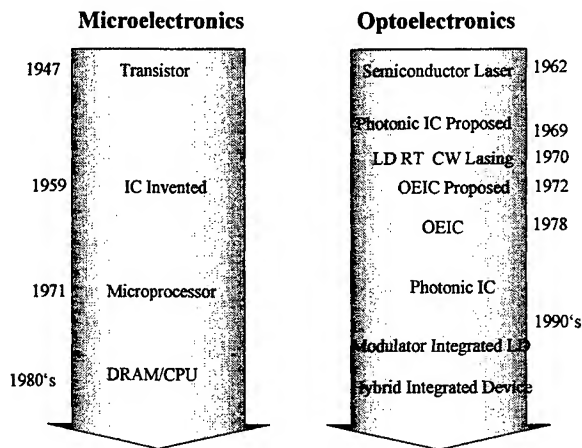


Fig. 3 Historical comparison between microelectronics and optoelectronics

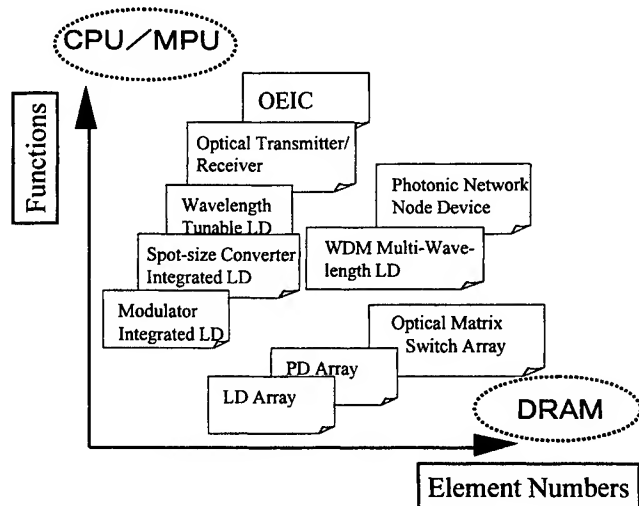


Fig. 4 Two main directions for photonic integration

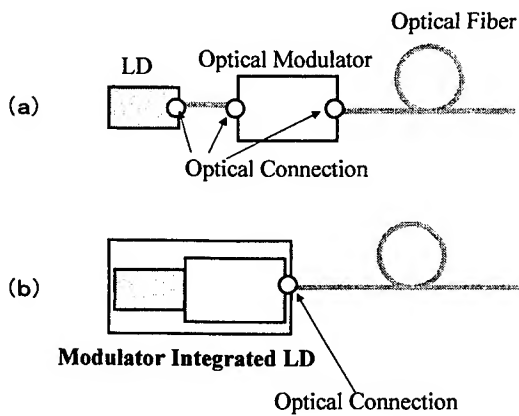


Fig. 5 Advantage of photonic integration

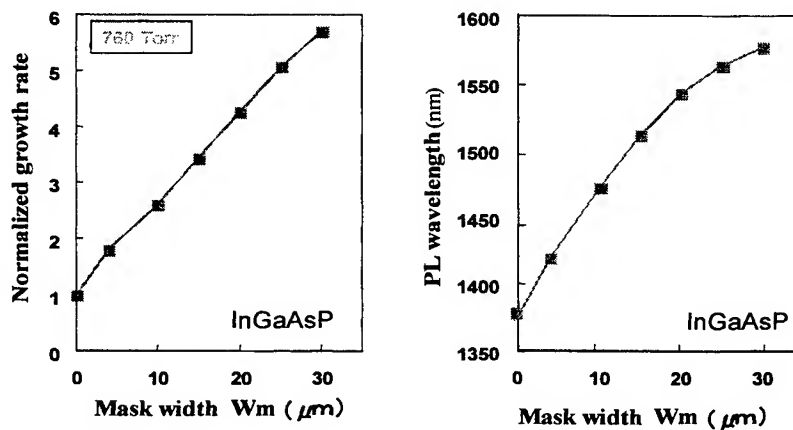
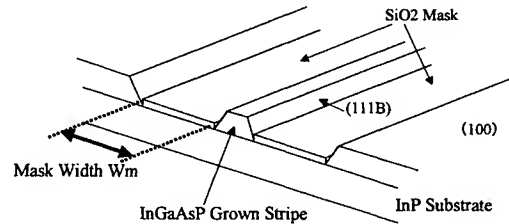


Fig. 6 Growth rate enhancement and compositional change with mask width in selective MOVPE technique

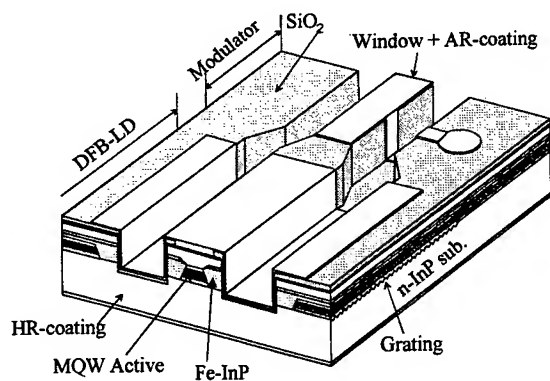


Fig. 7 Modulator integrated DFB-LD

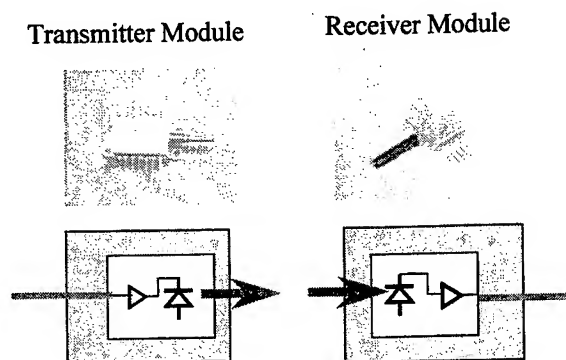


Fig. 8 Transmitter and receiver modules for 10-Gb/s transmission

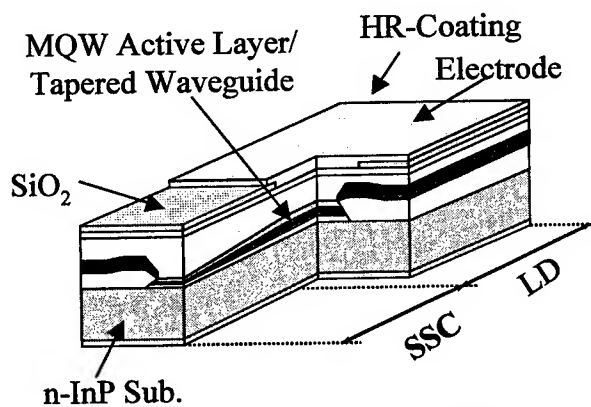


Fig.9 Spot-size converter integrated LD

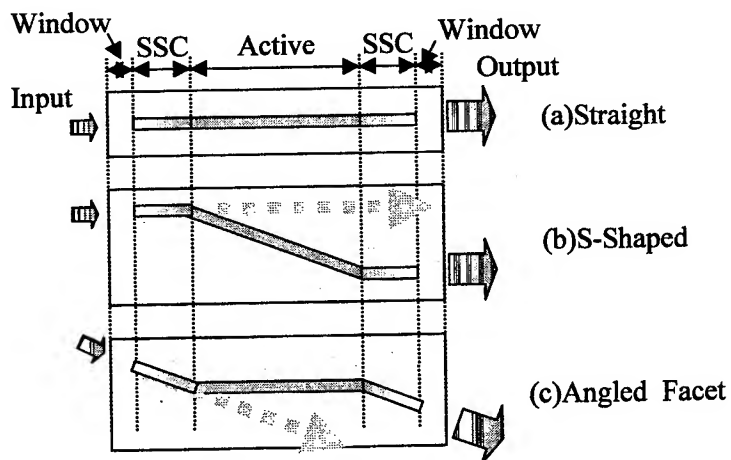


Fig. 10 Spot-size converter integrated semiconductor optical amplifier (SOA)

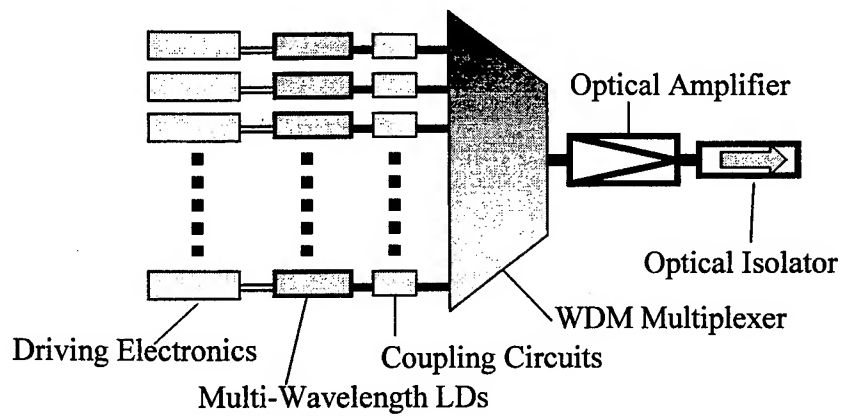


Fig. 11 A transmitter configuration of multi-channel dense WDM systems

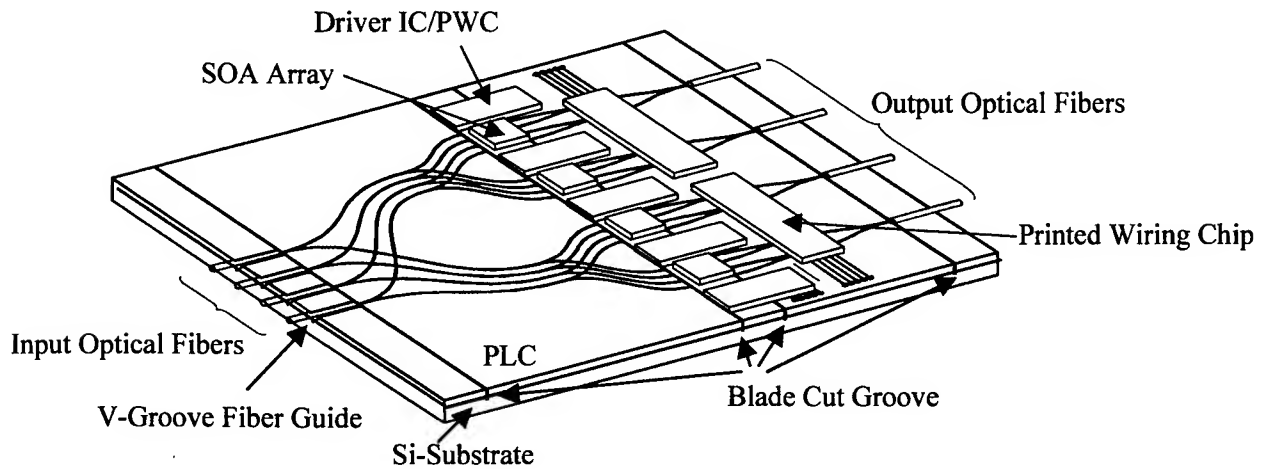


Fig. 12 A schematic of hybrid 4 x 4 optical matrix switch

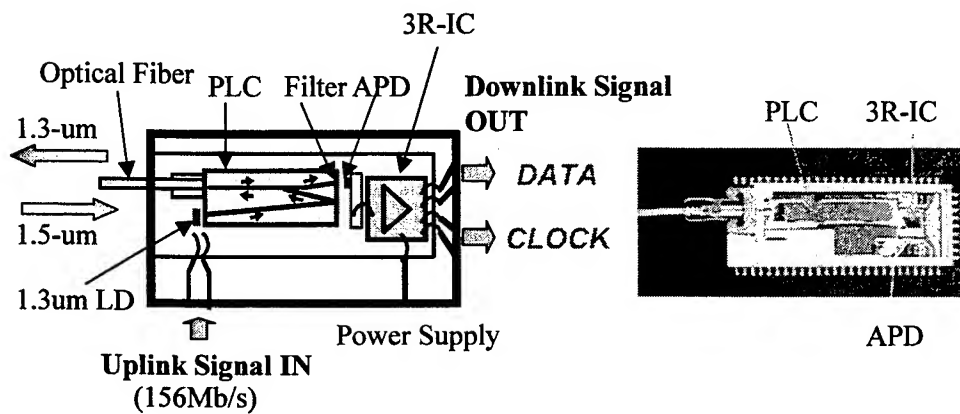


Fig. 13 Optical network unit (ONU) for ultra-wideband access systems

SESSION 1

High-Power Semiconductor Lasers

Measurement of mounting-induced strain in high-power laser diode arrays

J. W. Tomm^{* a}, R. Müller^a, A. Bärwolff^a, D. Lorenzen^b

^a Max-Born-Institut für Nichtlineare Optik und Kurzzeitspektroskopie,
Max-Born-Str. 2 A, D-12489 Berlin, Germany

^b Jenoptik Laserdiode GmbH, D-07745 Jena, Germany

ABSTRACT

Thermally induced strain caused by device packaging is studied in high-power semiconductor laser arrays by a novel non-invasive technique. Measurements with intentionally strained laser array devices for 808 nm emission reveal spectral shifts of quantum-confined optical transitions in the optical active region. These shifts by up to 10 meV serve as a measure for strain and are compared with model calculations. We demonstrate that different packaging techniques cause different packaging-induced strains. We also show that the packaging-induced strain portion, which gets transmitted through the solder material, differs for different packaging technologies. An intentionally strain-reduced packaging technique is shown to transmit about *one quarter* of the potential packaging-induced strain towards the optical active layer, whereas another packaging technique, which provides highly reliable 'single-chip' devices is found to transmit *about half* of the potential amount. Spatially resolved measurements demonstrate strain gradients within the devices. Also temporal strain evolution is monitored. We show that 'the burn-in' is accompanied by strain accumulation whereas for long-term operation strain relaxation occurs.

Keywords: high-power diode laser, packaging induced strain, strain homogeneity, photocurrent,

1. INTRODUCTION

High power diode lasers such as 'cm-bar arrays' are important for a wide range of applications, e.g. as pump sources and tools for material processing. The 'p-down packaging', i.e. the direct mounting of the epitaxial layer sequence on a heat spreader ensures sufficient thermal properties, however, in such a geometry, mechanical strain of the active region, being separated by only 2 μm from the solder between heat sink and laser structure, represents an important issue. Thus for this kind of devices the packaging technology is of crucial importance and is to be steadily checked. This report focuses on an adequate strain measurement technique that is applicable to packaged diode lasers. The principle is straightforward and easy to be understood. Our strain sensor is the laser structure itself. Within the Quantum Well (QW) there are a number of allowed optical transitions, the lowest of them ($1e \rightarrow 1hh$; e-electron, hh-heavy hole) being responsible for laser emission. These transition energies are known to be easily measured by absorption spectroscopy, that, however, is hardly done in a packaged device. Thus we replace the absorption measurement by the measurement of the Photo-Current (PC) spectrum of a laser structure. In the spectral region of the QW transitions PC spectra display a comparable spectral shape as the absorption coefficient and consequently the relevant transition energies can be determined.¹ Almost the same holds for the absorption edge of waveguide of the laser structure, that is expected to be affected by the packaging technology in the same way as the QW. Now the spectral shifts of the QW transitions as well as of the waveguide absorption edge serve as independent strain sensors.²

* Correspondence: Email: tomm@mbi-berlin.de; <http://www.mbi-berlin.de>; Telephone: +49-30-63921453; Fax: +49-30-63921459

Thus *packaging-induced strain modification* can be measured and the deformation of the semiconductor lattice (misfit parameter $\Delta a/a$, where a is the lattice constant of the respective epitaxial layer within the structure) can be *quantified*. This quantification of $\Delta a/a$ for layers within a packaged device represents the central idea of this report. The most promising way of measuring $\Delta a/a$ in a semiconductor lattice is to do X-ray diffraction. This straightforward way, however, demands direct access to the semiconductor lattice that is to be analyzed. Thus this kind of measurement is hardly done in p-side down mounted devices, that are additionally anti-reflection (AR) coated at their front facet.

Thus there is hardly another no other way than to monitor the strain-induced changes of the semiconductor band structure. There has been done a lot of work on such strain measurement in semiconductors and semiconductor QW's, that are reviewed for III-V materials e.g. by Jain et al.³ Most of the analytical techniques rely on polarization resolved measurements. Among others electroluminescence (EL) line scans are used as measure for strain distributions in devices.

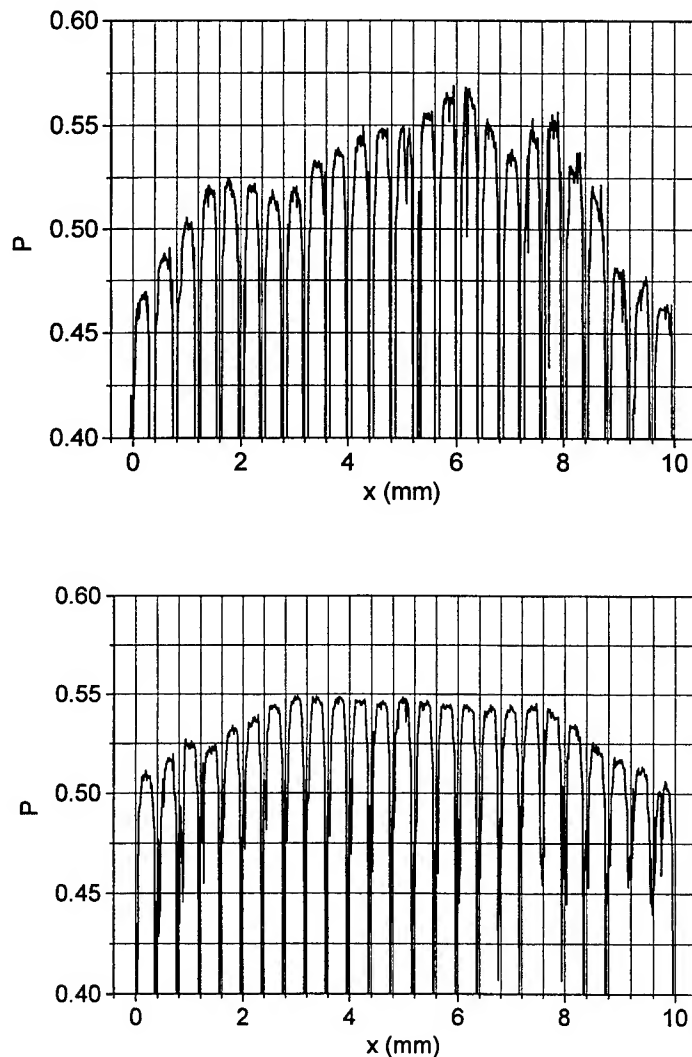


Fig. 1 Degree of polarization versus local position calculated from TE and TM EL line scans from fresh (top) and aged (bottom) 'cm-bar' devices with 25 emitters. The second one was operated at 25 °C in constant current mode with an operation current of 20 A.

Figs. 1 are examples for strain estimations based on polarization resolved measurements. Here the degree of polarization (P) was determined from TE and TM resolved EL data by using

$$P = (I_{EL}^{TE} - I_{EL}^{TM}) / (I_{EL}^{TE} + I_{EL}^{TM}) \quad (1)$$

The I_{EL} are the EL intensities and TE and TM refer to the direction of the E-vector perpendicular and parallel to the growth direction of the laser structure, respectively. Both devices are prepared from material of the same epitaxial run and mounted with In-solder at $T=160^\circ\text{C}$ on Cu heat sinks (resulting in compressive strain). This strain is expected to show its maximum in center of the device. Thus the hh-lh split should be increased there resulting in a higher value of P. Even this behavior is seen from Figs. 1. Since both devices have been prepared by the same technology the weaker P-modulation found for the aged device might be interpreted as relaxation of the packaging-induced strain.

However, such polarization resolved measurements imply disadvantages. The main one is that P is not exclusively determined by the strain but also by the quantum-confinement and waveguide effects. These effects determine the hh-lh split and the packaging-induced strain provides only a small modulation. Furthermore, there is no realistic way to get information about $\Delta a/a$ out of the P data. Thus we can conclude, that polarization resolved measurements have a certain potential for the estimation of strain distributions, however, quantitative measurements seem to be accompanied with major uncertainties.

Our new solution, that will be outlined in this report, also utilizes the strain dependence of the semiconductor band structure, however, exclusively spectral positions of optical transitions are taken into account. Basically we replace an intensity (ratio) measurement by a spectral line position measurement.

2. EXPERIMENTAL

We investigate several sets of 'cm-bars' as well as 'single-chip devices' based on $\text{In}_{0.06}\text{Al}_{0.08}\text{Ga}_{0.86}\text{As}/\text{Ga}_{0.7}\text{Al}_{0.3}\text{As}$ double QW structures grown by metalorganic vapor deposition on n-type GaAs substrates. The $1.5\ \mu\text{m}$ thick cladding layers consist of $\text{Al}_{0.6}\text{Ga}_{0.4}\text{As}$. The DQW region is embedded in an $\text{Al}_{0.3}\text{Ga}_{0.7}\text{As}$ waveguide having a width between 70 and 500 nm on each side. The typically 7 nm wide $\text{In}_{0.06}\text{Al}_{0.08}\text{Ga}_{0.86}\text{As}$ wells are separated by a 10 nm wide $\text{Al}_{0.3}\text{Ga}_{0.7}\text{As}$ barrier. 'Cm-bar' devices typically consist of 25 emitting stripes of $200\ \mu\text{m}$ width separated by $200\ \mu\text{m}$ passive areas (total lateral width 1 cm). The stripe region itself again consists of twenty $4\ \mu\text{m}$ wide sub-stripes. The photon energy of the laser emission of all devices was $\hbar\omega=1.53\ \text{eV}$ ($\lambda=808\ \text{nm}$). 'Single-chip devices' represent basically one of the 25 single emitter segments of a 'cm-bar' (total lateral width $400\ \mu\text{m}$). The most significant precondition for our experiments is excellent lateral homogeneity of the bars and from device to device. This is checked by several tests with unpackaged devices. Comparisons between different individual samples are exclusively done for samples coming from the same epitaxial run. The structures are mounted 'p-side down' on the heat sinks using In- and Au-Sn- based solder materials. For all devices of a given set care is taken to apply exactly the same packaging technique. The soldering temperatures are 160°C and 280°C for In- and Au-Sn- based solder materials, respectively.

In the PC measurement the diode laser device is operated similar to a photo-detector. The electrical signal created by the illumination of the diode laser front facet is taken from the power supply contacts and fed into the detector port of the FT spectrometer, that serves as radiation source and for data processing. The laser device was mounted on an adjustable heat sink ($T=296\ \text{K}$) and the front facet was irradiated by a light spot having a diameter $200\ \mu\text{m}$ to $1\ \text{cm}$. Typical excitation densities are on the order of $60\ \text{mW}/\text{cm}^2$. A reduction of the excitation density by more than four orders of magnitude does not affect the spectral positions of the interband transitions within the QW and the waveguide edge. For comparison a set of experiments with a conventional monochromator and lock-in detection was performed. Except the lower over-all operating efficiency of the dispersive system we do not find any modification of our results.

3. RESULTS AND DISCUSSION

3.1. Determination of Spectral Positions of Optical Transition

In Fig. 2 (top), we present PC spectra of a 'cm-bar'-sample in the spectral region around the fundamental bandgap of the QW. The onset of the spectrum for unpolarized excitation (solid line) is determined by the $1hh \rightarrow 1e$ transition of the DQW at 1.541 eV. The other two spectra were recorded with different linear polarization of the excitation light, namely TE (dashed line) and TM polarization (dotted line). Note the remarkable shift between the absorption edges for TE and TM polarized excitation as earlier demonstrated for absorption spectra in similar geometry.⁴

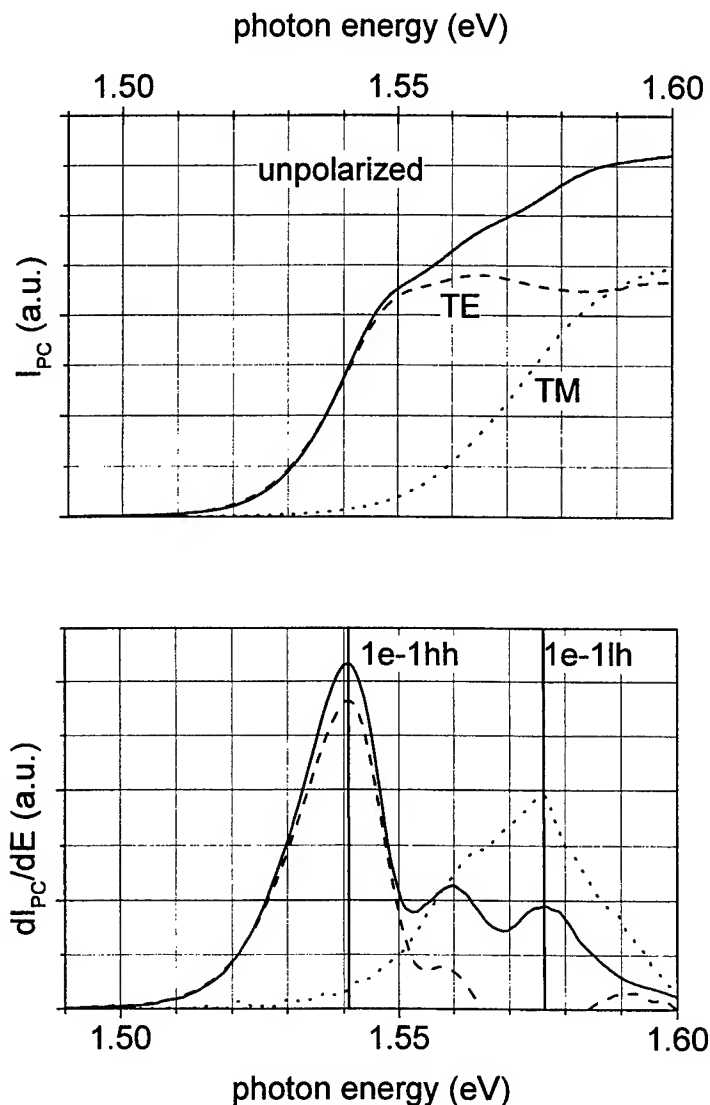


Fig. 2 PC spectra from a 'cm-bar' (top). The dashed line represents the TE PC spectrum and the dotted line marks a TM excited spectrum. The full line represents the spectrum measured with unpolarized light. The spectra at the bottom represent the first derivative of the data presented on top. The relevant optical transitions are marked.

The TM spectrum is dominated by the $1lh \rightarrow 1e$ transition at 1.577 eV. In Fig. 2 (bottom), the first derivatives of the spectra are displayed. We find excellent agreement between the transition energies derived from the PC spectra excited with unpolarized (full line), TE-polarized (dashed) and TM-polarized light (dotted). Thus for further investigation we use exclusively PC spectra excited with unpolarized light.

In Figs. 2 an additional optical transition is visible at about 1.56 eV. The nature of this transition is not cleared up yet. It may be related to the peculiarities of hh-lh mixing in the QW structure such as reported by Collins et al.⁵ Another possible explanation is resonant tunneling. However, this peak appears in spectra of devices having different epitaxial designs. Its influence gets increased if one reduces the 'information depth' of the measurement by tilting the device (cf. section 3.3.). Thus the additional line is likely to be related to the surface.

The same considerations as done for the QW transitions also may be done for the absorption edge of the waveguide at about 1.8 eV. The first derivation dI_{PC}/dE of this 'bulk-like' edge also provides a peak, which shifts in dependence on the external strain. Thus it is used as an additional and *independent* strain sensor. However, there is one peculiarity. Typical packaging-induced strains separate bulk hh- and lh related peaks by only a few meV and consequently they merge into one single peak. Its shift is determined by both shifts of lh- and hh-related peaks. Assuming that both contribute by about the same strength to the derivative spectra as shown in Ref.⁶, the resulting shift is expected to be about the averaged value of both, i.e. each of them determines the line shift in one wing of the line. Accordingly we provide guidance, how to determine 'optical transition positions' from the optical active region, namely the QW and the waveguide. Shifts of these 'optical transition positions' now will be used as measure for that strain contribution, that is caused by device packaging.

3.2. Strain Measurements in Packaged Devices

Now we measure these optical transition positions for devices mounted on different heat sinks materials. Furthermore, we calculate the 'thermal misfit' $\Delta a/a$ expected for the relevant soldering temperatures and heat sink materials from

$$\Delta a/a = \Delta \alpha \times \Delta T \quad , \quad (2)$$

where $\Delta \alpha$ is the difference between the thermal expansion coefficients of the semiconductor and heat sink materials and ΔT is the temperature difference between soldering and ambient temperatures.

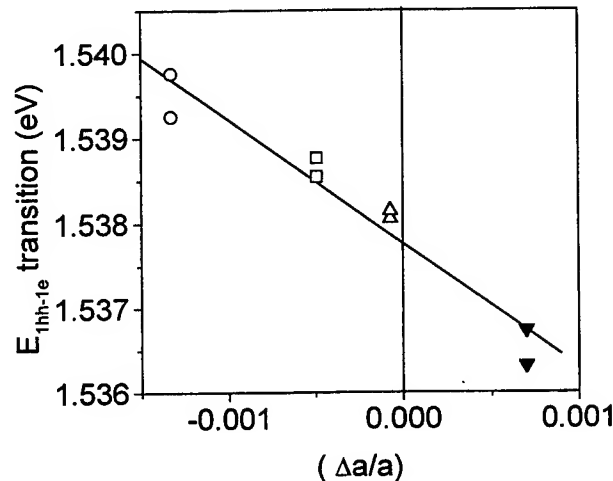


Fig. 3 Spectral position of the $1lh \rightarrow 1e$ transitions in 'cm-bar' devices determined from the first derivative of the PC spectra from 4 sample pairs versus calculated $\Delta a/a$. The full line is a linear least square fit to the data. Open symbols refer to compressive strain whereas full symbols indicate tensile strain. The heat sink materials are (from left to right): Cu, multilayer, Cu-W and diamond.

Fig. 3 shows positions of the 1hh→1e transitions in ‘cm-bar’ devices from 4 sample pairs versus calculated $\Delta a/a$. For estimates with equation (2) we used the following thermal expansion coefficients: $\alpha_{\text{GaAs}}=6.5 \times 10^6 \text{K}^{-1}$, $\alpha_{\text{multilayer}}=10 \times 10^6 \text{K}^{-1}$, $\alpha_{\text{Cu}}=16 \times 10^6 \text{K}^{-1}$, $\alpha_{\text{Cu-W}}=7 \times 10^6 \text{K}^{-1}$ and $\alpha_{\text{diamond}}=1.5 \times 10^6 \text{K}^{-1}$. The devices were soldered at 160°C with In solder. The same procedure was done for the 1hh→1e transitions as well as for the waveguide edge. A second packaging technique, applied to ‘single chip’ devices (Au-Sn solder, soldering temperature 280 °C) was examined in the same way.

Furthermore we calculated the expected shift for the optical transitions in strained QW’s and the bulk edge. Details of these calculations are given in Ref.⁷ As anticipated the experimental values are lower than the calculated shifts. This is due to plastic and elastic strain relaxation within the solder material and possibly the semiconductor (e.g. dislocation creation). Consequently the quotient between experimental slope in Fig. 3 and theoretical value (β , cf. Table I) is smaller than unity and is considered as measure for the ‘strain transmission’ towards the active region.

Table I. Comparison between measured and calculated strain-induced shifts for the three different optical transitions mentioned. Two packaging techniques are examined.

		1hh→1e	1lh→1e	waveguide edge
‘cm-bars’	$dE/d(\Delta a/a)$ (eV)	-1.45 ± 0.15	-2.6 ± 0.5	-1.7 ± 0.5
	β	0.27 ± 0.05	0.21 ± 0.07	0.18 ± 0.08
‘single chips’	$dE/d(\Delta a/a)$ (eV)	-3.0 ± 0.5	-5.7 ± 0.4	-5.5 ± 0.3
	β	0.57 ± 0.12	0.47 ± 0.07	0.60 ± 0.08

The conclusion from Table I is that the packaging-induced strain portion, which gets transmitted through the solder material, differs for different devices and packaging technologies. The intentionally strain-reduced packaging technique with In solder applied to the ‘cm-bars’ is shown to transmit about *one quarter* of the potential packaging-induced strain towards the optical active layer, whereas the second packaging technique, which provides highly reliable ‘single-chip’ devices by soldering them at 280 °C with Au-Sn solder is found to transmit *about half* of the potential amount (cf. row at the bottom of Table I).

3.3. Spatial Strain Distributions and Temporal Strain Evolution

Now we are enabled to measure strain distributions along front facets of ‘cm-bars’ by measuring PC spectra for different local positions along the device. Fig. 4 shows the $(\Delta a/a)$ modification along a 10 mm wide 808 nm emitting ‘cm-bar’ packaged with In solder. $(\Delta a/a)$ was calculated from the position shifts of the optical transitions by using the experimentally determined slopes $dE/d(\Delta a/a)$ for the corresponding sample set (cf. Table I). Since our technique is rather a ‘strain difference measurement’ we had to choose zero. We decided to take the sample edge as zero reference. This does not mean that the sample edge is unstrained. What we show is that packaging increases compression towards the center of the sample and we are able to quantify this increase with the ordinate scale in Fig. 4.

A certain depth resolution can be achieved as well. For this purpose we performed measurements with tilted devices. By tilting the device one can reduce the coupling efficiency into the laser waveguide and thus increases the PC contribution caused by unguided light passing the waveguide only once in a region nearby the surface (several μm). For perpendicular incidence (tilt angle 0°) information from a deeper region (on the order of 50 μm) is expected. A well-pronounced shift is observed which is again converted into a $\Delta a/a$ change. The result is plotted in Fig. 5. There is no clear local assignment, however a strain relaxation towards the laser facet is obvious. Since the laser cavity length is only 600 μm (compared to the 1 cm width) this relaxation is expected to be smaller as compared to the lateral relaxation, that is given in Fig. 4.

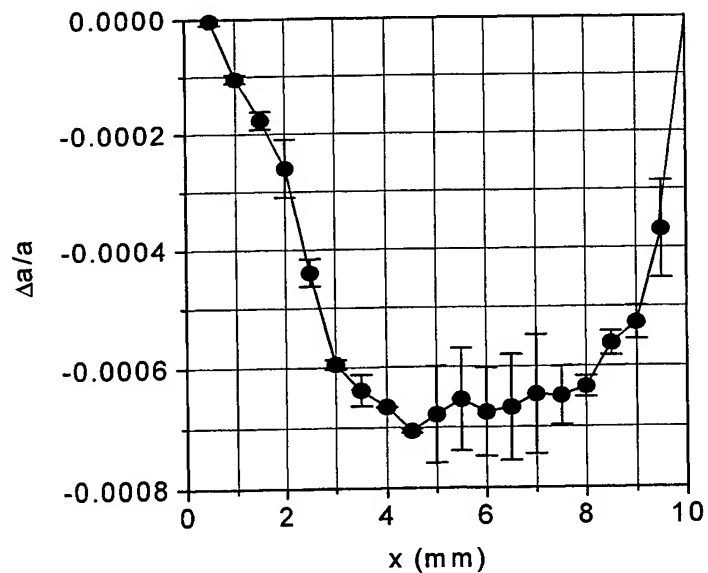


Fig. 4 Misfit parameter *change* ($\Delta a/a$) along a 10 mm wide 808 nm emitting 'cm-bar' packaged with In solder. The compressive strain value at the sample edge, determined by the packaging on the Cu-heat sink was set to zero.

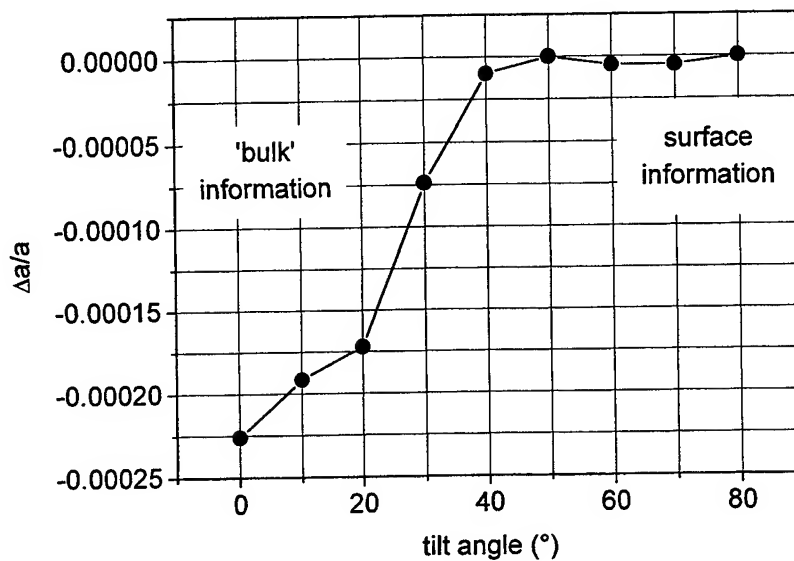


Fig. 5 Misfit parameter *change* ($\Delta a/a$) along a 10 mm wide 808 nm emitting 'cm-bar' packaged with In solder. The compressive strain value close to the partly relaxed surface, caused by packaging on the Cu-heat sink, was set to zero.

As shown in Fig. 6 temporal strain evolution is monitored as well. Up to 200-300 h operation time the particular 'cm-bar' device, which is also compressively packaged on Cu, experiences additional compression. Later strain relaxation appears and the additional compression accumulated during the first hundreds of hours of device operation gets overcompensated. Device manufactures know this rather critical first phase and call it the device 'burn-in'. Optimization of the 'burn in' conditions allows to increase the yield of device fabrication. Again we should mention that the zero strain value at zero hours of device operation does not indicate an unstrained device. This number was freely chosen, however, the $\Delta a/a$ -change after this initial situation are given quantitatively.

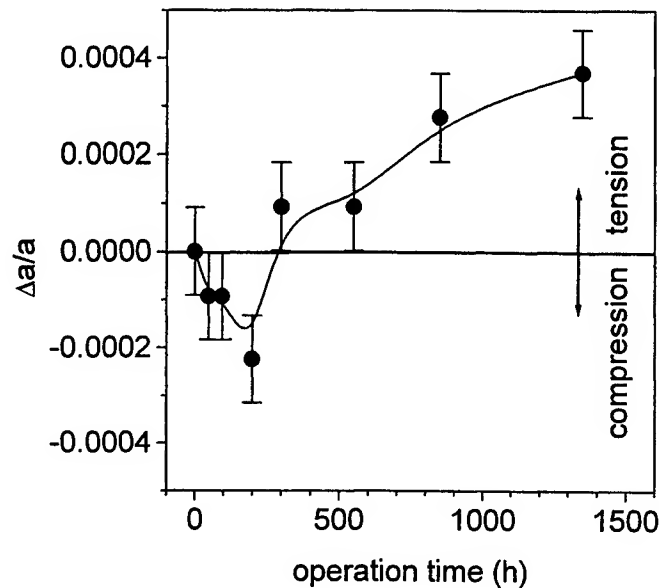


Fig. 6 Misfit parameter change ($\Delta a/a$) in center of an 808 nm emitting 'cm-bar' versus operation time. The initial compressive strain, caused by packaging on a Cu-heat sink was set to zero.

4. SUMMARY

Summarizing we present a novel non-invasive method for quantitative measurements of *strain differences and strain modifications* in laser devices. It takes reference to the spectral positions of the optical transitions within the waveguide of the laser devices. Therefore it crucially relies on sample homogeneity. We demonstrate the applicability to strain analysis in high-power diode lasers such as 'cm-bars'.

The strain-induced shift of interband transitions in the QW active layer as well as the strain-induced shift of the waveguide absorption edge provide *independent* access to sign and absolute value of the packaging-induced strain.

Spatial distributions of strain in high-power diode laser arrays are measured. Strain relaxation at the edges of the 'cm-bar' devices is demonstrated. For the first time we also show a reduction of the packaging-induced strain towards the laser front facet.

We demonstrate that different packaging techniques *reproducibly* cause certain packaging-induced strains. For two packaging architectures we determine the packaging-induced strain portion which gets transmitted through the solder towards the optically active layer. An intentionally strain-reduced packaging technique with In solder applied to the 'cm-bars' is shown to transmit about *one quarter* of the potential packaging-induced strain towards the optical active layer, whereas a second packaging technique, which provides highly reliable 'single-chip' devices by soldering them at 280 °C with Au-Sn solder is found to transmit *about half* of the potential amount.

We present a new experiment which gives insight into the evolution of the strain of the waveguide of high-power laser devices versus aging time. Here a significant discrepancy between the strain evolution during 'burn-in' and regular operation is shown.

The high accuracy, the non-invasive character, the short measurement times as well as the ability to perform measurements even at room-temperature make PC spectroscopy a promising tool for future device characterization and optimization also in other semiconductor devices such as all kinds of diode lasers, light emitting diodes and detectors.

ACKNOWLEDGMENTS

We would like to thank J. Luft, Osram AG Regensburg, and S. Weiß, Fraunhofer-Institut für Zuverlässigkeit und Mikrointegration Berlin, for valuable discussions and S. Schwirzke-Schaaf for expert technical assistance.

REFERENCES

1. J. W. Tamm, A. Jaeger, A. Bärwolff, T. Elsaesser, A. Gerhardt, and J. Donecker, „Aging Properties of High Power Laser Diode Arrays Analyzed by Fourier-Transform Photo-Current Measurements,“ *Appl. Phys. Lett.* **71**, pp. 2233-2235, 1997.
2. J. W. Tamm, R. Müller, A. Bärwolff, T. Elsaesser, D. Lorenzen, F. X. Daiminger, A. Gerhardt, and J. Donecker, „Direct spectroscopic measurement of thermally induced strain in high-power optoelectronic devices,“ *Appl. Phys. Lett.* **73**, pp. 3908-3910, 1998.
3. S. C. Jain, M. Willander, and H. Maes, „Stresses and strains in epilayers, stripes and quantum structures of III-V compound semiconductors,“ *Semicond. Sci. Tech.* **11**, pp. 641-671, 1996.
4. J. S. Weiner, D. S. Chemla, D. A. B. H. A. Haus, A. C. Gossard, W. Wiegmann, and C. A. Burrus, „Highly anisotropic optical properties of single quantum well waveguides,“ *Appl. Phys. Lett.* **47**, pp. 664-667, 1985.
5. R. T. Collins, L. Vina, W. I. Wang, L. L. Chang, L. Esaki, K. v. Klitzing, and K. Ploog, „Mixing between heavy-hole and light-hole excitons in GaAs/Al_xGa_{1-x}As quantum wells in an electric field,“ *Phys. Rev. B*, **36**, pp. 1531-1534, 1987.
6. K. H. Herrmann, J. W. Tamm, and Hessa Al-Otaibi, „Temperature Dependent Carrier Escape from Quantum-Well states in GaAs/GaAlAs Graded Index Laser Structures,“ *Semicond. Sci. Technol.* **14**, pp. 293-297, 1999.
7. J. W. Tamm, R. Müller, A. Bärwolff, M. Neuner, T. Elsaesser, D. Lorenzen, F. X. Daiminger, A. Gerhardt, J. Donecker, „Direct spectroscopic measurement of packaging-induced strains in high-power laser diode arrays,“ *SPIE Proc.* **3626**, 138-147, 1999.

Fabrication and characterization of high power diode lasers

Jürgen Jandeleit¹, Nicolas Wiedmann, Andreas Ostlender, Wolfgang Brandenburg,
Peter Loosen, Reinhart Poprawe

Fraunhofer-Institut für Lasertechnik, Steinbachstraße 15, D-52074 Aachen, Germany

ABSTRACT

High power diode lasers can be used for a lot of applications such as pumping of solid state lasers, direct material processing (for example welding, soldering, annealing) and printing. The successful use of high power diode lasers depends on their high efficiency and reliability in combination with a long lifetime. For a further increase in the quality of high power diode lasers the properties of semiconductor laser bars have to be improved as well as the mounting techniques for these bars onto specially designed heat sinks.

For most applications the electro-optical properties of the high power diode lasers have to be known exactly. Detailed information on the propagation characteristics and the transverse mode distribution of diode laser beams is necessary for the optimization of the overall performance. In addition the electro-optical characterization is a first test for the quality of high power diode lasers. An automated test set-up developed at the Fraunhofer-Institut für Lasertechnik will be presented. The electro-optical data such as threshold current, slope efficiency, center wavelength, spectral width, total conversion efficiency and cw-output power can be measured as a function of driving current as well as the beam divergence angles in fast and slow direction of the high power diode lasers. Different methods to determine the exact divergence angles will be discussed.

Keywords: high power diode lasers, fabrication methods, characterization methods, testing, reliability, divergence angle

1. INTRODUCTION

High power diode lasers serve as small and highly efficient laser-beam sources. Their output power has been increased in recent years.^{1,2,3} Nowadays, the output power of one diode laser bar is sufficient for many applications such as pumping of solid state lasers, direct material processing or printing.⁴ The successful use of high power diode lasers depends on their high reliability in combination with a long lifetime.

The electro-optical properties of high power diode lasers have to be known exactly for most applications. Detailed information on the propagation characteristics and the transverse mode distribution of diode laser beams is necessary for the optimization of the overall performance. For example, for material processing applications the laser radiation of high power diode lasers is often transmitted by an optical fiber due to greater flexibility and high radial symmetry of the delivered laser beam. However, the characteristic of the irradiated diode laser radiation do not show radial symmetry. The laser radiation is emitted from a small stripe with dimensions of $1\text{ }\mu\text{m} \times 10\text{ mm}$ where the smaller dimension is oriented perpendicular to the p-n junction of the diode laser. More precisely, the laser radiation is emitted from small facets positioned within this region. Depending on the specific structure of the diode laser bar, the emitting facets are separated by dead space which is optically inactive. Due to the specific design of the emitters within a diode laser bar the divergence angles parallel and perpendicular to the p-n junction show different values. Therefore, the beam of a diode laser bar is far away from having a radial symmetric shape. To obtain the circular focus spot needed for fiber coupling different beam-shaping techniques can be used, which in turn need to know the exact electro-optical properties of the diode lasers. In addition, the electro-optical characterization is a first test for the quality of high power diode lasers.

¹ Correspondence: Email: Jandeleit@ilt.fhg.de; WWW: <http://www.ilt.fhg.de>; Telephone: ++49-241-8906-0;
Fax: ++49-241-8906-121

2. PACKAGING AND FABRICATION OF HIGH POWER DIODE LASERS

Modern high power diode lasers have a wall plug efficiency about 50 % or more, which means in turn that almost as much as the optical power is generated as waste heat. To reach high output powers and to maintain long-term reliability the thermal management of diode laser bars is very important. Therefore, state of the art packaging technology consists of mounting the diode laser bars junction side down on micro channel heat sinks, which have a thermal resistance as small as 0.29 W/K.⁵

At the Fraunhofer-Institut für Lasertechnik high power diode laser bars are mounted on micro channel heat sinks in copper technology (fig. 1). The in- and outlet for the water cooling is located at the underside of the heat sinks. The heat sinks also serve as the p-contact of the diode laser bar. A thin copper sheet mounted on top of the diode laser bar serves as the n-contact. The diode laser bars are mounted at the front edge of the heat sinks with an overhang below 10 μm . For the electrical isolation of the p- and n-contact an isolation foil is used. To bridge the different expansion coefficients of the diode laser bar and the copper heat sink and to avoid induction of stress into the laser crystal a ductile solder like Indium is used for mounting. The soldering of the diode laser bar and the n-contact is done by reflow soldering processes.

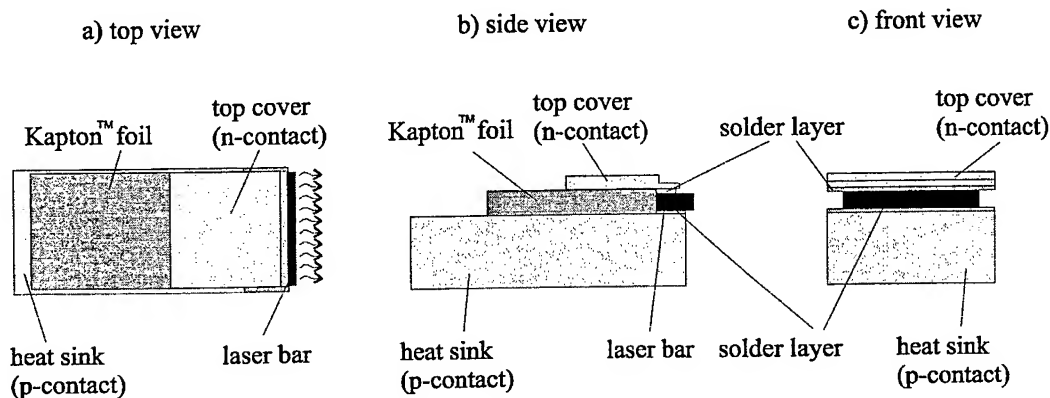


Fig. 1: Packaging of high power diode lasers used at Fraunhofer-Institut für Lasertechnik.

3. CHARACTERIZATION METHODS OF HIGH POWER DIODE LASERS

For the characterization of high power diode lasers different characterization methods and measuring stations are developed at the Fraunhofer-Institut für Lasertechnik. The standard data such as threshold current, slope efficiency, center wavelength, spectral width, total conversion efficiency and cw-output power as a function of driving current are measured in an automated measuring station (fig. 2). Driving currents up to 100 A can be applied to one diode laser bar.

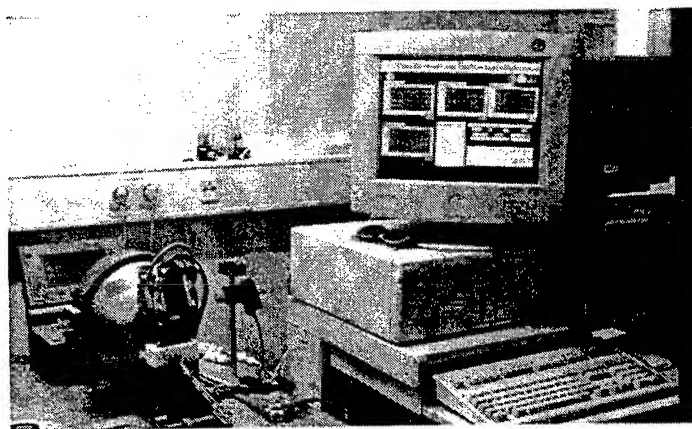


Fig. 2: Automated measuring station for the standard characterization of high power diode lasers.

In addition, the water flow rate of each micro channel heat sink is determined. The electro-optical standard characterization is a first test for the quality of high power diode lasers. Good diode lasers can be separated from bad diode lasers, whereas only good diode lasers are taken for burn-in.

To get knowledge about the limits of high power diode lasers a test set-up is developed which allows driving currents up to 280 A (fig. 3). An integrated water cooling of the n-contact ensures the effective removal of the waste heat also at the n-side of the diode laser. The cw-output power, the voltage and the total conversion efficiency are measured as a function of the driving current. The cooler for the n-contact also serves as the electrical connector and is fastened at a micro rail. The thermal and electrical connection of the n-contact is done by pressing down the cooler using a pneumatic cylinder. In contrast to the standard characterization the cw-output power is not measured using an integration sphere with a semiconductor detector but using a thermal detector. If higher driving currents than 280 A are needed further power supplies can be added to the test set-up.

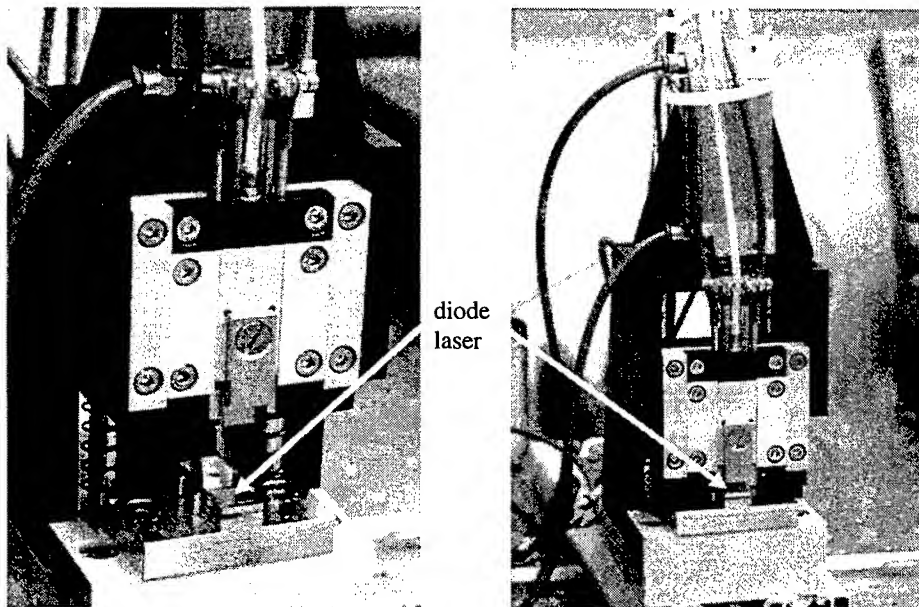


Fig. 3: High power test set-up for driving currents up to 280 A. Left side: opened diode laser holder, right side: closed diode laser holder.

For beam guiding and beam shaping techniques the beam divergence angles in fast and slow direction of high power diode lasers have to be known exactly. Therefore, a test set-up was developed which allows the determination of the divergence angles in fast and slow direction of a diode laser as well as the determination of the three-dimensional far-field distribution. For these measurements the diode laser has to be rotated in a plane perpendicular and parallel to the p-n junction, where the centers of these rotations have to coincide with the center of the front facet of the diode laser bar (fig. 4). The intensity of the diode laser bar is measured as a function of the angle. To achieve precise measuring results the measurement range of the angles has to be large to guarantee an accurate correction of the noise and the off-set of the measurement signal. A self-developed software program controls the measurement and calculates the divergence angles in fast and slow direction of the diode laser bar. For better comparison with data given by commercial diode laser suppliers the software program calculates the 95 %-, the $1/e^2$ - and the FWHM (Full Width Half Maximum)-value of the divergence angles. The 95 %- value defines the angle of enclosed power. It has to be mentioned, that the FWHM-value of the slow axis divergence has no special meaning because the far-field distribution of the slow axis has no clear shape like a Gaussian beam profile. Therefore, at the Fraunhofer-Institut für Lasertechnik the 95 %-value is used.

The overall efficiency of diode laser modules and the alignment of beam shaping components is strongly influenced by the smile of diode lasers. The smile describes the vertical position of each single-emitter within a diode laser bar. A test set-up was developed which allows the measurement of the smile of a diode laser (fig. 5). The radiation of a diode laser is emitted on a screen and detected by a CCD-camera. Differences in the vertical position of each single-emitter in the order of $1 \mu\text{m}$ can be determined.

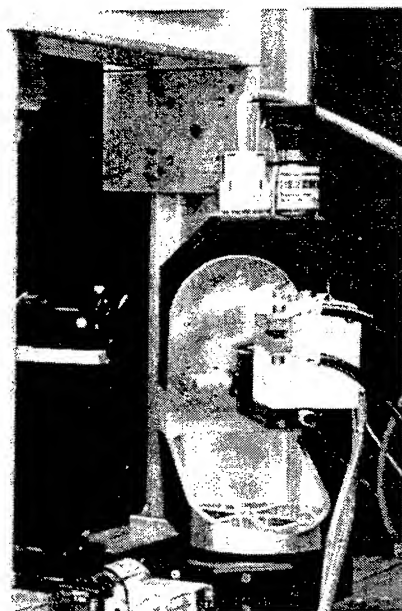


Fig. 4: Test set-up for the measurement of the fast and slow divergence of diode lasers.



Fig. 5: Test set-up for the measurement of the smile of diode lasers.

4. CHARACTERIZATION OF HIGH POWER DIODE LASERS

Every diode laser bar mounted on a copper micro channel heat sink at the Fraunhofer-Institut für Lasertechnik is characterized using the automated standard measuring station. The standard data are summarized on a characterization sheet (fig. 6).

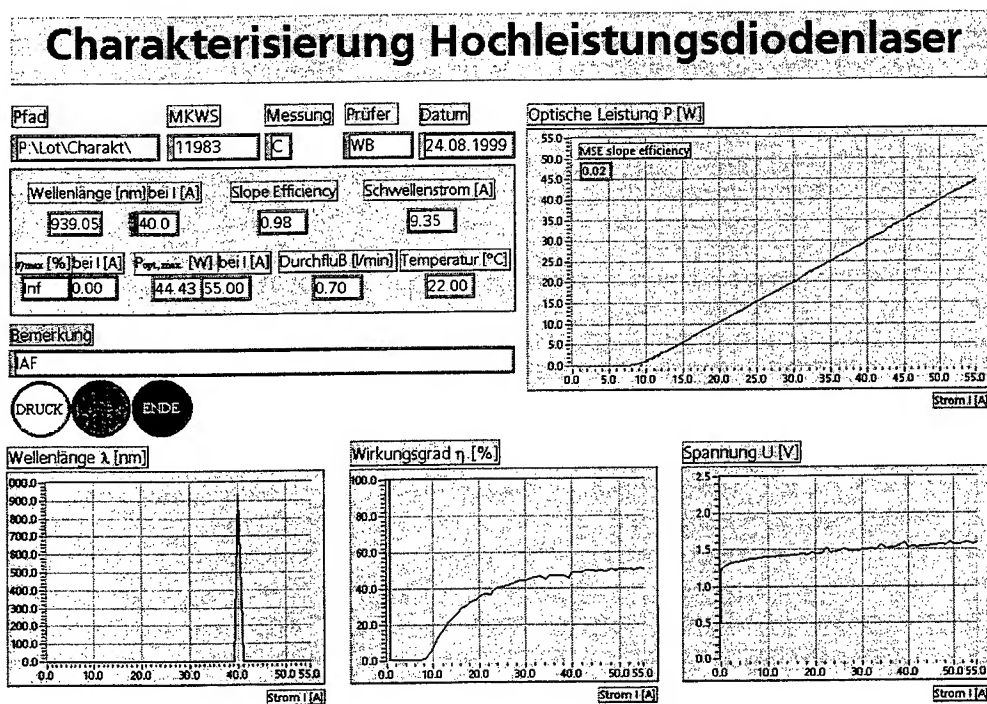


Fig. 6: Characterization sheet for the standard data of high power diode lasers.

The optical output power, the voltage and the total conversion efficiency are plotted versus the driving current, where the total conversion efficiency is calculated from the measured output power and voltage. The threshold current and the slope efficiency are determined from the P/I (power/current)-curve.

The beam divergence in fast and slow direction and the far-field distribution depend on the inner structure of high power diode lasers. The inner structure of high power diode lasers can be described by the pitch of the emitters within a bar and by the width of each emitter. Furthermore, the bars can consist of groups of multi-stripe arrays or of broad-area emitters. The far-field distribution of multi-stripe arrays and of broad-area emitters can be seen in figure 7. The far-field distributions in fast direction show a Gaussian-like shape, while the far-field distributions in slow direction differ from each other. For multi-stripe arrays two maxima can be seen, while broad-area emitters are characterized by one broad maximum. The divergence angles of different types of diode laser bars are summarized in table 1.

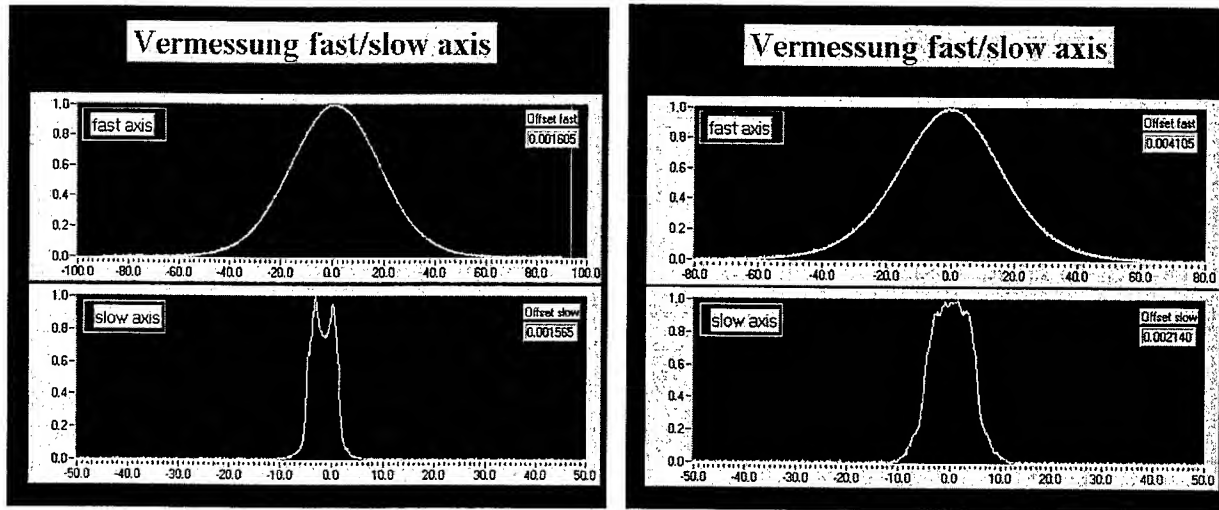


Fig. 7: Slow and fast axis divergence of high power diode lasers. Left side: bar consisting of multi-stripe arrays , right side: bar consisting of broad-area emitters.

wave-length	filling factor	pitch	emitter width	fast axis (full angle) [°]			slow axis (full angle) [°]		
				95%-value	1/e ² -value	FWHM	95%-value	1/e ² -value	FWHM
980 nm	25%	400 μ m	100 μ m	76,4	72,7	39,7	10,8	9,8	6,9
940 nm	50%	400 μ m	200 μ m	78,4	73,8	39,9	13	12,4	4,6
808 nm	30%	500 μ m	150 μ m	58,4	56,2	31,8	17,2	17,8	11,9
910 nm	30%	500 μ m	150 μ m	64,8	61,3	34,1	15,6	16,4	10,6
970 nm	30%	500 μ m	150 μ m	72,8	67,8	37,1	15	15,5	10,4
808 nm	50%	200 μ m	100 μ m	55,8	54,9	31,1	26,6	19,2	8
808 nm	90%	160 μ m	150 μ m	60,1	58,9	34,5	17,8	15,5	9,1
940 nm	50%	400 μ m	200 μ m	81,1	80,2	43,3	13,7	13,2	10,3
808 nm	50%	400 μ m	200 μ m	71,8	70,4	40,1	8,5	7,7	6,3

Table 1: Divergence angles of different types of high power diode lasers. Only the last two diode lasers consist of multi-stripe arrays.

The smile of different diode lasers mounted on copper micro channel heat sinks at the Fraunhofer-Institut für Lasertechnik was measured using the described test set-up. The diode laser bars under investigation consist of 19 single-emitters. During the measurements driving currents above the threshold current for laser radiation were applied to the diode lasers (fig. 8). The single-emitters of a high-quality diode laser are located on one straight line showing a smile below 1 μ m (fig. 8, left

side), while the single-emitters of bad diode lasers are arranged, for example, like a wave showing smiles above 1 - 2 μm (fig. 8, right side). The smile of diode lasers depends on the used mounting techniques and on the used mounting tools. To reduce the smile and to achieve reproducible mounting results the techniques as well as the tools have to be improved.

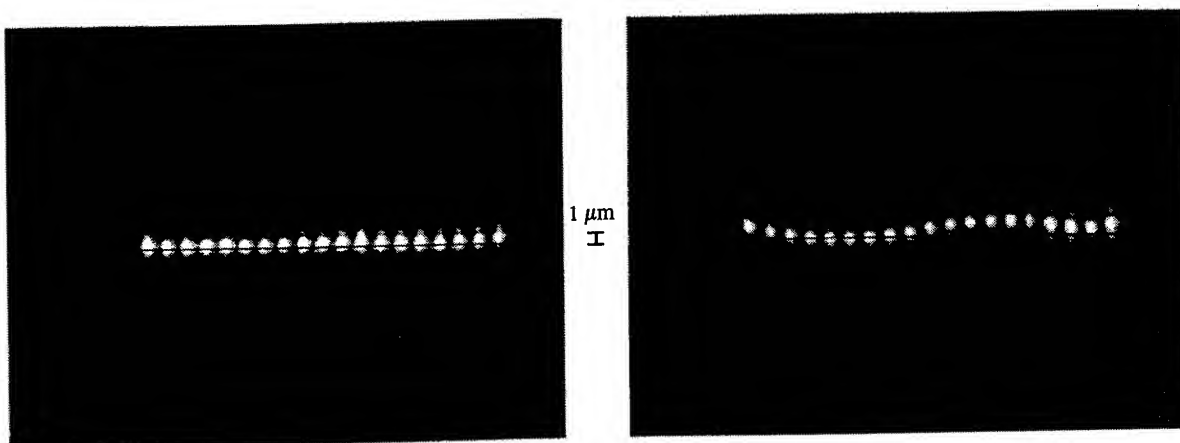


Fig. 8: Smile of diode lasers. Left side: good diode laser without smile, right side: bad diode laser showing a smile above 2 μm .

5. SUMMARY

For most applications the electro-optical properties of high power diode lasers have to be known exactly. Therefore, different test set-ups using different characterization methods are developed at the Fraunhofer-Institut für Lasertechnik.

The standard data such as threshold current, slope efficiency, center wavelength, spectral width, total conversion efficiency and cw-output power as a function of driving current can be measured in an automated measuring station. The standard data are summarized on a characterization sheet. To get knowledge about the limits of diode lasers a high power test set-up can be used, which allows driving currents up to 280 A. The divergence angles in fast and slow direction of a diode laser as well as the three-dimensional far-field distribution can be measured in a specially designed divergence test set-up. The divergence angles of different types of diode laser bars are summarized in table 1. To measure the smile of diode lasers a test set-up was developed which allows the determination of the position of a single-emitter within a bar with an accuracy in the order of 1 μm .

REFERENCES

1. D.Z. Garbuzov, N.Y. Antonishkis, A.D. Bondarev, A.B. Gulakov, S.N. Zhigulin, N.I. Katsavets, A.V. Kochergin, E.V. Rafailov, "High power 0.8 μm InGaAsP-GaAs SCH DQW lasers", IEEE, J. Quantum Electron., **27** (6), pp. 1531-1536, 1991.
2. J.K. Wade, L.J. Mawst, D. Botez, "High continuous wave power, 0.8 μm -band, Al-free active region diode lasers", Appl. Phys. Lett., **70** (2), pp. 149-151, 1997.
3. C. Hanke, L. Korte, B. Acklin, J. Luft, S. Grötsch, G. Herrmann, Z. Spika, M. Marciano, B. De Odorico, J. Wilhelmi, "Highly reliable 40 W-cw-InGaAlAs/GaAs-808 nm laser bars", SPIE, **3462**, pp. 47-53, 1999.
4. K. McEuren, Laser Focus Laser, Dec. 1997, pp. 121, 1997.
5. T. Ebert, J. Biesenbach, H.-G. Treusch, P. Loosen, R. Poprawe, "Optimization of micro channel heat sinks for high power diode lasers in copper technology", SPIE, **3285**, pp. 25-30, 1998.
6. M. Fukuda, *Reliability and Degradation of Semiconductor Lasers and LEDs*, Artech House, Boston • London, 1991.
7. O. Ueda, *Reliability and Degradation of III-V Optical Devices*, Artech House, Boston • London, 1996.

SESSION 2

Wide-Bandgap Materials

Stimulated emission and pump-probe studies of wide-gap nitrides for UV-blue photonic applications

Jin-Joo Song^a, Sergiy Bidnyk^a, and Theodore J. Schmidt^b

^aCenter for Laser and Photonics Research and Department of Physics,
Oklahoma State University, Stillwater, Oklahoma 74078

^bTechnology Development, Williams Communications,
Tulsa, Oklahoma 74172

ABSTRACT

Stimulated Emission and Pump-Probe studies were performed in GaN, InGa_N, and AlGa_N epilayers as well as GaN/AlGa_N separate confinement heterostructures (SCHs). We show that in GaN epilayers the near-threshold gain mechanism is inelastic exciton-exciton scattering for temperatures below ~150 K, whereas at elevated temperatures electron-hole plasma is the dominant gain mechanism. An analysis of the relative shift between the spontaneous emission and lasing peaks in SCH samples, combined with the temperature dependence of the lasing threshold, reveals that exciton-exciton scattering is the dominant gain mechanism leading to low-threshold ultraviolet lasing in the GaN/AlGa_N SCH over the entire temperature range studied. We further performed optical pumping of AlGa_N epilayers at different temperatures. Stimulated emission has been observed in Al_xGa_{1-x}N thin films for Al concentrations as high as $x = 0.26$, with a resultant stimulated emission wavelength as low as 328 nm at room temperature. This result indicated that AlGa_N-based structures are suitable not only for use in deep-ultraviolet detectors, but also as a potential source of deep-ultraviolet laser radiation. The interband optical transitions in GaN and InGa_N have also been studied at 10 K and room temperature using nondegenerate nanosecond optical pump-probe techniques. At low temperatures, strong, well-resolved features were seen in the absorption and reflection spectra corresponding to the 1s A and B exciton transitions. Broadening and decrease in intensity of these features were studied as the function of excitation pump density. We found that values of induced transparency and induced absorption are extremely large in GaN epilayers. The pump-probe results in GaN epilayers were directly compared to ones obtained from InGa_N films. Significant differences in near-bandedge absorption changes were clearly observed between the two materials.

Keywords: GaN, AlGa_N, InGa_N, separate confinement heterostructure, gain mechanisms, stimulated emission, pump-probe spectroscopy, induced transparency/absorption, exciton-exciton scattering, electron-hole plasma.

1. INTRODUCTION

GaN and its respective alloys (InGa_N and AlGa_N) have been attracting an ever increasing amount of attention due to their physical hardness, inert nature, and large direct band gaps, making them promising materials for UV-Blue-Green light emitting devices and detectors.¹ Current technological advances have made high brightness light-emitting diodes (LEDs) and cw laser diodes based on these materials a reality.² However, much information about the optical phenomena associated with the high carrier concentrations at which practical devices operate in these materials is still unknown. A better understanding of the optical phenomena associated with high carrier concentrations in this material system is important, not only for general physical insight, but also as an aid in the design and optimization of future group III nitride-based photonic devices.

In this work we describe the results of optical pumping and pump-probe studies in GaN, InGa_N, and AlGa_N epilayers as well as GaN/AlGa_N separate confinement heterostructures (SCHs). We identify the near-threshold gain mechanisms in GaN epilayers and GaN/AlGa_N SCHs. We demonstrate deep-ultraviolet stimulated emission by optically pumping Al_xGa_{1-x}N epilayers with high Al concentration. Through nondegenerate nanosecond optical pump-probe techniques we directly compare induced transparency and induced absorption in GaN and InGa_N epilayers.

2. SAMPLES

All samples used in this work were grown by metalorganic chemical vapor deposition (MOCVD). The GaN samples were all nominally undoped epitaxial films grown on (0001) sapphire and 6H-SiC substrates. Thin AlN buffers were deposited on the substrates at 775 °C before the growth of GaN. The GaN layers were deposited at 1040°C on AlN buffers. These conditions typically result in high quality single-crystal GaN layers.^{3,4} The thickness of the GaN layers ranged from 0.38 to 7.2 μm . Photoluminescence, absorption, reflection, and photoluminescence excitation spectra for these samples have been reported elsewhere.⁵

The SCH samples used in this work were grown by metalorganic chemical vapor deposition on 6H-SiC (0001) substrates with $\sim 3\text{-}\mu\text{m}$ -thick GaN epilayers deposited prior to the growth of the SCH region. The SCH sample under discussion has a 150-Å-thick GaN active layer, surrounded by 1000-Å-thick $\text{Al}_{0.05}\text{Ga}_{0.95}\text{N}$ cladding layers and 2500-Å-thick $\text{Al}_{0.10}\text{Ga}_{0.90}\text{N}$ waveguide layers symmetrically located on each side.

The $\text{Al}_x\text{Ga}_{1-x}\text{N}$ layers were grown on (0001) oriented sapphire at a temperature of 1050°C. Prior to $\text{Al}_x\text{Ga}_{1-x}\text{N}$ growth, a thin (~ 50 Å) AlN buffer layer was deposited on the sapphire at a temperature of 625°C. The $\text{Al}_x\text{Ga}_{1-x}\text{N}$ layer thickness was ~ 0.8 μm .

The InGaN layers used in this study were grown by MOCVD at 800 °C on a 1.8 μm thick GaN layer deposited at 1060 °C on (0001) oriented sapphire. The InGaN layers were capped by 0.05 μm GaN layers.

3. RESULTS AND DISCUSSIONS

3.1. Gain mechanisms in GaN epilayers

The first results on stimulated emission (SE) in GaN at low temperatures were reported in the literature more than a quarter of a century ago.⁶ Since then, SE has been demonstrated in samples grown on different substrates for temperatures as high as 700 K (Ref. 7). Understanding the SE (and hence, gain) mechanisms in this material is extremely important from both a fundamental physics and a device optimization standpoint. There have been several studies performed explaining the origin of SE in GaN films at various temperatures. Amano *et al.* suggested that electron-hole plasma (EHP) is the most plausible origin of gain in GaN epilayers at room temperature (RT) (Ref. 8). Catalano *et al.* suggested exciton-exciton (ex-ex) scattering to be the dominant gain mechanism at 80 K (Ref. 9). Recently Holst *et al.* performed gain spectroscopy on HVPE-

grown GaN films and concluded that biexcitonic decay is responsible for the gain at 1.8 K at low excitation densities, whereas EHP recombination dominates the spectra at higher excitation densities.¹⁰ However, the general picture of gain mechanisms in GaN and its implications towards laser diode (LD) structures with a GaN-active layer is still not well understood. In addition, the high RT SE threshold severely complicates the development of GaN active layer LDs.

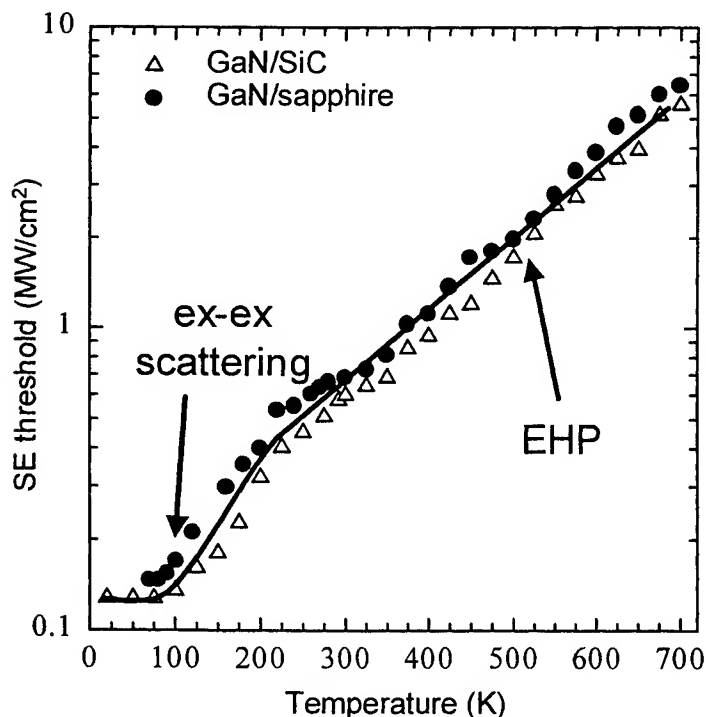


Figure 1. SE threshold as a function of temperature for GaN thin films grown on SiC (open triangles) and sapphire (filled circles). The SE threshold rises exponentially for temperatures exceeding 200 K, with a characteristic temperature of approximately 170 K. For temperatures below 200 K, the SE threshold is considerably reduced due to excitonic enhancement. The solid lines are given only as guides for the eye.

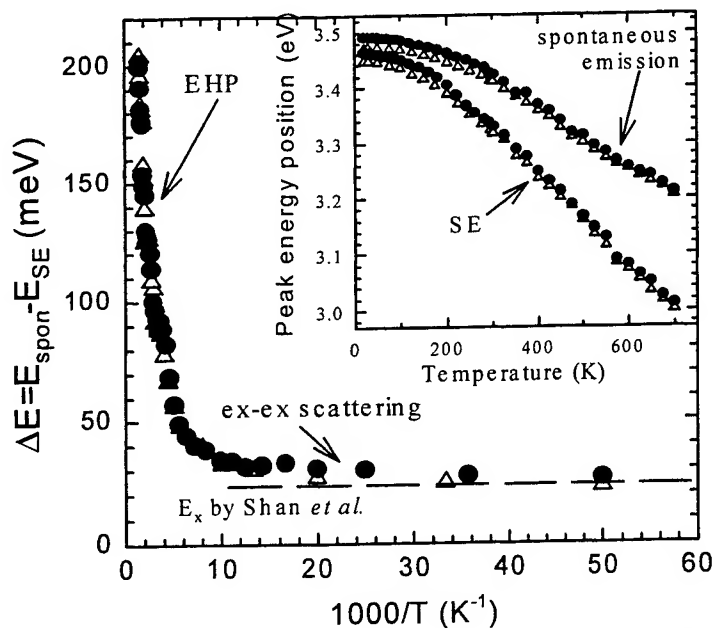


Figure 2. Energy difference (ΔE) between spontaneous and SE peaks as a function of temperature for GaN thin films grown on SiC (open triangles) and sapphire (filled circles). At low temperature, ΔE asymptotically approaches the exciton binding energy indicating the dominant near- I_{th} gain mechanism is inelastic ex-ex scattering. At elevated temperatures, the large value of ΔE indicates the increased presence of band-gap renormalization effects. The inset shows the absolute energy positions of the spontaneous and SE peaks. The difference in the energy positions between the two samples is a result of residual strain between the epilayers and the two different substrates.

We performed a study of the gain mechanisms in GaN epilayers using nanosecond optical pumping in the temperature range of 20 to 700 K. We observed that for temperatures below 150 K the dominant gain mechanism is inelastic ex-ex scattering characterized by band-filling phenomena and a comparatively low SE threshold. For temperatures in the vicinity of 150 K the SE threshold was found to abruptly increase and the energy position of the SE peak rapidly shifted towards lower energies due to bandgap renormalization. This transition was attributed to a change in the gain mechanism from ex-ex scattering to that of an EHP. EHP recombination was found to be the dominant recombination mechanism for all temperatures exceeding 150 K (up to 700 K). Based on our results, we discuss possibilities of reducing the room temperature lasing threshold in laser diode structures with a GaN active medium.

The SE part of this study was performed in an edge emission geometry. A tunable dye laser pumped by a frequency-doubled, injection-seeded Nd:YAG laser was used as the primary optical pumping source. The deep red output of the dye laser was frequency doubled to achieve a near ultraviolet (UV) pumping frequency. The laser beam was focused into a line on the sample surface using a cylindrical lens and the laser light intensity was continuously attenuated using a variable neutral density filter.¹¹ The emission was collected from one edge of the sample and coupled into a Spex 1.0 m spectrometer and spectrally analyzed with a UV enhanced multi-channel analyzer. Low power cw photoluminescence (PL) studies were also undertaken to measure the spontaneous emission as a function of temperature. A frequency doubled Ar⁺ laser (244 nm, 40 mW) was used as the excitation source. In order to avoid spectral distortion of spontaneous emission due to re-absorption, the laser beam was focused on the sample surface and spontaneous emission was collected from a direction near normal to the sample surface.¹²

Recently, Fischer *et al.* convincingly demonstrated the presence of excitonic resonances in GaN epilayers well above RT through optical absorption measurements.¹³ Excitons in GaN epilayers cannot be easily ionized due to the relatively large exciton binding energy. However, at near-SE-threshold (near- I_{th}) pump densities the picture is not straightforward since screening of the Coulomb-interaction weakens the binding of the exciton. In general, the existence of excitons depends on the strength of the Coulomb-interaction which in turn depends on the density and distribution of carriers among bound and unbound states.¹⁴ Therefore, the observation of excitons at low excitation powers at RT does not assure their presence at SE pump densities.

To determine if the SE threshold density occurs above or below the Mott density (the critical density beyond which excitons are no longer stable), we studied the temperature behavior of the SE threshold in GaN epilayers grown on sapphire and SiC substrates over a wide temperature range (20 to 700 K), as shown in Figure 1. For temperatures above 200 K, the SE thresholds roughly followed an exponential dependence: $I_{th} = I_0 \exp(T/T_0)$, with $T_0 \approx 170$ K (Ref. 7). This exponential behavior of the SE threshold is qualitatively similar to that observed in other material structures.¹⁵ However, as the temperature decreases to below 200 K, a significant (faster than exponential) reduction in the SE threshold was observed

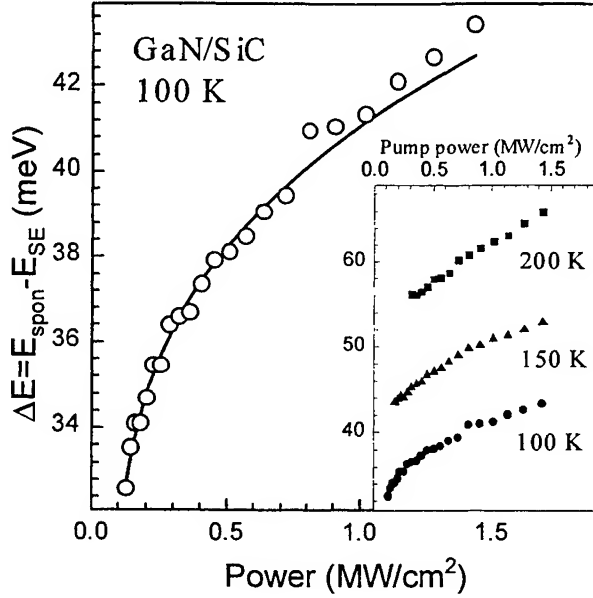


Figure 3. Energy difference (ΔE) between spontaneous and SE peaks as a function of excitation density at 100 K. The solid line represents a theoretical fit of the experimental data (open circles) in Eq. (2). The inset shows the change in the behavior of ΔE at different temperatures. An abrupt near- I_{th} shift in ΔE at 100 K is related to band-filling effects associated with increased values of kinetic energy E_k^{e-h} during the ex-ex scattering recombination process. At elevated temperatures and/or high excitation powers, EHP is the dominant gain mechanism.

scattering to have the lowest SE threshold at low temperatures.¹⁴

The effects of excitons on SE can be better understood by studying the temperature and power dependence of the SE peak position. We measured the energy position of the SE peak at near- I_{th} pump densities and the spontaneous emission peak using low power cw PL techniques in the temperature range of 20 to 700 K for two samples grown on sapphire and SiC substrates, as shown in the inset of Figure 2. The position of the spontaneous and SE peaks in the two GaN epilayers is influenced by residual strain resulting from thermal-expansion mismatch between the epilayers and the substrates.⁵ This difference in energy position for the two samples is largest at low temperature and gradually decreases as the temperature is increased.

To avoid strain-related complications we restricted ourselves to an analysis of the relative energy shift between the spontaneous and SE peaks, $\Delta E = E_{spon} - E_{SE}$, as depicted in Figure 1. As we approach low temperatures ($T < 150$ K), ΔE asymptotically approaches the exciton binding energy ($E_x = 21$ meV), measured by photoreflectance.¹⁶ However, at temperatures above 150 K, ΔE monotonically increases and reaches values as high as 200 meV at 700 K. The behavior of the energy difference between the spontaneous and SE peaks at low temperatures (< 150 K) can be well explained by inelastic ex-ex scattering. In the case of ex-ex scattering the energy difference between the two peaks can be estimated from:¹⁷

$$\Delta E = E_{spon} - E_{SE}^{ex-ex} = (E_g - E_x) - (E_g - 2E_x - E_k^{e-h}) = E_x + E_k^{e-h}, \quad (1)$$

where E_g is the bandgap energy and E_k^{e-h} is the kinetic energy of the unbound electron-hole pair created during the excitonic collision. At low excitation densities and low temperatures one can consider the bands to be empty. The unbound electron-hole pairs created during the process have a very small kinetic energy ($E_k^{e-h} \approx 0$), thus ΔE approaches E_x (as $T \rightarrow 0$ K), as shown in Figure 2.

For high temperatures ($T > 150$ K), the energy difference between spontaneous and SE peaks gradually increases from ~ 35 meV to a few hundred meV. Both the large energy difference and the relatively high SE thresholds in this temperature range (Figure 1) point to EHP recombination. In EHP recombination a large number of excited carriers cause band-gap renormalization effects leading to a large ΔE . Under such high excitation conditions, excitons are dissociated by many body interactions.⁸ As further evidence to support EHP in this temperature range, we point out that excitons have not been clearly observed in GaN at highly elevated temperatures, even under extremely low excitation conditions.¹³ We therefore conclude that EHP recombination is responsible for gain in GaN thin films at these elevated temperatures. Since no significant change in the behavior of the SE threshold and SE peak position was observed for temperatures between 150 K and 700 K (Figure 1 and Figure 2), we conclude that EHP recombination is the dominant gain mechanism for temperatures exceeding 150 K.

At temperatures below 150 K, the effect of the kinetic energy E_k^{e-h} on ex-ex scattering recombination process could be observed in the excitation density dependence of ΔE . As the excitation intensity or temperature is increased, the bottom of the bands become filled. Thus, unbound electron-hole pairs created in the process of ex-ex collision must have higher energies, and the kinetic energy E_k^{e-h} can no longer be neglected. The inset in Figure 3 shows the power dependence of ΔE at three different temperatures near the point when the gain mechanism experiences a transition from inelastic ex-ex scattering to EHP. For temperatures below 150 K, we observed a rapid increase of ΔE at near- I_{th} pump densities, as shown in the inset of Figure 3. This shift is most likely associated with the band-filling effect which causes increased values of E_k^{e-h} . For temperatures above 150 K, such a strong near- I_{th} shift in ΔE is not observed. At high temperatures ($T > 150$ K) SE originates from EHP recombination and the gradual increase in ΔE is caused by band-gap renormalization effects. For one photon pumping and elliptical bands, the band-filling effect associated with ex-ex scattering gives a calculated line shift E_k^{e-h} proportional to $(I - I_{th})^{1/3}$ (see Ref. 18). The substitution of this expression into Eq. (1) yields:

$$\Delta E = E_x + a(I - I_{th})^{1/3}, \quad (2)$$

A fit of the experimental data (open circles) taken at 100 K into Eq. (2) is shown in Figure 3 by a solid line. From the fit, we obtained the values of exciton binding energy $E_x = 28$ meV and the SE threshold $I_{th} = 100$ kW/cm², which is in a reasonable agreement with experimental results and supports the idea of ex-ex scattering being the dominant SE mechanism for temperatures below 150 K.

Since ex-ex scattering has a lower SE threshold than recombination from an EHP (Figure 1), it would be advantageous if SE was dominated by excitonic effects for RT and beyond.¹⁹ This could be achieved, for example, by introducing a 2-D spatial confinement.²⁰ By tailoring the width of a GaN active layer sandwiched between AlGaIn confinement layers, one would expect a significant increase in the exciton binding energy. For increased values of exciton binding energy, a strong reduction of the homogeneous broadening due

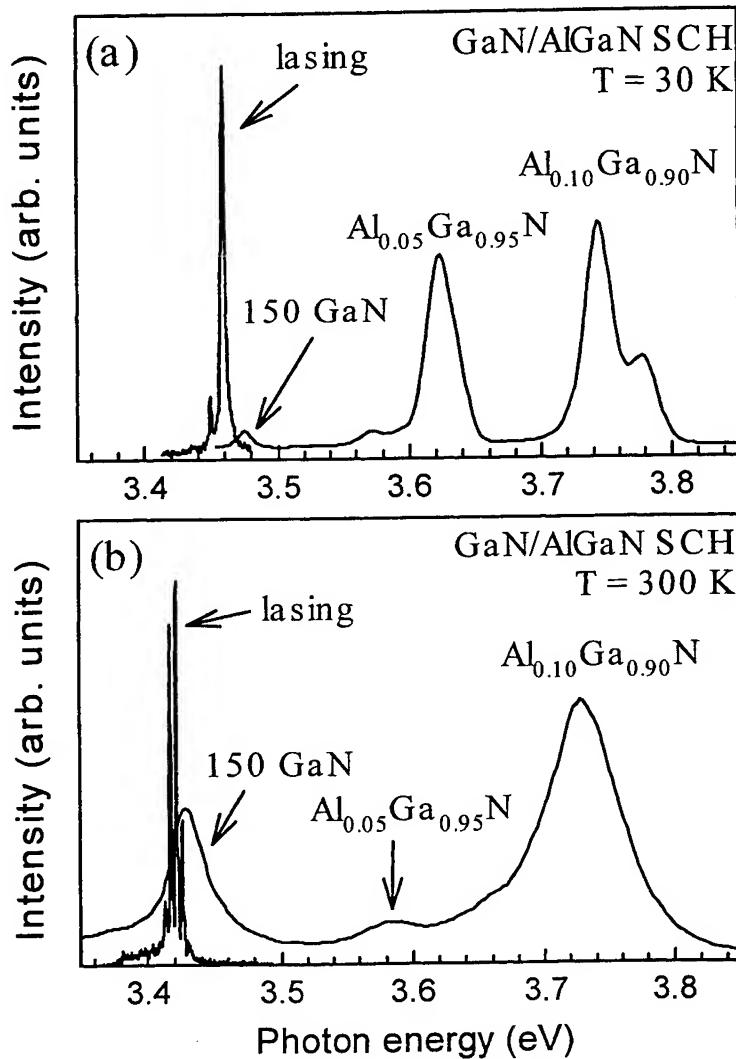


Figure 4. Lasing and low-density PL spectra from a GaN/AlGaIn separate confinement heterostructure taken at two different temperatures: (a) 30 K and (b) 300 K. Lasing spectra were obtained at pump densities of $1.3 \times I_{th}$ for each temperature. Lasing modes are highly polarized (TE:TM $> 300:1$) and originate from self-formed microcavities due to cracks in the AlGaIn and GaN layers. Low pump density PL spectra have three characteristic peaks associated with the 150-Å-thick GaN active region and the two AlGaIn confinement layers with different aluminum concentrations.

to reduced Fröhlich interactions is expected.²¹ This could potentially extend the ex-ex scattering gain mechanism to RT. The SE threshold for such structures would be significantly reduced due to carrier confinement²² and a shift in the dominant near- I_{th} gain mechanism to that of ex-ex scattering.

3.2. Mechanisms of efficient ultraviolet lasing in GaN/AlGaN separate confinement heterostructures.

The successful fabrication²³ of the 'blue laser' was largely due to the realization that the incorporation of indium into GaN was concomitant with a dramatic lowering of the lasing threshold,²⁴ enhancement of emission intensity,²⁵ and improvements in temperature characteristics.²⁶ The small bandgap of InN (1.9 eV), however, is disadvantageous for the development of near- and deep-ultraviolet (UV) LDs. Novel lasing structures, such as GaN-active medium structures, are required to fabricate LDs with emission wavelengths lying below 370 nm. Recently, Schmidt *et al.* observed a reduction of the stimulated emission (SE) threshold in a GaN/AlGaN separate confinement heterostructure (SCH).²⁷ However, the mechanisms leading to the observed blue-shift of the emission and reduction of the SE threshold compared to bulk-like epitaxial GaN layers have not been understood.

In this section we demonstrate UV laser action in optically pumped GaN/AlGaN SCHs with remarkably low lasing thresholds in the temperature range of 10 K to 300 K. Through an analysis of the lasing characteristics of these samples, such as the behavior of the temperature-induced shift between spontaneous emission and lasing modes, combined with the temperature dependence of the lasing threshold, we explain the gain mechanism leading to efficient lasing and discuss critical issues for the development of UV LDs with a GaN active medium.

Along with an SCH sample, we repeated the experiments on a 4.2- μm -thick GaN epilayer grown on (0001) 6H-SiC for comparison. The samples were mounted on a copper heat sink attached to a wide temperature range cryostat.

Conventional photoluminescence (PL) spectra were measured in the surface emitting geometry using a frequency-doubled Ar⁺ laser (244 nm) as the excitation source. In order to study the lasing phenomena, a tunable dye laser pumped by a frequency-doubled, injection-seeded Nd:YAG laser was used as the primary optical pumping source. The excitation beam was focused to a line on the sample using a cylindrical lens. The emission from the edge of the sample was coupled into a 1-m spectrometer with a side-mounted optical multi-channel analyzer and photomultiplier tube. Special precautions were taken to avoid fluctuations in sample position due to the thermal expansion of the mounting system. This allowed us to spatially "pin" the sample and obtain lasing modes from a single microcavity in the entire temperature range studied.

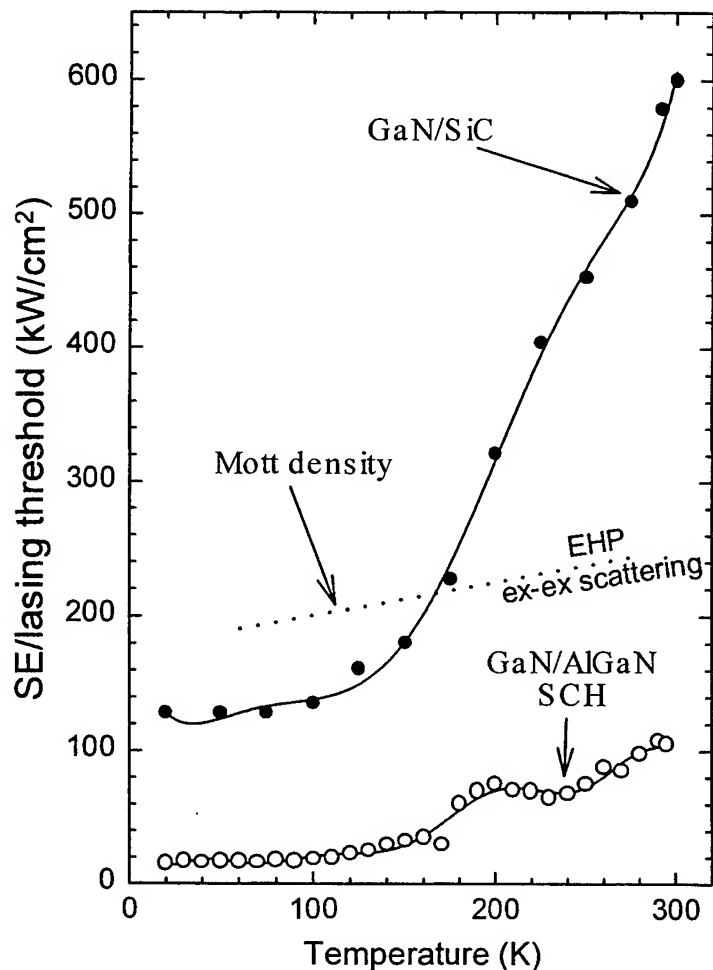


Figure 5. Temperature dependence of threshold pump densities for the 4.2- μm -thick GaN epilayer (closed circles) and GaN/AlGaN SCH (open circles). The lasing threshold of the SCH was measured to be 15 kW/cm² at 10 K and 105 kW/cm² at RT. Such a remarkably low lasing threshold is attributed to improved carrier confinement and optical waveguiding. Note that in the entire temperature range studied, lasing occurs at pump densities much lower than those required for exciton dissociation (Ref. 3). The solid lines are to guide the eye only.

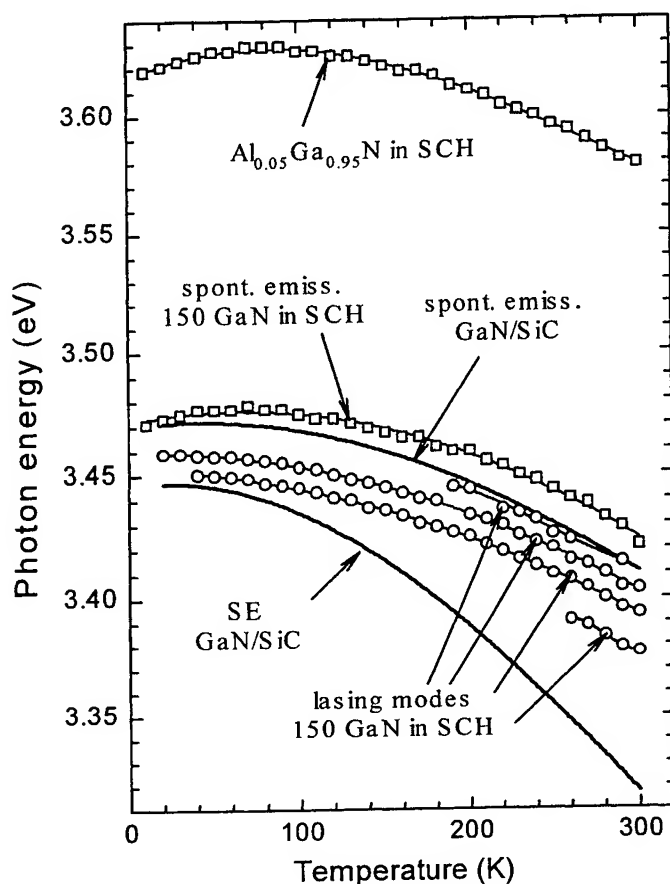


Figure 6. Temperature dependence of low density PL peak positions (open squares) and lasing modes (open circles) in a GaN/AlGaN SCH. For the purpose of comparison, we also plotted the position of spontaneous and SE peaks from a 4.2- μ m-thick GaN epilayer (solid lines). The two samples show distinctly different temperature evolution associated with the different origins of SE/lasing at elevated temperatures.

Typical low excitation emission spectra at 30 K [Figure 4(a)] and 300 K [Figure 4(b)] contain three distinct features associated with the active GaN layer, 5% aluminum cladding layer, and 10% aluminum waveguide layer. At low temperature the doublet spectral features related to the AlGaIn alloys in the SCH sample arise from a small alloy concentration difference between the two AlGaIn cladding and two waveguiding layers. It has been estimated that a 1% fluctuation in aluminum alloy concentration leads to a ~ 25 meV shift in the observed energy position.²² At increased excitation powers, a series of equally spaced lasing modes with full width at half maximum of ~ 3 Å appears on the low energy side of the GaN-active-region peak. The lasing modes

have a strong superlinear increase in intensity with excitation power. The laser emission has a narrow far field pattern and is strongly polarized, with TE:TM $\geq 300:1$ (limited by the signal/noise ratio of our instruments). Cracks were observed on the sample surface along all three cleave planes associated with the hexagonal structure, with the majority running parallel to the length of the bar. The spacing between the lasing modes was correlated to the length of microcavities formed by the cracks. Consequently, we believe that observed lasing is of a microcavity origin.²⁸ Further refinements in the cleaving process have allowed samples to be cleaved in a manner that resulted in no observable cracking, making them suitable for LD development.

A dramatic decrease in the lasing threshold of our SCH structure in comparison to a thick GaN epilayer was observed in the entire temperature range studied, as shown in Figure 5. The lasing threshold was estimated to be as low as 15 kW/cm² at 10 K and 105 kW/cm² at RT. Note that excitons in the GaN/AlGaIn SCH cannot be easily ionized with temperature due to the relatively large exciton binding energy.²⁹ The excitons are also unlikely to be dissociated by the presence of unbound states, since the threshold pump density is very low. It has been found experimentally that in order to weaken the excitonic Coulomb interaction by free carriers in GaN, a pump density of about 200-300 kW/cm² is required.³⁰ At this density the gain mechanism in GaN epilayers switches from exciton-exciton (ex-ex) scattering to electron-hole plasma (EHP), which is depicted in Figure 5 by a dotted line. Thus, in the SCH sample studied, excitons are expected to be present at densities above the lasing threshold and make major contributions to the recombination dynamics.

The consequences of exciton dynamics on lasing in the GaN/AlGaIn SCH can be better understood by studying the temperature dependence of the energy position of the emission peaks shown in Figure 6. The position of the spontaneous emission from the 150-Å-thick GaN active layer is located 0.15 eV below that of the Al_{0.05}Ga_{0.95}N cladding layer (open squares) and this difference remains temperature independent. The position of the lasing modes from a single microcavity was also plotted as a function of temperature in Figure 6 (open circles). As the temperature increases, the gain region broadens and additional modes are observed at elevated temperatures. For the purpose of comparison the temperature

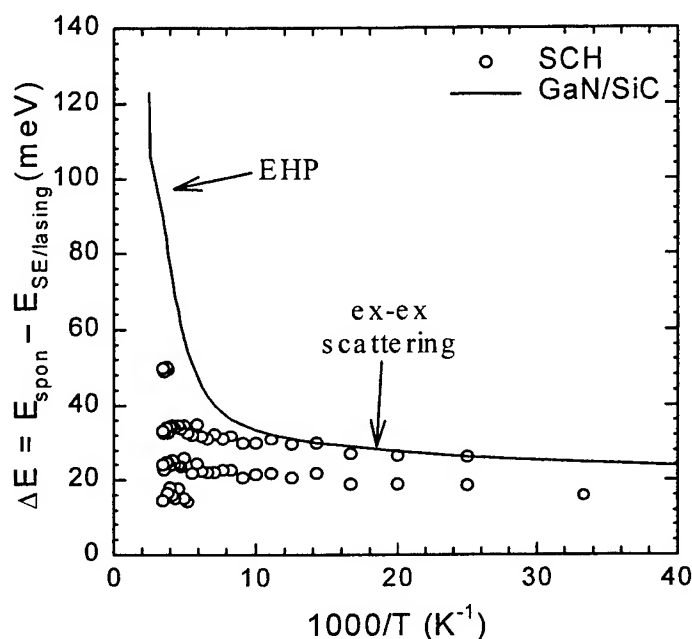


Figure 7. Energy position of lasing modes relative to spontaneous emission from the GaN active region in the SCH (open circles) and the energy difference between spontaneous and SE peaks in 4.2- μ m-thick GaN epilayer (solid line). The lasing modes in the SCH appear one exciton binding energy below the spontaneous emission peak over the entire temperature range studied, indicating that ex-ex scattering is the dominant lasing mechanism. On the contrary, the energy difference between the spontaneous and SE peaks in the GaN epilayer rapidly changes at ~ 150 K due to the gain mechanism transition from ex-ex scattering to EHP (Ref. 30).

evolution of the spontaneous and SE peaks of a thick GaN epilayer (solid lines) is also shown and appears to be distinctly different from that of the SCH sample. Note that the spontaneous

and lasing emission from the two samples could not be directly compared from this graph due to strain-related complications, such as the different thermal expansion coefficients of AlGaIn alloys compared to GaN.

In order to avoid complications arising from the effects of strain, we restricted ourselves to an analysis of the relative energy difference ΔE between the lasing modes and the GaN-active-region peak, as illustrated in Figure 6 (open circles). We ascertained that the position of the lasing modes is one exciton binding energy¹⁶ below the GaN peak and, most interestingly, remains temperature invariant from 10 to 300 K. This behavior is consistent with ex-ex scattering³⁰ being the dominant gain mechanism in the GaN/AlGaIn SCH over the entire temperature range studied. To further corroborate this point, on the same graph we plotted the energy difference (ΔE) between the spontaneous and SE peaks of a thick GaN epilayer (solid line). It has been demonstrated³⁰ that in GaN epilayers the dominant gain mechanism is ex-ex scattering at temperatures below 150 K. Similar to GaN epilayers, ΔE in the GaN/AlGaIn SCH lies one exciton binding energy below the spontaneous emission peak. However, at elevated temperatures ($T > 150$ K) ΔE in GaN epilayers rapidly increases, as opposed to the SCH sample. This was previously attributed to the transition of the gain mechanism from ex-ex scattering to EHP.³⁰ Since this transition was not observed in our SCH sample, we conclude that the ex-ex scattering mechanism remains dominant in our lasing structure, even at RT.

Note that we neither expected nor observed any enhancement of the exciton binding energy due to 2-D confinement, since the thickness of the active region is a factor of 5 larger than the Bohr radius of excitons in GaN. We also did not observe carrier recombination from localized states, which has been reported for InGaIn/GaN heterostructures.¹⁷ In spite of this, very low values of the lasing threshold were measured. In fact, these lasing threshold values are comparable to those of InGaIn/GaN multi-quantum well samples published in the literature.²⁶ We believe that the low lasing threshold of the GaN/AlGaIn SCH is due to improved carrier and optical confinement. Such a low lasing threshold combined with recent improvements in p-doping of AlGaIn alloys indicates that a realization of a GaN-active-medium UV laser diode is imminent.

3.3 Deep ultraviolet stimulated emission from $\text{Al}_x\text{Ga}_{1-x}\text{N}$ thin films.

The ternary compound $\text{Al}_x\text{Ga}_{1-x}\text{N}$ has the potential for use in light emitting devices and detectors covering nearly the entire deep ultraviolet (UV) region of the spectrum (190 - 350 nm). Applications of deep UV emitters and detectors include satellite to satellite communication shielded from Earth-based eavesdropping, remote sensing of chemical and biological contaminants, and medical applications where a compact, tunable UV laser source will find a myriad of uses, both known and presently unrealized. Despite a considerable amount of research directed towards AlGaIn based UV photodetectors,³¹ very little research has been conducted towards its use in UV laser diode development. Research conducted towards this end

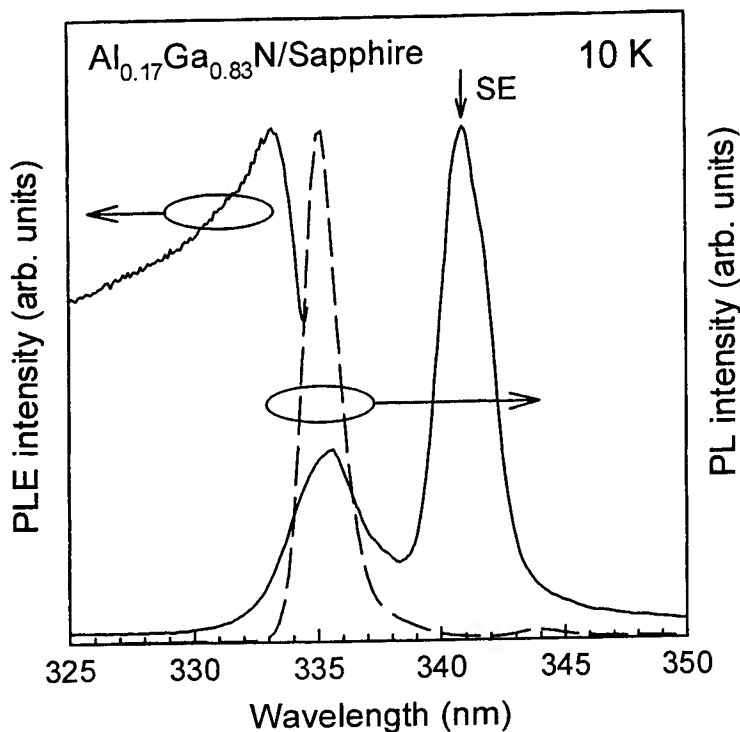


Figure 8. 10 K PLE, PL (dashed line), and SE spectra of an MOCVD-grown $\text{Al}_{0.17}\text{Ga}_{0.83}\text{N}$ thin film. The SE spectrum was taken with $I_{\text{exc}} = 2 \times I_{\text{th}}$.

has only been directed at low Al content AlGaN layers, whose emission wavelengths vary only slightly from that of GaN.^{32,33} We report here the observation of RT SE from optically pumped $\text{Al}_x\text{Ga}_{1-x}\text{N}$ thin films with x values as high as 26 %, putting the SE wavelengths well within the deep UV region of the spectrum (~ 328 nm). The recent demonstration of cw blue laser diodes with lifetimes in excess of 10,000 hours based on group-III nitride technology,³⁴ combined with the observation of RT deep UV SE from $\text{Al}_x\text{Ga}_{1-x}\text{N}$ reported here, makes the prospects of extending laser diode technology into the near and deep ultraviolet region of the spectrum using this material system look promising.

The $\text{Al}_x\text{Ga}_{1-x}\text{N}$ layers were optically pumped in an edge emission geometry using the second harmonic of the deep orange radiation

generated by an amplified dye laser pumped by the second harmonic of a Q-switched, injection seeded $\text{Nd}^{3+}:\text{YAG}$ (~ 4 ns pulse width and 10 Hz repetition rate). The deep UV radiation (310 nm) from the dye laser was focused to a line on the sample surface using a cylindrical lens. The emission was collected from one edge of the sample, coupled into a one meter spectrometer, and spectrally analyzed using a UV enhanced, gated CCD. Photoluminescence (PL) experiments were performed using the 244 nm line of a inter-cavity doubled cw Ar^+ laser as an excitation source. PL excitation (PLE) experiments were also carried out using the quasi-monochromatic emission from a Xe lamp dispersed by a $\frac{1}{2}$ meter monochromator as the excitation source. Both the PL and PLE experiments used a PMT in conjunction with a 1 meter double spectrometer as a detector.

Figure 8 shows a low temperature SE spectrum from an $\text{Al}_{0.17}\text{Ga}_{0.83}\text{N}$ layer superimposed on its low power cw PL peak (dashed line) and its band edge as measured by PLE (solid line). We see the spontaneous emission is Stokes shifted by approximately 2 nm from the band edge. The decrease in the PLE intensity above the band edge is a result of the decreasing intensity of the excitation source at these wavelengths. The SE originates at ~ 340 nm at threshold and redshifts with increasing excitation density (I_{exc}). The redshift of approximately 7 nm of the SE with respect to the band edge is consistent with the behavior of GaN at elevated I_{exc} . The SE spectrum shown in Fig. 1 was taken with an excitation density twice that of the SE threshold (I_{th}), i.e.: $I_{\text{exc}} = 2 \times I_{\text{th}}$.

Figure 9 shows RT emission spectra for (a) the $\text{Al}_{0.17}\text{Ga}_{0.83}\text{N}$ layer described above and (b) an $\text{Al}_{0.26}\text{Ga}_{0.74}\text{N}$ layer for several excitation densities below and above I_{th} . The low power cw PL peaks are also overlaid (dashed lines) for reference. The SE emerges out of the low energy spontaneous emission wing with increasing optical excitation for both layers. The separation between spontaneous and stimulated emission was measured to be ~ 10.5 and 8.5 nm, respectively, for the $x = 0.17$ and $x = 0.26$ layers. The red shift of the spontaneous emission peaks seen in the nanosecond excitation spectra of Figure 9(a) and Figure 9(b) compared to the cw spontaneous emission peaks is due to re-absorption of the emitted photons as they propagate along the excitation path in the edge-emission experiments. The larger shift in Figure 9(b) compared to that in Figure 9(a) is due to a larger band tail in the $x = 0.26$ layer compared to the $x = 0.17$, a result of increased compositional fluctuations in the $\text{Al}_x\text{Ga}_{1-x}\text{N}$ layers with increasing Al composition.

A comparison between the I_{exc} dependent behavior of these $\text{Al}_x\text{Ga}_{1-x}\text{N}$ films and that of GaN and InGaN films can now be made. We first note that the Stokes shift of the SE (~ 7 nm) with respect to the band edge exhibited by the $\text{Al}_{0.17}\text{Ga}_{0.83}\text{N}$ layer at 10 K is consistent with the SE behavior of GaN thin films at elevated temperatures and/or high I_{exc} (several times I_{th}), and is attributed to stimulated recombination of an electron-hole plasma (EHP). At low temperatures and

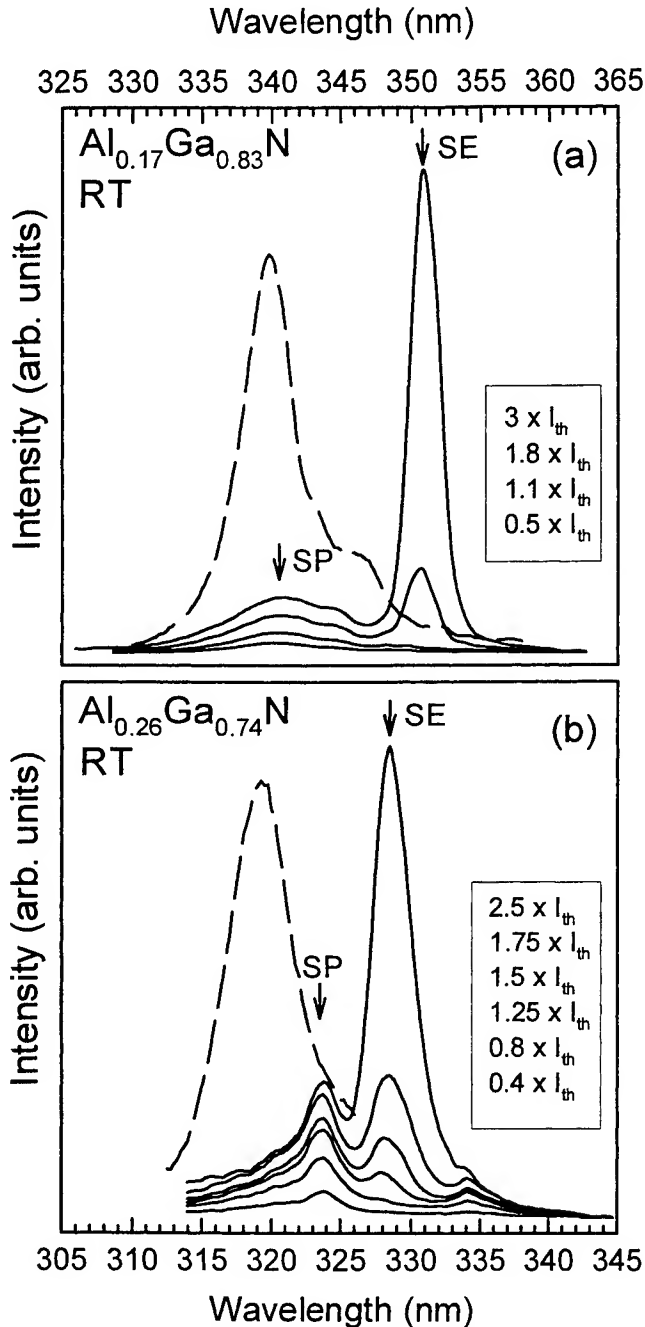


Figure 9. Dependence of emission intensity on excitation density (I_{exc}) for (a) an $Al_{0.17}Ga_{0.83}N$ and (b) an $Al_{0.26}Ga_{0.74}N$ thin film. The spontaneous (SP) and stimulated (SE) emission spectral positions are indicated by the arrows in Figure 8.

I_{exc} close to I_{th} , GaN stimulates approximately 21 meV (~ 2.1 nm) below the 1s A free exciton position, consistent with an exciton-exciton scattering related gain mechanism.^{35,36} The fact that the $Al_xGa_{1-x}N$ samples do not exhibit this behavior (and gain mechanism) is not surprising, nor expected, considering no excitonic features were observed in the PLE and photoreflectance spectra of these samples. At elevated temperatures and/or I_{exc} several times I_{th} , GaN exhibits a large Stokes shift of the SE compared to the band edge, exceeding 96 meV (~ 10.4 nm) near I_{th} at RT.³⁷ We note that InGaN films typically exhibit a large Stokes shift of the SE with respect to the band edge but only a slight redshift or even a blueshift with respect to the spontaneous emission. We also note that results for InGaN layers can vary strongly from sample to sample and with different experimental conditions,³⁸ whereas the results for GaN and $Al_xGa_{1-x}N$ layers are far more consistent from sample to sample.

Figure 10 shows the SE threshold of the $Al_xGa_{1-x}N$ samples studied here compared to a 4.2 μm GaN layer whose optical properties have been reported elsewhere^{39,40,41} and an MOCVD-grown $In_{0.18}Ga_{0.82}N$ layer of comparable alloy concentration to the $Al_{0.17}Ga_{0.83}N$ layer. The SE thresholds for the $Al_xGa_{1-x}N$ and $In_xGa_{1-x}N$ samples have been normalized to the GaN SE threshold for clarity. All samples were optically excited with the same nanosecond excitation source described above. More than an order of magnitude decrease in I_{th} for the $In_xGa_{1-x}N$ layer compared to the GaN layer is clearly seen, while incorporation of Al into GaN is seen to result in an increase in I_{th} with increasing Al concentration.

3.4. Optical nonlinearities in the band edge region of highly excited (In)GaN thin films

Nanosecond nondegenerate optical pump-probe absorption experiments on GaN have also been performed and the results have been compared to those obtained from InGaN films. Frequency doubled radiation from a nanosecond, Nd:YAG-pumped, amplified dye laser was used as a UV pumping source and broadband fluorescence from a dye solution was used as a probe source. The broadband transmitted probe spectra were analyzed using a 1-meter spectrometer in conjunction with a CCD. A pump wavelength of 342 nm was used for the GaN data presented in this report. For the InGaN study, the third harmonic (355 nm) of the same Nd:YAG laser (~ 5 ns pulses at 10 Hz) was used as the pumping source. The sample temperature was varied between 10 K and room temperature through the use of a closed cycle refrigerator.

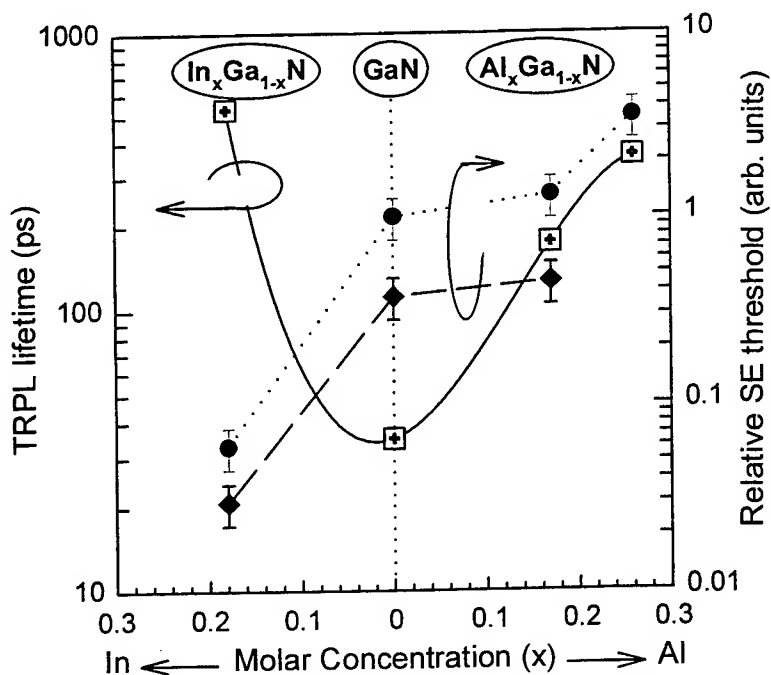


Figure 10. Relative SE thresholds for $\text{In}_{0.18}\text{Ga}_{0.82}\text{N}$, GaN , $\text{Al}_{0.17}\text{Ga}_{0.83}\text{N}$, and $\text{Al}_{0.26}\text{Ga}_{0.74}\text{N}$ thin films. The thresholds of the $\text{In}_{0.18}\text{Ga}_{0.82}\text{N}$ and $\text{Al}_x\text{Ga}_{1-x}\text{N}$ thin films are normalized to that of the GaN film ($I_{\text{th}} \sim 0.8 \text{ MW/cm}^2$). The TRPL lifetimes of the respective thin films are also shown. All samples were grown by MOCVD on (0001) oriented sapphire and optically excited with the same excitation source ($\lambda_{\text{exc}} = 310 \text{ nm}$).

body effects such as screening by free carriers, until at $I_{\text{exc}} \sim 3 \text{ MW/cm}^2$ they are no longer observable in the absorption spectra. The induced transparency associated with this saturation is large, exceeding $4 \times 10^4 \text{ cm}^{-1}$. In addition, the band edge is seen to flatten and shift to lower energies with increasing I_{exc} . The resulting below-gap induced absorption is also large, exceeding $4 \times 10^4 \text{ cm}^{-1}$. The below-gap induced absorption was found to reach a maximum several nanoseconds after the pump pulse, slowly returning to zero over approximately the next 100 ns.⁴³ Similar results were obtained in room temperature experiments. It has been suggested that the below-gap induced absorption is a result of lattice heating.^{44,45} We have estimated the amount of lattice heating generated by the nanosecond pump beam and have found it to be significantly less than is required to account for the observed band gap shift.⁴⁶ It will be shown later that this induced absorption is not present in InGaN films under similar excitation conditions. We believe the origin lies in the present crystalline quality of

GaN epitaxial film, where the multitude of crystalline defects and deep levels present in epitaxial GaN films contribute to the observed below-gap induced absorption.⁴⁷ The decrease in free exciton absorption with increasing I_{exc} is expected and attributed to many body effects, such as exciton screening by free carriers, causing a diminution of the excitonic oscillator strength.⁴⁸

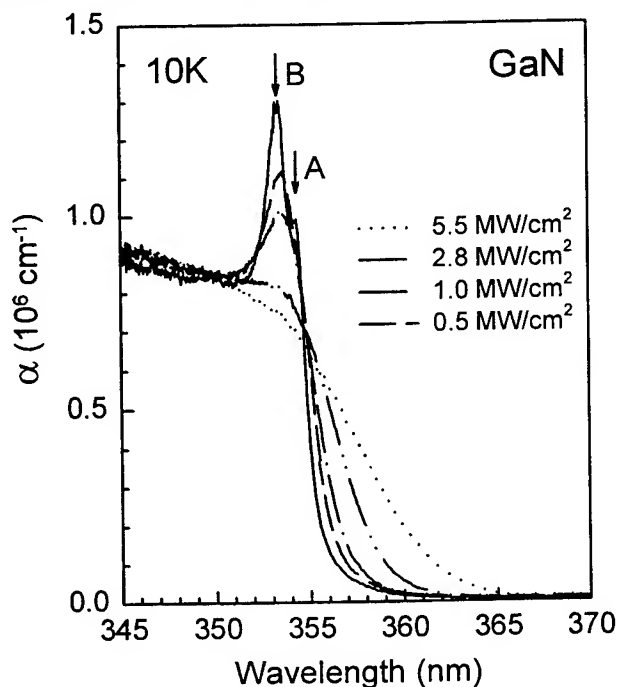


Figure 11. Nanosecond nondegenerate optical pump-probe absorption spectra of an MOCVD-grown GaN thin film at 10 K and RT as a function of increasing above-gap optical excitation. The 1 s A and B free exciton transitions are clearly seen in the unpumped spectrum. Clear induced transparency in the excitonic region and induced absorption in the below-gap region are seen with increasing optical excitation. The spectra are shown for zero time delay between the pump and probe pulses. The excitation wavelength was 342 nm.

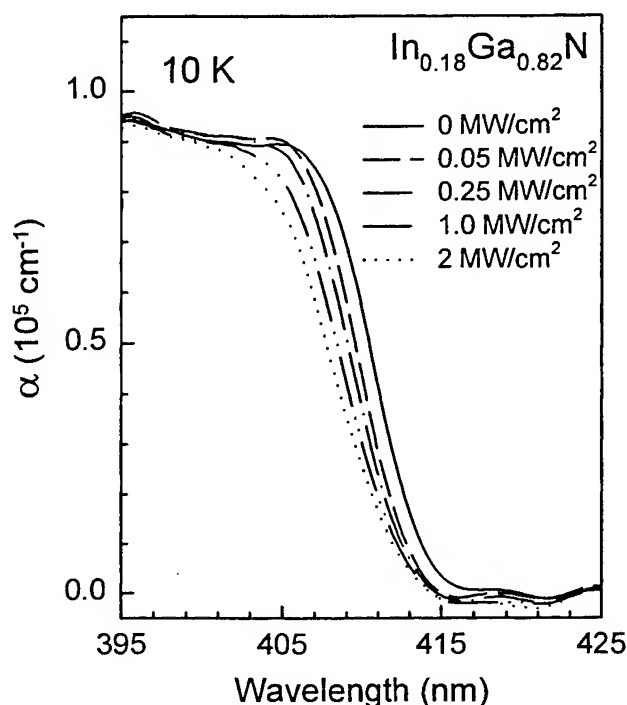


Figure 12. 10 K nanosecond nondegenerate optical pump-probe absorption spectra of an MOCVD-grown InGaN thin film as a function of above-gap optical excitation. The absorption edge of the InGaN film is significantly broader than that of GaN thin films, indicative of increased band tailing due to alloy fluctuations. Clear bleaching of these band tail states is observed with increasing excitation. Note the complete absence of below-gap induced absorption. The excitation wavelength was 355 nm.

Figure 12 shows the results of nanosecond nondegenerate optical pump-probe experiments performed on a 0.1 μm thick $\text{In}_{0.18}\text{Ga}_{0.82}\text{N}$ layer. The absorption edge of the $\text{In}_{0.18}\text{Ga}_{0.82}\text{N}$ layer is seen to be considerably broader than that of the GaN film. This band tailing is a result of difficulties in uniform indium incorporation. With increasing I_{exc} , absorption bleaching of the tail states is clearly observed, where the bleaching is seen to cover the entire spectral range of the absorption tail. We note that no induced absorption was observed in

the below-gap region of the InGaN layers. Instead, clear features attributed to net optical gain were observed in the below-gap region of the bleaching spectra.^{49,50} Similar experiments were performed on AlGaIn layers of similar alloy concentration ($x = 18\%$). AlGaIn films were observed to exhibit behavior similar to that of GaN, as opposed to InGaIn. The lack of induced absorption in the below-gap region of InGaIn-based materials is consistent with the order of magnitude reduction in stimulated emission threshold typically observed for InGaIn relative to GaN and AlGaIn films.⁵¹

4. CONCLUSIONS

We have studied the gain mechanisms in GaN epilayers in the temperature range of 20 to 700 K. We observed that for temperatures below 150 K the dominant near-threshold gain mechanism is inelastic exciton-exciton scattering, characterized by a low stimulated emission threshold. For temperatures exceeding 150 K the dominant gain mechanism was shown to be electron-hole plasma recombination, characterized by a relatively high SE threshold and a large separation between spontaneous and stimulated emission peaks. We also achieved efficient ultra-violet lasing in GaN/AlGaIn separate confinement heterostructures over a wide temperature range. Through an analysis of the relative shift between spontaneous emission and lasing peaks, combined with the temperature dependence of the lasing threshold, we demonstrate that exciton-exciton scattering is the dominant gain mechanism leading to low-threshold ultra-violet lasing over the entire temperature range studied. We showed that, in GaN/AlGaIn heterostructures, carrier and optical confinement play the decisive role in lowering the lasing threshold. We have also observed optically pumped SE at room temperatures from MOCVD-grown $\text{Al}_x\text{Ga}_{1-x}\text{N}$ films with SE wavelengths as low as 328 nm, putting the SE well within the deep UV region of the spectrum. To the best of our knowledge, this is the shortest room temperature SE wavelength ever reported from a semiconductor and illustrates that $\text{Al}_x\text{Ga}_{1-x}\text{N}$ based heterostructures have an unmatched capability for extending the range of semiconductor laser diodes deep into the UV. In addition, nanosecond and femtosecond nondegenerate optical pump-probe absorption experiments have been performed on GaN thin films and the results have been compared to those obtained for InGaIn films. The results suggest the high stimulated emission threshold of GaN relative to InGaIn results from induced absorption in the below-gap region of GaN with increasing carrier concentration, an effect absent in InGaIn.

5. ACKNOWLEDGEMENTS

The authors would like to thank ONR, AFOSR, BMDO, and DARPA for funding this work.

REFERENCES

- ¹ S. N. Mohammad and H. Morkoc, *Prog. Quant. Electr.* **20**, 361 (1996), and references therein.
- ² S. Nakamura, M. Senoh, S. Nagahama, N. Iwasa, T. Yamada, T. Matsushita, Y. Sugimoto, and H. Kiyoku, *Appl. Phys. Lett.* **70**, 868 (1997).
- ³ B. Goldenberg, J. D. Zook, and R. J. Ulmer, *Appl. Phys. Lett.* **62**, 381 (1993).
- ⁴ T. W. Weeks, Jr., M. D. Bremser, K. S. Ailey, E. Carlson, W. G. Perry, and R. F. Davis, *Appl. Phys. Lett.* **67**, 401 (1995).
- ⁵ W. Shan, A. J. Fischer, S. J. Hwang, B. D. Little, R. J. Hauenstein, X. C. Xie, J. J. Song, D. S. Kim, B. Goldenberg, R. Horning, S. Krishnankutty, W. G. Perry, M. D. Bremser, and R. F. Davis, *J. Appl. Phys.* **83**, 455 (1998).
- ⁶ R. Dingle, K. L. Shaklee, R. F. Leheny, and R. B. Zetterstrom, *Appl. Phys. Lett.* **19**, 5 (1971).
- ⁷ S. Bidnyk, B. D. Little, T. J. Schmidt, J. Krasinski, and J. J. Song, *Proc. SPIE* **3419**, 35 (1998).
- ⁸ H. Amano and I. Akasaki, *Proc. Topical Workshop on III-V Nitrides*, pp. 193-195, Nagoya, Japan (1995).
- ⁹ I. M. Catalano, A. Cingolani, M. Ferrara, M. Lugarà and A. Minafra, *Solid State Comm.* **25**, 349 (1978).
- ¹⁰ J. Holst, L. Eckey, A. Hoffman, I. Broser, B. Schöttker, D. J. As, D. Schikora, and K. Lischka, *Appl. Phys. Lett.* **72**, 1439 (1998).
- ¹¹ X. H. Yang, T. J. Schmidt, W. Shan, J. J. Song, and B. Goldenberg, *Appl. Phys. Lett.* **66**, 1 (1995).
- ¹² S. Bidnyk, T. J. Schmidt, G. H. Park, and J. J. Song, *Appl. Phys. Lett.* **71**, 729 (1997).
- ¹³ A. J. Fischer, W. Shan, J. J. Song, Y. C. Chang, R. Horning, and B. Goldenberg, *Appl. Phys. Lett.* **71**, 1981 (1997).
- ¹⁴ I. Galbraith and S. W. Koch, *J. Crystal Growth* **159**, 667 (1996).
- ¹⁵ See, for example, D. Wood, *Optoelectronic Semiconductor Devices*, (Prentice Hall, New York, 1994), pp. 136-138.
- ¹⁶ W. Shan, B. D. Little, A. J. Fischer, J. J. Song, B. Goldenberg, W. G. Perry, M. D. Bremser, and R. F. Davis, *Phys. Rev. B* **54**, 16369 (1996).
- ¹⁷ R. Levy and J. B. Grun, *Phys. Stat. Sol. (a)* **22**, 11 (1974).
- ¹⁸ X. H. Yang, J. M. Hays, W. Shan, J. J. Song, and E. Cantwell, *Appl. Phys. Lett.* **62**, 1071 (1992).
- ¹⁹ T. Uenoyama, *Phys. Rev. B* **51**, 10228 (1995).
- ²⁰ R. Dingle, *Semiconductors and Semimetals*, Vol. **24** (Academic Press, Inc., New York, 1987), pp. 18-23.
- ²¹ H. Jeon, J. Ding, A. V. Nurmikko, H. Luo, N. Samarth, J. K. Furdyna, *Appl. Phys. Lett.* **57** 23, 2413 (1990).
- ²² T. J. Schmidt, X. H. Yang, W. Shan, J. J. Song, A. Salvador, W. Kim, Ö. Aktas, A. Botchkarev, H. Morkoç, *Appl. Phys. Lett.* **68**, 1820 (1996).
- ²³ See homepage of Nichia America Corporation at <http://www.nichia.com>.
- ²⁴ S. Nakamura, M. Senoh, S. Nagahama, N. Iwasa, T. Yamada, T. Matsushita, Y. Sugimoto, and H. Kiyoku, *Appl. Phys. Lett.* **69**, 4056 (1996).
- ²⁵ S. Nakamura, M. Senoh, S. Nagahama, N. Iwasa, T. Matsushita, and T. Mukai, *MRS Internet J. Nitride Semicond. Res.* **4S1**, G1.1 (1999).
- ²⁶ Bidnyk, T. J. Schmidt, Y. H. Cho, G. H. Gainer, J. J. Song, S. Keller, U. K. Mishra, and S. P. DenBaars, *Appl. Phys. Lett.* **72**, 1623 (1998).
- ²⁷ T. J. Schmidt, X. H. Yang, W. Shan, J. J. Song, A. Salvador, W. Kim, Ö. Aktas, A. Botchkarev, and H. Morkoç, *Appl. Phys. Lett.* **68**, 1820 (1996).
- ²⁸ J. J. Song, A. J. Fischer, T. J. Schmidt, S. Bidnyk, and W. Shan, *Nonlinear Optics* **18**, 269 (1997).
- ²⁹ A. J. Fischer, W. Shan, J. J. Song, Y. C. Chang, R. Horning, and B. Goldenberg, *Appl. Phys. Lett.* **71**, 1981 (1997).
- ³⁰ S. Bidnyk, T. J. Schmidt, B. D. Little, and J. J. Song, *Appl. Phys. Lett.* **74**, 1 (1999).
- ³¹ For a review, see J. Y. Duboz and M. A. Khan in *Group III Nitride Semiconductor Compounds: Physics and Applications* (Oxford Univ. Press, New York, 1998) pp. 343-390.
- ³² A. I. Dirochka, M. N. Zargar'yants, A. A. Kiselev, E. V. Sinitsyn, *Sov. Phys. Semicond.* **13**, 113 (1979).
- ³³ D. Wiesmann, I. Brener, L. Pfeiffer, M. A. Khan, and C. J. Sun, *Appl. Phys. Lett.* **69**, 3384 (1996).
- ³⁴ S. Nakamura, M. Senoh, S. Nagahama, N. Iwasa, T. Yamada, T. Matsushita, H. Kiyoku, Y. Sugimoto, and T. Kozaki, H. Umemoto, M. Sano, and K. Chocho, *Jpn. J. Appl. Phys., Part 2* **36**, L1568 (1997).
- ³⁵ J. M. Hvam and E. Ejder, *J. of Lumin.* **12/13**, 611 (1976).
- ³⁶ J. Holst, L. Eckey, A. Hoffmann, I. Broser, B. Schottker, D. J. As, D. Schikora, and K. Lischka, *Appl. Phys. Lett.* **72**, 1439 (1998).
- ³⁷ S. Bidnyk, B. D. Little, T. J. Schmidt, J. Krasinski, and J. J. Song, *Proc. SPIE* **3419**, 35 (1998).

- ³⁸ T.J. Schmidt, S. Bidnyk, Y.H. Cho, A.J. Fischer, J.J. Song, S. Keller, U.K. Mishra, and S.P. DenBaars, Appl. Phys. Lett. **73**, 3689 (1998).
- ³⁹ X.H. Yang, T.J. Schmidt, W. Shan, J.J. Song, and B. Goldenberg, Appl. Phys. Lett. **66**, 1 (1995).
- ⁴⁰ W. Shan, T. J. Schmidt, X. H. Yang, S. J. Hwang, J. J. Song, and B. Goldenberg, Appl. Phys. Lett. **66**, 985 (1995).
- ⁴¹ T. J. Schmidt, J. J. Song, Y. C. Chang, R. Horning, and B. Goldenberg, Appl. Phys. Lett. **72**, 1504 (1998).
- ⁴² A. J. Fischer, W. Shan, J. J. Song, Y. C. Chang, R. Horning, and B. Goldenberg, Appl. Phys. Lett. **71**, 1 (1997).
- ⁴³ T. J. Schmidt, Ph. D. Thesis, Oklahoma State University (1998).
- ⁴⁴ H. Haag, P. Gilliot, R. Levy, B. Honerlage, O. Briot, S. Ruffenach-Clur, and R.L. Aulombard, Phys. Rev. B **59**, 2254 (1999).
- ⁴⁵ H. Haag, P. Gilliot, R. Levy, B. Honerlage, O. Briot, S. Ruffenach-Clur, and R.L. Aulombard, Appl. Phys. Lett. **74**, 1436 (1999).
- ⁴⁶ T.J. Schmidt, Y.C. Chang, and J.J. Song, Proc. SPIE **3419**, 61 (1998).
- ⁴⁷ See, for example, S. D. Lester, F. A. Ponce, M. G. Craford, and D. A. Steigerwald, Appl. Phys. Lett. **66**, 1249 (1995), or S. D. Hersee, J. C. Ramer, and K. J. Malloy, Mater. Res. Bull. **22**, 45 (1997).
- ⁴⁸ C. Klingshirn and H. Haug, Phys. Rep. **70**, 315 (1981), and references therein.
- ⁴⁹ T.J. Schmidt, J.J. Song, S. Keller, U.K. Mishra, and S.P. DenBaars, Mat. Res. Symp. Proc. **572**, 351(1999).
- ⁵⁰ T.J. Schmidt, Y.H. Cho, S. Bidnyk, J.J. Song, S. Keller, U.K. Mishra, and S.P. DenBaars, Proc. SPIE **3625**, 57 (1999).
- ⁵¹ T.J. Schmidt, Y.H. Cho, J.J. Song, and W. Yang, Appl. Phys. Lett. **74**, 245 (1999).

Optical properties of InGaN grown by MOCVD on sapphire and on bulk GaN

Marek Osinski^{*a}, Petr G. Eliseev^{ab}, Jinhyun Lee^a, Vladimir A. Smagley^a,
Tomoya Sugahara^c and Shiro Sakai^c

^aCenter for High Technology Materials, University of New Mexico, 1313 Goddard SE
Albuquerque, New Mexico 87106, USA

^bAlso at P. N. Lebedev Physics Institute, Russian Academy of Sciences, Moscow, Russia

^cDepartment of Electrical and Electronic Engineering, University of Tokushima
2-1 Minami-josanjima, Tokushima, Japan

ABSTRACT

Experimental data on photoluminescence of various bulk and quantum-well epitaxial InGaN/GaN structures grown by MOCVD are interpreted in terms of a band-tail model of inhomogeneously broadened radiative recombination. The anomalous temperature-induced blue spectral is shown to result from band-tail recombination under non-degenerate conditions. Significant differences are observed between epilayers grown on sapphire substrates and on GaN substrates prepared by the sublimation method, with no apparent evidence of band tails in homoepitaxial structures, indicating their higher crystalline quality.

Key words: Wide-bandgap semiconductors, InGaN, photoluminescence, band tails, homoepitaxy

1. INTRODUCTION

The ternary alloy $\text{In}_x\text{Ga}_{1-x}\text{N}$ has become a very important material in semiconductor physics. It can be fabricated as a thin film in different multilayer group-III nitride structures, and in spite of its poor crystalline quality it serves as efficient luminescent material in UV and visible light-emitting diodes and diode lasers.¹⁻⁴ It also seems promising for high-temperature optoelectronics, since its radiative quantum yield does not drop significantly as the ambient temperature is increased from 300 to 450 K.⁵

Even though InGaN-based devices have reached commercial maturity, the radiative emission processes in this material are not yet well understood. According to Ref. 6, emission in InGaN can be assigned to recombination of excitons localized at potential energy minima in the quantum well. From a study of multiple quantum wells, it was concluded that the exciton localization occurs at deep traps which could be originated from indium-rich regions acting as quantum dots.⁷ Some spectral features of InGaN-containing structures are rather unusual. As the ambient temperature increases, the emission peak undergoes an anomalous blue shift.⁸⁻¹¹ In addition, it was found that the emission peak spans continuously a wide spectral range (~ 0.2 eV) when the current passes ~ 6 decades.⁸ A strong contribution of non-thermal broadening is characteristic of the electroluminescence spectra of AlGaIn/GaN single quantum wells.⁹⁻¹⁰ A likely involvement of band-tail states was also pointed out.⁹⁻¹³

There are several issues with the InGaN alloy concerning its physical-chemical properties and fabrication methods. These are crystalline quality of hetero- and homoepitaxial material, residual stress/strain and piezoelectric fields, and alloy stability. All of these factors seem to influence the radiative recombination processes. In this paper, we present in detail a simple analytical model of recombination involving band-tail states that can be caused by a strong variation of the energy bandgap due to compositional non-uniformity and, possibly, to alloy instability associated with phase separation. The model

^{*}Correspondence: Email: osinski@chtm.unm.edu; WWW: <http://www.chtm.unm.edu>; Telephone: 505 272 7812;
Fax: 505 272 7801

is then applied to InGaN and compared with results of extensive spectral studies of photoluminescence from different InGaN-based epitaxial materials: bulk layers, single quantum wells, and multiple-quantum-well structures. We interpret the efficient radiative process in InGaN to be the result of fast capture of excess carriers into the band-tail states, with a subsequent radiative recombination. We focus on temperature dependence of the spectral peak position that allows us to describe different types of behavior in terms of the band-tail model and to derive the energy parameter of tails describing the broadening of the band edges. Such a broadening is the origin of the band tail states.

2. THE BAND-TAIL MODEL

2.1. General Remarks

Band tails can appear in the electron energy spectrum of solids as a result of disordering in the crystalline structure introduced by defects, impurities and non-uniformity of chemical composition. The best known examples of such tails are amorphous and heavily doped semiconductors (see, *e.g.* Ref. 14). Application of the band-tail concept to heavily-doped light-emitting diodes and diode lasers had been considered in Ref. 15, where occupation of the Gaussian density-of-states (DOS) tails was analyzed.

In a heavily doped semiconductor, disordering is associated with random Coulomb field of ionized impurities. In InGaN, the nature of band-tail states is different; they appear even in undoped material due to strong compositional non-uniformity. We emphasize that composition-related tail states are suitable to provide efficient luminescence because, as opposed to ionized impurities, these states attract both types of carriers: potential wells for both electrons and holes are associated with the same site (indium-rich cluster). Due to this, the matrix element for optical transitions can be as large as in the case of free carriers. In heavily doped semiconductors, the random electric potential of the Coulomb centers produces distant extremes of band edges that separate carriers of opposite sign. This leads to an increase in the lifetime of carriers captured into deep tail states, due to reduced matrix element.

Another particular feature of tail states in InGaN is that the composition variations are not statistical fluctuations, but rather a result of partial decay of the alloy, associated with its thermodynamic instability. This can produce more significant broadening of band edges than in heavily doped semiconductors.

In light-emitting structures, the tail states are very important, because they provide the lowest-energy levels available for the carriers. These states are occupied by excess minority carriers (or by both kinds of carriers) starting from very low pumping rates. Also, these states are the first ones to reach inverted population in lasers under higher pumping rate. The occupation of tails is more sensitive to the pumping rate than the occupation in regular energy bands because the DOS in tails is much lower. This produces strong band-filling effects characteristic of band tails (blue shift of the emission peak with an increasing pumping rate). On the other hand, the tails are a result of excessive inhomogeneous broadening in the system, and its contribution into spectral bandwidth leads to broader spontaneous emission spectra and higher lasing threshold.

We consider the language of band tails to be adequate for quantitative analysis of broad emission from InGaN. This is not in contradiction with a concept of localized excitons, which is more fruitful for very narrow linewidth emission in many semiconductors, including GaN. As an electron-hole pair is captured into tail states, the state occupation can be described as that of fermions, with the Fermi-Dirac statistics. This is an important tool for analysis that distinguishes localized excitons from the usual Bose-Einstein excitonic statistics.

Here we deal with certain DOS distribution in the band tails, without regard to what is a predominant cause of the energy level spreading. In agreement with traditional approach, we assume that multiple factors can lead to the Gaussian statistics of the spreading. These factors are: 1) a real shape of profiles for potential energy in cluster-related wells, 2) the Coulomb interaction of localized carriers, 3) free-carrier screening and other many-body effects, 4) exchange effects with neighboring clusters, 5) piezoelectric effect due to residual lattice strain. We believe that resulting DOS distribution is sufficiently stable in order to apply the regular distribution functions for occupation probability of tail states. If this approach were not producing satisfactory results, specific corrections would have to be introduced, for example, accounting for many-body effects.

2.2. Density-of-States Distribution

The local band edge (*1e*, *1hh* levels for quantum wells, conduction- and valence-band edges for bulk material) is assumed to fluctuate due to compositional variations. The average density of states (DOS) as a function of energy should be calculated as¹⁴

$$\rho(E) = \int \rho(E, V) P(V) dV, \quad (1)$$

where $\rho(E, V)$ is the local DOS function, $P(V)$ is the probability distribution, and V is the local band-edge position. The averaging procedure leads to smoothening of the sharp edge of the DOS distribution. Let us assume that the 2-dimensional DOS in quantum wells has a step-like shape:

$$\rho(E, V) = (m^*/\pi\hbar^2) \sum_i \vartheta(E - V_i), \quad (2)$$

where m^* is the effective mass, ϑ is the Heaviside step function [$\vartheta(x) = 1$ for $x > 0$ and $\vartheta(x) = 0$ for $x < 0$], and i is the subband index. We consider the shape modification of the lowest subband edge, $i = 1$. The probability function is assumed to be Gaussian:

$$P(V) = (2^{1/2}\pi^{1/2}\sigma)^{-1} \exp [-(V - V_0)^2/(2\sigma^2)], \quad (3)$$

where σ is the energy parameter of the distribution, and V_0 is the central position of the local band edge (the nominal band edge). The averaging procedure as in Eq. (1) gives

$$\rho(E) = (m^*/2\pi\hbar^2) \{1 + \operatorname{erf} [(E - V_0)/(2^{1/2}\sigma)]\}. \quad (4)$$

This expression predicts the DOS to be twice lower at the nominal edge $E = V_0$ than before averaging, and a decrease in the tail below the nominal edge. The asymptotic behavior (at energies deep inside the nominal bandgap) of $\rho(E)$ as given in Eq. (4) corresponds to the Gaussian form.

The parameter σ describes the broadening effect and the shape of the tail. In this simple approach, it is the only adjustable parameter. In general, this corresponds to the assumption of a distribution with non-vanishing moments only up to the second order. If higher-order moments are substantial, the distribution can be more complicated (asymmetric, *etc.*).

Under some circumstances, these assumptions can be modified. One case is correlation in compositional clusters (due to phase separation or chemical reordering). For example, phase separation caused by annealing may lead to formation of In-rich clusters of ultimate phase composition. If this process is completed, there will be a predominance of clusters with a definite composition. The random factor would be the size of clusters, but not their composition. There would be no states deeper than some cut level, corresponding to the ultimate phase composition. Thus, the asymptotic part of DOS distribution would deviate from the Gaussian shape.

2.3. Band-Tail Model: Carrier Occupation of Gaussian Band Tails

The model of quasi-equilibrium occupation with a Gaussian DOS was proposed earlier for heavily doped GaAs diode lasers.¹⁵ Under the increasing pumping rate, two types of behavior can in principle be observed in luminescence spectra: 1) a stable peak position, corresponding to non-degenerate occupation; and 2) blue-shifting peak corresponding to degenerate occupation (band-filling). It can be illustrated by a simple example of carrier distribution $N(E)$ in the energy scale of one of the tails, as shown in Fig. 1(a) for a range of Fermi-level positions. The DOS distribution corresponding to Eq. (4) is marked with a thick line. Thin lines in Fig. 1(a) represent carrier distributions with their maxima marked by dots. At low pumping rates, when the normalized Fermi level $(F - E_0)/\sigma < -3$, the peak of the carrier distribution has a stable position with a constant bandwidth. At higher pumping rates, the peak is pulled by the Fermi level towards the high-energy side. The non-degenerate occupation is typical for lower pumping rates and higher temperatures, while the degenerate occupation is typical for higher pumping rates and lower temperatures. An interesting feature of the redistribution of carriers with increasing temperature is shown in Fig. 1(b). As temperature rises, the peak of the curves moves towards higher energy. This effect is similar to ionization of local levels, but extended to the case of a continuous energy spectrum. It can lead to a blue temperature-induced shift of the emission peak, when the rate of the shift overcomes the rate of the temperature-induced bandgap shrinkage. Using the Gaussian approximation for the DOS distribution, we can obtain analytical expressions for this behavior.

We assume here that the DOS function $\rho_{e,h}(E)$ in the conduction and valence bands, respectively, has a Gaussian form:

$$\rho_{e,h}(E) = \rho_{0e,h} \exp [-(E - E_{0e,h})^2/2\sigma_{e,h}^2], \quad (5)$$

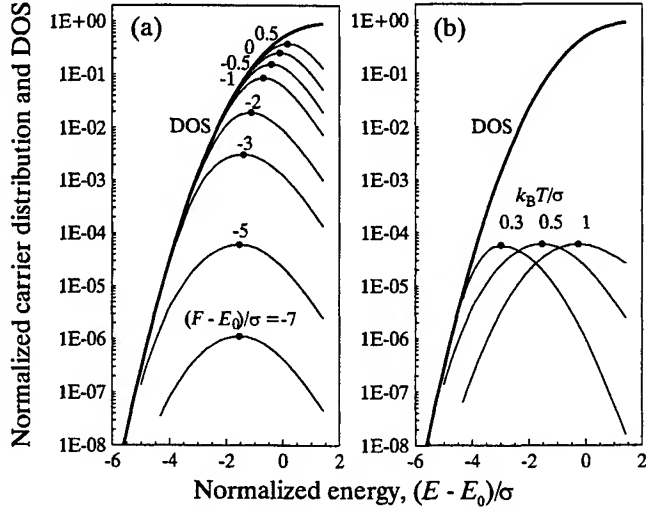


Fig. 1. Calculated normalized DOS distribution (thick lines) and carrier distributions (thin lines), both in units of $m^*/2\pi\hbar^2$, in function of the normalized energy $(E - E_0)/\sigma$, where E_0 is the nominal band edge. Dots mark the peak position. The DOS has a Gaussian asymptote deep inside the bandgap, but differs from the Gaussian function near the nominal (not-broadened) band edge E_0 . (a) Evolution of carrier distribution with increasing normalized Fermi energy $(F - E_0)/\sigma$ at constant temperature $T = \sigma/2k_B$. (b) Evolution of carrier distribution with temperature rise at approximately constant carrier density (normalized temperature is given in units of σ/k_B , where k_B is Boltzmann's constant).

where ρ_{0e} , ρ_{0h} , E_{0e} , E_{0h} , σ_e and σ_h are fixed parameters for band-tails of electron and hole states. In particular, E_{0e} and E_{0h} are the centers of the DOS Gaussians for the conduction and valence band tail, respectively, while σ_e^2 , σ_h^2 are the dispersions of both Gaussians. The optical transitions between the states of two tails are assumed to occur with no momentum conservation; hence the spectrum of spontaneous emission rate $r_{sp}(h\nu)$ can be represented by the integral convolution as follows:

$$r_{sp}(h\nu) = B(h\nu) \int \rho_e(E + h\nu) f_e(E + h\nu) \rho_h(E) f_h(E) dE, \quad (6)$$

where h is the Planck constant, ν is the photon frequency, $B(h\nu)$ is the recombination constant, and $f_e(E + h\nu)$, $f_h(E)$ are the occupation functions for both involved tails, respectively. We also assume that both occupation functions are Fermi-Dirac functions with a separate quasi-Fermi level F_e , F_h for each tail (the quasi-equilibrium approximation). In this consideration, we shall neglect the spectral dependence of $B(h\nu)$. Our focus is the behavior of the spectral peak $h\nu_p$ of the emission band. In the low-current case, we can suggest $h\nu_p - \Delta F > k_B T$, where $\Delta F = F_e - F_h$ is the quasi-Fermi-level separation and k_B is the Boltzmann constant. This condition corresponds to the *non-degenerate occupation*. Therefore, the Boltzmann's tails of the occupation function can be used:

$$f_e(E, T, F_e) \cong \exp[(F_e - E)/k_B T], \quad (7a)$$

$$f_h(E, T, F_h) \cong \exp[(E - F_h)/k_B T]. \quad (7b)$$

The carrier distributions $N(E)$, $P(E)$ for electrons and holes, respectively, can be calculated as follows:

$$N(E) = \rho_e(E) f_e(E, T, F_e) = \rho_{0e} \exp[(F_e - E_{0e}^*)/k_B T] \exp(-\sigma_e^2/2k_B^2 T^2) \exp[-(E - E_{0e}^*)^2/2\sigma_e^2], \quad (8a)$$

$$P(E) = \rho_h(E) f_h(E, T, F_h) = \rho_{0h} \exp[(E_{0h}^* - F_h)/k_B T] \exp(-\sigma_h^2/2k_B^2 T^2) \exp[-(E - E_{0h}^*)^2/2\sigma_h^2], \quad (8b)$$

where

$$E_{0e}^* = E_{0e} - \sigma_e^2/k_B T, \quad (9a)$$

$$E_{0h}^* = E_{0h} + \sigma_h^2/k_B T. \quad (9b)$$

As shown in Eq. (8), both carrier distributions over the energy scale are Gaussian with the same values of dispersion as in the corresponding DOS functions. The convolution of two Gaussians as specified in Eq. (6) gives again a Gaussian with the sum of partial dispersions,

$$r_{sp}(h\nu) = B \int N(E + h\nu) P(E) dE = B^* \rho_{0e} \rho_{0h} \int \exp[-(E + h\nu - E_{0e}^*)^2/2\sigma_e^2] \exp[-(E - E_{0h}^*)^2/2\sigma_h^2] dE$$

$$= B^* \rho_{0e} \rho_{0h} \exp[-(h\nu - h\nu_0)^2/2\sigma^2] , \quad (10)$$

where

$$B^* = B \exp[-(\sigma_e^2 + \sigma_h^2)/2k_B^2 T^2] \exp[(\Delta F - h\nu_0)/k_B T] , \quad (11a)$$

$$h\nu_0 = E_{0e}^* - E_{0h}^* , \quad (11b)$$

$$\sigma^2 = \sigma_e^2 + \sigma_h^2 . \quad (11c)$$

For a more general case, some non-Gaussian DOS distributions could be considered. Requirements for possible Gaussian-like distributions are: 1) reasonable asymptotic behavior deeply in the nominally forbidden band, 2) monotonic increase of the DOS from deep states to the nominal band edge, 3) smooth fitting to the undisturbed DOS somewhere near or above the nominal band edge.

A general rule for the position of the occupation maximum in a non-degenerate case for a monotonic DOS distribution is as follows:¹⁵

$$d \ln \rho / dE |_{\text{peak}} = (k_B T)^{-1} . \quad (12)$$

This position is rather stable with the increasing pumping range until degeneracy occurs [cf. Fig. 1(a)]. This means that the spontaneous emission peak is expected to be stable in the entire range of non-degenerate occupation (no band-filling effect). Therefore, any changes of the spectral position of the emission peak should be tested carefully with respect to: 1) occurrence of degeneracy with a transition to usual band-filling effect with peak position pulled by the quasi-Fermi levels; 2) change of DOS distribution by many-body effects; 3) total change of the dominant emission mechanism.

2.4. Temperature-Induced Shift of the Peak

Using Eq. (10), we can find that the spontaneous emission spectrum has a *temperature-dependent peak* at the photon energy

$$h\nu_0 = E_{0e}^* - E_{0h}^* = E_{0e} - \sigma_e^2/k_B T - E_{0h} - \sigma_h^2/k_B T = E_0^* - \sigma^2/k_B T , \quad (13)$$

where $E_0^* = E_{0e} - E_{0h}$ is the energy separation between the centers of Gaussian DOS distributions for electrons and holes, and $\sigma^2/k_B T$ is the "red" shift of the emission peak relative to the energy distance between the Gaussian centers. The energy E_0^* is close to the bandgap energy E_g , therefore, it can be assumed to depend on temperature in the same manner as E_g , namely,

$$E_0^*(T) = E_0^*(0) - \alpha T^2/(\beta + T) , \quad (14)$$

where α and β are expected to be close to the usual Varshni parameters. We use Eqs. (13) and (14) to obtain curves of $(h\nu_0 - E_0^*)$ plotted in Fig. 2 as function of temperature. The upper thick curve illustrates the temperature dependence of E_0^* , obtained with $\alpha = 1$ meV/K, $\beta = 1196$ K for the Varshni parameters. These values have been extracted from photoreflectance measurements¹⁶ of $\text{In}_{0.14}\text{Ga}_{0.86}\text{N}$ samples rather than from photoluminescence (PL) spectra. It was noticed in Ref. 16 that the PL peak was significantly red-shifted compared to the actual bandgap energy. We emphasize here that band-tailing effects influence PL spectra much more strongly than photoreflectance spectra. The calculated curves in Fig. 2 illustrate this effect.

Within the framework of the band-tail model, the temperature-induced shift of the low-current spectral peak position $h\nu_0$ is as follows:

$$d(h\nu_0)/dT = dE_0^*/dT - d[(\sigma_e^2 + \sigma_h^2)/k_B T]/dT = dE_g/dT + \sigma^2/k_B T^2 . \quad (15)$$

The sign of the temperature-induced shift is determined by dominant term on the right hand side of Eq. (15), with the negative bandgap term, and the positive band-tail term.

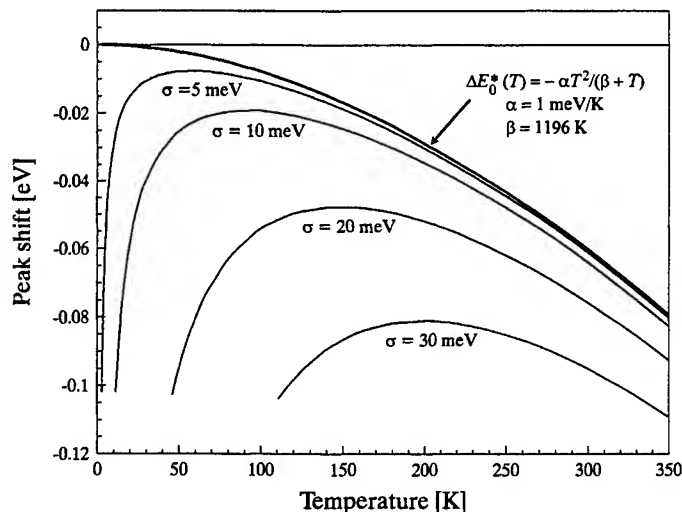


Fig. 2. Calculated peak position shift in function of temperature for a non-degenerate occupation of tail states. Thick curve corresponds to $\sigma = 0$ (no tails) and is given in the Varshni approximation. The peak position follows the thin lines corresponding to various values of the tail parameter σ . At very low temperatures, the dramatic decrease of the peak energy would actually be compensated due to degenerate occupation. In practice, degenerate occupation can be easily identified by observation of the emission peak shift with increasing pumping (due to the band-filling process). Such type of the peak position behavior has been clearly observed in electroluminescence studies of InGaN/AlGaIn/GaN quantum-well light-emitting diodes (LEDs).^{9-11,17-18}

3. EXPERIMENTAL

Epitaxial layers and multilayer structures used in this work have been grown at the University of Tokushima by horizontal atmospheric-pressure MOCVD epitaxy. TMG (trimethylgallium), TMI (trimethylindium) and NH_3 were used as source gases. A thin GaN buffer layer was grown at 500 °C, and then GaN layer was grown at 1050 °C.

Two types of substrates have been used: 1) sapphire, *c*-plane (0001), 2) "bulk" (needle-shaped) GaN (1010), *c*- and *m*-plane, grown by sublimation method.¹⁹ Single-heterostructure (SH) samples had an uncapped "bulk"-type InGaIn layer grown at 800 °C on a 2- μm -thick GaN buffer/substrate. The InGaIn layer thickness ranged from 50 nm to 110 nm. Two other types of samples are single- and multiple-quantum-well (SQW and MQW) structures with InGaIn wells and GaN barriers, sandwiched by GaN layers. Maximum cumulative InGaIn thickness was in MQW samples was 20 nm, minimum (in SQW samples) was 0.8 nm. The average composition of alloys was in the range of 5-25% and had been controlled by the growth process. The average indium content was determined using x-ray diffraction measurements. All samples prepared for PL characterization were undoped. Data on structural analysis of such epitaxial structures were reported earlier.²⁰⁻²³ For a single GaN layer, the transition of the film structure from grains with relatively independent orientation at about 300 nm to a uniform film with mosaic structure at 1.4 μm was observed. The threading dislocation density in epilayers ranges from 10^8 to 10^9 cm^{-2} in sapphire-substrate samples and is less than 10^6 cm^{-2} in homoepitaxial samples.

In PL measurements, a 325-nm UV line from He-Cd laser was used for surface pumping and a blue line at 442 nm was used for selective pumping of InGaIn layers covered by GaN. The illuminated spot was about 50 μm in diameter. The incident optical power density was up to 180 W/cm^2 . Measurements were performed using a closed-circuit refrigerator CTI-Cryogenics, model 22, to keep a sample at a fixed temperature. Spectra were recorded using a CVI double-grating spectrometer, model DK 242D, with a cooled GaAs-photocathode photomultiplier.

4. RESULTS OF MEASUREMENTS

We have observed several types of behavior of PL spectral peak. The main differences have been found between structures grown on sapphire and on bulk GaN substrates. In addition, even though the same PL pumping rate was maintained in all experiments, the actual excitation level could vary substantially from sample to sample, due to sample-dependent pumping efficiency (carrier collection into the InGaIn layer) and variable nonradiative recombination rate. The *first type* of behavior is a non-monotonic temperature dependence as shown in Fig. 3 for the case of a SH InGaIn structure with a 50-nm thick "bulk-type" InGaIn layer. Experimental points show a continuous blue shift by $\sim 20 \text{ meV}$ when temperature rises from 10 K to 110 K. At higher temperatures (70 - 300 K), the experimental points follow closely curve 2. This type of behavior includes a low-temperature part, where experimental points are above the "non-degenerate" curve 2, obviously because of some degeneracy, a middle-temperature part with an anomalous blue shift, and a high-temperature part with decreasing photon energy.

Fig. 4 presents the first type of the peak behavior at a low pumping rate of 0.7 W/cm^2 (full squares) and another, *second type* of behavior at a high pumping rate of 180 W/cm^2 . In the latter case (open circles) the peak energy decreases in a monotonic manner from low temperatures to room temperature by about 24 meV. However, this red shift is smaller than the corre-

sponding band-gap temperature dependence, as shown by curve 1. The open circles in Fig. 4 fall between curve 1 and curve 2, indicating that some contribution from tail-state filling is present even at high pump powers. An intermediate case, where the two effects almost cancel each other, leading to largely temperature-independent peak position, is shown by dots in Fig. 4 (pumping rate of 15 W/cm²). Along with a temperature rise from 10 K to 300 K, the spectral bandwidth of InGaN emission increased slowly from ~46 meV to ~70 meV.

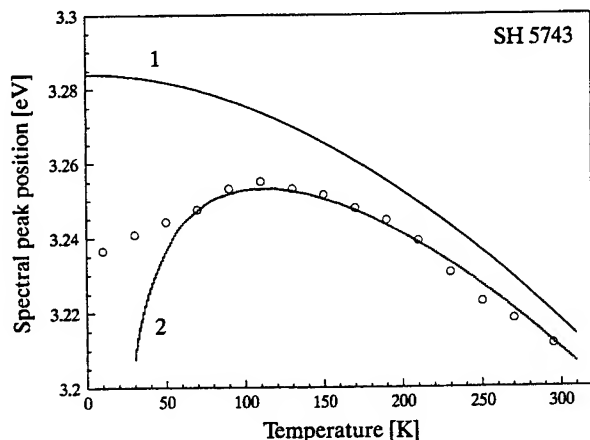
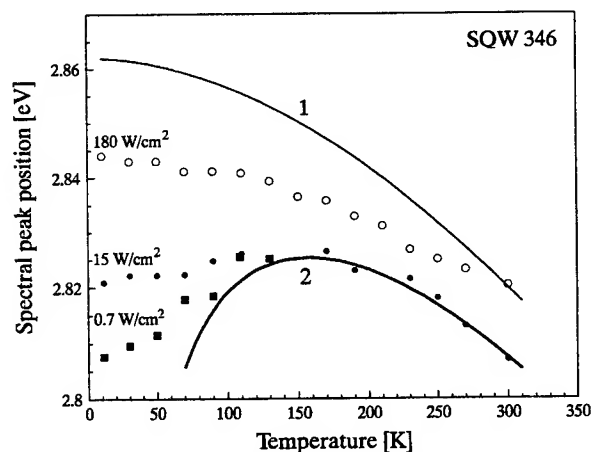


Fig. 3. PL peak position (circles) in function of temperature in a 110-nm-thick InGaN epilayer (single-heterostructure) No. 5743 emitting in the UV range. Curve 1 represents the nominal bandgap, curve 2 is for a non-degenerate occupation of band-tail states, calculated using Eqs. (13) and (14). Fitting parameters are $E_0^*(0) = 3.284$ eV, $\sigma = 14$ meV, $\alpha = 1.1$ meV. The value of β was fixed at 1196 K after Ref. 16. The maximum photon energy of 3.254 eV occurs at 110 K.

Fig. 4. PL peak position in function of temperature in a GaN/InGaN/GaN SQW sample (thickness of InGaN layer is 1.4 nm) emitting in blue range. Experimental points are for different pumping intensities at 325 nm, as indicated. Curve 1 is for a nominal band-gap variation with $E_0^*(0) = 2.862$ eV, $\alpha = 0.7$ meV/K, and $\beta = 1196$ K. Curve 2 is for a non-degenerate occupation of tail states with $\sigma = 18$ meV.



We inspected in more detail the low-temperature behavior (at 11 K) and have found that the pumping rate influences the peak position in accordance with the concept of degenerate occupation. With increasing pumping rate, the peak position marked by dots in Fig. 5 shifts continuously to higher photon energies by 26 meV. This behavior is qualitatively the same as that illustrated in Fig. 1a. Therefore, at low temperatures the spectral peak is rather sensitive to the pumping rate. At low pumping rates, the first type of behavior is observed; it converts into the second type at high pumping rates. Such evolution had been also observed in InGaN/AlGaIn/GaN SQW LED electroluminescence spectra.^{9-11,17-18}

In Fig. 6, we compare the spectral peak position curves for GaN and InGaN emissions from a single sample (SQW with the InGaN well layer thickness of 0.8 nm). A *third type* of behavior is observed for GaN (full dots), following closely the Varshni-like temperature dependence of Eq. (14). At low temperatures, the peak position is not much sensitive to the pumping rate, suggesting there is no substantial tailing. The low-temperature emission in undoped GaN is associated with excitons localized at point centers, rather than with band tails. The red shift of PL emission peak from low temperatures to 300 K is ~55 meV, much more than in samples with band tails. In contrast to GaN emission spectra, InGaN emission from the same sample is of the first type, namely, with some blue shift by a few meV in the middle-temperature range (100-150 K). The peaks at 30 K and at 250 K are at the same photon energy of ~3.16 eV, in sharp contrast to the Varshni-like behavior.

Perhaps the most important result of this study is that *all homoepitaxial samples displayed the Varshni-like behavior* (see Fig. 7), indicating that homogeneity of these samples may be much better than in samples grown on sapphire. However, luminescence efficiency of the homoepitaxial samples is not high, which in fact may well be related to their improved homogeneity. Consequently, it is difficult to follow the InGaN-related peak above ~200 K. Instead of a clear maximum,

some broad emission is observed at room temperature with multiple weak peaks. Low luminescence efficiency suggests that the actual excitation level (*i.e.* steady-state carrier concentration at any given level of pump power) is probably rather low even at low temperatures due to enhanced nonradiative recombination. The same conclusion can also be reached by integrating the spectra originating from the InGaN and GaN layers in the same samples. In addition, since the density of states in the bands is much higher than that in the tails, the temperature dependence of the spectral peak position is not influenced by the pumping rate as it was in the first two types of behavior. In summary, no evidence of band tailing was found in the homoepitaxial samples, in spite of their broad emission bandwidth (~ 62 meV at low temperatures).

Fig. 5. PL spectra of the same GaN/InGaN/GaN SQW sample as in Fig. 4, taken at 11 K with varying pumping intensity controlled by calibrated neutral density filters. Peak position is marked by dots. The behavior of the main peak can be compared with curves in Fig. 1a.

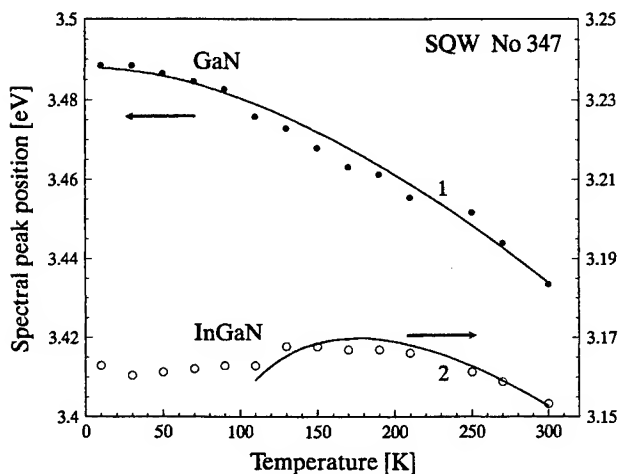
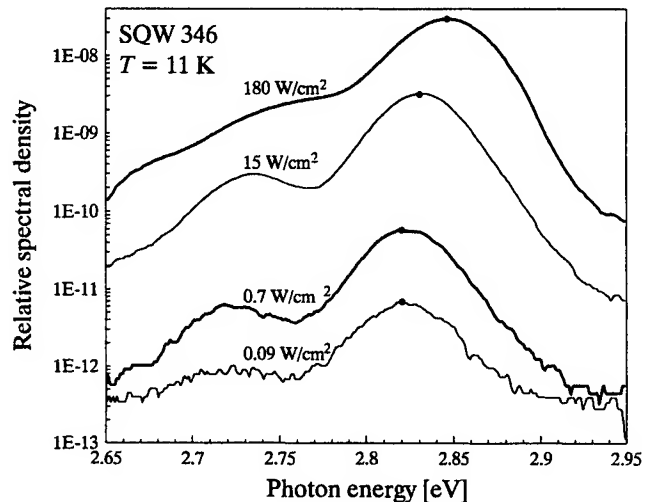


Fig. 6. PL peak position in function of temperature in GaN/InGaN/GaN 0.8-nm-thick SQW emitting in UV range for both GaN barrier emission (dots, left scale) and InGaN well emission (circles, right scale). Different types of behavior are identified with partial fitting by calculated curves 1 and 2. Curve 1 was obtained using $E_0^*(0) = 3.488$ eV, $\alpha = 0.6$ meV/K, and $\beta = 700$ K, reasonable for GaN. Above 110 K, the experimental points for InGaN are fitted by a “non-degenerate” curve 2 with tail parameter $\sigma = 24$ meV, $E_0(0) = 3.229$ eV, and $\alpha = 0.6$ meV. The value of β was taken here as 700 K, the same as in GaN. Note that fitting accuracy in β is rather poor, as it influences the temperature dependence in a rather weak fashion.

Improved homogeneity of InGaN in homoepitaxial samples correlates with reduced threading dislocation density in those samples. This points out that threading dislocations are likely to act as preferred sites for In deposition during growth, leading to In-rich clusters around the dislocation. This interpretation is further supported by direct observation of cathodoluminescence (CL) in MOCVD-grown InGaN-GaN quantum wells on sapphire, correlated with AFM imaging.²¹

5. DISCUSSION

5.1. Effect of Carrier Capture to Band-Tail States on Radiative Recombination Efficiency

Excess carriers are more likely to recombine radiatively when captured into In-rich clusters. Otherwise, they can diffuse to dislocations and other nonradiative sinks, and this is the most plausible explanation of poor radiative recombination efficiency of GaN and homoepitaxial InGaN. Observation of CL dark spots correlated with the TEM pattern of dislocations in

GaN strongly indicates that threading dislocations can act as nonradiative recombination centers.²⁴ The room-temperature hole diffusion length was estimated from that observation as ~50 nm. If capture into band-tail states shortens the diffusion length (below the average distance between dislocations), the band-tail recombination can restrict the nonradiative process at dislocations and other extended defects. In a simple approach, the radiative quantum yield η can be expressed as follows:²⁴

$$\eta = 1 - (r_0/a)^2 - (2/a^2) \int_{r_0}^a \exp[-(r-r_0)/L_D] r dr = 1 - (r_0/a)^2 - (2L_D/a^2) \{r_0 + L_D - (a + L_D) \exp[-(a-r_0)/L_D]\} \quad (16)$$

where r is the radial distance to the dislocation axis, r_0 is the radius of “dead zone” near the dislocation, $a = \frac{1}{2}N_d^{-1/2}$ is the average half-distance between dislocations, L_D is the bipolar diffusion length of carriers. Reported values of hole diffusion length L_p for GaN range from 50 nm²⁴ to an estimated upper limit of 250 nm²⁵, while r_0 was estimated to be 50 nm by observation of CL dark spots associated with threading dislocations²⁴. At $N_d = 10^8$ cm⁻², Eq. (16) gives $\eta \approx 95\%$ at $L_D = 50$ nm and $\eta \approx 79\%$ at $L_D = 150$ nm. At $N_d = 10^9$ cm⁻², the radiative efficiency falls to $\eta \approx 60\%$ at $L_D = 50$ nm and $\eta \approx 30\%$ at $L_D = 150$ nm. Therefore, the quantum yield can be of device quality in spite of the high dislocation density and high nonradiative recombination efficiency of dislocations, but will drop rapidly when N_d exceeds 10^8 cm⁻².

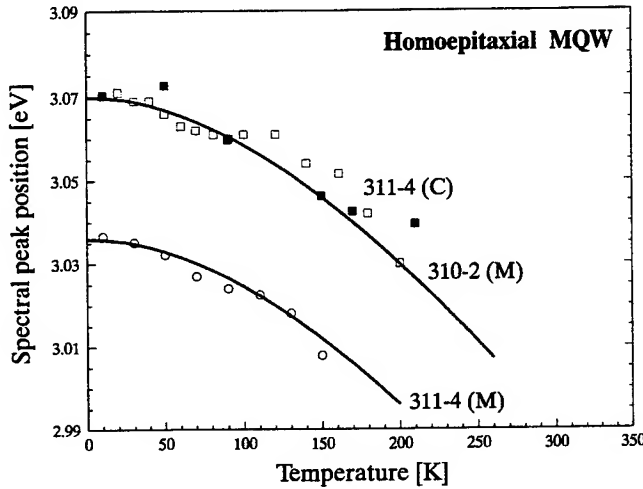


Fig. 7. PL peak position in function of temperature in homoeptaxial GaN/InGaIn/GaN MQWs emitting in violet range. C in brackets indicates a structure grown on the *c*-plane of GaN, M indicates a structure grown on *m*-plane of GaN. Experimental points are fitted using the Varshni expression (14).

It is rather unusual in optoelectronic semiconductors that a lower mobility of excess carriers could lead to a higher radiative quantum yield. However, in frame of this approach, Eq. (16) predicts higher η if the diffusion transport of excess carriers to dislocations is reduced by lower mobility of carriers captured into tail states. This can be an important factor leading to excellent light-emission performance of InGaIn with In content corresponding to blue and green light emission. Other defects and nonradiative centers can limit the positive effect of capture to the tail states in materials with high average content of In, approaching yellow light emission range.

5.2. Experimental Determination of σ Parameter

In previous section, we have fitted the experimental curves for the PL peak position vs temperature using Eqs. (13) and (14). The same procedure can also be applied to other published data where blue temperature-induced shift can be identified. The fitting results are summarized in Table I. It is clear that pronounced tailing is characteristic of InGaIn alloy, but not of GaN (at least in undoped samples). The tail parameter σ correlates with an average indium content and increases from about zero in GaN to 30-35 meV in green-light-emitting structures. The tailing is found in both thick epilayers and in QWs on sapphire, but not in homoeptaxial samples on sublimation-grown GaN substrates.

Consider now the tail parameter σ from the point of view of microscopic material properties. Our first hypothesis is that the tail states are not quantum-confined states, due to slow variation of the band edges. The effect can therefore be treated in the framework of tilted-band-edge approximation, used in the above calculation of the DOS distribution. Deeper tail states

are associated with clusters of larger indium molar fraction x . The magnitude of σ characterizes the energy scale for a substantial decrease in DOS. Using the average value of $dE_g/dx \approx -2$ eV in the range about $x = 0.20$, the composition variation corresponding to $\sigma = 30$ meV can be estimated to be ~ 0.015 , which is quite plausible. In the case of QWs, the variation of quantum-confined level could in principle be also associated with fluctuations of the well thickness L_z . Using the infinite-well approximation, sensitivity of the photon energy to QW thickness variation can be expressed as

$$d(h\nu)/dL_z \approx -\pi^2 \hbar^2 / (m_{\text{red}} L_z^3) , \quad (17)$$

where m_{red} is the reduced effective mass. When the average value of L_z is 3 nm, a change in the photon energy by 30 meV can result from a local increase in L_z to 5 nm. However, deep states inside the tail (3-5 times σ below nominal bandgap) would require an unreasonably high increase in L_z and may not even be attainable, since the bulk nominal bandgap represents the ultimate limit of well-thickness-related shift in energy level. In addition, the thickness variation interpretation is not applicable to a bulk material. We therefore conclude that In content fluctuations are a much more likely cause of the band tail states than the well thickness fluctuations.

Table I. Band-Tail Parameters in GaN and InGaN Epitaxial Structures
 ΔE is the temperature-induced *blue* spectral shift; $E_0^*(0)$ and σ are fitting parameters

Structure	Method	x [%]	ΔE [meV]	$E_0^*(0)$ [eV]	σ [meV]
GaN, thick ($\sim 1 \mu\text{m}$) epilayer	PL	0	~ 0	~ 3.48	< 2
InGaN, DH, $d = 40 \text{ nm}^{\text{a)}$	PL	2	~ 3	3.432	8
InGaN:Si, SH ^{b)}	PL	6	6	3.387	13.7
InGaN, MQW ^{c)}	PL	~ 20	7.6	~ 3.4	6.5
InGaN, SH, $d = 110 \text{ nm}$	PL	8.5 ± 1.5	20	3.34	10
InGaN, DH, $d = 40 \text{ nm}$	PL	7.5 ± 1.5	30	3.284	14
InGaN, SH, $d = 200 \text{ nm}^{\text{d)}$	PL	20	24	3.05	16
InGaN, SQW, $d = 1.4 \text{ nm}$	PL	~ 20	17	2.862	18
InGaN, SQW, $d = 2.5 \text{ nm}^{\text{e)}$	EL	15-30	52	2.78	31.5
InGaN, SQW, $d = 2.5 \text{ nm}^{\text{e)}$	EL	30-45	30	2.394	28.6
InGaN, SQW, $d = 2.5 \text{ nm}^{\text{e)}$	EL	30-45	59	2.392	35
InGaN, MQW, $d = 10 \times 2 \text{ nm}$ (homoepitaxial)	PL	~ 20	0	3.036	~ 0

^{a)} Derived from PL spectral peak position plot²⁶

^{b)} Derived from PL measurements²⁷

^{c)} PL study reported in Ref. 28. Peak near 3.4 eV suggests lower x than 20% indicated in the paper

^{d)} Derived from experimental plots²⁹

^{e)} Electroluminescence (EL) study reported in Ref. 11

Another hypothesis is that the tail states are quantum-confined states. We restrict the consideration to a particular case when the random variation in the lateral well size determines the dispersion of the energy level position in QWs, whereas composition variations are minimal (see Appendix). We use Eq. (A3) in order to estimate the average size of random wells by an order of value. We assume following numerical parameters: well depths $U_{\text{ce}} = U_{\text{oh}} = U_0 = 0.5$ eV, $m_e = 0.18 m_0$, $m_h = 0.8 m_0$, $\sigma = 30$ meV and assume large relative variation of size, $\sigma_R/R_0 \approx 1$. With these assumptions, we have an expression

$$R_0 = (\hbar/\sigma)(\sigma_R/R_0)(2U_0/m_{\text{red}})^{1/2} = 24 \text{ nm} . \quad (18)$$

This estimate looks reasonable, and such clusters are rather large. Considering the total number of In atoms in such a cluster, statistical fluctuations of indium composition can produce deviations not higher than 0.5% from the average composition of $x = 0.20$. Therefore, composition variations are not of purely statistical nature, but result from some segregation process. For example, presence of threading dislocations during growth can result in local enhancement of In content.²¹

6. CONCLUSIONS

Photoluminescence (PL) of InGaN/GaN bulk and quantum-well (QW) structures has been investigated and interpreted in terms of band-tail luminescence typical for structures grown on sapphire substrates. Different types of temperature dependence of the spectral peak position are identified. In the case of pronounced band-tailing, the dependence departs significantly from the usual Varshni-like bandgap shift. The PL peak is red-shifted with respect to the nominal bandgap energy, similarly to the Stokes shift, but due to different physical reasons. The tail-induced shift depends on temperature in a simple manner, producing an anomalous blue shift of the spectral peak with increasing temperature. Such shifts were observed in electroluminescence spectra of InGaN QWs^{9-11,17-18} and later reported in other studies of both electroluminescence and photoluminescence in InGaN. The anomalous temperature-induced blue shift of the peak position can be used to estimate the tail parameter σ which describes the density-of-states distribution in the tails. The σ parameter correlates with an average content of indium in alloy. The tailing effect is associated with alloy composition variations observed in both QW and bulk epilayers. Threading dislocations are a likely factor enhancing compositional inhomogeneities in InGaN. On the other hand, in homoepitaxial material (QW structures on sublimation-grown bulk GaN substrates) and in undoped GaN epilayers, the temperature anomaly is not observed and σ is estimated to be near zero.

From the above discussion, we can conclude the following:

- 1) There is a clear semi-quantitative agreement between the predicted effect of band tails on the spectral behavior of InGaN emission and the experimental PL data from InGaN-based epitaxial structures grown on sapphire substrates. The characteristic blue temperature-induced shift of the peak position was observed in all samples, including thick epilayers (50-110 nm) and different QW structures (with the well thickness as small as 0.8 nm). This phenomenon is associated with the band-tail formation due to compositional variations of the alloy, assisted by the presence of numerous dislocations.
- 2) The tail parameter σ is derived from the temperature dependence of the peak position and is found to correlate with the average In content in the InGaN alloy. This parameter is practically zero in undoped GaN and grows to 30-40 meV in green-light-emitting InGaN structures. The σ parameter is suggested to describe the inhomogeneous broadening of the band edges due to bandgap variation in the alloy.
- 3) In sharp contrast to InGaN samples grown on sapphire, there is no evidence for band tailing in homoepitaxial structures grown on bulk GaN needles as substrates. The PL efficiency in these structures is found to be rather low, indicating much stronger nonradiative recombination. We interpret this as evidence that the capture of carriers into tail states is favorable to radiative processes, preventing the diffusion of excess carriers to extended defects (dislocations, etc.).

ACKNOWLEDGMENTS

This work was supported by DARPA under the Optoelectronic Materials Center program. One of the authors (PGE) expresses his gratitude to the University of Tokushima for a possibility to stay there and to join the nitride studies at the Satellite Venture Business Laboratory during December 1998 - February 1999.

APPENDIX. TAIL PARAMETER σ IN THE CASE OF SIZE VARIATION

Consider the case of band-tail formation when the depth of wells is nearly constant, but their size can vary considerably. We use the "quantum disk" model for the In-rich clusters with a parabolic shape of the potential energy profile. The bottom of all wells is assumed to be at the same energy, whereas the energy of the quantum-confined level E_{loc} (the kinetic energy of localization, calculated from the bottom of the well) varies depending on the well size. E_{loc} is a function of the well radius R :

$$E_{loc} = (\hbar/R)(2U_0/m^*)^{1/2}, \quad (A1)$$

where U_0 is the well depth, and m^* is effective mass of the captured carrier. We consider the dispersion of E_{loc} to represent the parameter σ^2 for each type of carriers. For example, for electrons

$$\sigma_e^2 = 2\hbar^2 U_{0e} \sigma_R^2 / (R_0^4 m_e), \quad (A2)$$

where σ_R^2 is the dispersion of the well radius, R_0 is its average value, U_{0e} is the electron well depth, and m_e is the effective mass of electrons. Analogous expression can be written for holes with the well depth U_{0h} and the mass m_h . By adding

dispersions for both types of carriers, we obtain the total tail parameter

$$\sigma = (2^{1/2}\hbar/R_0)(\sigma_R/R_0)[(U_{0c}/m_e) + (U_{0h}/m_h)]^{1/2} . \quad (A3)$$

REFERENCES

1. S. N. Mohammad and H. Morkoç, *Prog. Quantum Electron.* **20**, pp. 361-525, 1996.
2. S. Nakamura and G. Fasol, *The Blue Laser Diode: GaN Based Light Emitters and Lasers*, Springer-Verlag, Heidelberg 1997.
3. J. W. Orton and C. T. Foxon, *Rep. Prog. Phys.* **61**, pp. 1-75, 1998.
4. O. Ambacher, *J. Phys. D: Appl. Phys.* **31**, pp. 2653-2710, 1998.
5. I. V. Akimova, P. G. Eliseev, and M. Osiński, *Quant. Electron.* **28**, pp. 987-990, 1998.
6. S. Chichibu, T. Azuhata, T. Sota, and S. Nakamura, *Appl. Phys. Lett.* **69**, pp. 4188-4190, 1996.
7. Y. Narukawa, Y. Kawakami, M. Funato, S. Fujita, S. Fujita, and S. Nakamura, *Appl. Phys. Lett.* **70**, pp. 981-983, 1997.
8. I. V. Akimova, P. G. Eliseev, M. A. Osiński, and P. Perlin, *Quant. Electron.* **26**, pp. 1039-1041, 1996.
9. M. Osiński, P. Perlin, P. G. Eliseev, and J. Furioli, in *Light-Emitting Diodes: Research, Manufacturing, and Applications* (E. F. Schubert, Ed.), San Jose, CA, 13-14 Feb. 1997, *SPIE Proc.* **3002** (Bellingham, WA: SPIE, 1997), pp. 15-25.
10. P. Perlin, M. Osiński, and P. G. Eliseev, in *III-V Nitrides* (F. A. Ponce, T. D. Moustakas, I. Akasaki, and B. A. Monemar, Eds.), Boston, MA, 2-6 Dec., 1996, *Mater. Res. Soc. Symp. Proc.* **449** (Pittsburgh, PA: Mater. Res. Soc., 1997), pp. 1173-1178.
11. P. G. Eliseev, P. Perlin, J. Lee, and M. Osiński, *Appl. Phys. Lett.* **71**, pp. 569-571 (1997).
12. K. G. Zolina, V. E. Kudryashov, A. N. Turkin, and A. E. Yunovich, *MRS Internet J. Nitride Semicond. Res.* **1**, Art. 11 (1996).
13. H. C. Casey, Jr., J. Muth, S. Krishnankutty, and J. M. Zavada, *Appl. Phys. Lett.* **68**, pp. 2867-2869, 1996.
14. E. O. Kane, *Solid-State Electron.* **28**, 3 (1985).
15. P. G. Eliseev, M. A. Manko, A. I. Krasilnikov, I. Z. Pinsker, *Phys. Stat. Solidi* **23**, 587 (1968).
16. B. D. Little, W. Shan, J. J. Song, Z. C. Feng, M. Schurman, and R. A. Stall, *III-V Nitrides* (F. A. Ponce, T. D. Moustakas, I. Akasaki, and B. A. Monemar, Eds.), Boston, MA, 2-6 Dec., 1996, *Mater. Res. Soc. Symp. Proc.* **449** (Pittsburgh, PA: Mater. Res. Soc., 1997), pp. 823-828.
17. M. Osiński, P. G. Eliseev, P. Perlin, V. A. Smagley, J. Furioli, and J.-H. Lee, *Record of the 16th Electron. Mater. Symp.*, Minoo, Osaka, Japan, 9-11 July, 1997, pp. 273-276.
18. M. Osiński, P. Perlin, P. G. Eliseev, J. Lee, and V. A. Smagley, *Nitride Semiconductors 1997, Proc. of the 2nd International Conf. on Nitride Semiconductors* (K. Hiramatsu, K. Kishino, S. Nakamura, and H. Amano, Eds.), *Special Issue J. Cryst. Growth* **189/190** (Amsterdam: North-Holland, 1998), pp. 803-807.
19. S. Sakai, H. Sato, T. Sugahara, Y. Naoi, S. Kurai, K. Yamashita, S. Tottori, M. Hao, and K. Nishino, *Mater. Science Forum* **264**, pp. 1107-1110, 1998.
20. H. Sato, T. Sugahara, Y. Naoi, and S. Sakai, *Jpn. J. Appl. Phys., Pt. 1* **37**, pp. 2013-2015, 1998.
21. T. Sugahara, M. Hao, T. Wang, D. Nakagawa, Y. Naoi, K. Nishino, and S. Sakai, *Jpn. J. Appl. Phys., Pt. 2 (Lett.)* **37**, L1195-L1198, 1998.
22. T. Wang, D. Nakagawa, M. Lachab, T. Sugahara, and S. Sakai, *Appl. Phys. Lett.* **74**, pp. 3128-3130, 1999.
23. S. Sakai, *J. Korean Phys. Soc.* **34**, pp. S220-S223, 1999.
24. T. Sugahara, H. Sato, M. Hao, Y. Naoi, S. Kurai, S. Tottori, K. Yanashita, K. Nishino, L. Romano, and S. Sakai, *Jpn. J. Appl. Phys., Pt. 2* **37**, pp. L398-L400, 1998.
25. S. J. Rosner, E. C. Carr, M. J. Ludowise, G. Girolami, and H. I. Erikson, *Appl. Phys. Lett.* **70**, pp. 420-422, 1997.
26. Y. Narukawa, S. Saijou, Y. Kawakami, S. Fujita, T. Mukai, and S. Nakamura, *Appl. Phys. Lett.* **74**, pp. 558-560, 1999.
27. T. Taguchi, T. Maeda, Y. Yamada, S. Nakamura, and G. Shinomiya, *Proc. Int. Symp. "Blue Laser and Light Emitting Diodes"* (A. Yoshikawa, K. Kishino, M. Kobayashi, and T. Yasuda, Eds.), Chiba, Japan, 5-7 March 1996, pp. 372-374.
28. K. L. Teo, J. S. Colton, P. Y. Yu, E. R. Weber, M. F. Li, W. Liu, K. Uchida, H. Tokunaga, N. Akutsu, and K. Matsumoto, *Appl. Phys. Lett.* **73**, pp. 1697-1699, 1998.
29. S. Chichibu, L. Sugiura, J. Nishio, A. Setoguchi, H. Nakanishi, and K. Itaya, *Proc. 2nd Int. Symp. "Blue Laser and Light Emitting Diodes"* (K. Onabe, K. Hiramatsu, K. Itaya, and Y. Nakano, Eds.), Kisarazu, Japan, 29 Sept. - 2 Oct. 1998, pp. 616-619.

Comparison of optical properties in GaN and InGaN quantum well structures

Shigefusa F. Chichibu^{*a}, Amane Shikanai^b, Takahiro Deguchi^b, Akiko Setoguchi^{**a}, Rikuro Nakai^{***a}, Kazumi Wada^c, Steven P. DenBaars^d, Takayuki Sota^b, Takashi Mukai^e, Shuji Nakamura^c

^aInstitute of Applied Physics, University of Tsukuba, 1-1-1 Tennodai, Tsukuba, Ibaraki 305-8573, Japan

^bDepartment of Electrical, Electronics, and Computer Engineering, Waseda University, 3-4-1 Ohkubo, Shinjuku, Tokyo 169-8555, Japan

^cDepartment of Materials Science and Engineering, Massachusetts Institute of Technology, 77 Massachusetts Ave., Cambridge, MA 02139

^dDepartment of Materials Engineering, University of California, Santa Barbara, CA 93106-5050

^eDepartment of Research and Development, Nichia Chemical Industries Ltd., 491 Oka, Kaminaka, Anan, Tokushima 774-8601, Japan

ABSTRACT

Static, field-modulated, and time-resolved spectroscopic measurements were carried out to compare the electronic structures between AlGaIn/GaN binary and GaN/InGaIn ternary single quantum wells (SQWs). The internal field exists across the quantum well (QW) naturally induces quantum-confined Stark effects, namely the redshift of the QW resonance energy and separation of electron-hole wavefunction overlap. Thus AlGaIn/GaN SQWs exhibited a weak luminescence peak due to the presence of nonradiative channels. However, optical absorption and degenerate pump-probe measurements revealed that excitonic character still remains for the thin QWs having the well width nearly the same as the bulk free exciton Bohr radius even under high electric field as high as 0.73 MV/cm. A slightly In-alloyed InGaIn SQW exhibited bright luminescence peak in spite of the pronounced effective bandgap inhomogeneity in the QW, which was confirmed by the point excitation and monochromatic cathodoluminescence mapping methods to have the lateral potential interval smaller than 40 nm. Therefore the light emitting area of the potential minima has the size defined as "quantum-disk" [M. Sugawara, Phys. Rev. B, 51, 10743 (1995)]. Carriers generated in the InGaIn QWs are effectively localized in these region to form localized QW excitons exhibiting highly efficient spontaneous emissions.

Keywords: InGaIn, Localization, Localized quantum well excitons, effective bandgap inhomogeneity, piezoelectric field, quantum-confined Stark effect.

1. INTRODUCTION

Major developments of III-nitride semiconductors¹⁻³ have led to the commercial production of blue and green single quantum well (SQW) light-emitting-diodes (LEDs) and to the demonstration of multiple quantum well (MQW) purplish-blue laser diodes (LDs).^{2,3-11} The growth of nearly threading dislocation (TD)-free GaN has been realized by the lateral epitaxial overgrowth (LEO) technique,¹¹⁻¹⁶ and the device lifetime of the cw MQW LDs has been extended up to 10,000 hours using low TD density GaN on sapphire¹⁴ and pure GaN substrates¹⁵ prepared by LEO technique. InGaIn alloys are attracting special interest because they serve as an active region of MQW LDs^{2,3-11} and bright UV,¹⁷ blue,² green,² and amber¹⁸ SQW LEDs and even for a red¹⁹ LED. Surprising evidence is that InGaIn QWs exhibit very high external quantum efficiency despite of the large TD density up to 10^{10} cm^{-2} .²⁰

In spite of these advances in device realization, emission mechanisms of InGaIn bulk materials and QW structures are not yet fully understood due to complex material physics and engineering, such as polarization induced internal electric field due to the wurtzite crystal lattice,^{21,22} and phase separating nature²³⁻²⁶ due to large lattice, thermal, and chemical mismatches. Importance of the recombination of QW excitons²⁷ localized at certain potential minima owing to the InN mole fraction fluctuation, which have later been estimated²⁸ to have quantum-disk (Q-disk)²⁹ size, in the InGaIn QWs has first been suggested by the authors.³⁰ The principal idea^{28,30-35} is that the QW exciton localization overcomes the disadvantageous electron-hole (e-h) pair separation due to the quantum confined Stark effect (QCSE) caused by the internal electric field, F ,

induced mainly by the piezoelectric field (F_{pz}). This model has later been supported by several groups claiming extended states,³⁶ quantum dots,^{37,38} compositional fluctuation of In,³⁹ or a band tail states.⁴⁰ On the other hand, Takeuchi *et al.*^{41,42} have pointed out the importance of the effects of F_{pz} in strained InGaN QWs. Then several researchers⁴³⁻⁴⁶ discussed the effect of F in AlGaIn/GaN or InGaIn QWs. In particular, the blueshift of the electroluminescence (EL) peak in InGaIn SQW LEDs² with increasing forward current has been explained^{30,34,35} by the combined effects of a reduction of QCSE due to Coulomb screening of F_{pz} and band-filling of the energy tail states. In order to obtain an insight into what dominates the emission properties of InGaIn QWs, it is necessary to investigate the effects of effective bandgap inhomogeneity and F in the QW separately and consistently.

In this article, several important physics which affect the emission properties of InGaIn QWs are discussed. First, the influence of F is reexamined on AlGaIn/GaN binary SQW to conclude that there exists polarization-induced and junction built-in high F across the strained QW. Presence of QW excitons is shown for the wells with the width (L) is nearly the same as the bulk free exciton Bohr radius (a_B) ($L \approx a_B$) even under high F by means of degenerate pump-probe method. Next the presence of effective bandgap inhomogeneity, which produces certain Q-disk-size localized potential minima, in practical InGaIn UV SQW LED is shown. Finally the origin of the QW exciton localization was discussed by investigating the InGaIn QWs grown on nearly TD-free GaN prepared by LEO technique.

2. EXPERIMENTAL

Samples investigated here were grown by metalorganic vapor phase epitaxy. AlGaIn/GaN SQW structure^{47,48} consisted of a 30-nm-thick $\text{Al}_{0.8}\text{Ga}_{0.2}\text{N}$ low-temperature (LT) nucleation layer (NL), a 1.0- μm -thick $\text{n-Al}_{0.3}\text{Ga}_{0.7}\text{N} : \text{Si}$ layer, a 0.15- μm -thick $\text{n-Al}_{0.15}\text{Ga}_{0.85}\text{N} : \text{Si}$ barrier layer, a 5-nm-thick undoped GaN SQW, a 0.15- μm -thick $\text{p-Al}_{0.15}\text{Ga}_{0.85}\text{N} : \text{Mg}$ barrier layer, a 0.5- μm -thick $\text{p-Al}_{0.3}\text{Ga}_{0.7}\text{N} : \text{Mg}$ layer, and a 0.5- μm -thick $\text{p-GaN} : \text{Mg}$ layer. The concentration of Si and Mg was $3 \times 10^{18} \text{ cm}^{-3}$ and $1 \times 10^{20} \text{ cm}^{-3}$, respectively. The InGaIn UV SQW LED¹⁹ consisted of a 30-nm-thick LT-NL, a 4- μm -thick $\text{n-GaN} : \text{Si}$ template, a 30-nm-thick $\text{n-Al}_{0.1}\text{Ga}_{0.9}\text{N} : \text{Si}$ barrier layer, a 5-nm-thick undoped InGaIn SQW, a 60-nm-thick $\text{p-Al}_{0.15}\text{Ga}_{0.85}\text{N} : \text{Mg}$ barrier layer, and a 0.12- μm -thick $\text{p-GaN} : \text{Mg}$ layer. The In concentration in the SQW was less than a few percent.¹⁹ For the monochromatic cathodoluminescence (CL) measurements, 3-nm-thick undoped $\text{In}_{0.02}\text{Ga}_{0.98}\text{N}$ and $\text{In}_{0.1}\text{Ga}_{0.9}\text{N}$ SQWs were grown on a 4- μm -thick $\text{n-GaN} : \text{Si}$ template capped with a 6-nm-thick undoped GaN.²⁸ They are grown on sapphire (0001) substrates. To eliminate the effect of TDs on the formation of the localized states,⁴⁹ 5 periods of 3-nm-thick undoped $\text{In}_{0.15}\text{Ga}_{0.85}\text{N}$ well and 7-nm-thick Si-doped ($2 \times 10^{18} \text{ cm}^{-3}$) GaN:Si barriers were grown on 8- μm -thick fully coalesced LEO GaN base, which was overgrown from 2- μm -thick GaN on sapphire using a SiO_2 pattern with 5- μm -wide openings separated by 15- μm -wide SiO_2 stripes oriented in the $\langle 1-100 \rangle$ direction. The edge-character TD density in GaN grown laterally over the SiO_2 mask (LEO wing) was less than 10^6 cm^{-2} .¹⁶ The InGaIn QWs were capped with 8-nm-thick GaN. In order to extract the optical information from the LEO wing, the samples were coated with a 150-nm-thick Al layer in which 5- μm -wide stripes were opened to reveal the wing region.

Electroluminescence (EL), photoluminescence (PL), photoluminescence excitation (PLE), electroreflectance (ER), photo-modulated electroreflectance (photorelectance: PR), optical transmittance, and spatially resolved monochromatic and spot-excitation CL measurements were carried out. Time-resolved photoluminescence (TR-PL) was excited by a frequency-tripled 150 fs pulse from a tunable Ti:sapphire laser operating at 80 MHz repetition rate. The excitation energy and power at the sample were typically 4.64 eV and 20 mW, respectively. Pump and probe measurements⁴⁸ were made at room temperature (RT). A mode-locked Ti:sapphire laser delivering 80 fs duration fundamental pulses was used. We measured the change in transmittance divided by the static transmittance ($\Delta T/T$) in the probe as a function of its delay relative to the pump at several wavelengths tuning the fundamental pulse wavelength.

3. ELECTRIC FIELD IN QUANTUM WELLS

Optical properties peculiar to wurtzite III-nitrides in comparison to familiar III-V semiconductors such as GaAs or InP known to date are summarized as follows: (i) Nitrides have an excitonic character in their optical properties. Indeed, dominant resonance structures due to A and B free excitons (FE) were found in both absorption⁵⁰ and photorelectance spectra⁵¹ of 3D GaN layers, and FE emission has been found even at RT,⁵¹ since the exciton binding energy, E_b , is as large as 26 meV and a_B is as small as 3.4 nm.⁵¹ It is also known that E_b is increased in QWs²⁷ due to confinement of wavefunctions. (ii) The wurtzite structure has the highest symmetry compatible with the existence of spontaneous polarization. Moreover, strain-induced piezoelectric tensor of wurtzite has three nonvanishing independent components. In the absence of the external fields, the total macroscopic polarization, P , is the sum of the spontaneous polarization in the equilibrium structure, P_0 , and of the strain induced piezoelectric polarization, P_{pz} . (iii) InGaIn alloys have an immiscible gap²³⁻²⁶ and they usually show broad luminescence band.² From (i) and (ii), physical scenarios of the optical transitions in

GaN and InGaN QWs are drawn as follows. Since the critical thickness of $\text{In}_x\text{Ga}_{1-x}\text{N}$ ($0 < x < 0.15$) is reported to be greater than 40 nm,^{3,41} coherent growth of InGaN is assumed. This strain causes F_{PZ} but excitons should also be significant.²⁷ Therefore the problem treated here is the behavior of confined energy levels in QWs under F , as discussed for GaAs/AlGaAs QWs in the 1980's.^{27,52,53} In QWs, FE absorption is observed even at RT under high F across the QW due to quantum confinement of the wavefunctions which enhances the Coulomb interaction between the e-h pair to increase E_b .²⁷ Miller et al.⁵² have observed an excitonic absorption in GaAs QWs, which was redshifted by 2.5 times the zero-field E_b for $F=10^5$ V/cm (50 times the ionization field F_i of 3D excitons). They have explained the redshift in terms of field modulation of quantized energy levels (QCSE).⁵² We estimate E_b in GaN / $\text{Al}_{0.1}\text{Ga}_{0.9}\text{N}$ QWs under $F=0$ as a function of L according to Bastard *et al.*²⁷ introducing finite barrier height. The obtained E_b value for $L=3$ nm is 47 meV and F_i is estimated to be 6.0×10^5 V/cm taking into account the shrinkage of e-h distance in z-direction down to 0.78 nm. E_b is 37 meV for $L=6$ nm.

Taking the small fraction (1/3) of the valence band discontinuity ΔE_v against the conduction band discontinuity ΔE_c into account,⁵³ schematic band diagrams of AlGaN/GaN or InGaN/GaN QWs are drawn in Fig. 1 for several cases; i.e. restrictions among $F \times L$, ΔE_v , and a_B . Since the restriction $F \times L > \Delta E_v$ breaks before breaking $F \times L > \Delta E_c$ with increasing F or L , restrictions between $F \times L$ and ΔE_v and between L and a_B (quantum size effect) only are drawn in Fig. 1. Note that in-plane (lateral) bandgap inhomogeneity is omitted. In CASE I, both e-h wavefunctions are confined in the well and have unique quantized energy levels where zero Stokes-like shift is expected though the resonance energy slightly shifts to lower energy due to QCSE. In CASE II, at least the hole wavefunction drops into the triangular shape potential well at one side of the well, and continuum states are formed at the rest of the potential slope inside the QW region. In addition the penetration of the barrier continuum wavefunction cannot be neglected. Therefore vertical component Stokes-like shift is produced. For the extreme situation of CASE II (pronounced CASE II), both the e-h wavefunctions drop into the triangular potential wells formed at opposite sides of the well resulting in z-directional separation. In CASE III and IV, the absorption tail would be modulated due primarily to QCSE⁵² and quantum-confined Franz-Keldysh effect (QCFK).⁵⁴

4. RESULTS AND DISCUSSION

4.1 Quantum confined Stark effect in AlGaN/GaN SQW

Optical absorbance, PR, and high excitation PL spectra of the binary GaN/AlGaN SQW structure are shown in Fig. 2. The absorbance and PR spectra of GaN SQW exhibited a clear excitonic resonance^{34,47} between 10 K and RT though multiple internal reflection fringes due to AlGaN thick base layer are superimposed on the absorbance spectra. It is noted that the peak energy is smaller by 128 meV than the FE energy of strain-free bulk GaN. This redshift against the quantum confinement effect is nothing but quantum confined Stark shift due to the spontaneous and piezoelectric fields, F . To estimate F , confined energy levels and wavefunctions in GaN/AlGaN SQW are calculated as functions of F , L , and carrier density n in the barrier by variational method neglecting the exciton binding energy E_b within the Hartree approximation by solving Schrödinger equation and Poisson equation simultaneously and self-consistently. Here the ratio $\Delta E_c : \Delta E_v$ is assumed to be 3:1. F is thus estimated to be 0.73 MV/cm.

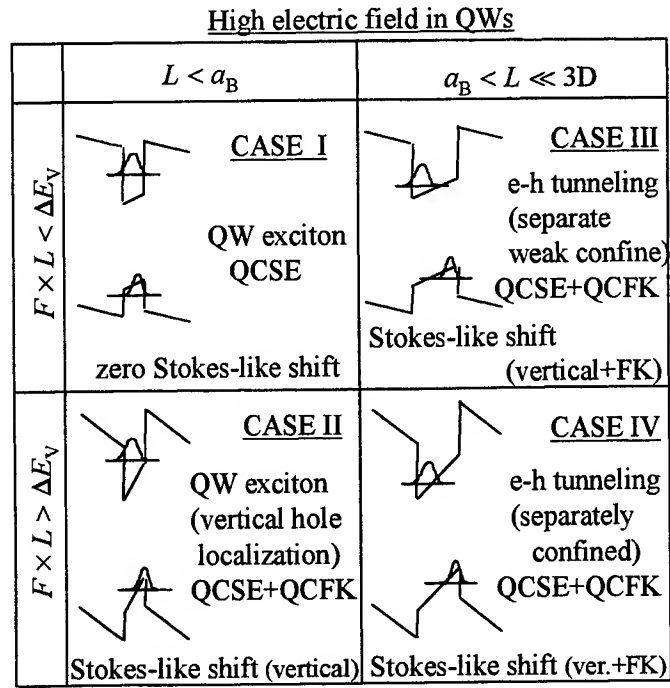


Fig. 1 Schematic band diagrams of AlGaN/GaN or GaN/InGaN QWs under the electric field F . Each case represents the restrictions determined among F , L , ΔE_v , and a_B .

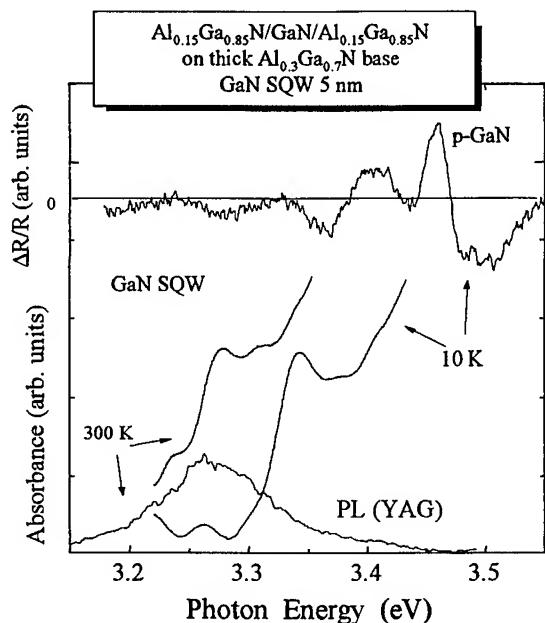
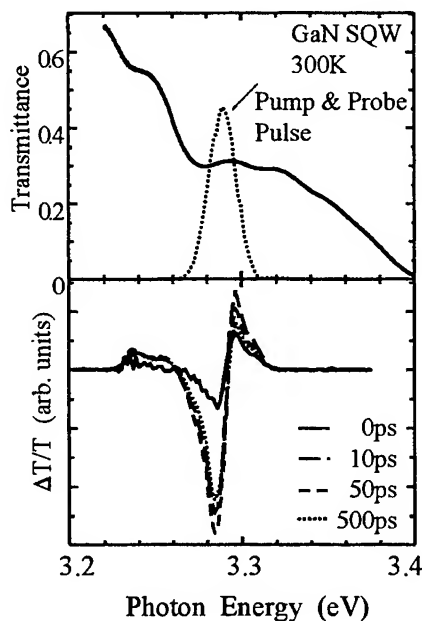


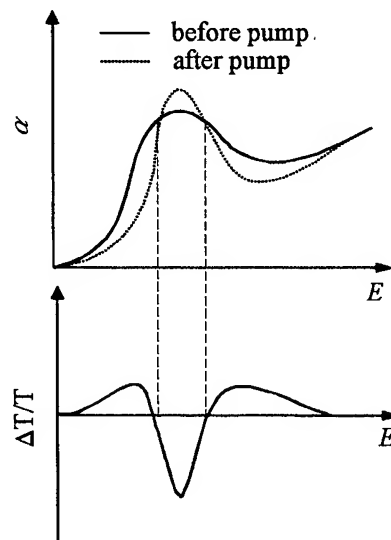
Fig.2 Optical absorbance and PR spectra at 10 K and absorbance and high excitation PL spectra at RT of the 5-nm-thick GaN/Al_{0.15}Ga_{0.85}N SQW structure grown on thick Al_{0.3}Ga_{0.7}N base layer.

Excitonic feature of the absorption peak at 3.28 eV at RT of this sample is examined by a degenerate pump and probe technique. Figure 3 (a) shows the energy dependence of $\Delta T/T$ for some delay times. The pump and probe beams profile used in measuring $\Delta T/T$ is also shown in Fig. 3 (a). Fig. 3 (a) indicates the following. The absorption increases around 3.275 eV corresponding to the exciton resonance and the transmittance increases in the energy region larger than 3.29 eV. For the energy region smaller than 3.26 eV, the transmittance increases again, though the corresponding clear spectrum is not shown here. Note that the behavior of the observed spectrum is similar to that of $\Delta T/T$ observed in GaAs self-electro-optic effect devices (SEEDs).⁵⁵ It takes about 25 ps for $\Delta T/T$ to reach its maximum or minimum value. A schematic illustration of the change in the absorption coefficient around the exciton resonance is shown in Fig. 3 (b), where expected change in the probe beam transmission is also shown. It can qualitatively explain the signals observed.

Observation of the excitonic absorption in this GaN/AlGaIn SQW at RT against such high F can be predicted^{27,52} from the increase in E_b in QWs.^{27,30,32,34,35,52} To confirm this, E_b in 5-nm-thick GaN QW is calculated by a variational method²⁷ with finite barrier height taking the e-h motion into account.³⁰ The value obtained is 40 meV under $F=0$. However, spontaneous emission intensity of the GaN SQW is very weak; the structure does not exhibit stimulated emission. The PL spectrum of GaN/AlGaIn in Fig. 2 was taken under high excitation condition using 3rd harmonic of YAG laser. In general, nonradiative recombination channels are frozen at low temperature. However,



(a)



(b)

Fig. 3 (a) Transmittance spectrum and the energy dependence of $\Delta T/T$ in the AlGaIn/GaN SQW at RT. The laser profile is also shown in (a). (b) Schematic illustration of the absorption coefficient change due to the photoinduced internal field screening (upper panel) and the expected energy dependence of $\Delta T/T$ (lower panel).

the GaN SQW exhibited very weak PL even at 10 K. This may be due to rapid separation of e-h pair^{34,35,45} due to F rather than to presence of nonradiative channels. Thus the presence of F in the QW is only disadvantageous for achieving high quantum efficiency. Note that the PL peak energy nearly agrees with the excitonic absorption peak at RT and excitons are delocalized for the GaN/AlGaIn SQW.

4.2 Potential fluctuation in GaN/InGaIn SQWs

In contrast to the weak, dim emission from the 5-nm-thick GaN SQW, the 5-nm-thick InGaIn UV LED having InN mole fraction smaller than a few percent exhibited bright UV emission even under low excitation condition using cw He-Cd laser or a current injection, as shown in Fig. 4, and showed the stimulated emission⁵⁶ from the sample edge under high excitation although the QW absorption structure is broadened. The ER spectrum clearly exhibits the resonance structures due to InGaIn SQW and AlGaIn barriers in which the bands are effectively modulated by the external field. It is clear that the energy tail expands to lower energy side down to 3.25 eV of the primary QW resonance around 3.4 eV. Mukai *et al.*⁵⁷ have reported that current and temperature dependences of the EL peak energy of 5.5-nm-thick $\text{In}_x\text{Ga}_{1-x}\text{N}$ SQW LEDs change drastically at a critical emission peak wavelength of 375 nm. When x is very small, the EL spectra do not show any blueshifts but show temperature dependence. Conversely, when x is larger than the value that corresponds to the emission peak of 375 nm, the EL spectrum shows nearly temperature-independent peak energy shows the blueshift with increasing forward current. Moreover, the output power of UV LEDs increase with increasing wavelength in UV region longer than 370 nm. These findings indicate that alloying or doping of In drastically changes the electronic structure of GaN, and the emission mechanisms change with x .

Typical wide-area and spot-excitation CL spectra at 10 K of a 3-nm-thick $\text{In}_{0.1}\text{Ga}_{0.9}\text{N}$ SQW are shown in Fig. 5. Although the effect of the multiple interference fringes on the CL spectra is not negligible, wide area ($10\ \mu\text{m} \times 10\ \mu\text{m}$) CL spectrum exhibits a broad CL band (FWHM nearly 100 meV), which consists of many sharp peaks (FWHM less than 20 meV)²⁸ at 10 K revealed by the spot-excitation CL spectra. This clearly shows that the broad CL band consists of sharper emission peaks having various peak energies. Therefore, there exist several structures composed of an InN-rich part surrounded by a GaN-rich part in each spot area. This structure is considered to be due to mesoscopic In compositional fluctuation and it can act as Q-disks,²⁹ dots, or segmented QWs³²⁻³⁵ having compositional and/or size inhomogeneity depending on the lateral size. A careful comparison between the two monochromatic scanning CL images taken at wavelengths of 400 nm and 420 nm using a triangular-shaped dark marker on the bottom-left corner indicates following results; (a) each bright (white in the figure) area consists of emissions from real spaces of about 60-400 nm in lateral size, (b) some dark areas in one figure correspond complementary to bright ones in the other figure, and (c) some areas exhibit both 400 and 420 nm CL emissions. These results can be explained by the existence of compositional fluctuation whose lateral interval is smaller than 60 nm, which value is the spatial resolution of the system (diffusion length). Supporting evidences of the short diffusion length in InGaIn QWs were reported by Rosner *et al.*^{58,59}. They showed less pronounced CL contrast in InGaIn SQW compared to GaN.⁵⁹ Sato *et al.*⁶⁰ estimated the PL intensity as a function of TD density and also supported the short diffusion length model in InGaIn QWs.²⁸ The result (c) indicates that the real area that emits CL is far smaller than the diffusion length (60 nm). Kisielowski *et al.*⁶¹ and Ponce *et al.*⁶² estimated the structural size of InN-rich clusters to be less than 10 nm and 20 nm, respectively. Such CL nanostructure was also found for the UV SQW LED having InN mole fraction as low as $x=0.02$, as shown in Fig. 6. This means that large FWHM of the PL peak and broadness of the PLE signal edge or the ER resonance for the CASE I QWs represent the in-plane effective emission bandgap inhomogeneity. Note that structures having lateral size between a_B exciton resonance wavelength (emission wavelength divided by the refractive index ≈ 160 nm) embedded in QWs are defined as Q-disks.²⁹ The e-h wavefunctions in the Q-disks are confined with respect to the z-direction, and Q-disks can improve the emission efficiency due to the lateral localization of QW

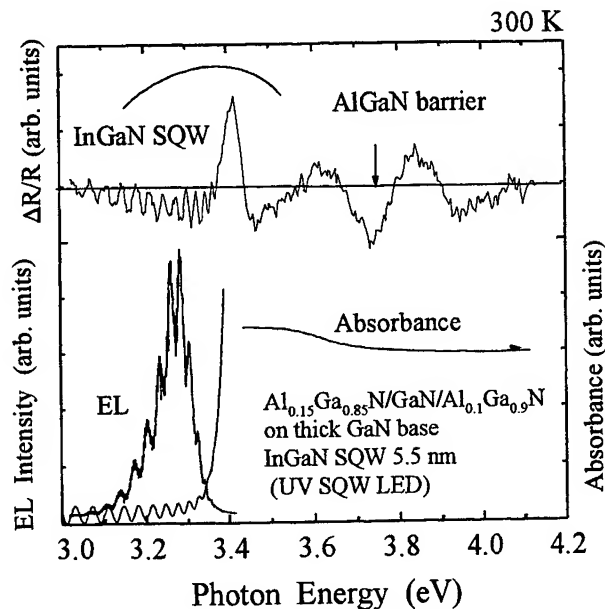


Fig. 4 ER, EL, and absorbance spectra of slightly In-alloyed InGaIn SQW LED structure measured at RT. The EL peak locates at the lower energy tail of the QW resonance observed in the ER spectrum.

3-nm-thick $\text{In}_{0.1}\text{Ga}_{0.9}\text{N}$ SQW

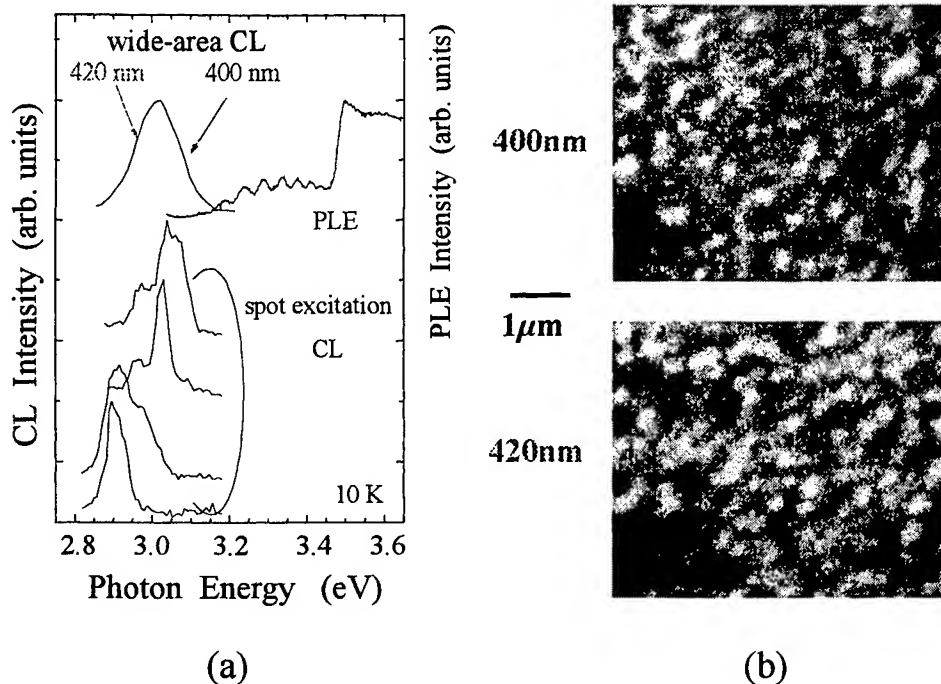


Fig. 5 Wide-area ($10\ \mu\text{m} \times 10\ \mu\text{m}$) scanning and spot excitation CL spectra of 3-nm-thick $\text{In}_{0.1}\text{Ga}_{0.9}\text{N}$ SQW capped by a 6-nm-thick GaN. The broad CL peak (FWHM=100 meV) consists of several sharp emission peaks (FWHM=20 meV) having different peak energies. Monochromatic CL images taken at 400 and 420 nm showed primarily the complimentary relation. The resolution of the CL mapping is limited by the diffusion length, which was nearly 60 nm in lateral direction.

excitons, that can reduce nonradiative pathways. This is the reason why InGaN exhibits bright spontaneous emissions. Naturally, it overcomes disadvantages of using wurtzite materials due to the polarization-induced electric fields. The e-h wavefunctions are still overlapped even in the pronounced CASE II. The emission lifetime τ is affected by both the e-h pair separation due to F_{pz} and in-plane localization for CASE II and pronounced CASE II. In Q-disks, the spontaneous emission lifetime becomes long since the emission is prohibited when the wave vector of exciton center-of-mass motion is above the critical energy.²⁹

The absorption spectrum of strained InGaN QWs is further modulated by QCfK⁵⁴ effect and bulky Franz-Keldysh effect from the barriers when the potential drop across the well ($F \times L$) exceeds ΔE_v . This produces apparent Stokes-like shift in addition to the in-plane net Stokes-like shift due to the potential inhomogeneity. It should be noted that InGaN amber SQW LEDs¹⁸ with InN mole fraction nearly 0.27 suffers from huge piezoelectric field F_{piezo} and showed the emission blueshift with increasing reverse bias on the pn junction when the well was selectively photo-excited.³⁰ The lower energy tail of

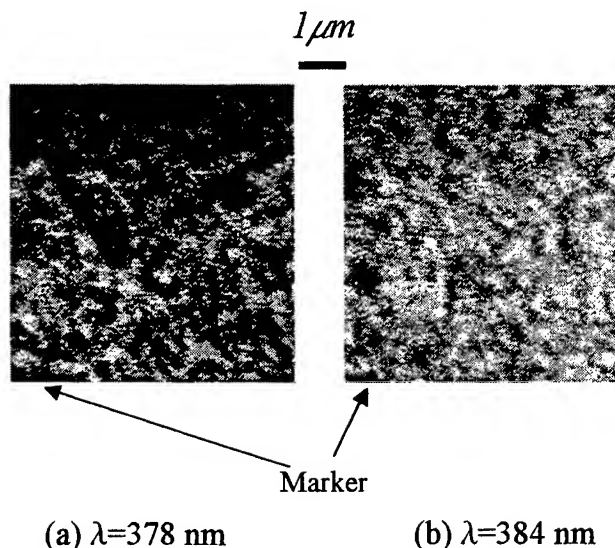


Fig. 6 Monochromatic CL images at 10 K of $\text{In}_{0.02}\text{Ga}_{0.98}\text{N}$ SQW structure taken at (a) 378 nm and (b) 384 nm whose PL peak wavelength is 381 nm.

the emission spectrum of amber SQW LEDs extends below the bulk InN bandgap, indicating that F_{piezo} is not completely screened by injected carriers. However, despite the large F_{piezo} , they exhibit reasonable efficient emission since $L < a_B$. From the fact that bulk InGa_{0.15}N also emits bright emission against F_{piezo} exists in it, effective localization is considered to serve as a bypass for the QW excitons into radiative recombination. Such acceptance of F_{piezo} indicates that structures are not quantum dots but Q-disks. It should be noted that cubic InGa_{0.15}N that does not suffer from spontaneous or piezoelectric fields along the a -axis also exhibits an emission from localized energy tails.^{63,64}

4.3 Origin of the QW exciton localization

The spacially-resolved monochromatic CL mapping shows that the lateral size of the light emitting area increases with increasing x and its density does not depend on the TD density. Note that nearly TD-free InGa_{0.15}N QWs also exhibited emissions due to localized excitons.⁴⁹ Figure 7 shows the time-integrated PL spectrum and decay time τ as a function of emission energy measured at RT. As shown, τ of nearly TD-free InGa_{0.15}N MQW increased with decreasing the photon energy. This is characteristics of the localized electronic system. The relation between τ and E was fitted using $\tau(E) = \tau_0 / \{1 + \exp[(E - E_{\text{me}})/E_0]\}$, where $E_0 = 60$ meV represents the depth in the tail states, $E_{\text{me}} = 2.88$ eV is the energy similar to the mobility edge, and $\tau_0 = 12$ ns is the radiative lifetime. These values are reasonable for the device-quality InGa_{0.15}N QW systems with highly lattice mismatched nonrandom alloy broadening. Therefore the in-plane effective bandgap inhomogeneity is caused by growth parameters, point defects, or thermodynamics rather than phase separation initiated by TDs. Anomalous temperature independence of the luminescence peak energy² cannot be explained only by an inhomogeneous F_{pz} . Since the change in x changes F_{pz} , the Q-disk size / segmented QW potential may, at least partly come from the nonrandom alloy potential fluctuation emphasized by the large bowing parameter in InGa_{0.15}N.⁶⁵

For LDs, the effective bandgap inhomogeneity more than 50 meV is too large to obtain a uniform electron-hole plasma (EHP) in the well. Indeed, some InGa_{0.15}N MQW LDs showed EHP lasing in tail states.^{32,35,66,67} This may cause the increase of threshold current density of InGa_{0.15}N LDs in terms of reduction in differential gain.⁶⁸

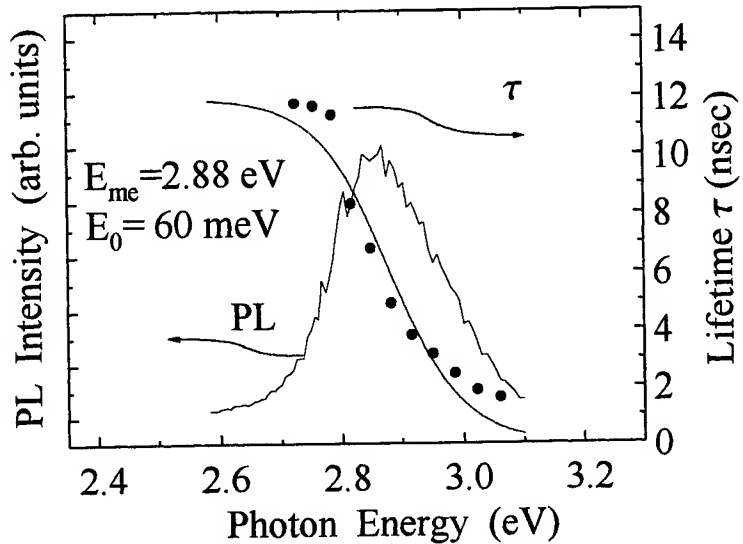


Fig. 7 Time-integrated PL spectrum and the decay time τ of In_{0.15}Ga_{0.85}N MQW structure grown on LEO wing as a function of emission energy taken at RT.

5. CONCLUSION

Electronic structure of GaN and InGa_{0.15}N SQWs was shown to be greatly affected by the internal field F , which induces QCSE to reduce the e-h wavefunction overlap. However, QW excitonic absorption peak was observed in GaN SQW up to 0.73 MV/cm. Evidence for the presence of QW excitons was clarified by the observation of photoinduced absorption change due to field screening around the QW exciton resonance energy. The Coulomb interaction between the e-h pair is maintained provided that $L < a_B$. The electronic structure of GaN SQW is modified by doping or alloying by In, which improve the emission efficiency despite the fact that effective bandgap inhomogeneity is increased. In is considered to produce Q-disk size effective bandgap fluctuation that helps effective localization of QW excitons.

ACKNOWLEDGMENTS

The authors are grateful to Professors U. K. Mishra, L. A. Coldren, J. E. Bowers, E. Hu, J. S. Speck, and K. Suzuki, and Drs. S. Keller, S. B. Fleischer, D. Cohen, J. Ibbetson, C. Bulutay, O. Brandt, H. Okumura, T. Azuhata, and T. Uenoyama for helpful discussions. The authors would like to thank A. C. Abare, M. P. Mack, M. S. Minsky, K. Torii, P.

Kozodoy, M. Hansen, P. T. Fini, H. Marchand, and M. Sugiyama for help in the experiments. The first author is thankful to Professor H. Nakanishi, Professor Y. Horikoshi, and Professor F. Hasegawa for continuous encouragement.

REFERENCES

1. S. Strite and H. Morcroc, *J. Vac. Sci. Technol. B* **10**, p. 1237, 1992.
2. S. Nakamura and G. Fasol, *The Blue Laser Diode* (Springer-Verlag, Berlin), 1997.
3. I. Akasaki and H. Amano, *Jpn. J. Appl. Phys.* **36**, p. 5393, 1997.
4. I. Akasaki, S. Sota, H. Sakai, T. Tanaka, M. Koike, and H. Amano, *Electron. Lett.* **32**, p. 1105, 1996.
5. K. Itaya, M. Onomura, J. Nishio, L. Sugiura, S. Saito, M. Suzuki, J. Rennie, S. Nunoue, M. Yamamoto, H. Fujimoto, Y. Kokubun, Y. Ohba, G. Hatakoshi, and M. Ishikawa, *Jpn. J. Appl. Phys.* **35**, p. L1315, 1996.
6. G. Bulman, K. Doverspike, S. Sheppard, T. Weeks, H. Kong, H. Dieringer, J. Edmond, J. Brown, J. Swindell, and J. Schetzina, *Electron. Lett.* **33**, p. 1556, 1997.
7. A. Kuramata, K. Domen, R. Soejima, K. Horino, S. Kubota, and T. Tanahashi, *Jpn. J. Appl. Phys.* **36**, p. L1130, 1997.
8. M. Mack, A. Abare, M. Aizcorbe, P. Kozodoy, S. Keller, U. Mishra, L. Coldren, and S. DenBaars, *MRS Internet J. Nitride Semicond. Res.* **2**, p. 41, 1997; *J. Cryst. Growth* **180/190**, p. 837, 1998.
9. F. Nakamura, T. Kobayashi, T. Asatsuma, K. Funato, K. Yanashima, S. Hashimoto, K. Naganuma, S. Tomioka, T. Miyajima, E. Morita, H. Kawai, and M. Ikeda, *J. Cryst. Growth* **180/190**, p. 841, 1998.
10. M. Kneissl, D. P. Bour, N. M. Johnson, L. T. Romano, B. S. Krusor, R. Donaldson, J. Walker, and C. Dunnrowicz, *Appl. Phys. Lett.* **72**, p. 1539, 1998.
11. Yamada, Y. Kaneko, S. Watanabe, Y. Yamaoka, T. Hidaka, S. Nakagawa, E. Marenger, T. Takeuchi, S. Yamaguchi, H. Amano, and I. Akasaki, *Proc. 10th IEEE Lasers and Electro-Optics Society Annual Meeting*, San Francisco, USA, Nov. 10-13, PD1.2, 1997.
12. A. Usui, H. Sunakawa, A. Sakai, and A. Yamaguchi, *Jpn. J. Appl. Phys.* **36**, p. L899, 1997; A. Sakai, H. Sunakawa, and A. Usui, *Appl. Phys. Lett.* **71**, p. 2259, 1997.
13. T. Zheleva, O-H. Nam, M. Bremser, and R. Davis, *Appl. Phys. Lett.* **71**, p. 2472, 1997; O-H. Nam, M. Bremser, T. Zheleva, and R. Davis, *Appl. Phys. Lett.* **71**, p. 2638, 1997.
14. S. Nakamura, M. Senoh, S. Nagahama, N. Iwasa, T. Yamada, T. Matsushita, H. Kiyoku, Y. Sugimoto, T. Kozaki, H. Umemoto, M. Sano, and K. Chocho, *Jpn. J. Appl. Phys.* **36**, p. L1568, 1997; *Appl. Phys. Lett.* **72**, p. 211, 1998.
15. S. Nakamura, M. Senoh, S. Nagahama, N. Iwasa, T. Yamada, T. Matsushita, H. Kiyoku, Y. Sugimoto, T. Kozaki, H. Umemoto, M. Sano, and K. Chocho, *Jpn. J. Appl. Phys.* **37**, p. L309, 1998.
16. H. Marchand, J. Ibbetson, P. Fini, P. Kozodoy, S. Keller, S. DenBaars, J. Speck, and U. Mishra, *MRS Internet J. Nitride Semicond. Res.* **3**, p. 3, 1998; H. Marchand, X. H. Wu, J. Ibbetson, P. Fini, P. Kozodoy, S. Keller, J. Speck, S. DenBaars, and U. Mishra, *Appl. Phys. Lett.* **73**, p. 747, 1998.
17. T. Mukai, D. Morita, and S. Nakamura, *J. Cryst. Growth* **189/190**, p. 778, 1998.
18. T. Mukai, H. Narimatsu, and S. Nakamura, *Jpn. J. Appl. Phys.* **37**, p. L479, 1998.
19. T. Mukai, M. Yamada, and S. Nakamura, *Jpn. J. Appl. Phys.* **38**, p. 3976, 1999.
20. F. Ponce and D. Bour, *Nature* **386**, p. 351, 1997.
21. F. Bernardini, V. Fiorentini, and D. Vanderbilt, *Phys. Rev. B* **56**, p. R10024, 1997.
22. polarity problem has been reviewed in E. Hellman, *MRS Internet J. Nitride Semicond. Res.* **3**, p. 11, 1998.
23. Osamura, S. Naka, and Y. Murakami, *J. Appl. Phys.* **46**, p. 3432, 1975.
24. A. Koukitsu, N. Takahashi, T. Taki, and H. Seki, *Jpn. J. Appl. Phys.* **35**, p. L673, 1996.
25. I-hsiu Ho and G. B. Stringfellow, *Appl. Phys. Lett.* **69**, p. 2701, 1996.
26. R. Singh, D. Doppalapudi, T. D. Moustakas, and L. Romano, *Appl. Phys. Lett.* **70**, p. 1089, 1997.
27. G. Bastard, E. E. Mendez, L. L. Cganga, and L. Esaki, *Phys. Rev. B* **26**, p. 1974, 1982.
28. S. Chichibu, K. Wada, and S. Nakamura, *Appl. Phys. Lett.* **71**, p. 2346, 1997.
29. M. Sugawara, *Phys. Rev. B* **51**, p. 10743, 1995.
30. S. Chichibu, T. Azuhata, T. Sota, and S. Nakamura, *Appl. Phys. Lett.* **69**, p. 4188, 1996.
31. S. Chichibu, T. Azuhata, T. Sota, and S. Nakamura, *Appl. Phys. Lett.* **70**, p. 2822, 1997.
32. S. Chichibu, T. Sota, K. Wada, and S. Nakamura, *J. Vac. Sci. Technol. B* **16**, p. 2204, 1998.
33. S. F. Chichibu, A. C. Abare, M. S. Minsky, S. Keller, S. B. Fleischer, J. E. Bowers, E. Hu, U. K. Mishra, L. A. Coldren, S. P. DenBaars, and T. Sota, *Appl. Phys. Lett.* **73**, p. 2006, 1998.

34. S. F. Chichibu, T. Sota, K. Wada, S. P. DenBaars, and S. Nakamura, *MRS Internet J. Nitride Semicond. Res.* **4S1**, p. G2.7, 1999.
35. S. F. Chichibu, A. C. Abare, M. P. Mack, M. S. Minsky, T. Deguchi, D. Cohen, P. Kozodoy, S. B. Fleischer, S. Keller, J. S. Speck, J. E. Bowers, E. Hu, U. K. Mishra, L. A. Coldren, S. P. DenBaars, K. Wada, T. Sota, and S. Nakamura, *Mater. Sci. Eng. B* **59**, p. 298, 1999.
36. E. Jeon, V. Kozlov, Y. Song, A. Vertikov, M. Kuball, A. Nurmikko, H. Liu, C. Chen, R. Kern, C. Kuo, and M. Crawford, *Appl. Phys. Lett.* **69**, p. 4194, 1996; A. Vertikov, A. Nurmikko, K. Doverspike, G. Bulman, and J. Edmond, *ibid* **73**, p. 493, 1998.
37. Y. Narukawa, Y. Kawakami, Sz. Fujita, Sg. Fujita, and S. Nakamura, *Phys. Rev. B* **55**, p. R1938, 1997.
38. Y. Narukawa, Y. Kawakami, M. Funato, Sz. Fujita, Sg. Fujita, and S. Nakamura, *Appl. Phys. Lett.* **70**, p. 981, 1997.
39. W. Shan, W. Walukiewicz, E. E. Haller, B. D. Little, J. J. Song, M. D. McCluskey, N. M. Johnson, Z. C. Feng, M. Schuman, and R. A. Stall, *J. Appl. Phys.* **84**, p. 4452, 1998.
40. P. Eliseev, P. Perlin, J. Lee, and M. Osinski, *Appl. Phys. Lett.* **71**, p. 569, 1997.
41. T. Takeuchi, H. Takeuchi, S. Sota, H. Sakai, H. Amano, and I. Akasaki, *Jpn. J. Appl. Phys.* **36**, p. L177, 1997.
42. T. Takeuchi, S. Sota, M. Katsuragawa, M. Komori, H. Takeuchi, H. Amano, and I. Akasaki, *Jpn. J. Appl. Phys.* **36**, p. L382, 1997.
43. C. Wetzel, H. Amano, I. Akasaki, T. Suski, J. Ager, E. Weber, E. Haller, and B. K. Meyer, *Mater. Res. Soc. Symp. Proc.* **482**, p. 489, 1998.
44. J. Bergman, N. Saksulv, J. Dalfors, P. Holtz, B. Monemar, H. Amano, and I. Akasaki, *Mater. Res. Soc. Symp. Proc.* **482**, p. 631, 1998.
45. J. Im, H. Kollmer, J. Off, A. Sohmer, F. Scholz, and A. Hangleiter, *Phys. Rev. B* **57**, p. R9435, 1998.
46. B. Gil, P. Lefebvre, J. Allègre, H. Mathieu, N. Grandjean, M. Leroux, J. Massies, P. Bigenwald, and P. Christol, *Phys. Rev. B* **59**, p. 10246, 1999.
47. T. Deguchi, K. Sekiguchi, A. Nakamura, T. Sota, R. Matsuo, S. Chichibu, and S. Nakamura, *Jpn. J. Appl. Phys.* **38**, p. L914, 1999.
48. A. Shikanai, T. Deguchi, T. Sota, T. Kuroda, A. Takeuchi, S. Chichibu, and S. Nakamura, *Physica E* (unpublished).
49. S. F. Chichibu, H. Marchand, M. S. Minski, S. Keller, P. T. Fini, J. P. Ibbetson, S. B. Fleischer, J. S. Speck, J. E. Bowers, E. Hu, U. K. Mishra, S. P. DenBaars, T. Deguchi, T. Sota, and S. Nakamura, *Appl. Phys. Lett.* **74**, p. 1460, 1999.
50. H. Amano, N. Watanabe, N. Kiode, and I. Akasaki, *Jpn. J. Appl. Phys.* **32**, p. L1000, 1993.
51. S. Chichibu, T. Azuhata, T. Sota, and S. Nakamura, *J. Appl. Phys.* **79**, p. 2784, 1996.
52. D. A. Miller, D. S. Chemla, T. C. Damen, A. C. Gossard, W. Wiegmann, T. H. Wood, and C. A. Burrus, *Phys. Rev. Lett.* **53**, p. 2173, 1984; *Phys. Rev. B* **32**, p. 1043, 1985.
53. C. G. Van de Walle and J. Neugebauer, *Appl. Phys. Lett.* **70**, p. 2577, 1997.
54. D. A. B. Miller, D. S. Chemla, and S. Schmitt-Rink, *Phys. Rev. B* **33**, p. 6976, 1986.
55. J. A. Cavaille, D. A. B. Miller, J. E. Cunningham, P. Li Kam Wa, and A. Miller, *Appl. Phys. Lett.* **61**, p. 426, 1992; *IEEE J. Quantum Electron.* **28**, p. 2486, 1992.
56. T. Deguchi, K. Torii, K. Shimada, T. Sota, R. Matsuo, M. Sugiyama, A. Setoguchi, S. Chichibu, and S. Nakamura, *Jpn. J. Appl. Phys.* **38**, 1999 (in press for 9/15 issue).
57. T. Mukai, M. Yamada, and S. Nakamura, *Jpn. J. Appl. Phys.* **37**, p. L1358, 1998.
58. S. Rosner, E. Carr, M. Ludwise, G. Girolami, and H. Erikson, *Appl. Phys. Lett.* **70**, p. 420, 1997.
59. J. Speck, H. Marchand, P. Kozodoy, P. Fini, X. Wu, J. Ibbetson, S. Keller, S. DenBaars, U. Mishra, and S. Rosner, *Proc. 2nd Int. Symp. on Blue Laser and Light Emitting Diodes* (Ohmsha, Tokyo), p. 37, 1998.
60. H. Sato, T. Sugahara, Y. Naoi, and S. Sakai, *Jpn. J. Appl. Phys.* **37**, p. 2013, 1998.
61. their results are summarized in C. Kisielowski, *Proc. 2nd Int. Symp. on Blue Laser and Light Emitting Diodes* (Ohmsha, Tokyo), p. 321, 1998.
62. F. Ponce, S. Galloway, W. Goetz, and R. Kern, *Mater. Res. Soc. Symp. Proc.* **482**, p. 625, 1998.
63. O. Brandt, J. Müllhäuser, A. Trampert, and K. Ploog, *Mat. Sci. Eng. B* **59**, p. 73, 1999.
64. J. Holst, A. Hoffmann, I. Broser, F. Bertram, T. Riemann, J. Christen, D. As, D. Schikora, B. Schoettker, and K. Lischka, presented at ICNS-3, to be published in *Phys. Status Solidi* **176**, 2000.
65. M. McCluskey, C. Van de Walle, C. Master, L. Romano, and N. Johnson, *Appl. Phys. Lett.* **72**, p. 2725, 1998.
66. T. Deguchi, T. Azuhata, T. Sota, S. Chichibu, and S. Nakamura, *Mater. Sci. Eng. B* **50**, p. 251, 1997.
67. T. Deguchi, A. Shikanai, K. Torii, T. Sota, S. Chichibu, and S. Nakamura, *Appl. Phys. Lett.* **72**, p. 3329, 1998.
68. K. Domen, A. Kuramata, and T. Tanahashi, *Appl. Phys. Lett.* **72**, p. 1359, 1998.

Low cost synthesis of ZnCdSe semiconducting thin films for optoelectronic applications

R.Chandramohan^a and T.Mahalingam^b

^a Physics Department, Sree Sevugan Annamalai College, Devakottai-630 303, India

^b Department of Physics, Alagappa University, Karaikudi-630003, India.

ABSTRACT

ZnCdSe ternary alloys form an important class of semiconducting system, which has a wide range of applications in optoelectronic devices in the entire visible spectrum. They are used in the fabrication of blue light emitting diodes, blue lasers, solar cells, thin film transistors and photoelectrochemical solar cells, etc.. Synthesis of such an important material using low cost technique is necessary for the effective application of this valuable system. Electrodeposition is a cost effective, versatile and viable technique for the synthesis of thin film materials. In this study, synthesis of thin films of (ZnCd) Se system from aqueous acidic mixture using potentiostatic electrodeposition is discussed. The physical properties of these films deposited onto transparent conducting tin oxide coated glasses are estimated. The optimised deposition conditions are determined and the films were used as photoelectrodes in poly sulphide electrolytes. The films are found to exhibit reproducible good photoelectrochemical (PEC) behavior. The results of these studies are reported.

Keywords: Low Cost Synthesis, Solar cells, Solid solution, Thin films, Compound semiconductors, II-VI Compounds, Zinc Cadmium Selenide, Chalcogenides, Electrosynthesis, Ternary Systems, Physical Properties.

1. INTRODUCTION

The synthesis of ternary Zn/Cd selenides opens up the possibility of their applications for novel opto-electronic devices in the visible region of electromagnetic radiation¹. The (ZnCd)Se system which enable a tunable band gap region between 1.7 and 2.8 eV at normal temperature facilitates the development of several new electronic and opto-electronic devices such as light emitting diodes, photo detectors, blue green lasers, etc..² Thin films of these materials are usually synthesised by molecular beam epitaxy³, electron beam evaporation⁴ and chemical formation⁵. However, it has been shown⁶ that electrodeposition is a simple and viable alternative to these cost intensive methods. Electrosynthesis of (ZnCd)Se thin films is difficult due to the wide difference in the reduction potentials of the different species present in the solution bath^{7,8}. In this report, the fabrication of composition modulated thin film structures in the (ZnCd)Se systems using the cost effective potentiostatic electrodeposition method and the characterization studies related to structural and optical behavior are reported. Photoelectrochemical solar cells have been fabricated by dipping the electrosynthesised (ZnCd)Se electrodes in polysulphide electrolyte and the results are discussed in detail. The thin film electrode surfaces are modified using various annealing ambients and etchants and the results are also reported.

2. EXPERIMENTAL DETAILS

The experimental synthesis of (ZnCd)Se thin films involves doing lot of preliminary studies before actual deposition. The foremost is cyclic voltammetry. The cyclic voltammograms are recorded for the zinc sulphate, cadmium sulphate and selenium dioxide at various concentrations and scan rate using a cyclic voltameter BAS 100A. These studies indicated the reduction of the various species in the potential range of -500 mV to -1200 mV with respect to SCE for tin oxide coated substrates. The thin films are prepared potentiostatically under various temperatures in the potential range of -500 mV to -1200 mV at various hydrogen ion concentrations. The cell

configuration was a conventional three electrode system. A platinum flag served as a counter electrode, the reference electrode was saturated calomel electrode and the working electrode comprised either precleaned titanium or tin oxide coated transparent conducting glass substrate with sheet resistance < 20 ohms square. The starting chemicals were GR grade ZnSO_4 , CdSO_4 and SeO_2 available from commercial sources and used as received (E Merck). All experiments were performed on carefully deaerated solution. The deposition parameters were optimised after series of experiments in cyclic voltammetry and after undertaking several depositions.

The deposition bath comprised 250 mM ZnSO_4 , 2 mM SeO_2 with various concentrations of CdSO_4 (0.5 to 9.5 mM) in triple distilled water. The pH was adjusted to 1.9 ± 0.1 . The films deposited at a bath temperature of 75°C were found to be uniform, shining and well adherent. It is found that the formation of middle composition of zinc cadmium selenide thin films is favoured when the ratio of Cd : Se ions are 2 : 1 in the solution bath. The deposited films are annealed in air at 450°C for 15 minutes before characterization.

Structural studies were carried out on these films of thickness 1.0 micron using an X-ray diffractometer (JEOL JDX 8030). The thickness of the films was estimated using multiple beam interferometer and weight loss methods in the appropriate ranges. The multiple beam interferometer is used to measure the film thickness up to 0.5 micron. The transmission and reflectance spectra were recorded using a double beam UV-Vis-NIR spectrophotometer (Hitachi U-3400). The surface morphology and EDAX studies were performed using a scanning electron microscope (JEOL JSM 35). The presence of impurities and contamination, which could not be detected by EDAX, are studied using ESCA and the compositions are also estimated⁹.

Photoelectrochemical solar cells have been fabricated by dipping the thin film (ZnCd)Se electrodes in an electrolyte comprising Na_2S , S and NaOH (1molar each). The current and voltages are measured in dark and under illumination. A platinum flag acted as a counter electrode. About 0.5 square cm of the electrode surface was illuminated with 550 mW radiation. Thin films deposited onto titanium to a thickness in the range of 1.2 to 2.0 microns were used for the PEC studies. The films were subjected to etching (chemical and photo etch) and the PEC performance were studied.

The annealing studies are carried out under both air and vacuum at various temperatures in the range of 300 - 600°C for different durations. The optimum annealing temperatures for the entire solid solutions are estimated. For surface modification studies both chemical etching and photoetching are used. The chemical etching of the films were done at 60°C by dipping the films in a dilute acid mixture containing HCl, HNO_3 , H_2SO_4 and acetic acid in the ratio of 4.0:1.0 : 0.2 : 0.1 by volume for few seconds. The etched films are thoroughly rinsed in triple distilled water and then dipped in polysulphide solution in order to remove oxidation products of the chemical etching. Photo etching of the films before and after chemical etching were also done in 1.5 M $\text{Na}_2\text{S}_2\text{O}_3$ to study the effect of photo etching on these samples. The flatband potentials were evaluated by illuminating the semiconductor electrolyte interface with a monochromatic light of wave length 580 nm in 1M KOH. The wave length is chosen to keep the absorption small.

3. RESULTS AND DISCUSSIONS

The deposition conditions optimised for the low cost synthesis of (ZnCd) Se thin films are presented in table 1. It is observed that the alloy films of this ternary system could be synthesised by altering the Cd content in the solution bath. The XRD patterns recorded for the electrodeposited thin films for various compositions onto tin oxide coated substrates show that the films are polycrystalline in nature with a hexagonal structure. Some peaks corresponding to cubic phase were also present. The d values obtained compare well with the available ASTM standards. However, it is observed that for $x=0$, cubic phase is obtained. Figure1 shows XRD pattern obtained for typical ZnSe, CdSe and ZnCdSe thin films coated onto tin oxide coated transparent conducting glass substrates.

The absorption studies were carried out using the transmission spectra which reveal an absorption edge at 700 nm for $x = 1$ corresponding to the band gap of the cadmium selenide thin film and the spectra obtained for $x = 0.8$, 0.6 and 0.2 indicated the shift of absorption edge towards the shorter wavelength side. The variation of band gap with the zinc content ' x ' is found to be linear and indicate the formation of a continuous series of solid solution. The variation of band gap for electrodeposited $\text{Zn}_{1-x}\text{Cd}_x\text{Se}$ thin films is found to obey Vegard's law with slight bowing.

Similar variation of ' E_g ' with x has been reported by Bassam et al for ZnCdSe crystals¹⁰. The variation of band gap with film composition determined from EDAX studies are presented in table 1 along with the solution composition. The refractive index ' n ' and extinction coefficient ' k ' obtained using a continuous differential descent method for $x = 0.3$ and 0.7 are illustrated in figure 2. The refractive index ' n ' is found to be maximum at a wavelength near 700 nm for $x = 1$ corresponding to the absorption edge. The addition of Zn to the deposit results in an increase of refractive index ' n ' and the extinction coefficient ' k '. The refractive index ' n ' and extinction coefficient ' k ' for $x = 0.3$ and 0.7 shows a maximum value of ' n ' which corresponds to the onset of absorption edge which is in conformity with earlier reports for CdS thin films¹¹.

The grain size of the electrodeposited films was found to be 0.01 micron using the full width at half maximum data obtained from XRD studies. The surface micrographs from the scanning electron microscope revealed a combination of needles and cauli flower shaped structure for a typical ZnCdSe film. The grains are found to be in good electrical contact. The surface of the films, as revealed by SEM micrographs, is found to have grains uniformly distributed through out the film¹².

EDAX studies revealed a small percentage of excess cadmium in all the electrodeposited alloy films. The EDAX studies on films electrodeposited by employing the concentration of CdSO_4 as greater than 10 mM do not show any zinc incorporation. The possible mechanism for the formation of ZnCdSe may be that selenous acid reduction to Se^{4+} precedes the reduction of CdSO_4 to Cd^{2+} followed by ZnSO_4 to Zn^{2+} reduction. When the cadmium concentration in the deposition bath is greater, cadmium reduction is found to be dominant when compared to Zn reduction and hence the metallic sites are preferentially occupied by Cd atoms. The EDAX studies indicated the substrate elements Sn and Si. Si presence is due to the glass substrate and the Sn is due to the tin oxide coating. Since EDAX is not suitable for the deduction of elements like oxygen the ESCA studies were also carried out for these films. The ESCA studies revealed the presence of oxygen and carbon contamination in all these films. The relative compositions of Zn, Cd and Se obtained for various solution compositions are shown in table 1.

The electrosynthesised films were used as photoelectrodes in polysulphide electrolyte. The films of ZnCdSe and CdSe are found to exhibit photoanodic behaviour while the films of ZnSe behaved as a photocathode. It is observed that the efficiency of the electrodes subjected to photoetching followed by chemical etching is maximum. The $\text{Zn}_{0.2}\text{Cd}_{0.8}\text{Se}$ electrode showed the maximum efficiency under unetched and etched conditions. The solar cell parameters evaluated under various annealing ambients at 450°C for CdSe and $\text{Zn}_{0.2}\text{Cd}_{0.8}\text{Se}$ are shown in table 2. It is clear from these studies that the vacuum annealed films behaviour is better than the air annealed ones. Figure 3 shows the Mott-Schottky plot obtained for a typical $\text{Zn}_{0.2}\text{Cd}_{0.8}\text{Se}$ thin film. The annealing studies were performed on these films. It is observed that annealing time greater than 15 seconds does not show any change in open circuit voltage. Hence for subsequent studies the annealing time was fixed as 15 seconds. It is observed that vacuum annealed films are superior photoelectrodes than the air annealed films for all the film compositions. Figure 4 shows the I-V characteristics obtained for a typical CdSe electrode under various etching conditions. Figure 5 shows the I-V characteristics obtained for $\text{Zn}_{0.2}\text{Cd}_{0.8}\text{Se}$ electrode under photoetch followed by chemical etched conditions. Table 3 shows the solar cell parameters estimated under various etching conditions for typical CdSe and $\text{Zn}_{0.2}\text{Cd}_{0.8}\text{Se}$. It is evident from these studies that the films which are vacuum annealed and photoetched followed by chemical etch showed the best photoelectrochemical results. It is observed that the Zn incorporation in CdSe thin film electrodes up to 20% of the metallic sites improved the photoelectrochemical behavior of the electrodes to an extent. The electrosynthesised films of (ZnCd)Se could be used for several other opto electronic devices like photovoltaic solar cell, thin film luminescent devices, etc... Further studies on these films are under progress.

4. CONCLUSION

The Synthesis of $Zn_{1-x}Cd_xSe$ thin films are performed using low cost method of electrodeposition. The reproducibility of the method is tested by the ability of the method to grow films of high quality and surface uniformity. The method though cost effective is found to yield films comparable to any other cost intensive methods. The physical properties of these films are studied. The structure of these films are found to be hexagonal for $0 < x < 1$ and cubic for $x = 0$. The optical properties of these films are studied and the band gap of these films is estimated. The optical constants of these films are also estimated and reported. The EDAX analysis showed an excess cadmium in the samples. The ESCA revealed the presence of carbon and oxygen traces in the films. Photoelectrochemical solar cells have been fabricated and important photoelectrochemical parameters are evaluated. The $Zn_{0.2}Cd_{0.8}Se$ electrode is found to behave as a better photoelectrode under etched and unetched conditions. Studies on the improvement of photoelectrochemical behavior of these electrodes using various surface modification techniques are being carried out. Further studies on the fabrication of several opto electronic devices like photovoltaic solar cells are under progress.

5. REFERENCES

1. R.Chandramohan, C. Sanjeeviraja and T. Mahalingam. 'Preparation of Zinc Selenide thin films for Solar Cell applications'. *Physica Status Solidi (a)* 163 (1997) R 11
2. K. Prior. 'The development of II-VI Semiconductors for blue diode lasers'. *Contemporary Physics*, **37**, pp.345-358, 1996.
3. Y.Z. Feng, S.P.Guo. 'The structure and strain relief in epitaxially grown CdSe on ZnSe by atomic layer epitaxy'. *J. Mater. Sci. Lett.* **15**, pp.1824-1827, 1996.
4. R. Islam and D. R. Rao. 'Electrical properties of polycrystalline ZnCdSe thin films grown by electron beam evaporation'. *J.Mater.Sci.Lett.* **13**, pp.1637-38, 1994.
5. R. K. Pandey, A. J. N. Rooz and R. B. Gore.'CdZnSe Photoanodes I-II'. *Semicon.Sci.Tech.* **3**, pp. 729-748, 1988.
6. K. Rajeshwar. 'Electrosynthesised thin films of group II-VI compound semiconductor alloys and superstructures'. *Adv. Mater.* **4**, pp.23-29, 1992.
7. A. Darkowski and A. Grabowski. 'Electrodeposition of Cd-Zn-Se thin films from Seleno Sulphite solutions'. *Solar Energy Mat.* **23**, pp. 75- 79, 1989.
8. C. Natarajan, G. Nogami and M. Sharon. 'Electrodeposition and Photovoltaic properties of Zinc Cadmium Selenide thin films'. *Bulletin of Electrochem.* **12**, pp.136-140, 1996.
9. R.Chandramohan. 'Studies on Electrosynthesised ZnCdSe Semiconducting thin films'. *Ph.D.Thesis Alagappa University, INDIA* 1998.
10. A. AL. Bassam, A. N. Brinkman G. J. Russel and J. Woods. 'Electrical Properties of ZnCdSe'. *J. Cryst. Growth* **86**, pp. 667- 671, 1988.
11. F. Tepehan and N.Ozer. 'A simple method for the determination of the Optical Constants, n and k of cadmium sulfide films from transmittance measurements'. *Solar Energy Mat. Solar Cells* **30**, pp. 353- 356, 1993.
12. R.Chandramohan, C.Sanjeeviraja, S.Rajendran, T.Mahalingam, M.Jayachandran and Mary Juliana Chockalingam. 'Electrosynthesis and Characterization of ZnCdSe thin films'. *Bulletin of Electrochem.* **14**, pp. 402- 406, 1998.

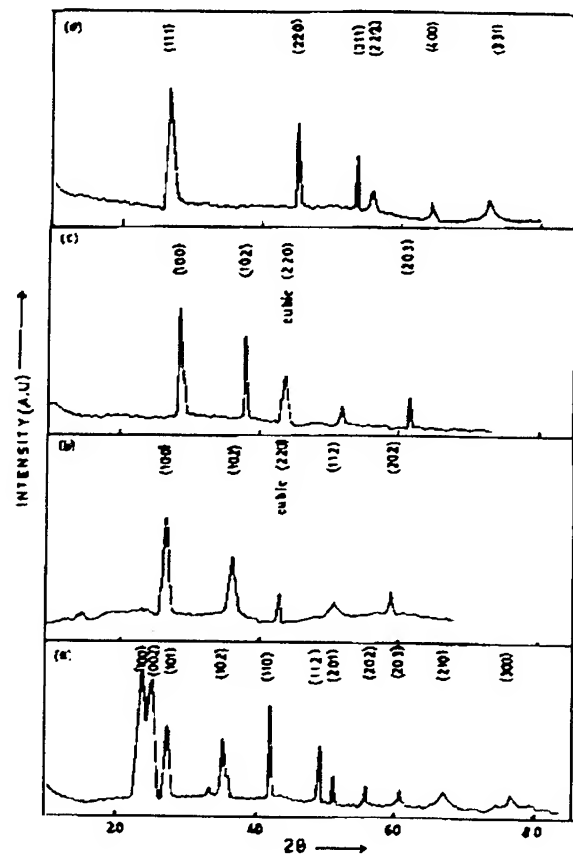


Fig.1 XRD patterns of $\text{Zn}_{1-x}\text{Cd}_x\text{Se}$ electrodeposited thin films for (a) $x = 1.0$, (b) $x = 0.6$, (c) $x = 0.2$ and (d) $x = 0$

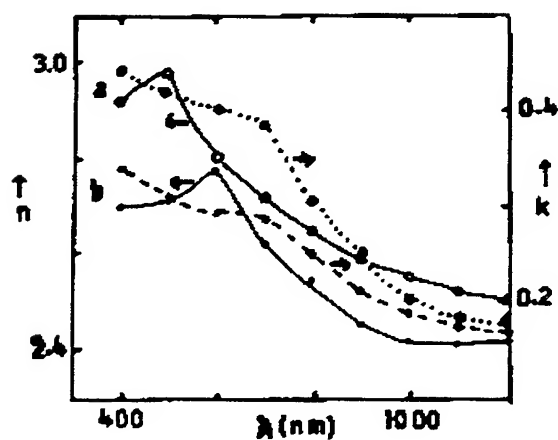


Fig.2 Variation of refractive index ' n ' and extinction coefficient ' k ' with wave length for (a) $\text{Zn}_{0.5}\text{Cd}_{0.5}\text{Se}$ and (b) $\text{Zn}_{0.3}\text{Cd}_{0.7}\text{Se}$ thin films.

Table 1 The variation of band gap with cadmium content 'x' in $Zn_{1-x}Cd_xSe$ thin film and the respective solution composition at solution pH= 2.0 and at 75°C bath temperature.

Concentration of			Cd content in film from EDAX	Band Gap E_g
ZnSO ₄ mM	CdSO ₄ mM	SeO ₂ mM		eV
250	0	2.5	0	2.82
250	2	2.5	0.2	2.52
250	5	2.5	0.5	2.25
250	8	2.5	0.8	1.94
250	9	2.5	0.9	1.82
250	10	2.5	1.0	1.72

Table 2 Solar Cell parameters at various annealing ambients at 450° C for CdSe and $Zn_{0.2}Cd_{0.8}Se$

Material	Ambients	Open Circuit Voltage V_{oc} V	Short Circuit Current Density J_{sc} mA/cm ²	Fill Factor FF	Efficiency η %
CdSe					
	Air	0.33	5.9	0.25	0.8
	Vacuum	0.50	6.8	0.33	1.1
$Zn_{0.2}Cd_{0.8}Se$					
	Air	0.42	7	0.34	1.35
	Vacuum	0.52	9	0.4	1.6

Table 3 Solar Cell parameters at various etching conditions for $Zn_{0.2}Cd_{0.8}Se$ and CdSe thin films annealed in vacuum at 450° C

S.No	Etching Conditions	Open Circuit Voltage V_{oc} V	Short Circuit Current Density J_{sc} mA/cm ²	Fill Factor FF	Efficiency η %
CdSe					
1	Unetched	0.50	6.8	0.33	1.1
2	Chemical etched	0.52	10.0	0.36	1.4
3	Photo etched	0.54	12.0	0.39	2.1
4	Photo etched followed by Chemical etch	0.56	15.0	0.52	4.9
$Zn_{0.2}Cd_{0.8}Se$					
1	Unetched	0.52	9.0	0.40	1.6
2	Chemical etched	0.57	12.5	0.45	4.2
3	Photo etched	0.58	19.0	0.53	5.3
4	Photo etched followed by Chemical etch	0.60	20.0	0.57	6.2

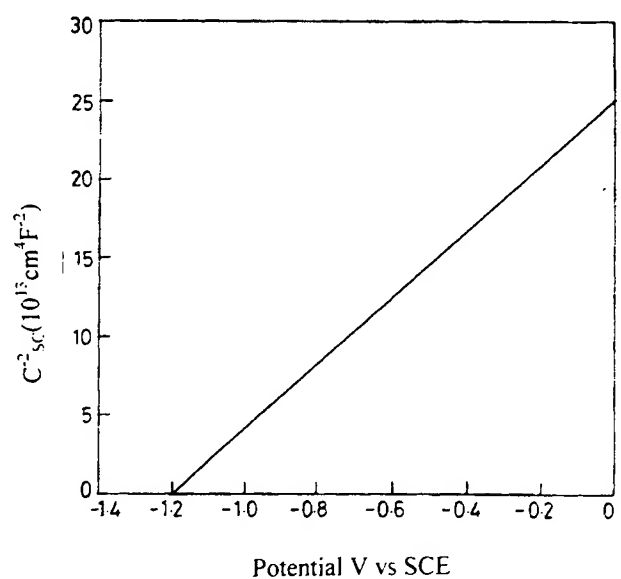


Fig.3 Mott- Schottky plot obtained for a typical ZnCdSe thin film.

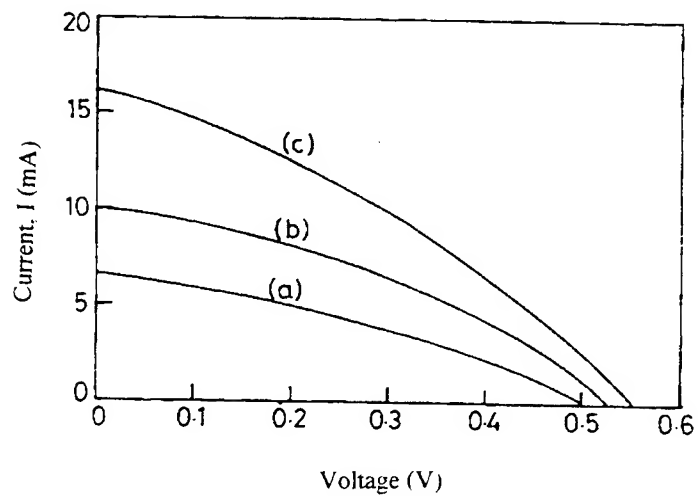


Fig.4 .I-V characteristics for a typical CdSe thin film under different etch conditions.

- (a) without etching
- (b) chemical etching
- (c) photoetching followed by chemical etching

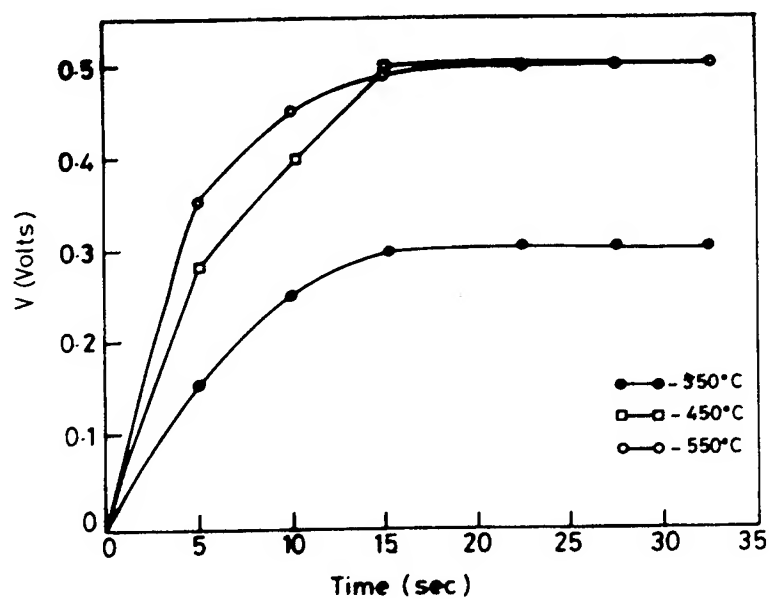


Figure.4. Variation of open circuit voltage with annealing time in vacuum for $\text{Zn}_{0.2}\text{Cd}_{0.8}\text{Se}$ thin films

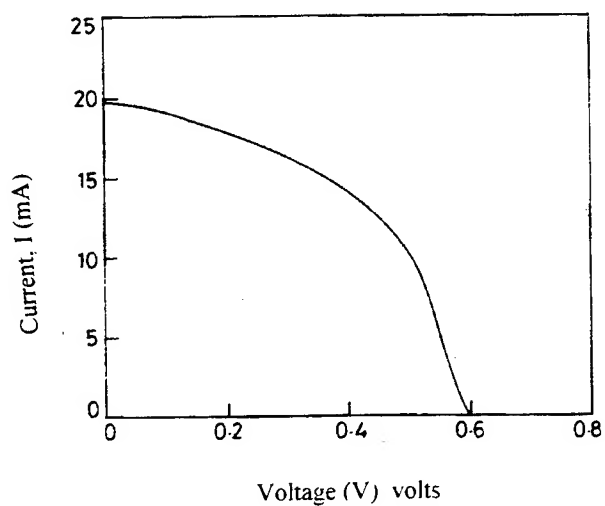


Fig.5. I-V characteristics of a typical $\text{Zn}_{0.2}\text{Cd}_{0.8}\text{Se}$ thin film photoetched followed by chemical etched in an etchant comprising of H_2SO_4 , HCl , HNO_3 and CH_3COOH in the volume ratio 0.2: 4.0:1.0:0.1

SESSION 3

Semiconductor Light Emitters

Shot noise limited VCSELs for high speed fiber optic data transmission

Jäger R., Wiedenmann D., Grabherr M., Jung C., Kicherer M., King R., Mederer F.,
Miller M., Schnitzer P., and Ebeling K.J.

Department of Optoelectronics,
University of Ulm,
D-89069 Ulm,
Germany

ABSTRACT

Oxide-confined vertical-cavity surface-emitting laser diodes (VCSELs) are optimized for multi-Gbit/s data rate optical transmission systems. Noise characteristics and small-signal modulation response of high-performance transverse single- and multi-mode devices under different operation conditions are investigated. We demonstrate for the first time 12.5 Gbit/s data rate fiber transmission with a bit-error rate of better than 10^{-11} for pseudo-random bit sequence (PRBS) signals over 100 m multimode fiber and 1 km single-mode fiber. Maximum electrical and optical bandwidths obtained at 3 mA driving current are 12 GHz and 13 GHz, respectively. For pumping levels above 2.8 times threshold current, the relative intensity noise (RIN) is below -150 dB/Hz up to 5 GHz for output powers of about 1 mW. In detail, we investigate the low frequency intensity noise of high efficiency small area selectively oxidized VCSELs emitting in the fundamental transverse mode up to 7 times threshold current at room temperature and in multiple transverse modes up to 20 times threshold current. For low temperature operation quantum efficiency of the VCSEL is increased leading to photon-number fluctuations 1.4 dB below the shot noise limit. This is to our best knowledge the largest amount of squeezing ever reported for VCSELs.

Keywords: laser noise, vertical cavity surface emitting lasers, optical interconnections, shot noise, optical data transmission, electrical bandwidth, optical bandwidth, modulation, semiconductor laser, squeezing

1. INTRODUCTION

In recent years the improvement of VCSELs has led to devices with excellent electrical and optical properties. Low threshold currents in the sub-100 μ A range,^{1,2} low threshold voltages close to the bandgap voltage, high wallplug efficiencies above 50%,³ and modulation bandwidths up to 21.5 GHz have been obtained.⁴ Considering system applications, high bit rate data transmission of 10 Gbit/s over 500 m multimode fiber (MMF) point-to-point interconnects using proton implanted 980 nm emission wavelength InGaAs quantum-well (QW) VCSELs as well as 10 Gbit/s for transmission distances up to 100 m using a p-type delta-doped InGaAs QW VCSEL have been reported.^{5,6} However, 800 to 850 nm is the preferred emission wavelength range owing to the availability of inexpensive Si or GaAs photodetectors. This wavelength regime was chosen as the standard for short-distance parallel optical interconnects. Recently, 10 Gbit/s transmission over 300 m low-loss graded-index perfluorinated plastic optical fibers (GI PF POFs) as well as 500 m over silica glass MMF using 850 nm emission wavelength VCSELs was demonstrated.^{7,8}

These results show that VCSELs are very attractive light sources for fiber based high-speed local area networks. The inherent possibility for creating one- or two-dimensional (1D or 2D) arrays make them the preferred emitters for parallel optical interconnects.⁹⁻¹¹ The rapid growth of the global communication networks is the main driving force for increasing transmission rates, input/output requirements, clock speeds, and parallel processing architectures.

Gigabit Ethernet is standardized for a data rate of 1 Gbit/s at 850 nm wavelength using 50 μ m core diameter MMF of lengths up to 550 m.¹² The continuously increasing need to provide higher network capacities mainly initiated by the Internet boom will require even faster networks than the Gigabit Ethernet. First developments for a 10 Gbit/s Ethernet multiplexer are reported.⁸

E-mail: roland.jaeger@e-technik.uni-ulm.de

The capability of a device to transmit data rates up to 10 Gbit/s can be investigated using analog small signal modulation and relative intensity noise (RIN). Usually, the frequency limits of electronic devices are determined by their parasitic elements. To understand the impedance behavior of VCSELs, an equivalent-circuit model is introduced and fitted to the modulation response of the device. RIN measurements provide data for parasitic-free small signal modulation behavior leading to the maximum intrinsic modulation bandwidth and efficiency. Generally, RIN restricts the minimum achievable bit-error rate (BER) especially for high-speed data transmission at 10 Gbit/s or above.¹³

The lower limit of the intensity noise in semiconductor lasers is given by the pump current fluctuations. Squeezed light with sub-poissonian noise can be generated in semiconductor lasers using suppressed pump noise.^{14,15} In principle, VCSELs are capable of producing intensity noise far below the shot noise limit.¹⁶ Experimentally, strong restrictions to this behavior are provided by thermal rollover, polarization instabilities as well as multi-transverse mode operation. Photon number squeezed states from a VCSEL were first demonstrated in 1997.¹⁷ Application of squeezed light to optical systems can, in principle, improve channel capacity and transmission error rates if attenuation in the link can be avoided.^{18,19} Shot noise limited light on the other hand is often considered an ideal signal for optical data transmission when losses are present.

In the following we discuss basic VCSEL device structures and output characteristics before we briefly demonstrate data transmission capabilities at 12.5 Gbit/s rates. We then study modulation behavior and noise properties in some detail including generation of squeezed light.

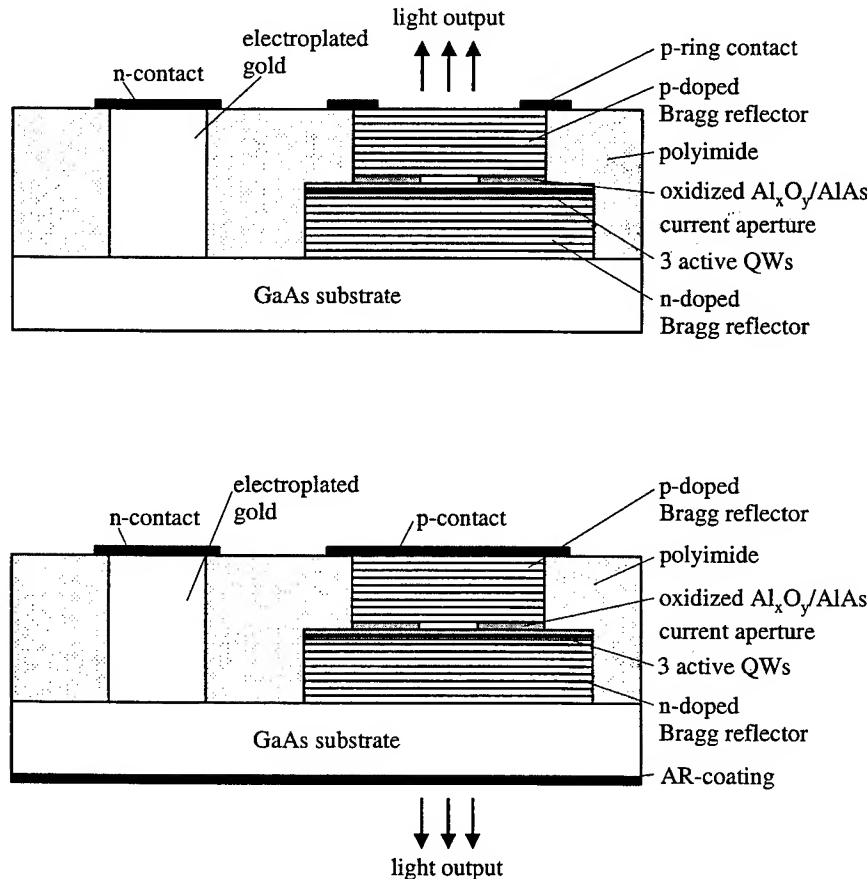


Fig. 1. Cross-sectional view of selectively oxidized top- and bottom-emitting VCSELs for emission wavelengths of 850 nm and 980 nm, respectively.

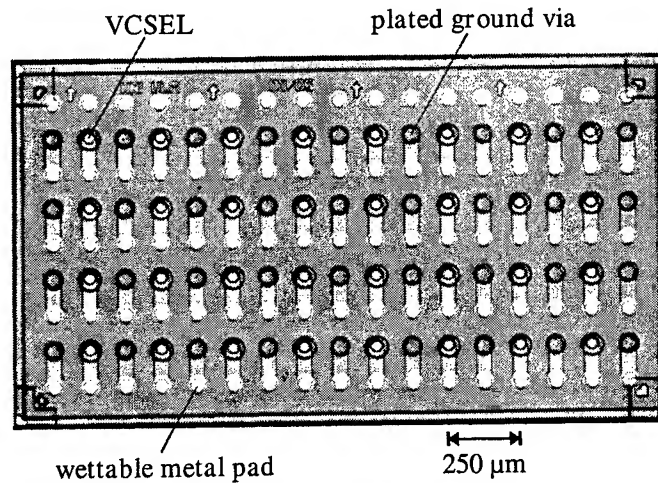


Fig. 2. Photograph of a bottom emitting 4×8 element VCSEL array with 250 μm pitch and two individual contacts per device.

2. BASIC DEVICE STRUCTURE AND OUTPUT CHARACTERISTICS

Fig. 1 shows schematics of selectively oxidized top and bottom-emitting GaAs and InGaAs QW based VCSELs, respectively. The layers are grown using solid source molecular beam epitaxy.²⁰ The active region is formed either by three 8 nm thick GaAs QWs embedded in $\text{Al}_{0.2}\text{Ga}_{0.8}\text{As}$ barriers for 850 nm emission wavelength, or by three 8 nm thick $\text{In}_{0.2}\text{Ga}_{0.8}\text{As}$ QWs embedded in GaAs barriers for 980 nm emission wavelength. For the 850 nm top emitting devices, the lower n-type Si-doped and the upper p-type C-doped Bragg reflectors consist respectively of 38 and 27 $\text{Al}_{0.2}\text{Ga}_{0.8}\text{As}/\text{Al}_{0.9}\text{Ga}_{0.1}\text{As}$ quarter-wavelength pairs, with graded interfaces and δ -doping to reduce series resistance.²¹ The optical cavity of a 980 nm bottom-emitting device is sandwiched between an upper p-type 30 pair C-doped and a lower 20.5 pair Si-doped Bragg reflector. Both mirrors consist of quarter-wavelength pairs of GaAs/ $\text{Al}_{0.9}\text{Ga}_{0.1}\text{As}$ stacks and are optimized for low series resistance.^{22,23} Current is injected through the upper Bragg reflector either by a ring contact, for the top emitting devices, or by a full contact for the bottom emitting devices. Current confinement is achieved by selective lateral oxidation of a 30 nm thick AlAs layer after mesa etching.²⁴ Stable single-mode emission is enforced by small oxide aperture and low optical confinement.²¹ Polarization can be controlled using tilted substrate²⁵ or elliptical current apertures.²⁶ Small diameter mesa with steep side-walls are required to obtain a low oxide capacitance. Therefore, mesa are formed by chemically assisted ion beam etching. The mesa is passivated and a second etching step gives access to the n-doped GaAs substrate on which a large area n-contact is evaporated. After planarization with photosensitive polyimide the n-contact is electroplated up to the height of the p-contact. For bottom emitting devices a single layer anti-reflection coating is evaporated on the polished 150 μm thick GaAs substrate.

The hybrid integration of VCSEL transmitters and III-V based photodetectors directly onto Si CMOS circuits seems to be an attractive solution for optical interconnects in future integrated circuit systems.²⁷ In order to demonstrate the potential of VCSELs as efficient transmitters in a high capacity bus, we have fabricated VCSEL arrays with 4×8 elements. Some transmitter chips have been flip-chip mounted on Si CMOS driver chips.²⁸ Fig. 2 shows a photograph of a bottom emitting selectively oxidized 4×8 InGaAs VCSEL array. Mounting the array junction-side down is done straightforward since all electrical contacts are on the top-side and laser emission occurs through the substrate at 980 nm wavelength. The layout concept can be carried forward to the optical interconnect standard 850 nm wavelength regime by employing, e.g. GaAs substrate removal after mounting.^{29,30} The VCSELs are arranged at 250 μm pitch and have two contacts per device for individual high bit rate modulation. Polyimide is used for electrical insulation and array planarization. The VCSELs as well as the plated vias, which connect the n-contact to the top-side metallization, are connected by tracks to remote wettable metal pads. We have studied single-mode VCSEL arrays with active device diameters of 3 μm . Fig. 3 shows the output and driving characteristics of all 32 devices in the array. The average threshold current is 0.6 mA and the average threshold voltage is 1.7 V. All

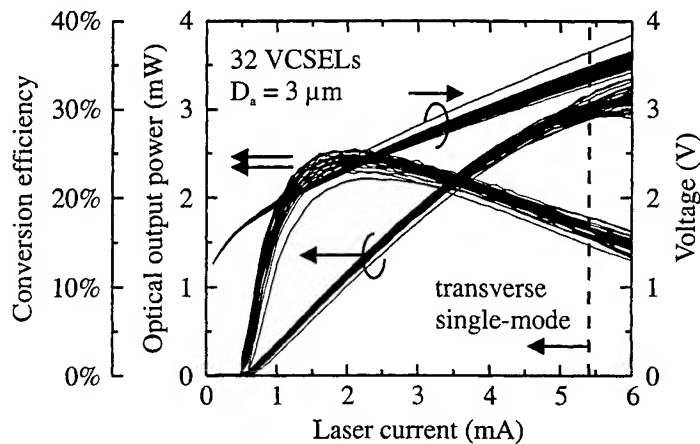


Fig. 3. Operation characteristics of all $3\ \mu\text{m}$ active diameter oxide-confined VCSELs within a 4×8 array.

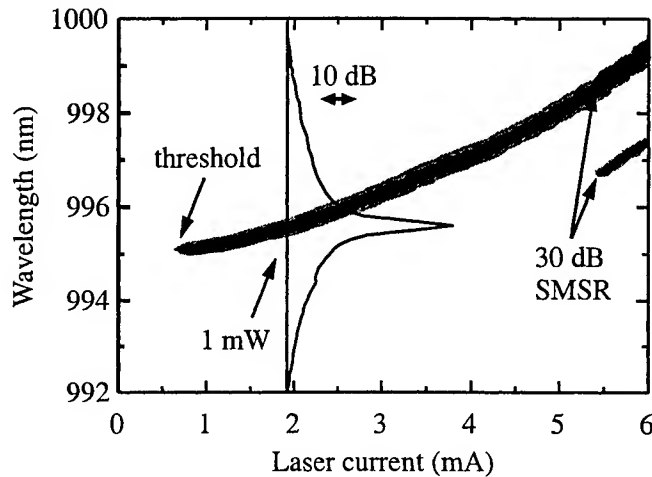


Fig. 4. Spectral current dependent mode map of a single-mode array VCSEL from the array of Fig. 3

VCSELs in the array are single-mode up to an output power of 3 mW with a side-mode suppression ratio (SMSR) of more than 30 dB as indicated in the emission spectrum of an individual laser of the array in Fig. 4. At an optical output power of 1 mW per element the conversion efficiency is 24% which corresponds to a dissipated power of 3.2 mW. The low-capacitance design of the array enables high-speed data transmission at 12.5 Gbit/s per element as discussed in section 3, far beyond the envisaged Gbit/s CMOS speeds. Fig. 5 shows a photograph of a VCSEL array flip-chip mounted on a $0.8\ \mu\text{m}$ gate length CMOS driver chip.

3. DATA TRANSMISSION

We have used the investigated VCSEL source as a transmitter in an optical data link. Fig. 6 shows a sketch of the test system. The VCSEL is contacted using a high frequency probe tip. Bias current and non-return-to-zero pseudo-random bit sequence (NRZ PRBS) signal are combined in a bias-tee and fed to the VCSEL. The optical fiber is butt-coupled to the VCSEL and connected via an optical attenuator to the pin InGaAs photodiode. After amplification the signal is analyzed in a sampling oscilloscope or in a bit error rate detector. We have used 1 km of $5\ \mu\text{m}$ core diameter single-mode fiber (SMF), 1.6 km of $9\ \mu\text{m}$ core diameter standard single-mode fiber (SSMF) and 100 m of $50\ \mu\text{m}$ core diameter graded index-multimode fiber (MMF).

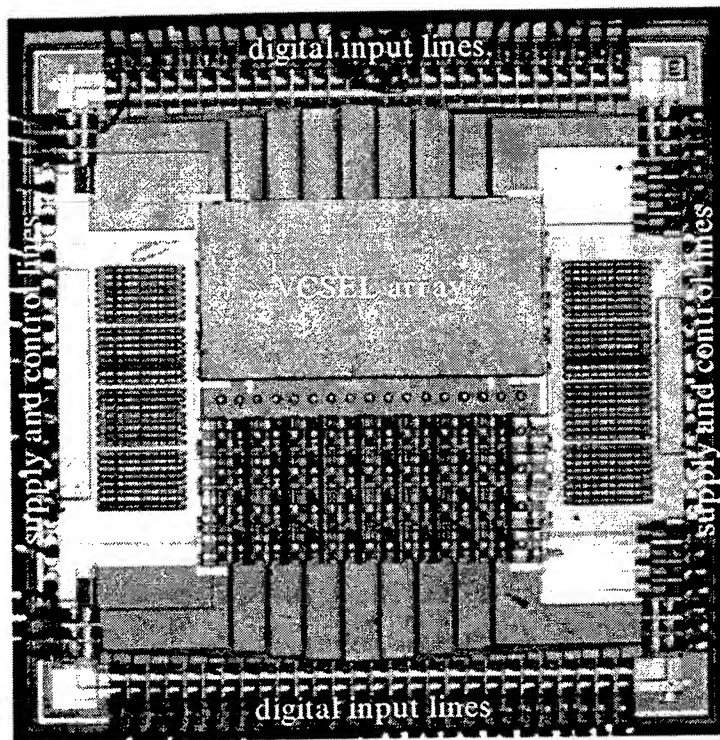


Fig. 5. 4×8 VCSEL array flip-chip mounted on Si CMOS driver circuits.³¹

The inset of Fig. 7 (left hand side) shows the eye diagram at 12.5 Gbit/s PRBS modulation of the 850 nm VCSEL for back to back transmission. The VCSEL is biased at three times threshold and modulated with 1 V_{pp}. Obviously, the laser is not modulated to below threshold, since the resulting turn-on delay would inhibit high data rate transmission. The broadened rising and falling edges of the eye are therefore attributed to pattern effects. Fig. 7 (left hand part) shows the bit error rate (BER) curves for the transmission experiments with an 850 nm single-mode VCSEL from the array in Fig. 3 using back to back (BTB) transmission, 100 m MMF and 1 km of SMF. In back to back transmission the minimum required optical power at the receiver is -11 dBm to achieve a bit error rate of 10^{-11} at 12.5 Gbit/s. This relatively high power is due to the high noise of the broad-band 50 Ω pin receiver used. Transmission distance was limited by fiber availability only. A transmission experiment using a 980 nm VCSEL and 1.6 km of standard single-mode fiber, supporting just one low loss fiber mode, was conducted as well. Fig. 7 (right hand part) shows the corresponding bit error rate curve. The minimum required power at the receiver is -11 dBm for a BER of 10^{-11} for the same transmission rate as above. These experiments are to be compared with similar studies at 850 nm wavelength, where fiber mode filters were required to suppress the effects of modal dispersion in the fiber.³²

4. SMALL SIGNAL MODULATION CHARACTERISTICS

Fig. 8 illustrates the physical origin of an equivalent-circuit model for the VCSEL impedance behavior, quite similar to that proposed in.⁴ Only a fraction of the injected current from outside contributes to electrons and holes which recombine in the active region. Therefore, the current flowing into the active region is distorted with respect to the terminal modulation signal. The equivalent-circuit model takes into account pad capacitance C_{pad} , series resistance R_s , oxide aperture capacitance C_{ox} and active layer resistance R_a . Quantities for the various elements are obtained by fitting the model to the measured rf S11 parameters. For the vector high frequency impedance measurements we use individual lasers from a polyimide planarized 4×8 array contacted with a coplanar probe tip. The model equivalent circuit well describes the measured data up to frequencies of 20 GHz. Table I gives determined parameters for three VCSELs of different active and mesa diameters. Only R_a significantly depends on the bias current, the

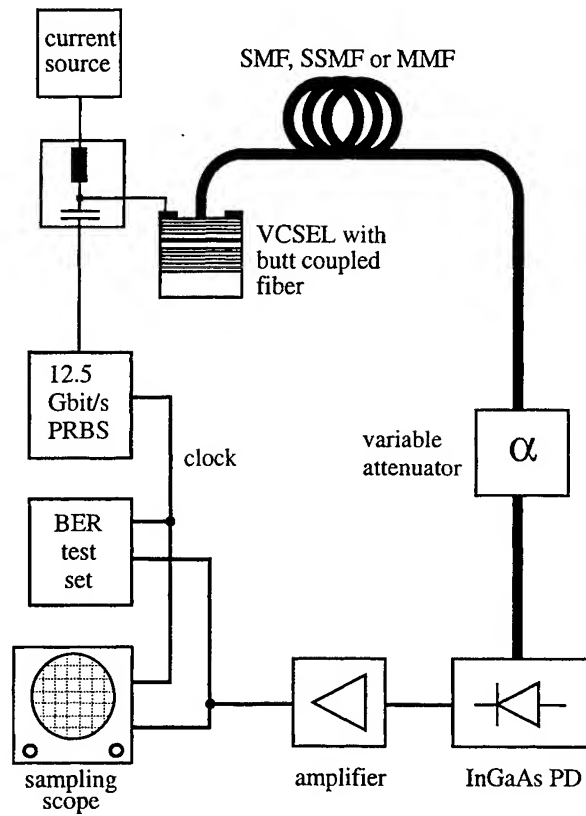


Fig. 6. Setup for data transmission experiments with 1 km single-mode fiber (SMF), 1.6 km standard single-mode fiber (SSMF) and 100 m graded index multimode fiber (MMF).

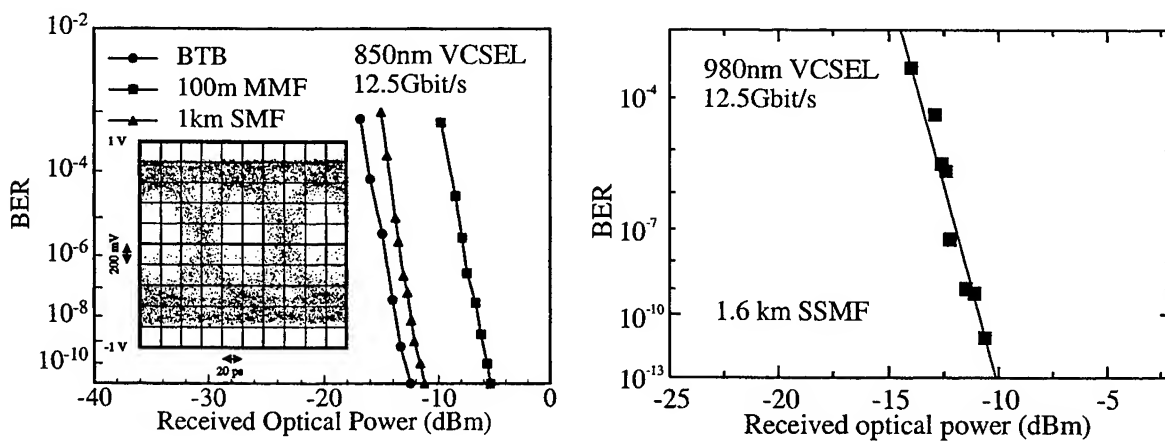


Fig. 7. Bit error rate curves for 12.5 Gbit/s PRBS transmission over different transmission channels using 850 nm (left hand part) and 980 nm emission wavelength VCSEL (right hand part). The eye diagram at this modulation of an 850 nm VCSEL is also depicted.

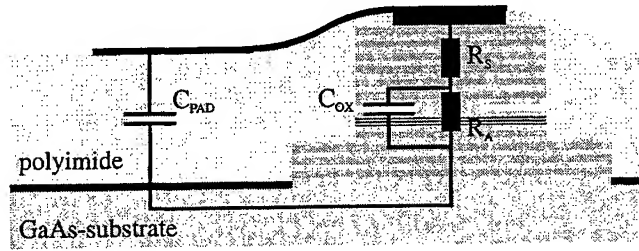


Fig. 8. An equivalent-circuit model for VCSELs and physical origin of various elements.

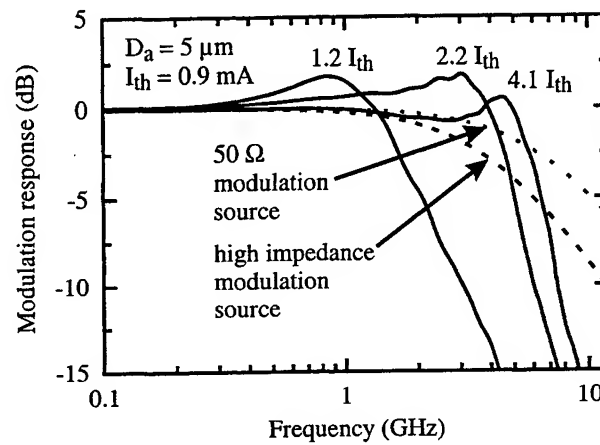


Fig. 9. Modulation response of a 960 nm VCSEL and calculated low-pass filter effect for 50 Ω and high impedance modulation source.

data listed in Table I are for a bias of far above threshold current. The parameters scale with the dimensions of the VCSEL indicating that the physical origin of the proposed circuit is reasonable.

Table 1. Equivalent-circuit parameters obtained by fitting the vector impedance of VCSELs with different active diameters (D_a) and mesa diameters (D_m).

D_a (μm)	D_m (μm)	R_s (Ω)	R_a (Ω)	C_{ox} (pF)	C_{pad} (pF)
3.5	32	55	86	0.56	0.13
5	34	46	46	0.68	0.13
8.5	38	36	24	1.0	0.13

Fig. 9 depicts the optical modulation response of a 5 μm VCSEL measured with a 50 Ω network analyzer. The VCSEL is contacted using a microwave probe tip and the light is detected by a 25 GHz photodiode. The fitted parameters from the equivalent-circuit model allow the calculation of the parasitic roll-off in the modulation response, also shown in Fig. 9 both for a high impedance and a 50 Ω modulation source. The VCSEL modulation bandwidth is seen to be limited by the electrical parasitics. The low-pass filter effect is stronger for a high impedance modulation

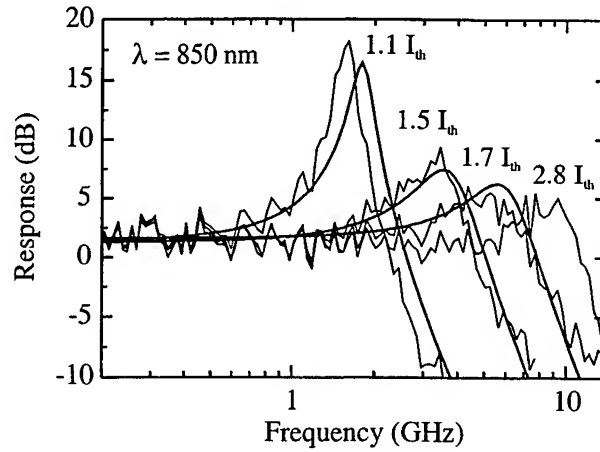


Fig. 10. Measured optical modulation response behavior of single-mode VCSEL for different bias levels. The intrinsic modulation response curves calculated from measured RIN data are also included as smooth solid lines.

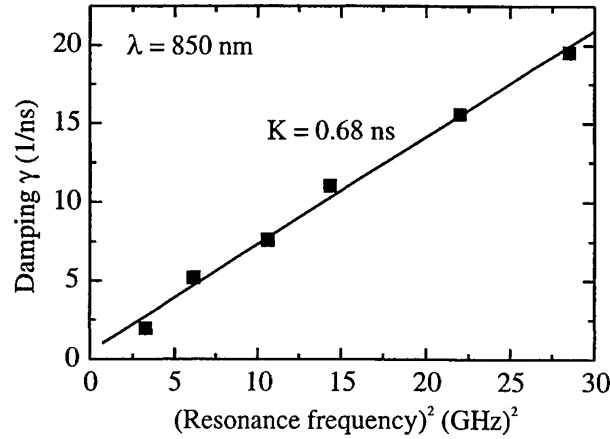


Fig. 11. Damping constant as a function of squared resonance frequency. The slope is the so called K-factor.

source. In order to reduce the effects of electrical parasitics on the modulation bandwidth devices with smaller mesa diameters are desirable. Another possibility to reduce the oxide capacitance is proton implantation passivation outside the active region.⁴

Fig. 10 shows the small signal modulation response of an 850 nm single-mode VCSEL with about 3 μm active diameter in a 20 μm mesa. At a bias current of 2.8 times threshold the modulation bandwidth $f_{3\text{dB}}$ reaches 12 GHz. Drawn as smooth solid lines are theoretical curves for the modulation response $M(\nu)$ of a parasitic free laser diode given by

$$M(\nu) = \frac{A}{4\pi^2(\nu_r^2 - \nu^2) + 2\pi i\gamma\nu}, \quad (1)$$

where the amplitude factor A is used as a fitting parameter, while the resonance frequency ν_r and the damping constant γ are extracted from the measured RIN spectra in Fig. 13. The good agreement between the intrinsic laser and the measured curves indicates the negligible influence of parasitic elements on the modulation response for the laser studied. In Fig. 11 we plot the damping constant as a function of the resonance frequency squared. From the slope, the so-called K-factor is obtained as $K=0.68\text{ ns}$ which results in a maximum modulation bandwidth of

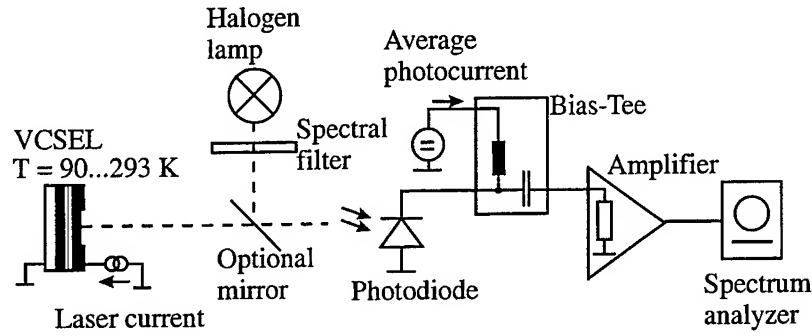


Fig. 12. Measurement setup for shot noise calibrated measurements of intensity noise and relative intensity noise of VCSELs.

$f_{3dB} = 13 \text{ GHz}$ according to³³

$$f_{3dB} = \sqrt{2} \frac{2\pi}{K}. \quad (2)$$

The good agreement between predicted and measured modulation bandwidth is a further indication for negligible parasitic elements. The comparatively large K-factor can be explained by the high threshold current of the laser, which is related to a comparatively high carrier density above threshold. The sub-linear dependence of gain on carrier density therefore leads to reduced differential gain and thus increased K-factor.³⁴ One method to reduce the K-factor is to increase mirror reflectivities and thereby lower the threshold carrier density.

5. NOISE CHARACTERISTICS

In optical transmission systems there are three major noise sources. The noise from the transmitter, the noise which is added in the transmission channel and the noise generated at the receiver. Here we focus on the noise generated by the transmitter, either by inherent sources or induced by optical reflections. The noise generated in the transmission channel is determined by the transmitter, but mainly depends on the properties of the optical fiber and is therefore of minor interest in the present context.³⁵⁻³⁸

5.1. Setup

Fig. 12 shows the measurement setup for shot noise calibrated measurement of intensity noise and relative intensity noise. The VCSEL is driven by a current source in order to suppress pump current fluctuations.¹⁴ For measuring intensity noise, a large area silicon pin photodiode is used as a light to current converter. The responsivity of the diode is approximately 0.55 A/W at the VCSEL emission wavelength of about 850 nm, corresponding to a quantum efficiency of 80 %. The photodiode is biased using a bias-tee. The average photocurrent, which is proportional to the average light intensity, can be measured at the dc input of the bias-tee. The ac current is fed to a low noise rf amplifier with a 50 Ω input resistance. The ac output signal of the amplifier is transmitted to an electrical spectrum analyzer to record the power spectral density of the photocurrent. From the relation between average photocurrent I_{avg} measured at the bias-tee and the power spectral density of the photocurrent at the amplifier input N_{elec} , the relative intensity noise (RIN) is obtained as

$$RIN = \frac{N_{elec}}{I_{avg}^2 50 \Omega}. \quad (3)$$

For shot noise calibration the photodiode is illuminated with a red-filtered halogen lamp, with the optical power adjusted to get the same average photocurrent as with the VCSEL. The shot noise limited RIN is given by

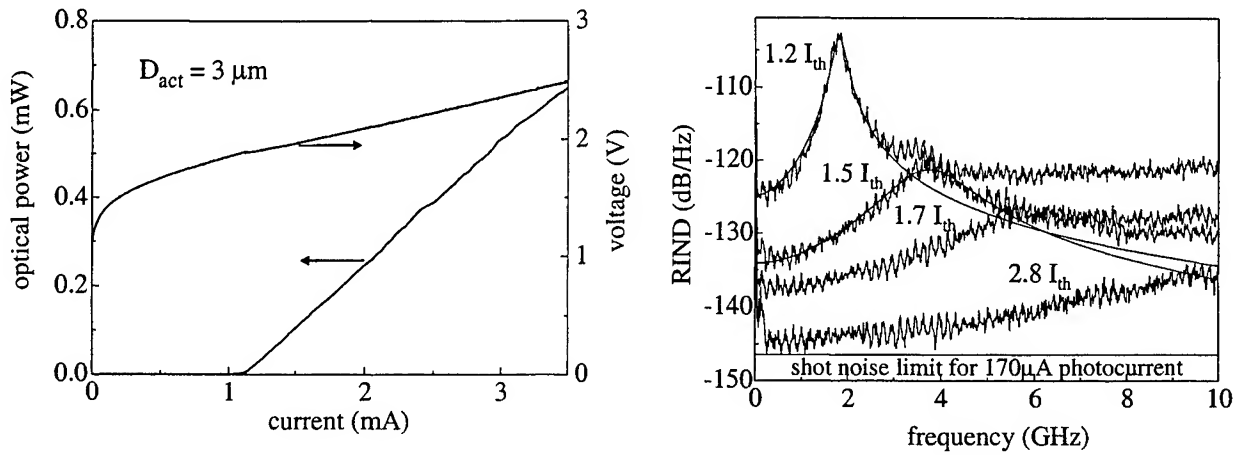


Fig. 13. Output characteristics and RIN spectra for different bias conditions of an 850 nm single-mode single-polarization VCSEL.

$$RIN_Q = \frac{2q}{I_{ph}} \quad (4)$$

Care is taken to exclude saturation effects in the photodiode due to different spatial power density distributions of the incident light on the detector surface. In our measurements variations of the spot diameter on the photodiode at high power levels gave no changes in the recorded photocurrent power spectral density.

5.2. RIN under cw-operation

Fig. 13 shows the cw characteristics and RIN spectra for different bias currents above threshold current I_{th} for an 850 nm single-mode VCSEL of $3 \mu\text{m}$ active diameter. Threshold current and voltage are close to 1 mA and 2 V, respectively. The VCSEL oscillates in the linearly polarized fundamental mode over the whole current range. The RIN spectra can be fitted using the theoretical form given in.³⁹ RIN decreases with increasing bias current reaching a minimum level of -145 dB/Hz at 3 mA, corresponding to an output power of 0.5 mW. From the measured photocurrent of $170 \mu\text{A}$ we can calculate a shot noise level of -147 dB/Hz , which is slightly below the measured data for the laser under study. At this bias point, we are not too far above the measurement system noise, which is determined by the thermal noise of the 50Ω load resistor. We should keep in mind that sub-poissonian noise in VCSELs has been observed.^{17,40}

Fig. 14 compares the average RIN in the frequency band from 100 MHz to 10 GHz for different types of VCSELs. The squares denote the average RIN of the single-mode linearly polarized VCSEL of Fig. 13. The average RIN of a single-mode VCSEL oscillating on two states of polarization for a certain current range is represented by triangles. For output powers up to $150 \mu\text{W}$ we get an increased average RIN, which is reduced to values 5 dB above those for the single-polarization single-mode VCSEL, when a stable emission on one polarization is reached for higher currents.^{41,42} The multimode VCSEL, denoted by circles in Fig. 14, has a strongly increased average RIN of about 120 dB/Hz at higher currents.⁴³ No special polarization control has been applied to the devices. It is worthwhile to mention that the average RIN needs to be kept below -112 dB/Hz to allow for a BER of 10^{-9} in 10 Gbit/s data transmission.⁴⁴

5.3. Feedback induced noise

We have studied the noise under distant optical feedback as well. The investigated VCSEL emits in the fundamental mode with one stable linear polarization and generates an output power of 2 mW at 3 mA of bias current. The VCSEL emission is coupled into a $5 \mu\text{m}$ diameter single-mode or a $50 \mu\text{m}$ diameter graded-index multimode optical

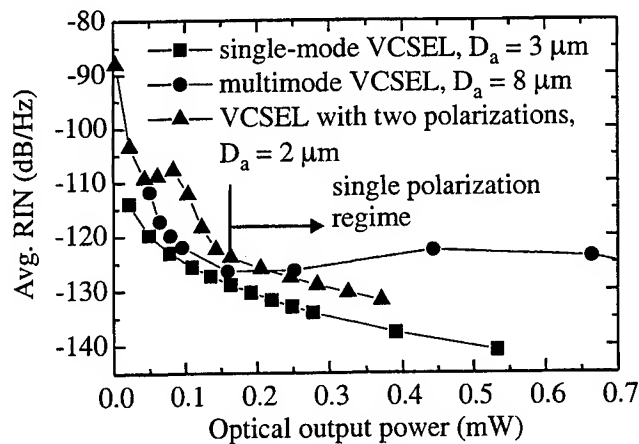


Fig. 14. Comparison of average RIN from 0.1–10 GHz for different 850 nm VCSELs as a function of output power.

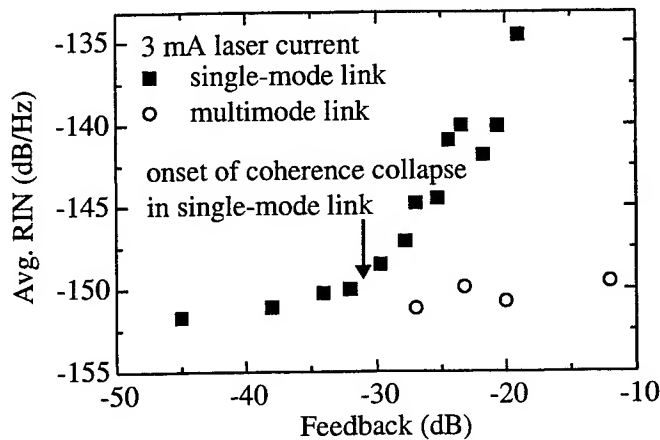


Fig. 15. Average RIN from 0.001 to 2 GHz of a single-mode single-polarization 850 nm VCSEL for different distant feedback levels in single-mode and multimode fiber link.

fiber. Coupling efficiency was measured to be 50% in both cases. Feedback from a distance of 30 m is introduced using an optical coupler and a gold mirror on one fiber endface beyond the coupler. The other coupler output is connected to a high sensitivity Ge avalanche photodiode. The feedback level is defined in the single-mode fiber link by the fraction of power reentering the laser, which is known due to reciprocity. In the multimode fiber link the feedback level is defined by the ratio of power emitted from the laser and the power reflected back towards the VCSEL. Fig. 15 shows the average RIN in a 2 GHz wide band at a bias current of 3 mA, which corresponds to about 6 times threshold current. For low feedback levels the average RIN is below -150 dB/Hz, which is again at the shot noise limit. In the multimode link we do not observe any increase of RIN with increasing feedback level, which is due to the low reverse coupling efficiency between the multimode fiber and the single-mode VCSEL. In the single-mode link an increase of RIN can be observed at feedback levels above -30 dB, reaching a level of -135 dB/Hz at a feedback level of -19 dB. This feedback regime is referred to as the coherence-collapse regime.⁴⁵ The onset of coherence-collapse is mainly determined by the mirror reflectivities, the cavity length, and the damping rate of the laser.^{45,46}

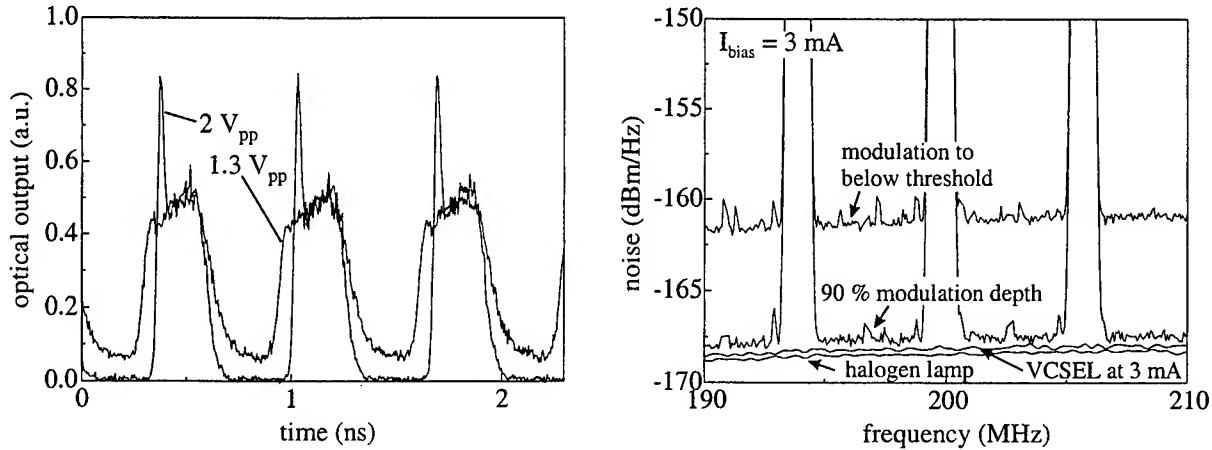


Fig. 16. Characteristics of an 850 nm single-mode single-polarization VCSEL. The left hand part shows optical output signals in the time domain for 1.3 V_{pp} and 2 V_{pp} modulation at 3 Gbit/s and 3 mA bias. The right hand part shows the corresponding RIN for cw excitation at 3 mA and PRBS modulation to below threshold (2 V_{pp}) and 90 % on-off ratio (1.3 V_{pp}). The shot noise of a halogen lamp is also shown for comparison.

5.4. RIN under large signal modulation

Since VCSELs are to be used as transmitters in optical transmission systems, we are interested in the intensity noise under large signal modulation. Modulated optical signals in the time domain are displayed in the left hand part of Fig. 16. The right hand part of Fig. 16 shows the intensity noise of a single-mode single-polarization VCSEL in a typical frequency band between 190 and 210 MHz for different modulation conditions. For comparison we measured the noise under cw operation at 6 times threshold current for 2 mW average output power using a pin photodiode. We obtain an intensity noise of -168 dBm/Hz in the 50 Ω load. Comparison with the shot noise generated by a halogen lamp at the same photocurrent shows almost the same intensity noise. When we modulate the laser with a NRZ coded PRBS we can detect the intensity noise between the strong spectral lines resulting from the PRBS modulation signal. Using a modulation amplitude of 1.3 V_{pp} corresponding to an on-off-ratio of about 10 dB, we find a minor increase in noise of about 1 dB. Using an amplitude of 2 V_{pp} we modulate the laser to below threshold and get an increase in noise of about 6 dB. However, intensity noise is still sufficiently low for error-free digital data transmission. The increase in noise for below-threshold modulation can be explained by photon and electron statistics. It can lead to bit error rate floors in transmission systems.⁴⁷ In multimode VCSELs a much stronger increase of noise is expected due to spatial hole burning and carrier diffusion.⁴⁸

5.5. Photon Number Squeezed States

We have measured the shot noise limited RIN of the halogen lamp using the measurement setup displayed in Fig. 12. To eliminate measurement errors in the spectrum analyzer or due to gain variations in the amplifier, the RIN of the VCSEL is normalized to the shot noise limit given by RIN_Q as shown in Fig. 17. At threshold, corresponding to approximately 5 μA photocurrent, relative intensity noise shows a maximum. For higher currents noise drops to the shot noise level. When the photocurrent exceeds 1.7 mA, a higher order mode starts to oscillate and intensity noise increases. Thermal rollover prevents from measuring in an operation range, where the two transverse modes are stable. It is clearly seen that for a certain current range before higher order modes start lasing, the intensity noise is close to or even below the shot noise level. In order to obtain stronger squeezing, higher output powers for fundamental mode emission are desirable.

To prevent early rollover of the light-current characteristics and to increase the single-mode operation range, we have studied VCSEL emission at reduced temperature of 90 K. The device is fabricated from the same wafer as the previous one, but due to inhomogeneous epitaxial growth, the resonance frequency of the cavity is detuned to the short wavelength side of the gain curve. Therefore, low substrate temperatures give reasonably good matching of the resonance frequency and the gain curve, depending on the bias point. In Fig. 18. the measured photocurrent

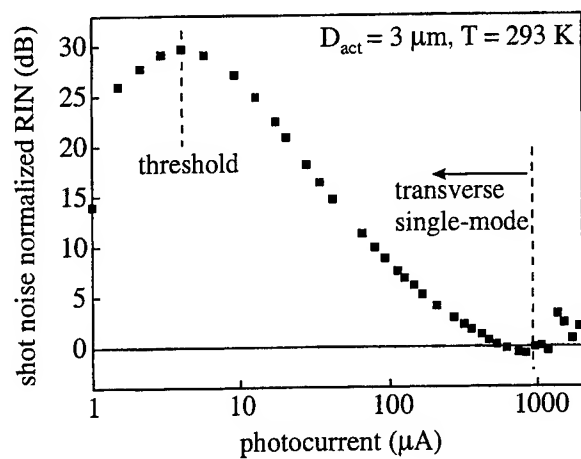


Fig. 17. Shot noise normalized RIN at 50 MHz as a function of photocurrent.

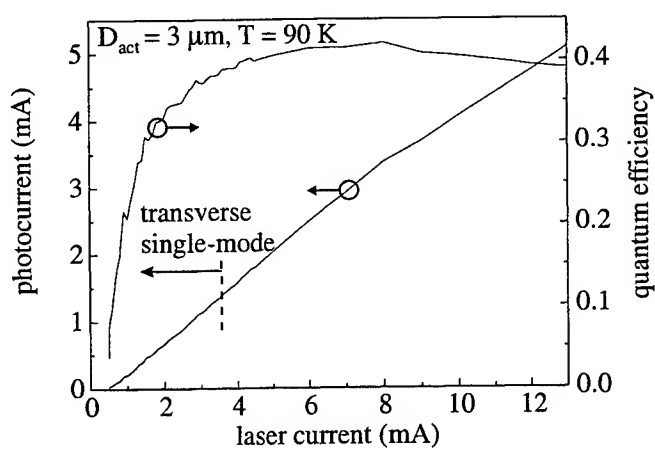


Fig. 18. Detector photocurrent and system quantum efficiency as a function of VCSEL driving current for operation of $T = 90 \text{ K}$.

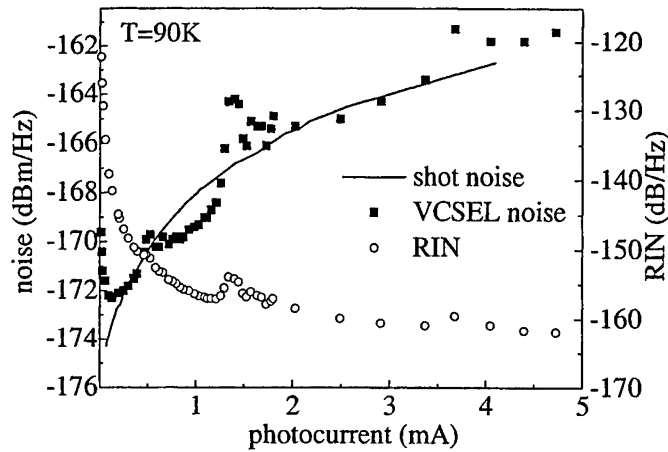


Fig. 19. Measured amplitude noise and RIN of VCSEL. For comparison the measured shot noise from a halogen lamp is included as solid line.

generated by the VCSEL emission is plotted as a function of laser current. From these data the quantum efficiency of the system is calculated and also included in Fig. 18. Threshold current is slightly above 0.5 mA, which is due to the residual mismatch between resonance and gain at this bias point. With increasing current internal heating shifts the gain curve to longer wavelengths. Laser current is increased up to 13 mA corresponding to a current density of approximately 180 kA/cm^2 . No rollover occurs. Measurement of the emission spectrum shows operation in the fundamental mode up to currents of 3.5 mA with a side mode suppression of better than 30 dB. For higher currents higher order modes begin to lase. The overall maximum quantum efficiency of the system is as high as 40%. In Fig. 19, the intensity noise of the VCSEL measured in an 1 MHz band around 55 MHz is displayed as a function of photocurrent. For comparison, the measured shot noise from the halogen lamp is also shown. From the intensity noise and the average current induced in the photodiode the relative intensity noise of the VCSEL is calculated and drawn as open circles. Above threshold, with increasing photocurrent the VCSEL intensity noise steeply drops reaching the shot noise level at a photocurrent of $250 \mu\text{A}$. At a photocurrent of approximately 0.5 mA minor polarization instability causes a slight increase of intensity noise above the shot noise level. At 1.14 mA photocurrent, intensity noise is 1.4 dB below the shot noise level. With further increased laser current, at 1.3 mA photocurrent, a higher order mode starts lasing which results in rising intensity noise. For still higher laser currents a stable operation range is reached, where intensity noise again approaches the shot noise level. Fig. 20 shows the intensity noise of the VCSEL in the frequency domain from 10 to 180 MHz for a photocurrent of 1.14 mA. The shot noise level, which was determined measuring the intensity noise of the halogen lamp, is also shown. For the whole frequency range VCSEL amplitude noise is about 1.4 dB below the shot noise level. Theoretically, from the overall quantum efficiency of the measuring system of 37% at the corresponding bias point, a maximum amplitude squeezing of 2 dB can be expected assuming Poissonian loss mechanisms.⁴⁹ The measured figure is in excellent agreement with the theoretical prediction.

6. CONCLUSION

We have designed, fabricated, and characterized selectively oxidized single-mode VCSELs and arrays to be used as transmitters in high-speed optical interconnects. Emission wavelengths are 850 and 980 nm. An optical modulation bandwidth of 13 GHz in combination with shot noise limited output under large signal modulation is demonstrated. Data transmission at 12.5 Gbit/s is realized over various kinds of fibers including $5 \mu\text{m}$ single-mode, $9 \mu\text{m}$ standard, and $50 \mu\text{m}$ graded-index multimode fiber. For parallel transmission 2D VCSEL arrays are flip-chip mounted on Si CMOS driver chips. The results obtained are encouraging for future implementations of 10 Gbit/s optical interconnect systems. Furthermore, we have thoroughly investigated low frequency intensity noise of high performance transverse single- and multi-mode VCSELs in the 850 nm wavelength regime, where high quantum efficiency silicon photodiodes are readily available. In a single-mode VCSEL emitter silicon photodiode detector transmitting system with an overall

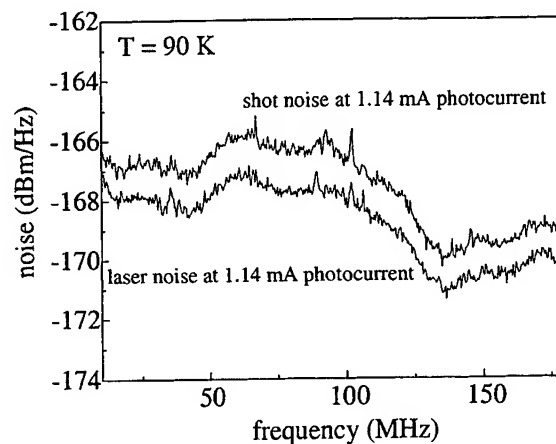


Fig. 20. VCSEL intensity noise from 10 to 180 MHz at a laser bias current of 2.9 mA. For comparison, the shot noise limited intensity noise from a halogen lamp is also shown.

quantum efficiency of 37% an intensity noise of 1.4 dB below the shot noise limit has been observed. This figure is the largest amount of squeezing ever reported for VCSELs. Polarization instability, mode competition noise and thermal rollover determine the noise characteristics. From an increased single-mode operation range and polarization stabilized emission, we expect to achieve still stronger amplitude squeezing.

7. ACKNOWLEDGMENTS

This work was supported by the European Commission within the ESPRIT MEL-ARI OPTO cluster under contract No. 22641 (OHC) as well as the German Science Foundation (DFG).

REFERENCES

1. D. Deppe, D. Huffaker, T. Oh, H. Deng, and Q. Deng, "Low-threshold vertical-cavity surface-emitting lasers based on oxide-confined and high contrast distributed bragg reflectors," *J. Sel. Topics Quantum Electron.* **3**, pp. 893–904, 1997.
2. Y. Hayashi, T. Mukaihara, N. Hatori, N. Ohnoki, A. Matsutani, F. Koyama, and K. Iga, "Lasing characteristics of low-threshold oxide confined InGaAs-GaAlAs vertical-cavity surface-emitting lasers," *IEEE Photon. Technol. Lett.* **7**, pp. 1324–1326, 1995.
3. R. Jäger, M. Grabherr, C. Jung, R. Michalzik, G. Reiner, B. Weigl, and K. Ebeling, "57% wallplug efficiency oxide-confined 850 nm wavelength VCSELs," *Electron. Lett.* **33**, pp. 330–331, 1997.
4. K. Lear, V. Hietala, H. Hou, M. Ochiai, J. Banas, B. Hammons, J. Zolper, and S. Kilcoyne, "Small and large signal modulation of 850 nm oxide-confined vertical cavity surface emitting lasers," *OSA Trends in Optics and Photonics* **15**, pp. 69–74, 1997.
5. U. Fiedler, G. Reiner, P. Schnitzer, and K.J. Ebeling, "Top-surface emitting laser diodes for 10 Gb/s data transmission," *IEEE Photon. Technol. Lett.* **8**, pp. 746–748, 1996.
6. N. Hatori, A. Mizutani, N. Nishiyama, A. Matsutani, T. Sakaguchi, F. Motomura, F. Koyama, and K. Iga, "An over 10-Gb/s transmission experiment using a p-type delta-doped InGaAs-GaAs quantum-well vertical-cavity surface emitting laser," *IEEE Photon. Technol. Lett.* **10**, pp. 194–196, 1998.
7. G. Giaretta, F. Mederer, R. Michalzik, W. White, R. Jaeger, G. Shevchuk, T. Onishi, M. Naritomi, R. Yoshida, P. Schnitzer, H. Unold, M. Kicherer, K. Al-Hemyari, J. Valdmánis, M. Nuss, X. Quan, and K.J. Ebeling, "Demonstration of 500 nm-wide transmission window at multi-Gb/s data rates in low-loss plastic optical fiber," *Proceedings of ECOC 99*, Nice, France, in press, 1999.
8. M. Nuss, "Lucent demonstrates 10 Gbit.s⁻¹ serial transmission," *III-V Review* **12**, p. 14, 1999.

9. H. Kosaka, M. Kajita, M. Yamada, Y. Sugimoto, K. Kurata, T. Tanabe, and Y. Kasukawa, "Plastic-based receptacle-type VCSEL-array modules with one and two dimensions fabricated using the self-alignment mounting technique," *47th Electron. Comp. & Technol. Conf. ECTC*, pp. 382-390, 1997.
10. L. Norton, F. Carney, N. Choi, C.K.Y. Chun, R.K. Denton Jr., D. Diaz, J. Knapp, M. Meyering, C. Ngo, S. Planer, G. Raskin, E. Reyes, J. Sauvageau, D.B. Schwartz, S. Shook, J. Yoder, and Y. Wen, "OptobusTH i:a production parallel fiber optical interconnect," *47th Electron. Comp. & Technol. Conf. ECTC*, pp. 204-209, 1997.
11. C. Jung, R. King, R. Jäger, M. Grabherr, F. Eberhard, R. Rösch, U. Martin, D. Wiedenmann, H. Unold, R. Michalzik, and K.J. Ebeling, "64 channel flip-chip mounted selectively oxidized GaAs VCSEL array for parallel optical interconnects," *Vertical-Cavity Surface-Emitting Lasers III*, 25-26 January 1999, San Jose, California, SPIE 3627, pp. 143-151, 1999.
12. http://www.gigabit-ethernet.org/technology/whitepapers/gige_97/technology.html
13. K.J. Ebeling, "Integrated Optoelectronics," *Springer Verlag*, Berlin 1993.
14. Y. Yamamoto, S. Machida, and O. Nilsson, "Amplitude squeezing in a pump-noise-suppressed laser oscillator," *Physical Rev. A* **34**, pp. 4025-4042, 1986.
15. S. Machida, Y. Yamamoto, and Y. Itaya, "Observation of amplitude squeezing in a constant-current-driven semiconductor laser," *Physical Review Letters* **58**, pp. 1000-1003, 1987.
16. J.-L. Vey, K. Auen, and W. Elsässer, "Semiclassical analysis and experimental investigations of vertical cavity surface emitting laser noise," *SPIE* **2994**, pp. 178-189, 1997.
17. D. Kilper, P. Roos, J. Carlsten, and K. Lear, "Squeezed light generated by a microcavity laser," *Physical Rev. A* **55**, pp. 3323-3326, 1997.
18. R. Slusher, and B. Yurke, "Squeezed Light for Coherent Communications," *J. Lightwave Technol.* **8**, pp. 466-477, 1990.
19. J. Ryan and M. Fox, "Semiconductors put the squeeze on light," *Physics World* **9**, pp. 40-45, 1996.
20. R. Jäger, J. Heerlein, E. Deichsel, and P. Unger, "63% wallplug efficiency MBE grown InGaAs/AlGaAs broad-area laser diodes and arrays with carbon p-type doping using CBr₄," *J. Crystal Growth* **201/202**, pp. 882-885, 1999.
21. B. Weigel, M. Grabherr, C. Jung, R. Jäger, G. Reiner and R. Michalzik, D. Sowada, and K.J. Ebeling, "High-performance oxide-confined GaAs VCSEL's," *IEEE J. Sel. Top. Quantum Electron.* **3**, pp. 409-415, 1997.
22. G. Reiner, E. Zeeb, B. Möller, M. Ries, and K.J. Ebeling, "Optimization of planar Be-doped InGaAs VCSELs with two-sided output," *IEEE Photon. Technol. Lett.* **7**, pp. 730-732, 1995.
23. K.L. Lear and R.P. Schneider, Jr., "Uniparabolic mirror grading for vertical cavity surface emitting lasers," *Appl. Phys. Lett.* **68**, pp. 605-607, 1996.
24. D.L. Huffaker, D.G. Deppe, K. Kumar, and T.J. Rogers, "Native-oxide defined ring contact for low threshold vertical-cavity lasers," *Appl. Phys. Lett.*, **65**, pp. 97-99, 1994.
25. Y. Kaneko, D. Mars, S. Nakagawa, Y. Ichimura, and N. Yamada, "Vertical-cavity surface-emitting lasers with stable polarization grown on (411)A-oriented GaAs substrates," *Jpn. J. Appl. Phys.* **38**, pp. L864-L866, 1999.
26. T. Mukaiharu, N. Ohnoki, Y. Hayashi, N. Hatori, F. Koyama, and K. Iga, "Polarization control of vertical-cavity surface-emitting lasers using a birefringent metal/dielectric polarizer loaded on top distributed Bragg reflector," *IEEE J. Sel. Top. Quantum Electron.*, **1**, pp. 667-673, 1995.
27. A.V. Krishnamoorthy, and D.A.B. Miller, "Scaling optoelectronic-VLSI circuits into the 21st century: a technology roadmap," *IEEE J. Sel. Top. Quantum Electron.*, **2**, pp. 55-76, 1996.
28. <http://www.intec.rug.ac.be/oic>
29. K.D. Choquette, K.M. Geib, B. Roberds, H.Q. Hou, R.D. Twisten, and B.E. Hammons, "Short wavelength bottom-emitting vertical cavity lasers fabricated using wafer bonding," *IEEE Electron. Lett.*, **34**, pp. 1404-1405, 1998.
30. S. Matsuo, T. Nakahara, K. Tateno, H. Tsuda, and T. Kurokawa, "Hybrid integration of smart pixel with vertical-cavity surface-emitting laser using polyimide bonding," *OSA Trends in Optics and Photonics*, **14**, pp. 39-46, 1997.
31. This work is part of the European OIIC project. Partners involved are ETH Zürich, IMEC Leuven, GMMT Caswell and University of Ulm.

32. P. Schnitzer, R. Jäger, C. Jung, R. Michalzik, D. Wiedenmann, F. Mederer, and K.J. Ebeling, "Biased and bias-free multi-Gb/s data links using GaAs VCSEL's and 1300 nm single-mode fiber," *IEEE Photon. Technol. Lett.*, **10**, pp. 1781-1783, 1998.
33. R. Olshansky, P. Hill, V. Lanzisera, and W. Powazinik, "Frequency response of 1.3 μm InGaAsP high speed semiconductor lasers," *IEEE J. Quantum Electron.*, **23**, pp. 1410-1418, 1987.
34. R. Nagarajan, T. Fukushima, M. Ishikawa, J.E. Bowers, R.S. Geels, and L.A. Coldren, "Transport limits in high-speed quantum-well lasers: experiment and theory," *IEEE Photon. Technol. Lett.*, **8**, pp. 1288-1290, 1996.
35. K. Petermann, "Nonlinear distortions and noise in optical communication systems due to fiber connectors," *IEEE J. Quantum Electron.*, **16**, pp. 761-770, 1980.
36. T. Kanada, "Evaluation of modal noise in multimode fiber-optic systems," *J. Lightwave Technol.*, **2**, pp. 11-18, 1984.
37. A.M.J. Koonen, "Bit-error-rate degradation in a multimode fiber optic transmission link due to modal noise," *IEEE J. Sel. Areas Comm.*, **4**, pp. 1515-1522, 1986.
38. R. Dändliker, A. Bertholds, and F. Maystre, "How modal noise in multimode fibers depends on source spectrum and fiber dispersion," *J. Lightwave Technol.*, **3**, pp. 7-12, 1985.
39. M.C. Tatham, I.F. Lealman, C.P. Seltzer, L.D. Westbrook, and D.M. Cooper, "Resonance frequency, damping, and differential gain in 1.5 μm multiple quantum-well lasers," *IEEE J. Quantum Electron.*, **28**, pp. 408-414, 1992.
40. D. Wiedenmann, P. Schnitzer, C. Jung, M. Grabherr, R. Jäger, R. Michalzik, and K.J. Ebeling, "Noise characteristics of 850 nm single-mode vertical cavity surface emitting lasers," *Appl. Phys. Lett.*, **73**, pp. 717-719, 1998.
41. D.V. Kuksenkov, H. Temkin, and S. Swirhun, "Polarization instability and relative intensity noise in vertical-cavity surface-emitting lasers," *Appl. Phys. Lett.*, **67**, pp. 2141-2143, 1995.
42. M.S. Wu, L.A. Buckman, G.S. Li, K.Y. Lau, and C.J. Chang-Hasnain, "Polarization induced enhancement of relative intensity noise and modulation distortion in vertical cavity surface emitting lasers," in *Proc. 14th Int. Semicond. Laser Conf.*, pp. 145-146, Maui, Hawaii, USA, Sept. 1994.
43. J.Y. Law and G.P. Agrawal, "Mode-partition noise in vertical-cavity surface-emitting lasers," *IEEE Photon. Technol. Lett.*, **9**, pp. 437-439, 1997.
44. K. Petermann, *Laser Diode Modulation and Noise*. Dordrecht: Kluwer Academic Publishers, 1991.
45. K. Petermann, "External optical feedback phenomena in semiconductor lasers," *IEEE J. Sel. Top. Quantum Electron.*, **1**, pp. 480-489, 1995.
46. J. Helms and K. Petermann, "A simple analytic expression for the stable operation range of laser diodes with optical feedback," *IEEE J. Quantum Electron.*, **26**, pp. 833-836, 1990.
47. T. Stephens, K. Hinton, T. Anderson, and B. Clarke, "Laser turn-on delay and chirp noise effects in Gbit/s intensity-modulated direct-detection systems," *J. Lightwave Technol.*, **13**, pp. 666-674, 1995.
48. J. Dellude, M.C. Torrent, J.M. Sancho, and K.A. Shore, "Statistics of transverse mode turn-on dynamics in VCSEL's," *IEEE J. Quantum Electron.*, **33**, pp. 1197-1204, 1997.
49. H.-A. Bachor, P. Rottengatter, and C.M. Savage, "Correlation effects in light sources with high quantum efficiency," *Appl. Phys. B*, **55**, pp. 258-264, 1992.

Manufacturing of lasers for DWDM systems

Kevin T. Campbell, Alex Robertson & Steven J. Wetzel

Lucent Technologies, Microelectronics Group 9999 Hamilton Blvd., Breinigsville, PA 18031

ABSTRACT

The evolution of dense wavelength division multiplexing (DWDM) has allowed service providers a convenient and cost effective method to dramatically increase transmission capacity over existing and new fiber network systems. As the demand for bandwidth continues to increase, systems designers are responding by increasing both the number of channels and the data rates. This trend has placed considerable pressure on many of the underlying system components. One component that has been particularly challenged by this trend is the manufacture of semiconductor lasers. This paper reviews the technical and logistical challenges faced in the high volume manufacture of lasers to support DWDM systems. As the product portfolio continues to expand, precise execution and teamwork among multiple organizations is required to assure reliable shipping performance. Production scheduling and manufacturing operations must work closely to continuously reprioritize the work in process in response to constantly changing channel demand and yield fluctuations. Wavelength prediction models must be developed that correlate in-process parameters to final device wavelength. These models are then applied to both in-process specification targeting and inventory management. Once the in-process specifications are properly targeted, the challenge moves to the fabrication processes, where processes are pushed to the limits of their control. Underpinning the entire effort must be an information management system in which parametric data is collected, wavelength prediction models are executed, and work in process inventory is controlled with respect to the required final output volume and wavelength distribution.

Keywords: Dense wavelength division multiplexing, distributed feedback lasers.

1. INTRODUCTION

Dense wavelength division multiplexing (DWDM) technology provides the capability to transmit multiple signals of different wavelength on a single fiber. Over the last five years, DWDM has been the single most important technology in the advancement of fiber optic networks. With the rapid growth of the Internet and demand for high speed data transmission, the existing backbone network capacity was quickly being exhausted. DWDM allowed for a very convenient, cost effective and flexible solution to rapidly increase the capacity of the existing networks.

The initial DWDM systems were introduced in the 1995 – 1996 timeframe. These systems were based on discrete distributed feedback (DFB) lasers transmitting at 2.5 Gbps, and typically contained eight channels.¹ At the time, the ability to increase the embedded fiber bandwidth capacity by a factor of eight was viewed as a tremendous breakthrough. The ability to deliver DFB lasers across eight channels was also viewed as a major challenge. Driven by a continual increase in bandwidth demand, and intense competition among system suppliers, the number of channels has quickly increased from 8 to 16, then 32, 40, 80 and even as high as 160.^{2,3,4} Along with this increase in the number of channels, the wavelength spacing between channels has decreased from 200 GHz to as low as 25 GHz. In addition to the channel explosion, electro-absorption modulated lasers (EMLs) were introduced as an alternative lower dispersion solution to the discrete DFB lasers, and individual channel bandwidths are migrating from 2.5 to 10 Gbps. The system bandwidth capability using the leading edge technology is truly incredible. The recently announced 160 channel system, at 10Gbps/channel, has a total system capacity of 1.6 terabits per optical fiber.

The evolution of the component technology has given the system designers multiple options. They have the option of directly modulating a DFB laser, combining a DFB laser with an external modulator, or using an EML. A full-stream supplier of laser components needs to provide product across all channels, with either a DFB or EML, and at either 2.5 or 10 Gbps. The situation promises to only get more challenging, with the anticipated introduction of narrow band and wide band wavelength selectable laser sources (NBWSL, WBWSL), and the inevitable migration to 40 Gbps per channel (figure 1).⁵

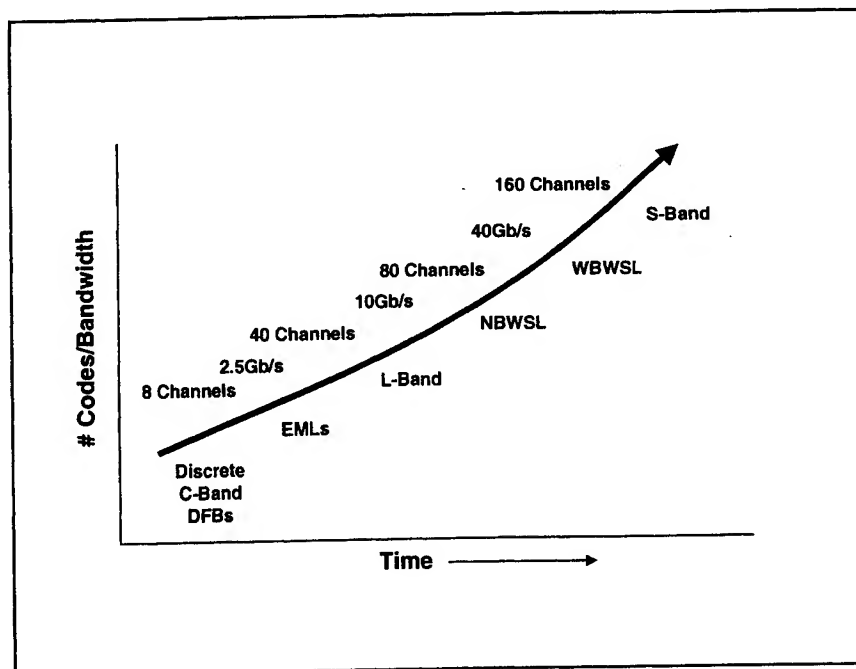


Figure 1.
Expanding Product Portfolio

The increasing number of channels, bandwidth migration and the addition of the EML devices, has resulted in a rapidly growing product portfolio. Until the WSL technology is fully in place, a separate laser device is required for each channel. A supplier that is offering both discrete DFBs and EMLs, 2.5 and 10 Gbps, and 40 different channels of each, is required to manufacture a separate device for each possibility resulting in 160 different product codes. The logistics of managing this portfolio has become as difficult as the device technology itself. Demand profiles across products and channels are continuously changing. With such an immature and difficult technology, yield fluctuations add to the variability.

A key metric for which all component suppliers are measured is shipping performance. Shipping performance is directly correlated to inventory. A supplier with a high level of inventory across all product families can quickly react and maintain shipping performance as yields and demand profiles changes. Unfortunately, maintaining such an inventory across so many individual products quickly becomes prohibitive from a financial standpoint. In addition to the overall cost of the inventory, the short life cycles of these products adds a significant risk that any inventory will become obsolete in place.

To meet the shipping performance metric challenges all aspects of the manufacturing organization. Product management/marketing provides the demand input to the system and is the interface to the customer. The internal interface for product management is production scheduling. Product management needs to maintain a close customer relationship, and to rapidly communicate demand profile changes. The key tool of production scheduling is the material requirements planning (MRP) system. The demand profile, work-in-process (WIP) inventory, and all process planning yields and intervals are contained in the MRP system. Based on the WIP, yields and intervals, production scheduling directs wafer starts and can forecast the device output over time.

Manufacturing operations is primarily responsible for executing the production schedule. One of the key responsibilities for manufacturing operations is interval. Short manufacturing interval is critical to meeting both shipping performance and inventory carrying metrics. With constantly changing demand, variable yields and the constraint of minimal inventory, speed is essential to maintaining shipping performance. There is also both a direct and indirect correlation between inventory and interval. The direct correlation is straight forward, in that as product moves through the manufacturing line quickly,

there is less product in process at any given time. The indirect correlation stems from the fact that, a supplier that does not have a short interval, will not be able to react quickly, and will need to maintain higher levels of inventory to handle the demand fluctuations. In addition to interval, manufacturing operations is responsible for accurately maintaining the inventory levels within the MRP system. With so many product lines, this task is difficult, but essential. For production scheduling to make the proper decisions, the inventory represented in the MRP system must match what is actually on the manufacturing line..

Last, but far from least, are the responsibilities for process engineering. Independent of wavelength, high volume manufacturing of advanced devices such as DFB lasers and EMLs presents significant process characterization and control challenges. The need to produce these devices at very specific and narrow wavelength targets adds considerably to the level of process control required. In addition to process control, a thorough understanding of the in-process parameters that impact final device wavelength is required. The ability to aim and consistently hit the wavelength target in the final device is critical. Unfortunately for the DWDM laser manufacturer, the final device wavelength is built into the device very early in the manufacturing process. Because of this inherent disadvantage, wavelength prediction models must be applied early in the process sequence to predict the final device wavelength profile for each wafer. The critical parametric data must be collected at each of the determining processes and automatically transferred to a database. The wavelength models are then applied and the data fed back to the MRP system to give a real-time picture of the wavelength distribution of the product moving through the line. Production scheduling can then modify wafer starts and reprioritize wafers in the line as necessary to assure that the product coming out at the end of the line meets the desired wavelength profile. The relationship of production scheduling, manufacturing operations, process engineering and the underlying information systems is shown in figure 2.

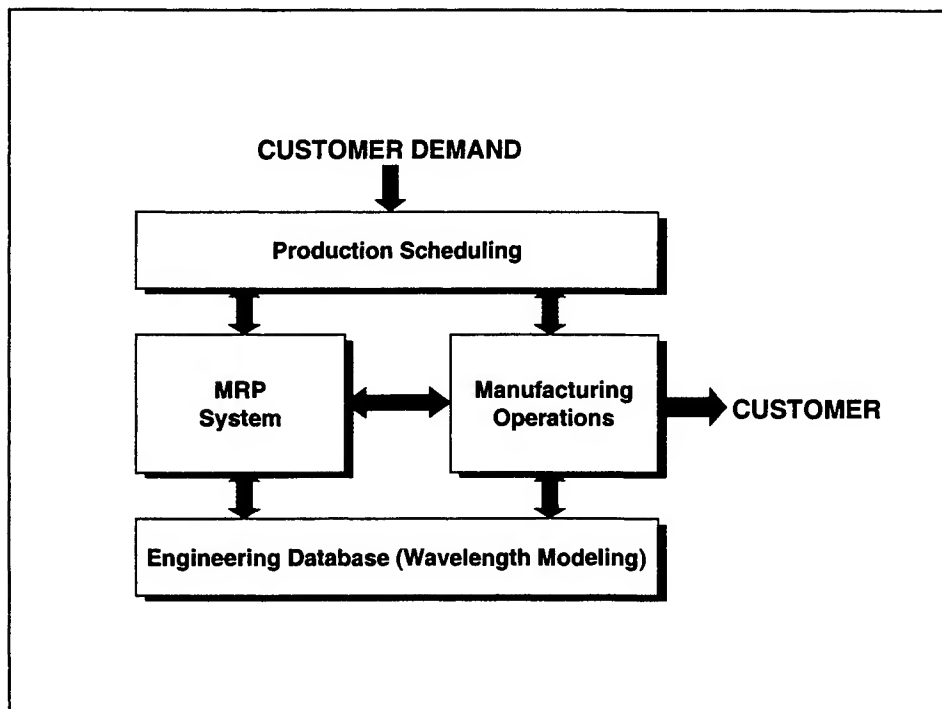


Figure 2.
Organizational Teamwork and Information Management

This paper will expand upon the challenges faced by a full-stream supplier of laser components for DWDM systems. The factors influencing the demand profile itself and why it is constantly changing will be reviewed first. The development of wavelength prediction models will then be presented, followed by a discussion on the implementation of these models as part of an overall manufacturing strategy for reliable high volume shipment of DWDM lasers. Finally, there will be a look to the future and impact of bandwidth migration and the introduction of WSLs.

2. DWDM LASER DEMAND PROFILE

A major supplier of DWDM lasers will have multiple customers, each with the potential for a different DWDM strategy. The systems will differ in the type of laser source, channel bandwidth, number of channels and individual channel spacing. At the current time, there are predominately two types of laser sources, DFBs and EMLs, and two bandwidths, 2.5 & 10 Gbps. The selection of the laser source will depend on the application and/or the strategy of that particular system supplier. The less demanding systems can simply use a DFB laser that will be directly modulated. For the more demanding applications, the primary strategy decision is to use either an EML or a DFB laser combined with an external lithium niobate modulator. At the current time, the choice varies among the system suppliers. The combinations of source type and bandwidth result in the possibility of four different product families at the laser chip level. The goal of the laser chip manufacturer is to reduce this to two product families, with both the DFB and EML chip being capable of meeting both the 2.5 and 10 Gbps specifications. This may or may not be possible depending on the chip performance and customer specifications.

The wavelengths and channel spacings have been defined by the International Telecommunications Union (ITU). There are currently two wavelength bands that have been established. The first of these to be defined is known as the conventional band, or C-band. It includes 45 channels spaced at 100 GHz between the wavelengths of 1528 – 1564 nm. In response to the growing demand for bandwidth, the long wavelength band, or L-band was added. It includes 55 channels spaced at 100GHz between the wavelengths of 1564 – 1610 nm. So, even at the standard 100GHz spacing, there are 100 possible channels. A third band, to be known as the short band, or S-band, is already being planned.

Table I shows a hypothetical C-band channel demand distribution for laser sources for DWDM applications. Depicted are the individual demands from several different customers across the 45 channels spaced at 100GHz. The cumulative demand by channel is shown graphically in figure 3. Immediately apparent is that the cumulative demand varies greatly across channels. Closer examination of the table reveals why. Each customer may have a different application and different demand by channel. Some customers have eight channel systems, others 16 channels, and some may have systems that span 40 channels. However, each customer may or may not be using all of the available channels. Some customers may install a 32 channel system and have low volume demand for each channel. Others may have 8 channel systems, and demand high volumes across every channel. Even when a customer uses every channel in their system, the demand within the channels being used is rarely level due to the number of systems they are deploying. Although the uneven demand across channels adds to the component supplier's challenges, it points to one of the primary advantages of DWDM systems. Large bandwidth capacity systems can be put in place, and then individual channels can be used as demand grows.

The fact that the demand across the various channels is not flat adds a great deal of difficulty that will be discussed later. However, in addition to not being flat, demand variation is not constant. First, each customer may have a fairly natural variation in demand based on changes in their yields and overall market demand. A second source is the common winning and losing of business within a competitive marketplace. A third source of variation is based on the fact that each of the system customers may have at least two suppliers for these critical components. In that case, it would not be unusual to have a customer with an urgent order as the result of a delivery shortcoming by another component supplier. The impacts of each type of variation, across each of the customers, results in a fairly large and unpredictable variation in both volume and channel distribution. As previously mentioned, with such a large number of end-item products, holding sufficient inventory to accommodate such large variation is not financially viable. The laser manufacturer must therefore be able to produce lasers at the desired wavelength at high confidence and within very short intervals.

Channel	Customer								Total
	A	B	C	D	E	F	G	H	
17	100	0	0	0	0	0	0	0	100
18	100	0	0	0	0	0	0	0	100
19	200	0	1,500	0	0	800	0	0	2,500
20	200	0	0	0	0	800	350	0	1,350
21	100	0	1,500	0	0	1,200	200	0	3,000
22	100	0	0	0	0	1,200	200	0	1,500
23	200	0	1,500	650	0	800	350	0	3,500
24	100	0	0	750	0	800	350	0	2,000
25	100	0	1,500	1,000	0	1,200	200	0	4,000
26	200	0	0	750	0	1,200	200	0	2,350
27	200	750	2,500	1,000	0	800	350	0	5,600
28	100	0	0	750	0	800	200	0	1,850
29	100	0	2,500	1,000	0	1,200	200	0	5,000
30	200	0	0	650	1,200	1,200	350	350	3,950
31	100	1,400	2,500	0	0	800	350	0	5,150
32	100	0	0	0	1,500	800	200	500	3,100
33	200	0	2,500	0	0	1,200	200	0	4,100
34	200	0	0	0	1,200	1,200	350	350	3,300
35	100	1,400	2,500	0	0	800	0	0	4,800
36	100	0	0	0	1,500	800	0	500	2,900
37	200	0	2,500	0	0	1,200	0	0	3,900
38	100	0	0	0	1,200	1,200	0	0	2,500
39	100	750	2,500	0	0	800	0	0	4,150
40	200	0	0	0	1,500	800	0	0	2,500
41	200	0	2,500	0	0	1,200	0	0	3,900
42	100	0	0	0	1,200	1,200	0	0	2,500
43	100	0	1,500	0	0	800	0	0	2,400
44	200	0	0	0	1,500	800	0	0	2,500
45	100	0	1,500	0	0	1,200	0	0	2,800
46	100	0	0	0	0	1,200	0	0	1,300
47	200	0	1,500	0	0	800	0	0	2,500
48	200	0	0	0	0	800	0	0	1,000
49	100	0	1,500	0	0	1,200	0	0	2,800
50	100	0	0	0	0	1,200	0	0	1,300
51	200	0	0	0	0	800	0	0	1,000
52	100	0	0	0	0	800	0	0	900
53	100	0	0	0	0	1,200	0	0	1,300
54	200	0	0	0	0	1,200	0	0	1,400
55	200	0	0	0	0	800	0	0	1,000
56	100	0	0	0	0	800	0	0	900
57	100	0	0	0	0	1,200	0	0	1,300
58	200	0	0	0	0	1,200	0	0	1,400
59	200	0	0	0	0	0	0	0	200
60	100	0	0	0	0	0	0	0	100
Total	6,300	4,300	32,000	6,550	10,800	40,000	4,050	1,700	105,700

Table 1. Hypothetical DWDM Laser Demand by Channel for Multiple Customers

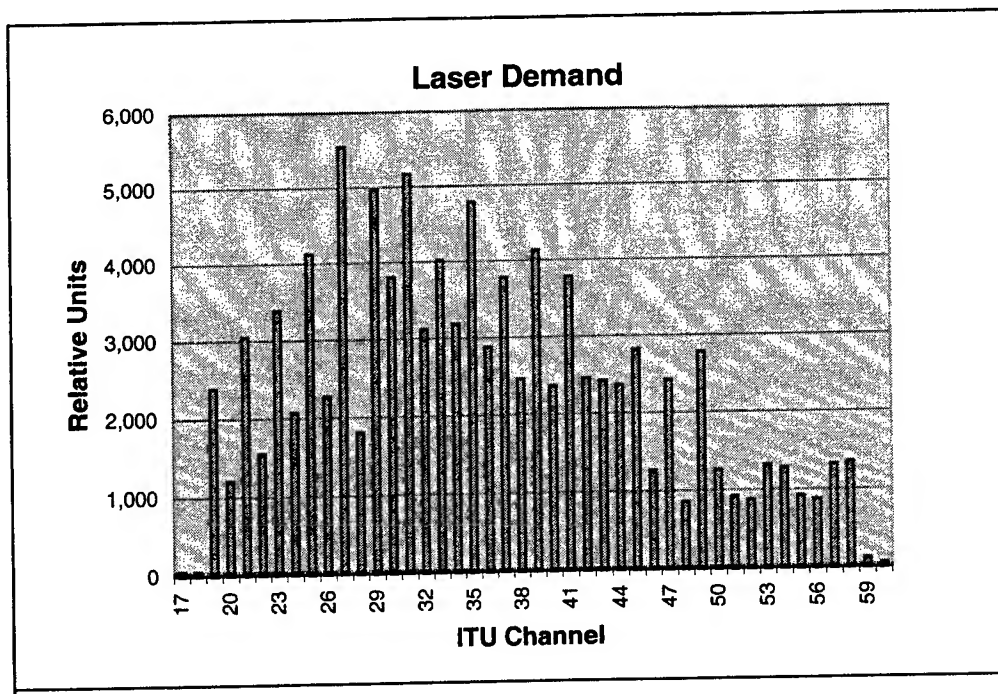


Figure 3.
Hypothetical DWDM Channel Demand Distribution

3. WAVELENGTH PREDICTION MODELS

As previously shown in figure 3, the demand for DWDM lasers typically varies greatly from channel to channel. Laser channels produced for which there is little or no demand have no value. Lasers produced for which there is already a large inventory also have no value. Such lasers are typically held as good inventory in anticipation of a customer order. The ability to very accurately pinpoint laser wavelength is therefore critical. The 100GHz spacing of the ITU grid corresponds to a fairly small wavelength spacing of 0.8 nm. The starting point for the ability to hit particular wavelength targets is a device model that relates the in-process variables to the final device wavelength.

The output wavelength of a DFB laser with a first-order grating is given by:

$$\lambda = 2\Lambda n_{\text{eff}}$$

Where λ is the device wavelength, Λ is the grating period, and n_{eff} is the effective-mode index. The grating period is straightforward and easily measured. The effective-mode index is a complex factor dependent upon the design of the MQW structure and active layer geometry. For a 1.5 μm DFB laser, this factor is typically around 3.4.⁶

This is the point at which laser chip designers start as they design DFB lasers for particular wavelength ranges. However, in practice, to confidently hit very narrow wavelength targets requires statistically developed models based on parameters that can be accurately and routinely measured and controlled within the manufacturing process.

Developing models sufficiently accurate to meet the tight DWDM targets requires well controlled measurements and a large amount of data. The critical parameters must be measured at several points across the wafer. Such characterization is typically referred to as wafer mapping. The output of the model is the distribution by channel on each particular wafer as shown in figure 4. The width of the distribution is dependent on the variation of the critical parameters across the wafer.

Within the manufacturing line, there will be multiple wafers, each with a particular wavelength target. The particular wavelength target will be set by varying the DFB grating period. As shown in figure 4, each wafer will produce not just lasers of the targeted wavelength channel, but a series of wavelength channels. The ability to center the distribution on the desired channel is dependent on the critical processes achieving the targeted in-process specifications. Knowing the total distribution that will be produced by the wafers in the manufacturing line is very valuable and can be obtained using the wavelength model. However, to make such predictions requires accurate data on each of the critical processes for both intra-wafer and inter-wafer process variation. Applying analysis of variance to this data will give the anticipated total variation of wavelength around each particular wavelength target. Summing these distributions for each of the particular wavelength targets in the manufacturing line then gives the total wavelength distribution that will be produced. This distribution can then be compared with the demand distribution such as the one shown in figure 3, and used to modify wafer target distributions to achieve a manufacturing distribution that matches the demand distribution.

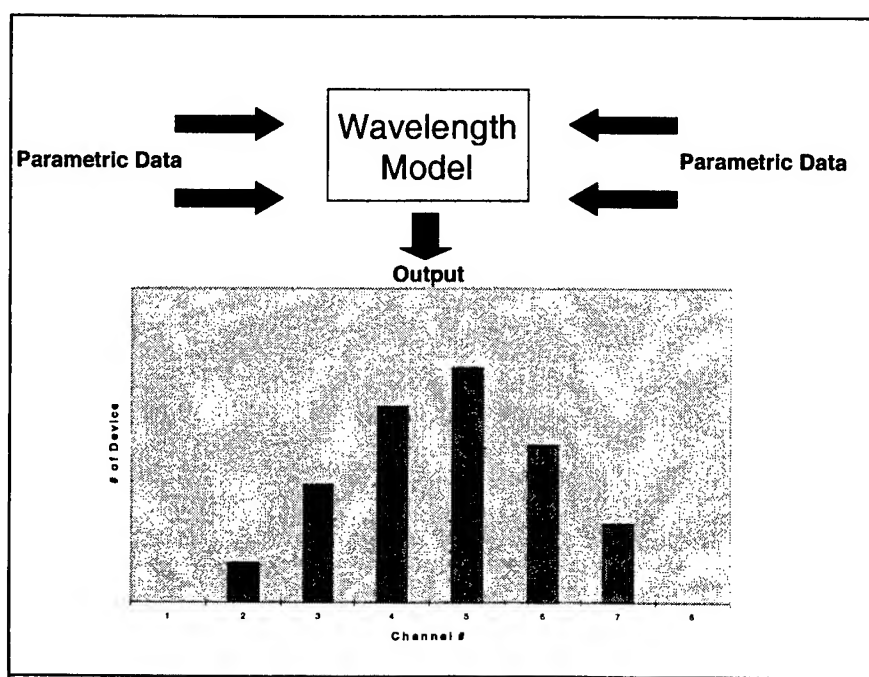


Figure 4.
Predicted Wafer Wavelength Distribution

4. REDEFINING PROCESS CONTROL

The foundation of a stable high volume manufacturing line, that can reliably meet customer demand across the ITU channel grid, is process control. Using the wavelength model, sensitivity analysis gives the impact of each of the individual parameters in determining the final device wavelength. To give an idea of the level of process control required, all other factors being constant, a 1 angstrom change in grating period will result in roughly 0.6 nm change in DFB wavelength. At 0.8 nm channel spacing, this very small change will most likely move the laser from one channel to another. With respect to the MQW structure, changes as small as one atomic layer will have a similar impact. Active width definition is dependent on two processes, lithography and etching control. Variation in the final active width of 0.1 μm will definitely move the wavelength one channel, and possibly two.

Considering the sensitivity of the lasing wavelength, relative to the 0.8 nm channel spacings, an incredible level of process control is required to hit any particular channel. Being off by an angstrom on the grating period and a few atomic layers on

the MQW period, and your three channels from where you were targeting. This level of control puts as much pressure on the measurement and test equipment as it does the process. If you can not measure to this level of accuracy, you will never be able to control the processes to this level. You will also have no chance of ever establishing models that correlate the measured in-process parameters to the device wavelength.

The process control effort must therefore start with metrology equipment. Measurement error studies must be completed and the equipment must be determined to be capable of the precision required. Testing standards must then be created and the equipment placed under strict process control. The starting point for the processes is to characterize them with respect to the relationship of the process input parameters to the desired outputs. The processes must then also be placed under strict control. As previously mentioned, the overall output of the line will be dependent on the cumulative effect of both the inter-wafer and intra-wafer variation, with the goal of most every manufacturing operation being to minimize variation.

5. Developing a Manufacturing Strategy

Given a demand forecast, well-controlled processes, and an empirical wavelength model, the organization needs to develop a manufacturing strategy. The goal of the strategy is to quickly and cost effectively produce the desired channel distribution. Implicit in being cost effective is that inventory levels be kept as minimal as possible, while maintaining acceptable shipping performance.

Figure 5 shows a typical process flow, from substrate to tested chip, for the fabrication of typical buried-heterostructure DFB lasers, with the grating under the active layer. As seen in the figure, the key wavelength determining processes occur very early in the fabrication sequence. The device wavelength is basically "locked-in" at the time the active width is defined. This fact points to having a real-time wavelength model as being almost a necessity. While being weeks away from final wavelength testing, knowing what you have in the wafer fabrication line is a real advantage. If the desired wavelength channel has been missed, new wafers can be started immediately. The impact this has on shipping performance is tremendous. In addition to knowing that you missed the target weeks earlier, you also have the advantage of identifying and then expediting wafers of the desired wavelength in the event of short interval orders, or downstream yield fluctuations. A third advantage is that you can minimize the value of the inventory in the line. The value of the wafer increases as it moves through the fabrication line. If you can identify that you don't need the particular wavelengths that a wafer will produce, you have the option of holding the wafer at lower value until there is a need for it.

As demonstrated in figure 3, each wafer produced will have a wavelength distribution dependent upon the level of variation across the wafer. A fundamental question is what is the optimal number of channels that each wafer should produce. Is it better to have wafers containing fewer channels, and a larger number of devices per channel, or is it better to have a large number of channels, but with a lower number of devices per channel. Several factors play into this decision. Clearly the demand distribution as depicted in figure 3 is a factor. If the distribution is fairly flat without large demand at specific channels, then wafers with large channel distributions are desirable. The decision also is dependent on the level of process control in the line. If trying to hit a specific channel, and process control is poor, then a broad distribution gives you a better chance of hitting the desired target, with at least some number of devices. On the other hand, if variation across the wafers is not well controlled, the channel distribution will inevitably be broad. On a manufacturing line in which process control is very good, the number of channels on a wafer is controllable, and becomes a significant part of the overall strategy.

Regardless of the level of process control and wavelength targeting strategy, shipping performance and inventory level are clear objectives for any manufacturing operation. Shown in figure 6 is an example of how the wavelength model is used in inventory management and production scheduling. The figure shows the inventory at three levels of the overall manufacturing sequence: wafer fabrication, completed wafers and tested chips.

The value of the inventory increases as you progress from fabrication, to completed wafer to tested chip. Certainly you want to hold a certain level of good tested chips, but what you really want is to hold the inventory at the lowest cost level, and still have confidence that you can react quickly to demand changes. This level is the completed wafer level.

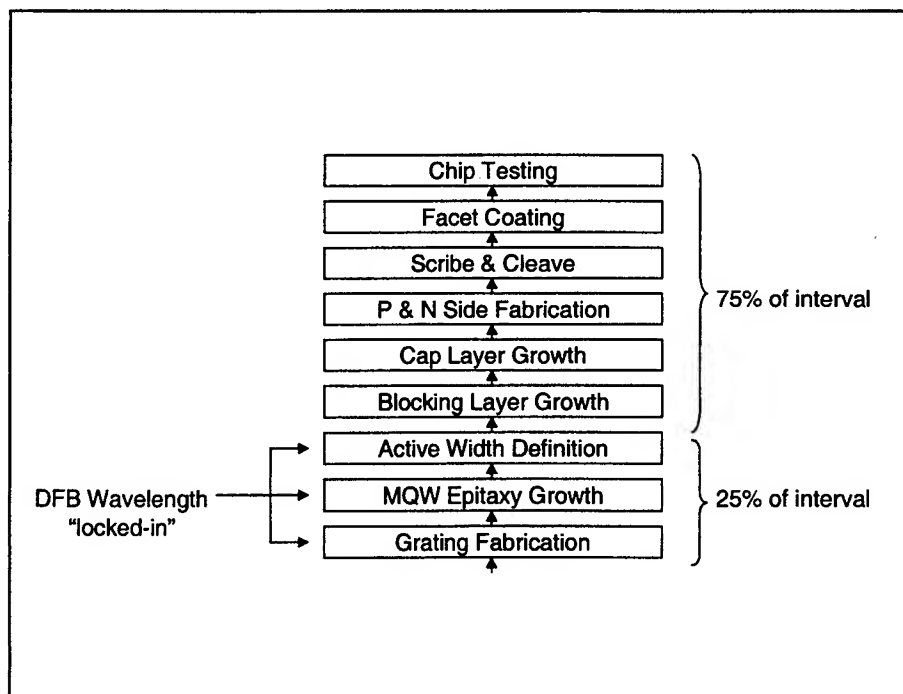


Figure 5. DFB Laser Chip Fabrication Sequence

Projected Laser Inventory

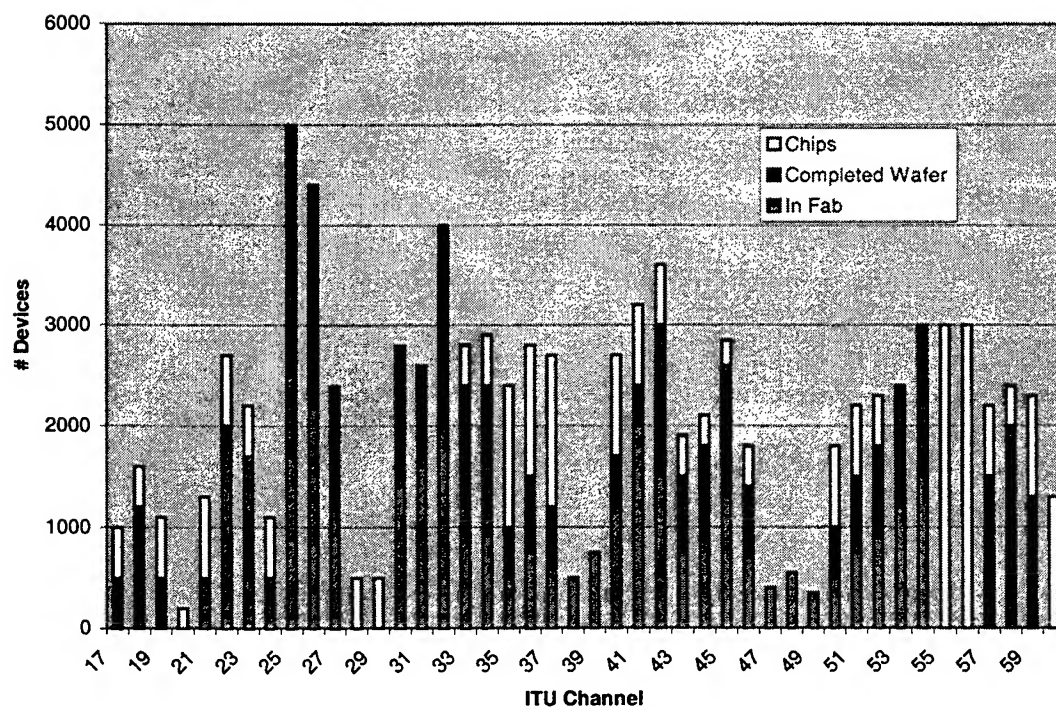


Figure 6. Projected Inventory Distribution by Channel

Although the data for figure 6 is fictitious, it is intended to make several points. There are certainly targets for the amount of inventory of each channel to be held as chips, and for the total inventory projection for each channel. Clear from the graph several problems. The most obvious is that there are a few holes in the inventory. These holes can happen quite easily. Maybe there was just a large demand for those channels that wiped out the chip and completed wafer inventory. Possibly the wafers targeted for those channels missed the target, or possibly they were scrapped due to not meeting all the other chip specifications. Another possibility is that maybe wafers targeted at these channels were never scheduled due to an oversight.

Also obvious from the figure is that some channels have a large amount of projected inventory. This can also happen quite easily. Maybe there was forecasted orders that were recently cancelled. Maybe wafers targeted for other channels fell into those channels, or possibly the yield of the wafers targeted for those channels was far exceeding the plan.

The bottom line is that the chart looks like it does because probably all of the above mentioned possibilities happened, and then happened again. The only constant is change: changing demand, changing yields and changing processes, and ultimately, incorporating this change into the strategy is the key to being successful.

6. SUMMARY

The ability to manufacture DWDM laser chips in high volumes to very specific wavelength channels has been one of the key enablers in the rapid expansion of the bandwidth capacity of today's fiber optic networks. In just five short years, system providers have been able to migrate from 8 x 2.5 Gbps DWDM systems to offering systems at 160 x 10 Gbps.

The challenges faced in the manufacture of these chips are as much logistical as technical. Meeting these challenges requires well controlled processes, accurate device wavelength models, and an overall manufacturing strategy that bridges several organizations.

Predicting the future is always difficult, especially in this technology. One thing that is not difficult to predict is that the technology will continue to evolve rapidly. Wavelength selectable lasers (WSLs) are almost certainly on the horizon, as is the migration to 40 Gbps and beyond. Although the introduction of the WSLs to manufacturing may be seen by some as simplifying the logistics of manufacturing DWDM lasers, it will certainly add to the technological challenges. Furthermore, at least in the near term, they will not totally displace the existing technology, they will simply add to the continuously growing product portfolio.

ACKNOWLEDGEMENTS

The authors would like to acknowledge the assistance of Arlon G. Martin and the strong management support of Vincent D. Mattera.

REFERENCES

1. R. Nering, "Demand triggers advances in dense WDM components", *Optoelectronics World*, Sept. 1998, pp. S5-S8.
2. W. Carter, "Lucent DWDM goes the distance", *Telephony*, March 9, 1998, p. 35.
3. W. Carter, "Lucent intros 400Gb/s DWDM system", Feb. 2, 1998.
4. Candian Corporate News via Dow Vision, June 6, 1999
5. M. Zirngibl, "Multifrequency Laser and Applications in WDM Networks", *IEEE Communications Magazine*, December 1998, pp. 39-41.
6. G. P. Agrawal and N. K. Dutta, *Long -Wavelength Semiconductor Lasers*, Van Nostrand Reinhold Co., New York, 1986.

Integrated thermal-electrical-optical simulator of vertical-cavity surface-emitting lasers

Marek Osinski* and Gennady A. Smolyakov

Center for High Technology Materials, University of New Mexico, 1313 Goddard SE
Albuquerque, New Mexico 87106, USA

ABSTRACT

An integrated thermal-electrical-optical solver of vertical-cavity surface-emitting lasers has been developed on the basis of the effective frequency method combined with the rate equations for photon and carrier densities. The integrated solver is applied to analyze the performance characteristics of GaAs-based proton-implanted top-surface-emitting lasers, oxide-confined surface-emitting lasers and intracavity-contacted oxide-confined surface-emitting lasers. Numerical results confirm the experimentally observed significant advantage of oxide-confined structures over proton-implanted devices, and identify the intracavity-contacted design as the most advantageous for oxide-confined structures.

Keywords: VCSELs, rate equations, effective frequency method, semiconductor laser design, optoelectronic device simulation.

1. INTRODUCTION

Vertical-cavity surface-emitting lasers (VCSELs) are a new class of semiconductor lasers of unique cavity geometry that have numerous advantages over edge-emitting lasers. Low threshold current, single-longitudinal-mode operation, circular output beam and easy wafer-scale integration make them very attractive as compact light sources for applications in optical communication and in various types of optical interconnects from single link to parallel one-dimensional (1D) and two-dimensional (2D) interconnects.

Optimization of VCSEL design to meet the requirements of telecommunication or optical interconnect applications remains a challenge and requires, in particular, development of elaborate models that would be capable of including multiple interdependent processes occurring within the device.

In this paper, we present a model in which coupling of thermal, electrical and optical phenomena is considered for practical design of VCSEL devices. Thermal-electrical analysis of VCSELs is based on the previously reported thermal-electrical model of proton-implanted top-surface-emitting lasers (PITSELs) [Nakwaski 1994]. The realistic distribution of heat sources is combined in the model with a semi-analytical 2D treatment of heat-flux spreading. In the analysis, all important heat-generation mechanisms are taken into account, including nonradiative recombination, reabsorption of spontaneous radiation, free-carrier absorption of laser radiation, and volume Joule heating. Thermal conductivities, electrical resistivities and absorption coefficients are all temperature dependent, allowing for reaching self-consistency in the model. The optical part of the model is based on the effective frequency method [Wenzel 1997], combined with the rate equations for photon and carrier densities (Section 2). The optical model can be used to calculate the lasing wavelength, modal intensity profile, emitted power and electromagnetic energy flux density inside the device. The model as a whole takes into account the phenomena most important in CW operation, and includes the major physical processes in a self-consistent manner.

In Section 3, the model is applied to analyze the performance characteristics of GaAs-based PITSELs, oxide-confined surface-emitting lasers (OCSELs) and intracavity-contacted oxide-confined surface-emitting lasers (IC-OCSELs).

*Correspondence: Email: osinski@chtm.unm.edu; WWW: <http://www.chtm.unm.edu>; Telephone: (505) 272 7812;
Fax: (505) 272 7801

2. MODEL DESCRIPTION

2.1. Carrier and Photon Rate Equations

The effective frequency method (EFM) (for details, see [Wenzel 1997] and [Smolyakov 1999]), as any waveguide-type analysis, provides us only with relative optical field distributions, without any information about the intensity of the optical field. In order to calculate the emitted power and the electromagnetic energy flux inside the VCSEL cavity, we combine the 2D solution of the scalar wave equation with the rate equations for photon and carrier densities. Assuming a constant carrier concentration within the active region of radius r_A and some constant level for resonant absorption in the active layer beyond that radius, we start from the well-known rate equations for carrier and photon densities n and S :

$$\frac{dn}{dt} = \frac{j}{ed} - \frac{n}{\tau_r} - \frac{n}{\tau_{nr}} - a(n - n_t)Sv_g, \quad (1)$$

$$\frac{dS}{dt} = \frac{\beta n}{\tau_r} + a(n - n_t)Sv_g - \frac{S}{\tau_{ph}}, \quad (2)$$

where j is the current density, e is the electron charge, d is the total thickness of all quantum-well layers, τ_r is the radiative lifetime for carriers, τ_{nr} is the nonradiative lifetime for carriers, a is the differential gain coefficient, n_t is the transparency carrier density, v_g is the group velocity, β is the spontaneous emission factor, and τ_{ph} is the photon lifetime that accounts for the decrease of the photon density due to output losses and other losses, not directly connected with radiating transitions.

Most importantly, the photon density S is not assumed uniform in the model, but is defined as

$$S = P\bar{n}^2(r, z)|E(r, z)|^2, \quad (3)$$

where P is the total number of photons in the mode, \bar{n} is the real part of the refractive index, and $E(r, z)$ is proportional to the electrical field profile calculated within the 2D EFM-based optical solver, normalized according to

$$2\pi \int_{V_M} \bar{n}^2(r, z)|E(r, z)|^2 r dr dz = 1, \quad (4)$$

where the integration is performed over the entire mode volume V_M . Note that $E(r, z)$ does not have the dimension of the electrical field, but instead is expressed in units of $(1/\text{volume})^{1/2}$. With this normalization condition, integration of Eq. (3) over the mode volume V_M produces the total number of photons in the mode P .

We integrate now Eqs. (1) and (2) over the mode volume V_M . In the case of the carrier density, the integration is reduced to the active region volume V_A , producing the following equation for the total number of carriers N in the active region:

$$\frac{dN}{dt} = \frac{I}{e} - \frac{N}{\tau_r} - \frac{N}{\tau_{nr}} - U_{stim}, \quad (5)$$

where $N = nV_A$, I is the total current, and U_{stim} represents the total number of carriers recombining via the stimulated emission process per unit time:

$$U_{stim} = 2\pi Pa(n - n_t) \int_{V_A} \bar{n}^2(r, z)|E(r, z)|^2 r dr dz. \quad (6)$$

Eq. (6) takes into account the fact that carrier density distribution inside the active region is assumed to be constant. Integration of Eq. (2) over the mode volume V_M gives the rate equation for the total number of photons in the mode P :

$$\frac{dP}{dt} = \frac{\beta}{\tau_r} N + U_{stim} - U_{res} - \frac{P}{\tau_{ph}} , \quad (7)$$

where U_{stim} represents the total number of photons generated by stimulated emission per unit time, and U_{res} represents the total number of photons lost due to resonant absorption per unit time, given by:

$$U_{res} = 2\pi\alpha P \int_{V_A'} \bar{n}^2(r, z) |E(r, z)|^2 r dr dz \equiv P U_{res}^* . \quad (8)$$

Here, α stands for the absorption coefficient, and V_A' is the volume of the unpumped part of the layers containing the active region.

Using Eq. (5), we can express U_{stim} under steady-state conditions as

$$U_{stim} = \frac{I}{e} - \frac{N}{\tau_r} - \frac{N}{\tau_{nr}} . \quad (9)$$

Substitution of this relation into Eq. (7) yields, again under steady-state conditions:

$$P = \frac{\frac{I}{e} - (1-\beta)\frac{N}{\tau_r} - \frac{N}{\tau_{nr}}}{\frac{1}{\tau_{ph}} + U_{res}^*} . \quad (10)$$

Eq. (6) combined with Eq. (9) gives the total number of carriers as follows:

$$N = \frac{\frac{I}{e} + 2\pi\alpha n_i P \int_{V_A'} \bar{n}^2(r, z) |E(r, z)|^2 r dr dz}{\frac{1}{\tau_r} + \frac{1}{\tau_{nr}} + \frac{2\pi\alpha P}{V_A'} \int_{V_A'} \bar{n}^2(r, z) |E(r, z)|^2 r dr dz} . \quad (11)$$

At very low excitation levels, the total number of carriers tends to its “below threshold” value

$$N = \frac{I\tau_r\tau_{nr}}{e(\tau_r + \tau_{nr})} . \quad (12)$$

On the other hand, at very high excitation levels, the total number of carriers tends to its “transparency” limit $N_t = n_i V_A$.

Once the total number of photons in the mode P is found, the value for the actual electrical field $E(r, z)$ is obtained by equating the calculated value for the electric energy density with that calculated according to the well-known formula of electrodynamics:

$$\hbar\omega P \bar{n}^2(r, z) |E(r, z)|^2 = \frac{1}{4} \bar{n}^2(r, z) \epsilon_0 |E(r, z)|^2 , \quad (13)$$

where the left-hand side is the calculated electric energy density and the right-hand side represents the time-averaged electric energy density for the electrical field $E(r, z)$.

2.2. Energy Flux and Emitted Power Calculations

To calculate the electromagnetic energy flux density, we use the standard formula for the time-averaged Poynting vector:

$$\bar{S} = \frac{1}{2} \text{Re}[\bar{E} \times \bar{H}^*] , \quad (14)$$

where complex representation is used for the fields.

Eq. (14) involves vectorial quantities, hence we need to identify at this stage a particular polarization chosen for the analysis. All LP modes in cylindrically symmetric waveguiding structures are two-fold degenerate with respect to polarization, with either $E_x = H_y = 0$, or $E_y = H_x = 0$. In what follows, we consider the modes with their electric field polarized along the x-axis.

Using the local-plane-wave approach, we can relate the longitudinal component of the Poynting vector to the only non-zero transverse components of the fields as

$$S_z = \frac{1}{2} \text{Re}\{E_x \cdot H_y^*\} . \quad (15)$$

Using Eq. (13), the electric field $E_x(r, z)$ can be expressed in terms of $E_x(r, z)$, calculated within the 2D EFM-based optical solver. The magnetic field component $H_y(r, z)$ can then be found from Maxwell's equations as

$$\frac{\partial E_x}{\partial z} = -i\omega\mu_0 H_y . \quad (16)$$

The exact knowledge of the electromagnetic energy flux density inside the VCSEL resonator is very important for accurate calculation of heat generation associated with the free-carrier absorption of laser radiation. In addition, it enables us to calculate the emitted power P_{out} as

$$P_{out} = 2\pi \int_0^{r_M} S_z(r, L) r dr , \quad (17)$$

where the upper integration limit r_M means that integration is performed over the mode area, and L indicates the z-coordinate of the top (emitting) surface of the cavity.

2.3. Integration of 2D Optical Solver with Thermal-Electrical Solver

The thermal-electrical solver [Nakwaski 1994] was developed as semi-analytical model of proton-implanted top-surface-emitting lasers (PITSELS). Being limited to analysis of thermal-electrical problem, it did not include any optical mode solver. Adding the optical part significantly enhances the capability of the model and makes it much more attractive as a comprehensive tool for device designers and application engineers.

The electromagnetic energy flux density calculated inside the optical solver is used by the thermal-electrical solver to calculate heat generation associated with the absorption of laser radiation. The heat sources associated with reabsorption of spontaneous emission and nonradiative carrier recombination are accounted for using the following expression:

$$q_A = \left(\frac{1}{\tau_r} + \frac{1}{\tau_{nr}} \right) \frac{NE_g}{\pi r_A^2} , \quad (18)$$

where τ_r is the radiative recombination lifetime, τ_{nr} is the nonradiative recombination lifetime, N is the total number of carriers in the active region, E_g is the active-region bandgap, and r_A is the active-region radius.

The heat sources associated with free-carrier absorption are found using the following expression:

$$q_{fc,i}(T) = P_{int,i}(T) \alpha_{fc,i}(T) d_i , \quad (19)$$

where T is the temperature, $P_{\text{int},i}$ is the internal optical power in region i , $\alpha_{\text{fc},i}$ is the free-carrier absorption coefficient in region i , and d_i is the thickness of region i . The carrier density calculated inside the optical solver is used by the thermal-electrical solver to calculate the free-carrier absorption coefficient in the active region. The free-carrier absorption in the DBRs is treated the same way as it was in the original version of the thermal-electrical solver [Nakwaski 1994], but using the actual calculated internal optical power, instead of previous analytical approximation that neglected longitudinal variations in the internal optical power.

At present time, the optical solver uses the average temperature increase in the active region, calculated by the thermal-electrical solver, to take into account the temperature-induced refractive index change in the VCSEL structure according to

$$\Delta \bar{n} = \frac{d\bar{n}}{dT} \Delta T, \quad (20)$$

where ΔT is the calculated average temperature increase in the active region, and $d\bar{n}/dT$ describes the temperature sensitivity of the refractive index. For example, for GaAs $d\bar{n}/dT = 3 \times 10^{-4} \text{ K}^{-1}$ [Seraphin 1967]. The model can be improved further to include temperature dependence of the refractive index in the entire volume of the device, using actual temperature profiles instead of the average temperature.

The peak gain reduction with increasing temperature is taken into account by assuming the following form for the temperature dependence of the differential gain coefficient:

$$a = a(0) \exp\left(-\frac{\Delta T_A}{T_0}\right), \quad (21)$$

where ΔT_A is the average active-region temperature increase and T_0 is the characteristic temperature. For GaAs-based VCSELs, we take $T_0 = 210 \text{ K}$ [Hasnain 1991]. A more sophisticated approach to temperature-variation of gain will be taken in the future, with independent temperature-dependent parameters for the transparency carrier density and for the differential gain.

A flow chart of self-consistent thermal-electrical-optical calculations is shown in Fig. 1. We solve the system of equations (10) and (11) self-consistently for P and N for each value of injection current I . In the process, we obtain also the value for clamped carrier density n . This part of the algorithm is represented by the "electro-optical self-consistency" loop in Fig. 1. The self-consistency in the thermal loop of Fig. 1 is achieved when the average active-region temperature increase ΔT_A does not change any more within the prescribed accuracy of calculations.

3. RESULTS

3.1. Implementations of Thermal-Electrical-Optical Solver

Although the thermal-electrical solver was originally developed for simulation of PITSELs [Nakwaski 1994], it is now possible to apply it to model at least a few types of oxide-confined VCSELs. The key element in this analysis is the 2D optical module, and it was prepared in such a way that it does not suffer from the thermal-electrical solver limitations. In particular, we can treat devices with varying optical properties along both radial and vertical directions.

The developed semi-analytical scheme of self-consistent calculations was adopted to three types of VCSEL structures - PITSELs (Fig. 2), OCSELs with annular contact on top of p -side DBR (Fig. 3), and OCSELs with intracavity contact on the p -side (IC-OCSELs) (Fig. 4). OCSEL and IC-OCSEL implementations can be expected to treat properly the devices with the diameter of the oxide-containing mesa sufficiently large for the optical field to decay practically to zero at the mesa edges and for the radial thermal flux to be largely unimpeded, just as it is in PITSELs. Alternatively, planar structure treatment can be expected to approximate quite well the OCSELs fabricated by etching of small circular or crescent-shaped vias from which oxidation proceeds, [Chua 1997], [Schneider 1998], [Chua 1998a], [Chua 1998b], [Alduino 1999]. Another approximation involved in using the thermal-electrical solver is that the difference in thermal conductivities between the oxide and the adjacent semiconductor is neglected. We believe that this approximation is quite reasonable and will not affect the results in any significant way, since the oxide layer thickness is typically very small.

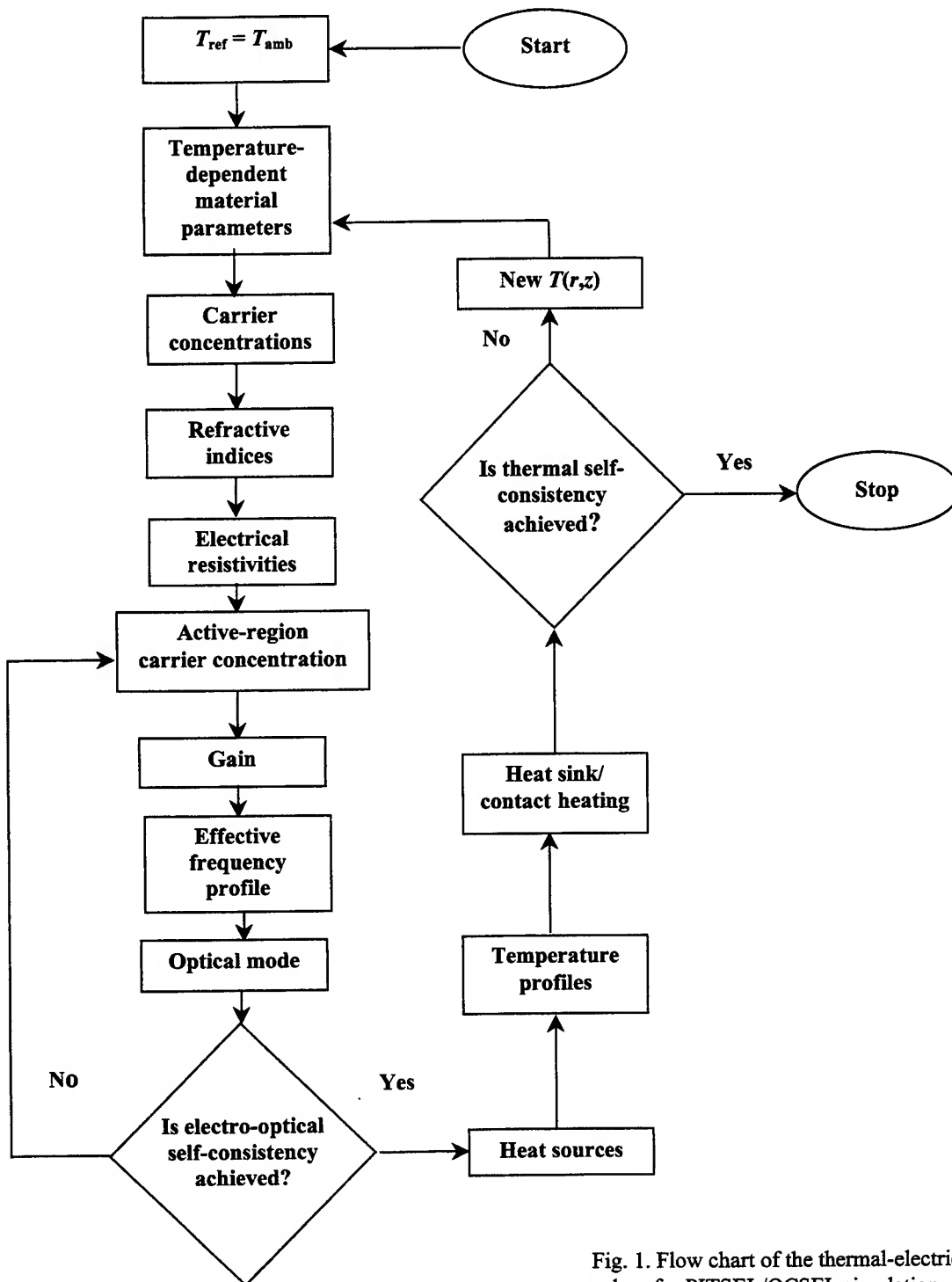


Fig. 1. Flow chart of the thermal-electrical-optical solver for PITSEL/OCSEL simulation.

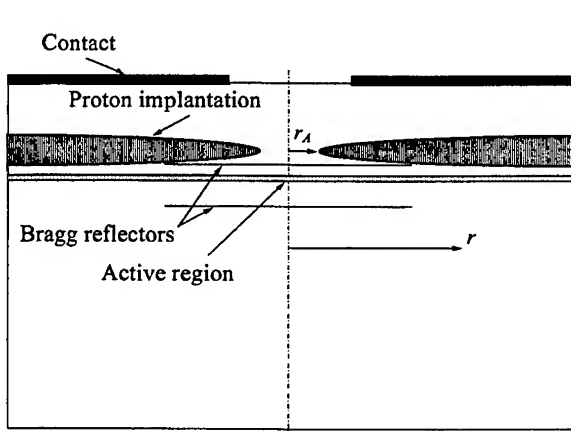


Fig. 2. Schematic structure of a PITSEL. r_A - the radius of the window in proton implanted region and of the active region.

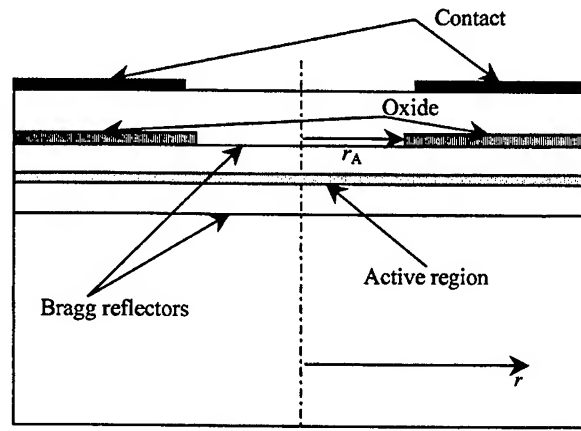


Fig. 3. Schematic structure of a planar OCSEL. r_A - the radius of the window in the oxidized layer and of the active region.

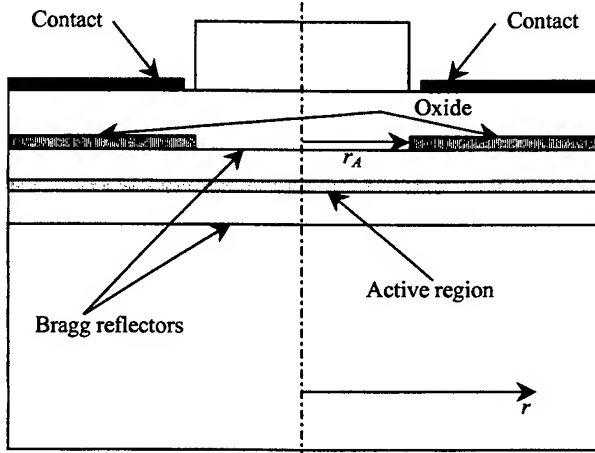


Fig. 4. Schematic structure of an intracavity-contacted (IC) OCSEL. r_A - the radius of the top DBR mesa, window in the oxidized layer and of the active region

3.2. Results of PITSEL Simulation

As a prototype for our simulations of PITSELS, we used the experimentally grown structure described in [Zhou 1991]. The PITSEL structure consists of an undoped active region bounded by the p -doped and n -doped DBR mirror stacks, all of which were grown on an n -GaAs substrate. The upper p -DBR mirror contains 24 pairs of quarter-wave $\text{Al}_x\text{Ga}_{1-x}\text{As}$ and AlAs layers. The Al content x of $\text{Al}_x\text{Ga}_{1-x}\text{As}$ is 15%, except at the heterointerfaces, where it is linearly graded from 15% to 100% over a distance of 12 nm. The lower n -doped DBR mirror contains 43.5 pairs of quarter-wave $\text{Al}_x\text{Ga}_{1-x}\text{As}$ and AlAs layers, with Al composition graded similarly as in the p -mirror. The active layer contains a symmetrical graded-index separate-confinement heterostructure (GRINSCH) with four 8-nm quantum wells separated by 2-nm barriers. Two different profiles of grading are applied on either side of the active region: first, a thin layer adjacent to the DBR mirror, graded from 100% down to 55%, and second, a thick layer adjacent to quantum wells, graded from 55% to 15%. The total thickness of the GRINSCH-MQW structure corresponds to a single wavelength of the cavity mode, which is designed to lase at 846 nm. The values of structural parameters used in the calculations are summarized in Table 1.

The phase and group refractive indices for $\text{Al}_x\text{Ga}_{1-x}\text{As}$ and AlAs layers were calculated using the approach of [Adachi 1985]. For the active GaAs region, the phase and group refractive indices were estimated using the Sellmeier equation:

$$n^2(\lambda) = A + B \left(\frac{\lambda^2}{\lambda^2 - C^2} \right), \quad (22)$$

where $A = 8.95$, $B = 2.05$, $C^2 = 0.39$ for GaAs at 300 K [Seraphin 1967].

Table 1. Device and material parameters assumed in calculations

Parameter	Value	Comments
r_A	5 μm	Active region radius
r_S	250 μm	Radius of the structure
r_{HS}	2.5 mm	Radius of the heat sink
t_{HS}	2 mm	Thickness of the heat sink
k_{HS}	398 W/(mK)	Thermal conductivity of the heat sink material
α	$2 \times 10^3 \text{ cm}^{-1}$	Resonant absorption coefficient
τ_r	1 ns	Radiative lifetime for carriers
τ_{nr}	10 ns	Nonradiative lifetime for carriers
$a(0)$	$2.5 \times 10^{-16} \text{ cm}^2$	Differential gain coefficient
T_0	210 K	Parameter of temperature dependence of a
n_t	$1 \times 10^{18} \text{ cm}^{-3}$	Transparency carrier concentration
N_A	$3 \times 10^{18} \text{ cm}^{-3}$	Acceptor concentration in p -type DBR layers
N_D	$3 \times 10^{18} \text{ cm}^{-3}$	Donor concentration in n -type DBR layers
β	10^{-4}	Spontaneous emission factor
dn/dT	$3 \times 10^{-4} \text{ K}^{-1}$	Parameter of refractive index temperature dependence

To illustrate the type of outputs produced by the integrated thermal-electrical-optical simulator, various PITSEL characteristics were calculated in the range of pumping currents from 0.2 mA to 5 mA, covering both below threshold and above threshold conditions. Fig. 5 shows the calculated average temperature increase in the active region ΔT_A as a function of current I . A pronounced change in the slope of $\Delta T_A(I)$ characteristic corresponds to the onset of lasing. Above threshold, a significant part of electrical energy is converted into stimulated emission rather than heat, hence a decrease in the rate of active-region heating should indeed be expected.

Fig. 6 clearly demonstrates a steadily growing carrier concentration n in the active region up to threshold, and clamped behavior of n above threshold. Since the active-region heating source associated with nonradiative recombination is proportional to the carrier density, contribution from this source to the active-region temperature increase is also clamped above threshold. This is the second factor behind the slower rate of active-region heating shown in Fig. 5.

A closer look at Fig. 6 reveals that the carrier concentration above threshold is not truly clamped. As a matter of fact, typical behavior in semiconductor lasers would be for n to increase slightly above threshold. Namely, due to increasing heating above threshold, peak gain at a fixed carrier density is reduced, and the carrier density has to increase to compensate for this effect. In contrast to this usual behavior, Fig. 6 reveals a rather anomalous feature of PITSELS, namely the carrier density slowly decreases above threshold. To our best knowledge, this effect has not yet been reported in any previous simulations, and this result alone illustrates the value of fully self-consistent thermal-electrical-optical modeling.

The mechanism of carrier density reduction above threshold can be understood by considering optical properties of PITSELS. Since the device structure, as shown in Fig. 2, contains no built-in lateral waveguide, the optical mode at low currents is formed via gain guiding. As the current increases, a lateral step in temperature, ΔT_A , causes a thermal lensing effect by increasing the refractive index in the active region, thus improving mode confinement in radial direction and reducing the gain required to maintain lasing in that mode. A change in the fundamental mode profile corresponding to this process is illustrated in Fig. 7.

Another indicator of the active region temperature variation is the emission wavelength drift. The refractive index increases with increasing temperature, and this shifts the Bragg resonance towards longer wavelengths. Consequently, the calculated resonant wavelength mirrors the active-region temperature increase, as illustrated in Fig. 8.

The on-axis distribution of light intensity along the PITSEL cavity is shown in Fig. 9 for the pumping current equal to 5 mA. The model allows us also to calculate the electromagnetic energy flux through the laser structure (Fig. 10), and the emitted power (Fig. 11). The negative values for energy flux in Fig. 10 mean that the electromagnetic energy propagates downwards

from the active region. We find the calculated light-current characteristic to be in a good qualitative agreement with the linear part of experimentally observed light-current characteristic (*cf.* Fig. 2(b) in [Zhou 1991]).

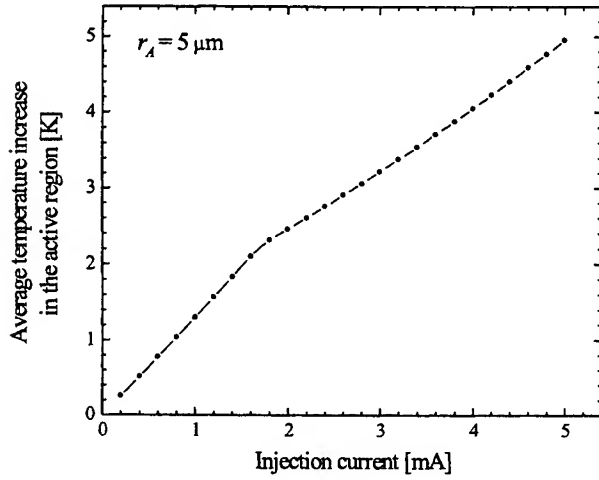


Fig. 5. Calculated average temperature increase in the active region versus injection current in a PITSEL.

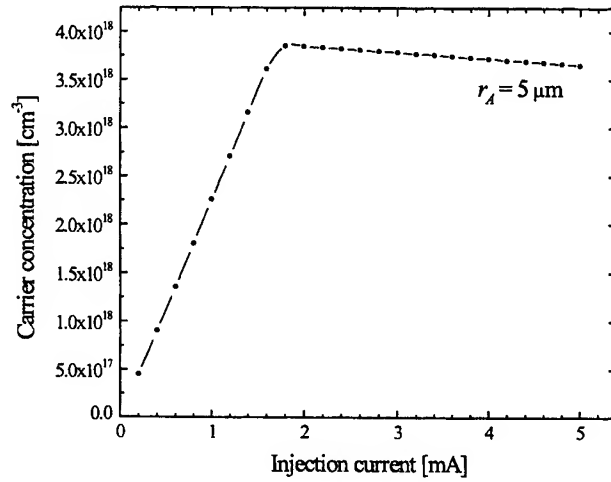


Fig. 6. Carrier concentration n in the active region versus the pumping current in the same PITSEL as in Fig. 5.

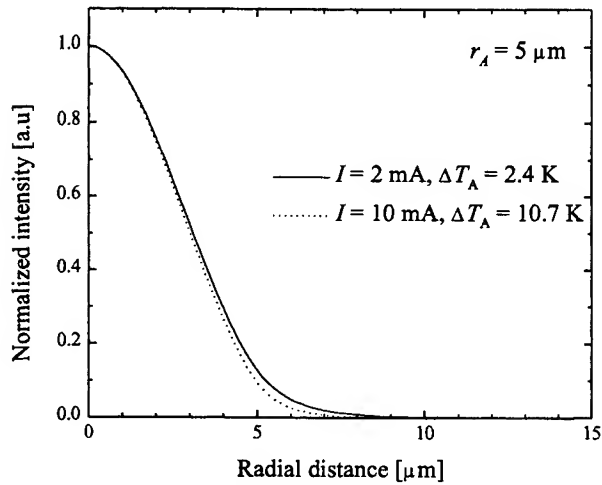


Fig. 7. Effect of temperature increase in the active region on the radial profile of the fundamental mode in the same PITSEL as in Fig. 5.

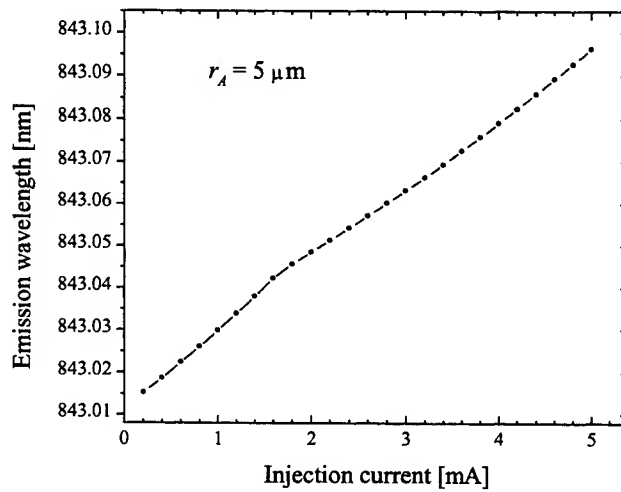


Fig. 8. Calculated emission wavelength versus injection current in the same PITSEL as in Fig. 5

3.3. Comparison of PITSEL, OCSEL, and IC-OCSEL Simulations

In this section, we discuss some of the first preliminary simulations of OCSELS and compare them with the results obtained for PITSELS. In order to facilitate the comparison, similarity of all structures has been maintained to the maximum possible extent. Thus, the DBR structure in all cases is assumed to be identical. Other parameters, such as the active-region radius, radius of the structure, thicknesses of all layers, *etc.*, were kept identical from structure to structure. The simulated OCSEL device had the first quarter-wave p -AlAs layer above the GRINSCH-MQW structure oxidized in the outer radial section of the device, but otherwise its structure was the same as in the case of the PITSEL discussed in Section 3.2. The IC-OCSEL

device had an intracavity contact located one $p\text{-Al}_{0.15}\text{Ga}_{0.85}\text{As}$ layer above the oxide layer and undoped top DBR mirror stack (with unintentional p -doping level of 10^{16} cm^{-3} , and the corresponding free-carrier absorption loss of 2.88 cm^{-1} instead of 16.87 cm^{-1} in p -doped DBR in PITSEL and OCSEL structures), but otherwise was identical to the first OCSEL. Other than the different doping level for the top DBR mirror in IC-OCSEL, the central part of the device in both OCSEL structures ($r \leq r_A$) is identical to that of the PITSEL considered in Section 3.2. The value of 1.575 for the refractive index of AlAs oxidized layer was extracted from Fig. 1 of [Knopp 1998].

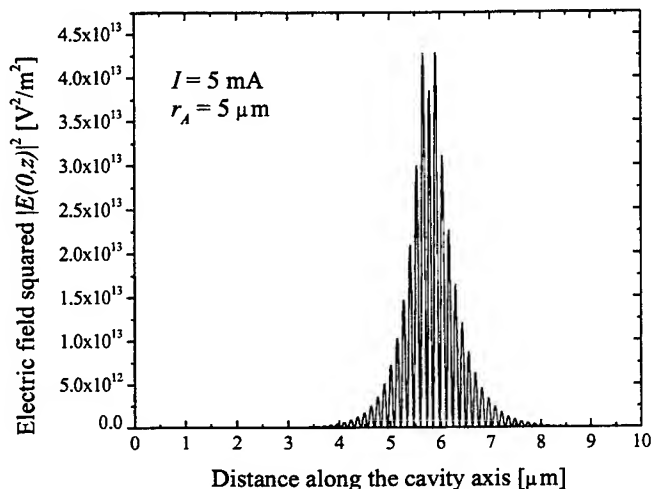


Fig. 9. Calculated intensity distribution along the cavity axis in the same PITSEL as in Fig. 5.

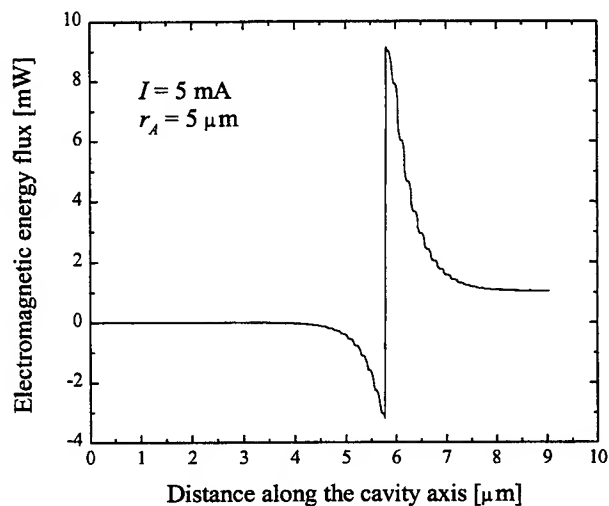


Fig. 10. Calculated distribution of electromagnetic energy flux in the same PITSEL as in Fig. 5.

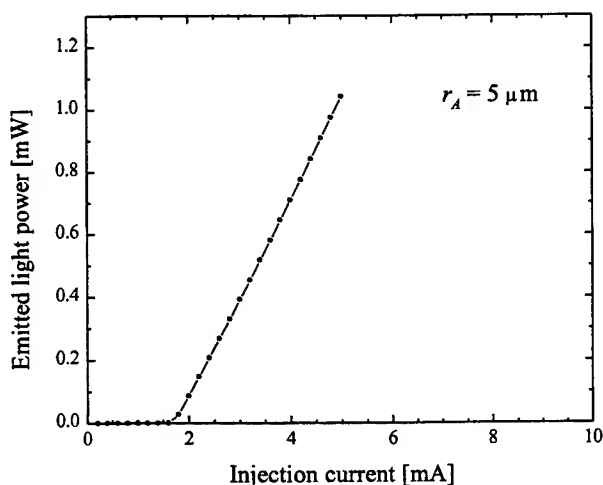


Fig. 11. Calculated light-current characteristic for the same PITSEL as in Fig. 5.

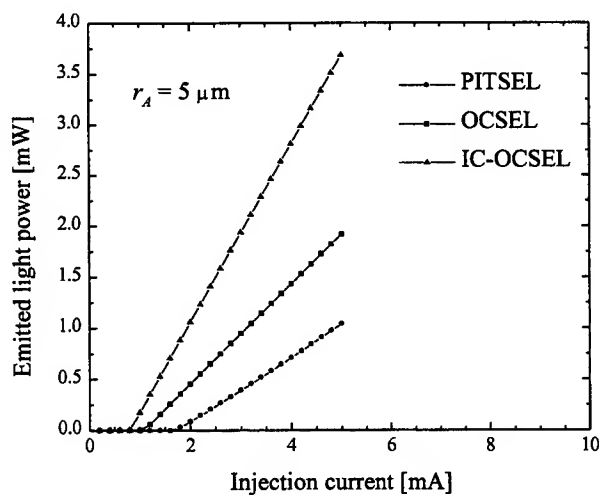


Fig. 12. Comparison of calculated light-current characteristics for three different VCSEL structures.

The most spectacular difference between OCSELS and PITSELS is illustrated in Fig. 12, where calculated light-current characteristics of three VCSEL structures are compared. Simple replacement of proton-implanted region with an oxidized layer results in a remarkable improvement in the threshold current, efficiency, and the output power. Inclusion of intracavity contact (IC-OCSEL) allows one to replace p -doped DBR with undoped layers, thus improving the resonator quality and gaining even more output power. Fig. 12 demonstrates the significant advantage of oxide-confined structures over proton-

implanted devices due to much better lateral (OCSEL and IC-OCSEL) and vertical (IC-OCSEL) mode confinement. This conclusion is in good agreement with experimental observations.

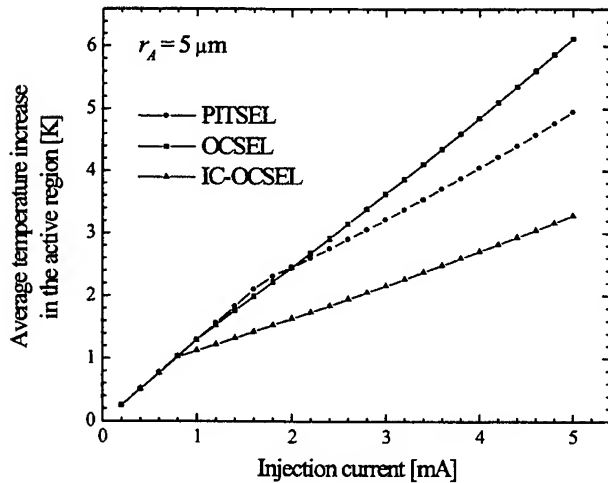


Fig. 13. Calculated average temperature increase in the active region versus injection current for the same three different VCSEL structures as in Fig. 12.

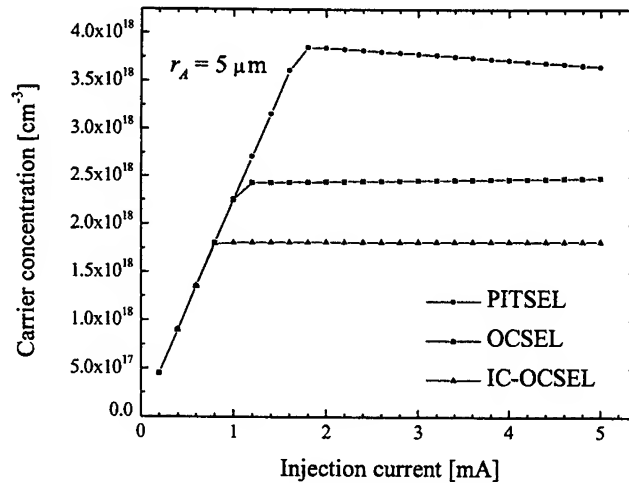


Fig. 14. Carrier concentration n in the active region versus the pumping current for the same three different VCSEL structures as in Fig. 12.

Other characteristics of OCSELs can also be easily extracted from our simulations. Fig. 13 shows that the active-region heating above threshold in OCSELs is significantly reduced due to lower threshold currents. In addition, heating in IC-OCSELs is less intense because the undoped top DBR mirror no longer represents a heat source of any significance. That means much better stability of operation for IC-OCSELs devices as compared to the other two types of devices.

Fig. 14 shows that the anomalous reduction in active region carrier concentration active region carrier concentration above threshold is limited to PITSELS, and both types of OCSELs display the usual clamped (and slowly raising) behavior. This results from a much stronger real-index guiding in oxide-confined structures which do not rely on thermal lensing for mode confinement.

4. CONCLUSIONS

We have developed an integrated thermal-electrical-optical solver of VCSELs. The optical part of the solver is based on the effective frequency method for the optical mode of VCSELs, combined with the rate equations for photon and carrier densities. The thermal-electrical part is based on the thermal-electrical solver developed originally for proton-implanted top-surface-emitting lasers (PITSELS) [Nakwaski 1994].

The integrated solver was applied to analyze and compare the performance characteristics of GaAs-based PITSELS, oxide-confined surface-emitting lasers (OCSELs) and intracavity-contacted oxide-confined surface-emitting lasers (IC-OCSELs). Effects of thermal lensing on PITSEL properties are illustrated. Numerical results confirm the experimentally observed significant advantage of oxide-confined structures over proton-implanted devices. The intracavity-contacted design ensuring the lowest threshold current and heat-generation rate has been identified as the most advantageous for oxide-confined structures.

ACKNOWLEDGMENTS

This work was supported by DARPA under the Optoelectronic Materials Center program and by CFD Research Corporation under the Phase II SBIR program.

REFERENCES

- [Adachi 1985] S. Adachi, "GaAs, AlAs, and $\text{Al}_x\text{Ga}_{1-x}\text{As}$: Material parameters for use in research and device applications", *J. Appl. Phys.*, vol. 58 (3), pp. R1-R29, 1985.
- [Alduino 1999] A. C. Alduino, S. Q. Luong, Y. Zhou, C. P. Hains, and J. Cheng, "Quasi-planar monolithic integration of high-speed VCSEL and resonant enhanced photodetector arrays", *IEEE Photon. Technol. Lett.*, vol. 11 (5), pp. 512-514, May 1999.
- [Chua 1997] C. L. Chua, R. L. Thornton, and D. W. Treat, "Planar laterally oxidized vertical-cavity lasers for low-threshold high-density top-surface-emitting arrays", *IEEE Photon. Technol. Lett.*, vol. 9 (8), pp. 1060-1062, Aug. 1997.
- [Chua 1998a] C. L. Chua, R. L. Thornton, D. W. Treat, M. Kneissl, and C. Dunnrowicz, "Low-threshold InAlGaAs vertical-cavity surface-emitting laser arrays using transparent contacts", *Appl. Phys. Lett.*, vol. 72 (9), pp. 1001-1003, 2 March 1998.
- [Chua 1998b] C. L. Chua, R. L. Thornton, D. W. Treat, and R. M. Donaldson, "Anisotropic apertures for polarization-stable laterally oxidized vertical-cavity lasers", *Appl. Phys. Lett.*, vol. 73 (12), pp. 1631-1633, 12 Sept. 1998.
- [Hasnain 1991] G. Hasnain, K. Tai, N. K. Dutta, Y. H. Wang, J. D. Wynn, B. E. Weir, and A. Y. Cho, "High temperature and high frequency performance of gain-guided surface-emitting lasers", *Electron. Lett.*, vol. 27, pp. 915-916, 23 May 1991.
- [Knopp 1998] K. J. Knopp, R. P. Mirin, D. H. Christensen, K. A. Bertness, A. Roshko, and R. A. Synowicki, "Optical constants of $(\text{Al}_{0.98}\text{Ga}_{0.02})_x\text{O}_y$ native oxides", *Appl. Phys. Lett.*, vol. 73 (24), pp. 3512-3514, 14 Dec. 1998.
- [Nakwaski 1994] W. Nakwaski and M. Osiński, "Self-consistent thermal-electrical modeling of proton-implanted top-surface-emitting semiconductor lasers", *Physics and Simulation of Optoelectronic Devices II* (W. W. Chow and M. Osiński, Eds.), Los Angeles, CA, 24-26 Jan. 1994, *SPIE Proc.*, Vol. 2146, pp. 365-387.
- [Schneider 1998] R. P. Schneider, Jr., "A new planar laser," *IEEE Spectrum*, vol. 35 (2), pp. 52-53, Feb. 1998.
- [Seraphin 1967] B. O. Seraphin and H. E. Bennet, in *Semiconductors and Semimetals* (R. K. Willardson and A. C. Beer, Eds.), vol. 3, p. 499, Academic Press, New York, 1967.
- [Smolyakov 1999] G. A. Smolyakov, V. A. Smagley, W. Nakwaski, P. G. Eliseev, and M. Osiński, "Design of InGa_{0.5}N/GaN/AlGa_{0.5}N VCSELs using the effective frequency method", *Physics and Simulation of Optoelectronic Devices VII* (P. Blood, A. Ishibashi, and M. Osiński, Eds.), *SPIE Proc.*, Vol. 3625, pp. 383-394 (1999).
- [Wenzel 1997] H. Wenzel and H.-J. Wünsche, "The effective frequency method in the analysis of vertical-cavity surface-emitting lasers", *IEEE J. Quantum Electron.*, vol. 33 (7), pp. 1156-1162, July 1997.
- [Zhou 1991] P. Zhou, J. Cheng, C. F. Schaus, S. Z. Sun, K. Zheng, E. Armour, C. Hains, W. Hsin, D. R. Myers, and G. A. Vawter, "Low series resistance high-efficiency GaAs/AlGaAs vertical-cavity surface-emitting lasers with continuously graded mirrors grown by MOCVD", *IEEE Photon. Technol. Lett.*, vol. 3 (7), pp. 591-593, July 1991.

Analysis and design of AlGaInP single-quantum-well LED

Liang Pao Lee^a, Soo Jin Chua^b

Dept. of Electrical Engineering, National University of Singapore, Singapore 119260

ABSTRACT

Calculations are done and compared for two AlGaInP single-quantum-well (SQW) LED structures: step separate-confinement-heterostructure (SCH) SQW structure and graded-index (GRIN) SCH-SQW structure. It is found that the latter has better performance in terms of spontaneous lifetime and injection efficiency. This is attributed to greater barrier height to electron leakage and substantial overlap between wavefunctions of different quantum numbers in the GRIN-SCH-SQW structure. Results also show that the GRIN layer thickness has no influence on the QW energy levels, spontaneous lifetime and injection efficiency in a GRIN-SCH-SQW.

Keywords: LED, AlGaInP, single-quantum-well, graded-index

1. INTRODUCTION

A new milestone in LED efficiency is achieved when the transparent-substrate (TS) double-heterostructure (DH) AlGaInP LED substrate - employing a thick GaP window layer - is successfully fabricated. An external quantum efficiency of 23.7% at 635.6nm and a luminous efficiency of 50.3 lm/W at 607.4nm^{1,2} was reported.

It was subsequently reported³ that AlGaInP MQW LEDs are not only brighter, but also more reliable than conventional AlGaInP DH LEDs. A thin active layer also serves to minimise self-absorption. In addition, quantum size effects (QSE) can be used to shorten the emission wavelength without a corresponding increase in Al composition.

In this paper, the spontaneous lifetime and injection efficiency of AlGaInP single-quantum-well (SQW) LEDs is theoretically analyzed. Two structures are studied and compared: the step separate-confinement-heterostructure (SCH) SQW structure (Fig. 1) and graded-index (GRIN) SCH-SQW structure (Fig. 2). The effect of the GRIN layer thickness on spontaneous emission rate and injection efficiency is also considered.

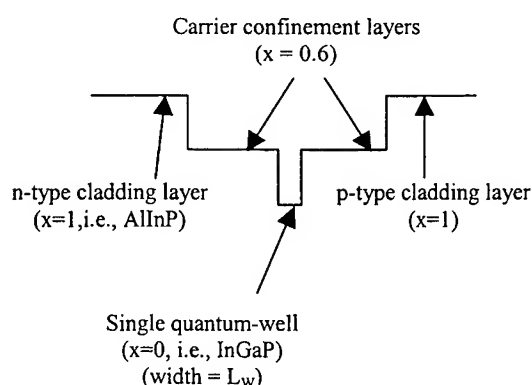


Fig. 1: Step SCH-SQW structure under study

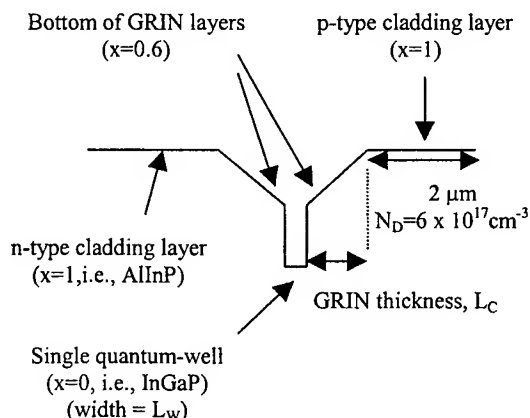


Fig. 2: GRIN-SCH-SQW structure under study

^a Correspondence: Email: eng60343@nus.edu.sg

^b Correspondence: Email: elecsj@nus.edu.sg

2. THEORY

2.1 Transfer matrix method for calculating allowable energy levels

The quasi-bound allowable energy levels are the basic information needed for QW calculations. These are obtained, using the transfer matrix method^{4,5,6}. The transfer matrix across each distinct interface is obtained by imposing the proper boundary conditions on the wavefunctions, namely the continuity of Ψ and the probability current $\frac{1}{m} \frac{\partial \Psi}{\partial x}$ across each heterojunction⁷. The wavefunction has the usual complex exponential form in regions of uniform composition. In regions of graded composition, the wavefunction can be expressed as the linear combination of Airy functions of the first and second types.

2.2 Quasi-Fermi level calculations for simple and step SCH-SQW structures

Using the principle of box quantization of kinetic energies (in the directions parallel to QW plane) and parabolic band approximation, i.e., $E = \frac{\hbar^2 k^2}{2m_{ci}}$, the density of electron states per unit volume for the i -th subband is given by⁸

$$g_{ci} = \frac{D_i}{L_z} = \frac{m_{ci}}{\pi \cdot \hbar^2 \cdot L_z}, \quad (1)$$

where m_{ci} is the effective mass of the electrons in the i -th subband of the conduction band and L_z is the QW width.

A similar equation holds for the holes in the valence band.

The simple model for the density of states described above neglects the effect of collisions between carriers, which would broaden the discrete energy levels in the x -direction. A necessary condition for the density of states for the validity of the model is that the collisional broadening of energies be small relative to the separation between discrete levels. If we assume an infinitely deep potential well to obtain the separation between the two lowest energy levels, the condition is, from⁹,

$$\frac{h}{2\pi\tau} \leq \frac{3\hbar^2}{8m_c L_z^2}, \quad (2)$$

where τ is the electron-electron scattering time. The term on the right side of Eq. (2) gives the energy separation between the first two levels for an infinitely deep rectangular well. Using $\tau = 24$ ns¹⁰ for $(\text{Al}_{0.2}\text{Ga}_{0.8})_{0.5}\text{In}_{0.5}\text{P}$, we get from Eq. (2) that $L_z \ll 12$ μm for electrons and $L_z \ll 8$ μm for heavy holes. This estimate shows that Eq. (1) for the density of states is an excellent approximation for a well thickness that is less than about 100 \AA . Eq. (1) should then hold for the quantum wells that are subsequently considered here.

If n is the number of electrons in the conduction band, the electron quasi-Fermi level can be obtained from

$$n = k_B T \cdot \sum_i g_{ci} \ln \left[1 + \exp \left(\frac{E_{fc} - E_{i0}}{k_B T} \right) \right], \quad (3)$$

where E_{fc} is the quasi-Fermi energy in the conduction band, and E_{i0} is the confined-particle energy level of the i -th subband.

Assuming further that only first subband is occupied,

$$E_{fc} - E_{i0} = k_B T \ln \left[\exp \left(\frac{n}{N_c} \right) - 1 \right], \quad (4)$$

where $N_c = g_c k_B T$

Similar relations hold for holes in the valence band.

2.3 Quasi-Fermi level calculations for GRIN-SCH-SQW structure

The DOS function and the carrier (electron or hole) quasi-Fermi levels are calculated in similar fashions as for the case of a step SCH-SQW structure. However, for a simple GRIN-SCH-SQW structure, it can be shown by a perturbation analysis of the eigenvalue equation that the appropriate lateral effective mass is a weighted average of the QW and cladding masses¹¹. Hence,

$$m_n^{-1} = \Gamma_n m_w^{-1} + (1 - \Gamma) m_g^{-1}, \quad (5)$$

where m_n is the GRIN effective mass for state n (n is the quantum number),

Γ_n is the wavefunction confinement factor in QW for state n ,

ψ_n is the normalised wavefunction for state n ,

m_w is the carrier effective mass in QW

and m_g is the carrier effective mass at bottom of GRIN.

For the case of the step SCH-SQW structure, carriers are strongly confined and Γ_n is almost unity, so that m_n is very nearly m_w for both electrons and holes.

2.4 Spontaneous emission rate

Weak carrier confinement in a GRIN-SCH-SQW structure also leads to invalidity of the quantum number selection rule for spontaneous emission. Hence, electron states and hole states with the same quantum number may have very different spatial extent, while electron states and hole state with differing quantum numbers may have wavefunctions that overlap considerably. The spatial overlap factor within the well between electron state i and hole state j is ¹²:

$$\Gamma_n = \left| \int_{-L_w/2}^{L_w/2} \Psi_i(x) * \Psi_j(x) dx \right|^2, \quad (6)$$

where $\psi_i(x)$ and $\psi_j(x)$ are the normalized wavefunctions for the electron state i and hole state j and L_w is the well width.

The overall spontaneous emission rate due to transitions between all possible states in a GRIN-SCH-SQW is given by:

$$R_{sp} = \sum_{i,j} C_{ij} \frac{32\pi^2 q^2 \eta |M_b|^2 m_\Gamma}{m_0^2 \epsilon_0 c^3 h^4 L_z} \cdot \int_{E_g}^{\infty} E f_c(E_c) f_v(E_v) dE, \quad (7)$$

where C_{ij} is the spatial overlap factor between states electron i and hole state j ,

q is the electron charge,

η is the refractive index,

m_0 is the free electron mass,

c is the velocity of light,

ϵ_0 is the permittivity of free space,

h is the Planck constant,

f_c and f_v are the Fermi factors for the electron at the energy E_c and hole at the energy E_v , where

$$E_c = \frac{m_\Gamma}{m_c} (E - E_q), \quad E_v = \frac{m_\Gamma}{m_h} (E - E_q), \quad m_\Gamma = \frac{m_c m_v}{(m_c + m_v)}, \quad (8)$$

(m_v and m_c are the effective heavy hole and electron masses respectively),

and $|M_b|$ is an average matrix element of transition for the Bloch states of the bands (in the x - and y - direction), as in the corresponding three-dimensional case. Using the Kane band model, $|M_b|^2$ in bulk semiconductors is given by [Casey]

$$|M_b|^2 = \frac{m_0^2 E_g (E_g + \Delta)}{12 m_e (E_g + \frac{2}{3} \Delta)} = \zeta m_0 E_g, \quad (9)$$

where ζ lies between 1 and 2 for most semiconductors. We assume that $|M_b|^2$ for a QW is given by

$$|M_b|^2 = \zeta m_0 E_q, \quad (10)$$

where E_q is the separation between the lowest electron energy level and lowest heavy hole energy level..

For a step SCH-SQW, the spatial overlap factor is close to unity between states with the same quantum numbers and close to zero for states with different quantum numbers.

The spontaneous radiative lifetime, τ_{sp} , is equal to $\frac{\Delta n}{R_{sp}}$, where Δn is the injected carrier density. When Δn is

very much larger than the equilibrium carrier density, Δn is equal to n .

The spontaneous recombination current density, J_{rad} , is equal to $q \cdot R_{sp} \cdot L_z$.

2.5 Current injection efficiency

Compared to the other major LED material systems, AlGaInP is characterized by low hole mobility, and high p-doping is also relatively difficult¹³. Therefore, hole leakage current is negligible compared to that of electrons. For this reason, valence band discontinuity and hole leakage current are ignored in current injection efficiency calculations.

The total leakage current density (J_L) is the sum of its drift and diffusion components ($J_L = J_{diffusion} + J_{drift}$) and is given by¹⁴

$$J_L = q \cdot D_n \cdot N_0 \cdot \left[\sqrt{\frac{1}{L_n^2} + \frac{1}{4z^2}} \cdot \text{Coth} \left(x_p \cdot \sqrt{\frac{1}{L_n^2} + \frac{1}{4z^2}} \right) + \frac{1}{2z} \right], \quad (11)$$

where q is the electronic charge,

x_p is the p-cladding layer thickness,

L_n is the minority electron diffusion length,

D_n is the minority electron diffusion coefficient (given by $D_n = \mu_n \left(\frac{kT}{q} \right)$, where μ_n is the minority electron mobility),

k is Boltzmann constant,

T is the absolute temperature,

z is a length characteristic of drift leakage, given by $z = \frac{kT}{q} \cdot \frac{\sigma_p}{J_{total}}$ (where σ_p is the electrical conductivity of the p-cladding layer and J_{total} is the total diode current density)

and N_0 is the concentration of minority electron at the edge of the p-cladding with energy greater than the conduction-band barrier height, ΔE_C .

It can be shown⁹ that

$$N_0 = 2 \left(\frac{2\pi m_n^* kT}{h^2} \right)^{3/2} \exp \left(- \frac{\Delta E}{kT} \right), \quad (12)$$

where ΔE is the effective potential barrier for electron at the active-confining layer interface and m_n^* is the density-of-states effective mass of electrons in the X valley of the AlGaInP p-cladding layer and h is the Planck's constant.

The barrier height to electron leakage, ΔE , can be estimated by summing up the barrier heights at the QW/confining layer interface, along with the potential step at the confining layer/P-cladding layer interface (Fig. 3). With uncertainties associated with band-filling, band-bending and material properties, the energy barrier estimated this way has been shown to be in reasonable agreement with the measured value¹⁴.

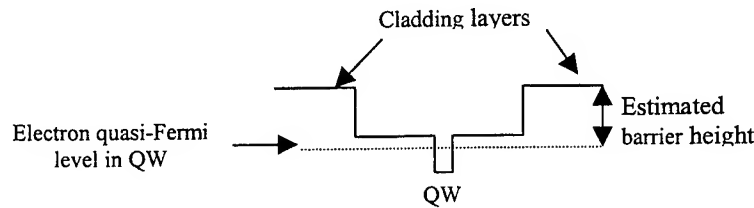


Fig. 3: Estimated barrier height to electron leakage

Eq. (11) is, in fact, an equation in J_L and J_{total} . Also,

$$J_{total} = J_{rad} + J_L, \quad (13)$$

Hence, Eq. (11) and (13) can be solved for the electron leakage current density, J_L , and total diode current density, J_{total} , since J_{rad} is known from spontaneous emission rate calculations. If nonradiative recombination is negligible, the internal quantum efficiency is equal to the injection efficiency.

3. RESULTS

3.1 Optimization of doping and thickness of p-cladding layer

The step SCH-SQW structure (Fig. 1) is analysed first. The well width is 80 Å; doping of the p-cladding layer is $6 \times 10^{17} \text{ cm}^{-3}$; thickness of the p-cladding layer is 1 µm and the thickness of the carrier confinement layers is about 1400 Å. $(\text{Al}_x\text{Ga}_{1-x})_{0.5} \text{In}_{0.5} \text{P}$ is the material system used with $x=1$ for the cladding layers, $x=0.6$ for the carrier confinement layers and $x=0$ for the QW.

The thickness of the p-cladding layer is varied. The maximum injection efficiency increases with the thickness of the p-cladding layer and begins to saturate at the thickness value of 2 µm (Fig. 4). This is expected from the form of Eq. (11), since the *Coth* function becomes nearly one, as its argument becomes very great.

With the value of 2 µm for the p-cladding layer thickness, calculations are performed to investigate how the doping of the p-cladding layer influences the maximum injection efficiency (Fig. 5). The maximum injection efficiency increases with the doping level in the p-cladding layer and begins to saturate when the doping is $6 \times 10^{17} \text{ cm}^{-3}$.

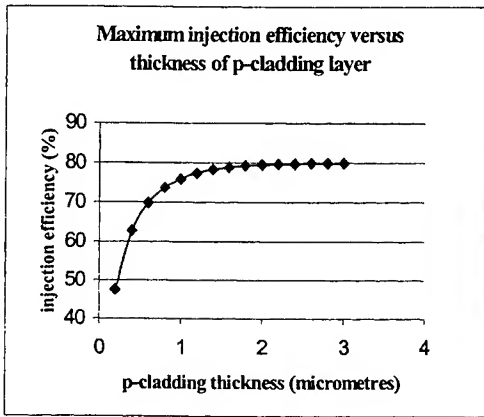


Fig. 4: Maximum injection efficiency as function of thickness of p-cladding layer

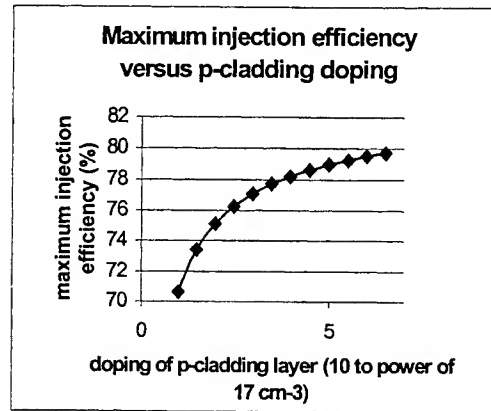


Fig. 5: Maximum injection efficiency as function of p-cladding layer doping

3.2 Comparison of step and GRIN SCH-SQW structures

Spontaneous lifetime and current injection efficiency are calculated for the step and GRIN SCH-SQW structures. Doping of the p-cladding layers are $6 \times 10^{17} \text{ cm}^{-3}$ for both structures; thickness of the GRIN layers are 300 Å; and the thickness of the cladding layers are 2 µm. $(\text{Al}_x\text{Ga}_{1-x})_{0.5} \text{In}_{0.5} \text{P}$ is the material system used with $x=1$ for the cladding layers, $x=0.6$ for the bottom of the GRIN layers or for the carrier confinement layers and $x=0$ for the QW (Fig. 1 and Fig. 2).

The injection efficiency is generally higher in a GRIN-SCH-SQW than in a step SCH-SQW for all well widths (Fig. 6). For a well width of 80 Å, the calculated maximum injection efficiency (which occurs at a carrier injection of $15 \times 10^{17} \text{ cm}^{-3}$ for both structures) is 85.3% in the GRIN-SCH-SQW and 80.4% in the step SCH-SQW. This improved performance is attributed to both shortening of the spontaneous lifetime and to reduction in electron leakage.

The presence of GRIN confinement layers tends to lower the allowable energy levels in the QW. This effect lowers the electron Fermi-level, thereby increasing the barrier height to electron leakage. For instance, for well width of 40 Å and carrier injection of $15 \times 10^{17} \text{ cm}^{-3}$, the barrier height is 243 meV in the GRIN-SCH-SQW and 237 meV in the step SCH-SQW (Fig. 8).

The improvement in spontaneous lifetime is much more pronounced. For example, for a well width of 80 Å and carrier injection of $15 \times 10^{17} \text{ cm}^{-3}$, the electron lifetime is 3.75 ns in the step SCH-SQW and only 2.80 ns in the GRIN-SCH-SQW (Fig. 7). This is attributed to the substantial overlap between wavefunctions of different quantum numbers in the GRIN-SCH-SQW. In a GRIN-SCH-SQW with 80 Å well width and 300 Å GRIN thickness, heavy hole and electron states with different quantum numbers overlap appreciably (Table A).

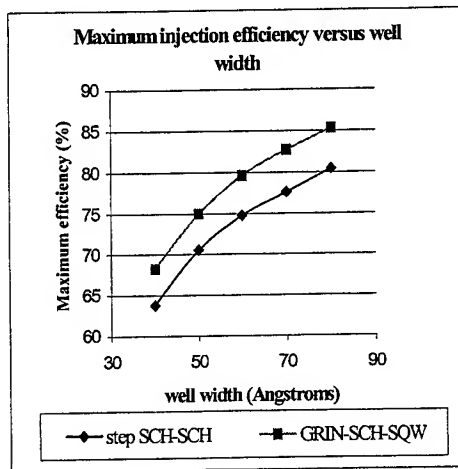


Fig. 6: Injection efficiency of step SCH and GRIN-SCH (with varying well widths)

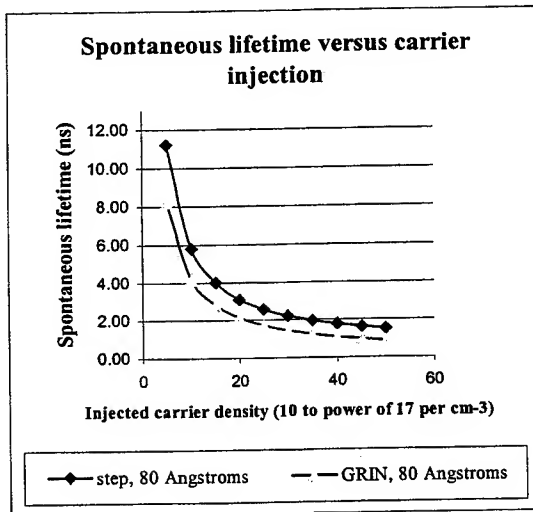


Fig. 7: Spontaneous lifetimes (both structures) as functions of carrier injection

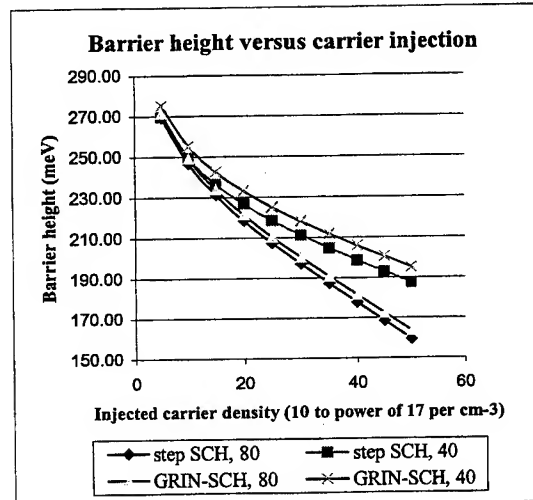


Fig. 8: Barrier heights (both structures) as functions of carrier injection

Table A: Spatial overlap factors between QW electron and heavy hole states

	Electron state 1	Electron state 2
Heavy hole state 1	93.67	52.60
Heavy hole state 2	83.89	87.83
Heavy hole state 3	4.37	41.94
Heavy hole state 4	1.42	2.40
Heavy hole state 5	2.94	2.23

3.3 Effect of varying GRIN thickness in GRIN-SCH-SQW structures

Calculated injection efficiency is the same for GRIN thickness of 100 Å, 300 Å and 1000 Å. An explanation for this is sought.

The heavy hole energy levels for GRIN thickness of 300 Å and 1000 Å are compared (Table B). While the GRIN energy levels are appreciably affected by the GRIN layer thickness, the QW energy levels are almost unaffected. In addition, the overall spontaneous emission rate in a GRIN-SCH-SQW is due almost entirely to transitions between the QW energy states. If we consider only transitions between the QW states (Table C), the spontaneous lifetime (correct to 3 significant figures) is 2.80 ns – identical to the value obtained when transitions between both GRIN and QW states are considered. Hence, the spontaneous emission rate in a GRIN-SCH-SQW is independent of the thickness of GRIN layers.

Table B: Influence of GRIN thickness on QW and GRIN energy levels (heavy holes)

	$L_c=300 \text{ Å}$	$L_c=1000 \text{ Å}$
QW energy levels	0.0072834	0.00726456
	0.0290371	0.0290207
	0.0648404	0.0648
	0.113729	0.113618
	0.172998	0.172627
GRIN energy levels	0.225847	0.218006
	0.233857	0.22008
	0.242125	0.225884
	0.252008	0.228402
	0.257083	0.232359

Table C: Spontaneous lifetimes for transitions between QW states

Lifetime	EE 1	EE 2
HH 1	4.42 ns	57.15 ns
HH 2	10.43 ns	72.16 ns
HH 3	746.81 ns	563.19 ns
HH 4	15.75 μs	18.73 μs
HH 5	140.21 μs	603.04 μs

4. SUMMARY & CONCLUSIONS

In this paper, the spontaneous lifetime and injection efficiency of AlGaInP single-quantum-well (SQW) LEDs has been theoretically analyzed. Two structures are studied and compared: the step separate-confinement-heterostructure (SCH) SQW structure and graded-index (GRIN) SCH-SQW structure.

For the designs studied (Fig. 1 and 2), the optimal doping and thickness of the p-cladding layers have been determined to be $6 \times 10^{17} \text{ cm}^{-3}$ and 2 μm respectively. For well width of 80 Å and carrier injection of $15 \times 10^{17} \text{ cm}^{-3}$, the electron lifetime is 3.75 ns in the step SCH-SQW and only 2.80 ns in the GRIN-SCH-SQW. For the same carrier injection and well width, the calculated injection efficiency is also higher in the GRIN-SCH-SQW: 85.3% in the GRIN-SCH-SQW and 80.4% in the step SCH-SQW. It has also been found that the QW energy levels, spontaneous lifetime and injection efficiency in a GRIN-SCH-SQW have no dependence on the GRIN thickness.

In conclusion, calculations have shown that the GRIN-SCH-SQW is superior to the step SCH-SQW in terms of spontaneous emission rate and injection efficiency.

REFERENCES

1. F. A. Kish, "Highly reliable and efficient semiconductor wafer-bonded AlGaInP/GaP light-emitting diodes", *Electronic Letters*, **32**, pp. 132-134, 1996.
2. D. A. Vanderwater, "High-Brightness AlGaInP Light Emitting Diodes", *Proceedings of the IEEE*, **85**, pp. 1752-1764, 1997.
3. S. J. Chang, "AlGaInP multiquantum well light-emitting diodes", *IEEE Proceedings – Optoelectronics*, **144**, pp. 405-409, 1997.
4. B. Jonsson et al., "Solving the Schrodinger equation in arbitrary quantum-well potential profiles using the transfer matrix method", *IEEE Journal of Quantum Electronics*, **26**, pp. 2025-2035, 1990.
5. A. K. Ghatak et al., "A novel numerical technique for solving the one-dimensional Schrodinger equation using

- matrix approach – Application to quantum well structures”, *IEEE Journal of Quantum Electronics*, **24**, pp. 1524-1531, 1988.
6. P. J. Stevens et al., “Computer modeling of the electric field dependent absorption spectrum of multiple quantum well material”, *IEEE Journal of Quantum Electronics*, **24**, pp. 2007-2016, 1990.
 7. G. Bastard, “Superlattice band structure in the envelop-function approximation”, *Physical Review B*, **24**, pp. 5693-5697, 1981.
 8. F. Capasso, *Heterojunction Band Discontinuities – physics & device applications*, Elsevier Science Publishers, 1987.
 9. G. P. Agrawal et al., *Long wavelength semiconductor lasers*, Van Nostrand Reinhold, 1986.
 10. J. Rennie et al., “High temperature (74 °C) CW operation of 634 nm InGaAlP laser diodes utilizing a MQW”, *IEEE Journal of Quantum Electronics*, **29**, pp. 1857-1862, 1993.
 11. S. R. Chinn, “A Model for GRIN-SCH-SQW Diode Lasers”, *IEEE Journal of Quantum Electronics*, **24**, pp. 2191-2214, 1988.
 12. P. K. Basu, *Theory of Optical Processes in Semiconductors – Bulk and Microstructures*, pp. 275, Oxford University Press, 1997.
 13. T. Yokotsuka et al., “Growth of heavily Be-doped AlInP by gas source molecular beam epitaxy”, *Applied Physics Letters*, **58**, pp. 1521-1523, 1991.
 14. D. P. Bour et al., “Drift Leakage Current in AlGaInP Quantum-Well Lasers”, *IEEE Journal of Quantum Electronics*, **29**, pp. 1337-1342, 1993.

Intracavity piezoelectric InGaAs/GaAs laser modulator

J.P.R. David, E. A. Khoo, A.S. Pabla*, J. Woodhead, R. Grey and G.J. Rees

Department of Electronic and Electrical Engineering
University of Sheffield, Mappin St., Sheffield S1 3JD, United Kingdom

* Currently at BT Research Laboratories, Martlesham Heath, Ipswich IP5 7RE,
United Kingdom

Abstract

Integration of a laser and modulator is shown to be possible in the InGaAs/AlGaAs material system by growing on a (111)B GaAs substrate and utilising the piezoelectric effect. The absorption characteristics of the modulator section are initially red shifted due to the built-in piezoelectric field and can be easily blue shifted with applied reverse bias. Since even under lasing conditions there is found to be a significant residual piezoelectric field in the quantum well, the modulator can be biased to a shorter wavelength than the lasing emission. Utilising these effects a simple two-section laser-modulator device in which the absorber section lies within the laser cavity has been fabricated. The results show that the threshold current of the laser-modulator structure is controlled by the reverse bias voltage and hence absorption in the modulator section.

Keywords : (111)B GaAs, piezoelectric, monolithic laser-modulator, intracavity absorber

1. Introduction

An important function in an optical communication system is the ability to modulate a light source at high speed in order to transmit data at large bit rates. At moderate data rates this can be done by directly modulating the semiconductor laser [1]. However at very high transmission rates over long distances the performance of directly modulated semiconductor lasers is limited by frequency chirp [2]. This phenomenon is the result of changes in the carrier density of the laser due to amplitude modulation and this in turn induces changes in the refractive index which also produces a phase modulation. The phase modulation leads to a frequency broadened pulse signal and hence degrades the transmission capability. To overcome this problem a scheme employing an external modulator is normally adopted with the laser continuously pumped [3]. A further improvement to this scheme is to integrate the laser and modulator monolithically in order to improve the optical coupling and achieve optoelectronic integration [4-9].

To realise this combination the absorption of the modulator section must be sufficiently controllable at the lasing wavelength to turn the laser on and off. In a conventional (001) device this requires selective area epitaxy or QW intermixing to shift the absorption edge of the modulator to the blue of the lasing wavelength [4-7]. The absorption edge can then be red-shifted back by the quantum-confined Stark effect (QCSE) to modulate the emission. Other methods rely on the built-in potential of the *p-n* junction in the modulator section which creates a field that red-shifts the absorption edge of the QW [8,9]. Since a conventional laser normally lases below the *e1-hh1* transition energy at flat-band [10], modulation of the laser light can be achieved by forward biasing the modulator section slightly in order to blue shift its absorption edge to produce a normally-off laser-modulator. However this method provides only a moderate contrast ratio because of the residual absorption in the modulator section and has the further disadvantage that carriers will be injected into the forward biased modulator which will affect the modulation speed when trying to extract the injected carriers.

In this paper an integrated laser-modulator using the novel piezoelectric effect in strained structures grown on (111)-oriented substrates will be described. This technique eliminates the need for the complex steps of disordering or regrowth of the QW to produce an integrated laser-modulator. The modulator section operates by conventional reverse biasing and an improvement in the contrast ratio over that of the conventional (001) device can be achieved by reducing the residual absorption at the lasing wavelength.

2. Background theory

Strained $\text{In}_x\text{Ga}_{1-x}\text{As}$ quantum wells grown on (111) GaAs will have a built-in piezoelectric field owing to the polar nature of the zinc-blende crystal [11]. This internal electric field can be as large as 10^7 V/m for 1% mismatch. The presence of the large electric field in the well will tilt the energy bands and separate the electron and hole wavefunctions, thus reducing the optical absorption and red-shifting the transitions (see Fig. 1). However these effects can be reversed by applying an appropriate bias opposing the well field, blue-shifting the absorption edge and restoring the wavefunction overlap [6]. The electric field in the quantum well can also be reduced by screening from charge injected into the well. Consequently spontaneous emission from piezoelectric lasers will blue-shift with injection current and at threshold the laser will emit at a wavelength shorter than if the internal field were unscreened [12,13]. Nevertheless it has been shown that even at carrier densities corresponding to lasing, there still remains a significant field in the quantum well [13,14]. This implies that the lasing wavelengths of piezoelectric lasers lie to the red of their $e1\text{-}hh1$ transition flat-band values.

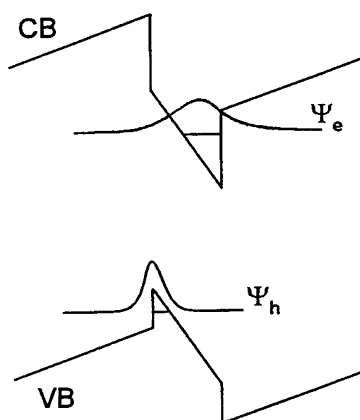


Fig. 1 Energy band diagram of a piezoelectric quantum well. The strained generated piezoelectric field in the well separates the electron and hole wavefunctions (Ψ_e and Ψ_h) and red shifts the optical transitions from the flat-band condition.

3. Growth and material characterisation

The growth on (111)B substrates is a major problem, limiting the development of piezoelectric devices. Unlike growth on (001) the exact misorientation angle of the (111) substrate, the III-V ratio and growth temperature are all important in determining surface morphology [10,11]. Previous work by us has shown that growth on n^+ (111)B GaAs substrates misoriented 2° towards $[2\bar{1}1]$ by conventional solid-source molecular beam epitaxy [12] can produce very high quality laser structures.

In our device the same single quantum well separate confinement heterostructure laser structure also acts as the modulator section. Growth was undertaken on the n^+ (111)B GaAs substrate with a layer sequence as follows: initially a 500\AA n^+ GaAs buffer was grown followed by $2\mu\text{m}$ of $n\text{-Al}_{0.66}\text{Ga}_{0.34}\text{As}$ and 1000\AA undoped $\text{Al}_{0.66}\text{Ga}_{0.34}\text{As}$ to form the lower

waveguide cladding layers, an active region consisting of an undoped $\text{In}_{0.2}\text{Ga}_{0.8}\text{As}$ strained quantum well (100Å) sandwiched between two undoped GaAs barriers (1000Å each) and a further 1000Å of undoped $\text{Al}_{0.66}\text{Ga}_{0.34}\text{As}$ and 1µm $p\text{-Al}_{0.66}\text{Ga}_{0.34}\text{As}$ as the upper cladding layers. Finally a 2000Å thick p^{++} GaAs capping layer was grown to reduce the contact resistance. The InGaAs quantum well was grown at a lower temperature of 530°C to avoid indium desorption while the AlGaAs cladding layers and the GaAs layers were grown at higher temperatures of 620°C and 605°C respectively to ensure smooth morphology of the finished surface

To characterise the material, photoluminescence (PL) measurements were undertaken at room temperature (RT, 293K) and at 10K using a closed loop helium cryostat. The excitation source used was the 514nm line of an argon ion laser and the PL was detected by a cooled Ge detector after being dispersed by a 0.5m monochromator. The spectra obtained are shown in Fig. 2. The RT PL spectra shows a peak at about 1020nm but several higher order transitions can also be clearly seen [15]. This is due to the fact that the large piezoelectric field relaxes the symmetry selection rule so that normally forbidden transitions are possible. As the temperature is reduced, these higher sub-bands cease to be populated and at 10K all the carriers relax to the lowest e1-hh1 level and only one peak is observed.

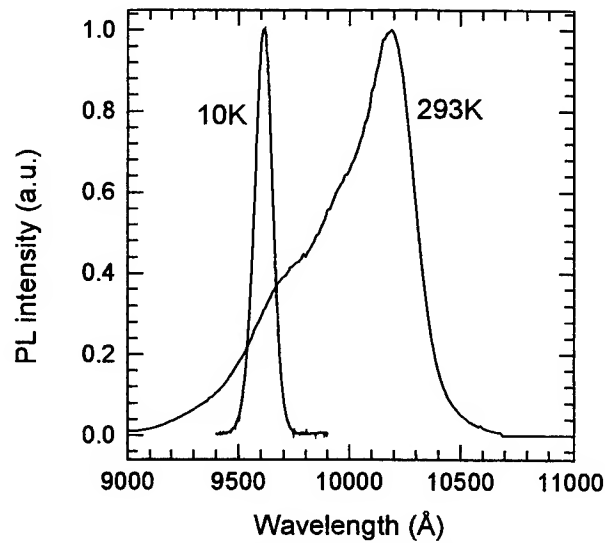


Fig. 2 293K and 10K photoluminescence spectra of the piezoelectric laser structure.

4. Device characterisation

Before making an integrated laser-modulator from this structure we need to understand its emission spectrum as a function of current injection and also of its absorption spectrum as a function of reverse bias. Broad area lasers previously fabricated from this material have shown a very low threshold current density (J_{th}) of 87A/cm² [12] suggesting that with optimised growth, the material is comparable to (001) devices. To study the lasing and spontaneous emission characteristics from the same device, 100µm wide broad area stripe lasers with narrow top optical windows (~10µm wide, 200µm long) were fabricated using Au-Zn for the top contact. To check that the unmetallized window was not resulting in any inhomogeneous current spreading, devices with full metal top contacts were also fabricated and similar threshold current and lasing characteristics were obtained. Emission from the top optical window reflects the spontaneous emission spectrum of the quantum well without being affected by the wavelength dependent absorption of the waveguide as in the case of edge emission [14].

Two sets of devices with top windows and of similar dimensions were fabricated. One set had parallel facets (410µm long) and one had non-parallel facets (a trapezium with sides of length 500µm and 320µm). The dependence of the spontaneous emission e1-hh1 peak position on injection current for both structures is shown in Fig. 3. As current is injected, the carriers start to screen the quantum well field and the e1-hh1 transition from both devices blue shift. The e1-hh1 transition

stops blue-shifting in the structure with parallel facets once threshold is reached since its carrier concentration is then pinned. However since lasing is suppressed in the device with non-parallel facets by poor feedback the e1-hh1 transition continues to blue-shift beyond the wavelength of the lasing device, indicating that the well field in the laser is only partially screened even at threshold, in agreement with previous studies [13,14]. A comparison of the edge emission to the spontaneous emission measurements from the top optical window in the piezoelectric stripe lasers show that the lasing wavelength is always longer than the e1-hh1 transitions, similar to observations in (001) lasers [10].

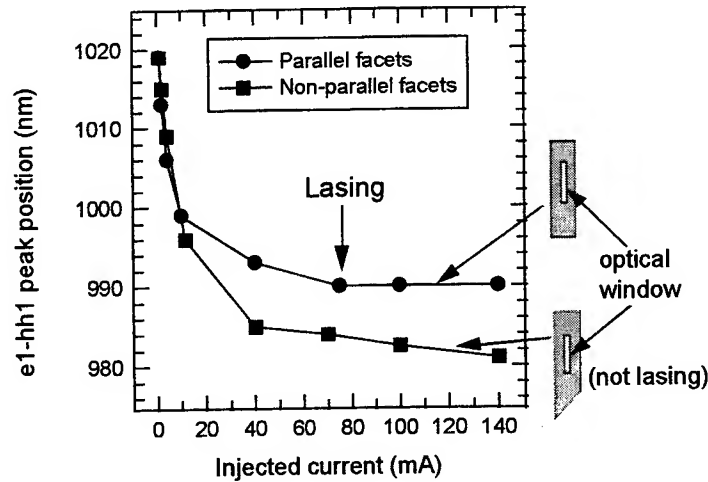


Fig. 3 e1-hh1 peak positions as observed from the spontaneous emission from top optical windows ($\sim 10\mu\text{m}$ wide) of two similar dimensioned devices (one with parallel laser facets, the other with non-parallel facets) as a function of injected current.

The gain spectrum of a laser depends on its carrier density and the gain peak which determines the lasing wavelength increases in energy as the threshold current density increases due to band filling effects. As the laser cavity becomes longer, the threshold gain reduces as the mirror loss term becomes less important. Short cavity lasers will therefore lase at shorter wavelengths and this effect should be observed for both conventional (001) as well as piezoelectric lasers.

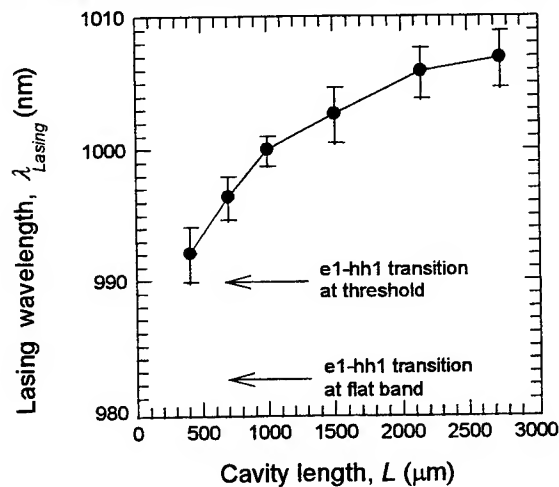


Fig. 4 Lasing wavelength versus cavity length of piezoelectric lasers. Also shown are the e1-hh1 peak position at lasing threshold and at flat-band.

Fig. 4 shows the dependence of the lasing wavelength, λ_L on cavity length, L for this piezoelectric structure. As expected λ_L increases with L due to the reducing threshold carrier concentration. Also shown in the figure is the approximate e1-

hh1 position at lasing threshold for the various devices and the e1-hh1 position at flat-band as determined from the top optical window spontaneous emission and the photocurrent spectra. The crucial point here is that the lasing wavelength always lies to the red of the flat-band e1-hh1 transition.

It is extremely difficult to undertake absorption measurements in a waveguide modulator since light must be coupled into the waveguide and the absorption would be non-uniform along its length. An easier alternative is to use *p-i-n* diode mesas with top optical windows fabricated from material adjacent to the lasers and measure their bias-dependent photocurrent spectra. Fig. 5 shows bias-dependent photocurrent spectra measured in mesa diodes fabricated from two similar InGaAs laser structures, one grown on a conventional (001) GaAs substrate and the other on the (111)B GaAs substrate. A clear difference between the red shifting (001) spectra with increasing reverse bias due to the QCSE and the blue shifting spectra in the piezoelectric structure can be seen. Also shown in the figure is the typical lasing wavelength for these structures. Although emission from the (001) laser will encounter a reducing absorption with increasing reverse bias, there will always be a significant residual absorption in the modulator section as shown, reducing the available absorption change and hence its contrast ratio. In the case of the piezoelectric quantum well the absorption edge shifts to the blue as the applied reverse bias reduces the well field, in contrast to the conventional (001) device behaviour. Consequently at the lasing wavelength indicated by the arrow the absorption initially *increases* with reverse bias. The peak absorption of the e1-hh1 transition in both cases are of similar magnitude. However at -6V, when the quantum well is close to flat band, the absorption at the lasing wavelength is at a minimum and the modulator produces little residual absorption. This combination of lasing and absorption characteristic in the same piezoelectric structure provides a simple alternative strategy for fabricating integrated laser-modulators.

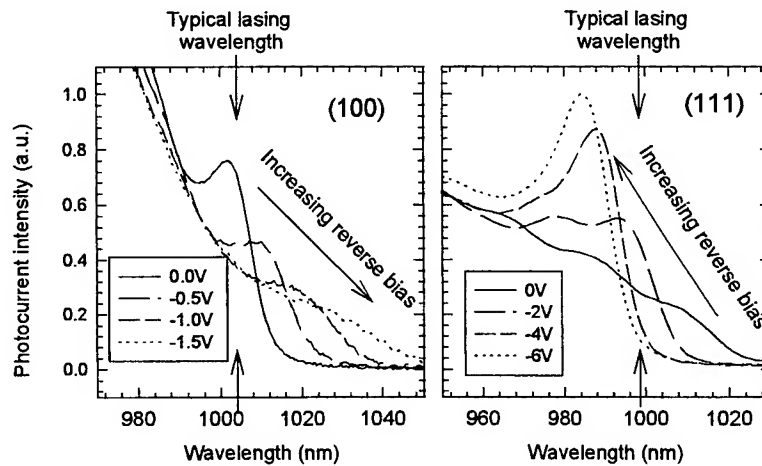


Fig. 5 Bias dependent photocurrent spectra measured in *p-i-n* mesa diodes of two similar laser structures grown on (001) and (111) GaAs substrates. The difference in applied voltage range is due to the different intrinsic region thickness. Note the difference in applied voltage range is caused by different intrinsic thickness.

5. Device implementation and results

In order to demonstrate the operating principle of the device, a simple laser with an intracavity absorber was fabricated in which the gain and absorption sections are combined within the same optical cavity. The metalisation was as for the laser fabrication but with a discontinuous top metal contact stripe separating the gain and absorption sections. The width of the electrodes was 50 μ m and they were separated by 20 μ m of bare semiconductor. This whole structure was then chemically etched to form a long stripe laser. The two top metal contact sections were then isolated electrically by wet-etching approximately 0.5 μ m into the *p*-doped AlGaAs cladding layer between them to form a trench. This creates a resistance of around 5 k Ω between the laser and modulator sections. The stripes were subsequently cleaved into two-section devices of different lengths in which the active and passive sections were around 500 μ m and 300 μ m long respectively (Fig. 6 (a)).

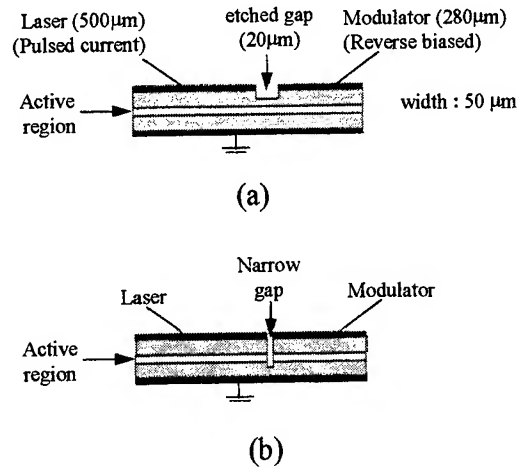


Fig. 6 (a) Schematic diagram of the laser with an intracavity absorber configuration. (b) Ideal integrated laser-modulator schematic diagram with external modulation.

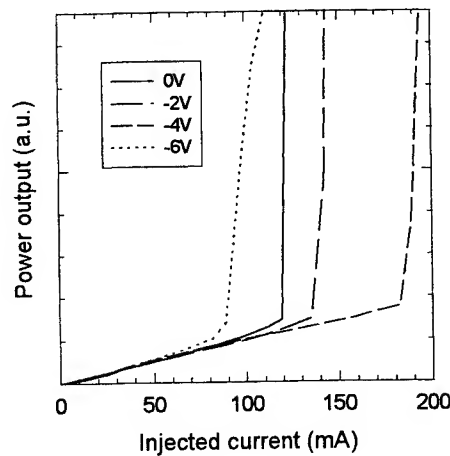


Fig. 7 *L-I* curves for the piezoelectric laser-modulator for different biases on the modulator section.

The fabricated devices were tested by injecting pulsed current ($1\mu\text{s}$ width, 1% duty cycle) into the gain section while the absorber section was subjected to DC reverse bias. The resulting light-current (*L-I*) curves of the laser with an intracavity absorber for various reverse bias voltages are shown in Fig. 7. At zero bias, the device can overcome the losses in the passive section and lase when enough current is injected into the active section. This is not surprising since the absorption at 0V of the absorber section is quite small as the electron and hole states are spatially separated by the large piezoelectric field. The 'sudden' light jump in the *L-I* characteristic is a typical lasing characteristic for this type of laser with an intracavity absorber [16]. With increasing absorber reverse bias, the threshold current first increases because of the increased absorption as shown in Fig. 5 and approaches a maximum at about -4V . However with further increase in absorber reverse bias the threshold current decreases and becomes a minimum at -6V , corresponding to the minimum absorption at the lasing wavelength of the structure. This type of lasing characteristic is unique to the piezoelectric structure and is not observed in conventional (001) devices. At higher levels of injected current, the bias-dependent *L-I* behaviour becomes complex, possibly due to the effects of absorption saturation in the coupled passive region within the cavity. This behaviour is currently under investigation.

Ideally the proposed monolithically integrated laser-modulator should be implemented as in Fig. 6(b) whereby the laser and modulator sections are isolated completely through reactive ion etching to form a narrow gap of a few micron apart in

order to get a good coupling between the two sections. To suppress any effects of absorption saturation on the active section, it may be necessary to antireflection-coat the other facet of the modulator to inhibit optical feedback into the active section. Modulation speed is expected to be comparable with that of conventional laser-modulators. Chirp, associated with variations in threshold carrier concentration as the loss in the passive section is modulated, will only be suppressed if feedback is inhibited by coating the exit facet of the modulator. It is expected that this approach will be applicable to the piezoelectric system of strained InGaAs on (111)B InP substrate where telecommunication applications are of interest [17].

6. Conclusions

This work shows that utilising the piezoelectric effect allows us to form a simple integrated laser-modulator without any difficult processes. The device relies on the fact that the lasing wavelength of piezoelectric lasers is always red-shifted from the fundamental transition at flat band because of the partial screening of the well-field at threshold. The lasing wavelengths in the piezoelectric lasers also increase with cavity length in a similar manner to the conventional (001) devices as the threshold current density decreases. The absorption of the piezoelectric modulator at these lasing wavelengths can then be altered by the applied reverse bias so that the laser can be turned on or off.

Acknowledgements

This work is supported by the EPSRC under grant GR/L11984 and the EU GHISO project. EAK is grateful to the University of Sheffield for financial support and CVCP for an ORS award.

References

- [1] J.D. Ralston, S. Weisser, K. Eisele, R.E. Sah, E.C. Larkins, J. Rosenzweig, J. Fleissner, and K. Bender : 'Low-bias-current direct modulation up to 33 GHz in InGaAs/GaAs/AlGaAs pseudomorphic MQW ridge-waveguide lasers', *IEEE Photon. Technol. Lett.*, 1994, **6**, (9), pp. 1076-1079
- [2] R.A. Linke : 'Modulation induced transient chirping in single frequency lasers', *IEEE J. Quantum Electron.*, 1985, **QE-21**, (6), pp. 593-597
- [3] R.C. Alferness : 'Waveguide electrooptic modulators', *IEEE Trans. Microwave Theory Tech.*, 1982, **MTT-30**, (8), pp. 1121-1137
- [4] M. Suzuki, Y. Noda, H. Tanaka, S. Akiba, Y. Kushiro, and H. Isshiki : 'Monolithic integration of InGaAsP/InP distributed feedback laser and electroabsorption modulator by vapor phase epitaxy', *J. Lightwave Technol.*, 1987, **LT-5**, (9), pp. 1277-1285
- [5] G. Raybon, U. Koren, M.G. Young, B.I. Miller, M. Chien, T.H. Wood, and H.M. Presby : 'Low chirp transmission at 5.0Gbit/s using an integrated DBR laser-modulator transmitter', *Electron. Lett.*, 1994, **30**, (16), pp. 1330-1331
- [6] R.M., Lammert, D.V. Forbes, G.M. Smith, M.L. Osowski, and J.J. Coleman : 'InGaAs-GaAs quantum-well lasers with monolithically integrated intracavity electroabsorption modulators by selective-area MOCVD', *IEEE Photon. Tech. Lett.*, 1996, **8**, (1), pp. 78-80
- [7] J. Werner, E. Kapon, N.G. Stoffel, E. Colas, S.A. Schwarz, C.L. Schwartz, and N. Andreadakis : 'Integrated external cavity GaAs/AlGaAs lasers using selective quantum well disordering', *Appl. Phys. Lett.*, 1989, **55**, (6), pp. 540-542
- [8] R.L. Thornton, W.J. Mosby, and T.L. Paoli : 'Monolithic waveguide coupled cavity lasers and modulators fabricated by impurity induced disordering', *J. Lightwave Technol.*, 1988, **6**, (6), pp. 786-792
- [9] S. Tarucha and H. Okamoto : 'Monolithic integration of a laser diode and an optical waveguide modulator having a GaAs/AlGaAs quantum well double heterostructure', *Appl. Phys. Lett.*, 1986, **48**, (1), pp. 1-3
- [10] P. Blood : 'Stimulated emission in quantum well laser-diodes', *Appl. Phys. Lett.*, 1989, **55**, pp. 1-3
- [11] D.L. Smith : 'Strain-generated electric fields in [111] growth axis strained-layer superlattices', *Solid State Commun.*, 1986, **57**, pp. 919-921

- [12] E.A. Khoo, A.S. Pabla, J. Woodhead, J.P.R. David, R. Grey, and G.J. Rees : 'Low threshold InGaAs/AlGaAs lasers grown on (111)B GaAs substrate', *Electron. Lett.*, 1997, **33**, pp. 957-958
- [13] A.S. Pabla, J. Woodhead, E.A. Khoo, R. Grey, J.P.R. David, and G.J. Rees : 'Partial screening of internal electric fields in strained piezoelectric quantum well lasers: Implications for optoelectronic integration', *Appl. Phys. Lett.*, 1996, **68**, pp. 1595-1597
- [14] C. Cooper, D.I. Westwood, and P. Blood : 'Laser diodes in piezoelectric quantum well structures', *Appl. Phys. Lett.*, 1996, **69**, pp. 2415-2417
- [15] R.A. Hogg, T.A. Fisher, A.R.K. Willcox, D.M. Whittaker, M.S. Skolnick, D.J. Mowbray, J.P.R. David, A.S. Pabla, G.J. Rees, R. Grey, J. Woodhead, J.L. Sanchez-Rojas, G. Hill, M.A. Pate, and P.N. Robson : 'Piezoelectric-field effects on transition energies, oscillator strength, and level widths in (111)B-grown (In,Ga)As/GaAs multiple quantum well', *Phys. Rev. B*, 1993, **48**, (11), pp. 8491-8494
- [16] W.X. Zou, D.B. Young, K-K. Law, and J.L. Merz : 'Low threshold InGaAs/GaAs/AlGaAs quantum well laser with an intracavity optical modulator by impurity-induced disordering', *Appl. Phys. Lett.*, 1993, **62**, pp. 556-558
- [17] A.S. Pabla, M. Hopkinson, J.P.R. David, E.A. Khoo, and G.J. Rees : 'Electroabsorption modulation in strained piezoelectric InGaAs/InP multi-quantum wells operating at $\lambda \approx 1.55 \mu\text{m}$ ', *Electron. Lett.*, 1994, **30**, pp. 1707-1708

SESSION 4

Semiconductor Device Processing

QUANTUM WELL INTERMIXING : FROM VISIBLE TO FAR-IR WAVELENGTH APPLICATIONS

E. Herbert Li

Department of Electrical and Electronic Engineering,

University of Hong Kong,

Pokfulam Road,

Hong Kong.

ABSTRACT

The Diffused Quantum Well (DFQW) structures created by both impurity induced and impurity free or vacancy promoted processes have recently been advanced to a higher level. The interdiffusion mechanism is no longer confined to two constituent atoms, but consists of two or multiple phase interdiffusion as well as multiple species, such as three cations interdiffusion and two pairs of cation-anion interdiffusion. Results show that the outcome of these interdiffusions is quite different. For instance, both compressive or tensile strain materials and both blue or red shifts in the bandgap can be achieved dependent on the type of interdiffusion. The advantage of being able to tune the material properties allows the realizations of higher performance lasers and modulators. Two lasing wavelengths (60 nm apart) are produced at $\lambda \approx 1.55\mu\text{m}$, on the same substrate, with threshold currents of 290mA, and an extremely large relative reflectance change (over 10000) is predicted with power consumption reduced by 67%. A six fold enhancement of the third order susceptibility over that of the bulk materials can be achieved by using the inter-subband transitions in the DFQW at $\lambda \approx 10\mu\text{m}$. Broadband (1000nm) detectors have also been realized due to the wide DFQW spectral bandwidth. Several state-of-the-art results of the DFQW will be summarized with an emphasis on the future developments and directions of the DFQW.

1. INTRODUCTION

Diffused quantum well (DFQW) is a non-square quantum well produced by interdiffusion of constituent atoms through the heterointerface. In the literature, DFQW is also referred to as quantum well mixing or intermixing (QWI) and quantum well disordering. Extensive work has recently been focused on the application of DFQWs since they provide post-growth tuning of the device operating wavelengths. The DFQWs can also be produced by a controlled interdiffusion process, which allows the rate of diffusion to be varied. This enables a selective area quantum well intermixing technology to laterally confine light for waveguiding. The process of achieving optical lateral confinement includes impurity induced disordering (IID) and impurity-free vacancy diffusion (IFVD). Performance of devices using DFQWs can also be improved and contribute to easy and effective realization of photonic integrated circuits.

The first work¹ on DFQW reported that Zn diffusion into an AlAs-GaAs superlattice, or into $\text{Al}_x\text{Ga}_{1-x}\text{As}$ -GaAs quantum well heterostructures can enhance the Al-Ga interdiffusion rate at the heterointerfaces and create uniform compositionally disordered $\text{Al}_x\text{Ga}_{1-x}\text{As}$ even at lower temperature. Following this, the disk-shaped IR-red GaAs-AlAs superlattice lasers were demonstrated (cw 300K), which were monolithically integrated into rectangular yellow-gap $\text{Al}_x\text{Ga}_{1-x}\text{As}$ cavities.² This process had become a first patent base on QW mixing.

In recent years, great effort has been put in using DFQW as a tool. Last year, several remarkable papers on lasers and modulators using DFQWs were published. For instance, the fabrication of multiple wavelength lasers and multi-channel wavelength division multiplexers in GaAs/AlGaAs structures have been achieved using the technique of "selective intermixing in selected area" (SISA), based on IFVD.³ Buried InGaAs/InP quantum wires with width down to 15nm was fabricated by lateral barrier modulation. The key technique involved was the local removal of the InP top barrier layer of the QW using high resolution electron beam lithography and selective wet chemical etching.⁴ Impurity-free disordering of InP based InGaAs/InGaAlAs QWs induced by three different dielectric thin cap films (SiO_2 , SiN_x , SrF_2) has been produced.⁵ Detail investigation of the in-plane spatial resolution of the disordering process was also developed.⁵ In fact, significant

reduction of threshold currents by IID in InGaAs/GaAs QW Ridge-Waveguide Lasers has succeeded.⁶ Vertical cavity surface emitting lasers employing a Zn diffused and disordered spatial mode filter were fabricated and tested.⁶¹ Low divergence output beam of surface emission was yielded and it is suitable for short haul optical fiber. Another device which is of interest is the superluminescent diode⁸ whose band emission spectrum is broad enough for high sensitivity in fiber optical gyroscopes. In addition, report of reviews have been made on IID by Holonyak in 1988,⁹ on the process of DFQW optoelectronics by Weiss in 1990,¹⁰ and on QWI by Marsh in 1993.¹¹

In this paper, we aim to make a comprehensive summary on the latest progress and development in DFQWs in different areas ranging from materials, production techniques, diffusion mechanisms, to device applications.

2. TECHNIQUES FOR MODIFYING INTERDIFFUSION RATES IN QWs

2.1. Ion Implantation

Ion Implantation is a technique in which direct injection of ionized, energetic atoms or molecules into a solid is employed. The ions injected will carry energies ranging from a few keV to several MeV, and implant doses from 10^{10} to more than 10^{16} ions/cm². Using small implantation energy, the damage introduced to the lattice structure will be reduced but with a decrease in the penetration depth, while with small dose of implants, there will be lesser enhancement of diffusion rate.

Ion Implantation will significantly enhance the interdiffusion rate, and control the lateral and vertical depth of diffusion precisely. Different combinations of ions and substrates are possible and the most commonly used ones are p-type ions (Zn, Be), n-type ions (Si), neutral type ions (O), and constituent ions (Al, Ga, As) in AlGaAs/GaAs. It was reported that the use of neutral ions (including constituent ions) can prevent the production of free carriers induced by the charged ions (n-type or p-type) which will introduce propagation loss and thus reduce the refractive index of the intermixed QW materials.⁴⁹ Recent application of different implants are discussed as follows.

Interdiffusion of Al-Ga in an Al_{0.3}Ga_{0.7}As/GaAs superlattice with focused-ion-beam implantation using Si has recently been studied.¹² This implantation technique provides maskless process with high spatial resolution and so, it enables precise patterning on the wafer for optoelectronics integrated circuits (OEIC) applications. Si ions are accelerated to 50 and 100 keV, and with rapid thermal annealing (RTA) at 950 °C for 10s. The diffusion coefficient was extracted to be 4.5×10^{-14} cm²/s (with a Si ion dose of 1×10^{14} cm²) and in comparison with RTA, which can only produce an interdiffusion coefficient of 1.3×10^{-16} cm²/s. This implies a 2 order magnitude enhancement.

In terms of constituent implantation, implanted gallium into both GaAs/AlGaAs and InGaAs/GaAs QWs have been performed and no significant effect on the diffusion coefficients was found in either systems. For arsenic implantation, the GaAs/AlGaAs system behaved identically to the Ga implanted sample, while in InGaAs/GaAs a region of enhanced interdiffusion was found, where the diffusion coefficient was enhanced by one order of magnitude.¹³

Photoluminescence of low-energy, low dose oxygen ion implantation into AlGaAs/GaAs QWs has been studied.¹⁴ Results showed that significant intermixing of both single and multiple AlGaAs/GaAs QWs has been achieved using 155 keV implantation energy with doses as small as 5×10^{13} cm⁻² after a moderate annealing step. A PL peak shift of 139 meV was observed in a 100Å GaAs QW after implanting 10^{14} cm⁻² oxygen ions at 155 keV and annealed at 1050 °C for 40s, while a shift of up to 100 meV was obtained in the MQW with a dose of 8×10^{14} cm⁻² ions at 450 keV with annealing at 950 °C for 120s.

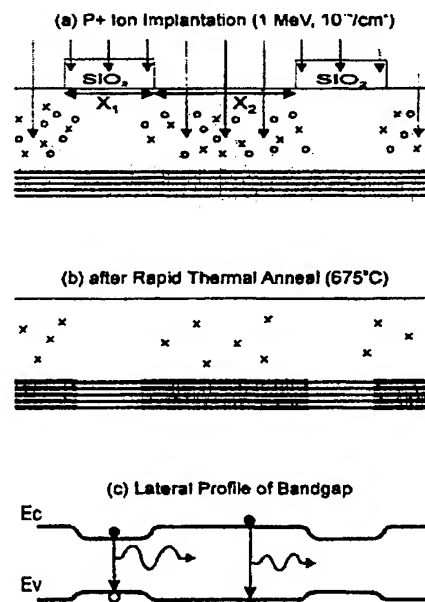


Figure 1 Schematic cross section through a sample illustrating selective area intermixing of five quantum wells located 1.77 μm below the surface: (a) ion implantation of P⁺ ions using a patterned 2.0 μm thick silicon dioxide mask; (b) after rapid thermal annealing, QW's underneath implanted regions and near the edges of masked regions have been intermixed; (c) the resultant change in the band-gap energy of the QW's along the lateral direction.

Quantum well intermixing using high-energy ion implantation is a promising technique for laterally selective, post-growth modification of a quantum well structure.⁴³ The lateral selectivity of the technique is a function of the ion straggling during implantation and the lateral diffusion of defects during post-implantation annealing, see Fig. 1. Low temperature photoluminescence was used to monitor the intermixing of quantum wells. A significant amount of intermixing, which resulted in a 57nm blueshift of the QW bandgap energy, was observed when the mask stripe width was less than 5 μ m, thus giving a lateral selectivity of 2.5 μ m.

In spite of these advantages, however, ion implantation technique will introduce more lattice damage and a large amount of defects in the materials. In order to reduce lattice damages, implantation energy is limited and thus, the penetration depth will be reduced.

2.2. Impurity Diffusion with Rapid Thermal Annealing

RTA is an essential step in impurity diffusion. Since impurity diffusion process undergoes a very slow rate on its own at conventional conditions, RTA is therefore used to promote its diffusion rate. RTA under temperature ranging from 900 to 1125 °C leads to substantial increase in interdiffusion rate. Most of the annealing is usually performed in the range from 400 to 1000 °C, and under a chemical environment with N₂ or even in vacuum to prevent oxidation to occur.

Marsh has demonstrated a method of RTA,¹¹ in which fluorine-implanted SCH and GRIN samples were capped with 1000Å of either SiO₂ or Si₃N₄ deposited by plasma-enhanced chemical vapour deposition. RTA is then performed at different temperatures (650 to 750 °C) in a nitrogen atmosphere. A more recent RTA experiment was performed in 1996 by Bacher which consists of samples annealed for one minute between 450 and 750 °C under a continuous flux of nitrogen to avoid surface oxidation.¹⁵

There is a report on a novel application of impurity diffusion.⁵⁰ The structure used is a 80-period GaAs/AlAs superlattice with each layer 34 Å thick, Si doped and annealed at 800 °C with a carbon source for 3 hours. PL spectra showed that the magnitude of the intermixing of Al and Ga increases with depth which is in contrast with the intermixing mechanism considering vacancy injection from the surface. This is because in theory, the diffusion coefficient of carbon is very small and hence carbon remains mainly at the surface of the MQW. Reduction of Si diffusion speed is mainly due to the combination of Si and carbon. As a result, the intermixing coefficient is small at the surface and increase gradually with depth.

The influence of RTA on the performance characteristic of GaInP/AlGaInP QW lasers which were grown by all-solid-source molecular-beam-epitaxy has been studied.⁴⁴ It was found that when the laser structure were annealed the threshold current density of the lasers decrease significantly. Another study on the influence of growth conditions on Al-Ga interdiffusion in low-temperature grown AlGaAs/GaAs MQW were characterized by photoluminescence (PL) spectroscopy.⁴⁵ The enhancement of interdiffusion was found to be strongly dependent on the growth and annealing conditions.

In general, flexibility of easy alteration of the compositional profile inside the material is made possible in impurity diffusion. However, unintentional intermixing may take place in regions other than those implanted and precise depth control cannot be achieved with this diffusion method. The volume concentration of impurity drops during interdiffusion and will eventually drop below the threshold concentration at which the implantation enhanced disordering occurs.

2.3. Impurity Free Vacancy Diffusion (IFVD)

The mechanism of IFVD requires the encapsulation of MQW samples by a dielectric cap such as SiO₂ or Si₃N₄ and then annealing at high temperature around 850 °C ~ 900 °C for 30 to 180 seconds. This will lead to out-diffusion of Ga into the cap and vacancies are generated on the group III sublattice that diffuse to the barriers and promote the interdiffusion in the MQWs. By using different combination of caps, selective area bandgap control is possible.

An experiment on IFVD¹⁶ was performed to investigate whether Ga vacancy is generated during SiO₂ capping and annealing. A uniformly Si doped GaAs epilayer of 10 μ m thick with $n = 4.8 \times 10^{18} \text{ cm}^{-3}$ grown by MBE was studied using photoluminescence and cathodoluminescence. As a result, an increase in the strength of the emission at 1.2 eV is observed which is attributed to the Ga vacancy. This evidence shown that Ga vacancy is the species responsible for IFVD.

The degree of intermixing for an impurity free interdiffusion enhancement technique using the dielectric cap layer depended on several factors, namely encapsulating dielectric material, the deposition conditions, and thermal treatment conditions. The strength of using this technique was that it was free from the influence of the related impurity and the damages of implanted ions. The oxidized AlGaAs as the dielectric cap layer was demonstrated to be useful as a diffusion mask.⁴⁶ A thick AlAs cap layer and AlGaAs interlayer were grown as a capping layer on the top of the InGaAs/GaAs QW structure. It was observed that the QW interdiffusion rate increased with the Al composition of the $\text{Al}_x\text{Ga}_{1-x}\text{As}$ interlayer until x reached about 0.5 and then saturate for $x \geq 0.5$.

The advantage of using IFVD is that it is a simple method which requires much less equipment to perform. As discussed above in using ion implantation, only neutral species IID can circumvent the large optical propagation losses associated. However, neutral impurities still introduce substantial changes in material resistivity and trap concentrations. IFVD can create large bandgap energy shifts without these disadvantages of IID. However, using IFVD will increase the number of etching steps needed to control the thickness of SiO_2 . Moreover, control of oxygen composition in SiO_xN_y is complex.

2.4. Laser Assisted Disordering

Laser assisted disordering is a direct write process that can pattern impurity induced layer disordering. This new technique employs a highly focused Ar^+ laser beam. For fabrication of AlGaAs-GaAs DFQW,¹⁷ the laser beam with lasing wavelength of 488 nm, is scanned through the heterostructure sample which is encapsulated with a 90 nm layer of $\text{Si-Si}_3\text{N}_4$. Its scan speed can be as high as 85 $\mu\text{m/s}$. The laser beam interaction region will result in a smooth cylindrical section on the micron scale. Annealing is then applied to drive the Si into the as-grown crystal, resulting in a local mixing of the crystal layers.

In a more recent report, pulsed photoabsorption-induced disordering technique was used to selectively intermix GaInAs/GaInAsP QW structure, which was studied by the use of high spatial resolution time-resolved PL. Measurements showed that a reduction in the non-radioactive recombination time of nearly two orders of magnitude as a result of this intermixing technique.⁵³

However the LAD can required high power densities to melt the material and can thus cause an undesirable redistribution of dopants out with the active region of the device. The spatial selectivity of PAID is also limited by lateral heat flow. For monolithic integration of optical devices, this leads to poor performance as the interface abruptness is $\sim 100 \mu\text{m}$. A variation of the PAID technique, which has a better spatial resolution has been developed using a pulsed laser irradiation.⁵⁸ It involves irradiating the InP-based QW material with high-energy Q-switched Nd:YAG laser pulses. Absorption of the high energy pulses results in bond breaking and disruption to the lattice, leading to a localized increase in the density of point defects. Measurements of the spatial resolution of this pulsed PAID technique show it to be better than 20 μm .

The laser assisted technique is a flexible process for optoelectronic device and circuit fabrication. However, a direct-write system is not an optimum configuration for many applications. For example, commercial production of diode lasers is based upon high yield, high throughput techniques such as photolithography. Further improvement is required.

3. DIFFUSION MECHANISM

3.1. One Phase, Group III in $\text{A}_x\text{B}_{1-x}\text{C}$ system

Simple calculations were made under Fick's Law of diffusion to determine the composition profile $x(z)$ for $\text{Al}_x\text{Ga}_{1-x}\text{As/GaAs}$ and $\text{In}_x\text{Ga}_{1-x}\text{As/GaAs}$ QWs.¹⁸ This simple model leads to error function solutions :

$$x(z) = x_0 \left\{ R_1 - \frac{1}{2} R_1 \left[\text{erf} \left(\frac{L_z + 2z}{4L_d} \right) + \text{erf} \left(\frac{L_z - 2z}{4L_d} \right) \right] \right\} \quad (1)$$

where z is the growth axis, x_0 is the as-grown composition of the QW material, L_D is the interdiffusion length and L_z is the well thickness. For AlGaAs/GaAs QW, $R_1 = R_2 = 1$ and for InGaAs/GaAs QW, $R_1 = 0$ & $R_2 = -1$. It has been reported that this equation accounts for a wide range of diffusion coefficient values obtained in various III-V semiconductor systems.^{51,52}

On the other hand, it has been found recently that the above Fick's diffusion equation may not properly describe the interdiffusion in the InGaAs/GaAs QW with strain.¹⁹ The strain is believed to introduce changes in crystal defect concentration and thus diffusivity is also influenced by strain. Therefore, the non-Fickian equation, which is an expanded form of Fick's second law, is introduced :

$$\frac{\partial C}{\partial t} = \frac{\partial}{\partial z} \left(D_0 \exp(\kappa C) \frac{\partial C}{\partial z} \right) \quad (2)$$

where C is the indium concentration, D_0 is the diffusivity when no stress is applied, κ is the parameter indicating the degree of strain enhancement and is also a function of In concentration.

This equation has included the effects of strains empirically. The experimental PL peak shifts as a function of annealing time were well fitted by this equation. Useful parameters, such as diffusivity of InGaAs/GaAs QW were found using this equation.

3.2. One Phase, Group III only in $A_xB_{1-x}C_yD_{1-y}$

Cation interdiffusion results in the formation of an InGaP/InGaAs abrupt interface from as-grown InGaAs/InP QW. Theoretical analysis²⁵ indicates that a large strain was built up across the well during early stage of interdiffusion. The strain and its effect on the bandgap profile of the disordered structure produces a distinctive quantum confinement profile which remains abrupt even after significant interdiffusion. This phenomenon together with a diffused well width which equals to that of the as-grown QW are in contrast to other material systems such as AlGaAs/GaAs and InGaAs/GaAs. The effect of strain results in a potential buildup in the barrier near the interface at the top of the well, while it gives rise to two miniwells at the bottom of the wells. The HH and LH band-edge splitting results in two distinct HH and LH confinement profiles with different depths.

3.3. One Phase, Group III plus V in $A_xB_{1-x}C_yD_{1-y}$ system

The effect of interdiffusion on the confinement profile of the quaternary material systems has been reported recently.²⁰ The intermixing of $In_{0.53}Ga_{0.47}As/InP$ has been modeled, taking into account different interdiffusion rates on the group III and group V sublattice. Error function distribution discussed above was used to represent the composition profile. A strained QW was resulted after intermixing. Theoretical results showed that when the cation interdiffusion rate is faster than that of the anion, the ground-state (C1-HH1) transition shifts to longer wavelengths. For prolonged interdiffusion, this shift to longer wavelengths, saturates and then decreases. This is in good agreement with the reported experimental results of Zn-diffused disordering²¹⁻²³ as well as thermal annealing of InGaAs/InP QWs.²⁴ When the anion diffusion rate is faster, results showed that the effective bandgap of the diffused QW would be the C1-LH1 ground state transition which shifts to shorter wavelength with interdiffusion. The tensile strain that is induced under these disordering conditions which moves the LH ground state above the HH ground state. Results obtained from these calculations showed that the control of relative extent of cation and anion interdiffusion offers different possibilities for optoelectronic device fabrication.

3.4. Two Phase, Group V in $A_xB_{1-x}C_yD_{1-y}$ system

Mukai²⁶ has derived a formula that describes the two-phase interdiffusion mechanism of the quaternary material system which includes the different interdiffusion coefficients between layers and interfacial discontinuity of interdiffused species. The formula was applied to analyze the dependence of an interdiffusion induced energy shift on annealing time, annealing temperature and well width in InGaAsP/InP QWs. Good agreement was achieved between the calculated and measured values.

Two phase Group V sublattice interdiffusion in $In_{0.53}Ga_{0.47}As/InP$ QW was also theoretically investigated²⁷ using the same formulation with a pseudo time dependence. This model has been validated with an even better agreement with experimental results. However, perfect fitting can not be obtained and further work must be continued.

3.5. Multiple Species, Group III

The most recent analysis on multiple cations interdiffusion in $\text{In}_{0.53}\text{Ga}_{0.47}\text{As}/\text{In}_{0.52}\text{Al}_{0.48}\text{As}$ is performed using a model base on the expanded form of Fick's second law²⁸:

$$\frac{\partial C_i}{\partial t} = \sum_{j=1}^{n-1} D_{ij} \nabla^2 C_{ij} \quad (3)$$

where n = the number of diffusable species, C is the indium concentration, D_0 is the diffusivity when no stress is applied. The model is fitted to the measured concentration data in order to determine their diffusion coefficients. It was found that the Ga-Ga diffusion coefficient is relatively large in comparison to the other rates so that the Ga concentration profiles show a more broadened distribution after annealing. The In-Ga diffusion is found to be negative which gives rise to the inverse process of diffusion, causes sudden abrupt change in the In profiles at the interfaces. Again, further experimental work should be done to enable a large set of data to be fully analyzed.

4. BAND STRUCTURE

Effects of interdiffusion on the subbands in an AlGaAs/GaAs QW has been investigated theoretically²⁹ in which the subband energies and wave functions in an interdiffusion-induced AlGaAs/GaAs single quantum well structure were calculated. The confinement profile was modeled by an error function. The spatially dependent electron effective mass was taken into consideration using a non-parabolic band model derived from a fourth-order expansion in k with the coefficients determined using a 14-band calculation. The valence subband mixing between the heavy and light holes were also considered. It was found that subband properties of the nonsquare QW was different from that of the conventional SQW. First of all, the subband-edge energy will initially increase and then decrease with interdiffusion, which could be explained by the evolution of the nonsquare QW shape in terms of crossover point, which is defined as the confinement profile intersection at the well barrier interface of the as-grown and interdiffused QWs. Enhancement of interband transition is predicted for the off-diagonal selection rule at the initial stages of interdiffusion, and a reduced confinement of the wave function was also observed. Lastly, the enhancement of the lowest energy light-hole negative mass was also obtained. The non-monotonic behavior of the subband-edge energies suggested that when only the lowest interband energy was used to characterize the interdiffusion process, errors are likely to occur. Analysis has also been done on InGaAs/GaAs QW and InGaAs/InP QW structures.^{30,31}

5. FAR-IR OPTICAL PROPERTIES

The first theoretical study of the linear and nonlinear intersubband absorption coefficients in AlGaAs/GaAs DFQW was reported by Li⁵⁹ following the first observation of an interdiffusion shifted intersubband transition energy by Ralston,⁶⁰ see Fig. 2. Results indicated that the well shape variation can provide a large tuning wavelength range in the far IR region with an almost constant absorption. This DFQW structure can be used to produce a wide bandwidth detector. The DFQW structure can also provide lower leakage currents due to reduced tunneling between the wells since the barrier thickness at the ground state energy is always thicker than that at the excited state energy. Effects of interdiffusion on the intersubband optical properties in a modulated doped QW structure have also been investigated theoretically.³² Linear and nonlinear intersubband electroabsorption and the change in refractive index with different well width, doping concentration, Aluminium concentration ratio in AlGaAs/GaAs QW were studied. A wide tuning range has been predicted which can be applied to the realization of multi-color and broadband photodetector. More recently, a DFQW has been employed to predict the enhancement of the third-harmonic susceptibility to an extent that it is six times better than the case of GaAs.³³ The obtained $\chi^{(3)}$ enhancement is as high as 2700 (nm/V)^2 , as shown in Fig. 3, and may also be carefully varied to produce a tuning range. However, there are still technical problems in fabricating with a high yield and low price.

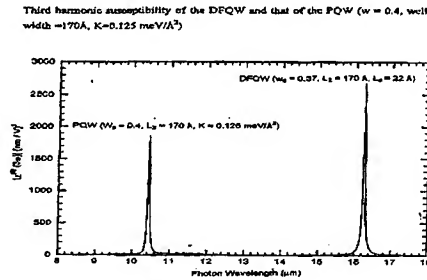


Figure 2

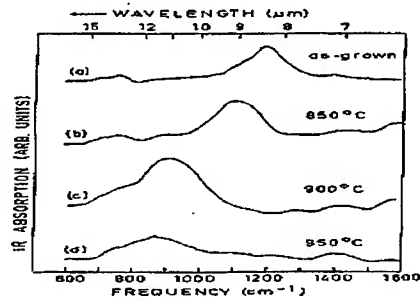


Figure 3

Figure 2 and 3 show the enhancement of $\chi^{(3)}$ in which shifting of intersubband absorption resonance occurs.

6. INTER-BAND IR OPTICAL PROPERTIES

6.1. Absorption

The most recent experimental work of partially intermixed QW waveguides is performed in 1989,³⁴ with the incident focused laser beam polarized both parallel (TE) and perpendicular (TM) to the plane of the QW layers. These spectra show the polarization anisotropy characteristic of QW absorption. In the TE spectra, both the lh and hh excitons appear while in the TM spectra, the hh exciton disappears and the lh exciton absorption strength increases. The intermixing induced band-edge shifts are clearly seen. There are theoretical studies in which a hyperbolic function has been used to model the confinement profile of a disordered $\text{Al}_{0.3}\text{Ga}_{0.7}\text{As}/\text{GaAs}$ QW⁵⁴ and results predict a different absorption spectra for the TE and TM polarization, and which is in good agreement with published measurements near the absorption edge. In a more recent investigation, theoretical calculations are performed on polarized absorption coefficients of interdiffused $\text{AlGaAs}/\text{GaAs}$ MQW.⁵⁵ Calculations were made without any approximation or presumption of the eigenstates. Results showed that for diffusion length ranging from 10 Å to 30 Å, the blue shift of the absorption edge is larger. The two dimensional QW properties were strongest in the beginning of interdiffusion.

6.2. Refractive Index

The effect of boron and fluorine IID on n_R of AlGaAs MQW was studied experimentally.³⁹ Substantial changes of > 1% in the refractive index were obtained in partially disordered material over the measured wavelength range. This implies that fluorine produces larger change than boron for similar annealing conditions. A few years later, experiment has been performed to investigate the effect of Zn IID on the refractive of $\text{AlGaAs}/\text{GaAs}$ MQWs.³⁸ This is a structure consisting of several uncoupled MQW ridge waveguides with tapered disordering across the transverse direction was employed. The refractive index changes have been deduced as a function of the Ga/Al interdiffusion length by the use of an interference technique. A maximum index change of 0.083 and 0.062 was measured for significant disordering ($L_d = 6.6$ nm) at 35 and 100 meV below the band edge energy of the as-grown MQW respectively.

Moreover, the polarization dependent refractive index for both $\text{Al}_{0.3}\text{Ga}_{0.7}\text{As}/\text{GaAs}$ and $\text{In}_{0.2}\text{Ga}_{0.8}\text{As}/\text{GaAs}$ single QWs are calculated.^{36,37} The confinement profile for the $\text{Al}_{0.3}\text{Ga}_{0.7}\text{As}/\text{GaAs}$ DFQW is modeled by an error function and n_R is determined by the real and imaginary parts of the dielectric function including contributions from the Γ , X and L Brillouin zones. It was found that at longer wavelengths, n_R decreases with increasing interdiffusion which normally provides a positive index step with respect to a less interdiffused QW. For shorter wavelengths, the wavelength range for a positive refractive index step increases as the extent of disordering between two interdiffused QWs is increasing. Polarization dependent n_R of disordered, strained $\text{InGaAs}/\text{GaAs}$ single QWs was also calculated using the same method applied to $\text{Al}_{0.3}\text{Ga}_{0.7}\text{As}/\text{GaAs}$ QW. In this calculation, decrease in refractive index with increase in the extent of disordering at longer wavelengths was observed. These structures also exhibit birefringence in a range of wavelengths from the QW band-edge to barrier band-edge, which decreases with interdiffusion.

6.3. Electro-absorption and Electro-Optic

There has been one experimental measurement on perpendicular field electroabsorption in GaAs/AlGaAs QW structures³⁴ which have been modified via partial interdiffusion of the well and barrier layers. Quantum well Stark effect has been observed in the DFQW where the room temperature exciton peaks are blue shifted by at least 40 meV via partial layer interdiffusion. On the other hand, the Quantum well Stark effect has also been analyzed theoretically in an AlGaAs/GaAs DFQW. Results showed a twofold enhancement of the Stark shift for the interdiffused QW over that of the square QW for the same 50 kV/cm applied field.⁵⁶ Excitonic absorption peak also shows a much larger reduction with increasing applied field in the more extensively DFQWs. These characteristics may be used to realize optical modulators with high on/off ratio and lower drive voltage.

In 1995, electric field induced refractive index change and absorption coefficient change in TE polarization are analyzed at room temperature for various interdiffusion modified $\text{Al}_{0.3}\text{Ga}_{0.7}\text{As}/\text{GaAs}$ QWs was also studied.³⁵ For small and medium interdiffusion lengths with fields of 100 and 50 kV/cm, respectively, improved chirping and electroabsorption can be obtained. In addition, in a selected set of interdiffusion lengths and fields, the material can be used for an electroabsorption modulator with reduced chirping in a wide range of operation wavelengths.

6.4. Optical Gain

Analyses are performed on laser gain and current density at room temperature for intermixed $\text{Al}_{0.3}\text{Ga}_{0.7}\text{As}/\text{GaAs}$ single quantum well structures.⁴¹ It was observed that small amount of intermixing will not affect the lasing quality much. Both the peak gain and current density remain about the same strength. However, for larger amount of intermixing, the lasing will diminish. A wide wavelength tuning range of 55 nm can be obtained without greatly affecting the quality of the lasing properties. Application of selective disordering to integrated optoelectronics devices on a planar substrate can be achieved.

7. DEVICES

The realization of gain coupled Distributed Feedback (DFB) lasers using the method of masked implantation induced QW intermixing was demonstrated.⁵⁷ The combination of Electron Beam Lithography and the implantation enhanced intermixing was successfully applied in the fabrication. It was found that the GaInAs/AlGaInAs material system has a high potential for tunable optoelectronic devices. A detail investigation on the integration processing steps such as implantation, subsequent annealing and re-growth with InP (MOVCD) was presented. Enhancement of side mode suppression ratio (SMSR) in $\lambda/4$ shifted DFB laser using DFQW is also proposed (Fig. 3). The suppression ratio can be increased significantly by introducing diffusion step along longitudinal direction of QW active region. Results show that large κL (>2.6) devices with step refractive index profile will exhibit stable, single-mode operation. The maximum power for single mode operation is obtained for >50 mW.⁴²

In the past two years the performance of VCSELs has dramatically improved. Following the discovery of using IID for carrier confinement in edge-emitting lasers, recently, there is an investigation on the dielectric-apertured VCL structure (see Fig. 4) using Zn IID to modify the perimeter of the QW active region for achieving enhanced carrier confinement.⁷ The laser is tested and it was found that threshold currents as low as 0.67 mA is obtained for IID-defined VCLs. The performance of IID-VCLs has been compared to air-gap apertured VCLs fabricated from adjacent material from the same wafer. SEM images of the active region and near field EL measurements indicated that the Zn-IID has resulted in confinement of the carriers in the lasers and such confinement should enable the generation of smaller diameter VCLs in the future.

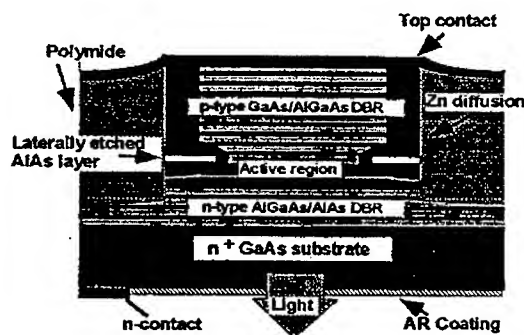


Figure 4

The fabrication of an antiguided laser array using zinc diffusion induced intermixing of a superlattice has been studied in order to create the necessary index step without the need for overgrowth.⁶² The fabrication made use of five-element, 10- μm center, antiguided array lasers (Fig. 5) in the GaAs-AlGaAs system operating at 0.860 μm , with the device

being operated at 1.2x diffraction limit to 3-W pulsed (total, both facets) and 1.6-W quasi-continuous-wave (CW) (100- μ s pulses; total, both facets). After the intermixing of GaAs-AlAs superlattices, the refractive index changed within the range 4.8%-5.2%, making it sufficient to create an effective index step, $\Delta n_{\text{eff}} \approx 0.015$ between the antiguide and interelement regions of the array.

A 1.5 μ m single mode coupled GaInAsP/InP DFB lasers by Focused ion beam (FIB) implantation lithography which combines an index grating with a self-aligned gain coupled grating was developed.⁶³ In this approach, the combination of a conventional ridge waveguide process with maskless patterning of laterally complex coupled gratings by FIB enhanced etching and FIB induced QW intermixing lateral refractive index gratings in antiphase with absorption grating are created. The devices showed that single mode emission at wavelengths around 1.55 μ m with line widths <2MHz and side mode suppression ratios of more than 40dB for cw operation at room temperature.

7.1. Modulators

The III-V semiconductor QW electrooptical phase modulators are of interest for a range of applications in optical communication and signal processing due to their large electrooptic effect. Waveguide phase modulators, with 0.5- and 1- μ m QW active regions defined by impurity induced disordering were reported.⁶⁴ By controlling the extent of the interdiffusion in the lateral claddings, the refractive index difference between the core and cladding was used to provide a single-mode operation. The structure of the phase modulator is shown in Fig. 6. Strong optical confinement required the peak impurity concentration to be at the centre of the QW active region. Moreover, the annealing time needed to be optimized so that single mode could be maintained at the desired bias field. A low dopant concentration was also expected to minimize the destruction of the modulator structure. The results showed that since the core/cladding interface was graded, the width of the metal contact would be important. A comparison of modulation efficiency for active layer thickness of 0.5 and 1.0 μ m showed that the 0.5- μ m one is a more efficient structure and its absorption loss could be reduced by increasing the applied field 50 to 100kV/cm.

Polarization-insensitive electroabsorptive III-V semiconductor QW modulation devices have been under intensive development because they can accommodate randomly polarized optical signals. A parabolic-like QW structure can be used to produce polarization-insensitive waveguide type modulators.⁶⁵ The use of interdiffusion of AlGaAs/GaAs QW to achieve the parabolic well shape was proposed. The theoretical results indicated that interdiffused QW could produce equal eigenstate spacing polarization insensitive Stark shifts, and modulation similar to an ideal parabolic quantum well. Three procedures were also proposed to develop polarization-insensitive on and off states in paraboliclike interdiffused QW. The modulation depth was compatible with that of the measured parabolic QWs. For diffused QWs one could take advantage of an as-grown rectangular QW with postgrowth thermal processing. These features demonstrate that an interdiffused QW structure could be used to produce a polarisation-insensitive electroabsorption modulator.

The QW electro-absorption (EA) modulator has been regarded recently as an important technique in the development of high speed optical communication systems. The effect of Al concentration in barrier and the thickness of the well layer on the modulation properties of AlGaAs/GaAs QWs was theoretically studied.^{1,66} The results showed that, with a larger Al concentration and a wider well depth, the range of interdiffusion for an enhanced electro-absorption change increased with both of these parameters, while insertion loss increased with the former and decreased with the latter. However, the increase in loss was lower than that of the rectangular QW for the same magnitude of absorption change. The range of a

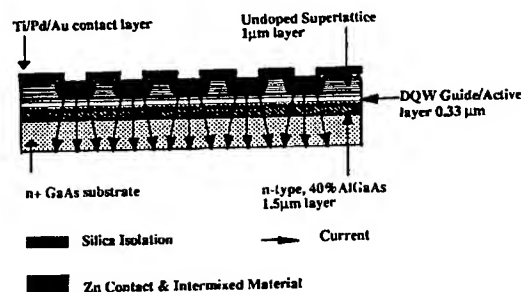


Figure 5 Structure of antiguided array laser

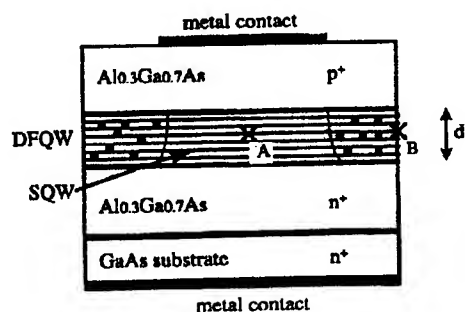


Figure 6 The cross section of the waveguide-type phase modulator, where the guiding region contains square QW's after interdiffusion.

tunable absorption-peak wavelength produced by interdiffusion increased with increasing Al concentration and decreased with increasing well width. Moreover, in a moderately interdiffused QW, the required bias was reduced for the same level of EA modulation. For the best device operation, interdiffused QWs with the Al concentration between 0.3 and 0.4 and well width between 10 and 12nm were the most suitable for developing a general-purpose electro-absorptive modulator. When applied in high-speed modulators, the EA of a wide and shallow QW active-region structure can be further enhanced with the use of corresponding interdiffusion.

7.2. Infrared Photodetector

The barrier layer and well of an infrared photodetector are partially intermixed and peak detection wavelength is red shifted.⁴⁷ Successive annealing at 850 °C were used to tune the 8.13µm detector to 9.13 µm continuously. The layer structure is grown by MBE on semi-insulating GaAs substrate. Each of the 32 periods of QW consists of 346Å AlGaAs barriers and 58Å GaAs well. The peak absorption strength reduces with increasing annealing time from 6% to 4%, but the overall quantum efficiency remains steady. The increase in dark current is mainly due to the details of subband energies and diffusion of Si through the layer structure can lower the device resistivity. The peak detection wavelength of the DFQW detector is beyond the half maximum point of that of the as-grown QW device. This indicates a clear-cut band-gap tuning between the two structures without crosstalk noise. The modified detector has responsivity comparable to as-grown material with larger spectral linewidth.

There is also a theoretical analysis of the intersubband infrared photodetector performance for various stages of interdiffusion in AlGaAs/GaAs QW.⁴⁰ It was found that the absorption strength and responsivity are enhanced for certain extents of interdiffusion and the peak detection wavelength red shifts continuously with a large tunable range from 7 to 38.4 µm. The dark current is at an acceptable value for small diffusion extent.

8. CONCLUSION

It can be seen that DFQW has introduced a very promising future in optoelectronics. In fact, development has advanced not only in improving performance, reliability, and integration of existing optical components, but also for cultivating novel optical functions. A planar, compatible OEIC in which a variety of different optical and electronic devices are composed of a common MQW structure, is proposed. It has been demonstrated that this concept is expected to be applicable to long-wavelength materials such as AlInAs/InGaAs and InGaAsP/InP MQW and is believed to focus an important direction of OEIC structure towards high performance and productivity. Another aspect which is of interest will be photonic integrated circuits. Integration of InGaAs/InP MQW laser and a low-loss waveguide in the long-wavelength region with high coupling efficiency using a cap-on-source-annealing technique has succeeded. This integration technique does not require a re-growth process, and it should prove useful for a variety of integrated devices, including mode-locked lasers and lasers integrated with optical modulators. In the future, further device enhancement and progressions are expected. In addition, wavelength demultiplexing modulator is foreseen as a new area of development.

REFERENCES

- [1] W. D. Laidig, N. Holonyak, Jr., and M. D. Camras, *Appl. Phys. Lett.* **38**, 776 (1981)
- [2] N. Holonyak, Jr., W. D. Laidig, and M. D. Camras, *Appl. Phys. Lett.* **39**, 102 (1981)
- [3] B.S.Ooi, S.G.Ayling, A.C.Bryce, and J.H.Marsh, *IEEE Phot. Tech. Lett.* **7**, 944 (1995)
- [4] K.Kerkel, J.Oshinowo, A.Forchel, J.Weber, and E.Zielinski, *Appl. Phys. Lett.* **67**, 3456 (1995)
- [5] S.Sudo, H.Onishi, Y.Nakano, Y.Shimogaki, K.Tada, M.J.Mondry, and L.A.Coldren, *Jpn. J. Appl. Phys.* **35** 1276 (1996)
- [6] S.Y.Hu, M.G.Peters, D.B.Young, A.C.Gossard, and L.A.Coldren, *Phot. Tech. Lett.* **7**, 712 (1995)
- [7] P.D.Floyd, B.J.Thibeault, J.Ko, D.B.Young, L.A.Coldren and J.L.Merz., *LEOS anneal meeting*, 207 (Boston, Nov 1996)
- [8] P.J.Poole, M.Davies, M.Dion, Y.Feng, S.Charbonneau, R.D.Goldberg, and I.V.Mitchell, *Phot. Tech. Lett.* **8**, 1145 (1996)
- [9] D. G. Deppe, and N. Holonyak, *J. Appl. Phys.* **64**, R93 (1988)
- [10] B. L. Weiss, Ed., *Special Issue, Opt. Quantum. Electron.* **23**, S799 (1991)

- [11] J. H. Marsh, *Semicond. Sci. Technol.*, **8**, 1136 (1993)
- [12] P. Chen and A. J. Steckl, *J. Appl. Phys.* **77**, 5616 (1995)
- [13] I.V.Bradley, W.P.Gillin, K.P.Homewood, and R.P.Webb., *J. Appl. Phys.* **73**, 1686 (1993)
- [14] B. L. Weiss, I. V. Bradley, and N. J. Whitehead, *J. Appl. Phys.* **71**, 5715 (1992)
- [15] G. Bacher, D. Tonnie, D. Eisert, and A. Forchel, *J. Appl. Phys.* **79**, 4368 (1996)
- [16] S.J.Lycett, A.J.Dewdney, M.Chisoni, C.E.Norman and R.Murray, *J. Elect. Mat.* **24**, 197 (1995)
- [17] J. E. Epler, R. L. Thornton, and T. L. Paoli, *Appl. Phys. Lett.* **52**, 1371 (1988)
- [18] S.Burkner, M.Maier, E.C.Larkins, W.Rothmund, E.P.O'Reilly, and J.D.Ralston, *J. Elec. Mat.* **24**, 805 (1995)
- [19] S. W. Ryu, I. Kim, and B. D. Choe, *Appl. Phys. Lett.* **67**, 1417 (1995)
- [20] W. C. Shiu, J. Micallef, I. Ng, and E. H. Li, *Jnp. J. Appl. Phys.* **34**, 1778 (1995)
- [21] I.J.Pape, P.LiKamWa, J.P.R.David, P.A.Clazton, P.N.Robson and D.Sykes, *Electron. Lett.* **24**, 910 (1988)
- [22] K. Nakashima, Y. Kawaguchi, Y. Kawamura, Y. Imamura and H. Asahi, *Appl. Phys. Lett.* **52**, 1383 (1988)
- [23] S. A. Schwarz, M. Koza, L. Nazar, and B. J. Skromme, *Appl. Phys. Lett.* **53**, 1051 (1988)
- [24] C. Francis, M. A. Bradley, P. Boucaud, F. H. Julien and M. Razeghi, *Appl. Phys. Lett.* **62**, 178 (1993)
- [25] J. Micallef, E. H. Li, and B. L. Weiss, *J. Appl. Phys.* **73**, 7524 (1993)
- [26] K. Mukai, M. Sugawara, and S. Yamzaki, *Phy. Rev. B.* **50**, 2273 (1993)
- [27] E. H. Li, J. Micallef, and W. C. Shiu, *Mat. Res. Soc. Symp. Proc.* **417**, 289 (1996)
- [28] Y.Chan, W.C.Shiu, W.K.Tsui, and E.H.Li, *MRS FALL O8.4* (Boston, Dec 1996)
- [29] E. H. Li, B. L. Weiss and K. S. Chan, *Phy. Rev. B.* **46**, 15181 (1992)
- [30] J.Micallef, E.H.Li, K.S.Chan, and B.L.Weiss, *Proc SPIE* **1675**, 211 (1992)
- [31] M.C.Y.Chan, K.S.Chan, and E.H.Li, *Proc SPIE* **2886**, 140 (1996)
- [32] E.H. Li, *IEEE J. Quantum Electron.* **34**, 1155 (1998)
- [33] E. H. Li, *Appl. Phys. Lett.* **69**, 460 (1996)
- [34] J.D.Ralston, W.J.Schaff, D.P.Bour, and L.F.Eastman, *Appl. Phys. Lett.* **54**, 534 (1989)
- [35] E. H. Li and W. C. H. Choy, *IEEE Phon. Tech. Lett.* **7**, 881 (1995)
- [36] E. H. Li, B. L. Weiss, K. S. Chan, and J. Micallef, *Appl. Phys. Lett.* **62**, 550 (1993)
- [37] J. Micallef, E. H. Li, and B. L. Weiss, *Appl. Phys. Lett.* **62**, 3164 (1993)
- [38] S. K. Han, S. Sinha, and R. V. Ramaswamy, *Appl. Phys. Lett.* **64**, 760 (1994)
- [39] S.I.Hansen, J.H.Marsh, J.S.Roberts, and R.Gwilliam, *Appl. Phys. Lett.* **58**, 1398 (1991)
- [40] A. S. W. Lee, and E. H. Li, *Appl. Phys. Lett.* **69**, 1 (1996)
- [41] E. H. Li, and K. S. Chan, *Elect. Lett.* **29**, 1233 (1993)
- [42] S. F. Yu and E. H. Li, *IEEE Phot. Tech. Lett.* **8**, 482 (1996)
- [43] J.E. Hayson, P.J. Poole, Y. Feng, E.S. Koteles, J.J. He, S. Charbonneau, R.D. Goldberg, I.V. Mitchell, *J.Vac.Sci.Technol. A* **16**, 817 (1998).
- [44] W. Feng, F. Chen, W.Q. Cheng, Q. Huang, and J.M. Zhou, *Appl. Phys. Lett.* **71**, 1676 (1997).
- [45] M. Jalonon, M. Toivonen, P. Savolainen, J. Kongas, and M. Pessa, *Appl. Phys. Lett.* **71**, 479 (1997).
- [46] J.-S. Choe, S.-W. Ryu, B.-D. Choe, H. Lim, *J. Appl. Phys.* **83**, 5779 (1998).
- [47] A.G.Steele, M.Buchanan, H.C.Liu, and Z.R.Wasilewski, *J. Appl. Phys.* **75**, 8234 (1994)
- [48] Y.Cheng, A.S.W.Lee, and E.H.Li, *IEEE TENCON'95*, 81 (1995); Y. Cheng, *MPhil Thesis* (University of Hong Kong, 1997)
- [49] I. V. Bradley, W. L. Weiss, and J. S. Roberts, *Opt. Quantum Elect.* **23**, S823 (1991)
- [50] Y.T.Oh, S.K.Kim, Y.H.Kim, T.W.Kang, and C.Y.Hong, *J. Appl. Phys.* **77**, 2415 (1995)
- [51] T. E. Schlesinger and T. Kuech, *Appl. Phys. Lett.* **49**, 519 (1986)
- [52] G. P. Kothiyal and P. Bhattacharya, *J. Appl. Phys.* **63**, 2760 (1988)
- [53] S. J. Fancey, G. S. Buller, J. S. Massa, A. C. Walker, C. J. McLean, A. McKee, A. C. Bryce, J. H. Marsh, and R. M. De La Rue, *J. Appl. Phys.* **79**, 9390 (1996)
- [54] E. H. Li and B. L. Weiss, *IEEE J. Quantum Elect.* **29**, 311 (1993)
- [55] E. H. Li, B. L. Weiss, and K. S. Chan, *IEEE J. Quantum Elect.* **32**, 1399 (1996)
- [56] E. H. Li, K. S. Chan B. L. Weiss, and J. Micallef, *Appl. Phys. Lett.* **63**, 533 (1993)
- [57] J. Kuhn, C. Kaden, V. Harle, H. Bolay, F. Scholz, H. Schweizer, H. Hillmer, R. Losch, and W. Schlapp, *Nuclear Instru. Meth. Phys. Res.* **B106**, 471 (1995)
- [58] B.S. Ooi, C.J. Hamilton, K. Mcilvaney, A.C. Bryce, R.M. Delarue, J.H. Marsh, and J.S. Roberts, *IEEE Photon. Technol. Lett.* **9**, 587 (1997).
- [59] E. H. Li, B. L. Weiss, and A. Laszcz, *Elect. Lett.* **28**, 885 (1992)

- [60] J.D.Ralston, M.Ramsteiner, B.Dischler, M.Maier, G.Brandt, P.Koidl, J. Appl. Phys. **70**, 2195 (1991)
- [61] P.D.Floyd, M.G.Peters, L.A.Coldren, and J.L.Merz, IEEE Phot. Tech. Lett. **7**, 1388 (1995)
- [62] J. M. Gray, J. H. Marsh, and J. S. Roberts, IEEE Photon. Technol. Lett. **10**, 328 (1998).
- [63] H. König, S. Rennon, J.P. Reithmaier, A. Forchel, J.L. Gentner and L. Goldstein, Appl. Phys. Lett. **75**, 1491, (1999)
- [64] W. C. H. Choy, B. L. Weiss, and E. H. Li, IEEE J. Quantum Electron. **34**, 84 (1998).
- [65] W. C. H. Choy and E. H. Li, Applied Optics **37**, 1674 (1998)
- [66] W. C. H. Choy and E. H. Li, IEEE J. Quantum Electron. **34**, 1162 (1998)

Email: ehli@eee.hku.hk; URL: <http://www-herbert.eee.hku.hk>; Telephone: 852 2859 7091; Fax: 852 2559 8738

Quantum Well Intermixing in GaAs/AlGaAs Laser Structure Using One-step Rapid Thermal Oxidation of AlAs

Seng Lee Ng, Oki Gunawan, Boon Siew Ooi*, Yee Loy Lam, Yan Zhou and Yuen Chuen Chan

Photonics Research Group, School of Electrical and Electronic Engineering
Nanyang Technological University

ABSTRACT

We report the development of a new quantum well intermixing technique in GaAs/AlGaAs laser structure. This technique uses a grown-in AlAs sacrificing layer as intermixing source and with the same layer, but oxidized using a one-step rapid thermal process (RTP), as the intermixing mask. Selective intermixing can therefore be achieved across the wafer using a one-step RTP cycle. Differential bandgap shift of as large as 47 meV has been observed from the masked and oxidized regions.

Keywords: GaAs, rapid thermal process, quantum well intermixing, thermal oxidation

1. INTRODUCTION

Quantum well intermixing (QWI) ¹ has been extensively studied in III-V quantum well structures. This is mainly due to the strong motivation from the search of an effective technology to modify the quantum well (QW) profile, and the potential applications in photonic integrated circuits (PICs) and opto-electronic integrated circuits (OEICs). QWI achieved using impurity-free vacancies diffusion (IFVD) is of great interest in the applications of PICs and OEICs. This method introduces no additional electrically charged impurities into the laser structures, hence, the material quality will not be degraded after the QWI process. Both good quality active and passive devices have been produced using this technique ^{2,3}. Besides dielectric caps induced QWI, surface oxide ⁴ and native oxides ⁵ also have been employed to achieve IFVD. Studies from Shi *et al* ⁴ found that the inter-diffusion rate of group III elements can be enhanced by the surface vacancies created during the removal of surface oxide of GaAs-AlGaAs structures. Native oxides using anodic oxidation technique was also found to induce QWI in similar material system ⁵. Hamilton *et al* ⁶, however, found that a few monolayer of Ga₂O₃, generated using hydrogen plasma processing technique on GaAs/AlGaAs multiple QW structure, can effectively be used to suppress the bandgap tuning of the system.

In this paper, we report a new technique for both enhancement and suppression of bandgap shifts by controlling the oxidation rate of the growth-in sacrificing AlAs cap layer using a one-step rapid thermal processing technique. This method is impurity-free, a much simpler and a one-step process, whereby both enhancement and suppression of QWI can be achieved a one process cycle.

2. EXPERIMENTS

A GaAs/AlGaAs double quantum well (DQW) laser structure, grown by metal-organic vapor phase epitaxy (MOVPE), was used in this study. The DQW region was undoped and consisted of two 10 nm wide GaAs QW's, separated by a 10 nm Al_{0.2}Ga_{0.8}As barrier. The top and bottom Al_{0.2}Ga_{0.8}As layers are 0.1 μ m thick to complete the waveguide core. Both the upper (1.5 μ m) and the lower (1.5 μ m) cladding layers are made of Al_{0.42}Ga_{0.58}As and doped to a concentration of $8 \times 10^{17} \text{cm}^{-3}$ and $9 \times 10^{17} \text{cm}^{-3}$ using carbon and silicon, respectively. The top contact layer consists of 0.1 μ m of GaAs doped with $1.3 \times 10^{19} \text{cm}^{-3}$ of zinc. A 0.1 μ m AlAs layer was grown on top of the GaAs contact layer to act as the sacrificing oxidation layer.

* Correspondence: E-mail: ebsooi@ntu.edu.sg; Tel: 65-790-4517; Fax: 65-791-2687

The oxidation of the AlAs layers was carried out using a rapid thermal processor (RTP) by annealing the samples between 600 °C and 800 °C for 60 seconds under O₂ ambient with flow rate of 50 sccm. The details of the oxidation process, as well as the oxide characterization, have been submitted for publication elsewhere ⁷. Energy dispersive X-ray and Raman spectroscopy measurements were performed on the oxidized samples to study the composition of the AlAs layer after processing. It was found that the oxidation of the AlAs layer was illustrated by the strong preferential oxidation of aluminum as compared to arsenic, because of the rapid out-diffusion of arsenic, the thermal in-diffusion of oxygen, and the surface segregation of both aluminum and oxygen atoms during the annealing step. From the AFM measurements, the film was found to be of good uniformity.

These samples were intermixed using the same RTP cycle at higher annealing temperatures, i.e. between 850°C and 925°C for 60 seconds, under N₂ rich conditions. As-grown samples were included into each run to act as the control sample. The samples were faced down on a piece of GaAs substrate to provide As overpressure to the surface and hence to minimize the out-diffusion of As during annealing.

3. INTERMIXED QUANTUM WELL BOUND STATES CALCULATION

In a QW structure, the effective mass of carriers (electrons or holes) varies across different layers. In an intermixed QW, the effective mass depends on the alloy concentration that in turn depends on the spatial position z . Here, we calculate the bound states in the QW active layer by solving the Schrodinger's equation in the form of Ben Daniel-Duke's equation.

The problem is first formulated by modeling the intermixing process in the QW. Assuming Fick's law and concentration independent diffusion coefficients (D), the concentration profile of the DQW can be derived in term of superposition of error functions ⁸:

$$C(z, L_d) = C_1 + \frac{(C_2 - C_1)}{2} \left[2 - \operatorname{erf}\left(\frac{z - b_1}{2L_d}\right) + \operatorname{erf}\left(\frac{z - b_2}{2L_d}\right) + \operatorname{erf}\left(\frac{z - a_1}{2L_d}\right) - \operatorname{erf}\left(\frac{z - a_2}{2L_d}\right) \right] \quad (1)$$

where C is the fractional Al concentration (i.e. x as in Al _{x} Ga_{1- x} As) across the well, L_d is the diffusion length, C_1 and C_2 are the initial Al concentrations in the well and at the barriers and z is the position in the QW growth direction. The diffusion length is defined as $L_d = \sqrt{Dt}$, where D is the diffusion coefficient and t is the annealing time. L_d characterizes the extent of intermixing in the QW. The coordinate system and the geometrical parameters are shown in Figure 1(a).

Symbol	Parameter	Al _{x} Ga _{1-x} As /GaAs	Units
$Q_c:Q_v$	Band offset splitting ratio	0.6 : 0.4	
$\Delta_0(x)$	Spin-orbit splitting	$0.34 - 0.04x$	eV
$\gamma_2(x)$	Luttinger parameter	$2.02 - 1.12x$	m_e
$m_c^*(x)$	Electron effective mass	$0.0665 + 0.0835x$	m_e
$m_{\perp HH}^*(x)$	Heavy Hole effective mass perpendicular to QW layer	$0.33 + 0.18x$	m_e
$m_{\perp LH}^*(x)$	Light Hole effective mass perpendicular to QW layer	$0.09 + 0.09x$	m_e
$m_{\parallel HH}^*(x)$	Heavy Hole effective mass parallel/transverse to QW layer	$0.11 + 0.10x$	m_e
$m_{\parallel LH}^*(x)$	Light Hole effective mass parallel / transverse to QW layer	$0.20 + 0.15x$	m_e
Γ_b	Lorentz Broadening Factor	10	meV
N_R	Bulk refractive Index	3.2	-

Table 1. Material Parameters for AlGaAs-GaAs Quantum Well Structures ⁹

The relevant material parameters of the GaAs/AlGaAs for the QW bound state calculation are given in Table 1. The bandgap energy profile that gives confinement of the carrier can be calculated using a given empirical formula:

$$E_g(x) = 1.424 + 1.594x + x(1-x)(0.127 - 1.31x) \text{ eV} \quad (2)$$

where x is the Al fractional concentration. $\text{Al}_x\text{Ga}_{1-x}\text{As}$ has a lattice constant very close to GaAs for $x < 0.4$ as used in this experiment. Therefore the strain effect can be neglected in this model. The band offset splitting ratio is taken as 60:40, i.e., $Q_c = 0.6$ and $Q_v = 0.4$. The DQW bandgap profile with respect to diffusion length across the growth direction z is plotted in Figure 1(b). The potential function that confine the carriers (electrons in conduction band and holes in the valence band) are given as:

$$V_r(z) = Q_r [E_g(z) - E_{g0}] \quad (3)$$

where the subscript r denotes either the conduction or valence band of the QW. E_{g0} is the bandgap of the binary alloy GaAs that corresponds to the minimum bandgap in the as-grown QW.

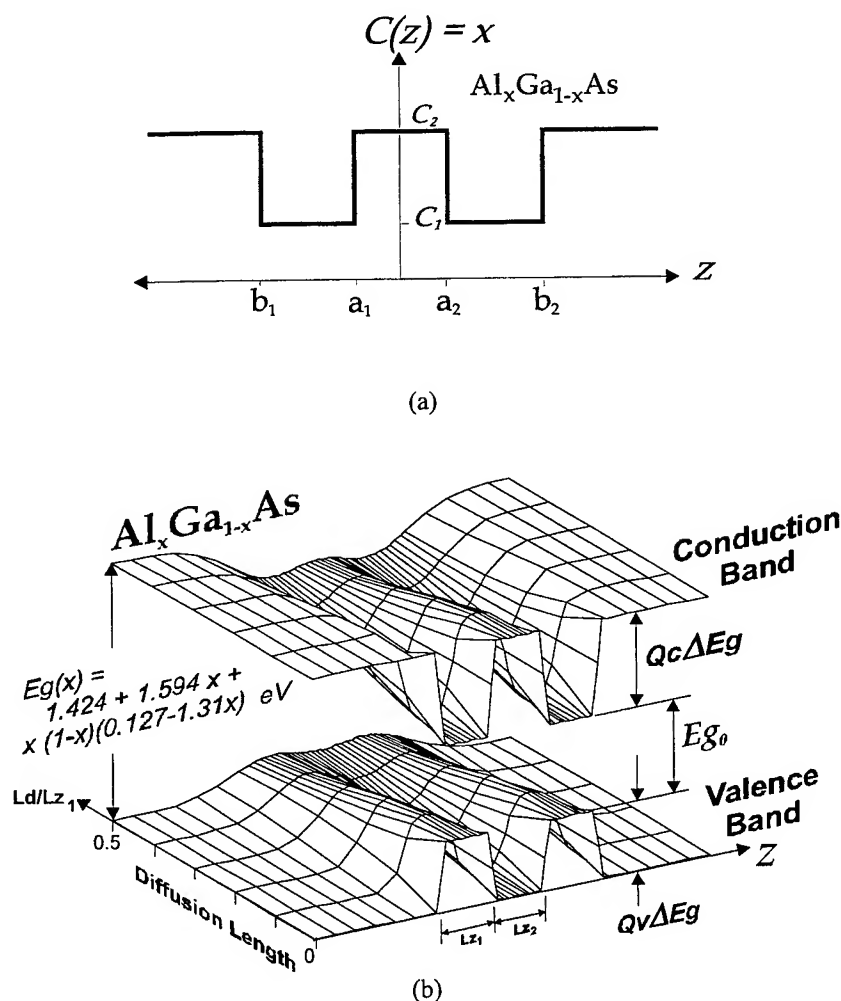


Figure 1. (a) The coordinate system for Al concentration profile, and (b) the band-edge potential confinement profile due to the intermixing process in a DQW.

Quantum mechanics requires the probability current density of the carrier to be conserved, i.e. the $\frac{1}{m^*} \frac{\partial \psi}{\partial z}$ and $\frac{\partial \psi}{\partial z}$ are both continuous along z . This leads to a modification of the Schrödinger's equation to the Ben Daniel-Duke's equation in effective mass approximation:

$$-\frac{\hbar^2}{2} \frac{\partial}{\partial z} \frac{1}{m^*(z)} \frac{\partial \psi_n(z)}{\partial z} + V(z) \psi_n(z) = E_n \psi_n(z) \quad (4)$$

where $m^*(z)$, $\psi_n(z)$, $V(z)$, E_n are the local carrier effective mass, eigen wave functions, potential function (in this case the band edge of either the conduction/valence band) and the eigen energies respectively.

Transforming the differential equation into an eigen-value matrix, called Finite Difference Eigen Value (FDEV) ¹⁰ method is used to solve the Ben-Daniel Duke's equation. The differential equation is represented as finite difference equations along the QW growth direction (z) that is divided into n mesh points. The finite difference equations are derived from the 4th order Taylor series of derivatives:

$$\begin{aligned} \frac{\partial \Psi(z_i)}{\partial z} &\approx \frac{\Psi(z_{i-2}) - 8\Psi(z_{i-1}) + 8\Psi(z_{i+1}) - \Psi(z_{i+2})}{12\Delta z} \\ \frac{\partial^2 \Psi(z_i)}{\partial z^2} &\approx \frac{-\Psi(z_{i-2}) + 16\Psi(z_{i-1}) - 30\Psi(z_i) + 16\Psi(z_{i+1}) - \Psi(z_{i+2})}{12\Delta z^2} \end{aligned} \quad (5)$$

Now the Ben-Daniel Duke's equation at every mesh point (z_i) becomes:

$$C_1(z_i)\Psi(z_{i-2}) + B_1(z_i)\Psi(z_{i-1}) + [A(z_i) - E]\Psi(z_i) + B_2(z_i)\Psi(z_{i+1}) + C_2(z_i)\Psi(z_{i+2}) = 0 \quad (6a)$$

where

$$\begin{aligned} C_1(z_i) &= \frac{\hbar^2}{24 m^*(z_i) \Delta z^2} \left[\frac{1}{m^*(z_i)} \frac{\partial m^*(z_i)}{\partial z} + 1 \right] \\ B_1(z_i) &= -\frac{\hbar^2}{24 m^*(z_i) \Delta z^2} \left[8 \frac{1}{m^*(z_i)} \frac{\partial m^*(z_i)}{\partial z} + 16 \right] \\ A(z_i) &= \frac{5 \hbar^2}{4 m^*(z_i) \Delta z^2} + V(z_i) \\ B_2(z_i) &= -\frac{\hbar^2}{24 m^*(z_i) \Delta z^2} \left[-8 \frac{1}{m^*(z_i)} \frac{\partial m^*(z_i)}{\partial z} + 16 \right] \\ C_2(z_i) &= \frac{\hbar^2}{24 m^*(z_i) \Delta z^2} \left[-\frac{1}{m^*(z_i)} \frac{\partial m^*(z_i)}{\partial z} + 1 \right] \end{aligned} \quad (6b)$$

All the finite difference equations (5a) for every mesh points will construct a generalized eigen value matrix equation:

$$[H][\Psi] = E[\Psi] \quad (7)$$

The elements of the Hamiltonian matrix can be expressed as:

$$H_{mn} = C_1(z_n)\delta_{m,n-2} + B_1(z_n)\delta_{m,n-1} + A(z_n)\delta_{m,n} + B_2(z_n)\delta_{m,n+1} + C_2(z_n)\delta_{m,n+2} \quad (8)$$

where $\delta_{m,n}$ is the usual Kronecker delta function.

All the mesh points construct $n \times n$ matrix equation (Eq. 7) representing eigen values problem that can be solved numerically. The eigen values of this matrix equation are the eigen energies (E_n) and their eigen vectors are the corresponding wavefunctions (Ψ_n). From the bound states calculation, the transitional energy $e_1 \rightarrow hh_1$ can be calculated that corresponds to the peak excitonic wavelength measured from the PL spectroscopy. In this way the diffusion length of the intermixed QW can be deduced.

4. RESULTS AND DISCUSSION

The bandgap shift, relative to the as-grown samples, as a function of the oxidation temperature is given in Figure 2. It can be seen from Figure 2 that the peak wavelength of the control samples (samples with unoxidized AlAs cap) relative to the as-grown sample have been shifted to as far as 45 nm and 70 nm at annealing temperatures between 850 °C and 925 °C for 60 s respectively. Figure 2 also shows that the degree of intermixing decreases with increasing of the oxidation temperature, as it was found that oxide thickness increases with the process temperature⁷. This implies that the change in energy bandgap decreases with increasing of oxide thickness. It is also seen from Figure 2 that the differential bandgap shift between the aluminum oxide cap, prepared at 800 °C, and grown-in sacrificing AlAs cap, i.e. unoxidized region, is as large as 47 meV after annealed at 925 °C for 60 seconds.

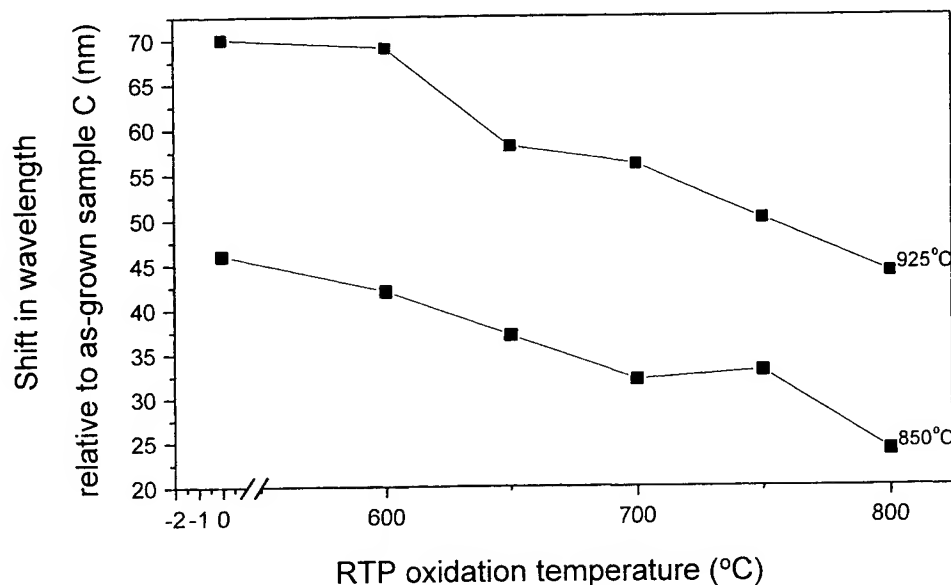


Figure 2. Plot of shift in wavelength relative to as-grown sample against RTP oxidation temperature. The intermixing annealing temperatures are 850°C and 925°C.

The QWI mechanism for this dielectric capping technique is not known, even though it is well known that for IFVD, the inter-diffusion rate of group III elements is enhanced by the surface Ga vacancies generated by the dielectric cap layer on the GaAs-AlGaAs structures. The detailed mechanism for this QWI is currently under investigation.

To extract more information from the experiments, the DQW sub-band bound energy states were calculated by solving the Schrodinger's equation in effective mass approximation using finite difference Eigen-value method¹⁰. The diffusion length, hence the degree of QWI, was calculated using the model introduced in Section 3. Figure 3 shows the transitional energy of the ground states of electron in the conduction band to the heavy holes in the valence band at various diffusion lengths. It shows the blue-shift phenomena as a consequence of the disordered band edge profile due to QWI. Given the PL peak, the

diffusion coefficients of the group III elements can be deduced. In calculating the effective diffusion lengths the ramp-up and ramp-down time during the RTP were taken into account in order to improve the accuracy of the calculation ¹¹.

The group III diffusion coefficients, as well as the activation energies of the QWI process were calculated (Figure 4). The group III diffusion coefficients calculated are in the range between 10^{-15} and 10^{-14} cm^2/s . These values agree well to the diffusion coefficients observed by other groups in similar material systems ^{12,13}. The diffusion coefficients were found to decrease with increasing in the oxide thickness (Figure 4). Since Ga vacancies play an important role in the QWI of AlGaAs/GaAs material systems ¹¹, smaller diffusion coefficients indicate lesser Ga vacancies being generated in the vicinity of QW, which is in agreement with the previous observation. Assuming temperature dependent interdiffusion process that obeys Arrhenius equation, the activation energy of the group III diffusion can also be estimated to be in a range of 1.2 eV to 3.2 eV. Despite the drift involved, the results clearly show a decreasing trend of the activation energy. Sample with oxide layer grown at higher temperature has lower activation energy. Selective QWI can therefore be obtained from regions masked between AlAs and Al_xO_y .

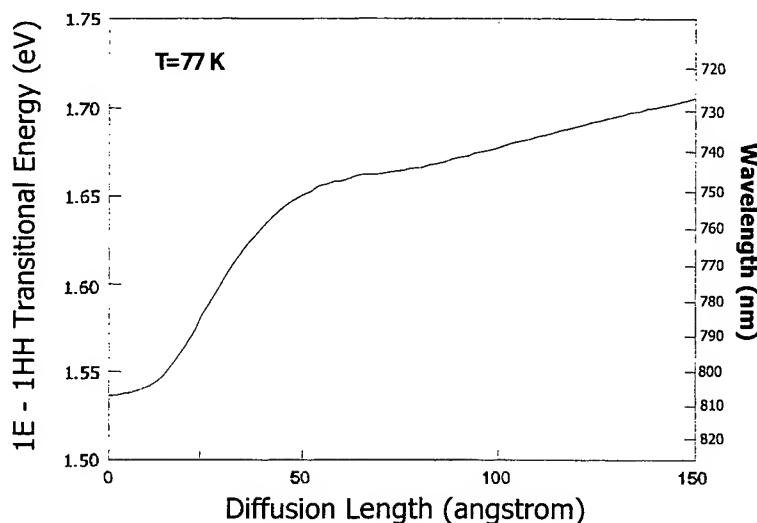


Figure 3. Energy and the wavelength of the DQW's photoluminescence peak at various diffusion lengths at 77 K

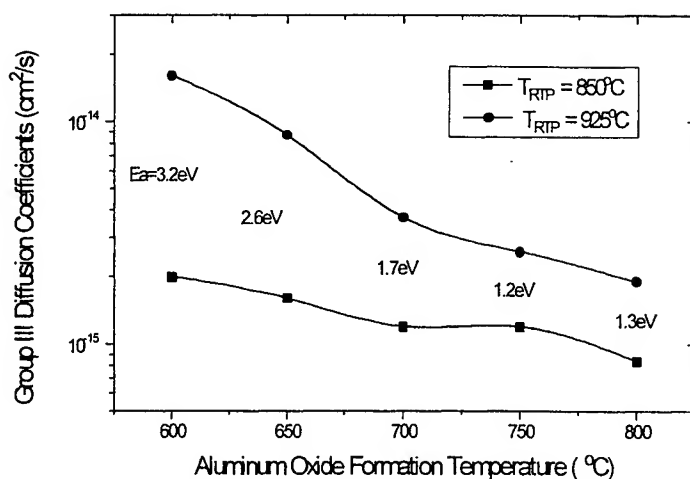


Figure 4. Diffusion coefficients of the samples of different oxidation temperature

5. CONCLUSION

We have developed a new quantum well intermixing process using aluminum oxide cap as QWI source and un-oxidized AlAs layer as QWI mask. The oxidation of the AlAs layers was carried out using a rapid thermal processor (RTP) by annealing the samples between 600 °C and 800 °C for 60 seconds under O₂ ambient with flow rate of 50 sccm. These samples were intermixed using the same RTP cycle at higher annealing temperatures, i.e. between 850°C and 925°C for 60 seconds, under N₂ rich conditions. It was found that the pure AlAs cap, i.e. unoxidized region, enhanced QWI rate in GaAs/AlGaAs as far up to 70 nm relative shift, whereas the oxide cap, prepared at higher oxidation temperature, suppresses QWI rate.

Using error function model to calculate the bandgap profile in a QWI process, the PL measurement of excitonic peak can be related to the diffusion length of the intermixed QW. Then the value of the diffusion coefficients can be deduced. The model incorporates the numerical solution of Ben-Daniel Duke's equation for carriers' bound-state in conduction band and valence band. Theoretical calculation shows that the activation energy of the group III interdiffusion decreases with increasing oxide layer thickness, i.e. from 3.2 eV to 1.2 eV.

ACKNOWLEDGEMENTS

This project has been supported by Academic Research Funds, Ministry of Education, RG47/96 and RG18/97.

REFERENCES

1. J. H. Marsh, "Quantum well intermixing", *Semicon. Sci. Technol.*, **8**, pp. 1136-1155, 1993.
2. B.S. Ooi, S.G. Ayling, A.C. Bryce and J.H. Marsh, "Fabrication of Multiple Wavelength Lasers in GaAs-AlGaAs Structures Using a One-Step Spatially Controlled Quantum-Well Intermixing Technique", *IEEE Photonics Technology Letters*, **7**, pp. 944-946, 1995.
3. B.S. Ooi, M.W. Street, S.G. Ayling, A.C. Bryce, J.H. Marsh and J.S. Roberts, "The application of the selective intermixing in selected area (SISA) technique to the fabrication of photonic devices in GaAs/AlGaAs structures", *International Journal of Optoelectronics*, **10**, pp. 257-263, 1995.
4. S. Shi, P. Li Kam Wa, A. Miller, J. Pamulapat, P. Cooke and Mitra Dutta, "The controlled disordering of quantum wells using surface oxidation", *Semicon. Sci. Technol.*, **9**, pp. 1564-1566, 1994.
5. S. Yuan, C. Jagadish, Y. Kim, Y. Chang, H.H. Tan, R.M. Cohen, M. Petravic, L.V. Dao, M. Gal, M.C.Y. Chan, E.H. Li, J.O and P.S. Zory, Jr., "Anodic-Oxide- Induced Intermixing in GaAs-AlGaAs Quantum-Well and Quantum-Wire Structures", *J. Selected Topics in Quantum Electronics*, **4**, pp. 629-635, 1998.
6. C.J. Hamilton, S.E. Hicks, B. Voge, J.H. Marsh and J.S. Aitchison, "Suppression of Bandgap Shifts in GaAs/AlGaAs Multiple Quantum Wells using Hydrogen Plasma Processing", *Electronics Letters*, **31**, pp. 1393-1399, 1995.
7. S.L. Ng, B.S. Ooi*, Y.L. Lam, Y.C. Chan, Y. Zhou and S. Buddhudu, "Characterization of Rapid Thermal Oxidation of AlAs on GaAs/AlGaAs Structure", *Surface and Interface Analysis (submitted)*.
8. I. Gontijo, Y.S. Tang, R.M. De La Rue and C.M. Sotomayor Torres, "Photoreflectance and Photoluminescence of Partially Intermixed GaAs/AlGaAs Double Quantum Wells", *Journal of Applied Physics*, **76**, pp. 5434-5438, 1994.
9. E. H. Li, B.L. Weiss, K.S. Chan, 'EigenStates and Absorption Spectra of Interdiffused AlGaAs-GaAs Multiple-Quantum-Well Structures', *IEEE Journal of Quantum Electronics*, **32**, pp. 1399-1404, 1996
10. Y. L. Lam and J. Singh, "Monte Carlo Analysis of the Carrier Relaxation Processes in Linear and Parabolic-GRINSCH Quantum Well Laser Structures", *IEEE J. Quantum Electronics*, **30**, pp. 1196-1203, 1994.
11. K.B. Kahan, D.L. Peterson, G. Rajeswaran and D.J. Lawrence, "Properties of Ga vacancies in AlGaAs materials", *Applied Physics Letters*, **55**, 651-653, 1989.
12. I. Gontijo, T. Krauss, J.H. Marsh, and R.M. De La Rue, "Postgrowth Control of GaAs/AlGaAs Quantum Well Shapes by Impurity-Free Vacancy Diffusion", *IEEE J. Quantum Electronics*, **30**, pp. 1189-1194, 1994.
13. B.S. Ooi, K. McIlvaney, Michael W. Street, A.S. Helmy, S.G. Ayling, A.C. Bryce, J.H. Marsh, J.S. Roberts, "Selective Quantum-Well Intermixing in GaAlAs Structures Using Impurity-Free Vacancy Diffusion", *IEEE J. Quantum Electronics*, **33**, pp. 1784-1793, 1997.

Multi-wavelength lasers fabricated by a novel impurity-free quantum well intermixing technology

J. H. Teng^a, S. J. Chua^{*a,b}, Y. H. Huang^b, Z. H. Zhang^a, G. Li^b, A. Saher Helmy^c, and J. H. Marsh^c

^aCenter for Optoelectronics, Dept. of Electrical Engineering, National University of Singapore

^bInstitute of Material Research and Engineering, National University of Singapore

^cDept. of Electronics and Electrical Engineering, University of Glasgow, UK

ABSTRACT

Using impurity free vacancy enhanced disordering (IFVD), the shift in the band gap of $\text{Al}_{0.3}\text{Ga}_{0.7}\text{As}/\text{GaAs}$ QW structures can be precisely controlled by an Al layer buried between a spin-on silica film and wet-oxidized GaAs surface. The blue shift in wavelength of $\text{Al}_{0.3}\text{Ga}_{0.7}\text{As}/\text{GaAs}$ QW photoluminescence (PL) depends linearly on the thickness of the buried Al layer. By changing the Al layer thickness, the PL peak wavelength can be tuned from 7870 Å for the as-grown sample to 7300 Å and 7050 Å after 20s and 45s rapid thermal annealing at 850°C respectively. Applying this technology, three wavelength lasers were successfully fabricated in a single chip. The laser is a $\text{GaAs}/\text{Al}_{0.3}\text{Ga}_{0.7}\text{As}$ three quantum well GRIN-SCH structure. Al layers with different thickness, i.e., no Al, 200 Å and 300 Å thick respectively, were buried between the oxidized GaAs surface and the silica film by two step photo-lithography and lift-off in three adjacent regions with 200µm spacing. After one step rapid thermal annealing, the wafer was processed into 6µm oxide-stripe lasers. At room temperature the intermixed lasers covered with different thickness of Al layer show different lasing wavelengths. All the lasers have similar threshold current and slope efficiency.

Key words: quantum well, quantum well laser, quantum well intermixing, photonic integrated circuit, multi-wavelength laser.

1. INTRODUCTION

The tremendous need for high data rate transfer in this information age demands the use of optical communication systems. This is also one of the driving forces for the development of photonic integrated circuit (PIC) and optoelectronic integrated circuit (OEIC). The development of PIC, which requires the integration of both the active and passive devices, such as semiconductor lasers, switches, modulators, functional waveguides, photodetectors, etc., will produce breakthroughs in the areas of information processing and transfer. One key technology to implement monolithic integration of opto-electronic and photonic devices is the spatially selective modification of the band gap energy of QWs across a wafer. The band gap energy of quantum well (QW) structures determines the operating wavelength of photonic devices, such as semiconductor lasers and modulators. Other opto-electronic components, such as passive waveguides and optical interconnects, require the band gap energy to be larger than that of the operating photon energy to avoid absorption.

There are several methods to realize the monolithic integrated photonic circuit. One method involves the growth-etch-regrowth technique^{1, 2} and one is the selective epitaxy growth^{3, 4}. Both of them need regrowth and hence lead to low production yield. Also the contamination and defects at the etch and regrowth interfaces are difficult to avoid. An alternative method is the post growth quantum well intermixing QWI, which has attracted much interest in the past decade. In this technique, the band gap of a QW structure is modified selectively by intermixing the group III/or group V atoms in the well and barrier to form an alloy. In addition, the refractive index is also modified due to the increase in band gap energy. Most GaAs based semiconductor heterostructures are thermally stable at elevated temperatures. For example, the

* E-mail: elecjsj@nus.edu.sg

diffusion coefficient of Al in an undoped AlAs-GaAs heterostructure is of the order of $10^{-19} \text{ cm}^2/\text{s}$ at 850°C . However, the intermixing process can be greatly enhanced due to the existence of point defects, either vacancies or interstitials, in the vicinity of the interface of QWs. Several methods have, therefore, been developed to enhance inter-diffusion through controlling the point defect concentration at QWs^{6, 7}. Methods to enhance QWI can be differentiated by the means of introducing point defects such as dopant diffusion,⁸ ion-implantation,⁹ physical surface damage,^{10, 11} and interfacial reactions.^{12, 13, 14} Localized QW intermixing is capable of blue shifting the QW band gap energy by several tenths of meVs in predefined regions on the wafer. Previous work has demonstrated that the impurity-free vacancy disordering (IFVD) has minimum effect on the electric properties, crystal quality and optical propagation losses.⁷ It is an especially advantageous technique if the intermixed QWs are to be used as active device regions.

For IFVD, the degree of QW intermixing could be spatially controlled across a wafer if one were capable of laterally controlling the number of generated vacancies, which subsequently re-distribute within a heterostructure.⁶ IFVD is usually implemented by coating the semiconductor with a dielectric encapsulant layer followed by thermal annealing. Although the exact mechanism by which Ga out-diffuses from the semiconductor surface (usually GaAs) into the dielectric layer (usually SiO_2) is not yet fully understood, group III vacancies are generated at the interface as a result of the Ga out-diffusion. Diffusion of these vacancies through a heterostructure substantially enhances QWI. Recently, S. Yuan *et al.* reported that the anodic GaAs oxide can enhance the quantum well intermixing¹⁵, and R. M. Cohen *et al.* reported that the inter-diffusion coefficient could be changed by one order of magnitude if the surface condition is controlled.¹³ In this work, we reported that band gap shifts can be precisely controlled by an Al layer buried between a SiO_2 dielectric encapsulant film and the oxidized GaAs surface of $\text{Al}_{0.3}\text{Ga}_{0.7}\text{As}/\text{GaAs}$ QW structures. By applying this technology, a three-wavelength laser was successfully fabricated in a single wafer. This method has the potential of being an effective means of fabricating integrated opto-electronic and photonic devices.

QW structure		3QWs GRIN-SCH Laser structure		
GaAs	30nm	GaAs	100nm	$C > 2 \times 10^{19} \text{ cm}^{-3}$
$\text{Al}_{0.3}\text{Ga}_{0.7}\text{As}$	300nm	$\text{Al}_{0.7}\text{Ga}_{0.3}\text{As} \rightarrow \text{GaAs}$	100nm	$C \sim 2 \times 10^{19} \text{ cm}^{-3}$
GaAs	7nm	$\text{Al}_{0.7}\text{Ga}_{0.3}\text{As}$	900nm	$C \sim 5 \times 10^{17} \text{ cm}^{-3}$
$\text{Al}_{0.3}\text{Ga}_{0.7}\text{As}$	25nm	$\text{Al}_{0.3}\text{Ga}_{0.7}\text{As} \rightarrow \text{Al}_{0.7}\text{Ga}_{0.3}\text{As}$	100nm	undoped
GaAs	7nm	$\text{Al}_{0.3}\text{Ga}_{0.7}\text{As}$	25nm	undoped
$\text{Al}_{0.3}\text{Ga}_{0.7}\text{As}$	25nm	GaAs	7nm	undoped
GaAs	7nm	$\text{Al}_{0.3}\text{Ga}_{0.7}\text{As}$	25nm	undoped
$\text{Al}_{0.3}\text{Ga}_{0.7}\text{As}$	20nm	GaAs	7nm	undoped
GaAs	200nm	$\text{Al}_{0.3}\text{Ga}_{0.7}\text{As}$	25nm	undoped
GaAs substrate		GaAs	7nm	undoped
		$\text{Al}_{0.3}\text{Ga}_{0.7}\text{As}$	25nm	undoped
		$\text{Al}_{0.7}\text{Ga}_{0.3}\text{As} \rightarrow \text{Al}_{0.3}\text{Ga}_{0.7}\text{As}$	100nm	undoped
		$\text{Al}_{0.7}\text{Ga}_{0.3}\text{As}$	800nm	$\text{Si} \sim 2 \times 10^{18} \text{ cm}^{-3}$
		$\text{GaAs} \rightarrow \text{Al}_{0.7}\text{Ga}_{0.3}\text{As}$	100nm	$\text{Si} \sim 2 \times 10^{18} \text{ cm}^{-3}$
		GaAs	200nm	$\text{Si} \sim 2 \times 10^{18} \text{ cm}^{-3}$
		GaAs substrate N^+		

Figure1. The structures of the sample used in QW intermixing and laser fabrication. For the QW structure, all the layers are undoped.

2. SAMPLES AND EXPERIMENTS

A $\text{Al}_{0.3}\text{Ga}_{0.7}\text{As}/\text{GaAs}$ three QWs sample was used in the QW intermixing experiment and a GRIN-SCH $\text{Al}_{0.3}\text{Ga}_{0.7}\text{As}/\text{GaAs}$ laser sample which has exactly the same active region structure as the three QW sample was used in the multi-wavelength laser fabrication, as showed in Figure1. They were all grown by metal organic vapour phase epitaxy (MOVPE). The QW intermixing experiments were done with the $\text{Al}_{0.3}\text{Ga}_{0.7}\text{As}/\text{GaAs}$ three QWs structure. Samples were first dipped in HCl to get rid of the surface oxide layer and then oxidised at 450°C for 2 hours in wet- O_2 ambient. The wet- O_2 was obtained by bubbling O_2 through the DI water held in a bath at 90°C . An Al layer was then deposited on the oxidised GaAs surface using e-beam evaporation. For the QW intermixing experiment, the Al layer thickness was varied from 0 to 50nm for different samples. After the Al layer evaporation, all the samples were immediately coated with a spin-on silica layer. The silica layer was formed by spinning commercial liquid silica on the surface at a rotation speed of 5000 rpm for 30s and repeated after an interval of 10s. The coated wafers were then baked at 120°C for 1 hour. The formed silica layer has a thickness of 150nm. Previous studies have shown that spin-on silica is an effective dielectric encapsulant layer in IFVD¹². Thermal annealing was conducted in a rapid thermal processor with temperature controlled by a pyrometer. The samples were proximity capped and placed side-by-side in a quartz chamber in N_2 ambient. Photoluminescence (PL) measurements were performed at 8 K. Samples were mounted on the same cold finger in a cryostat. The excitation source was an Ar^+ laser tuned to a wavelength of 488nm. The PL signals were dispersed by a 0.75m monochromator and detected by a GaAs photo-multiplier.

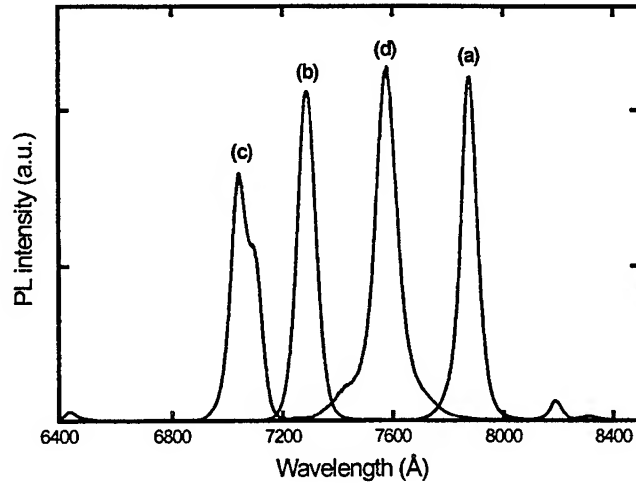


Figure 2. Low temperature photoluminescence (7K) spectra of $\text{Al}_{0.3}\text{Ga}_{0.7}\text{As}/\text{GaAs}$ QW structures. (a) As grown sample. (b) After 20s of thermal annealing with a silica layer coated on an oxidised surface. (c) After 45s of thermal annealing with a silica layer coated on an oxidised surface. (d) After 20s of thermal annealing with a 20nm thick Al layer buried between a coated silica layer and an oxidised surface. The annealing temperature was 850°C .

3. QW INTERMIXING RESULTS

For the impurity free vacancy enhanced interdiffusion (IFVD) in GaAs systems induced by a deposited SiO_2 layer, it is believed that an increased Ga vacancy concentration generated by the chemical reaction between GaAs and SiO_2 at an elevated temperature is responsible for the enhanced interdiffusion. The properties of SiO_2 may have a great effect on enhancing QW intermixing.¹⁶ The spin-on silica film can reduce the threshold temperature at which significant QW intermixing takes place. From previous study, it is clear that, compared to a bare surface, the oxidation of GaAs surface can enhance the QW intermixing.^{13, 15} Even though the exact reason is not clear, it is assumed that Ga vacancies were

generated by the chemical reaction during oxidation. The spin-on silica coated on the GaAs native oxide surface strongly enhances the quantum well intermixing, as shown in Fig. 1 (see Curve a, b and c). It can be seen that with the spin-on silica and oxidized GaAs surface, the blue shift of $\text{Al}_{0.3}\text{Ga}_{0.7}\text{As}/\text{GaAs}$ QW was about 59nm and 82nm after 20s and 45s of thermal annealing at 850°C, respectively. This is consistent with our previous report.⁸ If we assume the intermixing process to be independent of Al concentration, the diffused Al composition profile $w(z)$ across the QW structure is given by the double error function:¹⁷

$$W(z) = W_0 \left\{ 1 + \frac{1}{2} \operatorname{erf} \left(\frac{z - \frac{l}{2}}{2L_D} \right) - \frac{1}{2} \operatorname{erf} \left(\frac{z + \frac{l}{2}}{2L_D} \right) \right\} \quad (1)$$

where W_0 is the initial Al concentration in the barrier, l is the width of the as-grown quantum well, z is the growth direction, L_D is the diffusion length defined as:

$$L_D = 2\sqrt{Dt} \quad (2)$$

where D is the Al-Ga interdiffusion coefficient and t is the annealing time. By using these equations and the measured PL peak energy blue shift, the calculated interdiffusion coefficient was found to be $\sim 1.7 \times 10^{-15} \text{ cm}^2/\text{s}$. The same inter-diffusion coefficient was obtained for both annealing times, implying that the vacancy concentration at the QW remains constant over this period of time. To a first approximation, this implies that the rate of Ga out-diffusion from the oxidised GaAs surface into the spin-on silica cap remains unchanged within the annealing period. The concentration gradient of Ga vacancies present in the region adjacent to the surface, resulting from the Ga out-diffusion, drives a constant flux of Ga vacancies through the structure. As a result, QW intermixing progresses with a constant inter-diffusion coefficient, as the thermal annealing time increases.

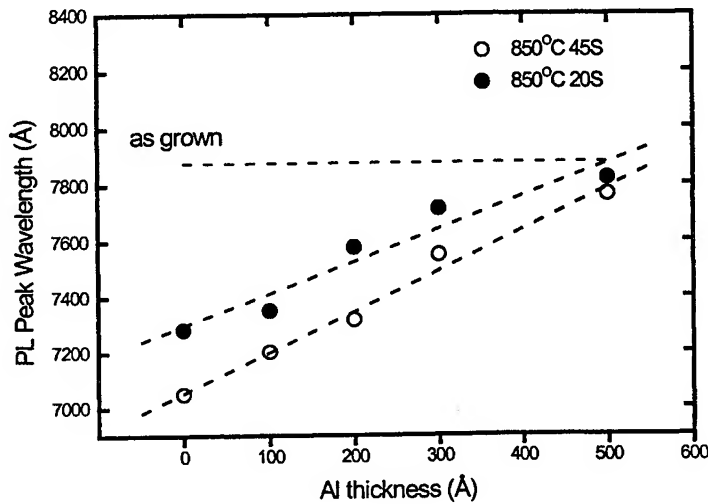


Fig. 2 Low temperature photoluminescence peak wavelength as a function of the thickness of the Al layer buried between the spin-on silica layer and the oxidised GaAs surface of $\text{Al}_{0.3}\text{Ga}_{0.7}\text{As}/\text{GaAs}$ QW structure. Thermal annealing was conducted at 850°C for 20 s (solid circles) and 45 s (open circles). Dashed lines are the guides to eyes.

One sample with a 20nm thick Al layer buried between the spin-on silica layer and oxidised GaAs surface was subjected to the same 20s thermal annealing process as that without a buried Al layer. It can be seen in Fig. 1 when comparing to the PL peak wavelength of the as-grown sample (Curve a), the Al layer suppresses the blue shift from 59nm (see Curve b) to

30nm (see Curve d). The amount by which blue shift is suppressed depends on the thickness of the Al layer. As can be seen in Fig. 2, for the two annealing times used (20s and 45s), the blue shift decreases almost linearly with an increase of the Al layer thickness. Using a 50nm thick Al layer, the QW intermixing is almost totally suppressed. The inter-diffusion coefficient was calculated and plotted as a function of the Al layer thickness in Fig. 3. As can be seen, the inter-diffusion coefficient can be changed by more than one order of magnitude simply by changing the Al layer thickness. The dependence of inter-diffusion coefficients on the Al layer thickness is well fitted by an exponential function.

From previous results, a thin Al layer (27.5nm) on the oxidised surface substantially reduces the interdiffusion coefficient from $3 \times 10^{-17} \text{ cm}^2/\text{s}$ to less than $2 \times 10^{-19} \text{ cm}^2/\text{s}$ at 950°C .¹³ The QW intermixing is therefore almost totally suppressed. With a spin-on silica layer, a considerable blue shift still occurs even with a 30nm thick Al layer on the oxidised GaAs surface when annealed at 850°C (see Fig. 2). The inter-diffusion coefficient is in this case of the order of $10^{-16} \text{ cm}^2/\text{s}$ (see Fig. 3). As postulated in Ref.13, the chemical potential still drives diffusion of atomic Ga out of the GaAs beneath the oxidised surface into the spin-on silica at an elevated temperature.

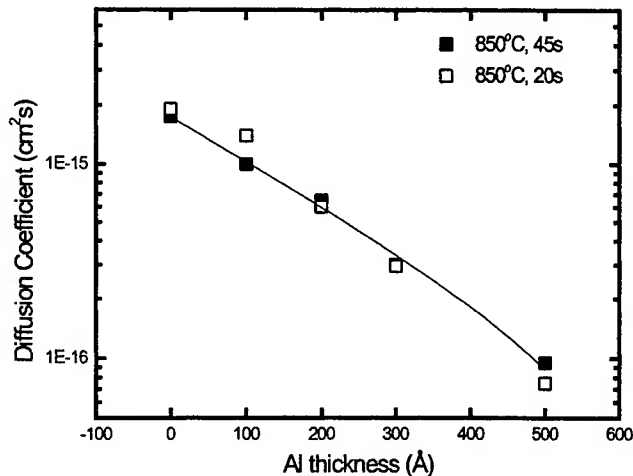


Fig. 3 Inter-diffusion coefficient at 850°C as a function of the thickness of the Al layer buried between the spin-on silica layer and the oxidised GaAs surface of $\text{Al}_{0.3}\text{Ga}_{0.7}\text{As}/\text{GaAs}$ QW structure. Thermal annealing time was 20 s (open squares) and 45 s (solid squares). The solid line is an exponential fitting curve.

In our structures, a buried Al layer can react with SiO_2 or Ga_2O_3 during thermal annealing. Reactions of SiO_2 with Al produce Al_2O_3 and Si. The diffusion of atomic Si into the structure would lead to impurity-induced QW intermixing.⁷ This does not appear to be happening here since QW intermixing is suppressed with increasing Al layer thickness. Reactions of the buried Al layer with Ga_2O_3 would reduce the oxide to produce atomic Ga and Al_2O_3 . Partial annihilation of Ga vacancies by the atomic Ga would reduce the inter-diffusion coefficient and consequently the degree of QW intermixing. Another explanation for the reduced QWI is that the Al_2O_3 layer acts as a diffusion barrier. Oxidation of the evaporated Al layers in air before coating the silica layer, and oxidation induced by residual oxygen and H_2O in the spin-on silica layer during high temperature annealing may also play a role in transforming the Al to Al_2O_3 . The dense and thermally stable Al_2O_3 layer formed after Al evaporation, together with the layer of Ga atoms left behind after reducing the oxide, may both play a role in impeding the Ga out-diffusion. The low diffusion coefficient of atomic Ga through this barrier layer would limit the mass-transport flux of atomic Ga from the GaAs into the spin-on silica layer. This oxide barrier may also act as a sink for Ga vacancies beneath the Al_2O_3 . Both picture match well with the experimental results since an increased Al layer thickness will both increase the barrier thickness of Al_2O_3 and the capacity of producing more atomic Ga and sinking more Ga vacancies. Those effects will consequently limit the number of out-diffused Ga and, hence the number of vacancies available in heterostructure for inter-diffusion.

Using appropriate mask and lift-off technology, the deposition of Al layers with varying thickness on different regions on the oxidised GaAs surface can result in different degrees of QWI across a wafer. This technology is a very promising means for lateral band gap control. Below we will demonstrate the laser device fabricated by applying this technology.

4. MULTI-WAVELENGTH LASER

The wafer used in fabricating multi-wavelength laser is a three quantum well GRIN-SCH structure grown by low pressure MOCVD as showed in Figure 1. It has the same active region structures as the three QWs sample used in the QW intermixing experiment. The wafer was first cleaned by diluted HCl solution and then oxidised at the same condition as described above. After the wet thermal oxidation, Al layers with different thickness, i.e., no Al, 200Å Al and 300Å Al respectively, were deposited on the GaAs native oxide surface by two step photolithography and lift-off technology in three adjacent regions with 200µm space. Then silica was spun on the whole wafer and baked at 120°C for 1 hour. RTP was conducted in N₂ ambient at 875°C for 45s. The temperature selected here was higher than that used in the QW intermixing experiment. This is because the laser structure has a thicker and highly p-type doped upper-cladding and top-capping layer. Previous report and our study showed that the high concentration p-type doping would suppress the bandgap blue shift due to the negatively charged Ga vacancies.^{8, 18} After RTP the GaAs oxide/Al/SiO₂ layers were all removed with buffered HF and a new 200nm SiO₂ was deposited on the GaAs surface. Oxide stripe lasers with 6µm width were formed at the centre of each intermixed region with a space of 200µm by lithography and etching. P-type contact of Cr(200 Å)/Au (2000 Å) was formed using lift-off technology. N-type metal of AuGe (800 Å)/Ni (100 Å)/Au(1500 Å) was deposited on the backside of the substrate after thinning the wafer to 100µm. After alloying, lasers with 500µm length were cleaved from the wafer and mounted p side up on copper sink for laser characteristic measurement.

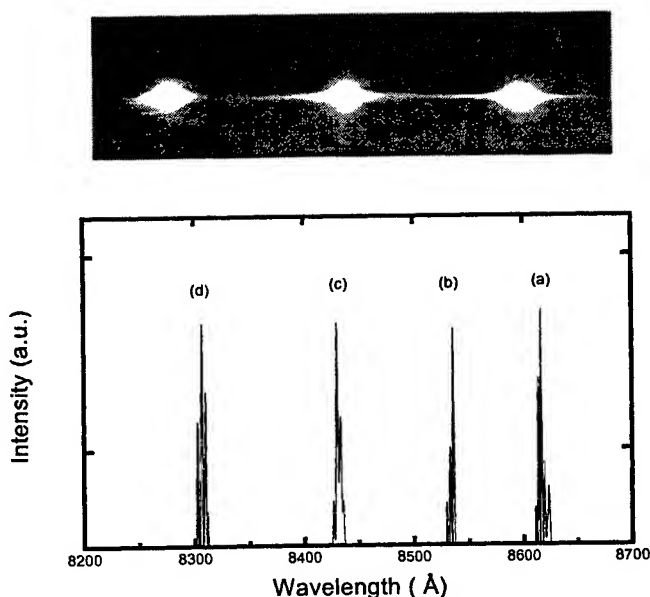


Figure 5. Laser spectra with different blue shift by controlling the degree of quantum well intermixing with an Al layer buried between the native oxide of GaAs and the silica film. (a) As-grown laser as reference, (b) with 300Å Al layer, (c) with 200 Å Al layer, (d) without any Al layer, only silica on top of the oxidized GaAs surface, the RTP was conducted at 875°C for 45s. The upper picture is the light spot pattern of the three-wavelength laser.

The lasers were tested under pulse conditions at room temperature. The current pulse width was 400ns and repetition rate was 5KHz. Figure 5 shows the spectra of lasers with different lasing wavelengths. Lasers operating at three different wavelengths of 8307 Å, 8430 Å and 8536 Å, which correspond to no Al, 200 Å and 300 Å thick Al layer buried between the GaAs oxide and the silica film, were integrated in one chip with a size of 600µm×500µm. The integrated laser can emit

either three wavelengths simultaneously or each wavelength separately. The upper part of Figure 5 showed the three light spots pattern captured by a CCD camera when the three lasers were pumped simultaneously. The distance between the light spots is 200 μ m. The spectrum of lasers fabricated from the as-grown sample were also illustrated in Figure 5 as a reference, which showed a lasing wavelength of 8616 Å. Multi-mode spectra were observed since they were gain-guided Fabry-Perot lasers without any special mode-selection design.

Maintaining device performance is very important for the integration of different optoelectronic component on a single wafer. Any serious degradation in the performance of the Al covered and band gap tuned laser will negate the advantages of this technique. Figure 6 illustrates the light-current characteristics for the lasers fabricated in the material of as-grown, SiO₂ capped and intermixed, 200 Å and 300 Å thick Al covered plus SiO₂ capping and intermixed. The lasers fabricated from the as-grown sample had a threshold current of 52mA and an external differential quantum efficiency of 22% facet. The wavelength tuned lasers from either silica covered only region or from Al covered region all showed a similar threshold current of about 57mA and external differential quantum efficiency of 20% facet. This is a 5mA increase in threshold current and a slight decrease in differential quantum efficiency compared to the as-grown one. This small difference means that the quality of the material remains good with this Al controlled band gap tuning technology.

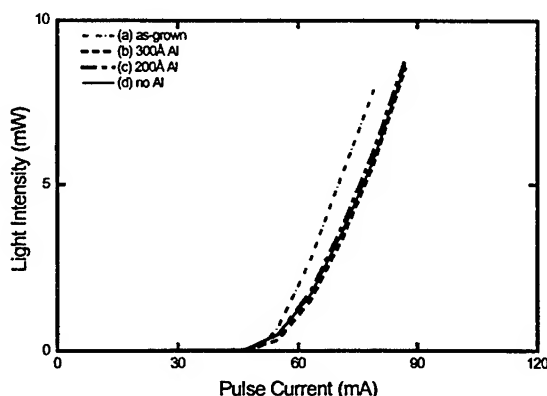


Figure 6. Light-current characteristics for the oxide stripe lasers with bandgap tuned by Al controlled QW intermixing operating at room temperature.

5. CONCLUSIONS

In conclusion, an Al layer located between the wet-oxidised GaAs surface and spin-on silica cap was used to control the band gap shift of QW structures. The blue shift of Al_{0.3}Ga_{0.7}As/GaAs QW decreases linearly as the Al layer thickness increases. Using this process, the inter-diffusion coefficient could be changed from 1.5×10^{-15} cm²/s to 7.5×10^{-17} cm²/s at 850°C. Lasers operated at three different wavelengths were successfully integrated on one chip by applying different thickness of Al coverage during quantum well intermixing. No significant increase in threshold current and differential quantum efficiency were observed in band gap tuned lasers by a buried Al layer compared to the lasers fabricated from the as-grown material. This process has the potential of being a reliable means to achieve spatially localised selective QW intermixing across a wafer, an essential technology for fabricating integrated opto-electronic and photonic devices.

ACKNOWLEDGMENT

The assistance from the technical staff Ms. H. Musni and Mr. B. H. Tan are gratefully acknowledged. One of the authors (J. H. T) acknowledges the research scholarship awarded by the National University of Singapore.

REFERENCE

1. I. Kotaka, K. Wkita, M. Okamoto, H. Asai, and Y. Kondo, "A low-drive-voltage, high speed monolithic multiple-quantum-well modulator /DFB laser light source," *IEEE Photon. Technol. Lett.* **5**, pp. 61-63, 1993.
2. R. C. Alferness, U. Koren, L. L. Buhl, B. I. Miller, M. G. Young, T. L. Koch, G. Raybon, and C. A. Burrus, "Broadly tuneable InGaAsP/InP laser based on a vertical coupler filter with 57nm tuning range," *Appl. Phys. Lett.* **60**, pp. 3209-3211, 1992.
3. M. Aoki, H. Sano, M. Suzuki, M. Takahashi, K. Uomi, and A. Takai, "Novel structure MQW electroabsorption modulator/DFB Laser integrated device fabricated by selective area MOCVD growth," *Electron. Lett.* **27**, pp. 2138-2140, 1991.
4. A. R. Pratt, R. L. Williams, C. E. Norman, M. R. Fahy, A. Marinopoulou, and F. Chatenoud, "Indium migration control on patterned substrates for optoelectronic device applications," *Appl. Phys. Lett.* **65**, pp. 1009-1011, 1994.
5. T. E. Schlesinger and T. Kuech, "Determination of the interdiffusion of Al and Ga in undoped AlGaAs/GaAs quantum wells," *Appl. Phys. Lett.* **49**, pp. 519-521, 1986.
6. R. M. Cohen, "Point defects and diffusion in thin films of GaAs," *Mater. Sci. Eng.* **R20**, pp. 167-280, 1997.
7. J. H. Marsh, "Quantum well intermixing," *Semicon. Sci. Technol.*, **8**, pp. 1136-1155, 1993.
8. D. G. Deppe and N. Holonyak, Jr., "Atom diffusion and impurity induced layer disordering in quantum well III-V semiconductor heterostructures," *J. Appl. Phys.* **64**, pp. R93-R113, 1988.
9. H. H. Tan, J. S. Williams, C. Jagadish, P. T. Burke and M. Gal, "Large energy shifts in GaAs-AlGaAs quantum wells by proton irradiation-induced intermixing," *Appl. Phys. Lett.* **68**, pp. 2401-2403, 1996.
10. O. P. Kowalski, C. J. Hamilton, S. D. McDougall, J. H. Marsh, A. C. Bryce, R. M. De La Rue, B. Vögele, C. R. Stanley, C. C. Button, and J. S. Roberts, "A universal damage induced technique for quantum well intermixing," *Appl. Phys. Lett.*, **72**, pp. 581-583, 1998.
11. A. Saher Helmy, J. S. Aitchison, and J. H. Marsh, "The kinetics of intermixing of GaAs/AlGaAs quantum confined heterostructures," *Appl. Phys. Lett.* **71**, pp. 2998-2930, 1997.
12. G. Li, S. J. Chua, S. J. Xu, X. C. Wang, A. Saher Helmy, Mao-Long Ke and J. H. Marsh, "Silica capping for $\text{Al}_{0.3}\text{Ga}_{0.7}\text{As}/\text{GaAs}$ and $\text{In}_{0.2}\text{Ga}_{0.8}\text{As}/\text{GaAs}$ quantum well intermixing," *Appl. Phys. Lett.* **73**, pp. 3393-3395, 1998.
13. R. M. Cohen, Gang Li, C. Jagadish, Patrick T. Burke and Michael Gal, "Native defect engineering of interdiffusion using thermally grown oxides of GaAs," *Appl. Phys. Lett.*, **73**, pp. 803-805, 1998.
14. Chao-Kun Lin, Xingang Zhang, P. Daniel Dapkus, and Daniel H. Rich, "Spatially selective disordering of InGaAs/GaAs quantum wells using an AlAs native oxide and thermal annealing technique," *Appl. Phys. Lett.*, **71**, pp. 3108-3110 1997.
15. S. Yuan, Y. Kim, C. Jagadish, P. T. Burke, M. Gal, J. Zou, D. Q. Cai, D. J. H. Cockayne, and R. M. Cohen, "Novel impurity-free interdiffusion in GaAs/AlGaAs quantum wells by anodization and rapid thermal annealing," *Appl. Phys. Lett.* **70**, pp. 1269-1271, 1997.
16. A. Saher Helmy, S. K. Murad, A. C. Bryce, J. S. Aitchison, J. H. Marsh, S. E. Hicks, and C. D. W. Wilkinson, "Control of silica cap properties by oxygen plasma treatment for single-cap selective impurity free vacancy disordering," *Appl. Phys. Lett.* **74**, pp. 732-735, 1999.
17. H. Leier, A. Forchel, G. Hörcher, J. Hommel, S. Bayer, H. Rothfritz, G. Weimann, and W. Schlapp Mass, "Dose dependence of ion-implantation-induced intermixing of GaAs/GaAlAs quantum-well structures," *J. Appl. Phys. Lett.* **67**, pp. 1805-1813, 1990.
18. B. S. Ooi, K. McIlvaney, M. W. Street, A. Saher Helmy, S. G. Ayling, A. C. Bryce, J. H. Marsh, and J. S. Roberts, "Selective quantum-well intermixing in GaAs-AlGaAs structures using impurity-free vacancy diffusion," *IEEE J. Quantum Elect.* **33**, pp. 1784-1793, 1997.

Dry plasma etching of GaAs vias in BCl_3/Ar and Cl_2/Ar plasmas

Y. W. Chen*, B. S. Ooi, G. I. Ng, C. L. Tan and Y.C. Chan

Microelectronics Centre, School of Electrical and Electronic Engineering,
Nanyang Technological University, Singapore 639798

ABSTRACT

We report the development and characterizations of GaAs via hole processes using BCl_3/Ar and Cl_2/Ar plasmas generated by an electron cyclotron resonance (ECR) system. The effect of the in- and out-diffuse of the reactive species and etch by-products, of the BCl_3/Ar plasma, on the etch rate of the GaAs vias has been studied. The average GaAs etch rate was found to increase with increasing of both BCl_3 and Cl_2 flow rates. Under similar conditions, namely 800W microwave power, 150W RF power, 10sccm Ar flow rate, same (BCl_3 or Cl_2) flow rate, the etch rates of Cl_2/Ar plasma were found to be 7-16 times higher than those of BCl_3/Ar plasma. As the microwave power increased from 0 to 1500W, the etch rate increased by a factor of as large as 124 for the Cl_2/Ar process. Etch rate as high as $6.7\mu\text{m}/\text{min}$ was observed from sample etched in Cl_2/Ar plasma using a microwave power, RF power and process pressure of 800W, 150W and 50mTorr, respectively. Compared to the BCl_3/Ar plasma, Cl_2/Ar plasma is a better candidate, as this process gives higher etch rate and smoother etched surface.

Key words: Vias, dry etching, GaAs, electron cyclotron resonance

1. INTRODUCTION

The fabrication of GaAs monolithic microwave integrated circuits (MMICs) with through-the-wafer via connections is of great interest¹. The existing of vias can lead to higher packing densities, improved gain, and layout simplification. Recently, interest in the application of via hole etching in photonic devices and packaging such as transmission modulators, photodetectors, and vertical cavity surface emitting lasers (VCSELs), has been growing². GaAs substrate absorbs the wavelength of operation for many GaAs-based photonic devices, therefore, it is necessary to remove the substrate of these devices by forming via holes. In addition, smooth, anisotropy GaAs via holes may also be used in photonic device packaging as alignment guide to couple optical fibers to the devices.

GaAs via hole etching has been demonstrated and achieved using various technologies and process gases to a certain degree of success. They can be processed in the conventional reactive ion etching (RIE) systems. A two-step reliable via hole dry etching process, using $\text{BCl}_3/\text{Cl}_2/\text{Ar}$ followed by CCl_2F_2 gas mixtures, was reported for GaAs MMICs fabrication³. High pressure RIE vias through 200 μm thick GaAs, using CCl_2F_2 plasma has been reported⁴.

High-density plasma etching of III-V semiconductors has significant advantages on the fabrication of photonic and electronic devices over the conventional RIE techniques⁵. High-density plasma etch systems, including electron cyclotron resonance (ECR) and inductively coupled plasma (ICP), generate ion densities of 3 to 4 orders of magnitude higher than those in the RIE systems. Cl_2/BCl_3 ECR-generated plasma was reported to be used to achieve GaAs etch rate of greater than $3.2\mu\text{m}/\text{min}$ ⁶. Etching of small diameter ($\leq 30\mu\text{m}$) GaAs via holes has also been reported⁷ using ECR. This process allows the fabrication of via with closer proximity and, therefore, higher density of devices can be produced onto a single chip. GaAs vias have also been obtained by ICP² and non-plasma based micro-machining⁸.

GaAs via holes are typically etched in chlorine-based plasma due to the higher volatility of Ga- and As-chloride etch products as compared to the etched products formed in other halogen-based plasma⁹. In this paper, we report the

* Corresponding author: p2680731z@ntu.edu.sg

development and characterizations of GaAs via hole processes using BCl_3/Ar and Cl_2/Ar plasmas generated by an ECR system.

2. EXPERIMENT

The samples used in this experiment were n-type (Te-doped) and (100) oriented GaAs substrate. Via hole patterns, with windows diameter of $70\mu\text{m}$, masked with 10nmTi and 200nm Ni, were transferred onto the GaAs wafers using photolithography and metal lift-off process. After etching, the average GaAs etch rate was measured using a Dektak stylus profilometer. The surface morphology was investigated using an optical microscope.

The etching process was developed in an ECR system equipped with an RF-biased chuck capable of accommodating various sizes of samples and operating at various temperature ranges. The RF chuck is powered with a 13.56MHz, 500W generator. The reactor is configured with a Nd-Fe-B permanent magnet to generate the resonance zone. The process chamber is surrounded by a permanent magnet jacket, which helps to focus the plasma ions into the center of the chamber away from the chamber walls. Ar gas enters the reactor chamber through an upstream gas manifold, whilst Cl_2 and BCl_3 enter the chamber through the downstream. Unless otherwise mentioned, etches were performed at; 5 minutes etching, room temperature, 10mTorr process pressure, 800W microwave power, and 150W RF power.

3. RESULTS AND DISCUSSION

Fig. 1 shows the plot of the etch rate as a function of etch time, varied from 2 to 40 minutes, for BCl_3/Ar processes using parameters as specified above. In these experiments, the flow rates of BCl_3 and Ar were set to 20sccm and 10sccm, respectively. Etch rate as high as $0.34\mu\text{m}/\text{min}$ has been obtained from samples etched for 5 minutes. The etch rate, however, dropped to about $0.1\mu\text{m}/\text{min}$ for samples etched under exposure time of greater than 5 minutes. The decrease in etch rate might be due to the decrease in the transport rate of the reactive species and etch by-products from the via ^{3,6}. In order to minimize the influence of etch time on the etch rates, samples should be etched to a deeper depth when studying the effects of other variables on the etch rate.

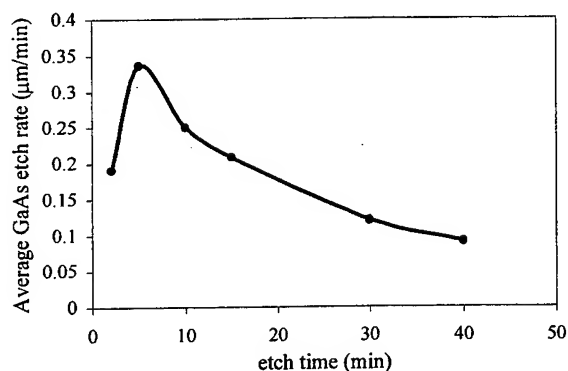
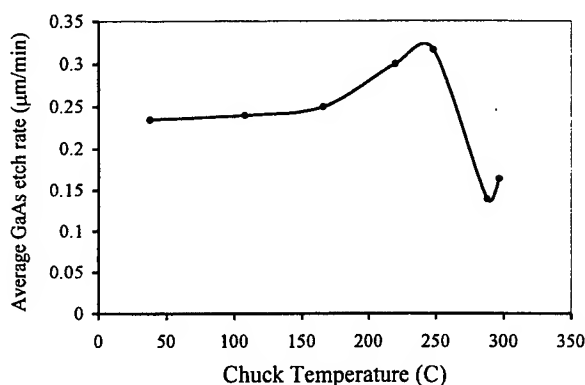


Fig. 1 Average GaAs etch rates as a function of the etch time for BCl_3/Ar processes.

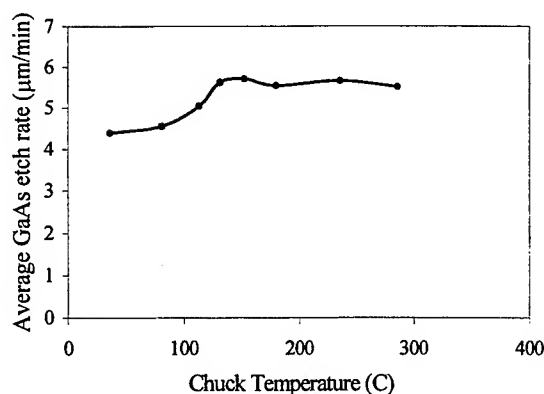
The GaAs etch rates in BCl_3/Ar and Cl_2/Ar plasmas versus chuck temperature are shown in Fig. 2(a) and Fig. 2(b) respectively. In the BCl_3/Ar processes, the flow rates of BCl_3 and Ar were fixed at 20sccm and 10sccm respectively, with process pressure of 10mTorr. The etch time for this process was fixed at 10 minutes. In the Cl_2/Ar processes, the flow rates of Cl_2 and Ar were set to 30sccm and 10sccm respectively, with process pressure of 10mTorr. The etch time for the Cl_2/Ar process was 5 minutes.

The etch rate was found to increase gradually as the chuck temperature increased (Fig. 2(a) and Fig. 2(b)). This may be attributed to the increased etch reaction and effectiveness of removal of the by-products at higher temperature¹⁰. For BCl_3/Ar plasma, only a very insignificant change in etch rate was observed for the chuck temperature of below 150°C . A sharp drop in the etch rate was however observed when the temperature was increased to $>250^\circ\text{C}$. A possible explanation may be that the increase in etch reaction of reactive species was hindered by the increased formation of surface contaminated layer formed by the BCl_3 by-products when the temperature is increased.

For Cl_2/Ar plasma, the etch rate was found to stay at about $5 \pm 0.5 \mu\text{m}/\text{min}$ when the temperature was varied between 35°C and 290°C . This implies that the chuck temperature plays a minor role in enhancing the etch rate in this process. Room temperature was therefore chosen for the subsequent process, as low temperature will increase the flexibility of the choice of the etch-mask. The etch rate was found to increase by a factor of 1.3 when the chuck temperature increased from room temperature to 150°C (i.e. from $4.4 \mu\text{m}/\text{min}$ to $5.5 \mu\text{m}/\text{min}$).



(a)

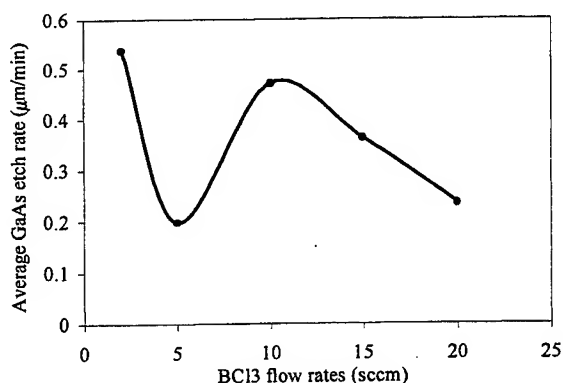


(b)

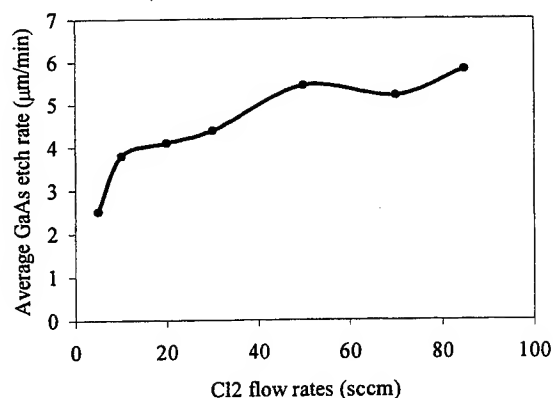
Fig. 2. GaAs etch rates as a function of chuck temperature for BCl_3/Ar (a) and Cl_2/Ar (b) processes.

The effects of the BCl_3 and Cl_2 flow rates in the BCl_3/Ar and Cl_2/Ar plasmas on the GaAs etch rate were studied (Fig. 3). During these runs, the Ar flow rate was held constant at 10sccm , whilst the BCl_3 and Cl_2 flow rates were varied from 2sccm to 20sccm , and 5sccm to 85sccm , respectively. A sharp drop in the etch rate was observed from the samples etched with a BCl_3 flow rate of 5sccm (Fig 3(a)).

The Cl_2 flow rate was varied from 5sccm to 85sccm for the Cl_2/Ar processes, causing an increase of dc bias from about 25V to 75V at RF power of 150W. The average GaAs etch rate increased by a factor of 2.3, as the Cl_2 flow rate increased from 5sccm to 85sccm (i.e. from $2.5\mu\text{m}/\text{min}$ to $5.8\mu\text{m}/\text{min}$). The surfaces of the processed samples remained good after etching for 5 minutes under these conditions. Comparing Fig. 3 (a) and Fig. 3 (b), we find that under process conditions of 800W microwave power, 150W RF power, 10sccm Ar flow rate, same flow rate, the etch rates of Cl_2/Ar plasma were about 7-16 times higher than those of BCl_3/Ar plasma. In addition, the etched surface of samples exposed to Cl_2/Ar plasma is smoother and cleaner than that etched by the BCl_3/Ar plasma.



(a)

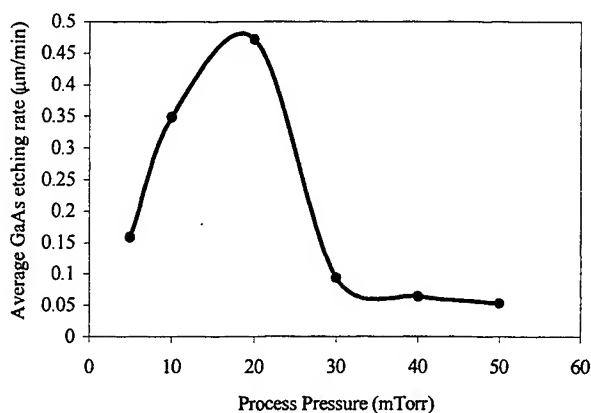


(b)

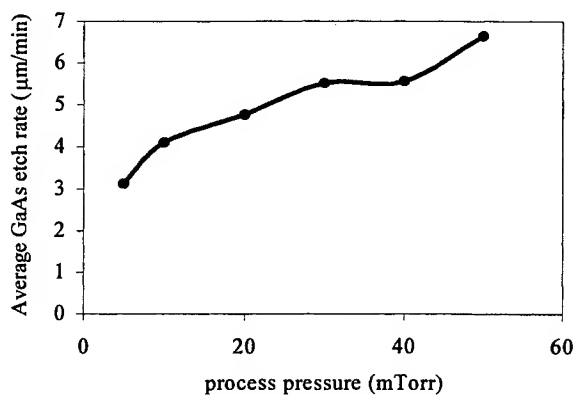
Fig. 3. GaAs etch rate as a function of BCl_3 and Cl_2 flow rates for BCl_3/Ar (a) and Cl_2/Ar (b) processes.

The relationship between the average GaAs etch rates and the process pressure in BCl_3/Ar and Cl_2/Ar plasmas are shown in Fig. 4. During these runs, both BCl_3/Ar and Cl_2/Ar flow rates were fixed at 20sccm /10sccm. For the BCl_3/Ar processes (Fig. 4(a)), the etch rate was found to increase from $0.16\mu\text{m}/\text{min}$ to $0.47\mu\text{m}/\text{min}$, when the process pressure increased from 5mTorr to 20mTorr. The process was in the reactant-limited regime, which results in the increase of etch rate at low process pressure. A decrease in etch rate was observed when the process pressure was in the range of 25-50mTorr. This may be due to the formation of deposits, due to low sputtered energy (60-70V dc bias), or saturation of reactive chlorine at the GaAs surface⁶.

As for the Cl_2/Ar plasma (Fig. 4(b)), the etch rate was found to increase from $3.1\mu\text{m}/\text{min}$ to $6.7\mu\text{m}/\text{min}$, when the process pressure increased from 5mTorr to 50mTorr. The process pressure was varied from 5mTorr to 50mTorr, resulting in an increase in dc-bias from 30V to 105V at a RF power of 150W. The etch rate increased almost linearly as the process pressure increased from 5mTorr to 30mTorr, suggesting that the process is at a reactant limited regime at the low process pressure window⁶. The etch rate is expected to increase with increasing of the process pressure as more chlorine reactants will be transported to the substrate surface and made available for GaAs to react. Etch rate as high as $6.7\mu\text{m}/\text{min}$ has been obtained at a process pressure of 50mTorr. A relatively smooth etch surface was observed from the samples etched at process pressure of below 30mTorr.



(a)



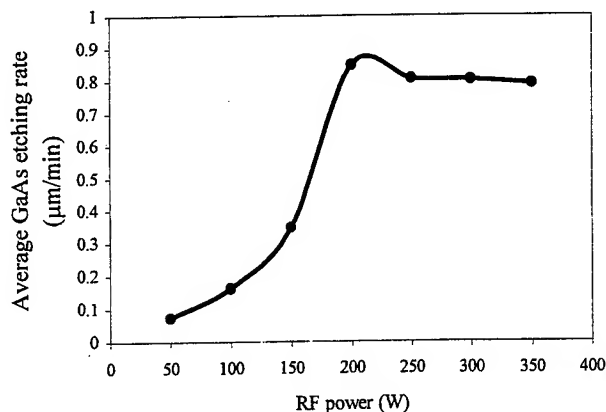
(b)

Fig. 4. GaAs etch rate as a function of process pressure for BCl_3/Ar (a) and Cl_2/Ar (b) processes.

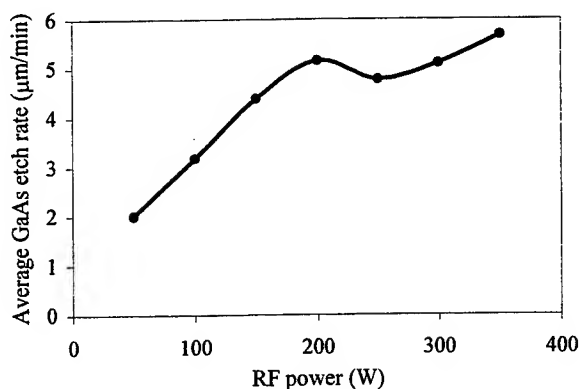
The GaAs etch rates as a function of RF power for both BCl_3/Ar and Cl_2/Ar processes are given in Fig. 5. In these processes, the BCl_3/Ar and Cl_2/Ar flow rates were fixed at 20sccm/10sccm, and 30sccm/10sccm, respectively.

For the BCl_3/Ar process, the GaAs etch rate was found to increase with increasing of RF power (Fig. 5(a)). This may be due to the increased excitation of reactive species at higher ion energies and hence, improved sputter desorption of the etch products. There was a slight decrease when RF power was increased to $>200\text{W}$. This may be due to sputter desorption of active species before they can react at the GaAs surface.

For the Cl_2/Ar process, the dc bias increased from $\sim 10\text{V}$ to $\sim 110\text{V}$, when the RF power was varied from 50W to 350W . The etch rate increased by approximately a factor of 2.9 as the RF power increased from 50W to 200W (i.e. from $2.0\mu\text{m}/\text{min}$ to $5.7\mu\text{m}/\text{min}$). At high RF power, the etch rate might be enhanced by the effect of sputter desorption of the etch products, due to high ion bombardment energy, from the surface.



(a)

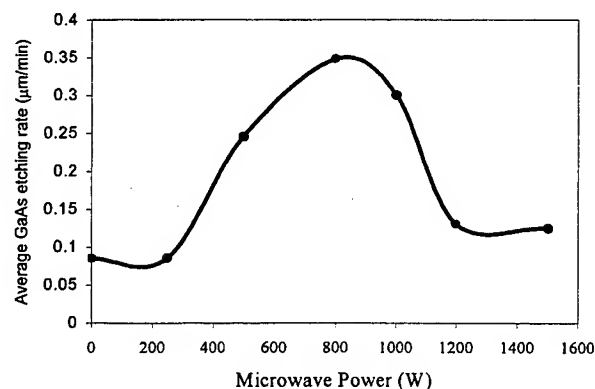


(b)

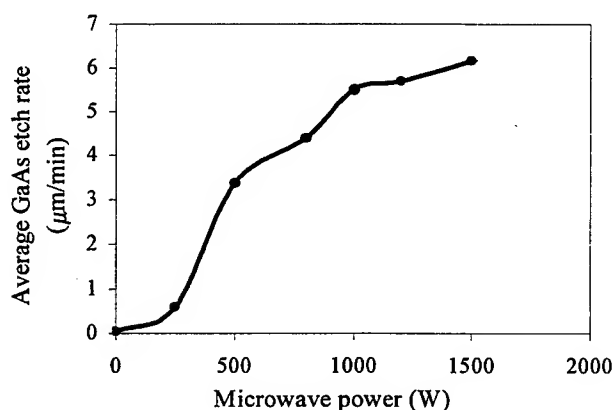
Fig. 5. GaAs etch rate as a function of RF power for BCl_3/Ar (a) and Cl_2/Ar (b) processes.

Fig. 6 shows the relationship between GaAs etch rates and the microwave power for BCl_3/Ar (Fig. 6(a)) and Cl_2/Ar processes (Fig. 6(b)). In these runs, the BCl_3/Ar and Cl_2/Ar flow rates were set to $20\text{sccm}/10\text{sccm}$, and $30\text{sccm}/10\text{sccm}$, respectively. For BCl_3/Ar processes (Fig. 6(a)), a drop in the etch rate was observed when the microwave power was increased to $> 800\text{W}$. A possible explanation may be that the increase in the etch rate was hindered by the increased formation of surface contaminated layer, formed by the BCl_3 by-products, when the microwave power is increased.

In contrast, the etch rate was found to increase by approximately a factor of 124 (i.e. from $0.05\mu\text{m}/\text{min}$ to $6.2\mu\text{m}/\text{min}$) as the microwave power increased from 0 to 1500W (Fig. 6(b)) for the Cl_2/Ar processes. The enhancement of the etch rates at high microwave powers is mainly attributed to the high plasma densities generated at high microwave power environment. Rough surfaces were, however, observed from the samples etched under the microwave power between 1200W and 1500W .



(a)



(b)

Fig. 6. GaAs etch rate as a function of microwave power for BCl₃/Ar (a) and Cl₂/Ar (b) processes.

4. CONCLUSIONS

We report the development and characterizations of GaAs via hole processes using BCl₃/Ar and Cl₂/Ar plasmas generated by an electron cyclotron resonance (ECR) system. The effect of the in- and out-diffuse of the reactive species and etch by-products, of the BCl₃/Ar plasma, on the etch rate of the GaAs vias has been studied. The average GaAs etch rate was found to increase with increasing of both BCl₃ and Cl₂ flow rates. Under similar conditions, namely 800W microwave power, 150W RF power, 10sccm Ar flow rate, same flow rate, the etch rates of Cl₂/Ar plasma were found to be 7-16 times higher than those of BCl₃/Ar plasma. As the microwave power increased from 0 to 1500W, the etch rate increased by a factor of as large as 124 for the Cl₂/Ar process. Etch rate as high as 6.7μm/min was observed from sample etched in Cl₂/Ar plasma using a microwave power, RF power and process pressure of 800W, 150W and 50mTorr, respectively. Compared to the BCl₃/Ar plasma, Cl₂/Ar plasma is a better candidate, as this process gives higher etch rate and smoother etched surface.

REFERENCES

1. M. Barsky, R. Lai, Y. L. Kok, M. Sholley, D. C. Streit, "190 GHz InP HEMT MMIC LNA with dry etched backside vias," Proc. of 11th International Conference on Indium Phosphide and Related materials, pp. 423-425 (1999).
2. R. J. Shul, A. G. Baca, R. D. Briggs, and G. B. McClellan, "ICP etching of GaAs via hole contacts," *Electrochemical Society Proc.* No. 2, pp. 515 (1996).
3. M. S. Chung, H. R. Kim, J. E. Lee, B. K. Kang, and B. M. Kim, "Via hole process for GaAs monolithic microwave integrated circuit using two-step dry etching," *J. Vac. Sci. Technol.* B11 (2), 159 (1993).
4. L. G. Hipwood and P. N. Wood, "Etching of through substrate via holes for GaAs MMIC's," *J. Vac. Sci. Technol.* B3 (1), 395 (1985).
5. A. Grill, *Cold Plasma in Materials Fabrication*, IEEE press, Inc., New York, (1993).
6. R. J. Shul, M. L. Lovejoy, J. C. Word, A. J. Howard, D. J. Rieger, and S. H. Kravitz, "High rate reactive ion etch and electron cyclotron resonance etching of GaAs via holes using thick polymide and photoresist masks," *J. Vac. Sci. Technol.* B15 (3), 657 (1997).
7. S. J. Pearton, F. Ren, A. Katz, J. R. Lothian, T. R. Fullowan, and B. Tseng, "Dry processed, through-wafer via holes for GaAs power devices," *J. Vac. Sci. Technol.* B11 (2), 152 (1993).
8. F. Foulon and M. Green, "Through-wafer via fabrication in gallium arsenide by excimer laser projection patterned etching," *J. Vac. Sci. Technol.* B11 (5), 1854 (1993).
9. K. P. Hilton and J. Woodward, "Via holes for GaAs MMICs fabricated using reactive ion etching," *Electronics Lett.* Vol. 21, No. 21, 962 (1985).
10. R. J. Shul and A. J. Howard, "Temperature dependent electron cyclotron resonance etching of InP, GaP, and GaAs," *J. Vac. Sci. Technol.* A14 (3), 1102 (1996).

Effect of etch pit density of InP substrate on the stability of InGaAs/InGaAsP quantum well laser materials

Hwi Siong Lim, Teik Kooi Ong, Boon Siew Ooi*, Yee Loy Lam, Yuen Chuen Chan and Yan Zhou
Photonics Research Group, School of Electrical and Electronic Engineering,
Nanyang Technological University, Singapore 639798

ABSTRACT

InGaAs/InGaAsP quantum well structures have wide applications, such as the integration of optoelectronic devices and low threshold current density lasers, as well as low loss waveguides and optical switching elements. In many cases, high temperature operations (such as during selective area epitaxy or regrowth) are necessary during the course of processing a wafer. Here, we report the influence of low and high etch pit densities (EPD) InP substrates on the thermal stability of InGaAs/InGaAsP quantum well laser structure. Both the n-type of S-doped ($\text{EPD} < 500 \text{ cm}^{-2}$) and Sn-doped ($\text{EPD} \approx 5 \times 10^4 \text{ cm}^{-2}$) InP substrates were grown under the same run with half wafer each. To assess the thermal stability, the samples were annealed, using a rapid thermal processor, between 650°C and 750°C , for 60 seconds. 77 K photoluminescence measurements were performed on the samples after annealing to study the degree of bandgap shift. It was found that S-doped InP substrate with low EPD, i.e. low point defect density, is thermally stable up to an annealing temperature of 625°C for 60 seconds. Compared to the S-doped materials, laser structure grown on the Sn-doped InP substrate was found to exhibit larger degree of bandgap shift resulted from defects induced quantum well intermixing.

Keywords: Etch pit density, thermal stability, InGaAs/InGaAsP, quantum well, rapid thermal processing.

1. INTRODUCTION

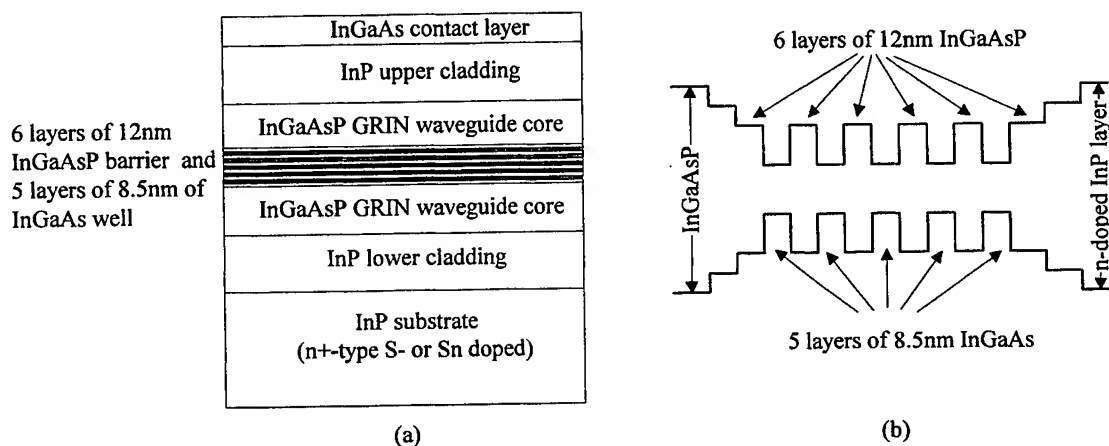
InGaAs/InGaAsP quantum well (QW) structures, lattice matched to InP, have been widely used in wavelength division multiplexing (WDM) system for long haul optical fiber communication. This is mainly due to its capability in the integration of optoelectronics devices such as low threshold current density lasers, low loss waveguides, semi-absorbing regions of electro-optic modulator and optical switching elements onto a single chip¹. The integration process is highly desirable in order to reduce chip size, production cost and also to increase the efficiency of the performance. However, in many cases, high temperature operations, such as during selective area epitaxy growth or growth and regrowth process, are necessary during the course of processing a wafer². High temperature induces not only strain but also interdiffusion phenomenon which strongly modifies the abruptness of the interfaces between wells and barriers. This modification will in turn affect the electrical and optical properties of the device performance.

Etch pit density (EPD) of the InP substrate plays an important role in determining the thermal stability of the InGaAs/InGaAsP structure. Low EPD is defined as substrate with a relatively low etch rate and low point defect density and vice versa for high EPD substrate. It is known that high temperature enhances the interdiffusion between As and P

* Correspondence: Email: ebsooi@ntu.edu.sg; Tel: (65)-7904517; Fax: (65)-7912687.

atoms in InGaAs/InGaAsP wafer structures, which results in a blue-shifting of the bandgap energy of QW³. This effect is also known as quantum well intermixing (QWI)⁴ and is attributed to the diffusion of point defects in the materials. These point defects from InP-substrate will further enhance the interdiffusion rate between wells and barriers which have high concentration gradient. Though the current epitaxy techniques can minimize the grow-in point defects to an insignificant level, the propagation and diffusion of point defects from the substrate layer are possible and cannot be overlooked during high temperature processes. Furthermore, by considering the poor thermal stability of InGaAs/InGaAsP laser materials as compared to GaAs/AlGaAs laser materials⁵, it is more critical to choose a suitable dopant for InP substrate during the growing process.

2. EXPERIMENT



The samples of each wafers were first cleaved into $2 \times 2 \text{ mm}^2$ for the experiment. The samples were annealed using RTP at temperatures vary from 650°C to 750°C for 60s in nitrogen-rich and oxidation-free environment. During annealing, two GaAs proximity caps were used to sandwich the sample in order to provide arsenic overpressure to the epilayers³. 77 K PL measurements were then carried out to study the degree of bandgap shift of the samples after RTP.

3. RESULTS AND DISSCUSSION

The PL spectra obtained from both S-doped (low EPD) and Sn-doped (high EPD) structured were normalized and are shown in Figure 3 and 4 respectively. The blue-shifted wavelength relative to the as-grown sample, as a function of RTP temperature for both samples is given in Figure 2. It was observed from the excitonic peak that the PL wavelength for Sn-doped samples show large degree of intermixing ($\geq 30 \text{ nm}$) compared to the S-doped samples at RTP temperatures below 700°C . This is mainly due to the fact that Sn-doped substrate, with high EPD and hence high grown-in defect density, promoting group V interdiffusion at high temperature which resulted in QWI. This implies that QW structures grown on S-doped substrate is more thermally stable than the Sn-doped substrate. It was found that the blue-shift of Sn-doped substrate was saturated at temperature above 700°C , which could be attributed to the saturation of the point defects in the substrate.

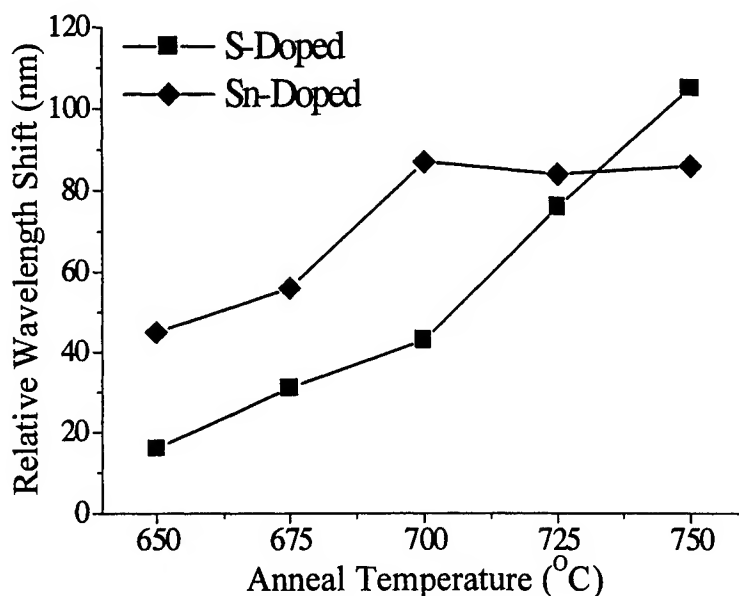


Figure 2: Comparison of wavelength blue-shift for S-doped and Sn-doped substrates

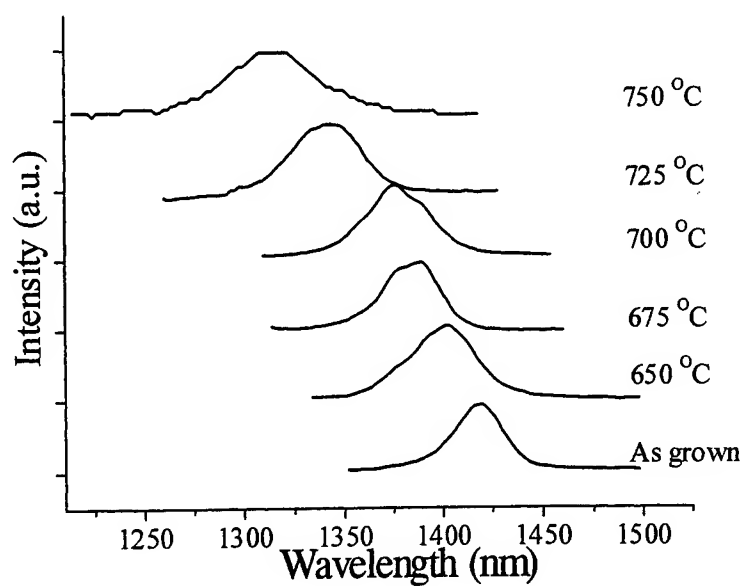


Figure 3: Normalized PL spectra from the laser structures grown on S-doped structure at different annealing temperatures.

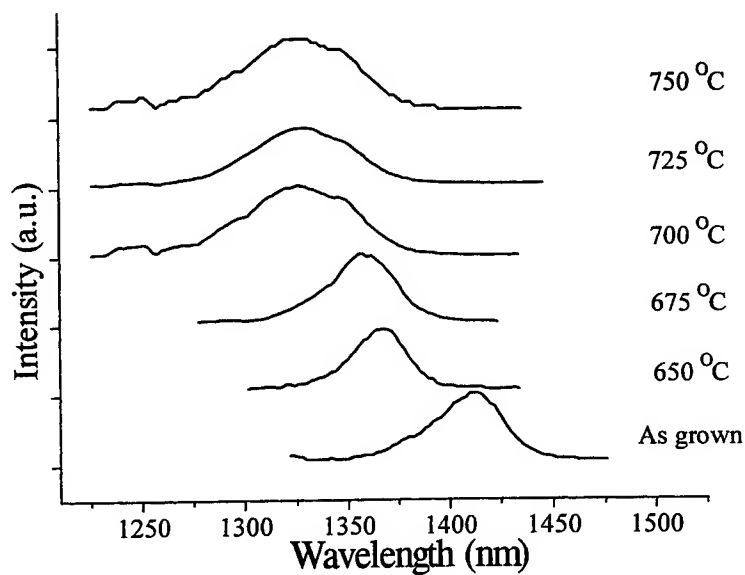


Figure 4: Normalized PL spectra from the laser structures grown on Sn-doped structure at different annealing temperatures.

The relationship between full width at half maximum (FWHM), relative to the as-grown samples, as a function of temperature is shown in Figure 5. At temperatures below 675°C, the FWHM of Sn-doped samples do not show to broaden significantly. At RTP temperatures of 700 °C and above, the quality of the material degraded significantly (i.e. broadened spectra), as can be seen from Figure 5. In the case of S-doped substrate, the relative FWHM was almost constant for samples annealed at 700 °C and below. The broadening in FWHM for samples intermixed to large degree of QWI can be explained by the change in QW shape from abrupt to parabolic, and hence loss of confinement of the carriers in the QWs.

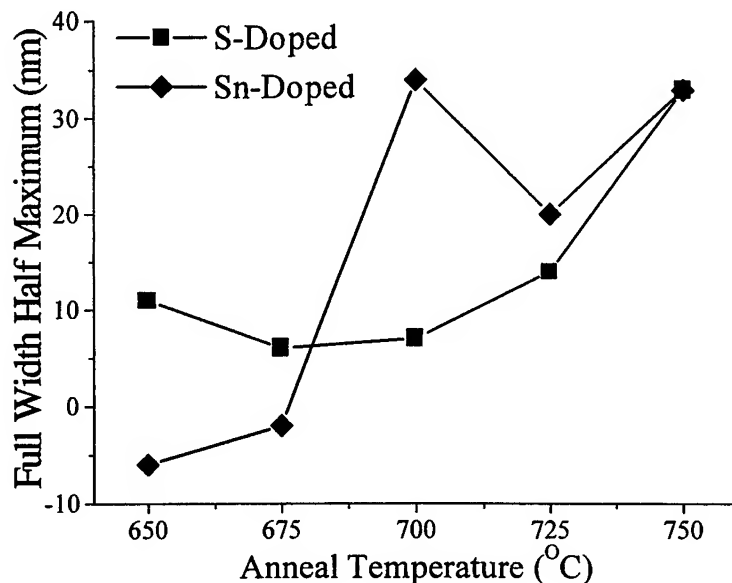


Figure 5: FWHM relative to as-grown samples versus different annealing temperatures.

4. CONCLUSION

We have studied the thermal stability of InGaAs/InGaAsP QW structures grown on high and low EPD InP-substrate. It was found that Sn-doped substrate with high EPD density resulted in lower degree of thermal stability. In contrast, QW samples grown on S-doped substrate are thermally stable up to 625 °C for 60 seconds.

REFERENCES

1. F. Delorme, J. Hourany, H. Nakajima, N. Kalonji, J. Semo, M. Billard and R. Lefevre, "12 wavelength-channel fast switching operation of compact DBR laser modules including IC-drivers," *Electron. Lett.*, **32**, pp. 1670-1671, 1996.
2. Yasumasa Kashima, Tsutomu Munakata, "Broad Spectrum InGaAsP Edge-emitting light-emitting diode using selective area metal-organic vapor-phase epitaxy," *IEEE Photonics Techno. Lett.*, **1**, 1998.

3. D.G. Deppe and N. Holonyak, Jr., "Atom diffusion and impurity-induced layer disordering in quantum well III-V semiconductor heterostructures", *J. Appl. Phys.*, **64**, R93, 1988.
4. J. H. Marsh, "Quantum well intermixing," *Semicond. Sci. Technol.*, **8**, pp. 1136-1155, 1993.
5. H. Peyre, F. Alsina, J. Camassel, J. Pascual, R.W. Glew, "Thermal stability of InGaAs/InGaAsP quantum wells," *J. Appl. Phys.*, **73**, pp. 3760, 1993.
6. S. Charbonneau, E.S. Koteles, P.J. Poole, J.J. He, G.C. Aers, J. Haysom, M. Buchanan, Y. Feng, A. Delage, F. Yang, M. Davies, T.D. Goldberg, P.G. Piva, and I.V. Mitchell, "Photonics Integrated Circuits Fabricated using Ion Implantation," *IEEE J. Selected topics in Quan. Electron.*, **4**, pp. 772, 1998.

SESSION 5

Polymeric Materials and Devices

Highly scattering optical transmission polymers for liquid crystal display

Akihiro Tagaya^{*a, b}, and Yasuhiro Koike^{*a, b}

^aFaculty of Science and Technology, Keio University,
3-14-1, Hiyoshi, Kohoku-ku, Yokohama 223, JAPAN

^bKanagawa Academy of Science and Technology,
3-2-1, Sakado, Takatsu-ku, Kawasaki 213, JAPAN

ABSTRACT

We proposed highly scattering optical transmission (HSOT) polymers and applied it to a light pipe of a backlighting system for liquid crystal displays (LCDs). The HSOT polymer backlighting system having not only approximately twice the brightness but also twice the efficiency of the conventional one was realized based on analysis of multiple scattering in the HSOT polymers. The problem of color dispersion which had been believed to be the nature of scattering phenomenon was solved by optimizing the heterogeneous structures in the HSOT polymers. As a result, the HSOT polymer backlighting system with sufficient color uniformity was achieved. In addition, the HSOT polymer backlighting system was composed of fewer parts than those of the conventional transparent one. The HSOT polymer backlighting system is suitable for recent thin LCDs because of these advantages.

Keywords: highly scattering optical transmission polymers, liquid crystal displays, backlighting, multiple scattering

1. INTRODUCTION

In the market of portable information terminals, lower electric power consumption liquid crystal displays (LCDs) are strongly required for longer battery lifetime. The electric power consumption and image quality of recent LCDs, however, are still insufficient for use as portable display devices. The power consumption of a typical backlighting system is about 60 % of total power consumption of a typical LCD unit. In addition to this, decrease in thickness of the backlighting system is the one of the most important targets to realize thinner LCDs. In the case of a typical polymer light pipe in the backlighting system, the minimum thickness is limited by thermostability of the polymer. Reduction the number of other parts in the backlighting system such as a diffusing film and a brightness enhancement film, therefore, is desirable for the thinner LCDs.

We proposed highly scattering optical transmission (HSOT) polymers for use as a high efficiency illumination medium and applied it to the light pipe of the backlighting system for LCDs¹⁻⁴. The incident light is scattered repeatedly and homogenized effectively inside the HSOT polymers because of the internal microscopic heterogeneous structures, and then radiated uniformly from the entire surface of the HSOT polymers. Before our proposal, it had been believed that the light pipe of the backlighting system should be transparent, because scattering phenomenon due to heterogeneous structures inside the light pipe seems to cause transmission loss and degrade color uniformity. Thus, a lot of efforts had been made in order to decrease scattering in the light pipe. Nevertheless, we developed the HSOT backlighting system which showed approximately twice the brightness, in other words, twice the efficiency of the conventional one and sufficient color uniformity by introducing and controlling the microscopic heterogeneous structures. Furthermore, reduction of the number of parts in the backlighting system was achieved. Details of the development are described in this paper.

2. STRUCTURE OF HSOT BACKLIGHTING SYSTEM

Schematic diagram of the HSOT and conventional backlighting systems is shown in Figure 1. In all conventional edge-light type backlighting systems, a transparent PMMA light pipe with printed dot patterns and other surrounding light-controlling devices (shown in Figure 1 (a)) are used. The printed dot patterns are necessary at the bottom of the light pipe in order to obtain uniform luminance. Also, a diffusing film is indispensable to hide the printed dot pattern. Furthermore, two brightness enhancement films (BEF, trade name of 3M) are employed to achieve higher luminance in the vertical direction to the output surface. On the other hand, in the HSOT backlighting system (shown in Figure 1 (b)), only the prism film optimized for the HSOT light pipe is necessary on the output surface. The luminance from all over the surface of the light pipe is almost uniform without the printed dot patterns or the diffusing film because high-order multiple scattering inside the HSOT polymer makes the luminance from the surface uniform.

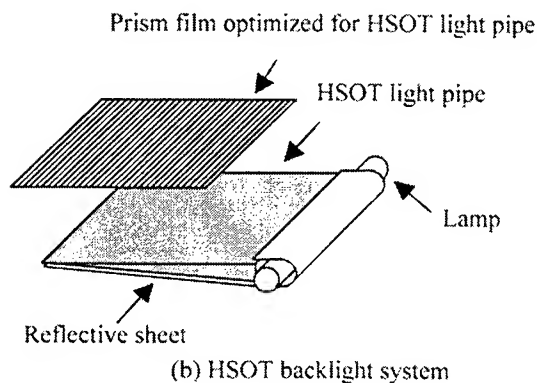
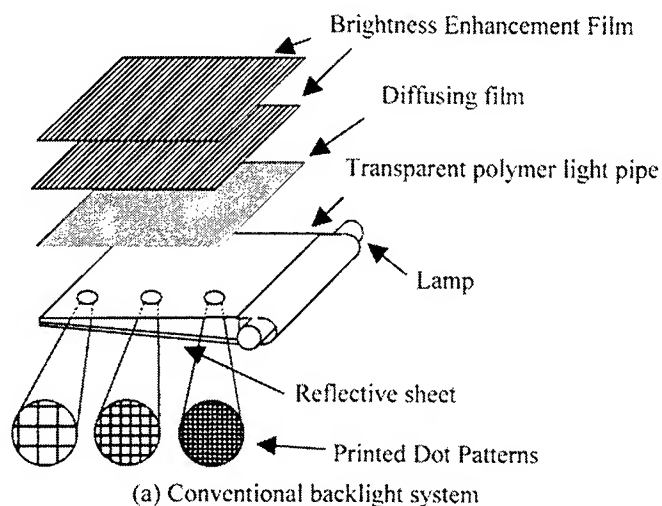


Figure 1 Schematic diagram of LCD backlighting systems.

3. HSOT DESIGNING SIMULATION

The light homogenization effect caused by the multiple light scattering phenomenon in the HSOT polymer was analyzed by the HSOT designing simulation using the Monte Carlo method⁵ based on Mie scattering theory⁶⁻⁷. Mie scattering theory

describes scattering phenomenon caused by a spherical particle in a homogeneous medium exactly. Mie scattering theory was applicable to analysis of scattering in the HSOT polymers in which polymer particles were doped to introduce the microscopic heterogeneous structure. The Monte Carlo method was used to analyze random and repeating processes in the multiple light scattering phenomenon, because the Monte Carlo method is a powerful method to solve problems that have no immediate probabilistic interpretation.

Light scattering intensity profile and scattering efficiency of a single particle can be calculated by using equations

$$I(\alpha, m, \theta) = \lambda^2 (i_1 + i_2) / 8\pi^2, \quad (1)$$

$$K(\alpha, m) = \left(\frac{\lambda^2}{2\pi^2 r^2} \right) \sum_{v=1}^{\infty} (2v+1) \left\{ |a_v|^2 + |b_v|^2 \right\}, \quad (2)$$

$$i_1 = \left| \sum_{v=1}^{\infty} \frac{2v+1}{v(v+1)} \left\{ a_v \frac{P_v^1(\cos\theta)}{\sin\theta} + b_v \frac{dP_v^1(\cos\theta)}{d\theta} \right\} \right|^2, \quad (3)$$

$$i_2 = \left| \sum_{v=1}^{\infty} \frac{2v+1}{v(v+1)} \left\{ b_v \frac{P_v^1(\cos\theta)}{\sin\theta} + a_v \frac{dP_v^1(\cos\theta)}{d\theta} \right\} \right|^2$$

$$a_v = \frac{\psi'_v(m\alpha)\psi_v(\alpha) - m\psi_v(m\alpha)\psi'_v(\alpha)}{\psi'_v(m\alpha)\zeta_v(\alpha) - m\psi_v(m\alpha)\zeta'_v(\alpha)}, \quad (4)$$

$$b_v = \frac{m\psi'_v(m\alpha)\psi_v(\alpha) - \psi_v(m\alpha)\psi'_v(\alpha)}{m\psi'_v(m\alpha)\zeta_v(\alpha) - \psi_v(m\alpha)\zeta'_v(\alpha)}$$

$$\alpha = 2\pi r n_m / \lambda_0, \quad (5)$$

$$m = n_s / n_m, \quad (6)$$

which are derived from Mie scattering theory, where $I(\alpha, m, \theta)$ and $K(\alpha, m)$ mean scattering intensity and scattering efficiency, α is a size parameter, m is a relative refractive index between particle (n_s) and matrix (n_m). r means particle radius, and λ means wavelength of incident light in the matrix. $P_v^1(\cos\theta)$ is a Legendre polynomial, ψ_v, ζ_v are the first two orders of the Ricatti-Bessel functions.

By the Monte Carlo method, scattering angle θ , expected photon path length L , probability density distribution function $F(\theta)$ of scattering angle and extinction coefficient σ are defined as

$$\sigma = \pi \int_0^{\infty} \int_0^{\infty} r^2 n_a(r) f(\lambda) K(\alpha, m) dr d\lambda, \quad (7)$$

$$L = -\ln(\text{random } 1) / \sigma, \quad (8)$$

$$F(\theta) = \frac{I(\theta)W(\theta)}{\int_0^{\pi} I(\theta)W(\theta) d\theta}, \quad (9)$$

$$\theta = F^{-1}(\text{random } 2), \quad (10)$$

where $n_a(r)$ is particle concentration, $f(\lambda)$ is probability density distribution function of wavelength, $random$ 1 and 2 are uniform random numbers generated between 0 and 1, $I(\theta)$ is scattering intensity profile and $W(\theta)$ is solid angle. This Monte Carlo simulation method was applied to examine the multiple light scattering phenomenon in the HSOT polymer with using more than ten thousands photons.

As shown in Figure 2, size of the heterogeneous structure has a significant influence on scattering behavior. Therefore, it is important to control the heterogeneous structure in order to achieve high luminance and uniformity of the HSOT backlighting system. Analysis of the scattering behavior should be carried out with consideration to the distribution of particle diameter, since typical polymer particles has a diameter distribution. Precise control of the size of the heterogeneous structure was realized by doping polymer particles having a narrow distribution of particle diameter.

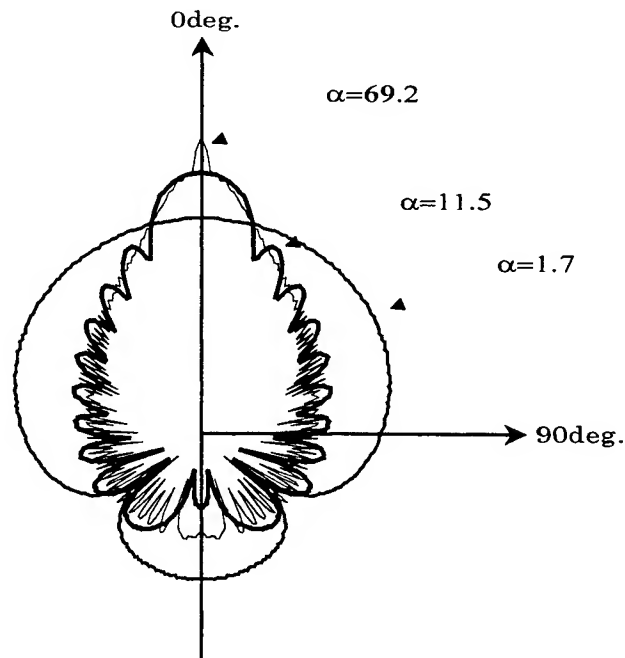


Figure 2 Calculated single scattering profile based on Mie scattering theory. The vector from the origin of the coordinates to each curve is proportional to logarithmic intensity scattered at the corresponding angle. Size parameters: $\alpha = 1.7, 11.5, 69.2$. Relative refractive index: $m = 0.961$.

Calculated and experimental luminance profiles radiated from the output surface of the HSOT light pipe whose size was 2.5-inch diagonal is shown in Figure 3. Angle of the luminance profile was defined as Figure 4. Validity of the simulation for multiple light scattering phenomenon was confirmed based on the good agreement between the calculated and experimental profiles.

Symmetric prism film for converting the illuminating light at 63 degree into vertical direction to the output surface (0 degree) was developed based on the ray tracing analysis. The illuminating light was refracted and reflected, and finally converted with the optimized prism film as shown in Figure 5 in which $\theta_1 = \theta_2 = 31.5$ degree. The HSOT backlighting system of 2.5 inch-diagonal using this symmetric prism film showed approximately twice the brightness (8870 lx) of the conventional one (4530 lx) at the center of the backlight under the same conditions.

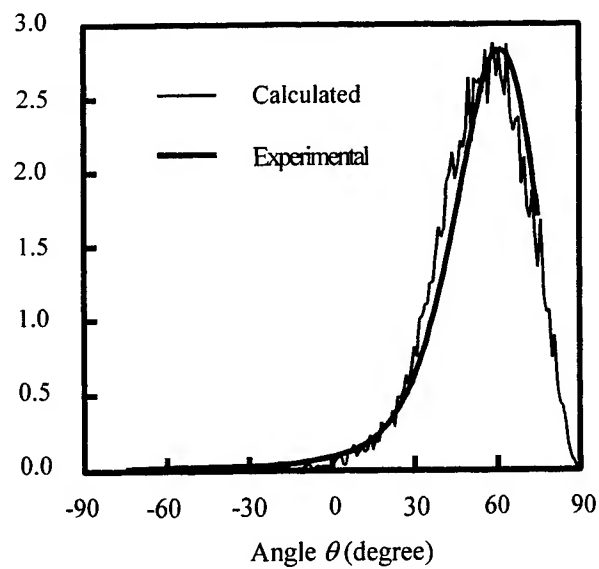


Figure 3 Calculated and experimental luminance profiles radiated from the HSOT light pipe whose size was 2.5-inch diagonal.

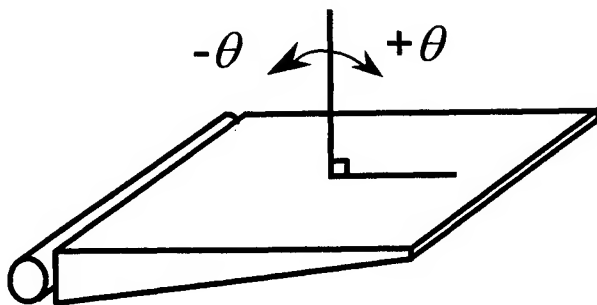


Figure 4 Definition of angle θ for luminance profile.

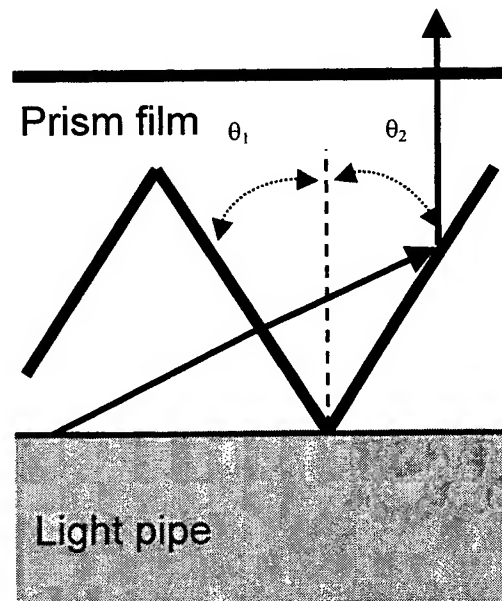


Figure 5 A typical locus of ray in the symmetric prism film optimized for the HSOT light pipe.

4. COLOR UNIFORMITY

Red color of sunset is caused by scattering in the atmosphere in which blue light is scattered stronger than red light. Rayleigh scattering theory accounts for this phenomenon and tells the relation between intensity of scattered light I_S and wavelength λ ,

$$I_S \propto \lambda^{-4}, \quad (11)$$

A general concept of scattering is based on Rayleigh scattering theory because it is simple, familiar and useful for describing a lot of scattering phenomena of nature. Therefore, it had been believed that scattering phenomenon inside the light pipe caused the degradation of the color uniformity so that the output light became yellowish in proportion to the distance from the lamp. Rayleigh scattering theory, however, doesn't hold when a scatterer is larger than $\lambda/20$.

Disproving the general concept of scattering, we found the method for realizing sufficient color uniformity based on Mie scattering theory. The method is to optimize size of the heterogeneous structures (diameter of the particles). Figure 6 shows the scattering efficiency curves of a single particle for 435, 545 and 615 nm-wavelength, respectively. These wavelengths correspond to RGB wavelengths of typical cold fluorescent lamps. Each curve oscillates and converges the limit $K = 2$. As shown in Figure 6, in the case of a smaller particle (A), blue light is scattered stronger than red, however, in the case of a larger particle (B), blue light is not scattered stronger than red. Therefore, the color of illumination can be controlled by changing the size of the heterogeneous structures, even if all materials forming the HSOT polymers are transparent.

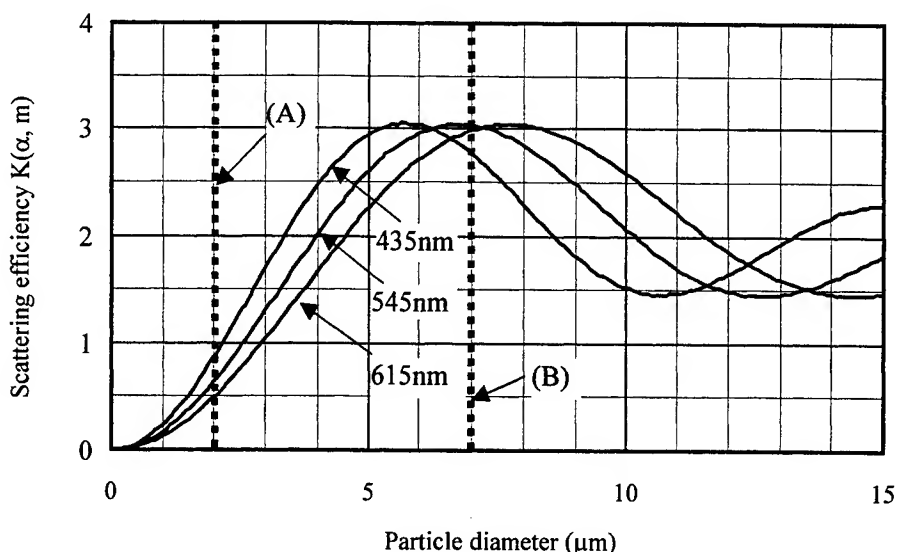


Figure 6 Scattering efficiency curves of a single particle for 435, 545 and 615 nm-wavelength, respectively. Typical cold fluorescent lamps have peaks of spectrum around these wavelengths. $m = 0.965$.

Figure 7 shows the color temperature for 4.0-inch diagonal HSOT backlighting systems containing the particles (A) and (B), respectively. Although the HSOT backlighting system containing the particle (A) showed poor uniformity of color temperature which can be explained by the general concept, the HSOT backlighting system including the optimized particle (B) showed higher uniformity without dependence of the distance from the lamp. The uniformity by the optimized particle (B) was sufficient for recent LCDs. Actually, a 10.4-inch diagonal HSOT backlighting system containing the optimized particle has been used in a notebook computer released to the market in 1998. It follows from what has been described that optimization of the heterogeneous structures realizes scattering phenomenon without color dispersion and the HSOT backlighting system with sufficient color uniformity.

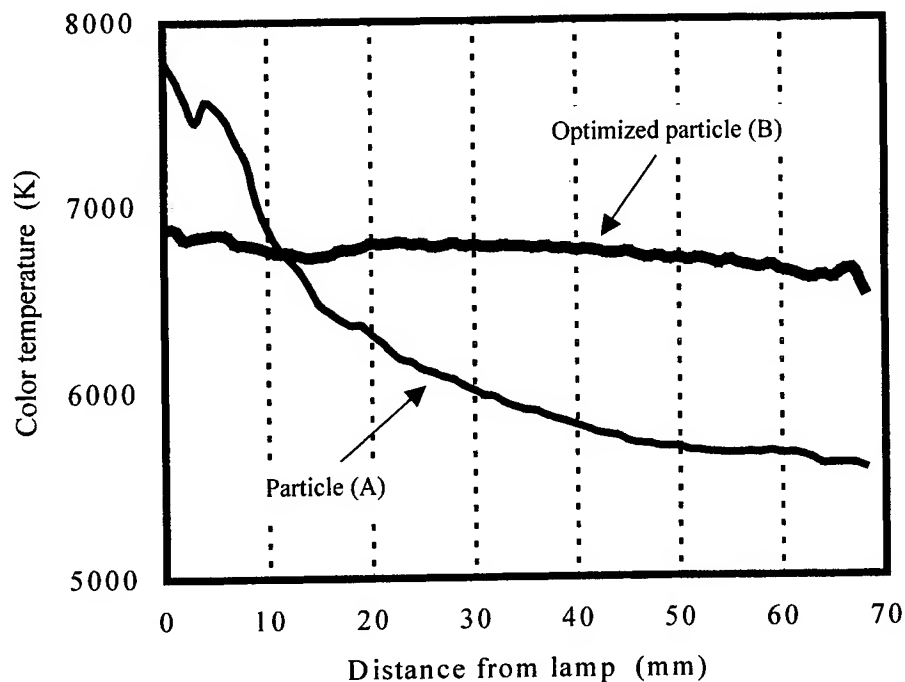


Figure 7 Color temperature for 4.0-inch diagonal HSOT backlighting systems containing the particles (A) and (B), respectively.

5. NOVEL ASYMMETRIC PRISM FILM FOR THE HSOT

We proposed a novel asymmetric prism film to achieve high luminance compared to the symmetric prism film which had been optimized for the HSOT light pipe. Figure 8 shows typical loci of ray in the asymmetric prism film. Here, angle of the prism was divided into two parts θ_1 and θ_2 . In the case of the asymmetric one, θ_1 is not equal to θ_2 . Although only one locus with an angle from the light pipe can be converted into 0 degree in the symmetric type prism sheet, two loci with different angles can be converted into 0 degree in the asymmetric one. Furthermore, the luminance profile with the asymmetric one is narrow compared to symmetric one.

The asymmetric prism film was optimized for the 2.5-inch HSOT light pipe by using our prism film simulation program based on a ray tracing technique. Calculated and experimental output profiles from the asymmetric and symmetric prism films are shown in Figure 9. Optimized angles of the prism θ_1 - θ_2 were 5.6-35.0 for the asymmetric type and 31.5-31.5 for the symmetric type, respectively. Luminance with the asymmetric prism film was about 30% higher than that of the symmetric one.

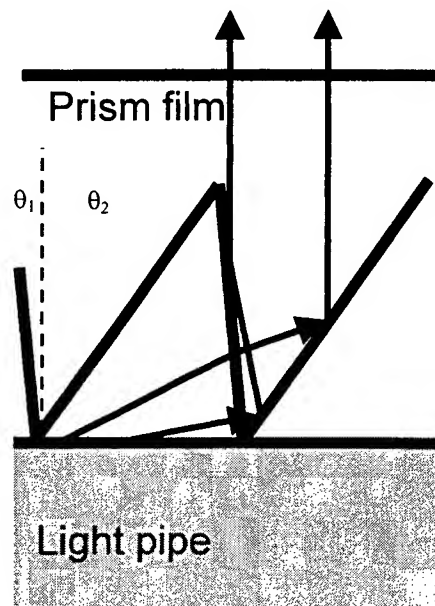


Figure 8 Typical loci in the asymmetric prism film.

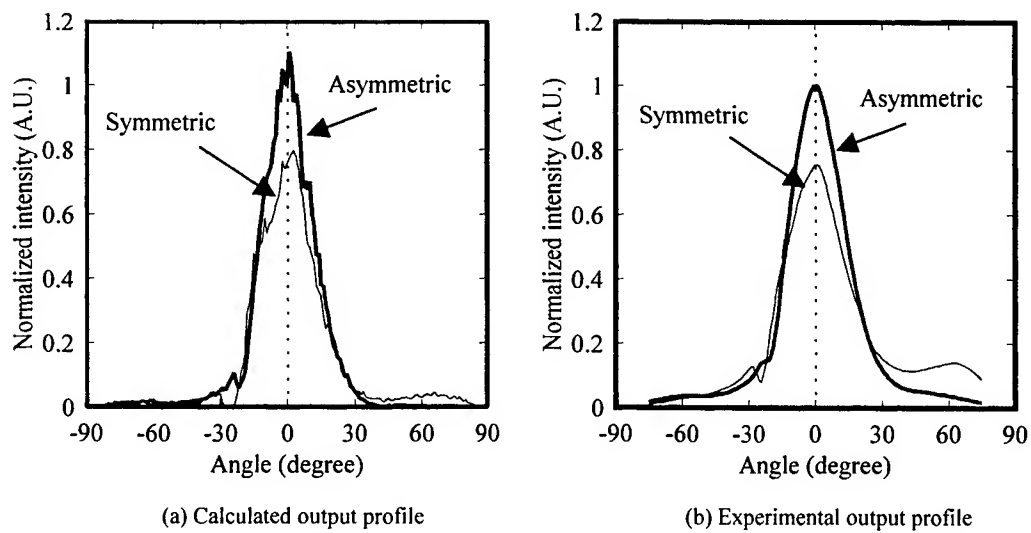


Figure 9 Calculated and experimental output profiles from the asymmetric and symmetric prism films.

CONCLUSION

Analysis of the multiple light scattering inside the HSOT polymer and optimization of the HSOT polymer for a LCD backlight were carried out by using the HSOT designing simulation. As a result, the HSOT backlighting system including the symmetric prism film optimized for the HSOT light pipe showed twice the brightness and efficiency of the conventional transparent PMMA plate backlighting system, and the uniform color temperature without dependence of the distance from the lamp. Furthermore, the asymmetric prism film was proposed and prepared for the HSOT light pipe by using the prism film simulation program based on the ray trace technique. The optimized asymmetric prism film system showed about 30% higher luminance than that of the symmetric prism system. Finally, it should be emphasized that optimization of the heterogeneous structures realized scattering phenomenon without color dispersion, which disproved the general concept of scattering.

REFERENCES

1. A. Horibe, M. Izuhara, E. Nihei, and Y. Koike, "Brighter backlights using highly scattered optical transmission polymer," J. of SID, 3, pp.169-171, 1995.
2. A. Horibe, E. Nihei, and Y. Koike, "Bright LCD Backlight using high-scattering optical-transmission polymer," SID'96 Digest, pp. 577-579, 1996.
3. A. Horibe, M. Baba, E. Nihei, and Y. Koike, "High-efficiency and high-quality LCD backlight using highly scattering optical transmission polymer," IEICE TRANS. ELECTRON., E81-C, pp. 1697-1702, 1998.
4. A. Tagaya, and Y. Koike, "Highly scattering optical transmission polymers for bright display," Polymer Preprints, 40, pp. 1163-1164, 1999.
5. I. Lux, and L. Koblinger, Monte Carlo Particle Transport Methods: Neutron and Photon Calculations, CRC Press, Boca Raton, 1991
6. G. Mie, "Beiträge zur optik trüber medien, speziell kolloidaler metallösungen," Ann. der Phys., 25, pp. 377-445, 1908.
7. M. Kerker, The Scattering of Light and Other Electromagnetic Radiation, Academic Press, San Diego, 1969.

Development of Metal Containing Polymers For Optoelectronic Applications

Wai Kin Chan*, Sijian Hou, Po King Ng, Chi Tak Wong, Sze Chit Yu

Department of Chemistry, University of Hong Kong, Pokfulam Road, Hong Kong, China

ABSTRACT

Most of the work in organic electroluminescent polymers has been focused on organic conjugated polymers. However, polymers attached with transition metal complex have received relatively less attention. We have synthesized and studied the light emitting properties of some metal containing polymers based on the polypyridine complexes of rhenium and ruthenium. These complexes exhibit long-lived excited states caused by the metal to ligand charge transfer (MLCT) transitions. By varying the structure of the ligand and/or the transition metal, we are able to fine-tune the electronic properties of the resulting metal complexes.

We have synthesized a series of poly(phenylenevinylene) (PPV) derivatives which are functionalized with ruthenium polypyridine complexes at the polymer mainchain or side chain. These complexes are able to act as photosensitizers which enhance the photoconductivity of these polymers at longer wavelength. Both the conjugated backbone and the metal complex can emit light upon excitation. As a result, it is possible to tune the color by loading different amount of ruthenium complex to the polymer. Luminescence studies showed that the ruthenium complex could quench the emission of the conjugated backbone in some polymers, which suggests an energy transfer process between the backbone and the metal complexes. It was also found that the presence of metal complexes could enhance the charge carrier mobilities of the polymers, as the metal and/or ligands can act as extra charge carriers in the charge transport process.

Keywords: poly(p-phenylenevinylene), PPV, ruthenium, bipyridine, terpyridine, light emitting device

1. INTRODUCTION

Since the first report of electroluminescence (EL) in poly(*p*-phenylenevinylene) (PPV),¹ different examples of EL devices based on a variety of materials including conjugated polymers²⁻³ and fluorescent dye-doped polymeric systems⁴⁻⁵ have been reported. The use of transition or rare earth metal complexes for EL devices⁶⁻⁸ has been gaining more attention because of the flexibility in structure design and modification. In normal organic materials, the maximum quantum efficiency for an EL process originated from the emission of singlet excitons is 25 % due to the spin statistic for the production of singlet and triplet excited states by charge recombination. This limits the quantum efficiency and performance of the EL devices based on ordinary organic molecular or polymeric materials.

Our group has developed different types of conjugated polymers functionalized with ruthenium (II) bipyridyl (bpy) or terpyridyl (tpy) complexes.⁹⁻¹³ The chemistry and photophysics of ruthenium bipyridyl¹⁴⁻¹⁵ and terpyridyl¹⁶⁻¹⁸ complexes have been studied extensively. They exhibit a relatively long-lived metal-to-ligand charge transfer (MLCT) excited state which makes it a promising candidate for EL devices. Upon excitation, the singlet excited state undergo intersystem crossing to the lowest triplet ³MLCT excited states and the quantum yield for this process is essentially unity. This triplet excited state is able to emit light at around 600-650 nm depending on the nature of the bipyridine ligand. By utilizing the emission from the triplet states, it is possible to exceed the theoretical 25 % limit for traditional organic light emitting devices.¹⁹ In addition, the ruthenium polypyridine complexes exhibit a reversible ruthenium

* Correspondence Email: waichan@hkucc.hku.hk; Telephone: (852) 2859-8943; Fax: (852) 2857-1586

centered $\text{Ru}^{\text{II/III}}$ oxidation and several other ligand-based reductions. As a result, the ruthenium complexes may also play the role as charge transporting species and thus enhance the charge carrier mobilities, which is very important to the performance of EL devices.

Fine tuning of the light emitting properties can be achieved by modifying the structure of the ligand or by using different transition metals. There are several approaches to incorporate transition metal complexes to the polymer molecule. In the first approach, the metal center constitutes part of the polymer mainchain (Figure 1). The second approach involves the use of the polymer mainchain as the site for coordination. Alternatively, the metal complexes can also be attached to the polymer molecule as pendant group. In these polymers, there are two light emitting moieties: the π -conjugated main chain and the ruthenium complexes. Usually the PPV mainchain emits in the green region while the ruthenium complex emits in the red region. Therefore, the emission color is a combination of these two colors. Tuning of the emission properties can be adjusted by changing the metal content in the polymers.

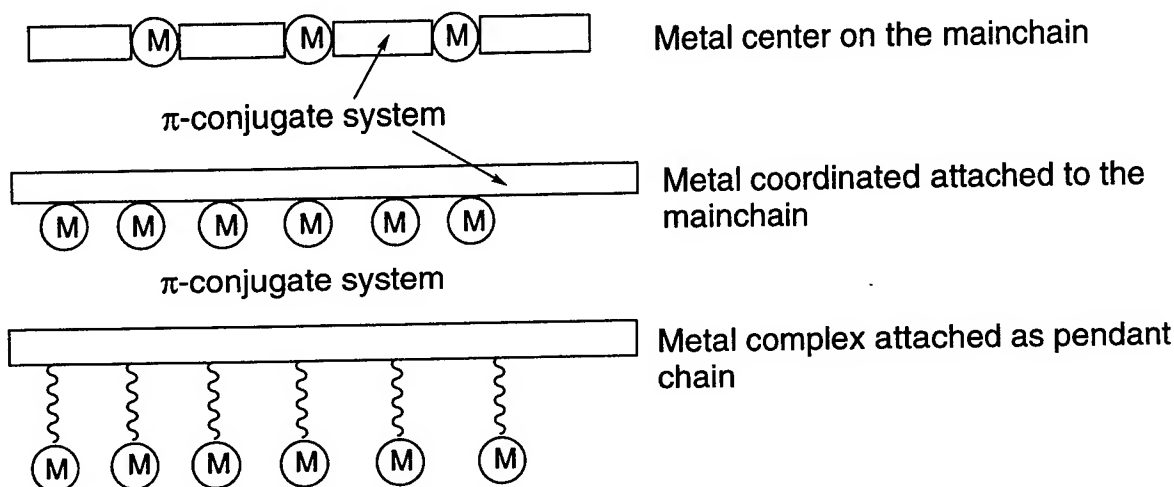


Figure 1. Design of different types of metal containing polymers.

2. RESULTS AND DISCUSSION

The ruthenium containing PPVs were synthesized by the palladium catalyzed Heck coupling reaction.²⁰ Compared to other PPV synthetic methods such as Mc Murray condensation, Wittig reaction, and the precursor polymer approach, the mild reaction condition can tolerate a variety of functional groups and hence different types of functionalized PPV can be easily prepared. We have synthesized three types of PPV (polymers A-C) derived from three ruthenium containing monomers (Figures 2-3). These polymers are soluble in common organic solvents and can be processed into optical quality thin film by spin coating or solution casting techniques. For those polymers with lower metal content, they are soluble in non polar solvents such as 1,2-dichloroethane or 1,1,2,2-tetrachloroethane. Those polymers with higher ruthenium content are soluble in polar aprotic solvents such as *N,N*-dimethylformamide (DMF) or *N*-methylpyrrolidinone (NMP).

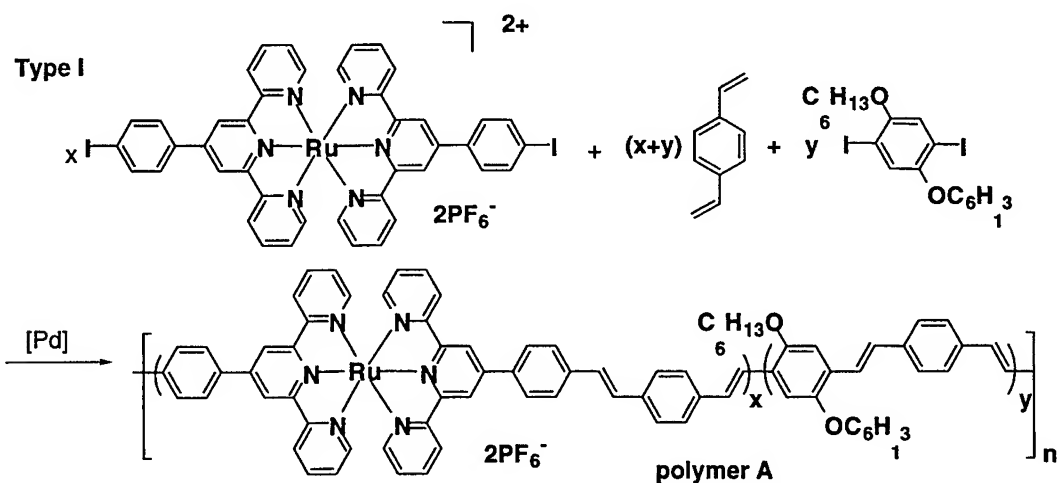


Figure 2. Synthesis of ruthenium functionalized **polymer A** with ruthenium center as part of the main chain.

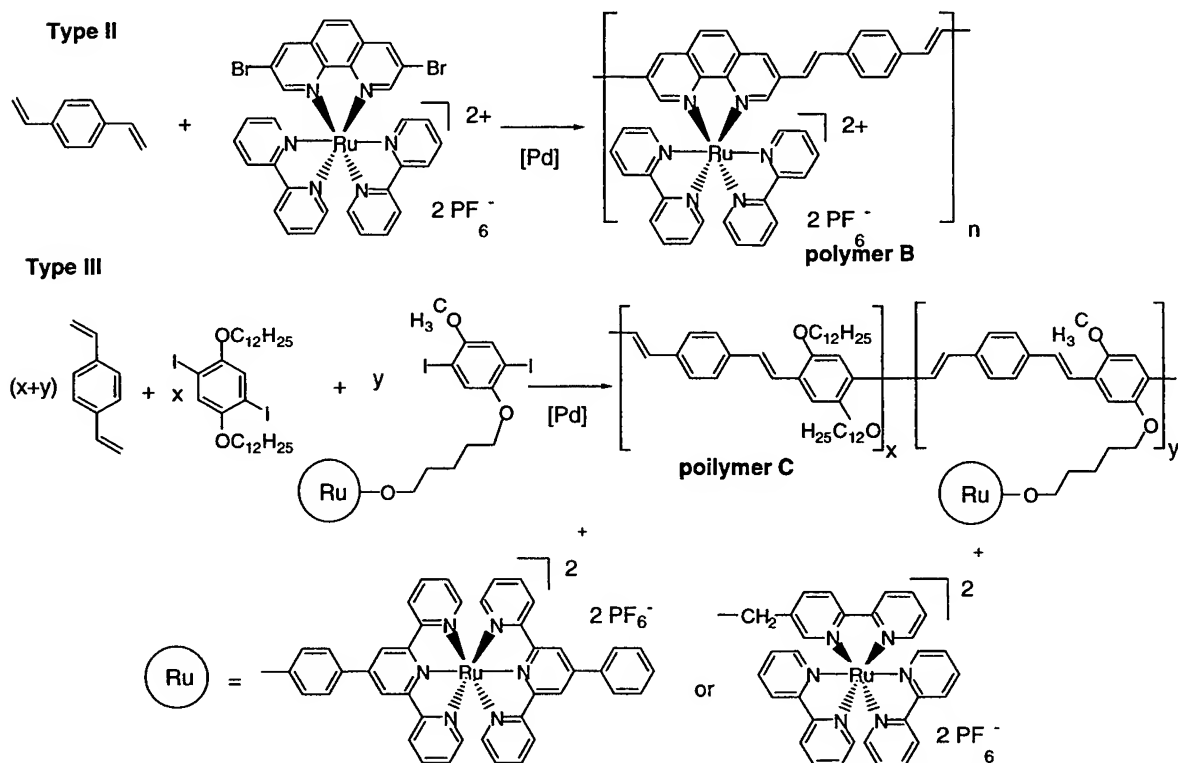


Figure 3. Syntheses of polymers **B** and **C** with the ruthenium polypyridine complexes attached to the polymer main chain or side chain.

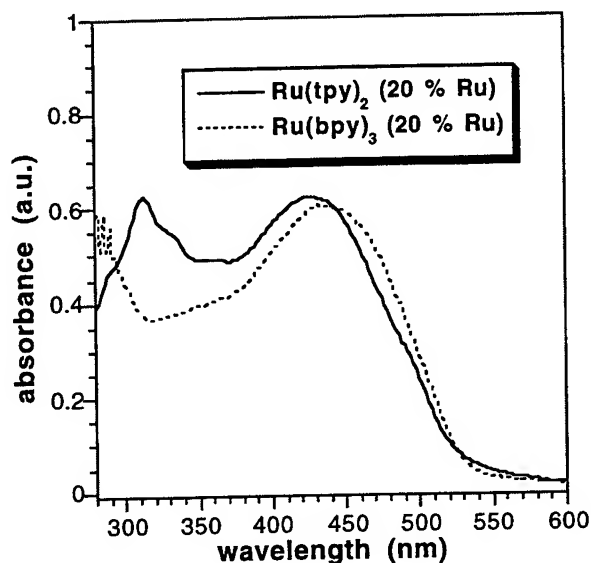


Figure 4. Electronic absorption spectra of polymer C with pendant ruthenium bipyridine or terpyridine complexes.

The electronic absorption spectra of these polymers mainly consist of two components. Two strong absorption bands are usually observed at ca. 290 and 460 nm which are due to the π - π^* transition of the polypyridine ligand and the π -conjugated mainchain, respectively. In addition, there is also another absorption peak centered at the vicinities of 500-550 nm which is assigned to be the metal-to-ligand charge transfer transition. It is considered to be the promotion of an electron from the $d\pi(\text{Ru})$ to the $\pi^*(\text{bpy}$ or $\text{tpy})$ orbitals, and is a characteristic absorption features for ruthenium polypyridine complexes. Figure 4 shows the typical absorption spectra for polymer C functionalized with pendant ruthenium bipyridine and terpyridine complexes. The spectra are dominated by the absorption due to the conjugated main chain, while the absorption due to the metal complex only appears as a small shoulder. However, in the PL spectra, the intensities of the emissions originated from the MLCT excited states are comparable to those from the main chain.

The charge carrier mobilities of these polymers were studied by the conventional time-of-flight technique. A polymer film with thickness of approximately 1 μm was prepared by solution casting on an indium-tin-oxide (ITO) coated glass slide. A layer of semi-transparent gold electrode (thickness ~ 100 Å) was coated on the polymer surface by evaporation under high vacuum. A nitrogen laser (337 nm, pulse width = 5 ns) was used to generate a sheet of charge carriers. Under an externally applied electric field, the movement of charge carriers was monitored with an oscilloscope. The drift mobility μ was calculated according to the equation $\mu = L/t_T E$ where L is the film thickness, E is the applied electric field, and t_T is the transit time which corresponds to the time when the leading part of the carrier distribution reaches the opposite electrode. The transient photocurrent profile indicates a dispersive charge transport with non-Gaussian carrier distribution. The charge carrier mobilities under different applied field strength and temperature were also studied. An Arrhenius plot of the charge mobility at different temperature indicates a thermally activated charge migration process and the activation energies were estimated to be in the range between 0.1 to 0.2 eV.

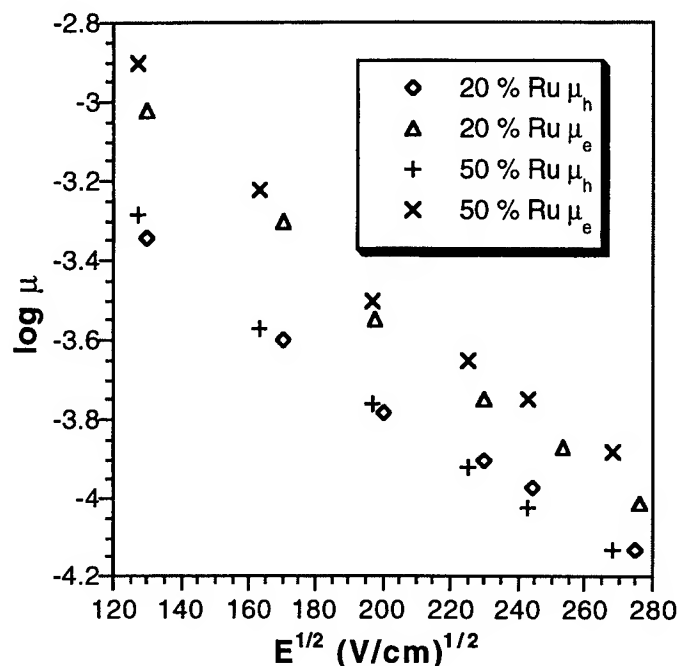


Figure 5. Field dependence hole and electron carrier mobilities for polymer **B** with different ruthenium content.

The field dependent charge carrier mobilities show a very interesting feature. A plot of hole mobility at different applied electric field strength for polymer **B** with different ruthenium content is shown in Figure 5. The electron carrier mobilities μ_e of the polymers are in general higher than the hole carrier mobilities μ_h . Those polymers with higher ruthenium content also exhibit higher mobilities. This is probably due to the fact that the ruthenium bipyridine complexes are able to enhance the carrier mobility by providing more charge carrier to the polymers. Since an electric field reduces the barrier for jumps along the field direction, the drift mobility is expected to increase with increasing field strength. However, the $\log \mu$ vs. $E^{1/2}$ plot shows a nearly linear relationship with negative slope, indicating that increasing the electric field would decrease the carrier mobility. This interesting phenomenon can be explained by the presence of off-diagonal disorder in the hopping sites. There are enhanced routes for charge transport which involve some short hops not in the direction of the electric field.²¹

The electroluminescence behavior of the polymers were evaluated by preparing a simple single layer light emitting device with the configuration ITO/polymer/Al. Typical polymer film thickness is approximately 50-70 μm . The device is subjected to forward bias with the ITO as the anode and aluminium as the cathode. The current voltage characteristics of the polymer **C** with pendant ruthenium bipyridine or terpyridine complexes are shown in Figure 6. Both systems show typical diode character and exhibit turn-on voltage at 5 V with rectification ratio greater than 1000 at 15 V. The external quantum efficiencies of the devices are estimated to be 0.1 %, and the maximum luminance of the device was approximately 360 cd/m^2 .

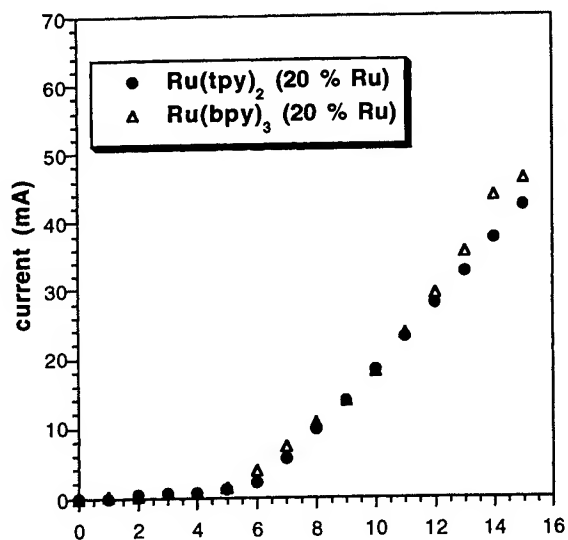


Figure 6. Current-voltage characteristic of the light emitting devices fabricated from polymer C with pendant ruthenium bipyridine or terpyridine complexes.

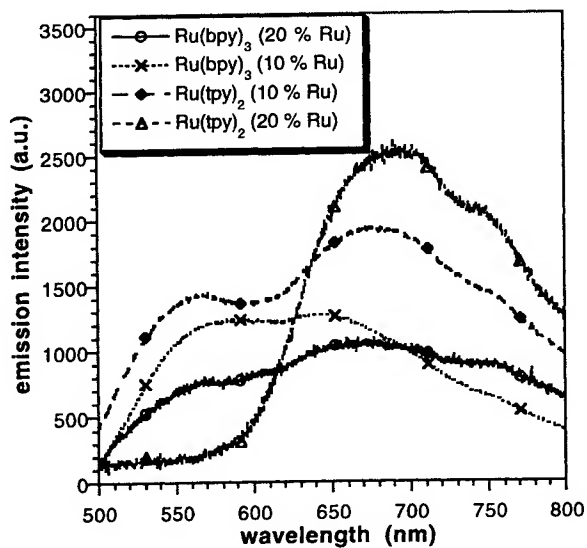


Figure 7. Electroluminescence spectra of the light emitting devices fabricated from polymer C with pendant ruthenium bipyridine or terpyridine complexes under a forward bias of 20 V.

Figure 7 shows the EL spectra of polymer C with pendant ruthenium bipyridine and terpyridine complexes under the forward bias condition. Two emission bands at 560 and 650 nm are observed in the ruthenium terpyridine containing polymers whose intensity ratio correlates to the $[\text{Ru}(\text{tpy})_2]^{2+}$ content in the polymer. Similar emission properties are also observed in the ruthenium bipyridine containing polymers with 10 % ruthenium except that the peak of the MLCT emission shifts to 680 nm. In these polymers, the resulting yellow light originates from the simultaneous emission from the PPV backbone (green light) and the ruthenium polypyridine complexes (red light). For the polymer which contains 20 % $[\text{Ru}(\text{bpy})_3]^{2+}$ complex, however, only one red emission peak is found at 690 nm. We attribute this interesting phenomenon to the energy transfer between the ruthenium bipyridyl complexes and the polymer mainchain. When the metal complex content is low, quenching of the backbone is not efficient because the backbone and the metal complex moieties are separated by a hexamethylene spacer linkage. When the $[\text{Ru}(\text{bpy})_3]^{2+}$ content is increased to 20 %, the quenching process becomes dominant. It can also be seen that the $[\text{Ru}(\text{tpy})_2]^{2+}$ complex is not an efficient quencher compared to the bipyridyl analog. It is not fully understood why there was no quenching in the PL process. The difference between PL and EL spectra may suggest that these two processes undergo different mechanisms. Nevertheless, these results demonstrate that the emission color of the polymers can be tuned by adjusting the metal complex content or by using different transition metals. In addition, by preparing mix-metal complexes, it is also possible to prepare multicolor display devices.

The schematic diagram for the energy transfer process is shown in Figure 8. Upon excitation, the π -conjugated backbone can either undergoes light emission ($\pi^*\text{-}\pi$) or an energy transfer process in which its energy is transferred to the metal complexes. The excited state of the metal complex can subsequently undergoes light emission from the MLCT excited states. As a result, the emission from the conjugated mainchain is apparently quenched by the metal complexes, and the resulting color of light emission is dependant on several factors such as the distance between the metal and main chain, nature of the spacer group, and overlap of the absorption and emission spectra etc. It was found that in the derivatives of polymer B, this quenching process is more efficient. Only red light emission was observed when the ruthenium content was 20 %. By understanding the detail of this energy transfer process, it is possible to tune the emission color by simply varying the metal content without modifying the structure of the polymers.

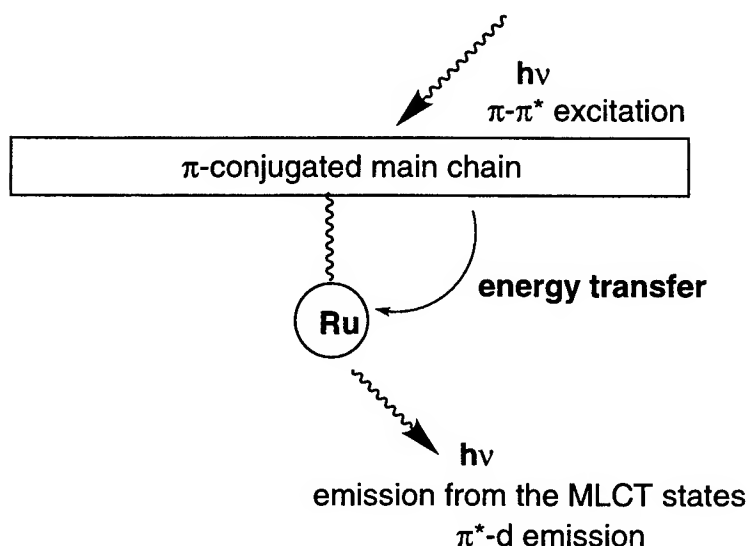


Figure 8. Schematic diagram representing the energy transfer process in the ruthenium containing polymers.

3. CONCLUSIONS

We have developed different series of conjugated polymers functionalized with ruthenium bipyridine or terpyridine complexes on the polymer main chain or side chain. It was found that the content and the nature of the metal complexes might affect the physical properties of the polymers such as photosensitivity, charge carrier mobilities, and luminescence properties. Moreover, the metal complexes are able to quench the emission from the π -conjugated main chain and it is possible to tune the emission color by varying the structure or metal content of the polymers.

4. ACKNOWLEDGMENTS

This work was supported by the Research Grants Council of The Hong Kong Special Administrative Region, China (Project No. HKU 7093/97P and HKU 7090/98P) and The University Research Committee, University of Hong Kong. Partially financial support from the Hung Hing Ying Physical Science Research Fund and the Run Run Shaw/Leung Kau Kui Research and Teaching Endowment Fund is also acknowledged.

5. REFERENCES

1. J. H. Burroughes, D. D. C. Bradley, A. R. Brown, R. N. Marks, K. Mackay, R. H. Friend, P. L. Burns, and A. B. Holmes, *Nature* **347**, pp. 539, 1990.
2. G. Gustafsson, Y. Cao, G. M. Treacy, F. Klavetter, N. Colaneri, and A. J. Heeger, *Nature* **357**, pp. 477, 1992.
3. N. C. Greenham, S. C. Moratti, D. D. C. Bradley, R. H. Friend, and A. B. Holmes, *Nature* **365**, pp. 628, 1995.
4. J. Kido, K. Hongawa, K. Okuyama, and K. Nagai, *Appl. Phys. Lett.* **64**, pp. 815, 1994.
5. T. A. Hopkins, K. Meerholz, S. Shaheen, M. L. Anderson, A. Schmidt, B. Kippelen, A. B. Padias, H. K. Hall, N. Peyghambarian, and N. R. Armstrong, *Chem. Mater.* **8**, pp. 344, 1996.
6. J. Kido, H. Hayase, K. Honogawa, K. Nagai, and K. Okuyama, *Appl. Phys. Lett.* **65**, pp. 2124, 1994.
7. D. L. Thomsen III and F. Papadimitrakopoulos, *Polymer Preprint* **38**(1), pp. 398, 1997.
8. J.-K. Lee, D. Yoo, and M. F. Rubner, *Chem. Mater.* **9**, pp. 1710, 1997.
9. W. Y. Ng and W. K. Chan, *Adv. Mater.* **9**, pp. 716, 1997.
10. W. K. Chan, X. Gong and W. Y. Ng, *Appl. Phys. Lett.* **71**, pp. 2919, 1997.
11. S. C. Yu, X. Gong and W. K. Chan, *Macromolecules* **31**, pp. 5639, 1998.
12. X. Gong, P. K. Ng, W. K. Chan, *Adv. Mater.* **10**, pp. 1337, 1998.
13. C. T. Wong, W. K. Chan, *Adv. Mater.* **11**, pp. 455, 1999.
14. K. Kalyanasundaram, *Coord. Chem. Rev.* **46**, pp. 159, 1982.
15. A. Juris, V. Balzani, F. Barigelli, S. Campagna, P. Belser, A. Von Zelewsky, *Coord. Chem. Rev.* **84**, pp. 85, 1988.
16. E. C. Constable, *Adv. Inorg. Chem. Radiochem.* **30**, pp. 69, 1986.
17. E. C. Constable, J. Lewis, M. C. Liptrot, P. R. Raithby, *Inorg. Chim. Acta.* **178**, pp. 47, 1990.
18. J.-P. Sauvage, J.-P. Collin, J.-C. Chambron, S. Guillerez, C. Coudret, V. Balzani, F. Barigelli, L. De Cola, L. Flamigni, *Chem. Rev.* **94**, pp. 993, 1994.
19. W. Helfrich, W. G. Schneider, *J. Chem. Phys.* **44**, pp. 2902, 1966.
20. R. F. Heck, *Organic Reactions* **27**, pp. 345, 1982.
21. M. Van der Auweraer, F. C. De Schryver, P. M. Borsenberger, H. Bässler, *Adv. Mater.* **6**, pp. 199, 1994.

Polymer light-emitting diodes based on novel soluble poly(p-phenylene vinylene)

Hongjin Jiang^{*a}, Yan Zhou^a, Jingsong Huang^b, Boon-Siew Ooi^a, Yee-Loy Lam^a, Yuen-Chuen Chan^a
^aPhotonics Research Group, School of Electrical & Electronic Engineering, Nanyang Technological University, Singapore, 639798

^bNational Lab of Integrated Optoelectronics, Jilin University, Changchun, P.R.China, 130023

ABSTRACT

Conjugated polymers are a novel class of semiconductors that combine the optical and electronic properties of semiconductors with the processing advantages and mechanical properties of polymers. Since the first discovery of electroluminescence from conjugated polymer, poly(p-phenylene vinylene)(PPV) has been reported by J.H.Burroughes, et.al, in 1990, the research on polymer light emitting diodes (PLEDs) has progressed rapidly. However, the number of soluble conjugated polymers with relatively high luminescence efficiency is still limited. In this paper, a recently synthesized soluble PPV derivative poly(2-methoxy-5-butoxy-p-phenylene vinylene)(MBPPV) is adopted to fabricate PLEDs. We studied the photoluminescence and electroluminescence properties of MBPPV and its polyblend with poly(N-vinylcarbazole)(PVK). The energy transfer between MBPPV and PVK matrix in different blending concentration is also investigated. The emission peak and efficiency of the device ITO/MBPPV: PVK/Alq₃/Al are 570nm and 1.35% respectively.

Keyword: Soluble conjugated polymers, polymer blend, light emitting diode, energy transfer

1. INTRODUCTION

As a novel class of semiconductor materials, conjugated polymers combine the optical and electronic properties of conventional semiconductors with the processing advantages and mechanical properties of polymers. Since the report¹ by Burroughes et al in 1990, electroluminescence (EL) in conjugated polymers has attracted significant interest. The major advantages of polymers over inorganic semiconductor LEDs are low-cost, easy processing, heat stability, mechanical properties and the relative ease to tune the emission spectra from UV to IR by modifying the main chain structure and/or the side chain of the polymers¹⁻⁵. At same time, these polymers are free of the problems related to crystallization and aggregation, which are the detrimental factors to the quality of evaporated films made with low molecular weight organic compounds. Molecular doped polymers (MDPs)⁶⁻⁹, polymer blends¹⁰⁻¹² and polymer multilayers¹³⁻¹⁵ are typical effective methods to obtain highly efficient EL, long lifetime and variable color polymer devices.

Although research has progressed rapidly on polymer LEDs, the number of soluble conjugated polymers with relatively high luminescence efficiency is still limited. Poly(p-phenylene vinylene)(PPV), which was the first well-studied conjugated polymer that shows electroluminescence¹, has excellent thermal and chemical stability. Several soluble derivatives of PPV have been synthesized and used to fabricate LEDs and the EL films of these polymer solutions require no subsequent processing or treatment. Examples of such soluble derivatives of PPV include poly(2-methoxy-5-(2'-ethyl-hexyloxy)-p-phenylene vinylene)(MEH-PPV)², poly(2,5-dialkoxy-p-phenylene vinylene)(RO-PPV)³, and poly(2,5-diheptyl-p-phenylene vinylene)(CN-PPV)⁴.

* Correspondence E-mail: p145390240@ntu.edu.sg; Fax: 65-7904161

Among them, MEH-PPV is a typical and widely used material because of the excellent EL performance of the devices based on it. Unfortunately, MEH-PPV is soluble only at elevated temperatures; at room temperature, its solution is unstable and gel can be easily formed in the solution. As a result, the solution casting of uniform films of MEH-PPV requires special care. In this work, the photoluminescence (PL) and EL performances of a novel soluble PPV derivative have been investigated.

2. DEVICE FABRICATION AND EXPERIMENT

Poly (2-methoxy-5-p-phenylene vinylene)(MBPPV), a novel derivative of PPV, in which the introduction of the methoxy and butoxy side groups makes it soluble, is adopted for the fabrication of our polymer LEDs. The chemical structure of MBPPV is illustrated in Figure 1. MBPPV has excellent solubility in the conjugated form, at room temperature and in common organic solvents. A thin film of MBPPV can be obtained by spin coating directly from the solution and the precursor route, which is necessary for the preparation of other PPV thin films, can be avoided. Additionally, MBPPV has high thermal stability and it shows no thermal degradation below 420°C. Such properties are desirable for good device performance. However, MBPPV shows relatively low PL quantum yield. Its film forming property is not very ideal, the spin-coated film is not uniform. In order to overcome these problems, polymer blends have been employed to fabricate the emitting layer.

Polyblending, i.e. blending polymers with different emission and charge-transport characteristics, is a usual approach to tune the color of emission and to improve the EL efficiency^{10,11}. The tuning of the color and the improvement of the EL efficiency result from the exciton transfer from the high band gap to the low band gap material between the blended polymers and the balance between two types of charge carrier in the devices. This exciton transfer depends on the overlap of the emission and absorption spectra of the blended materials. Poly (N-vinylcarbazole) (PVK) was adopted as the active matrix in our polyblend system. PVK has been widely used as a hole-transporting polymer^{10, 11, 16} as it has good film-forming property and relatively high hole-transporting capability. Moreover, the PL spectrum of PVK overlaps well with the absorption spectrum of MBPPV and this enables efficient energy transfer from the transport material (PVK) to the emitter (MBPPV). The experimental analysis of this blend showed that the PL intensity of MBPPV in the blend could be far greater than that of the pure MBPPV, which indicates that MBPPV in the PVK matrix can improve the EL efficiency and stability of the devices.

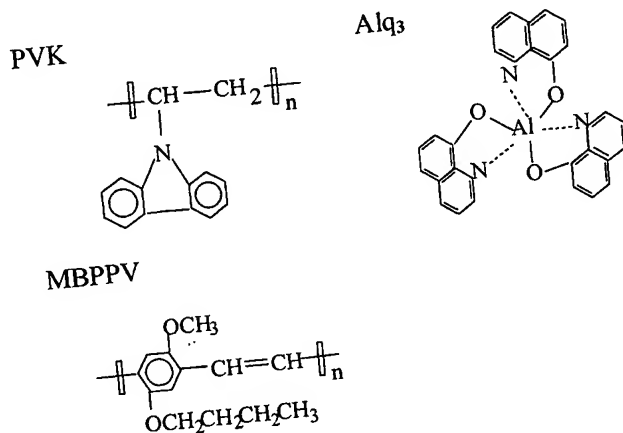


Figure 1. Molecular structures of MBPPV, PVK and Alq₃.

The blend solution of PVK: MBPPV in chloroform with various blend concentrations were prepared to study the energy transfer between them. The weight ratios between the PVK and MBPPV are 15:1, 12:1, 10:1, 5:1 and 2:1 respectively. Two kinds of EL device based on this polyblend were fabricated: indium-tin-oxide (ITO)/PVK:MBPPV/Al and ITO/ PVK: MBPPV/8-(quinolinolate)-aluminum (Alq₃)/Al. Alq₃ serves as an electron transporting layer in the latter device structure. PVK and Alq₃ were purchased from Aldrich Co. Inc. Their molecular structures are depicted in Figure 1. ITO glass with a sheet

resistance of about 50Ω per square was used as the substrate of the devices. Prior to the polymer layer deposition, the ITO substrate was thoroughly cleaned by ultra-sonication in organic detergents, and de-ionized water, then blown dried with filtered nitrogen. Al was used as the electron injection electrode of the devices. Films of the polymer blends were deposited by spin coating at room temperature without subsequent processing or heat treatment. The films are dense, uniform and have excellent reproducibility. The thickness of the film is about 150nm, depending on the concentration of the solution and the spin rate, etc. Alq_3 and Al electrode were deposited at a pressure below 3×10^{-7} Torr, and their deposition rates were controlled by a quartz oscillating thickness monitor to be 0.1nm/s and 0.2nm/s respectively. The thickness of Alq_3 and Al is 8 and 300nm respectively. The emitting area is $2 \times 2 \text{mm}^2$. The luminance was measured by a Luminance Meter (Handy Model ST-86LA), and the emission spectra were measured with a RF-530Pc Spectrofluorophotometer. Absorption spectrum was measured with UV-3100, UV-VIS-NIR Recording Spectrophotometer. All measurements were carried out at room temperature under ambient atmosphere.

3. RESULTS AND DISCUSSION

The MBPPV solution (10% in chloroform) was first spin-coated on a quartz glass substrate to measure the absorption and PL spectra at room temperature. Figure 2 displays absorption and PL spectra of MBPPV film. The excitation wavelength of PL spectrum is 482nm. The absorption peak corresponding to π - π^* transitions of the MBPPV film is observed at the wavelength of 468nm. The broad absorption band is the result of the superposition of the absorption of species with different transition energies. However, there is no mirror image relation between absorption and PL spectra in Figure 2. The PL peak of the spectrum is at 585nm, and the PL spectrum has a relatively narrow half-width (36nm). This can be explained by the fact that emission always occurs from the lowest energy states of the upper band, since energy is transferred from higher π - π^* states to lower energy states before radiative deactivation takes place.

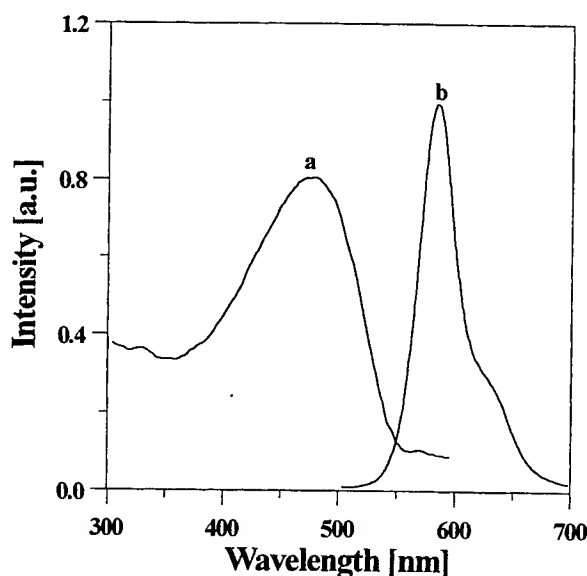


Figure 2. Absorption (a) and PL (b) spectra of a MBPPV film. The excitation wavelength for the PL spectrum is 482nm.

Figure 3 shows the PL intensity of various polyblend concentrations. We find that the PL spectra of different polyblends have the same shape and emission peak at 570nm. However, the PL intensity varies with the variation of the blend concentration, which indicates that there are interactions between the matrix (PVK) and emitter (MBPPV). The emission intensity increases with the increase of the MBPPV concentration in the PVK matrix. However, in the PVK:MBPPV system, the emission intensity is maximum at the weight ratio of 10:1. Beyond that, the emission intensity decreases with the increase of MBPPV concentration. The intensity decrease may be attributed to concentration quenching in this blend system. The emission peaks of the blended film PL spectra are blue-shifted by 15nm in comparison to the peak of the pure MBPPV film as shown in Figure 2. This is

possibly due to the variation of the MBPPV chain conformation in the PVK matrix and the interaction between them. As we know, the emitted photon energy of conjugated polymer, i.e. the $\pi-\pi^*$ transition energy, is always correlated with the conjugation length. The conjugation length of MBPPV in the blends probably becomes smaller because of the dispersing function of the PVK molecule, and this may result in the higher $\pi-\pi^*$ transition energy.

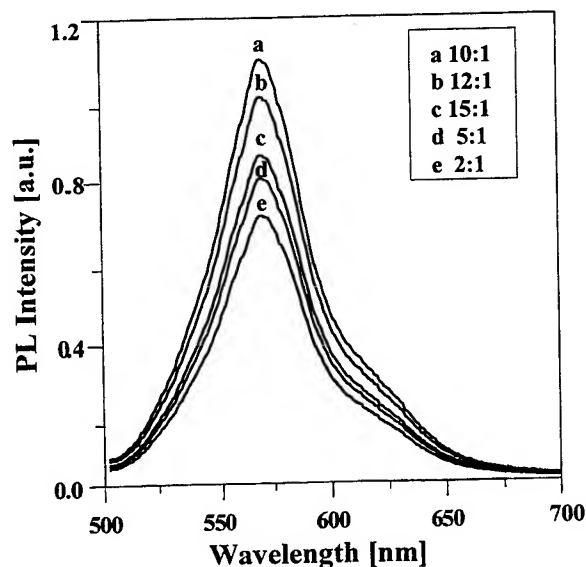


Figure 3. PL spectra of polyblend of PVK:MBPPV with various blend concentration excited at 480nm.

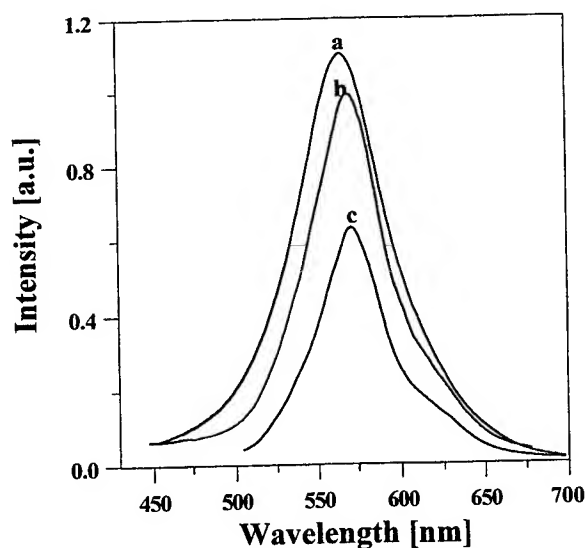


Figure 4. EL (a) and PL (b) spectra of a double-layer structure, PL (c) spectrum of a single-layer structure. The excitation wavelengths for (b) and (c) are 400nm and 482nm respectively.

EL devices are fabricated using the blend of PVK and MBPPV at 10:1 weight ratio, since the polyblend film has the strongest emission intensity at this blend concentration. The EL spectrum of a double-layer LED, and the PL spectra of both a

single-layer and a double-layer structure are illustrated in Figure 4. Although, the PL spectrum of the double-layer structure was obtained by exciting at 400nm which is the absorption peak of Alq_3 , the two PL spectra have the same emission peak at 570nm and the same spectral shape, which indicates that the emitting region is located in the polyblend layer. EL spectra of the two structures are of the same shape, and they are almost identical to their PL spectrum. As there is no luminescence from Alq_3 at the wavelength of 520nm, this indicates that Alq_3 only serves as electron transporter and it has no contribution to the PL and EL of the double layer structure.

The current-voltage curves of the double-layer and the single-layer LEDs are depicted in Figure 5. The turn-on voltages of the double-layer and the single-layer LEDs are about 3.5V and 4.2V respectively.

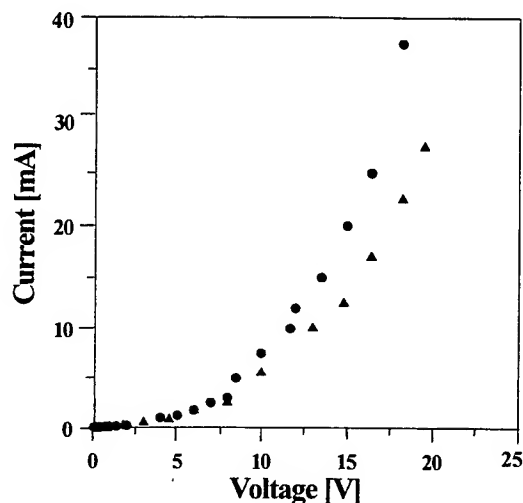


Figure 5. Current-voltage curves of a double-layer (•) and a single-layer (▲) LEDs.

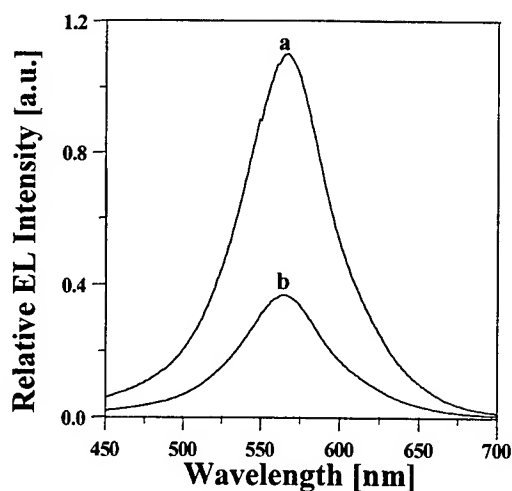


Figure 6. EL spectra of double layer structure (b) and single layer structure (a) devices at the same operation voltage (8V).

When the bias voltage was increased beyond the turn-on voltage, bright yellow light was observed in both devices. Figure 6 compares the EL spectra of single layer and double layer, it shows that at the same operation voltage (8V), the double layer structure device have a stronger EL intensity than the single layer device. The maximum external quantum efficiency of the double-layer LEDs reaches 1.35% (at 28.3mA/cm²), which is almost twice that of the single-layer LEDs (0.84% at 16.8mA/cm²). This is attributed to the introduction of Alq₃, which improves the efficiency of electron-injection and meanwhile balances the injection of the two charge carriers.

4. CONCLUSION

PL and EL characteristics of polymer LEDs made from a novel soluble derivative of PPV, MBPPV and its polyblends with PVK matrix have been studied. Energy transfer between them has also been investigated. A single-layer and double-layer structure LEDs with polyblends as the active layer are fabricated. It has been demonstrated that the turn-on voltages and external quantum efficiencies of the double-layer LEDs (3.5V, 1.35%) are better than those of the single-layer structure (4.2V, 0.84%). The emission peak is located at 570nm. MBPPV is a potential polymer in organic light emitting field, and further research work on device optimization will be carried out to obtain a better device performance based on this material.

- [1] J.H. Burroughes, D.D.C. Bradley, A.R.Brown, R.N.Marks, K.Mackay, R.H.Friend, P.L.Burns, A.B.Holmes, *Nature (London)*, 347(1990) 539.
- [2] G.Yu, C.Zhang, Q.Pei, Y.Cao, Y.Yang, A.J.Heeger, *Material Research Society Conference*, San Francisco, April 1996.
- [3] D.Braun, E.G.J.Staring, R.C.J.E.Demandt, etc, *Synth.Met.*,66(1994)75.
- [4] N.C.Greenham, A.R.Brown, D.D.C.Bradly, R.H.Friend, and A.B.Holmes, *Nature*365(1993)628.
- [5] Y.Yang, Q.Pei, A.J.Heeger, *J.Appl.Phys.*, 79(1996)934.
- [6] J.Kido, M.Kohda, K.Hongawa, K.Okuyama, K.Nagai, *Mol.Cryst.Liq.Cryst.*, 227(1993)77.
- [7] J.Kido, M.Kohda, K. Okuyama, K.Nagai, *Appl.Phys.Lett.*,61(1992)762.
- [8] Y.Yang, H.J.Jiang, S.Y.Liu,X.M.Zhou,F.Wu,W.J.Tian,Y.G.Ma,J.C.Shen, *Synth.Met.*,91(1997)335.
- [9] J.Kalinowski G.Giro, P.Di Marco, V.Fattori, *Synth.Met.*,98(1998)1.
- [10] H.Nishino, G.Yu, A.J.Heeger, T.-A.Chen, R.D.Rieke, *Synth.Met.*, 68(1995)243.
- [11] J.S.Huang, H.F.Zhang, W.J.Tian, J.Y.Hou, Y.G.Ma, J.C.Shen, S.Y.Liu, *Synth.Met.*, 87(1997)105.
- [12] S.Tasch, E.J.W.List, O.Ekstrom, W.Graupner, G.Leising, P.Schlichting, U.Rohr, Y.Geerts, U.Scherf, K.Mullen, *Appl.Phys.Lett.*,71(1997)2883.
- [13] I.D.Park, Q.Pei, M.Marrocco, *Appl.Phys.Lett.*,65(1994)1272
- [14] A.J.Heeger, I.D.Park, F.Klavetter, C.Zhang, Y.Yang, Q.Pei, N.Colaneri, *MRS Spring Meeting, Symposium L on Electroluminescent Polymers*, San Francisco(1994)
- [15] Y.He, S.Gong, R.Hattori, J.Kanicki, *Appl.Phys.Lett.*,74(1999)2265.
- [16] Y.Zhang, Y.Cui, P.N.Prasad, *Phys.Rev.B* 46(1992) 9900.

Optical properties and waveguiding in films of a nonlinear polymer: Difluorophenyl-polydiphenylenevinylene (DFP-PDPV).

Anna Samoc^a, Barry Luther-Davies^a, Marek Samoc^a, Heike Liebegott^b, Regina Stockmann^b and Hans-Heinrich Hoerhold^b

^a Laser Physics Centre, RSPHysSE, Australian Photonics CRC, Australian National University, Canberra, ACT 0200, Australia

^b Institut fuer Organische Chemie und Makromolekulare Chemie, Friedrich-Schiller-Universitaet Jena, 07743 Jena, Germany

ABSTRACT

Third-order optically nonlinear polymeric materials built of rigid-rod molecules are often insoluble and transmit visible light poorly. We report on optical and waveguiding properties of a new soluble derivative of poly(*p*-phenylenevinylene) (PPV): a π -conjugated polymer poly[biphenyl-4,4'-diyl-1,2-di(4-fluorophenyl)vinylene], (DFP-PDPV). We found that solvents used for processing of the DFP-PDPV polymer may influence the film optical properties. Changes in absorption spectra, birefringence, optical attenuation and the nonlinear refractive index were observed in the films made by spin coating and solution cast using different solvents.

The films are birefringent and dispersive. Refractive indices vary from 1.76 to 1.63 for the TE polarisation of the incident light and from 1.70 to 1.60 for the TM polarisation for wavelengths from 476.5 nm to 1.55 μ m, respectively. The birefringence is an order of magnitude lower than that in films of unsubstituted PPV.

DFP-PDPV is suitable for fabrication of optical waveguides. Low loss waveguiding layers could be prepared. Propagation losses were measured at 632.8nm, 810nm and 1064nm. The losses decrease at longer wavelengths reaching the level of 1 dB/cm at 1.06 μ m. The waveguiding properties of DFP-PDPV films depend on the solvents used in processing of the polymer.

We investigated thin films of DFP-PDPV for their potential for nonlinear waveguide applications. The modulus of nonlinear refractive index $|n_2|$ in the range $(0.9-1.5) \times 10^{-14} \text{ cm}^2/\text{W}$ was measured in DFP-PDPV films at 800nm using a femtosecond degenerate four wave mixing (DFWM) technique. These studies supplement the results of nonlinear optical studies of this polymer in solution using the Z-scan technique described in Proceedings of SPIE 3473, 79-90 (1998) ¹.

Keywords: soluble conjugated polymer, difluorophenyl-polydiphenylenevinylene, poly[1,4-phenylenevinylene], absorption spectra, refractive index, third-order nonlinear optical (NLO) properties

1. INTRODUCTION

Photonics, which uses photons for signal transmission and processing has been labelled as the emerging technology for the "information era" leading to the next millennium and revolutionising communication, flow of information and data storage.

The full realisation of the potential of photonics for information processing is, however, not possible without careful studies of optical properties of materials. This includes materials for producing passive waveguide structures, materials with gain, useful for laser and optical amplifier structures and materials with nonlinear optical (NLO) properties, useful for various schemes of frequency conversion, switching and controlling of light beams.

Further author information –

A.S.(correspondence): E-mail: anna.samoc@anu.edu.au; WWW: <http://laserspark.anu.edu.au/~asa111>;

Telephone: +61-2-6249-4611; FAX: +61-2-6249-0029

H.-H.H.: E-mail: hoerhold@rz.uni-jena.de; Telephone: +49-3641-948270; FAX: +49-3641-948202

The nonlinear optical effects provide the key functions for high speed signal processing. It is expected that high data rate modulation will be available through all-optical technologies in which switching can be achieved either by changing the intensity of the transmitted light due to the intensity dependence of the refractive index of the third-order nonlinear optical material or using an optical control pulse.

Advances in the future development and processing of materials with enhanced linear and nonlinear optical properties are anticipated. There are many different types of materials that could be synthesised and fabricated into optical waveguides to exhibit nonlinear optical modulation or switching. The main advantages of organic materials are their great diversity that results in widely varying optical nonlinearities and the ease of assembly into device configurations^{2,3}. There is an effort to understand the macroscopic nonlinear optical properties of materials in terms of microscopic properties of the atoms and molecules forming them. This is especially important for organic materials, which are built of well-defined microscopic structural elements and in which the bonds holding atoms in molecules are much stronger than the forces between the molecules. It is known that molecules with double bonds exhibit larger molecular refraction and much larger polarizabilities than σ -bonded organic molecules. Understanding of the structure-property relationship⁴⁻⁶ is helpful for material optimisation, designing new materials, preparing them and evaluating their suitability for photonic devices.

In the π conjugated polymers the p_z carbon orbitals overlap stronger along the chains compared to the weaker overlap between chains. The conjugation of π electrons gives these materials their unique quasi-one-dimensional electronic and optical properties. Organic conjugated polymers have been the subject of intense research in recent years due to their semiconducting properties and due to their potential application as an active layer in electroluminescent devices. The third-order nonlinear optical properties of π conjugated polymers can vary considerably depending on the details of the chain structure and the type of substituents attached to the backbone⁵⁻⁸. A key to the successful development of optical polymer technologies is to achieve processible and environmentally stable transparent materials. In particular, optical materials need to be processed in a carefully controlled way to achieve reproducible refractive index profiles required in optical devices.

We have been interested in the development of π conjugated optical polymers based on the molecular structure of poly(*p*-phenylenevinylene) (PPV) and its derivatives. These materials possess strong nonlinearities, which may be potentially useful in all-optical switching applications⁸⁻¹⁰. Poly(*p*-phenylenevinylene) ($-\text{C}_6\text{H}_4-\text{CH}=\text{CH}-$)_n is an example of the nonlinear optical polymer built of rigid-rod molecules with a strong third-order nonlinearity. The nonlinear refractive index $|n_2|$ is in the range $10^{-12} - 10^{-11} \text{ cm}^2/\text{W}$ ⁹. PPV films can be obtained by the soluble precursor route¹¹ where the film of the precursor polymer can be transformed at high temperature into the insoluble PPV polymer. The position of electronic levels determined by π conjugation, the linear optical properties (refractive indices, film transparency) and third order nonlinearities of the films depend strongly on the conditions of the conversion of the precursor polymer¹⁰. PPV films show large optical losses of the order of 10^2 dB/cm preventing the use of the polymer in waveguiding applications. A large improvement in optical properties of PPV films can be obtained if the conversion of the precursor polymer proceeds in the environment of a host polymer, poly(1-vinyl-2-pyrrolidone) (PVP)^{10,12}. We observed low loss waveguiding of laser beams in the visible wavelength range in the films of PPV-PVP composites¹². An enhancement of nonlinear refractive index at low concentrations of PPV in the composites was detected^{10,12}.

The development of synthetic routes to PPV derivative molecules modified by introduction of solubilizing substituents has led to tractable polymeric materials, easily soluble in popular solvents¹³⁻¹⁵. Novel substituted PPV derivatives were synthesised, where mono-phenyl, di-phenyl and di-phenoxy groups substituted hydrogen atoms at the vinylene bond in the molecule of PPV. The amorphous polymers were reported to have good film-forming properties, the waveguiding films being light and air stable. Their nonresonant third-order nonlinearity, n_2 was on the order of $10^{-14} \text{ cm}^2/\text{W}$ in the wavelength range 880-990 nm¹⁶⁻¹⁹. The broadening of the signal spectrum due to self-phase modulation was observed in planar polymer waveguides made of some of these polymers^{20,21}.

Recently, a new PPV polymer: poly[biphenyl-4,4'-diyl-1,2-di(4-fluorophenyl)vinylene] known as difluorophenyl-polydiphenylenevinylene (DFP-PDPV) has been synthesised. The molecular structure of the polymer differs from the PPV molecule by the presence of bulky fluorophenyl groups substituting hydrogen atoms at the vinylene position and by the presence of diphenyl structure in the main chain modifying properties of the polymer and its solubility. The fluorine atoms replacing the hydrogen atoms may also have influence on intensity of the C-H overtone absorption in the polymer in the telecommunication important near-infrared wavelength range.

We have been interested in how optical nonlinearities and waveguiding properties may vary with the type of substituent attached to the PPV backbone⁷. Recently we reported results of Z-scan experiments performed with femtosecond pulses at 800 nm in dioxane solutions of PPV derivatives substituted with the phenoxyphenyl groups and fluorophenyl groups at the vinylene position¹. We found that the nonlinear refractive index was on the order of $10^{-14} \text{ cm}^2/\text{W}$ in both polymers, the real

part of n_2 being positive. The polymers had remarkably low values of the two-photon absorption coefficient: $(6-8) \times 10^{-16} \text{ cm}^2/\text{W}^1$ and the imaginary part of nonlinear refractive index at 800 nm.

In this paper we show new results of studies of linear and nonlinear optical properties in films of DFP-PDPV. The films were prepared from the material processed in different solvents. We observed that optical transparency, waveguiding and the propagation losses were distinctly different in these films. The refractive index dispersion was measured in two orthogonal polarizations of the incident light in the wavelength range 476.5 nm to 1550 nm. The films were studied with Degenerate Four Wave Mixing (DFWM). An instantaneous, delayed-component-free response was observed in the phase-matched and non-phase-matched DFWM geometry.

2. EXPERIMENTAL STUDIES AND DISCUSSION

2.1. Polymer and film preparation

The synthesis of poly[biphenyl-4,4'-diyl-1,2-di(4-fluorophenyl)vinylene] (DFP-PDPV) was performed at the University of Jena following the reaction scheme presented in Figure 1.

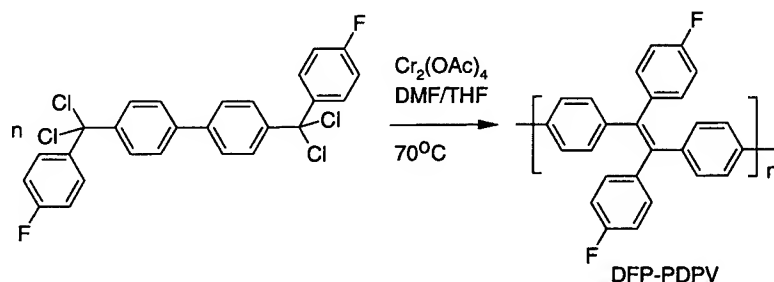


Figure 1.

Synthesis of poly[biphenyl-4,4'-diyl-1,2-di(4-fluorophenyl)vinylene] (DFP-PDPV).

The polymer was prepared by dehalogenation polycondensation of the biphenyl tetrachloride with chromium (II) acetate as the reducing agent in N,N-dimethylformamide/ tetrahydrofuran (DMF/THF) solution with the method described in Refs¹³⁻¹⁵. The molecular weight of the polymer studied here was $M_n(\text{VPO}) = 22,200$. The polymer has a high glass transition temperature $T_g = 310^\circ\text{C}$. The polymer formed yellow fibres. The solid could be readily dissolved in 1,4-dioxane (the polymer content can be >11 wt%), chloroform (>9 wt%), THF (>12%), toluene, 1,1,2,2-tetrachloroethane (TCE) (1.1 wt%). The polymer forms intensively fluorescent yellow-greenish solutions. Films were prepared from filtered solutions (0.2 μ PTFE) by spinning or solution casting on 1 mm thick fused silica (Infrasil) or glass slides (Fisher-Finest) under nitrogen atmosphere. Film thicknesses were of the order of submicron to a few tens of microns. Films were transparent except when they were prepared from the 1,4-dioxane solutions, where an opaque thick layer was formed by solution cast or spinning. These films showed island-type morphology. Some traces of opacity could be found in the films made by spinning of the polymer in TCE solutions.

2.2. Linear optical properties

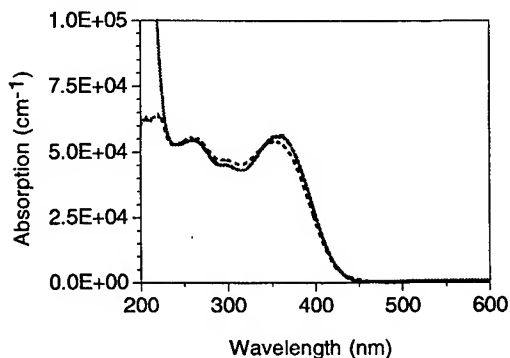


Figure 2.

Absorption in DFP-PDPV films deposited from tetrahydrofuran solution (solid line), $\lambda_{\text{max}} = 361 \text{ nm}$ and 1,1,2,2-tetrachloroethane solution (broken line), $\lambda_{\text{max}} = 352.5 \text{ nm}$.

Figure 2 shows optical absorption spectra of DFP-PDPV in the films deposited from THF and TCE solutions. The spectra were measured with a UV-VIS-NIR spectrophotometer (SHIMADZU, model UV-3101PC). A film prepared from THF solution had absorption maximum at 361 nm, decadic absorption coefficient was measured to be $\alpha = 5.6 \times 10^4 \text{ cm}^{-1}$ in the film. The absorption band appeared at 352 nm, $\alpha = 5.4 \times 10^4 \text{ cm}^{-1}$ in the film prepared from TCE solution spun on a fused silica (Infrasil) slide. The maximum appeared at 356 nm, $\alpha = 5.9 \times 10^4 \text{ cm}^{-1}$ if the film was deposited from TCE solution on Fisher glass slide. We interpret the shift as being a result of the polymorphism changing orientation of molecules in the films. Absorption maximum of DFP-PDPV in dioxane solution¹ appeared at 361 nm, extinction coefficient was equal to $2.8 \times 10^4 \text{ L mole}^{-1} \text{ cm}^{-1}$.

The long-wavelength absorption maximum in DFP-PDPV film is closely related to a π - π^* transition assigned for the conjugated electron system in the parent molecule poly(4,4'-diphenylenediphenylvinylene) (PDPV) which has a maximum close to 354 nm²², $\alpha = 1.6 \times 10^4 \text{ L mole}^{-1} \text{ cm}^{-1}$. It indicates that the substitution of the C-H bond with a C-F bond in the phenyl group attached to the vinylene group of the polymer backbone does not change substantially the π - π^* energy gap. However, one can notice a big difference in the optical absorption if one compares optical spectra of the soluble derivatives of phenyl substituted PPV with the spectra of pristine PPV film showing an absorption maximum in the range 430-460 nm¹⁰.

The blue shift of the absorption maximum to higher energy in DFP-PDPV can be caused by reduction in the π conjugation due to the presence of the biphenyl segment in the vicinity of the phenylvinylene unit in the polymer backbone and to the substitution of hydrogen atoms at vinylene position with bulky fluorophenyl groups. These may induce a steric hindrance in the phenylenevinylene unit, reduce the planarity of the phenylenevinylene part and affect the conjugation of π electrons in the molecule. The increase of the energy of electronic excitation in the molecules may influence linear and nonlinear optical polarization of the material.

2.2.1. Refractive index data and dispersion

The index of refraction is a fundamental property of a material. It may give an insight into the electronic structure of a molecule but also may be an indication of the purity and reproducible fabrication of a material. We measured refractive indices in the polymer films of DFP-PDPV with a Metricon, model 2010 prism coupler at wavelengths: 476.5 nm, 488 nm, 514.5 nm, 632.8 nm and 810 nm available at the Laser Physics Centre, ANU and the Metricon, model 2010 prism coupler at 632.8 nm and 1550 nm available at the Physics Department, UNSW. The measurements proceeded with light beams obtained from various laser sources. The measurement accuracy and resolution were within specification of the prism coupler: index accuracy ± 0.001 , index resolution ± 0.0005 . The investigated area of the film where the film was in contact with the measuring prism was of about 1 mm diameter.

We measured the dispersion of refractive indices in DFP-PDPV films for TE and TM polarisation of the incident light. Figure 3 shows the refractive index measured in the films of DFP-PDPV prepared from THF, chloroform and 1,1,2,2-tetrachloroethane solutions. The films were birefringent. The index varied from 1.76 to 1.63 for TE polarisation of the incident light and from 1.70 to 1.60 for TM polarisation between the wavelengths of 476.5 nm and 1.55 μm , respectively. The birefringence was wavelength dependent. The average value of the difference of the indices $n_{\text{TE}} - n_{\text{TM}}$ was found to be 4.5×10^{-2} in the measured wavelength range.

The birefringence in the films is caused by orientation of polymer molecules in the film formation process. They can be ordered with the longer axis aligned parallel to the surface of substrate. The DFP-PDPV polymer molecules are anisotropic similar to the rigid rod shaped unsubstituted PPV molecules. However, the birefringence in this PPV derivative is more than an order of magnitude lower than that in PPV films. Refractive indices of PPV films were found to be 2.2 for TE polarisation and 1.6 for TM polarisation at 632.8 nm, the index values depending on the history of film preparation¹⁰

The dispersion curves were analysed with various types of Sellmeier equations. The data were fitted with polynomial functions presented in Figures 4 and 5. The dispersion constants were calculated using averaged data from all films.

The examination of the results of measurements provides information about the uniformity of the refractive index in polymer films. The index uniformity in DFP-PDPV was determined from calculation of the standard deviation of the results measured within the film. The maximum index variation within the specimen was between 1 to 5 units in the third decimal place. The standard deviation was rather independent on the solvent used for the film preparation. The interspecimen variation was as low as 1 and as large as 10 units of 10^{-3} in the films prepared from various solvents. The differences in the index data were stronger at shorter wavelengths and for TE polarization of the light beams.

The lowest values of the refractive indices were found in the films deposited from THF. The indices in films obtained from chloroform solutions were bigger by 2-3 units of 10^{-3} . The biggest indices and the biggest variation in the index data were

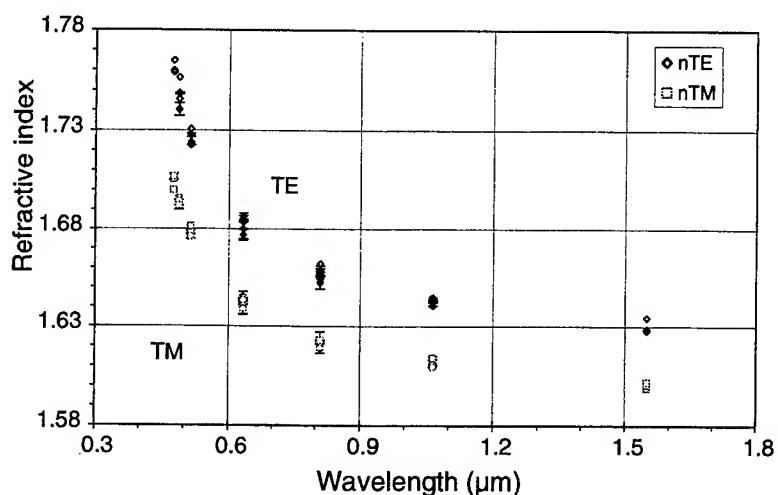


Figure 3.
Refractive index dispersion in DFP-PDPV films measured for two polarisations of the incident light: TE: E field parallel and TM: E field perpendicular to the waveguiding layer.

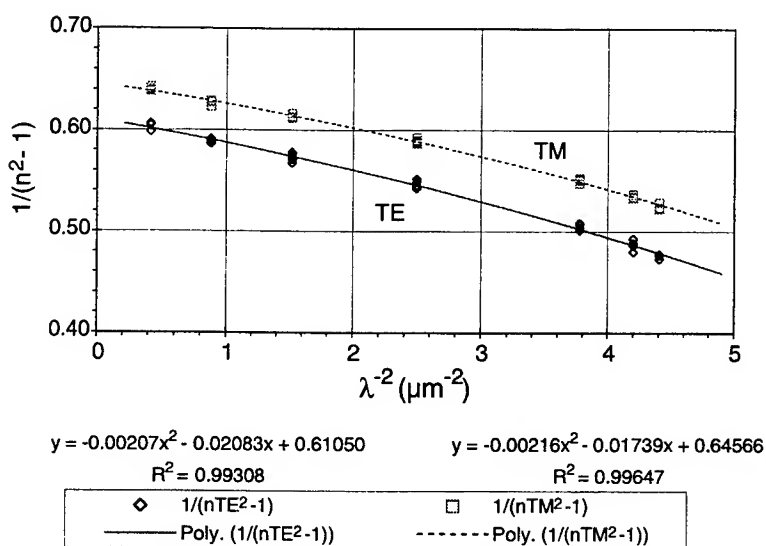


Figure 4
Fit of the experimental data of dispersion of refractive indices in DFP-PDPV films with a linear form of the Sellmeier equation $1/(n^2-1)$ vs. $1/\lambda^2$.

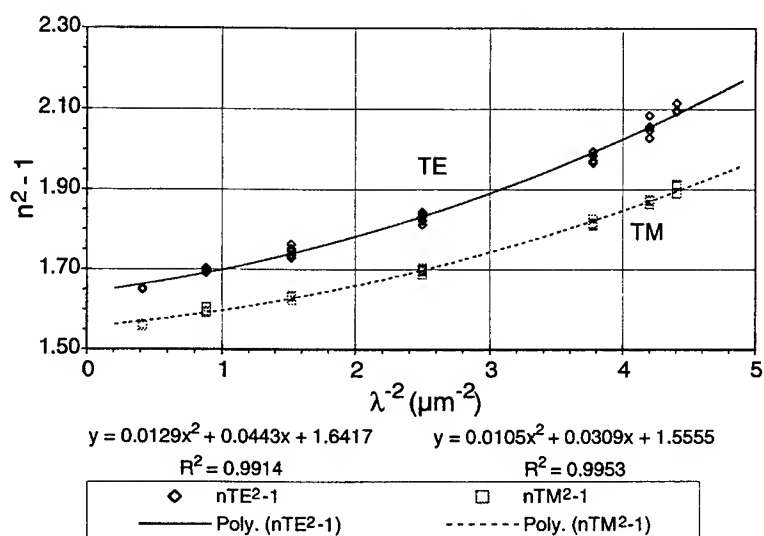


Figure 5.
Dispersion of refractive indices in DFP-PDPV films fitted with a polynomial function n^2-1 vs. $1/\lambda^2$

measured in the films deposited from 1,1,2,2-tetrachloroethane solutions. The differences were more evident in the indices measured for TE than for TM polarisation.

Since these samples have been measured under identical conditions all the differences could not be accounted for by experimental errors alone. The variations could be caused by microcrystalline domains within the non-crystalline amorphous structure induced by temperature gradient, which exists during solvent evaporation in the course of film preparation. The variation in the index data may indicate microstructures with different orientation of polymer molecules. Small traces of impurities formed in the reaction with the solvent would rise the index. Because of the optical differences between crystalline and amorphous regions, optical scattering may occur depending on the size of crystallites.

2.2.2. Waveguiding properties

The waveguiding properties of DFP-PDPV films are remarkably good, however, their optical quality depend on the film processing conditions. Highly transparent films were obtained from THF, chloroform (solution-cast) and 1,1,2,2-tetrachloroethane solution (spin-cast). Strong scattering of light was observed in the films obtained from 1,4-dioxane solutions (solution-cast). We measured waveguiding optical losses in transparent polymer films with a CCD camera. Figure 6 shows a part of our experimental setup used for measurements of waveguiding. Laser light is coupled through the prism at an angle suitable for one of the modes propagating in a waveguiding film. A CCD camera captures a streak of light scattered out of the guided beam.

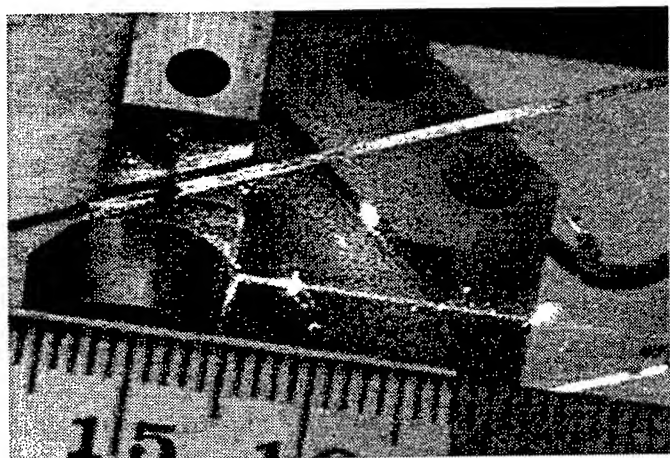


Figure 6

The view of a part of experimental arrangement used for detection of optical losses in planar waveguides with a CCD camera. The incident light beam is coupled into the film through a prism using a proper incident angle. The guided beam propagates in the film. A streak of light scattered on imperfections indicates the presence of the laser beam propagating in the film.

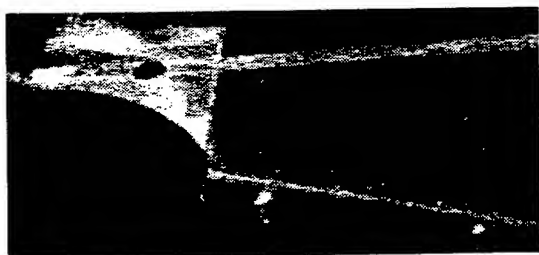


Figure 7

A side-view image of a waveguiding film of DFP-PDPV ($3\ \mu$ thick) deposited from chloroform solution on a silica glass substrate. The decay of the intensity of scattered light along the streak can be recorded with a CCD camera. A blackened aluminium foil placed under the sample provides dark background during measurements.

10 mm

The optical losses were derived through analysis of the intensity of the streak of scattered light beam measured along the film. The attenuation of intensity of guided light occurs mainly due to the intrinsic material losses. A decay of intensity of propagating beam causes a reduction of the intensity of light scattered out of the waveguide along the propagation distance. Figure 7 shows an example of a streak of scattered light induced by a light beam propagating within a $3\ \mu$ thick film of DFP-PDPV prepared from chloroform solution.

The waveguide loss factor was calculated from Lambert's Law analysis of the slope of the linear dependence $\log(I-I_b)$ on the distance of a propagating beam, where I denotes intensity of scattered light and I_b is the background intensity. Figure 8 shows an example of intensity distribution measured and optical losses evaluated in one of the films.

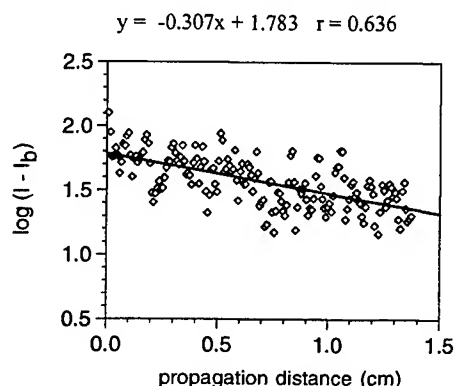


Figure 8

A distribution of the light intensity scattered on imperfections along the path of the laser beam. Waveguide losses are determined through the analysis of the decay of intensity of the streak of light showed in Figure 7. The loss coefficient derived from the slope of the dependence of $\log(I-I_b)$ vs. propagation distance is equal to 3.1 dB/cm at 632.8 nm.

Optical losses measured with a CCD camera technique depend on the absorption and scattering contributions. The losses in films of DFP-PDPV are wavelength dependent. Table 1 shows optical losses measured at three wavelengths and two orthogonal polarizations of light beams propagating in DFP-PDPV films deposited from chloroform and TCE solutions. The data obtained in the films deposited from THF solutions were within the range reported in Table 1.

Table 1a, 1b

The propagation losses in DFP-PDPV waveguiding films measured in the visible and near infrared wavelength range.

a) 3 μ thick film (F1284) prepared from chloroform solution

Wavelength (nm)	α_{TE} (dB/cm)	α_{TM} (dB/cm)
632.8	2.6 ± 0.6	4.6 ± 0.5
810	1.1 ± 0.3	2.4 ± 1.6
1064	1.0 ± 0.5	2.4

b) 0.6 μ thick film (F1351) prepared from 1,1,2,2-tetrachloroethane solution

Wavelength (nm)	α_{TE} (dB/cm)	α_{TM} (dB/cm)
632.8	11.1 ± 1.5	10.1 ± 1.9
810	4.7 ± 0.4	4.2 ± 0.4
1064	1.5 ± 0.8	1.4

The data presented here show that optical losses of DFP-PDPV in the films prepared from 1,1,2,2-tetrachloroethane are higher than in films deposited from chloroform (or THF). The difference is stronger at shorter wavelengths. The losses reach the level 1 dB/cm at 1.06 μ in both films.

It is difficult to state what part of optical loss is due to scattering or to material linear absorption. Photodeflection spectroscopy provides an independent information on absorption losses. Such measurements are planned.

One can expect that, if the scattering contributes the most, then this is due to refractive indices variation in these films. Indeed, such variation was observed as mentioned in the previous paragraph. The index variation was explained there by the possibility of the formation of small crystalline domains. The optical losses may increase in the regions of a microdomain grain-like structure with different densities and refractive indices.

It is known that PPV and some other PPV derivatives scatter visible light due to rigid-rod molecular structure, which has a strong tendency for crystallisation. The waveguiding properties of PPV can be improved if the polymer is

mixed into the matrix of PVP or sol-gel glasses^{10,12}, which may prevent formation of large crystallites and reduce scattering.

The molecular structure helps in reducing the tendency of the polymer for crystallisation. The PPV derivative studied here has a nonplanar molecular structure due to the presence of diphenylene segments and bulky groups attached to the main chain. They improve solubility of the material but also may reduce the tendency for crystallisation and improve the waveguiding properties. Other members of the family of soluble PPV derivatives also form stable low optical loss waveguides. For example, films of monophenyl substituted PPV (MP-PPV) prepared from chlorobenzene solutions had losses (4.4 ± 0.3) dB/cm for TE₀ and (7.1 ± 0.3) dB/cm for TM₀ modes at 632.8 nm¹⁶. Optical losses reported in the films of diphenoxyphenyl substituted PPV (DPOP-PPV) were 3.5 ± 0.3 dB/cm at 632.8 nm and 1.0 ± 0.3 dB/cm at 830 nm¹⁷ and 2 dB/cm at 885.6 nm²⁰. These processible polymers can be good candidates for photonic devices fabrication.

2.3. Nonlinear optical properties

Nonlinear optical properties of DFP-PDPV films were studied with the Degenerate Four Wave Mixing (DFWM) technique. The measurements of the nonlinear refractive index were performed in the forward BOXCARS geometry^{23,24} using an amplified Ti-sapphire femtosecond laser system operating at 800 nm. This system consists of an Ar ion laser (Coherent Innova 300) pumped Ti-sapphire oscillator (Coherent Mira) and an Nd:YAG laser (Spectra Physics GCR-130) pumped Ti-sapphire amplifier with diffraction grating pulse decompression and compression stages. It produced nominally 100 femtosecond long pulses of energies in the range 0.1-100 microjoules with the repetition rate of 30 Hz. The laser pulses used in the measurements were usually of the order of 2 μJ/pulse. The beam spot size on the sample was approximately $w_0=150$ μm. Two types of DFWM signals were simultaneously measured: the usual phase-matched signal and the non-phase-matched signal appearing in the applied experimental geometry^{1,7,24}.

The principle of using the two types of signals is that the phase matched interactions cause the appearance of a signal of the intensity proportional to the square of the interaction length that is $I_{DFWM,pm} \propto L^2$ whereas the non-phase-matched interactions give nonlinear signals which show, in principle, oscillating behaviour and can be considered to have a quadratic dependence on the interaction length only if this length is much less than the coherence length $l_c = \pi/|\Delta k|$, Δk being the phase mismatch. Thus, for a sample consisting of a relatively thin polymer film (usually thinner than the coherence length which is on the order of 10 microns) on a 1mm thick glass substrate, the phase-matched DFWM signal is often a result of two contributions of similar magnitude: that from the film and that from the substrate.

It is generally difficult to separate these contributions to the intensity of DFWM signal since the signal coming out of the film and the substrate can have different phases due to the presence of both the real and imaginary components in the nonlinearity. However, the non-phase-matched signal is still useable for the determination of the film nonlinearity since only a thickness of glass on the order of the coherence length (15-20 μm) contributes to that signal. This has an advantage of being able to perform a measurement of nonlinearity of a thin film of a polymer even in the presence of relatively strong NLO signals due to the nonlinearity of the glass or silica substrate.

We used the following relation for the determination of the nonlinearity of the investigated polymer:

$$|n_{2,film}| = \frac{1}{\sqrt{K}} \sqrt{\frac{I_{DFWM,np}}{I_{DFWM,pm,silica}}} \frac{L_{silica,eff}}{L_{film}} n_{2,silica}$$

where $n_{2,silica}$ is the nonlinear refractive index of the silica plate, taken to be 3×10^{-16} cm²/W, $n_{2,film}$ is the nonlinear refractive index of the polymer film, $I_{DFWM,np}$ is the intensity of the non-phase-matched signal obtained for a polymer film on a substrate and $I_{DFWM,pm}$ is the intensity of the phase-matched signal obtained for a standard 1mm thick silica plate at the same input intensity. L_{film} is the film thickness and $L_{silica,eff}$ is the effective thickness of the silica plate, which was about 500 μm in our experiments, the number being smaller than the geometrical thickness of 1 mm because of incomplete overlap of the beams in the sample. Finally, K is the experimental factor taking into account the relative sensitivity of the phase-matched and non-phase-matched signal detection, determined by a measurement of the non-phase-matched/phase-matched signals ratio on a highly nonlinear film. Using the above relation, $|n_2|$ values of polymer films were determined.

Films of DFP-PDPV showed instantaneous, delayed-component-free responses to the femtosecond pulses. Figure 9 shows an example of a phase-matched and Figure 10 of a non-phase-matched DFWM signal measured in a film of the

polymer, deposited from chloroform solution on 1mm thick silica glass. The signals were normalised to their peak intensities.

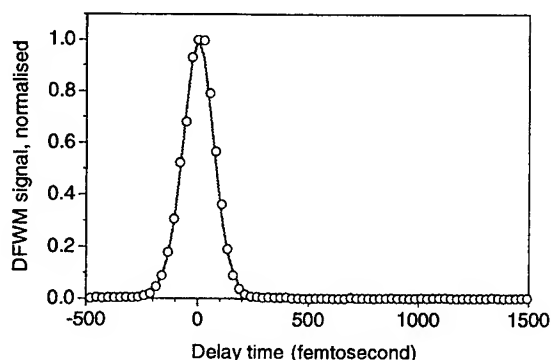


Figure 9

DFWM phase-matched signal measured at 800 nm in an 8.6 μm thick film of DFP-PDPV, deposited from chloroform solution on a 1 mm silica glass substrate. The solid line shows a theoretical instantaneous DFWM response for a sech^2 intensity profile of the pulses with intensity full width at half-maximum, FWHM=116 femtoseconds. This signal was 1.8 times stronger than the signal measured for the substrate alone.

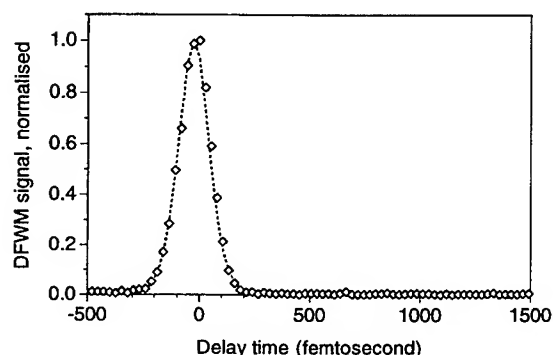


Figure 10

DFWM non-phase-matched signal measured at 800 nm in an 8.6- μm thick film of DFP-PDPV, deposited from chloroform solution on a 1 mm silica glass substrate. The line corresponds to a theoretical DFWM signal for a sech^2 pulse with FWHM equal to 115 femtoseconds. The signal intensity was about 100 times bigger than the intensity of non-phase-matched signal measured in the substrate.

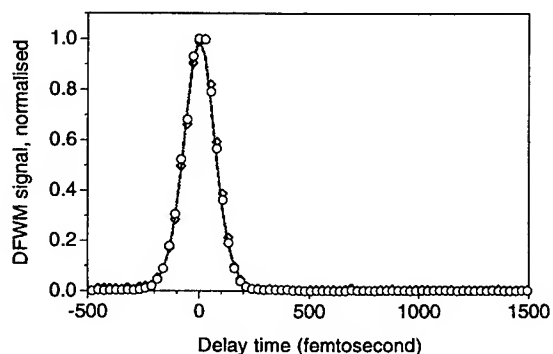


Figure 11

A comparison of the nonlinear responses measured with DFWM at 800 nm in the film studied in Figure 9 and Figure 10. The phase-matched signal is denoted with open circles showing experimental points, the solid line shows the fitting curve. The non-phase-matched DFWM experimental data are represented by diamonds, the broken line shows the fitting curve.

The nonlinear response in a DFP-PDPV film is practically instantaneous. Least square fits²⁵ of the signals gave FWHM of the laser pulses equal to 116 fs (the phase-matched signal) and 115 fs (the non-phase-matched signal). This agreed well with the pulse duration measured with the autocorrelation technique. Figure 11 shows a perfect overlap of the normalised signals measured at the same power of incident beams in the phase-matched and non-phase-matched arrangements in the film of DFP-PDPV.

We studied power dependencies of the DFWM signals to verify whether they were proportional to the cube of the input intensity, as predicted for the signal due to the Kerr nonlinearity (i.e. the electronic nonlinearity described by a linear intensity dependence $\Delta n = n_2 I$). Studies of an 8.6 μm thick film of DFP-PDPV deposited from chloroform solution showed cubic power dependence. In a thicker film (23 μm) prepared from THF we found the power coefficient close to four.

Table 2 shows the modulus of nonlinear refractive index $|n_2|$ measured with non-phase-matched DFWM technique in DFP-PDPV films. The data were calculated assuming the cubic dependence of DFWM signal. The measurements were

repeated on the same films in two or three measurement series. The scatter of data is given by the value of standard deviation.

Table 2.

Non-linear refractive index measured at 800 nm with DFWM in the non-phase-matched geometry in DFP-PDPV films of various origin .

Thickness of DFP-PDPV films (μm), (solvent used for film preparation)	$ n_2 _{800\text{nm}} (10^{-14} \text{ cm}^2/\text{W})$
9.7, 23.4 (THF)	0.9 ± 0.3
3.3, 8.6 (chloroform)	1.4 ± 0.4
2.0, 3.3, 5.2 (1,1,2,2-tetrachloroethane)	1.5 ± 0.4

The data show that the modulus of the nonlinear refractive index in DFP-PDPV films at 800 nm is in the range $|n_2|=(0.9-1.5)\times 10^{-14} \text{ cm}^2/\text{W}$. The difference in the values obtained in the films of different origin was as large as 40-60%. This might be related to differences in material morphology indicated earlier in the measurements of optical losses and the linear refractive index .

The nonlinearity determined here corresponds well to the results of Z-scan measurements of the real and imaginary part of the electronic nonlinearity, $n_{2,\text{real}}=8.3\times 10^{-15} \text{ cm}^2/\text{W}$ (positive nonlinearity) and $n_{2,\text{im}}=6.6\times 10^{-16} \text{ cm}^2/\text{W}^1$.

$|n_2|$ in DFP-PDPV is substantially smaller than $|n_2|$ in neat PPV: $(10^{-12} - 10^{-11}) \text{ cm}^2/\text{W}$ at 800 nm⁹.

DFP-PDPV possesses a low value of the figure of merit, the two-photon absorption merit factor T ($T = 4\pi n_{2,\text{imag}}/n_{2,\text{real}} = \beta\lambda/n_2$). We found $T=1$ in the Z-scan measurements of the polymer in 1,4-dioxane solutions¹. The dominant loss factor, the two-photon absorption coefficient $\beta=1\times 10^{-10} \text{ cm/W}$ in DFP-PDPV is remarkably lower than the coefficient measured at the same wavelength in neat PPV, $\beta=(2-8)\times 10^{-8} \text{ cm/W}^{9,10}$.

The difference in the real and imaginary part in DFP-PDPV compared to PPV may be correlated with the blue shift of the linear and possibly also nonlinear absorption transitions occurring in of these polymers. A study of dispersion of nonlinear optical properties would be useful to understand the correlation.

Due to low linear and nonlinear absorption losses DFP-PDPV can be better candidate for fabrication of nonlinear optical waveguides than neat PPV despite its lower value of real part of nonlinearity. Indeed, low nonlinearities of soluble, substituted-PPVs were utilised for observation of nonlinear optical phenomena in channel waveguides. Spectral broadening of the signal due to self-phase modulation was successfully demonstrated in the conjugated polymer waveguides^{20,21} using material nonlinearities: DPOP-PPV where $n_2=0.85\times 10^{-14} \text{ cm}^2/\text{W}$, $\beta=8\times 10^{-11} \text{ cm/W}$ in the transparent region at 885.6 nm ($\lambda_{\text{max}}=363 \text{ nm}$) and the damage threshold was $> 16 \text{ GW/cm}^2$ ²⁰, and DP-PPV/DP-PFV where the real part of focusing nonlinearity is $n_2=2.7\times 10^{-14} \text{ cm}^2/\text{W}$ and $\beta=1.8\times 10^{-10} \text{ cm/W}$ at 900 nm (absorption maximum at 375 nm)²¹. The values for DPOP-PPV reported in¹⁸⁻²⁰ were in good agreement with the results of our Z-scan measurements of this polymer in dioxane solutions¹

3. CONCLUSIONS

We studied linear and nonlinear optical properties of a new member of the conjugated polymer family based on the structure of poly(*p*-phenylenevinylene): difluorophenyl-polydiphenylenevinylene (DFP-PDPV). We investigated optical properties of thin films of DFP-PDPV for their potential for nonlinear waveguide applications.

The results indicate that the polymer can be useful in the studies of nonlinear optical effects, modulation or switching in optical waveguides. The blue shift of the position and decreasing strength of the $\pi-\pi^*$ absorption transition in UV spectrum in comparison to PPV films correlates with decreasing value of $|n_2|$ at 800 nm. A study of dispersion of nonlinear optical properties would be worth to undertake to understand the correlation between optical absorption and third-order nonlinearities in the material.

We observed the influence of the solvents used for film casting on optical properties of DFP-PDPV films: a shift of absorption spectra, change of birefringence, modification of optical losses and a weak change in the modulus of nonlinear refractive index. Detection and investigation of microdomain structures in films of the polymer would be useful to explain the results of optical studies.

Low loss waveguiding layers can be fabricated from polymer solutions using common solvents: tetrahydrofuran, chloroform and 1,1,2,2-tetrachloroethane. They may cause different tendency for crystallisation of the polymer when solvent evaporates during film formation. The crystallites can induce scattering. However, the absorption losses due to impurities introduced, for example, by the solvent interacting with the polymer may also be responsible for propagation losses in the waveguides. A study of optical absorption in waveguiding films with the method of photodeflection spectroscopy would be worth to undertake to detect the origin of the losses.

The third-order nonlinear optical properties of DFP-PDPV films deposited from various solvents and determined by DFWM are in the range $|n_2| = (0.9-1.5) \times 10^{-14} \text{ cm}^2/\text{W}$. This is similar to the data obtained from previous Z-scan studies of the polymer in dioxane solutions¹

We conclude that the DFP-PDPV polymer is well suited for investigations of nonlinear optical effects involving the use of ultrashort pulse lasers in nonlinear waveguides. The nonlinear optical response measured by DFWM is practically instantaneous and likely to be mostly of electronic nature.

4. ACKNOWLEDGMENTS

The authors thank Dr. Michael Bazylenko of the School of Electrical and Electronic Engineering, University of New South Wales for providing access to a prism coupler for 1550 nm measurements. Support of the polymer synthesis (H. H. H.) by Fonds der Chemischen Industrie is gratefully acknowledged.

5. REFERENCES

- 1 A. Samoc, M. Samoc, B. Luther-Davies, H. Liebegott, R. Stockmann, and H. H. Hoerhold, "Third-order nonlinear optical properties of poly(*p*-phenylenevinylene) derivatives substituted at vinylene position", *Proceedings of SPIE 3473 (Third-Order Nonlinear Optical Materials)*, pp. 79-90, 1998.
- 2 *Organic Thin Films for Waveguiding Nonlinear Optics*, edited by F. Kajzar and J. D. Swalen (Gordon and Breach Publishers, Amsterdam, The Netherlands, 1996).
- 3 *Characterization Techniques and Tabulations for Organic Nonlinear Optical Materials; Vol. 60*, edited by M. G. Kuzyk and C. W. Dirk (Marcel Dekker, Inc., New York, Basel, Hong Kong, 1998).
- 4 C. Flytzanis, "Impact of dimensionality in the optical nonlinearities", *Nonlinear Optical Effects in Organic Polymers*, edited by J. Messier, F. Kajzar, P. Prasad, and D. Ulrich, 162, pp. 1-12, Kluwer Academic Publishers, Dordrecht /Boston /London, 1989
- 5 J. L. Bredas, C. Adant, P. Tackx, A. Persoons, and B. M. Pierce, "Third-Order Nonlinear Optical Response in Organic Materials: Theoretical And Experimental Aspects", *Chem. Rev.* **94**, pp. 243-278, 1994.
- 6 C. Bubeck, "Relations between structure and third-order nonlinearities of molecules and polymers", *Organic Thin Films for Waveguiding nonlinear Optics*, edited by F. Kajzar and J. D. Swalen, 3, pp. 137-161, Gordon and Breach Publishers, Amsterdam, The Netherlands, 1996
- 7 M. Samoc, A. Samoc, B. Luther-Davies, Z. Bao, L. Yu, B. Hsieh, and U. Scherf, "Femtosecond Z-scan and degenerate four-wave mixing measurements of real and imaginary parts of the third-order nonlinearity of soluble conjugated polymers", *J. Opt. Soc. Am. B* **15**, pp. 817-825, 1998.
- 8 M. Samoc, A. Samoc, B. Luther-Davies, Z. Bao, S. K. Deb, L. Yu, B. Hsieh, and U. Scherf, "Prospects Of Third-Order Nonlinear Optical Polymers For Guided Wave Applications: "Rigid Rod", "Hairy Rod", "Ladder" And "Picket Fence" Polymers", *Nonlinear Optics* **20**, pp. 183-196, 1999.
- 9 A. Samoc, M. Samoc, M. Woodruff, and B. Luther-Davies, "Tuning the Properties of Poly(*p*-phenylenevinylene) for Use in All-optical Switching", *Optics Letters* **20**, pp. 1241-1243, 1995.
- 10 A. Samoc, M. Samoc, M. Woodruff, and B. Luther-Davies, "Poly(*p*-phenylenevinylene): an attractive material for photonic applications", *Photonic Polymer Systems: Fundamentals, Methods and Applications*, edited by D. L.

- Wise, G. E. Wnek, D. J. Trantolo, T. M. Cooper, and J. D. Gresser, pp. 373-436, Marcel Dekker, Inc, New York, Basel, Hong Kong, 1998
- 11 F. R. Denton III and P. M. Lahti, "Synthesis and properties of poly(phenylene vinylene)s and related poly(arylene vinylene)s", *Photonic Polymer Systems: Fundamentals, Methods and Applications*, edited by D. L. Wise, G. E. Wnek, D. J. Trantolo, T. M. Cooper, and J. D. Gresser, pp. 61-102, Marcel Dekker, Inc, New York, Basel, Hong Kong, 1998
- 12 A. Samoc, M. Samoc, and B. Luther-Davies, "Linear and nonlinear optical properties of poly(p-phenylenevinylene)- poly(N-vinylpyrrolidone) (PPV-PVP) composites", *Proceedings of SPIE 3147 (Nonlinear Optical Properties of Organic Materials X)*, pp. 166-177, 1997.
- 13 H. H. Hoerhold, M. Helbig, D. Raabe, J. Opfermann, U. Scherf, R. Stockmann, and D. Weiss, "Poly(phenylenevinylene); Entwicklung eines elektroactiven Polymermaterials vom unschmelzbaren Pulver zum transparenten Film", *Z. Chem.* **27**, pp. 126-137., 1987.
- 14 H. H. Hoerhold and M. Helbig, "Poly(phenylene vinylene)s - synthesis and redoxchemistry of electroactive polymers", *Makromol. Chem. Macromol. Symp.* **12**, pp. 229-258, 1987.
- 15 H. H. Hoerhold, M. Helbig, and A. Bleyer, "Phenyl-substituted poly(phenylene-vinylene)s, electrical and optical properties", *Macromolecules 1992*, edited by J. Kahovec, , pp. 301-311, VSP International Science Publishers, The Netherlands, Utrecht, 1993
- 16 U. Bartuch, A. Braeuer, P. Dannberg, H. H. Hoerhold, and D. Raabe, "Measurements of high nonresonant third-order nonlinearity in MP-PPV waveguides", *Int. J. Optoelectron.* **7**, pp. 275-279, 1992.
- 17 F. Michelotti, T. Gabler, H. Hoerhold, R. Waldhaeusl and A. Braeuer, "Prism coupling in DMOP-PPV optical waveguides", *Opt. Comm.* **114**, pp. 247-254., 1995.
- 18 T. Gabler, R. Waldhaeusl, A. Braeuer, U. Bartuch, R. Stockmann, and H. H. Hoerhold, "Nonresonant n_2 and two-photon-absorption dispersion measurements of DPOP- PPV and DP- PPV /DP-PFV polymer strip waveguides", *Opt. Commun.* **137**, pp. 31-36, 1997.
- 19 T. Gabler, A. Brauer, R. Waldhaeusl, U. Bartuch, H. H. Hoerhold, and F. Michelotti, "Nonresonant n_2 and TPA coefficient measurement in polymer waveguides by different measurement techniques", *Pure Appl. Opt.* **7**, pp. 159-168, 1998.
- 20 T. Gabler, R. Waldhaeusl, A. Braeuer, F. Michelotti, H. H. Hoerhold, and U. Bartuch, "Spectral broadening measurements in poly(phenylene vinylene) polymer channel waveguides", *Appl. Phys. Lett.* **70**, pp. 928-930, 1997.
- 21 U. Bartuch, U. Peschel, T. Gabler, R. Waldhaeusl, and H. H. Hoerhold, "Experimental investigations and numerical simulations of spatial solitons in planar polymer waveguides", *Opt. Commun.* **134**, pp. 49-54, 1997.
- 22 D. D. C. Bradley, R. H. Friend, and W. J. Feast, "Infrared and optical absorption in poly(4,4'-diphenylenediphenylvinylene)", *Springer Ser. Solid State Sci.* **63**, pp. 196-9, 1985.
- 23 G. M. Carter, "Excited State Dynamics and Temporally Resolved Nonresonant nonlinear-optical processes in polydiacetylenes", *J. Opt. Soc. Am. B* **4**, pp. 1018-1024, 1987.
- 24 F. P. Strohkendl, L. R. Dalton, R. W. Hellwarth, H. W. Sarkas, and Z. H. Kafafi, "Phase-Mismatched Degenerate Four-wave Mixing: Complex Third-Order Susceptibility Tensor Elements of C60 at 768 nm", *J. Opt. Soc. Am. B* **14**, pp. 92-98, 1997.
- 25 M. Samoc, unpublished.

SESSION 6

Polymeric Devices and Optical Links

High-Speed Plastic Optical Fibers and Amplifiers

Yasuhiro Koike

Faculty of Science and Technology, Keio University / Kanagawa Academy of Science and Technology

ABSTRACT

Recent status of the polymer optical fiber (POF) for high speed data communication and telecommunication is reviewed. The GI POF was proposed for the first time at Keio University, and several methodologies to fabricate GI POF have been currently proposed. In this paper, we clarify the great advantage of perfluorinated (PF) polymer as the polymer matrix of low-loss and high bandwidth graded-index (GI) POF. It is generally known that the PF polymer can decrease the intrinsic absorption loss compared with poly methyl methacrylate (PMMA), which is the conventional material of POF. Furthermore, it was found that low material dispersion of the PF polymer is another advantage to obtain the high bandwidth GI POF.

It was clarified for the first time that the power distribution of modes formed by the mode dependent attenuation was the dominant factors of the higher bandwidth of the GI POF than theoretically predicted bandwidth, while the effect of the mode coupling was small.

Keywords: Graded-Index polymer optical fiber, perfluorinated polymer, modal dispersion, material dispersion, differential mode attenuation, mode coupling

1. INTRODUCTION

Considerable research activity lately has been devoted to the development of the optical component and devices that have the capability to support the high-speed telecommunication. Silica base single mode optical fiber has been widely utilized in the long distance trunk area for the order of giga bit per second transmission because of its high bandwidth and transparency. Introduction of the single mode fiber into all trunk area in Japan was completed in December 1997, and construction of the fiber network in access area which is called " π system" has just started. In the π system, the single mode optical fiber system is introduced to the carve at first, and drop line is operated by the conventional metallic cables. Realization of all optical networks by the single mode fiber requires many breakthroughs in the total system cost. Because of the small core size such as 5 to 10 μm , accurate alignment is necessary in the light coupling to the fiber and the connection of fibers, which increases the total system cost including fiber connectors, transceiver, packaging, and installation, etc.

On the other hand, use of the silica base multimode fiber is a recent trend in the field of local area network (LAN) and interconnection, because the large core diameter of the multimode fiber such as 50 and 62.5 μm increases the tolerance of misalignment in the fiber connection compared to that of single mode fiber. However, even in the case of the multimode fiber, the accurate connection by using ferrule is still required by the following two reasons: One is that the misalignment of connectors even by precise injection molding is still $\pm 20\sim 30\ \mu\text{m}$ and is too large for the core of 50 μm or 62.5 μm of multimode glass fiber. Second is the serious modal noise caused by coherent light source such as vertical cavity surface emitting laser (VCSEL)¹.

A large-core, high-bandwidth, and low-loss GI POF² was reported for the breakthrough of above issue. Large core such as 200 ~ 1000 μm of the GI POF enables the use of inexpensive plastic connector by the injection molding without a ferrule, eliminating the problem of the modal noise. The poly (methyl methacrylate) (PMMA) has been generally used as the core material of step-index type POF commercially available and its attenuation limit is approximately 100 dB/km at the visible region². Therefore, the high attenuation of POF compared to the silica base fiber has been one of the big barriers for POF in data communication application for more than 100-m distance.

The development of the perfluorinated (PF) amorphous polymer base GI POF³ opened the way for great advantage in the high-speed POF network. Since serious intrinsic absorption loss due to the carbon hydrogen vibration that existed in PMMA base POF was completely eliminated in the PF polymer base POF, the experimental total attenuation of the PF polymer base GI POF decreased to 40 dB/km even in the near infra-red region⁴. It was clarified that the theoretical attenuation limit of the PF polymer base POF is much comparable to that of the silica base fiber (0.3 dB/km). In this paper, the bandwidth and transmission distance achieved by the POF is described by considering the inherent attenuation and dispersion factors.

2. DEVELOPMENT POF FOR HIGH-SPEED DATA COMMUNICATION

First report of POF was in 1960's, which was almost the same as the invention of silica-base optical fiber. However, the POF has not necessarily played a main role in the field of telecommunication, because of its intrinsic high attenuation. Poly methyl methacrylate (PMMA), which has been the typical polymer material for the core of POF, shows the lowest attenuation at the visible region, while the attenuation abruptly increases from near infrared to infrared region. This is due to the intrinsic absorption loss of carbon-hydrogen stretching vibration. Therefore, theoretical attenuation limit of PMMA base POF is around 100 dB/km at 0.65- μ m wavelength, which has been the big problem of POF so far for telecommunication use. However, in 1990's, innovative polymer material, perfluorinated polymer was invented. As the PF polymer has no carbon-hydrogen bonding in it, the intrinsic absorption loss dramatically decreases⁵. Development of POF attenuation is summarized in Fig. 1.

With decreasing the attenuation of POF, high bandwidth came to be also required for POF. All commercially available POF has been of SI POF. Therefore, bit rate of the POF has been limited to less than 10 Mb/s. On the other hand, we proposed the high-bandwidth GI POF for the first time, and demonstrated a 2.5 Gb/s 100 m transmission in 1994. Proposal of the GI POF has triggered the research and development of high speed POF data link. Reported experimental results of high speed data transmission by POF is shown in Fig. 2. With using low loss PF polymer base GI POF, 2.5 Gb/s 450 m transmission was succeeded in 1998⁶.

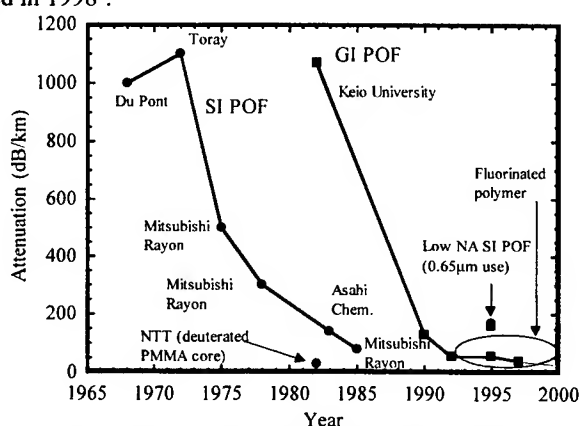


Fig. 1 Development in the attenuation of POF.

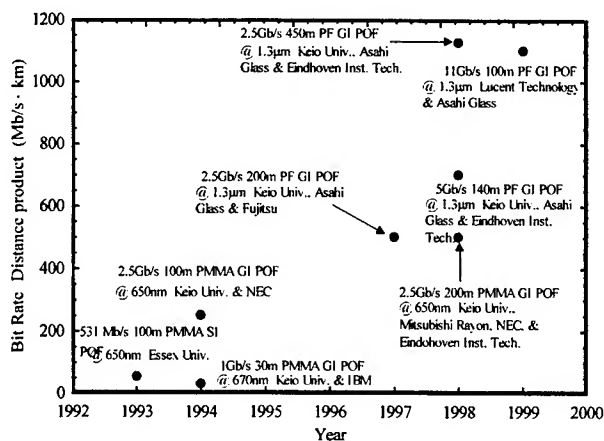


Fig. 2 Development in the high-bit rate trial in the POF link

3. PF POLYMER BASE GI POF

3.1. Material Dispersion

Birth of the PF polymer having no carbon-hydrogen bonding in the molecule has brought a new concept of optical data link. Great advantage of the PF polymer is low intrinsic absorption loss. Because of the low intrinsic loss, very wide wavelength range from visible to near infrared region (for instance 1.3- μ m) can be adopted for signal wavelength in the PF polymer base GI POF link. Currently the lowest attenuation of the PF polymer base GI POF is around 30 dB/km at 1.3- μ m⁷.

On the other hand, we found another advantage in the PF polymer, that is the low material dispersion. The material dispersion of the PF polymer estimated by measuring the wavelength dependence of the refractive index of polymer is shown in Fig. 3 compared with those of PMMA and silica. Since the material dispersion generally decreases with increasing the wavelength, operating wavelength of POF network should be in near infrared region rather than in visible region for high-speed data transmission. However, the light source of 0.65- μm wavelength has been required for the conventional PMMA base POF network so far, because one of low attenuation window is located at 0.65- μm .

Low attenuation of the PF polymer base GI POF at near infrared region gives an advantage even in the dispersion limitation because the material dispersion decreases with increasing the wavelength as mentioned above. In the case of the PF polymer, the material dispersion at 0.65- μm wavelength is 0.13 ns/nm·km which is much lower than that (0.32 ns/nm·km) of the PMMA at the same wavelength. Further, the material dispersions of the PF polymer at 0.85 and 1.3- μm wavelengths decrease to 0.054 and 0.009 ns/nm·km, respectively.

Although the material dispersion of silica is almost zero at 1.3- μm wavelength, the high material dispersion of the GeO_2 doped silica from visible to near infrared region limits the bandwidth of GeO_2 - SiO_2 base fiber. On the other hand, it should be noteworthy that addition of dopant in the PF polymer causes little change in value of material dispersion. Since perfluorinated substance is used as the dopant, the material dispersion of the dopant is low. Furthermore, the material dispersion of PF homopolymer is almost the same as that of dopant added PF polymer in the wavelength range from 0.45 to 1.3 μm , which indicates that the higher bandwidth PF polymer base GI POF is expected in wide wavelength range from visible to near infrared region rather than the multimode silica fiber.

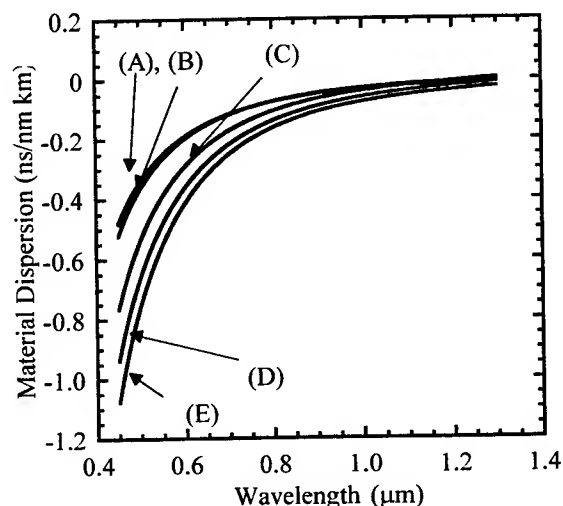


Fig. 3 Material dispersion of PMMA, PF polymer and silica.
(A): PF homopolymer (B): 15 wt. % PF dopant added PF polymer (C): pure SiO_2
(D): 13.5 mol % GeO_2 doped SiO_2 (E): PMMA homopolymer

3.2. Dispersion Induced by Refractive Index Profile

Total dispersion is estimated by using WKB method, considering material, modal and profile dispersions, as described in detail in this section. Approximation of power-law index profile in eq. (1) enabled to calculate the root mean square (r.m.s.) width σ of the impulse response of GI POF as a function of index exponent g by the WKB method⁸⁻¹⁰.

$$n(r) = n_1 \left[1 - 2\Delta \left(\frac{r}{a} \right)^g \right]^{\frac{1}{2}} \quad 0 \leq r \leq a \quad (1)$$

$$n(r) = n_2 \quad r > a$$

where, n_1 and n_2 are the refractive indices of center axis and the cladding, respectively, a is the core radius, g is index exponent, that is the parameter of the index profile, and Δ is called relative index difference which is expressed as Eq. (2)

$$\Delta = \frac{n_1^2 - n_2^2}{2n_1^2} \quad (2)$$

Subsequently, the relation between the refractive index profile and the bandwidth of the GI POF was obtained by using the simple relation between the width of impulse response and the bandwidth as shown in eq. (3).

$$f_{-3dB} = \sqrt{\frac{\ln 2}{2\pi^2}} \frac{1}{\sigma} = \frac{0.188}{\sigma} \quad (3)$$

where σ is the root mean square width of the impulse response function. Here, -3 dB bandwidth of the GI POF was calculated by assuming that the output pulse waveform was approximated by Gaussian shape.

It should be noted that the difference of the optimum index exponent value between 0.65 and 1.3- μ m wavelengths is caused by the inherent polarization properties of material itself. The optimum index profile of the GI fiber for giving maximum bandwidth is described by eq. (4) when the index profile is approximated by the power-law equation shown in eq. (1)¹⁰.

$$g_{opt} = 2 - \frac{2n_1}{N_1} \cdot P - \Delta \frac{\left(4 - \frac{2n_1}{N_1} \cdot P\right) \left(3 - \frac{2n_1}{N_1} \cdot P\right)}{5 - \frac{4n_1}{N_1} \cdot P} \quad (4)$$

$$N_1 = n_1 - \lambda \frac{dn_1}{d\lambda} \quad (5)$$

where g_{opt} signifies the optimum index exponent, and P that is called as profile dispersion is written as follows.

$$P = \frac{\lambda}{\Delta} \frac{d\Delta}{d\lambda} \quad (6)$$

Since the profile dispersion P is the function of the differentiation of the relative index difference Δ with respect to wavelength λ , the optimum index profile depends on refractive index of the core material, which means that index increment by the dopant material is key issue. The wavelength dependence of the bandwidth characteristics of PF polymer base GI POF is shown in Fig. 4, compared to that of the GeO_2 - SiO_2 base multimode glass fiber. Selected index exponents of 2.03, 2.07 and 2.23 are the optimum index exponents of the PF polymer base GI POF when the source wavelengths are 0.65, 0.85 and 1.3 μ m, respectively, while 2.01 and 1.78 are optimum for 0.85 and 1.3- μ m wavelength, respectively, in the silica base multimode fiber. It was already confirmed that³ if the index exponent g is controlled to around 2.0, several hundreds $\text{MHz} \cdot \text{km}$ can be achieved in wide wavelength range from 0.6 to 1.3 μ m, because of low material dispersion. On the other hand, in

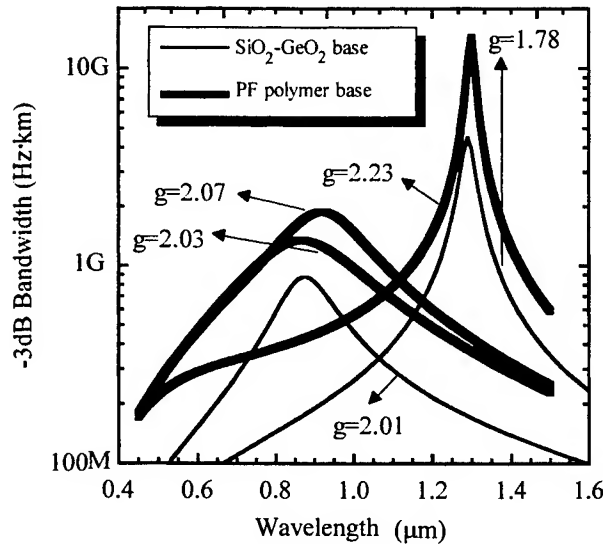


Fig. 4 Wavelength dependence of the bandwidth of PF polymer base GI POF and GeO_2 - SiO_2 base GI multimode glass fiber.

the case of the SiO_2 - GeO_2 base GI multimode fiber, accurate index profile control for specified wavelength of used laser is necessary to achieve several hundreds $\text{MHz} \cdot \text{km}$, since the wavelength dependence of the bandwidth is much stronger than that of the PF polymer as shown in Fig. 4. It can be emphasized that the low material dispersion of PF polymer allows the tolerance in the index profile of the PF polymer base GI POF even for higher-speed transmission rather than silica fiber.

On the other hand, for 1.3- μ m use, optimum index exponent g_{opt} is 2.23, by which approximately 10 $\text{GHz} \cdot \text{km}$ can be achieved, while the same GI POF having 2.23 of index exponent exhibits only 400 $\text{MHz} \cdot \text{km}$ when the wavelength of the light source is 0.65 μ m. In order to further decrease the wavelength dependence of the optimum index profile, suitable dopant which can decrease the profile dispersion (i.e. the wavelength dependence of the relative index difference. See Eq.

(6.) should be selected. The shift of the optimum index exponent of the PF polymer base GI POF between 0.85- μm and 1.3- μm wavelengths is 0.16 (from 2.07 to 2.23) which is smaller than that (0.23) of $\text{GeO}_2\text{-SiO}_2$ base GI multimode glass fiber (from 2.01 to 1.78). This is because the profile dispersion of the PF polymer base GI POF is smaller than that of $\text{GeO}_2\text{-SiO}_2$ base GI multimode glass fiber.

4. BANDWIDTH CHARACTERISTICS OF GI POF

To cover the high-bit rate such as several hundred mega bit per second, which must be required even in office and home-network, we proposed the high-bandwidth GI POF for the first time², and have reported its bandwidth characteristic³. Recently interests focused on POF accelerates the research and development of POF particularly in its bandwidth improvement. In this paper, we clarified that the launch condition and mode dependent attenuation are the dominant factors determining the bandwidth of the GI POF. It was also shown that the mode coupling effect on the bandwidth characteristics of the GI POF is considered to be small compared to the above two factors within 100 m. We show a precise bandwidth prediction of the GI POF by considering the power distribution among the propagating modes and differential mode attenuation for the first time, resulting in a good agreement with the experimentally measured property.

We reported that the refractive index profile of the GI POF could be widely controlled by the interfacial-gel polymerization technique². Bandwidth characteristics of the prepared GI POF were analyzed, and we succeeded in predicting the impulse response function of the GI POF having arbitral index profile. In this analysis, uniform launch of all modes is usually assumed because of easy calculation. Fig. 5 shows the experimental and calculated pulse broadening through 100-m PMMA base GI POF. Here, the GI POF whose index profile is slightly deviated from the ideal one was used for measurement in order to clearly observe the pulse broadening. Even for this GI POF, more than 1 GHz of bandwidth for 100m was obtained. The pulsed light signal was launched into the GI POF via a 1-m length, 1-mm core diameter step-index (SI) POF having NA of 0.5 which is much higher than that of the GI POF, in order to realize the uniform excitation of all modes including both meridional and skew modes. A large disagreement is observed between the calculated and measured output waveforms. It was confirmed by the detail analysis that the second peak existing in the calculated waveform shown by the open circle is attributed to the higher order modes having large group delay. On the other hand, an excellent agreement with the measured waveform was observed when the mode dependent attenuation obtained from the near-field power distribution was taken into consideration as shown by close circle.

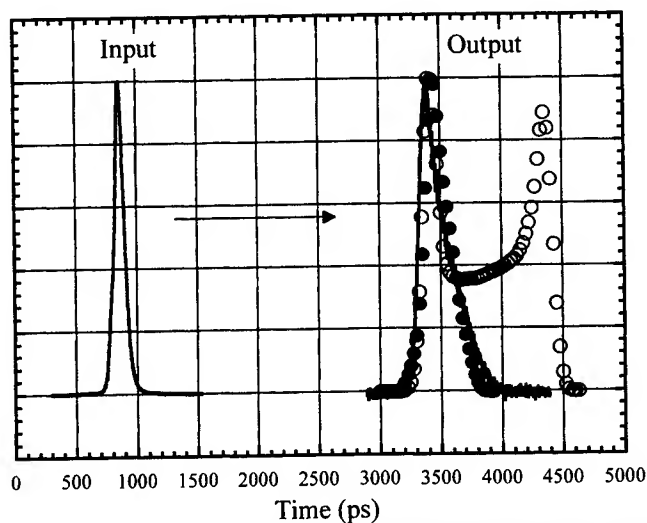


Fig.5 Comparison of measured and calculated bandwidth characteristics of the GI POF having an index exponent of 2.7

Solid line: measured waveform

●: Predicted waveform when all modes were assumed to equally launched.

○: Predicted waveform when the differential mode attenuation describe in the following section was taken into account

5. PROPAGATING MODE CHARACTERISTICS

5.1. Launch Condition Dependence of Far-Field Pattern from GI and SI POF

There have been several reports concerning the dispersion property of GI POF. In these articles, bandwidth characteristic of the POF was tried to theoretically calculated. However, the theoretical bandwidth properties of the GI POF often have some amount of disagreement with the measured one. The reason of the disagreement was generally explained by the mode coupling, which was derived from the similar discussion in the silica base multimode fiber. Although the detail modal property has not been analyzed, higher measured bandwidth than theoretically predicted bandwidth was reported as the result of strong mode coupling. However, we found that the mode coupling effect on the bandwidth characteristics in the GI POF is much smaller than that in the SI POF. In order to investigate the mode coupling effect on the bandwidth in both GI and SI POFs, the launch condition dependence and transmission distance dependence of the far-field pattern (FFP) were investigated at first. In this measurement, the lower order modes were selectively launched in both GI and SI POFs. In the case of GI POF, the order of mode number relates to both launching beam diameter and launching angle, while the launching angle directly corresponds to the mode number. Therefore, a single mode silica fiber was butted to the center of the GI POF to launch the lowest order mode group, while collimator lens are used for SI POF as the low order mode exciter. Results are shown in Fig. 6. It was noteworthy that the angular distribution of the output power from the SI POF gradually expands with increasing the transmission distance, although the input NA is very small. This result indicates that strong mode coupling, which scrambles the mode power distribution within 40-m transmission, exists in the SI POF.

On the other hand, the angle distribution from the GI POF with 50-m length is just the same as that with 10-m length, which means that the mode coupling in the GI POF is much weaker than that in the SI POF.

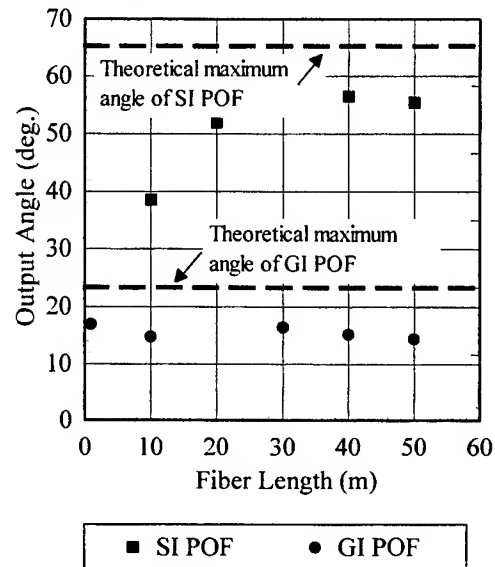


Fig. 6 Comparison of fiber length dependence of the far-field pattern of the conventional SI POF and GI POF.

5.2. Differential Mode Delay

The group delay of each mode in the GI POF was investigated by the measurement of the differential mode delay (DMD). In the DMD measurement, optical pulse is coupled into the GI POF via a 1-m single mode silica fiber in order to launch a specified mode group of the GI POF. By shifting the position of the single mode fiber attaching to the GI POF from the core center to the periphery, each mode from the low order to high order is independently launched. The results of the DMD measurement in 100-m GI POF are shown in Fig.7. Here, the lengths 0 μm , 130 μm , ... 200 μm shown in Fig. 7 signify the distance from the core center to launching position by the single mode fiber. Output near-field patterns (NFPs), which directly relate to the mode number of transmitted mode, are also shown in Fig.7. When the higher order modes are selectively launched by shifting the launch position 200 μm apart from the core center, the ring pattern is clearly observed, which indicates that the higher order modes are independently transmitted with little energy transfer to the lower order modes. The group delay of each mode in the GI POF was investigated by the measurement of the differential mode delay (DMD). It was observed that with increasing the mode number, larger time delay is observed in which each peak in Fig. 7 is exactly the same as the theoretical value assuming no mode coupling. The fiber length dependence of the DMD is shown in Fig. 8. Generally, the degree of mode coupling in the multi-mode optical fiber is evaluated by the relation between the fiber length and the output pulse width. When the output pulse width is plotted with respect to the fiber length, the slope is an important parameter. The slope close to 1 signifies weak mode coupling, while the slope less than 1 large mode coupling. However, the output pulse width decreases when the higher order modes have very high attenuation, which means that the slope between the fiber length and the output pulse width becomes less than 1 even if the mode coupling is much weak. Therefore, it can be concluded that the mode coupling in the SI POF is stronger than that in the GI POF because the core-cladding boundary strongly affects the propagating mode characteristics. It is also concluded that the mode coupling effect on the bandwidth of the GI POF is very small for 100m distance.

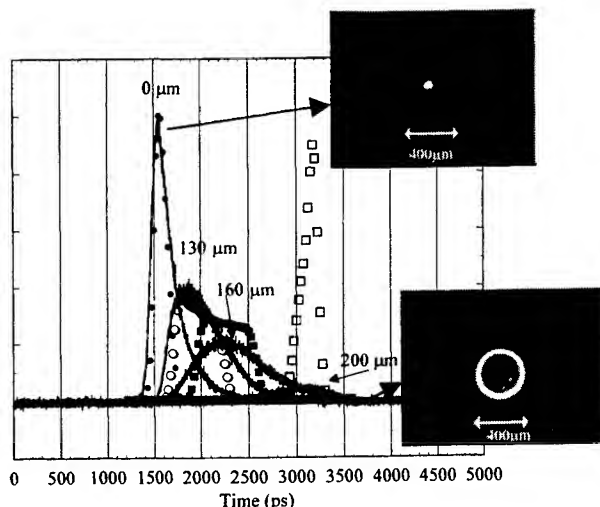


Fig. 7 Measured and calculated result of differential mode delay in 100-m PMMA base GI POF Core diameter: 450 μ m. Photograph: Output Near-Field Pattern from the GI POF, where arrows show the core diameter Plots: Calculated DMD

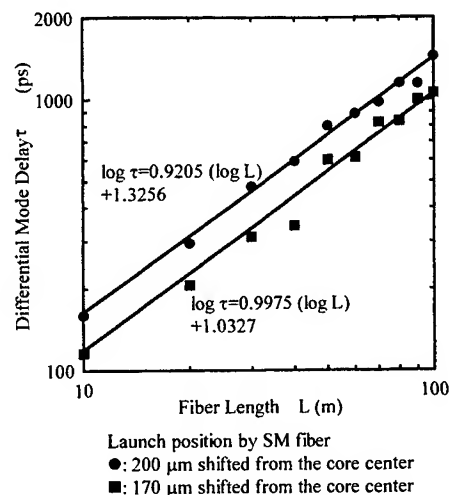


Fig. 8: DMD versus fiber length of the GI POF.

5.3. Differential Mode Attenuation

Differential mode attenuation was measured directly with using the modified method of the DMD measurement. Similar to the DMD measurement, small mode groups were launched via a single mode fiber butted to the one end of GI POF. The output power distribution with respect to the fiber radius was measured. Since the numerical aperture (NA) of the GI POF varies in the radial direction according to the refractive index profile, acceptable light power, which is highest at the core center, gradually decreases from the core center to periphery. In order to compensate such launch power difference along with the fiber radius, cut-back method was adopted for differential mode attenuation measurement. Measured result of the differential mode attenuation of the GI POF used in the DMD measurement shown in Fig. 7 is shown in Fig. 9. The attenuation of the low order modes is about 150 dB/km, while abrupt increase was observed with increasing the mode number.

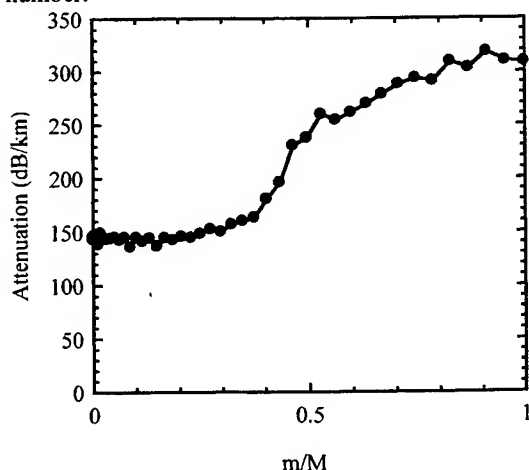


Fig. 9
Measured differential mode attenuation of the GI POF.

m is defined as the principal mode number:
 $m=2\mu+v$, where μ and v are radial and azimuthal mode number, respectively.
 M is the maximum principal mode number.

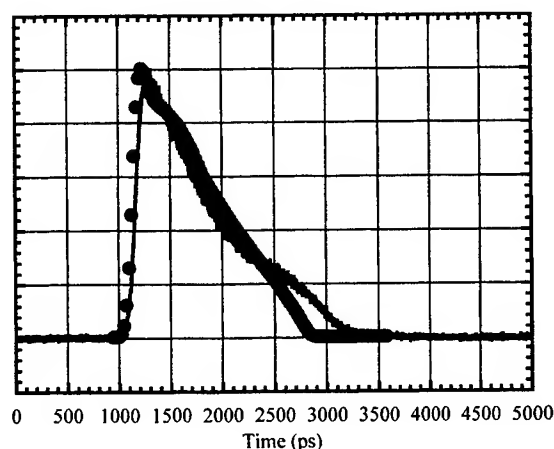


Fig. 10 Comparison of measured output waveform from 100-m length GI POF used in DMD measurement shown in Fig. 10 and the calculated waveform by considering measured differential mode attenuation shown in Fig.13.

It is calculated from Fig. 9 that approximately 17 dB of power difference exists between the lowest and the highest order mode after 100-m transmission. By considering the differential mode attenuation as shown in Fig. 9, output pulse waveform from 100-m GI POF was calculated with using WKB computation method as described above. The result is shown in Fig. 10. This result of the differential mode attenuation was introduced into the calculation procedure of the output waveform. As shown in Fig. 9, the mode group whose principal mode number is in $0 \leq m/M \leq 0.5$ have almost the same power, while the transmitted power by the modes whose principal mode number is larger than $M/2$ decreases dramatically. By taking into account the differential mode attenuation, excellent agreement was observed between measured and calculated waveforms.

6. PREPARATION OF POLIMER OPTICAL FIBER AMPLIFIERS

Since the active dopants in the low intensity portion of pump profile remain uninverted and reabsorb the signal, the overlap between the spatial modes of the pump light and the distribution of the active dopants is crucial for efficient excitation. We employed the interfacial gel polymerization technique to form the active dopant distribution as well as refractive index profile. Herein we describe the preparation of the fibers. First, we prepared a poly (methyl methacrylate) (PMMA) cylindrical tube with 6-mm inner diameter and 10-mm outer diameter. Then, a MMA monomer solution containing specified amounts of t-butyl peroxy isopropylcarbonate (initiator), n-butyl mercaptan (chain transfer agent), low molecular weight high refractive index dopant for a graded index profile, and active dopant was poured into the tube. The polymerization was carried out at 90 °C for 24 hours. The preform rod obtained was heat treated at 110 °C to complete the polymerization. The preform rod was heat-drawn into a fiber at 200 °C. The fiber diameter and the core diameter were 500 μm and 300 μm , respectively. Figure 11 shows refractive index and dye distribution profiles in a preform fabricated from MMA solution containing 20 wt% of benzyl n-butyl phthalate and 20 ppm-wt of Rhodamine B. The refractive index profile was determined by an interferometric method^{10,11}, and dye distribution profile by an absorbance measurement. The quadratic profiles are successfully formed because low molecular weight dopants and organic dyes are progressively confined to the center region of the preform during the interfacial gel polymerization process.

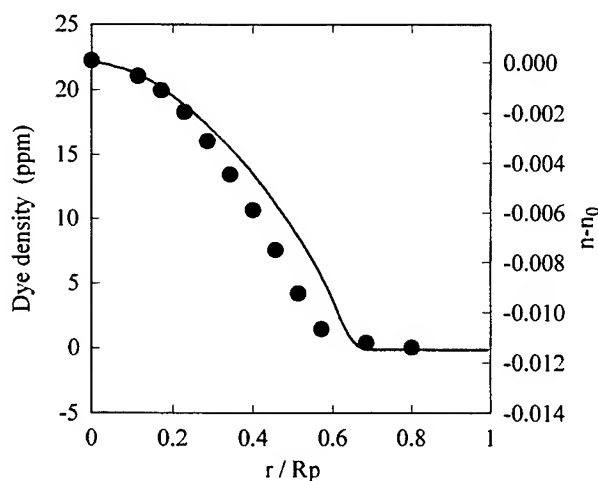


Fig. 11 Refractive index and dye distribution profiles in a preform fabricated from MMA solution containing 20 wt% of benzyl n-butyl phthalate and 20 ppm-wt of Rhodamine B.

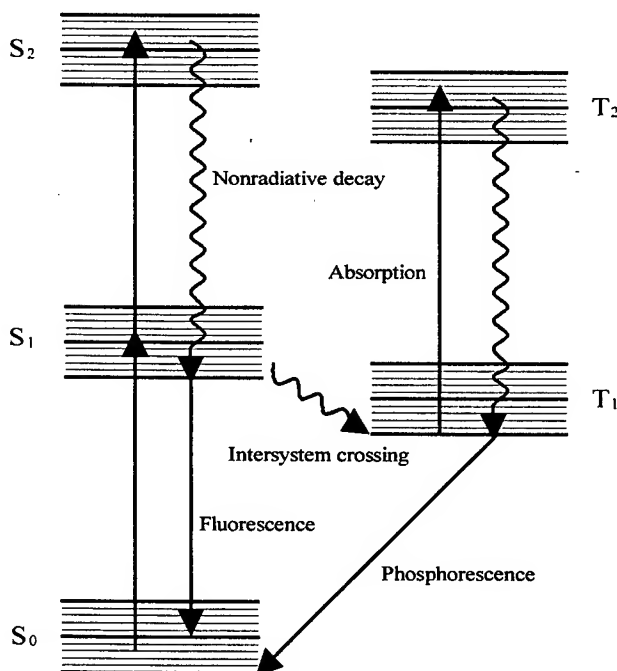


Fig. 12 Schematic energy levels of a dye molecule.

7. ORGANIC DYE-DOPED POLYMER OPTICAL FIBER AMPLIFIERS

7.1. Spectroscopic properties of organic dyes

Figure 12 shows the energy levels of an organic dye. Each electric level is a band composed of a continuum of vibrational and rotational levels. The absorption band of dyes is due to the transition from the electronic ground state S_0 to the first excited singlet state S_1 . The reverse process, the transition between S_1 and S_0 , is responsible for the spontaneous emission known as fluorescence and for the stimulated emission.

When the organic dye-doped POFA is pumped with an intense light source, the dye molecules are excited typically to some higher level in the singlet manifold, from which they relax within picoseconds to the lowest vibronic level of S_1 , that is, the metastable level for stimulated emission. The allowed transition from the lowest vibronic level of the first excited singlet state to some higher vibronic level of the ground state gives a high amplification factor. However, there are some processes that can be deleterious to the optical amplification. These processes can be grouped into those that cause a direct relaxation to the ground state S_0 or an excitation to higher singlet states S_n ($n = 2, 3 \dots$) (internal conversion), and those that are responsible for intersystem crossing to the triplet manifold. The radiative transition from the lowest triplet state T_1 to the ground state S_0 is termed phosphorescence. The population of the lowest triplet state has a two-fold consequence: Firstly, it reduces the population of the excited singlet state, and hence amplification factor; and secondly, it enhances the triplet-triplet absorption losses by increasing the population of the lowest triplet state.

Figures 13 and 14 show the absorption and emission cross section spectra for Rhodamine B and Oxazine 4 in PMMA, respectively. We determined absorption and emission cross sections based on quantum yield, absorbance, and fluorescence lifetime measurements. The quantum yields for Rhodamine B, and Oxazine 4 in PMMA were measured to be 0.76, and 0.10, respectively. The smaller emission cross section of Oxazine 4 is mainly due to the lower quantum yield compared with that of Rhodamine B. A peculiarity of the spectra of organic dyes is the widths of the absorption and emission bands, which cover several tens of nanometers. The breadth of the absorption spectrum offers alternative excitation sources such as a frequency-doubled Nd: YAG laser, copper vapor lasers, excimer lasers, and the broad emission spectrum provides wide tunability.

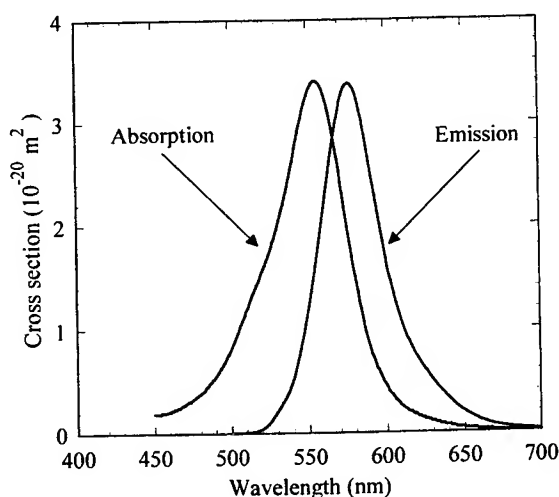


Fig. 13 Absorption and emission cross section spectra of Rhodamine B in PMMA.

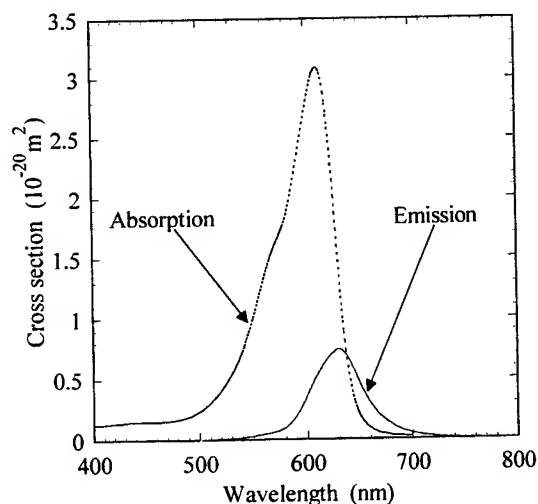


Fig. 14 Absorption and emission cross section spectra of Oxazine 4 in PMMA.

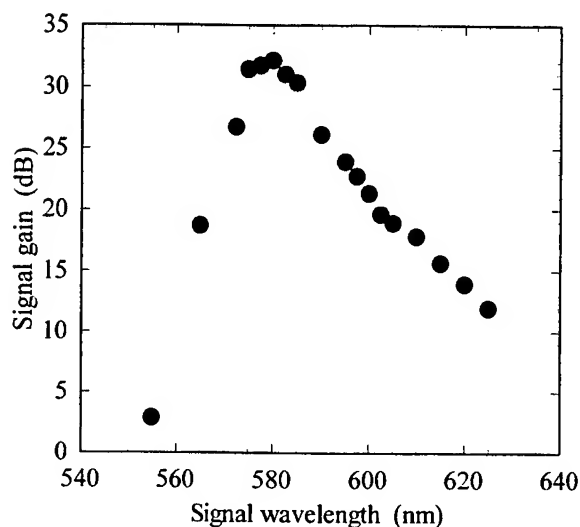


Fig. 15 Experimental gain versus signal wavelengths, obtained with a Rhodamine B-doped POFA with 1-m length, for launched pump power of 2.8 kW at 532 nm.

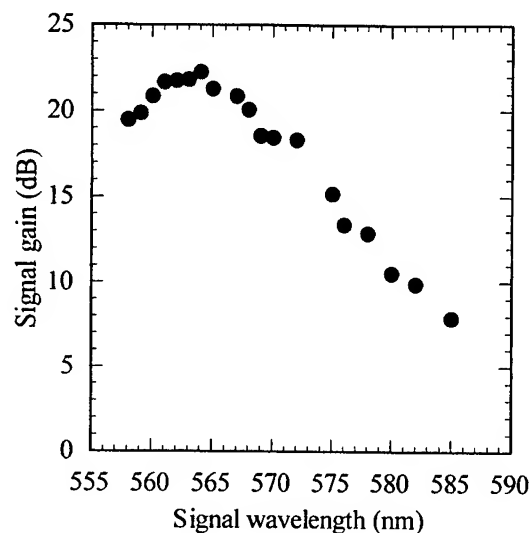


Fig. 16 Experimental gain versus signal wavelengths, obtained with a Rhodamine 6G-doped POFA with 1.6-m length, for launched pump power of 2 kW at 532 nm.

7.3 Gain characteristics of organic dye-doped POFAs

7.3.1 Gain spectra

A large gain bandwidth of organic dye-doped POFAs suggests that they can be tuned over a wavelength range of tens of nanometers. We investigated signal wavelength dependence for a Rhodamine B-doped POFA, and a Rhodamine 6G-doped POFA. The fiber was end-pumped at 532 nm with a frequency-doubled Nd: YAG laser. A dye laser pumped at 532 nm with the frequency-doubled Nd: YAG laser was used as a signal source. A neutral density filter (ND) was inserted to vary the pump rate. A spectroscope was used to separate the amplified output signal from any broad band spontaneous emission or remnant pump before detection with a photomultiplier. The launched pump and signal power was estimated by replacing the doped fiber with an undoped fiber.

Figure 15 shows experimental gain versus the signal wavelength for a Rhodamine B doped-POFA with 1-m length for 2.8 kW of pump power at 532 nm. Signal inputs were 0.3 W. More than 20 dB gain and 30 W output power have been achieved for signal wavelength spanning the 40 nm range between 560 nm and 600 nm with a best observed gain of 33 dB at 580 nm.

Figure 16 shows the signal gain as a function of signal wavelengths for a Rhodamine 6G-doped POFA with 1.6-m length for 2 kW of launched pump power. The fiber was fabricated from MMA solution containing 1 ppm-wt of Rhodamine 6G. The best observed gain was 22 dB at 564 nm. Optimization of the fiber parameter is expected to provide higher gains for a Rhodamine 6G-doped POFA. A remarkable advantage of organic dye-doped POFAs is the enormous selection of wavelengths for amplification due to the large variation in dye structure. The number of possible signal wavelengths and corresponding tunability range are greatly extended by the variety of organic dyes that can be used as active dopants. Hence the most important characteristic of organic dye-doped POFAs for practical applications is their ability to provide high-power output tunable over a wide range of wavelength

7.3.2 Pump wavelength dependence

We investigated pump wavelength dependence of organic dye-doped POFAs. We used an optical parametric oscillator as a pump source, and a dye laser as a signal source. The dye laser was pumped with a 532 nm output of the optical parametric oscillator.

Figure 17 shows the gain as a function of pump wavelength obtained for a POFA with 1-m length, fabricated from MMA solution containing 1 ppm-wt of Rhodamine B. For 600 W of launched pump power, the best observed gain was 22

dB for the fiber when pumped at 550 nm. The optimum pump wavelength for the Rhodamine B-doped POFA was found to be 550 nm, which corresponds to the peak absorption wavelength of Rhodamine B in PMMA. Figure 18 shows launched pump power dependence of the Rhodamine B-doped POFA with 1-m length, pumped at 550 nm. The maximum gain of 37 dB was obtained for the fiber for 3 kW of pump power at 550 nm.

Figure 19 shows pump wavelength dependence for a POFA fabricated from MMA solution containing 10 ppm-wt of Oxazine 4. The optimum pump wavelength for the Oxazine 4-doped POFA was found to be 605 nm. The maximum gain of 20 dB was obtained for the Oxazine 4-doped POFA for 3 kW of launched pump power at 605 nm. When pumped at 532 nm, the maximum gain obtained was 13 dB. It has been shown that pumping at the peak absorption wavelength optimizes the POFA performance. The regions around 580 nm and 650 nm attract most attention because they coincide with the low-loss windows of PMMA-based polymer optical fibers. A Rhodamine B-doped POFA operates in the region around 580 nm, and an Oxazine 4-doped POFA in the region around 650 nm.

4.2.3 Photostability

Organic dyes in solid matrices such as polymers and sol-gel glasses have attracted increasing attentions as gain media for laser applications¹¹⁻¹⁴. Whereas it is of lesser importance in lasers and amplifiers in liquid phase, the photostability can be a serious problem in solid state devices such as polymer optical fiber amplifiers, where the dye cannot be circulated.

We investigated the photostability of a Rhodamine B-doped POFA with 0.9-m length, for 2.7 kW of launched pump power at a 10 Hz repetition rate. Throughout the 10 hours of continuous operation at 10 Hz (approximately 3.6×10^5 shots), the gain remained 33 dB and no photodegradation of doped dye was observed. The operation lifetime is longer than those of dyes in solid matrices for laser applications. Since the dye concentration (in order of one ppm-wt) is much lower than those in conventional solid state dye lasers (typically, in order of hundreds of ppm-wt), the energy release from the dye molecules is so efficient that the thermal effect, which leads to decomposition of fluorescent species, is suppressed. The low dye concentration can be realized only in active components in a fiber form because of their long interaction length between gain media and propagating beams.

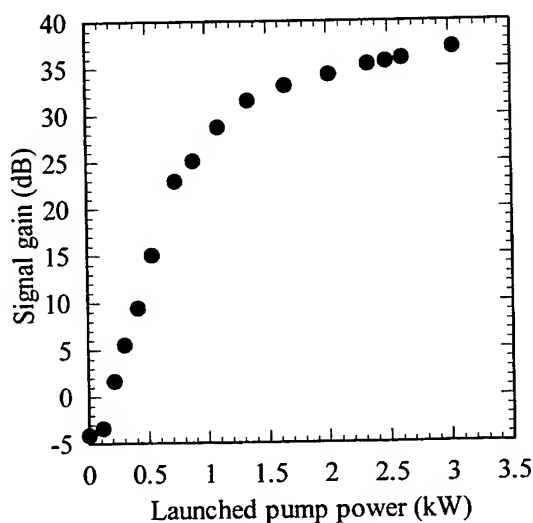


Fig. 17 Experimental gain versus launched pump power, obtained with a Rhodamine B-doped POFA with 1-m length, pumped at 550 nm. Signal wavelength was 580 nm.

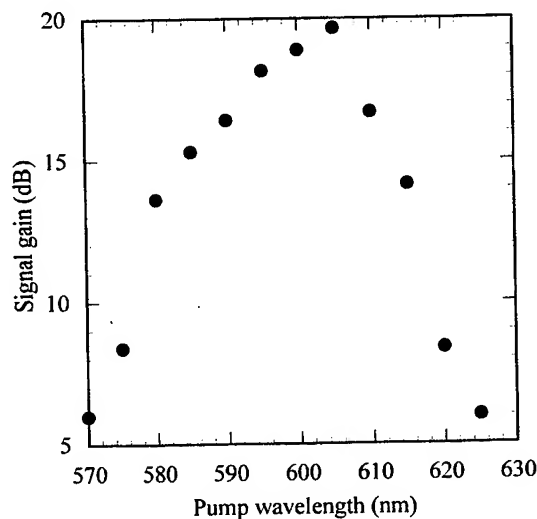


Fig. 18 Experimental gain versus pump wavelengths, obtained with an Oxazine 4-doped POFA with 0.4-m length, for launched pump power of 3 kW. Signal wavelength was 644 nm.

8. RARE EARTH CHELATE-DOPED POLYMER OPTICAL FIBERS

8.1 Spectroscopic properties of rare earth chelates

Rare earth chelates, especially, those of Eu, were the first compounds used for laser action in the liquid phase¹⁵. The required pump energy was as high as 1000 J. However, it is much easier to attain the required degree of inversion in a fiber form because of the confined pump light in the core region. Furthermore, the synthetic polymer shows much better compatibility with organic compounds and is amenable to high dopant concentrations, which result in a high gain in a short length of fiber.

The refractive index of GI POFs has a maximum along the axis and decreases gradually in the radial direction until it merges into the constant cladding index. We use low molecular weight dopants immobilized in a polymer host to form a concentration profile in GI POFs. Since optical properties of fluorescent materials are strongly host-dependent, we investigated fluorescence intensities and fluorescence lifetimes of Eu chelate in PMMA with and without low molecular weight dopants. We chose β -diketones of trifluoroacetylacetone and hexafluoroacetylacetone as chelating agents, and synthesized Eu chelates of trifluoroacetylacetone and hexafluoroacetylacetone in tris forms ($\text{Eu}(\text{TFAA})_3$ and $\text{Eu}(\text{HFAA})_3$). For spectroscopic investigations, we prepared MMA solutions with 800 ppm-wt of $\text{Eu}(\text{TFAA})_3$ and 20 wt% of low molecular weight dopants, and carried out polymerization using t-butyl peroxy isopropylcarbonate as an initiator, and n-butyl mercaptan as a chain transfer agent. The temperature of polymerization was maintained at 90 °C for 24 hours. Then, the polymer bulks obtained were heat treated at 110 °C to complete the polymerization. For all spectroscopic studies, we used polished rectangular parallelepiped samples. The dimensions of these samples were 40 × 10 × 10 mm, with europium chelate concentrations of 800 ppm-wt in the PMMA host. We measured fluorescence intensities with a spectrophotometer, and determined fluorescence lifetimes using a dye laser pumped at 337 nm with a nitrogen laser.

Table 1 shows fluorescence intensities and fluorescence lifetimes of $\text{Eu}(\text{TFAA})_3$ in PMMA with and without low molecular weight dopants. Adding 20 wt% of a low molecular weight dopant, triphenyl phosphate (TPP), resulted in significant increase in fluorescence intensity of $\text{Eu}(\text{TFAA})_3$, while appreciable decrease was observed when benzyl n-butyl phthalate (BBP) was used. The fluorescence intensity of $\text{Eu}(\text{TFAA})_3$ in PMMA doped with 20 wt% of TPP was twice as high as that without TPP. Similarly, the fluorescence lifetime of the $\text{Eu}(\text{TFAA})_3$ in PMMA was found to be less than 300 μs , while, in PMMA doped with TPP, $\text{Eu}(\text{TFAA})_3$ showed a fluorescence lifetime as long as 450 μs . The mechanism of the fluorescence enhancement by doping of TPP is currently under investigation. Based on the available data, TPP is the most suitable dopant for the rare earth chelate-doped POFs.

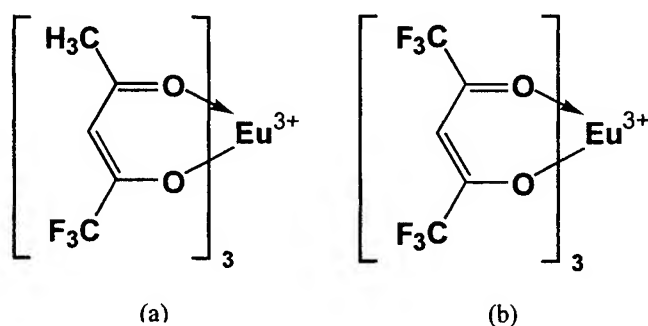


Fig. 19 Molecular structures of (a) $\text{Eu}(\text{TFAA})_3$ and (b) $\text{Eu}(\text{HFAA})_3$.

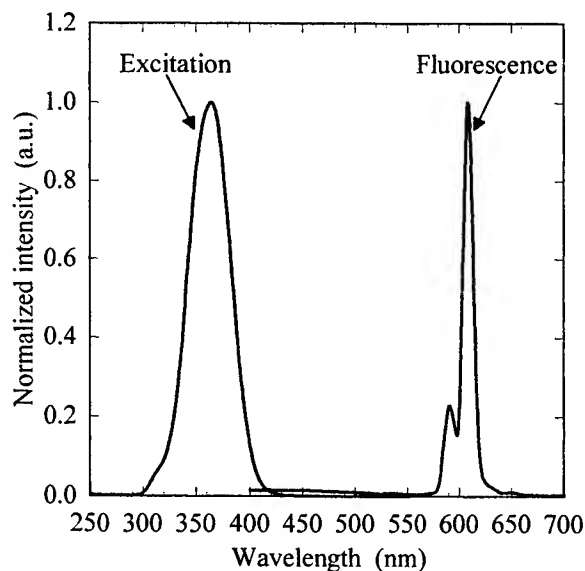


Fig. 20 Excitation and fluorescence spectra of $\text{Eu}(\text{HFAA})_3$ in PMMA.

Table 1 Fluorescence intensities and lifetimes of Eu (TFAA)₃ in PMMA with various kinds of dopants for refractive index profile. TPP: triphenyl phosphate, BBP: benzyl n-butyl phthalate.

	Dopant		
	Without dopant	TPP	BBP
Fluorescence intensity (a.u.)	1.0	2.0	0.4
Fluorescence lifetime (μs)	271	445	...

8.2. Optical properties of rare earth chelate-doped polymer optical fibers

Figure 23 shows the attenuation spectrum of the GI POF doped with 1 wt% of Eu(HFAA)₃. The attenuation loss around 650 nm is found to be 0.4 dB/m, which is three times as high as that of an undoped GI POF. As an in-line polymer optical fiber amplifier, which will be used in several meters of fiber, the loss is considered to be negligibly small.

We measured the emission characteristics of the fiber side-pumped with xenon flashlamps. We employed a close-coupled multiple coaxial geometry with 6 xenon lamps. Approximately 70 cm of the fiber was excited. Fig. 24 shows temporal profiles of pumping and fiber output pulses at 300 J of total input energy to the lamps. The full width at half maximum were 3.5 μs for the pump pulse, and 6 μs for the fiber output pulse. The measured spontaneous decay time of Eu(HFAA)₃ in PMMA doped with 20 wt% of TPP is 560 μs, and the fiber output shows much shorter lifetime, which

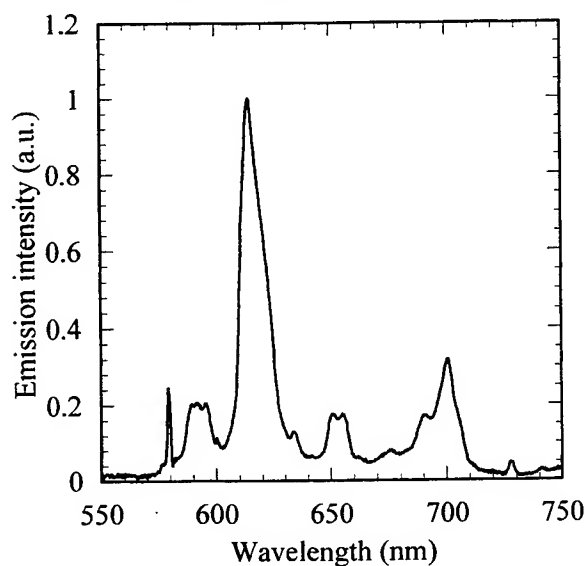


Fig. 21 Fluorescence spectrum of an Eu(HFAA)₃-doped POF.

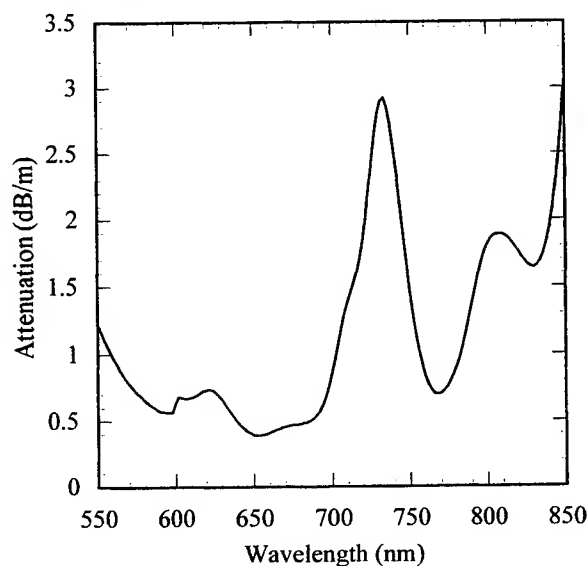


Fig. 22 Transmission loss spectrum of an Eu(HFAA)₃-doped POF. The chelate concentration was 1 wt%.

indicates the occurrence of superfluorescence. Figure 25 shows the superfluorescence spectrum of the fiber at 108 J of total input energy to the lamps, coupled with the fluorescence spectrum. To measure superfluorescence from the fiber, we used a spectroscope to separate the ⁵D₀-⁷F₂ line at 614 nm from any other emission before detection with a CCD array. The halfwidth of the fluorescence was 13 nm, while the emission spectrum exhibits 8 nm. The linewidth was reduced to about 60% of the initial value. Because we did not optimize the pump geometry, only a small fraction of the pump light was absorbed by the chelate. The input power into the lamps could be reduced with an optimized excitation geometry. Rare earth chelate-doped POFs are appealing as superfluorescent sources in fiber sensor applications.

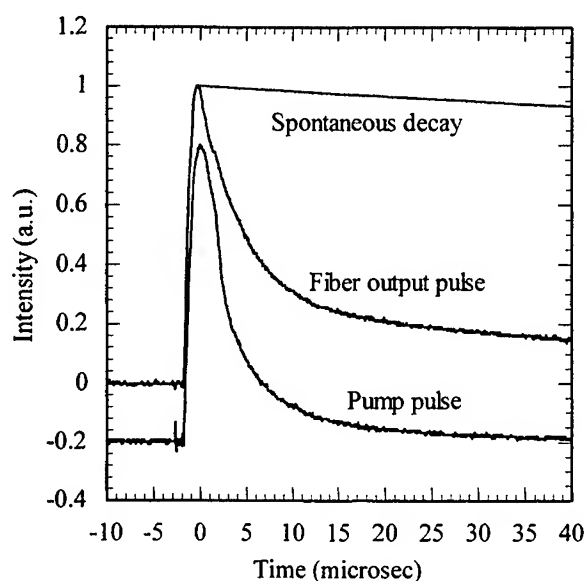


Fig. 23 Temporal profiles of pump and fiber output pulses.

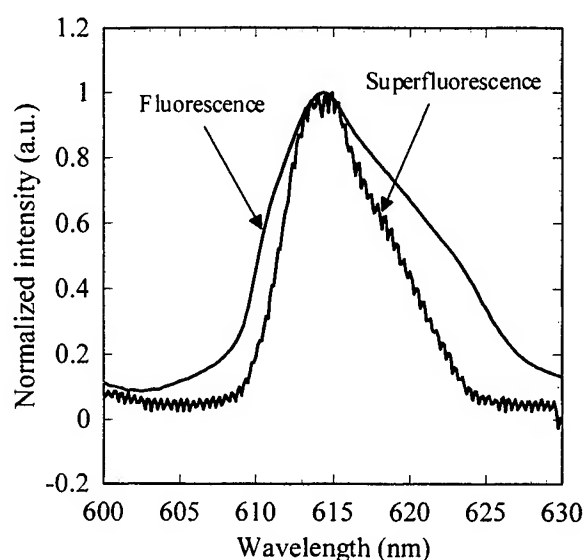


Fig. 24 Fluorescence and superfluorescence spectra of an $\text{Eu}(\text{HFAA})_3$ -doped POF. The chelate concentration was 1 wt%.

9. CONCLUSION

Lower material dispersion of the PF polymer than PMMA and even silica gives the great advantage in the bandwidth. It was clarified for the first time that higher bandwidth than PMMA base GI POF and $\text{GeO}_2\text{-SiO}_2$ base multimode fiber can be expected. Furthermore, low attenuation, which is another advantage of the PF polymer base GI POF, enabled much high bandwidth at $1.3\ \mu\text{m}$ because the material dispersion decreases with increasing the wavelength.

It was theoretically and experimentally confirmed that the bandwidth characteristics of the PMMA base GI POF is strongly influenced by the mode dependent attenuation and not by the mode coupling. The conclusion that the effect of differential mode attenuation is large rather than the mode coupling on the bandwidth characteristic of the GI POF is derived from the following three reasons:

- (1) Each mode are transmitted independently in the DMD analysis even after 100-m transmission, and their delay times are precisely predicted by the group delay calculation in which no mode coupling effect was considered.
- (2) Linear relation between the DMD τ and fiber length L was observed in the DMD analysis.
- (3) Theoretically estimated output pulse waveforms showed an excellent agreement with that experimentally measured by considering the differential mode attenuation effect.

Since the POF link length is considered to be less than 100 m, the result of the weak mode coupling effect indicates that the steady state mode distribution is not necessarily established in the GI POF. Therefore, these propagating mode characteristics are very important issues for designing the POF data link system.

It has been demonstrated that organic dye-doped POFAs cover the wide spectral coverage in the visible. It has also been verified that pumping organic dye-doped POFAs at their peak absorption wavelength yields the maximum gain. The first demonstration of superfluorescence in the Eu chelate-doped GI POF, evidenced by the lifetime shortening and the spectral narrowing, shows that rare earth chelate-doped GI POF are promising as optical amplifiers and superfluorescent sources in a variety of communication and sensor applications. We have prospect that the wide choice of rare earth ions offers light amplification in several wavelength regions ranging from visible to infrared with rare earth chelate-doped GI POFs.

10. ACKNOWLEDGEMENT

This work is supported by the research fund of Plastic Optical Fiber Project from the Ministry of Posts and Telecommunications.

11. REFERENCES

1. R. E. Epworth, The phenomenon of modal noise in analogue and digital optical fiber systems, Proc. 4th European Conf. on Opt. Commun., Genoa, Italy, pp.492-501, Sept. 1978.
2. Y. Koike, T. Ishigure, and E. Nihei, , High-Bandwidth Graded-Index Polymer Optical Fiber, IEEE J. Lightwave Technol., 13, pp. 1475-1489, 1995
3. Y. Koike, Progress of Plastic Optical Fiber Technology, Proc. European Conf. on Opt. Commun. Oslo, Norway, I, pp. 41-48, Sept. 1996
4. Y. Koike and T. Ishigure, Progress of low-loss GI polymer optical fiber from visible to 1.5- μ m wavelength, Proc. European Conf. on Opt. Commun. Edinburgh, Scotland, I, pp. 41-48, Sept. 1997
5. T. Onishi, H. Murofushim Y. Watanabe, Y. Takano, R. Yoshida, M. Naritomi, "Recent progress of perfluorinated GI POF," The 7 th. Intenational POF Conference, Post Deadline Paper, October, Berlin (1998)
6. W. Li, G. D. Khoe, H. P. A. v.d. Boom, G. Yabre, H. de Waardt, Y. Koike, M. Naritomi, N Yoshihara, and S. Yamazaki, "Record 2.5 Gbit/s Transmission Via Polymer Optical Fiber At 645 nm Visible Light," The 7 th. Intenational POF Conference, Post Deadline Paper, October, Berlin (1998)
7. G. Giaretta, W. White, M. Wegmueller, R. V. Yelamatry, and T. Onishi, "11 Gb/sec Data Transmission Through 100m of Perfluorinated Graded-Index Polymer Optical Fiber," Optical Fiber Communication Conference, Post deadline paper, PD14. February, San Diego (1999)
8. J. W. Fleming, Material and mode dispersion in $\text{GeO}_2 \cdot \text{B}_2\text{O}_3 \cdot \text{SiO}_2$ glasses, J. Am. Cer. Soc., vol. 59, no. 11-12, pp. 503-507, 1976.
9. T. Ishigure, E. Nihei, and Y. Koike, Optimum refractive-index profile of the graded-index polymer optical fiber, toward gigabit data links, Appl. Opt., vol.35 no.12, p.2048-2053, 1996
10. R. Olshansky and D. B. Keck, Pulse Broadening in Graded-Index Optical Fibers, Appl. Opt., 15, (2), 483-491, 1976
11. Y. Ohtsuka, and Y. Koike, "Determination of the refractive-index profile of light focusing rods: accuracy of a method using Interphako inference microscopy," Appl. Opt. Vol. 19, pp. 2866-2872, 1980.
12. B. H. Soffer, and B. B. McFarland, "Continuously tunable, narrow-band organic dye lasers," Appl. Phys. Lett. Vol. 10, pp. 266-267, 1967.
13. A. Costela, F. Florido, I. Garcia-Moreno, R. Duchowicz, F. Amat-Guerri, J. M. Figuera, and R. Sastre, "Solid-state dye lasers based on copolymers of 2-hydroxyethyl methacrylate and methyl methacrylate doped with rhodamine 6G," Appl. Phys. B. vol. 60, pp. 383-389, 1995.
14. F. Salin, G. Le Saux, P. Georges, A. Baum, C. Bagnall, and J. Zarzycki, "Efficient tunable solid-state laser near 630 nm using sulforhodamine 640-doped silica gel," Opt. Lett. Vol. 14, pp. 785-787, 1989.
15. M. D. Rahn, and T. A. King, "Comparison of laser performance of dye molecules in sol-gel, polycom, ormosil, and poly(methyl methacrylate) host media," Appl. Opt. Vol. 34, p. 8260, 1995.
16. H. Samelson, A. Lempicki, C. Brecher, and V. Brophy, "Room-temperature operation of a europium chelate liquid laser," Appl. Phys. Lett. Vol. 5, pp. 173-174, 1964.

Development of microlens arrays for integration with optoelectronic devices

C. Wang*, Y. C. Chan, Y. L. Lam and B. S. Ooi

Photonics Research Group, School of Electrical and Electronic Engineering
Nanyang Technological University, Block S1, Nanyang Avenue, Singapore 639798

ABSTRACT

Optoelectronic integrated devices can be found in an increasing number of applications in optical systems and are expected to play a major role in future optical systems. They offer the potential of compact, lightweight optics that can be mass-produced in polymeric materials by low-cost replication techniques. The fabrication technology that can achieve such micro-optical elements has been well developed. The direct He-Cd laser writing system is adopted to fabricate micro-optical elements in this work. Continuous-relief microlens elements and microlens arrays fabrication process, which can be used in applications requiring integration of optoelectronic devices, are described. The continuous-relief microlens elements and microlens arrays are fabricated at different conditions and the optimum conditions have been determined. The intensity of the laser beam, the moving speed of the movable stages, the distance between the top surface of the photoresist coated on the substrate to the UV objective lens, and the overlap of the adjacent patterns are the key parameters that significantly influence the surface roughness, profile and surface-relief height of the drawn continuous-relief microlens elements.

Keywords: Continuous-relief microlens element and microlens arrays, direct laser writing

1. INTRODUCTION

Computer clock speeds have been increasing steadily over the past decade. In contrast, electrical interconnects between chips and boards are approaching the limits of their performance. The issues of electromagnetic cross-talk, capacitive loading, and signal distortion can be alleviated by use of optical carriers to transmit parallel data¹.

Driven by the practical need to reduce the weight, size and cost of complex optical systems as well as the desire to create optics with novel functionality, researchers fabricated and tested subwavelength structures, such as the hybrid diffractive/refractive optics, and large arrays of continuous-relief micro-optics.

In most practical cases, the optical performance (efficiency and image uniformity in particular) of continuous-relief micro-optical elements is superior to that of their binary optical counterparts, the performance of which generally improves with increased complexity and number of levels².

Direct writing in photoresist by a focused laser beam, in which accurate control of the process parameters enables a complex continuous-relief microstructure to be fabricated in a single exposure scan and development, has been shown to produce excellent results²⁻⁷. Laser writing, as a form of maskless lithography, has the advantage of enabling rapid prototyping of electronic and optoelectronic devices with low setup and running costs. It offers great flexibility due to its maskless and discretionary nature^{4, 8-9}.

In this paper, we report the development of the fabrication of continuous-relief microlens elements using direct laser writing. We have shown that the laser intensity, writing speed, writing height, laser intensity variation, overlap and diameter are the major parameters that all determine the optical performance of the fabricated micro-optical elements. The laser writing system has been successfully proven to be highly suited to the fabrication of quality micro-optical devices.

* Corresponding author: Email: p145740294@ntu.edu.sg; Telephone: +65-7905449; Fax: +65-7933318

2. EXPERIMENT

The experimental studies are carried out using a laser writing system, optical microscope, surface profiler and scanning electron microscopy (SEM). The laser writing system⁴ consists essentially of a laser source that provides the optical energy for transforming the photoresist, an optical subsystem that focuses the laser beam to a writing spot on the wafer surface and enables controlled exposure times, a movable stage that holds the wafer to be exposed, a computer with special software interfaced with a motion controller for the movable stage, and an observation and alignment subsystem.

An acousto-optic modulator (AOM) is used to control the ultraviolet laser beam intensity, and it is driven by a radio frequency (RF) driver. The AOM value is actually the signal from the computer that has been converted to an analog input to the RF driver for modulating the ultraviolet laser beam intensity. Thus, the AOM value, which is an arbitrary unit, represents the intensity of the laser beam.

Figure 1 shows the variation of the AOM value and laser intensity at the focal point of the objective lens. When the AOM value is smaller than 3, the laser intensity is almost the same, but when the AOM value is larger than 3, the laser intensity changes quickly as the AOM value increases.

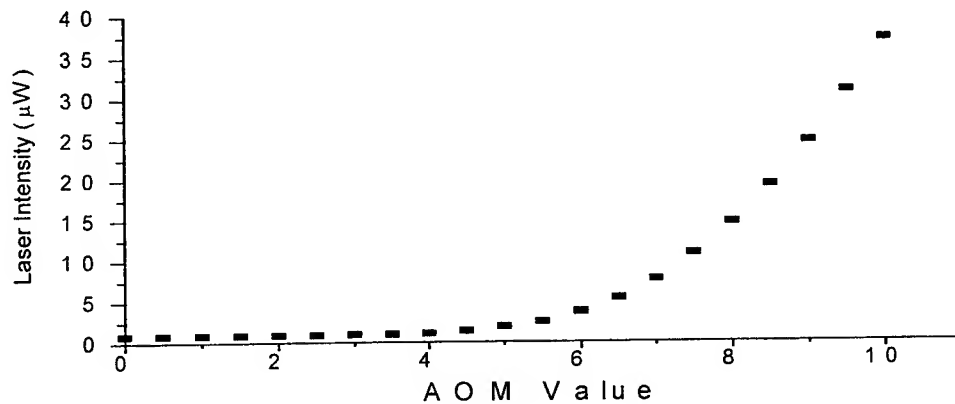


Fig. 1. Variation of the AOM value and laser intensity

Control of the laser writing system is executed via a system computer with a user-friendly interface. Data entry tables enable the definition of system parameters, such as the intensity of the laser beam, the laser beam spot size, the movable stage speed and scale of the basic pattern's dimensional unit to the step resolution, and the pattern of the drawing.

Generally, there are two methods to write the sample pattern onto the photoresist-coated sample: namely, the spiral method and the raster scan method shown in Figure 2. Currently, the spiral lines are used to draw the lens patterns and the raster lines for the lines patterns because the spiral line has fewer turning points, consequently a smooth surface of the written patterns can be achieved.

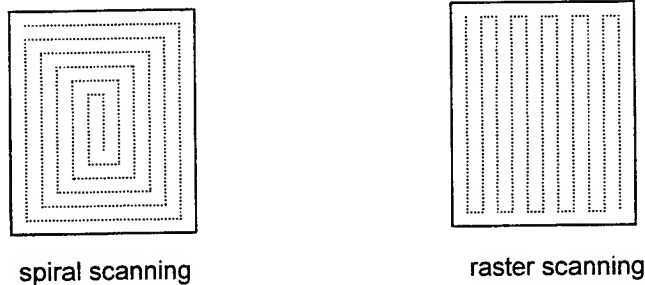


Fig. 2. Writing paths for spiral scanning and raster scanning

A He-Cd laser emitting at 325-nm with a cw power of 15mW is used in the experiment. A glass sample of area $1 \times 1 \text{ cm}^2$ is cut and coated, exposed and developed in a yellow illuminated room. The fact that the emission wavelength of 325-nm is relatively close to the i-line (365-nm) emission of the mercury lamp also means that high-performance commercial i-line photoresist chemicals can be used as the writing medium for pattern transfer. Here, the positive photoresist TSMR of Tokyo Ohka Kogyo is adopted for coating and the NMD-3 solution for developing.

The continuous-relief microlens elements can be fabricated by controlling the intensity of the laser beam, the moving speed of the movable stages, the distance between the top surface of the photoresist coated on the substrate to the UV objective lens, and the overlap of the adjacent patterns. All of these data are input to the computer and the program then executes the necessary parameter determination.

3. CONTINUOUS-RELIEF MICROLENS ELEMENTS FABRICATION

3.1 Surface-Relief Profile Fidelity

The ultimate test of the quality of a micro-optical element is its optical performance, which is measured in terms of parameters such as imaging quality, efficiency and scattered light. In the fabrication process, it is useful to consider and monitor physical parameters which are a measure of how well the design surface relief is realized, in particular the absolute relief height, profile form, lateral resolution and the surface roughness.

3.1.1 Surface-relief height on photoresist

The precision to which the surface-relief height is reproduced in unstructured, uniform areas is dependent upon the photoresist film sensitivity, laser beam intensity control and the development process.

Figure 3 shows the variation curve for surface-relief height of the drawn microlens elements at different AOM values. The surface-relief height of the drawn microlens elements could be changed from about $0.1 \mu\text{m}$ to $1 \mu\text{m}$, as the AOM value is varied from about 3.5 to 12. As a result, the maximum surface-relief height of the drawn microlens elements that can be achieved currently is $0.9 \mu\text{m}$. In practice, in order to draw a correct microlens element profile, the AOM value should be determined according to the overlap of the adjacent patterns, AOM value change step and the microlens element design parameters. Thus the surface-relief height of the fine microlens element profile is smaller than the maximum value of $0.9 \mu\text{m}$ in practice.

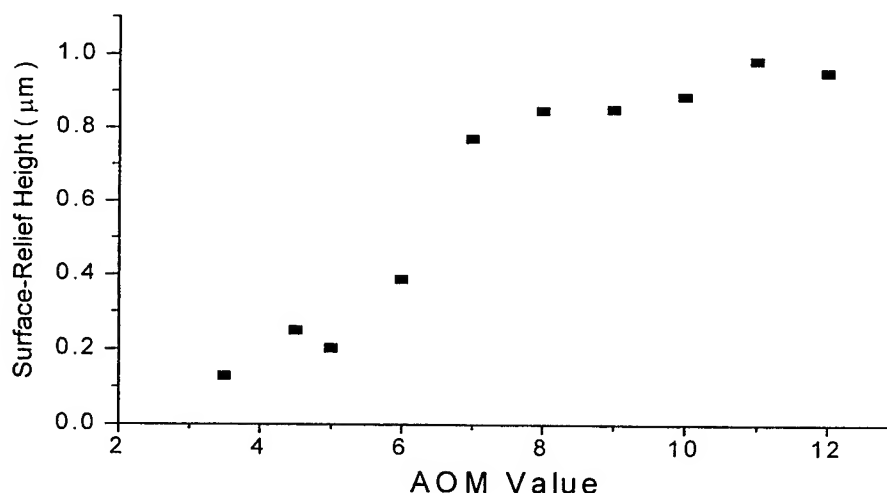


Fig. 3. Variation of the writing thickness of the drawn microlens elements at different AOM values

3.1.2 Profile of continuous-relief microlens elements fabricated on photoresist

Two factors, overlap and AOM step value, significantly influence the profile of the drawn continuous-relief microlens elements. Overlap means the center distance between two adjacent written patterns. The AOM step value is the decremental AOM value between two continuous sub-patterns.

Figure 4 shows the profile of the drawn continuous-relief microlens elements with different AOM step values via a surface profiler. The AOM step value is changed from 0.06 to 0.03. The diameters of these microlens elements are 270 μm , 300 μm , 360 μm and 480 μm respectively. The starting AOM value is 6, the overlap is 6 μm and writing height is 3 μm .

The AOM step value is a key parameter that influenced the surface roughness, profile and writing thickness for drawing the microlens elements. Analyzing the experiment results in Figure 4, it can be seen that a better surface profile of the microlens element could be attained when the AOM step value is 0.04 and 0.03. When the AOM step value is less than 0.03, the surface roughness of the microlens elements drawn by the direct laser writing system is small enough and we also could obtain a satisfactory profile of the microlens elements. However, in the current direct laser writing system, one written pattern can only consist of no more than 100 sub-patterns, because of the limitation of the memory of the motion controller. So if the AOM step value is very small, it will lead to one written pattern having more than 100 sub-patterns and the system will not be able to get the correct writing patterns. Hence, there is a need to pay more attention in choosing the optimum AOM step value, while considering the other parameters, such as the overlap, the writing height and diameter of the microlens element.

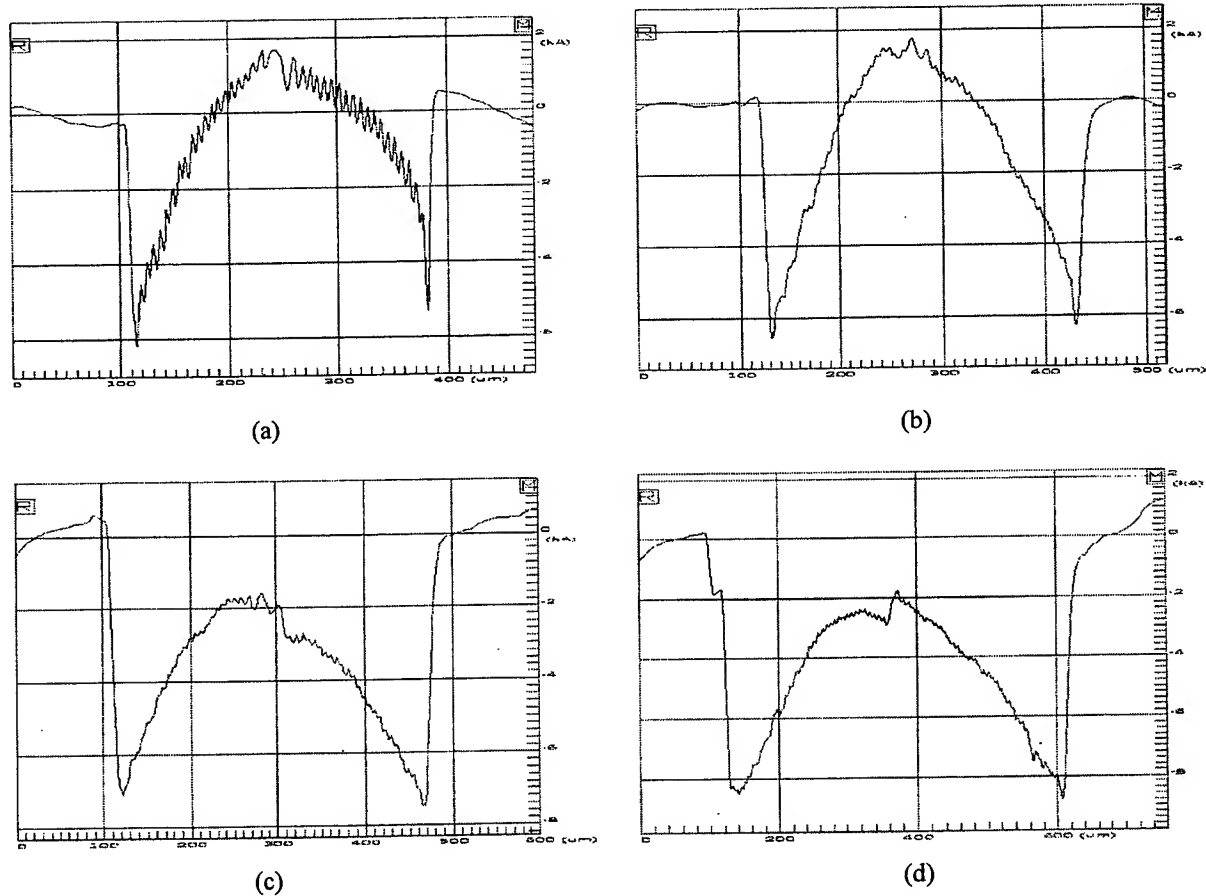


Fig. 4. Profile of the drawn continuous-relief microlens elements with different AOM step values via surface profiler, (a) AOM step value = 0.06, (b) AOM step value = 0.05, (c) AOM step value = 0.04, (d) AOM step value = 0.03.

The profile of the drawn continuous-relief microlens elements with different overlaps is shown in Figure 5. The overlap is changed from 8 μm to 3 μm . The diameters of these microlens elements are 640 μm , 360 μm , 480 μm , 400 μm , 320 μm and 240 μm respectively. The starting AOM value is 6, AOM step value is 0.03 and writing height is 3 μm . A good surface profile of the microlens element can be achieved when the overlap is 5 μm and 6 μm from Figures 5 (c) and (d). In the case where the overlap is more than 6 μm , the profile of the microlens elements has a lot of noise, and the surface roughness is significant. On the other hand, if the overlap is less than 5 μm , we could not draw the profile of the microlens elements correctly.

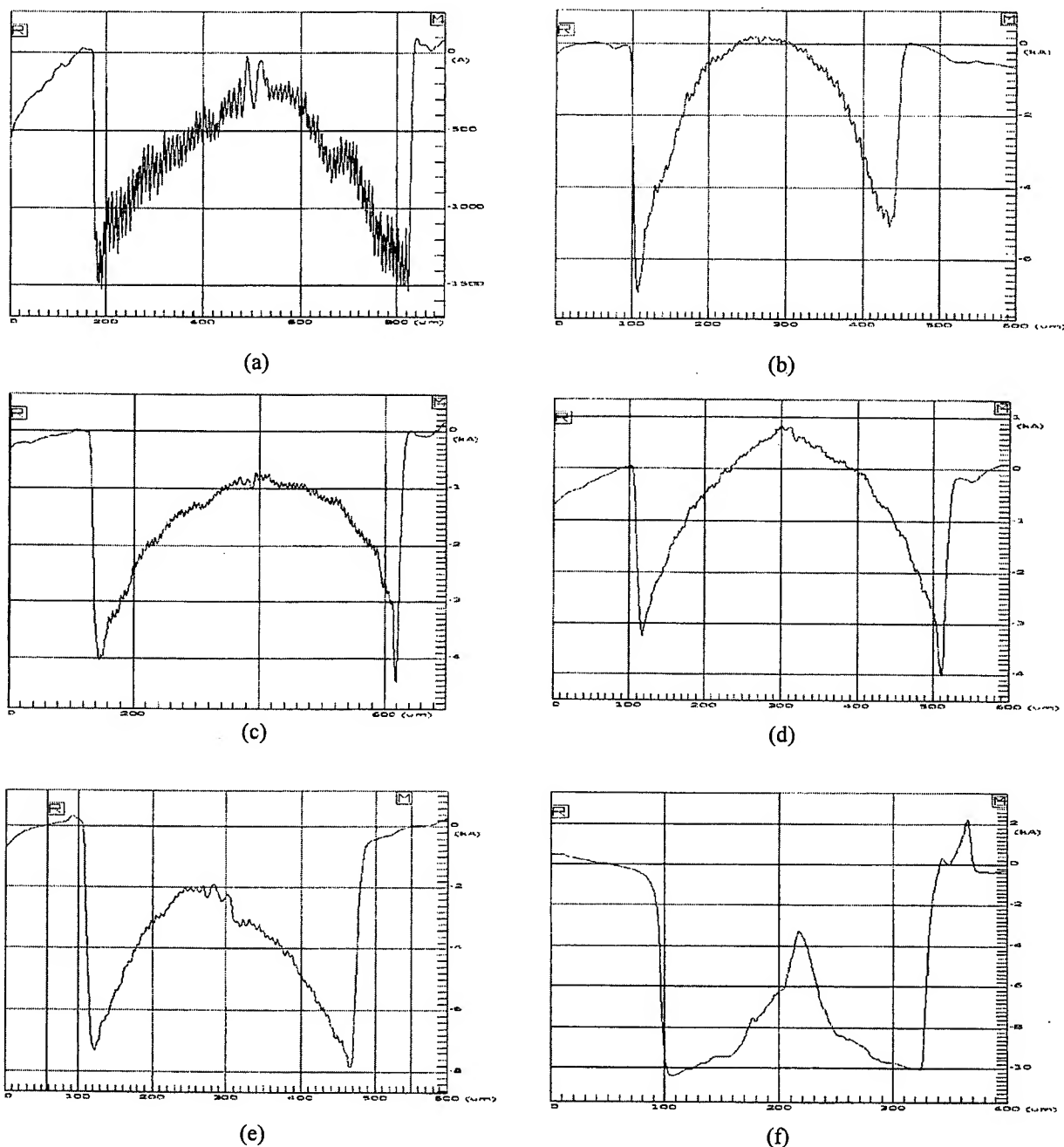


Fig. 5. Profile of the drawn continuous-relief microlens elements with different overlaps via surface profiler, (a) Overlap = 8 μm , (b) Overlap = 7 μm , (c) Overlap = 6 μm , (d) Overlap = 5 μm , (e) Overlap = 4 μm , (f) Overlap = 3 μm .

Defining the optimal parameters, such as the overlap, starting AOM value, AOM step value, diameter, writing height and writing speed is a key point for producing the fine profile of the continuous-relief microlens elements.

In the next section, we will present examples of single microlens element and microlens arrays fabricated by direct laser writing using the system constructed at Photonics Lab II of School of Electrical & Electronics Engineering, Nanyang Technological University.

3.2 Examples of the Fabricated Single Microlens Element and Microlens Array on Photoresist

Figure 6 shows the photos and profile of the fabricated single microlens element. The single microlens element diameter is $480\text{ }\mu\text{m}$. The starting AOM value is 6, AOM step value is 0.03, the overlap is $6\text{ }\mu\text{m}$ and writing height is $3\text{ }\mu\text{m}$. The spiral lines are used to draw microlens patterns.

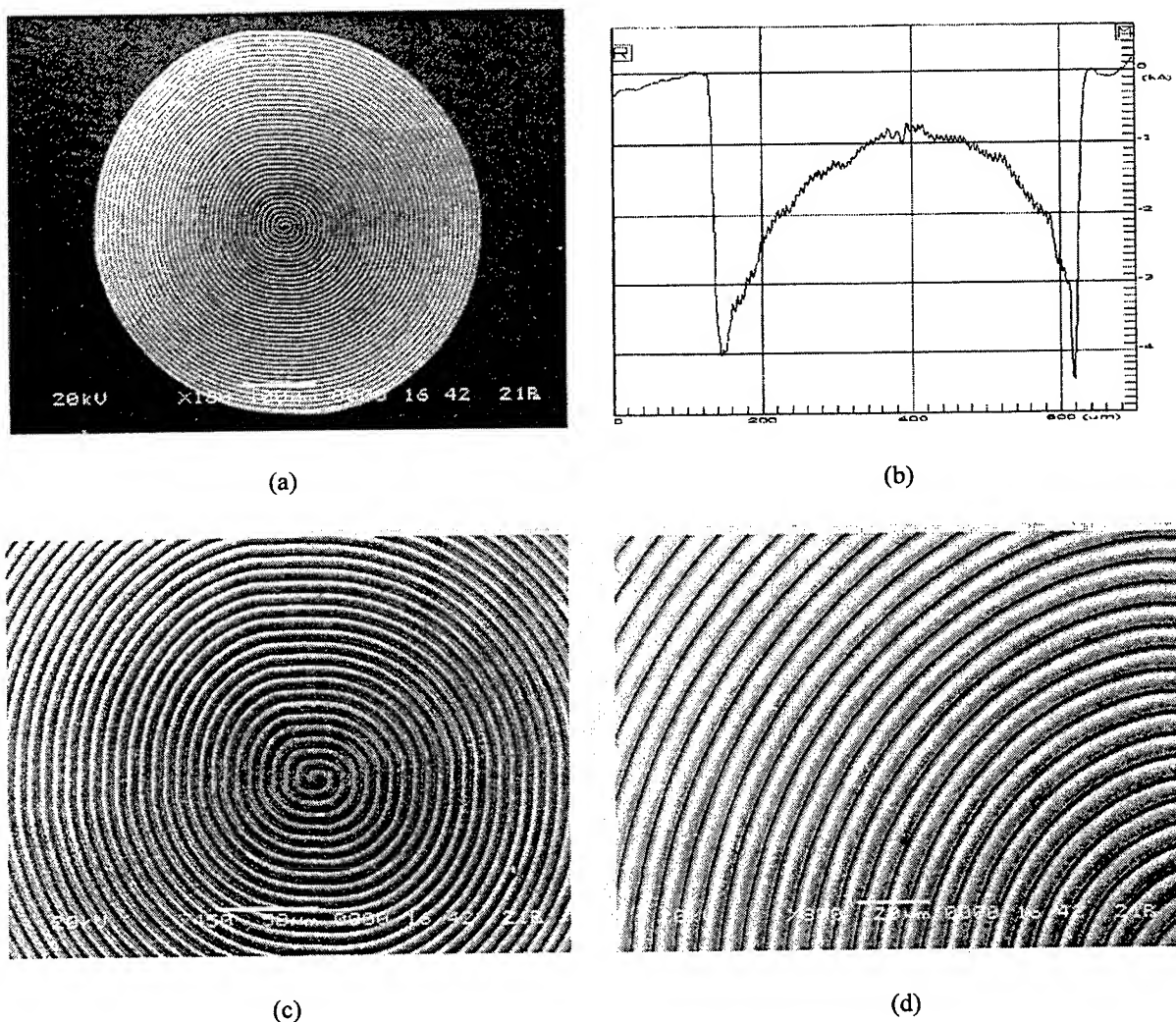


Fig. 6. Examples of the fabricated single microlens element, (a) Photo of a single microlens element with overlap of $6\text{ }\mu\text{m}$ and AOM step value of 0.03 via SEM, (b) Profile of the single microlens element via surface profiler, (c) Photo of the central part of the single microlens element via SEM, (d) Photo of the edge of the single microlens element via SEM.

The photo and profile of the fabricated microlens array of 9 elements are shown in the Figure 7. The diameter of one element of the microlens array is 300 μm .

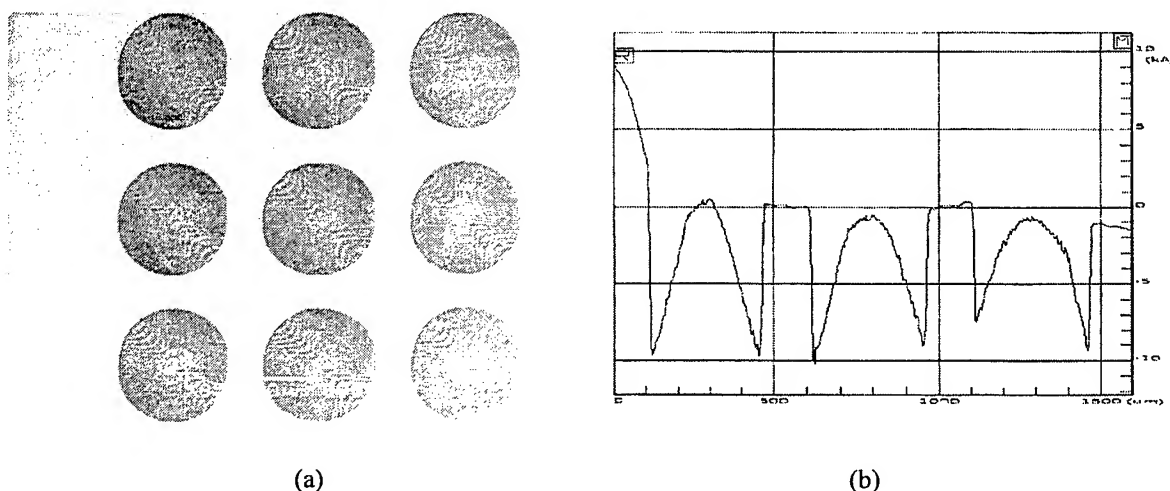


Fig. 7. Examples of the fabricated microlens array, (a) Photo of the microlens array with overlap of 6 μm and AOM step value of 0.03 via SEM, (b) Profile of the microlens array via surface profile.

From above figures, it can be seen that the microlens elements have good surface profile and small surface roughness. Experiments have also been carried out to assess the optical performance of the fabricated single microlens element and microlens array.

The capabilities of the laser writing technology are illustrated in Figures 6 and 7. We expect that the performance of the fabricated micro-optical elements can be improved by using a deep UV 266-nm laser in future.

4. CONCLUSIONS

The laser writing system has been successfully proven to be highly suited for the fabrication of the continuous-relief of microlens elements and microlens arrays. The fabrication process of forming continuous-relief microlens elements on photoresist by direct laser writing system has been studied. The variation of surface-relief height of drawn microlens elements at different AOM values is discussed. The optimal values of overlap ($= 5 \mu\text{m}$ or $6 \mu\text{m}$) and AOM step values ($= 0.03$ or 0.04) are given. Examples of the fabricated continuous-relief single microlens element and microlens array are presented. It can be observed that the microlens elements have a good surface profile and surface roughness. The high optical quality of the fabricated micro-optical elements and devices can be achieved by determining the optimum parameters, such as the intensity of the laser beam, laser intensity variation, overlap of the adjacent patterns, diameter, writing height and writing speed.

REFERENCES

1. Eva M. Strzelecka, Duane A. Loudervack, Brian J. Thibeault, Geoff B. Thompson, Kent Bertilsson, and Larry A. Coldren, "Parallel free-space optical interconnect based on arrays of vertical-cavity lasers and detectors with monolithic micro-lenses", *Appl. Opt.* **27**, pp. 2811-2821, 1998.
2. M. T. Gale, M. Rossi, J. Pedersen, H. Schütz, "Fabrication of continuous-relief micro-optical elements by direct laser writing in photoresists", *Opt. Eng.* **33**, pp. 3556-3566, 1994.
3. H. P. Herzing, ed, *MICRO-OPTICS: Elements, systems and applications*, Taylor & Francis, London, 1997.
4. Y. C. Chan, Y. L. Lam, Y. Zhou, F. L. Xu, C. Y. Liaw, W. Jiang, J. Ahn, "Development and applications of a laser writing lithography system for maskless patterning", *Opt. Eng.* **37**, pp. 2521-2530, 1998.
5. M. Haruna, M. Takahashi, K. Wakabayashi, and H. Nishihara, "Laser beam lithographed micro-Fresnel lenses", *Appl. Opt.* **29**, pp. 5120-5126, 1990.

6. M. T. Gale, G. K. Lang, T. M. Raynor and H. Schütz, "Fabrication of micro optical components by laser beam writing in photoresist", *SPIE, 1506, Micro-optics*, pp. 65-70, 1991.
7. A. Y. Smuk, and N. M. Lawandy, "Direct laser writing of diffractive optical elements", *CLEO'97*, pp. 177, 1997.
8. Y. S. Liu, "Sources, optics, and laser microfabrication systems for direct writing and projection lithography," Chap. 1 in *Laser Micro-fabrication: Thin Film Processes and Lithography*, D. J. Ehrlich and J. Y. Tsao, Eds., pp. 3-84, Academic Press, Boston, 1989.
9. C. Y. Fu, B. Law, R. Hsu, N. F. Raley, V. Malba, R. Hills, and C. Lai, "A laser direct write double-level-metal technology for rapid fabrication," in *Proc. IEEE 1990 Custom Integrated Circuits Conf.*, pp. 18.1/1-4, 1990.

Multi-Gigabit/s perfluorinated graded-index plastic-optical-fiber data links with butt-coupled single-mode InGaAs VCSEL

F. Mederer^{†a}, R. Jäger^a, P. Schnitzer^a, H. Unold^a, M. Kicherer^a and K.J. Ebeling^a,
M. Naritomi^{‡b} and R. Yoshida^b

^aUniversity of Ulm, Dept. of Optoelectronics, Albert-Einstein-Allee 45, D-89069 Ulm, Germany

^bAsahi Glass Co., LTD., 2-1-2, Marunouchi, Chiyoda-ku, Tokyo 100-8305, Japan

ABSTRACT

Vertical-cavity surface-emitting lasers (VCSELs) with emission wavelengths in the range from 850 nm to 950 nm are highly attractive light sources for low-cost, high-speed data transmission over several hundred meters of perfluorinated graded-index plastic-optical fibers (GI-POFs). Multi-Gigabit/s data transmission over common PMMA-based step-index POFs is generally limited to several meters predominantly due to dispersion. Here, we demonstrate 3 Gbit/s and 7 Gbit/s pseudo-random-bit-sequence non-return-to-zero data transmission over 80 m perfluorinated GI-POF made of CYTOP[®] using a single-mode butt-coupled selectively oxidized InGaAs VCSEL source emitting at 935 nm emission wavelength. For 3 Gbit/s data rate the received optical power for a bit error rate (BER) of 10^{-11} is -22.5 dBm for back-to-back (BTB). A power penalty of 1 dB is found for transmission over 100 m graded-index multimode glass fiber and 2 dB for 80 m GI-POF. For 7 Gbit/s the required optical power for a BER of 10^{-11} is -10.2 dBm for BTB with a power penalty of 0.5 dB for 80 m GI-POF transmission. Reduced power penalty observed at 7 Gbit/s is attributed to the restricted modulation bandwidth of the VCSEL used in the experiment.

Keywords: Vertical-cavity surface-emitting lasers (VCSEL), graded-index plastic-optical fibers (GI-POF), optical fiber communication, NRZ modulation, InGaAs

1. INTRODUCTION

VCSELs with emission wavelengths in the range of 850 nm or 950 nm are highly attractive light sources for low-cost, high-speed data transmission over several hundred meters of perfluorinated GI-POF¹. Outstanding electrical and optical properties of VCSELs include threshold currents of below $100 \mu A^2$, high wallplug efficiencies above 50 %³, and modulation bandwidths above 20 GHz⁴. On-wafer testing without the need for cleaving and simple but highly effective butt-coupling to fibers lead to potentially inexpensive transmitters for multi-gigabit/s local area networks, like Gigabit Ethernet⁵. Due to the high bandwidth-length-product of up to 10 GHz×km, comparatively low attenuation of less than 100 dB/km and large core diameter providing increased connector tolerances, the GI-POF will be one of the promising candidates for "the last one mile" transmission in fiber to the home efforts⁶.

2. FIBER CHARACTERISTICS

The two limiting factors in digital data transmission over optical fibers are attenuation and bandwidth of the used fiber. Due to limited optical input power in the fiber and the required output power into the photodiode, the attenuation restricts the possible length of a data link. The material absorption loss in fibers is mainly caused by stretching vibrations of the different atomic bonds in the material, as indicated in Figure 1.

Correspondence:

[†]F. Mederer: Telephone: +49-731-5026037, Fax: +49-731-5026049, Email: felix.mederer@e-technik.uni-ulm.de

[‡]M. Naritomi: Telephone: +81-3-3218-5622, Fax: +81-3-3287-0771, Email: masaki-naritomi@om.agc.co.jp

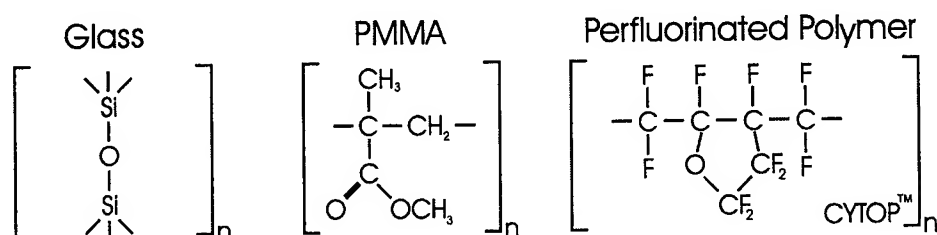


Figure 1. Chemical structure of silica glass, PMMA and perfluorinated polymer (CYTOP®)

Atomic bond	λ_0 (μm)
Si-O	9.0-10.0
C-C	7.6-10.0
C-H	3.3-3.6
C-O	7.9-10.0
C=O	5.3-6.5
C-F	7.9-10.0

Table 1. Wavelength of fundamental stretching vibrations of different fiber materials

Table 1 shows the wavelength λ_0 of the fundamental stretching vibration (FSVW) for different molecular bonds. Silica glass with Si-O bonds has a FSVW of 9.0-10.0 μm . This high λ_0 has the advantage to get low absorption for overtones in the range of 800 to 900 nm. PMMA consists of C-C, C-H, C-O, and C=O bonds. The FSVW of C-C and C-O bonds are in the range of silica, but the C-H and C=O bonds, with their low λ_0 , cause high absorption at wavelengths larger than 500 nm, as shown in Figure 2. In perfluorinated polymers, these two high absorbing bonds are replaced by C-F bonds having high λ_0 . Therefore, perfluorinated materials have the potential to decrease the attenuation of polymers getting close to the range of silica material.

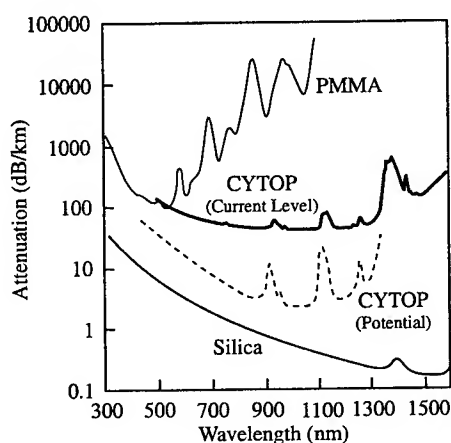


Figure 2. Attenuation characteristics of perfluorinated polymer (CYTOP®) compared with silica and PMMA.

Figure 2 compares the attenuation of different fiber materials. At a wavelength of 935 nm typical attenuations of glass-based fiber and PMMA-POF are about 1 dB/km and 10000 dB/km, respectively. The attenuation of the perfluorinated polymer is less than 90 dB/km. The used GI-POF has a 155 μm core diameter made of CYTOP®, a glass-state perfluorinated polymer¹, and a 95 μm thick cladding layer.

The second important characteristic is the maximum data transmission rate determined by the fiber bandwidth. For estimating the bandwidth, the GI-POF refractive index profile is approximated by the power-law profile

$$n(r) = \begin{cases} n_1 \left[1 - 2\Delta \left(\frac{r}{a}\right)^g\right]^{\frac{1}{2}} & \text{for } 0 \leq r \leq a \\ n_2 & \text{for } r > a \end{cases} \quad (1)$$

where n_1 and n_2 are the refractive indices on axis and in the cladding, respectively, a is the core radius, g characterizes the refractive index profile, and Δ is the relative index difference given by

$$\Delta = \frac{n_1^2 - n_2^2}{2n_1^2} \quad (2)$$

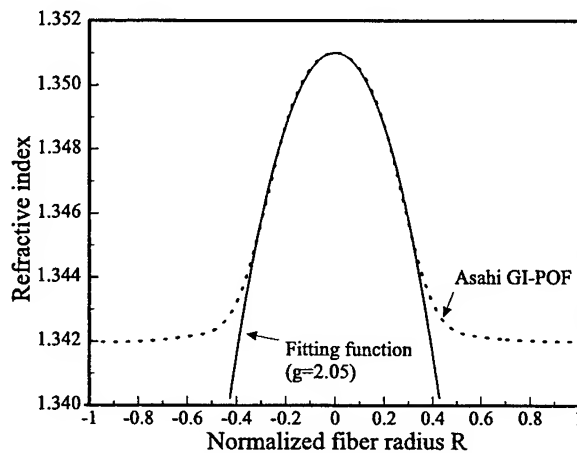


Figure 3. GI-POF refractive index profile and power-law profile fitting function.

Figure 3 shows the refractive index profile of the used GI-POF and the fitting function. The refractive index in the center axis is 1.351 and increases nearly with a power-law function to the refractive index of 1.342 of the cladding. The bandwidth per kilometer is estimated by Gloge's method⁷ as

$$B = \left(\frac{n_1}{c} \left[\frac{g-2}{g+2} \Delta + \frac{3g-2}{g+2} \frac{\Delta^2}{2} \right] \right)^{-1} \quad (3)$$

For the used GI-POF made by Asahi Glass the index exponent g is about 2.05 and the bandwidth-length-product is estimated to be 2.2 GHz×km. Underfilled mode-launching from butt-coupled single-mode VCSELs may lead to higher bandwidth-length-products. Simulations for optimized refractive index profiles indicate potential bandwidth-length-products of up to 10 GHz×km¹ allowing multi-gigabit/s data transmission over several hundred meters of fiber. In contrast, data transmission over PMMA-based step-index POF is limited to several meters predominantly by dispersion⁸.

3. VCSEL CHARACTERISTICS

Top-emitting selectively oxidized InGaAs based 935 nm emission wavelength VCSELs shown in Figure 4 are fabricated using solid source molecular beam epitaxy. The bottom AlAs-Al_{0.2}Ga_{0.8}As distributed Bragg reflector (DBR) consists of 40 n-type Silicon doped layer pairs. The active region contains three 8 nm thick In_{0.18}Ga_{0.82}As quantum-wells embedded in GaAs spacer layers to provide efficient carrier confinement. The top DBR consists of 17 Carbon doped Al_{0.9}Ga_{0.1}As-Al_{0.2}Ga_{0.8}As layer pairs. For current confinement a selectively oxidized 27 nm thick AlAs layer is inserted in the top mirror. Planarizing polyimide passivation is used to reduce bondpad capacitance. The laser is wire-bonded from a Ti/Au bondpad to an SMA socket to keep feeding lines as short as possible.

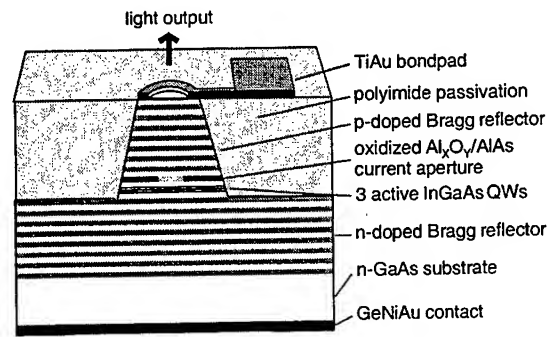


Figure 4. Cross-sectional view of a selectively oxidized polyimide passivated InGaAs VCSEL.

Output characteristics of a $4\text{ }\mu\text{m}$ diameter VCSEL are given in Figure 5. Threshold current and voltage is as low as 1.3 mA and 1.75 V, respectively. The maximum output power is 4.5 mW at a current of 10 mA. The differential resistance at an operating current of 5 mA is about $190\text{ }\Omega$.

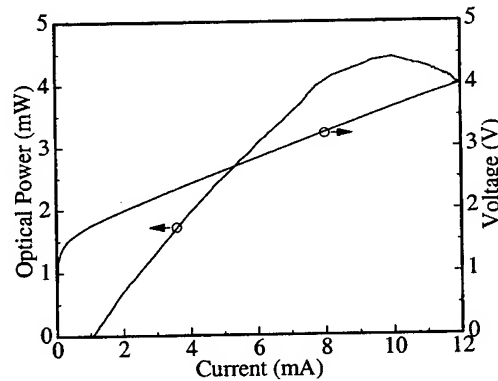


Figure 5. Output characteristics for a $4\text{ }\mu\text{m}$ diameter laterally oxidized InGaAs VCSEL.

The CW emission spectrum in Figure 6 for 5 mA driving current corresponding to 3 mW output power is single-mode centered at 934.2 nm wavelength. For 7 Gb/s modulation with $V_{pp}=1.3\text{ V}$ at 5 mA bias current the emission wavelength is shifted to 934.4 nm. Side-mode suppression slightly decreases but still remains better than 24 dB.

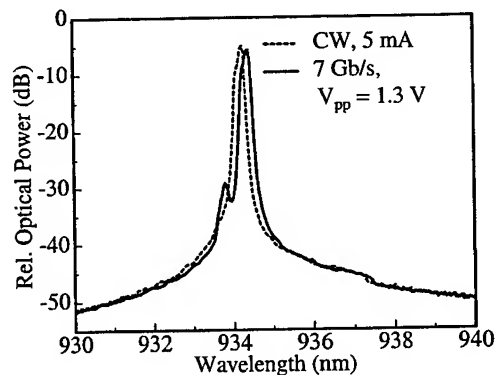


Figure 6. Emission spectra for CW operation and 7 Gb/s modulation at 5 mA driving current for a $4\text{ }\mu\text{m}$ diameter laterally oxidized InGaAs VCSEL.

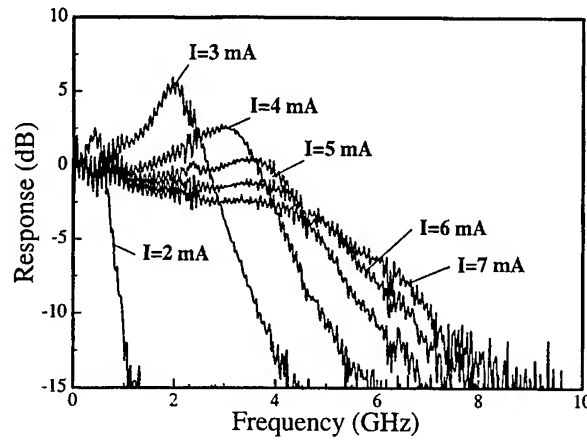


Figure 7. Small-signal frequency response of a 4 μm diameter laterally oxidized InGaAs VCSEL for various bias currents.

Figure 7 shows the small-signal frequency response characteristics of a 4 μm diameter laterally oxidized InGaAs VCSEL for various bias currents. The maximum 3dB bandwidth is limited to about 5 GHz due to the parasitic mesa and bondpad capacitance of about 1 pF.

4. DATA TRANSMISSION RESULTS

The setup for the transmission experiments is shown in Figure 8. The light is either launched in a butt-coupled 100 m long 50 μm diameter graded-index multimode glass fiber (MMF) or in a 80 m long GI-POF. For transmission experiments the laser is driven with a pattern generator at a voltage of $V_{pp}=1.3$ V and a bias current of 5 mA, combined in a bias-tee and fed to the VCSEL. After transmission over the fiber the signal is passed through a variable attenuator and detected either with a 50 μm diameter Germanium avalanche photodiode of 2 GHz bandwidth or with a $16 \times 16 \mu\text{m}^2$ InGaAs PIN photodiode of 15 GHz bandwidth using demagnifying imaging of the far end of the fiber. The amplified digital signal is monitored with an electrical sampling oscilloscope and analysed with a BER detector.

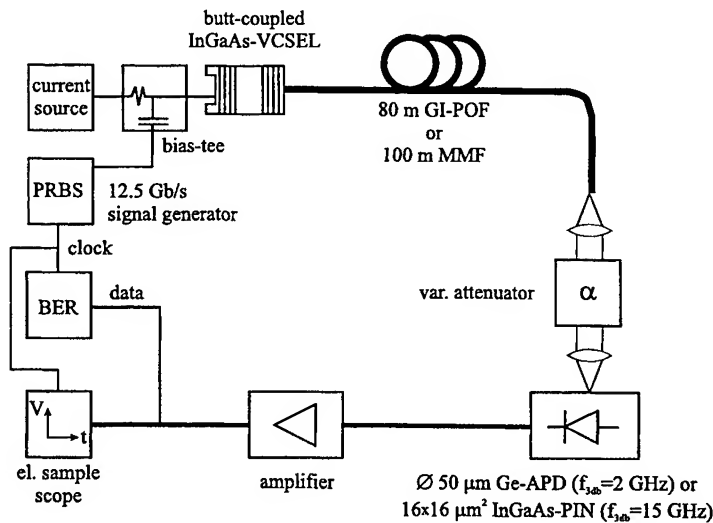


Figure 8. Setup for the transmission experiments.

It is worth to mention that in the case of the $16 \times 16 \mu\text{m}^2$ photodiode with the imaging optics applied long term modal noise was not fully suppressed since it was difficult to collect all the output light on the detector surface.

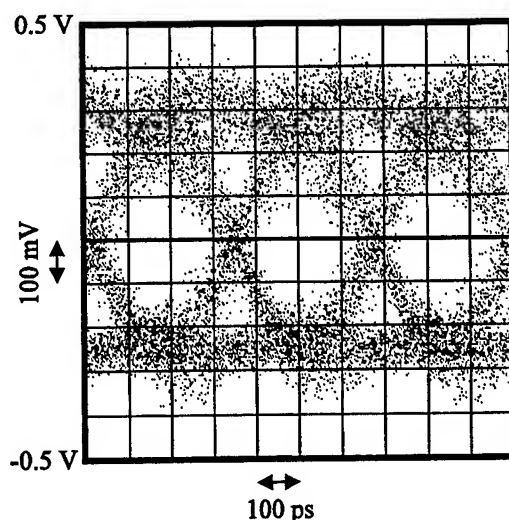


Figure 9. Eye diagram recorded for a 3 Gb/s PRBS, $2^{31} - 1$ word length signal with $V_{pp}=1.3$ V modulation at a bias-current of 5 mA after transmission over 80 m GI-POF.

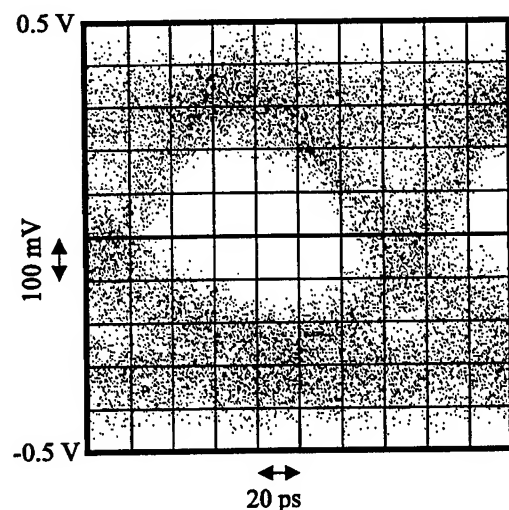


Figure 10. Eye diagram recorded for a 7 Gb/s PRBS, $2^7 - 1$ word length signal with $V_{pp}=1.3$ V modulation at a bias-current of 5 mA after transmission over 80 m GI-POF.

Figure 9 illustrates the eye diagram for 3 Gb/s pseudo-random bit sequence (PRBS) with $V_{pp}=1.3$ V modulation voltage and $2^{31} - 1$ word length and Figure 10 for 7 Gb/s PRBS with $2^7 - 1$ word length recorded after 80 m GI-POF transmission. The BER is 10^{-11} and the on-off-ratio 10 dB. In the case of 7 Gb/s we have used a PRBS with a word length of $2^7 - 1$ because it is common to perform data encoding in LANs using short run length codes like 8B/10B⁹. These sequences avoid low frequency spectral components which may cause trouble in commonly available broadband amplifiers having a comparatively small lower cut-off frequency. For 3 Gb/s in Fig. 9, the eye is symmetric and without significant relaxation oscillations. Similarly, the amplified eye at 7 Gb/s in Fig. 10 shows no significant effects of relaxation oscillations.

Figure 11 and Figure 12 show the results of the transmission experiments where the BER is plotted versus the received optical power for 3 Gb/s and 7 Gb/s data rates.

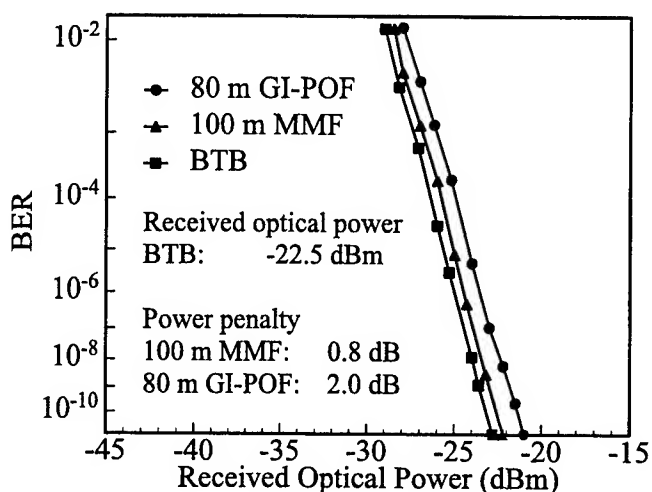


Figure 11. BER recorded for 3 Gb/s data transmission with PRBS of $2^{31} - 1$ word length.

For 3 Gb/s signals the received optical power for a BER of 10^{-11} is -22.5 dBm under back-to-back operation (BTB, open circles). A power penalty of 1 dB and 2 dB is found for transmission over 100 m MMF (open squares) and 80 m GI-POF (open triangles), respectively.

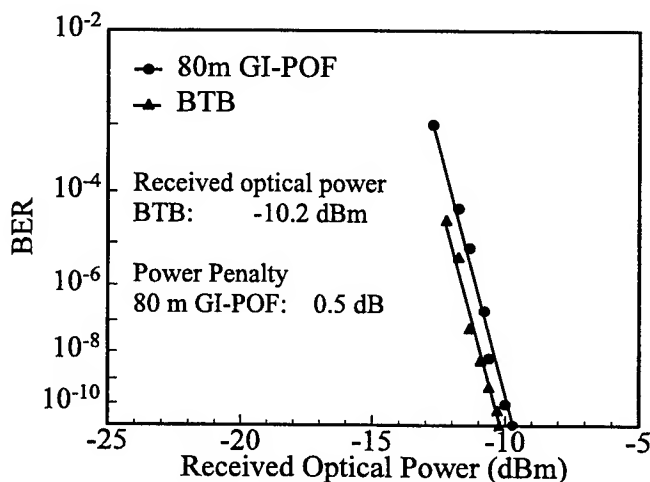


Figure 12. BER recorded for 7 Gb/s data transmission with PRBS of $2^7 - 1$ word length.

For 7 Gb/s signals the received optical power for a BER of 10^{-11} is -10.2 dBm BTB (filled circles) with a power penalty of 0.5 dB for 80 m GI-POF transmission (filled triangles). Reduced power penalty observed at 7 Gb/s is attributed to the restricted modulation bandwidth of about 5 GHz of the VCSEL used in the experiment.

5. CONCLUSION

We have successfully demonstrated data transmission using 935 nm InGaAs VCSEL and butt-coupled GI-POF. Data rates up to 7 Gb/s have been transmitted over 80 m of GI-POF. Transmission behavior is similar to graded-index MMF¹⁰. Easy butt-coupling between VCSEL and GI-POF with lateral alignment tolerances of 50 μm ¹¹ make such modules very attractive for low-cost local area network solutions, e.g. the Gigabit Ethernet.

ACKNOWLEDGMENTS

This work was supported by the German Ministry of Research and Technology (BMBF), the German Science Foundation (DFG), and the European Commission within the ESPRIT MEL-ARI OPTO program under contract No. 22641 (OIIC).

REFERENCES

1. T. Onishi, H. Murofushi, Y. Watanabe, Y. Takano, R. Yoshida, and M. Naritomi, "Recent progress of perfluorinated GI-POF," in *Proc. 7th International POF Conference 98*, pp. 39–42, (Berlin, Germany), 1998.
2. D. Deppe, D. Huffaker, T. Oh, H. Deng, and Q. Deng, "Low-threshold vertical-cavity surface-emitting lasers based on oxide-confined and high contrast distributed Bragg reflectors," *IEEE J. Sel. Topics Quantum Electron.* **3**, pp. 893–904, 1997.
3. R. Jäger, M. Grabherr, C. Jung, R. Michalzik, G. Reiner, B. Weigl, and K. Ebeling, "57 % wallplug efficiency oxide-confined 850 nm wavelength VCSELs," *Electron. Lett.* **33**, pp. 330–331, 1997.
4. K. Lear, V. Hietala, H. Hou, M. Ochiai, J. Banas, B. Hammons, J. Zolper, and S. Kilcoyne, "Small and large signal modulation of 850 nm oxide-confined vertical cavity surface emitting lasers," *OSA Trends in Optics and Photonics* **15**, pp. 69–74, 1997.
5. Gigabit Ethernet Alliance, "Gigabit Ethernet Whitepaper 1997," *Gigabit Ethernet Technology*, [Online], Available [HTTP://www.gigabit-ethernet.org](http://www.gigabit-ethernet.org), Directory: /technology/whitepapers/gige_97/, File: gigabit2.pdf, 1997.
6. Y. Koike, "GI POF in high-speed telecommunication," in *Proc. 6th International POF Conference 97*, (Kauai, Hawaii, USA), 1997.
7. D. Gloge and E. Marcetili, "Multi mode theory of graded-core fibers," *Bell Syst. Tech. J.* **52**, pp. 1563–1578, 1973.
8. P. Schnitzer, M. Grabherr, R. Jäger, R. King, R. Michalzik, D. Wiedenmann, F. Mederer, and K. Ebeling, "Vertical cavity surface emitting lasers for plastic optical fibre data links," in *Proc. 7th International POF Conference 98*, pp. 157–162, (Berlin, Germany), 1998.
9. L. Aronson, B. Lemoff, L. Buckmann, and D. Dolfi, "Low-Cost Multimode WDM for Local Area Networks Up to 10 Gb/s," *IEEE Photon. Technol. Lett.* **10**, pp. 1489–1491, 1998.
10. U. Fiedler, G. Reiner, P. Schnitzer, and K. Ebeling, "Top-surface emitting laser diodes for 10 Gb/s data transmission," *IEEE Photon. Technol. Lett.* **8**, pp. 746–748, 1996.
11. T. Kaneko, S. Kitamura, T. Ide, T. Kawase, T. Shimoda, Y. Watanabe, R. Yoshida, and Y. Takano, "VCSEL module for optical data links using perfluorinated GI POF," in *Proc. 7th International POF Conference 98*, pp. 27–32, (Berlin, Germany), 1998.

Monolithically Integrated Detector/Receiver in standard CMOS Operating at 250 Mbit/s for low-cost Plastic Optical Fiber data links

Maarten Kuijk, Daniël Coppée & Roger Vounckx

ETRO division IMEC, University of Brussels, Pleinlaan 2, 1050 Brussels Belgium.

Email: mkuijk@vub.ac.be

ABSTRACT

To solve the "lower frequency gain" that limits the speed of conventional CMOS detectors, we spatially modulate CMOS photo diode junctions. This gives a differential photodiode with a flat responsivity curve up to a -3dB bit rate of more than 500 Mbit/s. Detector and circuitry (for receiver, digitizing, decoding etc), can now be combined on a single -low cost- CMOS chip for datacom applications. Here we report on the first integration of a receiver (including decision circuitry) with a 300 μm diameter detector intended for use in plastic optical fiber (POF) links. The diameter of the detector allows to choose for large multimode POF cores (e.g. 250 μm) and low precision mechanical connectors. The receiver circuit is fully differential from the detector onwards, for improved power supply rejection. A differential feedback mechanism filters out the DC-level. A final symmetric OTA converts the differential signal to a single ended digital output. The total chip area including bonding pads is 440 μm x 600 μm . The received optical power to obtain a BER of 10^{-9} (635 nm wavelength with PRBS $2^{15}-1$) is -17.6 dBm (17.2 μW) at a bit rate of 155 Mbit/s and -12.2 dBm (60 μW) at 250 Mbit/s bit rate. The chip dissipates only 25.3 mW at a 3.3V power supply. The bit rate is receiver limited. A design in a smaller feature size CMOS technology will show even better bit-rate and/or sensitivity performance. In conclusion, it is now possible to make detector/receivers combinations in standard CMOS lowering the overall cost of a POF data link system.

Keywords: CMOS detector, optical receiver, integrated detector, Si-OEIC, differential receiver.

1. INTRODUCTION

For an increasing number of optoelectronic applications the use of sub-micron and visible wavelengths is becoming more important than the use of longer wavelengths ($> 1 \mu\text{m}$). For data storage, the use of shorter wavelength allows denser packing of information and consequently leads to a higher storage capacity per disk. For fiber communication, the low absorption window in plastic optical fibers (POF) for the red wavelength region encourages the use of visible light. Eye safety is an extra welcome feature. Another advantage is that light with these wavelengths absorbs relatively well in Silicon. This feeds the expectation that it becomes possible to integrate detector and receiver in CMOS technology, and even in a *standard* CMOS technology. We present a way to achieve relative good bit rates with relative good sensitivity for monolithic detector/receiver circuits in *standard* CMOS.

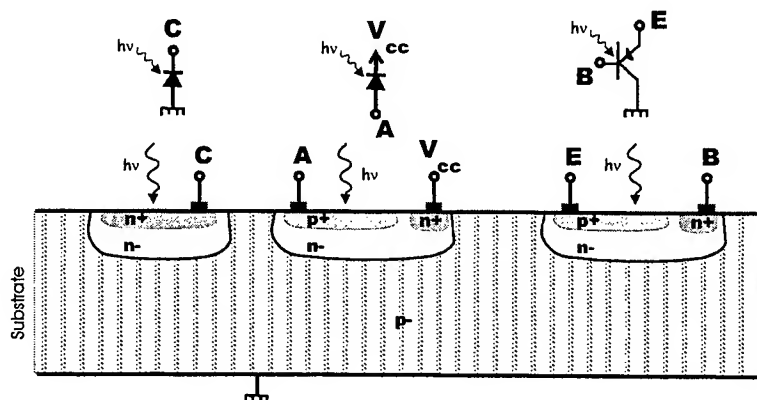


Figure 1: Three available schemes for light detection in a standard N-well CMOS process.

Therefore we spatially modulate the light and the detector [1,2]. The principle works well for wavelengths smaller than or equal to 860 nm. In this paper we report on the monolithic combination of such a detector with a receiver, whereby the detector is relatively large to accommodate serial communication systems with low precision connectors and large core plastic optical fibers (POF). These issues are important to converge to a *low cost* communication system for e.g. automotive and household applications. At the same time, other circuits that are normally used in a telecom receiver can be integrated as well, such as a clock recovery circuit, a serial to parallel conversion unit, a 10 bit to 8 bit decoder, error correction, etc.

In the following text we will discuss the separate schemes to make photo-diodes in CMOS, including their limitations, then we explain how the Spatially Modulated Light detector (SML-detector) increases bandwidth. Further we will show how to integrate this differential detector in CMOS and to get rid of mismatch problems. We conclude with the results of first measurements.

2. DETECTORS IN STANDARD CMOS

In an standard N-well CMOS process, there are several junctions available for the collection of photo-generated carriers. Figure 1 shows three available options.

The *first scheme* is to use an n-region in the p⁺ substrate. The N-well together with the available highly doped n⁺ diffusion gives a good cathode. The N-well serves to obtain a thicker absorption layer. Its low doping concentration gives a low detector capacitance. The n⁺ lowers the lateral resistance of the N-region, and generates a back surface field, reflecting minority carriers (i.e. holes) towards the junction. The main *problem* with this first solution is that carriers, generated by photons below the junction (deeper in the substrate), get collected at the junction many nanoseconds or even microseconds later. This slow response is due to the diffusive nature of the carriers in the neutral zone. The used wavelength (absorption coefficient) and the thickness of the N-well layer determine the percentage of diffusive carriers on the total of absorbed photo-generated carriers. Figure 2 shows the effect of these carriers in time and in frequency domain. When a light pulse impinges, the detector current increases quite similarly. However, when the light input remains at the same level, the detector current will not remain at its value but will increase in time. The complementary effect happens when the light input is turned off. This phenomenon is due to the build-up of a cloud of photo-generated carriers in the p⁺ substrate. In the frequency domain this effect can be seen as gain at lower frequency.

In typical telecom receivers one works with a threshold level, to distinguish between HIGH and LOW. This level is determined by averaging the detector signal. When lower frequency gain is present this digitizing principle fails.

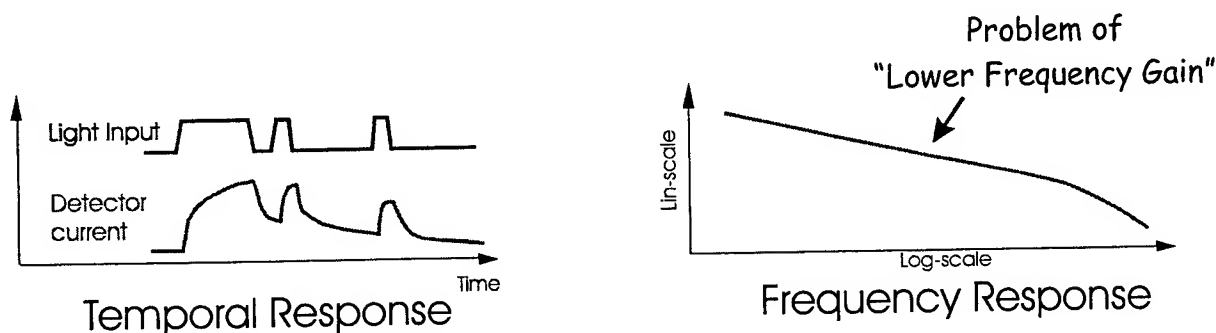


Figure 2: Effect of slowly diffusive substrate carriers in the time and frequency domain.

The *second scheme* in Fig. 1 uses the N-well connected to V_{cc} (or any fixed positive voltage) to screen off the diffusive substrate carriers. The active junction is between the p⁺ diffusion and the N-well. In this way a flat responsivity versus frequency is obtained. This gives however only a very limited responsivity of 0.01 A/W up to 0.04 A/W at higher voltages [3]. Moreover, the junction has at one side a high doping level, increasing the capacitance of this detector junction considerably.

The *third scheme* in Fig. 1 uses the available parasitic bipolar PNP transistor as a phototransistor. Again, lower frequency gain will cause trouble. Therefore this configuration is a good option for low frequency applications, including a CMOS camera. Another problem with this scheme is that in general this PNP transistor shows a poor high frequency performance.

In literature, several other ways to integrate high-speed photo-detectors in silicon have been presented. However they deviate considerably from the standard CMOS processing. To get rid of the effect of the substrate carriers, they use a buried highly doped layer [4], or an oxide layer[5]. In another case, a high voltage is used to generate a very large depletion layer in a lowly doped substrate [6].

3. SPATIALLY MODULATED LIGHT DETECTOR

Figure 3 shows the top-view and a cross-section of the Spatially Modulated Light detector (SML-detector). It can be fabricated in *any standard CMOS technology* (0.8 μm , 0.6 μm , 0.35 μm , 0.25 μm), lowering the cost of design iterations, speeding up time-to-market, and lowering the final fabrication cost. It is based on the diode junctions of the first scheme in Fig. 1.

A row of N-well fingers is alternatingly covered and non-covered with a light blocking material. In CMOS we can use metal 1 or metal 2 for this purpose.

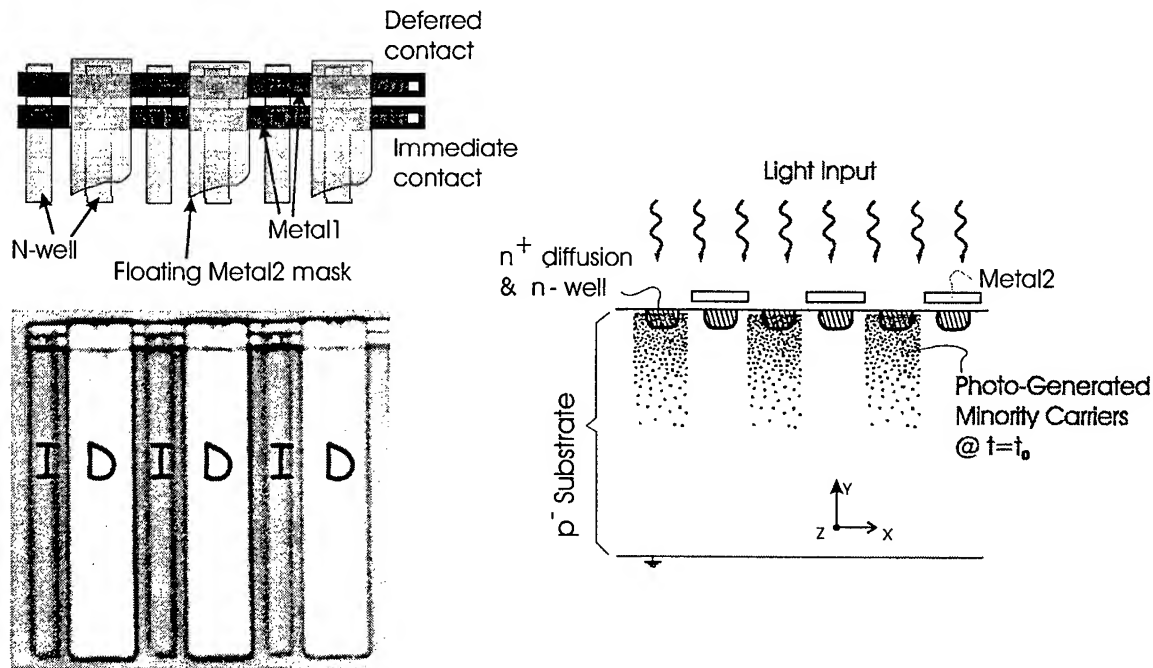


Figure 3: Top-view and cross-section of the Spatially Modulated Light detector.

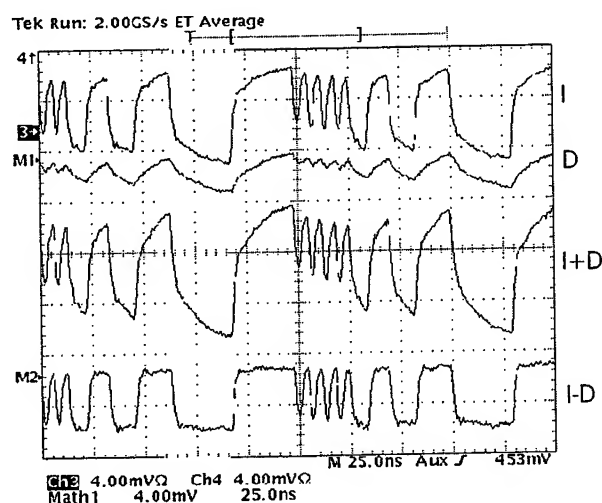
The uncovered fingers are grouped together forming the so-called *immediate* detector (I). The covered fingers form the *deferred* detector (D). In Figure 3 we show three Immediate fingers, and three Deferred fingers. The number and the length of the fingers can be adjusted to define the total area of the detector.

In this way, the incident light is *spatially modulated*, and the photo-generated carriers in the Silicon are similarly spatially modulated (see Fig. 3, at the right) at the moment of absorption. Electron-hole pairs, photo-generated in the depletion zone of the n-well p-substrate junction will instantaneously split due to the electric field and contribute to the Immediate detector current. Photo-generated carriers in the neutral zone of the N-well will diffuse quite fast (they have to bridge a small distance) to the junction and also contribute to the Immediate detector current. Carriers, photo-generated in the substrate, diffuse to the immediate detector fingers, to the deferred detector fingers, and outside the detector or towards the bottom of the substrate. Or even they may recombine (with a time constant of milliseconds). Carriers that are generated *close* to an

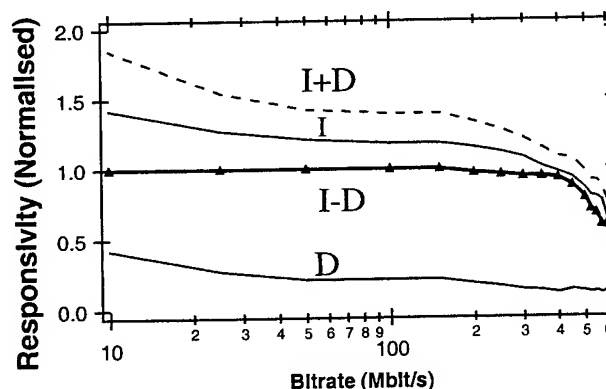
immediate finger will have a higher probability to reach this Immediate finger than to reach one of the neighboring deferred fingers. Carriers generated *deep* in the substrate will require a long time to reach the detector surface, and have more or less equal probability to reach an immediate finger or a deferred finger. In short, the deferred detector gives a temporal response that is in proportion to the useless cloud of slow diffusive carriers. The immediate detector response contains the fast response and this slow response. All that has to be done is to subtract the deferred detector response from the immediate detector response in order to isolate the fast response.

This is nicely confirmed by measurements on an SML detector with 8 micron finger pitch at 860 nm wavelength (Fig. 4). A digital sequence of light pulses was used to illuminate the SML detector. The left figure shows the immediate (I) response and the deferred (D) response. The Oscilloscope's sum and subtraction functions were used to generate the two other signals.

The deferred signal shows a slow trailing behavior, the immediate signal has on the contrary steep edges, followed by the same trailing behavior. The sum signal reflects what a homogenous CMOS detector would give (like the sketched curves in Fig.2). It is very difficult to recover the initial bit stream from this signal. The difference signal (I-D) is a useful signal, reflecting the initial (not shown) digital sequence of light pulses. The measurement shown on the right of Figure 4, is the frequency response for the same signals (I, D) and combination of signals. The difference response (I-D) is the useful curve. That response is flat with a -3 dB bit rate of about 500 Mbit/s, for the given parameters. For finer pitch technology, the fingers can be made smaller and put on a finer pitch resulting in an improved frequency response.



Temporal Response



Frequency Response

Figure 4: The time and frequency response of I, D, I+D and I-D.

As a consequence of the unknown thickness of dielectric layers in the CMOS above the Silicon surface (used as insulation between metal layers and a passivating top layer), there is a relatively large uncertainty on the precise responsivity. Depending on the wavelength and this thickness, the dielectric layer can operate as an antireflection coating, as well as a reflection coating. The measured responsivity is 0.1 A/W for 860 nm, when the light is impinging on as well the deferred as the immediate area's (when the light is focussed into the open slits -on immediate fingers only- the responsivity doubles to 0.2 A/W). The measured responsivity for 635 nm was 0.132 A/W, which is about 25 % quantum efficiency.

4. THE INTEGRATED RECEIVER

Since the useful signal is the Immediate minus the Deferred signal, we have to make a subtraction somewhere. This can easily be achieved at the start of the receiver by making a differential trans-impedance amplifier. The dual input signal can then be considered as the sum of a *common mode* signal and a *differential mode* signal. The differential mode signal is the useful part (the fast part). The common mode contains non-essential information, like the slow part of the detector response. A differential amplifier is thus quite useful, since it mainly amplifies the differential part of the signal.

The total receiver is shown in Figure 5. OTA1 is configured as the differential trans-impedance amplifier, which determines the noise and attainable bit rate. The 2k resistors were made by means of two N-wells. The calculated capacitance of this large $300 \times 300 \mu\text{m}^2$ detector is between 2.5 pF and 3 pF.

The subsequent OTA2, OTA3 and OTA4 are internally limited to an amplification factor of 5, extending the bandwidth of the separate amplifiers to 125 MHz. We chose for a single ended digital output, and placed the conversion from differential to single ended signal as far in the amplifying chain as possible. OTA5 does this conversion. This OTA was designed to give an output voltage of half the power supply ($V_{cc}/2 = 1.65\text{V}$) at zero volt differential input. In this way it matches the switching point of the following inverter. The final inverter is intended to give a boost such that the chip can immediately deliver enough current to drive a 10 pF load capacitance with digital values (rail to rail).

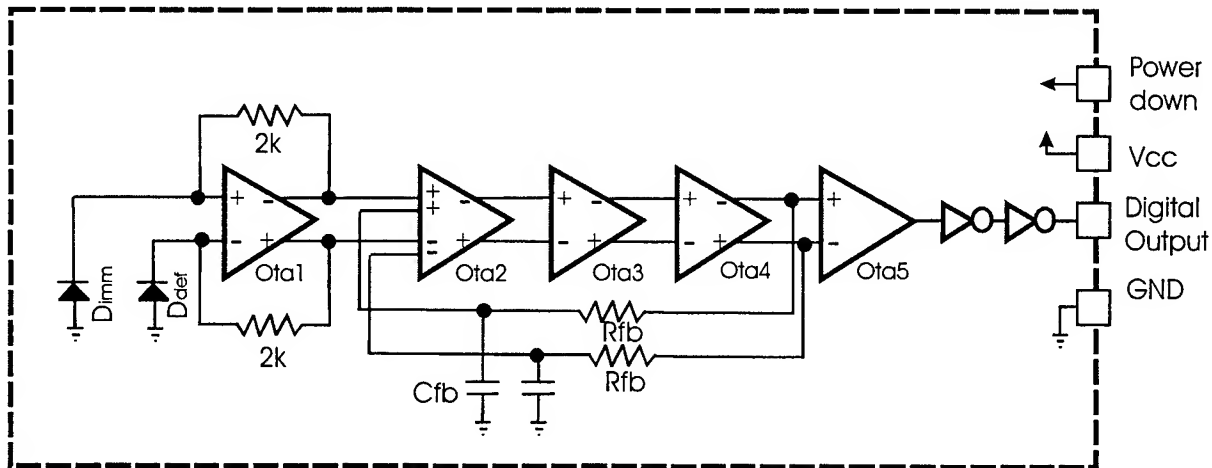


Figure 5: The hart of the receiver.

In Figure 5, a differential *feedback* is organized by means of resistors R_{fb} and capacitors C_{fb} . They form a negative feed back path between the differential output voltage of OTA4 to a second differential input of OTA2. In this way, low frequent components in the signal passing the amplifying chain are filtered out.

The *first* reason for this filtering is to attenuate the effect of offset mismatch in pairs of transistors. If a mismatch error signal is for example larger then the useful signal and if it gets amplified by the same factor, the output will always remain in the same state, determined by the sign of the mismatch. Especially mismatches in transistor pairs in the beginning of the amplification chain are more destructive since the effect of these mismatches is amplified the most. By attenuating the lower frequency component, the mismatch effect (that can be regarded as DC signal) will effectively be filtered out. The *second* use of this filtering action is to get a positive differential voltage for a HIGH input, and a negative differential voltage for a LOW input. By filtering out the DC component, this goal is reached when assuming that the transmitted data is DC-balanced.

The dominant pole in the feedback loop had to be designed at a frequency low enough to fulfill stability requirements. Therefor the Capacitors C_{fb} and Resistors R_{fb} of the feedback loop had to be made very large. The feedback resistors R_{fb} were therefor made with very long PMOS transistors with the gate connected to GND, operating in their triode region. The capacitors C_{fb} were made with verly large NMOS and PMOS transistors. The NMOS transistors were connected with

source and drain to GND, and the Gate was used as the connection terminal. The PMOS transistors were similarly connected to Vcc, and the gate used as terminal.

Figure 6 shows the simulated output voltages in response to a 3 μ A of photo-diode input current. The output of OTA1 doesn't show the filtering effect below 100 kHz since it isn't part of the feedback loop. Every stage amplifies with a factor of 5. The -3dB cut-off frequency of OTA4 is at about 100 MHz, enough to support 155 Mbit/s, and somewhat low to support the 250 Mbit/s data rate. With more input light the maximum bit rate is rather determined by the output of OTA3, that has a 130 MHz -3dB cut-off. The larger signal, associated to more light, gives that OTA4 is not able to amplify, and consequently the maximum bit rate is not any longer determined by its *small signal* -3dB point. In other words, the output of OTA3 is fast enough, and OTA4 only passes the digital signal through.

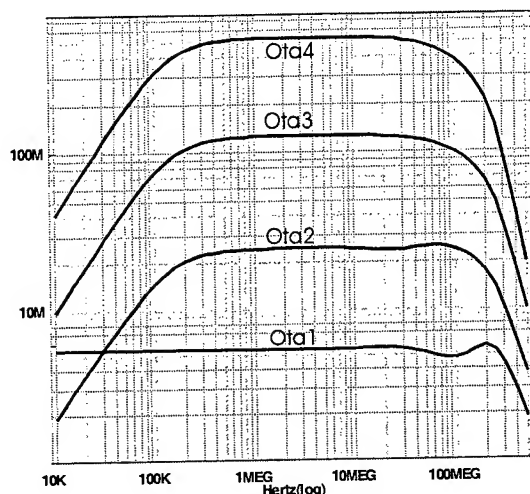


Figure 6: Voltage at the outputs of the amplification stages, in response to a 3 μ A detector input current.

The circuit shown in Fig. 5 is fully symmetric from the detector onwards, up to OTA5. This is very important for the power supply rejection. Any spike or ripple on the power supply, generated by the circuit itself or entering from outside, will have its consequences on the voltage of all electrical nodes in the circuit. When operating single ended, it is quite likely that these error voltages get amplified themselves. Again, the more the error voltages get injected at the beginning of the amplifying chain, the more destructive they will be. By operating differential, symmetric nodes get the same error voltages. For this to be true these symmetric nodes need to have same node impedance. If error voltages on symmetric nodes have same amplitude and same phase, they do not contribute to the effective signal that is defined as the difference voltage between those nodes. For very good power supply rejection, one has to work -if possible- from the detector onwards with differential signaling. The fact that the SML detector has two connection nodes with equal impedance is an important advantage of the SML detector not present with most other integrated detectors.

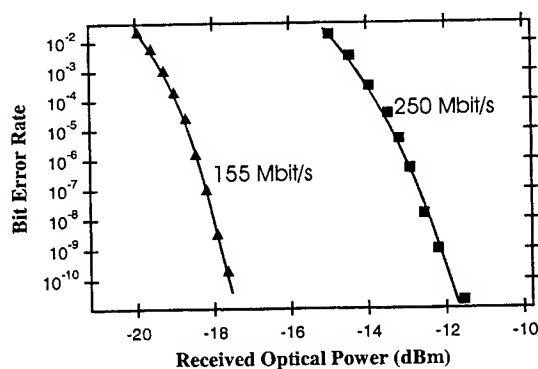


Figure 7: Measured Bit Error Rate plots at two different bit rates, for 635 nm wavelength.

A laser with wavelength of 635 nm was focussed on the detector. The receiver was powered with 3.3V. A Bit Error Rate (BER) plot was measured, given by Fig. 7. The received optical power to obtain a BER of 10^{-9} (with PRBS $2^{15}-1$) was found to be -17.6 dBm ($17.2 \mu\text{W}$) at a bit rate of 155 Mbit/s and -12.2 dBm ($60 \mu\text{W}$) at 250 Mbit/s bit rate. The current consumption (at 250 Mbit/s bit rate but with disconnected output) was 7.65 mA. Power dissipation of the receiver circuit is thus 25.3 mW.

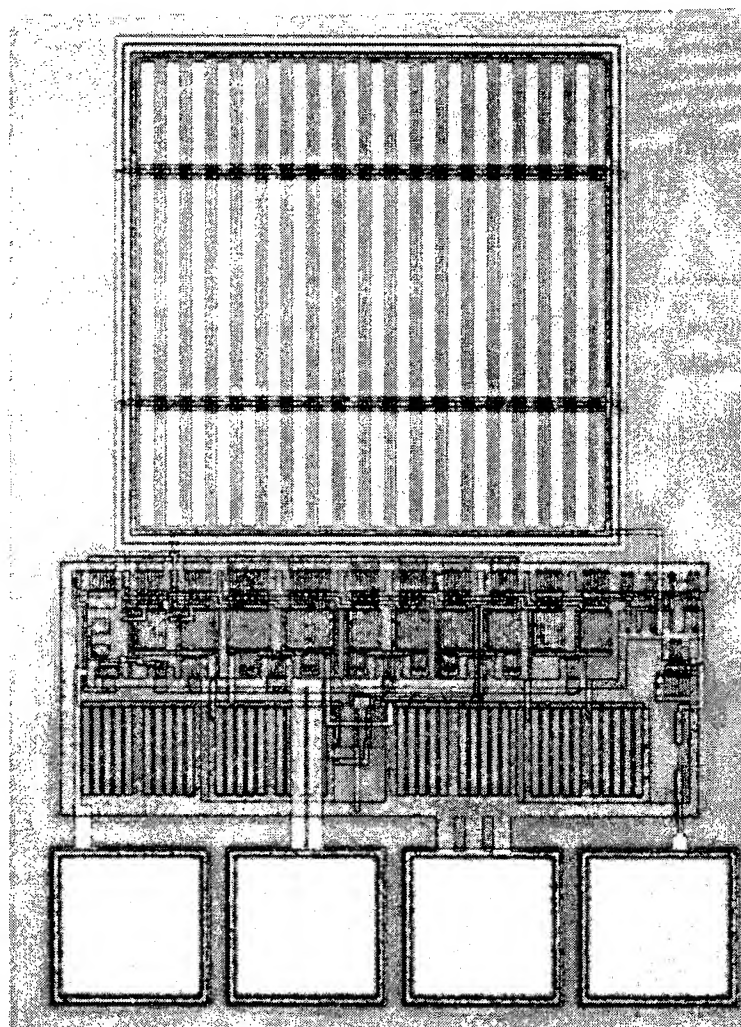


Figure 8: Photograph of the detector/receiver. At the top the $300 \times 300 \mu\text{m}^2$ detector, below the receiver circuit, and at the bottom the four bond pads. The total chip area including bonding pads is $440 \mu\text{m} \times 600 \mu\text{m}$.

For the given 0.6 micron technology, the achieved performance can still be improved further. First of all, the input transistors of OTA1 could have been designed with a much larger W/L, increasing their g_m and improving consequently signal to noise ratio. The optimum (for maximum sensitivity) is to increase W/L until the capacitance of the input transistors is the same as the capacitance of the detector. Moreover, the amplifier chain can be designed to amplify smaller light input signals.

For a smaller feature CMOS technology, e.g. 0.25 micron, both detector and receiver performance can be improved considerably. The use of finer detector fingers are expected to improve detector bit rate to beyond the Gbit/s. In 0.25-micron technology a gigabit/s receiver can also be designed without too much difficulty.

5. CONCLUSIONS

In conclusion, it is now possible to make detector/receivers combinations in *standard* CMOS operating at respectable bit rates and hence lowering the overall cost of a POF data link system. This was demonstrated by integrating the Spatially Modulated Light detector with a differential receiver system in a 0.6 micron CMOS technology.

6. ACKNOWLEDGEMENTS

The authors thank for partial funding the following institutions: EC: ESPRIT IV-MELARI-OIIC, FWOV, DWTC: IUAP IV/13 and AWI: GOA 20325.

7. REFERENCES

1. M. Kuijk, D. Coppée, and R. Vounckx: "Spatially Modulated Light Detector in CMOS with Sense-Amplifier Receiver Operating at 180 Mb/s for Optical Data Link Applications and Parallel Optical Interconnects Between Chips", IEEE J. of JSTQE Vol. 4, p1040-1045, 1998.
2. D. Coppée, W. Pan, J. Stiens R. Vounckx and M. Kuijk: "Experimental study of the Spatially Modulated Light Detector", Solid State Electronics, Vol. 43/3, p. 609-613, 1999.
3. T. K. Woodward, and A. V. Krishnamoorthy: "1 Gbit/s CMOS photoreceiver with integrated detector operating at 850 nm", Electronics Letters, Vol. 34, p. 1252, 1998.
4. T. Takimoto, N. Fukunaga, M. Kubo and N. Okabayashi: "High Speed Si-OEIC for Optical Pickup", IEEE transactions on Consumer Electronics, Vol. 44, p. 137, 1998.
5. M. Ghiono, F. Zappa, V.P. Kesan and J. Warnock, "A VLSI-compatible High Speed Silicon Photodetector for Optical Data Link Applications", IEEE trans. on electron devices, Vol. 43, p. 1054, 1996.
6. C. L. Schow, J. D. Schaub, R. Li, J. Qi and J. C. Campbell: "A 1-Gb/s Monolithically Integrated Silicon NMOS Optical Receiver", IEEE J. of Selected Topics in Quantum Electronics, Vol. 4, p. 1035, 1999.

SESSION 7

Fiber Lasers and Amplifiers

Passive mode locking in erbium-ytterbium fiber lasers

Serey Thai^a and Michael Hayduk^b

U.S. Air Force Research Lab, Sensors Directorate, 25 Electronic Pkwy, Rome, New York 13441

^aTel. (315) 330-3724, Fax (315) 330-7901, Email: thais@rl.af.mil

^bTel. (315) 330-7753, Fax (315) 330-7901, Email: hayduk@rl.af.mil

ABSTRACT

A novel mode-locked erbium-ytterbium fiber laser operating at 1550 nm using multiple quantum well (MQW) saturable absorbers was developed. The laser was constructed in a Fabry-Perot configuration using a fiber Bragg grating as a front reflector and a fiber Bragg grating output as a back reflector of the laser cavity. The passive mode-locking element placed inside the laser cavity is a 75 period InGaAs/InAlAs MQW saturable absorber grown lattice matched on an InP substrate. The output of the laser was taken through the other available port of a wavelength-division demultiplexer. The laser produced mode-locked output pulse trains at 16.67-MHz repetition rate and 10 mW of average output power.

Keywords: fiber laser, passive mode locking, multiple quantum well, saturable absorber, erbium-ytterbium.

INTRODUCTION

An extensive research effort aimed at the refinement of rare-earth-doped and co-doped fiber has led to the development of high speed and compact sources of ultrashort pulses. Erbium-doped and erbium-ytterbium co-doped fiber can be used in optical amplifier and laser applications. The significance of these devices is the operating wavelength in the 1.55- μm region, where silica fiber has the lowest attenuation window. One of the advantages of the erbium-ytterbium co-doped fiber is an energy transfer from ytterbium ions to erbium ions in a silica fiber. The ytterbium ions exhibit strong absorption over a wavelength range extending from 800-1100 nm, in which the energy transfer excites the erbium ions.¹ The ytterbium ions absorb the pump light, and the absorbed energy is transferred to the erbium ions inducing a population inversion between the $^4I_{3/2}$ and $^4I_{15/2}$ states, that is responsible for laser action around 1.55 μm as a three-level laser at room temperature.^{2,3,5} The presence of ytterbium ions increases the pump absorption compared to erbium alone, which in turn, enables construction of a short Fabry-Perot fiber laser with low thresholds and high output powers.⁴ The lasing can occur only if the gain available from the bleached section exceeds the loss of the remaining length of the fiber.⁵ Hence, in this co-doped system a strong pump power can yield a high output power. Furthermore, erbium-ytterbium is a stable system with respect to temperature that will not lead to a change in performance as does an erbium laser.⁵ Therefore, passively mode-

locked erbium-ytterbium co-doped fiber lasers can produce stable, self-starting high repetition rate, high power, picosecond and subpicosecond pulses in the 1.55- μm region.

Applications of ultrashort pulsed fiber lasers include high-speed optical networks, optical communications, and photonic analog to digital converters. Note that fiber based lasers and fiber amplifier technologies are inherently compatible. Hence, using both of these systems will significantly compensate for the distribution and splitting losses encountered in real applications.⁶ Furthermore, fiber based systems can be designed to achieve soliton pulse generation and shaping, and minimize dispersion induced limits.⁶ Passive mode locking provides an effective and practical alternative approach to active mode locking.⁷ There are a variety of cavity configurations of passively mode-locked fiber lasers ranging from ring lasers to a Fabry-Perot configuration using a saturable absorber as a back reflector of the cavity. This paper introduces a novel cavity configuration of an erbium-ytterbium co-doped fiber laser using a multiple quantum well saturable absorber based on InGaAs/InAlAs structure as a passive mode locker.

PASSIVELY MODE-LOCKED FIBER LASER SYSTEM

A Fabry-Perot erbium-ytterbium co-doped fiber laser passively mode locked by the MQW saturable absorber, as shown in Fig. 1, is a novel configuration using Bragg gratings as front and back reflectors of the laser cavity. A Neodymium:Yttrium Lithium Fluoride (Nd: YLF) CW laser operating at 1047-nm is used as a pump source, and is protected by an OFR fiber-optic isolator (ISO). The isolation at the peak wavelength is greater than 36 dB. The isolator is to ensure no beam feedback into the pump source. The cavity is defined by two fiber Bragg gratings as a front and back reflector of a lasing wavelength. A 1555-nm center wavelength fiber Bragg grating (FBG) with bandwidth of 1.61 nm and 54.4-dB reflectivity is used as a front reflector. Note that the FBGs are completely transparent to the pump beam. A laser gain medium is placed after the front reflector. Approximately 5 m of erbium-ytterbium (Er/Yb) co-doped fiber is used as the gain medium. The geometry of the co-doped fiber is very much similar to a standard single mode fiber. An output

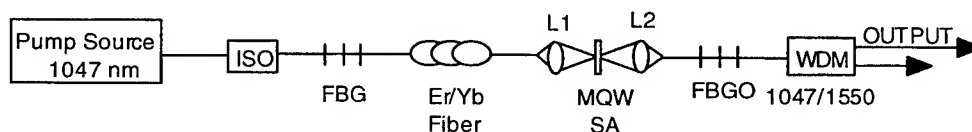


Fig. 1 Schematic diagram of a passively mode-locked Er/Yb codoped fiber laser system.

beam of the co-doped fiber is focused by lens L1, where a saturable absorber element is placed at the focal plane. This passive mode-locking element is a 75 period InGaAs/InAlAs MQW saturable absorber grown lattice matched on an InP substrate. Lens L2 is positioned at a focal length away from the focal point to focus the signal back into fiber Bragg grating output (FBGO). Lenses L1 and L2 are composed of two microscope objective lenses in back-to-back configuration. This

arrangement induces collimating and focusing functions. The FBGO is utilized as a 1.55- μm back reflector with 80% reflectance. This reflector is also transparent to the pump beam. However, a wavelength division demultiplexer (WDM) demultiplexes the pump beam and the lasing beam. The laser output is taken through 1550-nm port of the WDM and the 1047-nm port can be fed back into the cavity. The saturable absorber mostly absorbs the pump beam because the absorption is much greater at the pump wavelength than the lasing wavelength. This wavelength-dependent absorption will be discussed in detail in the following section.

EXPERIMENTAL RESULTS AND DISCUSSION

Discussions will first focus on experimental data of absorbance spectrum of the MQW passive saturable absorber, and the following section will discuss experimental results of the pulse spectrum, the output power characteristics as a function of pump power, Q-switched mode-locked pulses, and CW mode-locked pulses using the absorber. The saturable absorber is a mechanism to build up mode-locked pulses from a very weak initial noise or spontaneous-emission distribution composed of many axial modes with random phases and amplitudes. A continued pumping continues to increase the initial noise distribution until noise spikes within cavity have enough gain to saturate the absorber. Eventually, gain saturation is reached, and a stable pulse is produced by the laser. In this laser, the pulse train is transmitted through the FBGO rear reflector. A uniform train of pulses is created corresponding to one pulse per cavity round trip. These pulses are mode locked or all-in phase.

ABSORBANCE SPECTRUM OF MQW SATURABLE ABSORBER

The absorption plot, as shown in Fig. 2, is the absorbance spectrum of the MQW saturable absorber grown by molecular beam epitaxy (MBE). The structure consists of 75 periods alternating layers of 100 Å $\text{In}_{0.53}\text{Ga}_{0.47}\text{As}$ quantum wells and 100 Å $\text{In}_{0.52}\text{Al}_{0.48}\text{As}$ barriers grown lattice matched on top of a semi-insulating InP substrate.

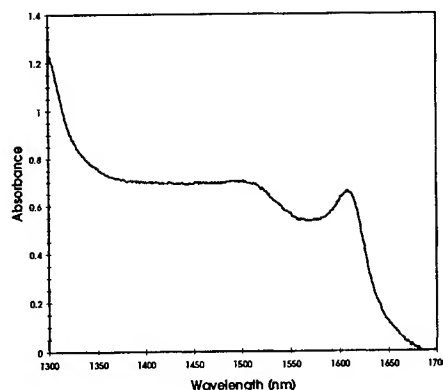


Fig. 2 Absorbance spectrum of a 75 period InGaAs/InAlAs MQW saturable absorber.

The absorbance (αd) of the MQW saturable absorber is governed by Beer's law ($\alpha d = -\ln(I/I_0)$), where α is the absorption coefficient, d is the total thickness of the sample, I is the intensity transmitted through the sample, and I_0 is the intensity of the source. Accordingly, the absorption coefficient is determined by dividing the absorbance by the total thickness. For instance, the absorption coefficient at 1.55- μm wavelength is approximately 0.367Np/ μm since the total thickness of the MQW saturable absorber is 1.5 μm . Furthermore, the graph exhibits light-hole excitonic features at 1525 nm and heavy-hole excitonic features at 1610 nm. The observation of the excitons even at room temperature indicates a well grown sample.

LASER OUTPUT CHARACTERISTICS

The output spectrum, as shown in Fig. 3, indicates the lasing wavelength at 1555.97 nm, and it was produced by a 230-mW pump power. The full-width at half-maximum (FWHM) is approximately 0.229 nm.

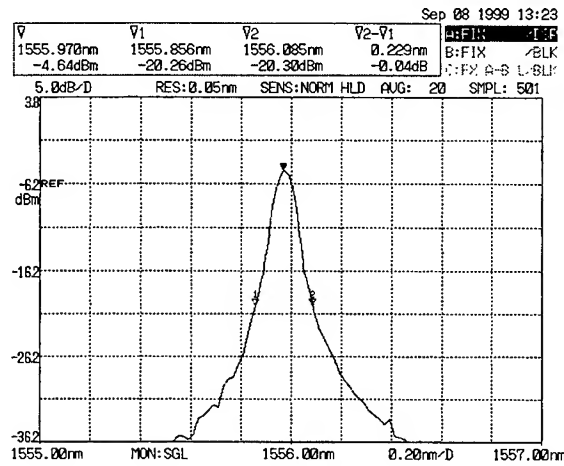


Fig. 3 Optical spectrum of the mode-locked pulses.

Information given in the figure can be utilized to obtain the corresponding frequency width. The frequency width can be determined by a standard differential relation as follows:

$$|\Delta f| = \frac{\Delta \lambda c}{n \lambda^2} \quad (1)$$

where n is the index of the fiber. The pulse shape for many types of mode locked lasers can be represented by the Gaussian function. Thus, the Gaussian time-bandwidth product is given by $\Delta t \Delta f = 0.4413$.⁸ The product of the temporal and frequency bandwidths was obtained from a Fourier Transform relationship between time and frequency amplitude profiles. The relation indicates that a very narrow time interval Δt requires a broad spectral emission bandwidth $\Delta \lambda$. Hence, the expression of a FWHM pulse width can be written

$$\Delta t = \frac{0.4413n\lambda^2}{\Delta\lambda c} \quad (2)$$

Assuming the pulse profile in the frequency domain is analogous to the transform of the pulse in the time domain, then the pulse is transform limited and the intensity format becomes a Gaussian shape. The assumption implies a pulse duration of about 23.33 ps.

The power plot, as shown in Fig. 4, demonstrates laser's output power at 1555 nm as a function of pump power. The output power increases proportionally with the pump power until saturation is approached at approximately 10 mW. The pump power operating at was limited to approximately 700 mW.

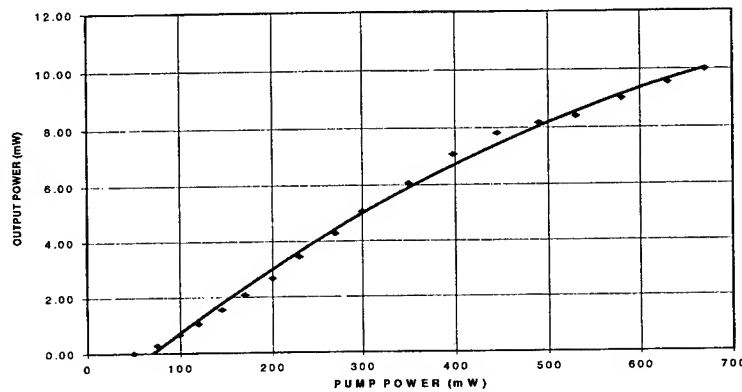


Fig. 4 Output power's behavior as a function of pump power.

Placing the saturable absorber near the focus generated the passive Q-switching mode-locked pulse train as shown in Fig. 5. Positioning the absorber in this manner allows the laser pumping process to build up lasing signal by effectively blocking the rear reflector over some period of time. The lasing gain continues to increase until it exceeds the absorber's threshold, then laser oscillation begins to take place inside the cavity. This initial build-up creates an intense burst of laser oscillation, which translates to higher output pulses. Note that there is no direct control over a repetition period. It strongly depends on the build-up and emission rate of the lasing gain by the saturable absorber. Hence, the absorber's characteristics define the Q-switching repetition rate. The experimental repetition period of the lasing Q-switched pulse train is approximately 14 μ s. Since repetition rate is inversely proportional to repetition period, then the Q-switching repetition rate is about 71 KHz.

A periodic repetition rate of a standing-wave cavity is governed by the following equation:

$$T = \frac{2nL}{c} \quad (3)$$

where L is the cavity length. Since the length in the experimental setup is about 6.5-m long, the repetition period becomes 65 ns which is much shorter than the Q-switched repetition period. The Q-switched pulse width at FWHM is approximately 600 ns. Thus, each Q-switched pulse should contain many CW mode-locked pulses.

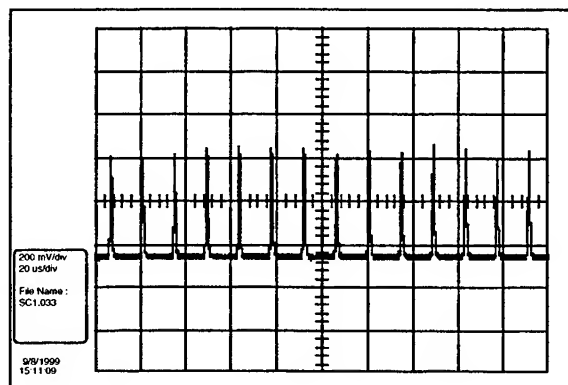


Fig. 5 Passive Q-switching pulse train with a repetition period of 14 μ s.

Figure 6 illustrates a periodic signal pattern inside one of the Q-switched pulses. The Q-switched pulse contains many oscillation spikes with all in phase, and amplitudes followed the Q-switched pulse envelope. There are eleven spikes at the FWHM pulse width. This Q-switched mode-locking is created by the MQW saturable absorber when the mode-locked pulses are also circulating within the cavity.⁷

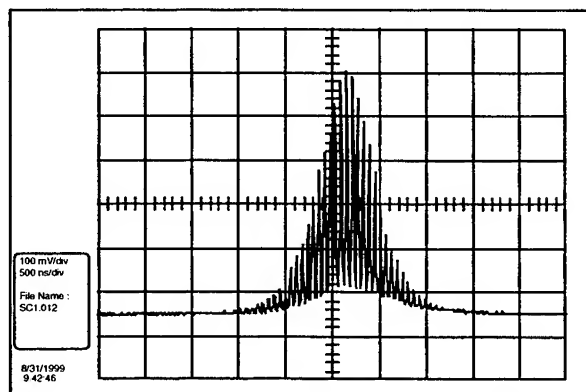


Fig. 6 Periodic signal pattern inside a passive laser Q-switching pulse.

The periodic pulse train of the CW mode-locked laser, as shown in Fig. 7, was generated by positioning the saturable absorber at the focus of the lens. Placing the absorber at the focal plane allows lasing signal distribution to circulate inside the laser cavity without experiencing an initial build-up delay as in the laser Q-switching case. Hence, mode-locked pulses do not have as high peak power pulses as in the Q-switched laser. According to the experimental results, peak power of

passive mode-locked pulses is about twenty-two times lower than for the Q-switched peak power. However, the repetition rate of a mode-locked laser is a controllable parameter, as shown in Equ. (3), since it is directly proportional to the cavity length. The repetition period of the periodic pulse train shown in the figure is approximately 60 ns which is close to the calculated value. The minor deviation between the two values is mainly due to the general assumption of the refractive index value for the fiber. Thus, the repetition rate of the mode-locked laser is 16.67 MHz. This rate can be increased further by simply shortening the cavity length. However, the length of the laser gain medium should be long enough to optimize population inversion efficiency by allowing a significant fraction of the pump power to be absorbed, but short enough to minimize the reabsorption process. For instance, an unbleached portion at the output end of the long fiber length reabsorbs a short lasing wavelength region, resulting a long lasing wavelength.

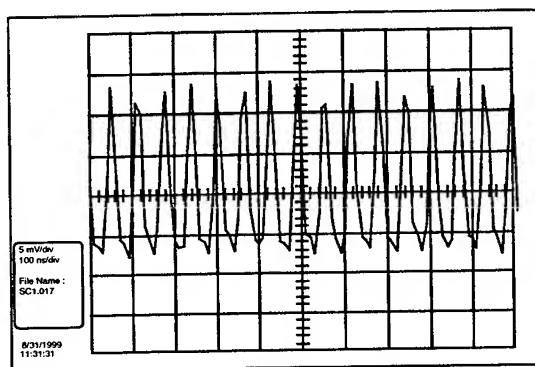


Fig. 7 Periodic pulse train of the passive mode-locked laser.

CONCLUDING REMARKS

A passive mode-locked laser was constructed in a Fabry-Perot configuration using fiber Bragg gratings for front and rear reflectors with a MQW intra-cavity saturable absorber. The mode-locked laser output is centered at 1555.97 nm with a spectral width at FWHM 0.229 nm. The laser can either produce Q-switched mode-locked pulse trains or CW mode-locked pulse trains by simply changing the location of the saturable absorber with respect to the focal plane. The Q-switched pulse train operates at a 71-KHz repetition rate with a 600 ns pulse width at FWHM when the position of the absorber is near the focus. Peak power of the Q-switched pulses is about twenty-two times higher than for the CW mode-locking which occurs when the absorber is placed exactly at the focal plane. The CW mode-locked pulse trains have a 16.67-MHz repetition rate with 10-mW average output power.

ACKNOWLEDGMENTS

The authors wish to acknowledge Reinhard K. Erdmann and Michael Parker of the Air Force Research Laboratory, Sensors Directorate, Rome Research Site for numerous discussions concerning mode-locked fiber lasers.

REFERENCES

1. J. D. Minelly, W. L. Barnes, R. I. Laming, P. R. Morkel, J. E. Townsend, S. G. Grubb, and D. N. Payne, "Diode-array pumping of $\text{Er}^{3+}/\text{Yb}^{3+}$ co-doped filter lasers and amplifiers," IEEE Photonics Tech. Letts., Vol. 5, No. 3, pp. 301-303, March 1993.
2. G. D. Geronimo, S. Taccheo, and P. Laporta, "Optoelectronic feedback control for intensity noise suppression in a codoped erbium-ytterbium glass laser," Electronics Letters, Vol. 3315, pp. 1336-1337, 17 July 1997.
3. E. Snitzer and R. Woodcock, " Yb^{3+} - Er^{3+} Glass Laser," App. Phys. Letts. Vol. 6, No. 3, pp. 45-46, 1 Feb. 1965.
4. J. T. Kringlebotn, P. R. Morkel, L. Reekie, J. L. Archambault, and D. N. Payne, "Efficient diode-pumped single-frequency Erbium:Ytterbium fiber laser," IEEE Photonics Tech. Letts, Vol. 5, No. 10, pp. 1162-1164, Oct. 1993.
5. W. L. Barnes, S. B. Poole, J. E. Townsend, L. Reekie, D. J. Taylor, and D. N. Payne, " Er^{3+} - Yb^{3+} and Er^{3+} Doped Fiber Lasers," J. Lightwave Technology, Vol. 7, No. 10, pp. 1461-1465, 10 October 1989.
6. K. Teegarden, Mode locked fiber lasers and their applications, Final Tech. Report, AFRL-SN-RS-TR-1998-97, June 1998.
7. A. E. Siegman, LASERS, University Science Books, Mill Valley, CA, 1986.
8. R. Erdmann, Applications of optical gain media, Final Tech. Report, RL-TR-96-197, March 1997.

Spectroscopy of Nd^{3+} , Tm^{3+} and Er^{3+} ions in tellurite glasses and fibres for broadband optical fibre amplifiers in the 1350-nm to 1600-nm range

M. Naftaly, S. Shen, A. Jha

Department of Materials, University of Leeds, Leeds LS2 9JT, UK

ABSTRACT

Tellurite glasses doped with Er^{3+} , Tm^{3+} and Nd^{3+} are investigated for broadband amplifiers in the third telecommunications window. Fluorescence spectra and lifetimes of Er^{3+} , Tm^{3+} and Nd^{3+} in tellurite glass were measured. Stimulated emission cross-sections were calculated using the McCumber method for Er^{3+} and the Judd-Ofelt analysis for Tm^{3+} and Nd^{3+} . The obtained emission parameters are compared with those in other glass hosts. The potential advantages of tellurite glass as amplifier host are discussed.

Keywords: Er-doped amplifier, Tm-doped amplifier, Nd-doped amplifier tellurite glass fibres

1. INTRODUCTION

The rapid worldwide growth of telecommunications demands accelerated bandwidth expansion. The development on WDM technologies made possible multichannel transmission, while dense WDM increased the number of available channels. However, channel density is constrained by technological limitations and by fibre dispersion. Ultimately, the number of channels can only be increased by expanding the transmission "window" of the fibres. The recently developed All-Wave Fibre from Lucent, which is essentially OH⁻-free, has a transmission window of 420 nm, extending from 1260 nm to 1680 nm. However, for practical purposes, the range of wavelength available for long-distance transmission (>50 km) is determined by the gain bandwidth of optical fibre amplifiers.

At wavelengths around 1550 nm, where the erbium doped silica fibre amplifier (EDFA) operates, early iterations of these devices exhibited bandwidths of 30-40 nm, depending on the constituents of the host glass. More recently, considerable effort has been devoted to gain flattening and gain extension, often involving quite complex redesigns of the basic amplifier. By these techniques, the useful amplifier range can be extended so that some amplifier designs now cover as much as 70-80 nm [1,2]. While this is a significant improvement, it is still only a small fraction of the fibre transmission window. The limitations on the bandwidth of the silica EDFA are intrinsic, so while further improvement may be possible, it will not be significant. Hence there is currently a strong commercial imperative among designers of components for optical systems to provide more sources of optical amplification that will cover all of the available bandwidth, and thereby allow further channels to be multiplexed over the same fibre.

A recent development in this direction has been the demonstration of tellurite glass EDFA having broadband flat gain bandwidth of 70 nm [3-8]. This device takes advantage of the broad emission and large cross-section of Er^{3+} in tellurite glass host. The gain bandwidth of tellurite EDFA can be extended further by combining it with a Tm^{3+} -doped amplifier, which offers gain on the short wavelength wing of the EDFA band [9-11]. A combined device comprising a Tm^{3+} -doped fluoride amplifier and a tellurite EDFA has already been demonstrated [8]. However, the device exhibited two separate gain bands, at 1443-1484 nm (Tm^{3+} -fluoride band) and 1532-1608 nm (Er^{3+} -tellurite band). Clearly, a continuous gain band would be preferable. In this paper we discuss Er^{3+} spectroscopy in tellurite glasses and show that a further extension of the gain band as demonstrated by NTT can be achieved by modifying the glass composition. We also present evidence that continuous gain should be achievable in an all-tellurite device comprising a Tm^{3+} - and an Er^{3+} -doped amplifier modules. This would more than double the available bandwidth, possibly to as short as 1400 nm.

The amplifier bandwidth can be further extended to shorter wavelengths by adding a Nd³⁺-doped tellurite glass module operating around 1340 nm. Over the years, a variety of Nd³⁺-doped glasses have been investigated as hosts for a 1.3 μ m fibre amplifier [12,13,14]. Although the Nd³⁺ amplifier is highly efficient, the difficulty was to obtain gain below 1320 nm. Recently, gain at 1310-1360 nm was demonstrated in fluoroaluminate glass [13,14]. Nd³⁺ experiences a strong nephelauxetic shift [12]; as a result, in tellurite glass the Nd³⁺ emission peak is red-shifted to 1340 nm. In a fibre geometry, the 1.3 μ m amplifying transition of Nd³⁺ suffers from competition with amplified spontaneous emission (ASE) at 1.1 μ m. Several methods of ASE filtering have been developed [14], and are applicable to tellurite fibres. Nd³⁺-doped tellurite fibre amplifier can therefore fill the gap between the Tm³⁺-doped tellurite amplifier at 1.46 μ m and the Nd³⁺-doped fluoroaluminate amplifier at 1.32 μ m. In this paper we present results on Nd³⁺ spectroscopy in tellurite glass, and show that a Nd³⁺ amplifier would complement Tm³⁺ and Er³⁺ devices in increasing further the available bandwidth. A continuous gain band extending from 1310 nm to 1600 nm may become possible by using a combination of Nd³⁺, Tm³⁺ and Er³⁺ amplifiers.

2. EXPERIMENTAL

The composition of the tellurite glass was 80TeO₂:10ZnO:10Na₂O; this glass, therefore, will be referred to as TZN. In doped glasses Er₂O₃, Tm₂O₃ and Nd₂O₃ substituted for TeO₂. High purity (99.99%) starting materials were used to avoid contamination with transition metals. Glass samples were melted at 650°C in air in a gold crucible, cast into a brass mould, and annealed at 260°C for 1 hour. Bulk glass samples were cast into rectangular moulds 50x40x5 mm.

TZN glasses were melted under a dry air purge in an unsealed silica vessel. Melting under dry air reduced OH⁻ content approximately by a factor of 2 compared with glasses melted under ambient atmosphere.

Fluorescence spectra and lifetimes were measured in bulk glasses. A Ti-sapphire laser was used to pump Er³⁺-doped glasses at 0.98 μ m, Tm³⁺-doped glasses at 0.79 μ m, and Nd³⁺-doped glasses at 0.8 μ m. Emission spectra were recorded using a scanning spectrometer with an InGaS detector (Macam Photometrics). Resolution was approximately 1 nm. The bulk glass sample was positioned so that the pump beam struck near the edge of the sample, and the optical path of emitted light through the sample to the detector was approximately 1 mm. This was done to reduce the effects of radiation trapping which can distort the observed emission spectrum. This setup was also used to measure lifetimes in bulk glass samples. A mechanical chopper was used to modulate the pump, and fluorescence decay curves were recorded by a digital storage adaptor. Lifetimes were calculated by fitting an exponential function to the data. Absorption spectra were recorded by a UV-VIS-NIR spectrophotometer (Perkin-Elmer Lambda-19).

3. RESULTS

3.1 Er³⁺ fluorescence spectra at 1.55 μ m

Figures 1a and 1b show respectively the absorption and emission cross-sections of Er³⁺ for the 1.55 μ m transition in a number of tellurite glass hosts. Tellurite glass compositions are listed in Table 1. Absorbance spectra were measured in bulk glass samples, and absorption cross-sections were calculated using the Beer-Lambert law. Fluorescence spectra were obtained as described above, and the values of stimulated emission cross-sections were calculated from absorption cross-sections using the McCumber method [15]. It is seen that both heights and widths of absorption and emission vary significantly with the host glass composition. Having investigated over 30 different tellurite glass compositions, it was concluded that the glass containing 80TeO₂:10Na₂O:10ZnO offered the best combination of high glass stability and good spectroscopic properties (large absorption and emission cross-sections and broad emission spectra).

Table 1. Compositions of tellurite glasses shown in Figures 1a and 1b.

Glass	Composition
N2	80TeO ₂ :10Na ₂ O:9ZnO:1Er ₂ O ₃
N4	70TeO ₂ :20Na ₂ O:9ZnO:1Er ₂ O ₃
K2	75TeO ₂ :15K ₂ O:9ZnO:1Er ₂ O ₃

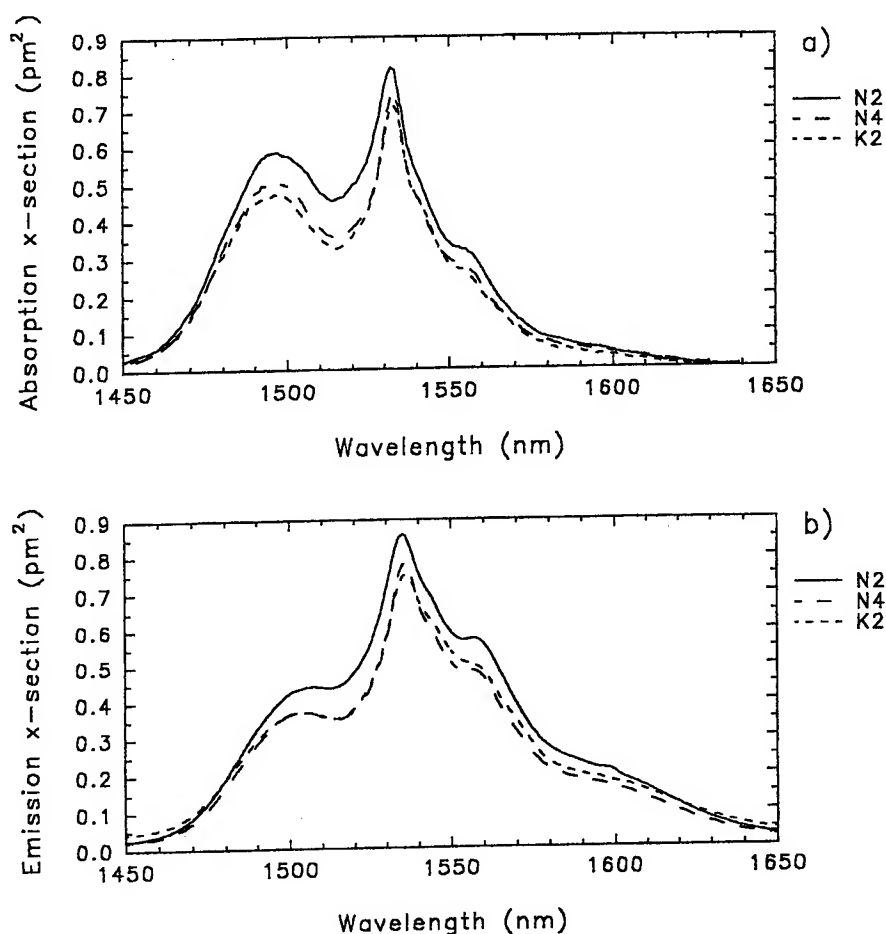


Figure 1. a) Absorption, and b) Emission spectra of Er^{3+} in 3 tellurite glass compositions.

Figure 2 compares the $^4\text{I}_{13/2} \rightarrow ^4\text{I}_{15/2}$ fluorescence of Er^{3+} in TZN tellurite glass with that in other amplifier hosts, Al/Silica, fluoride ZBLAN, and tellurite developed by NTT [3,7]. In TZN glass the fluorescence is broader and the stimulated emission cross-section is higher than in other hosts. Table 2 summarises the salient features. The gain bandwidth of an amplifier is determined largely by the width of the emission spectrum and the stimulated emission cross-section. We may therefore define a figure-of-merit (FOM) for bandwidth as the product $\sigma_e \times \text{FWHM}$. The data in Figure 2 and Table 2 point to the advantages of TZN glass as a host for a broadband Er^{3+} -doped amplifier.

The Er^{3+} emission spectrum in TZN tellurite glass is significantly broader (75 nm FWHM) than in other glasses studied as EDFA hosts. Multicomponent fluoride glasses, such as ZBLAN, are known to have multiple dopant sites resulting in broad emission spectra [16]. Ligand fields in different dopant sites can variously affect the amount of Stark splitting and/or the strengths of transitions between Stark sub-levels, which are thermalised at room temperature. In the case of different Er^{3+} -doped glass hosts, the energies of Stark sub-levels involved in the 1.55 μm emission remain approximately constant, and variations in spectra are caused primarily by changes in transition intensities [16]. Dopant populations in different sites will therefore have different emission spectra, and the aggregate spectrum will be inhomogeneously broadened. The width and shape of Er^{3+} emission spectrum in TZN glass is broadly similar to that in a multi-site ZBLAN glass; moreover, the width varies considerably among different tellurite compositions. Therefore broad Er^{3+} emission in TZN glass may be attributed to multiple dopant sites with large variations among them. The structure of TZN glass also points to the existence of multiple sites [17]. TeO_2 does not form a glassy state, but requires network modifiers, such as divalent and monovalent oxides, to form stable glass. Network modifiers create a variety of dopant sites in the glass, associated with TeO_4 , TeO_3 , and distorted TeO_{3+x} units. A range of dopant sites is therefore clearly desirable for a broadband EDFA glass host.

Table 2. Emission parameters of Er^{3+} in different hosts.

Parameter	TZN	tellurite/NTT [3]	ZBLAN	Al/Silica
Stimulated emission cross-section σ_s , pm^2	0.86	0.66	0.48	0.55
Width at 3 dB or full width at half-maximum, FWHM, nm	75	60	65	45
Width at 1 dB	10	9	10	7
FOM for bandwidth, $\sigma_s \times \text{FWHM}$	65	40	30	25
Lasing level lifetime τ , ms	7.6	4	10	10
FOM for gain $\sigma_s \times \tau$	6.5	2.6	4.8	5.5

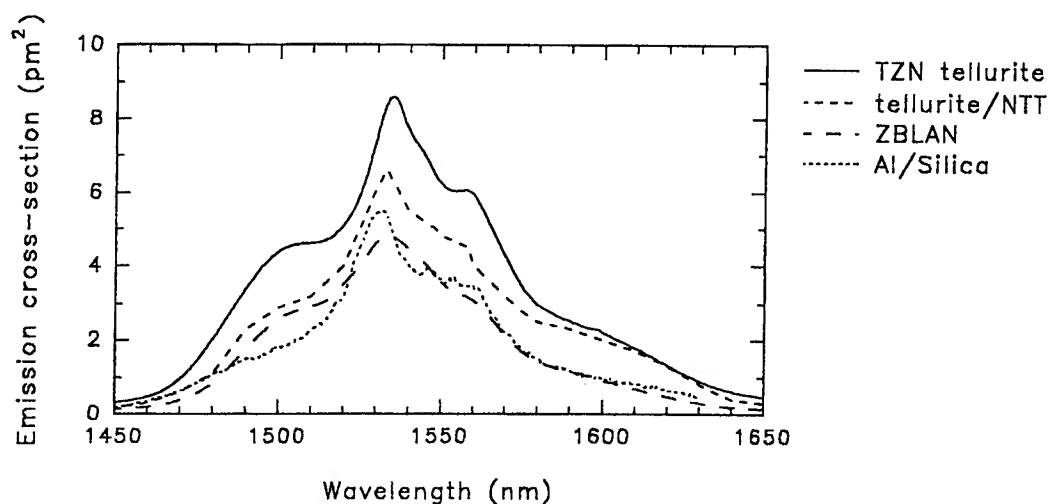


Figure 2. Emission spectra of Er^{3+} in TZN tellurite glass, in the tellurite glass developed by NTT, in fluoride ZBLAN glass and in Al/Silica glass.

Fluorescence spectra of Er^{3+} were measured in TZN glasses doped with varying amounts of Er^{3+} . For easier comparison of spectral profiles, Figure 3 shows normalised spectra in glasses doped with 0.5, 1 and 2 mol% of Er_2O_3 . A significant broadening of emission with increased concentration is clearly observed. A possible cause may be that as the concentration of Er^{3+} ions increases, more dopant sites become populated.

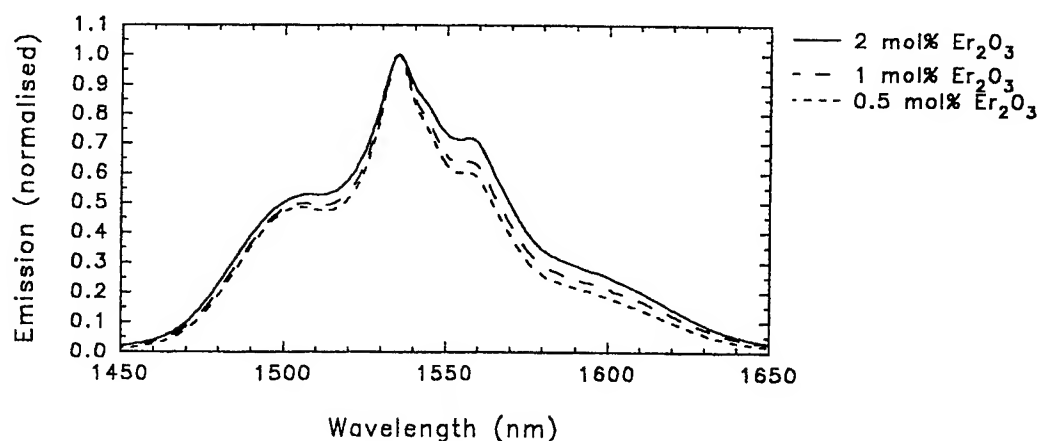


Figure 3. Emission spectra of Er^{3+} in TZN tellurite glass doped with 0.5, 1 and 2 mol% Er_2O_3 .

3.2 Er³⁺ fluorescence lifetimes at 1.55 μm

The decay of the $^4\text{I}_{13/2}$ lasing level in TZN glass was found to be single exponential in all samples, regardless of Er³⁺ concentration. Figure 4 shows an example of a logarithmic plot of fluorescence intensity versus time; the straight solid line is a least-squares fit to the data, showing that the data conform to the single-exponential relationship. Single-exponential decay indicates the absence of Er³⁺ ion clustering even at high doping levels. Since Er³⁺ ions have been shown to reside in multiple dopant sites in TZN glass, single-exponential behaviour of fluorescence decay demonstrates that fast energy transfer re-distributes excitation among ions on time-scales much shorter than fluorescence lifetime.

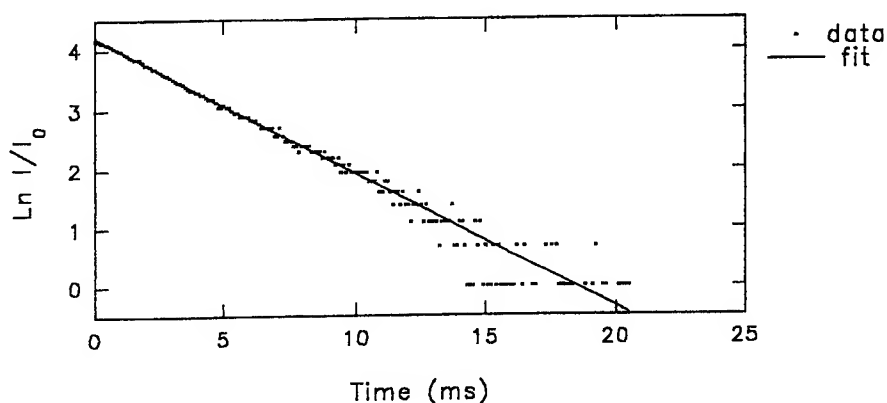


Figure 4. Fluorescence decay of Er³⁺ in TZN glass.

In order to investigate concentration quenching in TZN glass, fluorescence lifetimes were measured in glasses doped with varying amounts of Er³⁺. Figure 5 plots the dependence of fluorescence lifetime on Er₂O₃ concentration. The lifetime increases sharply with increasing concentration, then declines more slowly. The slow decline in the lifetime indicates a slow onset of concentration quenching. The initial increase of the lifetime with concentration is attributed to Er-Er energy transfer, which acts to delay emission. This behaviour is consistent with the strong spectral broadening in heavily doped glasses, which also points to energy transfer increasing with concentration. Maximum lifetime of 7.6 ms occurs around 0.5 mol% Er₂O₃, and decreases by less than 10% at 1 mol% Er₂O₃. The lasing level lifetime of Er³⁺ in TZN glasses is listed in Table 2, where it can be compared with that in other glass hosts. The figure-of-merit (FOM) for amplifier gain is usually defined as the product of stimulated emission cross-section and lifetime ($\sigma_s \times \tau$), and is also listed in Table 2.

The high doping levels and the delayed onset of quenching in TZN glass confirm the absence of ion clustering in TZN glass. Heavily doped devices are therefore possible, greatly reducing the required device length and enabling planar devices. By implementing improved glass processing, to reduce OH⁻ content, it is expected that considerably longer lifetimes, with a later onset of concentration quenching, can be obtained.

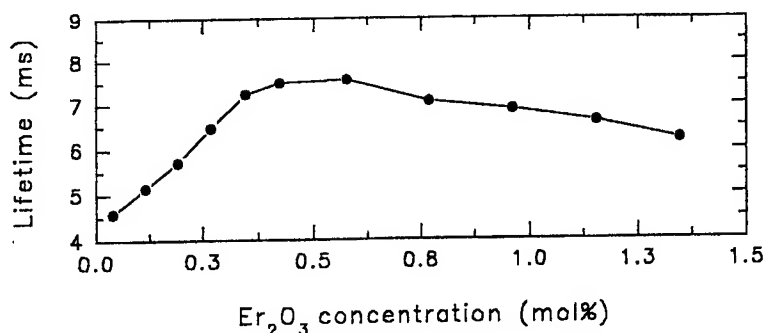


Figure 5. Fluorescence lifetime of Er³⁺ in TZN glass as a function of dopant concentration.

3.3 1.46 μm fluorescence of Tm^{3+}

TZN tellurite glass was also investigated as host for the Tm^{3+} -doped amplifier. Figure 6 shows the normalised emission spectra of Tm^{3+} at 1.46 μm in tellurite glass and in ZBLAN. In order to clarify the issues related to combining two devices, the normalised 1.55 μm emission of Er^{3+} in tellurite glass is also shown. Tm^{3+} fluorescence is seen to be significantly broader in tellurite glass, with FWHM of 114 nm, than in ZBLAN where FWHM is 76 nm. As in the case of Er^{3+} , the broadening is due to multiple dopant sites in tellurite glass. The Tm^{3+} peak in tellurite glass is also red-shifted by approximately 6 nm to 1458 nm, compared with 1452 nm in ZBLAN. The nephelauxetic shift observed in tellurite glass is related to its high refractive index (2-2.1 in tellurite, 1.5 in ZBLAN). The Tm^{3+} -tellurite and Er^{3+} -tellurite emission spectra in Figure 6 intersect at a higher level and longer wavelength than do the Tm^{3+} -ZBLAN and Er^{3+} -tellurite spectra. The data therefore indicate that a Tm^{3+} -doped tellurite fibre amplifier will be more suitable for providing continuous gain when combined with a tellurite EDFA. This may be achieved, in particular, by pumping the tellurite EDFA at 980 nm, thus allowing gain at shorter wavelengths.

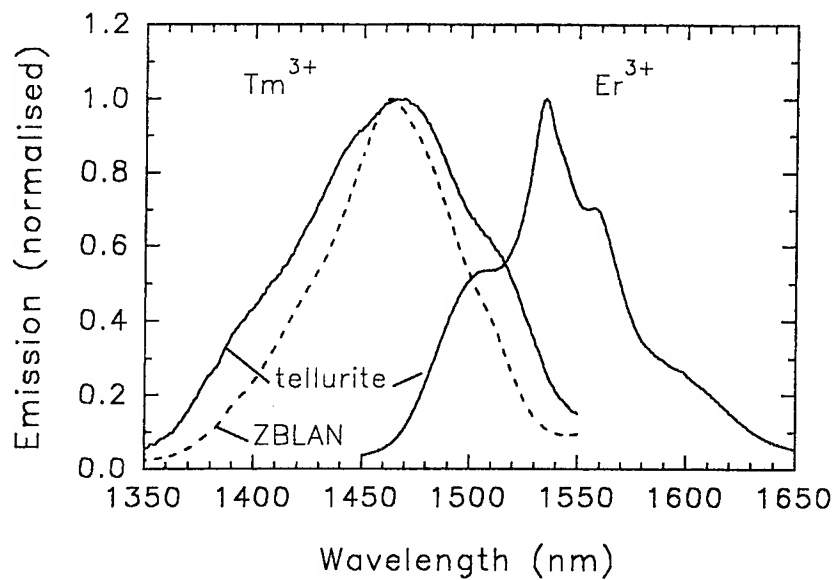


Figure 6. Emission spectra of Tm^{3+} in TZN tellurite glass and in fluoride ZBLAN glass.

Table 3 lists spectroscopic parameters of Tm^{3+} in tellurite and ZBLAN glasses. Stimulated emission cross-sections were calculated using the Judd-Ofelt analysis [18]. The high refractive index of tellurite glass causes the emission cross-section to be larger and the lifetime shorter than in ZBLAN. The FOM for amplifier gain tends to decrease in high refractive index hosts. As a result, the FOM for gain is 30% lower in tellurite than in ZBLAN. However, the FOM for bandwidth is nearly 3 times larger in tellurite glass than in ZBLAN. Yamada et al [8] describe a Tm^{3+} -doped fluoride (ZBLAN) amplifier operating at wavelengths 1443-1484 nm with a bandwidth of 37 nm. The presented results suggest that a similar Tm^{3+} -tellurite amplifier may have an extended bandwidth of up to ~ 120 nm over wavelengths of 1400-1520 nm.

Table 3. Emission parameters of Tm^{3+} -doped TZN and ZBLAN glasses.

Parameter	TZN	ZBLAN
Peak emission wavelength, nm	1458	1452
FWHM of emission, nm	114	76
Fluorescence lifetime τ , μs	280	740
Stimulated emission cross-section σ_s , pm^2	0.45	0.23
FOM gain, $\sigma_s \times \tau$	130	170
FOM bandwidth, $\sigma_s \times \text{FWHM}$	51	18

3.4 1.34 μm fluorescence of Nd^{3+}

TZN tellurite glass was also investigated as host for a Nd^{3+} -doped amplifier which will operate at around 1.34 μm , bridging the gap between the 2nd and 3rd telecom windows. Figure 7 shows the normalised emission spectra in TZN tellurite glass of Nd^{3+} , Tm^{3+} and Er^{3+} .

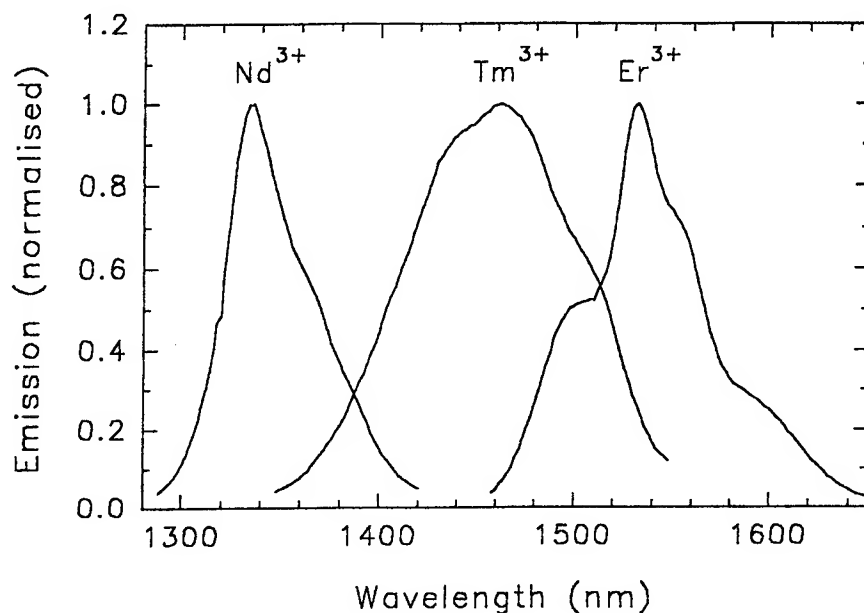


Figure 6. Emission spectra of Nd^{3+} , Tm^{3+} and Er^{3+} in TZN tellurite glass.

Table 4 compares spectroscopic parameters of Nd^{3+} in tellurite and silicate [12] glasses. Silicate glass was chosen for comparison because it has the longest emission wavelength of all investigated (non-tellurite) glasses, and is the preferred host for commercial devices. As was the case when Tm^{3+} emission was compared in tellurite and ZBLAN (see above), the high refractive index of tellurite glass causes the emission cross-section of Nd^{3+} to be larger and the lifetime shorter than in silicate. As a result, the FOM for gain is 35% lower in tellurite than in silicate. In contrast with Tm^{3+} and Er^{3+} , the width of Nd^{3+} emission does not increase in tellurite glass and is similar to that in silicate. The FOM for bandwidth nevertheless benefits from the increased cross-section, and is 50% larger in tellurite than in silicate. However, the advantages of Nd^{3+} -doped tellurite glass as compared to silicate are not as great as in the case of Tm^{3+} and Er^{3+} , primarily because its emission profile does not change significantly and its width does not increase.

Table 4. Emission parameters of Nd^{3+} -doped TZN and silicate glasses.

Parameter	TZN	silicate [12]
Peak emission wavelength, nm	1337	1334
FWHM of emission, nm	51	54
Fluorescence lifetime τ , μs	200	436
Stimulated emission cross-section σ_s , pm^2	0.98	0.62
FOM gain, $\sigma_s \times \tau$	196	270
FOM bandwidth, $\sigma_s \times \text{FWHM}$	50	33

4. CONCLUSIONS

Tellurite TZN glass doped with Er^{3+} and Tm^{3+} has been investigated as a host for a broadband fibre amplifier in the third telecommunications window. Both Er^{3+} - and Tm^{3+} -doped TZN glasses demonstrated extended broad emission spectra and large stimulated emission cross-sections. In both glasses the FOM for bandwidth exceed those in other glass hosts. These results indicate that tellurite glasses specifically designed for broad emission and large cross-sections are promising hosts for extra-broadband amplifiers. The results also suggest that a combined amplifier device comprising Tm^{3+} - and Er^{3+} -doped tellurite fibres may produce a continuous gain band extending from around 1400 nm to around 1600 nm. A Nd^{3+} doped amplifier operating around 1.34 μm is clearly desirable, since it would fill the wavelength gap in that region, complementing other amplifier devices. However, more work is required to determine whether TZN tellurite glass is the most advantageous host for such a device, or whether the glass composition can be redesigned to improve its performance.

ACKNOWLEDGEMENTS

The authors gratefully acknowledge DTI/SMART and ORS/Tetley Lupton Scholarship for supporting this research.

REFERENCES

1. P F Wysocki, J Judkins, R Espinola, M Andrejco, A Vengsarkar, K Walker: "Erbium-doped fiber amplifier flattened beyond 40 nm using long-period grating", OFC'97, 1997, paper PD2-1.
2. Y Sun, J W Sulhoff, A K Srivastava, A Abramov, T A Strasser, P F Wysocki, J R Pedrazzani, J B Judkins, R P Espinola, C Wolf, J L Zyskind, A M Vengsarkar, J Zhou: "A gain-flattened ultra wide band EDFA for high capacity WDM optical communications systems", ECOC'98, v 1-3, ch 351, pp 53-54.
3. A Mori, Y Ohishi, M Yamada, H Ono, Y Nishida, K Oikawa, S Sudo: "1.5 μm Broadband Amplification by tellurite-based EDFAs", OFC'97, 1997, paper PD1-1.
4. M Yamada, H Ono, A Mori, T Kanamori, S Sudo and Y Ohishi: "Ultra-broadband and gain-flattened EDFA's for WDM signals", OAA'97, 1997, paper MB1.
5. M Yamada, A Mori, H Ono, K Kobayashi, T Kanamori and Y Ohishi: "Broadband and gain-flattened Er^{3+} -doped tellurite fibre amplifier constructed using a gain equaliser", Electron Lett, v 34, 1998, pp 370-371.
6. A Mori, K Kobayashi, M Yamada, T Kanamori, K Oikawa, Y Nishida and Y Ohishi: "Low noise broadband tellurite-based Er^{3+} -doped fibre amplifiers", Electron Lett, v 34, 1998, pp 887-888.
7. A Mori, Y Ohishi, S Sudo: "Erbium-doped tellurite glass fibre laser and amplifier", Electron Lett, v 33, 1997, pp 863-864.
8. M Yamada, A Mori, K Kobayashi, H Ono, T Kanamori, K Oikawa, Y Nishida and Y Ohishi: "Gain-flattened tellurite-based EDFA with a flat amplification bandwidth of 76nm", IEEE Photon Tech Lett, v 10, 1998, pp 1244-1246.
9. R M Percival and J R Williams: "Highly efficient 1.064 μm upconversion pumped 1.47 μm thulium doped fluoride fibre amplifier", Electron Lett, v 30, 1994, pp 1684-1685.
10. T Sakamoto, M Shimizu, T Kanamori, Y Terunuma, Y Ohishi, M Yamada and S Sudo: "1.4 μm band gain characteristics of a Tm-Ho-doped ZBLAN fiber amplifier pumped in the 0.8 μm band", IEEE Photon Tech Lett, v 7, 1995, pp 983-985.
11. J Kani, T Sakamoto, M Jinno, T Kanamori, M Yamada and K Oguchi: "1470 nm band wavelength division multiplexing transmission", Electron Lett, v 34, 1998, pp 1118-1119.
12. S Zemon, W J Miniscalco, G Lambert, B A Thomson, M A Newhouse, P A Tick, L J Button, D W Hall: "Comparison of Nd^{3+} -doped glasses for amplification in the 1300-nm region", Proc SPIE, Vol 1789, 1993.
13. M Naftaly, A Jha, E R Taylor: "Spectroscopic properties of Nd^{3+} in fluoroaluminate glasses for an efficient 1.3 μm optical amplifier", accepted for publication in J Non-Cryst Solids.
14. A Jha, M Naftaly, E R Taylor, B N Samson, D Marchese, D N Payne: "1310-1320 nm emission in Nd^{3+} -ion doped fluoroaluminate glasses", IR Glass Optical Fibres & Applications, v 3416, ch 29, pp 115-123, 1998.
15. W J Miniscalco, R S Quimby: "General procedure for the analysis of Er^{3+} cross-sections", Optics Lett, v 16, 1991, pp 258-260.
16. W J Miniscalco: "Erbium-doped glasses for fibre amplifiers at 1500 nm", J Lightwave Tech, v 9, 1991, pp 234-250.
17. J C Sabadel, P Armand, D Cachau-Herreillat, P Baldeck, O Doclot, A Ibanez, E Philipot: "Structural and nonlinear optical characterizations of tellurium oxide-based glasses: TeO_2 - BaO - TiO_2 ", J Solid State Chem, v 132, 1997, pp 411-419.
18. W T Carnall, H Crosswhite, H M Crosswhite: "Energy level structures and transition probabilities in the spectra of the trivalent lanthanides in LaF_3 ", Argonne National Laboratory, 1978.

SESSION 8

Measurement Techniques for Optoelectronics

Metrology for Optoelectronics

Gordon W. Day*
Optoelectronics Division
National Institute of Standards and Technology
Boulder, Colorado, 80303 USA

ABSTRACT

This paper discusses measurement technology, standards, and traceability for the optoelectronics industry. Examples include the development of artifact standards, known as Standard Reference Materials (SRMs), for the calibration of instrumentation, and the calibration of laser and optical fiber power meters and detectors.

Keywords: Optoelectronics, optical fiber, lasers, optical detectors, measurement technology, standards, calibrations, traceability

1. INTRODUCTION

Optoelectronic components have enabled many of the most significant, high technology products and processes of the latter part of the 20th century. Modern telephone systems and the Internet depend on high-speed communications made possible by semiconductor lasers and optical fiber. A tiny laser and a few other optical elements are the essential components in consumer audio and CD-ROM computer storage systems. Fax machines, laser printers, retail checkout systems, and new medical diagnostic and treatment procedures are other examples of the enabling power of optoelectronic components. But these familiar products and techniques may be only the start. The optoelectronics industry continues to grow rapidly. In 1997, the market for optoelectronic components approached \$40 billion and was growing at 15% to 20% per year.

As with any high technology field, metrology is an essential part of the technological and commercial infrastructure. Sound measurements permit effective product specification and enable fair trade. As importantly, well-designed measurements can improve manufacturing efficiency, leading to the development of high-volume markets.

For example, around 1980, when optical fiber began to be used in telecommunications systems, a meter of fiber cost between \$1 and \$2. Manufacturers estimated that 20% of the cost of production could be attributed to measurements, yet studies showed that the accuracy of measurements underlying product specification was very poor. Today, optical fiber is manufactured in huge volumes; estimates suggest 35 million kilometers were installed in 1998. The price is around \$0.05 per meter, of which perhaps 10% is attributable to measurements. And measurement quality in the industry is generally very good.

Several factors contributed to this transformation. Standards developing organizations (SDOs), especially the Telecommunications Industry Association, in the United States, and the International Electrotechnical Commission and the International Telecommunications Union, internationally, have developed and verified hundreds of standard methods for characterizing optical fiber. Instrument manufacturers have developed a wide range of products for the characterization of fiber and related components in accord with agreed standards—the market for instrumentation in optoelectronics is thought to be over \$500M/year, worldwide, and growing rapidly. And national standards laboratories have provided artifact standards for instrument calibration, calibration services, and, more generally, assistance in the development and verification of the standard measurement methods.

In the following two sections, the artifact standards, known as Standard Reference Materials (SRMs), and the calibration services that NIST provides for the optoelectronics industry are briefly described.

* Correspondence: gwd@boulder.nist.gov; <http://boulder.nist.gov/div815>

2. STANDARD REFERENCE MATERIALS

As the selection of commercial instrumentation for characterizing optoelectronic components has grown, the demand for appropriate methods of calibration has also grown. In many areas, instrument calibration is most effectively achieved by using an artifact standard with stable and well-established characteristics. This permits recalibration, by the instrument user at his own site, at whatever interval is deemed appropriate. If, in addition, the artifact has been characterized with traceability to appropriate national standards, such calibrations may be an efficient method of meeting requirements of quality standards, such as those promulgated by organizations such as the International Organization for Standards (ISO).

NIST currently provides twelve Standard Reference Materials to meet these needs, and has several others under development (See Table 1 and Figure 1). Several are designed to assist optical fiber and connector manufacturers meet dimensional specifications. Others can be used to calibrate instruments designed to determine optical fiber propagation characteristics such as chromatic dispersion or polarization mode dispersion. Two recently-developed SRMs permit the wavelength calibration of instruments such as optical spectrum analyzers and are especially useful in wavelength division multiplexed system development.

Table 1 NIST Standard Reference Materials for calibrating optoelectronic instrumentation**

Number	Name	Availability
2513	Mode Field Diameter Standard for Single-Mode Fiber	Available
2517	Wavelength Reference Absorption Cell - Acetylene ($^{12}\text{C}_2\text{H}_2$)	Available
2518	Polarization Mode Dispersion Standard	Available
2519	Wavelength Reference Absorption Cell - Hydrogen Cyanide (H^{13}CN)	Available
2520	Optical Fiber Diameter Standard	Available
2522	Pin Gauge Standard for Optical Fiber Ferrules	Available
2523	Optical Fiber Ferrule Geometry Standard	Available
2524	Optical Fiber Chromatic Dispersion Standard	Available
2525	Optical Retardance Standard	Available
2553	Optical Fiber Coating Diameter	Available
2554	Optical Fiber Coating Diameter	Available
2555	Optical Fiber Coating Diameter	Available
xxxx	Polarization Dependent Loss Standard	In 2000
xxxx	Deterministic Polarization Mode Dispersion Standard	In 2000
xxxx	Optical Disc Retardance Standards	In 2000
xxxx	Composition Standards for Compound Semiconductors	In 2000

** NIST Standard Reference Materials Catalog, SP 260, available from the National Institute of Standards and Technology, Standard Reference Materials Program, Gaithersburg, MD 20899



Figure 1 NIST Standard Reference Materials for calibrating optoelectronic instrumentation. Large box in back center contains approximately 10 km of optical fiber with its zero dispersion wavelength specified to within 0.08 nm. Small items in front are for fiber and connector dimensional calibrations. Boxes at right and left are for wavelength calibration. Black units are for polarization mode dispersion (left) and retardance (right).

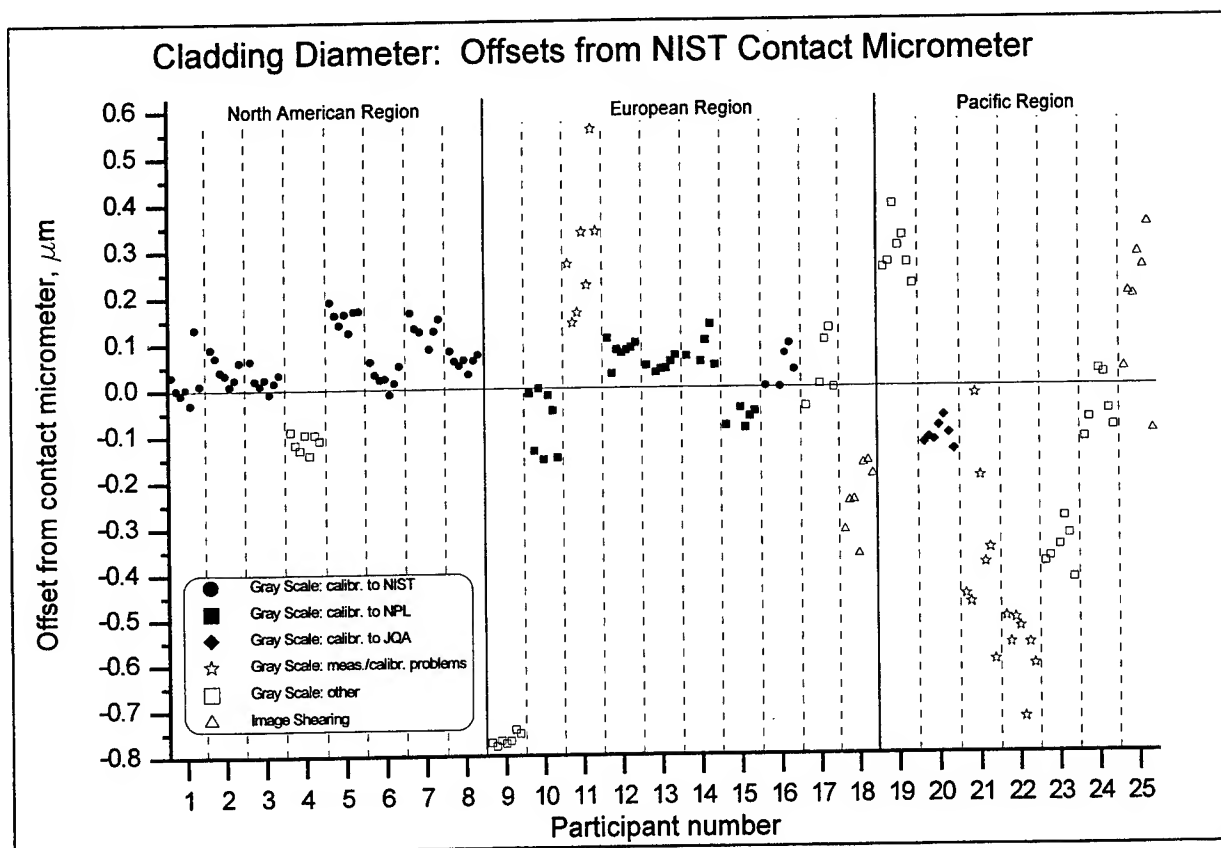


Figure 2 Results of an international comparison of optical fiber diameter measurements. Solid symbols represent measurements that are traceable to an artifact standard.

The value of artifact standards in reducing measurement uncertainties within the industry is well illustrated by the results of an international comparison of optical fiber diameter measurements conducted in 1995. The results are shown in Figure 2. Seven fiber specimens were measured in 25 laboratories in North America, Europe, and the Pacific region. Most of the measurements made in North America were traceable to NIST SRM 2520, which has an estimated uncertainty of about 40 nm. Some of the measurements made in Europe were traceable to an artifact standard produced by National Physical Laboratory (NPL) in the United Kingdom and one set in the Pacific region was traceable to a standard produced by Japanese Quality Assurance Organization (JQA) in Japan. As can be seen from the Figure 2, measurements traceable to artifact standards produced by the national standards laboratories provided the greatest consistency.

3. CALIBRATIONS

For some instruments, especially optical power meters and detectors, where standards and calibration systems are more complex, high quality measurements are best assured through periodic calibration in a standards laboratory. Many national standards laboratories provide such calibrations.

NIST maintains seven primary standards for laser power and energy, as indicated in Figure 3. Each is designed for a specific wavelength and power or energy range and for either pulsed or cw radiation. Each operates on the principle of comparing the temperature rise resulting from absorbed optical power or energy to that caused by dissipated electrical power or energy. They are thus traceable to SI units through electrical standards for voltage and resistance. Figure 4 shows one of the standards. Figure 5, a cuaway drawing of the same standard, shows the cavity in which laser light is absorbed, the thermocouples which measure the temperature rise, and the heaters which permit a dissipation of a known amount of electrical energy. The principal uncertainty in these instruments is establishing the degree to which heating from the two sources provides the same temperature rise, per unit of energy deposited.

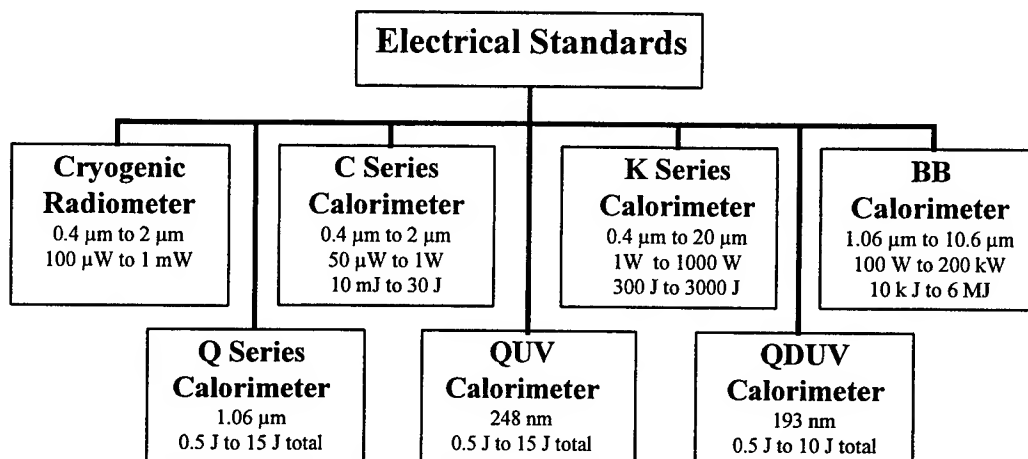


Figure 3 NIST primary standards for laser power and energy measurement

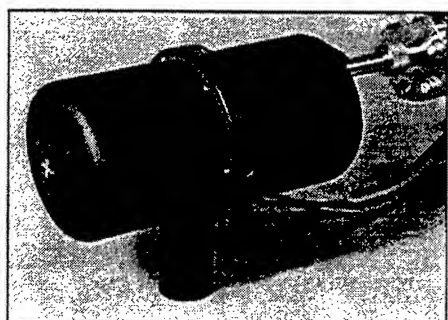


Figure 4 C-series calorimeter

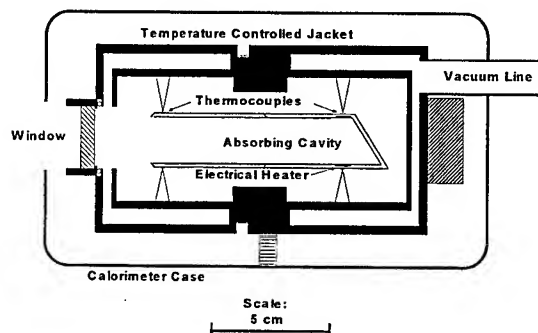


Figure 5 Cut-away view of C-series calorimeter

In most cases at NIST, laser power (or energy) meters and detectors intended for use with lasers are calibrated directly against the appropriate primary standard represented in Figure 3 using a system similar to that shown in Figure 6. The system is based on a wedged beamsplitter which serves as a calibrated attenuator. The standard is placed in the transmitted beam and the instrument to be tested is placed in any one of the reflected or higher order transmitted beams. The ratios of each of these beams to the primary transmitted beam can be calculated from first principles of measured directly.

Detectors and power meters with optical fiber-coupled inputs can also be calibrated, though these require the use of a transfer standard, and the calibrations are performed by direct substitution.

For detectors and optical receivers, frequency response is another parameter of importance. A particularly effective approach to frequency response calibrations is to use the beat frequency signal between two tunable single frequency lasers, as shown in Figure 7. Currently, NIST can provide calibrations with this system to at least 50GHz; in most cases the detector and microwave power sensors are calibrated together as a unit.

Tables 2 and 3 summarize the calibration services currently provided by the NIST Optoelectronics Division. NIST also provides calibration services for detectors intended to be used with incoherent radiation and for photometric quantities through its Optical Technology Division. Full details of NIST calibration services are available in NIST Special Publication 250.^{***}

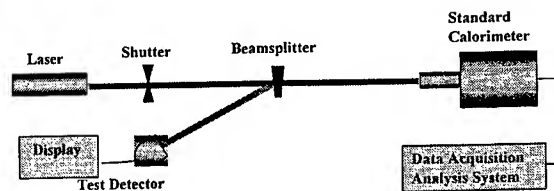


Figure 6 Beamsplitter-based calibration system

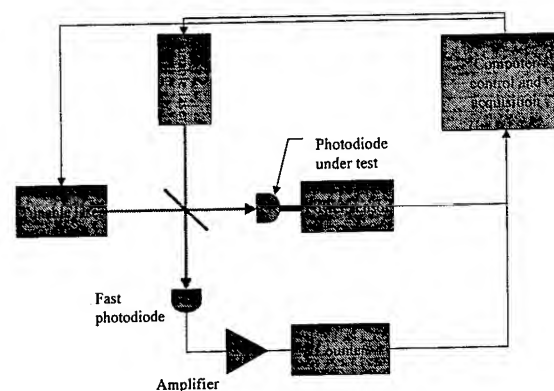


Figure 7 Heterodyne frequency response calibration system

Table 2 Laser Power and Energy Calibrations			
	Laser	Wavelength	Range
CW	Argon	488,514 nm	1 μ W - 1 W
	HeNe	633 nm	1 μ W - 20 mW
	Diode	830 nm	100 μ W - 20 mW
	Nd:YAG	1064 nm	100 μ W - 450 W
		1319 nm	100 μ W - 20 mW
	Erbium	1550 nm	100 μ W - 50 mW
	CO ₂	10.6 μ m	100 mW - 1kW
Pulsed	KrF	48 nm	5 μ J/pulse - 150 mJ/pulse 50 μ W - 7 W average
	Nd:YAG	1064 nm	1mJ - 50 mJ/pulse (1-20 Hz prf)
			10 ⁻⁴ - 10 ⁻⁸ W(peak) 10 ⁻¹¹ - 10 ⁻¹⁵ J/pulse

Table 3 Optical Fiber Power Meters and Detectors			
Parameter	Wavelength	Range	Status
Absolute Power Calibration	670, 780, 850, 1310, 1550 nm	10 - 100 μ W	Calibration Service
Optical Receiver Frequency Response	1319 nm	300 kHz - 50 GHz	Special Test
	850 nm	1 MHz - 26 GHz	Special Test
Optical Fiber Power Meter Linearity	850, 1310, 1550 nm	60 - 90 dB	Special Test
Optical Detector Impulse Response	800 nm	100 fs impulse source	Special Test
Optical Detector Spatial Uniformity	635, 850, 1300, 1550 nm		Special Test
Optical Fiber Power Meter Spectral Responsivity	400 - 1700 nm		Special Test

^{***} NIST Calibrations Services Users Guide, SP 250, available from the National Institute of Standards and Technology, Calibration Program, Gaithersburg, MD 20899.

Imaging the evanescent intensity gradients of an optical waveguide using a tapping-mode near-field scanning optical microscope

Chi Wen Yang

Department of Physics, National Chung Cheng University, Chia Yi 621, Taiwan

Din Ping Tsai

Department of Physics, National Taiwan University, Taipei 10617, Taiwan

Howard E. Jackson

Department of Physics, University of Cincinnati, Cincinnati, Ohio 45221-0011, USA

ABSTRACT

Imaging the local evanescent intensity gradients by using a tapping-mode near-field scanning optical microscope is developed. Two different optical structures, one a well-characterized BK-7 glass prism in the total internal reflection configuration, and the other a side-polished optical fiber waveguide with a step index of refraction, were studied. Results show distinct imaging contrasts of the intensity gradients, and reveal the variations of the local index of refraction of waveguide. This is a novel near-field optical method, and can be used in the imaging of local index of refraction of a variety of optical waveguide structures.

KEY WORDS: near-field optics, evanescent intensity, intensity gradients, local index of refraction, scanning near-field optical microscope.

1. INTRODUCTION

Imaging the evanescent intensity distribution of the integrated optical waveguides was first reported by Tsai et al. in 1990¹. Lately, similar studies have been applied to various waveguide structures including directional couplers, y branches, semiconductor optical channel waveguides, and multimode interference structures²⁻⁴ by using near-field scanning optical microscopy (NSOM). The advantage of NSOM is its spatial resolution with no diffraction limit. Because the very local optical properties can be revealed by the evanescent intensity of various structures of waveguides, the NSOM became a useful tool for the measurements. In this paper a recent developed tapping-mode NSOM is introduced to image the near-field intensity and intensity gradients on waveguides. The working principle and the performance of this novel method are shown. The gradients of the evanescent intensity could lead to the local optical property of waveguide, for example, the local index of refraction. Both the intrinsic character and the performance of optical waveguide structures can be examined by the imaging of evanescent intensity gradients. Two samples, a well-understood BK-7 prism in the total internal reflection configuration, and an optical waveguide structure, were studied to show the usefulness of this new method.

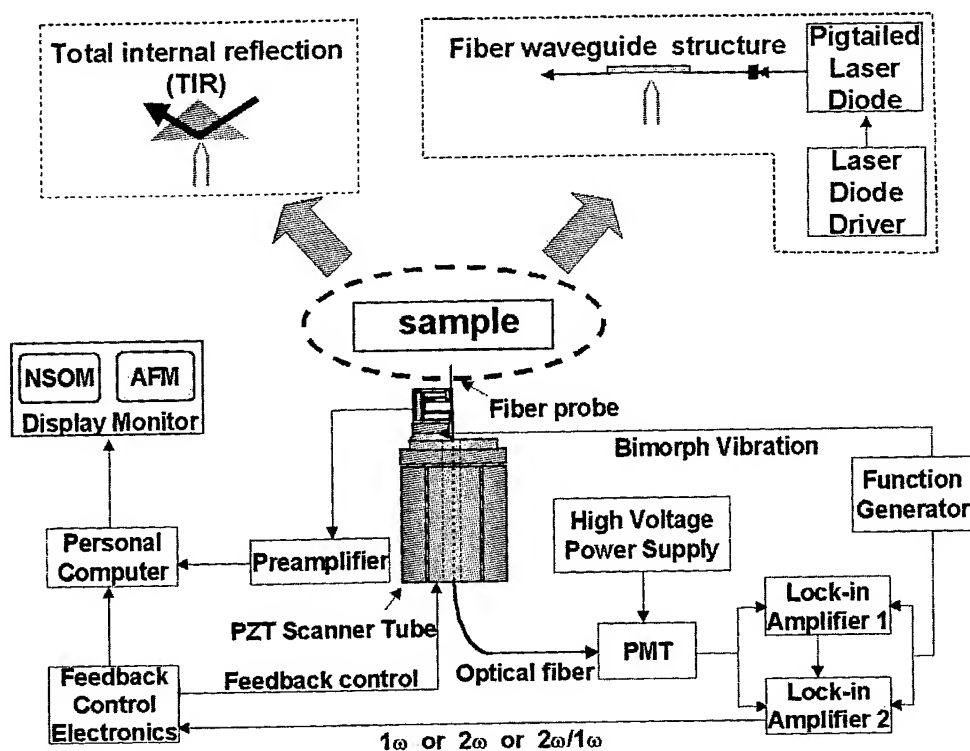


FIG. 1. A schematic of the experimental setup for the near-field intensity gradient measurements is shown.

2. EXPERIMENTAL

For the evanescent intensity measurements, a recently developed tapping-mode tuning-fork near-field scanning optical microscope (TMTF-NSOM)⁵ was used. A schematic of the experimental setup is shown in Fig. 1. An inverted TMTF-NSOM was used to probe the evanescent field intensity at the surface of the sample. Light coupled to the tapered fiber tip operated in the near-field was detected by a photomultiplier tube whose signal was fed to two external lock-in amplifiers which acquired signals at the tapping (modulation) frequency ω , at 2ω and provided their ratio $(I(2\omega)/(I(\omega)))$. The feedback control of the near-field optical fiber probe was provided by an internal lock-in amplifier of a commercial electronic control unit of an atomic force microscope (AFM)⁶, which is described elsewhere⁵. This is a non-optical method, has all the advantages of the tapping-mode, high spatial resolution, high sensitivity, and excellent stability. The setup is compact, simple, rigid, and inexpensive, and can be used in various environments⁵. The simultaneous imaging of topography and near-field optical signals could be achieved easily using our setup. Two different optical samples were studied in our experiments. A schematic of the samples, a BK-7 prism and a side-polished single mode step index fiber (Newport, F-SA) is displayed in Fig. 1. The BK-7 prism of index 1.517 is operated in the total internal reflection configuration with an excitation wavelength of 632.8 nm. The optical fiber waveguide sample had core and cladding diameters of 125 μm and 3.8 μm respectively, and a polished depth of the core of 0.43 μm . The width of the air/core interface region is 2.4 μm . The nominal index of refraction of the core and cladding are 1.4616 and

1.4571 respectively, and thus the difference in index of refraction is only 0.0045. A laser diode operating at 656 nm was used to excite this waveguide.

3. PRINCIPLE

The optical evanescent intensity above an optical waveguide or prism is given by

$$I = I_s + I_o \exp(-2qz), \quad (1)$$

where I_o is the intensity at the surface of the waveguide, z is the probe height above the waveguide surface, I_s is the scattered background intensity, $q = k(n_{\text{eff}}^2 - 1)^{1/2}$, and k is $2\pi/\lambda$, where λ is the wavelength of the light coupled into the optical waveguide or prism. Instead of operating a near-field microscope in the conventional constant height (constant z) mode, consider a mode where z is modulated: $z = z_o + A \cos \omega t$. If the amplitude (A) is small, we can expand the evanescent intensity expected above the waveguide or prism in the following manner:

$$I = I_o \exp(-2qz_o) [1 + q^2 A^2 - 2qA \cos(\omega t) + q^2 A^2 \cos(2\omega t) - \dots] + I_s, \quad (2)$$

and we can measure the ratio of the evanescent intensity at both the modulation frequency (ω) and at twice that frequency (2ω) by

$$I(2\omega)/I(\omega) = I_o \exp(-2qz_o) \cdot q^2 A^2 / I_o \exp(-2qz_o) \cdot (-2qA) = -Aq/2, \quad (3)$$

For the known tapping amplitude A , we then obtain q , a measure of the local optical property. The imaging of this ratio $I(2\omega)/I(\omega)$ gives the image of the local near-field intensity gradients because of

$$\frac{dI}{dZ} = 0 - 2qI_o \exp(-2qZ) = -2q[I - I_s]. \quad (4)$$

4. RESULTS AND DISCUSSION

A $20 \mu\text{m} \times 20 \mu\text{m}$ scan acquired simultaneously at the total internal reflection region on the hypotenuse face of a BK-7 ($\lambda/4$) glass prism is shown in Fig. 2. Fig. 2a is an AFM image, which displays the topography of the prism surface with a *rms* roughness over a $20 \mu\text{m} \times 20 \mu\text{m}$ area of 0.65 nm. Figures 2b and 2c are, respectively, the NSOM images of near-field intensity, and the ratio (R) of optical signals acquired at the frequency of 2ω and 1ω . Basically the image of Fig. 2b shows no distinct features. For a high optical quality material like BK-7, we expect only exceedingly small variations in index, and thus the observed fluctuations in the image in Fig. 2b are a measure of the noise.

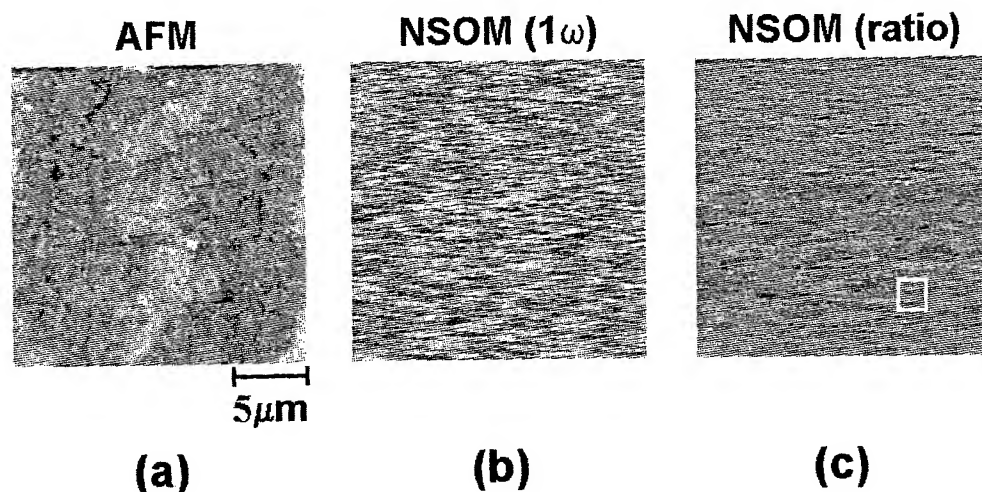


FIG. 2. A $20\ \mu\text{m} \times 20\ \mu\text{m}$ scan of AFM and NSOM images at the total internal reflection region on the hypotenuse face of a BK-7 glass prism. (a) AFM image; (b) NSOM intensity image; (c) NSOM image of the ratio R of the optical signals acquired at a frequency of $2\ \omega$ and $1\ \omega$. This image displays the contrast of the near-field intensity gradients or the index of refraction.

By Eq. 3, with the known values of n (1.517), λ (632.8 nm), θ (45°), and thus the q ($3.854 \times 10^{-3}\ \text{nm}^{-1}$) in our experiments, we can find out the tapping amplitude A from the measured value of R . Figure 2c displays the contrast image of the ratio R when the amplitude of the driving voltage of the piezoelectric bimorph is 3.5 V. By measuring the mean value of a 2×2 microns area indicated by a square box in the Fig. 2c, a mean value of $R = -0.065$ is found, and the derived tapping amplitude A is found in this case to be $33.7 \pm 0.3\ \text{nm}$. A commercial optical interferometer⁷ was used to measure the vibrating displacements of the force sensing tine of a separate tuning fork in free oscillating condition with the driving amplitude of the bimorph at 3.5 V. The measured vibrating amplitude was $35 \pm 0.4\ \text{nm}$, in reasonable agreement with the tapping amplitude derived from the near-field data of Fig. 2c.

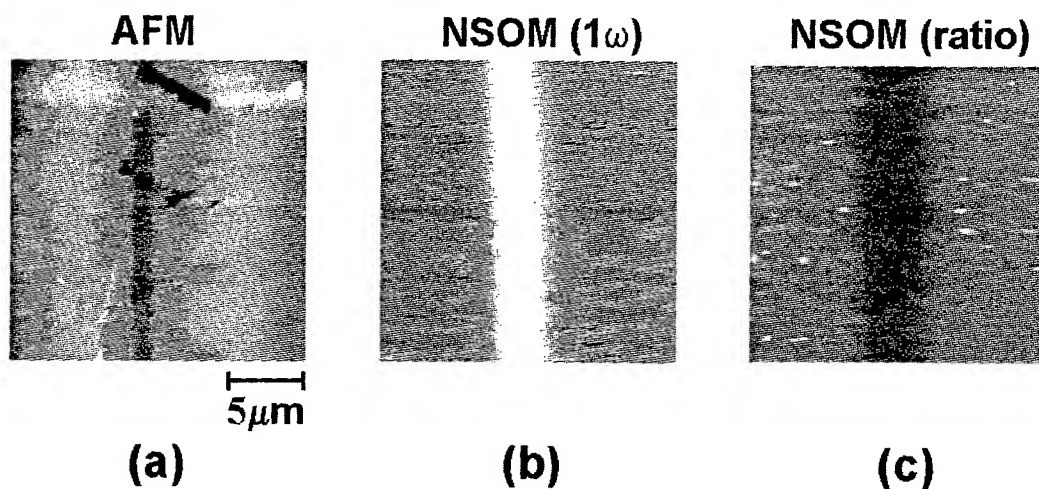


FIG. 3. A $20\text{ }\mu\text{m} \times 20\text{ }\mu\text{m}$ scan of AFM and NSOM images simultaneously acquired on a side polished optical fiber waveguide sample. (a) AFM image; (b) NSOM intensity image. (c) is a NSOM image of the ratio R of the optical signals acquired at a frequency of 2ω and 1ω , and displays the contrast of the index of refraction.

Figure 3 shows the several images obtained simultaneously from the side-polished single mode step index optical fiber waveguide sample. Figure 3a shows a $20\text{ }\mu\text{m} \times 20\text{ }\mu\text{m}$ AFM image which is simply a measure of the polishing flatness; the sample waveguide width of 2.4 microns, a *rms* roughness inside the waveguide of 0.38 nm, and a *rms* roughness outside the waveguide region of 0.31 nm. A tapping-mode near-field measurement of the intensity above this optical fiber is displayed in Fig. 3b. Distinct confinement of the waveguided light displays good signal to noise. The peak signal was around 3.896 V, and the width of the optical waveguide intensity distribution was measured to be 4.68 microns ($1/e^2$ to $1/e^2$), in reasonable agreement with that expected from geometry of our optical waveguide sample. In Fig. 3c we display the *ratio* of the evanescent intensity detected at 2ω to that at 1ω : $R = I(2\omega)/I(\omega)$. This image contains the information of the local index variations in this structure. Inside the optical waveguide core region this ratio is seen to be reasonably uniform; the measured variation is less than 2% for a $1\text{ }\mu\text{m} \times 1\text{ }\mu\text{m}$ area inside the core region, and with a *rms* value of - 0.17. The *rms* ratio value outside the waveguide of a $1\text{ }\mu\text{m} \times 1\text{ }\mu\text{m}$ region is measured at 0.031 which is due to a very small imbalance of the two lock-in amplifiers. The difference in values of R in the two areas of Fig. 3c reflects the index difference between core and cladding regions.

In summary, we have demonstrated a new method for imaging directly the local index of refraction of optical waveguide structures using tapping-mode near-field techniques.

5. ACKNOWLEDGEMENTS

We are grateful for the support by the National Science Council of R. O. C. under Grant No. NSC89-2112-M-002-050.

6. REFERENCES

1. Din Ping Tsai, Howard E. Jackson, R. C. Reddick, S. H. Sharp, R. J. Warmack, *Appl. Phys. Lett.* **56**, 1515 (1990).
2. A. G. Choo, H. E. Jackson, U. Thiel, G. N. De Brabander, J. T. Boyd, *Appl. Phys. Lett.* **65**, 947 (1994).
3. Y. Toda, M. Ohtsu, *IEEE Photon. Techn. Lett.*, **7**, 84 (1995).
4. E. G. Borgonjen, M. H. P. Moers, A. G. T. Ruiter, N. F. van Hulst, *Proc. SPIE* **2535**, 125 (1995).
5. Din Ping Tsai, Yuan Ying Lu, *Appl. Phys. Lett.* **73**, 2724 (1998).
6. The Nanoscope IIIa from Digital Instruments Inc., Santa Barbara, CA 93117.
7. Advanced Vibrometer Interferometer Device, Ahead Optoelectronics, Inc., B1, 130, Section 3, Keelung Road, Taipei, Taiwan.

Effective index measurement of propagated modes in planar waveguide

John E. Batubara^{*a}, Hendik R. Yulianto^a, Henri P. Uranus^{a,b} and Muljono^a

^aUniversity of Pelita Harapan, Lippo Karawaci, Tangerang 15811, Indonesia

^bUniversity of Indonesia, Salemba 4, Jakarta 10430, Indonesia

ABSTRACT

A method of index measurement, the so-called m-line technique has been applied to measure the refractive index of planar waveguides fabricated by ion exchange method in BK7 substrate. By placing a prism coupler on the surface of the planar waveguide, the coupling angle of modes guided in the waveguide was measured. The prism has apex angle of 44.9° and is made of ZnSe with refractive index 2.59073. The values of the coupling angles were then processed mathematically to obtain the effective indices of the guided modes. The number of modes guided in the waveguide depends on the duration of ion exchange process, and the effective refractive indices have been determined for the respective modes. The result for zero order mode, ranging from 1.5183 to 1.6887 for TM modes and from 1.5182 to 1.6891 for TE modes. On the other hand, for the duration of ion exchange process of 48 hours, five modes were guided in the waveguide and the effective refractive indices were 1.6887; 1.6167; 1.5818; 1.5649 and 1.5465 for zeroth, the first, the second, the third and the fourth modes, respectively. The use of the m-line technique has been proved to be simple and effective with high accuracy in the characterization purpose of waveguides.

Keywords: effective index, planar waveguide, ion exchange, m-line technique, prism coupler.

1. INTRODUCTION

Prism coupler is one passive component in integrated optical circuits⁽¹⁾ functions to couple light from a planar waveguide to the prism or from the prism to a planar waveguide. The planar waveguide used in coupling light by this method has a form of thin dielectric film of light guide with a simple structure⁽²⁾ such that a characterization can be treated theoretically and can be verified by experiment and investigation. The prism coupler is accomplished with m-line technique with a purpose to determine the characteristics of planar waveguides as a follow up of the fabrication method.

M-line technique is sometimes also called as m-line spectroscopy because the intensity pattern of light formed on the observation screen has several lines of light beam representing certain modes arranged as light spectrum. The term spectroscopy is no longer used for this technique because the intensity pattern is not a real spectrum.

The prism coupler using m-line technique was introduced by Osterberg and Smith⁽²⁾ in 1964. In principle, the method is similar with the edge coupling where the light is coupled from light source to a planar waveguide. This method has a disadvantage in the alignment problem with a relatively high loss of greater than 0.2 up to 0.5 dB. The alignment problem was then improved by Bell Telephone Laboratories in 1969 achieving a low loss, both for light coupling to the waveguide through the prism and for light coupling from the waveguide to the air through the prism. Thereafter, the loss was gradually improved in broadband communication systems.

There are some merits of the m-line technique using prism coupler, namely: (a) simple, easy and rapid process; (b) accurate result with high efficiency; (c) if the thickness of the waveguide film is large, the refractive index and the thickness of the film can be determined⁽³⁾. By overcome some difficulties in the application of the m-line technique with prism coupler, the m-line method will be very useful tool in the characterization of the planar waveguides⁽⁴⁾.

*Correspondence: Department of Electrical Engineering, Faculty of Industrial Technology, University of Pelita Harapan ,
Lippo Karawaci, Tangerang 15811, Indonesia,
Telephone : 62-21-5460901; Fax: 62-21-5460910

In this study, planar waveguides fabricated by ion exchange method⁽⁵⁾ on BK7 substrates were characterized by measuring their effective index by the use of m-line technique. Some developments in preparing the measurement and its result are reported in this paper.

2. THEORETICAL CONSIDERATIONS

Planar waveguides have simple wave guiding property, particularly for step index type of planar waveguide. Geometrical structure of planar dielectric waveguide can be described⁽²⁾ using Fig. 1. Basically, there are three layers in a planar waveguide as shown in figure where refractive indices of the layers are denoted by n_1 , n_2 , and n_3 respectively. The layer between n_1 and n_3 is a very thin layer such as we call it as film where the light is guided in z direction. The condition of light to be guided in the film is $n_2 > n_3 \geq n_1$ which means that total internal reflection should be existed in the film.

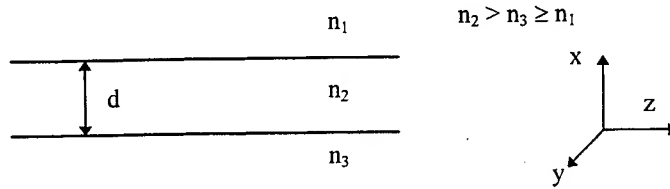


Fig.1 Basic structure of planar waveguide

The wave equation for the electric field in y direction for TE (transverse electric) polarized mode can be written as

$$(\partial^2 E_y) / (\partial x^2) = (\beta^2 - n^2 k^2) E_y \quad (1)$$

where E_y is the electric field in y direction; β is the propagation constant in the propagation axis; n is the refractive index; $k = 2\pi/\lambda$ is the wave vector; and λ is the wavelength of light.

The equation of magnetic field wave in z axis (H_z) for TE mode is

$$(\partial E_y) / (\partial x) = -j\omega\mu H_z \quad (2)$$

where ω and μ are constants.

By solving the equation (1) into (2), eigen value equation of TE mode for step index waveguide can be obtained by the application of boundary condition for the magnetic field wave equation in z axis as follows,

$$(\kappa^2 - \gamma\delta) \sin(\kappa d) - \kappa(\gamma + \delta) \cos(\kappa d) = 0 \quad (3)$$

where $\kappa^2 = k^2 n_2^2 - \beta^2$; $\gamma^2 = \beta^2 - k^2 n_3^2$; $\delta^2 = \beta^2 - k^2 n_1^2$.

Similarly, the equation for TM mode can written as

$$(\partial^2 E_y) / (\partial x^2) = (\beta^2 - n^2 k^2) E_y \quad (4)$$

and the electric field wave equation in z axis is written as

$$(\partial E_y) / (\partial x) = -j\omega\mu H_z \quad (5)$$

and therefore the eigen value of TM mode can be derived by substituting eq. (4) into (5) giving

$$\kappa (n_1^2 n_2^2 \gamma + n_2^2 n_3^2 \delta) \cos(\kappa d) - (\kappa^2 n_1^2 n_3^2 - \gamma \delta n_2^4) \sin(\kappa d) = 0 \quad (6)$$

Those eigen value equations (3) and (4) are used to derive the formulation in determining the refractive indices of TE and TM modes, respectively.

3. M-LINE MEASUREMENT

3.1 Concept of Prism Coupler

The method of prism coupler is a general technique used to substitute the problem of alignment of light coupling from a light source to the surface of waveguide on the edge coupling. This method of light coupling consists of two types of prism coupler, namely the coupling of light from the prism to the film (prism input coupling) and from the film to the prism (prism output coupling). The principle of prism input coupling is actually used as a reference of the prism output coupling.

In this study, light propagation mode traveling in the prism is coupled to the film layer and then the light propagates in the film as shown in Fig. 2. The figure shows a collimated light beam from a laser source enters the prism through the slope surface and then is coupled to the film layer of the waveguide. The air gap between the prism base and the film surface is negligibly small. The field pattern of the light wave decreases exponentially at the base of the prism. If the air gap is small enough, less than or equal to $\lambda/2$, an interaction among the the modes coupled fromt the prism to the film will exist. The coupling of light modes causes a transfer of energy from the prism to the film by the tunneling effect or optical tunneling.

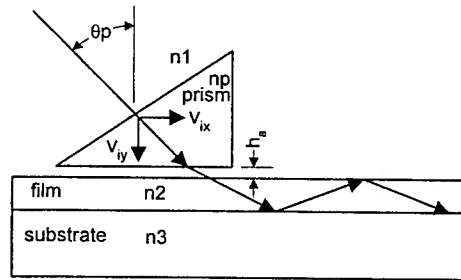


Fig.2 The light propagation in prism input coupling

The important property of the coupled modes is the possibility of energy to be exchanged in the coupling area with a condition that there are two modes with equal phase velocity, the so-called phase matched. In this case, the phase velocity of light in horizontal direction entering the prism equal to the phase velocity of one of the light modes in horizontal direction guiding in the waveguide. This condition can be written in equation

$$k_p \sin \theta_p = \beta_{sw} \quad (7)$$

where k_p indicates the propagation constant of light in the prism; θ_p indicates the angle between the incident light to the prism base and the normal line of the prism base; and β_{sw} indicates the propagation constant of light on the surface of the film layer. The exchange of light energy for a number of coupled modes will reach a maximum if the interaction length L along the wave propagation direction is

$$\kappa L = \pi/2 \quad (8)$$

where κ is the coefficient of the light coupling on the coupling area.

3.2 M-line Technique

Measurement by m-line technique using prism coupler was applied to determine effective refractive index of waveguide as important parameter in characterizing the waveguide. In this study, a waveguide with step index type was used as sample of the measurement.

Some basic equipments used in the experiment were laser source with monochromatic red light ($\lambda = 633 \text{ nm}$) to detect the pattern of guided modes. A prism of right angle type was used as laser light coupler. The prism is made of zinc-sulfide (ZnSe) with refractive index $n_p = 2.59073$ for $\lambda = 633 \text{ nm}$ and prism angle $\epsilon = 44.9^\circ$ as shown in Fig. 3. The sample of film used as waveguide for m-line measurement was BK7 substrate fabricated by ion exchange. The refractive index of BK is $n_s = 1.5151$ for $\lambda = 633 \text{ nm}$.

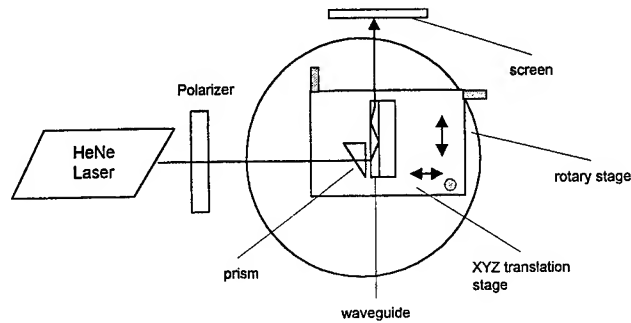


Fig.3 Schematic diagram of m-line measurement

For the purpose of identification of the samples, each sample was labelled with numbers BK71, BK72, ... and so on. Therefore each sample was processed and characterized in order according to the given label.

The whole process of m-line measurement consists of three steps, namely (1) the adjustment of position of the prism coupler on the center point of the rotating table; (2) measurement of the reference angle; and (3) measurement set up of the light coupling angle.

3.2.1 Position adjustment of the prism coupler

To adjust the position of the rotating table into the center point of the prism, a laser light hang from a static rod was used. The laser beam was directed precisely to the center point of the prism located on the XYZ stage and rotating table. See Fig. 4.

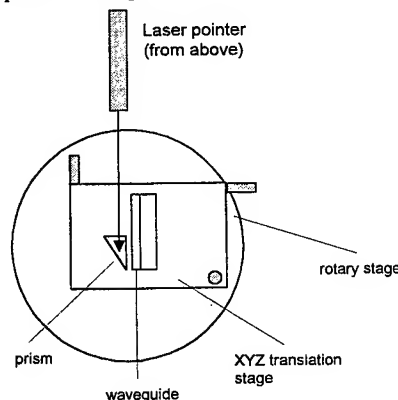


Fig. 4 Position adjustment of the prism coupler

The adjustment of the position of the prism was done by sliding the XYZ stage until the position of the light spot striking the prism was unchanged when the rotating table was slowly rotated. By achieving the position of the prism coupler, the measurement of the reference angle in the next step can be worked out.

3.2.2 Measurement of the reference angle

The purpose of the measurement of the reference angle is to determine the normal line of the prism surface such that the coupling angle of light can be measured. Here again, a laser light was used as light source for aligning the measurement. The set up is shown in Fig. 5.

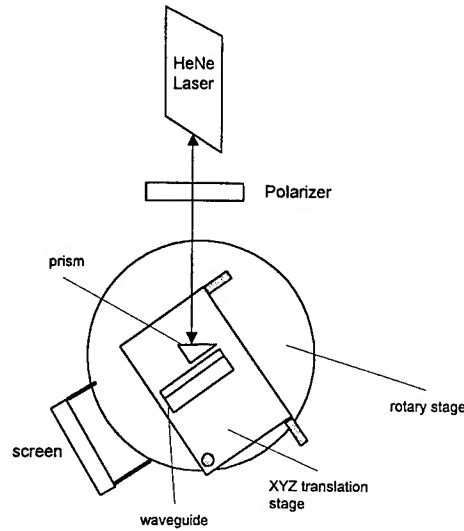


Fig. 5 Measurement set up of reference angle

If the reflected light striking the prisme surface is precisely coincidence and in opposite direction with the incident light, then the reference angle θ_r can be read on the angle scale of the rotating table.

3.2.3 Measurement of the coupling angle

From eq. (7) in the previous section, a relation between the effective index n_{eff} and the light coupling angle can be obtained as follows,

$$n_{eff} = n_p \sin \theta_p \quad (9)$$

Based on Snell's lawn for light refraction, it is obtained

$$n_p \sin \rho = n_1 \sin \alpha \quad (10)$$

and the solution gives

$$\rho = \sin^{-1}[\sin \alpha / n_p] \quad (11)$$

$$\alpha = \varepsilon - \rho \quad (12)$$

Substituting eq. (11) to eq. (12) gives

$$\theta_p = \varepsilon + \sin^{-1}[\sin \alpha / n_p] \quad (13)$$

Furthermore, substituting eq. (12) to eq. (13) we then abtain

$$n_{eff} = n_p \sin (\varepsilon + \sin^{-1}[\sin \alpha / n_p]) \quad (14)$$

Equation (14) is used to determine the values of the refractive index of the modes guided in the film layer of the substrate, both for TE and TM modes.

Similarly, the solution for the guided mode making an angle α from the coupling area is given by

$$n_{\text{eff}} = n_p \sin \left(\varepsilon - \sin^{-1} [\sin \alpha / n_p] \right) \quad (15)$$

Equation (14 and (15) are used as references to determine the values of effective indices of guided modes, both for TE and TM modes.

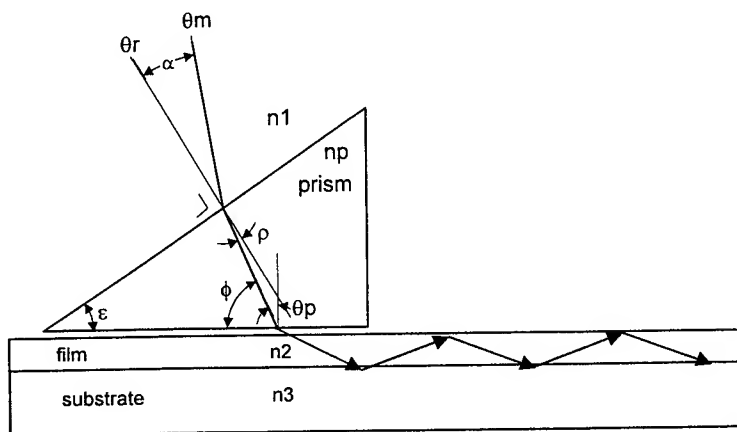


Fig. 6 Measurement scene of coupling angle

The measurement set up of the coupling angle has been shown in Fig. 2. The figure shows an angle formed by the light beam moving farther from the interface of the film layer and the air layer.

First, the reference angle θ_r should be measured to obtain the normal line of the prism surface. This line is perpendicular to the of the prism as shown in the figure. Then the angle α can be achieved from the difference of θ_m and θ_r , or $\alpha = \theta_m \pm \theta_r$. Furthermore, using eq. (14) and (15) the effective index can be calculated, substituting the values of n_p and ε .

4. RESULT AND DISCUSSION

The measurement was worked out on the samples of planar waveguide fabricated by K^+ - Na^+ ion exchange on BK7 substrate for various time duration of process at the temperature of 385° . KNO_3 was used as K^+ ion source. From the result of coupling angle measurement, the effective index was calculated by the use of eq. (14). The values of n_p was taken from the Sellmeir equation as 2.59073 and the apex angle $\varepsilon = 44.9^\circ$.

The results were tabulated in Table 1 for TE modes and in Table 2 for TM modes. The tables show the values obtained for reference angle, coupling angle of the prism, and effective index for various time duration of ion exchange process. The coupling angle of the prism is divided into two columns, one was read on the measurement and the other was measured with respects to the reference. The study also shows that the ion exchange process is not effective to fabricate the waveguide for time duration less than 1.5 hours.

The relation between the effective refractive index of each mode and the time duration of the ion exchange is shown in Fig. 7. The values of effective index were ranging in an interval $1.5151 < n_{\text{eff}} < 1.60$ giving an index difference of 5.7%. The effective index of TE mode and TM mode does not have a large difference.

Table 1 Data of the m-line measurement of TE modes for various time duration of ion exchange process

Sample	t (hour)	Reference angle θ_r (°)	Read prism coupling angle θ_m (°)	Prism coupling angle with respect to reference $\alpha = \theta_r - \theta_m$ (°)	Effective index refractive (n_{eff})
BK71	0,5				
BK72	1				
BK73	1,5	244.47	$m_0 = 220.53$	23.94	1.5182
BK74	2	246.57	$m_0 = 223.55$	23.02	1.5303
BK75	3	241.27	$m_0 = 221.67$	19.60	1.5752
			$m_1 = 218.43$	22.84	1.5326
BK76	4	240.18	$m_0 = 222.27$	17.91	1.5974
			$m_1 = 219.13$	21.05	1.5561
BK77	6	240.67	$m_0 = 222.57$	18.10	1.5949
			$m_1 = 220.60$	20.07	1.5690
BK78	12	244.83	$m_0 = 230.33$	14.50	1.6423
			$m_1 = 227.68$	17.15	1.6074
			$m_1 = 221.03$	23.80	1.5200
BK79	24	240.77	$m_0 = 226.73$	14.04	1.6483
			$m_1 = 224.10$	16.67	1.6138
			$m_2 = 220.92$	19.85	1.5719
			$m_3 = 217.50$	23.27	1.5269
BK710	48	240,02	$m_0 = 229.10$	10.92	1.6891
			$m_1 = 227.28$	12.74	1.6654
			$m_2 = 224.08$	15.94	1.6234
			$m_3 = 222.80$	17.84	1.6065
			$m_4 = 217.50$	21.19	1.5543

Moreover, the number of modes with respects to the time duration of the ion exchange process for both TE and TM modes is shown in Fig. 8. The figure shows that the number of modes will increase when the time duration increases. It can be understood because the increase of ion exchange time duration will increase the thickness of film and the refractive index of the film surface. Particularly, for BK71 and BK72 for time $t = 0.5$ hour and $t = 1$ hour, the number of modes guided in the film was not detected because the intensity of light caught on the screen is very weak. This is not due to the experimental condition but because the length of the waveguide is too short. Therefore the coupling process does not reach an effective condition such that the mode image was weakly or almost cannot be detected.

Table 2 Data of the m-line measurement of TM modes for various time duration of ion exchange process

Sample	t (hour)	Reference angle θ_r (°)	Read prism coupling angle θ_m (°)	Prism coupling angle with respect to reference $\alpha = \theta_r - \theta_m$ (°)	Effective index refractive (n_{eff})
BK71	0,5				
BK72	1				
BK73	1,5	238.87	$m_0 = 214.93$	23.94	1.5183
BK74	2	242.42	$m_0 = 219.35$	23.07	1.5296
BK75	3	242.25	$m_0 = 222.78$	19.47	1.5769
			$m_1 = 221.33$	20.92	1.5578
BK76	4	241.67	$m_0 = 222.77$	18.90	1.5844
			$m_1 = 221.65$	20.02	1.5697
BK77	6	243.05	$m_0 = 224.08$	18.97	1.5835
			$m_1 = 223.12$	19.93	1.5709
BK78	12	244.52	$m_0 = 228.55$	15.97	1.6230
			$m_1 = 225.78$	18.74	1.5866
			$m_2 = 221.33$	23.19	1.5280
BK79	24	241.7	$m_0 = 226.57$	15.13	1.6399
			$m_1 = 224.77$	16.93	1.6103
			$m_2 = 222.85$	18.85	1.5851
			$m_3 = 218.63$	23.07	1.5296
BK710	48	243.28	$m_0 = 232.33$	10.95	1.6887
			$m_1 = 226.83$	16.45	1.6167
			$m_2 = 224.18$	19.10	1.5818
			$m_3 = 223.28$	20.00	1.5699
			$m_4 = 221.50$	21.78	1.5465

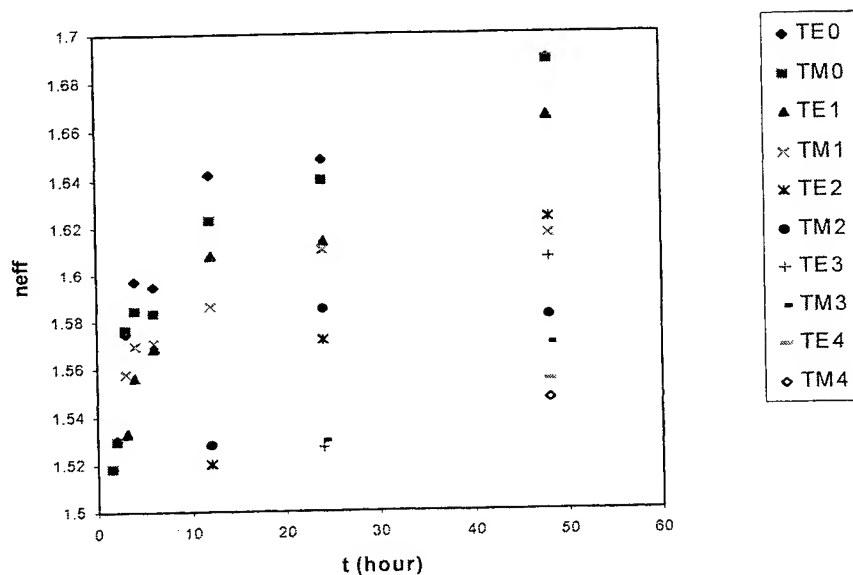


Fig. 7 The profile of effective index for TE/TM modes with respects to time duration

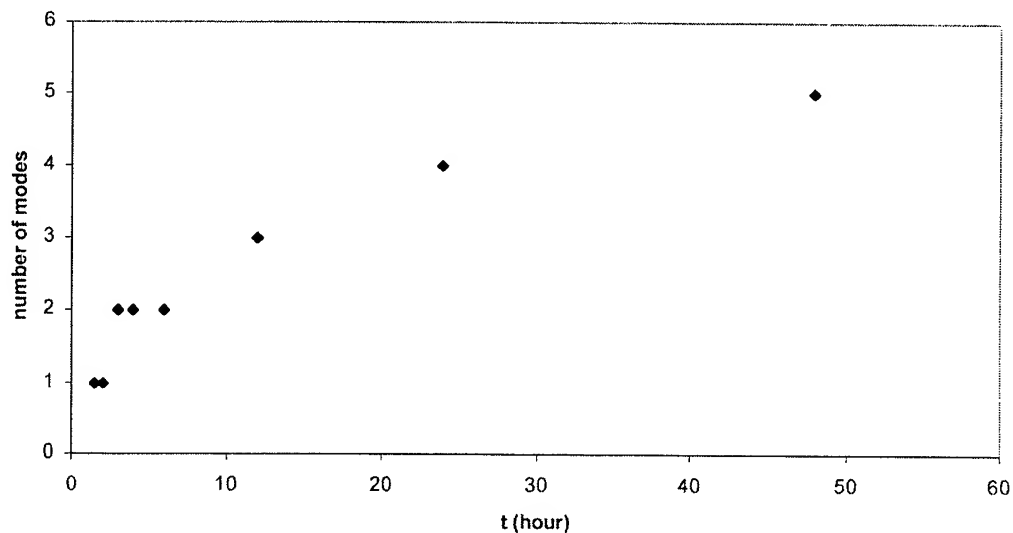


Fig. 8 The number of guided modes with respects to the time duration

5. CONCLUSION

A study on the characterization of planar waveguide has been proposed by developing an m-line technique to measure the effective index of the waveguide. A prism coupler was accomplished in this technique and the result is represented in terms of effective index and number of modes respectively, as a function of time duration of fabrication process. The proposed technique has been proved to be simple and effective characterization method of planar waveguides with accuracy.

ACKNOWLEDGEMENTS

The authors would like to acknowledge their colleagues from University of Indonesia, Dr. Hamdani Zain and Mrs Retno Wigayatri for technical assistance and discussion, and Mr. Masagus Densi for providing the samples.

REFERENCES

1. R. Ulrich and R. Torge, "Measurement of thin film parameters with a prism coupler," *Applied Optics*, Vol. 12, No.12, pp. 2901-2908, 1973.
2. H. Kogelnik, *Integrated Optics: Topics in Applied Physics* (ed. T.Tamir), Springer Verlag, New York, 1985.
3. Steven T. Kirsch, "Determining of refractive index and thickness of thin films from prism coupler measurement," *Applied Optics*, Vol. 20, No. 12, pp. 2085-2088, 1981.
4. Joanna Jansson, "Prism coupling selectivity in anisotropic uniaxial waveguide," *Applied Optics*, Vol.20, No. 2, pp. 374-379, 1981.
5. Joseph E. Gortych and Dennis G. Hall, "Fabrication of planar optical waveguide by K⁺-ion exchanged in BK7 and pyrex glass," *IEEE journal of Quantum Electronics*, Vol. QE-22, No.6, pp. 892-895, 1986.

Determination of white and $1/f$ FM noise components of semiconductor laser spectrum by a delayed self-heterodyne interferometer using short delay fiber

Mohammed Nazrul Islam^{a*}, Tadakazu Nomura^b, Masaaki Imai^c and Md. Quamrul Huda^a

^a Department of Electrical and Electronic Engineering, Bangladesh University of Engineering and Technology, Dhaka-1000, Bangladesh

^b Toshiba Corporation, Yokohama 247-0006, Japan

^c Department of Electrical and Electronic Engineering, Muroran Institute of Technology, Muroran 050-8585, Japan

ABSTRACT

The measurement and evaluation of power spectrum of a semiconductor laser by delayed self-heterodyne interferometer is demonstrated with the use of a short delay fiber. The measured spectrum is analyzed numerically including the effect of a delay time much less than the laser coherence time. The theoretical formulation developed here is found to be accurate since it exhibits a peak with finite width at the center frequency of the measured lineshape. The white and $1/f$ components of the laser FM noise are then separated successfully by fitting numerical analysis to the experimental results.

Keywords: Delayed self-heterodyne interferometer, Frequency modulation, Power spectrum, Semiconductor laser, White noise.

1. INTRODUCTION

With increasing growth of optical communication and sensing systems, the development of narrow linewidth semiconductor lasers has drawn considerable research interests. In addition to the white frequency modulation (FM) noise, a residual noise component is observed, termed as the $1/f$ FM noise, which imposes limitation upon narrowing the laser spectral linewidth¹. The spectral density of this $1/f$ FM noise is inversely proportional to the frequency, but is independent of the laser output power². Thus it determines the ultimate receiver sensitivity limit in coherent optical communication system³. The accurate measurement of these white and $1/f$ FM noise components of semiconductor laser spectrum has, therefore, become necessary to characterize their effects on the system performance. The delayed self-heterodyne interferometer (DSHI) has been widely used for estimating the spectral linewidth of semiconductor laser due to its feature that a resolution of better than several hundred kilohertz can easily be achieved without the use of a stable local oscillator⁵.

In this study, the power spectrum of a semiconductor laser is determined by a delayed self-heterodyne interferometer which uses a short delay fiber rather than a long fiber required in the original method. A theoretical formulation is developed to analyze the obtained spectral nature of the laser. Then the white and $1/f$ FM noise components of the laser linewidth are separately determined through numerical solution of the laser spectrum.

2. THEORETICAL DEVELOPMENT

In a delayed self-heterodyne interferometer, the output of a semiconductor laser is split into two beams, one of which is time-delayed while passing through a single-mode optical fiber and the other beam is frequency shifted by an acousto-optic modulator (AOM), as shown in Fig. 1. The present method utilizes a short fiber having a delay time (τ_d) which is less than the laser coherence time (τ_c). The beat signal beam at the output of the interferometer is detected by a photodetector and then analyzed.

The spectrum of the laser output is given by

$$S(\omega) = \int_{-\infty}^{\infty} \gamma(\tau) \exp[-j\omega\tau] d\tau \quad (1)$$

where $\gamma(\tau)$ can be determined as follows⁵

$$\begin{aligned} \gamma(\tau) &= \cos(\Omega\tau) \exp \left[-4 \int_{-\infty}^{\infty} S_{FM}(f) \left(\frac{\sin(\pi f \tau)}{f} \right)^2 (1 - \cos 2\pi f \tau_d) df \right] \\ &= \cos(\Omega\tau) \times \gamma_W(\tau) \times \gamma_F(\tau) \end{aligned} \quad (2)$$

Here, $\Omega = 2\pi f_m$, f_m is the frequency shift occurred due to the AOM and $S_{FM}(f)$ is the spectrum of laser FM noise. The laser FM noise consists of a white noise component and a $1/f$ noise component which are defined as follows²

$$S_{FM}(f) = \frac{C}{P} + \frac{K}{f} \quad (3)$$

where P is the laser output power, C and K are constants. The two terms in the above equation are responsible for the two FM noise components, respectively. Therefore, the white noise component of laser spectrum can be determined and simplified as³

$$\gamma_W(\tau) = \begin{cases} \exp\left(-2\pi^2 \frac{C}{P} |\tau|\right), & |\tau| < \tau_d \\ \exp\left(-2\pi^2 \frac{C}{P} \tau_d\right), & |\tau| > \tau_d \end{cases} \quad (4)$$

Therefore, we can determine the spectrum of white FM noise as

$$\begin{aligned} S_W(\omega) &= \exp\left[-2\pi^2 \frac{C}{P} \tau_d\right] \cdot \delta(\omega) \\ &+ \frac{2\pi^2 C/P}{\omega^2 + (2\pi^2 C/P)^2} \left[1 - \exp\left[-2\pi^2 \frac{C}{P} \tau_d\right] \left\{ \cos(\omega\tau_d) + 2\pi^2 \frac{C}{P} \tau_d \frac{\sin(\omega\tau_d)}{\omega\tau_d} \right\} \right] \end{aligned} \quad (5)$$

While using a long delay fiber, the measured lineshape, $S_W(\omega)$, becomes Lorentzian as we can understand from the above equation.

$$S_W(\omega) = \frac{2\pi^2 C/P}{\omega^2 + (2\pi^2 C/P)^2}, \quad \text{for } \tau_d \gg \tau_c \quad (6)$$

Thus the half width at half maximum (HWHM) of the laser spectrum due to white FM noise, B_c , can be defined as $2 B_c = \pi C/P$. Note that a factor of 2 is included here because of the fact that the measured spectral linewidth by DSHI method is twice the original linewidth of semiconductor laser³.

Now, the spectrum of $1/f$ FM noise is known to be Gaussian when the delay time (τ_d) is large. But for small values of τ_d , the spectrum deviates from the Gaussian distribution [4] and then it becomes difficult to evaluate

the spectrum. However, for practical purposes, the $1/f$ FM noise spectrum can well be approximated as a Lorentzian distribution and thus $\gamma_F(\tau)$ can be assumed to have the following form.

$$\gamma_F(\tau) = \exp[-2\pi(2r_s)|\tau|] \quad (7)$$

where r_s is the full width at half maximum (FWHM) linewidth of the laser spectrum due to $1/f$ FM noise.

Finally, the resultant laser spectrum can be found by taking Fourier transformation of equation (2) using equations (4) and (7).

$$\begin{aligned} S(\omega) = & \frac{4\pi(2B_c + 2r_s)}{(4\pi B_c + 4\pi r_s)^2 + (\omega - \Omega)^2} \\ & \times \left\{ 1 - \exp[-2\pi(2B_c + 2r_s)\tau_d] \left[\cos(\omega - \Omega)\tau_d + \frac{\omega - \Omega}{2B_c + 2r_s} \sin(\omega - \Omega)\tau_d \right] \right\} \\ & + \frac{4\pi r_s}{(4\pi r_s)^2 + (\omega - \Omega)^2} \exp[-2\pi(2B_c + 2r_s)\tau_d] \\ & \times \left[\cos(\omega - \Omega)\tau_d - \frac{\omega - \Omega}{2r_s} \sin(\omega - \Omega)\tau_d \right] \end{aligned} \quad (8)$$

where the total HWHM linewidth of the semiconductor laser spectrum is given by

$$\delta f = B_c + \frac{r_s}{2} \quad (9)$$

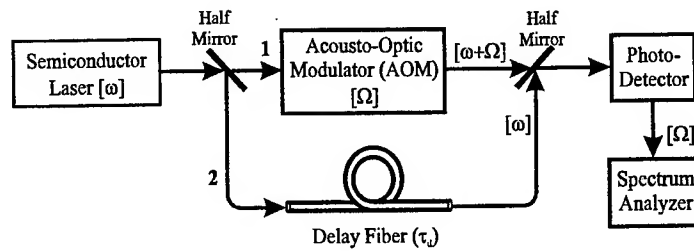


Fig. 1: Principle of delayed self-heterodyne interferometer

3. RESULTS AND DISCUSSION

When a short delay fiber is used, the two beams of the interferometer are no longer uncorrelated. Hence, the measured spectrum deviates from the original Lorentzian lineshape of the laser spectrum. Figure 2 shows the spectral lineshape by the dotted line for a single-mode semiconductor laser. The acousto-optic modulator (AOM) frequency is 80 MHz. A short fiber of length 2 m is utilized as the delay fiber. The results show that the lineshape has ripples in the sidebands and a spike at the center frequency having a finite width.

When the delay time (τ_d) is large enough, the laser spectrum is Lorentzian and hence it is difficult to separate the white and $1/f$ FM noise components of the laser linewidth. However, using short delay time, the spectrum can be analyzed by equation (11) which allows the separation of the noise components. The theoretical lineshape was fitted to the experimental results. As shown in Fig. 2, the theoretical formulation closely depicts the practical lineshape of the laser output. From the best-fitting of the theoretical equation to the experimental data, we obtained that $B_c = 2.1$ MHz and $r_s = 600$ kHz. Similar measurement and analysis were also carried out with a 3 m

fiber used as the delay line. The well approximation of the experimental results by the theoretical formulation was verified and the values of $B_c = 2.2$ MHz and $r_s = 900$ kHz were found from the best fitting analysis. These findings indicate that the laser spectral width due to white FM noise (B_c) is maintained within 2.1 to 2.2 MHz irrespective of the delay fiber length when the injection current is 71.5 mA. However, the linewidth due to $1/f$ FM noise (r_s) increases with increase in delay time.

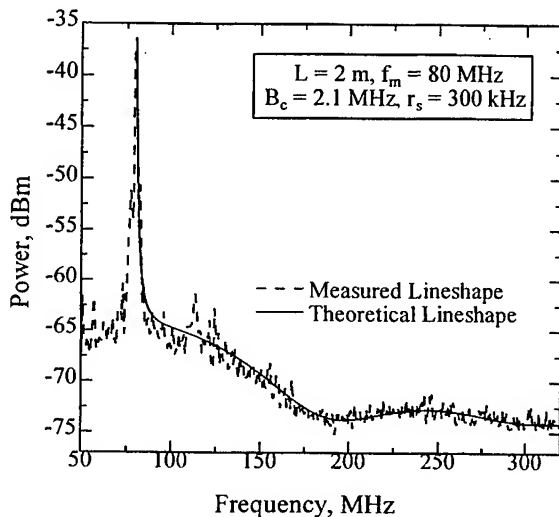


Fig. 2: Laser power spectrum measured by DSHI; dotted: measured, solid: theoretical

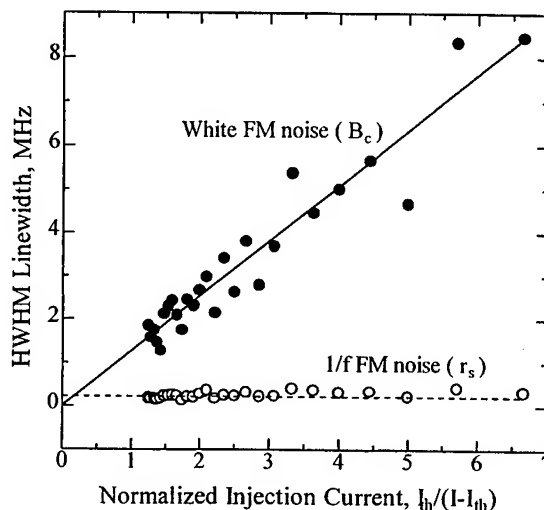


Fig. 3: Variation of white and $1/f$ FM noise components with injection current

Then the spectral linewidth of the laser output was measured by varying the injection current of the laser. With the values of B_c and r_s obtained from the curve-fitting in each case, the white and $1/f$ FM noise components of the laser spectrum were separately determined and the results are shown in Fig. 3. The linewidth due to white FM noise increases with decreasing injection current and hence decreasing power. However, the linewidth due to $1/f$ FM noise does not change with changes in current and thus it determines the residual linewidth in the measurement of the laser spectrum.

4. CONCLUSION

The spectral linewidth of a semiconductor laser is determined by a delayed self-heterodyne interferometer using a short delay fiber. A mathematical analysis for the lineshape and spectral width of a semiconductor laser is developed assuming the $1/f$ noise spectrum to be Lorentzian. The formulation clearly describes the lineshape of the laser output including a the finite width of the peak at the center frequency. Also it provides efficiently the separation of the white and $1/f$ noise components of the laser FM noise.

REFERENCES

1. D. Welford and A. Mooradian, "Output power and temperature dependence of the linewidth of single-frequency CW (GaAl)As diode lasers," *Appl. Phys. Lett.*, **40**, pp. 865-867, 1982.
2. K. Kikuchi and T. Okoshi, "Dependence of semiconductor laser linewidth on measurement time: evidence of predominance of $1/f$ noise," *Electron. Lett.*, **21**(22), pp. 1011-1012, 1985.

3. K. Kikuchi, "Effect of $1/f$ -type FM noise on semiconductor-laser linewidth residual in high-power limit," *IEEE J. Quantum Electron.*, **25**(4), pp. 684-688, 1989.
4. L. B. Mercer, " $1/f$ frequency noise effects on self-heterodyne linewidth measurements," *J. Lightwave Technol.*, **9**(4), pp. 485-493, 1991.
5. T. Okoshi, K. Kikuchi and A. Nakayama, "Novel method for high resolution measurement of laser output," *Electron. Lett.*, **16**(16), pp. 630-631, 1980.
6. L. E. Richter, H. I. Mandelberg, M. S. Kruger and P. A. McGrath, "Linewidth determination from self-heterodyne measurements with subcoherence delay times," *IEEE J. Quantum Electron.*, **22**(11), pp. 2070-2074, 1986.
7. M. Okai, T. Tsuchiya, A. Takai and N. Chinone, "Factors limiting the spectral linewidth of CPM-MQW-DFB lasers," *IEEE Photon. Technol. Lett.*, **4**(6), pp. 526-528, 1992.

SESSION 9

Planar Waveguides and Devices

Reconstruction of Refractive Index Profile of Planar Waveguide using Inverse WKB Method

Andrew Supit^{*a}, Henri P. Uranus^{a,b}, Muljono^a, John E. Batubara^a

^aUniversity of Pelita Harapan, Lippo Karawaci, Tangerang 15811, Indonesia

^bUniversity of Indonesia, Salemba 4, Jakarta 10430, Indonesia

ABSTRACT

A characterization method of planar waveguides, namely m-line measurement has been utilized to reconstruct refractive index profile in planar waveguide. This method gives some values of incident angle that can be coupled in to waveguide, which after some mathematical calculations can provide its mode indices. To reconstruct the refractive index profile from mode indices as a function of normalized film thickness we use Inverse Wentzel-Kramers-Brillouin method. Furthermore, we select the value of n_0 that give the smoothest refractive index profile by finding the minimum sum of the squares of second differences of the profile. For this purpose, we implement reiterative, trial and error method on some values above the measured fundamental effective index value as a guess of the surface index. The result has been smoothed using curve fitting algorithm to exponential and Gaussian profile. The results confirm that index profile of planar waveguide can be reconstructed mathematically and the profile can be obtained more accurate by the proposed curve fitting technique than the basic IWKB method.

Keywords: Refractive index profile, m-line measurement, Inverse WKB, curve fitting, planar waveguide.

1. INTRODUCTION

Planar waveguide structures have been widely used for many optical components, for example: directional coupler, optical splitter, optical waveguide harmonic generator, etc. The rapid growth of implementation of planar waveguide-based optical components in telecommunication and electronics industry makes planar waveguide design become more important and must be developed to meet the industry demand.

In designing optical waveguides, characterization processes are needed to establish some fabrication parameters. The most important part of these characterization processes is determination of refractive index distribution. Because the refractive index distribution of waveguides prepared by various methods are different, then by determining the refractive index distribution of planar waveguides, we can analyze it as a function of fabrication parameters. According to Shiozawa et al.³ methods for determining the refractive index distribution are classified into three groups: 1) Far-field exit radiation pattern of the guided mode. 2) Near-field exit radiation pattern of the guided mode^{8,9}. 3) Effective index method. This effective index method has advantages of being relatively simple and non-destructive. This method is accomplished by measuring the propagation angles of the various modes (namely m-line measurement)^{5,6}, computing the effective indices of guided modes and then by extending the inverse WKB approximation we can derive the refractive index profile from the measured effective index indices. The inverse WKB method proposed by White and Heidrich¹ is based on certain approximations, that each point is connected to its turning point by piecewise linear lines. This leads to some error, particularly for extreme order modes and waveguides with only limited number of mode indices. Regarding the approximations, this method in some cases also can't reconstruct a smooth refractive index profile, especially at turning points, although a method that minimizes the sum of the squares of the second differences of the profile has been implemented.

In this paper we apply a fitting method namely Gauss-Newton⁴ to determine the parameters of refractive index distribution function based on the IWKB method. Firstly we implement IWKB method on sets of mode indices of the waveguide

*Correspondence: Department of Electrical Engineering, Faculty of Industrial Technology, University of Pelita Harapan, Lippo Karawaci, Tangerang 15811, Telephone: 62-21-5460901; Fax: 62-21-5460910

samples to reconstruct the refractive index profiles, then by choosing appropriate distribution functions and processing the obtained IWKB data using Gauss-Newton method, we determine the parameters of refractive index distribution function better. Application of this method to exponential and Gaussian refractive index profile samples are demonstrated to show that this method can determine the parameters more accurately.

2. THEORY

According to WKB method, the eigenvalue equation for a TE mode of a graded index waveguide that slightly decreasing from the waveguide surface can be written as¹:

$$\int_0^{x_m} \left[n^2(x) - n_m^2 \right]^{1/2} dx = \frac{4m-1}{8} \quad m = 1, 2, \dots, M. \quad (1)$$

Where $n(x)$ is the refractive index distribution function of a waveguide, x_m is the turning point of mode number- m and n_m is the effective refractive index of mode number- m . The x_m is defined by $n(x_m) = n_m$. Phase shift at the waveguide surface is $\pi/2$ and phase shift at the turning point is $\pi/4$. By assuming that each turning point is connected to its adjacent turning point by piecewise linear lines, we can derive an approximate solution of equation (1) in term of x_m . The solution is¹:

$$x_m = x_{m-1} + \left[\frac{3}{2} \left(\frac{n_{m-1} + 3n_m}{2} \right)^{-1/2} (n_{m-1} - n_m)^{-1/2} \right] \times \left\{ \left(\frac{4m-1}{8} \right) - \frac{2}{3} \sum_{k=1}^{m-1} \left(\frac{n_{k-1} + n_k}{2} + n_m \right)^{1/2} \frac{(x_k - x_{k-1})}{(n_{k-1} - n_k)} \left[(n_{k-1} - n_m)^{3/2} - (n_k - n_m)^{3/2} \right] \right\} \quad (2)$$

for $m=2, 3, \dots, M$.

Where x_1 is defined by¹:

$$x_1 = \frac{9}{16} \left(\frac{n_0 + 3n_1}{2} \right)^{-1/2} (n_0 - n_1)^{-1/2} \quad (3)$$

By using m -line measurement, we only measure the mode indices n_1, n_2, \dots, n_M . Therefore, the value of surface index (n_0) must be obtained by selecting a value larger than value of n_1 that gives the smoothest profile. The smoothest profile can be achieved by minimizing the sum of the squares of the second differences of the profile with respect to every guessed surface index value as discribed (by reiterative trial and error). Usually, in order to save computation time, we limit the range of the trial surface index value from n_1 to n_1+2 .

By implementing IWKB technique as described above, we obtain a set of data pairs that consist of turning points and refractive indices of mode number- m respectively, e.g. $(x_0, n_0), (x_1, n_1), (x_2, n_2), \dots, (x_M, n_M)$, where M is the highest order of guided modes. By choosing an appropriate distribution function, we fit this function to these data pairs using Gauss-Newton method.

Matrix equation for Gauss-Newton method can be written as⁴:

$$[Z_j]^T [Z_j] \{\Delta A\} = [Z]^T \{D\} \quad (4)$$

Where $[Z_j]$ and $[Z_j]^T$ are partial derivative matrix and its tranposed matrix of fitted function respectively, evaluated at j -th guess.

Matrix $[Z_j]$ can be written as:

$$[Z_j] = \begin{bmatrix} \frac{\partial n(x_1)}{\partial a} & \frac{\partial n(x_1)}{\partial b} \\ \frac{\partial n(x_2)}{\partial a} & \frac{\partial n(x_2)}{\partial b} \\ \vdots & \vdots \\ \frac{\partial n(x_M)}{\partial a} & \frac{\partial n(x_M)}{\partial b} \end{bmatrix} \quad (5)$$

Where a and b are the parameters to be determined.

$\{\Delta A\}$ is a column matrix containing changes of parameters, that can be written as:

$$\{\Delta A\} = \begin{Bmatrix} \Delta a \\ \Delta b \end{Bmatrix} \quad (6)$$

Where Δa and Δb define changes of parameter a and b respectively.

$\{D\}$ is a matrix vector containing differences between measured and function value. $\{D\}$ can be written as:

$$\{D\} = \begin{Bmatrix} n_1 - n_j(x_1) \\ n_2 - n_j(x_2) \\ \vdots \\ n_M - n_j(x_M) \end{Bmatrix} \quad (7)$$

Where $n_j(x_1), n_j(x_2), \dots, n_j(x_M)$ define the function value evaluated at j -th guess.

Equation (2) is iterated for:

$$a_{j+1} = a_j + \Delta a \quad (8)$$

$$b_{j+1} = b_j + \Delta b \quad (9)$$

until sufficient small percentage value of relative error of parameter a and b can be reached.

It should be noted that the selection of initial guess is very important, that some values of initial guess must be tried until the iteration converges. To make this process faster, we choose the closest value to actual parameters which we try to find.

3. DEMONSTRATION OF THE METHOD

In order to test the method, we consider two types of refractive index distribution function, i.e. exponential distribution and Gaussian distribution. Each of the two distribution functions has two parameters, which will be obtained by implementing the IWKB and fitting method. Firstly we get sets of mode indices calculated using Characteristic Matrix method proposed by Uranus and Batubara² from each distribution function. We regard these calculated mode indices as the measured mode indices, then we retrieve the distribution function from sets of the calculated mode indices using IWKB technique and finally we reconstruct the refractive index distribution function using Gauss-Newton fitting technique.

3.1. Exponential distribution

For a planar waveguide, the exponential refractive index distribution function is represented by³:

$$n(x,a,b) = n_c \quad x < 0 \quad (10)$$

$$n(x,a,b) = a \exp(-bx) + n_s \quad x \geq 0 \quad (11)$$

Where n_c is the refractive index in the cladding region, n_s is the refractive index of substrate, $a=\Delta n=n_0-n_s$, n_0 determine the surface index and $b=1/d$ where d determine the depth factor of the waveguide.

In first case, we refer to profile provided by Shiozawa et al.³ as a sample with nine modes, with $n_c=1$, $n_s=2.177$, $\Delta n=0.0987$ and $d=2.230 \mu\text{m}$. We regard these values as the actual values. A set of mode indices is calculated using characteristic matrix method² for $\lambda=0.6328 \mu\text{m}$. The calculated mode indices are shown in Table 1 and the parameter $a=\Delta n$ and $b=1/d$ are computed for both IWKB method and fitting technique as described in previous section. In fitting process, initial guess $a_j=2.177$ and $b_j=1$ were chosen for this sample.

The result of refractive index profile reconstruction for Sample 1 is shown in Figure 1. It is obvious that by using fitting technique, we can obtain smoother profile than if only IWKB method is used. The fitted results are $n_0=2.2729$ and $d=2.3422$ which show better agreement with the actual values, compared to basic IWKB method results. For comparison we list the results in Table 2.

White and Heidrich have noted that the arbitrariness in n_0 is most critical for the first mode. Then, with regards to this behavior, we have reconstructed another profile of Sample 1 with n_0 is intentionally incorrectly guessed to 2.25565 to show how it mainly effect the result of fitting technique. The computational result is shown in Figure 2. It visually shows that by using the fitting technique we can reduce fluctuation of the lower order modes of the resulted profile even when wrong surface index value is used. For comparison, we list the results in Table 3. It also shows that the value of n_0 obtained by the fitting technique is still closer to its actual value, although we fail to obtain better result for d .

Table 1. Mode Indices of sample with exponential refractive index distribution (Sample 1)

Sample 1	
$n_c=1$; $n_s=2.177$; $\Delta n=0.0987$; $d=2.2230 \mu\text{m}$; $\lambda=0.6328 \mu\text{m}$	
Mode Number	Mode Indices
1	2.242989516519558
2	2.221795099435605
3	2.207573653993736
4	2.197319920849242
5	2.189818803149381
6	2.184411020621575
7	2.180680312363579
8	2.178335536357855
9	2.177027803400416

Table 2. Parameters comparison of Sample 1.

Parameters	Actual Value	Plain IWKB Value	Fitted Value
n_0	2.2757	2.2711	2.2729
$d (\mu\text{m})$	2.2230	2.3549	2.3422

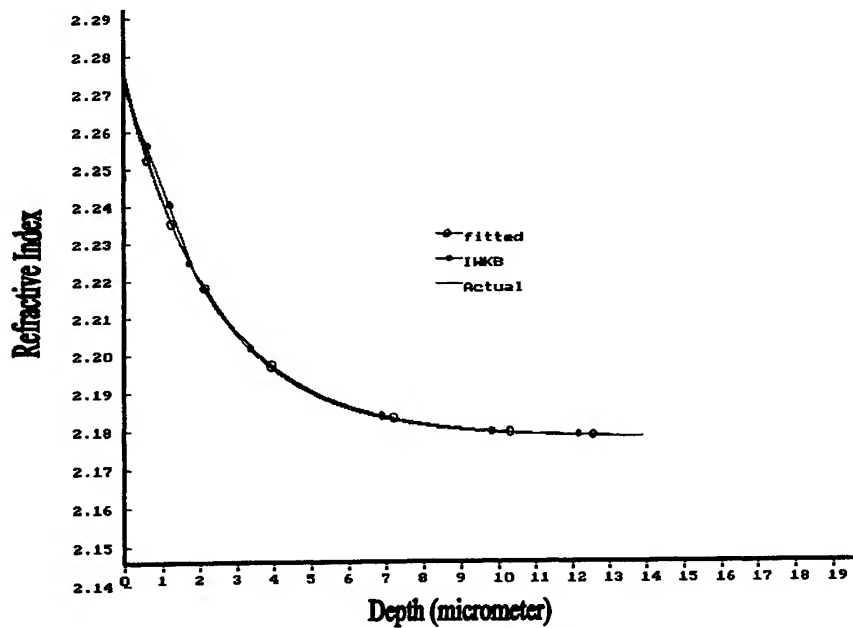


Figure 1. Refractive Index profile reconstruction result for Sample 1.
Actual exponential profile, IWKB profile and fitted profile based on the set of mode indices.

Table 3. Parameters comparison of Sample 1 with $n_0=2.5565$

Parameters	Actual Value	Plain IWKB Value	Fitted Value
n_0	2.2757	2.25565	2.26130
d (μm)	2.2230	2.34534	2.80156

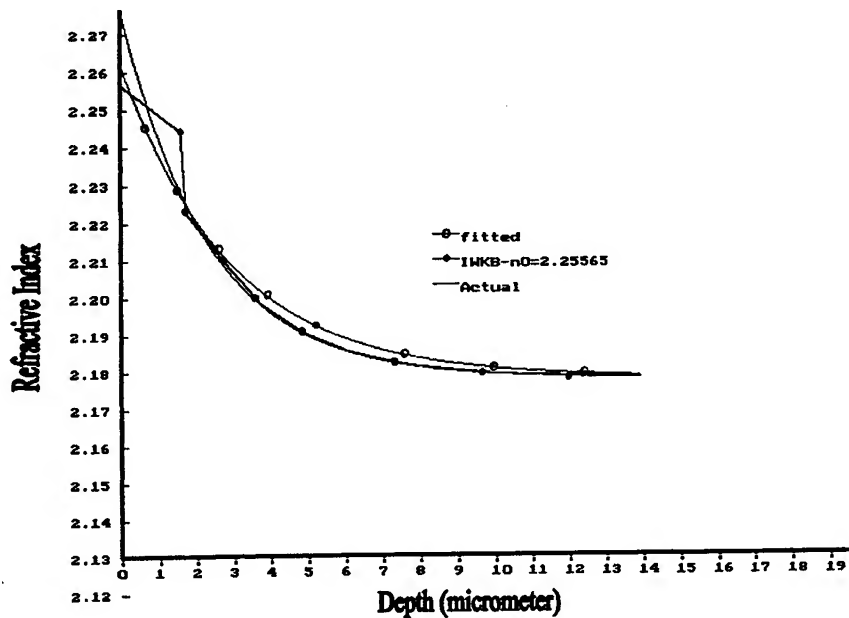


Figure 2. Refractive Index profile reconstruction result for Sample 1 with $n_0=2.5565$ (wrong guess).
Actual exponential profile, IWKB profile with $n_0=2.5565$ and fitted profile based on the set of mode indices.

3.2 Gaussian Distribution

For a planar waveguide, the Gaussian refractive index distribution function is represented by^{3,7}:

$$n(x,a,b) = n_c \quad x < 0 \quad (12)$$

$$n(x,a,b) = a \exp(-(bx)^2) + n_s \quad x \geq 0 \quad (13)$$

Where n_c is the refractive index in the cladding region, n_s is the refractive index of substrate, $a=\Delta n=n_0-n_s$, n_0 determine the surface index and $b=1/d^2$ where d determine the depth factor of the waveguide. The parameter a and parameter b are the parameters to be determined.

In this case, we generate a sample of Ti-diffused LiNbO₃ with five guided modes², $n_c=1$, $n_s=2.16596569$, $\Delta n=0.02$ and $d=10 \mu\text{m}$. We regard these values as the actual values, a set of mode indices is calculated using characteristic matrix method² for $\lambda=1.3 \mu\text{m}$. The calculated mode indices are shown in Table 4 and the parameter $a=\Delta n$ and $b=1/d^2$ are computed for both IWKB method and fitting technique as described in previous section. In fitting process, initial guess $a_j=2.16596569$ and $b_j=1$ were chosen for this Sample.

The result of refractive index profile reconstruction for Sample 2 is shown in Figure 3. It visually shows that also by using the fitting technique, we can obtain smoother profile than if only IWKB method is used. The fitted results are $n_0=2.1672$ and $d=9.641$ which show better agreement with the actual values, compared to plain IWKB method results. For comparison we list the results in Table 5.

We also conduct the same experiment as we have done before for exponential distribution to show how the arbitrariness in n_0 for the first mode mainly effects the result of fitting technique. The results also show good agreement with the results obtained in the previous experiment.

Table 4. Mode Indices of sample with Gaussian Refractive Index Distribution (Sample 2)

Sample 2 $n_c=1$; $n_s=2.16596569$; $\Delta n=0.02$; $d=10 \mu\text{m}$; $\lambda=1.3 \mu\text{m}$	
Mode Number	Mode Indices
1	2.161999741644183
2	2.157201667998022
3	2.153051043965975
4	2.149646635147939
5	2.147146233342612

Table 5. Parameters comparison of Sample 2

Parameters	Actual Value	Plain IWKB Value	Fitted Value
n_0	2.1659	2.1680	2.1672
$d (\mu\text{m})$	10	10.838	9.641

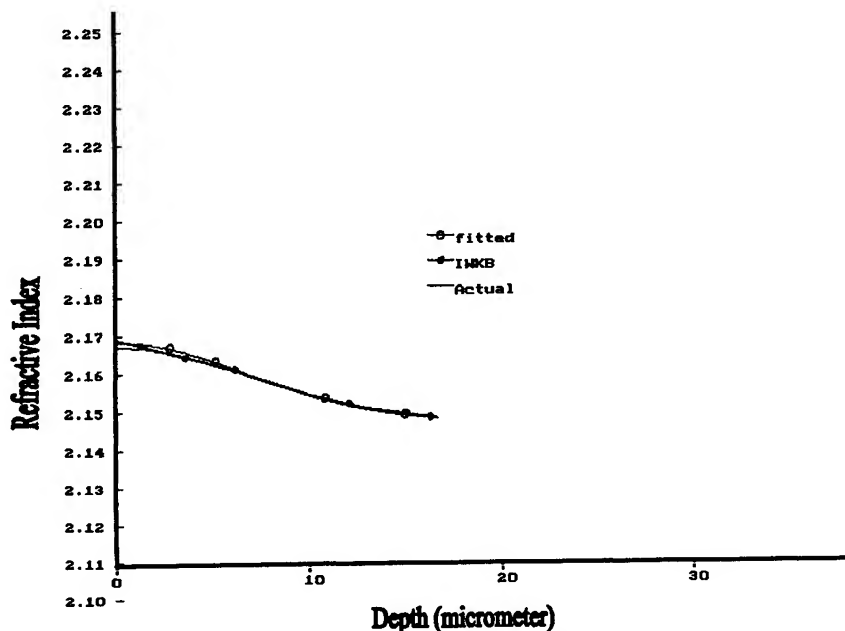


Figure 3. Refractive Index profile reconstruction result for Sample 2.
Actual Gaussian profile, IWKB profile and fitted profile based on the set of mode indices.

4. CONCLUSION

Gauss-Newton fitting technique has been implemented to determine the parameters of graded index planar waveguide. This method extends the IWKB technique and shows that it can determine the parameters of waveguide's refractive index distribution function more accurate than the plain IWKB technique. Two refractive index profile cases were considered in this paper, i.e. an exponential refractive index distribution waveguide and Gaussian refractive index distribution waveguide. The fitted parameters for these samples were in better agreement with the actual value than the parameters obtained from plain IWKB technique. For disturbed measured data of mode indices, particularly for wrong-determined surface index, this technique still has a better agreement-with the actual value for n_0 parameter-compared to basic IWKB technique.

ACKNOWLEDGEMENT

The First author would like to acknowledge Mrs. Rita Kencanawati, Ms. Elizabeth, Mr. Michael for their encouragement and Mr. Danny Handoko for technical assistance and encouraging this work.

REFERENCES

1. J.M White and P.F. Heidrich, "Optical waveguide refractive index profiles determined from measurement of mode indices: a simple analysis", *Applied Optics* **15**, pp. 151-155, 1976.
2. H. P. Uranus and J. E. Batubara, "Analisis Moda pada pandu gelombang optik berlapis jamak", *Optronika* **1**, pp. 34-42, 1997.
3. T. Shiozawa, H. Miyamoto, H. Ohta, M. Yamaguchi, and T. Oki, "Determination of two-dimensional Optical Waveguide Index Distribution Function Parameters from Effective Indexes", *Journal of Lightwave Technology* **8**, pp. 497-504, 1990.
4. S. C. Chapra and R. P. Canale, *Numerical Methods for Engineers*, Mc Graw-Hill Book Company, 1989.
5. R. Ulrich and R. Torge, "Measurement of Thin Film Parameters with a Prism Coupler", *Applied Optics* **12**, pp. 2901-2908, 1973.

6. S. T.Kirsch, "Determining the refractive index and thickness of thin films from prism coupler measurements", *Applied Optics* 20, pp. 2085-2089, 1981.
7. H. Kogelnik,"Theory of Optical Waveguides", in *Guided-Wave Optoelectronics*, Theodor Tamir, 26, pp. 7-88, Springer-Verlag, Berlin Heidelberg, 1998 .
8. K. Morishita, "Index profiling of three-dimensional optical waveguides by the propagation-mode near-field method", *J. Lightwave Technology* 4, pp. 1120-1124, 1986.
9. J. Helms, J. Schmidtchen, B. Schuppert, and K. Petermann, "Error analysis for refractive-index profile determination from near-field measurements", *J. Lightwave Technology* 8, pp. 625-633, 1990,

A planar add/drop 2-wavelength filter employing a blazed Bragg grating and a 3x3 asymmetric coupler

Keith W. Gaff#, François Ladouceur* and John D. Love#

Optical Sciences Centre
The Australian National University
Canberra ACT 0200
Australia

* Virtual Photonics Inc
Helmholtzstrasse, 2-9
10587 Berlin
Germany

ABSTRACT

We propose a novel 6-port planar waveguide coupler device for adding and/or dropping two different wavelengths from a WDM channel using a single grating. By writing a blazed Bragg grating into a few-moded core at a slight angle to the waveguide propagation direction, power can be coupled from the fundamental mode into higher-order, backward-propagating modes and vice-versa. Each such mode is channelled into a particular output port using an adiabatic splitter. Modelling results indicate that more than 99.99% of the power in the fundamental mode can be coupled into the higher-order modes at their respective Bragg wavelengths.

Keywords: gratings, couplers, multiplexing, demultiplexing, planar waveguides, asymmetric couplers

1. INTRODUCTION

Typically fibre Bragg gratings are written into optical fibres designed to support just one mode - the fundamental. In order to maximise the reflection of the fundamental mode at its Bragg wavelength, these gratings are written with the index modulation phase fronts perpendicular to the optical fibre axis and, therefore, parallel to the modal phase front. However, if the Bragg grating written in the single-moded fibre is tilted slightly away from the perpendicular to the optical fibre axis, i.e. is blazed, power can be coupled, and hence reflected, into any higher-order, backward-propagating cladding modes¹. Power is strongly reflected when the Bragg condition is satisfied for coupling between the forward-propagating fundamental mode and the particular backward-propagating cladding mode in question, i.e. when

$$\beta_m(\lambda_m) + \beta_0(\lambda_m) = 2\pi \cos(\theta)/d \quad (1)$$

where $\beta_0(\lambda_m)$ is the propagation constant for the fundamental mode, $\beta_m(\lambda_m)$ is the propagation constant for the m 'th core mode, λ_m is the Bragg wavelength, d is the grating period, and θ is the angle from the perpendicular to the waveguide transmission axis.

If the core is large enough to support several modes, i.e. the fibre becomes few-moded, it is possible to reflect power into a particular backward-propagating core mode when the wavelength satisfies the Bragg condition in eqn.1. This idea was applied to two-core couplers by writing an angled grating in the waist region of an adiabatic, single-mode fused taper coupler², to produce a 4-port fibre wavelength add/drop device. An equivalent, adiabatic twin-core planar coupler device has also been designed and fabricated³.

2. DEVICE DESCRIPTION

However, by using a single waveguide core supporting several modes, it is possible to design a grating which couples power between the forward-propagating fundamental mode and backward-propagating, higher-order core modes, as shown schematically in Fig.1. Such a grating could be used to add and drop several wavelengths from a WDM network, since the Bragg reflection conditions between the fundamental mode and successive higher-order modes are satisfied at decreasing wavelengths.

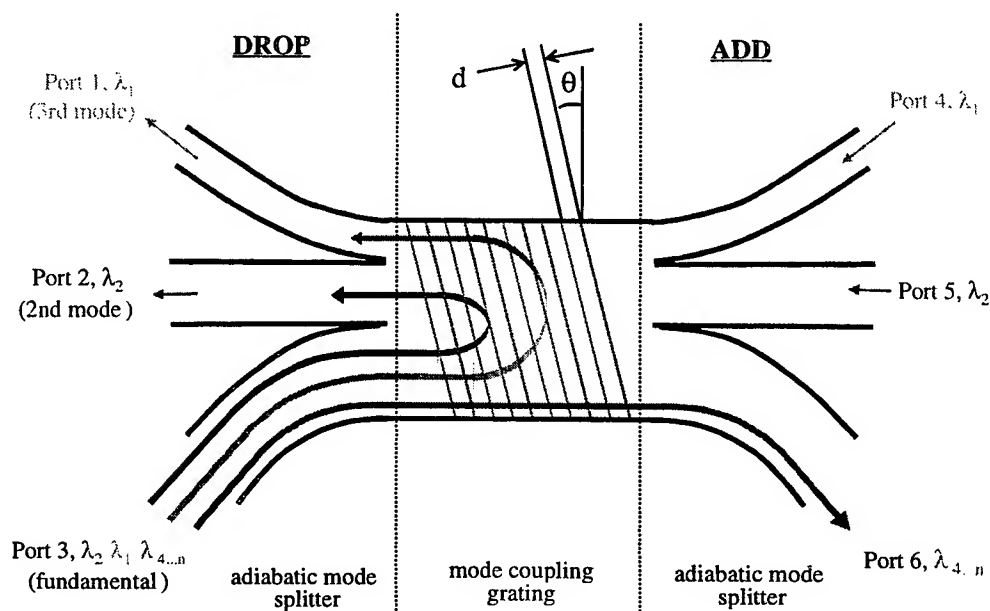


Fig.1. Schematic diagram of the proposed 6-port add/drop filter

At the left hand end of the device in Fig.1, we use an asymmetric mode splitter⁴ to channel successive higher-order mode into successively narrower output ports. Thus the second mode exits through port 2 at wavelength λ_2 , and the third mode exits through port 1 at wavelength λ_3 . Since the grating and asymmetric splitter are linear devices, signals at wavelengths λ_2 and λ_3 can be also be added to the network by reversing the direction of propagation and inserting them through the right hand ports 4 and 5, respectively. The cross-talk between adjacent input ports and adjacent output channels can be minimised to 30dB or better through optimal design of the asymmetric splitters to ensure adiabatic propagation of each higher-order through the splitting region⁴. Although each input/output port must have a distinctly different width to its neighbour in Fig.1, tapering of each port away from the splitting region will bring each port to the standard single-mode width.

3. THEORY

The centre of the coupler is assumed to have a nominally step profile with core index n_0 and cladding index n_{ck} , and a core half-width ρ . The grating is represented as a modulation of the core index with period d and amplitude $\delta n(z) \ll n_0$, where the z direction is parallel to the coupler axis, and is written at an angle θ to the transverse x -axis as shown in Fig.1. Thus the core refractive index of the region containing the grating can be expressed as a perturbation of the planar waveguide core given by:

$$n_{\text{core}}(x, z) = n_0 + \delta n(z) \cdot \sin(\Omega_x x + \Omega_z z) \quad (2)$$

where the x - and z -components of the grating frequency are $\Omega_x = 2\pi \sin(\vartheta)/d$ and $\Omega_z = 2\pi \cos(\vartheta)/d$. For a uniform grating, δn is constant along the length of the grating, whereas when a Gaussian apodized grating is used to suppress side lobes, $\delta n(z)$ is a continuous function of z :

$$\delta n(z) = \delta n_0 \exp\left[-\frac{(z - z_0)^2}{\sigma^2}\right] \quad (3)$$

where z_0 denotes the position of the centre of the grating and σ is the half-width or spot size of the Gaussian. We assume that the core and cladding indices of the rectangular-core coupler are similar, so that the weak-guidance approximation holds, in which case the scalar transverse field $\psi_m(x, y)$ and propagation constant β for the m 'th core mode are solutions of the two-dimensional scalar wave equation in x and y , and the eigenvalue equation, respectively. The complete modal field dependence is:

$$a_m(z) \psi_m(x, y) \exp(i\beta_m z) \quad (4)$$

where $a_m(z)$ is the modal amplitude. If b_m combines the amplitude and phase dependence of the mode in eqn.4, i.e. all the longitudinal z dependence, then the relationship between the $b_m(z)$ in the region containing the grating are governed by the set of coupled mode equations⁵

$$\frac{db_{\pm m}}{dz} \mp i\beta_m b_{\pm m} = \pm i \sum_{n=\text{all modes}} C_{mn} (b_n + b_{-n}) \quad (5)$$

where we have used \pm to designate the forward (+) and backward (-) propagating modes, and the coefficients, C_{mn} , are related to the normalized modal field distributions by:

$$\begin{aligned} C_{mn} &= \frac{k\delta n}{2\bar{n}_{co}} \left[\cos(\Omega_z z) \int_{-\infty}^{\infty} \Psi_m \Psi_n \sin(\Omega_x x) dx + \sin(\Omega_z z) \int_{-\infty}^{\infty} \Psi_m \Psi_n \cos(\Omega_x x) dx \right] \\ &= C'_{mn} \cos(\Omega_z z) + C''_{mn} \sin(\Omega_z z) \end{aligned} \quad (6)$$

When both of the modes m and n are even or odd, $C'_{mn}=0$, whereas $C''_{mn}=0$ when they have opposite symmetry. By employing the transformation

$$b_{\pm m} = X_{\pm m} \exp(\pm i\beta_{\pm m} z)$$

and following the procedure ⁵ for the reflection of a single mode from a grating, the coupled mode equations reduce to:

$$\frac{dX_{\pm m}}{dz} = \sum_{\substack{m,n \\ \text{same} \\ \text{parity}}} X_{\mp n} C''_{mn} \exp[\pm i(\Omega_z - \beta_n - \beta_m)z] \pm i \sum_{\substack{m,n \\ \text{different} \\ \text{parity}}} X_{\mp n} C'_{mn} \exp[\pm i(\Omega_z - \beta_n - \beta_m)z] \quad (7)$$

if it is assumed that $|\beta_m - \beta_n| \ll \Omega_z$ and $|\Omega_z - (\beta_m + \beta_n)| \ll |\Omega_z - |\beta_m - \beta_n||$.

The first condition is always true when the weak guidance approximation holds. The second assumption is valid when considering wavelengths close to those for which the Bragg condition for reflection, i.e. $\Omega_z = \beta_m + \beta_n$, is satisfied. Since we are particularly interested in the transmission spectra for wavelengths very close to those satisfying the Bragg condition for reflection from the grating, the second assumption is also valid.

4. NUMERICAL SOLUTION

While eqn. 7 can be solved analytically for a coupler with a one-dimensional slab cross-section, solutions for the rectangular cross-section of the coupler must be found numerically. To do this, we employ the Fourier Decomposition Method to solve for the modes of the scalar wave equation. The coupling coefficients were then calculated using eqn.6, and the coupled mode equations are then solved by numerical integration over the length of the grating. When modelling apodised gratings using the Gaussian function in eqn.3, we set $z=0$ at the start of the grating, $z_0 = L/2$ and $\sigma = s \cdot L/2$, where L is the grating length and s is a parameter describing the spread or spot size of the Gaussian function.

For the current investigation, we have used a planar waveguide with $V=3.46$ in the width at a wavelength $\lambda=1.55\mu\text{m}$, an aspect ratio (thickness to width) of 0.90, and core and cladding refractive indices of 1.46 and 1.453 respectively. This waveguide supports the three modes with the field shapes shown quantitatively in Fig.2. These modes are, from top to bottom, the fundamental mode with a single maximum on the core axis, the first odd mode (in the x -direction) and the second even mode (in the x -direction). In the y -direction all three modes are essentially single-moded, i.e. have only a single extremum in the field.

When using the Fourier Decomposition Method, the domain over which the problem is solved must be sufficiently large compared to the dimensions of the coupler waist, to ensure that the scalar solutions and their derivatives are vanishingly small at the boundary of the surrounding rectangular domain. If the domain and/or the order of the Fourier expansion are too small, the solutions may be the "guided" modes of the domain boundary rather than true guided modes of the core resulting in incorrect predictions of the field distributions, propagation constants and coupling coefficients in eqn. 6. We found that the field distributions of the modes were adequately described by a 12th order Fourier series combined with a domain six times the size of the core.

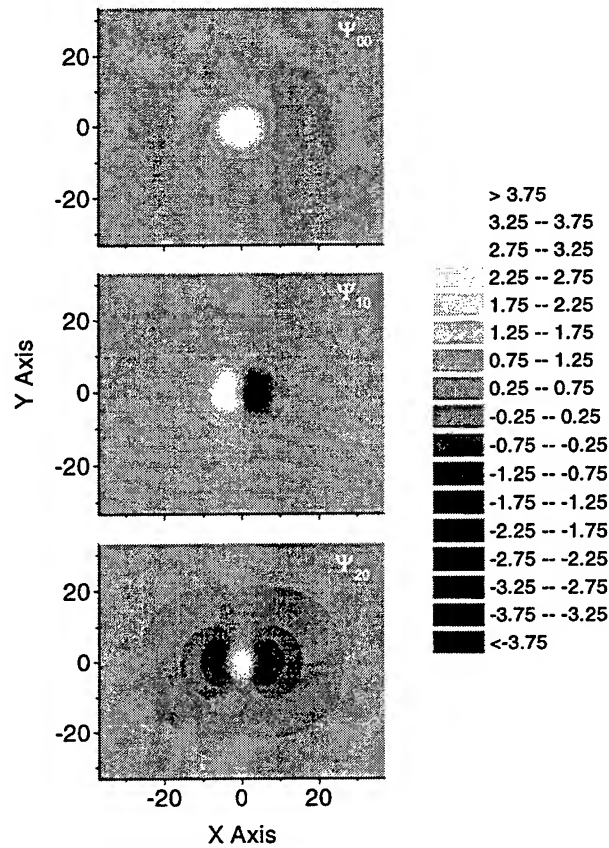


Fig. 2. Normalised Fourier decomposition solutions of the scalar wave equations for a waveguide with $V=3.46$ at 1550nm, an aspect ratio of 0.90, $n_{co}=1.46$ and $n_{cl}=1.453$, for the first three higher-order modes in the width of the waveguide.

As there is no established convention for labelling the modes of planar waveguides, we have chosen to designate the solutions of the scalar wave equations by the symbol, Ψ_{mn} , where the first subscript, m , is the number of zeros along the (transverse) x-axis, and the second subscript the number of zeros along the (vertical) y-axis. Thus the top fundamental mode in Fig.2 is designated by the symbol Ψ_{00} , the middle mode by Ψ_{10} and the third mode by Ψ_{20} .

5. RESULTS AND DISCUSSION

From eqn.6, it is apparent that the coupling coefficients depend on the grating angle θ . Fig. 3 shows the angular dependence of the strength of the reflection of the forward-propagating mode into the backward-propagating fundamental mode and likewise the other backward-propagating modes. As can be seen, there exists an angle of approximately 3.83° that minimizes the back reflection of the fundamental mode onto itself. The reflection of the fundamental mode must be minimized to reduce losses and cross-talk in the network since the reflected fundamental will propagate back out port 3 and back along the network. For the present set of waveguide parameters the predicted reflection of the fundamental mode at 1551.3nm is less than -30dB when the grating angle is 3.83° . The transmission spectrum in Fig. 4 for gratings written with this angle exhibits two reflection bands 1.6nm apart. The two reflection bands correspond to reflections into the Ψ_{10} mode (1550.0nm) and the Ψ_{20} mode (1548.4nm), respectively, from the fundamental mode.

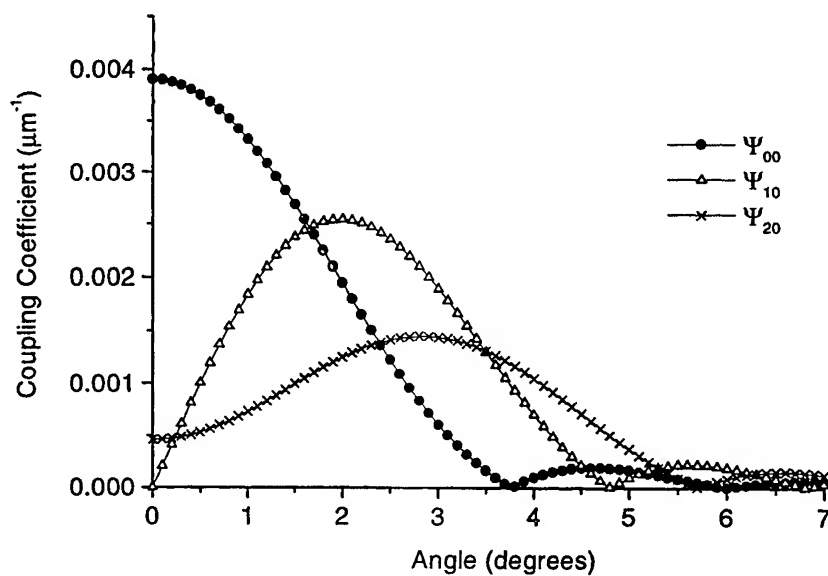


Fig. 3. Dependence of the coupling coefficients C'_{mn} or C''_{mn} in eqn. 6 on the angle for coupling between the fundamental mode Ψ_{00} and itself, Ψ_{10} and Ψ_{20} .

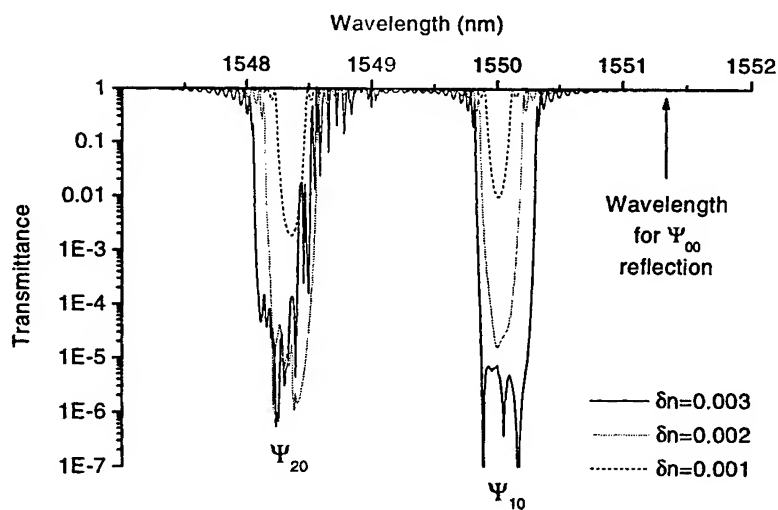


Fig. 4. Transmission spectrum from a gratings with a 3.83 angle and different amplitudes for the index modulation.

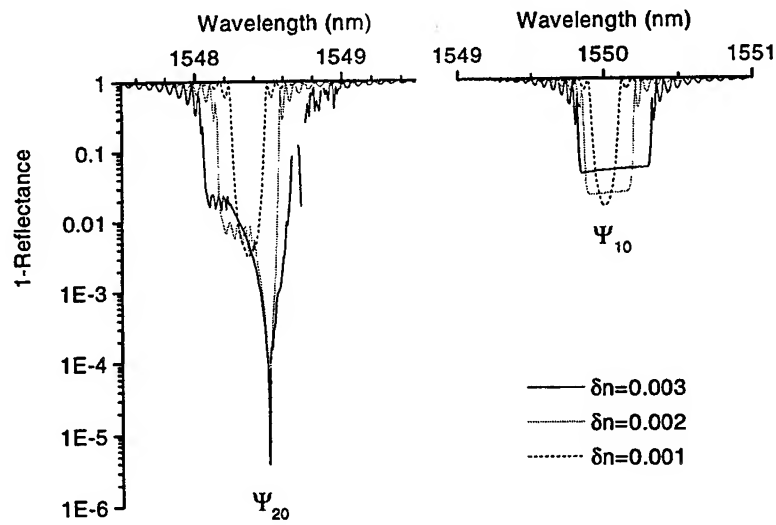


Fig. 5. Effect of the grating amplitude, δn , on the reflection bands of the Ψ_{10} and Ψ_{20} modes

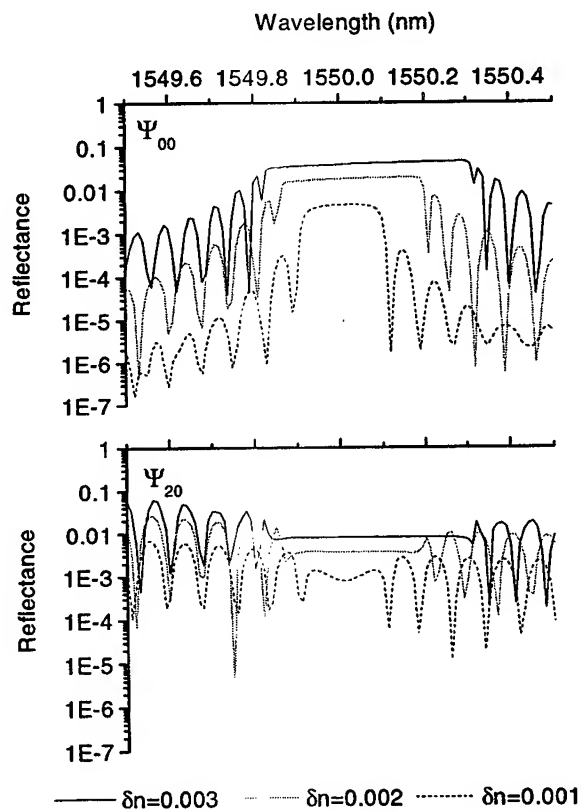


Fig. 6 Reflectance of the fundamental mode, Ψ_{00} , and the Ψ_{20} mode at the Ψ_{10} reflection band

When the amplitude δn of an un-apodized, mode-coupling grating is increased from 0.001 to 0.003, extinction ratios greater than 40dB can be obtained, as shown in Fig. 4. However ripples appear in the transmission spectrum at the Ψ_{10} and Ψ_{20} reflection bands. Moreover, the increased extinction of the forward-propagating fundamental mode is not matched by an increase in the power transferred to the desired Ψ_{10} mode at 1550nm. Surprisingly, the reflectance of the Ψ_{10} mode at 1550nm decreases from 0.9848 to 0.9513, as shown in Fig. 5, when the grating amplitude is increased from 0.001 to 0.003. The reflectance of the Ψ_{20} remains approximately constant when the grating amplitude is increased.

The ripples in the transmission spectrum of the strongly-reflecting gratings and the decreased reflectance of the Ψ_{10} mode at 1550nm are due to undesirable reflection of power into the other modes, i.e. due to increased crosstalk (Fig. 6). Crosstalk at 1550nm with the backward propagating Ψ_{00} mode increases from -23.4dB to -14.1dB when the grating amplitude is increased from 0.001 to 0.003, and crosstalk with the Ψ_{20} mode increases from -28.8dB to -21.0dB.

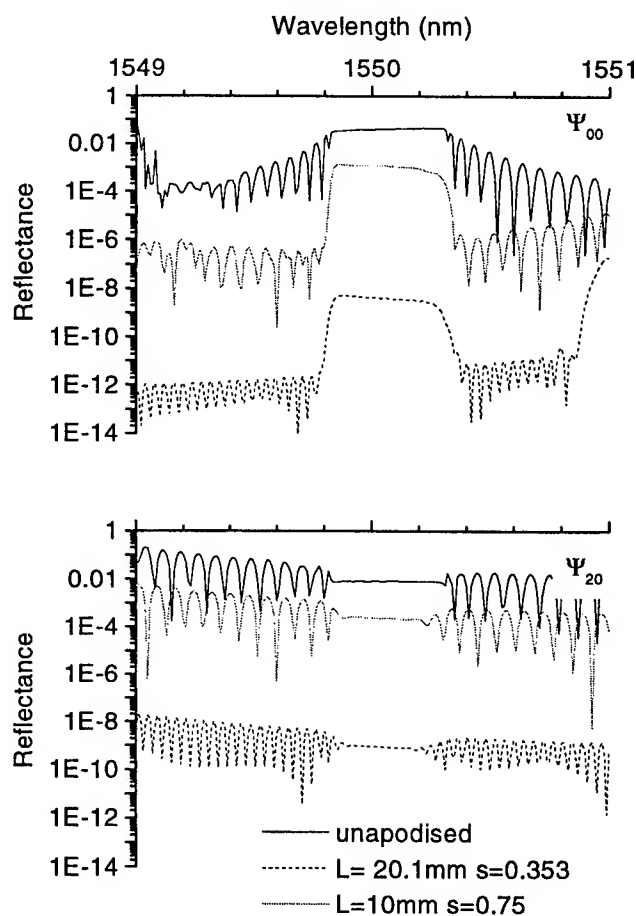


Fig. 7. Effect of apodizing the grating on the reflection of Ψ_{00} and Ψ_{20} at 1550nm

Crosstalk between the modes can be greatly reduced by apodizing the grating, as shown in Fig. 7, which compares the reflection of the Ψ_{00} and Ψ_{20} modes at 1550nm from a 10mm unapodized grating, a 10mm mildly apodized grating ($s=0.75$) and a long, strongly apodized grating ($s=0.353$, $L=20.1$ mm). Although the three gratings have similar transmission spectra, as in Fig. 8, the reflection of the undesirable Ψ_{20} mode at 1550nm is less than -80 dB from the strongly apodized grating and -36 dB from the shorter mildly apodized. These crosstalk values are significantly less than the -21 dB reflected into the Ψ_{20} mode at 1550nm from the unapodized grating. Furthermore, apodizing the grating removes the ripples in the transmission spectrum inside the reflections bands, as shown in Fig. 8.

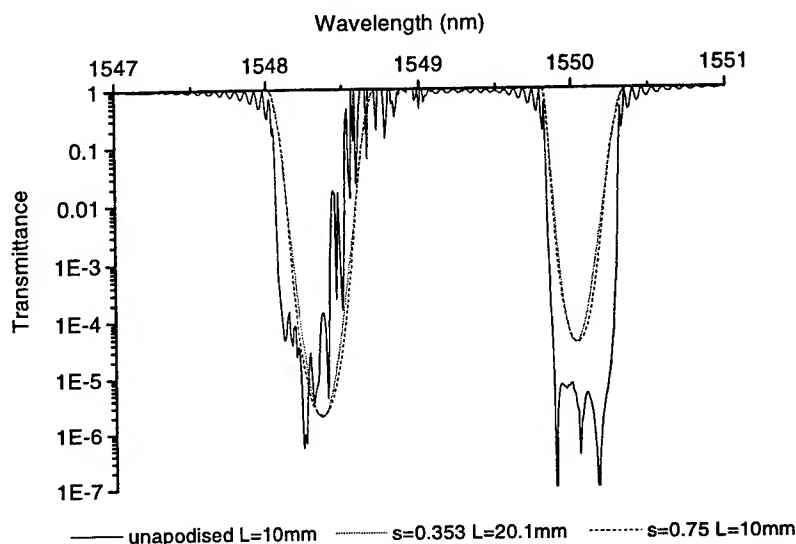


Fig. 8. Transmission spectra from an unapodized grating, a short mildly apodized grating ($L=10$ mm, $s=0.75$) and a longer, more strongly apodized grating ($L=20.1$ mm, $s=0.353$)

6. CONCLUSIONS

Modelling of a mode-coupling, angled grating in a planar waveguide indicates that it is possible to design a grating that has negligible reflection of the fundamental mode back on itself, yet strongly reflects power from the fundamental mode into the higher-order modes. Our modelling predicts that the reflection of the fundamental mode, will be less than a low -30 dB from a 10nm grating with a ripple amplitude of 0.003, written at an angle of 3.83° into a planar waveguide with $V=3.46$ at 1550nm, $n_{co}=1.46$, $n_{cl}=1.453$ and an aspect ratio of 0.90. On the other hand, the predicted extinction ratios of the fundamental mode at the reflection bands of the Ψ_{10} and Ψ_{20} modes (1550nm and 1548.4nm respectively) are greater than 40dB.

The modelling also suggests apodization of the grating is necessary to reduce power losses and crosstalk. By apodizing the grating, we obtained predicted crosstalk less than -35 dB from a 10mm grating, and less than -80 dB from a more strongly apodized grating 20.1mm long.

Our modeling demonstrates that an angled grating written into a single waveguide core supporting three modes could be used in conjunction with an adiabatic splitter as a WDM add/drop filter which simultaneously adds/drops two channels 1.6nm apart.

7. ACKNOWLEDGEMENTS

Keith Gaff is the recipient of an Australian Postgraduate Award (Industry) supported by ADC-AOFR Pty Ltd. This work was supported by the Australian Photonics Cooperative Research Centre

8. REFERENCES

1. S. J. Hewlett, J. D. Love, G. Meltz, T. J. Bailey, and W. W. Morey, "Coupling characteristics of photo-induced Bragg gratings in depressed- and matched-cladding fibre," *Optical and Quantum Electronics*, **28**, 1641-54 (1996).
2. A. S. Kewitsch, G. A. Rakuljic, P. A. Willems, and A. Yariv, "An all-fiber, zero insertion loss, add/drop filter for wavelength division multiplexing," *Bragg Grating, Photosensitivity, and Poling in Glass Fibers and Waveguides: Applications and Fundamentals. Technical Digest. Postconference Edition.*, pp. 256-8, Opt. Soc. America, Washington, DC, USA, 1997.
3. C. K. Madsen, T. A. Strasser, M. A. Milbrodt, C. H. Henry, A. J. Bruce, and J. DeMarco, "Planar waveguide add/drop filter employing a mode-converting grating in an adiabatic coupler," *Integrated Photonics Research. Technical digest.*, pp. 102-4, Optical Society of America, Washington, DC, USA, 1998.
4. R. W. C. Vance and J. D. Love, "Asymmetric adiabatic multi-prong splitters for mode-multiplexed systems," *Electronics Letters*, **29**, 2134-6 (1993).
5. A. W. Snyder and J. D. Love, *Optical Waveguide Theory*, Chapter 27, Chapman & Hall Medical, London, 1983, pp. 543-52.

3C(β)-SiC-on insulator waveguide structures for modulators and sensor systems

Adrian Vonsovici^{a*}, Graham T. Reed^{a**}, M. Josey^b, P. Routley^b, Alan G.R. Evans^b, F. Namavar^c
^aUniversity of Surrey, School of Electronics, Information Technology and Mathematics, Guildford
GU2 5XH, UK

^bUniversity of Southampton, Department of Electronics and Computer Science, Highfield,
Southampton SO17 1BJ, UK

^cSpire Corporation, One Patriots Park, Bedford, MA 01730-2396, USA

ABSTRACT

In this work planar and rib β -SiC-on-insulator waveguides were investigated. The waveguides were fabricated by two different methods. In the first a technological process similar to that of SIMOX was used, a buried SiO₂ layer was formed by a two-step high-energy ion implantation of oxygen in SiC/Si wafers. For the second type of waveguides we used heteroepitaxy of SiC on SOI(SIMOX). The losses have been measured at 1.3 and 1.55 μ m. Rib waveguides were fabricated using dry-etching (RIE). These types of waveguides have great potential for high-speed silicon-based photonic devices compatible with silicon technology.

Keywords: Si-based optoelectronics, silicon on insulator, SiC planar waveguides, SiC rib waveguides, Pockels modulator, high-speed modulators.

1. INTRODUCTION

In recent years Si-based optoelectronics has emerged in the field of optical communication devices. For fiber-to-the-home (FTTH) networks cost targets are extremely stringent, therefore the possibility to realize such systems using mature silicon technology was investigated by many groups. Since the linear electro-optic effect (Pockels effect) vanishes in crystalline silicon due to the centrosymmetric crystal structure, active devices such as modulators and switches must be designed using the free carrier dispersion effect¹. Furthermore, the transparent wavelength range of Si is limited to the region of above 1.2 μ m and therefore integrated optics applications in the visible range are excluded. There is a great demand for photonic integrated devices compatible with silicon technology and the use of silicon based alloys (SiGe, SiGeC, SiC) could offer a solution to some specific problems.

SiC polytypes have long been considered as good candidates for high-power and high-temperature devices because of their attractive electronic properties. The cubic polytype (3C or β) of the silicon carbide (SiC) has a wide bandgap (2.2eV), transparent in the range 0.54-2 μ m and therefore suitable for waveguiding over the visible and near-infrared optical spectrum range as well as the longer communication wavelengths. Cubic SiC is a crystal with a zincblende structure and possesses a $\bar{4}3m$ point-group lattice structure which is non-centrosymmetric. The electro-optic coefficient, is more than 70% higher than that for GaAs². Optical devices fabricated from β -SiC can be operated in the visible range (the absorption edge at room-temperature is 539nm) offering much greater scope for a variety of applications: shorter wavelength interferometers with better resolution, visible signal routing for optical data storage, compatibility with the new GaN visible light emitting devices. Other important characteristics like high mechanical strength, chemical inertness and excellent thermal conductivity make SiC very attractive for use in sensor systems in harsh environments (highly corrosive and at high-temperatures).

β -SiC waveguides, formed by attaching a SiC film to a sapphire substrate, were experimentally studied by Tang et al.³. Prucnal and Liu⁴ proposed planar SiC waveguides on SiO₂, in structures similar to silicon-on-insulator ones. Recently, waveguiding in SiC-on insulator (SICOI) and SiC-on SOI (SICSOI) was thoroughly investigated in planar waveguides⁵.

* -E-mail: eeslav@ee.surrey.ac.uk ** -E-mail: G.Reed@ee.surrey.ac.uk *** -Fax 44-(0)1483-534 139.

The SiCOI waveguides were made using a process similar to the SIMOX fabrication method using a one step high-energy implantation of oxygen. The losses were reasonably low for both SICOI and SICSOI materials (8.8-9dB/cm).

In this paper we investigated at 1.3 and 1.55 μ m planar and rib-waveguides made using both SiCOI and SICSOI materials. We improved the fabrication of the SICOI material by using a two-step high-energy implantation of oxygen. A thicker buried layer was obtained allowing us to reduce the loss by leakage toward the substrate for the TE polarization where the previous SICOI material had losses of approximately 26dB/cm at 1.55 μ m.

The Reactive Ion Etching method (RIE) was used for the fabrication of rib waveguides which is fully compatible with silicon processing technology, offering the opportunity to develop high-speed, low cost photonic circuits.

2. FABRICATION OF SICOI AND SICSOI WAVEGUIDES

2.1 SICOI planar waveguides fabrication.

A β -SiC epilayer ($\sim 2\mu$ m thick), grown using CVD by Cree Research Inc. (USA) on a Si substrate, has been used as a substrate for fabricating the SICOI waveguides. The SiC layer has a high-resistivity (30 Ω -cm) and therefore little free-carrier absorption is expected from it. The buried oxide layer was produced by a two-step high-energy ion implantation of oxygen. We used high-energy (1.6 and 2MeV) oxygen ions implanted to a dose of 10^{18}cm^{-2} . This gives a predicted range of about 1.14 and 1.3 μ m respectively and an R_{straggle} of about 85 and 95nm respectively (using the ion implantation simulation software TRIM⁶). The superposition of the two implantation profiles gives a range of about 1.23 μ m and a R_{straggle} of about 175nm. Therefore we expect a guiding SiC layer of approximately 1.05 μ m and a buried layer of approximately 0.35 μ m. During the implantation the sample was maintained at $\sim 600^\circ\text{C}$ by using a heated sample stage to minimize the implantation damage⁷. A full-analysis of the buried layer formed in a similar process but using lower implantation energy (200keV), was made by XTEM and RBS. While the Si concentration at the O-rich layer is reduced leading to a silicon dioxide, the C is practically all ejected from this layer. The RBS results indicate a predominantly SiO_x ($x=2.04$) layer with a thickness equal to approximately $2 \cdot R_{\text{straggle}}$. The SiO_2 /bulk-SiC interface is sharper than the surface-SiC/ SiO_2 one. Furthermore, channeling results show that crystalline quality of the SiC surface layer is good with minimum yield $\chi_{\text{min}}=14.1\%$. The dual implant process has been used to reduce leakage loss from the waveguides reported in our previous work⁵.

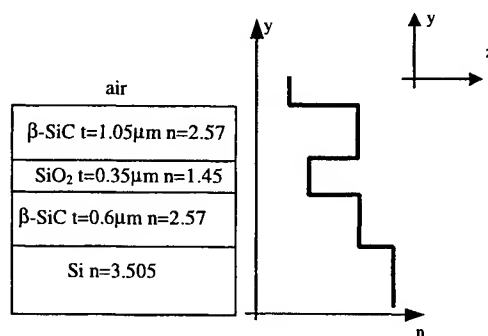


Figure 1. The schematic cross-sectional view of the SiCOI waveguide formed by ion implantation. The associated refractive index profile is also shown.

2.2 SICSOI planar waveguides fabrication.

β -SiC thin films ($\sim 4.8\mu$ m) were grown using CVD by SPIRE CORPORATION (USA) on SOI-Unibond($0.2\mu\text{mSi}/0.4\mu\text{mSiO}_2$) substrates (see figure 2 for a schematic of this type of planar waveguide). The SiC epilayer has a relatively high residual n-doping $\sim 5 \cdot 10^{17}\text{cm}^{-3}$. The recently reported method of epitaxy called site-competition epitaxy⁸ was used. This allowed a more accurate control of the epi-layer quality during the epitaxy by appropriately adjusting the Si/C ratio within the growth reactor to effectively control the amount of dopant incorporated into substitutional SiC crystal lattice sites. The temperature of growth was relatively low for the SiC epitaxy 1330-1350 $^\circ\text{C}$ due to problems

related to voids that appear in the SiO₂ buried layer. Despite this the quality of the layers was very good. Further work was initiated in order to reduce the doping concentration (n-type, nitrogen) to less than 10^{16}cm^{-3} for practical active devices, which will provide lower loss waveguides in the future.

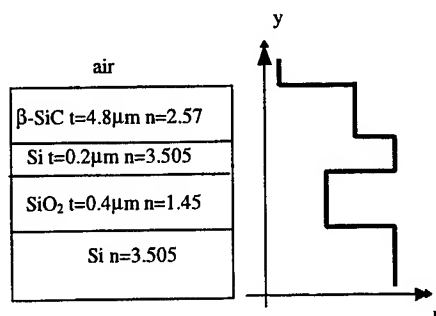


Figure 2. The schematic cross-sectional view of the SICOSI waveguide formed by epitaxial growth on SOI. The associated refractive index profile is also shown.

2.3 Rib waveguides fabrication.

The SICOI and SICOSI substrates were used for the fabrication of 3D waveguide structures using standard silicon processing technology steps. Firstly a thick PECVD oxide layer ($\sim 1\mu\text{m}$) was deposited on top of the substrates. Subsequently standard lithography was used to pattern parallel straight rib waveguides and different integrated optics devices (y-junctions, tapers, Mach-Zehnder interferometers). The patterns were etched in the oxide using a $\text{CHF}_3+(2\%)\text{Ar}$ RIE. The oxide mask was needed as a supplementary mask for the next step of dry-etching of the SiC using a mixture of $\text{CHF}_3+33\%\text{O}_2$. The etching of the SiC has a very slow rate ($\sim 15\text{-}20\text{nm/min}$) but excellent anisotropy. Also, smooth and almost vertical ($<5^\circ$ of tilt) rib walls were obtained (see figure 3a and 3b). Other etching recipes are faster ($35\text{-}40\text{nm/min}$) as for example the mixtures of $\text{SF}_6+(10\text{-}50\%)\text{O}_2$, but the anisotropy is not as good and let significant residue on the bottom surface together with significant waveguide wall roughness. As the roughness of the rib walls is important for low surface scattering losses we preferred to use the low-rate etching recipe using CHF_3+O_2 . The etched depth in SiC was $0.2\mu\text{m}$ for SICOI rib waveguides and $0.5\mu\text{m}$ for SICOSI waveguides, measured using a Dektak surface profile measuring instrument.

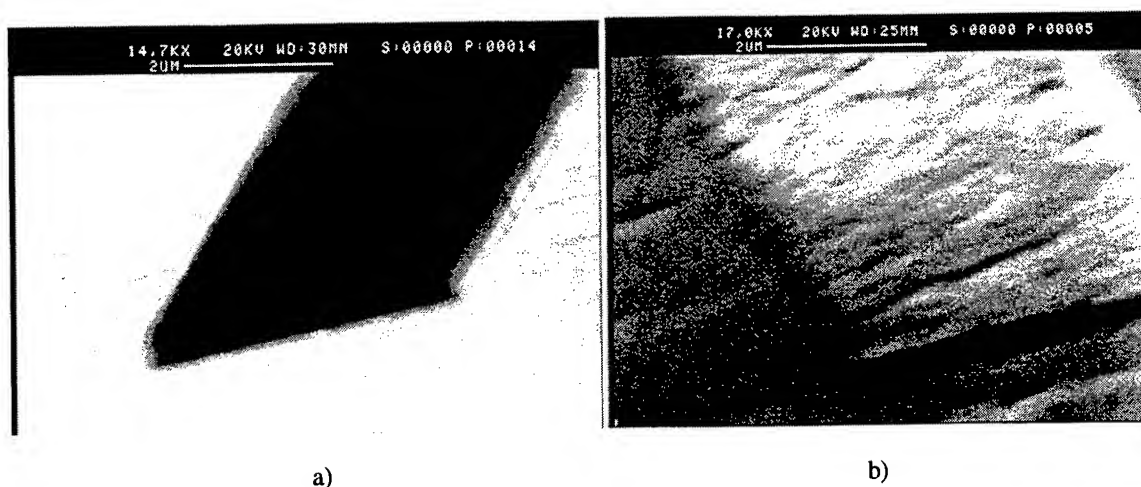


Figure 3 Etched rib waveguides using a) SICOI material ($0.2\mu\text{m}$ rib height) and b) SICOSI material ($0.5\mu\text{m}$ rib height).

3. WAVEGUIDE LOSS MEASUREMENTS

Waveguide insertion loss measurements for planar and rib waveguides were carried out at 1.3 and 1.55 μm for both the TE and TM polarizations. For these experiments, the SiC waveguides were cleaved and then polished at the ends to form the waveguide facets. Insertion loss results from coupling loss due to the mismatch between the field profile of the input beam and guided mode, propagation loss of the guided mode and Fresnel reflection loss at both endfaces. Assuming a normally incident beam the total Fresnel reflection loss was estimated to be 1.9dB.

The schematic of the experimental setup used for the 1.3 and 1.55 μm measurements is presented in figure 4.

The first light source is a pigtailed DFB laser diode emitting at 1.3 μm with an output power of 2mW, and the second light source is a pigtailed FP laser diode operating at 1.55 μm with a nominal power of 1.5mW at the output of the fibre. An in-line fibre polarization controller is used for adjusting for both TE and TM guided mode excitation. The fibre output is collimated and focused onto the waveguide input using two objective lenses. The advantage of this setup is the ability to change the polarization without changing the mechanical positioning at the input of the waveguide. The output of the waveguide is imaged using an objective lens onto an infrared Ge detector. Using a beamsplitter and an infrared video camera positioned at 90° from the optical axis we could observe the image of the waveguide output and make the adjustments for optimum waveguide coupling. Both the input and the output objective lenses are mounted on precision positioning stages that allows precise control of the alignment with the waveguide input-output. The waveguide mount is fixed on top of a precision 4-axis waveguide manipulator that allows supplementary flexure rotations for optimum tilting and alignment of the waveguide input with the laser beam.

Three different lengths of waveguides were used for the loss measurement. This is known generically as the cutback method¹⁰. As the net propagation loss varies exponentially with the length of the waveguide, using at least three different waveguide lengths we could eliminate the insertion and Fresnel losses (assumed to be the same for all waveguides) from the total loss measured. The averaged error due mainly to errors in measuring the length of the waveguides or different polishing quality from waveguide to waveguide is estimated at $\pm 0.3\text{dB/cm}$.

Since there may be the possibility of inconsistent coupling to multimode waveguides, the experiments were repeated several times for each set of waveguides, and the mean of the results taken, and the spread giving an indication of the uncertainty associated with the measurements. It must be emphasized that due to the leaky nature of the SICOI planar waveguides modes of higher order than the fundamental will have leakage loss greater than 50dB/cm (e.g TE 1st order mode 60dB/cm at 1.3 μm). This is a very different situation from that of mode excitation in truly multimode waveguides with no leakage. The higher order leaky-modes are "stripped" from the waveguide after a short distance ($\sim 2\text{-}3\text{mm}$) so that the measured value is related to the fundamental mode of the waveguides, although any light initially coupled into the higher order modes will contribute to the overall loss.

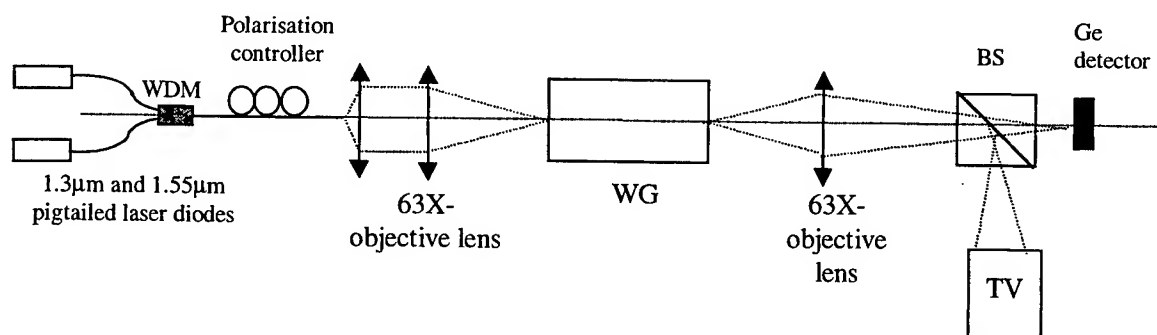


Figure 4. Schematic representation of the experimental setup. A fibre in-line polarization controller is used to control the polarization without the movement of the beam in front of the waveguide input.

4. RESULTS AND DISCUSSIONS

4.1 Loss mechanisms in SiCOI and SiCSOI waveguides.

Planar waveguide losses for SiCOI and SiCSOI can originate from three main causes.

- Leakage into the substrate for waveguides fabricated on a high-refractive index substrate (leaky-waveguides).
- Interface scattering losses resulting from imperfections of interfaces in the waveguide geometry after the fabrication process.
- Bulk material losses, due to imperfections in the refractive index of the guiding layer material and to absorption of free-carriers.

We will neglect the residual absorption of the SiC as it has been shown that the β -SiC is highly transparent in the 0.54-2 μm range^{11,12}. These loss mechanisms have been reviewed previously for Sic waveguides in⁵.

4.2 Losses of SiCOI planar waveguides.

The results obtained for SiCOI waveguide propagation loss (α_{exp}) for TE and TM polarizations at 1.3 and 1.55 μm are summarized in Table I, together with predicted leakage loss (α_{leak}), the latter being discussed further below. Whilst these losses are not low when compared to silica waveguides ($\sim 0.01\text{dB/cm}$) or silicon waveguides ($\sim 0.5\text{dB/cm}$), they are the lowest losses yet reported for silicon carbide thin film waveguides, and the lowest of these quoted losses (6.9dB/cm at 1.3 μm TM polarization) is tolerable for active devices 2-3mm long.

The degree of leakage loss is determined by the buried oxide thickness as the light propagating in such a waveguide could escape into the substrate by an effect analogous to the tunnel effect in quantum mechanics. For the SiCOI planar waveguide, starting with a 2 μm SiC layer on a silicon substrate, using a two-step implant we expect a waveguide with about 1.05 μm of SiC, separated by 0.35 μm of buried oxide from a remaining 0.6 μm SiC layer and the Si underlying substrate (the cross section of this SiCOI planar waveguide is depicted in figure 1).

In figure 5 we have shown the losses by leakage into the substrate as a function of the buried oxide thickness, for TE₀ and TM₀ modes, at 1.3 μm and 1.55 μm respectively¹³. A 0.35 μm buried oxide layer is sufficiently thick in order to ensure less than 0.7dB/cm leakage loss at 1.3 μm for a 1.05 μm SiC layer. About 4dB/cm of loss are predicted for TE polarisation and 2dB/cm for TM polarisation at 1.55 μm .

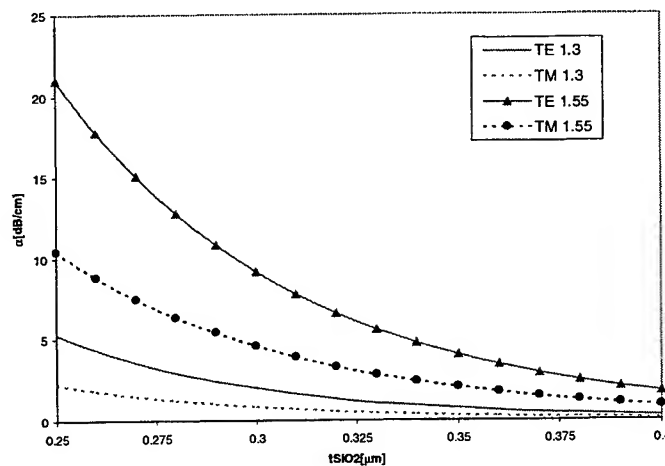


Figure 5. Predicted leakage into the substrate loss at 1.3 and 1.55 μm for TE,TM polarizations.

The remaining loss can be attributed to bulk and interface scattering⁵. However, the important conclusion is that by using additional ion implantation the buried oxide layer can be thickened, thus reducing the loss due to leakage. A significant

reduction of the leakage loss is observed compared to the one-step implanted SICOI waveguides reported previously ⁵, which had leakage losses greater than 5dB/cm for a TE polarization and about 2dB/cm for a TM polarization at 1.3μm. Total waveguide losses of less than 10dB/cm were measured at 1.55μm, a significant improvement compared to the one-step implanted SICOI waveguides that were very lossy (15-27dB/cm) due to the leakage. The losses due to propagation (leakage) have been reduced to less than 4dB/cm at 1.55μm before any additional scattering loss is considered. Furthermore, it is reasonable to expect that losses of the order of 6dB/cm can be obtained at 1.3 and 1.55μm by increasing the thickness of the buried oxide layer.

Table I. Experimental total loss for SICOI waveguides and the estimated loss by leakage toward the substrate.

Wavelength(μm)/Polarization		$\alpha_{exp}(dB/cm)$	$\alpha_{leak}(dB/cm)$
1.3	TE	7.4	0.7
	TM	6.9	0.3
1.55	TE	9.8	4.0
	TM	7.5	2.0

4.3 Losses of planar SICSOI waveguides.

For the SICSOI waveguides the total waveguide losses at 1.3 and 1.55μm are reported in Table II. No significant polarization dependence was observed indicating a relatively low interface scattering (less than 0.5dB/cm for a SiC layer thickness greater than 3μm). The loss due to the volume scattering is proportional to $1/\lambda^3$ ¹⁴ and the free carrier absorption loss that is proportional to λ^2 ¹⁵. The bulk scattering for the SICSOI waveguides should be similar to that of SICOI waveguides because the confinement factor is greater than 0.99 in both cases.

The total waveguide loss coefficient could be expressed as:

$$\alpha_{tot}(\lambda) = \alpha_{bulk_scatt}(\lambda) + \alpha_{free_carr}(\lambda) = A \frac{1}{\lambda^3} + B\lambda^2 \quad (1)$$

The A and B coefficients can be determined from a fit of measurements at two wavelengths 1.3 and 1.55μm.

TABLE II. Experimental total insertion loss for SICSOI waveguides.

Sample	$\lambda(\mu m)$	$\alpha_{exp}(dB/cm)$
M6-2310-1	1.3μm	11.2
	1.55μm	14.3

Thus, we determined that the contribution of the bulk scattering is ~2dB/cm at 1.3μm. The remaining loss at the same wavelength are therefore due to absorption and is about 9.2dB/cm

The free-carrier absorption losses could be interpreted using the model of Drude-Lorentz ¹⁵ which describes this type of absorption in semiconductors:

$$\Delta\alpha = \frac{e^3\lambda^2}{4\pi^2c^3\epsilon_0n} \left(\frac{\Delta N}{\mu_e(m_{ce}^*)^2} + \frac{\Delta P}{\mu_h(m_{ch}^*)^2} \right) \quad (2)$$

where the c is the speed of light in vacuum, ϵ_0 is the absolute permittivity of the vacuum, the refractive index of the semiconductor, e the electron charge, ΔN and ΔP the free electron and hole concentrations, μ the mobilities and the m^* the effective masses of the carriers¹⁶. The SiC layers have a residual doping of $5 \cdot 10^{17} - 10^{18} \text{cm}^{-3}$. The absorption attributed to free-carriers corresponds to a free-carrier concentration of $\sim 8 \cdot 10^{17} \text{cm}^{-3}$. Reducing the residual doping of the SiC layers to less than 10^{17}cm^{-3} will reduce this cause of loss to less than 1dB/cm.

4.3 Losses of the rib waveguides.

In figure 6 we present the images of the outputs of the rib waveguides made using the SICOI (figure 5a) and the SICSOI (figure 5b) materials. The losses of these waveguides were estimated at $1.3 \mu\text{m}$ and they are about 1.5dB/cm and 1dB/cm higher than that for the respective planar cases (see TABLE III). This extra loss is most probably due to additional surface scattering of the rib walls.

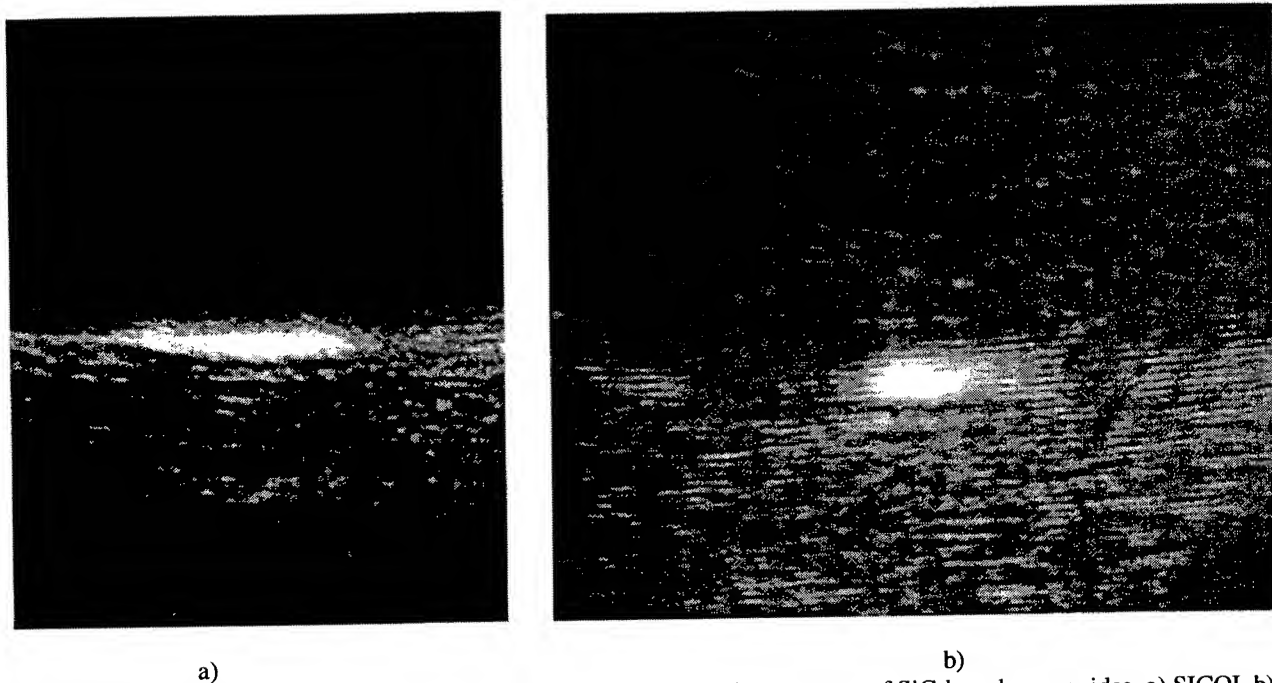


Figure 6. Images of the outputs of the rib waveguides made using the two types of SiC-based waveguides. a) SICOI. b) SICSOI. For the figure a) the polarisation is TM and for figure b) is TE and the wavelength is $1.3 \mu\text{m}$.

TABLE III. Experimental total propagation loss for SICOI and SICSOI rib waveguides.

Waveguide(rib width)	$\alpha_{\text{exp}}(\text{dB/cm}), \lambda=1.3 \mu\text{m}$
SICOI($5.5 \mu\text{m}$)	8.5
SICSOI($5.5 \mu\text{m}$)	12.1

5. CONCLUSION

We have presented an investigation of waveguide loss of $(\beta\text{-})\text{SiCOI}$ and $(\beta\text{-})\text{SiCSOI}$ planar and rib waveguides. The planar waveguides loss measurements were carried out at the telecommunications wavelengths of 1.3 and $1.55 \mu\text{m}$ and resulted in the lowest SiC thin film waveguide losses yet reported, of less than 7dB/cm at $1.3 \mu\text{m}$, for a TM polarization. This result is obtained for a SICOI planar waveguide made by a two-step high-energy implantation of oxygen to create a

buried oxide layer ($\sim 0.35\mu\text{m}$). A total propagation loss of 7 dB/cm would be equivalent to 2dB of insertion loss for a 3mm phase modulator that will use the high-speed Pockels effect. For the SICOI waveguides further reduction of the residual doping will determine lower absorption loss at $1.3\mu\text{m}$ and losses less than 5dB/cm are obtainable if the residual doping is reduced at less than 10^{17}cm^{-3} .

We have also reported the first fabrication and loss measurements on rib waveguides made using both types of materials. The lowest loss was 8.5dB/cm. The supplemental loss due to the imperfections of the rib walls is in the range 1-1.5dB/cm so the waveguides could be used successfully for high-speed Pockels modulators. In particular, the thin SICOI waveguides could be used for interferometric evanescent-type waveguide sensors that could be used in harsh-environments (highly corrosive and/or high-temperature).

6. REFERENCES

1. C.K. Tang, G.T. Reed, A.J. Walton and A.G. Rickman, "Low-loss single mode optical phase modulator in SIMOX material" *IEEE J. Lightwave Technology*, **12**, pp. 1394-1400, 1994.
2. X. Tang, K.J. Irvine, D. Zang and M. Spencer, "Linear electro-optic effect in cubic silicon carbide", *Appl. Phys. Lett.*, **59**, pp.1938-1939, 1991.
3. X.Tang, K. Wongchotigul and M. Spencer, "Optical waveguide formed by cubic silicon carbide on sapphire substrates", *Appl. Phys. Lett.*, **58**, pp. 917-918, 1991.
4. Y.M. Liu and P.R. Prucnal, "Low-loss silicon carbide optical waveguides for silicon-based optoelectronic devices", *IEEE Photonics Technology Letters*, **5**, pp. 704-707, 1993.
5. A. Vonsovici, G.T. Reed, A.G.R. Evans, "Loss measurements for β -SiC-on-insulator waveguides for high-speed silicon-based photonic devices" *Proceedings of SPIE*, vol 3630, pp.115-124, 1999.
6. J.F. Ziegler, J.P. Biersack and U. Littmark: "The Stopping and Range of Ions in Solids", Pergamon Press, New York, 1985 (ISBN 0-08 021603-X).
7. J.A. Edmond, S.P. Withrow, W. Wadlin and R.F. Davis: "High temperature implantation of single crystal beta silicon carbide thin films", *Mater. Res. Soc. Symp. Proc.*, **77**, pp. 193-198, 1987.
8. D.J. Larkin, P.G. Neudeck, J.A. Powell and L.G. Matus, "Site competition epitaxy for superior silicon carbide electronics", *Appl. Phys. Letters*, **65**, pp. 1659-1661, 1994.
9. P.H. Yih, A. J. Steckl, "Residue free reactive ion etching of 3C-SiC and 6H-SiC in fluorinated mixture plasmas" *J. Electrochem. Soc.*, vol. 142, no. 8, pp. 2853-2860, 1995.
10. G. Tittelbach, B. Richter and W. Karthe, "Comparison of three transmission methods for integrated optical waveguide propagation loss measurement", *Pure and Applied Optics*, **2**, pp 683-706, 1993.
11. S.A. Self, "Focusing of spherical gaussian beams", *Appl. Opt.*, **22**, pp. 658-661, 1983.
12. W.G. Spitzer, D.A. Kleinman and C.J. Frosch, "Infrared properties of cubic silicon carbide films", *Physical Review*, **113**, pp. 133-136, 1959.
13. P. Shaffer and R. Naum, "Refractive index and dispersion of beta silicon carbide", *J.Opt. Soc. Am.*, **59**, pp. 1498-1500, 1969.
14. K.H. Schlereth and M. Tacke, "The complex propagation constant of multilayer waveguides: an algorithm for a personal computer", *IEEE J. Quantum Electr.*, **26**, pp. 627-630, 1990.
15. J. Nayyer, Y. Suematsu and H. Tokiwa, "Mode coupling and radiation loss of clad-type optical waveguides due to the index inhomogeneities of the core material", *Opt. and Quantum Electron.*, **7**, pp. 481-492, 1975.
16. T.S. Moss, G.J. Burrell and B. Ellis, *Semiconductor Opto-electronics*. London, UK: Butterworth & Co., 1973.
17. G.L. Harris, H.S. Henry, A. Jackson and S. Yoshida, "Carrier Properties and Band Structure", *Properties of Silicon Carbide*, pp 63-81, ed. G.L. Harris, EMIS Datareviews Series No.13, published by INSPEC, 1995.

Blazed grating couplers in Unibond SOI

T.W. Ang, G.T. Reed, A. Vonsovici, A.G.R. Evans*, P.R. Routley*, M.R. Josey*

School of Electronic Engineering, Information Technology, and Mathematics, University of Surrey,
Guildford, GU2 5XH, UK.

* Department of Electronics and Computer Science, University of Southampton, Highfield, SO17 1BJ,
UK.

ABSTRACT

Grating couplers can be more efficient than end-fire coupling, in coupling light into a thin film waveguide (thickness of $\sim 1 \mu\text{m}$ and below). The aim of this work is to fabricate a low cost, highly efficient silicon waveguide grating coupler which is to be used at the telecommunication wavelength of $1.3 \mu\text{m}$. Silicon-on-insulator (SOI) is chosen for fabricating the gratings as it is low cost using the existing silicon technology. Unibond wafers were used because they offer flexibility in the choice of the thickness of both the silicon film and the buried oxide layer, and they have low optical waveguide loss. The wafers used in this work have a Si film thickness of $1.14 \mu\text{m}$ and a SiO_2 buried layer thickness of $0.67 \mu\text{m}$. Gratings that have asymmetrical profiles, such as blazed gratings are known to have higher directionality than the symmetrical rectangular gratings, and hence a higher output efficiency. Using perturbation theory, Si blazed gratings with an optimum grating height were predicted to have a maximum output efficiency of the order of 90 % towards the substrate. The design and fabrication of the blazed gratings will be discussed in this paper.

Key words: Unibond, silicon-on-insulators, blazed gratings, waveguide grating couplers, ion beam milling.

1. INTRODUCTION

Silicon-based guided-wave optics has demanded attention because of the possibility of expansion of broadband network delivered to the business/home [1-2]. Integrated optical transceivers intended for optical networks, such as local area networks and fibre to home connections can be fabricated using silicon-on-insulator (SOI) technology [1-2].

Integrated optics in SOI usually utilises a silicon layer of several microns in thickness, in order to ensure high efficiency coupling between external devices such as optical fibres and integrated optical chips. However, because the only efficient optical modulation mechanism in silicon is via the injection of free carriers [3], this relatively large silicon layer results in modulators limited to a few tens of MHz [4-5]. An alternative method of efficiently coupling to thin silicon layers will result in higher speed modulators [6]. Grating couplers offer such a possibility. Hence, our aim in this work is to design and fabricate an highly efficient thin film SOI waveguide grating coupler which can be developed for low cost high-speed modulation in Si-based optoelectronics.

Waveguide grating couplers have been widely used for integrated optics applications as input or output devices. To have an high output efficiency, the output beam of the coupler should be radiating into either the upper air or lower substrate, at a specific diffraction order [7]. However, for a symmetrical grating, which is usually a rectangular or sinusoidal profile, the output beam is typically divided equally between the air and substrate regions and hence the maximum efficiency is limited to 50 % [7].

Methods to divert most of the output beam to the desired region and hence maximise the efficiency, include the use of blazed gratings which utilise sawtooth [8-9] and parallelogramic profiles [10-11] and the use of single [12] or multi-layered reflective claddings or substrates [13].

In our previous work, we achieved an output efficiency of the order of 70 % towards the superstrate using rectangular gratings with a reflective buried oxide layer and an optimum grating height in SOI [14]. To our knowledge, this output efficiency is the highest reported in SOI for a symmetrical grating profile.

Sawtooth blazed grating couplers are typically known to have almost twice the output efficiency of the rectangular gratings, due to the blazing effect [8-9]. The sawtooth blazed profile can either be produced directly by tilting the wafer at an angle during the ion beam etching, or by the technique of direct electron beam writing with variable electron dose. The latter method is however less effective in creating a good asymmetrical profile due to the scattering of electrons during the lithography process [15], especially when the pitch of the grating is in the submicron range. Various sawtooth blaze angles can be fabricated by tilting the wafer at different angles in the ion beam chamber [16].

Unibond SOI wafers were chosen for fabricating our grating couplers because they allow us to select the Si film and the buried SiO₂ and hence give greater flexibility in grating coupler design. Furthermore, they exhibit a very low optical loss of 0.15 ± 0.05 dB/cm [17] which is the among the lowest SOI waveguide losses reported [18]. To compromise between the cost and the specification of the thickness, the Unibond SOI wafers were chosen to have the Si film thickness of 1.14 μm (approximately 1 μm after device fabrication) and the SiO₂ thickness of 0.67 μm [14].

Grating couplers fabricated on SOI waveguides operating at an infrared wavelength of 1.3 μm require submicron grating pitch. To realise this feature size on the device, we used electron-beam lithography to write the rectangular grating pattern in a nitride mask. The blaze profile was then transferred to the Si layer by tilting the wafer at an angle in an Argon (Ar) ion beam chamber.

2. THEORY

2.1 Blazed gratings in SOI

The basic structure of blazed grating couplers in SOI is shown in Fig. 1. The grating consists of grating height, t_g , grating period, d , and the output beam angle, ϕ_1 . To maximise output efficiency, we designed the grating at the diffraction order of -1 and its period, d , using the following equations [7]:

$$d = \frac{\lambda}{N - \sin \phi_{-1}} \quad (1)$$

$$d < \frac{2\lambda}{n_s + N} \quad (2)$$

where N is the effective refractive index of the guiding layer with the grating, λ is the input laser wavelength in the air, n_s is the refractive index of SiO₂ and the remainder of the parameters are defined above.

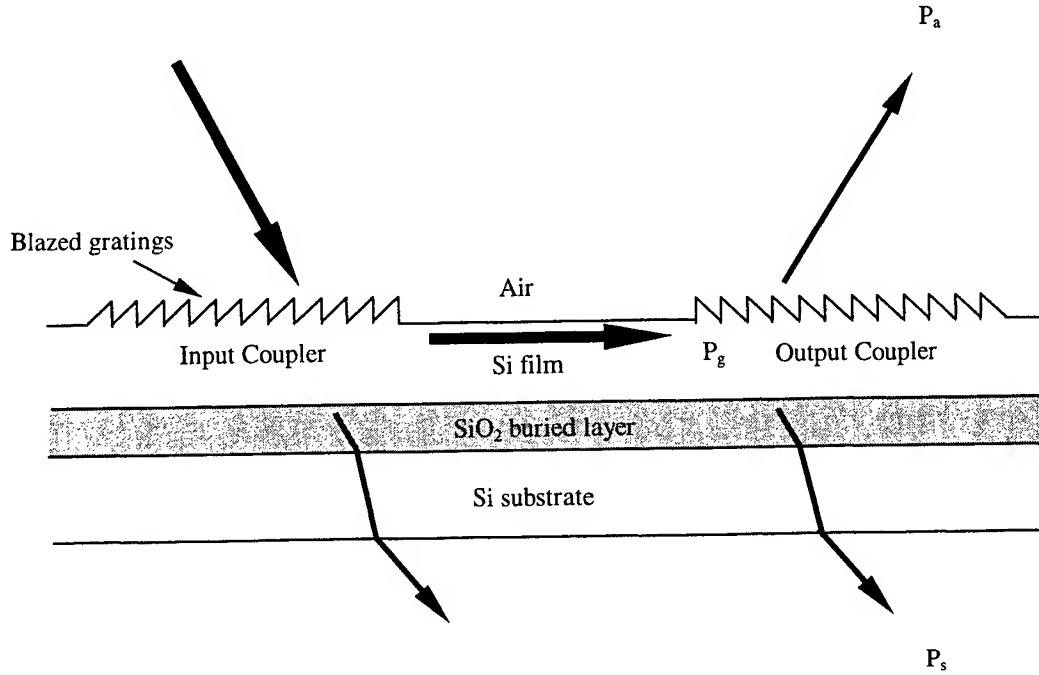


Fig. 1 Geometry of input and output blazed grating couplers in SOI waveguide.

From Fig. 1, the output efficiency of the blazed grating coupler can either be:

$$\eta_a = \frac{P_a}{P_g} \quad (3)$$

or

$$\eta_{sub} = \frac{P_s}{P_g} \quad (4)$$

where η_a is the output efficiency towards the superstrate (air), η_{sub} is the output efficiency towards the substrate, P_a is the output power diffracted towards the superstrate, P_g is the incident surface wave power propagating in the guiding layer and P_s is the transmitted beam power towards the substrate.

3. EXPECTED OUTPUT EFFICIENCY

3.1 Predicted output efficiency of ideal right-angled Si blaze profile

The designs of Si blazed gratings were based on perturbation by constructive Bragg-reflection inside the grating in which most of the surface wave in the output coupler can be radiated into either the upper air region or the lower substrate region [8-9]. The output efficiency of an ideal right-angled Si blazed profile in SOI with the film thickness of $1\text{ }\mu\text{m}$ can be predicted using the perturbation theory [14, 19]. However in reality, the blazed grating is more likely to be of variable triangular shape which has its vertical side slanted by a few degrees or of a trapezoidal shape which has its top portion removed, due to the difficulties of etching the precise right-angle triangular profiles during fabrication. Therefore it is necessary for us to predict the output coupling efficiency for this non-ideal trapezoidal blazed profile.

3.2 Predicted output efficiency of trapezoidal Si blaze profile

Fig. 2 shows the theoretical output efficiency of a trapezoidal Si blazed grating. It has a constant grating height of $0.2\text{ }\mu\text{m}$ and a grating period of $0.4\text{ }\mu\text{m}$.

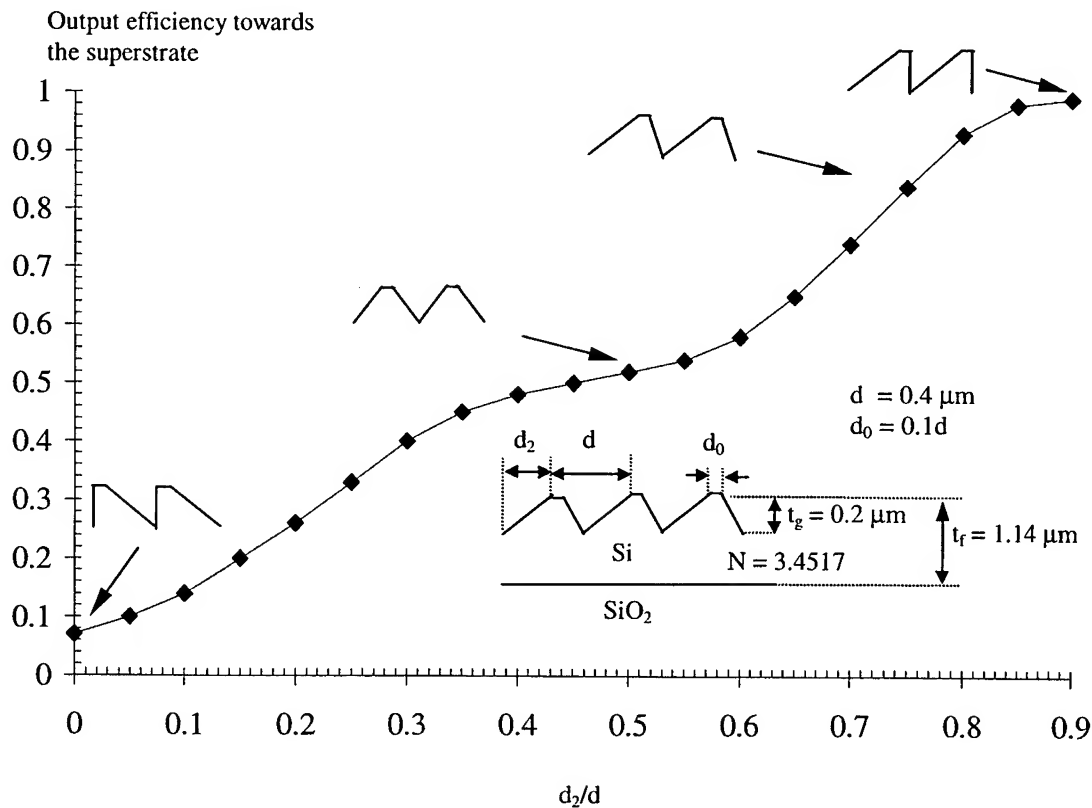


Fig. 2 Output efficiency of a non-ideal trapezoidal Si blazed grating on SOI waveguide at the period of $0.4\text{ }\mu\text{m}$, grating height of $0.2\text{ }\mu\text{m}$ at $1.3\text{ }\mu\text{m}$ in TE mode.

The trapezoidal grating has a non-ideal flat-top portion, d_0 , fixed at $0.1d$ which has the value of 40 nm. We then varied the slanting width of the grating, d_2 , which in turn determines the output efficiency towards the surface (superstrate) of the grating coupler.

The output efficiency decreases from a maximum of 99 % when $d_2/d = 0.9$ (a right-angle blazed with a flat-top portion) to a minimum of 7 % when $d_2/d = 0$ (becomes a laterally mirrored blaze profile). Hence, by keeping the flat-top width to a minimum, we can still achieve a maximum output efficiency towards the surface close to 100 % which is that of an ideal right-angled blazed grating [14]. When $d_2/d = 0.5$, output efficiency drops to almost that of a symmetrical profile (50 %).

The reason that the output efficiency falls below that of a symmetrical rectangular grating in SOI which has a value of the order of 80 % [14], is probably due to the fact that the grating height in this case is not at its optimum value. Hence, we can deduce that the non-ideal slanting wall of the blazed gratings ($d_2/d \neq 1$) has a greater effect upon determining the output efficiency of the grating coupler towards the surface than the small flat-top width. This conclusion agrees well with the results shown by other workers [8-9, 20] where the second slanting side of the blazed grating diverts some of the guided wave into the lower region and hence increases the output efficiency of the grating coupler towards the substrate.

In reality, since it is difficult to fabricate an ideal right-angled blazed gratings to attain a maximum output efficiency towards the superstrate [e.g. 20], we have decided to design our SOI blazed grating coupler with the maximum output efficiency diffracts towards the substrate since the fabricated slanting wall of the blazed grating will help to increase the output efficiency towards the lower substrate as shown in Fig. 2.

Hence, an output efficiency towards the substrate of a non-ideal blaze profile which has a second slanting slope (20 % of grating period) at Si film thickness of $1\text{ }\mu\text{m}$ was plotted as shown in Fig. 3. It can be seen that the output efficiency reaches its maximum of the order of 90 % at the grating height below 80 nm.

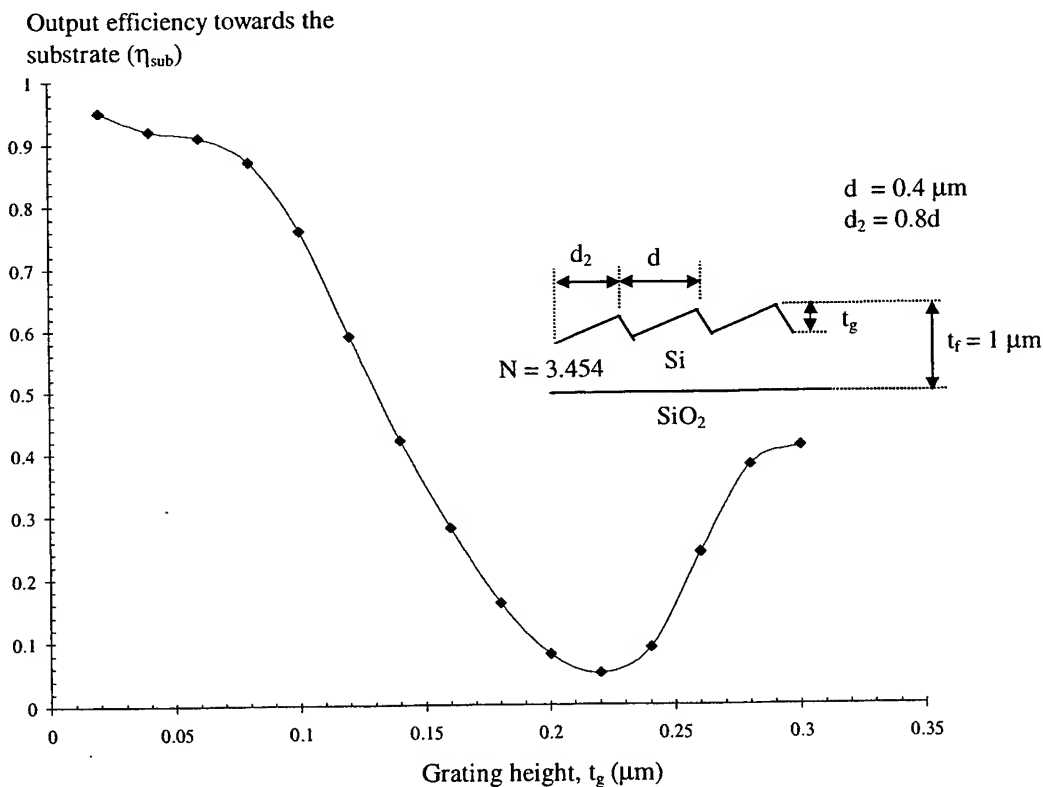


Fig. 3 Theoretical perturbation output efficiency with various grating heights of the fabricated SOI blazed grating couplers.

4. FABRICATION

The SOI wafer was first RCA cleaned and then deposited with a layer of 200 nm thick silicon nitride (Si_3N_4) by LPCVD (Low Pressure Chemical Vapour Deposition) growth. Before ion etching the wafer, rectangular gratings were formed in the Si_3N_4 mask with a period of 400 nm using electron-beam lithography, followed by reactive ion etching. The wafer was then dry etched with Argon (Ar) in the Ion Beam Miller chamber with the condition as shown in Table 1.

Gas content for Si etch	Argon (Ar)
Base pressure	4 μT
RF power	311 W
Bias voltage	390 V
Bias current	200 A
Accelerating voltage	275 V
Accelerating current	20 A

Table 1 Condition of the Ar beam etching for the Si blazed gratings.

The wafers were tilted at various angles as shown in Fig. 4 to investigate the characteristic of the ion beam etching on the blaze profile and the blaze angle of the Si gratings. The wafer tilt angle ranged from 27° to 67° and the etch time was selected as 4 minutes. The blaze angle was expected to range from 63° to 23° (90° - wafer tilt angle) and the etch depth was expected to be of the order of 100 nm.

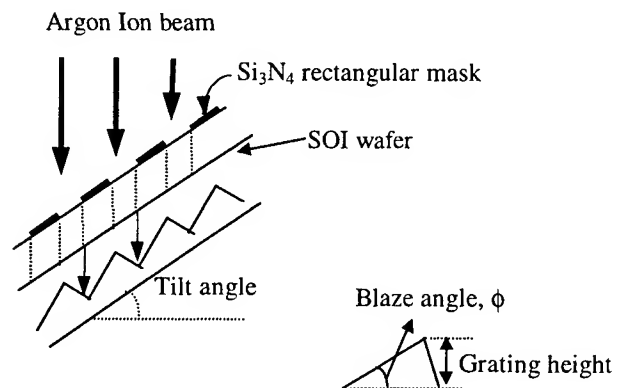


Fig. 4 SOI wafer etched with Argon in Ion Beam Miller at a tilt angle.

Fig. 5 shows the outcome of the relation between the blaze angle and the wafer tilt angle. It can be seen that the resultant blaze angle, ϕ , was determined by (77°- wafer tilt angle), instead of (90°- wafer tilt angle) as achieved by [16]. This could be due to the fact that the blaze angle is also dependent on the grating height, i.e. the vertical etch depth of the Si blazed gratings.

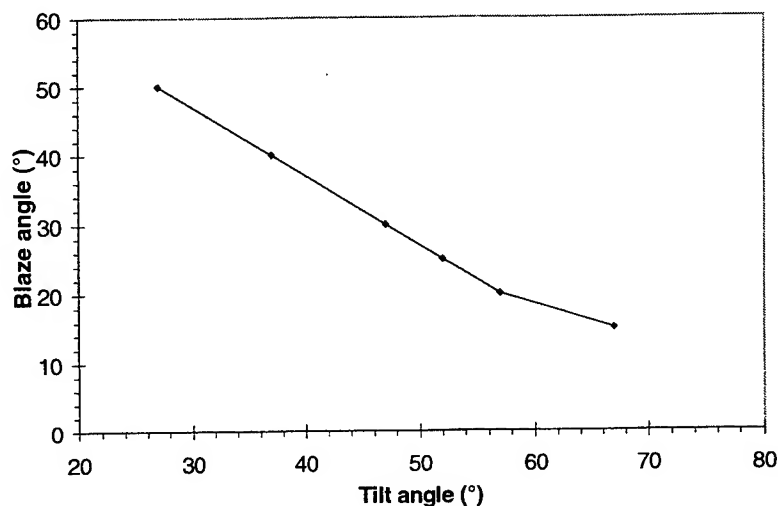


Fig. 5 Relation between the tilt wafer angle and the blaze angle.

Different duty cycles of the nitride rectangular masks ranging from 30 to 50 % were also fabricated to determine whether the mark to space ratio of the mask had any effect upon the blaze profile. The experiments indicated that the duty cycle of the mask had little effect upon the outcome of the blazed gratings, as compared to the tilt angle and etching time. Consequently, the rectangular grating mask was usually fabricated in the duty cycle of 50 %.

5. RESULT

5.1 Fabricated SOI blazed grating coupler

The best asymmetrical Si blazed profile using the grating mask period of 400 nm was successfully fabricated in SOI Unibond wafers at the tilt angle of 70°, as shown in Fig. 6. The middle section under the gratings shown in the photograph is the SiO₂ buried layer in the Unibond wafer. Under the inspection of an SEM (Scanning Electron Microscopy), the resulting fabricated Si blazed gratings were found to have a grating pitch of 380 nm, a grating height of 80 nm and the resulting Si film thickness is 1 μ m. In addition, it can be seen that the top portion of the blaze is sharp and the blaze angle is approximately 10°.

The measured output efficiency of this SOI blazed grating coupler will be evaluated and reported elsewhere, but is expected to be of the order of 85 %, and certainly in excess of 80 %.

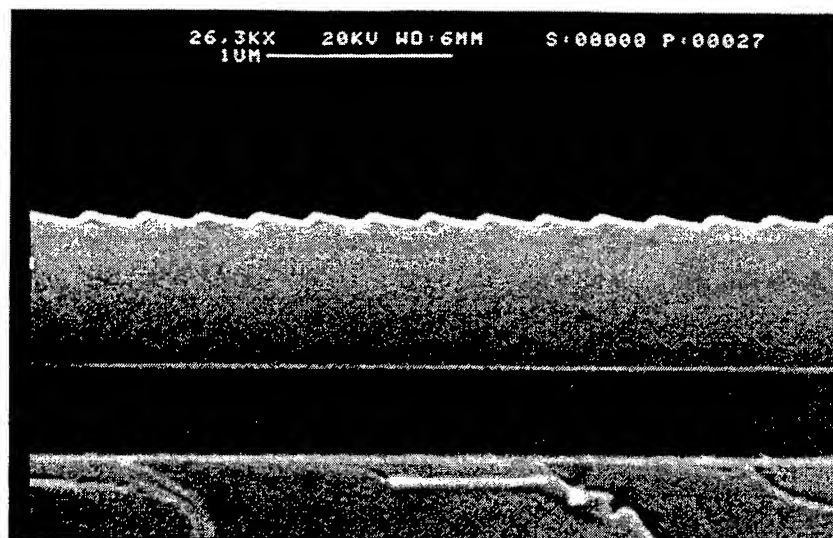


Fig. 6 SEM photograph of a good asymmetrical Si blazed profile in Unibond SOI which has the pitch of 383 nm and a grating height of 80 nm with a Si film thickness of 1 μ m.

6. CONCLUSION

We have shown using the perturbation theory that the blazed grating has a maximum output efficiency of the order of 90 % towards the substrate which is higher than that of the rectangular gratings. In addition, we have successfully fabricated good asymmetrical Si sawtooth blazed gratings which have a pitch of less than 400 nm using the angled ion beam etching. To our knowledge, this is the first blazed gratings fabricated in SOI. The coupling efficiency of the gratings will be evaluated and reported elsewhere.

7. ACKNOWLEDGEMENT

The first author is grateful for an Overseas Research Studentship (ORS) and a Faculty Scholarship from the University of Surrey awarded to him to pursue his Ph.D. and all the authors wish to express their thanks to Bookham Technology Limited for financial support.

REFERENCES

- [1] A. Harpin, "Integrated optics in silicon: coming of age", Proc. of SPIE, **3007**, pp. 128-135, 1997.
- [2] R. Morris, "Silicon-on-insulator integrated optic transceivers", Proc. of SPIE, **3007**, pp. 56-67, 1997.
- [3] R. A. Soref and B. R. Bennett, "Electrooptical effects in silicon", IEEE J. Quant. Elect., **QE-23**, 1, pp. 123-129, 1987.
- [4] G.V. Treyz, P.G. May, and J.M. Halbout, "Silicon Mach-Zehnder waveguide interferometer based on the plasma dispersion effect", Appl. Phys. Lett., **59**, 7, pp. 771-773, 1991.
- [5] C.Z. Zhao, G.Z. Li, E.K. Liu, Y. Guo and X.D. Liu, "Silicon-on-insulator Mach-Zehnder waveguide interferometers operating at 1.3 μ m", Appl. Phys. Lett., **67**, 17, pp. 2448-2449, 1995.
- [6] T.W. Ang, P.D. Hewitt, A. Vonsovici, G.T. Reed, A.G.R. Evans, P.R. Routley, T. Blackburn and M.R. Josey,

- "Integrated optics in Unibond for greater flexibility", *Proc. of Electrochemical Soc.*, **99-3**, pp. 353-360, 1999.
- [7] T. Tamir and S.T. Peng, "Analysis and design of grating couplers", *Appl. Phys.*, **14**, pp. 235-254, 1977.
 - [8] S.T. Peng and T. Tamir, "Directional blazing of waves guided by asymmetrical dielectric gratings", *Opt. Comm.*, **11**, 4, pp. 405-409, 1974.
 - [9] K.C. Chang and T. Tamir, "Bragg-reflection approach for blazed dielectric gratings", **26**, 3, pp. 327-330, 1978.
 - [10] A. Larsson, N. Eriksson, M. Li, S. Kristjansson and M. Hagberg, "Grating coupled surface emitters with built-in beam control", *Proc. of SPIE*, **3004**, pp. 49-59, 1997.
 - [11] M. Hagberg, N. Eriksson and A. Larsson, "High efficiency surface emitting lasers using blazed grating outcouplers", *Appl. Phys. Lett.*, **67**, 25, pp. 3685-3687, 1995.
 - [12] R.M. Emmons and D.G. Hall, "Buried-Oxide Silicon-on-Insulator Structures II : Waveguide Grating Couplers", *IEEE J. of Quant. Elect.*, **28**, 1, pp. 164-175, 1992.
 - [13] N. Eriksson, M. Hagberg and A. Larsson, "Highly efficient grating-coupled surface-emitters with single outcoupling elements", *IEEE Photo. Tech. Lett.*, **7**, 12, pp. 1394-1396, 1995.
 - [14] T.W. Ang, G. T. Reed, A. Vonsovici, A. G. R. Evans, P. R. Routley, T. Blackburn, M. R. Josey, "Grating couplers using silicon-on-insulator", *Proc. of SPIE*, **3620**, pp. 79-86, 1999.
 - [15] A.N. Broers, "Fabrication limits of electron beam lithography and of UV, X-ray and ion-beam lithographies", *Phil. Trans. R. Soc. Lond.*, **A**, **353**, pp. 291-311, 1995.
 - [16] A. Yoshinobu and N. Susumu, "Blazing of holographic grating by ion etching technique", *Jap. J. Appl. Phys.*, **15**, 4, pp. 721-722, 1976.
 - [17] T.W. Ang, G. T. Reed, A. Vonsovici, A. G. R. Evans, P. R. Routley, M. R. Josey, "0.15 dB/cm loss in Unibond SOI waveguides", *Elect. Lett.*, **35**, 12, pp. 977-978, 1999.
 - [18] U. Fischer, T. Zinke, J. -R. Kropp, F. Arndt and K. Petermann, "0.1 dB/cm waveguide losses in single-mode SOI rib waveguides", *IEEE Photo. Tech. Lett.*, **8**, 5, pp. 633-635, 1996.
 - [19] K.C. Chang, "Surface-Wave Scattering by Dielectric Gratings with Arbitrary Profiles," Ph.D. Dissertation, Polytechnic Institute of New York (June 1979).
 - [20] R. Waldhäusl, P. Dannberg, E.B. Kley, A. Bräuer and W. Karthe, "Highly efficient blazed grating couplers in planar polymer waveguides", *Int. J. of Optoelectronics*, **8**, 5/6, pp. 529-536, 1993.

Effective-index method with built-in perturbation correction for the design of polarization-insensitive optical waveguide directional couplers

Kin Seng Chiang and Chung Ho Kwan

Optoelectronics Research Center and Department of Electronic Engineering
City University of Hong Kong, Hong Kong, P. R. China

ABSTRACT

In this paper, we apply the recently proposed effective-index method with built-in perturbation correction to the study of directional coupler that consists of two parallel rectangular-core waveguides. We show with numerical examples that the splitting ratio of the directional coupler can be made insensitive to the polarization state of the input light by using proper waveguide parameters.

Keywords: Couplers, integrated optics, polarization, waveguides

1. INTRODUCTION

Optical waveguide directional couplers are the building blocks of many integrated optic circuits. The behavior of a directional coupler in the form of two parallel identical optical waveguides is characterized by a coupling coefficient, which is a measure of the difference of the propagation constants for the symmetric and antisymmetric modes of the composite waveguide structure.¹ In general, the coupling coefficient, and hence, the splitting ratio of a coupler, depends on the polarization state of light. This can give rise to polarization noise when light is launched into the coupler from a single-mode fiber. It is of practical interest to search for designs of directional couplers that have polarization-independent coupling coefficients.

Our study involves the calculation of the coupling coefficients for both polarized modes of the couplers, and requires a method that can discriminate between the polarized modes with a good accuracy. Because intensive computation is necessary for finding the conditions to achieve polarization independence, conventional numerical methods for solving the vector wave equation,² such as the finite-element method and the finite-difference method, are just too inefficient for the task. In the case of a coupler that consists of two parallel rib waveguides, the spectral-index method has been used for finding the polarization-independence conditions.³ Recently, we have developed a new approximate method, namely, the effective-index method with built-in perturbation correction (EIMPC), for the analysis of the polarized modes of rectangular-core waveguides.⁴ The idea of the method is to convert a rectangular-core waveguide into an equivalent

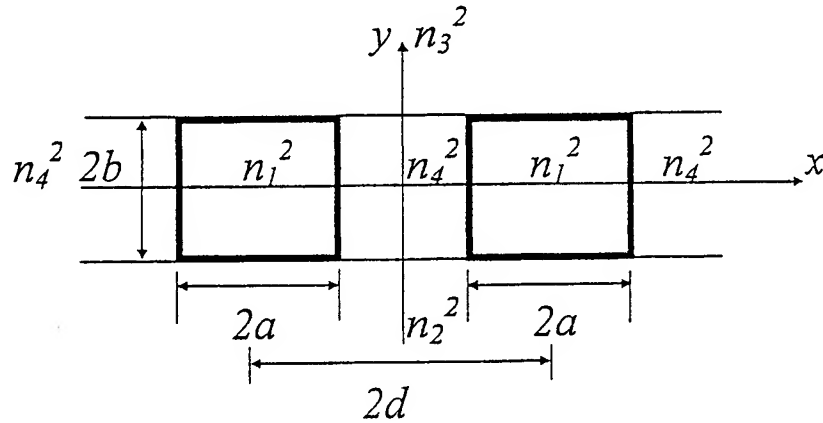


Figure 1: Cross section of a directional coupler consisting of two parallel rectangular-core waveguides.

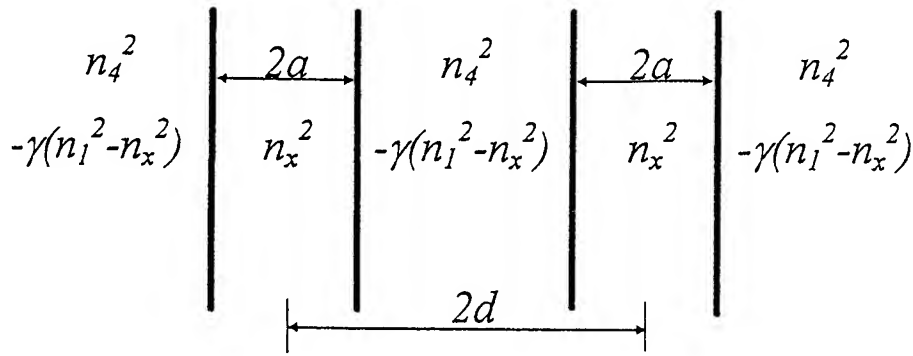
slab waveguide. The method is highly efficient and can differentiate between the polarized modes with a good accuracy. In this paper, we apply the method to the design of polarization-insensitive coupler that consists of two parallel rectangular-core waveguides.

2. METHOD OF ANALYSIS

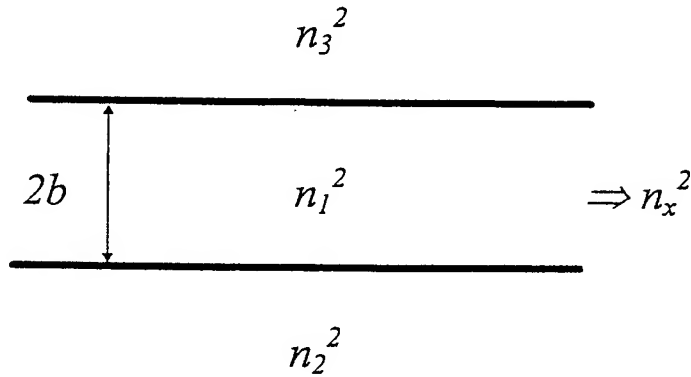
The cross section of a directional coupler consisting of two parallel identical rectangular-core waveguides is shown in Fig.1, where $2a$ and $2b$ are the width and the thickness of the individual core, respectively, $2d$ is the separation between the centers of the cores, and n_1 , n_2 , n_3 , and n_4 are the refractive indices of the core and the surrounding claddings with $n_1 > n_2 \geq n_3, n_4$. The refractive-index profile of this composite waveguide structure is characterized by three relative index steps: $\Delta_i = (n_1^2 - n_i^2)/2n_1^2$ for $i = 2, 3, 4$. This structure is general enough to represent several important classes of optical waveguides, including fully buried waveguides ($\Delta_2 = \Delta_3 = \Delta_4$), channel waveguides ($\Delta_3 > \Delta_2 = \Delta_4$), and strip or ridge waveguides ($\Delta_3 = \Delta_4 > \Delta_2$). In practice, the refractive index of the cores is only slightly larger than that of a surrounding cladding, i.e., at least one of Δ_i is much smaller than unity. As a result, the guided mode of the composite waveguide is approximately linearly polarized.² In general, the guided mode can be designated as the E_{mn}^p mode with $m - 1$ and $n - 1$ field zeros along the x and y axes, respectively, where $p = x$ or y indicates the direction of the predominant transverse electric field.

The power transfer between the two waveguides, which are assumed single-moded in isolation, can be described by the beating between the symmetric (E_{11}^p) and antisymmetric (E_{21}^p) modes of the composite two-core waveguide.¹ The beatlength of the coupler, i.e., the minimum length of the coupler required for 100% power transfer, is given by $\pi/2C$, where C is the coupling coefficient, which is equal to half the difference between the propagation constants for the E_{11}^p and E_{21}^p modes. In general, the coupling coefficient and hence the beatlength depend on which polarization of light is used, i.e., whether $p = x$ or y . In the present study, we employ the effective-index method with built-in perturbation correction (EIMPC)⁴ to study the polarization dependence of the coupling coefficient.

The idea of the EIMPC is to approximate the rectangular waveguide coupler in Fig.1 by a slab waveguide coupler shown in Fig.2(a), where the refractive index n_x is determined from the three-layer



(a)



(b)

Figure 2: The idea of the effective-index method with built-in perturbation correction is to approximate the rectangular waveguide coupler in Fig.1 by (a) a slab waveguide coupler, where the effective index n_x is determined from (b) a three-layer slab waveguide.

slab waveguide in Fig.2(b). To be specific, the mode index (the propagation constant divided by the free-space wavenumber) for the TE_{n-1} (TM_{n-1}) mode of the slab waveguide in Fig.2(b) is used as the effective refractive index n_x of the coupler in Fig.2(a). The propagation constant for the TM_{m-1} (TE_{m-1}) mode of the slab waveguide coupler is then regarded as the approximate propagation constant for the E_{mn}^x (E_{mn}^y) mode of the rectangular waveguide coupler. As shown in Fig.2(a), a parameter γ is introduced in the claddings of the slab waveguide coupler. The conventional effective-index method corresponds to the case $\gamma = 0$.^{5,6} The EIMPC employs an optimal value of γ to eliminate the first-order perturbation error in the propagation constant.⁴⁻⁶

Analytical expressions for γ have been derived for the polarized modes of a single rectangular-core waveguide.⁴ The same expressions can be used for the analysis of rectangular waveguide couplers. For the E_{mn}^x mode, the result is the same as that for the scalar mode:^{4,6}

$$\gamma = 1 - \frac{(\Delta_4/\Delta_3)W_2 + (\Delta_4/\Delta_2)W_3}{2W_2W_3 + W_2 + W_3} \quad (1)$$

where $W_2 = bk(n_x^2 - n_2^2)^{1/2}$ and $W_3 = bk(n_x^2 - n_3^2)^{1/2}$ with k the free-space wavenumber. For the E_{mn}^y

mode, γ is given by⁴

$$\gamma = 1 - \left(\frac{\Delta_4}{\Delta_2}\right) \left(\frac{V}{U}\right)^2 \frac{\left[1 + \frac{4\Delta_2}{1-2\Delta_2} \left(\frac{W_2}{V}\right)^2\right] P_2 + \left[1 + \frac{4\Delta_2}{1-2\Delta_3} \left(\frac{W_3}{V}\right)^2\right] P_3}{1 + \frac{4\Delta_2}{1-2\Delta_2} \left(\frac{W_2}{V}\right)^2 P_2 + \frac{4\Delta_2}{1-2\Delta_3} \left(\frac{W_3}{V}\right)^2 P_3} \quad (2)$$

where $U = bk(n_1^2 - n_x^2)^{1/2}$, and $V = bk(n_1^2 - n_2^2)^{1/2}$ is the normalized frequency. P_2 and P_3 are given by $P_2 = f_2/f$ and $P_3 = f_3/f$ with $f = f_1 + f_2 + f_3$, where

$$f_1 = 2 + \left(\frac{W_2}{U}\right)^2 f_2 + \left(\frac{W_3}{U}\right)^2 f_3 \quad (3)$$

$$f_2 = \frac{U^2}{W_2 \left[(1 - 2\Delta_2)U^2 + \left(\frac{1}{1-2\Delta_2}\right) W_2^2 \right]} \quad (4)$$

$$f_3 = \frac{U^2}{W_3 \left[(1 - 2\Delta_3)U^2 + \left(\frac{1}{1-2\Delta_3}\right) W_3^2 \right]} \quad (5)$$

It can be shown that, in the limit $\Delta_2 \rightarrow 0$, Eq.(2) reduces to Eq.(1). It should be noted that only the solutions for the slab waveguide in Fig.2(b) are required for the evaluation of γ . In comparison with the effort of solving the slab waveguides, the extra effort of computing γ from Eq.(1) or Eq.(2) is negligible. The EIMPC is practically as efficient as the conventional effective-index method, yet produces far more accurate results.⁴⁻⁶ The EIMPC can differentiate the polarized modes with a good accuracy,⁴ and, therefore, is suitable for the study of the polarization-dependent properties of the waveguides.

In the analysis of the couplers, what we actually calculate are the normalized coupling coefficients C_x and C_y for the x - and y -polarized modes:

$$C_p = \frac{V}{4}(P_{11p}^2 - P_{21p}^2), \quad p = x, y \quad (6)$$

where P_{11p}^2 and P_{21p}^2 are the normalized propagation constants for the E_{11}^p and E_{21}^p modes, respectively, with

$$P_{mnp}^2 = \frac{(\beta_{mnp}^2/k)^2 - n_2^2}{n_1^2 - n_2^2} \quad (7)$$

where β_{mnp} is the propagation constant for the E_{mn}^p mode. By using the normalized parameters, the results can be presented in a more universal way.

3. POLARIZATION NOISE

The coupling coefficients C_x and C_y are in general different. This can cause polarization noise. To see this, we consider a coupler that is half-beatlength long for light linearly polarized in the x direction. For this particular polarization state of light, the coupler functions as a 50/50 power divider. For light linearly polarized in the y direction, however, the splitting ratio is no longer strictly 50%, because the coupling coefficient (and hence the beatlength) is slightly different from that for the x -polarized light. A variation

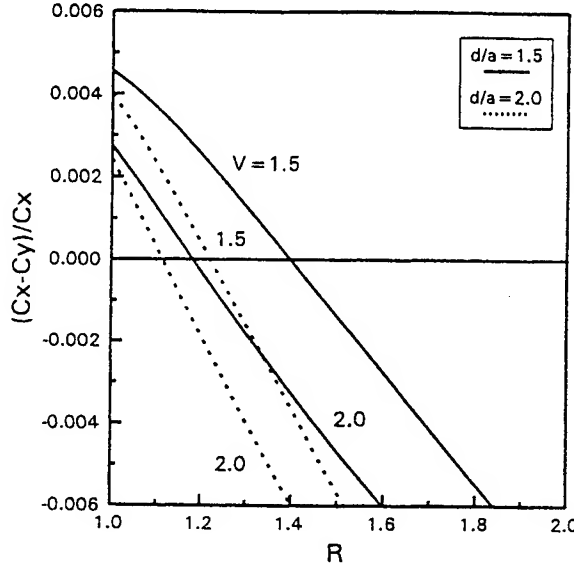


Figure 3: The relative difference between C_x and C_y as a function of R for a fully buried waveguide coupler with $\Delta_2 = \Delta_3 = \Delta_4 = 0.01$.

in the polarization state of the input light to the coupler can thus cause a variation in the output power from the coupler. This gives rise to noise when the polarization state of the input light varies randomly.

The polarization noise in a half-beatlength coupler can be calculated from the following expression:

$$N = \left| 1 - 2 \cos^2 \left(\frac{\pi C_y}{4 C_x} \right) \right| \quad (8)$$

which is a measure of the relative output power fluctuation. For a fully buried coupler with $\Delta_2 = \Delta_3 = \Delta_4 = 0.01$, $a/b = 1$, and $d/a = 1.5$, operated at $V = 1.5$, we find $C_y/C_x = 0.9954$, which gives a fluctuation of about 0.7%. When the relative index step of the coupler is increased to 0.05 (with other parameters unchanged), the power fluctuation increases to about 3.7%. In the next section, we show that the noise of this kind can be eliminated by choosing the waveguide parameters properly.

4. POLARIZATION-INSENSITIVE COUPLERS

4.1 Fully Buried Waveguide Couplers

We first consider a fully buried waveguide coupler with $\Delta_2 = \Delta_3 = \Delta_4 = 0.01$. The relative difference between C_x and C_y is shown in Fig.3 as a function of the aspect ratio $R = a/b$ of the cores for two core separations: $d/a = 1.5$ and 2.0. It is clear from Fig.3 that, in each case, the difference between C_x and C_y changes sign as R increases and there exists a particular value of R at which $C_x = C_y$, i.e., the coupler becomes polarization-insensitive.

The aspect ratio R required for achieving polarization independence ($C_x = C_y$) is presented in Fig.4(a) as a function of V for several core separations, and the corresponding coupling coefficient is shown in

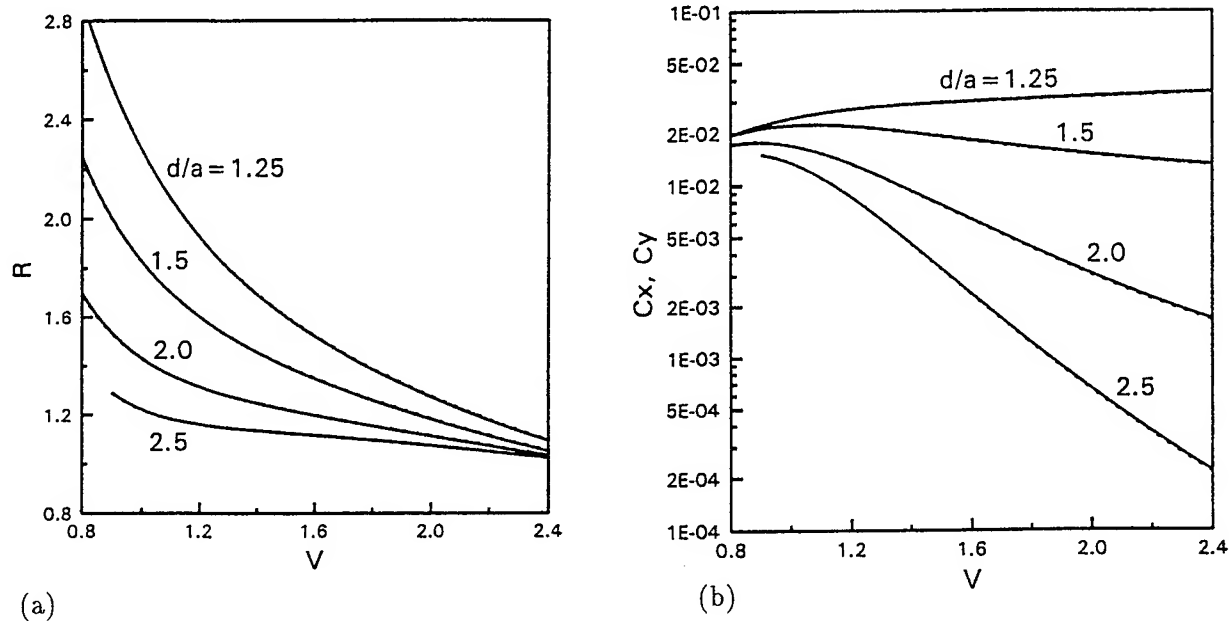


Figure 4: (a) The aspect ratio R required for achieving polarization independence as a function of V and (b) the corresponding normalized coupling coefficient as a function of V for a fully buried waveguide coupler with $\Delta_2 = \Delta_3 = \Delta_4 = 0.01$ (solid curves) or $\Delta_2 = \Delta_3 = \Delta_4 = 0.005$ (dotted curves).

Fig.4(b). Figure 4 actually contains two sets of results, one for $\Delta_2 = \Delta_3 = \Delta_4 = 0.01$ (solid curves) and the other for $\Delta_2 = \Delta_3 = \Delta_4 = 0.005$ (dotted curves), but they are hardly distinguishable. This implies that the polarization-independence conditions as well as the corresponding normalized coupling coefficients are insensitive to the relative index difference between the cores and the cladding. In general, the aspect ratio required decreases with increasing V and d/a . As far as matching the spot size of a single-mode fiber is concerned, a square core ($R = 1$) is desired. As can be seen from Fig.4(a), the shape of the core gets closer and closer to a square as V and d/a get larger and larger, i.e., when the coupling between the two waveguides gets weaker and weaker.

It should be noted that, when V falls below the cutoff frequency of the E_{21}^p mode, the coupler does not function as a power divider any more. On the other hand, to avoid the guidance of higher-order modes, V should not be larger than the cutoff frequency of the E_{31}^p mode. In Fig.5, the cutoff normalized frequency V_c is shown as a function of R for the E_{11}^p , E_{21}^p , and E_{31}^p modes at several values of d/a ($\Delta_2 = \Delta_3 = \Delta_4 = 0.01$). V_c is found to be insensitive to the polarization of the mode and the relative index difference between the cores and the cladding.

4.2 Channel Waveguide Couplers

We next consider a channel waveguide coupler with $\Delta_3 > \Delta_2 = \Delta_4$. The aspect ratio $R = a/b$ required for achieving $C_x = C_y$ is shown in Fig.6 as a function of V . In Fig.6(a), the results for $\Delta_2 = \Delta_4 = 0.01$ and 0.005 are presented with Δ_3 fixed at 0.3, while in Fig.6(b), the results for $\Delta_3 = 0.3$ and 0.45 are presented with Δ_2 (Δ_4) fixed at 0.01. As can be seen from Fig.6, the polarization-independence conditions are

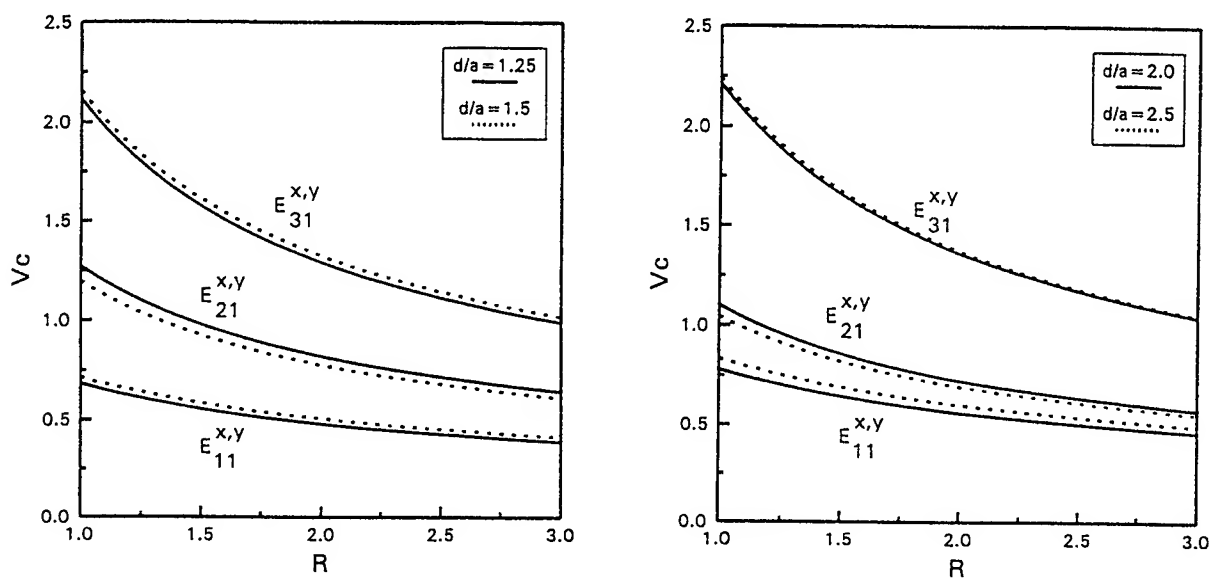


Figure 5: The cutoff normalized frequency V_c as a function of R for the E_{11}^p , E_{21}^p , and E_{31}^p modes of a fully buried waveguide coupler with $\Delta_2 = \Delta_3 = \Delta_4 = 0.01$.

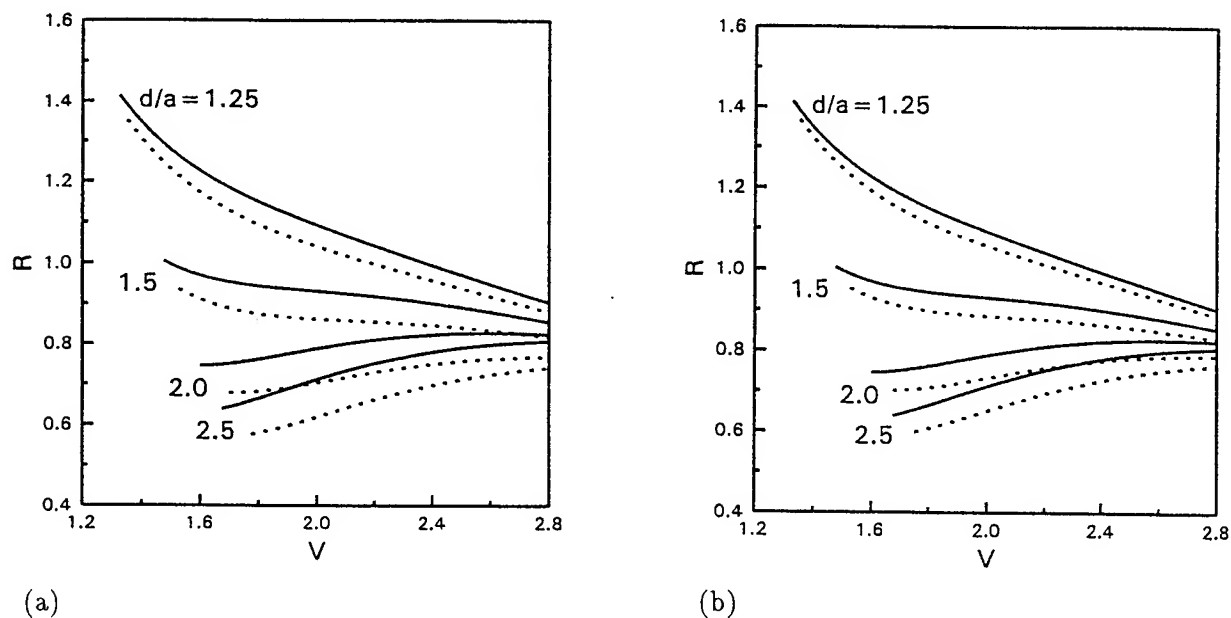


Figure 6: The aspect ratio R required for achieving polarization independence as a function of V for a channel waveguide coupler with (a) $\Delta_3 = 0.3$ and $\Delta_2 = \Delta_4 = 0.01$ (solid curves) or $\Delta_2 = \Delta_4 = 0.005$ (dotted curves); (b) $\Delta_2 = \Delta_4 = 0.01$ and $\Delta_3 = 0.3$ (solid curves) or $\Delta_3 = 0.45$ (dotted curves).

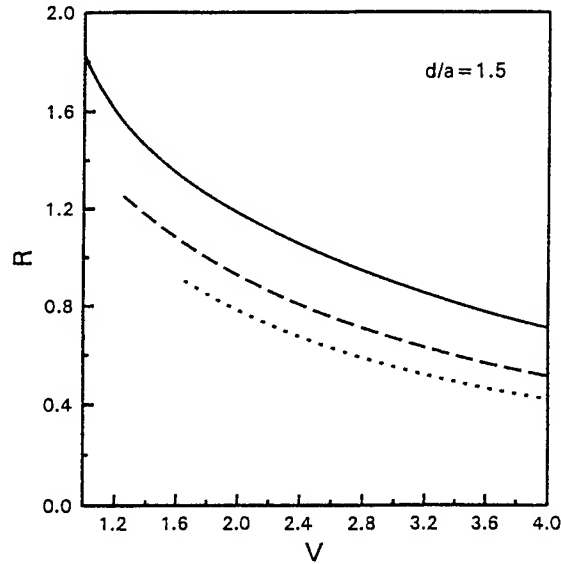


Figure 7: The aspect ratio R required for achieving polarization independence as a function of V for a strip waveguide coupler with $d/a = 1.5$ and $\Delta_2 = 0.01$ at three values of Δ_3 (Δ_4): 0.01 (solid curve), 0.02 (dashed curve), and 0.03 (dotted curve).

sensitive to both Δ_2 and Δ_3 . A comparison of Fig.4(a) and Fig.6 shows that the aspect ratio required for a channel waveguide coupler to achieve polarization independence is in general smaller than that required for a fully buried waveguide coupler.

4.3 Strip Waveguide Couplers

In the case of a strip waveguide coupler with $\Delta_3 = \Delta_4 > \Delta_2$, the polarization-independence conditions are shown in Fig.7, where the results are calculated for $d/a = 1.5$, $\Delta_2 = 0.01$, and three values of Δ_3 (Δ_4): 0.01 (fully buried waveguides), 0.02, and 0.03. As shown in Fig.7, the aspect ratio required can be reduced by increasing Δ_3 (i.e., lowering the cladding index n_3). This can be an effective means of controlling the spot size of a polarization-insensitive coupler.

5. CONCLUSION

By using the effective-index method with built-in perturbation correction, we have analyzed several types of rectangular waveguide directional couplers with emphasis on the calculation of their polarization-dependent properties. We have shown with numerical examples that polarization-independent coupling can be achieved by choosing the waveguide parameters properly. Typical polarization-independence conditions have been presented for several important waveguide geometries, including fully buried waveguides, channel waveguides, and strip waveguides. Our results, though approximate, should serve as useful guidelines for the design of polarization-insensitive couplers based on rectangular-core waveguides.

6. ACKNOWLEDGMENTS

This research work is supported by a University Grants Committee (Hong Kong Government) Research Grant.

7. REFERENCES

1. A. W. Snyder, "Coupled-mode theory for optical fibers," *J. Opt. Soc. Amer.*, Vol.62, pp.1267-1277, 1972.
2. K. S. Chiang, "Review of numerical and approximate methods for the modal analysis of general optical dielectric waveguides," *Opt. Quantum Electron.*, Vol.26, pp.S113-S134, 1994.
3. K. S. Chiang and W. P. Wong, "Design of zero-birefringence semiconductor waveguides," *SPIE Proceedings Vol.3278, Integrated Optic Devices II*, pp.168-178 1998.
4. K. S. Chiang, C. H. Kwan, and K. M. Lo, "Effective-index method with built-in perturbation correction for the vector modes of rectangular-core optical waveguides," *J. Lightwave Technol.*, Vol.17, pp.716-722, 1999.
5. K. S. Chiang, "Analysis of rectangular dielectric waveguides: effective-index method with built-in perturbation correction," *Electron. Lett.*, Vol.28, pp.388-389, 1992.
6. K. S. Chiang, K. M. Lo, and K. S. Kwok, "Effective-index method with built-in perturbation correction for integrated optical waveguides," *J. Lightwave Technol.*, Vol.14, pp.223-228, 1996.

SESSION 10

WDM and Optical Link Components

Arbitrary-response gain-flattening filters with low amplitude and phase noise and in-built ASE suppression.

Mark Janos, Ben Smith, Simon Poole
JDS Uniphase Pty Ltd
4A Byfield St, N.Ryde
NSW, Australia
Tel: +61 2 8875 2900, Fax +61 2 8875 2901

ABSTRACT

We present a Fibre Bragg Gratings for amplifier gain flattening which combine both an extremely high performance gain flattening response with a high-rejection ASE filter. The maximum shape error on the filter is $< \pm 10\%$ with an insertion loss of $< 0.15\text{dB}$ and Group Delay variation of $< \pm 0.6\text{psec}$.

1. INTRODUCTION

Dense Wavelength Division Multiplexed (DWDM) communication systems are now commercially available with 32- and 40- channels whilst 128-channel and above systems have been announced. A key component in all such systems is a gain-flattened erbium-doped fibre amplifier¹. As DWDM systems evolve from simple point-to-point connections (where appropriate pre-emphasis can be used to overcome any non-uniformity in the system response) to ring and, ultimately, mesh architectures, the requirements for uniformity across the amplifier gain band become more stringent. Similarly, for ultra-long haul systems such as undersea networks, several hundred amplifiers may be concatenated in a single chain and any amplifier gain non-uniformity will dramatically affect the system performance.

This is clearly demonstrated in Fig 1 which shows the effect of gain peaking in a cascade of 12 unflattened in-line amplifiers. The distance between each amplifier is 70km. Each graph shows the ASE spectrum (1nm bandwidth) after a specific number of amplifiers. The horizontal axis spans 1500-1600nm and the vertical axis spans 80dB. (Courtesy R.Tench, Lucent Technologies, Breiningsville)

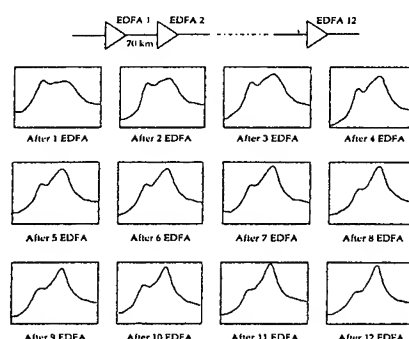


Fig 1 Gain Peaking in an EDFA cascade

A number of techniques for amplifier gain flattening have been proposed and implemented including thin film filter², micro-optics³, blazed Fibre Bragg Gratings (FBGs)⁴ and long-period gratings⁵.

We report here chirped FBGs for amplifier gain flattening, which can be manufactured to an arbitrary shape and have the lowest amplitude and phase noise yet reported. The gratings also include an ASE filter and, by appropriate design, can flatten an amplifier over $> 40\text{nm}$. Environmental performance of the packaged gratings is also reported.

2. CHIRPED FBGS FOR GAIN FLATTENING

Chirped FBGs have received considerable attention as potential dispersion compensation components for high bit-rate DWDM systems. Chirped, unblazed FBGs for amplifier gain flattening have received less research attention but can, with suitable design and control of manufacturing process provide a very precise and flexible solution to the requirements of EDFA manufacturers. Of critical importance is the need to remove any systematic errors in the amplitude of the grating response since in a multi-amplifier system these will add linearly and can cause imbalance in the channel power levels and hence degradation in the system performance. Similarly, any systematic effects in the phase response of a grating can also affect system performance by introducing an additional wavelength-dependent dispersion penalty.

Chirped FBGs for amplifier gain flattening are manufactured by writing a grating with uniform chirp and controlling the reflectivity at different wavelengths by varying the apodisation along the length of the grating. The apodisation profile for a grating combining gain flattening and ASE rejection is shown in Fig 2.

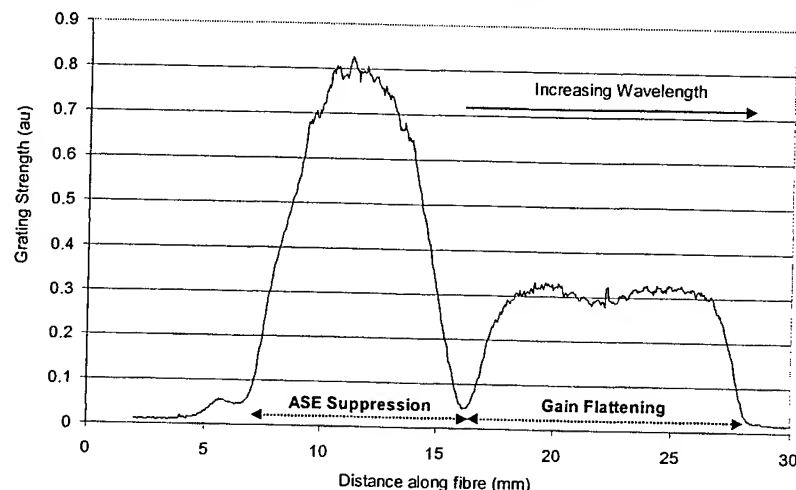


Fig 2 Apodisation profile of gain-flattening grating measured by sidescan technique

3. OPTICAL PERFORMANCE

Typical spectrum of filter combining both a gain flattening filter and ASE suppression is shown in Fig 2. The filter shape, including manufacturing tolerances, matches the required amplitude to within $\pm 0.05\text{dB}$ over the operating range of

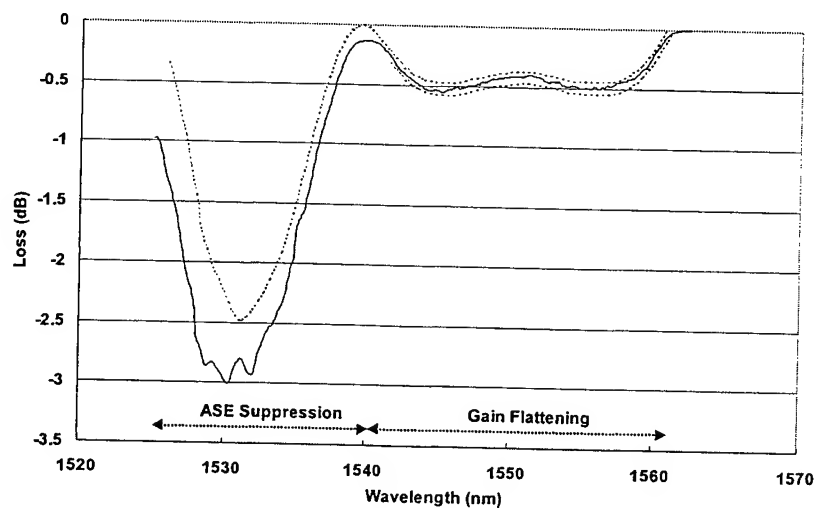


Fig 3 Amplitude response of typical grating.
Error bands are $\pm 0.05\text{dB}$ from the nominal spectrum in gain flattening region

>20nm with an excess loss of <0.15dB. The strength of the ASE suppression peak around 1535nm can be independently controlled and, if required, the high-accuracy gain flattening section can be extended to include the ASE peak, thus further increasing the useable bandwidth.

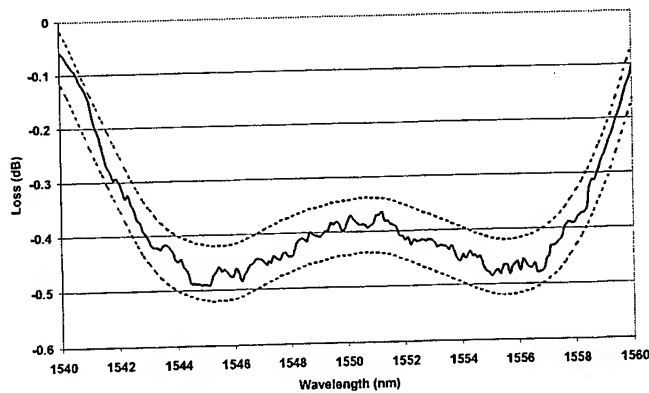


Fig 4 Normalised response of 10 Concatenated Filters
Error bars are set at ± 0.05 dB from nominal specification

As noted above, systematic errors in filter shape can cause significant degradation in system performance.

Fig 4 shows the normalised response of 10 gratings, which shows that any systematic error in the filter response is negligible.

High bandwidth (OC-192 and above) systems require low levels of chromatic and polarisation mode dispersion. The measured Group Delay of an FBG gain-flattening filter is shown in Fig 4. Of particular note is the extremely low noise level in the measurement system (<200fsec), as well as the overall low level of group delay ripple across the grating bandwidth.

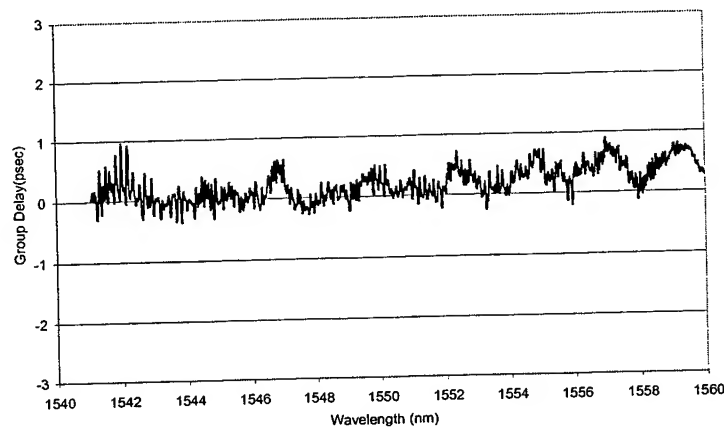


Fig 5 Group Delay Ripple of Gain Equalisation Filter

4. PACKAGING

To maintain the filter performance over the specified operating conditions and throughout the required operational life, the grating must be packaged in an environmentally-stable package. The principle of operation of the package is to compensate for the increase in grating wavelength with temperature (primarily due to the increase in the refractive index of the fibre with temperature) by reducing the strain on the grating as the temperature increases. This is achieved by the package shown schematically in Fig 6 below.

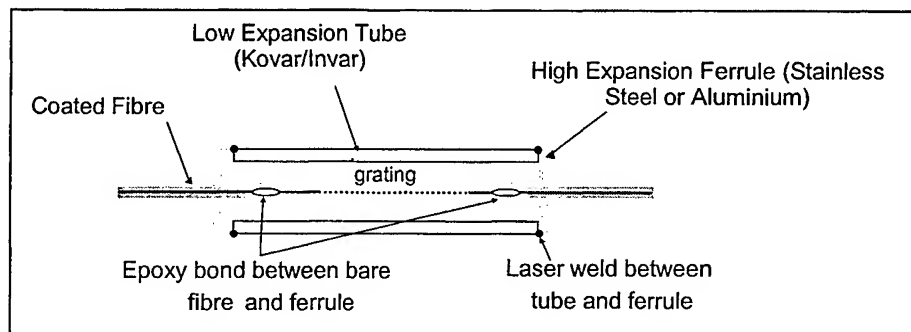


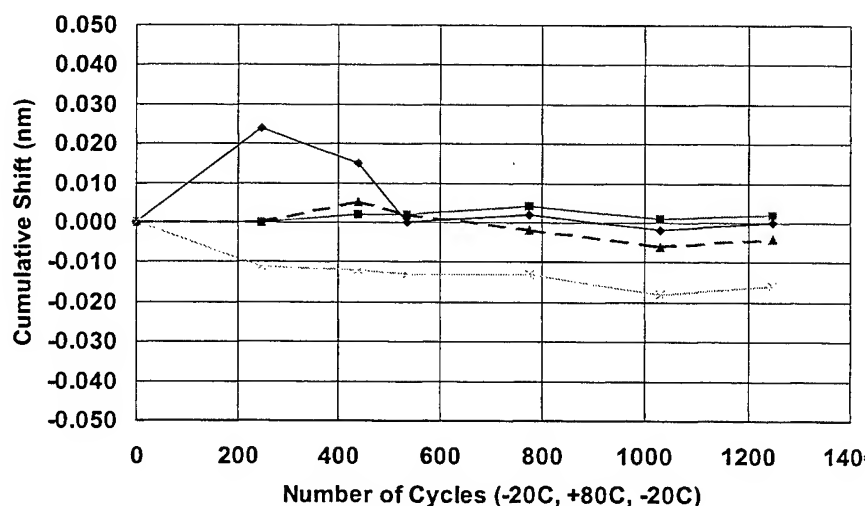
Fig 6 Schematic of Package Design

Variants of the package outlined above have been, qualified for either Undersea (Wet-plant) <0.25 FIT or Terrestrial (Dry-plant) <100 FIT use. The terrestrial package variant complies with the qualification requirements of Bellcore 1209 and 1221.

5. ENVIRONMENTAL PERFORMANCE

To maintain the filter performance over the specified operating conditions and operational life, the grating must be packaged in an environmentally-stable package⁶. Extensive environmental proving of the package design is required to guarantee the required FIT levels for telecommunications applications. Typical FIT requirements are <100 for terrestrial applications and <0.25 for undersea applications.

A complete analysis of the package performance is beyond the scope of this paper, so only illustrative measurements indicating the temperature dependence (Fig 5(a)) and long-term temperature cycling results (Fig 5(b)) are shown here. These show that, over the device operating temperature (in this case from 0 to 40°C) and during extended temperature cycling (20/+80/-20°C) the grating performance will not be affected



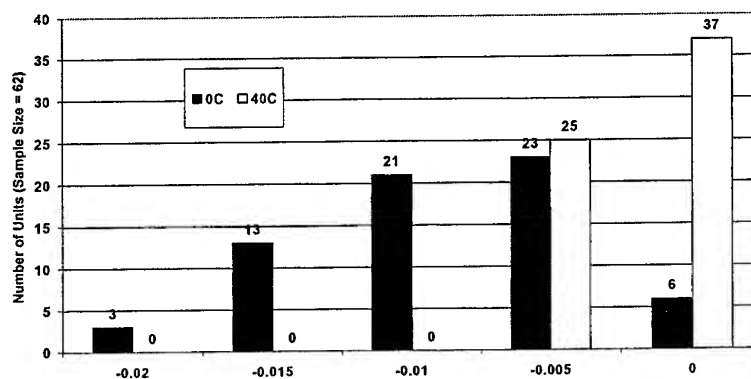


Fig 8 Temperature Dependence of Undersea-qualified Package

6. CONCLUSIONS

We have demonstrated for the first time an arbitrary-response gain-flattening filter with better than ± 0.05 dB absolute amplitude accuracy, < 0.15 dB excess loss, negligible group delay ripple and in-built ASE-suppression. This device will find application in both terrestrial and undersea communication systems.

7. ACKNOWLEDGEMENTS

The authors would like to thank their many colleagues in JDS Uniphase who have contributed to the development of the components described in this paper.

8. REFERENCES

1. Erbium-Doped Fiber Amplifiers: Principles and Applications by E.Desurvire, Wiley, pp.480ff, 1994
2. EG JDS Uniphase Type 1515
3. R.A.Betts, S.J.Frisken, D.Wong, "Split-beam fourier filter and its application in a gain-flattened EDFA", Proc OFC'95, San Jose, 1995 paper TuP4
4. R.Kashyap et al, Electron.Lett., **29**, 1025, 1993.
5. A.M.Vengsarkar *et al*, OFC'95, San Jose, 1995, paper PD4.
6. T. Hammon, J.Bulman, F.Ouellette, S.B.Poole, "A temperature compensated optical fibre Bragg grating rejection filter and wavelength reference", Proc OECC, Chiba, 1996, paper 18C1-2

Avalanche multiplication in $\text{Al}_x\text{Ga}_{1-x}\text{As}/\text{GaAs}$ multilayer structures

C. K. Chia^{*a}, J. P. R. David^{**b}, G. J. Rees^b, S. A. Plimmer^b and R. Grey^b

^aSchool of Physics, Universiti Sains Malaysia, 11800 Minden, Penang, Malaysia

^bElectronic and Electrical Engineering Department, University of Sheffield,
Mappin street, Sheffield S1 3JD, United Kingdom

ABSTRACT

A systematic study has been carried out to understand how avalanche multiplication is modified by heterojunction band-edge discontinuities in $\text{Al}_x\text{Ga}_{1-x}\text{As}/\text{GaAs}$ PIN diodes. A series of $\text{Al}_x\text{Ga}_{1-x}\text{As}/\text{GaAs}$ structures have been investigated with well and barrier thicknesses fixed at 500 Å while the periods range from one up to twenty-five. Whereas the band-edge discontinuity of these structures has previously been suggested as responsible for producing large ratios of electron to hole ionization coefficients, this investigation shows that a significant ratio is only present in the thinnest 0.1 μm single period devices and that this is due to 'dead-space' effects rather than that of the heterojunction. In fact the multiplication characteristics of all structures are shown to approach those of the average alloy of the device as the number of periods increases, which also strongly suggests that the role of the heterojunction is insignificant. Varying the Al composition had little or no effect on the ionization coefficient ratio. The measured multiplication behaviour is interpreted using a simple Monte-Carlo model which shows that the effect of the band-edge discontinuity is negligible because it is offset by different rates of energy relaxation in GaAs and $\text{Al}_x\text{Ga}_{1-x}\text{As}$.

Keywords: Avalanche photodiodes, APD, pin, multiple quantum wells, photomultiplication, noise, GaAs.

1. INTRODUCTION

The use of heterojunction band-edge discontinuities has been suggested¹ as a way to enhance the electron to hole ionization coefficient ratio (α/β) in avalanche photodiodes (APDs) and thereby obtain low noise performance.² However, groups working with $\text{Al}_x\text{Ga}_{1-x}\text{As}/\text{GaAs}$ multiple quantum well (MQW) APD have observed widely variable results.³⁻⁸ Capasso et al.³ and Kagawa et al.⁴ observed substantial electron ionization enhancement, in contrast to others like Susa and Okamoto,⁵ Franks,⁶ Juang et al.⁷ and Bhattacharya et al.⁸ Recent work⁹⁻¹¹ on $\text{Al}_x\text{Ga}_{1-x}\text{As}/\text{GaAs}$ structures suggests that electron ionization enhancement via the conduction band-edge discontinuity is unlikely to occur in this material system. In this work we have carried out detail investigations in a series of $\text{Al}_x\text{Ga}_{1-x}\text{As}/\text{GaAs}$ multilayer structures with well and barrier thicknesses fixed at 500 Å and with periods ranging from one to twenty-five.

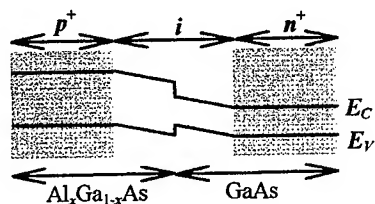
2. EXPERIMENTS AND MODELLING

2.1. Structure details

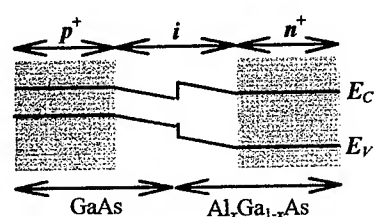
All the devices used in this work, grown on n^+ (001) GaAs substrate, were prepared by conventional solid source molecular beam epitaxy. The impurity concentration in p^+ and n^+ cladding layers were doped at $1.5 - 2.0 \times 10^{18} \text{ cm}^{-3}$. The 'i'-region consists of the $\text{Al}_x\text{Ga}_{1-x}\text{As}$ and GaAs layers with equal barrier and well widths of 500 Å. Two types of structure were grown as shown in Fig. 1. In type A structures, electrons travelling in the high field region start from $\text{Al}_x\text{Ga}_{1-x}\text{As}$ and end in GaAs, whereas in type B structures they start in GaAs and end in $\text{Al}_x\text{Ga}_{1-x}\text{As}$. Structures with Al content x of 0.30 and 0.45 were investigated with one, three and five periods corresponding to 'i'-region thickness w of 0.1, 0.3 and 0.5 μm respectively. In addition, two MQW structures with Al content x of 0.45 and device configuration similar to that used by Capasso et al.³ were also grown. Both p^+ and n^+ cladding layers were 1 μm thick GaAs. The intrinsic region consists of the multilayer with equal barrier and well width of 500 Å, starting and ending with GaAs undoped layers. The 'i'-regions are 1.55 μm and 2.55 μm for structures with 15½ and 25½ periods respectively. Schematic band diagrams for these structures are also shown in Fig. 1 with details of all the structures summarized in Table 1.

* Email: ckchia@usm.my; ** email: j.p.david@sheffield.ac.uk

Type A: $p^+ = \text{Al}_x\text{Ga}_{1-x}\text{As}$, $n^+ = \text{GaAs}$
(electrons travelling in the high field region start from $\text{Al}_x\text{Ga}_{1-x}\text{As}$ and end in GaAs)



Type B: $p^+ = \text{GaAs}$, $n^+ = \text{Al}_x\text{Ga}_{1-x}\text{As}$
(electrons travelling in the high field region start from GaAs and end in $\text{Al}_x\text{Ga}_{1-x}\text{As}$)



MQW structure similar to that used by Capasso et al.³:
 $p^+ = n^+ = \text{GaAs}$
(electrons travelling in the high field region start and end in GaAs)

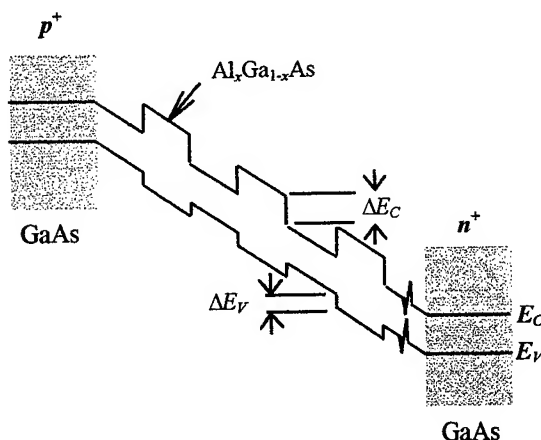


Fig.1. Schematic band diagrams of the type A and type B heterostructures. Multilayer type A and type B structures have the same configurations as shown on the left but with more periods in the *i*-region. The band-edge profile of the MQW structure similar to that used by Capasso et al. is shown on the right (E_C = conduction band-edge; E_V = valence band-edge. ΔE_C and ΔE_V are the conduction and valence band-edge discontinuities, respectively).

Table 1. Details of the *p-i-n* structures used in this study.

Heterogeneous <i>pin</i> structures	p^+ (top) (~1.0 μm)	<i>i</i>		n^+ (bottom) (~1.0 μm)	<i>w</i> (\AA)
		Repeating unit 500 \AA /500 \AA	period(s)		
<i>pin30A1</i>	Al 30%	Al 30%/GaAs	1	GaAs	1000
<i>pin30B1</i>	GaAs	GaAs/Al 30%	1	Al 30%	1000
<i>pin45A1</i>	Al 45%	Al 45%/GaAs	1	GaAs	1000
<i>pin45B1</i>	GaAs	GaAs/Al 45%	1	Al 45%	1000
<i>pin60A1</i>	Al 60%	Al 60%/GaAs	1	GaAs	1000
<i>pin60B1</i>	GaAs	GaAs/Al 60%	1	Al 60%	1000
<i>pin30A3</i>	Al 30%	Al 30%/GaAs	3	GaAs	3000
<i>pin30B3</i>	GaAs	GaAs/Al 30%	3	Al 30%	3000
<i>pin30A5</i>	Al 30%	Al 30%/GaAs	5	GaAs	5000
<i>pin45A5</i>	Al 45%	Al 45%/GaAs	5	GaAs	5000
<i>pin45B5</i>	GaAs	GaAs/Al 45%	5	Al 45%	5000
<i>pin45C15</i>	GaAs	GaAs/Al 45%	15½	GaAs	15500
<i>pin45C25</i>	GaAs	GaAs/Al 45%	25½	GaAs	25500
Homogeneous <i>pin</i> structures	p^+ (top) (~1.0 μm)	<i>i</i>		n^+ (bottom) (~1.0 μm)	<i>w</i> (\AA)
<i>GaAs1</i>	GaAs	GaAs		GaAs	1000
<i>GaAs3</i>	GaAs	GaAs		GaAs	3000
<i>GaAs5</i>	GaAs	GaAs		GaAs	5000
<i>Al301</i>	Al 30%	Al 30%		Al 30%	1000
<i>Al305</i>	Al 30%	Al 30%		Al 30%	5000
<i>Al601</i>	Al 60%	Al 60%		Al 60%	1000

In order to understand the avalanche multiplication behavior in the heterogeneous structures it is instructive to understand the intrinsic properties of the homogeneous counterparts. For short multiplication lengths ($w < 0.3 \mu\text{m}$) the multiplication behavior differs greatly from that of the bulk because the ionization dead space (the distance carriers must travel to attain the ionization energy) becomes a significant proportion of the multiplication region.¹² Therefore, some $\text{Al}_x\text{Ga}_{1-x}\text{As}$ and GaAs homojunction control layers were also grown and characterized. The nominal details of the structures are as listed in Table 1. It has been shown¹² that for structures with $w > 0.3 \mu\text{m}$, the multiplication characteristics agree well with the bulk values so the data of Bulman¹³ for GaAs and of Robbins¹⁴ for $\text{Al}_x\text{Ga}_{1-x}\text{As}$ ($x = 0.1$ to 0.4) can be used.

2.2. Characterization

The dimension and Al composition of the structures were first checked by modeling the x-ray rocking curves obtained using a double-crystal diffractometer. The structures were then fabricated into circular mesa diodes using conventional photolithography techniques. I-V measurements were performed at room temperature in the dark. For each layer leakage current measurements were repeated on several devices of different size to check the consistency of current density. Only devices with low leakage current, sharp and well-defined breakdown voltage were selected for photomultiplication measurement. C-V measurements were also conducted to deduce the doping profiles and i -region thicknesses. Details of the parameters obtained from these measurements are listed in Table 2.

Table 2. Summary of device parameters deduced from x-ray and C-V measurements.

Layers	X-ray					C-V		
	AlGaAs undoped	GaAs undoped	Period(s)	w (Å)	Al content x	$p = n$ ($\times 10^{18} \text{cm}^{-3}$)	i ($\times 10^{16} \text{cm}^{-3}$)	w (Å)
<i>pin30A1</i>	480	495	1	975	0.29	1.5	0.1	990
<i>pin30B1</i>	452	500	1	952	0.29	1.5	0.1	1000
<i>pin45A1</i>	520	500	1	1020	0.45	1.9	0.1	990
<i>pin45B1</i>	490	505	1	995	0.47	1.9	0.1	1000
<i>pin60A1</i>	548	500	1	1048	0.60	1.8	0.1	1000
<i>pin60B1</i>	524	429	1	953	0.64	2.0	0.1	1020
<i>pin30A3</i>	500	500	3	3000	0.31	1.8	1.0	2900
<i>pin30B3</i>	500	500	3	3000	0.30	2.0	1.0	2950
<i>pin30A5</i>	500	500	5	5000	0.30	1.5	0.1	5300
<i>pin45A5</i>	540	540	5	5400	0.43	1.5	0.1	5650
<i>pin45B5</i>	550	550	5	5500	0.44	1.5	0.1	5750
<i>pin45C15</i>	510	510	15½	15810	0.45	2.0	0.15	16000
<i>pin45C25</i>	480	480	25½	24480	0.45	1.8	0.1	25000
<i>GaAs1</i>	GaAs homojunction <i>pin</i>				-	1.5	0.1	1000
<i>GaAs3</i>	GaAs homojunction <i>pin</i>				-	2.8	0.1	2800
<i>GaAs5</i>	GaAs homojunction <i>pin</i>				-	1.5	0.1	4500
<i>Al301</i>	Al 30% homojunction <i>pin</i>				0.31	2.4	0.1	1030
<i>Al305</i>	Al 30% homojunction <i>pin</i>				0.30	1.5	1.0	5050
<i>Al601</i>	Al 60% homojunction <i>pin</i>				0.61	3.2	0.1	865

The electron and hole initiated multiplication characteristics, M_e and M_h , were measured as a function of electric field using the technique described by Stillman and Wolfe.¹⁵ A 442nm He-Cd laser was used to produce minority carrier injection. The short wavelength resulted in near total absorption of the light in the GaAs or $\text{Al}_x\text{Ga}_{1-x}\text{As}$ cladding layer¹⁶ resulting in pure electron or hole carrier injection. Pure electron injection was effected by illuminating the p^+ cladding layer of the mesa diode with the laser beam from top while in some cases, pure hole injection was achieved by illuminating the n^+ cladding layer on devices where the substrate had been selectively etched away. The incident laser beam is modulated by a mechanical chopper and the resulting photocurrent is measured using a lock-in amplifier, to ensure that only the multiplied primary photocurrent is measured. Reliable measurement of multiplication values were obtained down to 1.002.

2.3. Modelling

A simple Monte Carlo model is used to interpret the experimental results. Detail of the model has been reported elsewhere.¹⁰ The impact ionization rate R at energy E above the threshold energy E_{th} is described by a modified Keldysh¹⁷ equation

$$R = C [(E/E_{th}) - 1]^3 \quad (1)$$

where C is a fitted scattering rate. A common phonon energy $\hbar\omega$ was used for electrons and holes. The strength of phonon scattering for electrons and holes is obtained by fitting to the multiplication characteristics of the $\text{Al}_x\text{Ga}_{1-x}\text{As}$ homojunction structures and is represented by energy-independent phonon scattering mean free paths, λ_e and λ_h , respectively. In the simulation of transport in periodic structures, regions are defined for the specified materials. The simulation in each individual region is exactly the same as for the case of homogeneous material but the material parameters and scattering probabilities are updated every time a carrier enters a new region. Quantum mechanical treatment of transmission, reflection and tunneling probabilities at the heterointerfaces are used. No size quantization effects are included in the simulation because the well widths are rather wide in our structures (~ 500 Å) and our interest in impact ionization only concerns carriers with a relatively high energy. The conduction and valence band discontinuities at the heterojunctions are aligned using a 60:40 ratio of the band gap difference at Γ . Parameters used in simulation are as shown in Table 3. Using the device dimensions and doping profiles listed in Table 2, the simulated multiplication values are in very good agreement with the measured values for all the structures.

Table 3. Parameters used in the Monte Carlo simulations.

Al content x	Particle	λ_e, λ_h (Å)	Al _x Ga _{1-x} As-GaAs band offsets (meV)		C ($\times 10^{13} \text{ s}^{-1}$)	E_{th} (eV)	$\hbar\omega$ (meV)
			ΔE_C	ΔE_V			
$x = 0$	electron	51	0	-	1.20	1.75	29.0
	hole	46	-	0			
$x = 0.30$	electron	43	227	-	1.30	1.91	31.0
	hole	41	-	151			
$x = 0.45$	electron	40	336	-	1.35	1.99	32.5
	hole	38	-	224			

3. RESULTS

The multiplication characteristics measured in the single period $\text{Al}_x\text{Ga}_{1-x}\text{As}/\text{GaAs}$ heterostructures with Al content $x = 0.3$, 0.45 and 0.6 have been reported elsewhere^{9,10} so only M_e of the type A and type B heterostructures with Al content $x = 0.45$ are shown in Fig.2. For heterostructures with Al content $x = 0.3$ and 0.6 a similar trend is observed. Also shown in Fig.2 are the M_e characteristics of GaAs and $\text{Al}_x\text{Ga}_{1-x}\text{As}$ homojunctions with similar thickness. In all the type A heterostructures, in which injected electrons travel from $\text{Al}_x\text{Ga}_{1-x}\text{As}$ to GaAs, at low electric fields M_e is similar to that of the GaAs homojunction structure. Conversely, at low fields in the type B heterostructures, in which injected electrons travel from GaAs to $\text{Al}_x\text{Ga}_{1-x}\text{As}$, M_e is similar to that of the $\text{Al}_x\text{Ga}_{1-x}\text{As}$ homojunction structure. As the electric field increases however, the M_e curves diverge from these homojunction characteristics and converge towards the multiplication curve of the equivalent average alloy for the 'i'-region. The M_h characteristic measured in the type A heterostructures is similar to the M_e characteristic of the type B heterostructures.^{9,10} The field-dependent electron and hole ionization coefficients, $\alpha(F)$ and $\beta(F)$, shown in Fig.3 were extracted from M_e and M_h using the expressions¹⁵

$$\alpha(F) = [(M_e - 1)/(M_e - M_h)] \ln(M_e/M_h)/w \quad (2)$$

$$\beta(F) = [(M_h - 1)/(M_e - M_h)] \ln(M_e/M_h)/w.$$

A large effective α/β ratio is obtained for the type A heterostructures at low fields but this converges to nearly unity at higher fields. Such phenomena are primarily due to the dead-space effects.^{10,12} The effects of the band-edge discontinuities at the heterointerface on M_e and M_h are compensated by the different energy-loss rates due to phonon cooling in $\text{Al}_x\text{Ga}_{1-x}\text{As}$ and GaAs.¹⁰

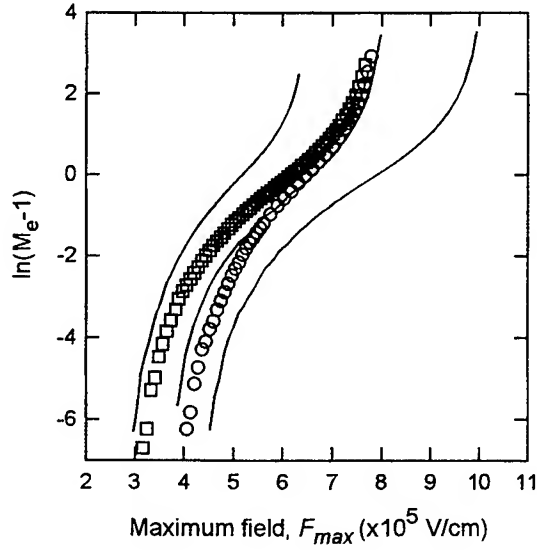


Fig. 2. M_e measured in $Al_{0.45}Ga_{0.55}As/GaAs$ heterostructures and $Al_xGa_{1-x}As$ homojunctions plotted as $\ln(M_e - 1)$ against maximum field. Symbols (\square) and (\circ) represent M_e of the $Al_{0.45}Ga_{0.55}As/GaAs$ type A and type B heterostructures, respectively. Solid lines are M_e for $Al_xGa_{1-x}As$ homojunctions with $x=0, 0.3$ and 0.6 , from left to right, plotted for comparison.

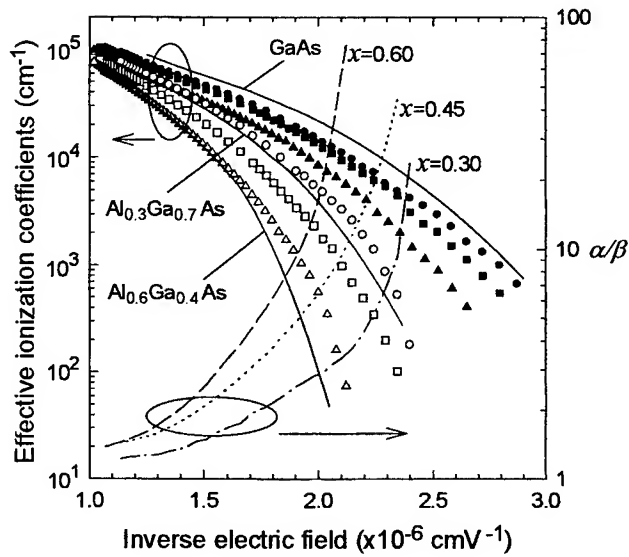


Fig. 3. Effective $\alpha(F)$ (filled symbols) and $\beta(F)$ (hollow symbols) for $Al_xGa_{1-x}As/GaAs$ type A heterostructures with $x = 0.30$ (\bullet, \circ), $x = 0.45$ (\blacksquare, \square) and $x = 0.60$ ($\blacktriangle, \triangle$). Solid lines are $\alpha(F)$ [$\approx \beta(F)$] for $Al_xGa_{1-x}As$ homojunctions with $x = 0, 0.3$, and 0.6 . Also shown are the field dependence of α/β ratios for each heterostructure.

The M_e measured from the 3, 5, 15½ and 25½ period MQWs are plotted as $\ln(M_e - 1)$ together with the simulated results as a function of maximum electric field. Fig. 4 shows the M_e obtained from the $Al_{0.3}Ga_{0.7}As/GaAs$ 3 and 5 period structures. Also shown for comparison are the M_e of the homojunction structures of similar thicknesses. The 3 period type A and type B structures show very little difference in M_e where a small discrepancy is observed at low multiplication values. Comparison with the M_e for GaAs and $Al_{0.3}Ga_{0.7}As$ homojunctions shows that M_e in the 3 period structures are intermediate between those of the homojunctions. Although no type B structure for the 5 period $Al_{0.3}Ga_{0.7}As/GaAs$ structure was measured, the simulation carried out for an inverse structure (electron starting from GaAs instead of $Al_{0.3}Ga_{0.7}As$) to the type A structure shows identical M_e characteristics. Fig. 5 shows the measured and simulated M_e for two 5 period structures with Al content $x \approx 0.45$. The simulated results agreed well with the measured values for both type A ($x = 0.43$, $w = 0.565 \mu m$) and type B ($x = 0.44$, $w = 0.575 \mu m$) structures. These M_e are identical and show equivalent alloy behavior from the comparison with M_e in GaAs and $Al_{0.45}Ga_{0.55}As$ homojunctions. The M_e in 5 period structures ($w \approx 0.5 \mu m$) for electrons starting from GaAs or $Al_xGa_{1-x}As$ show no difference because in thicker structures ($w > 0.3 \mu m$) the dead space becomes less significant.

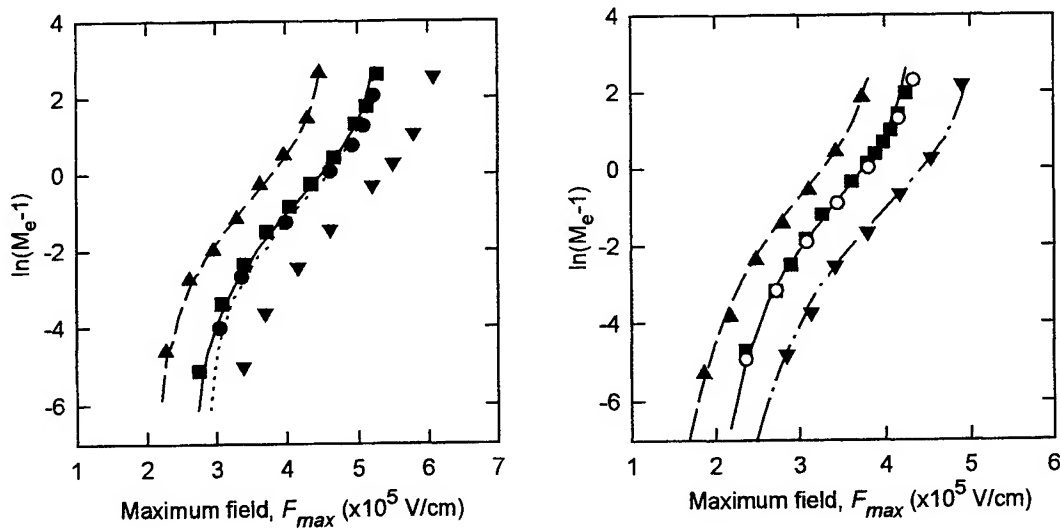


Fig.4. Monte Carlo simulated (symbols) M_e for 3 (left) and 5 (right) period $Al_{0.3}Ga_{0.7}As/GaAs$ structures plotted as $\ln(M_e - 1)$ versus maximum field. Lines are the experimental data. Left: solid line and symbol (\blacksquare) for the 3 period type A structure ($w = 0.29 \mu m$) and dotted line and symbol (\bullet) for 3 period type B structure ($w = 0.295 \mu m$). Right: Solid line and symbol (\blacksquare) for the 5 period type A structure ($w = 0.53 \mu m$) and symbol (\circ) represents the simulated M_e for a type B structure (inverse structure of type A). Also shown are the M_e for GaAs and $Al_{0.3}Ga_{0.7}As$ homojunction with similar thickness. Left: broken line and symbol (\blacktriangle) for GaAs ($w = 0.28 \mu m$), and symbol (\blacktriangledown) for M_e simulated for a $0.3 \mu m$ $Al_{0.3}Ga_{0.7}As$ structure. Right: broken line and symbol (\blacktriangle) for GaAs ($w = 0.45 \mu m$), and dot-dashed line and symbol (\blacktriangledown) for $Al_{0.3}Ga_{0.7}As$ ($w = 0.505 \mu m$).

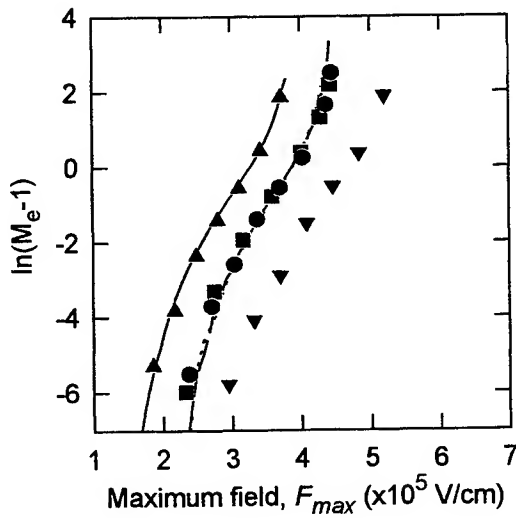


Fig.5. Measured (lines) and Monte Carlo simulated (symbols) M_e for the 5 period type A ($w = 0.565 \mu m$: dotted line, \blacksquare) and type B ($w = 0.575 \mu m$: broken line, \bullet) $Al_{0.45}Ga_{0.55}As/GaAs$ structures. Also shown are the simulated (symbols) and measured (lines) M_e characteristics of GaAs (solid line, \blacktriangle) and of $Al_{0.45}Ga_{0.55}As$ (\blacktriangledown) homojunctions with $w = 0.5 \mu m$.

The measured and modelled M_e for the $15\frac{1}{2}$ and the $25\frac{1}{2}$ period MQWs similar to that used by Capasso et al.³ are compared in Figs.6(a) and (b) together with the M_e for GaAs and $Al_{0.4}Ga_{0.6}As$ homojunctions, generated using Bulman's and Robbins' data for structures of similar thickness. The M_e predicted using the simple Monte Carlo model are in good agreement with those measured experimentally. These M_e again show equivalent alloy behavior, lying in between those of the homojunctions. This suggests that no additional effect occurs in thick $Al_xGa_{1-x}As/GaAs$ MQWs that might enhance the

ionization coefficients. The breakdown voltages obtained from modelling and from experiments (both dark current and photocurrent) all show the same value. By contrast the M_e and M_h reported by Capasso et al.³ exhibit breakdown at a voltage much lower than that measured in our MQW, as plotted in Fig.6(b) for comparison.

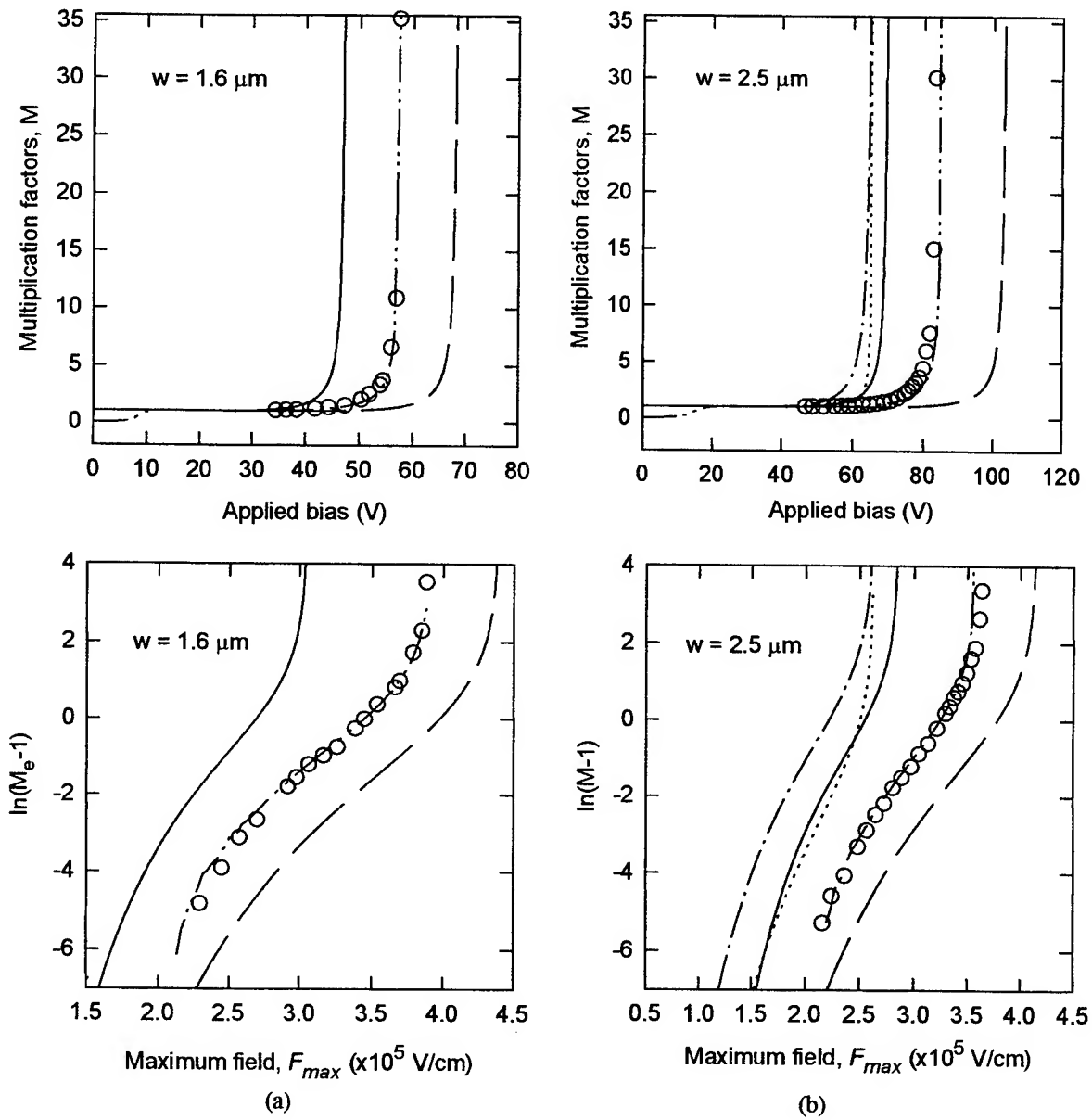


Fig.6. Simulated (symbols \circ) electron multiplication factors in (a) $15\frac{1}{2}$ period MQW ($L_W = L_B = 510 \text{ \AA}$, $w = 1.6 \text{ \mu m}$) and in (b) $25\frac{1}{2}$ period MQW ($L_W = L_B = 480 \text{ \AA}$, $w = 2.5 \text{ \mu m}$) plotted in M_e versus applied bias (top) and $\ln(M_e - 1)$ against maximum electric field (bottom). Dot-dot-dashed lines: MQW, solid lines: Bulman's data for bulk GaAs and broken lines: Robbins' data for bulk $Al_{0.4}Ga_{0.6}As$. Also plotted for comparison in (b) are the electron (dot-dashed line) and hole (dotted line) multiplication factors reported by Capasso et al.

4. DISCUSSION

The electron multiplication characteristics M_e modelled in the single and multilayer $\text{Al}_x\text{Ga}_{1-x}\text{As}/\text{GaAs}$ structures with equal barrier and well widths ($\sim 500 \text{ \AA}$) are summarised in Fig.7 for $x = 0.30$ and in Fig.8 for $x = 0.45$. In thin structures ($w \approx 0.1 \mu\text{m}$) M_e is determined by the ionization properties of the material in the latter half of the structure because of the dead space effects. As a consequence the multiplication characteristics obtained by injecting electrons from $\text{Al}_x\text{Ga}_{1-x}\text{As}$ to GaAs (type A) and from GaAs to $\text{Al}_x\text{Ga}_{1-x}\text{As}$ (type B) are very different, especially at low electric fields. As the electric field increases the multiplication behavior converges to that of the equivalent alloy because the feedback from holes causes ionization in the other half of the structure. The advantage obtained from the conduction band-edge step down from $\text{Al}_x\text{Ga}_{1-x}\text{As}$ to GaAs is offset by the energy loss via the higher phonon emission rate in the $\text{Al}_x\text{Ga}_{1-x}\text{As}$ layer. As the multiplication length increases ($w > 0.3 \mu\text{m}$) the dead space becomes insignificant and M_e in the multilayer structures samples the ionization properties of both the barrier and the well materials. As a result only equivalent alloy behavior is observed. M_e for both type A and type B structures converge to identical characteristics when the layer thickness approaches $0.5 \mu\text{m}$.

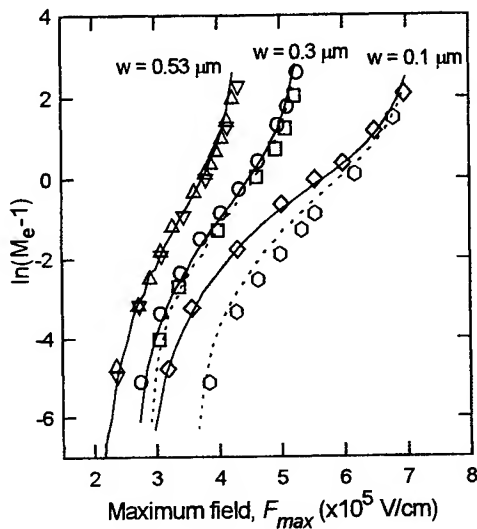


Fig.7. Simulated (symbols) electron multiplication characteristics in $\text{Al}_{0.3}\text{Ga}_{0.7}\text{As}/\text{GaAs}$ heterojunction and multilayer structures with $L_w = L_B \approx 500 \text{ \AA}$. Type A ($p^+ = \text{Al}_{0.3}\text{Ga}_{0.7}\text{As}$, $n^+ = \text{GaAs}$): (\diamond): $w = 0.1 \mu\text{m}$, (\circ): $w = 0.3 \mu\text{m}$ and (Δ): $w = 0.53 \mu\text{m}$, and type B ($p^+ = \text{GaAs}$, $n^+ = \text{Al}_{0.3}\text{Ga}_{0.7}\text{As}$): hexagon: $w = 0.1 \mu\text{m}$, (\square): $w = 0.3 \mu\text{m}$ and (∇): $w = 0.53 \mu\text{m}$. Solid and dotted lines represent the measured values for type A and type B structures respectively.

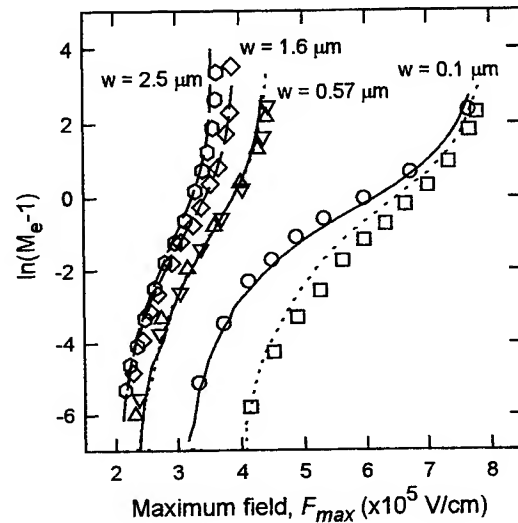


Fig.8. Simulated (symbols) electron multiplication characteristics in $\text{Al}_{0.45}\text{Ga}_{0.55}\text{As}/\text{GaAs}$ heterojunction and multilayer structures with $L_w = L_B \approx 500 \text{ \AA}$. Type A ($p^+ = \text{Al}_{0.45}\text{Ga}_{0.55}\text{As}$, $n^+ = \text{GaAs}$): (\circ): $w = 0.1 \mu\text{m}$, and (Δ): $w = 0.57 \mu\text{m}$, and type B ($p^+ = \text{GaAs}$, $n^+ = \text{Al}_{0.45}\text{Ga}_{0.55}\text{As}$): (\square): $w = 0.1 \mu\text{m}$, and (∇): $w = 0.57 \mu\text{m}$. Solid and dotted lines represent the measured values for type A and type B structures respectively. Symbols (\diamond) and hexagon represent the simulated values for the $15\frac{1}{2}$ ($w = 1.6 \mu\text{m}$) and $25\frac{1}{2}$ ($w = 2.5 \mu\text{m}$) period Capasso-type ($p^+ = n^+ = \text{GaAs}$) MQWs with the measured values represented by the broken lines.

Although no hole multiplication factors were measured in the multilayer structures, knowing that $\alpha > \beta$ (i.e. $M_e > M_h$) we can still estimate the $\alpha(F)$ by considering two extreme cases, namely when $\beta = \alpha$ ($M_h = M_e$) or $\beta = 0$ ($M_h = 1$).¹⁸ The true ionization coefficients should lie between these two extreme limits. The field dependent ionization coefficients $\alpha(F)$ and $\beta(F)$, as expressed in equations (2), for the 5 period and the $25\frac{1}{2}$ period MQWs estimated from experiments and by simulation are plotted together in Fig.9 for comparison. The $\alpha(F)$ simulated for these two MQWs lie between those estimated from experimental M_e assuming $\beta = 0$ ($M_h = 1$) and $\beta = \alpha$ ($M_h = M_e$). The $\alpha(F)$ and $\beta(F)$ simulated for the $15\frac{1}{2}$ period MQW also lie on the same lines and are not shown for clarity. The simulated $\beta(F)$ are just slightly lower than the

$\alpha(F)$, which means no significant improvement in the α/β ratio is obtained in the $\text{Al}_{0.45}\text{Ga}_{0.55}\text{As}/\text{GaAs}$ MQW structure. Noise measurements show the excess noise factors in these MQWs have $k = \beta/\alpha = 0.5$ ¹⁹, in contrast to the results reported by Kagawa et al.⁴ where $k = 0.14$ is observed.

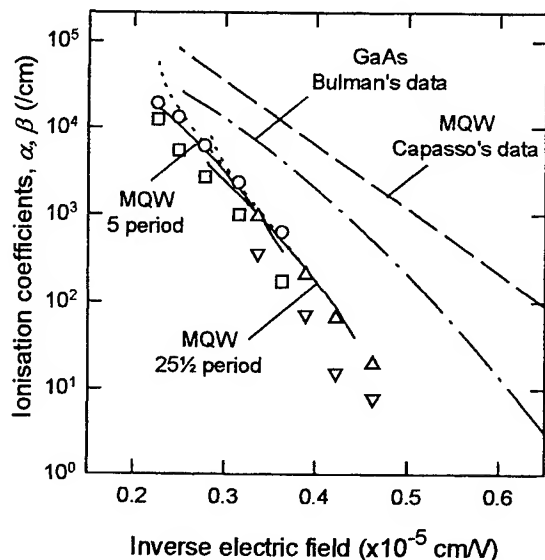


Fig. 9. Modelled ionization coefficients for thick $\text{Al}_{0.45}\text{Ga}_{0.55}\text{As}/\text{GaAs}$ MQWs. The simulated values for the 5 period MQW are represented by symbols (○) for $\alpha(F)$ and (□) for $\beta(F)$. $\alpha(F)$ and $\beta(F)$ for the $25\frac{1}{2}$ period MQW are represented by symbols (Δ) and (▽) respectively. The $\alpha(F)$ estimated using experimental data are shown as dotted line for case I: $M_h = 1$ and as solid line for case II: $M_h \approx M_e$. Also plotted for comparison are the $\alpha(F)$ for bulk GaAs (Bulman's data) represented by the dot-dashed line, and the $\alpha(F)$ of $\text{Al}_{0.45}\text{Ga}_{0.55}\text{As}/\text{GaAs}$ MQW structure reported by Capasso et al., represented by the broken line.

5. CONCLUSION

The role of band-edge discontinuities on impact ionization in $\text{Al}_x\text{Ga}_{1-x}\text{As}/\text{GaAs}$ multilayer structures has been studied in detail. This was investigated initially by measuring the electron and hole multiplication characteristics, M_e and M_h , in a series of short $\text{Al}_x\text{Ga}_{1-x}\text{As}/\text{GaAs}$ single heterojunction structures with x ranging from 0.3 to 0.6, and with an equally thick 500\AA $\text{Al}_x\text{Ga}_{1-x}\text{As}$ barrier (L_B) and GaAs (L_W) well. In these devices, at low electric fields, the electron multiplication occurs mainly in the latter half of the i -region because of dead space effects. As the electric field increases the electron multiplication behavior converges to that of the equivalent alloy because the feedback of holes causes ionization in the other half of the structure. Investigations were then extended to $\text{Al}_x\text{Ga}_{1-x}\text{As}/\text{GaAs}$ multilayer structures with 3, 5, $15\frac{1}{2}$ and $25\frac{1}{2}$ periods, again, with $L_B = L_W = 500\text{\AA}$. As the multiplication length increases ($w > 0.3\text{ }\mu\text{m}$) the dead space becomes less significant and electron multiplication samples the ionization properties of both the $\text{Al}_x\text{Ga}_{1-x}\text{As}$ barriers and the GaAs wells. As a result only equivalent alloy behavior is observed.

Comparison of multiplication characteristics measured in all of these $\text{Al}_x\text{Ga}_{1-x}\text{As}/\text{GaAs}$ devices with those measured in the $\text{Al}_x\text{Ga}_{1-x}\text{As}$ and GaAs homojunction devices with similar multiplication thicknesses shows that the electron multiplication curves of the $\text{Al}_x\text{Ga}_{1-x}\text{As}/\text{GaAs}$ multilayer structures always lie between those of the GaAs and $\text{Al}_x\text{Ga}_{1-x}\text{As}$ homojunctions. The electron multiplication and ionization coefficient in these structures never exceed those of GaAs. This is strong evidence that electron ionization enhancement is not present in $\text{Al}_x\text{Ga}_{1-x}\text{As}/\text{GaAs}$ multilayer structures.

The microscopic aspects of hot carrier transport across an $\text{Al}_x\text{Ga}_{1-x}\text{As}$ -GaAs heterointerface were studied numerically using a simple Monte Carlo model. Modelling suggests that the advantage obtained from the conduction band-edge step down from $\text{Al}_x\text{Ga}_{1-x}\text{As}$ to GaAs is offset by the energy loss via stronger phonon emission in the $\text{Al}_x\text{Ga}_{1-x}\text{As}$ layer. The multiplication and ionization behavior in the $\text{Al}_x\text{Ga}_{1-x}\text{As}/\text{GaAs}$ MQWs were predictable after the effect of a single heterojunction on carrier ionization had been deduced. Since any energy gain associated with the band-edge discontinuity is offset by the difference in the energy loss rates in $\text{Al}_x\text{Ga}_{1-x}\text{As}$ and GaAs, only equivalent alloy behavior is expected. The measured and modelled results were found to be in good agreement.

ACKNOWLEDGEMENT

This work was supported by the EPSRC (U.K.) under grants GR/J49549 and GR/L71674.

REFERENCE

1. R. Chin, N. Holonyak, G.E. Stillman, J.Y. Tang. and K. Hess, "Impact ionization in multilayered heterojunction structures", *Electron. Lett.*, **16**, 467, 1980.
2. R.J. McIntyre, "Multiplication noise in uniform avalanche diodes", *IEEE Trans. Elec. Dev.*, **ED-13**, 164, 1966.
3. F. Capasso, W.T. Tsang, A.L. Hutchingson and G.F. Williams, "Enhancement of electron impact ionization in a superlattice: A new avalanche photodiode with a large ionization rate ratio", *Appl. Phys. Lett.*, **40**, 38, 1982.
4. T. Kagawa, H. Iwamura and O. Mikami, "Dependence of the GaAs/AlGaAs superlattice ionization rate on Al content", *Appl. Phys. Lett.*, **54**, 33, 1989.
5. N. Susa and H. Okamoto, "Properties of GaAs/Al_{0.53}Ga_{0.47}As avalanche photodiode with superlattice fabricated by Molecular Beam Epitaxy", *Jpn. J. Appl. Phys., Part 1*, **23**, 317, 1984.
6. R.B. Franks, "Dependence of ionization coefficients on well and barrier widths for GaAs/AlGaAs multiple quantum wells", *Solid State Electron.*, **33**, 1235, 1990.
7. F.Y. Juang, U. Das, Y. Nashimoto and P.K. Bhattacharya, "Electron and hole impact ionization coefficients in GaAs/Al_xGa_{1-x}As superlattices", *Appl. Phys. Lett.*, **47**, 972, 1985.
8. P.K. Bhattacharya, Y. Zebda and J. Singh, "Electron and hole impact ionization coefficients in GaAs/Al_{0.45}Ga_{0.55}As/Al_{0.3}Ga_{0.7}As coupled well systems", *Appl. Phys. Lett.*, **58**, 2791, 1991.
9. C.K. Chia, J.P.R. David, G.J. Rees, P.N. Robson, S.A. Plimmer and R. Grey, "Electron multiplication in Al_xGa_{1-x}As/GaAs heterostructures", *Appl. Phys. Lett.*, **71**, 3877, 1997.
10. C.K. Chia, J.P.R. David, G.J. Rees, S.A. Plimmer, R. Grey and P.N. Robson, "Impact ionization in Al_xGa_{1-x}As/GaAs single heterostructures", *J. Appl. Phys.*, **84**, 4363, 1998.
11. T.P. Pearsall, "Impact ionization in AlGaAs/GaAs superlattices", *Appl. Phys. Lett.*, **73**, 1227, 1998.
12. S.A. Plimmer, "Avalanche multiplication in Al_xGa_{1-x}As", Ph.D. thesis, University of Sheffield, U.K., 1997.
13. G.E. Bulman, V.M. Robbins and G.E. Stillman, "The determination of impact ionization coefficients in (100) Gallium Arsenide using avalanche noise and photocurrent multiplication measurements", *IEEE Trans. Elec. Dev.*, **32**, 2454, 1985.
14. V.M. Robbins, S.C. Smith and G.E. Stillman, "Impact ionization in Al_xGa_{1-x}As for x = 0.1 - 0.4", *Appl. Phys. Lett.*, **52**, 296, 1988.
15. G.E. Stillman and C.M. Wolfe, "Semiconductors and Semimetals", edited by R.K. Willardson and A.C. Beer, Academic Press, New York, **vol.12**, 1977.
16. B. Monemar, K.K. Shih and G.D. Pettit, "Some optical properties of the Al_xGa_{1-x}As alloy system", *J. Appl. Phys.*, **47**, 2604, 1976.
17. L.V. Keldysh, "Kinetic theory of impact ionization in semiconductors", *Soviet Phys. JETP*, **37**, 509, 1960.
18. J.P.R. David, J.S. Marsland and J.S. Roberts, "The electron impact ionization rate and breakdown voltage in GaAs/Ga_{0.7}Al_{0.3}As MQW structures", *IEEE Elec. Dev. Lett.*, **10**, 294, 1989.
19. K.F. Li, University of Sheffield, private communication, 1998.

Quantum mechanical analysis of a Muller effect plasma wave optical modulator/switch

Sina Khorasani, Alireza Nojeh, Bizhan Rashidian*

Dept. of Electrical Engineering, Sharif University of Technology, P. O. Box 11365-9363, Tehran, Iran

ABSTRACT

Feasibility of a new integrated waveguide amplitude modulator/switch with more than 100GHz bandwidth in the visible and IR spectrum, based on the absorption of light due to linear interaction of the incident laser and a two-dimensional plasma layer has recently been demonstrated¹. Plasma layers were generated via Muller's effect at the waveguide's interfaces.

In this article, properties of the charge layers are investigated using quantum mechanics. First, the density of states and unperturbed energy eigenvalues are calculated. Then electron wave functions are obtained using the solution of Schrödinger's equation in the presence of an external applied electrostatic field in the structure. In the next step, energy eigenvalues are estimated by means of a perturbation technique. The electron density in the interfaces and the effective thickness of the charge layers are obtained using the calculated wave functions. The reflection problem is treated classically by direct solution of Maxwell's equations¹.

Keywords: Plasma, Optical Modulator, Optical Switch, Muller Effect, Waveguide, Quantum Mechanics, Schrödinger's equation, Perturbation Technique.

1. INTRODUCTION

In a recent study, it has been discussed how the propagation of plasma waves in a High Electron Mobility Transistor (HEMT) can be used to implement a new generation of terahertz devices². In near future, light beam, instead of electric current, will be responsible for carrying information between different parts of these devices and optical circuits. Several approaches for light modulation have been proposed based on electro-optical, magneto-optical and acousto-optical effects³, however there still exist some fundamental limitations in their sizes and speeds.

Another approach makes use of the interaction of electric charge and electromagnetic wave. McQuistan and Schultz⁴ proposed an infrared modulator in which free carrier absorption in germanium had been utilized to modulate the radiation. Allen, Tsui and Vinter⁵ investigated the absorption of infrared radiation by electrons in semiconductor inversion layers. Kovacs and Scott⁶ demonstrated the optical excitation of surface plasma waves in metal-dielectric interfaces, from both theoretical and experimental points of view. A valuable review on optical plasma resonance has been published by Steinmann⁷. The coupling of light to plasmon oscillations has also been investigated by Lindau and Nilsson⁸, and Fontana⁹. Also, far-infrared light modulator and switch has been proposed and developed in 400 KHz range by Kuijk, Vounckx, Stiens and Borghs¹⁰⁻¹². They have used the concept of reflection of light from an inversion layer that acts as a mirror for light frequencies below the layer's plasma frequency. However, it seems that very fast modulation had not been achieved because of the slow dynamics of the inversion layer.

In a recent article, the authors have demonstrated the feasibility of a new voltage controlled integrated optical modulator/switch, which may be fabricated by existing microtechnology methods¹. In that device, the TE or TM polarized laser beam propagates in a planar optical waveguide structure. By means of the Muller effect that has been discussed in detail, two-dimensional electron gases (2DEGs) are generated at the waveguide's film-cover and film-substrate interfaces. These two dimensional plasmas can be excited by the light and thus, energy transfer between the light beam and the 2DEGs could happen as the result of this interaction. As the amount of light absorption by the electron gases depends on the properties of the 2DEGs such as the charge density in them, it is possible to have a modulator if one is able to change these properties in a convenient manner. In the Muller effect, a transverse voltage is responsible for the generation and control of the electron gas, and thus the modulation or the switching of the light beam intensity. As has been demonstrated, the device

*Correspondence: Email: rashidia@ee.sharif.ac.ir, Telephone: +98-21-9182631, Fax: +98-21-6036008

could be operated with low voltages (<3 V) and high switching/modulation speed (<10 ps), and because of its vertical structure it can be fabricated in small dimensions.

The present work mainly deals with the properties of the charge layer under discussion. Schrödinger's wave equation is first solved for the electrons in the charge layer. An electrostatic field is applied externally to the structure. Electron wave functions are thus obtained for the film-cover interface states. The density of states (DOS) and the unperturbed energy eigenvalues are also calculated. In the next step, energy eigenvalues are estimated by means of a perturbation technique. Using the calculated wave functions, the electron density in the interfaces and the effective thickness of the charge layers are estimated. The calculation of the reflection coefficient of the laser beam from the structure is then performed using the solution of Maxwell's equations.

2. DEVICE STRUCTURE

The proposed structure is shown in Fig. 1. The illustrated device consists of a planar dielectric waveguide in which the light beam propagates. Two metal electrodes make it possible to apply a transverse electric field to the waveguide. As is known from Muller's effect, such a voltage will produce a surface electric charge in the interfaces of the dielectrics, if the conductivity to permittivity ratios of these dielectrics are different. It can be easily shown that for the film-cover interface, the density of this surface charge is given by:

$$\sigma_{fc} = (\rho_s t_s + \rho_f t_f + \rho_c t_c) / (\rho_f \epsilon_f - \rho_c \epsilon_c) V. \quad (1)$$

where V is the transverse voltage, t stands for a layer's thickness and ρ and ϵ denote resistivity and permittivity, respectively. f , s , and c subscripts refer to film, substrate, and cover layers. It is seen that the surface charge density is proportional to the applied voltage. If this voltage is changed, the density of the two dimensional plasma will be changed, causing a change in the reflection coefficient of light, thus modulating the output beam intensity. Proper layer characteristics could be chosen in order to obtain the desired surface charge density with typical voltage values in state-of-the-art CMOS technology (<3 V).

3. METHOD OF ANALYSIS

3.1. Quantum mechanical analysis

It is assumed that a transverse electric field is applied to the structure so that the electrostatic potential $\Phi(z)$ in the film and cover regions can be approximated as typically shown in Fig. 2a. Obviously, corrections should be made to it because of the presence of the charge layer itself, which are imposed within the solution of the unperturbed system. Schrödinger's wave equation is written in the form

$$\mathbf{H}|n\rangle = \lambda_n |n\rangle, \quad (2)$$

when $|n\rangle$ represents the eigenket of n th state in the system and λ_n is the eigenvalue associated with it. The electronic Hamiltonian which is defined as¹³

$$\mathbf{H} = -\frac{\hbar^2}{2m^*} \frac{d^2}{dz^2} + V(z). \quad (3)$$

The constituting materials and the interface are assumed to be isotropic with regards to the electron effective mass which is represented by m^* , and the effect of the periodic background lattice potential is considered in the value of m^* . The potential energy is related to the electrostatic potential $\Phi(z)$ by the relationship

$$V(z) = -e\Phi(z) + \Delta E_c \theta(-z), \quad (4)$$

in which $-e$ stands for the electron charge and ΔE_c is the conduction band energy difference between the film and the cover materials. θ represents the unit step function. A typical $V(z)$ is shown in Fig. 2b. The density of occupied states may be written as¹⁴

$$N_n = D_n \frac{kT}{q} \ln \left[1 + \exp \left(\frac{E_F - \lambda_n}{kT} \right) \right], \quad (5)$$

where D_n is the density of the n th state¹⁵ defined as

$$D_n = \frac{qm^*}{\pi \hbar^2}. \quad (6)$$

The energy levels of the unperturbed system (i.e. no applied voltage) are given by¹⁶

$$\lambda_n = \left(\frac{\hbar^2}{2m^*} \right)^{1/3} \left[\frac{3}{2} q |E_s(0)| \left(n + \frac{3}{4} \right) \right]^{2/3}. \quad (7)$$

Here, $E_s(0)$ stands for the discontinuity of normal electric field at the interface due to the 2D electron gas¹⁶ and is given by

$$|E_s(0)| = q \frac{n_s}{\epsilon_{eff}}, \quad (8)$$

in which the effective dielectric permittivity at the interface is defined as

$$\epsilon_{eff} = \epsilon_0 \frac{\epsilon_c + \epsilon_f}{2}. \quad (9)$$

The numerical approach solves the following system of second order differential equations

$$\frac{d^2}{dz^2} \begin{bmatrix} \Phi(z) \\ \langle z|0 \rangle \\ \langle z|1 \rangle \\ \vdots \\ \langle z|n \rangle \end{bmatrix} = \begin{bmatrix} -\frac{q}{\epsilon_{eff}} \sum_n N_n |\langle z|n \rangle_0|^2 \\ \frac{2m^*}{\hbar^2} [V(z) - \lambda_{00}] \langle z|0 \rangle_0 \\ \frac{2m^*}{\hbar^2} [V(z) - \lambda_{10}] \langle z|1 \rangle_0 \\ \vdots \\ \frac{2m^*}{\hbar^2} [V(z) - \lambda_{n0}] \langle z|n \rangle_0 \end{bmatrix}, \quad (10)$$

in which the 0 subscript represents the unperturbed system. This set of differential equations are subject to the boundary conditions

$$\langle z|n \rangle|_{z=-l_f} = 0, \quad \langle z|n \rangle|_{z=l_c} = 0 \quad (11a)$$

$$\Phi(z)|_{z=-l_c} = V, \quad \text{and} \quad \Phi(z)|_{z=l_f} = 0. \quad (11b)$$

FDM^{17,18} with the following discretization operator is applied to solve (10):

$$\frac{d^2}{dz^2} A(z) \approx \frac{A(z_{n+1}) + A(z_{n-1}) - 2A(z_n)}{\Delta z^2}. \quad (12)$$

After solving the above system, the perturbed eigenvalues are found from¹⁹:

$$\lambda_k = \lambda_{k0} + \Delta\lambda_k \text{ and } \Delta\lambda_k \approx \langle k | \Delta H | k \rangle, \quad (13)$$

and then the system of equations (10) is solved again for perturbed eigenfunctions. Finally, the average density of electron gas $\langle \rho \rangle$ and effective thickness $\langle t \rangle$ are derived from:

$$\langle \rho \rangle = \sum_n N_n \langle |z| n \rangle^2, \quad (14a)$$

$$\text{and } \langle t \rangle = -\frac{\sigma_{fc}}{q\langle \rho \rangle}. \quad (14b)$$

These information are used in the next section to calculate the reflection coefficient, where the 2D electron gas is treated as a thin slab of one-component-plasma.

3.2. Solution of Maxwell's equations

In order to calculate the reflection coefficient of light by the structure, one has to solve the Maxwell equations for the system. As the waveguide itself imposes a dispersion relation on the propagation of light in it, the simple structure shown in Fig. 3 is considered here for simplicity, and its reflection coefficient is calculated. The Ag layer which is shown in the structure represents the metal electrode. The results obtained in this subsection will serve the complete analysis of the waveguide modulator problem. The detailed classical method of analysis is published elsewhere¹, and is not repeated here.

However, the present work differs from the former in its definition of interface currents. There, an infinitely thin interface current density was inserted in the formulation as a discontinuity in the tangential magnetic field \mathbf{H} that shall not be confused with the Hamiltonian. Here, the interface charge layer is considered as a plasma slab with finite thickness whose associated bulk charge density and thickness have been estimated by quantum mechanics as described in the previous subsection, and enters the formulation described in reference 1 as a separate layer. The corresponding complex permittivity is defined as

$$\varepsilon = \left(1 - \frac{\omega_p^2}{\omega^2} \right) + j \left(\frac{q\mu}{\omega} \langle \rho \rangle \right), \quad (15)$$

with the average carrier density $\langle \rho \rangle$ given by the relation (14a), and j and ω being the unit imaginary number and angular frequency of light, respectively. Also, $\omega_p^2 = q^2 \langle \rho \rangle / m^* \varepsilon_{eff}$ is the plasma frequency of the electron gas¹². The real part of the relation (15) is adopted from the conventional model for the plasma¹² and the imaginary part represents the conduction loss resulting from carrier density at the interface.

4. RESULTS AND DISCUSSIONS

A typical structure has been analyzed based on the above formulation. The dielectric regions can be made up of transparent conductors such as ITO (Indium Tin Oxide) or ZnO (Zinc Oxide). One can control the degree of transparency and conductivity to a large extent in the process of depositing these materials. In our example, an index of refraction equal to 1.8 is assumed for the film region. It should be pointed out that interface mobility is greater than the bulk mobility, because electronic states are present at the interface and carriers in these states are not bounded to the lattice to the degree that are the bulk states. This is why the use of dielectrics in the structure does not cause any difficulty. In addition, the interface

mobility has to be increased by depositing a thin layer of a high electron mobility material. For the second region (the cover), a refractive index equal to 1.4 has been assumed. For the Ag electrode, the value of the relative permittivity has been taken as $-12 + j 0.4$ for the wavelength used in the analysis²⁰. Also, $t_c = 100$ nm and $t_{\text{electrode}} = 20$ nm with resistivities $\rho_s = \rho_c = 10^{-2} \Omega\text{m}$ and $\rho_f = 10^{-1} \Omega\text{m}$ have been chosen for the calculations.

The effective thickness of the charge layer and the volume electron density in it are plotted as functions of the applied voltage in Fig. 4. It is observed that the volume charge density exhibits little change by changing the applied voltage, but the effective thickness varies almost linearly. It should be noted that the layer's surface charge density that is the product of the two parameters in question is a linear function of the applied voltage as imposed by Muller's effect.

Fig. 5(a) and 5(b) show the electron ground and first excited state wave functions for an applied voltage of 0.1V. The confinement of the 2DEG near the interface is seen in the figures. Increasing the applied voltage to 1V results in more confinement of electrons as in Fig. 5(c). Reflection coefficients calculated using the semi-classical method described in this article are plotted versus the angle of incidence in Fig. 6 for both TM and TE polarized lights, at different values of the applied voltage. The considerable change of the reflection coefficients in response to the voltage demonstrates the structures ability to act as an electro-optic modulator. Similar curves are also calculated by the full-classical method¹ and are shown in Fig. 7 for comparison. The considerable similarity between the results obtained using full-classical and semi-classical methods is evident.

It should be pointed out that a complete analysis of the waveguide structure can be carried out as is done in reference 1. This analysis is not the purpose of the present work.

5. CONCLUSIONS

The plasma wave modulator that had recently been proposed and analyzed using classical electromagnetics was reviewed and the characteristics of its two-dimensional plasma layer were investigated using quantum mechanics. The semi-classical approach to the analysis of the modulator gives results that are relatively similar to the full-classical results.

REFERENCES

1. B. Rashidian, A. Nojeh, and S. Khorasani, "A new plasma wave micro-optical modulator/switch," *Proc. MOEMS'99*, pp. 66-73, Mainz, 1999.
2. M. I. Dyakonov and M. S. Shur, "Plasma wave electronics: Novel terahertz devices using two dimensional electron fluid," *IEEE Trans. on Electron Devices*, **43**, pp. 1640-1645, 1996.
3. A. Yariv, and P. Yeh, *Optical Waves in Crystals*, John Wiley and Sons, New York, 1984.
4. R. B. McQuistan and J. W. Schultz, "Modulation of infrared by free carrier absorption," *J. of Appl. Phys.*, **35**, pp. 1243-1248, 1964.
5. S. J. Allen, Jr., D. C. Tsui, and B. Vinter, "On the absorption of infrared radiation by electrons in semiconductor inversion layers," *Solid State Commun.*, **20**, pp. 425-428, 1976.
6. G. J. Kovacs and G. D. Scott, "Optical excitation of surface plasma waves in layered media," *Phys. Rev. B*, **16**, pp. 1297-1311, 1977.
7. W. Steinmann, "Optical plasma resonances in solids," *Phys. Stat. Sol.*, **28**, pp. 437-462, 1968.
8. I. Lindau and P. O. Nilsson, "Experimental evidence for excitation of longitudinal plasmons by photons" *Phys. Lett.*, **31A**, pp. 352-353, 1970.
9. E. Fontana, "A theoretical analysis of the coupling of light to surface-plasmon oscillations at the edge of a slab waveguide," *IEEE Trans. on Microwave Theory and Tech.*, **46**, pp. 234-241, 1998.
10. M. Kuijk and R. Vounckx, "Use of two-dimensional electron gas in optical information processing: Proposal for integrated mirror optical switch," *Electron. Lett.*, **25**, pp. 231-233, 1989.
11. J. Stiens, M. Kuijk, R. Vounckx, and G. Borghs, "New modulator for far-infrared light: Integrated mirror optical switch," *Appl. Phys. Lett.*, **59**, pp. 3210-3212, 1991.
12. M. Kuijk and R. Vounckx, "Optical plasma resonance in semiconductors: Novel concepts for modulating far-infrared light," *J. of Appl. Phys.*, **66**, pp. 1544-1548, 1989.
13. F. Stern and S. D. Sarma, "Electron energy levels in GaAs-Ga_{1-x}Al_xAs heterojunctions," *Phys. Rev. B*, **30**, pp. 840-848, 1984.

14. T. Ando, "Density-functional calculations of sub-band structure in accumulation and inversion layers," *Phys. Rev. B*, 13, pp. 3468-3477, 1976.
15. F. Ali and A. Gupta, eds., *HEMTs and HBTs: Devices, Fabrication and Circuits*, Artech House, Boston, 1991.
16. F. Stern, "Quantum properties of surface space charge layers," *CRC Crit. Rev. Solid-State Sci.*, pp. 499-512, 1974.
17. M. N. O. Sadiku, *Numerical Techniques in Electromagnetics*, CRC Press, Boca Raton, 1992.
18. C. F. Gerlad and P. O. Wheatley, *Applied Numerical Analysis*, 4th ed., Addison Wesley, Reading, 1989.
19. J. J. Sakurai, *Modern Quantum Mechanics*, Addison Wesley, Redwood City, 1985.
20. P. B. Johnson and R. W. Christy, "Optical constants of the noble metals," *Phys. Rev. B*, 6, pp. 4370-4379, 1972.

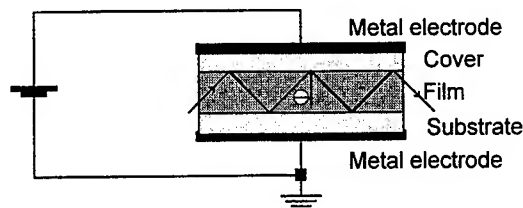


Fig. 1. Device structure for the plasma wave optical modulator/switch.

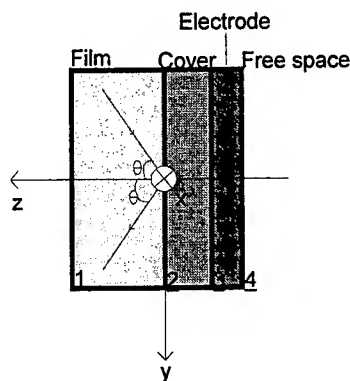
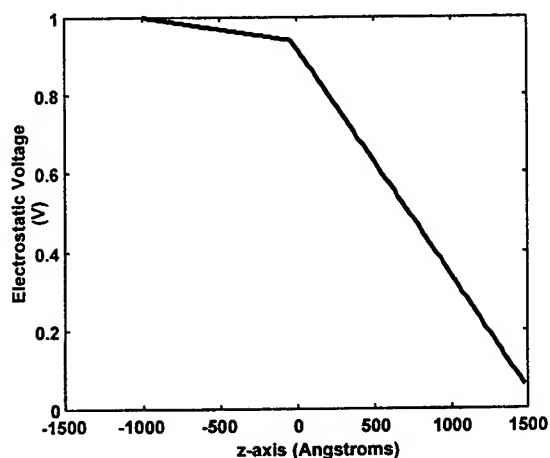
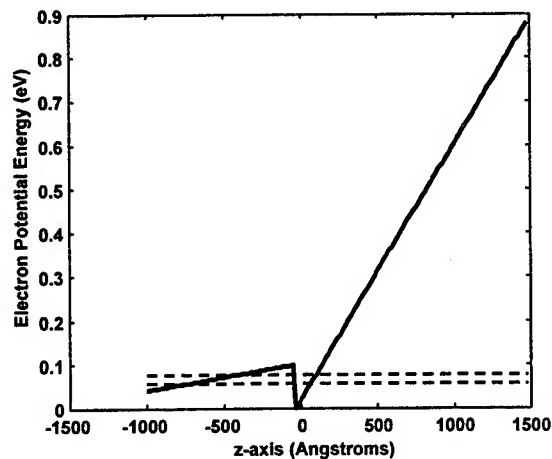


Fig. 2. Basic structure used in the analysis of the optical modulator/switch in Fig. 1.

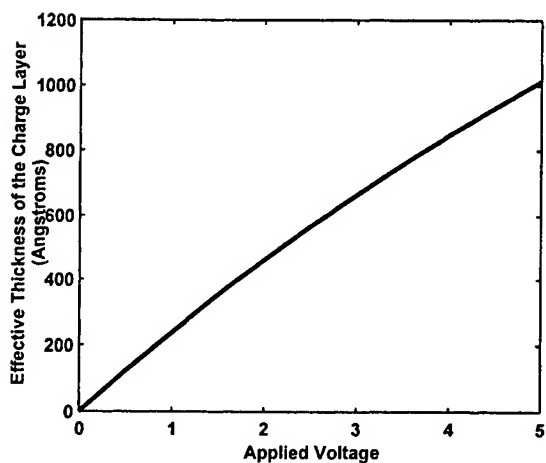


(a)

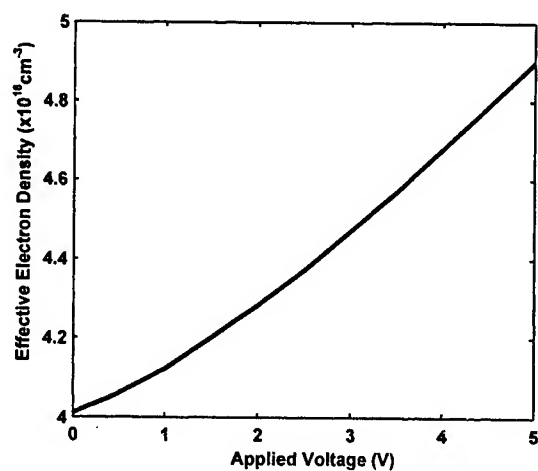


(b)

Fig. 3. (a) Initial electrostatic potential in the structure. (b) Electron potential energy in the structure and the two first energy states. 1 V external voltage has been applied.

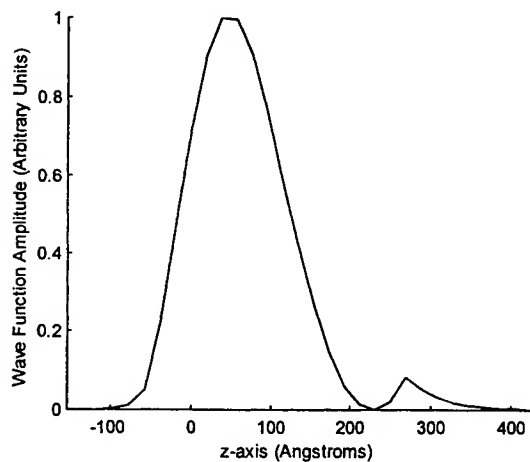


(a)

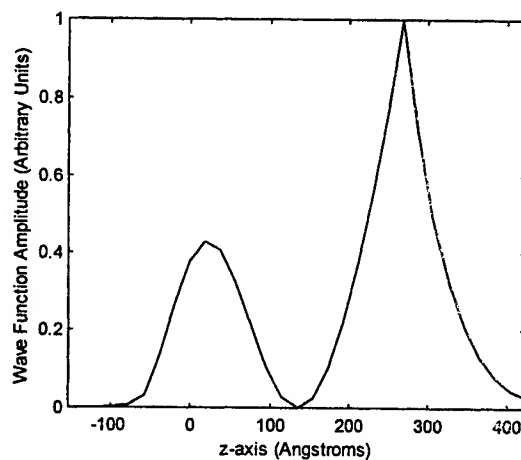


(b)

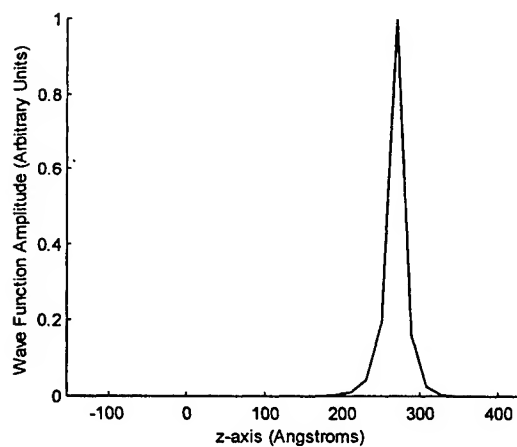
Fig. 4. a) Charge layer's effective thickness vs. applied voltage.
b) Charge layer's electron density vs. applied voltage.



(a)

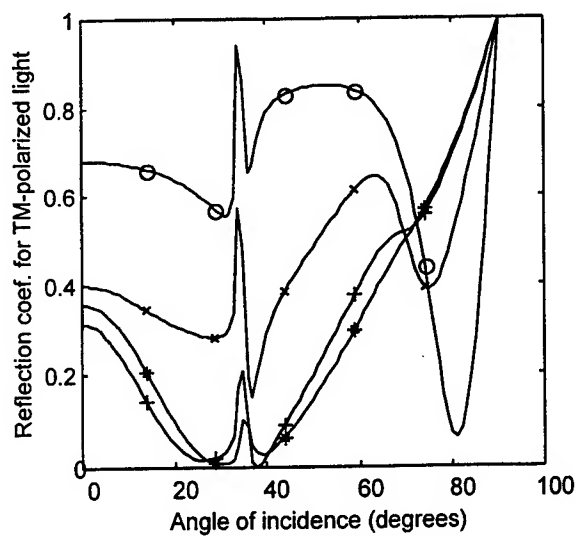


(b)

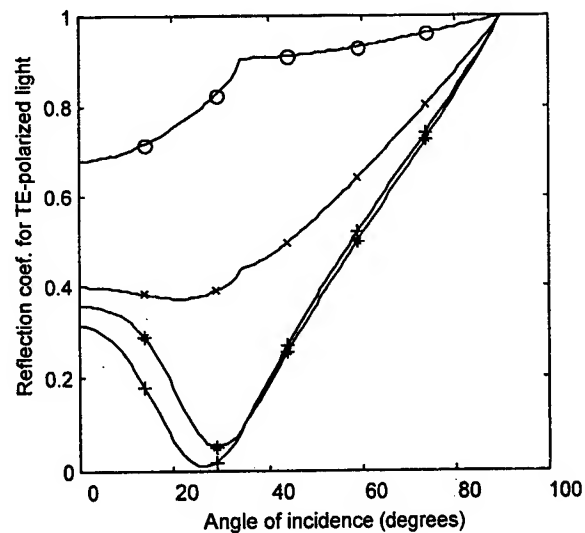


(c)

Fig. 5. (a) Ground state electron wave function for 0.1 V applied voltage. (b) First excited state electron wave function for 0.1 V applied voltage. (c) Ground state electron wave function for 1 V applied voltage.

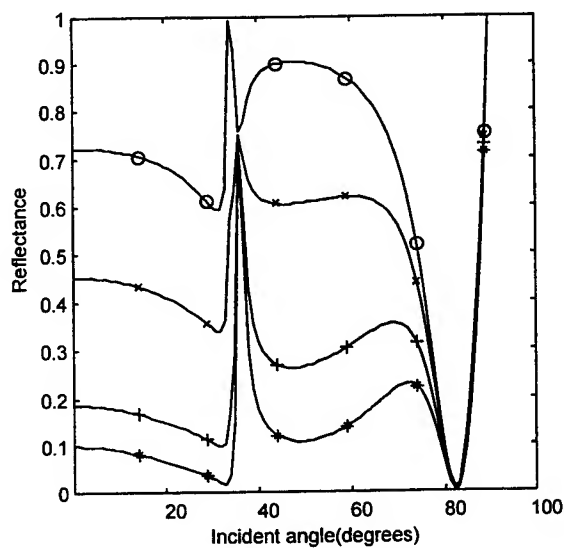


(a)

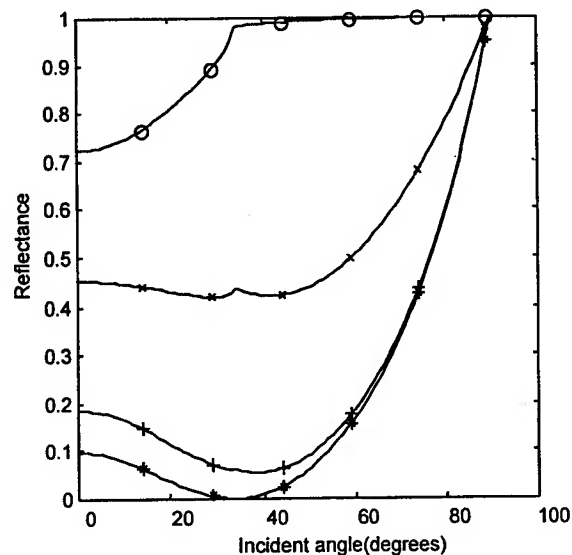


(b)

Fig. 6. Dependence of reflectivity on incident angle - Semi classical analysis:
(o) $V=0.1V$, (x) $V=1V$, (+) $V=3V$, (*) $V=5V$. (Interface mobility = $5 \text{ m}^2/V\cdot\text{sec}$)
(a) TM polarization. (b) TE polarization.



(a)



(b)

Fig. 7. Dependence of reflectivity on incident angle - Full classical analysis (figures from ref. 1):
(o) No applied voltage, (x) $V=1V$, (+) $V=3V$, (*) $V=5V$. (Interface mobility = $5 \text{ m}^2/V\cdot\text{sec}$)
(a) TM polarization. (b) TE polarization.

Integrated acousto-optic tunable filter, equalizer and switch in WDM communication system

Dai Enguang*, Wu Deming and Xu Anshi

National Laboratory on Local Fiber-Optic Communication Networks & Advanced
Optical Communication Systems
Department of Electronics, Peking University, Beijing 100871 China

ABSTRACT

Acousto-optic tunable filter (AOTF), acousto-optic switch (AOS) and acousto-optic equalizer with high acousto-optic interaction efficiency are important devices in WDM networks. The technologies of unidirectional and focused transducer were adopted for the design of integrated acousto-optic device. Extensive usage for the acousto-optic device such as optical switches, gain equalizer and optical add-drop multiplexer have been studied. The concept that changing the radius of focus transducer can adjust the switching speed and FWHM of the filter was proposed for the first time.

Keywords: acousto-optic tunable filter, acousto-optic switch, curved transducer, optical add-drop multiplexer

1. INTRODUCTION

The integrated acousto-optic tunable filter (AOTF), acousto-optic equalizer and acousto-optic switch (AOS) are rapidly gaining importance in fiber-optic communication systems because these devices have combined features of rapid switching time, broad tuning range and parallel processing capability.

As for conventional transducer in integrated acousto-optic devices, its aperture was usually small, the impedance was much higher than $50\ \Omega$. It was usually bi-directional, there was large interfinger reflections and there was 3dB transduction loss. Because the aperture is small, the spread of SAW propagation is very severe.

In different usage, the design requirements for the acousto-optic device are different. For optical switch, first of all, the high extinction ratio and high speed target should be considered. As far as optical filter, the sidelobe should be controlled at a low level and the FWHM should be narrow enough to decrease the interchannel interference.

Sufficient extinction ratio and high switching speed are indispensable for modern fiber-optic communication system. Mechanical switch has higher extinction ratio, but its switching speed is in the range of milliseconds. Waveguide travel-wave modulator has higher speed, but its extinction ratio is usually below 20dB. As far as AOS, unfortunately, switching speed and extinction ratio are contradictory. Longer interaction length is needed to obtain higher extinction ratio, which will result in slower switching speed. The usual speed of AOS reported is in several microseconds with extinction ratio below 25dB^{1-3} . In this paper, we will develop new technologies to solve this problem.

EDFA is widely recognized as an ideal repeater for long distance lightwave transmission systems. However, as for cascaded EDFAs, even a fraction variation of a decibel in the gain spectrum flatness of individual amplifier would lead to larger difference after propagation through long EDFA chains. Gain equalizers are essential to equalize the signal power and the signal-to-noise ratio. The results in the paper will show gain compensations for two arbitrary injected wavelength.

*Correspondence: Email: daieg@pku.edu.cn; Telephone: (8610)62754170; Fax: (8610)62751763;

2. DESIGN OF THE INTEGRATED ACOUSTO-OPTIC DEVICE

The integrated acousto-optic devices consisted of a single-mode Ti-indiffused optical waveguide placed along surface acoustic wave propagation direction. To launch SAW effectively and decrease the reflection between fingers, the technology of both electrode-width controlled (EWC) single phase unidirectional transducer (SPUDT) and focused transducer were adopted simultaneously. SPUDT was designed with coupled-mode theory. Based upon a set of coupled-of-mode equations, the width of the electrode can be determined.

Coupled-mode theory is a very useful tool for the design of low loss IDT. If we denote periodic length, the particle velocities of the forward going and backward going surface acoustic waves by λ_a , $A^+(x)$ and $A^-(x)$, respectively, the differential equations can be expressed as follows

$$\frac{dA^+(x)}{dx} = -jk_{11}A^+(x) - jk_{12}e^{j2\delta x}A^-(x) + \alpha e^{j\delta x}V \quad (1)$$

$$\frac{dA^-(x)}{dx} = jk_{11}A^-(x) + jk_{12}^*e^{-j2\delta x}A^+(x) - \alpha^*e^{-j\delta x}V \quad (2)$$

$$\frac{dI}{dx} = 2\alpha^*e^{-j\delta x}A^+(x) + 2\alpha e^{j\delta x}A^-(x) + j\omega CV \quad (3)$$

where $\delta = k - k_0$, $k = \omega/V_p$, $k_0 = 2\pi/\lambda_a$ and V is the voltage, $I(x)$ is the bus bar current, α , α^* are the transduction coefficient, C is the capacitance per unit length, and V_p is the phase velocity of the SAW on the electrically free surface. By solving these equations, the mixed matrixes are obtained as

$$S_{11} = P_{11} + \frac{2P_{13}^2}{G_L + P_{33}} \quad (4)$$

$$S_{13} = \frac{2\sqrt{G_L}P_{13}}{G_L + P_{33}} \quad (5)$$

where P_{11} is the reflection coefficient at the forward acoustic port, P_{13} is the generated acoustic wave amplitude in the forward direction. G_L is the combined effective electrical load conductance.

$$P_{33} = G_A + jB_A + j\omega C_T - j/(\omega L_M) \quad (6)$$

G_A is the acoustic radiation conductance, B_A is the acoustic radiation susceptance, C_T is the transducer static capacitance, and L_M is the matching inductance. The approach for the design of low loss transducer is to solve a self-consistent set of P_{11} , P_{13} and P_{33} such that S_{11} is zero under matched conditions.

The developed SPUDT is unique in that it consists of curved interdigital electrodes which can be used to generate SAW and focus acoustic power at the middle of the interaction length and thus the SPUDT can facilitate decreasing the spread of SAW along optic waveguide. The acoustic walk-off effect for X-Y LiNbO_3 can be avoided when the curved IDT is compensated. Because acoustic focus is located at a different position from the geometric focus of the curved IDT for the kind of material, the offset distance should also be compensated.

It should be noted that the unidirectional transducer can only decrease the 3dB transduction loss partially, not totally. This is because that the interdigital transducer is not designed for narrow RF bandwidth, but for mediate bandwidth to make the devices adjustable.

The fabrication conditions are identical for both EWC-SPUDT and conventional splitter finger IDT. Above all, the EWC-SPUDT can also effectively decrease the inter-finger reflections that will degrade the frequency response of the IDT.

Another consideration is that the unidirectional operation will minimize the reflections from the substrate edge on the side the transducer placed.

3. EXPERIMENTS

In this section, three kinds of application of the acousto-optic device will be discussed. The devices were designed differently for different usage.

3.1. Acousto-optic switch

By carefully designing the structure of the transducer, above all, the focus radius of the curved SPUDT, the intensive surface acoustic wave was confined in a narrow interaction area between optical waveguide and acoustic propagation with a short interaction length.

The frequency of the driving signal applied to the transducer was at 176MHz. With an optical spectrum analyzer, the spectrums for the "off" state and the "on" state are depicted in Fig. 2 and Fig. 3. The extinction ratio with a single stage AOS was up to 32dB, the extinction-ratio up to 60dB can be expected for the two-stage structure. The overall insertion loss

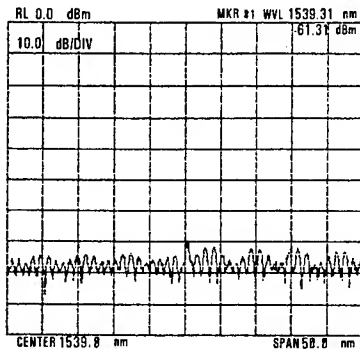


Fig.2. The "off" state

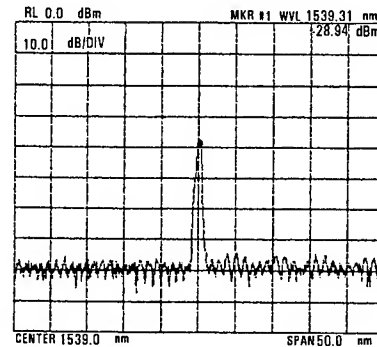


Fig.3. The "on" state

was less than 4dB. Based upon HP8510C network analyzer, it is shown that the impedance of the transducer is 46Ω , which means that the transducer can match 50Ω RF signal efficiently.

The experimental apparatus for switching speed demonstration is shown in Fig.4. The output of a DFB laser was passed through the AOS and a self-fabricated high-speed external modulator, then the light was coupled into a detector. The RF signal at 176MHz was passed through a RF switch driven by square-wave clock signals.

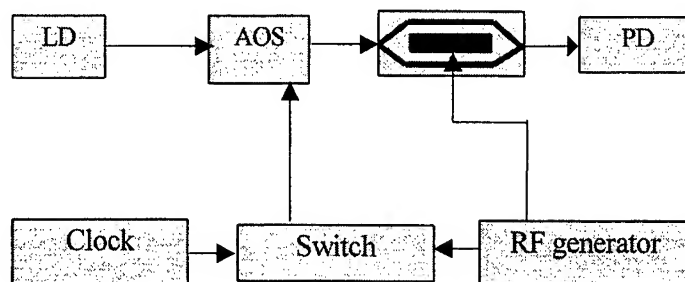


Fig.4. The Experimental setup for the measurement of switching speed

Fig. 5 shows traces of the switching signal (lower trace) and the modulated signal (upper trace). The rise time, defined as the time required to reach 90% of the steady-state transmission⁴, was 300ns (the delay of the RF pulse was also included), much higher than that reported on AOS. The RF driving power needed was 200mW.

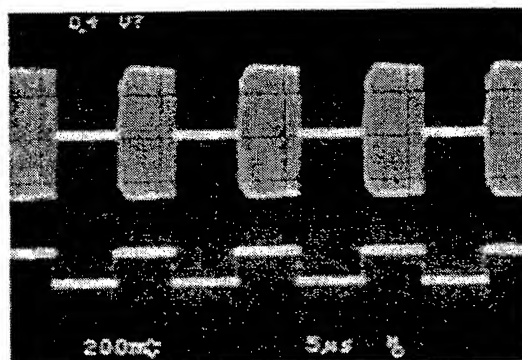


Fig.5. The time-domain display. Time scale is 5 μ s per division

Fig.6 shows the traces of the modulated signal at the time scale of 500 μ s per division. It can be proved from the frequency-domain and time-domain display that the extinction ratio and the switching speed are definitely very high. To authors knowledge, it is the highest-speed integrated acousto-optic switch with high extinction ratio ever been fabricated.

Curved electrodes is not used for the suppression of the sidelobe usually adopted in acousto-optic tunable filter but for the decreasing of the spread of SAW along optic waveguide, and thus the acoustic waveguide is not needed. The vast advantage of the curved and unidirectional transducer is that it can effectively decrease the power needed for the conventional AOS with shorter interaction length to arrive at the same extinction ratio and switching speed. The transducer can not withstand high power.

The switching speed was controlled by the design of different radius of the curved transducer. The radius was limited to several millimeters to arrive at high-speed operation. Acoustic absorber must be pasted at a suitable place, which means that the distance between the SPUDT transducer and the absorber is twice that of the radius of the SPUDT.

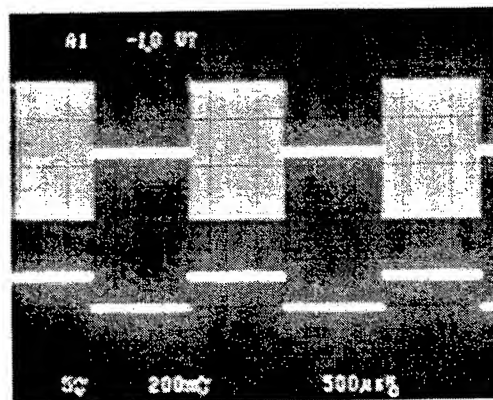


Fig.6. The time-domain display. Time scale is 500 μ s per division

From both of the Figures as displayed above, it is shown that no overshoot was generated which is common to some kinds of optical switches. This will make the acousto-optic switch more fit for the system application in which require little interference when the channels or signals are switched.

3.2. Acousto-optic equalizer for multi-wavelength system

In WDM system and networks, the maintenance of all signals at a high fidelity will require careful control over changing conditions. There are a large number of key technologies needed in network control and management, in which channel power equalization is an essential one. Robust networks require that the power difference among WDM channels remains small so as to ensure adequate gain for all channels⁵. A significant power and signal-to-noise ratio difference among many channels will be accumulated after an amplifier chain.

Since the EDFA gain is not uniform with wavelength, the lower gain channels progressively lose power relative to the higher gain channels⁶. The equalization approach of power management is based upon node isolation principle that the channel power at the output of each node is equalized to a preset level and thus the power difference between channels introduced by non-flat gain profile or dynamic reconfiguration of network will not be passed on to the subsequent nodes.

Traditional approaches for the channel power equalization are compensating the power variation by tuning optical attenuators and EDFAs. Channel powers are monitored using couplers and electronics feedback circuit.

Our method for equalizing WDM channel powers is to use an AOTF for notch filters. AOTF can provide an excellent means for gain equalization because it is capable of controlling the signal levels of the multiple wavelengths simultaneously and independently. Arbitrary filter shapes could be produced by applying several RF signals simultaneously to the device. The experimental setup shown in Fig.7 contained four wavelength, three EDFAs, an AOTF, an isolator, and an attenuator. The AOTF's RF driving frequency centered at two separate values. To compensate for the wavelength variation, the individual RF power levels applied to the AOTF should be adjusted.

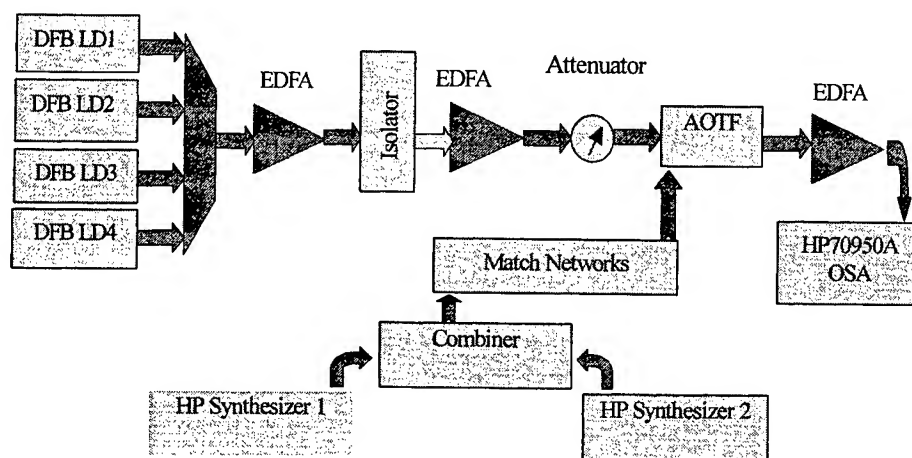


Fig.7. Experimental setup for multi-wavelength equalization

After the four wavelength shown in Fig.8 was equalized, the four wavelength was almost in the same power levels, which is denoted in Fig.9. It has been proved that the adjustment of the channel power level was convenient and fast. If an active feedback circuit is added into the system, a much higher equalizing speed can be achieved.

It should be noted that all-fiber acousto-optic tunable filters can experimentally demonstrate gain equalization of EDFAs in the range of 35nm⁷. This wide equalizing range is mainly from its wide 3-dB bandwidth. Integrated AOTF can also realize the performance of wide-range equalization on the condition that the acousto-optic interaction length should be designed as short as possible and suitable doped-metal film should be selected to handle high power operation. The surface acoustic wave transducer of the integrated AOTF is integrated into the substrate, whereas the flexural acoustic wave transducer of all-fiber AOTF is bulk structure. It can be seen that the integrated acousto-optic equalizer is more compact in structure than its all-fiber counterpart at a expense of larger insertion loss in the order of 3 to 4dB.

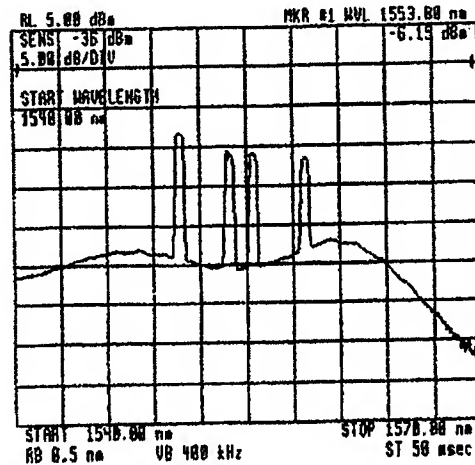


Fig.8. To be equalized wavelength in WDM system with three EDFAs

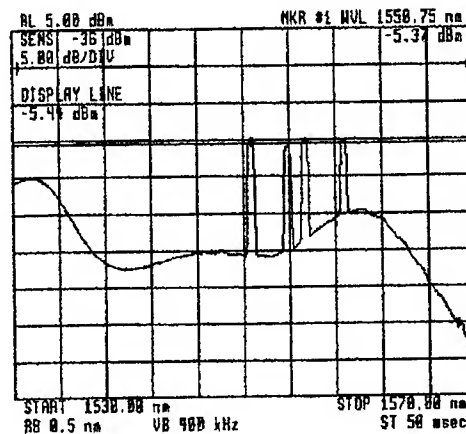


Fig.9. Equalized four wavelength

3.3. Optical add-drop multiplexer for multi-wavelength system

The most unique applications of the AOTF is as an optical add-drop multiplexer (OADM) in fully transparent WDM networks nodes. It was used as a multiplexer for dropping a wavelength or adding another wavelength when the appropriate set of RF frequencies were shut down or applied.

A high degree of extinction is necessary in the operation of the AOTF as a channel add-drop multiplexer. Under the condition that a node has extracted a given wavelength channel with only a modest degree of extinction, if the same wavelength is added at later nodes, the previously-leaked intensity will constitute directly-added intensity noise², and even if no new signal has been added into the node, receivers at subsequent nodes may detect the residual signal.

Four wavelength denoted in Fig. 10 was used. In this application, the filter acts as 2×2 nodes. Experimental results on dropping of one wavelength is demonstrated in Fig. 11.

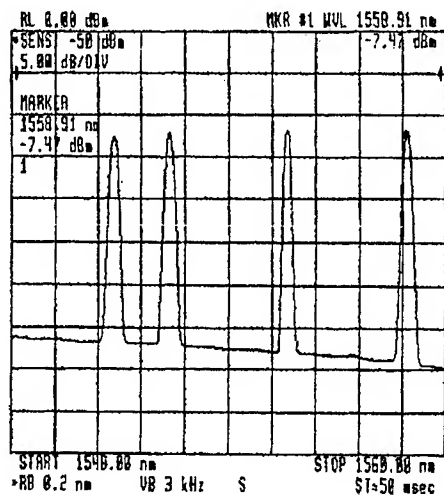


Fig. 10. Four original wavelength

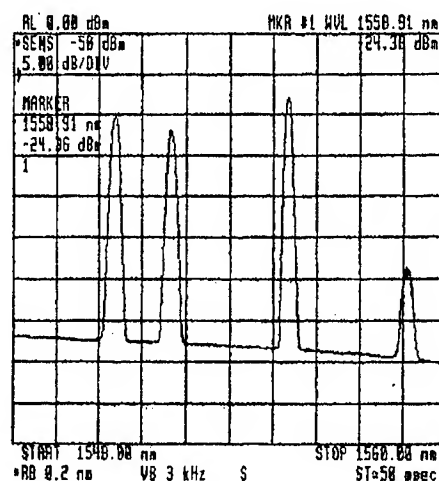


Fig. 11. Drop of one wavelength

As for as AOTF used as OADM, the optical spectrum should be more narrow than that of acousto-optic switch. As a result, the interaction length of the optical waveguide and the acoustic propagation should be much longer than that of acousto-optic switch. Lengthening the radius of the curved SPUDT will produce longer interaction length. Curved electrodes are used as the suppression of the sidelobe and the decreasing the spread of SAW along optic waveguide. The radius was extend to 20 millimeters to make the FWHM as narrow as 1.2nm.

4. CONCLUSION

The main usage such as switch, OADM and optical equalizer were intensively studied in WDM network. A single-stage AOS with SPUDT electrode was fabricated. Its extinction ratio is up to 32dB and switching speed is at about 300ns. No acoustic waveguide was needed. The acousto-optic device can also be used as equalizer in WDM+EDFA system with the advantages of continuous and fast equalization of optical wavelength. It is shown that the design methods are suitable for these acousto-optic devices' future usage in the field.

Low loss surface acoustic wave technologies^{8,9} are key in the fabrication of practical integrated acousto-optic devices. Unidirectional transduction technology is the main approach for the design of low loss IDT. Focused transducer is used as increasing the acoustic power near the optic waveguide to make the acousto-optic interaction intensive. If both of unidirectional and focus technology are adopted simultaneously, the device will be more suitable for the complex and stringent requirements for the future optical fiber communication.

ACKNOWLEDGMENTS

Authors will thank the supports of High Technology Research and Development Program of China and supports of Natural Science Foundation of China (69877002).

REFERENCES

1. F. Tian and H. Herrmann. interchannel interference in multiwavelength operation of integrated acousto-optical filters and switches. *Journal of lightwave technology*, 13, 1995.
2. David A. Smith, John J. Johnson. Integrated acoustically tuned optical filters for filtering and switching applications, *ultrasonic symposium*. pp. 547-557, 1991
3. K. W. Cheung, D. A. Smith, Multiple channel operation of integrated acousto-optic tunable filter, *Electronics letters*,

Vol. 25, No. 6, 375-376, 1989

4. D.A. Smith. Switching speed of integrated acoustically-tunable optical filter. Electronics letters, 27, pp. 1202-1203, 1991
5. A. E. Willner. Towards uniform channel performance in dynamic WDM systems and networks. OFC'99. pp.224-226.
6. S. H. Huang, X. Y. Zou, A. E. Willner. Experimental demonstration of active equalization and ASE suppression of three 2.5Gb/s WDM network channels over 2500km using AOTF as transmission filters. IEEE photonics technology letters, vol. 9, no. 3, 1997. pp. 389-391
7. H. Sang Kim. Dynamic gain equalization of erbium-doped fiber amplifier with all-fiber acousto-optic tunable filters. OFC'98, pp.136-138
8. Dai Enguang. Miniature Radar Based upon SAW ID-tags . Proceeding of IEEE MTT-S International Microwave and Optoelectronics Conference, Brazil, pp. 130-135, 1997
9. Dai Enguang. SAW filter with insertion loss of 2dB and fractional bandwidth of 30%. IEEE ultrasonics symposium, 1999.

SESSION 11

Sol-Gel Processing

Fabrication of gratings and design of diffractive optical elements embossed on sol-gel films

G. Tan*, Y. C. Chan, J. Liu, C. Y. Liaw, Y. L. Lam and Y. Zhou

Photonics Research Group, School of Electrical and Electronic Engineering
Nanyang Technological University, Block S1, Nanyang Avenue, Singapore 639798

ABSTRACT

Ion exchange, plasma deposition and flame hydrolysis are typically employed techniques for fabricating glass waveguides and gratings. These techniques have several drawbacks such as involvement of expensive instruments, multi-step procedure and high temperature treatment. These drawbacks make it difficult for their adoption in mass production. The sol-gel process is a simple and inexpensive way for making glass, and embossing into sol-gel films provides a simple alternative for fabricating surface profile gratings and other integrated optical devices. In this paper, we report the usage of the embossing technique to fabricate gratings and diffractive optical elements (DOEs) in the sol-gel cladding layer of a waveguide. The designed DOEs manipulate out-coupled light from a slab waveguide and form 3 lines of equal intensity at a stipulated distance. The DOEs were designed as two-level optics by the direct binary search method based on the scalar diffractive theory, and the master molders used in the embossing were fabricated by ultraviolet laser writing on photoresist combined with reactive ion etching. We chose organic modified silane in the sol-gel process and no baking was needed, greatly minimizing possible shrinkage of the thin film.

Keywords: Diffractive Optical Elements, Sol-Gel, Embossing

1. INTRODUCTION

Ion exchange¹, plasma deposition and flame hydrolysis² are typically employed techniques for fabricating glass waveguides and gratings. These techniques have several drawbacks such as involvement of expensive instruments, multi-step procedure and requirement of high temperature treatment. These drawbacks make their adoption difficult for mass production.

The sol-gel process provides a simple, low cost and low temperature solution for making bulk doped-glass and thin films, which are promising materials in integrated optics due to its excellent transparency, high thermal, mechanical stability, and low coupling losses with the optical fiber. Embossing into sol-gel thin films offers a practical way for the production of surface corrugation gratings, as well as other integrated optic components. It has been reported that embossing onto organic gel layers has the problem of serious shrinkage of up to 40-70%, while embossing onto inorganic layers suffers from thickness limitation and restricted plasticity³⁻⁷. Hybrid organic-inorganic sol-gel can thus provide both good plasticity and relatively little shrinkage during the embossing process.

In this paper, we present our experimental results in the fabrication of gratings by embossing on the hybrid organic-inorganic sol-gel film and simulation results of diffractive optical elements based on the parameters of the embossed sol-gel film.

2. FABRICTION OF GRATING BY EMBOSSING

In our experiment, the sol-gel precursors used are γ -glycidyloxypropyltrimethoxy silane (GLYMO) and titanium tetraisopropoxide. By changing the ratio of the two precursors, the refractive index of the resulting

* Corresponding author: Email: p145522710@ntu.edu.sg; Telephone: +65-7905449; Fax: +65-7933318

film can be easily adjusted, and this provides a route for refractive index design in the fabrication of optical waveguides⁸.

The sol solution is achieved by firstly mixing GLYMO with ethanol and water in the molar ratio of $C_9H_{20}O_5Si : C_2H_5OH : H_2O = 1 : 4 : 4.5$ (mol ratio) as sol <1>, and secondly mixing titanium tetraisopropoxide with acetylacetone in the molar ratio of $C_{12}H_{28}O_4Ti : C_5H_8O_2 = 1 : 4$ as sol <2>, and finally we proceed with the mixing of sol <1> and <2> in the molar ratio of 0.7 : 0.3. In such prepared solutions, the molar ratio of Si : Ti is 3 : 2. Next, the solutions are applied to the substrate after filtering with a 0.2 μm filter. Then the gel is spin-coated onto a cleaned Si substrate with a spin speed of 4000rpm for 35 seconds. A film with a thickness of 6.43 μm is achieved in a single coating step. After that, the samples are put in a clean air environment for drying. We measured the dependence of film thickness on drying time and obtained an empirical relation as given below:

$$y = 5.63 + 0.8 \exp(-t/280)$$

where y is the film thickness in μm and t is the drying duration in minutes. According to this relation, the total shrinkage of a pattern embossed on the film is no more than 5% if the pattern is embossed after drying the film for 4 hours.

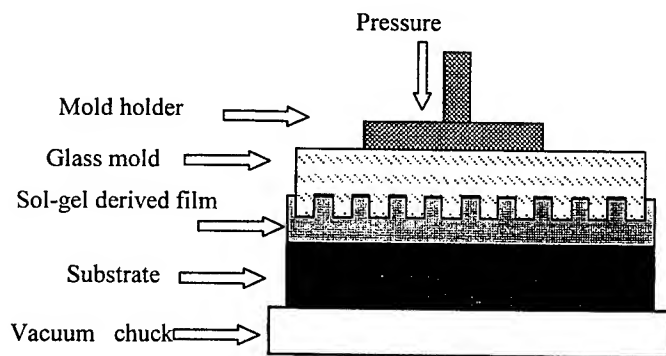


Fig.1 Schematic apparatus for embossing on sol-gel derived glass films

Embossing is carried out by the system shown in Fig. 1. An embossing pressure of about 200N/cm² is applied to the mold, forcing the grating pattern into the gel film, which has been dried in air for about 4 hours. In our experiments, a commercially available glass grating with a period of 1.103 μm is chosen as the mold. After keeping the pressure on the sample for 20 minutes, the mold is separated from the film. During the whole embossing procedure, no other method, such as UV irradiation or heating, is employed to help cure the pattern. The sample is then placed in a clean air environment for another 4 days before characterizing the embossed pattern.

Gratings on the embossed film and the mold are measured using atomic force microscopy (AFM). The measurement result is presented in Fig. 2. The grating period of the embossed film is found to be 1.102 μm , which is consistent with that of the mold. The grating depth achieved on the film is 57.2nm, smaller than the mold depth of 84.2nm, and achieving a depth-to-width aspect ratio of 1 : 10. We believe that the difference in the depth comes from the compressed air trapped between the mold and the film during embossing.

3. DESIGN OF DOES ON SOL-GEL FILM

Based on the above described sol-gel film with a refractive index of 1.46, a DOE has been designed, which is intended to manipulate light coupled out from a waveguide by focusing the light into 3 lines at a distance of 400mm. The Kirschhoff scalar diffraction theory is adopted to model the propagation from the DOE to

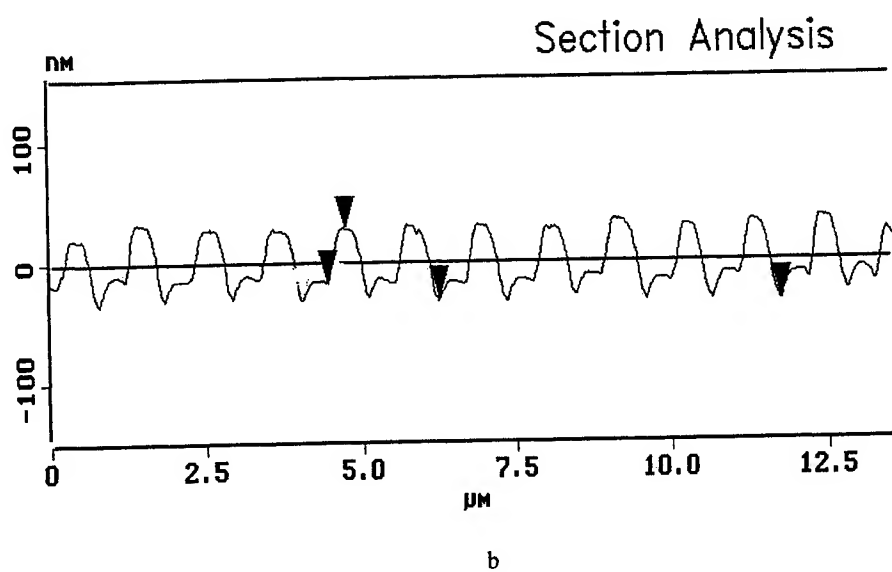
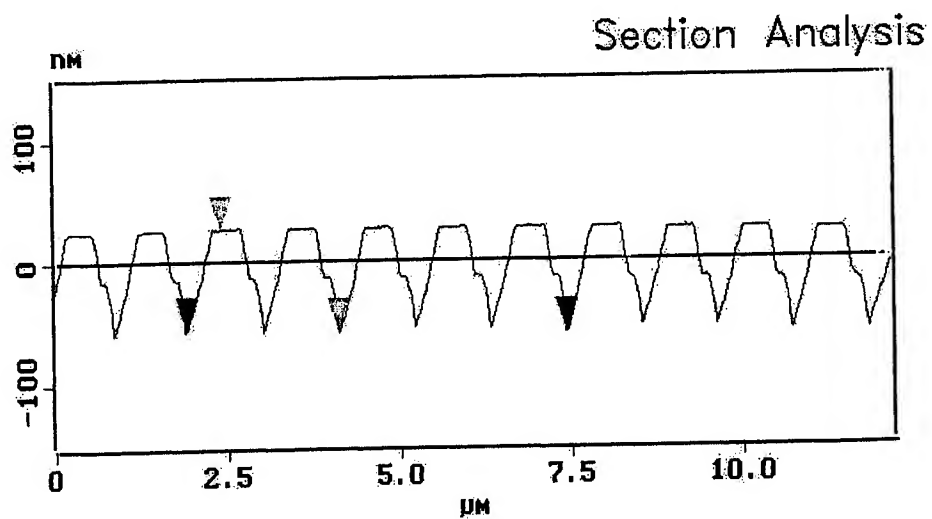


Fig.2 AFM section analysis of grating. a) grating on the mold, with period of $1.102\mu\text{m}$ and depth of 84.2nm b) embossed grating on the film with period of $1.102\mu\text{m}$ and depth of 57.2nm

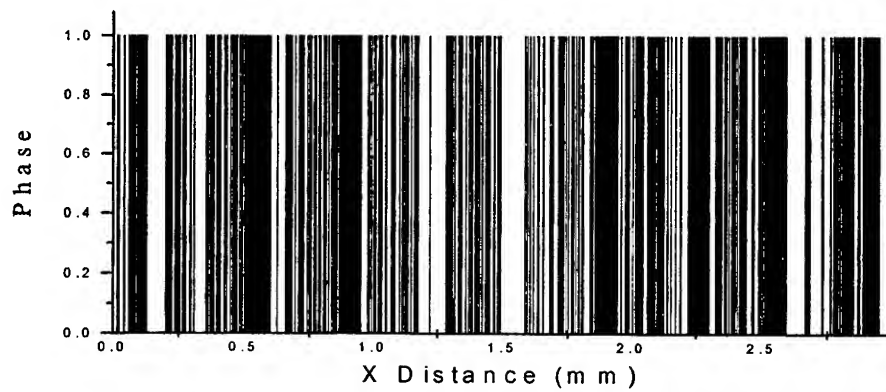


Fig. 3 Calculated phase distribution of the DOE

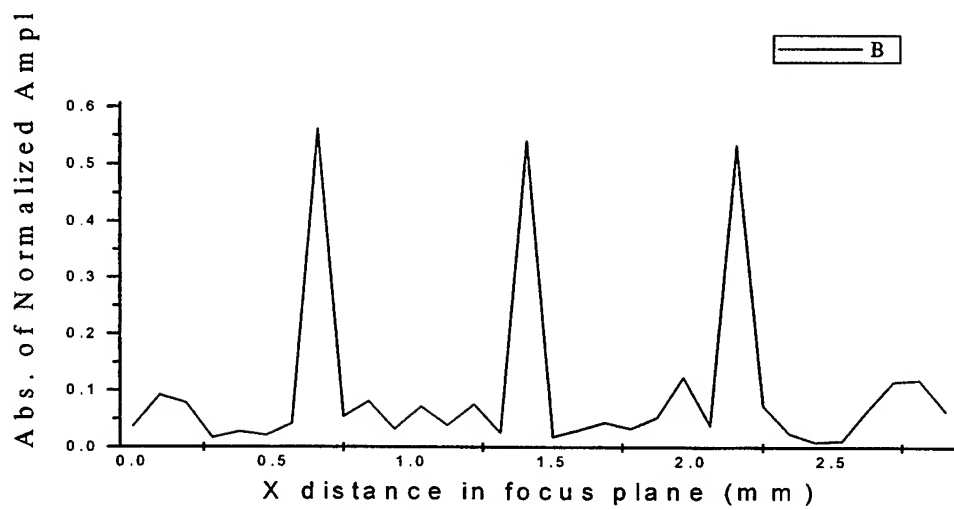


Fig.4 Absolute complex amplitude distribution on the focus plane (perpendicular to the designed focus lines), which is at a distance of 400 mm from the DOE

the focus plane. The DOE is designed to be a two-level element, i.e. only phase differences of 0 and π exist. The direct binary search (DBS) algorithm⁹ is employed to generate the phase structure.

The input window, i.e. the illuminated area of the DOE, is designed to be 3x3 mm, and is same as the dimension of the focus plane. The wavelength of the incident light is chosen to be 0.6328 μ m. The distance from the DOE to the focus plane, i.e. focus length, is set to be 400mm. Sampled point numbers in the DOE and focus plane are 1000 and 36, respectively. The distance between adjacent focused lines is 0.25mm. Thus, the complex amplitude in the DOE and focus plane can be represented by 2 vectors, and the propagation transformation becomes a matrix with 1000 rows and 36 columns.

The calculated discrete phase distribution on the DOE is shown in Fig. 3. Plane light incident on the DOE will be focused at the distance of 400mm and the distribution of the absolute value of the complex amplitude on the focus plane is shown in Fig. 4.

In the simulation, it is found that with the increase of the sampling number in the DOE, the result becomes better, but an increasing number of sampled points in the focus plane show no improvement. This is reasonable because a larger number of sampling points in the DOE results in the phase distribution being more continuous and thus closer to the ideal profile.

4. CONCLUSIONS

We have demonstrated embossing gratings into organically modified sol-gel film. The embossed grating has the same period as the mold while the embossed depth is smaller than that of the mold. Further work is needed to improve the aspect ratio of the embossed pattern. There is also the need to resolve the problem of adhesion of the sol-gel film to the mold.

A DOE on sol-gel film has been designed by the DBS algorithm. There are several ways to improve the performance of the DOE. The first is to employ a phase-amplitude retrieval algorithm, e.g., Y-G algorithm. Unlike direct phase search, the Y-G algorithm is based on the functional relationship between the phase plane and the focus plane, and thus a better, and maybe the most optimal solution, could be found. The second way is to fabricate a multi-layer or even continuous profile DOE, and the closer to continuous profile is the DOE surface, the more ideal the result will be. Combined with the embossing technology, it is possible to fabricate micro-optical elements in mass volume and capacity.

REFERENCES

1. S.I.Najafi (ed.), *Introduction to Glass Integrated Optics*, Artech House, Boston, 1992.
2. M. Grant, "Glass integrated optical devices on silicon for optical communications", *Glass Integrated Optics and Optical Fiber Devices, SPIE Proc. CR53*, pp.55-79, 1994.
3. H. Krug et al., "Fine patterning of thin sol-gel films", *J. Non-Cryst. Solids* **147&148**, pp. 447-450, 1992.
4. N. Tohge et al., *J. Non-Cryst. Solids* **100**, p501, 1988.
5. A. Matsuda et al., *SPIE* **1328**, p71, 1990.
6. K. Tiefenthaler et al., *Proc. Soc. Photo-Opt. Instrum. Eng.* **401**, p165, 1983.
7. W. Lukosz and K. Tiefenthaler, *Opt. Lett.* **8**, p537, 1983.
8. J. Liu et al. "Fabrication of sol-gel derived optical glass waveguide on InP for integrated optics", *CThW1, CLEO'99*, Baltimore, USA, 1999.
9. Michael A. Seldowitz et al., "Synthesis of digital holograms by direct binary search", *Appl. Opt.* **26**, No. 14, p.2788, 1987.

Deposition of Sol-gel Derived Inorganic and Composite Material Films on InP for Integrated Optics

J. Liu, Y. L. Lam, Y. C. Chan, Y. Zhou, W. X. Que, G. Tan, and B. S. Ooi

Photonics Research Group, School of EEE,
Nanyang Technological University,
Nanyang Avenue, Singapore 639798.
Phone: 0065-7905461, Email: p143506720@ntu.edu.sg

ABSTRACT

In this paper, we present the fabrication of sol-gel derived silica based films on InP using both inorganic and composite material precursors. Thin silica films with thicknesses less than $0.5\mu\text{m}$ are achieved using an inorganic precursor by means of multiple spin coatings and rapid thermal processing (RTP) at an annealing temperature of 450°C . The cracking pattern of the inorganic silica film on InP is analyzed. Thick films are derived from composite materials by multiple spin coatings with only furnace baking at 150°C . In addition, the different properties of each type of films and their potential applications in terms of monolithic integration are discussed.

1. INTRODUCTION

The sol-gel process is a wet chemistry technique for making solid materials by hydrolysis and condensation of liquid precursors and it has been proven to be a promising technique for integrated photonic device fabrication¹⁻³. On the other hand, the III-V semiconductors, such as GaAs, InP, and related ternary compounds, are very important for making sensors, solid-state lasers, high-frequency devices, and integrated circuits⁴⁻⁵. They have unique and promising optical and electrophysical properties compared to silicon and germanium. Particularly, in making photonics devices, InP has potential performance advantages over either silicon or GaAs in such diverse applications as electro-optical devices, microwave and millimeter wave components, and in high speed logic circuits. Furthermore, many applications can be found for amorphous silica⁶⁻⁸. As such, we believe that deposition of sol-gel derived silica on InP can effectively combine their useful properties for applications in integrated devices. We also expect the successful coating of high quality and versatile sol-gel waveguide films on III-V semiconductor to lead to new optical integrated circuit (OIC) designs. Specifically, since InP is the substrate for manufacturing semiconductor lasers, photodetectors and other optoelectronic devices operating in the long wavelength region, the fabrication of waveguide devices on sol-gel films on the InP substrate can potentially lead to interesting hybridized OIC. In addition, such coating is expected to find applications in other microelectronics fabrication. For example, the coating of amorphous SiO_2 on InP can be used as an interlevel dielectric⁹.

To date, deposition of SiO_2 on InP substrate is generally done by plasma enhanced chemical vapor deposition (PECVD)¹⁰, distributed electron cyclotron resonance plasma technique¹¹, or photochemical vapor deposition¹². Sol-gel process is a compelling alternative to the above methods because it provides a simple, low cost and low temperature solution for depositing films of various compositions on a substrate. Such films are promising as they can be easily made into integrated optical waveguides and be monolithically integrated with a semiconductor device. In addition, sol-gel derived films can be made to offer excellent transparency, high thermal, mechanical and chemical stability, and low coupling losses with optical fibers, as well as an outstanding range of material properties and compositions that extend its capability to active devices for modulation, lasing, and switching.

So far, coating SiO_2 on InP substrates by the sol-gel technique has not been much explored, probably because of the difficulty to do so as a result of the quite different structures and thermal expansion coefficients between these two materials. In this paper, we present the fabrication of sol-gel derived silica based films on InP using both inorganic and composite material precursors. The inorganic silica film is made by means of multiple spin-coatings and rapid thermal processing (RTP) at an annealing

* Correspondence: Email: p143506720@ntu.edu.sg; Telephone: 0065-7905461.

temperature of 450°C, and the composite material film is also made by multiple spin coatings but with only furnace baking at 150°C. The different properties of each type of films, and their potential applications in terms of monolithic integration are also discussed.

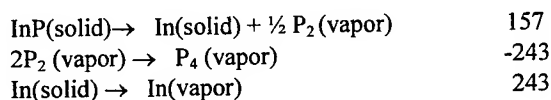
2. EXPERIMENTAL

The main factor leading to the decomposition of semiconductor compounds under thermal processing is loss of stoichiometry by evaporation. Atom evaporation and condensation keep the stoichiometric balance at the surface. The competition between the evaporation and condensation rates determines the overall evaporation rate.

Changes in stoichiometry are initiated by decomposition of the semiconductor compound and by the loss of one of the components, usually a group-V element at high temperatures. Surface evaporation causes diffusion of these atoms from the bulk to the surface. An increase in processing temperature, producing higher evaporation and diffusion rates, as well as a longer processing duration, leads to greater variation in stoichiometry from the bulk of the semiconductor crystal.

Solid-vapor equilibrium for InP is characterized by the reactions at the surface, shown as follows¹³:

Enthalpy of the reaction ($\times 10^3$ J/mol)



InP is quite sensitive to temperature. The thermal stabilities of related III-V semiconductors are ranked as : GaP > GaAs > InAs > InP. At a relatively high temperature, volatility of In and P can be a problem when the InP substrate is heated. In this case, sulfur implanted InP substrate is selected since the formation of In-S bonds can improve the thermal stability of InP¹⁴. Specifically, the InP wafer substrate we used is of <100> orientation and doped n-type with sulfur to a concentration of $3 \times 10^{18}/\text{cm}^3$. Polished wafers, obtained from ATRAMET INC., were cleaned by the following procedures prior to coating: First, the wafer is soaked in an ultrasonic bath of trichloroethylene (TCE) for 5 minutes, followed by acetone and methanol rinses and a light etch in a 0.1% Br-methanol solution for 1 minute. Then the wafer is rinsed again using deionized water for several times and dried by pure nitrogen gas. The solution was applied to the substrate from a syringe containing a 0.2 μm disposable filter. Multiple layers were deposited to increase the coating thickness. Deposition of the sol-gel coating is accomplished with a spincoater at a spin speed of 4000rpm for 45seconds in a nitrogen-purged glovebox. The annealing process is carried out in an atmosphere of purified nitrogen gas.

In addition, rapid thermal processing (RTP)¹⁵⁻¹⁶, which allows for comparatively much shorter heat treatment schedules than a conventional furnace, is chosen for the experiment. It has been proven that RTP is one effective method to solve the problem of III-V semiconductor decomposition¹⁷.

In the preparation of the inorganic films by the sol-gel route, silicon tetraethoxide (or tetraethoxysilane TEOS) is used. During the sol-gel process, many factors can influence the structure of the inorganic polymers. The most important factors are the water to alkoxide ratio, pH, and aging conditions¹⁸⁻²² of the initial solutions. Film porosity is largely determined by the polymer structure. The whole process is shown in Figure 1.

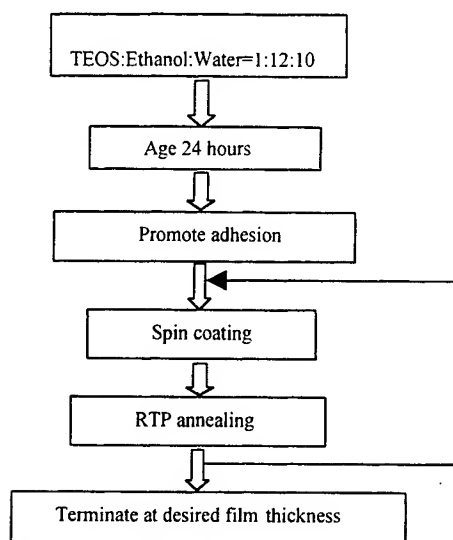
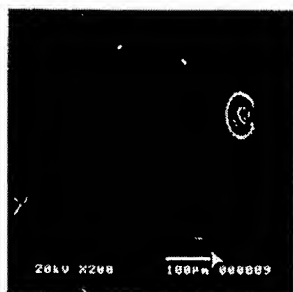
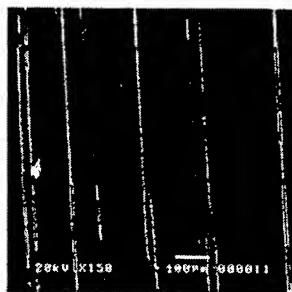


Fig.1 Sol-gel processing procedure

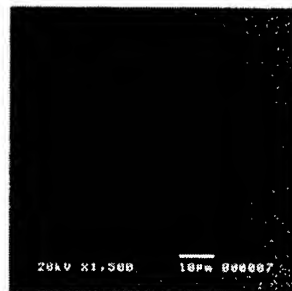
For making the inorganic film, the heat processing temperature is 450°C for 30seconds. The heat treatment allows for sufficient condensation of the inorganic film whose refractive index is about 1.44. However, a thick film is hard to achieve. Experimentally, a critical thickness of about 0.5 μ m is obtained. This is compared with that of about 1.5 μ m for a film on silicon substrates. The volatility of InP can be a trigger to induce the film cracking, and all the failure films have a crack orientation of parallel or perpendicular to $\langle 100 \rangle$, as shown in the SEM images in Figure 2. Figure 2(a) indicates the cracking situation when the volatility of In and P begins to take place. Figure 2(b) shows the final cracking triggered by the InP volatility. Figure 2(c) is the picture for the successful SiO₂/InP coating.



a) The slightly cracking when the volatility of InP begin to happen



b) The final crack of sol-gel derived silica films on InP substrates



c) The surface condition of successful SiO₂/InP

Fig.2 SEM images of sol-gel derived inorganic silica films on InP

The cracking pattern and smaller critical thickness of a sol-gel derived silica film on InP can be explained by energetics analysis of the cracking process as follows. For an InP substrate with $\langle 100 \rangle$ orientation, the Young's modulus changes with the directions, while the biaxial modulus of the film is isotropic. In this case, the biaxial stress existing in the isotropic sol-gel film is independent of direction. Since the tensile strain modulus in the plane of the substrate is variable, certain directions are more compliant than others. As the film stress and film elastic constants are independent of direction, the most compliant direction corresponds to the direction of lowest critical thickness in the film.

Cracking of the film corresponds to the state where the energy release rate of the crack reaches a critical value. The energy release rate G_{ss} is given by²³

$$G_{ss} = \frac{1}{2} \frac{\sigma^2 h}{\bar{E}_f} \pi g(\alpha, \beta), \quad (1)$$

where h is the thickness of the film, σ is the stress in the film, and \bar{E}_f is the plane tensile strain modulus of the film, which is a function of elastic modulus and Poisson's ratio. When the energy release rate G_{ss} reaches the critical value G_c , h becomes h_c , the critical thickness for the crack-free film. $g(\alpha, \beta)$ is the nondimensionalized crack opening displacement, and is a function of the Dundurs parameters α and β . For the plane strain problem, α and β can be obtained by²⁴

$$\alpha = \frac{\bar{E}_f - \bar{E}_s}{\bar{E}_f + \bar{E}_s}, \quad (2)$$

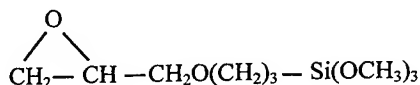
$$\beta = \frac{\mu_f(1 - 2\nu_s) - \mu_s(1 - 2\nu_f)}{2\mu_f(1 - \nu) + 2\mu_s(1 - \nu_f)}, \quad (3)$$

where μ and ν are the shear modulus and Poisson's ratio, and the f and s indicate the film and substrate, respectively.

The nondimensionalized integral of the crack opening displacement g depends on direction in a $\langle 100 \rangle$ InP substrate because α in the plane of the $\langle 100 \rangle$ InP wafer has orientation dependence. Since the film stress, G_c and \bar{E}_f are constants, h_c will vary inversely with $g(\alpha, \beta)$ according to Equation (1). It has been proven that $g(\alpha, \beta)$ is a weak function of β , and also an increasing function of α ²³. In this case, for a film of given elastic constants, $g(\alpha, \beta)$ increases with the substrate compliance. Hence, when the substrate compliance decreases, the critical thickness will increase. As Young's modulus of the InP substrate, which is the inverse of the material compliance, is only about half of the value of Si, the critical thickness of sol-gel films on InP will be smaller than that on silicon.

For a $\langle 100 \rangle$ InP substrate, the direction of lowest \bar{E}_s in the plane of the wafer is $[100]$. Therefore it is expected that the films on InP will crack preferentially perpendicular or parallel to this direction.

In the experiment, thick silica films whose thicknesses are larger than $1\mu\text{m}$ are hard to achieve by using pure inorganic precursor. However, they can be achieved by using organically modified silane. To make the organically modified silica film, the sol-gel precursor used is γ -glycidyloxypropyltrimethoxy silane (GLYMO) ($\text{C}_9\text{H}_{20}\text{O}_5$, Si : $\text{C}_2\text{H}_5\text{OH}$: H_2O = 1 : 4 : 4.5). Control of the properties of the final material is achieved by controlling the chemical nature of the organic and inorganic phases, the size and morphology of these domains (nm to sub- μm scale) and the nature of the interface interaction. The molecular structure of GLYMO is as follows:



After spin-coating, the GLYMO/InP sample is baked in a furnace at a temperature of 150°C for 10 minutes. The sol-gel process is shown in Figure 3.

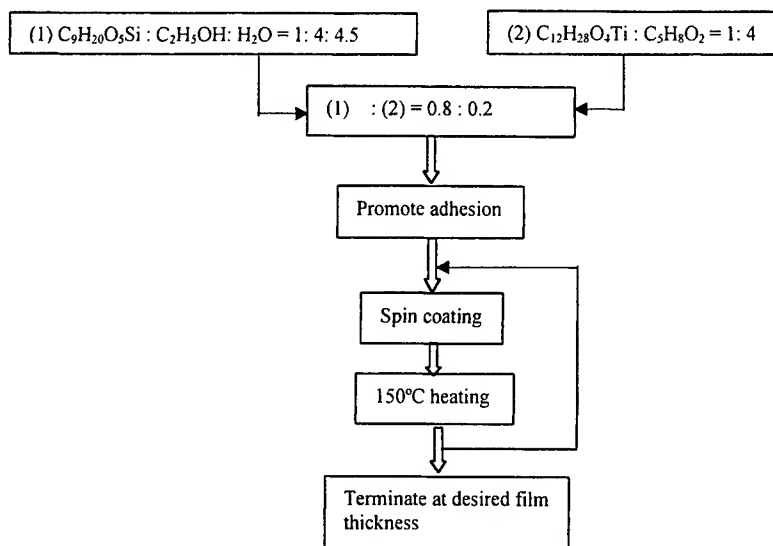


Fig 3 Sol-gel processing procedure for TiO₂-GLYMO silane film

3. DISCUSSIONS

Inorganic silica films can be used as a dielectric²⁵, buffer layer²⁶, or for passivation²⁷ and a silica film on InP can be used to fabricate InP-based field-effect devices²⁸. Deposition of a silica film on InP by the sol-gel route can greatly reduce the expenses involved. However, two points limit the optical waveguide applications on InP using pure inorganic precursors. The first problem is that the critical thickness of submicrons which is not sufficient for waveguiding, and the other is that fabrication of optical waveguides by the sol-gel route requires high temperature processing to reduce its attenuation, which will damage the InP substrate.

Technological progress is always dependent on the materials possessing new or vastly enhanced properties. Few pure materials can individually owe all of the physical and mechanical properties required for certain applications. In this case, most materials are used either as alloys or hybrid materials. Hybrid materials can contain both inorganic and organic components combined into intimate, new morphologies. The degree of phase separation in these materials can change but domain sizes are typically on the nanometer scale. In some cases, the domain sizes are reduced to a level such that "molecular composites" can be formed. As a result of this intimate mixing, these composites often possess good transparency and elastic properties. In addition, a low temperature processing will be possible.

The good transparency of composite materials may be explained as follows. For the spherical particles embedded in a matrix, the reduction of light intensity due to scattering is given by Equation 4²⁹, in which x is the optical pathlength, V_p is the volume fraction of particles, r is radius of the particle, λ is the wavelength of light, and n_p and n_m are the refractive indexes of the particles and matrix, respectively.

$$\frac{I}{I_0} = \exp \left[\frac{-3V_p x r^3}{4\lambda^4} \left(\frac{n_p}{n_m} - 1 \right) \right] \quad (4)$$

Comparing the ratio of refractive indices for porous glass ($n_p/n_m = 0.685$), with that of a glass/poly (methyl methacrylate) blend ($n_p/n_m = 1.02$), we can find that organic-inorganic composite is more transparent than the porous silica gel formed in the absence of polymer. This is due to a substantial decrease in the pores as they are filled with polymer rather than air.

The application of composite materials is wide, ranging from inorganically modified organic polymer to inorganic glasses modified by organic polymers. At a specific organic/inorganic ratio, the properties of these materials will be influenced by the phase behavior, degree of inter-penetration, and inter-phase connectivity. Two factors limit the method of forming composites by incorporation of polymers into sol-gel glasses. Firstly, only a finite number of polymers are soluble in the tri-component sol-gel solution. Secondly, the shrinkage associated with their drying introduces a considerable degree of stress within the dried glasses, thereby precluding most of the molding applications. To solve these problems, our efforts have focused on methods involving the in situ formation of both the organic polymer and inorganic matrix. Under certain conditions, the polymer can be kinetically trapped into the inorganic matrix before significant phase separation. In this way, transparent organic-inorganic composite materials can be prepared which contain organic polymers that would normally be insoluble in typical sol-gel solutions.

Control of the properties of the final material is achieved by controlling the chemical nature of the organic and inorganic phases, the size and morphology of these domains (nm to sub- μm scale) and the nature of the interface interaction. In the experiment, the sol-gel glass was synthesized by combining γ -glycidyoxypropyltrimethoxysilane ($\text{C}_9\text{H}_{20}\text{O}_5\text{Si}$) and titanium tetraisopropoxide ($\text{C}_{12}\text{H}_{28}\text{O}_4\text{Ti}$). Thick films of organic modified silica on InP can be easily obtained. In addition, the thickness and refractive index can be controlled by means of adding dopants with different concentrations. By controlling the refractive index and thickness, the buffer and guiding layers can be tailored and the optical glass waveguide is successfully fabricated on InP³⁰. Further development of buried waveguide has also been achieved by laser writing, reactive ion etching (RIE) and sol-gel re-coating. The output image of the buried waveguide is shown in Figure 4.

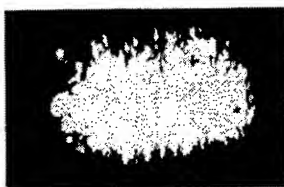
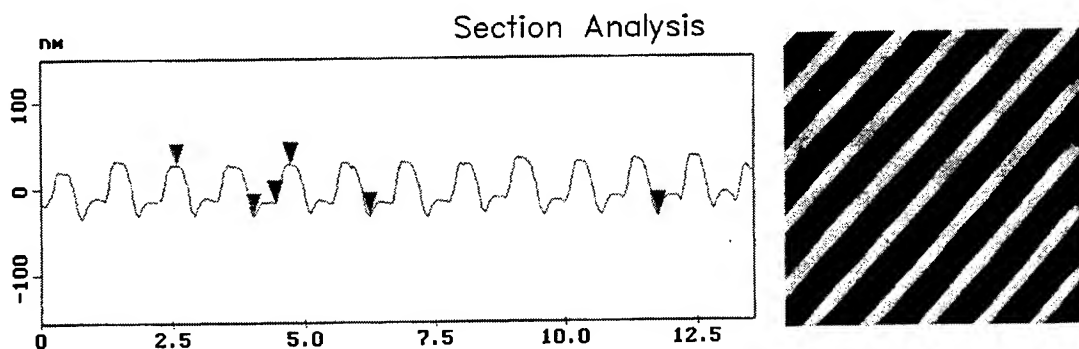


Fig.4 Output of buried glass waveguide made by laser writing and RIE

In addition, embossing into sol-gel thin films offers a practical way for the production of surface corrugation gratings, as well as other integrated optic components. Using organically modified silane, which has better elastic properties than pure inorganic glass, embossed glass gratings are successfully fabricated on InP, as shown in Figure 5.



We also have tried using inorganic film as the buffer layer during the fabrication of optical waveguide, as shown in Figure 6, it is found that the surface roughness of the waveguide can be improved compared with that made by two-step coating using composite materials. This is probably because the surface of inorganic film is not as sticky as composite film, and thus the second spin-coating is more homogeneous at a certain spin speed. In this point of view, using inorganic film as the buffer layer can reduce some amount of scattering loss of the waveguide. However, because the thickness of buffer layer can only reach $0.5\mu\text{m}$ on InP, the waveguide confinement is not satisfied.

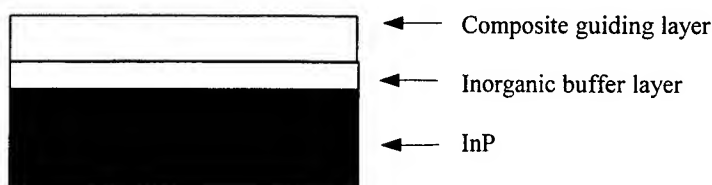


Fig.6 Glass waveguide fabricated on InP using both inorganic and composite materials

It is well known that the transmission capability of optical fiber communication systems has been significantly increased by the advent of the wavelength division multiplexing (WDM) technique. Tunable wavelength filters with a narrow bandwidth and a wide tuning range are useful devices for the purpose of selecting one wavelength carrying the desired information among the WDM signals. Besides, InP based III-V compounds are playing important roles in integrated optics because active devices are usually constructed from them. Based on our experiments, it is very hopeful to achieve integration of the active devices such as semiconductor lasers and passive components including sol-gel derived wavelength filters.

4. CONCLUSION

Considering that InP has its unique advantages over Si and GaAs in many applications such as electro-optical devices, microwave and millimeter wave components, and in high speed logic circuits, and that the sol-gel technique is a simple, versatile, flexible, and low-cost technique for the fabrication of integrated photonics device, we have succeeded in applying the sol-gel technique to coat SiO_2 layers on InP substrates using both inorganic and composite material precursors. Thin silica films with thicknesses less than $0.5\mu\text{m}$ are achieved using inorganic precursor by means of multiple spin coatings and rapid thermal processing (RTP). The cracking pattern of silica film on InP is also theoretically analyzed. Thick films derived from composite materials are obtained by multiple spin coatings with only a furnace baking at 150°C . In addition, the different properties of each type of film, and their potential applications in terms of monolithic integration are discussed. Based on our experiments, we conclude that the inorganic film on InP can be used as dielectric or buffer layer, and organically modified silane is suitable for making waveguide and mold application. We feel that it is possible to achieve integration of the active devices and passive components through the sol-gel route.

The authors gratefully acknowledge the helpful discussions from Mr. S. D. Cheng, and AFM testing from Ms. B. G. Neo.

REFERENCES

1. A. Fardad, M. P. Andrews, and S. I. Najafi, "Novel sol-gel fabrication of integrated optical waveguides," in *Conf. On Integrated Optics Devices: Potential for Commercialization*, San Jose, Proc. SPIE 2997, 72-78 (1997).
2. Y. Zhou, Y. L. Lam, S. S. Wang, H. L. Liu, C. H. Kam, Y. C. Chan, "Fluorescence enhancement of Er^{3+} -doped Sol-gel Glass by Aluminium Co-doping", *Appl. Phys. Lett.*, Vol.71, No. 5, 4 August 1997.
3. M. P. Andrews and S. I. Najafi, Eds., *Critical Review Conference on Sol-gel and Polymer Photonics Devices*, San Diego, Proc., SPIE CR68 (July 1997).
4. *GaAs Microelectronics*, edited by N.G. Einspruch and W. R. Wisseman (Academic Press, New York, 1985).
5. L. Sharma, *Implantation in InP technology*, *Solid State Technol.* 32(11), 113-117 (1989).

6. Ito, Y. Winkler, D. Jain, H. Williams, D B. "Application of extended energy loss fine structure in determining the structure of amorphous SiO₂", *Journal of Non-Crystalline Solids*, v 222, Dec 2 1997, p. 83-93.
7. Weiping, Ming Tan, Guozhong Wang, and Lide Zhang, "Reversible transition between transparency and opacity for the porous silica host dispersed with silver nanometer particles within its pores", *Appl. Phys. Lett.* 69 (20), 1996, 2980-2982.
8. D. P. Yu, Q. L. Hang, Y. Ding, "Amorphous silica nanowires: Intensive blue light emitters", *Appl. Phys. Lett.* Vol. 73, No. 21, 1998, 3076-3078.
9. W. L. Warren C. J. Brinker, "Sol-gel silicate thin-film electronic properties", *J. Appl. Phys.* 69 (8), 1991, 4404-4408.
10. Lambrinos, M. F. Besland, M. P. Gagnaire, A. Louis, P. Callard, "In situ photoluminescence control during fabrication of SiO₂/InP structures." *Journal of the Electrochemical Society*. V 144 n 6 Jun. 1997. P 2086-2095.
11. F. Plais and B. Agius "Electrical properties of distributed electron cyclotron resonance plasma-deposited SiO₂-InP diodes", *Applied Physics Letters*, Volume 59, Issue 7, 1991, pp. 837-839.
12. F. Houzay and J. M. Moison "Surface localization of the photochemical vapor deposition of SiO₂ on InP at low pressure and room temperature", *Applied Physics Letters*, Volume 58, Issue 10, 1991, pp. 107.
13. R. F. C. Farrow, The evaporation of InP under Knudsen (equilibrium) and Langmuir (free) evaporation conditions, *J. Phys.* D7(17), 2436-2448, (1974).
14. Han, Il Ki. Her, June. "Low dark current and high-speed metal-semiconductor-metal photodetector on sulfur-treated InP." *Japanese Journal Applied Physics Part2-Letters*. V33n12A Dec 1 1994. P6454-6457.
15. Hill, Chris. "Advances in rapid thermal and integrated processing", *Microelectronic Engineering*. V34n2 sept. 1997. P215-216.
16. Daviet, Jean-Francois. "Rapid thermal processing of semiconductor wafer." *Journal of Electrochemical Society*. V144n2. Feb 1997. P753-758.
17. V. E. Borisenko, V. V. Gribkovskii, V. A. Labunov, and S. G. Yudin, Pulsed heating of semiconductors, *Phys. Status Solidi A* 86(2), 573-583 (1984).
18. C. J. Brinker, K. D. Keefer, D. W. Schafer, R.A. Assink, B. D. Kay, and C. S. Ashley, *J. Non-Cryst. Solids* 63, 45 (1984).
19. K.D. Keefer, in *Better Ceramics through Chemistry*, Materials Research Society Symposium Proceedings, edited by C. J. Brinker, D. E. Clark, and D. R. Ulrich (North Holland, Amsterdam, 1984), Vol. 32, p. 15.
20. C. J. Brinker, A. J. Hurd, and K. J. Ward, *Ultrastructure Proceeding of Advanced Ceramics* (Wiley, New York, 1998), p223.
21. D. W. Schafer, J. E. Martin, K. J. Ward, and K. D. Keefer, in *Physics of Finely Divided Matter*, edited by N. Boccara and M. Daoud (Spring, Berlin, 1985), p.13.
22. S. Sakka, K. Kamiya, K. Makita, and Y. Yamamoto, *J. Non-Cryst. Solid*, 63, 223 (1984).
23. J. L. Beuth, "Cracking of thin bonded films in residual tension", *Int. J. Solids Structures* Vol.29, 1657-1675 (1992).
24. J. Dundurs, "Edge-bonded dissimilar orthogonal elastic wedges under normal and shear loading", *J. Appl. Mech.* 36, 650-652 (1969).
25. Jo, Moon-Ho. Hong, Jung-Kyun. Park, Hyung-Ho. Kim, Joong-Jung. Hyun, Sang-Hoon. Choi, Se-Young. "Application of SiO₂ aerogel film with low dielectric constant to intermetal dielectrics". *Thin Solid Films*. v 308-309 Oct 31, 1997. p 490-494.
26. Callender, Claire L. Robitaille, Lucie. Noad, Julian P. Gouin, Francois. Almeida, Carlos A. "Optical signal distribution to MSM photodetector arrays via integrated polyimide waveguides", *Journal of Lightwave Technology*. v 15 n 9 Sep 1997. p 1700-1707.
27. Ban, Masahito. Suzuki, Katsumi. Enomoto, Youichi. "SiO₂ passivation film effects on microwave characteristics of YBa₂Cu₃O₇ minus x-based resonators", *Physica C: Superconductivity*. v 290 n 3-4 Nov 1 1997. p 345-353.
28. C. Licoppe, F. Wattine, C. Meriadec, J. Flicstein, and Y. I. Nissim "A combination of rapid thermal processing and photochemical deposition for the growth of SiO₂ suitable for InP device applications", *Journal of Applied Physics*, Volume 68, Issue 11, 1990, pp. 5636-5640.
29. D. W. Richerson. *Modern Ceramic Engineering*. Marcel Dekker. New York. 1982.
30. J. Liu, Y. L. Lam, Y.C. Chan, Y. Zhou, W. X. Que, and B. S. Ooi, "Fabrication of sol-gel derived optical glass waveguide on InP for integrated optics", *CThW1, CLEO'99*, Baltimore, USA, 1999.

Deposition of potassium lithium niobate films by sol-gel method

H. X. Zhang, Y. Zhou, C. H. Kam, X. Q. Han, S. D. Cheng, B. S. Ooi, Y. L. Lam, Y. C. Chan

Photonics Research Group, Microelectronics Division, School of Electrical and Electronic Engineering
Nanyang Technological University, Nanyang Avenue, Singapore 639798

Z. Sun, M. B. Yu, X. Shi, S. F. Yoon

Microelectronics Center, School of Electrical and Electronic Engineering, Nanyang Technological
University, Nanyang Avenue, Singapore 639798

ABSTRACT

Potassium lithium niobate (KLN) films have been prepared by sol-gel method using metal ethoxides as starting materials. The films were deposited by spin coating and were annealed in air in a conventional oven as well as in a rapid thermal processor (RTP). X-ray diffraction and Raman scattering measurements have shown that polycrystalline KLN films with tetragonal tungsten-bronze-type structure could be obtained on both SiO₂ buffered Si and fused quartz substrates. Surface morphology studies indicated that RTP annealing could avoid film cracking and enable nanostructured low-surface roughness KLN films to be formed. Optical waveguiding experiments showed that the films have refractive indices close to those of their single crystal and could support several modes. The films deposited on fused quartz were highly transparent in the visible-near infrared spectral range and the absorption edges of the films, as determined from the absorption data, were found to shift towards the violet spectral side.

Keywords: potassium lithium niobate, sol-gel, XRD, Raman scattering, absorption edge, optical waveguiding

1. INTRODUCTION

Potassium lithium niobate in composition of K₃Li_{2-x}Nb_{5+x}O₅ (KLN, 0.15 < x < 0.5) is a tetragonal ferroelectric material with the tungsten-bronze-type structure. KLN has been expected as a promising medium for blue laser operation by second harmonic generation (SHG) of commercially available GaAs/(Al,Ga)As diode lasers because of its large optical nonlinearity, short cutoff wavelength, high optical damage threshold, and wide non-critical phase matching properties at room temperature.¹⁻³ It also exhibits better mechanical stability than KNbO₃, which substantially scales down depoling caused by mechanical shock and temperature fluctuation. Moreover, the phase-matching wavelength in SHG can be adjusted to the laser wavelength by varying the content of lithium in the composition. KLN crystals have been previously grown by Kyropoulos, Czochralski⁴ and top-seed solution growth (TSSG)^{5,6} methods. These techniques often result in cracked crystals because of the difference in lattice change with temperature during growth and the compositional fluctuation due to the non-unit effective segregation coefficients of solutes. Recently, both micro-pulling-down (μ -PD) technique⁷ and laser heated pedestal growth (LHPG) method⁸⁻¹⁰ were used to grow KLN fiber crystal, but it is still difficult to grow homogeneous crystals with sufficient size and uniform composition. Compared with the research of bulk crystal growth, little attention has been paid to the preparation of KLN films. KLN film obviously offers an alternative for the fabrication of compact and integrated blue lasers, and a good recent example related to this scheme was the realization of blue-violet laser via SHG in a waveguide.¹¹ In this scheme, large index difference between the film and the substrate enables highly confining waveguides to be formed and as a result, extremely high power density can be achieved with modest total incident power, a characteristics that is conducive to SHG and low-threshold gain devices. In addition, KLN films can also find applications in surface acoustic wave (SAW), pyroelectric and piezoelectric devices because of their ferroelectric and piezoelectric effects.

Methods such as chemical vapor deposition, sputtering, pulse laser deposition and sol-gel deposition have been used to prepare ferroelectric films. In addition to the advantages of low-temperature processing and molecule-level mixing of starting materials, sol-gel can produce films with high purity, controlled composition and desired compositional homogeneity. Recently there are some reports about the preparation of powders and films of several tungsten-bronze-type ferroelectric materials such as barium sodium niobate (Ba₂NaNb₅O₁₅, BNN), Sr_{1-x}Ba_xNbO₆ (SBN) series and potassium

strontium barium niobate (KsBN) by sol-gel.¹²⁻¹⁵ In this paper, we report the sol-gel preparation and characterization of KLN nanocrystalline films.

2. EXPERIMENTS

Lithium, potassium and niobium ethoxides [LiOC_2H_5 , KOC_2H_5 and $\text{Nb}(\text{OC}_2\text{H}_5)_5$], were used as starting materials. Acetyl acetone (AcAc, $\text{C}_5\text{H}_8\text{O}_2$), acetic acid (HAc, CH_3COOH) and 2-methoxy ethanol [2-ME, $\text{CH}_3\text{O}(\text{CH}_2)_2\text{OH}$] or their mixture (1:1:1 in volume) were adopted as solvent. The scheme outlining the synthesis of KLN precursor, gel and films is depicted in Fig. 1.

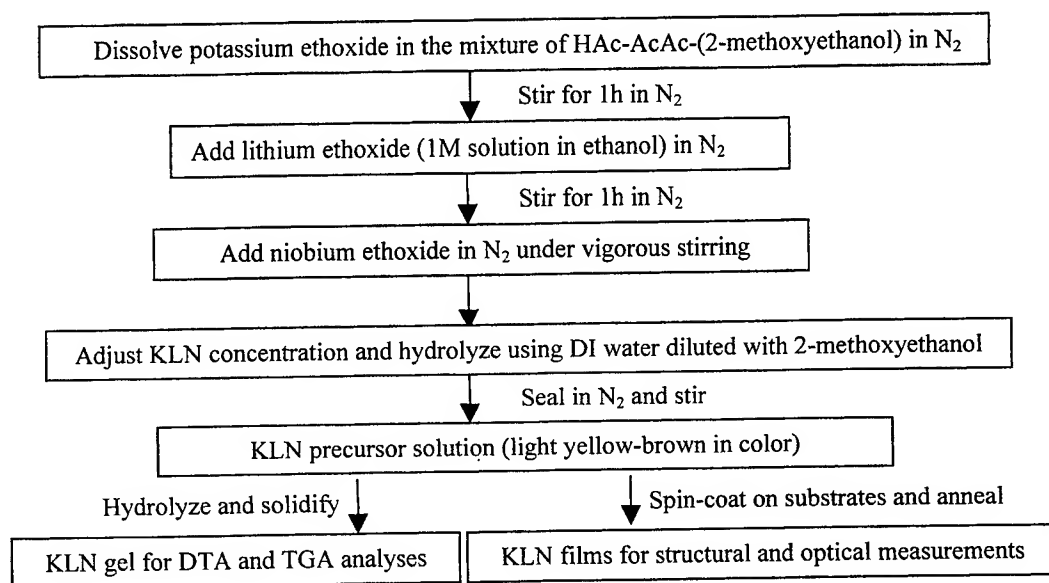


Fig. 1 Schematic flow chart of sol-gel process for KLN gel and films

Potassium ethoxide was firstly dissolved in the mixture of AcAc, HAc and 2-ME. Then LiOC_2H_5 and $\text{Nb}(\text{OC}_2\text{H}_5)_5$ were added drop-by-drop successively under vigorous stirring, with the resultant solution having a final K:Li:Nb mole ration of 3:2:5. The concentration of the solution was adjusted using 2-ME to about 0.08 M KLN. The precursor thus obtained was a transparent solution with a light yellow-brown color. Hydrolysis was initiated by adding an appropriate amount of water diluted with 2-ME. A portion of KLN precursor was gelled by further hydrolysis in air. The as-prepared wet gel was baked at 80 °C to form a dry gel of KLN, and the dry gel was then characterized by thermogravimetric and differential thermal analyzers (PERKIN ELMER TGA-DTA analyzer 1700). The rest of the precursor was used to deposit KLN films on SiO_2 buffered (001) Si and fused quartz (10 mm×10 mm×1 mm, MTI Corporation) by spin-coating in N_2 with a speed of 3,000 rpm for 30 s. The films were then annealed in air at different temperatures from 600°C to 700°C for 5 min in a conventional oven and for 2 min in a RTP, respectively. The structure of the films was examined using an XRD (Simens D5005, with a working voltage of 40 kV and a current of 40 mA) and a Microraman Spectrometer (Nanoscope MicroRaman 100, the 514 nm line of an Ar^+ laser is used for excitation). Surface morphology characterization of the films was completed with an optical microscope (Olympus BX60) and a scanning probe microscope (AFM, Nanoscope IIIa). The refractive indices and the thickness of the films were measured with a dark-line prism-coupling configuration at 632.8 nm (Metricon). The optical transmission and absorption spectra of the films deposited on fused quartz substrates were measured on a HP 1845 Spectrometer. All the measurements were carried out at room temperature.

3. RESULTS AND DISCUSSION

The DTA and TGA curves for the KLN dry gel from room temperature to 800 °C are shown in Fig. 2. The TGA curve indicates that there is a sudden weight loss at about 230 °C followed by a continuous weight loss up to 650 °C due to the combustion of remaining organic compounds. Meanwhile, a sharp and strong exothermal peak appears at 650 °C on the

DTA curve, indicating the crystallization of KLN. The XRD profiles from the KLN films annealed in a conventional oven at different temperatures (see Fig. 3) show the formation of tetragonal tungsten-bronze-type KLN. We have previously found that the films do not have as good crystallinity as compared to the powders (see Fig. 3).¹⁶ At the same annealing temperature and period, the films have impurity phase or phases which have distinct diffraction peaks at $2\theta=17.5$, 23.5 and 32.5° , the intensity of which decreases with the increase of annealing temperature. Nearly pure tetragonal tungsten-bronze-type structure could be obtained.

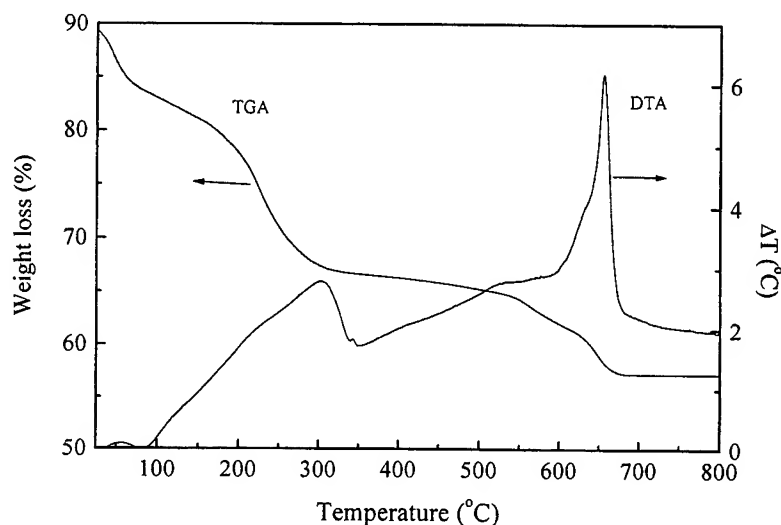


Fig. 2 DTA and TGA curves for KLN dry gel with a heating rate of $8^\circ/\text{min}$

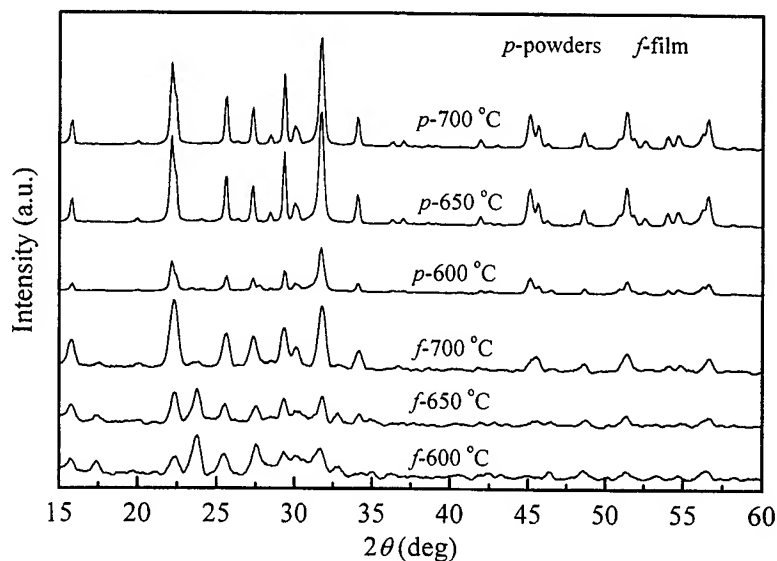


Fig. 3 XRD profiles of the KLN films (*f*) and powders (*p*) annealed in a conventional oven

The formation of tungsten-bronze-type KLN was further confirmed by Raman spectra of the films. As shown in Fig. 4, typical Raman scattering behavior of tungsten-bronze-type ferroelectrics was observed except for a slight shift of the spectra in comparison with that of the KLN single crystal. The peaks at 881 cm^{-1} and 650 cm^{-1} belong to two of the characteristic Raman modes of $[\text{NbO}_6]$ octahedrons, ν_1 and ν_2 , respectively. The broad band from 150 cm^{-1} to 350 cm^{-1} is attributed to the

broadening and splitting of the third mode ν_3 resulting from the distorted octahedrons and deviation from O_h symmetry. The weak peak at 375 cm^{-1} belongs to an external vibration mode of $[\text{NbO}_6]$.¹⁷ Even though the films have impurity phase, their Raman spectra are nearly the same as that of KLN crystals. It is thus deduced that the impurity phase or phases of the film may have the same or similar structure type as KLN. The formation of LiNbO_3 was ruled out because it has more complicated Raman spectra. Two possible phases are KNbO_3 and $\text{K}_3\text{LiNb}_6\text{O}_{17}$, which can be produced when there is a Li deficiency. Li deficiency often occurs at high annealing temperature because of the high volatility of Li oxide.

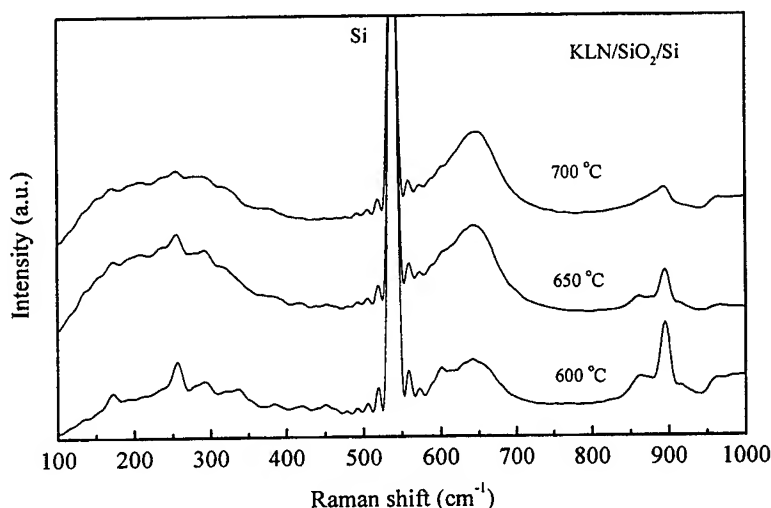


Fig. 4 Raman spectra of KLN films deposited on SiO_2/Si and annealed at different temperatures in a conventional oven

Fig. 5 shows the surface morphology of the films (two layers) on SiO_2/Si and fused quartz annealed in a conventional oven and in a RTP. It is clear that needle-like cracks are very obvious in the conventionally annealed film deposited on SiO_2/Si (Fig. 5a); while no cracks are observed in the RTP annealed films deposited on both SiO_2/Si and fused quartz. That means that rapid thermal annealing can greatly improve the surface quality of the films. The AFM observation of a RTP annealed $\text{KLN}/\text{SiO}_2/\text{Si}$ film, as given in Fig. 6, shows an average grain size of 35 nm and an RMS (root mean square) surface roughness of 3.3 nm.

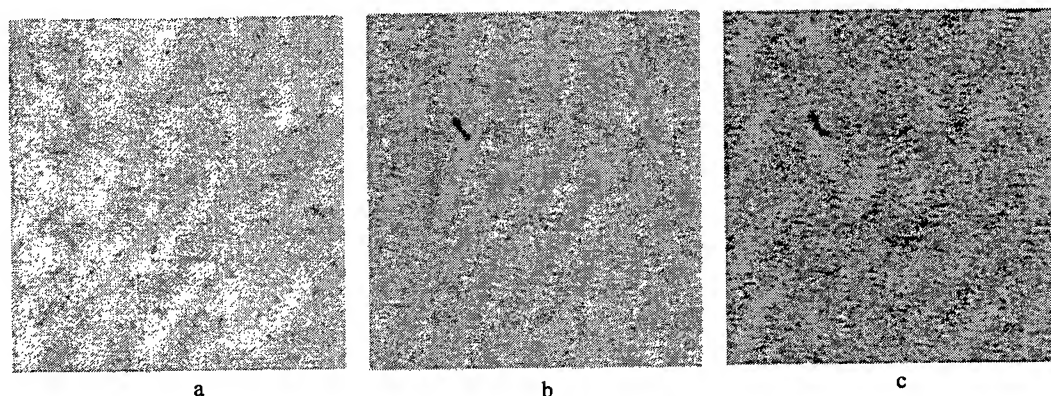


Fig. 5 Surface morphology of KLN films deposited on SiO_2/Si (a, b) and fused quartz (c) and annealed at $700\text{ }^\circ\text{C}$ in a conventional oven (a) and in a RTP (b, c) ($\times 500$)

Fig. 7 shows the light guiding property of a 2-layer KLN film and a 3-layer one annealed in a RTP at 700 °C. Two transverse magnetic modes (TM) and two transverse electric (TE) modes (not shown here) were observed for the 2-layer film, while three TM and TE modes were observed for the 3-layer film. From the dark line spectra, the refractive indices of the films are determined to be 2.1443 and 2.1706 with thickness being 0.4443 μm and 0.6444 μm for the 2-layer and 3-layer films, respectively. The refractive index values of the films are close to those of KLN crystal ($n_o=2.2770$, $n_e=2.1630$).¹⁸

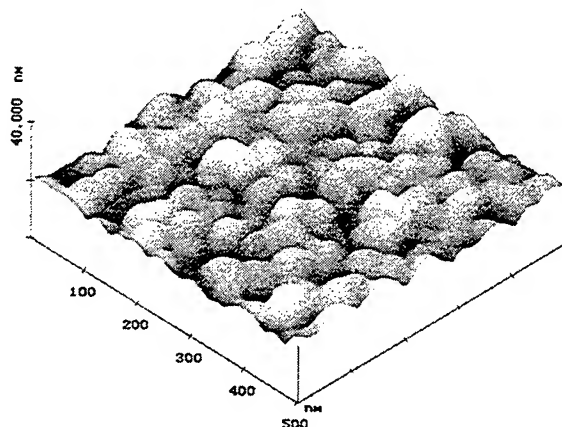


Fig. 6 AFM micrograph of a KLN film deposited on SiO_2/Si and annealed in a RTP at 700 °C

The transmission spectra of our KLN films deposited on fused quartz and annealed in a RTP are shown in Fig. 8. It is noted that the films were highly transparent in the visible-near infrared spectral range, which is very important for second harmonic generation of blue-green laser through near infrared laser diode pumping. The transmission rapidly decreases when the wavelength is reduced to around 320 nm, showing a direct band transition. It was also surprising to find that the absorption edges of the films extended greatly to the violet side in comparison with those of the bulk KLN crystals.⁴⁻⁶

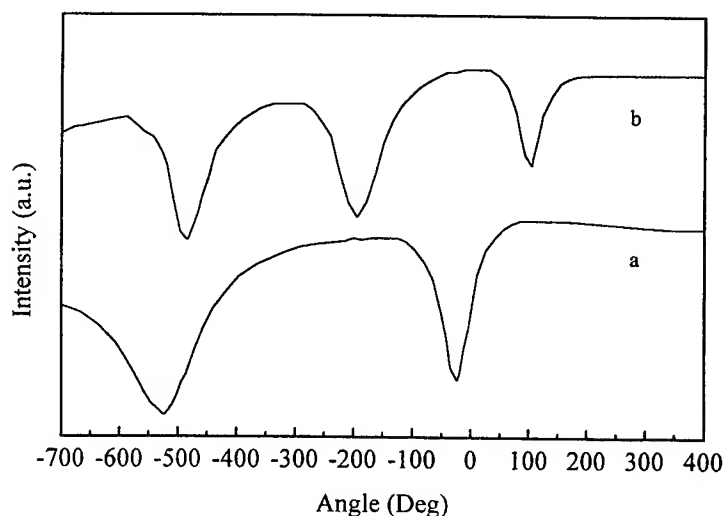


Fig. 7 Dark-line prism-coupling spectra of a 2-layer (a) and 3-layer (b) KLN films deposited on SiO_2/Si and annealed at 700 °C in a RTP ($N_p=2.8659$)

For crystalline dielectric materials with high absorption (α in the order of 10^5 - 10^6 cm⁻¹), the absorption coefficient has the following energy dependence:¹⁹ $(\alpha h\nu)^2 \sim (h\nu - E_g)$, where $h\nu$ is the photon energy and E_g is the band gap. Thus E_g can be determined by plotting $(\alpha h\nu)^2$ vs. $h\nu$ and extrapolating the linear portion of the plot to $(\alpha h\nu)^2 = 0$ (see Fig. 9). α was measured using a bare fused quartz substrate as blank and calculated according to $\alpha = 2.303A/d$, where A is the measured absorbance and d is the thickness of the film. Surface reflection loss was not calibrated in the calculation. For the film annealed at 700 °C, the absorption edge is 4.40 eV, corresponding to 282 nm. The absorption edges of KLN crystals may be different, depending on the growth methods employed and the crystal composition. Recently, three absorption edges have been reported for KLN crystal of the same composition ($x=0$): 3.13 eV (396 nm, flux pulling method),⁵ 376 nm (3.30 eV, TSSG method)⁶ and 354 nm (3.50 eV, micro-pulling-down technique).⁷ It is known that the band gap of the niobate crystals corresponds to the electron transition from the $5d$ orbits of Nb to the $2p$ orbits of O. From the point of view of crystal structure and stoichiometry, KLN has a site occupancy formula written as $(A_1)_2(A_2)_4(C)_4(B_1)_2(B_2)_8O_{30}$. For fully occupied KLN lattice, A_1 and A_2 are occupied by the larger K^+ ions and all the C sites (nine-oxygen coordination) are occupied by the smaller Li^+ ions. B_1 and B_2 (six-oxygen coordination) are occupied by Nb^{5+} ions.²⁰

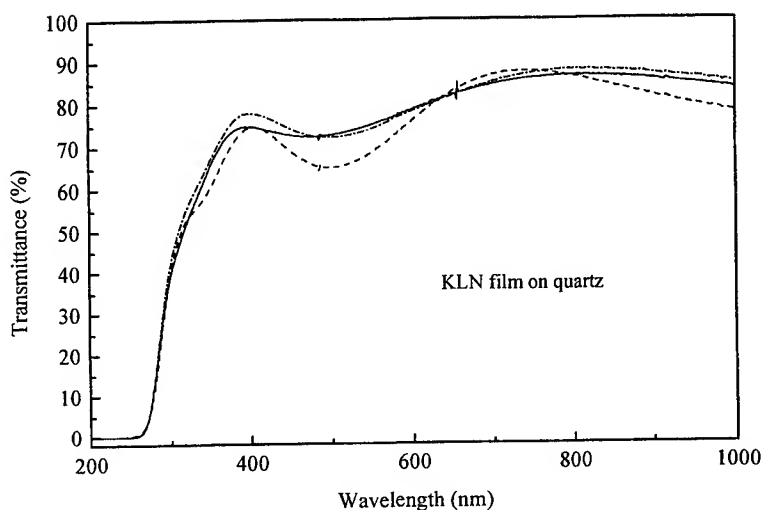


Fig. 8 Transmission spectra of 2-layer KLN films deposited on fused quartz and annealed in a RTP at 600 (-----), 650 (—) and 700 °C (— · —), respectively

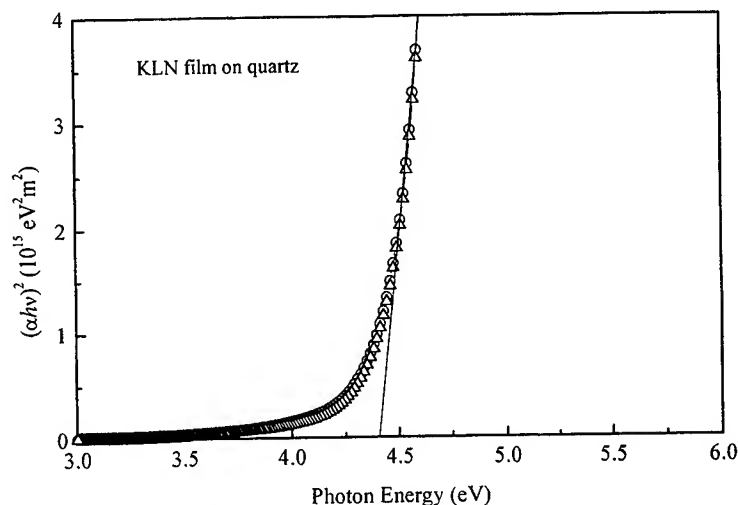


Fig. 9 $(\alpha h\nu)^2 \sim h\nu$ dependencies of KLN films deposited on fused quartz and annealed in a RTP at 650 (Δ) and 700 °C (O), respectively

As discussed earlier, volatility of Li is possible at high temperature, resulting in vacant C sites. The vacant C sites can be occupied by Nb^{5+} ions, the d -orbit splitting of which will be greatly increased because of the stronger crystal field in the C sites, yielding lower-energy d orbits (d_{xy} , d_{xz} , d_{yz}) filled with electrons. Thus, the electron transition from Nb $5d$ to O $2p$ needs higher energy, corresponding to larger absorption edge. Another consideration is the quantum confinement effect. For a nanostructured material, the band gap increases with the decrease of the grain size because of the caused lattice contraction, and a 20~80 nm-violet shift has been observed in BaTiO_3 films with different grain size and thickness.²¹ So the nanocrystalline structure of the present KLN films possibly contributes to the larger band gap. The results show that the optical property of KLN material can be tailored to some extent to meet the practical application requirement, though detailed quantitative studies remain to be carried out.

4. CONCLUSIONS

The preparation and characterization of sol-gel derived KLN films have been reported in this paper. All the results have shown that tetragonal tungsten-bronze-type KLN films could be obtained on both SiO_2/Si and quartz. RTP annealing was significant for preparing nanostructured crack-free films. The films can support optical modes and has a refractive index close to that of a KLN crystal. It was found that the absorption edges of the films had large shift to the violet spectral side and the tentative reasons were discussed. At present, only polycrystalline films were obtained on the studied substrates because of the lattice mismatch between the films and the substrates. Other substrates and buffer layers are under consideration to improve the film orientation.

REFERENCES

1. J. J. E. Reid, Ouwerkerk, and L. J. A. M. Berkers, "Potassium lithium niobate and its application to intercavity frequency doubling," *Philips J. Research* **46**, pp. 199, 1992.
2. J. J. E. Reid, "Resonantly enhanced, frequency doubling of an 820 nm GaAlAs diode laser in a potassium lithium niobate crystal," *Appl. Phys. Lett.* **62**, pp. 19, 1989.
3. T. Karaki, K. Miyashita, M. Nakatsuji and M. Adachi, "Growth and optical properties of ferroelectric $\text{K}_3\text{Li}_2\text{Nb}_5\text{O}_{15}$," *Jpn. J. Appl. Phys.* **37**, pp. 5277, 1998.
4. Z. Chen, M. Tago, M. Adachi and A. Kawabata, "Growth and properties of tungsten-bronze ferroelectrics potassium lithium niobate single crystals," *Ferroelectrics* **196**, pp. 265, 1997.
5. H. R. Xia, L. J. Hu, J. Q. Wei, J. Y. Wang and Y. G. Liu, "Growth and properties of tetragonal tungsten bronze type potassium lithium niobate single crystals," *Cryst. Res. & Technol.* **32**, pp. 311, 1997.
6. Y. Furukawa, S. Makio, T. Miyai, and M. Sato, "Growth and characterization of $\text{K}_3\text{Li}_2(\text{Ta}_x\text{Nb}_{1-x})_5\text{O}_{15}$ crystals for blue second harmonic generation applications," *Appl. Phys. Lett.* **68**, pp. 744, 1996.
7. D. H. Yoon, M. Hashimoto and T. Fukuda, "Growth and characterization of $\text{K}_3\text{Li}_{2-x}\text{Nb}_{5+x}\text{O}_{15+2x}$ micro single crystals formed by the μ -pulling down method for blue SHG applications," *Jpn. J. Appl. Phys.* **33**, pp. 3510, 1994. K. Imai, M. Imaeda, S. Uda, T. Taniuchi and T. Fukuda, "Homogeneity and SHG properties of $\text{K}_3\text{Li}_{2-x}\text{Nb}_{5+x}\text{O}_{15+2x}$ single crystals grown by micro-pulling-down technique," *J. Crystal Growth* **177**, pp. 79, 1997.
8. M. Ferriol, G. Foulon, A. Brenier, M. T. Cohen-Adad and G. Boulon, "Laser heated pedestal growth of pure and Nd^{3+} -doped potassium lithium niobate single-crystal fibers," *J. Cryst. Growth* **173**, pp. 226, 1997.
9. M. Matsukura, Z. Chen, M. Adachi and A. Kawabata, "Growth of potassium lithium niobate single-crystal fibers by the laser-heated pedestal growth method," *Jpn. J. Appl. Phys.* **36**(Pt 1), pp. 5947, 1997.
10. G. Foulon, B. Brenier, M. Ferriol, and G. Boulon, "Nonlinear laser crystal as a blue converter: laser heated pedestal growth, spectroscopic properties and second harmonic generation of pure and Nd^{3+} -doped $\text{K}_3\text{Li}_{2-x}\text{Nb}_{5+x}\text{O}_{15+2x}$ single crystal fibers," *J. Phys. D: Appl. Phys.* **29**, pp. 3003, 1996.
11. See special report "Blue lasers extend optical storage to 15 GB," *Nikkei Electronics Asia* No. 4, pp. 46, 1998.
12. W. Sakamoto, T. Yogo, K. Kikuta, T. Arimoto and S. Hirano, "Synthesis of lead barium niobate powders and thin films by the sol-gel method," *J. Am. Ceram. Soc.* **79**, pp. 889, 1996.
13. W. Sakamoto, T. Yogo, K. Kikuta, K. Ogoso, A. Kawase and S. Hirano, "Synthesis of strontium barium niobate thin films through metal alkoxides," *J. Am. Ceram. Soc.* **79**, pp. 2283, 1996.
14. T. Yogo, W. Sakamoto, T. Isaji, K. Kikuta and S. Hirano, "Synthesis of $\text{Ba}_2\text{NaNb}_5\text{O}_{15}$ powders and thin films using metal alkoxides," *J. Am. Ceram. Soc.* **80**, pp. 1767, 1997.
15. W. Sakamoto, A. Kawase, T. Yogo and S. Hirano, "Preparation and properties of $\text{K}(\text{Sr}_{0.75}\text{Ba}_{0.25})_2\text{Nb}_5\text{O}_{15}$ thin films by chemical solution deposition method," *Jpn. J. Appl. Phys.* **36**, pp. 5930, 1997.

16. H. X. Zhang, C. H. Kam, Y. Zhou, X. Q. Han, S. D. Cheng, Y. L. Lam, C. Y. Chan, "Preparation of potassium lithium niobate nanocrystalline powders and films," submitted to *J. Mater. Res.*
17. H. R. Xia, H. Yu, H. Yang, K. X. Wang, B. Y. Zhao, J. Q. Wei, J. Y. Wang and Y. G. Liu, "Raman and infrared reflectivity spectra of potassium lithium niobate single crystals," *Physical Review* **B55**, pp. 14892, 1997.
18. V. G. Dmitriev, G. G. Gurzadyan, and D. N. Nikogosyan, *Handbook of Nonlinear Optical Crystals*, Springer, Heidelberg, 1997.
19. J. C. Tauc, *Optical Properties of Solids*, North-Holland, Amsterdam, 1972.
20. Y. H. Xu, *Ferroelectric Materials and their Applications*, North-Holland, Amsterdam, 1991.
21. J. S. Zhu, X. M. Lu, W. Jiang, W. Tian, M. Zhu, M. S. Zhang, X. B. Chen, X. Liu, and Y. N. Wang, "Optical study on the size effects in BaTiO₃ thin films," *J. Appl. Phys.* **81**, pp. 1392, 1997.

Influence of Al/Nd ratio on light emitting properties of Nd-doped glass prepared by sol-gel process

Q. Xiang, Y. Zhou, Y. L. Lam, B. S. Ooi, Y. C. Chan and C. H. Kam

Photonics Research Group, School of Electrical and Electronic Engineering
Nanyang Technological University, Nanyang Avenue, Singapore 639798

ABSTRACT

For rare earth doped silica-based glasses derived by sol-gel process, Al was used as a modifier in order to improve the dispersion of the rare earth ion in silica lattices, and thus, make the higher rare earth doped silica glasses without clustering possible. In this research, the influence of the ratio of Al to Nd on the fluorescence intensity and lifetime was studied in details to get the material which has a strong fluorescence intensity as well as the long fluorescence lifetime enough for integrated amplifier and laser use. Ten samples in the form of powder with different Al/Nd (in the range of 10 to 80) and different Nd (from 0.25 mole to 3 mole) concentration were prepared by sol-gel process. These powders were gotten by heating the dried gels in a furnace in air environment. The results of the fluorescence intensity and lifetime show that the Al/Nd=10 with 1 mole Nd, that is the recipe $100\text{SiO}_2 : 10\text{AlO}_{1.5} : 1\text{NdO}_{1.5}$ has the strongest fluorescence intensity in the ten samples. But its $\tau_{1/e}$ is only 110 μs . For $100\text{SiO}_2 : 20\text{AlO}_{1.5} : 0.25\text{NdO}_{1.5}$, the obtained $\tau_{1/e}$ is 216 μs without special OH movement treatment. The research results show that we need to balance the fluorescence intensity and the lifetime to choose the suitable recipe for practice use.

Keywords: Nd doped glass, Al/Nd ratio, Active properties

1. INTRODUCTION

The rare earth doped glasses derived by sol-gel process is a promising candidate for material fabrication of integrated optical amplifiers and lasers. By the sol-gel process, it is very easy to tailor the materials composition to realize different functions. The process is also very flexible as the final materials can be made in the form of bulk, film, powder, and even special shapes. Meanwhile, the dopants can disperse in the host homogeneously with relatively high concentration due to the wet chemistry nature of the process. For optical amplifier and laser use, the active properties, such as fluorescence strength, transmission lifetime, are essential. Since the optical interaction path in integrated optics is much shorter than in fiber, a large rare earth concentration is needed. But the large rare earth concentration will lead to rare earth ion cluster, which will reduce the fluorescence intensity and the lifetime because of the concentration quench and cross relaxation between ions. In rare earth doped silica glass derived by sol-gel process, aluminum or phosphate are added to disperse the rare earth ion in host lattices homogeneously. What is the optimum ratio of aluminum (or phosphate) to rare earth (Nd^{3+} or Er^{3+}) ion? Some researchers adopt the ratio (atom ratio) of 10 : 1, and less than 2(at)% rare earth concentration^{1,2,3}. In general, there exist a optimum rare earth concentration for a certain amount Al or P dopants for the strongest PL intensity. But on that rare earth concentration, the fluorescence lifetime is relatively short. So, what is the suitable rare earth concentration for both strong photoluminescence (PL) intensity and long lifetime enough for lasing operation?

In this research, we focused on Nd-doped $\text{SiO}_2\text{-Al}_2\text{O}_3$ material system and prepared ten samples with different ratio of Al to Nd and different Nd concentration. Their PL spectra and lifetime were measured and analyzed. Because powder is easier than thin film to prepare and to get the active optical properties, we analyzed the properties of the powders. But the results are also available for relevant films. The main purpose of this research is to compare the material properties of different compositions for further research. The processing parameters are not optimized.

2. SAMPLE PREPARATION

Following the conventional sol-gel processing⁴, tetraethylorthosilicate (TEOS) was diluted in ethanol (EtOH) and water, with HCl added as a catalyst, let it hydrolyze in 60°C for one hour. $\text{Al}(\text{NO}_3)_3 \cdot 9\text{H}_2\text{O}$ and $\text{Nd}(\text{NO}_3)_3 \cdot 6\text{H}_2\text{O}$ were used as precursors

Correspondence: Email: qxjiang@ntu.edu.sg; Tel: +65-7905461; Fax: +65-7904161

of Al_2O_3 and Nd_2O_3 respectively. They are dissolved in EtOH, and then dropped into the pre-hydrolyzed TEOS solution. The end solutions stirred at room temperature in a covered bottle for one week, and then removed the cover. Several days later, they became dried gels. The high temperature treatment was carried out on all dried gels in a furnace by heating to 1000°C in 12.5 hours and then holding at 1000°C for 5 hours. The ten samples with different ratio of Al to Nd and Nd concentration are listed in Table I.

Table I Sample List

Sample No.	Compositions	Al/Nd ratio	Nd (mole)
1	$100\text{SiO}_2 : 10 \text{AlO}_{1.5} : 0.25 \text{NdO}_{1.5}$	40	0.25
2	$100\text{SiO}_2 : 10 \text{AlO}_{1.5} : 0.5 \text{NdO}_{1.5}$	20	0.5
3	$100\text{SiO}_2 : 10 \text{AlO}_{1.5} : 1 \text{NdO}_{1.5}$	10	1
4	$100\text{SiO}_2 : 20 \text{AlO}_{1.5} : 0.25 \text{NdO}_{1.5}$	80	0.25
5	$100\text{SiO}_2 : 20 \text{AlO}_{1.5} : 0.5 \text{NdO}_{1.5}$	40	0.5
6	$100\text{SiO}_2 : 20 \text{AlO}_{1.5} : 1 \text{NdO}_{1.5}$	20	1
7	$100\text{SiO}_2 : 20 \text{AlO}_{1.5} : 2 \text{NdO}_{1.5}$	10	2
8	$100\text{SiO}_2 : 40 \text{AlO}_{1.5} : 1 \text{NdO}_{1.5}$	40	1
9	$100\text{SiO}_2 : 40 \text{AlO}_{1.5} : 2 \text{NdO}_{1.5}$	20	2
10	$100\text{SiO}_2 : 40 \text{AlO}_{1.5} : 3 \text{NdO}_{1.5}$	133.3	3

3. PHOTOLUMINESCENCE PROPERTIES

The experimental apparatus used for obtaining the photoluminescence spectra of Nd-doped $\text{SiO}_2\text{-Al}_2\text{O}_3$ glass powder is shown in Figure.1. An Ar^+ laser with 488nm emission was used as the pump source. The pump signal was mechanically chopped at 80Hz. The fluorescence light emitted is collected by two lenses, analyzed with an ORIEL (model 77200) monochromator and detected with an ORIEL (model 71905) detector associated with a high pass optical filter. The reflected pump light was cut by a long pass filter located in front of the monochromator. All the spectra are recorded at room temperature. In order to get comparable results, every sample was held in a same quartz cell, all the other parameters in the measurement system kept constant during the measurement. The results are shown in Figure 2.

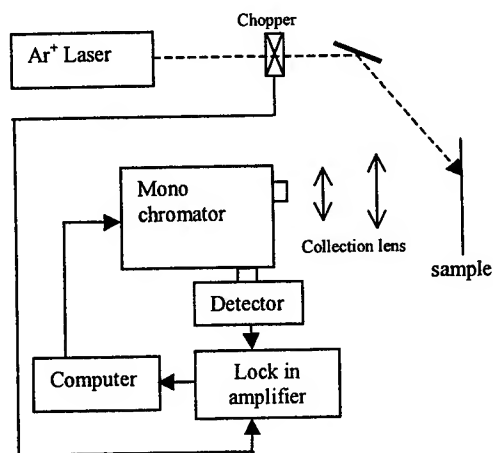
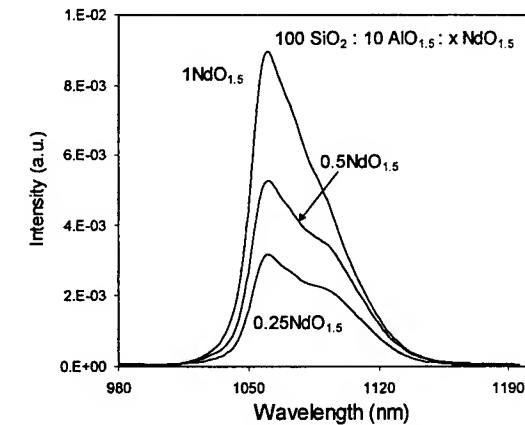


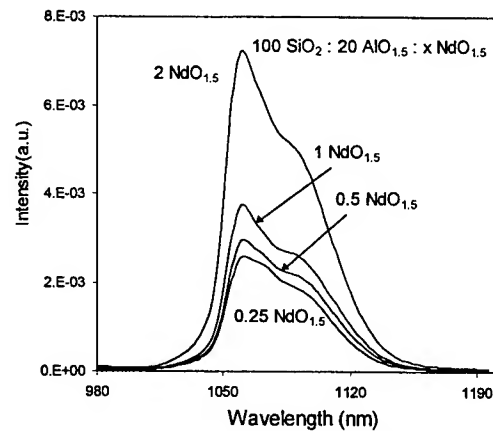
Fig.1 Setup for measurement of PL

Sample 1 to 3(called group one) has the same 10 mole Al but the Nd concentration was changed from 0.25 to 1 mole. As you can see in the Figure 2(a), the sample with $100\text{SiO}_2 : 10\text{AlO}_{1.5} : 1\text{NdO}_{1.5}$ composition has strongest PL in this group. There exist no any difference of the peak wavelength, they are all at 1060nm. The FWHM (full width of half maximum) are 56nm, 52nm and 44nm for 0.25at%Nd, 0.5at%Nd sample and 1at%Nd respectively. Sample 4 to 7(called group two) has the same 20 mole Al but Nd concentration was changed from 0.25 to 2 mole. The results in Figure 2(b) show that the sample with

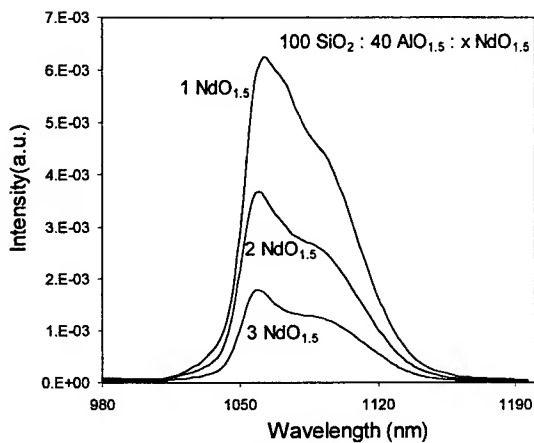
100SiO₂: 20AlO_{1.5}: 2NdO_{1.5} composition has the strongest PL in this group. The peak wavelengths are all 1060nm as well. The FWHM are 58nm, 58nm, 56nm, and 54nm for 0.25at%Nd, 0.5at%Nd, 1at%Nd and 2at%Nd sample respectively. Similarly, in group three (sample 8 to 10) with 40 mole Al concentration, the recipe 100SiO₂: 40AlO_{1.5}: 1NdO_{1.5} has the strongest PL shown in Figure 2(c). The FWHM are 55nm, 57nm and 60nm for 1at%Nd, 2at%Nd, and 3at%Nd sample respectively. No peak wavelength shift is observed for the ten samples. We think this results from the wavelength resolution limitation (2nm) of our measurement system. But the FWHM increases with the increment of Al concentration due to the wide distribution of Nd bonding sites with the presence of Al in host lattices. The maximum in each group is compared in figure 3. As you can see, the peak of the recipe 100SiO₂:10AlO_{1.5}: 1NdO_{1.5} is highest and also strongest in ten samples. But the intensity difference among the three samples in Figure 3 is not great. That implies these three recipes are available only considering the PL intensity.



(a) Al/Nd = 10: x (x = 0.25~1)



(b) Al/Nd = 20 : x (x = 0.25~2)



(c) Al/Nd = 40 : x (x = 1~3)

Fig. 2 PL spectra of Nd : SiO₂-Al₂O₃ of Nd:SiO₂-Al₂O₃ glasses

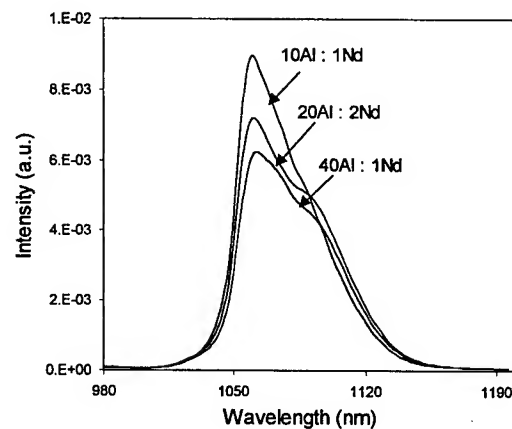


Fig. 3 Comparing of the PL spectra

4. LIFETIME

The fluorescence lifetimes for Nd doped silica glass were measured by exciting the samples with a pulsed semiconductor laser with the wavelength of 808nm. The pulse duration is about 100 ns, and the repeating rate is set at 1000 times per second. A Hamamatsu R5108 photomultiplier tube (PMT) was used as the detector, whose anode pulse rising time is 1.2 ns and the electron transiting time is 18 ns. A Tektronix TDS 360 digital oscilloscope was used in this system to record the decay. Figure 4 shows this setup.

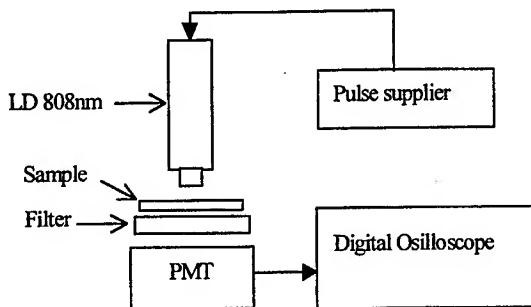


Fig.4 setup for measurement of the fluorescence decay of Nd:SiO₂-AlO_{1.5}

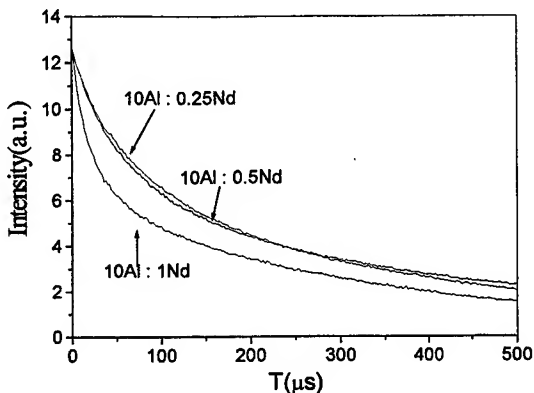
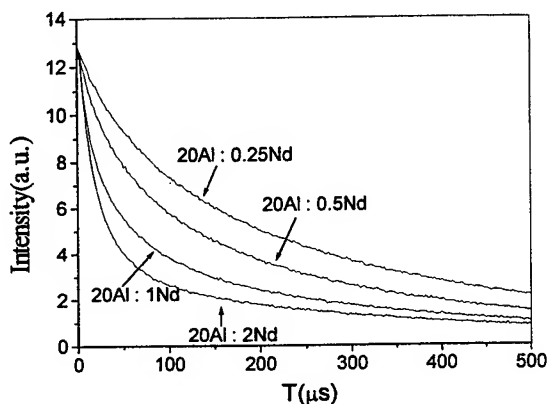
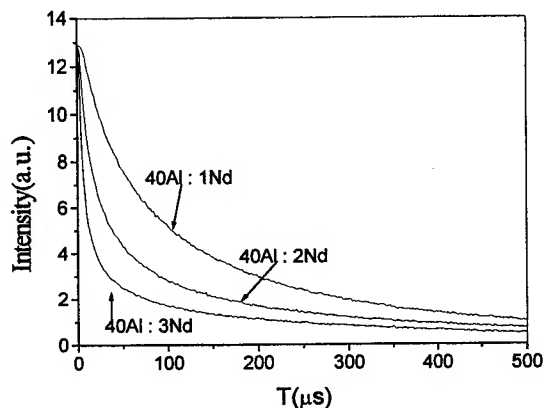


Fig.5(a) Al/Nd = 10:x (x = 0.25~1)



(b) Al/Nd = 20:x (x = 0.25~2)



(c) Al/Nd = 40:x (x = 1~3)

Fig.5 Fluorescence decay

Figure 5(a), (b) and (c) shows the fluorescence decay of group one, two and three respectively. In each group, the higher the Nd concentration is, the faster the fluorescence decays. The decay curve of the samples from No.1 to No.5 is pure exponential, the samples from No.6 to No.10 is non-exponential. When the Nd concentration is increased, the average distance between ions is smaller and some degree of non-exponentiality starts to occur, even without clustering, because of cross relaxation.

Cross-relaxation is a special case of energy transfer where the original system (E_3-E_2) losses the energy by decaying to the lower state E_2 (which may also be the ground state E_1 in Figure 6) and another system ($E_3'-E_2'$) acquires the energy by going to a higher state E_2' . The cross-relaxation between a pair of RE ions is graphically presented in Figure 6. It may take place between the same lanthanide (being a major mechanism for quenching at higher concentration in a given material) or between two differing elements, which happen to have two pairs of energy levels separated by the same amount. The two energy gaps may be equal or can be matched by one or two phonons. The possible cross-relaxation channels for Nd³⁺ are $^4F_{9/2} \rightarrow ^4I_{15/2} \rightarrow ^4I_{9/2} \rightarrow ^4I_{15/2}$.

$\tau_{1/e}$ is the fluorescence lifetime (the time is the time for fluorescence signal reaches a value of $I(0)/e$ where $I(0)$ is the value of the fluorescence signal at $t=0$). The $\tau_{1/e}$ value for the ten samples is listed in Table II. At lower Nd concentration (0.25at%), the increment of Al can obviously increase the $\tau_{1/e}$, for example, 10Al : 0.25Nd, $\tau_{1/e} = 172\mu s$, and 20Al : 0.25Nd, $\tau_{1/e} = 216\mu s$. But at higher Nd concentration (more than 0.5at%), the increment of Al can not only increase the $\tau_{1/e}$, but also decrease the $\tau_{1/e}$. As examples, 10Al : 0.5Nd, $\tau_{1/e} = 156\mu s$, 20Al:0.5Nd, $\tau_{1/e} = 140\mu s$; 10Al : 1Nd, $\tau_{1/e} = 110\mu s$, 20Al:2Nd, $\tau_{1/e} = 68\mu s$. So, the function of the Al is more effective at low Nd concentration than at higher concentration (more than 0.5at%).

Table II Lifetime of Different Al/Nd and Nd samples

Samples No	Al/Nd ratio	Nd (mole)	$\tau_{J/e}$
1	40	0.25	172
2	20	0.5	156
3	10	1	110
4	80	0.25	216
5	40	0.5	140
6	20	1	68
7	10	2	38
8	40	1	114
9	20	2	42
10	133.3	3	14

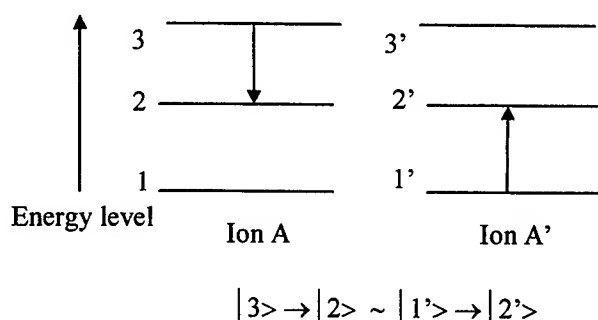


Fig.6 Scheme for cross-relaxation between two ions of the same or different nature

5. DISCUSSION AND CONCLUSION

For 10at%Al sample group, the PL intensity increases as the increment of Nd up to 1at%, the samples with Nd concentration more than 1at% were not prepared, we don't find the maximum Nd concentration in this group. For 20at%Al sample group, the PL intensity also increases with the increment of Nd concentration up to 2at%. But the PL intensity of 20Al : 2Nd sample is a little lower than the intensity of 10Al : 1Nd sample. Moreover the lifetime of 20Al : 2Nd sample is much shorter than that of 10Al : 1Nd sample. So, in practical, it is impossible increasing Nd concentration any more in group two samples. As above said, the intensity difference among the three samples in Figure 3 is not great, but their lifetime are quite different. For practical use, at the same level PL intensity and lifetime, we should choose the lower Nd and Al concentration recipe considering the possible crystalline and quench. Thus, as a conclusion, we think the recipe $100\text{SiO}_2 : 10\text{NdO}_{1.5} : 1\text{NdO}_{1.5}$ is the suitable one.

REFERENCES

1. Y. Zhou, Y. L. Lam, S. S. Wang, H. L. Liu, C. H. Kam, and Y. C. Chan, "Fluorescence enhancement of Er^{3+} -doped sol-gel glass by aluminium codoping" *Appl. Phys. Lett.* **71**(5), August 1997, pp587-589.
2. S.R. Natarajan, T.Srinivas, M. J. Joseph, and A. Selvarajan, "Fabrication of rare-earth doped sol-gel based composite planar optical waveguides on glass", 1998 International Conference on Applications of Photonic Technology, Ottawa, CANADA, July 27-30, 1998.
3. X. Origaac, D. Barbier, X. M. Du, and R. M. Almeida, "Fabrication and characterization of sol-gel planer waveguides doped with rare earth ions", *Appl. Phys. Lett.* **69**(7), 12 August 1996, 895-897.
4. Ian M. Thomas, Stephen A. Payne and Gary D. Wilke, "Optical properties and laser demonstration of Nd-doped sol-gel Silica glasses", *J. Non-Cry Solids*, **151**(1992) 183-194.

Characterization of Reactive Ion Etching of Sol-Gel SiO₂ Using Taguchi Optimization Method

Terence C.L. Wee*, Boon Siew Ooi, Yan Zhou, Yuen Chuen Chan, and Yee Loy Lam

Photonics Research Group, School of Electrical and Electronic Engineering,

Nanyang Technological University, Singapore 639798

ABSTRACT

SiO₂ films prepared using sol-gel technique have found enormous potential applications in photonics, electronics and sensor devices. However, the feasibility of the devices utilizing sol-gel technology lies on the ease of the fabrication processes such as patterns transfer using wet or dry etchings. Dry etching is preferred over wet etching as it is able to produce finer features with high anisotropic etch profile. In this paper, we report the development of a dry reactive ion etching (RIE) process for sol-gel SiO₂ using a mixture of CF₄ and O₂ plasma. Parameters such as RF power, chamber pressure, CF₄ and O₂ flow rate, were optimized using a statistical method called Taguchi Technique. Etch rate of as high as 50nm/min, with high anisotropy etched profile, has been obtained.

Key words: Sol-gel, Reactive ion etching, SiO₂, Taguchi, optimization

1. INTRODUCTION

In recent years, the sol-gel method, which is a technique for forming glass and ceramic materials by low temperature reaction of liquid metal-organic precursors, has gained considered attention in the development of materials and devices for optical and photonics integrated circuits (PIC) applications. This is due to the fact that sol-gel provides a highly convenient route for the preparation of uniform high quality thin films and monoliths of oxide glasses. The material could be easily used in interesting applications such as passive waveguides, optical amplifiers, lasers and non-linear switching devices¹. The precursor solutions are simply mixed, cast into molds or coated onto surfaces by spinning or dipping, and followed by gelation at low temperature. These features have interesting potential, allowing the possibility to prepare amorphous materials, which cannot be obtained by traditional melting techniques². This includes incorporating thermally weak substances in inorganic matrixes. For these reasons, a wide range of novel materials could be prepared for PIC applications. In the aspect of semiconductor processing, sol-gel is a simple and low cost method for depositing films such as SiO₂ as compared to plasma enhanced chemical vapor deposition (PECVD), which involves the use of specialized equipment. The simplicity and low cost is attractive to PIC researchers.

In order to fully utilize the usage of sol-gel derived film such as SiO₂ in the different PIC fabrication processes, it must be ensured that this technique does not obstruct the fabrication flow. In other words, the films derived from this technique has to be feasible in all the fabrication processes, such as etching, as compared to the films deposited using chemical vapor deposition (CVD) processes. Thus, it is important to study the compatibility of using the sol-gel films in the different processes as compared to the CVD films.

Etching of sol-gel SiO₂ film is being studied in this paper as it has not been substantially studied and characterized previously. The etching process is divided into dry and wet etching. However, in most cases, dry etching is preferred over wet etching as it is able to produce finer features with higher anisotropic etch profile. A reactive ion etching (RIE) dry etch process for sol-gel SiO₂, using a mixture of CF₄ and O₂ plasma has been developed. A few parameters, such as the CF₄ and

* Corresponding author: Email: pa3509463@ntu.edu.sg; Telephone: +65-7905461; Fax: +65-7933318

O₂ flow rate, RF power and chamber pressure was found to affect the etching process strongly. Thus optimization of these parameters to obtain a high anisotropic profile and high etch rate process was carried out.

The process of achieving the optimal etch rate of the sol-gel SiO₂ film involves the experimentation of the etch rate by changing the process parameters. Experiment with the process variables one at a time or by trial and error until a first feasible combination is found, is a common approach in attaining optimization. However, this approach can lead to a very long and tedious time span for completing the experiment. Thus, Taguchi method ³, a more systematic and efficient approach for determining near optimum settings of the process parameters is used for the optimization process.

Taguchi method is a statistical method, which reduces the variations in experiments. The robust design method uses orthogonal arrays (OA) to study the parameter space, usually containing a large number of process parameters, with a small number of experiments. Based on design of experiment (DOE) theory, Taguchi's orthogonal arrays provide a method for selecting an intelligent subset of the parameter space. Using orthogonal arrays significantly reduces the number of experimental configurations. Table 1 shows a common orthogonal array comparing with number of equivalent full factorial experiments. As can be seen from the table, using an OA approach called L9 requires only 9 experiments to be carried out in search of an 81 control factor combination. This will provide the near optimal mean, and also the minimal variation away from the mean. The L9 OA approach is used to optimize the RIE etching of sol-gel derived SiO₂, with the 4 factors being O₂ and CF₂ flow rate, RF power and process pressure, and each factors is taken with 3 different levels.

Orthogonal Array	Factors & Levels	No. of Experiments
L4	3 Factors at 2 Levels	8
L8	7 Factors at 2 Levels	128
L9	4 Factors at 3 Levels	81
L16	15 Factors at 2 Levels	32,768
L27	13 Factors at 3 Levels	1,594,323
L64	21 Factors at 4 Levels	4.4x10 ¹²

Table 1. Common orthogonal arrays (OA) with number of equivalent full factorial experiment

2. EXPERIMENT

2.1 Sol-gel preparation

The undoped sol-gel solution was prepared by mixing solution of TEOS, ethanol, DI water and HF of different percentage. The corresponding weightage of the individual solution is shown in table 2.

Solution	Weight (g)	Wt %
TEOS	20.8	100
Ethanol	46	-
DI Water	21.6	-
HF(4%)	2 drops	-

Table 2. Composition and weight of undoped sol-gel SiO₂ solution

The solution was then allowed to age for 24 hours before using. The aging process is essential to control its viscosity, necessary in the spinning process. The ready solution was then spun onto a cleaned Si substrate using a spin coater. The spin speed was set to 4000rpm and the duration was set to 30s, the thickness of the sol-gel coated was about 200nm. Next, the sample was processed using a rapid thermal processor (RTP) at 600°C for 120 seconds to convert the porous gel into dense glass.

2.2 Taguchi Optimization

In the experiment, RF power, process pressure, CF₄ and O₂ flow rates were identified to be the control factors. In the optimization process, three levels were selected for each factor. The level of a control parameter refers to how many test values of the parameters are to be analyzed. The first level was taken to be the initial operating condition. The subsequent level were taken sufficiently far apart to capture non-linearity.

The selection of the appropriate orthogonal array to fit the experiment requires the calculation of the total degrees of freedom to find the minimum number of experiments that must be performed to reach a near optimum parameter set. One degree of freedom is associated with the overall mean regardless of the number of control factor, and for the other factors,

$$\text{Degree of freedom} = \text{No. of Levels} - 1, \quad (1)$$

The tabulated values assigned to the different levels of each parameter are shown in Table 3.

Level	Pressure (mTorr) (F4)	CF ₄ flow (sccm) (F2)	O ₂ flow (sccm) (F3)	RF power (W) (F1)
1	24	20	10	24
2	30	60	30	45
3	50	100	50	65

Table 3. Values assigned to different levels of control parameters for sol-gel etching

For each factor, the degree of freedom is $3-1=2$, together with one more degree of freedom associated with the overall mean, the total degree of freedom is calculated to be 9. Thus, 9 experiments have to be carried out in order to reach a near optimum case. This fits nicely into Taguchi's standard L9 array. The array and corresponding parameter assignment is shown in table 4.

Exp. No.	Column No.				Actual parameter values			
	1	2	3	4	Pressure (mTorr)	CF ₄ (sccm)	O ₂ (sccm)	RF power (W)
1	1	1	1	1	24	20	10	24
2	1	2	2	2	24	60	30	45
3	1	3	3	3	24	100	50	65
4	2	1	2	3	30	20	30	65
5	2	2	3	1	30	60	50	24
6	2	3	1	2	30	100	10	45
7	3	1	3	2	50	20	50	45
8	3	2	1	3	50	60	10	65
9	3	3	2	1	50	100	30	24

Table 4. The array and corresponding parameter assignment of etching of sol-gel

Upon obtaining the table for the experiment, the etching was done on the samples using a conventional parallel plate RIE system. The samples were etched for 3 minutes with different process parameters. After the etching process, the photoresist on the samples were removed using acetone, and the profile of the samples was measured using a DEKTEK³ surface profiler.

3. RESULTS AND DISCUSSION

After etching, the etched depth of the samples were measured, and the etch rate for each set of experiment was calculated. The results of the experiment were tabulated and are shown in Table 5.

Experiment No	Setting level for each etching parameter				Average etch rate (nm/min)
	Pressure	CF ₄ flow	O ₂ flow	RF power	
1	24	20	10	24	8.68
2	24	60	30	45	18.74
3	24	100	50	65	27.54
4	30	20	30	65	10.28
5	30	60	50	24	5.26
6	30	100	10	45	32.60
7	50	20	50	45	11.73
8	50	60	10	65	50.10
9	50	100	30	24	14.39

Table 5. Results of matrix experiment for etching of sol-gel

Since the experiment design was orthogonal, it was possible to separate out the effect of each factor. For example, RF power (control factor number four -F4) was at level one in experiment 1, 5 and 9. Thus, the corresponding mean for F4 at this level could be calculated by summing up its corresponding etch rates and taking the mean, and the result was found to be 9.44nm/min. The mean etch rate for each level of the 4 control factors were calculated and is displayed in Table 6. This table provides the data for plotting of response graphs, which enables the analysis of the sensitivity of the different control factors on the etch rate.

Parameter Level	Mean etch rate (nm/min)			
	Pressure	CF ₄ flow	O ₂ flow	RF power
1	16.05	10.23	30.46	9.44
2	18.32	24.70	14.47	21.02
3	25.41	24.84	14.84	29.31

Table 6. Mean etch rate of sol-gel

Figure 1 shows the response graph for process pressure. As can be seen from the graph, the mean etch rate increases as the process pressure increases. This phenomenon could be due to the fact that the increase in process pressure increases the density of the neutral and ionized species in the chamber⁴. However, when the pressure was increased to subsequent level well beyond 50mTorr during the sol-gel RIE process, a decrease in etch rate was observed. This is attributed to the decrease in mean free path (MFP) of the bombarding ions. If the mean free path is smaller than the sheath, a significant amount of collision and ionization will occur in the sheath region. However, at higher pressures many ions will not be accelerated across the full sheath potential, thus bringing about a decrease in the etch rate.

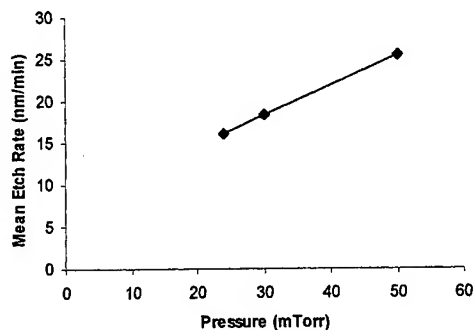


Figure 1. Response graph of process pressure on sol-gel etching

Figure 2 shows the response graph for CF_4 flow rate. From the graph, it is found that increasing CF_4 flow rate increases the etch rate. This could be attributed to the fact that the increase of the flow rate increases the density of F atoms dissociated from CF_4 in the plasma, thus enhance the etch rate of SiO_2 .

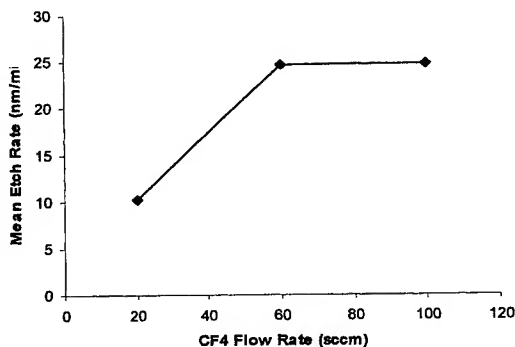


Figure 2. Response graph of CF_4 flow rate on sol-gel etching

Figure 3 shows the response graph for O_2 flow rate. The graph showed decrease in etch rate as the O_2 flow rate increases. O_2 is used in the process to form volatile products such as CO , CO_2 and COF_2 . Formation of these products would decrease the concentration of CF_x/F recombination rate. Thus increases the F concentration. However, beyond a certain limit, the O_2 starts to dilute the CF_4 and thus slowing down the etching process. In order to prevent the dilution of CF_4 feed gas, a gas ration of 10:1 of CF_4 : O_2 is chosen for the final optimization.

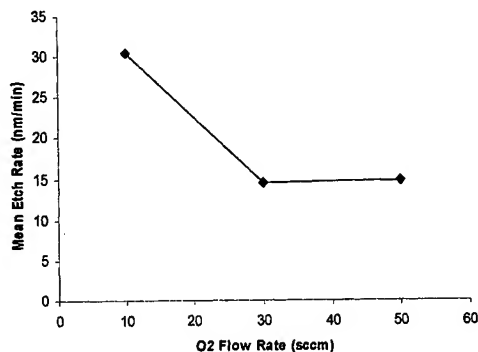


Figure 3. Response graph of O_2 flow rate on sol-gel etching

The effect of RF power on sol-gel SiO_2 etch rate is shown in Figure 4. As can be seen from the graph, the etch rate of sol-gel SiO_2 increased almost linearly with increasing RF power. Comparing all the graphs obtained, RF power was found to be the most significant control factor for the RIE etching of the sol-gel.

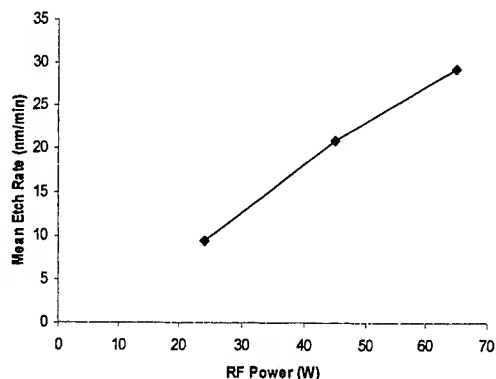


Figure 4. Response Graph of RF power on sol-gel etching

The increase in etch rate with RF power is mainly due to the fact that increasing RF power dissipated in the plasma increases the sheath potential. This provides the gas molecules in the plasma with greater energy and thus a higher concentration of reactive species will be formed.

Upon analyzing the graphs obtained, a near optimum level for the 4 control parameters has to be selected and further confirm for optimum results. The four optimum values for the four controllable factors was chosen to be RF power of 65W, process pressure of 50mTorr, CF_4 flow rate of 100sccm and O_2 flow rate of 10sccm. These values were chosen in a range near the maximum etch rate region of the response graph. As can be seen, the optimum value combination was not considered during the 9 experiments that were carried out. However, in the optimization using Taguchi's technique the predicted near optimum setting need not correspond to one of the rows of the matrix experiment.

The verification experiment was carried out for 3 times with the identical process parameters. The average etch rate was calculated and was found to be $47.5 \pm 2.5 \text{ nm/min}$. This etch rate is higher than all the previous obtained etch rate and is considered to be the highest etch rate obtainable within the ranges of values chosen for the control factors.

The resultant surface profile obtained is shown in Figure 6.

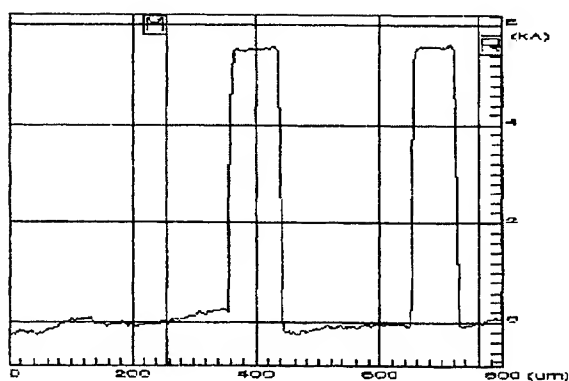


Figure 6. Surface profile of etched sol-gel samples

From the figure above, it can be observed that a good anisotropic etch profile is obtained. The waviness seen in the profile and the difference in the bottom edge level is due to the limitation of the surface profiler.

4. CONCLUSION

Dry etching using RIE was studied on sol-gel derived SiO_2 . The different parameters governing the etching process, such as RF power, chamber pressure, CF_4 and O_2 flow rate was optimised using statistical Taguchi method. It was found that RF power was the most significant control factor for the RIE etching of so-gel SiO_2 , and a gas ratio of 10:1 of CF_4 : O_2 was needed for optimum etching. The optimized parameters were found to be RF power of 65W, process pressure of 50mTorr, CF_4 and O_2 flow rate of 100sccm and 10sccm respectively. Confirmation run shows that the optimized parameters produced a mean etch rate as high as $47.5 \pm 2.5 \text{ nm/min}$. The obtained profile was also highly anisotropic.

ACKNOWLEDGEMENTS

The authors would like to thank Mr Leong Chee Hoi and Mr Lui Whye Hoe, for their substantial aid in conducting the experiments for this paper.

REFERENCES

1. C.J. Brinker & G.W. Scherer, *Sol-gel science: the physics and chemistry of sol-gel processing*, Academic Press, 1990.
2. L.H. Lee, B.S. Ooi, Y.L. Lam, Y.C. Chan, C.H. Kam, "Quantum Well Intermixing in GaAs-AlGaAs Laser Structure Using Sol-gel SiO_2 Dielectric Cap," *SPIE Photonics China 98*, 3547, pp 319-323, 1998.
3. Phillip J. Ross, *Taguchi techniques for Quality Engineering*, McGraw-Hill, 1998.
4. S.M. Sze, *VLSI Technology*, McGraw-Hill International Edition, 1998.

SESSION 12

Sol-Gel Devices

TiO₂/SiO₂/ORMOSIL hybrid material planar waveguides prepared at low temperature by sol-gel processing

Wenxiu Que*, Y. Zhou, Y. L. Lam, Y. C. Chan, S. D. Cheng, H. P. Li, J. Liu, C. H. Kam

Photonics Research Group, School of Electrical & Electronic Engineering,
Nanyang Technological University, Nanyang Avenue, Singapore 639798, Singapore

ABSTRACT

We report the preparation of sol-gel derived planar waveguides from high titanium content hybrid materials. By incorporating organic molecules into the inorganic TiO₂-SiO₂ sol-gel glass matrix, porous-free waveguide films are obtained with low temperature heat treatment. The single spin-on thickness is measured to be more than 1.7 μm , enough to support light guiding and the refractive index of the film is found to depend on the heat treatment temperature. We also studied the microstructural and optical properties of the waveguide films using atomic force microscopy, ellipsometry, thermal gravimetric analysis, and UV-visible spectroscopy. Based on these experimental results, we found that heat-treatment at a temperature about 100°C is sufficient to produce a relatively dense film with high transmission in the visible and near infrared range. We believe that this process is very useful for the fabrication of passive photonic circuits on temperature sensitive substrates such as III-V compound semiconductors. Meanwhile, it has also been noted that a purely inorganic and crack-free silica-titan films could be obtained after baking the hybrid material film at 500°C or higher.

Keywords: Sol-gel processing, Hybrid materials, Planar waveguides, Films, Microstructural properties, Optical properties

1. INTRODUCTION

Optical quality films of a few μm thicknesses are a basic requirement for integrated-photonic devices that are fabricated on silicon substrates. Since such films are thick by normal coating standards, a number of specialized methods have been developed to form them. These include wet thermal oxidation and thermal nitridation,¹⁻⁴ sputtering,⁵⁻⁶ low-pressure chemical vapor deposition,⁷⁻⁸ and flame hydrolysis.⁹⁻¹¹ Each method has its own advantages and disadvantages.

The sol-gel method is one of the most important techniques for the synthesis of various functional thin films. A distinctive feature of the sol-gel process is that it enables one to prepare silicate glasses at lower temperatures that are impossible with the above-mentioned methods. In addition, the sol-gel process makes use of low-cost materials and equipment, and is thus an interesting alternative for the fabrication of basic integrated optical circuits. With channel waveguides being the basic component of integrated optics, the development of its fabrication technology is hence essential to the realization of high-performance devices such as splitters, couplers, deflectors, and optical amplifiers.¹²⁻¹⁴ As with any sol-gel process, three basic stages are involved, namely, the formation of a sol (a stable suspension of particles within a liquid), the processing of the sol to form a gel (a continuous solid network permeated by liquid), and the drying of the gel to form a porous glass. Typically, in order to deposit a film, the sol is applied to the surface of a solid either by spin coating or by dip coating. Gel formation then follows as a result of solvent evaporation. The drying stage may simply involve heating the gel to evaporate the liquid phase, although higher temperature processing is often employed to remove any residual organic material by combustion and to sinter the glass. In general, sol-gel derived optical material based solely inorganic systems such as tetraethoxysilane (TEOS)-derived gels can be very porous unless densification has been carried out at high temperature. An attractive way to overcome the problem is to combine properties of very different materials in one, and to produce molecular-scale composite materials via sol-gel processing. Another process developed recently is to incorporate organic molecules into the inorganic matrix using basically the same sol-gel technique.¹⁵⁻¹⁶ When organic groups are integrated in the glass, the shrinkage is low because the bulky organic components fill the pores between the inorganic oxide chains. The composite materials can reach its final density at a temperature of less than 200°C, especially if the organic groups can cross-link by epoxy or methacryl polymerization.

* correspondence: Email: ewxque@ntu.edu.sg; Telephone: (65)7905642; Fax: (65)7912687

In this work, we have investigated the preparation of high optical quality organic-inorganic hybrid material waveguide films made from acid catalyzed solutions of γ -Glycidoxypropyltrimethoxysilane (GLYMO) mixed with tetraethoxysilane (TEOS) and tetrapropylorthotitanate (TPOT) based on the sol-gel technique. We have also studied the characteristics and properties of the waveguiding films by atomic force microscopy (AFM), X-ray diffractometry (XRD), ellipsometry, thermal gravimetric analysis (TGA), and UV-visible spectroscopy (UV-VIS).

2. EXPERIMENTAL SECTIONS

Three solutions containing TEOS, GLYMO and TPOT respectively were initially prepared. For a solution A, 1 mole of TEOS was mixed with 4 moles of ethanol and 4 moles of de-ionized water. After the solution was stirred for 30 minutes, 0.1 mole hydrochloric acid was added and the solution was further stirred for 60 minutes. For Solution B, 1 mole of GLYMO was mixed with 4 moles of ethanol and 4 moles of de-ionized water, and the solution was stirred for about 30 minutes. For solution C, TPOT was added to acetylacetone at a molar ratio of 1:4 under a nitrogen environment and the solution was stirred until homogenization was reached. The three solutions (solution A, B, and C) were then mixed with a $\text{SiO}_2\text{:TiO}_2$ molar ratio of 2, while the molar ratio of GLYMO to SiO_2 was fixed to be 1:1. Accordingly, the studied molar ratio of GLYMO: $\text{SiO}_2\text{:TiO}_2$ was 0.40:0.40:0.20. The final mixture solution was stirred for 25 hours at room temperature. The experimental procedure is schematically shown in Fig.1.

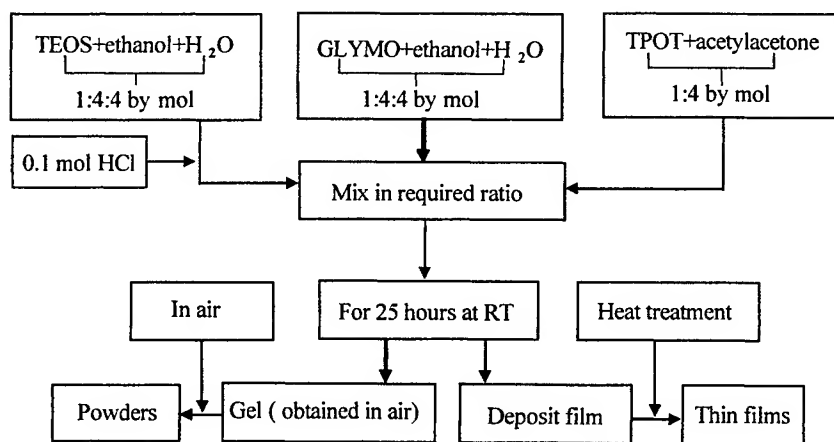


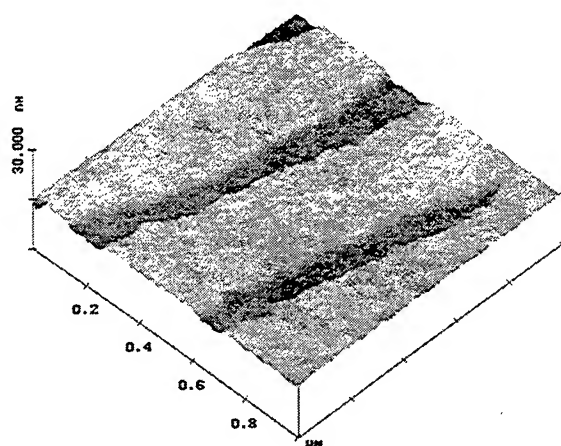
Figure 1 Flow chart of the synthesis of composite films and powders by a sol-gel process

It should be noted that cleaning of the substrate is important for proper adhesion of the films. The substrates (Si and glass slide) were ultrasonically cleaned in acetone and ethanol respectively, rinsed with de-ionized water and dried with pure nitrogen. After one sol-gel layer was spun in a clean room environment (class 100) on the substrate at 4000 rpm for 35 seconds, the coated film was then heated at different temperatures of 100, 200, 300, 400, and 500°C, for about 20 minutes. It was found that a dense, stable and crack-free film could be obtained after a heat treatment at about 100°C, and this result is in agreement with that reported by Ref.[16]. A film thickness of about 1.7 μm could be easily obtained on a Si substrate by a single-coating process. When such a film was deposited on a glass slide or a silica-on-silicon substrate, light wave guiding was easily demonstrated. In the following sections, we will present our study on the film characterization by using AFM, XRD, ellipsometry, TGA, and UV-VIS spectroscopy.

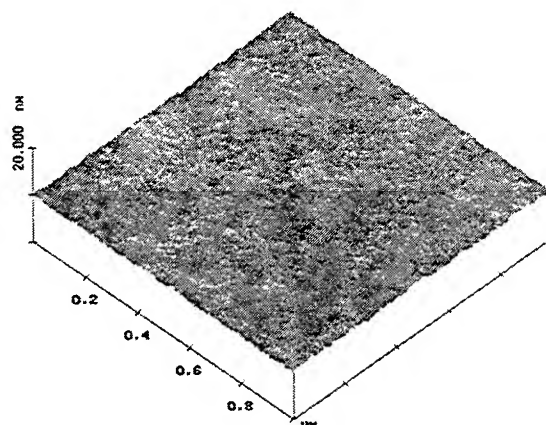
3. RESULTS AND DISCUSSION

The sol-gel films were characterized using XRD, AFM, TGA, ellipsometry, and UV-VIS spectroscopy. XRD was carried out for the waveguide films by using a Rigaku Rint 2000 Series X-ray diffractometer equipped with a thin film attachment unit. The X-ray radiation source used was Cu K α , operated at 40 kV, 35 mA and the scanning speed was 4°/min at a step of 0.02°. TGA was done using a Perkin Elmer 7 Series system on the hybrid material powders obtained from solutions at a heating rate 2°C/min. The morphology of the film was examined under an AFM (Digital Instruments, Nanoscope IIIa) using the tapping mode. The thickness and refractive index of the films were measured with a spectroscopic phase modulated ellipsometer. For those films coated on microscope glass slides, their UV-visible transmission spectra were measured in the range of 250-800 nm using a Perkin Elmer Lambda 16 UV/VIS Spectrometer.

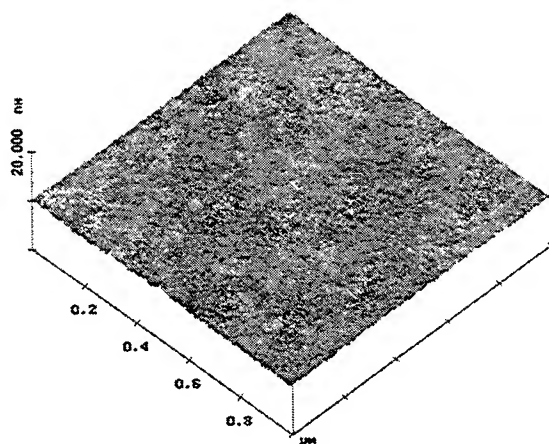
3.1 Morphology of the film



(a) 80°C



(b) 300°C



(c) 500

Figure 2 AFM pictures of the films baked at different temperature

Figures 2 (a), (b), and (c) show the AFM images of the films baked at different temperatures. It can be seen from Fig.2(a) that the film baked at about 80°C has a relatively big surface roughness, but a porous-free morphology. The big roughness may be related to the organic solvents that remain in the film. When baked at 500°C (Fig.2(c)), a dense, smooth and uniform morphology with relatively small surface roughness can be obtained. However, the film baked at 300°C (Fig.2(b)) shows a relatively porous surface as compared to that of Fig.2(c). This porosity observed in the 300°C treated film could be a direct result of the large weight loss that occurs during heat treatment at this temperature. These results of Fig. 2 indicate that when the organic groups are integrated in the inorganic system, the shrinkage of the composite material is low because the bulky organic components fill the pores between the inorganic oxide chains. The composite materials can thus be made to reach its final density at a low temperature. For example, the result in Fig.2(a) actually shows that a porous-free film can be obtained at the baking temperature of 80°C. Fig.2(c) indicates that when the organic compounds have been completely combusted and decomposed at the baking temperature of 500°C, the observed film becomes a purely inorganic coating. When the baking temperature is in the middle as is shown in Fig.2(b), the organic compounds are partially combusted or decomposed, and therefore, pores could be observed.

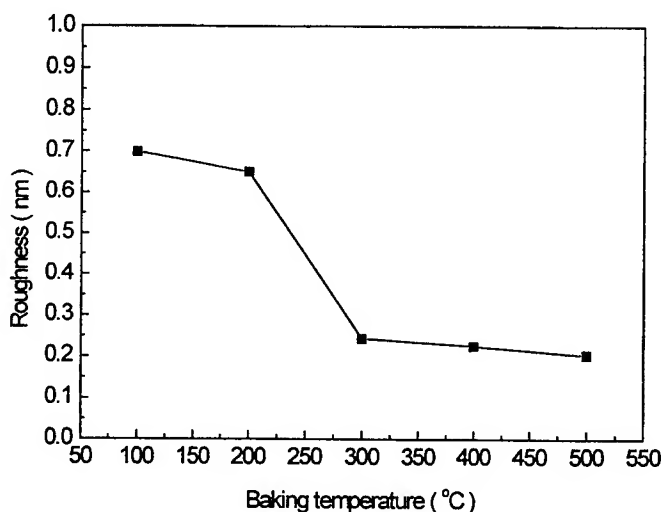


Figure 3 Dependence of the RMS roughness of the films on baking temperature

Fig.3 shows the dependence of the root mean square (RMS) surface roughness of the films on the baking temperature. It is obvious that the surface roughness is relatively big when the baking temperature is below 200°C. But when the baking temperature is increased, the volatilization and the thermal decomposition of the organic solvents or the combustion of organic compounds occur, the RMS roughness thus reduces and the film becomes relatively smooth. Obviously, the surface roughness of the film obtained under the present processing condition is sufficiently small (less than 0.7 nm) for optical waveguide applications. To better understand the heat treatment process, TGA and DTA were used to examine the thermal properties of the composite materials.

3.2 Results and discussion of TGA

The powder used for the thermal analysis was obtained by pouring the sols into petri dishes and drying them at room temperature for about two weeks. Crushed powders of 30-40mg were put into an Au crucible for TGA. Figure 4 shows the TGA curves of the gel powders. It can be seen that there are three weight loss stages, namely, below 200°C, between 200 and 310°C, and from 310 to 480°C. Below 200°C, the weight loss is due to the evaporation of water and the volatilization and thermal decomposition of the remnant organic solvents. Between 200 and 310°C, the weight loss is attributed to the carbonization or the combustion of organic compounds, in other words, this weight reduction is due to the loss of carbon, hydrogen and oxygen. Between 310 and 480°C, the weight losses are probably ascribed to the further combustion of organic compounds. It can be seen that when the coating was heated at 500°C or above, there is basically no further weight loss, which infers that the organic groups are burnt off and a purely inorganic material has been formed. Evidently, These results

can be used to understand further the AFM results. The reason for the existence of relatively large pores in the film when the heat treatment temperature is at 300°C is thus due to the organic compounds being partially combusted or decomposed.

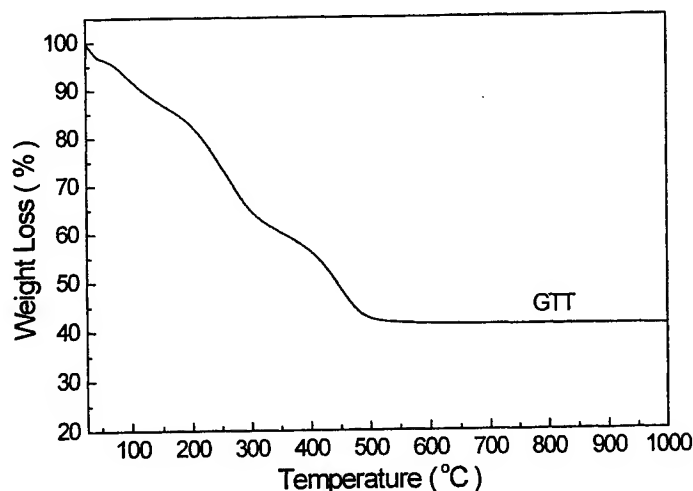


Fig.4 The TGA curves of the gel powders

3.3 Results and discussion of ellipsometry

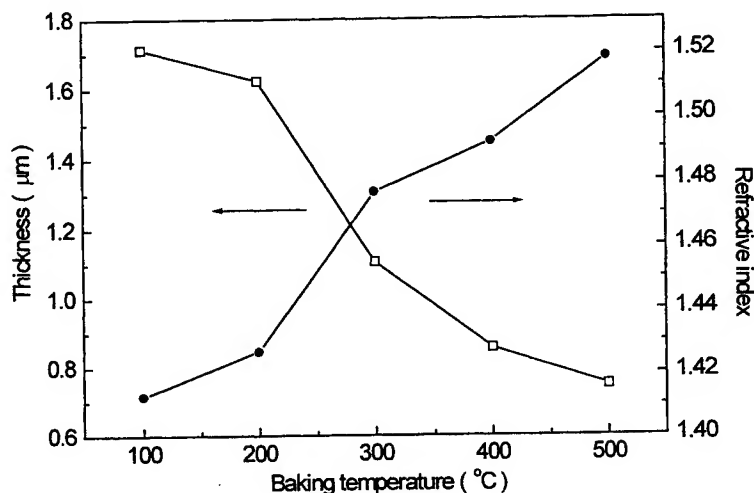


Figure 5 Dependence of the thickness and refractive index of the films on the baking temperature

Figure 5 shows the dependence of the film thickness and refractive index on the baking temperature. Here, the film was baked at 100, 200, 300, 400, and 500°C for 20 minutes respectively. It can be seen that with the temperature set at 100°C, a single spin-on layer with a thickness of more than 1.7 μm could be obtained on a silicon substrate. It can also be clearly seen that within the baking temperature range, the refractive index of the waveguide film can be varied from 1.40 to 1.52 at the wavelength of 633 nm. In addition, as the baking temperature rises, the refractive index increases and the film thickness drops. This is expected as the film would be more condensed when it is baked at a higher temperature. However, it should be noticed that the decrease in the film thickness is a lot more substantial when the baking temperature is between 200 and

400°C, which is probably due to the thermal decomposition and the combustion of the organic compounds. In fact, as have discussed in TGA section, the film could become purely inorganic $\text{SiO}_2\text{-TiO}_2$ film if the baking temperature is further increased. These results indicate that dense sol-gel GLYMO/ $\text{SiO}_2\text{/TiO}_2$ films can be obtained at a baking temperature between 100 and 200°C. In other words, a heat treatment temperature of between 100°C and 200°C is sufficient to obtain a dense and stable $\text{SiO}_2\text{/TiO}_2\text{/GLYMO}$ hybrid material planar waveguide films.

3.4 Results and discussion of UV-VIS transmission properties

Figure 6 shows the optical transmittance spectra of the films baked at different temperatures. Note that these films are single layer films with a thickness from about 0.7 μm to 1.7 μm (Fig.5). It can be seen that the films obtained at room temperature, or baked at 100 and 200°C all have relatively high transmittance, except for the absorption from organic solvents in the range between 300 nm and 360 nm. Evidently, the absorption of organic solvents disappears gradually with the increase of the baking temperature. However, the films baked at 300 and 400°C have a significantly larger absorption up to 700 nm, and in fact, noticeable discoloration was observed. On the other hand, the film baked at 500°C has a much higher transmittance than those baked at 300 and 400°C. In addition, no discoloration was observed, and the absorption of organic solvents has disappeared completely. Based on the results obtained by TGA in Fig. 4, this behavior can be explained as follows. The films baked at 300 and 400°C were porous due to the incomplete decomposition of the organic compounds. As a result, in addition to the absorption by the remaining acetylacetate complex, a relatively large degree of scattering of light from the pores was expected. When the baking temperature was increased to 500°C, the organic compounds would have been completely decomposed and a purely inorganic dense film was obtained. Consequently, the scattering and absorption caused by the relatively large pores and the remaining acetylacetate complex was thus substantially suppressed.

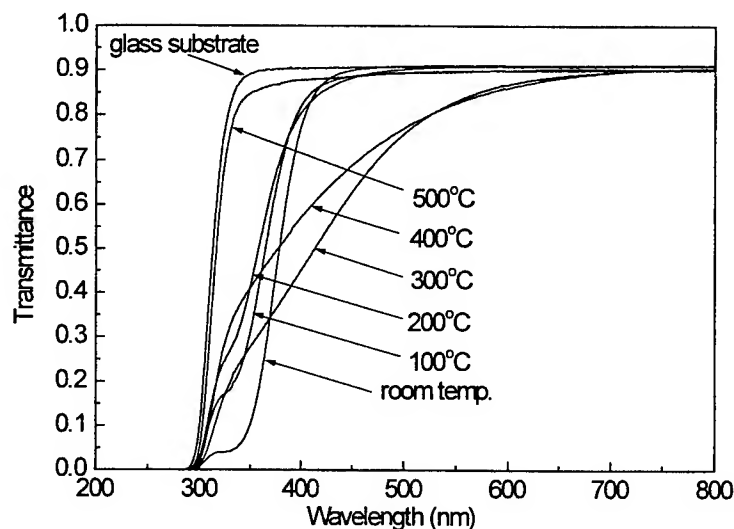


Figure 6 Dependence of optical transmittance of the films on the baking temperature

4. CONCLUSIONS

We have successfully developed a recipe to incorporate organic molecules into the inorganic sol-gel glass matrix and have obtained a single coating layer with a thickness of about 1.7 μm that is thick enough to enable the imprinting of optical channel waveguides or other passive devices for photonic applications. We have also studied the material structure and the optical properties of the planar waveguide films and have found that thickness and the refractive index of the films can be controlled by the processing conditions such as the baking temperature. The hybrid material waveguide films have also been studied using AFM, ellipsometry, and UV-VIS spectroscopy. These results indicate that a heat-treatment temperature below 200°C is sufficient to produce a sol-gel composite film, which is dense, stable, pore-free, and highly transparent. It

has also been noted that a purely inorganic and crack-free silica-titan films could be obtained after baking the hybrid material films at 500°C or higher.

REFERENCES

1. D. E. Zelmon, H. E. Jackson, J. T. Boyd, A. Naumaan, and D. B. Anderson, "A low scattering graded-index SiO_2 optical waveguide thermally grown on silicon," *Appl. Phys. Lett.*, **42**, pp. 565-566, 1983.
2. D. E. Zelmon, J. T. Boyd, and H. E. Jackson, "Low-loss optical waveguides fabricated by thermal nitridation of oxidized silicon," *Appl. Phys. Lett.*, **47**, pp. 353-355, 1985.
3. P. Gidon, S. Valette, and P. Mottier, "Integrated lenses on silicon nitride waveguides," *Opt. Eng.*, **24**, pp. 235-240, 1985.
4. G. Grand and S. Valette, "Optical polarizers of high extinction ratio integrated on oxidized silicon substrate," *Electron. Lett.*, **20**, pp. 730-731, 1984.
5. N. Imoto, N. Shimizu, H. Mori, and M. Ikeda, "Sputtered silica waveguides with an embedded three-dimensional structure," *J. Lightwave Technol.*, **LT-1**, pp. 289-293, 1983.
6. J. T. Boyd, R. W. Wu, D. E. Zelmon, A. Naumaan, H. A. Timlin, and H. E. Jackson, "Guided wave optical structures utilizing silicon," *Opt. Eng.*, **24**, pp. 230-234, 1985.
7. W. Stutius and W. Streifer, "Silicon nitride films on silicon for optical waveguides," *Appl. Opt.*, **16**, pp. 3218-3222, 1977.
8. C. H. Henry, R. F. Kazarinow, H. J. Lee, K. J. Orlowsky, and L. E. Katz, "Low loss Si_3N_4 - SiO_2 optical waveguides on Si," *Appl. Opt.*, **26**, pp. 2621-2624, 1987.
9. M. Kawachi, M. Yasu, and T. Edauro, "Fabrication of SiO_2 - TiO_2 glass planar optical waveguides by flame Hydrolysis deposition," *Electron. Lett.*, **19**, pp. 583-584, 1983.
10. N. Takao, M. Yasu, and M. Kawachi, "Low Loss high-silica single-mode channel waveguides," *Electron. Lett.*, **22**, pp. 321-322, 1986.
11. M. Kawachi, "Silica waveguides on silicon and their application to integrated-optics components," *Opt. Quantum Electron.*, **22**, pp. 391-416, 1990.
12. X. M. Du, T. Touam, L. Degachi, J. L. Guibault, M. P. Andrews, and S. I. Najafi, "Sol-gel waveguide fabrication parameters: an experimental investigation," *Opt. Eng.* **37**(4), pp. 1104-1104, 1998.
13. S. Holmes, R. R. A. Syms, Ming Li, and Mino Green, "Fabrication of buried channel waveguides on silicon substrates using spin-on glass," *Appl. Opt.* **32**(25), pp. 4916-4921, 1993.
14. S. Motakef, J. M. Boulton, and D.R. Uhlmann, "Organic-inorganic optical materials," *Opt. Lett.*, **19**, pp. 1125-1127, 1994.
15. Y. Sorek, M. Zevin, R. Reisfeld, T. Hurvits, and S. Ruschin, "Zirconia and zirconia-ORMOSIL planar waveguides prepared at room temperature," *Chem. Mater.*, **9**, pp. 670-676, 1977.
16. Y. Sorek, R. Reisfeld, I. Finkelstein, and S. Ruschin, "Sol-gel glass waveguides prepared at low temperature," *Appl. Phys. Lett.*, **63**, pp. 3256-3258, 1993.

Light emitting properties of sol-gel derived Er^{3+} -doped, Yb^{3+} -co-doped $\text{SiO}_2\text{-TiO}_2\text{-Al}_2\text{O}_3$ planar waveguide

Q. Xiang*, Y. Zhou, Y. L. Lam, Y. C. Chan and C. H. Kam

Photonics Research Group, School of Electrical and Electronic Engineering,
Nanyang Technological University, Nanyang Avenue, Singapore 639798

ABSTRACT

In this research, silica based planar waveguide and powdered glasses doped with Er_2O_3 , Yb_2O_3 , TiO_2 and Al_2O_3 have been fabricated by sol-gel process. The photoluminescence enhancement has been demonstrated to be seven and four times that without Yb co-doping when pumped by a 980 nm laser diode and a 488 nm Ar^+ laser respectively. The strongest fluorescence is observed from the 93 SiO_2 : 7 TiO_2 : 10 $\text{AlO}_{1.5}$: 0.5 $\text{ErO}_{1.5}$: 1 $\text{YbO}_{1.5}$ glass. Dependence of the photoluminescence intensity and lifetime on Er^{3+} as well as Yb^{3+} concentration has been experimentally studied.

Keywords: Yb codoped, Photoluminescence enhancement, Light emitting properties

1. INTRODUCTION

The $^4\text{I}_{13/2}$ to $^4\text{I}_{15/2}$ transition in Er^{3+} -doped thin films and glasses has generated considerable interest in recent years because its wavelength of 1.5 μm is within the third transmission window of silica-based fiber communication systems. Erbium-doped fiber amplifier (EDFA) pumped at 980nm has rapidly turned out to be a key component in all modern optical transmission systems. However, EDFA is still rather space consuming and does not allow for the integration of several functions on one chip. Thus, integrated optical devices, such as waveguide based amplifiers, and lasers that might be fully compatible with the well-established silicon technology, are of particular interest. A major drawback of Er^{3+} -doped optical devices integrated on Si is their inherent small size that requires a high doping level to be achieved. But, at a high Er^{3+} concentration, cooperative interactions such as up-conversion and fast energy migration between the Er^{3+} ions become apparent and will limit the 1.55 μm emission efficiency¹⁻³. This drawback can be overcome to a certain extent by co-doping Yb^{3+} ⁴⁻⁷. In such a case, the dominant mechanism of excitation of Er^{3+} ions is the energy transfer from the $\text{Yb}^{3+}\text{-}^2\text{F}_{5/2}$ level to the $\text{Er}^{3+}\text{-}^4\text{I}_{11/2}$ level.

In the last few years many authors have successfully demonstrated pulsed as well as continuous wave (CW) operation of Er^{3+} doped, and Yb^{3+} co-doped active materials in different hosts, such as bulk Er-Yb:phosphate glasses⁸⁻⁹, the silicate Er-Yb: Y_2SiO_5 (YSO)¹⁰⁻¹², the garnet Er-Yb: $\text{Y}_3\text{Al}_5\text{O}_{12}$ (YAG)^{12,13}, the oxyapatite Er-Yb: $\text{SrY}_4(\text{SiO}_4)$ ¹⁴, the Er-Yb: $\text{Ce:Ca}_2\text{Al}_2\text{SiO}_7$ (CAS) crystals¹⁵, and Er^{3+} - Yb^{3+} phosphate-based glass fibers¹⁶⁻¹⁷. All the above mentioned erbium-doped materials co-doped with ytterbium are generally used to decrease the threshold pump rate owing to an effective ytterbium to erbium transfer mechanism of the excitation energy.

In this research, using sol-gel process, we prepared Er-doped, Yb co-doped $\text{SiO}_2\text{-TiO}_2\text{-Al}_2\text{O}_3$ powdered glasses as well as planar waveguides. The luminescence enhancement resulting from Yb^{3+} co-doping was demonstrated. The photoluminescence at 1.55 μm and the lifetime of $\text{Er}^{3+}\text{-}^4\text{I}_{13/2}$ were measured by using 980 nm laser diode and 488 nm Ar^+ laser as pump sources.

2. SAMPLE PREPARATION CHARACTERIZATION

We previously reported the preparation steps of Er^{3+} -doped $\text{SiO}_2\text{-TiO}_2\text{-Al}_2\text{O}_3$ planar waveguides by sol-gel process¹⁸. We also described the processing procedures of powdered glasses of Er^{3+} -doped $\text{SiO}_2\text{-TiO}_2\text{-Al}_2\text{O}_3$ ¹⁹. Here the preparation steps of powdered glasses and planar waveguides are almost same as stated in reference 18 and 19 except for the Yb^{3+} element included in the solution here. $\text{Yb}(\text{CH}_3\text{COO})_3 \cdot 4\text{H}_2\text{O}$ was used as the precursor of Yb_2O_3 . It was dissolved in DI water before being added to the solution of $\text{SiO}_2\text{-TiO}_2\text{-Al}_2\text{O}_3\text{-Er}_2\text{O}_3$. 11 solutions with different constituent composition were prepared in

*Correspondence: Email: eqxiang@ntu.edu.sg; Tel: +65-7905461; Fax: +65-7904161

this experiment. Table I shows the recipes used. 11 powdered glasses corresponding to the 11 recipes in Table I were fabricated. We fabricated the 15-layer planar waveguide using only recipe 10.

The measurement of the PL intensity was carried out on all the 11 powdered glasses. The measurement system is shown in Figure 1, in which a single mode fiber pig-tailed 980 nm laser diode had its output beam collimated and was employed as the pumping source. The other parts of the system are the same as stated in reference 20. The fluorescence lifetime of Er^{3+} - ${}^4\text{I}_{13/2}$ from the 11 powdered glasses was measured using the setup as shown in Figure 2. The pump source is again the 980nm laser diode but it is mechanically chopped at 10 Hz. In the case of the 15-layer planar waveguide, the photoluminescence spectrum and lifetime were obtained by coupling a 488nm Ar^+ laser beam through a prism into the waveguide¹⁸⁻¹⁹.

Table I The sample compositions and their corresponding lifetime

Sample No.	Recipes used	Lifetime (ms)	
		Powder Glasses(at 980 nm)	Planar waveguide (at 488nm)
1	93 SiO_2 : 7 TiO_2 : 15 $\text{AlO}_{1.5}$: 1 $\text{ErO}_{1.5}$: 0.5 $\text{YbO}_{1.5}$	0.989	
2	93 SiO_2 : 7 TiO_2 : 15 $\text{AlO}_{1.5}$: 1 $\text{ErO}_{1.5}$: 1 $\text{YbO}_{1.5}$	0.959	
3	93 SiO_2 : 7 TiO_2 : 15 $\text{AlO}_{1.5}$: 1 $\text{ErO}_{1.5}$: 1.5 $\text{YbO}_{1.5}$	0.750	
4	93 SiO_2 : 7 TiO_2 : 15 $\text{AlO}_{1.5}$: 1 $\text{ErO}_{1.5}$: 2 $\text{YbO}_{1.5}$	1.13	
5	93 SiO_2 : 7 TiO_2 : 15 $\text{AlO}_{1.5}$: 0.05 $\text{ErO}_{1.5}$: 1 $\text{YbO}_{1.5}$	4.27	
6	93 SiO_2 : 7 TiO_2 : 15 $\text{AlO}_{1.5}$: 0.1 $\text{ErO}_{1.5}$: 1 $\text{YbO}_{1.5}$	4.14	
7	93 SiO_2 : 7 TiO_2 : 15 $\text{AlO}_{1.5}$: 0.5 $\text{ErO}_{1.5}$: 1 $\text{YbO}_{1.5}$	1.92	
8	93 SiO_2 : 7 TiO_2 : 15 $\text{AlO}_{1.5}$: 1.5 $\text{ErO}_{1.5}$: 1 $\text{YbO}_{1.5}$	0.72	
9	93 SiO_2 : 7 TiO_2 : 15 $\text{AlO}_{1.5}$: 2 $\text{ErO}_{1.5}$: 1 $\text{YbO}_{1.5}$	0.583	
10	93 SiO_2 : 7 TiO_2 : 10 $\text{AlO}_{1.5}$: 1 $\text{ErO}_{1.5}$: 2 $\text{YbO}_{1.5}$	0.976	3
11	93 SiO_2 : 7 TiO_2 : 10 $\text{AlO}_{1.5}$: 1 $\text{ErO}_{1.5}$	1.11	

Our intention was to find out the amount of enhancement of the photoluminescence intensity by co-doping Yb^{3+} . Samples 10 and 11 were thus meant for such a comparison, as sample 11 has no Yb^{3+} codoping while sample 10 has. In order to figure out the influence of Er and Yb concentrations on the overall photoluminescence properties, the rest of the samples were prepared. In samples 1-4, the Er^{3+} concentration was fixed and the Yb^{3+} concentration was varied. The dependence of photoluminescence (PL) intensity and lifetime on Yb^{3+} concentration was thus obtained from these four samples. Meanwhile, in sample 5-9 and 2, the Yb^{3+} concentration was fixed and different Er^{3+} concentration was used. By analyzing the photoluminescence intensity and lifetimes, we intended to get a suitable recipe for waveguide amplifier preparation.

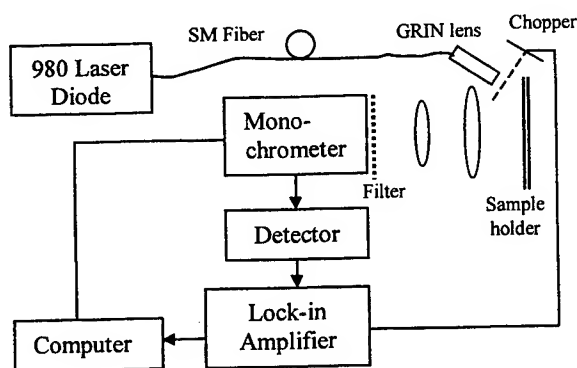


Figure 1 the measurement system of the PL spectra for Er-doped and Yb co-doped glasses by sol-gel process

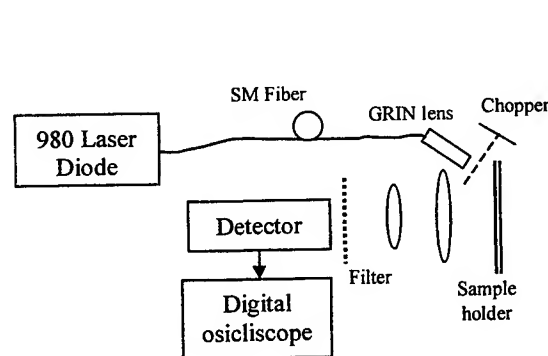


Figure 2 the measurement setup of the lifetime of Er-doped and Yb codoped glasses by sol-gel process

3. RESULTS

3.1 The photoluminescence of Er-doped, Yb-co-doped powdered glasses

Figure 3 shows the PL spectrum of Yb³⁺ co-doped sample as compared to the sample without Yb³⁺ co-doping (sample 10 and 11). As we can see, the PL intensity of the Yb³⁺ co-doped sample is seven times higher than that of the Yb-free sample. Figure 4 shows a simply energy level diagram of the Er-Yb material system. In the case of fluorescence enhancement, the emission of 1.55μm light from Er³⁺ includes the following four processes: (a) absorption of a pump photon from the ²F_{7/2} to ²F_{5/2} level of Yb³⁺, (b) energy transfer from the Yb³⁺ - ²F_{5/2} to Er³⁺ - ⁴I_{11/2} level, (c) non-radiative decay of Er³⁺ from ⁴I_{11/2} level to ⁴I_{13/2} level, and (d) radiative decay of Er³⁺ from ⁴I_{13/2} to ⁴I_{15/2}.

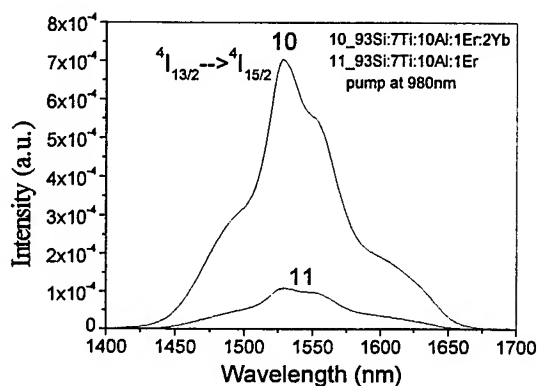


Figure 3 The PL enhancement of Yb³⁺ co-doped sample as compared with the Yb³⁺-free sample pumped at 980 nm

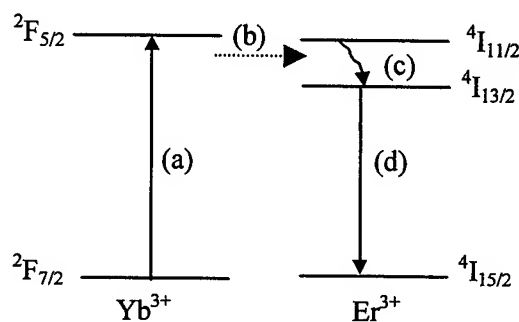


Figure 4 Energy level diagram of Er-Yb system

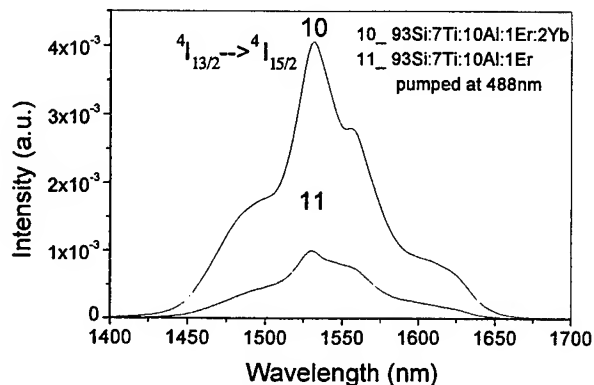


Figure 5 The PL enhancement of Yb³⁺ co-doped sample compared with the Yb³⁺-free sample pumped at 488 nm

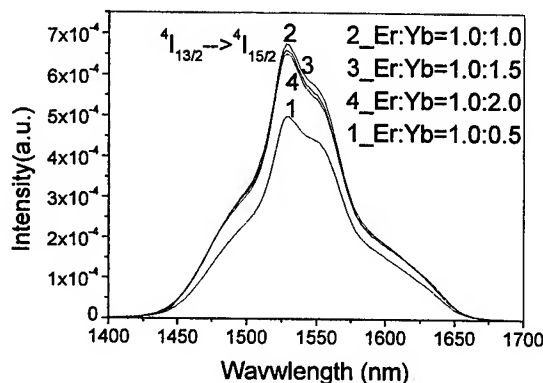


Figure 6 Dependence of the PL intensity of Er³⁺ on Yb³⁺ concentration pumped by 980nm laser diode

We also measured the PL of the same two samples using 488 nm Ar⁺ laser as the pump source, the spectrum curves are shown in Figure 5. As can be seen, four times higher PL intensity from the Yb³⁺ co-doped sample as compared to the Yb³⁺-free sample was obtained. Sensitization of the Er³⁺ emission by Yb³⁺ ions at an excitation wavelength of 488 nm (energy ~ 2.5eV) is an unexpected phenomenon, as the Yb³⁺ - ²F_{5/2} excited state is about 1.2-1.3 eV above the ground state ²F_{7/2} (the absorption wavelength is centered around 950 nm). However, the same phenomenon of PL enhancement via Yb co-doping under 488nm excitation has also been found in Er³⁺ and Yb³⁺ implanted SiO₂/Si films⁴. These results suggest that Yb³⁺ atoms in SiO₂ based glass networks form some complexes (excited Yb³⁺ center) that can perhaps absorb the 488nm light. These complexes mediate energy transfer from the excitation laser beam to the Er³⁺ ions. There exist two possible ways of energy

transfer from the excited Yb^{3+} center ($\text{Yb}^{\#}$). (a) The Er^{3+} ion is excited via the transfer of energy from the $\text{Yb}^{\#}$ center to one of the highly excited states of Er^{3+} such as $^4\text{F}_{7/2}$ and $^4\text{S}_{3/2}$, which is followed by rapid nonradiative relaxation to the $^4\text{I}_{13/2}$ metastable state. (b) The first stage of the process is intracenter nonradiative relaxation of the excited $\text{Yb}^{\#}$ complex, which brings the Yb^{3+} ion to its $^2\text{F}_{5/2}$ excited state. Excitation energy is then transferred to the Er^{3+} - $^4\text{I}_{11/2}$ state followed by relaxation to the $^4\text{I}_{13/2}$ emitting level. The fact that the enhancement pumped at 488 nm is less than the enhancement pumped at 980 nm shows that the absorption of the suggested complex for the 488nm pump is weaker than that of the Yb^{3+} ion for the 980 nm pump.

Figure 6 shows the photoluminescence spectra of sample 1- 4 where the Er^{3+} concentration is fixed and the Yb^{3+} concentration is changed. As can be seen, samples 2, 3 and 4 have almost the same photoluminescence intensity, while sample 1 has a slightly lower PL intensity. These results imply that the ion ratio of Yb/Er should not be less than one in order to enable to effective energy transfer, in other words at least Yb ion is needed for one Er ion. Meanwhile, it can be found that when the Yb/Er ratio is more than one, the enhancement seems to have somehow saturated. The lifetime difference of these four samples is found very small and this means that Yb^{3+} has little influence on the lifetime of Er ion at $^4\text{I}_{13/2}$. Meanwhile, the lifetime of all the four samples is relatively short and most likely, this comes from the concentration quenching effect because of the relatively high total rare earth ion concentration (2-3.5 mole).

Figure 7 is the photoluminescence spectra of the samples 5 - 9 and 2. The six samples have the same Yb^{3+} concentration but different Er^{3+} concentration. The results show that sample 7 has the strongest photoluminescence intensity among the six samples and its recipe is $93\text{SiO}_2:7\text{TiO}_2:15\text{AlO}_{1.5}:0.5\text{ErO}_{1.5}:1\text{YbO}_{1.5}$. The mole ratio of Yb/Er is two. However, the corresponding lifetime is relatively short as compared to that of samples 5 and 6. Referring to the lifetime as shown in Table I, it can be seen that the lifetime generally decreases relatively quickly with the increment of Er^{3+} concentration, especially in the range of 0.1 to 1.0 mole. Figure 8 is the curve of lifetime against the Er^{3+} concentration. The quenching concentration of Er^{3+} , that is, the Er^{3+} concentration for which the fluorescence lifetime of the metastable level $^4\text{I}_{13/2}$ is half of that found at very low concentration⁶, of our sample series is around 0.5 mole and is thus that of recipe 7.

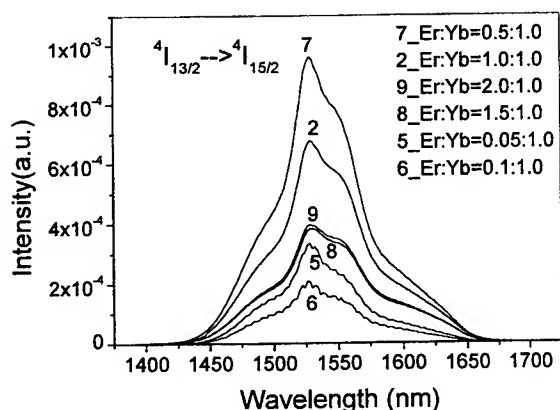


Figure 7 The PL spectra of the samples which have the different Er^{3+} concentration and same Yb^{3+} concentration

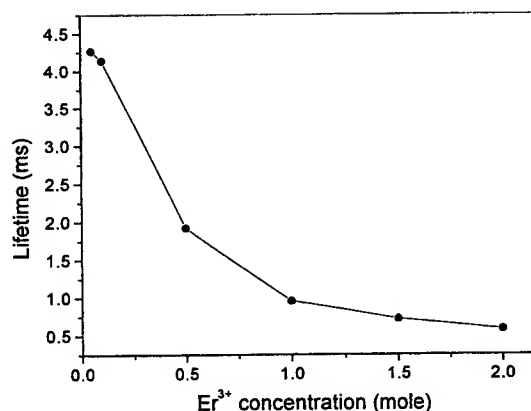


Figure 8 The dependence of the $\text{Er } ^4\text{I}_{13/2}$ lifetime on the Er concentration

3.2 Active properties of the planar waveguide

As stated above, the recipe used to fabricate the planar waveguide is $93 \text{ SiO}_2 : 7 \text{ TiO}_2 : 10 \text{ AlO}_{1.5} : 1 \text{ ErO}_{1.5} : 2 \text{ YbO}_{1.5}$. The planar waveguide was deposited on SOS substrate by using multiple spin-coating and rapid thermal annealing in a rapid thermal processor (RTP). In the RTP, the film was heated up to 900°C in 30 seconds, kept at 900°C for 15 seconds, and then cooled down to room temperature in 30 seconds. A post-annealing was carried out on the planar waveguide after 15 layers were deposited. We measured the photoluminescence and lifetime of Er^{3+} - $^4\text{I}_{13/2}$ under 488 nm Ar⁺ laser pump.

Figure 9 is the photoluminescence spectrum of the 15-layer planar waveguide pumped at 488 nm. Figure 10 shows the fluorescence decay of this 15-layer planar waveguide. A lifetime $t_{1/e}$ of 3.0 ms was obtained by a first order exponential fitting. It is noted that the $t_{1/e}$ of the powdered glass with same composition as that of the planar waveguide is only 0.976 ms

under 980 nm pump (shown in Table I). The difference may come from two possible reasons, firstly, the different OH concentration in the powdered glass and in the planar waveguides, secondly, the different sample volume that is exposed to the pump light, and thirdly, the different pump wavelength and pump power. Apparently, more studies need to be carried out.

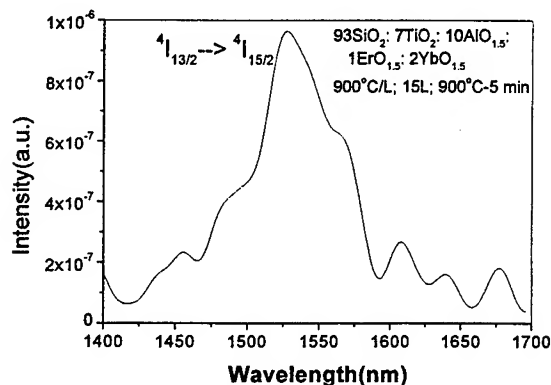


Figure 9 The PL spectrum of Er^{3+} doped, Yb^{3+} codoped 15-layer planar waveguide pumped by 488 nm

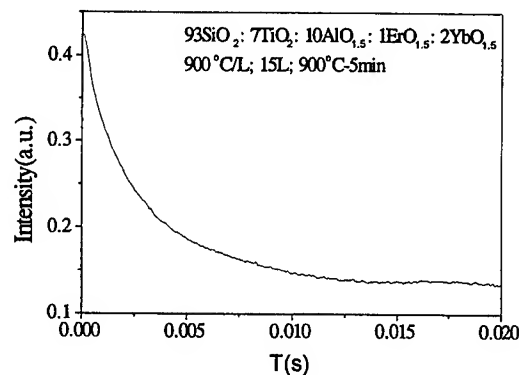


Figure 10 The fluorescence decay of the Er^{3+} doped, Yb^{3+} codoped 15-layer planar waveguide pumped by 488 nm

4. CONCLUSION

Silica based planar waveguides and powders doped with Er_2O_3 , Yb_2O_3 , TiO_2 , and Al_2O_3 have been fabricated by sol-gel process. We studied the influence of the material's Er^{3+} and Yb^{3+} composition on its fluorescence properties and demonstrated that Yb^{3+} co-doping can indeed enhance the 1.55 μm fluorescence substantially. Using a molar ratio of $93\text{SiO}_2:7\text{TiO}_2:10\text{AlO}_{1.5}:1\text{ErO}_{1.5}:2\text{YbO}_{1.5}$, a 15 layer planar waveguide with a relatively strong fluorescence and a relatively long lifetime (3ms) has been fabricated on a silica-on-silicon substrate. The fluorescence spectrum and lifetime of the powder glasses with different Er^{3+} and Yb^{3+} mole contents are compared and experimentally we found that a Yb/Er ratio of about one is a good choice for an efficient enhancement of the 1.55 μm light emission and also that the quenching concentration of Er is about 0.5 mole%.

REFERENCES

1. V. P. Gapontsev, S. M. Matitsin, A. A. Isineev, and V. B. Kravchenko, *Opt. Laser Technol.* **14**, 189 (1982).
2. E. Snoeks, G. N. van den Hoven, and A. Polman, *J. Appl. Phys.* **73**, 8179 (1983).
3. E. Snoeks, G. N. van den Hoven, A. Polman, B. Hendriksen, M. B. J. Diemeer, and F. Priolo, *J. Opt. Soc. Am. B* **12**, 1468 (1997).
4. A. Kozanecki, K. Homewood, and B. J. Sealy, "Sensitization of Er^{3+} emission at 1.5 μm in SiO_2 thermally grown on silicon by coimplantation of Yb", *Appl. Phys. Lett.*, **75**, 793 (1999).
5. Gang Gu, P.P. Ong, Jinhua Cai, Wei Yang, Youwei Du, Shihe Yang, "Enhanced luminescence of silica thin films co-doped with Er^{3+} and Yb^{3+} ", *Thin Solid Films*, **340**, 230-232(1999).
6. Xavier Orignac, Denis Barbier, Xin Min Du, Rui M. Almeida, Orla McCarthy, Eric Yeatman, "Sol-gel silica/titania-on-silicon Er/Yb-doped waveguides for optical amplification at 1.5 μm ", *Optical Materials*, **12**, 1-18(1999).
7. A. Shooshtari, T. Touam, S. I. Najafi, " Yb^{3+} sensitized Er^{3+} -doped waveguide amplifiers: a theoretical approach", *Optical and Quantum Electronics* **30**, 249-264(1998).
8. J. A. Hutchinson, T. H. Allik, *Appl. Phys. Lett.* **60**, 1424(1992).
9. B. Labranche, A. Mailloux, M. Levesque, Y. Taillon, M. Morin, P. Mathieu, *OSA Proceedings on Advanced Solid-State Lasers*, **24**, 379(1993).
10. C. Li, R. Moncge, J. C. Sourieau, C. Borel, C. Wyon, *Opt. Commun.* **107**, 61(1994).
11. K. Spariosu, R. D. Stultz, M. b. Camargo, S. Montgomery, M. Birbaum, B.H.T. Chai, *OSA Proceedings on Advanced Solid-State Lasers*, **20**, 156(1994).
12. T. Schweizerr, T. Jensen, E. Heumann, G. Huber, *Opt. Commun.* **118**, 557(1995).
13. K. Spariosu, M. Birbaum, *OSA Proceedings on Advanced Solid-State Lasers*, **13**, 127(1992).

14. J. C. Sourian, P. Romero, C. Borel, C. Wyon, C. Li, R. Moncroe, *Appl. Phys. Lett.* **64**, 2024(1994).
15. B. Simondi-Teisseire, B. Viana, A.-M. Lejus, J.-M. Benitez, D. Vivien, C. Borel, R. Templier, C. Wyon, *IEEE J. Quantum Electron.* **QE-32**, 2024(1996).
16. K. Hsu, C. H. Miller, J. T. Kringlebotn, E. M. Taylor, J. E. Townsend, D. N. Payne, *Opt. Lett.* **19**, 886(1994).
17. K. Hsu, C. H. Miller, J. T. Kringlebotn, D. N. Payne, *Opt. Lett.* **20**, 337(1995).
18. Q. Xiang, Y. Zhou, Y.L. Lam, Y.C. Chan and C.H. Kam, "Preparation and Characterization of Er-doped SiO₂-TiO₂-Al₂O₃ planar optical waveguide by Sol-gel Method", *Photonics West '99*, **SPIE.3622**, 18(S4), San Jose, California, USA, 23 – 29 January 1999.
19. Q. Xiang, Y. Zhou, Y.L. Lam, Y.C. Chan, and C.H. Kam, "Comparison of Er-doped sol-gel glasses with various hosts", *ISPA'99*, Singapore, 29 Nov.- 3 Dec. 1999.
20. Q. Xiang, Y. Zhou, Y.L. Lam, Y.C. Chan, and C.H. Kam, "Influence of Al/Nd ratio on light emitting properties of Nd doped glass by sol-gel process", *ISPA'99*, Singapore, 29 Nov.- 3 Dec. 1999.

Temperature-dependent luminescence and energy transfer in Europium and rare earth codoped nanostructured Sol-gel SiO₂ glasses

S. Buddhudu*, M. Morita⁺, Hong Xi Zhang, C.H.Kam, Yee Loy Lam, Yan Zhou,
Terence K.S. Wong, Yuen Chuen Chan, Boon Siew Ooi, Seng Lee Ng and Wenxiu Que

Photonics Research Group, Microelectronics Division, School of Electrical and Electronic
Engineering Nanyang Technological University, Singapore 639798

⁺Department of Industrial Chemistry, Seikei University, Tokyo-180, Japan

ABSTRACT

Temperature- dependent luminescence spectra, lifetimes and energy transfer in Eu³⁺ and other rare earths (La³⁺, Pr³⁺, Nd³⁺, Sm³⁺, Gd³⁺, Dy³⁺, Er³⁺ & Yb³⁺) codoped sol-gel SiO₂ glasses, were investigated in the temperature range from 10K to 300K. Due to the addition of the other rare earths as co-dopants, luminescence spectra of Eu³⁺ have shown significant changes not only in spectral intensities but also in emission peak features. Evaluation of the temperature- dependent energy transfer rates and lifetimes and the computation of critical energy transfer distances by employing two different energy transfer model schemes, have provided evidence for such luminescence behavior in the nanometer- size confined glass matrices.

Keywords: Eu³⁺ sol-gel glasses, luminescence spectra, energy transfer

1. INTRODUCTION

Sol-gel glasses have been considered to be more promising and strategic materials to realize quantum confined luminescence phenomena and as new phosphor materials for high density TV and compact lasers.^{1,2} Sol gel method provides a convenient alternative to the traditional melting method for the preparation of rare earth ions doped glasses for optical studies, this method permits lower temperature processing, higher sample homogeneity and purity and the opportunity to prepare a variety of new optical materials in both bulk and film form with ease. There has been a great deal of interest in the luminescence of impurity ions doped sol-gel SiO₂ glasses in which bright emission in the visible spectral regions has been observed at room temperature due to ligand to metal charge transfer.³ Strong surface effects and nanometer size limited optical properties have been reported for sol-gel glasses.⁴⁻⁷ Excitation energy transfer processes of rare earth ions in conventional glasses have also been reported in literature.⁸ However, no report has so far been made available in literature on energy transfer of rare earth ions in sol gel glasses. Keeping in view of the technological importance of these sol-gel materials, it would therefore be of more interest to study systematically the excitation energy transfer in such rare earth ions co-doped glasses which possess nano-structured networks. In the present paper, we report the luminescence spectra and decay profiles of Eu³⁺ ions co-doped glasses. The purpose is to investigate the presence of any phase transitions in the optical materials with the change in temperatures (10K to 300K) through the measurement of temperature dependent luminescence and lifetimes. Such a study is considered very important for the preparation of phosphor based luminescence display devices without phase transitions both at room and low temperatures as well. The luminescence spectra and the decay times of Eu³⁺ doped sol-gel glasses in the absence and the presence of co-dopants, were analyzed by two different models namely Dexter and Krol.

* Correspondence: email: ebsrin@ntu.edu.sg, Telephone (65)7905985; Fax (65)791-2687

2. EXPERIMENTAL STUDIES

We have prepared sol-gel SiO_2 glasses doped with Eu^{3+} (1mol%) and RE^{3+} ($\text{RE}=\text{La, Pr, Nd, Sm, Gd, Dy, Er, Yb}$) ions by mixing tetraethylortho-silicate (TEOS), diethoxydimethyl-silane (DEDMS) and rare earth nitrates in suitable proportions by the method described earlier.⁹ We have carried out measurements of luminescence and lifetimes under a N_2 laser (337.1nm) excitation with a microcomputer controlled Spex-1401 spectrophotometer system fitted with a PMT (Hamamatsu Model C-3350), a lock-in amplifier (of the model Sr-400) and two channel gated photon counter. The luminescence spectral studies were carried out for different Eu^{3+} dopant ion concentrations (0.5 to 2.0). Brighter luminescence was observed at 1 mole%, hence the dopant rare earth ion concentration has been fixed at 1 mol% in sol gel glasses for investigation in the present work. The decay curves in the absence of co-dopants were non-exponential and hence for the codoped glasses, double exponential fitting was carried out. The decay curves of the emission transitions were measured at different temperatures by using a Tektronix TDS-420 four channel digital oscilloscope. The low temperature cryogenic system was a Helium Unit from M/s Displex Air Products fitted with a temperature controller (9600-1 Silicon diode from Scientific Inst. Inc. Tokyo, Japan).

3. RESULTS AND DISCUSSION

Figure 1 presents the luminescence spectra of Eu^{3+} doped xerogel (dried glass) and sol gel (annealed) silica glasses. Eu^{3+} ions excited to the $^5\text{D}_0$ metastable level emit luminescence through the $^5\text{D}_0 \rightarrow ^7\text{F}_J$ ($J=0,1,2,3,4$) transitions in the 0.55 to 0.72 μm wavelength. From this it is found that the intensity of the prominent red emission band ($^5\text{D}_0 \rightarrow ^7\text{F}_2$ at 612nm) in the annealed sample is approximately 2 times more than that in the unannealed sample. However, the other transitions have not shown such a significant change, so for the production of rich luminescent phosphor devices, annealing is considered quite essential, as we understand from Fig. 1.

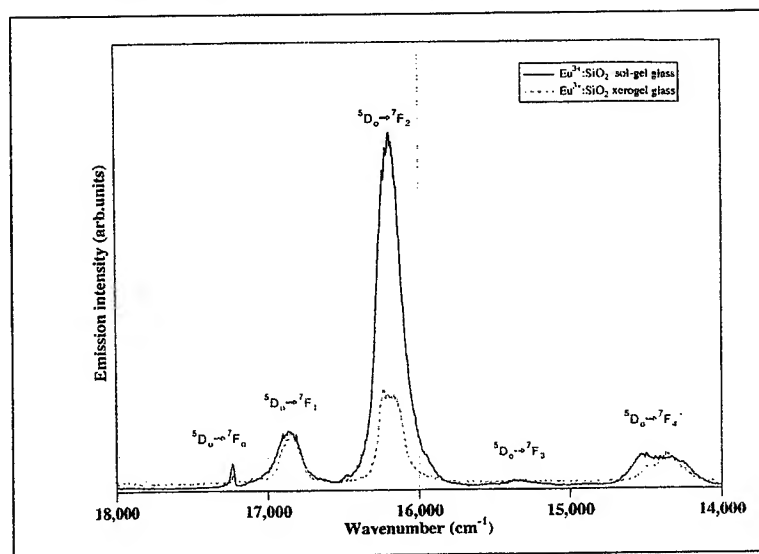


Figure 1 Luminescence spectra of unannealed and annealed $\text{Eu}^{3+}:\text{SiO}_2$ glasses at 300K

The $^5\text{D}_0 \rightarrow ^7\text{F}_0$ transition is very weak, as is expected from the selection rules. It appears in the spectrum only because of J mixing. The $^5\text{D}_0 \rightarrow ^7\text{F}_1$ is allowed by the magnetic dipole process. This is the only magnetic dipole transition, in agreement with the selection rules. All the other transitions are electric dipole in character, being induced by odd-parity components. Both $^5\text{D}_0 \rightarrow ^7\text{F}_{2,4}$ transitions are strong, whereas the $^5\text{D}_0 \rightarrow ^7\text{F}_3$ transition is weak, in general agreement with the Judd-Ofelt selection rules for electric dipole transitions. For rare earth ions in sol-gel glasses there exist two types of non-radiative transition processes, one is the interaction between the rare earth ions, and the other is that between the rare earth ions and the hosts. The non-radiative transition caused by the interaction of rare earth ions is a process of resonant energy transfer. The interactions of the same rare earth ions bring about concentration quenching effect, while those of different rare earth ions cause dopant quenching and sensitizing. The preliminary condition for resonant energy transfer is the energy gap between transition energy levels of two ions. In the sensitized fluorescence the energy absorbed by sensitizing ions could be transferred to fluorescence ions by

means of resonant energy transfer. The energy transfer process in inorganic materials has theoretically been explained by Forster and Dexter ¹⁴⁻¹⁶, where the excitation is transferred from a donor ion (D) to an acceptor (A), separated by a distance R_0 (nm). The Figure 2 shows the temperature dependent luminescence in the absence of codopants, dependence of luminescence upon the temperature change is linear and there are no changes in the emission band shapes due to substantial reduction of multiphonon process to suppress the non-radiative transitions and hence a significant enhancement of radiative luminescence intensity at lower temperatures. Figure 3 shows the temperature dependent luminescence of Eu^{3+} and Dy^{3+} doped sol gel glasses that have very short lifetimes. The non-radiative transition caused by the interaction of rare earth ions is a process of resonant energy transfer. Dexter has indicated the resonant energy transfer probability is inversely proportional to the sixth power of the distance between the two centers (R_0), if two centers belong to the dipolar transition, and energy transfer probability will be inversely proportional to higher magnitude of distance (R_0) ($>6^{\text{th}}$ power) in case of quadripole transitions. Experiments show the non-radiative transition probability of Eu^{3+} - Eu^{3+} is proportional to N_0^2 , so it is inversely proportional to the sixth power of the distance (R_0) and the interaction of Eu^{3+} - Eu^{3+} might be considered as dipole resonant energy transfer. In the case of sensitized fluorescence(Eu^{3+} - Ln^{3+}), the energy absorbed by sensitized ions(Ln^{3+}) can be transferred to the fluorescence ions(Eu^{3+}) by means of resonant energy transfer. The non-radiative transition process has been considered as a multiphonon relaxation process. The non-radiative transition probability of multiphonon process relies first of all on the phonon order i.e. the energy gap of the energy levels, and also the phonon energy. The former determines the energy level structure of rare earth ions and the latter is dependent on the structure of hosts. From fig.1, it is clear that the annealed sample reveals better luminescence spectra with a significantly controlled multiphonon process, due to the uniform distribution of dopant rare earth ions in the sol gel silica glass compared to the unannealed xerogel glass.

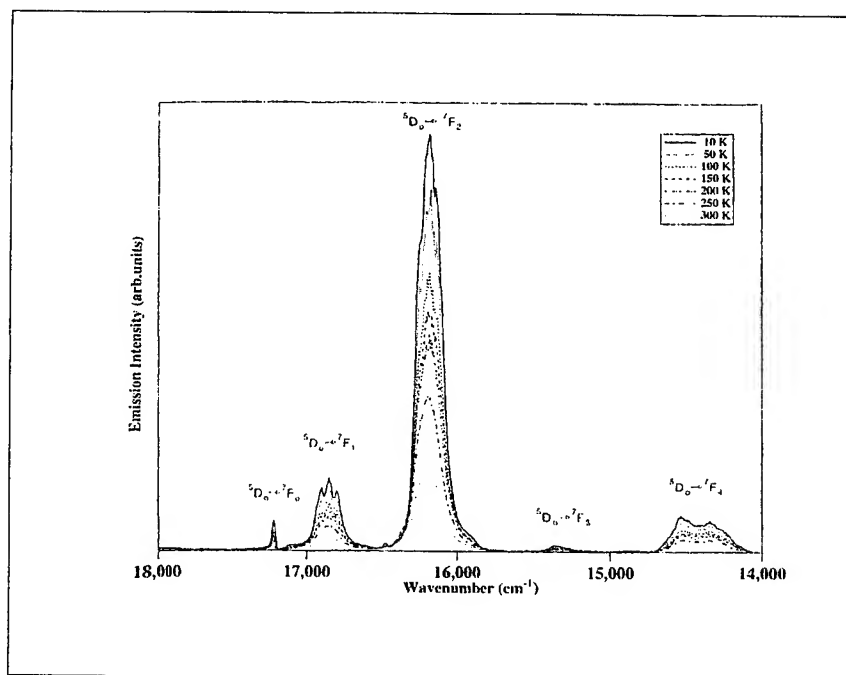


Figure 2 Temperature dependence of luminescence spectra of Eu^{3+} (1mol%) doped sol-gel SiO_2 glass between 10K and 300K.

Emission intensities are normalized to the spectrum at 10K. The decay curves of the Eu^{3+} , Dy^{3+} doped sol gel silica glass are shown in Figure 4, and Figure 5 reveals the broadening and structural changes in the emission bands of Eu^{3+} due to the presence of Yb^{3+} . The spectral features of Eu^{3+} are very significantly influenced by four other lanthanide (La, Pr, Dy, Nd) codopants as well, as we can see from the data given in Tables 1 and 2 respectively. For the optical materials investigated, due to the presence of the codopants, their decay curves have short lifetimes and non-exponential decay patterns because of D-D migration as well as D-A transfer. At lower temperatures, the D-D migration is slow as compared with the D-A transfer; consequently, the decay behavior represents diffusion-limited transfer. The weakness of the donor migration at low temperatures could be seen with $^5\text{D}_0 \rightarrow ^7\text{F}_0$ (forbidden transition). At higher temperatures the higher J states of the ground $^7\text{F}_J$ manifold are occupied the Eu-Eu migration

that involves the stronger $^5D_0 \rightarrow ^7F_{1,2}$ transitions and becomes more effective. Particularly in Eu-Dy, Eu-Yb, Eu-La, Eu-Pr, Eu-Nd, the D-A energy transfer is more predominant as the codopant ions occupy irregular sites with distinct absorption and emission transitions.

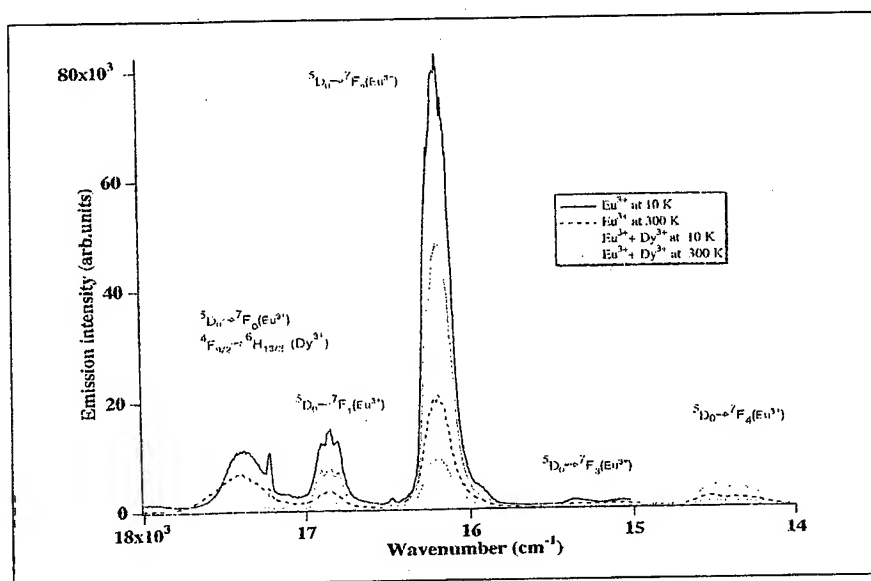


Figure 3 Spectral changes of luminescence from Eu^{3+} (1mol%), $\text{Eu}^{3+} + \text{Dy}^{3+}$ (1mol%) SiO_2 glasses at 300K and 10K

Measurement of the luminescence and lifetime shows that in the dual rare earths doped sol-gel glasses, the lifetimes are found to be shorter compared to singly doped Eu^{3+} doped glasses (Fig.4 and Table 1).

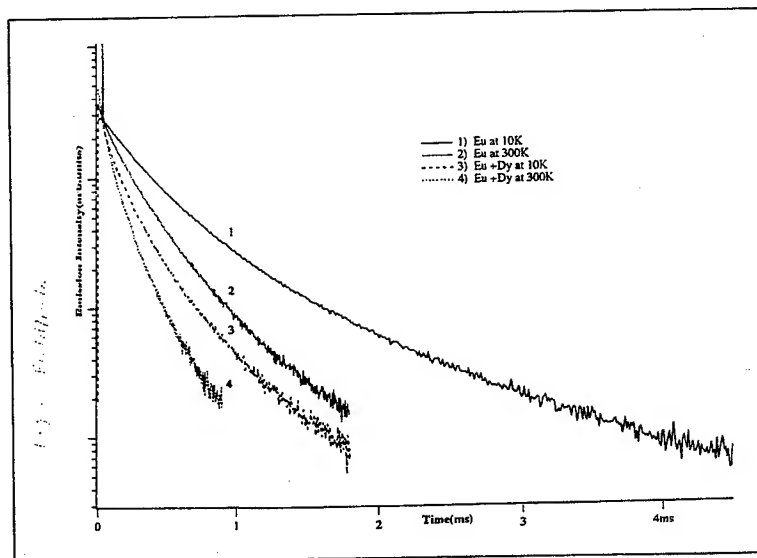


Figure 4 Decay curves of the prominent emission transition ($^5D_0 \rightarrow ^7F_2$ at 612nm) of $\text{Eu}^{3+}:\text{SiO}_2$ sol gel glasses with and without the codopant Dy^{3+} ions at 300K and 10K

Table 1 Comparison of the measured (double exponential fitted) average lifetimes (μs) of the prominent red emission transition ($^5\text{D}_0 \rightarrow ^7\text{F}_2$) at 612 nm of Eu^{3+} and Eu^{3+} codoped with other lanthanide ions at 300 K and 10 K

Sol-gel Glass	$^5\text{D}_0 \rightarrow ^7\text{F}_2$ at 612 nm	
	Γ at 300K (μs)	Γ at 10K (μs)
Eu^{3+}	419	671
$\text{Eu}^{3+}, \text{La}^{3+}$	109	186
$\text{Eu}^{3+}, \text{Pr}^{3+}$	105	180
$\text{Eu}^{3+}, \text{Nd}^{3+}$	121	193
$\text{Eu}^{3+}, \text{Sm}^{3+}$	126	206
$\text{Eu}^{3+}, \text{Gd}^{3+}$	217	374
$\text{Eu}^{3+}, \text{Dy}^{3+}$	92	137
$\text{Eu}^{3+}, \text{Er}^{3+}$	152	240
$\text{Eu}^{3+}, \text{Yb}^{3+}$	99	150

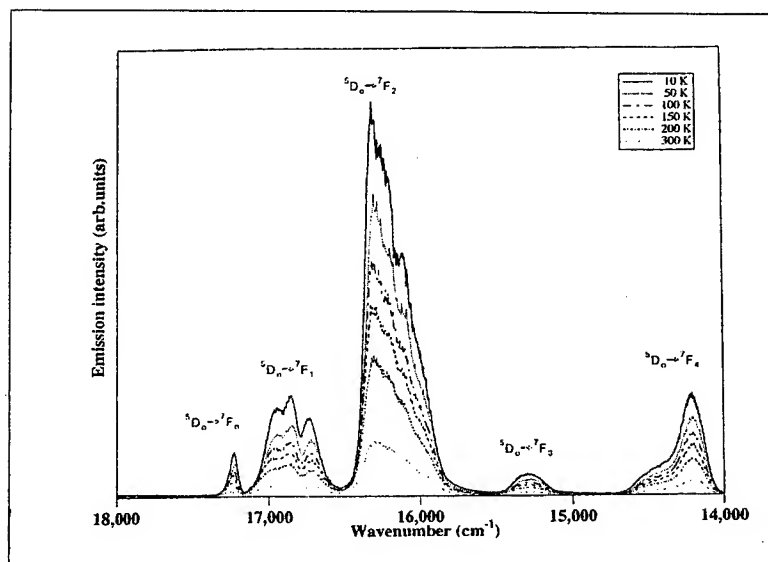


Figure 5 Temperature dependence of luminescence spectra of $\text{Eu}^{3+}:\text{SiO}_2$ sol gel glass with Yb^{3+} as the co-dopant ions

The decay curves of the emission transitions (one prominent $^5\text{D}_0 \rightarrow ^7\text{F}_2$ and other transitions $^5\text{D}_0 \rightarrow ^7\text{F}_{0,1,3,4}$) of the Eu^{3+} luminescence in singly doped and co-doped sol-gel glasses have been analyzed by deducing the energy transfer rate (W_{ET}), critical distance (R_0), energy transfer efficiency (η_{ET}), as detailed below.¹⁰⁻¹² The luminescence intensity $I(t)$ is approximated by sum of two exponential decay components from

$$I(t) = A_1 \exp(-t/\Gamma_1) + A_2 \exp(-t/\Gamma_2) \quad (1)$$

where Γ_1 and Γ_2 are faster and slow decay components respectively. Parameters A_1 and A_2 are weighting factors of fitting to provide reasonable estimate of average values in the cases of complicated decay profiles. Using the above equation, the average lifetime $\langle \Gamma \rangle$ could be given by

$$\langle \Gamma \rangle = (A_1 \Gamma_1^2 + A_2 \Gamma_2^2) / (A_1 \Gamma_1 + A_2 \Gamma_2) \quad (2)$$

Two different models of the energy transfer have been employed while determining the energy transfer. The first one is based on Dexter-Inokuchi model for resonant energy transfer by considering the energy transfer in rare earth ions in sol glasses due to resonant energy transfer from donor to acceptor levels. The energy transfer probability (s^{-1}) in each glass is obtained from¹³⁻¹⁴

$$W_{tr} = \langle \Gamma_0 \rangle^{-1} + \langle \Gamma \rangle^{-1} \quad (3)$$

Where Γ_0 & Γ are the lifetimes of the donor (Eu^{3+}) ion in the absence and presence of acceptor ion (Ln^{3+}) respectively. In the second model namely the Krol model,¹¹ total transfer rate (W_{tr}^t) is obtained from

$$W_{tr}^t = \sum W_{tr} ({}^5D_0 \rightarrow {}^7F_{J=0,1,2,3,4}) \quad (4)$$

In Krol model the average lifetime is computed from

$$\langle \Gamma \rangle^{-1} = \langle \Gamma_1 \rangle^{-1} + \langle \Gamma_2 \rangle^{-1} \quad (5)$$

This equation is comparable with the first model expression with the neglect of weighting factors A_1 and A_2 . In addition to the prominent transition lifetime, the lifetimes of other emission transitions have also been taken into account to evaluate the transfer rate and the efficiency in the sol gel glasses examined in the present work. The computed critical distances of energy transfer at 300K and 10K in sol-gel glasses are shown in Table 2.

Table 2 Critical distance R_0 (nm) for the energy transfer process in Eu^{3+} and codopant rare earth ions in sol-gel glasses at 10K and 300K

Sol-gel glasses	Dexter Model		Krol Model	
	300K	10K	300K	10K
Eu^{3+}, La^{3+}	0.84	0.81	0.86	0.82
Eu^{3+}, Pr^{3+}	0.96	0.90	0.99	0.96
Eu^{3+}, Nd^{3+}	0.90	0.88	0.92	0.89
Eu^{3+}, Sm^{3+}	0.79	0.76	0.81	0.80
Eu^{3+}, Gd^{3+}	0.87	0.84	0.90	0.89
Eu^{3+}, Dy^{3+}	0.99	0.93	1.07	1.03
Eu^{3+}, Er^{3+}	0.86	0.85	0.89	0.87
Eu^{3+}, Yb^{3+}	0.92	0.90	0.97	0.95

In the Dexter model only the prominent peak (${}^5D_0 \rightarrow {}^7F_2$) was considered, however in the Krol model all terminal levels are considered, because the relative emission intensities are found to be varying due to the change of codopants with Eu^{3+} dopants in sol-gel silica glasses. The critical distance of the energy transfer (R_0) is derived from¹⁵⁻¹⁶

$$R_0 = (9W_{tr} \langle \Gamma_0 \rangle / 16\pi^2 C^2)^{1/6} \quad (6)$$

where C is the concentration of an acceptor (Ln^{3+}) ion. The energy transfer efficiency η_{tr} has been evaluated from the expression

$$\eta_{tr} = W_{tr} \Gamma = 1 - (\Gamma / \Gamma_0) \quad (7)$$

where Γ_0 and Γ are average lifetimes of the donor ion (Eu^{3+}) in the presence and absence of acceptor ions, respectively. Smooth and continuous increase in the luminescence intensity was observed with the lowering of the temperature down to 10K from the room temperature 300K. Meanwhile no phase transitions was found in these sol-gel glasses. Due to absence of low temperature phase transitions, it should be stated that these novel optical materials could be used to carry out investigations on the multiphonon relaxation process by measuring the fluorescence line narrowing. They can also be used with other laser techniques to study confined amorphous structures. Sharp emission levels observed in our sol-gel glasses (Figs.1 and 2) confirm that due to homogenous distribution of dopant rare earth ions in the host matrices, broadening of lines results from a combination of the sharp line emissions at different frequencies from dopant ions (co-dopant rare earth) at distinct sites.

4. CONCLUSION

We have investigated luminescence, decay times and energy transfer processes in sol-gel SiO_2 glasses doped with Eu^{3+} and other codopants in the temperature range between 10K and 300K. We have not observed any phase transitions below 300K, hence temperature dependent luminescence and decay time behavior of the Eu^{3+} ion can serve as good probes to monitor the dynamics of energy transfer in the nanometer size sol-gel glasses. The decay curves were analyzed by two models: resonant energy transfer by Dexter-Inokuch¹³⁻¹⁶ and trapping limited energy transfer by Krol and Roos¹¹. We have fitted the decay curve with two exponents and used two methods to derive the average decay times from these the decay times. By phenomenological derivation of critical distance (R in nm) of the energy transfer, we have found that the critical distances are about 1 nm in the sol gel glasses at both 10K and 300K. This paper provides the evidence of excitation energy transfer that is confined in nano-structured sol-gel glass networks. The luminescence intensity was not satisfactory in the dried xerogel glasses due to nonhomogeneous distribution of dopant rare earth ions in the glasses. The pore size confinement affects the optically active rare earth ions. In the case of annealed sol-gel glasses, the temperature dependent luminescence spectra and lifetimes of the Eu^{3+} singly doped and codoped with other rare earth ions show that there exist no phase transitions. We believe that these sol-gel luminescent phosphor materials are useful for screen coating of TVs and CRTs.

REFERENCES

1. C.J.Brinker,G.W.Scherer,*Sol Gel Science*, Academic Press,San Diego,1990
2. M Guglielmi, P.Colombo,L.Mancinelli Degli Esponsti, G.C.Righini,S.Pelli, *Glasses for optoelectronics-II*, SPIE,1513(1991)2
3. B.T.Stone and K.L.Bray *Er^{3+} doped silica and hybrid organic/inorganic silica gels* Mat.Res.Soc.Symp.Proc. 435(1996)617
4. C.J.Brinker, G.W.Scherer, *Sol-gel Science, The Physics and Chemistry of Sol-Gel Processing* Academic Press ,San Diego,CA,1990
5. L.C.Klein,*Sol-gel technology*, Noyes, Park Ridge,NJ,1988
6. Y.Sorek, R.Reisfeld, I.Finkelstein and S. Ruschin *Sol-gel glass waveguides prepared at low temperature*,Appl.Phys.Lett.63(1993)3256
7. T.Jin,S.Inoue,T.Shuji and K.I.Machida,G.Y.Adachi,*Luminescence properties of lanthanide complexes incorporated into sol-gel derived inorganic and organic composite materials*, J.Non.Crystalline Solids.223(1998)123-132
8. R.Reisfeld and C.K.Jorgensen, *Chemistry, Spectroscopy and Applications of Sol-Gel Glasses*, Springer Verlag, Berlin, 1992.
9. M.Morita and M.Herren *Preparation of Sol-gel Glasses* Journal of the SID,5(2)(1997) 127
10. B.Henderson and G.F.Imbusch, *Optical Spectroscopy of Inorganic Solids*, Oxford University Press, England(1989)
11. D.M.Krol and A.Roos, Phys.Rev.23(1981)2135
12. G.Fuxi, *Optical and Spectroscopic Properties of Glass*, Springer Verlag,Berlin,1991
13. R.Reisfeld, *Lasers and Excited States of Rare Earths*, Springer Verlag,Berlin,Heidelberg,1977
14. B.Di Bartolo, *Spectroscopy of Solid State Laser Type Materials*, Plenum Press,New York,1988
15. G. Boulon, *Spectroscopic Studies of Energy Transfer in Solids in Energy Transfer Processes in Condensed Matter* by B.DiBartolo,Plenum Press, New York, 1984.
16. W.M. Yen, *Experimental Studies of Energy Transfer in Rare Earth Ions in Crystals in Spectroscopy of Solids Containing Rare Earth Ions* Edited by Kaplyanskii, A.A. and R.M. Macfarlane, North Holland Publishers, Amsterdam, 1989.

Structural, electrical and optical properties of sol-gel processed thin films of BaTiO₃ on ITO glass

C.H. Kam ^a, S.D. Cheng ^{a*}, Y. Zhou ^a, K. Pita ^b, X.Q. Han ^a, W.X. Que ^a, H.X. Zhang ^a
Y.L. Lam ^a, Y.C. Chan ^a, W.S. Gan ^c, Z. Sun ^a, and X. Shi ^a

^a Microelectronics Division, School of Electrical and Electronic Engineering
Nanyang Technological University, Nanyang Avenue, S639798, Singapore

^b Material Technology and Application Center, Technology Development Division
Singapore Productivity and Standards Board, 1 Science Park Drive, S118221, Singapore

^c Acoustical Technologies Singapore Pte. Ltd., 209-212 Innovation Center
Nanyang Avenue, S639798, Singapore

ABSTRACT

BaTiO₃ thin films are prepared on ITO-coated Corning 1737 glass. The solution is prepared from a double metal ethoxide and the films are deposited by spin coating and annealing at 700°C for 2 hours in an O₂ atmosphere. The films are characterized using X-ray diffraction, atomic force microscopy, micro-Raman, UV-VIS spectroscopy, and Sawyer-Tower Bridge. The pure perovskite phase of BaTiO₃ is identified by X-ray diffraction. The tetragonality is revealed from Raman study by identifying the symmetrical dependent Raman shift at about 306 cm⁻¹. The ferroelectricity of the film is confirmed by the P-E hysteresis loop. The films are highly transparent, with an absorption edge at 3.73eV. These desirable features indicate that the films have potential in electronic display and electro-optical applications.

Keywords: BaTiO₃, Sol-gel, X-ray diffraction, micro-Raman, Optical properties, Electrical properties.

1. INTRODUCTION

Barium titanate (BaTiO₃) is very useful in optical and electrical applications due to its electro-optic, ferroelectric and dielectric properties. Different deposition methods, including rf sputtering ^{1, 2}, metal-organic chemical vapor deposition (MOCVD) ³⁻⁵, dipping-pyrolysis ⁶, pulsed laser deposition (PLD) ^{7, 8}, molecular beam epitaxy (MBE) ⁹, and sol-gel ¹⁰⁻¹⁵, have been employed in the preparation of such films. These films are generally prepared on crystalline materials, such as MgO ^{3, 4, 7, 8}, SrTiO₃ ^{6, 9}, LaAlO₃ ¹⁰, MgO/GaAs ⁷, Si ¹¹⁻¹³, MgO/Si ², and Pt/Si ¹²⁻¹⁴.

Corning 1737 is a new type of glass, which is introduced mainly for the active-matrix liquid crystal displays (AM-LCD) ¹⁶. It has a high softening point of over 900°C, which is even higher than that of Corning 7059 (~844°C). It is thus a suitable glass substrate for the preparation of sol-gel BaTiO₃ films which have a relatively high sintering temperature of about 650°C ¹⁵. It is also of importance in the preparation of ferroelectric films, such as BaTiO₃ film on glass substrate, for electronic display and electro-optic applications.

In this work, BaTiO₃ thin films are prepared on ITO-coated Corning 1737 glass. The solution is prepared from a double metal ethoxide and the films are deposited by spin coating. The films are characterized using X-ray diffraction (XRD), atomic force microscopy (AFM), micro-Raman, UV-VIS spectroscopy, and Sawyer-Tower Bridge (RT66A). The pure perovskite phase of BaTiO₃ is identified by XRD. The tetragonality is revealed from Raman study by identifying the symmetry dependent Raman shift at about 306 cm⁻¹. The ferroelectricity of the films is confirmed by the P-E hysteresis loop. The films are highly transparent, with an absorption edge at 3.73eV. These desirable features indicate that the films have potential in electronic display, and electro-optical applications.

2. EXPERIMENTAL

The sol was prepared by mixing barium ethoxide (10%w/v in ethanol) with tetrapropyl orthotitanate (TPOT) at a molar ratio of Ba/Ti = 1, and a molar concentration of 0.14M in ethanol. A precipitation in the solution might occur in 24 to 48 hours.

* Corresponding author, Tel: +65-7905461; Fax: +65-7933318; E-mail: P142977657@ntu.edu.sg.

The solution was continuously stirred and the films were prepared within 24 hours. Multiple coatings were employed with 650°C/15minutes preheating in-between each coating. The three-layer films were finally annealed at 700°C for 2 hours in an O₂ atmosphere. The films were studied by means of X-ray diffraction (Rigaku RINT 2000), micro-Raman (Renishaw Ramascope), atomic force microscopy (Digital Instrument, Nanoscope IIIa), Sawyer-Tower Bridge (RT66A, Radiant Technology), and UV-VIS spectrometry (HP8453).

3. RESULTS AND DISCUSSION

3.1 Structural Properties

3.1.1 XRD results

The XRD results shown in Fig. 1 are obtained at different glancing angles of 0.5°, 1.0°, 2.0°, and 3.0°. For comparison, the result for ITO glass substrate is also shown in the figure. At a low glancing angle of 0.5°, we can only see the diffraction from Perovskite BaTiO₃. When the glancing angle increases, diffraction from both BaTiO₃ and ITO can be identified. However, we cannot see any other impurity phases, which suggests that the interdiffusion between the film and substrate is not obvious.

Although the perovskite phase of BaTiO₃ is confirmed by XRD, we need to further determine whether it is in the tetragonal or cubic phase. It is well known that the tetragonal BaTiO₃ has a low c/a ratio of 1.01, and thus it is very difficult to distinguish whether it is in tetragonal or cubic form from XRD experiments.

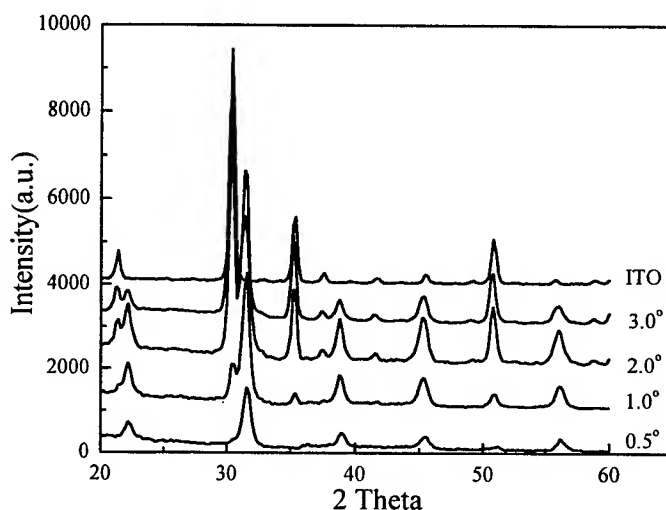


Fig. 1 XRD results obtained at different glancing angles of 0.5°, 1.0°, 2.0°, 3.0° and that for ITO glass substrate. Pure perovskite phase of BaTiO₃ can be found in the film.

3.1.2 Micro-Raman study

Raman spectroscopy is a characterization method that measures the frequencies of the long wavelength lattice vibrations (phonons). Unlike XRD, Raman spectroscopy does not provide a direct determination of the crystal structure. However, it has several advantages over the diffraction method. Raman spectroscopy can detect low concentration impurity phases that may be missed by XRD, and it is more sensitive to non-crystalline phases than diffraction. In addition, crystal symmetry related structural changes often have a large effect on the Raman spectrum. Thus Raman spectroscopy can distinguish more easily between crystalline phases which possess different symmetries but with similar lattice parameters, such as the cubic and tetragonal phases of BaTiO₃^{5, 18}.

Our micro-Raman is performed by using an Ar⁺ laser operating at the wavelength of 514.5nm. The results of our BaTiO₃ film, the substrates both with and without ITO coating are shown in Fig. 2. As we can see from the figure, the vibration mode specifically belonging to the tetragonal phase of BaTiO₃ appears at 306cm⁻¹, which is very close to the crystal value

of 305cm^{-1} . In the meantime, a phonon mode of 519cm^{-1} also appears, which corresponds to the vibration of both the cubic and tetragonal phase. Note that the single crystal value is about 515cm^{-1} . Similar to the XRD results, no other impurity phase can be found in the Raman study.

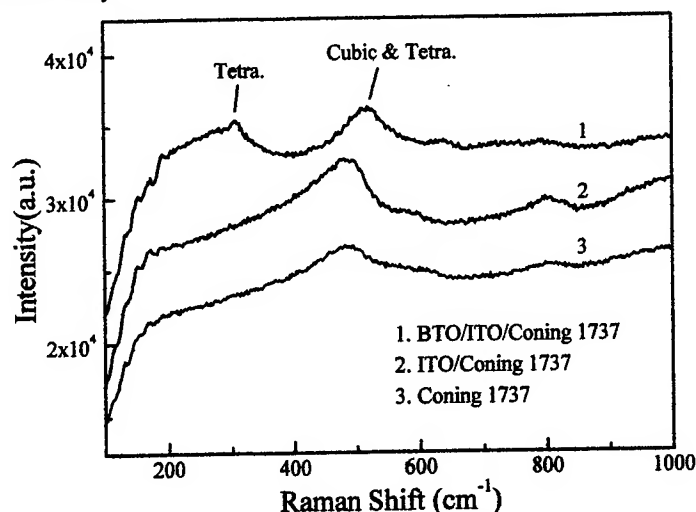


Fig. 2 Raman shift of different phonon modes in the film (line 1), and the glass substrate (Corning 1737) with (line 2) and without ITO (line 3). The tetragonality of the film can be identified by the phonon mode of 306cm^{-1} .

From the XRD and Raman studies, we can conclude that our film is made up of tetragonal perovskite phase of BaTiO_3 , with no other impurity phases. The tetragonality of the film is also confirmed by the P-E hysteresis loop of the film as will be shown later.

3.1.2 Surface morphology

The surface morphology of the film is examined under an AFM and Fig. 3 shows the image. As we can see, small crystallites with well-defined facets can be found. Due to the presence of these crystallites, the surface of the film is relatively rough, and the root mean square (RMS) roughness is about 9.8nm .

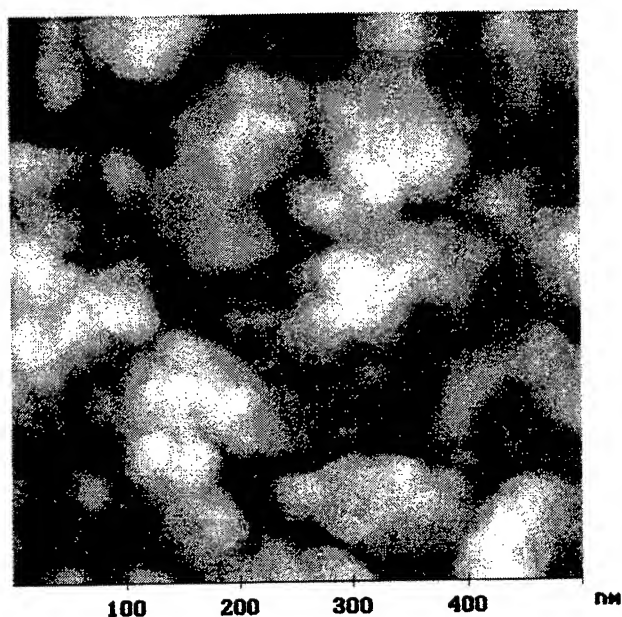


Fig. 3 Surface morphology of the film revealed by AFM. Here, crystallites with well-defined facets can be found.

3.2 Electrical Properties

The electrical properties are studied by a Sawyer-Tower Bridge operating at a frequency of 50Hz. In this experiment, a top Al electrode is deposited on the BaTiO₃ film and the measured P-E hysteresis loop is shown in Fig. 4. The opening of the loop is due to the difference in work functions between the bottom and top electrode materials. The P-E loop confirms the ferroelectricity and the tetragonality of the film.

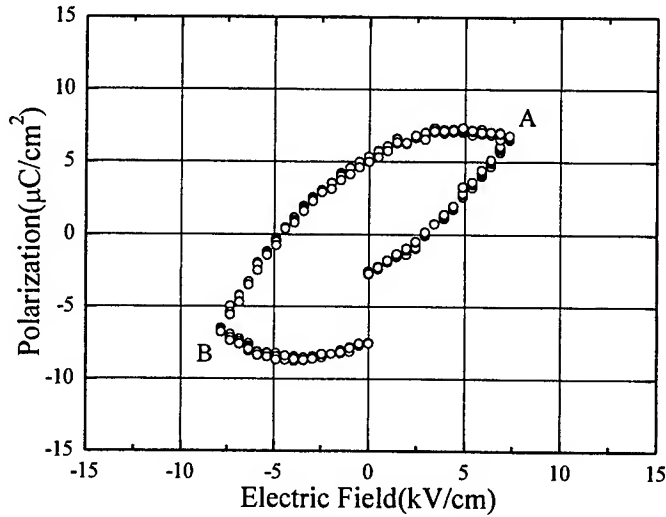


Fig. 4 P-E hysteresis loop obtained with Al/BaTiO₃/ITO sandwiched structure.

3.3 Optical Properties

The optical transmittance of the film is obtained with UV-VIS spectrometry. Figure 5 shows the direct measurement result of the BTO/ITO/glass together with that of the ITO/glass. We can see that the transmission range of the film is over ~330nm. The transmittance of the film (T_f) can be calculated with the measured transmittance (T_m) of the sample (substrate + film) and that of the substrate (T_s)¹⁷,

$$T_f = \frac{1}{1 + \frac{1}{T_m} - \frac{1}{T_s}} \quad (1)$$

In the transmission range, T_f is found to be approximately 100%, indicating that the film is highly transparent.

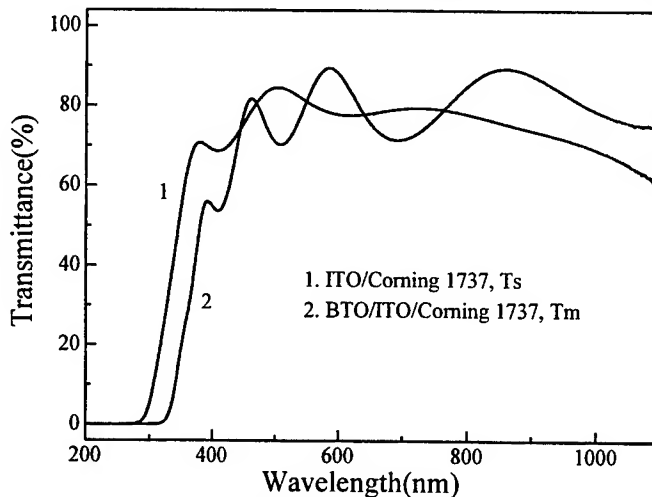


Fig. 5 Optical transmittance of ITO glass substrate (line 1) and BaTiO₃ film on the substrate (line 2).

The bandgap energy can be determined by the measurement of the optical absorption edge of the film, which lies in the UV spectral region. For direct transitions, the absorption coefficient α is given by ¹:

$$\alpha h\nu = A'(h\nu - E_g)^{1/2} \quad (2)$$

where $h\nu$ is the photon energy, A' is a constant, and E_g is the transition bandgap energy. The plot of $(\alpha h\nu)^2$ vs. $h\nu$ is given in Fig. 6.

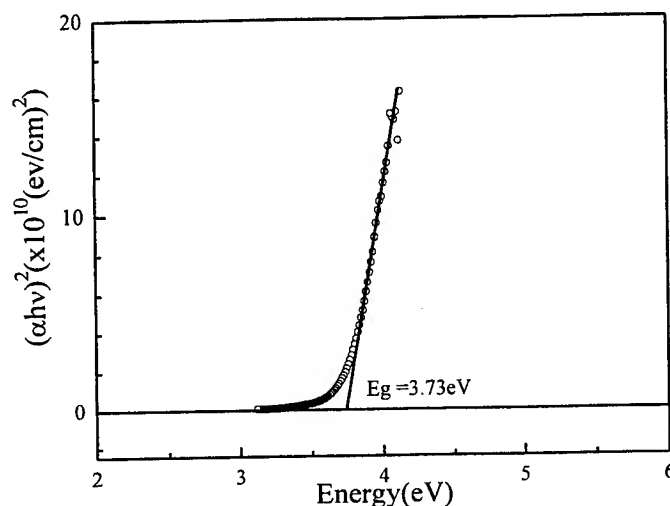


Fig. 6 Plot of $(\alpha h\nu)^2$ vs. $h\nu$; the bandgap is determined by extrapolating the linear part of the plot to zero.

By extrapolating the linear portion of the curve to zero, a bandgap energy of 3.73 eV is obtained for our films, which is higher than that of the bulk BaTiO_3 ($E_g=3.15$ eV). Others authors have also reported similar result ¹. The bandgap widening can be due to a stress-induced distortion of the band by the film-substrate interaction and it thus is dependent on the film processing condition. Furthermore, defects such as point, line and planar defects in the crystalline film and the nanocrystalline size effect can all lead to the variation of the bandgap energy ²⁰.

In conclusion, we have successfully prepared BaTiO_3 thin films on ITO-coated Corning 1737 glass. The films are highly transparent with pure tetragonal perovskite phase. The ferroelectricity of the films is confirmed by the P-E hysteresis loop. The films have potential in electronic display and electro-optical applications.

ACKNOWLEDGEMENTS

We would like to express our thanks to Ms. B.G. Neo, and Ms. L.C. Wong for their kind assistance in the AFM and XRD measurements, and to Singapore National Science & Technology Board (NSTB) for the support to one of us (K. Pita) under project number OC0008.

REFERENCES

1. P. Pasierb, S. Komornicki, and M. Radecka, "Structural and optical properties of $\text{Sr}_{1-x}\text{Ba}_x\text{TiO}_3$ thin films prepared by rf sputtering", *Thin Solid Films*, **324**, pp. 134-140, 1998.
2. S. Kim, and S. Hishita, "Growing BaTiO_3 thin films on Si(100) with MgO-buffer layer by sputtering", *Thin Solid Films*, **281-282**, pp. 449-452, 1996.
3. C.S. Hwang, M.D. Vaudin, and G.T. Stauff, "Influence of substrate annealing on the epitaxial growth of BaTiO_3 thin films by metal-organic chemical vapor deposition", *J. Mater. Res.*, **12**(6), pp. 1625-1633, 1997.
4. H.A. Lu, L.A. Wills, and B.W. Wessels, "Electrical properties and poling of BaTiO_3 thin films", *Appl. Phys. Lett.*, **64**(22), pp. 2973-2975, 1994.
5. D.L. Kaiser, M.D. Vaudin, G. Gillen, C-S. Hwang, L.H. Robins and L.D. Rotter, "Growth of BaTiO_3 thin films by MOCVD", *Mat. Res. Soc. Symp. Proc.*, **335**, pp. 47-52, 1994.

6. S. Kim, T. Manabe, I. Yamaguchi, T. Kumagai, and S. Mizuta, "Preparation of epitaxial BaTiO₃ thin films by the dipping-pyrolysis process", *J. Mater. Res.*, **12**(4), pp. 1141-1144, 1997.
7. V. Srikant, E.J. Tarsa, D.R. Clarke, and J.S. Speck, "Crystallographic orientation of epitaxial BaTiO₃ films: the role of thermal-expansion mismatch with the substrate", *J. Appl. Phys.*, **77**(4), pp. 1517-1522, 1995.
8. L. Beckers, J. Schubert, W. Zander, J. Ziesmann, A. Eckau, P. Leinenbach, and Ch. Buchal, "Structural and optical characterization of epitaxial waveguiding BaTiO₃ thin films on MgO", *J. Appl. Phys.*, **83**(6), pp. 3305-3310, 1998.
9. H. Shigetani, K. Kobayashi, M. Fujimoto, W. Sugimura, Y. Matsui and J. Tanaka, "BaTiO₃ thin films grown on SrTiO₃ substrates by a molecular-beam-epitaxy method using oxygen radicals", *J. Appl. Phys.*, **81**(2), pp. 693-697, 1997.
10. A.D. Li, C.Z. Ge, P. Lü, D. Wu, S.B. Xiong, and N.B. Ming, "Fabrication and electrical properties of sol-gel derived BaTiO₃ films with metallic LaNiO₃ electrode", *Appl. Phys. Lett.*, **70**(12), pp. 1616-1618, 1997.
11. C.R. Cho, A. D. Kwun, T. W. Noh, and M.S. Jang, "Electrical properties of sol-gel deposited BaTiO₃ thin films on Si(100) substrate", *Jpn. J. Appl. Phys.*, **36**(4A), pt. 1, pp. 2196-2199, 1997.
12. S. Nourbakhsh, I. Vasilyeva, and J.N. Carter, "Novel metalorganic route for fabrication of BaTiO₃ thin ferroelectric films", *Appl. Phys. Lett.*, **66**(21), pp. 2904-2806, 1995.
13. M.C. Gust, N.D. Evans, L.A. Momoda, and M.L. McCartney, "In-situ transmission electron microscopy crystallization studies of sol-gel-derived Barium Titanate thin films", *J. Am. Ceram. Soc.*, **80**(11), pp. 2828-2836, 1997.
14. M.N. Kamalasanan, N.D. Kumar, and S. Chandra, "Dielectric and ferroelectric properties of BaTiO₃ thin films grown by the sol-gel process", *J. Appl. Phys.*, **74**(9), pp. 5679-5686, 1993.
15. K. Pita, S.D. Cheng, C.H. Kam, Y. Zhou, Y.L. Lam, and Y.C. Chan, "The crystallinity, the surface morphology and the optical constant of sol-gel derived thin films of BaTiO₃ on SiO₂/Si and Si substrates", *Ferroelectrics*, 1999. To appear.
16. J.C. Lapp, "Glass substrates for AMLCD applications: properties and application", *Proc. of SPIE*, **3014**, pp. 2-9, 1997.
17. E. Dogheche, B. Jaber, and D. Rémiens, "Optical waveguiding in epitaxial PbTiO₃ thin films", *Appl. Opt.*, **37**(19), pp. 4245-4248, 1998.
18. L.H. Robins, D.L. Kaiser, L.D. Rotter, P.K. Schenck, G.T. Stauff, and D. Rytz, "Investigation of the structure of barium titanate thin films by Raman spectroscopy", *J. Appl. Phys.*, **76**(11), pp. 7487-7498, 1994.
19. N.F. Mott, and E.A. Davis, *Electronic Processes in Non-Crystalline Materials*, Oxford University Press, London, 1979.
20. V. Srikant, and D.R. Clarke, "Optical absorption edge of ZnO thin films: the effect of substrate", *J. Appl. Phys.*, **81**(9), pp. 6357-6364, 1997.

SESSION 13

Solar Cells

Electrochemical synthesis of SnS thin films for photoelectrochemical cells

B. Subramanian[@], C. Sanjeeviraja[#]
M. Jayachandran^{*} and Mary Juliana Chockalingam^{*}

[@]Jayaram College of Engineering & Technology, Karattampatti-621 014, India

[#]Dept. of Physics, Alagappa University, Karaikudi-630 003, India

^{*}Central Electrochemical Research Institute, Karaikudi-630 003, India

ABSTRACT

Tin Sulphide (SnS), a layered semiconducting material which finds wide applications in optoelectronic devices and window material for heterojunction solar cell. This paper reports on the materials properties of thin films of SnS prepared by electrodeposition and brush plating. Brush plating is an electroplating process usually adopted to coat large area thin metal or alloy film. The films of 0.6 – 1.0 μm and 1.0 – 2.5 μm thickness were prepared by electrodeposition and brush plating respectively. X-ray diffraction studies showed that the as prepared films of both techniques revealed polycrystalline nature of the films and the lattice parameter values are: $a = 0.403 \text{ nm}$; $b = 1.145 \text{ nm}$; and $c = 0.399 \text{ nm}$. The surfaces were analyzed by electron spectroscopy for chemical analysis (ESCA) and Scanning Electron Microscopy (SEM) for surface morphology. The band gap, refractive index and extinction coefficient values were estimated from the optical studies in the wavelength region of 400-1500 nm. The adhesion of the films prepared by brush plating was found to be excellent. Photoelectrochemical (PEC) solar cells were fabricated using SnS photoelectrodes. Capacitance-Voltage (C-V) studies revealed the p-type nature of all the films. The flat band potentials were 0.52 V and 0.47 V respectively. The quality of the films prepared by electrodeposition and brush plating are compared.

Key words: Tin sulphide, Brush plating and Photoelectrochemical Solar Cells

1. INTRODUCTION

The utility of tin sulphide (SnS) semiconducting thin film in photoelectrochemical conversion of solar energy and its photovoltaic properties have already been demonstrated.^{1,2} Tin sulfide is a IV-VI compound semiconductor and orthorhombic structure with the distorted NaCl type.³ In chalcogenides, within each layer, the atoms are bound together by predominantly covalent forces. The bonds between the layers are extremely weak due to Van der Waal's forces.⁴ They can be synthesized by means of low temperature chemical precipitation and vapour deposition techniques as described in previous works.^{3,5} Electron probe microanalysis and X-ray photoelectron spectroscopy studies were carried out for electrodeposited SnS thin films by Mishra et al.⁶

In this study the SnS films were prepared by cathodic electrodeposition and brush plating techniques. The main advantages of electrodeposition is the apparatus simplicity, low energy consumption and ease in control of film thickness, its composition and morphology by means of changes in deposition potential or current density.⁷ The brush plating technique is also simple, convenient and low cost method⁸ for obtaining large area films. This technique is employed for the first time by the authors in synthesizing SnS films for application in solar energy conversion. The objective of this paper is to study and compare the structural, morphological, optical and photoelectrochemical properties of the SnS films obtained by electrodeposition and brush plating techniques and to compare the quality of the films.

2. EXPERIMENTAL

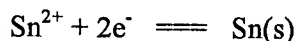
The SnS films were cathodically electrodeposited on TO-coated glass substrates with exposed area ranging between 0.5 – 2.5 cm². An EG&G Princeton Applied Research (PAR) potentiostat Model 270 was employed in performing cyclic voltammetry experiments and controlling deposition potential. saturated calomel electrode (SCE) and platinum electrode were employed as the reference and counter electrodes respectively. The electrodeposition bath consisted of 5 mM of SnCl₂, 0.01 M of Na₂S₂O₃ and few drops of HCl.

SnS films of thickness 2-3 μm were deposited on TO coated conducting glass substrates which is the negative electrode by brush plating technique using Selectron Power Pack Model 150A-40 V. To obtain very good adhesion, pretreatment of the substrate was done using the solution containing equal volumes 2 : 1 HNO₃ and 1:1 HCl and finally treated for 60s in 10% by volume of NaOH. The plating bath consisted of 3-5 mM of SnCl₂ and 0.01 M of Na₂S₂O₃ (pH about 1.5). The stylus, consisting of a carbon rod wrapped in cotton wool served as the anode. The anode and cathode were connected to the power pack, the anode was wetted with the plating solution and the substrate was brushed with it.

The films were characterized by X-ray diffraction for structural analysis using JEOL JDX 803 a X-ray diffractometer with CuKα radiation (λ = 1.5418 Å). A Carry – 5E UV-VIS-NIR Spectrophotometer was used to carry out the optical studies in the range 400-1500 nm. Morphological studies were carried out by employing JSM 6400 JEOL Scanning Electron Microscope. Mott-Schottky studies were done with Vasavi (VCLR 7) LCR meter. The photoelectrochemical solar cells were set up with SUNLUX 500 W/250 V tungsten filament-halogen lamp, for white light illumination at 100 mW cm⁻². The photon flux was measured by a CEL Suryamapi instrument. The redox electrolyte used for photoelectrochemical studies was (aq.) 0.1 M FeCl₂, FeCl₃ (0.05 M H₂SO₄) using analytical reagent (AR) grade chemicals. The counter electrode was graphite, the reference electrode was a saturated calomel electrode (SCE) attached very near to p-SnS photoelectrode.

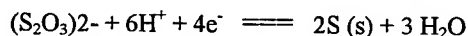
3. RESULTS AND DISCUSSION

The selection of the composition of the electroplating bath to obtain SnS thin films were made through several attempts. The deposition of binary compounds are governed by the factors (i) electrode potential of individual ions of the electrolyte (ii) cathodic polarization caused by difference in deposition potential and (iii) relative ion concentrations in the electrolyte. The basic individual electrochemical reactions of Sn and S and their corresponding Nernst equation as follows⁹.



$$E = E^\circ (\text{Sn}^{2+} / \text{Sn}) + (RT / 2F) \ln (a_{\text{Sn}^{2+}} / a_{\text{Sn}})$$

$$= -0.38 \text{ V SCE} + 0.0295 \ln (a_{\text{Sn}^{2+}} / a_{\text{Sn}})$$



$$E = E^\circ (\text{S}_2\text{O}_3^{2-} / \text{S}) + (RT / 4F) \ln (a_{\text{S}_2\text{O}_3^{2-}} / a_{\text{S}})$$

$$(3 RT / 6 F) \ln \text{OH}^+ \rightleftharpoons + 0.26 \text{ V SCE} + 0.0148$$

Hence E° is the equilibrium electrode potential expressed with reference to SCE, 'a' are activities of ions in the bulk solution and the deposit (a = 1, for an ion in the solid deposit) and CH⁺ is the concentration of hydrogen ions, Sn(s) and S(s) are the respective species in the deposition.

For simultaneous deposition of Sn and S, the concentration and pH of the electrolyte should be adjusted such that the electrode potentials of the individual deposits come closer to each other. This has been achieved by varying the potential in the cathodic direction.

Cyclic voltammetry (CV) experiments were carried out under different potential scan rate for the individual species of Sn^{2+} and $\text{S}_2\text{O}_3^{2-}$ ions. A strong cathodic peak was observed at $\sim -0.55 \text{ V}_{\text{SCE}}$ which is associated with Sn (II) reduction process in the C-V pattern obtained for Sn species alone. When 10 mM of $\text{S}_2\text{O}_3^{2-}$ species were added, the cathodic current onset shifted to -0.60 V followed by a small wave at -0.64 V . It corresponds to the reduction of thiosulphate ions in the mixed bath. This is corroborated by the reduction peak at about -0.7 V in the CV curve for $\text{S}_2\text{O}_3^{2-}$ species alone. A similar observation was made by other workers.¹⁰ At more negative potential a tin rich film was observed. The deposition was carried out by keeping the potential constant at -0.8 V versus SCE for 10-15 minutes. A smooth and uniform deposit with grey-brown colour was observed at this potential. A near stoichiometry of the films were confirmed through XRD and XPS analysis.

The electrochemistry involved in brush plating process is similar to that of electrodeposition. SnS thin films were brush plated with various potentials in the range of 2 to 7 volts and also with different time duration in the range of 3 to 10 minutes. Films deposition were carried out at different temperatures (i.e.) RT, 50 and 60°C . A good polycrystalline nature was observed for the films plated at a plating potential of 3 volt, 4 minutes of plating time and at the room temperature. The current density was always maintained at 0.01 amp.hr.

At higher potentials the film gets peeled off. XRD and XPS analyses show the films plated for 4 minutes are near stoichiometry. The electrolyte bath temperature does not play a major role in the crystallinity of the SnS films. XPS studies reveal the presence of Sn and S on the grey-brown samples synthesized by electrodeposition as well as brush plating techniques.

3.1. Structure

The X-ray diffraction pattern of brush plated SnS films on a conducting glass substrate is shown in Fig.1. The calculated interplanar spacings (d-values) from these patterns were found to agree well with those of electrodeposited films prepared by us and ASTM data as given in Table 1.⁹ The diffractogram indicates the polycrystalline nature with all major peaks corresponding to the orthorhombic lattice with $a = 0.403 \text{ nm}$, $b = 1.145 \text{ nm}$ and $c = 0.399 \text{ nm}$. They compare well with the reported value.⁶ One peak corresponding to SnO_2 is noticed. Elemental Sn or S is not detected in the diffractogram. As far as structure is concerned no difference in the XRD pattern is observed between electrodeposited and brush plated SnS films. By the hot probe method it was observed that all the films were found to be p-type in nature.

$D_{\text{brush}} (\text{\AA})$	$D_{\text{electro}} (\text{\AA})$	ASTM	hkl
3.324	3.336	3.423	120
2.901	2.910	2.931	101
2.778	2.769	2.797	040
2.360	2.384	2.305	131
2.061	2.030	2.024	141
1.773	1.763	1.779	151

3.2. Morphology

Fig. 2 indicate the surface morphology of the brush plated and electrodeposited SnS films. Prior to SEM analysis, all the specimens were sputter-coated with a 7 nm thin film of gold to enhance their electrical conductivity. The grain size (GS) was calculated from the intercept method.¹²

$$\text{GS} = 1.5 (l / m) \quad \dots (1)$$

Where l is the length of the line drawn on the photograph cutting the grains, n is the number of grains cut by the line and m is the magnification of the photograph and 1.5 is a constant assuming spherical grains. The grain size was found to be about $\sim 400 \text{ \AA}$ for electrodeposits and $\sim 3000 \text{ \AA}$ for brush plated films. SEM photograph of brush plated SnS film, Fig. 2 (a) revealed that the closely packed grains provide a pin hole free morphology leading to

better spatial contact between the grains and thus they can be used for photoelectrochemical cells. It is observed that the films prepared by electrodeposition techniques contains lot of cracks may be because of poor adhesion with the substrate.

3.3. Optical Studies

Optical absorbance and transmittance spectra in the wavelength region of 400-1500 nm for the brush plated and electrodeposited SnS films were taken. The plot of $(\alpha h\nu)^{1/2}$ versus $h\nu$ yielded a straight line which indicated the indirect optical transition near the absorption edge of the SnS films prepared by both techniques. The intercept of the plots yielded a band gap value of 1.05 eV and 1.1 eV for brush plated and electrodeposited SnS films respectively as shown in Fig. 3 which are consistent with other reported values.²

The thickness of the films were calculated using the relation

$$d = \frac{\lambda_1 \lambda_2}{2 (n_2 \lambda_1 - n_1 \lambda_2)} \quad \dots (2)$$

Where n_1 and n_2 are the refractive indices at two adjacent maxima (or minima) λ_1 and λ_2 . Electrodeposited SnS films are found to be thinner (0.6 – 1.0 μm) than the films prepared by brush plating method (1.0 – 2.5 μm) as evidenced by interference pattern obtained for electrodeposited films as shown in Fig. 4. The continuous differential descent (CDD) method has been used to determine the optical constants, the refractive index (n) and the extinction coefficient (k). All the films exhibited variation of refractive index at the shorter wavelength but almost constant in the longer wavelength (near infra red) region. The refractive index values varies from 4.1 to 2.1 for electrodeposited and 3.2 to 2.4 for brush plated films and these values agreed with the values reported in the literature. The extinction coefficients for these films were observed to be low in the order of 0.003 for electrodeposited and 0.008 for brush plated films.

3.4. Characterization of p-SnS Thin Films / Ferro-ferricyanide Photoelectrochemical Solar Cells

3.4.1. Mott-Schottky plot analysis

The semiconductor-electrolyte junction can be conceived as a series connection of two capacitances, that of the space charge layer per unit area C_{sc} and that of the Helmholtz layer per unit area, C_H . The contribution to the total capacitance from C_H is negligible. Thus for a PEC cell the Mott-Schottky relation is given by

$$\frac{1}{C_{sc}^2} = \frac{2}{q \epsilon_o \epsilon_s N_A} \left[V - V_{FB} - \frac{K_B T}{q} \right] \quad \dots (3)$$

Where q is the electronic charge, K_B is the Boltzmann constant, T is the absolute temperature, V is the electrode potential, V_{FB} is the flat band potential, N_A is the acceptor concentration, ϵ_s is the static permittivity of the semiconductor and ϵ_o is the permittivity of free space.

Fig. 5 shows the typical Mott-Schottky plot drawn using the capacitance data at the frequency of 1 kHz (in the dark) for the p-SnS film / ferro-ferricyanide electrolyte/graphite PEC cell. The intercept at the electrode potential axis (for $1/C_{sc}^2 = 0$), gives the flat band potentials of about 0.52 V_{SCE} for electrodeposited and 0.47 V_{SCE} for brush plated SnS film. From the nature of the curves it is confirmed that all the films were p-type in nature.

3.4.2. Power output characteristics

As the films prepared by brush plating technique are having good adhesion with the substrate and more thicker than electrodeposited films, these films were represented here for PEC studies. To investigate the nature of the junction

formed with SnS and the electrolyte, dynamic current-voltage (I-V) characteristics of the PEC cells were studied. The curve obtained under illumination of film is shifted from that for dark, which indicates the photosensitizing ability of the film. The estimated values of the energy conversion efficiency, η and the fill factor, ff , were found to be 0.029% and 71.2% respectively which are in agreement with the reported values.¹² The low efficiency may be due to the series and parallel resistances of the cell or the low carrier concentration, low mobility of the carriers and grain boundaries which can act as recombination centres for photogenerated carriers. Still lower efficiency of 0.012% was found for electrodeposited films but the films prepared by both techniques are found to have a good stability against photocorrosion as already reported by Sharon et al.². Surface modification by etching and annealing process in various conditions is in progress to improve the PEC performance of SnS photoelectrodes.

4. CONCLUSION

SnS films have been synthesized by electrodeposition and brush plating techniques on SnO₂ coated conducting glass substrates from aqueous solution containing SnCl₂ and S₂O₃²⁻ ions at room temperature. X-ray diffraction studies indicated that all the films were polycrystalline in nature. The d-values obtained for the films prepared by both techniques are found to be similar. A pin hole free and closely packed grains arrangement are observed from SEM pictures for the brush plated SnS films which is a prerequisite for the semiconductor films to be used in solar cells. The films of SnS grown by electrodeposition and brush plating were found to be exhibiting photoactivity in Fe²⁺ / Fe³⁺ electrolyte. The power conversion efficiency is very poor for all the films. Though a good stability against photocorrosion is observed, optimization of films for better PEC performance is in progress. Thicker films were obtained through brush plating technique and also these films were more adherent with the substrate than electrodeposited films.

REFERENCES

1. H. Noguchi, A. Setiyadi, H. Tanamura, T. Nagatomo and O. Omoto, "Characterization of vacuum-evaporated tin sulfide film for solar cell materials", *Solar Energy Materials and Solar Cells*, 35, PP.325-331, 1994.
2. M. Sharon, K. Basavaswan and N.P. Sathe, "Chemically Stable and Cheaply Available Chalcogenides for a Solar Chargeable Battery (Saur Vidyut Kosh. III) – A Survey", *J. Sci. and Ind. Res.*, 44, PP.593-598, 1985.
3. R.D. Engelken, H.E. McCloud, C. Lee, M. Slayton and H. Ghoreishi, "Low temperature chemical precipitation and vapour deposition of SnxS thin films", *J. Electrochem. Soc.*, 134, PP.2696-2707, 1987.
4. R.K. Bedi, "Characterization of SnSe films for device applications", *Conference on Physics and Technology of Semiconductor Devices and Integrated Circuits*, B.S.V. Gopalan and J. Majhi, PP.104-112, SPIE Publication, 1992.
5. P.K. Nair and M.T.S. Nair, "Chemically deposited SnS-Cu_xS thin films with high solar acceptance : new approach to all-glass tubular solar collectors", *J. Phys. D. Appl. Phys.* 24, PP. 83-87, 1991.
6. K. Mishra, K. Rajeshwar, Alex Weiss, M. Murley, R.D. Engelken, M. Slayton and McCloud, "Electrodeposition and Characterization of SnS thin films", *J. Electrochem. Soc.*, 136 (7), PP.1915-1923, 1989.
7. A.N. Molin and A.I. DiKusar, "Electrochemical Deposition of PbSe thin films from aqueous solutions", *Thin Solid Films*, 265, PP.3-6, 1995.
8. J.C. Morris, "Brush Plating – Part I", *Metal Finishing*, July, PP.45-48, 1988.
9. B. Subramanian, T. Mahalingam, C. Sanjeeviraja, M. Jayachandran and M.J. Chockalingam, "Electrodeposition of SnS thin films from aqueous medium", *Bull. Electrochem.*, 14 (11), PP.398-401, 1998.
10. Z. Zainel, M.Z. Hussein, A. Ghazali, "Cathodic electrodeposition of SnS thin films from aqueous solution", *Solar Energy Materials and Solar Cells*, 40, PP.347-357, 1996.

11. V. Damodara Das and L. Damodane, "Power Conversion efficiency studies of vacuum evaporated n-CdSe_{0.6}Te_{0.4} Semiconducting thin film / (aq) ferro-ferri cyanide electrolyte photoelectrochemical solar cells", Solid State Communications, 103, PP.173-178, 1997.
12. S.A. Jodgudri and C.D. Lokhande, "Studies on Photoelectrochemical (PEC) Properties of Electrodeposited SnSe Electrode", Bull. Electrochem., 11 (10), PP.487-489, 1995.

Further author information:

@B. Subramanian

Dept. of Physics

Jayaram College of Engineering & Technology, Karattampatti-621 014, India

E-mail: tspseenthil@yahoo.com

Telephone: (091) 04327-43870

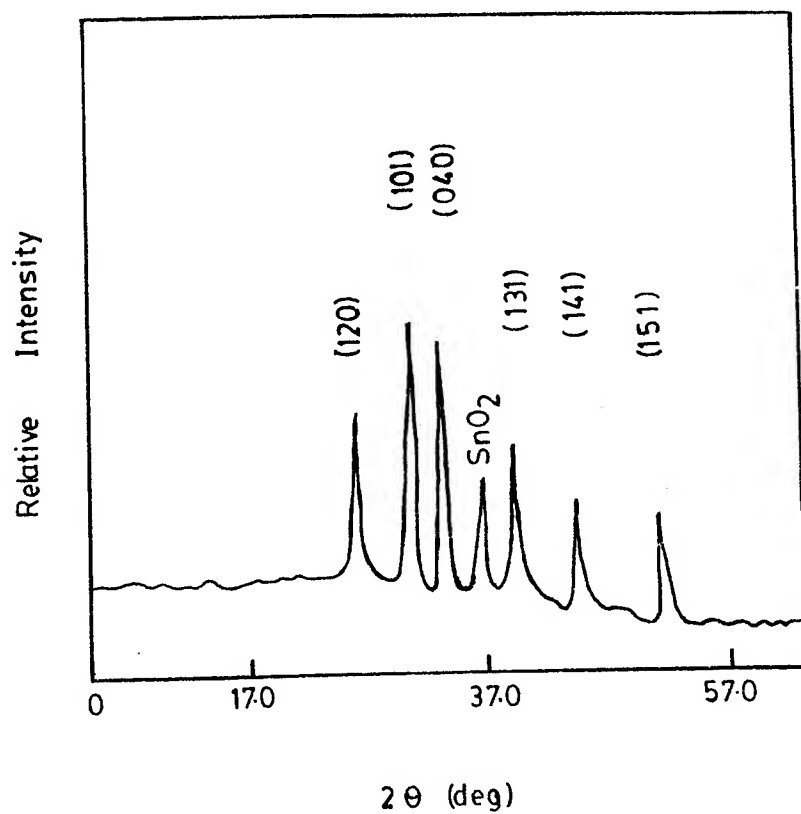


Fig. 1.XRD pattern of brush plated SnS thin film.

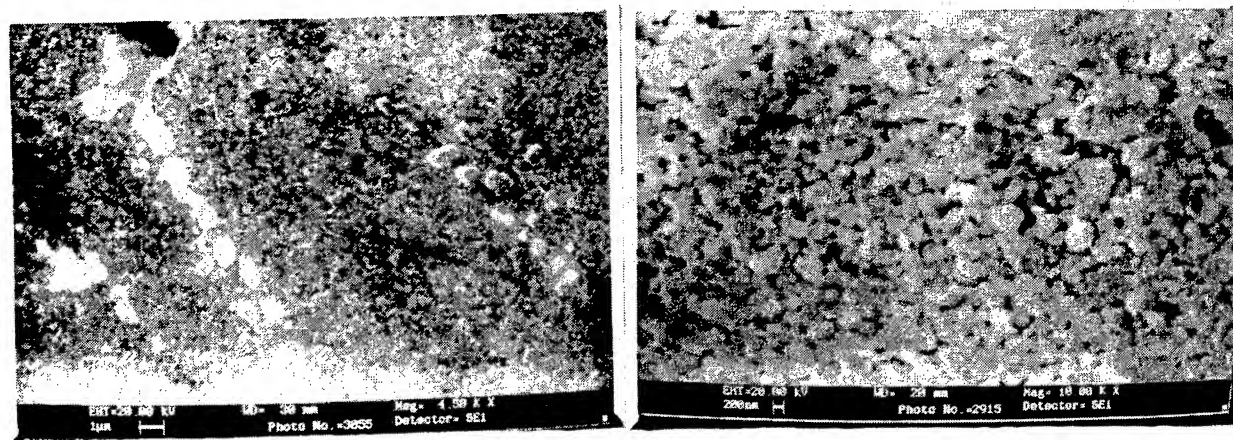


Fig. 2. Scanning Electron Micrographs of SnS film.
(A) Brush plated (B) Electrodeposited

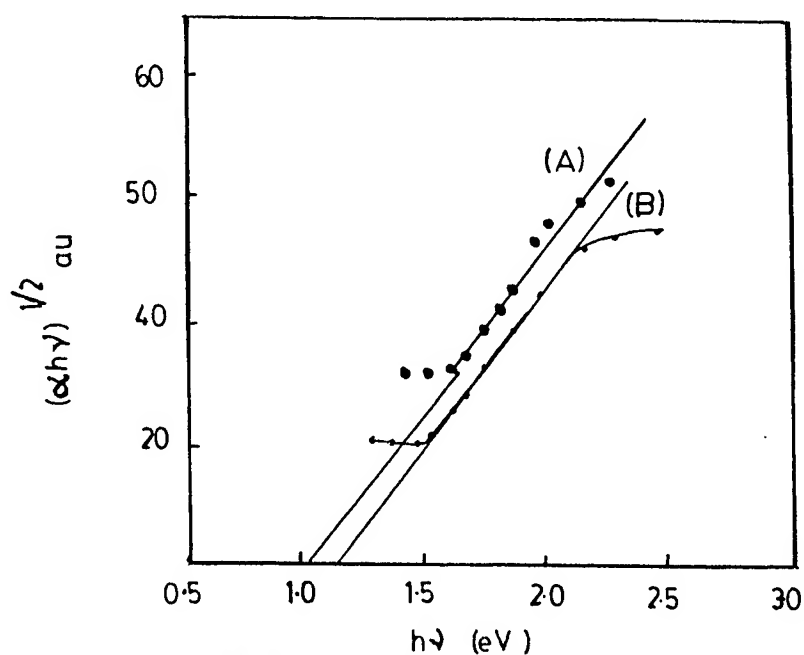


Fig.3 A plot between $(\alpha h\nu)^{1/2}$ and $h\nu$ (eV) for SnS thin film.
(A) Brush plated (B) Electrodeposited

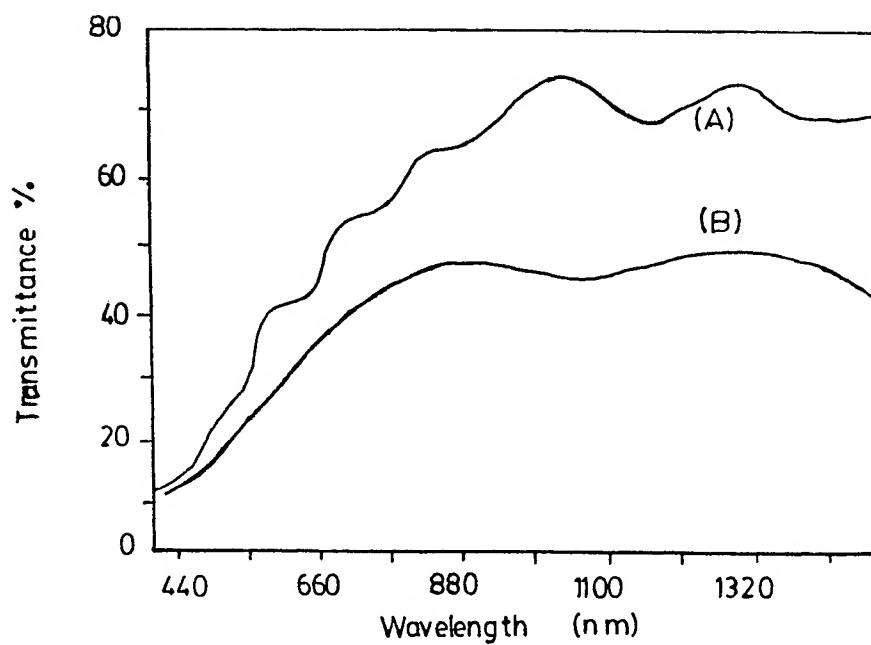


Fig.4. Transmission spectrum of SnS thin film.
(A) Electrodeposited (B) Brush plated

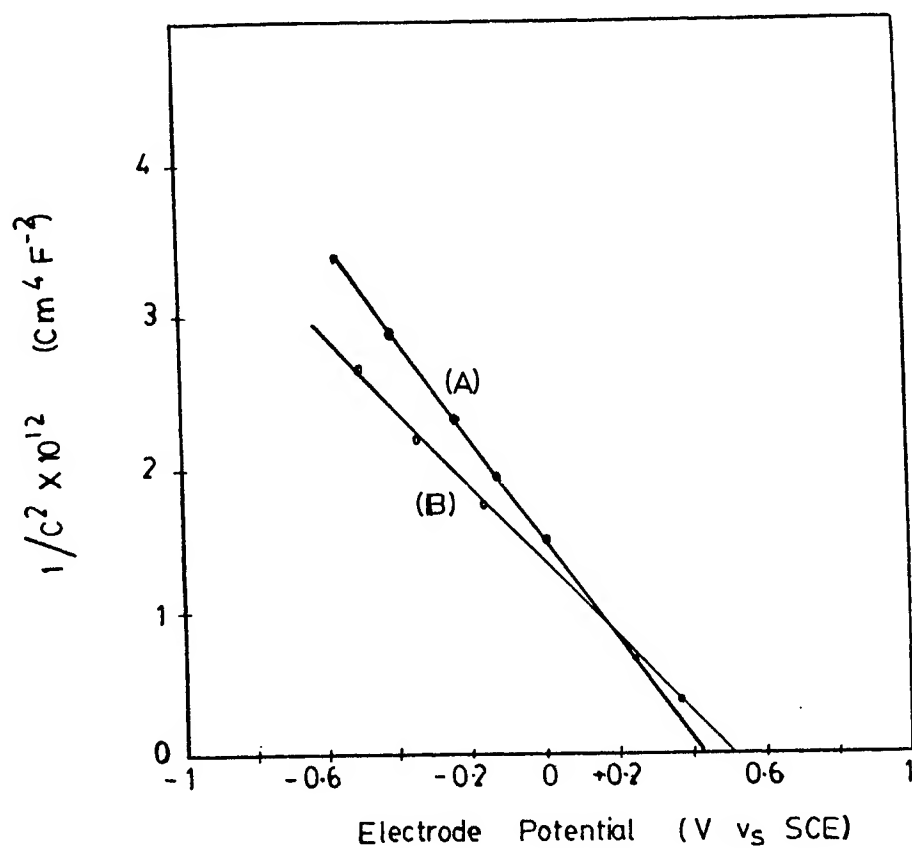


Fig.5. Mott - Schottky plot for a p-SnS /Fe³⁺,Fe²⁺/Pt system.

(A)Brush plated (B) Electrodeposited

SESSION 14

Unconventional Photonic Devices

Influence of the Hole-Carrier Layer Controlled by Electrochemical Method on Electroluminescence

Guangming Wang¹, Xiao Hu¹, and Terence K.S Wong²

¹Polymer laboratory, School of Applied Science, Nanyang Technological University, Nanyang Avenue, Singapore 639798.

²School of Electrical & Electronic Engineering, Nanyang Technological University, Nanyang Avenue, Singapore 639798.

ABSTRACT

Two-layer light emitting devices were fabricated using electrochemical deposited polybithiophene (PBTh) as the hole-transport layer and spin coated blend of polyoctylthiophene and a butadiene derivative as the emitting layer. It was found that the current density used for depositing polybithiophene greatly affects the effectiveness of the PBTh films as the hole-transport layers in enhancing the electroluminescent (EL) intensity and efficiency. Through analyzing the oxidation-reduction properties and conductivity of the PBTh films and the EL efficiency of the device, it can be concluded that there is an optimal current density for depositing the PBTh hole transport layer for the EL devices.

Key Words: Polybithiophene, Electropolymerization, Electroluminescence, Hole layer, Emitting layer

1. INTRODUCTION

Since the report of the electroluminescence of low molecular weight organic materials in the mid-1980s, EL devices using fluorescent organic dyes have been developed Tang and Van Slyke¹ showing brightness and operating voltages suitable for practical applications. More recently, EL phenomenon and devices from π -conjugated polymer has generated increasingly interests among many researchers during the last decade². In order to enhance both EL intensity and EL efficiency, improve the stability of the EL devices and change the emitting-light color, research work has been mainly concentrated on two respects, i.e., synthesis of new materials³⁻⁹ and developing novel structures for the EL devices.¹⁰⁻¹⁴

The forming-film technique is very important for fabricating the organic EL devices, especially for the multilayer devices. Several techniques such as vacuum evaporation, spin-coating, and self-assembly methods were reported for depositing the organic films. For the evaporation method, it requires costly machines and more complex techniques to create the more uniform thin films. For the spin coating, it is difficult to control the thickness of the film. And for the self-assembly method, it takes much longer time to fabricate a suitable thickness of the organic film for the EL devices. However, few reported the deposition such layers using the electrochemical method although it is commonly used to generate various electroactive polymer films. Comparing with the other methods mentioned above, electrochemical deposition is a relatively simple and requires no high complex system. Film thickness can also be controlled with relative ease and yet it is also flexible and versatile as many different types of electroactive polymer films can be obtained. In fabrication of multilayer devices, the second organic layer (emitting layer) on indium-tin oxide (ITO) coated glass is usually deposited by vacuum evaporating method rather than via spin coating. This is because the first organic layer is easily damaged in some solvents even if it is insoluble in these solutions.

Electrochemical polymerization of monomers such as thiophene, pyrrole, aniline and their derivative leads to the direct deposition of redox active conductive polymer films on the anode. These conducting polymers (polythiophene (PTh), polypyrrole (PPy) and polyaniline (PAni)) can be easily doped electrochemically and have been studied widely due to their many promising applications.¹⁵⁻¹⁷ Although all these films are generated through oxidation, and could be used as p-type

semiconductors, to our experience the film of thiophene based polymer films are more uniform than those of PPy and PANi. For the electropolymerization of thiophene in organic media, it is well recognized that the presence of water depresses the efficiency of the electropolymerizing process for thiophene dramatically.¹⁸ Bithiophene can be electropolymerized at very low potential, compared with PTh in the aqueous solution mixed with acetonitrile, and the polymer polybithiophene (PBTh) is also insoluble in general solvents and highly uniform on ITO. It was reported that oligothiophene film deposited by vacuum evaporation method, could enhance hole injection to the emitting layer in the EL device since it known as p-type semiconductor of low ionization energy (5.2 eV) and has considerably large hole mobility ($0.1 \text{ cm}^2/\text{V s}$) in a thin-film transistor.¹⁹ In this work, PBTh films are used in the EL devices as hole-transport to enhance the EL properties.

In this paper, we report the electropolymerization of bithiophene on the ITO in an aqueous acid solution mixed with organic solvent, acetonitrile and discuss the influence of the conditions of electrochemical deposition of PBTh hole-transport layer on the properties of EL devices.

2. EXPERIMENTS

2. 1. Materials

Chemicals: Bithiophene as monomer was used to electropolymerize PBTh, and polyoctylthiophene (P3OT) and butadiene derivative (DEAB) were blended to fabricate the emitting layer. BTh, DEAB and P3OT were purified by vacuum distillation, recrystallization and Soxhlet extraction respectively. Their molecular structures are shown in Fig. 1.

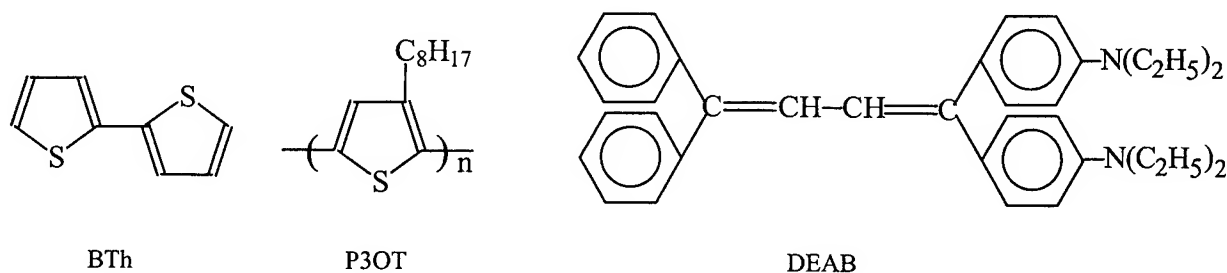


Fig.1. Chemical structures of bithiophene (BT), polyoctylthiophene (P3OT) and butadiene derivative (DEAB)

2. 2. Electrochemical Synthesis

System: An EG&G PAR Model 273 potentiostat/galvanostat was employed for electrochemical polymerization and cyclic voltammetry studies. Electrochemical measurements were carried out using a three-electrode system. Ag/AgCl and platinum (Pt) foil were used as the reference electrode and counter electrode respectively, and ITO as working electrode. The deposition of PBTh was carried out on ITO electrode in a 0.02 M bithiophene and 1.0 M HClO_4 water/acetonitrile mixed solution of volume ratio of 1:1. The same electrolyte/solvent system, without monomer, was used for doping-dedoping study. The solutions were purged prior to experiments by argon bubbling.

Treatment for Electrodes: Pt electrode was cleaned in boiling 50% H_2SO_4 aqueous solution and rinsed in ultra pure water (Millipore SUPERQ). ITO glass was cleaned using deionized water, ethanol, acetone, and mixture of isopropyl alcohol and deionized water (volume ration: 1:1).

Procedure in deposition: The ultra thin film of PBTh was electropolymerized by using chronopotential method. The amount of the polymer deposited on the working electrode was controlled by the total amount of charge consumed by the reaction system. After each polymerization, the polymer was thoroughly dedoped electrochemically. The polymer films were then washed with acetonitrile and deionized water. After that they were dried under vacuum at 100°C overnight.

2. 3. Fabrication of devices

The mixed solution of P3OT (5.0 mg/ml) and DEAB (10 mg/ml) was used for fabricating the emitting layer by using spin-coating method. The top aluminum electrode was prepared using a vacuum vapor evaporator at a vacuum of 10^{-5} Torr. The emitting area was $3 \times 4 \text{ mm}^2$. All measurements on device were carried out at room temperature in air.

3. RESULTS AND DISCUSSION

3.1. Properties of hole-transport layer

PBTh film can be electropolymerized in pure organic solvent, but the potential is much higher than that in the mixed solvents of water and acetonitrile. Fig.2 shows the cyclic voltammograms of 0.02M bithiophene in the mixed solutions of 1.0 M HClO₄ and acetonitrile with volume ratio of 1:1 and in the pure acetonitrile. It shows that the mixed solution has significant effect on the onset oxidation potential of bithiophene.

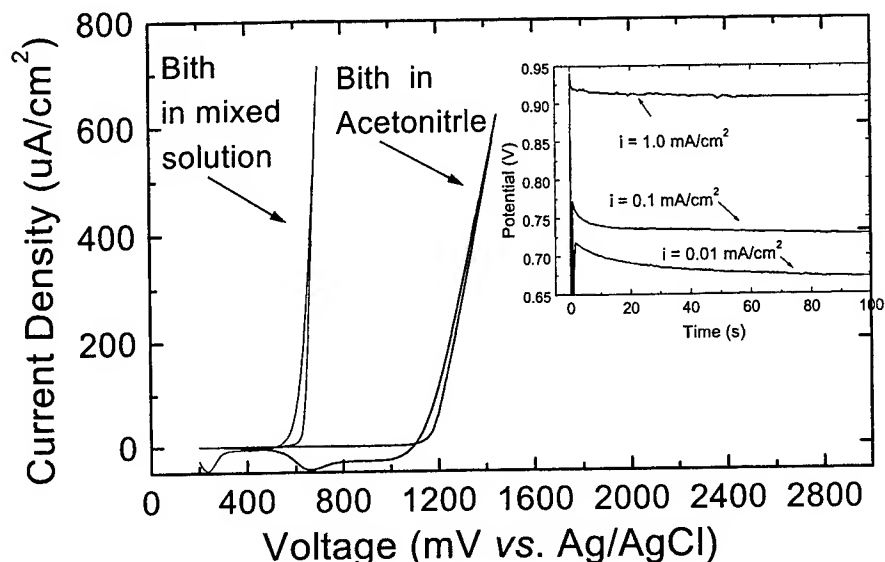


Fig.2. Cyclic voltammograms of 0.02M bithiophene (Bith) in the HClO₄(1.0M)/acetonitrile mixed solution with volume ratio of 1:1, and in the pure acetonitrile with 0.1M Tetraethylammonium tetrafluoroborate (>99%, Fluka) as electrolyte. Inset in this figure shows the chronopotentiograms of bithiophene at different anodic current densities of 0.01, 0.1 and 1.0 mA/cm² in the mixed solvent.

The potential for electropolymerizing PBTh is also very different at different anodic current densities of 0.01, 0.1 and 1.0 mA/cm², shown in inset of Fig.2. The PBTh films, as hole-transport layer in the devices were electropolymerized at these current densities on ITO. The low potential in the mixed solution may be due to the presence of the acids or Lewis acids, leading to the formation of π -complexes between monomers and the acids, which are more easily electrooxidized.²⁰

3.1.1. Electrochemical properties

In order to understand the influence of current density of electropolymerization on the properties of polybithiophene films, cyclic voltammograms of different films generated in this mixed solution were recorded. Fig. 3 shows the linear relationship between the anodic peak current density and the scan rate in the range from 10 to 200 mVs⁻¹ for the films deposited with different current densities. The inset of Fig.3 are the cyclic voltammograms of the film generated at the current density of 0.01 mA/cm², which serve as an example due to the similarity for the cyclic voltammograms of the films electropolymerized at different current densities. The following equations can be obtained by linear regression of the data in Fig. 3:

$$i = 1.97 v + 11.2 \quad (1-1)$$

$$i = 2.04 v + 34.7 \quad (1-2)$$

$$i = 2.71 v + 0.1, \quad (1-3)$$

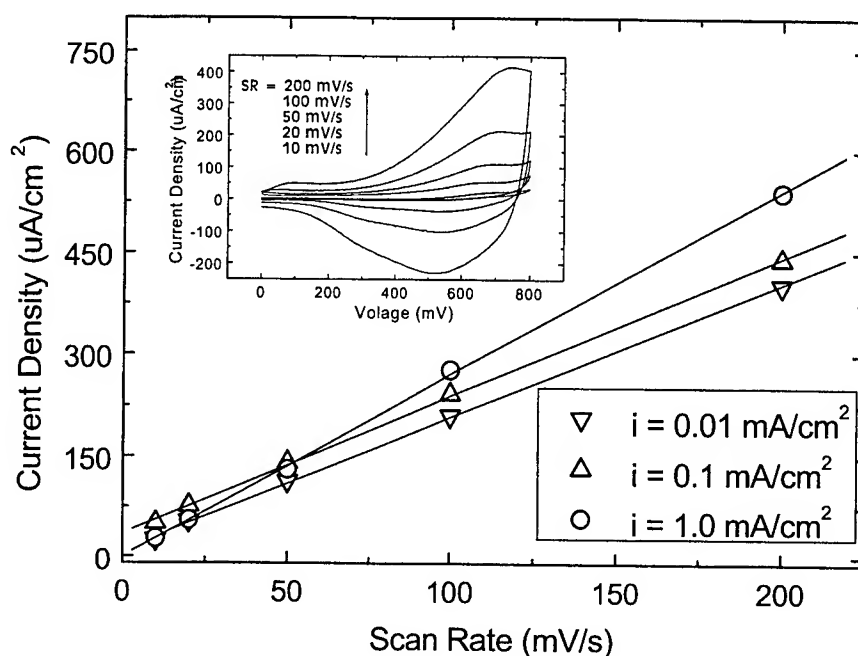


Fig.3. Relationship between the anodic peak current density and the scan rate for the films deposited with different current densities. Inset in this figure shows cyclic voltammograms of PBTh deposited anodic current densities of 0.01 mA/cm^2 in the $\text{HClO}_4(1.0\text{M})/\text{acetonitrile}$ mixed solution with volume ratio of 1:1.

where i and v are the current density and the scan rate respectively. Since the slopes of the lines 1.97, 2.04, and 2.71 correspond to the current densities of electropolymerization of 0.01, 0.1, and 1.0 mA/cm^2 , respectively, it is clear that the dependence of the peak current density on the scan rate increases with the current densities of electropolymerization. According to the mechanisms of oxidation or doping of polymers, the charges first transfer from the electrode to the polymer film, and then migrate to the film-solution interface. The above electrochemical analysis suggests that, during doping, the charges migrate faster in the polymer films electrosynthesised at higher current density.

3.1.2. Influence of the current density of electropolymerization on conductivity of PBTh film

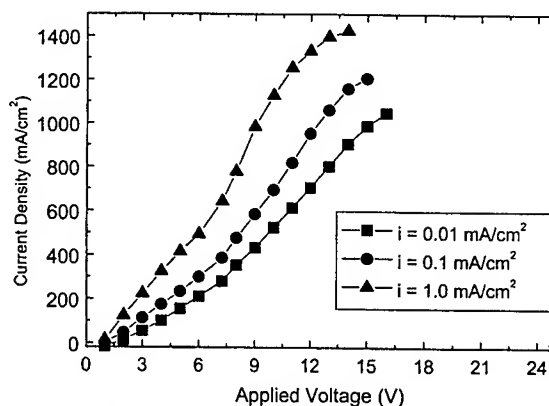


Fig.4. Current density changing with the applied voltage for films of PBTh deposited at different current densities in the mixed solution.

In order to discuss the influence of the current density of electropolymerization on the conductivity of the polymer film, the aluminum as top electrode was deposited on the surface on the PBTH for measuring the relationship between the current and the applied voltage. The thin film of PBTh was electropolymerized by using chronopotentiometric method, and the thickness of the film deposited on the working electrode was controlled by the total amount of charge consumed by the reaction system. It was kept to be constant at 8 mQ/cm^2 for film deposition at different current densities of 0.01, 0.1 and 1.0 mA/cm^2 .

Fig.4 depicts the variation of the current density through the PBTh film with the applied voltage for these films with ITO as positive electrode and aluminum as negative electrode. It can be seen that the higher deposition current density results in higher current density through the dry PBTh film between ITO and aluminum electrode. For the film deposited at 1.0 mA/cm^2 the current through the film rises quickly at about 8 to 9 V. In this case, there may be some degree of tunneling current probably due to the existence of pin holes in the film. For films deposited at lower current densities, the current density through the film increases more gradually and the tunneling effect seems to be less significant. This is also supported by the EL results shown in Figs. 7 and 8.

3.2. Characteristics of EL devices

The schematics of the EL device is shown in Fig.5. The thickness of the hole-transport layer is about 5 nm, and that of emitting layer about 50~80 nm. The PBTh films deposited at the three current densities were used as hole transport layer.

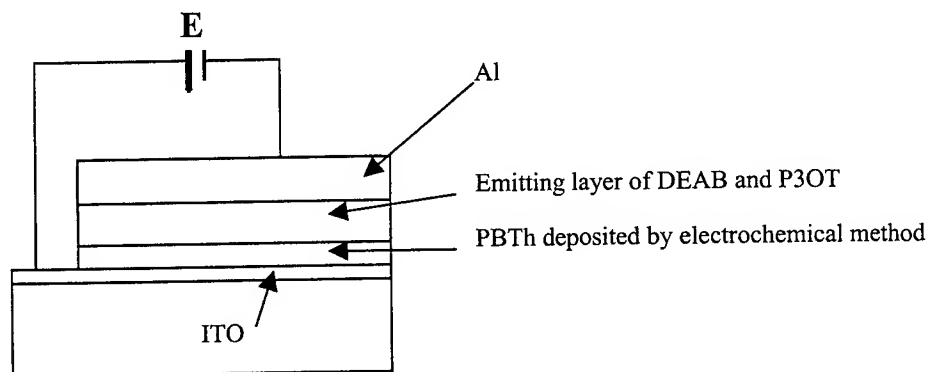


Fig.5. Construction of the EL device with electropolymerized PBTh as hole-transport layer

The EL spectra were generally similar when the three different PBTh films were used. Fig.6 compares the EL spectra of two kinds of devices with and without the hole transport layer at 10 V. The PBTh film results in red shift of EL spectra and a increase of the half width from 82 to 86 nm. These observations can be attributed to ease of recombination of electron and hole in the molecules of P3OT in the emitting layer due to the hole-transport hole used in these devices.

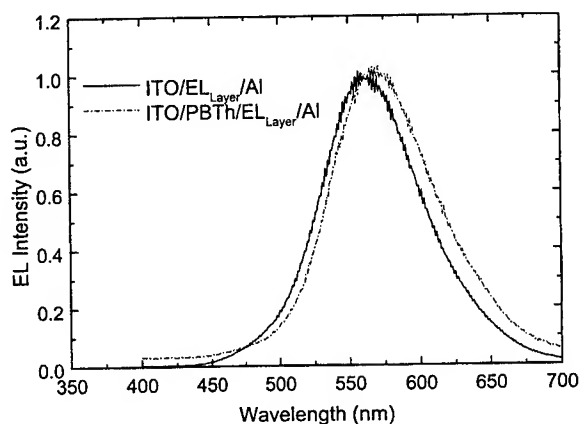


Fig.6. Normalized EL spectra of different devices obtained at 10V.

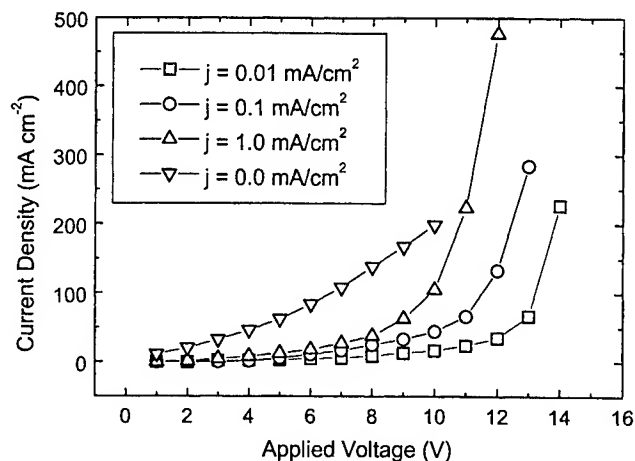


Fig.7. Current density-voltage characteristics for the EL devices with the hole-transport layers electropolymerized at different conditions

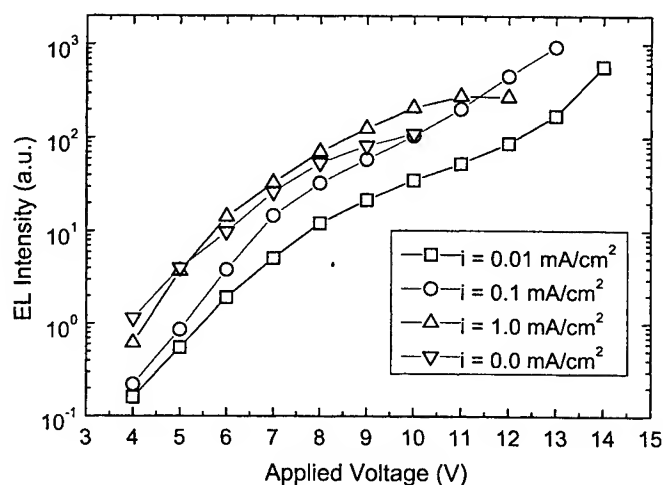


Fig.8. Relationship between EL intensity and applied voltage for the EL devices with the electropolymerized hole-transport layer.

The current and EL intensity for two-layer EL devices are quite different. Figs.7 and 8 show the current density and EL intensity changing with the applied voltage for these devices. It could be seen that the current intensity through the EL devices increases with elevation of current density of electropolymerization, but the change in EL intensity reflects inconsistency relative to the I-V plots (Fig. 7), suggesting that there is an optimal current density of electropolymerization of hole-transport layer for the EL devices.

The influence of current density of electropolymerizing film on the EL properties can be seen from Fig.8 and the relationship between the current through the film and applied voltage shown in Figs. 4 and 7. For hole-transport layer deposited at low current density such as 0.01 mA/cm^2 , the EL intensity is lowest among all devices fabricated. However, the consumed electrical energy for this device is much lower than that for all other devices. On the other hand, at higher current density

such as 1.0 mA/cm^2 to generate the polymer, the EL intensity of the EL device is lower than that for the double-layer device with the PBTh deposited at 0.1 mA/cm^2 at the beginning of 11V although higher current intensity passes through the device. By analyzing the Raman spectra of PBTh films deposited at the different current densities, we found they are the same as each other. Thus, the conductivity of the PBTh (see Fig.4) here is mainly determined by the structure of the film. In fact, we also found from the images of atomic force microscopy (AFM) that the roughness and the grain size of the film change with the deposition conditions. Therefore, as the hole-transport layer (PBTh) deposited at high current density of 1.0 mA/cm^2 , many carriers in the devices cannot recombine to generate the excitons, leading to lower EL intensity probably due to higher tunneling current because of existence of pinholes.

4. CONCLUSION

Based on the above discussion, the following conclusions can be drawn. The PBTh films can be electropolymerized directly on the ITO conducting glass. These PBTh films were successfully used as carrier-transport layer in fabrication of the EL device to enhance the EL intensity and EL efficiency. It was found that the condition for PBTh deposition is important because it affects the structure and morphology of the film, which in turn has a great influence on the efficiency of the recombination of carriers.

ACKNOWLEDGMENTS

The work is supported by an academic Research Funds, RG61/94 and RGM 44/97, of Nanyang Technological University, Singapore.

REFERENCES

1. C.W. Tang and S.A. Van Slyke, "Organic electroluminescent diodes," *Appl. Phys. Lett.* **51**, pp. 913-915, 1987.
2. J.H. Burroughes, D.D.C. Bradley, A.R. Brown, R.N. Marks, K. Mackay, R.H. Friend, P.L. Burns, and A.B. Holmes, "Light-emitting diodes based on conjugated polymers," *Nature* **347**, pp. 539-541, 1990.
3. C. Adachi, T. Tsutsui, and S. Saito, "Blue light-emitting organic electroluminescent devices," *Appl. Phys. Lett.* **56**, pp. 799-801, 1990.
4. M. Berggren, O. Inganäs, G. Gustafsson, J. Rasmussen, M.R. Andersson, T. Hjertberg, and O. Wennerström, "Light-emitting diodes with variable colors from polymer blends," *Nature* **372**, pp. 444-446, 1994.
5. M. Strukelj, F. Papadimitrakopoulos, T.M. Miller, and L.J. Rothberg, "Design and application of electron-transporting organic materials," *Science* **267**, pp. 1969-1972, 1995.
6. S. Son, A. Dodabalapur, A.J. Lovinger, and M.E. Galvin, "Luminescence enhancement by the introduction of disorder into poly(p-phenylene vinylene)," *Science* **269**, pp. 376-378, 1995.
7. C. Adachi, K. Nagai, and N. Tamoto, "Molecular design of hole transport material for obtaining high durability in organic electroluminescent diodes," *Appl. Phys. Lett.* **66**, pp. 2679-2681, 1995.
8. D. O. Brien, A. Bleyer, D.G. Lidzey, D.D.C. Bradley, and T. Tsutsui, "Efficient multilayer electroluminescence devices with poly(m-phenylenevinylene-co-2,5-dioctyloxy-p-phenylenevinylene) as the emissive layer," *J. Appl. Phys.* **82**, pp. 2662-2670, 1997.
9. A. W. Grice, D.D.C. Bradley, M.T. Bernius, M. Inbasekaran, W.W. Wu, and E.P. Woo, "High brightness and efficiency blue light-emitting polymer diodes," *Appl. Phys. Lett.* **73**, pp. 629-631, 1988.
10. N. Takada, T. Tsutsui, and S. Saito, "Control of emission characteristics in organic thin film electroluminescent diodes using an optical-microcavity structure," *Appl. Phys. Lett.* **63**, pp. 2032-2034, 1993.
11. J. Kido, M. Kimura, and K. Nagai, "Multilayer white light-emitting organic electroluminescent device," *Science* **267**, pp. 1332-1334, 1995.
12. M. Granström, M. Berggren, L. Inganäs, "Micrometer- and nanometer-sized polymeric light-emitting diodes," *Science* **267**, pp. 1479-1481, 1995.
13. M. Hamaguchi and K. Yoshino, "Color-variable electroluminescence from multilayer polymer films," *Appl. Phys. Lett.* **69**, pp. 143-145, 1996.
14. J.R. Sheats, "Stacked organic light-emitting diode in full color," *Science* **277**, pp. 191-192, 1997.
15. S. Chao and M.S. Wrighton, "Solid-state microelectrochemistry: Electrical characteristics of a solid-state microelectrochemical transistor based on poly(3-methylthiophene)," *J. Am. Chem. Soc.* **109**, pp. 2197-2199, 1987.

16. C.T. Kuo and W.H. Chiou, "Field-effect transistor with polyaniline thin films as semiconductor," *Synth. Met.* **88**, pp. 23-30, 1997.
17. G.M. Wang, H. Chen, H. Zhang, C.W. Yuan, Z.H. Lu, G. Wang, and W. Yang, "TiO₂/polypyrrole diodes prepared by electrochemical deposition of polypyrrole on microporous TiO₂ film," *Appl. Surf. Science* **135**, pp. 97-100, 1998.
18. F. Beck and U. Barsch, "The role of water in the electrodeposition and doping of polythiophene and two of its derivatives," *Makromol. Chem.* **194**, pp. 2725-2739, 1993.
19. C. Hosokawa, H. Higashi, and T. Kusumoto, "Novel structure of organic electroluminescence cells with conjugated oligomers," *Appl. Phys. Lett.* **62**, pp. 3238-3240, 1993.
20. E.A. Bazzouai, S. Aeiya, and P.C. Lacaze, "Low potential electropolymerization of thiophene in aqueous perchloric acid," *J. Electroanal. Chem.* **364**, pp. 63-69, 1994.

SESSION 15

Poster Session

A study on the polarization-sensitive performance of the strained quantum well semiconductor optical amplifiers

Deming Liu*, Wenchao Xu, Zigang Duan, Dexiu Huang

(Huazhong Univ. of Science and Technology, Dept. of Optoelectronic Engineering)

ABSTRACT

Comparing with Erbium Doped Fiber Amplifiers (EDFA), one prominent disadvantage of Semiconductor Optical Amplifier (SOA) is that its gain is sensitive to the state of polarization (SOP) of incident light. Reducing the polarization sensitivity of SOA is one of the important aims that man goes in for in the research of SOA. In this paper, we analyze the polarization performance of SOA, and also successfully develop a mixed-strain quantum well, polarization insensitive SOA. Ultra low residual reflectivity film is coated on the cleaved ends of active-layer to eliminate the resonant effect of the cavity and suppress self-simulated emission, thus the incident optical signals could obtain single path gain while travelling through the active-layer, which forms the travelling-wave amplification.

Key words: SOA, optical communication, strained quantum well, polarization

1. INTRODUCTION

With the integrated development of all-optic communication technique, the research of SOA becomes a heat subject again all over the world. SOA will play an important role in the futural all-optic communication systems. SOA could be used to construct optical switch arrays and optical interconnecting systems. Furthermore SOA wavelength conversion has many important applications in WDM all-optic network. Many researches of SOAs and their applications have been reported in a great deal of documents.¹⁻⁴

The following requirements are needed for SOA in the optical communication systems: high small-signal gain (in line amplification) or high-saturation output, broadband and flat gain spectrum, low noise figures and polarization insensitive gain. The major key technique, which influences the performance of SOA most, includes two aspects: structure design of the chip material of SOA and research of growth techniques, suppression technique of resonant cavity effect on the cleaved ends. Early SOA directly used the chip material of LD, and antireflection (AR) film was coated on the cleaved ends of the active-layer to suppress resonant effect of the cavity, thus incident optical signals obtained single path gain while travelling through the active-layer, which formed travelling-wave amplification. Due to the confinement of bulk material, the performance index of SOA stayed in low level till late 1980s, and especially its higher polarization sensitivity ($\sim 7\text{dB}$) and higher noise figures ($7\sim 8\text{dB}$) were unacceptable by the optical communication systems, which once made researchers to doubt the future of SOA. From early 1990s, with the development of "energy band engineering" and the maturation of theory and technique of strained quantum well (SQW), researchers can highly enhance the performance of SOA through the proper design of the energy band of semiconductor material. From then SOA obtain the new life and the strong competitive power.

The authors have successfully developed a polarization-insensitive SOA. The active chips of the SOA adopt the multi-layer SQW structure, and ultra low residual reflectivity film is coated on the cleaved ends of active-layer to suppress self-simulated emission resonance, which forms the travelling-wave amplification. The key technique for SOA, the theoretical analysis of the performance of SOA and the experimental research will also be presented in this paper.

* Correspondence: Email: dmliu@mail.hust.edu.cn; Telephone/Fax: 0086-27-87543355

2. DEVELOPMENT OF SOA

One fatal disadvantage of SOA with the common structure is that its transverse electric (TE) mode gain is not equal to transverse magnetic (TM) mode gain (Generally TE mode gain is much greater than TM's), which results in the polarization-sensitive performance of SOA. This drawback now can be overcome with a tensile strained and compressive strained multi-layer quantum well structure. The structure of mixed SQW is shown in Fig. 1, where the solid line denotes that a heavy hole (hh) band moves up to the top of the valence band while the dashed line denotes that a light hole (lh) band moves up to the top of the valence band. Tensile strain makes a light hole band moves up to the top of the valence band. The transition of electron to light hole mainly generates TM polarization-state photons and few TE polarization-state photons, thus tensile strained quantum well enhances TM mode gain by suppression of TE mode gain. Compressive strain makes a heavy hole band moves to the top of the valence band. But the transition of electron to heavy hole only generates TE polarization-state photons, thus compressive strained quantum well only provides TE mode gain. If the active-layer contains two types of strained quantum well at the same time, such type of active-layer can provide TE and TM modes gain meanwhile. Hence we can adjust TE mode gain to be approximately equal to TM mode gain by properly designing the composition of the grown material, well width, the amount of strain and layer number to reduce the polarization sensitivity.

Metalorganic chemical vapor deposition (MOCVD) system provided by Wuhan Telecommunication Device Company (WTD) is used for crystal growth. This system is manufactured by ALEXTRON Lt.d. of Germany and equipped with RUN/VENT fast trigger. Phosphine (PH_3) and Arsine (AsH_3) are used for group V sources, while Trimethylindium (TMIn) and Trimethylgallium (TMGa) are used for group III sources. Hydrogen diffused by palladium tube is the carrier gas.

In order to acquire excellent mixed-strain quantum well material, good tensile strained and compressive strained quantum well material is necessary. The foremost technological parameters which influence the performance of SOA most are well width, well number and the amount of strain of tensile strained and compressive strained material. Thus we firstly adjusted technological parameters of tensile strained and compressive strained quantum well respectively, then high spot studied up on the flow of group III sources and group V sources and lastly decided the optimum growth technology. Basing on these results, we successfully grew the pure tensile strained and compressive strained quantum well material its fluorescent and dual-crystals diffraction performance met the design requirements well. Two types of SQW were then grown up in different combination. We also used commercial HRS software based on Tagaki-Taupin equation to theoretical simulation analyze the diffraction curve of mix dual-crystal structure. We find the following rules from the X-ray diffraction cure through the theoretical simulation analysis and calculation of different mixed-strained quantum structure, such as 3C2T, 3T2C, 3T3C, 3C3T, 4C3T, 4T3C, 4T4C, 4C4T (where C denotes compressive strained quantum well, T denotes tensile strained quantum well, respectively):

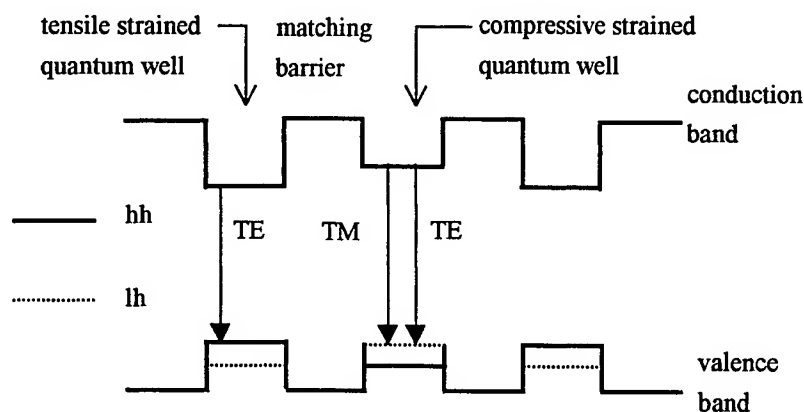


Fig.1 The top band diagram of tensile strained quantum well, matching barrier and compressive strained quantum well

2.1. The periodic frame corresponding to the angle spacing of diffraction satellite peaks consists of a tensile strained quantum well, a compressive quantum well and two barrier layers. Period Λ and the average amount of strain of zero order peak ε_{avr} is respectively given by:

$$\Lambda = w_t + w_c + 2w_b \quad (1)$$

$$\varepsilon_{avr} = (\varepsilon_t w_t + \varepsilon_c w_c + 2\varepsilon_b w_b) / \Lambda ; \quad (2)$$

here, w_i and ε_i ($i=t,c,b$) are the width and the amount of strain of tensile strained quantum well, compressive strained quantum well and barrier layer.

2.2. The more the periodic of mixed-strained quantum well is, the greater the intensity is. The narrower the satellite peak is, the greater the intensity is.

2.3. When the number of two types of strained quantum well are identical, adding a tensile strained quantum well and a compressive strained quantum well at the same time will not influence the position of zero order satellite peak, but increase the intensity of satellite peaks.

2.4. The order of tensile strained and compressive strained quantum well in periodic structure doesn't have a great influence on diffraction curve.

Through optimization design analysis, we chose the mix structure of 4T3C and adopted the width of compressive strained quantum well as 2nm while the amount of its strain as 0.6%, the width of tensile strained quantum well as 12nm while the amount of its strain as -0.75%, the width of barrier as 14nm while the amount of its strain as 0.14% to grow the material of mixed-strained quantum well. The subsequent technique of device introduced the Double Channel Planar Buried Heterostructure (DCPBH) extension chip. The chip was 600um in length and 2um in width after cleavage, and AR film was coated on the two cleaved ends to reduce the residual reflectivity to 5×10^{-4} , thus the SOA chip was produced.

3. MEASUREMENT AND ANALYSIS FOR THE PERFORMANCES OF SOA

The net gain and polarization sensitivity is the foremost parameters of SOA. The measurement setup is shown in Fig. 2. The modulated optical signal (1kHz) output from LD travels through the Polarization Controller (PC) and single mode fiber which is used to couple the light to the SOA chip. A crystal analyzer with high extinction ratio is set up at the output end of SOA chip. A PIN detector receives the output power. The above equipment forms a setup to measure the polarization sensitivity gain of SOA. In the measurement, the working current I_{drive} is applied to SOA. TE and TM modes could be obtained by rotating the PC. Then we can detect the output light power of SOA for TE and TM modes respectively by rotating the polarization analyzer. The gain is related to the polarization through the coefficient of correlation P as:

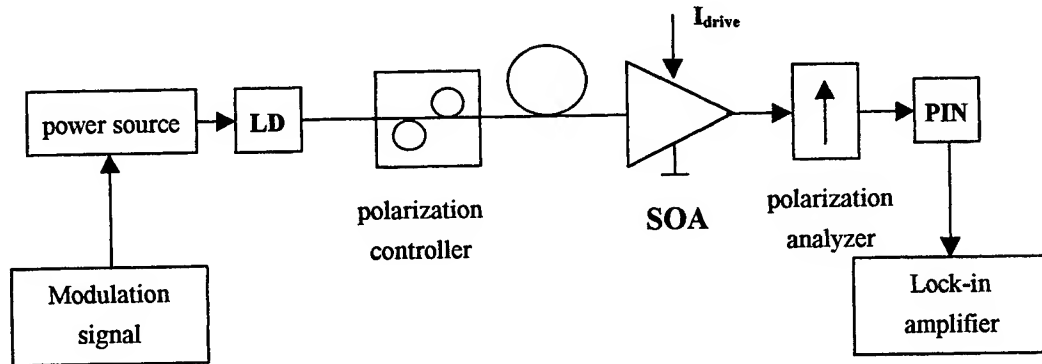


Fig.2 The schematic diagram of measurement setup

$$P = |G_{TE} - G_{TM}| \quad (3)$$

A few curves of output power of SOA for TE and TM modes versus driving current are shown in Fig.3. Where (a) corresponds to the conventional quantum well (QW) chip, (b) corresponds to the mixed-strain quantum well chip, and (c) corresponds to the mixed-strain quantum well chip with AR film (AR-SQW). Comparing among the above there, we can obviously see:

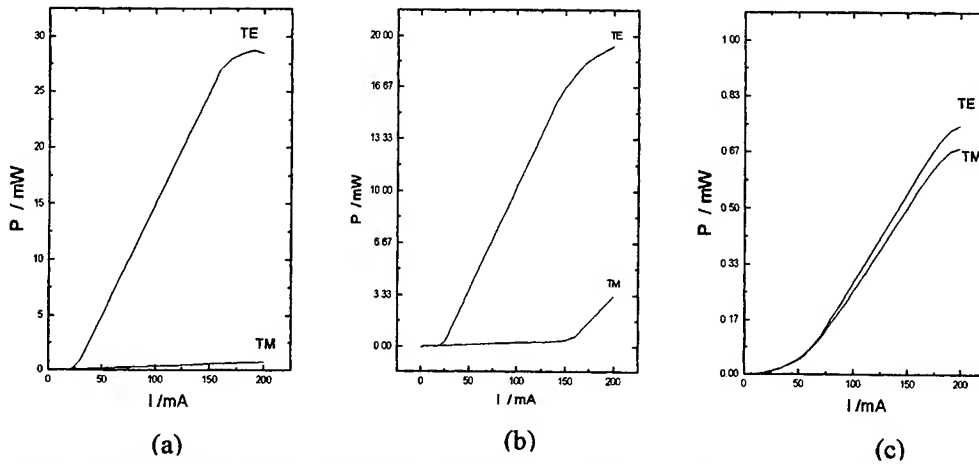


Fig. 3 The comparing of the output power of SOA versus driving current for TE and TM polarization

3.1. For the QW wafers there was only TE mode lasing and no TM mode lasing.

3.2. For the mixed-strain quantum well LD both of the TE and TM modes will lase, which indicates that the tensile strained quantum well has taken in effect and the TM mode gain is upgraded. But the lasing threshold current of TM mode is greater than that of TE's. Owing to the cutoff dimension of TE mode is smaller than that of TM's, TE mode is easier to lase. So when TM mode lases, due to the mode competition effect, TM mode is difficult to lase. Only with the higher driving current (i.e. the internal gain is very high), TM mode could be possible to lase.

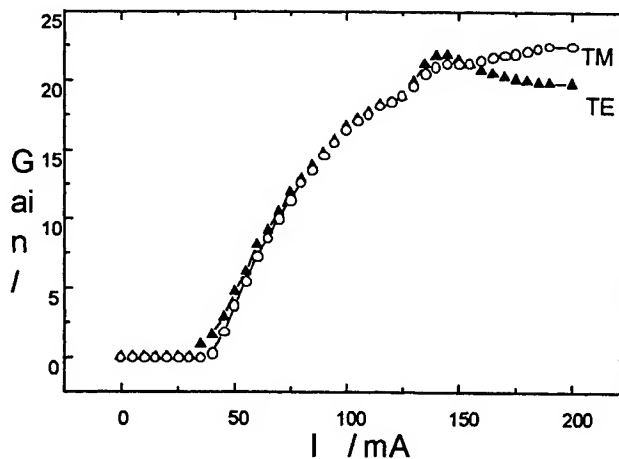


Fig.4. Chip gain of SOA versus driving current for TE and TM polarization

3.3. After AR film is coated on the cleaved ends of chip, the P-I curves of both TE and TM modes have no obvious threshold, which forms the superradiance output, and the curve of TE mode is very close to that of TM mode too. This indicates that TE and TM modes obtain approximately same gain with the joint contribution of SQW and AR film, which is also demonstrated by the later measurement results.

The output spectrum of the AR-SOA is very close to the spontaneous emission spectrum of LED, but it will present obvious modulation by lasing when the driving current is too high. The gain bandwidth of SOA may be approximately equal to the spontaneous radiation spectrum bandwidth of SOA, and is measured to be 46nm. The curve of TE and TM modes gain versus driving current is shown in Fig.4. The gain difference between TE and TM mode (i.e. P) is less than 0.5dB below the saturation current, and the maximum unsaturated gain achieved is 22.5 dB. Due to the influence of residual reflectivity of cleaved ends, the saturation output current is only 150 mA, which doesn't achieve the theoretical expected value. The performance of SOA could be continuously greatly improved by reducing the residual reflectivity.

4. CONCLUSION

In this paper the relationship between the well width, well number and strained quantum of the SQW as well as the reflectivity of the AR film were studied. The results of the theoretical and experimental analysis showed that the P-I curves of TE and TM modes for the QW, SQW and AR-SQW wafers were much different. For the QW wafers there was only TE mode lasing and no TM lasing. For the SQW wafers the lasing of TM mode occurred because of introducing the extensively strained quantum well and the competition between TE mode and TM mode was observed. For the AR-SQW wafer the P-I curves for both TE and TM modes were nearly consistent and linear till the maximum operation current. An optimum balance was achieved through adjusting the related design parameters and the operation conditions. A real polarization-insensitive SOA with the polarization-related gain ripple lower than 0.5 dB in the whole range of the driven currents and the gain-bandwidth was fabricated. The SOA were designed to operate at two wavelengths, i.e. 1310 nm and 1550 nm. A maximum gain of 22 dB and gain-bandwidth of 45 nm were reached.

ACKNOWLEDGEMENT

The authors would like to thank the leaders and researchers of WTD for their encouragement and cooperation through this work. Also the acknowledgement should be given to the National 863-Program who aids the project.

REFERENCES

1. P. Doussiere, S.Dubovitsky, "1.55 μm polarization independent semiconductor optical amplifier with 25 dB fiber to fiber gain," *IEEE Photon. Technol. Lett.* **6**(2), pp. 170-173, 1994.
2. Holtmann C, T Mukai, T Saitoh, "Polarization independent bulk active region semiconductor optical amplifier for 1300 nm wavelength," *IEEE Photon. Technol. Lett.* **8**(3), pp. 343, 1996.

Phase calculation of (100) oriented InGaAsSb grown with liquid phase epitaxy

Xiang-jun Mao*, Yuen-Chuen Chan and Yee-Loy Lam

Photonics Research Group, School of Electrical and Electronic Engineering
Nanyang Technological University, Block S1, Nanyang Ave., Singapore 639798

ABSTRACT

The solidus-liquidus phase diagram of (100) oriented $\text{In}_x\text{Ga}_{1-x}\text{As}_y\text{Sb}_{1-y}$ quaternary alloy, which is lattice-matched to the GaSb substrate, has been calculated. We used the Levenberg-Marquardt method (least squares minimization) to deal with the nonlinear equations and find the phase curves at different temperatures. We obtained a series of phase diagrams from 500°C to 730°C. The phase plots of the indium content in the GaSb-lattice matched $\text{In}_x\text{Ga}_{1-x}\text{As}_y\text{Sb}_{1-y}$ quaternary as a function of the antimony content of the melt at different temperatures bear three kinds of shapes. The plots below 532.7°C are similar, displaying a hyperbola with two branches, and the lower the temperature, the larger is the gap between the branches. The phase plot changes to two intersected lines at 532.7°C. At temperatures higher than 532.7°C, the phase diagram includes a nearly symmetrical curve and a segment. The higher is the temperature, the shorter is the segment. A new growth region have been discovered, where GaSb-lattice matched $\text{In}_x\text{Ga}_{1-x}\text{As}_y\text{Sb}_{1-y}$ with high indium content can be grown.

Keywords: Liquid phase epitaxy, GaSb, $\text{In}_x\text{Ga}_{1-x}\text{As}_y\text{Sb}_{1-y}$, mid-infrared, phase diagram

1. INTRODUCTION

The $\text{In}_x\text{Ga}_{1-x}\text{As}_y\text{Sb}_{1-y}$ solid solution has a wide range of applications in high resolution gas spectroscopy, pollution monitor, industrial process control, space technology, medical diagnostics, free space communications, low loss fiber optic communication, and military counter measure systems¹⁻⁶.

It is well known that infrared detectors are very important for pollution monitor. For such applications, HgCdTe is the dominant material system used. However, some disadvantages, such as instability and nonuniformity, evidently exist for this material due to the high Hg vapor pressure that is noted during the growth. The toxic properties of the component materials Hg, Cd and Te, also pose problems in the production process. It is anticipated that long wavelength materials from $\text{In}_x\text{Ga}_{1-x}\text{As}_y\text{Sb}_{1-y}$ alloy may offer an alternative to HgCdTe³.

There are several methods to grow the InGaAsSb quaternary alloy including liquid-phase epitaxy(LPE), metalorganic chemical vapor deposition(MOCVD), molecular beam epitaxy(MBE) and so on. In this paper the discussion will be focused on LPE¹⁻⁶.

The successful InGaAsSb growth by LPE motivated studies of the phase diagrams in In-Ga-As-Sb system. Since the experimental determination of a quaternary phase diagram is very cumbersome, there is an obvious need for reliable thermodynamic techniques to predict them from ternary data. A lot of calculation models were brought out, in which the solution model derived by Ilegems and Panish is practical and efficient. It consists of a set of equations based on the successive decomposition of the quaternary solid solution into regular mixtures of ternary and then binary compounds. These liquidus equations are employed in the calculation of solid-liquid equilibria in the In-Ga-As-Sb system^{1,7,8}.

*Correspondence: Email: p145714704@ntu.edu.sg; Telephone: 65 790 5461;

2. PHASE DIAGRAM CALCULATION EQUATIONS AND METHODS

We use the thermodynamical model brought forth by Ilegems and M.B. Panish to calculate the phase diagram. For the solidus-liquidus phase diagram of (100) oriented $\text{In}_x\text{Ga}_{1-x}\text{As}_y\text{Sb}_{1-y}$ quaternary alloy, which is lattice-matched to GaSb substrate, the related equations are as follows^{7,8}:

$$\begin{aligned}\Delta H_F^{\text{InAs}} - T\Delta S_F^{\text{InAs}} - RT\ln xy + RT\ln 4X_L^{\text{In}}X_L^{\text{As}} \\ = M_L^{\text{InAs}} + \alpha_{\text{In-Ga}}(1-x)^2 + \alpha_{\text{As-Sb}}(1-y)^2 - \alpha_c(1-x)(1-y); \\ \Delta H_F^{\text{InSb}} - T\Delta S_F^{\text{InSb}} - RT\ln x(1-y) + RT\ln 4X_L^{\text{In}}X_L^{\text{Sb}} \\ = M_L^{\text{InSb}} + \alpha_{\text{In-Ga}}(1-x)^2 + \alpha_{\text{As-Sb}}y^2 + \alpha_c(1-x)y; \\ \Delta H_F^{\text{GaAs}} - T\Delta S_F^{\text{GaAs}} - RT\ln(1-x)y + RT\ln 4X_L^{\text{Ga}}X_L^{\text{As}} \\ = M_L^{\text{GaAs}} + \alpha_{\text{In-Ga}}x^2 + \alpha_{\text{As-Sb}}(1-y)^2 + \alpha_cx(1-y); \\ \Delta H_F^{\text{GaSb}} - T\Delta S_F^{\text{GaSb}} - RT\ln(1-x)(1-y) + RT\ln 4X_L^{\text{Ga}}X_L^{\text{Sb}} \\ = M_L^{\text{GaSb}} + \alpha_{\text{In-Ga}}x^2 + \alpha_{\text{As-Sb}}y^2 - \alpha_cxy;\end{aligned}\quad (1)$$

$$\begin{aligned}\alpha_c = \Delta H_F^{\text{InSb}} - T\Delta S_F^{\text{InSb}} + \Delta H_F^{\text{GaAs}} - T\Delta S_F^{\text{GaAs}} - \Delta H_F^{\text{InAs}} + T\Delta S_F^{\text{InAs}} - \\ \Delta H_F^{\text{GaSb}} + T\Delta S_F^{\text{GaSb}} + 0.5(\alpha_{\text{InAs}} + \alpha_{\text{GaSb}} - \alpha_{\text{GaAs}} - \alpha_{\text{InSb}});\end{aligned}\quad (2)$$

According to the definition of the function M_L^{ij} , we can get:

$$\begin{aligned}M_L^{\text{InAs}} &= \alpha_{\text{InAs}}(1/2 - X_L^{\text{In}}(1 - X_L^{\text{As}}) - X_L^{\text{As}}(1 - X_L^{\text{In}})) + (\alpha_{\text{InGa}}X_L^{\text{Ga}} + \alpha_{\text{InSb}}X_L^{\text{Sb}})(2X_L^{\text{In}} - 1) + \\ &\quad (\alpha_{\text{GaAs}}X_L^{\text{Ga}} + \alpha_{\text{AsSb}}X_L^{\text{Sb}})(2X_L^{\text{As}} - 1) + 2\alpha_{\text{GaSb}}X_L^{\text{Ga}}X_L^{\text{Sb}}; \\ M_L^{\text{InSb}} &= \alpha_{\text{InSb}}(1/2 - X_L^{\text{In}}(1 - X_L^{\text{Sb}}) - X_L^{\text{Sb}}(1 - X_L^{\text{In}})) + (\alpha_{\text{InGa}}X_L^{\text{Ga}} + \alpha_{\text{InAs}}X_L^{\text{As}})(2X_L^{\text{In}} - 1) + \\ &\quad (\alpha_{\text{GaSb}}X_L^{\text{Ga}} + \alpha_{\text{AsSb}}X_L^{\text{As}})(2X_L^{\text{Sb}} - 1) + 2\alpha_{\text{GaAs}}X_L^{\text{Ga}}X_L^{\text{As}}; \\ M_L^{\text{GaAs}} &= \alpha_{\text{GaAs}}(1/2 - X_L^{\text{Ga}}(1 - X_L^{\text{As}}) - X_L^{\text{As}}(1 - X_L^{\text{Ga}})) + (\alpha_{\text{InGa}}X_L^{\text{In}} + \alpha_{\text{GaSb}}X_L^{\text{Sb}})(2X_L^{\text{Ga}} - 1) + \\ &\quad (\alpha_{\text{InAs}}X_L^{\text{In}} + \alpha_{\text{AsSb}}X_L^{\text{Sb}})(2X_L^{\text{As}} - 1) + 2\alpha_{\text{InSb}}X_L^{\text{In}}X_L^{\text{Sb}}; \\ M_L^{\text{GaSb}} &= \alpha_{\text{GaSb}}(1/2 - X_L^{\text{Ga}}(1 - X_L^{\text{Sb}}) - X_L^{\text{Sb}}(1 - X_L^{\text{Ga}})) + (\alpha_{\text{InGa}}X_L^{\text{In}} + \alpha_{\text{GaAs}}X_L^{\text{As}})(2X_L^{\text{Ga}} - 1) + \\ &\quad (\alpha_{\text{InSb}}X_L^{\text{In}} + \alpha_{\text{AsSb}}X_L^{\text{As}})(2X_L^{\text{Sb}} - 1) + 2\alpha_{\text{InAs}}X_L^{\text{In}}X_L^{\text{As}};\end{aligned}\quad (3)$$

Accordingly, $\alpha_{\text{In-Ga}}$ and $\alpha_{\text{As-Sb}}$ in the quaternary solid solution are given by the linear relations⁹:

$$\begin{aligned}\alpha_{\text{In-Ga}} &= y\alpha_{\text{InAs-GaAs}} + (1-y)\alpha_{\text{InSb-GaSb}}; \\ \alpha_{\text{As-Sb}} &= x\alpha_{\text{InAs-InSb}} + (1-x)\alpha_{\text{GaAs-GaSb}};\end{aligned}\quad (4)$$

In this work, the thermodynamical parameters of Dolginov¹⁰⁻¹² are used (Table 1). The equation group is not easily solved by the normal method. However, it is possible to convert the equation problem to an optimization problem. From the equation group, we can get an optimization function:

$$\begin{aligned}F(X_L^{\text{In}}, X_L^{\text{Ga}}, X_L^{\text{As}}) = \\ (\Delta H_F^{\text{InAs}} - T\Delta S_F^{\text{InAs}} - RT\ln xy + RT\ln 4X_L^{\text{In}}X_L^{\text{As}} - (M_L^{\text{InAs}} + \alpha_{\text{In-Ga}}(1-x)^2 + \alpha_{\text{As-Sb}}(1-y)^2 - \alpha_c(1-x)(1-y)))^2 + \\ (\Delta H_F^{\text{InSb}} - T\Delta S_F^{\text{InSb}} - RT\ln x(1-y) + RT\ln 4X_L^{\text{In}}X_L^{\text{Sb}} - (M_L^{\text{InSb}} + \alpha_{\text{In-Ga}}(1-x)^2 + \alpha_{\text{As-Sb}}y^2 + \alpha_c(1-x)y))^2 + \\ (\Delta H_F^{\text{GaAs}} - T\Delta S_F^{\text{GaAs}} - RT\ln(1-x)y + RT\ln 4X_L^{\text{Ga}}X_L^{\text{As}} - (M_L^{\text{GaAs}} + \alpha_{\text{In-Ga}}x^2 + \alpha_{\text{As-Sb}}(1-y)^2 + \alpha_cx(1-y)))^2 \\ \text{with } X_L^{\text{In}} + X_L^{\text{Ga}} + X_L^{\text{As}} + X_L^{\text{Sb}} = 1\end{aligned}\quad (5)$$

The problem is to search for an optimization solution where the value of $F(X_L^{\text{In}}, X_L^{\text{Ga}}, X_L^{\text{As}})$ is smallest, which is a least squares minimization problem. There are mainly six methods, and they are:

- (1) Levenberg-Marquardt Method

- (2) Broyden-Fletcher-Goldfarb-Shanno Method
- (3) Davidon-Fletcher-Powell Method
- (4) Steepest Descent Method
- (5) Nelder-Mead Method
- (6) Gauss-Newton Method

In the course of calculation, we find that the Levenberg-Marquardt Method is most efficient for the iteration. The reason is that the Levenberg-Marquardt Method is very efficient for solving the least squares minimization problem. Hence this method was chosen¹³.

Table 1. Thermodynamical parameters of Dolginov used in this work.

<i>Parameter</i>	<i>Compound or system</i>	<i>Value</i>
Melting point : T^F (K)	InAs	1215
	InSb	798
	GaAs	1511
	GaSb	983
Entropy of fusion ΔS^F (cal mol ⁻¹ K ⁻¹)	InAs	14.52
	InSb	14.32
	GaAs	16.64
	GaSb	15.80
Interaction parameters in solid phase: (cal mol ⁻¹)	InAs-InSb	1600
	GaAs-GaSb	4000
	GaAs-InAs	2000
	GaSb-InSb	1450
Interaction parameters in liquid phase: (cal mol ⁻¹)	In-As	1645-7.49T
	In-Sb	-4111+0.82T
	Ga-As	-2793-0.46T
	Ga-Sb	3154-4.02T
	Ga-In	1066
	As-Sb	750

So far, the remaining problem is how to search for the initial value for the iterations. Substituting the expression M_L^{ij} to the equation group(1), it is obvious that the coefficient ΔH_F^{ij} is linear, which means that if we assume that X_L^i is known and that ΔH_F^{ij} is unknown, we can work out it very easily because the new equations are linear. This merit brings forth a very good way to improve on optimization algorithms. Taking ΔH_F^{ij} and X_L^{in} as unknown in turn, we can design a unique algorithm, and its ability of convergence is excellent. No matter what the initial values are, the optimization solution can be found easily.

3. DISCUSSION

We obtained a series of phase diagrams from 500°C to 730°C. The phase plots of the indium content in the GaSb-lattice matched $In_xGa_{1-x}As_ySb_{1-y}$ quaternary as a function of the antimony content of the melt at different temperatures display three kinds of shapes: 1) a hyperbola with two branches; 2) two intersected lines; 3) a nearly symmetrical curve and a segment. Through the computations, we define the feasible growth region of GaSb-lattice matched $InGaAsSb$, and found a new growth region with higher indium content for LPE growth.

The plots below 532.7°C are similar, displaying a hyperbola with two branches. The lower is the temperature, the larger is the gap between the branches(Figure 1).

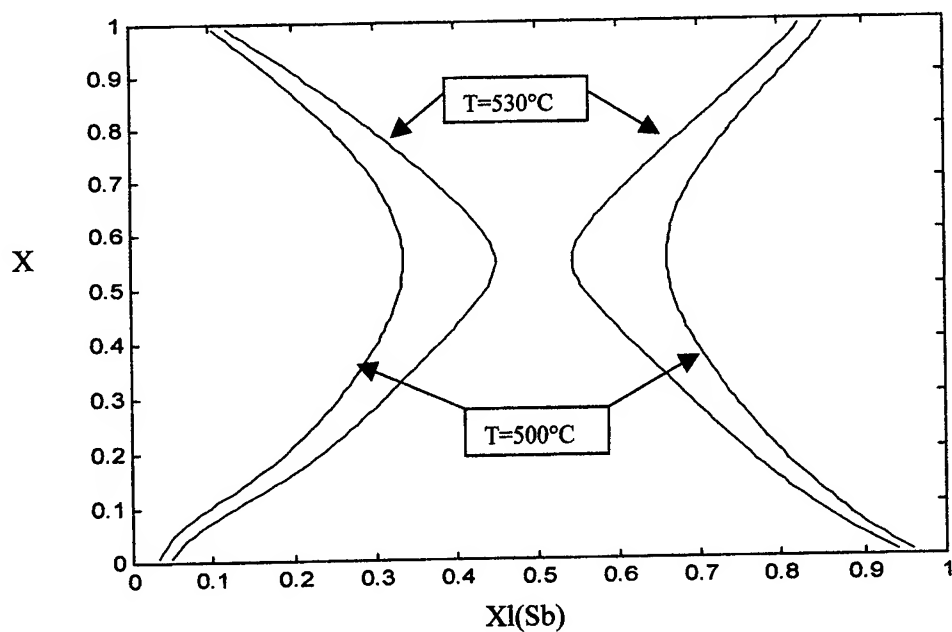


Figure 1. Equilibrium solidus isotherms for GaSb-lattice matched $\text{In}_x\text{Ga}_{1-x}\text{As}_y\text{Sb}_{1-y}$ quaternary alloys as a function of antimony content of the melt: x versus $Xl(\text{Sb})$

The phase plot changes to two intersected lines at 532.7°C (Figure 2).

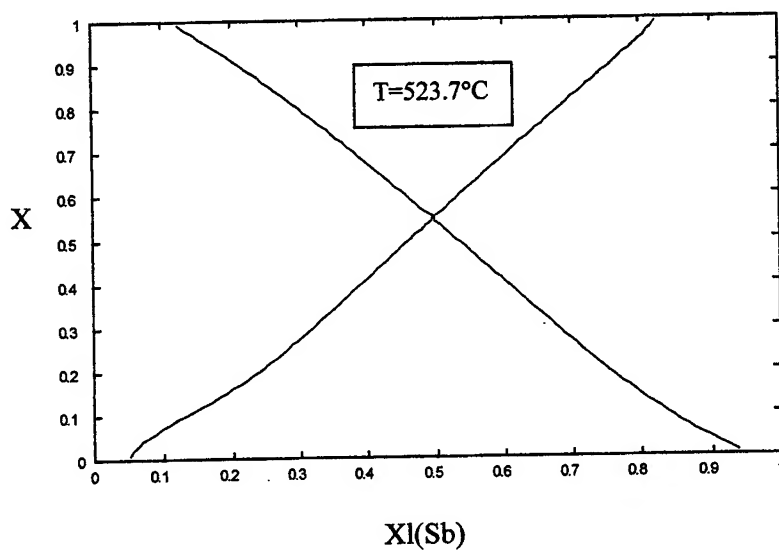


Figure 2. Equilibrium solidus isotherms for GaSb-lattice matched $\text{In}_x\text{Ga}_{1-x}\text{As}_y\text{Sb}_{1-y}$ quaternary alloys as a function of antimony content of the melt: x versus $Xl(\text{Sb})$.

At temperatures higher than 532.7°C , the phase diagram includes a nearly symmetrical curve and a segment (Figure 3). The higher is the temperature, the shorter is the segment.

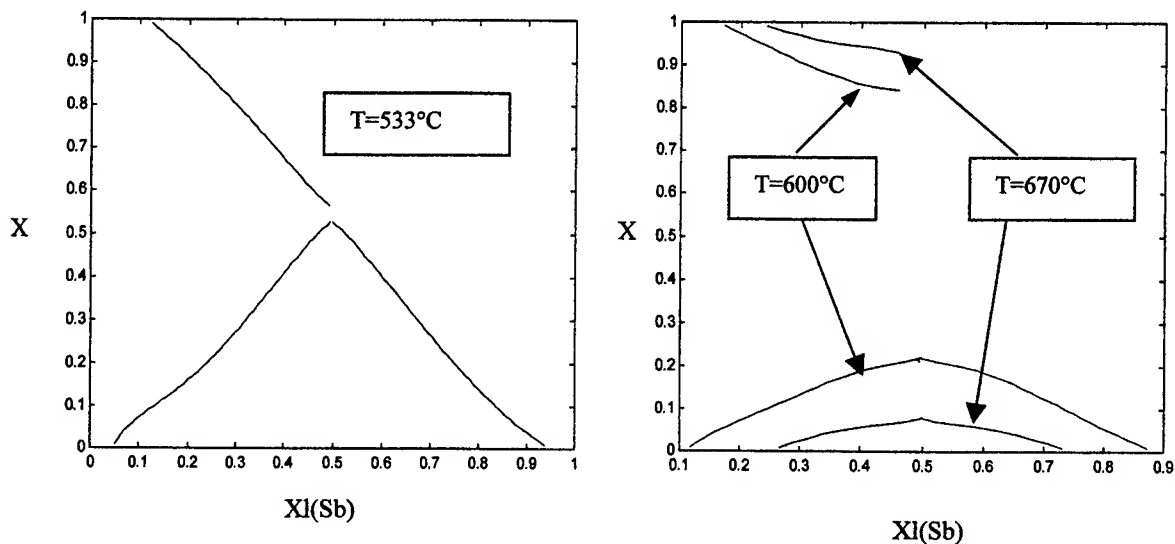


Figure 3. Equilibrium solidus isotherms for GaSb-lattice matched $\text{In}_x\text{Ga}_{1-x}\text{As}_y\text{Sb}_{1-y}$ quaternary alloys as a function of antimony content of the melt: x versus $Xl(\text{Sb})$.

Many growth experiments of $\text{In}_x\text{Ga}_{1-x}\text{As}_y\text{Sb}_{1-y}$ on GaSb substrate with LPE are carried out at a temperature of 600°C . It is useful to compute the atom fractions of composition X_L^{In} , X_L^{Ga} , X_L^{As} and X_L^{Sb} in the melt in equilibrium with solid $\text{In}_x\text{Ga}_{1-x}\text{As}_y\text{Sb}_{1-y}$ at 600°C (Figure 4). This is an example, and the computation at other temperatures is similar.

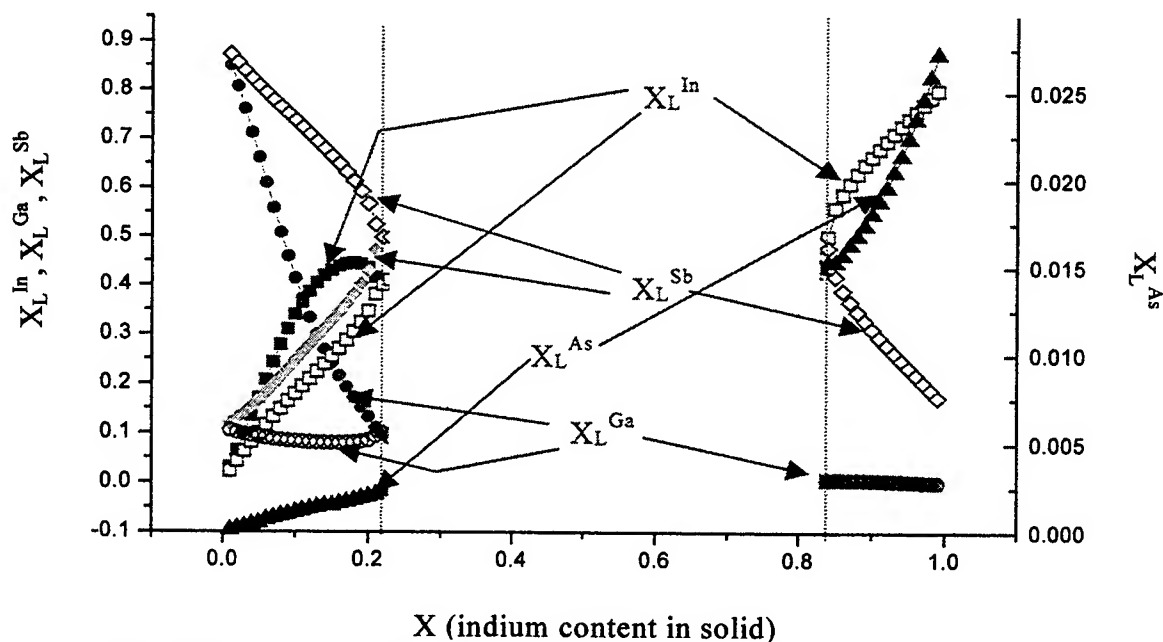


Figure 4. The atomic fractions X_L^{In} , X_L^{Ga} , X_L^{As} and X_L^{Sb} as a function of x (indium content in solid) for the growth of lattice matched $\text{In}_x\text{Ga}_{1-x}\text{As}_y\text{Sb}_{1-y}$ on GaSb(100) substrates at 600°C .

Summarizing these calculation results, we can get the feasible growth region of InGaAsSb.

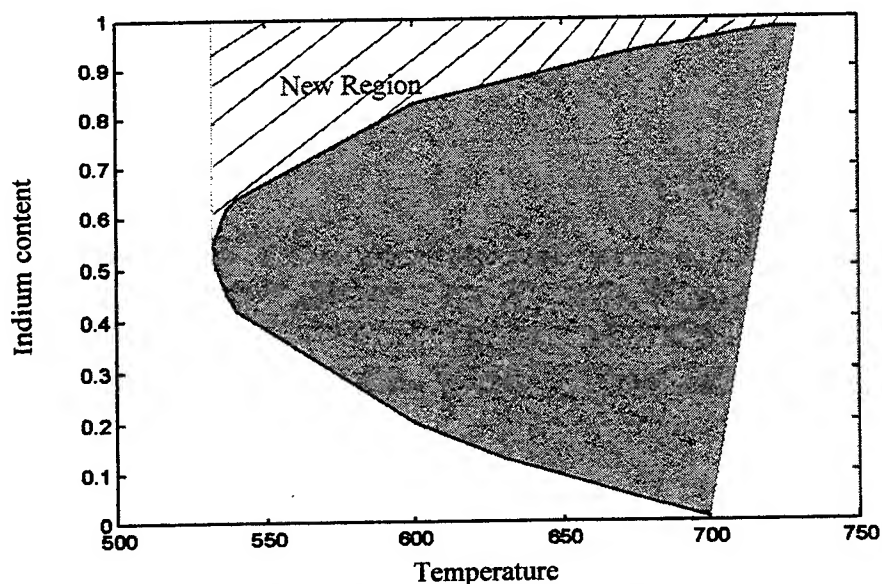


Figure 5. Feasible growth region of $\text{In}_x\text{Ga}_{1-x}\text{As}_y\text{Sb}_{1-y}$ on GaSb substrate with LPE.

Quaternary $\text{In}_x\text{Ga}_{1-x}\text{As}_y\text{Sb}_{1-y}$ on GaSb substrate can be grown outside the shaded region in Figure 5. Most of the LPE growth on GaSb substrates so far were performed in the region under the shaded region. These studies showed the limitation in the solid phase composition due to a large miscibility gap. For example, the content x of indium in solid $\text{In}_x\text{Ga}_{1-x}\text{As}_y\text{Sb}_{1-y}$ can't exceed 0.24 and thus wavelength is limited up to $2.4\mu\text{m}$ (Figure 6) at 610°C . In the present calculation, a new growth region is found which shows that $\text{In}_x\text{Ga}_{1-x}\text{As}_y\text{Sb}_{1-y}$ with x larger than 0.84 can be grown at a temperature of 610°C . According to Spinodal isotherms¹⁴ for $\text{In}_x\text{Ga}_{1-x}\text{As}_y\text{Sb}_{1-y}$ lattice-matched to GaSb, the new region exists outside the miscibility gap. Hence, growth in the new region can improve crystal quality and allow for a higher indium content in the alloy.

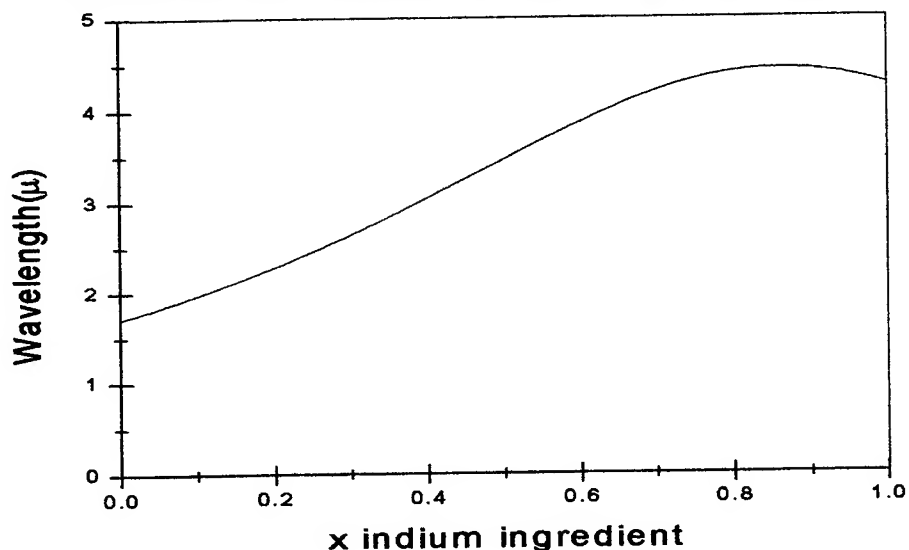


Figure 6. Relation between indium content of $\text{In}_x\text{Ga}_{1-x}\text{As}_y\text{Sb}_{1-y}$ lattice-matched to GaSb and wavelength.

Consequently, it is practicable to produce an $\text{In}_x\text{Ga}_{1-x}\text{As}_y\text{Sb}_{1-y}$ film with a bandgap cut off wavelength of $4.2\mu\text{m}$.

When the indium content x is kept constant, X_L^{As} and X_L^{Sb} increase with the growth of temperature (Figure 7). Conversely, X_L^{In} and X_L^{Ga} decrease when the temperature goes up (Figure 7). This may be caused by the fact that it becomes harder for As and Sb to crystallize when the growth temperature rises.

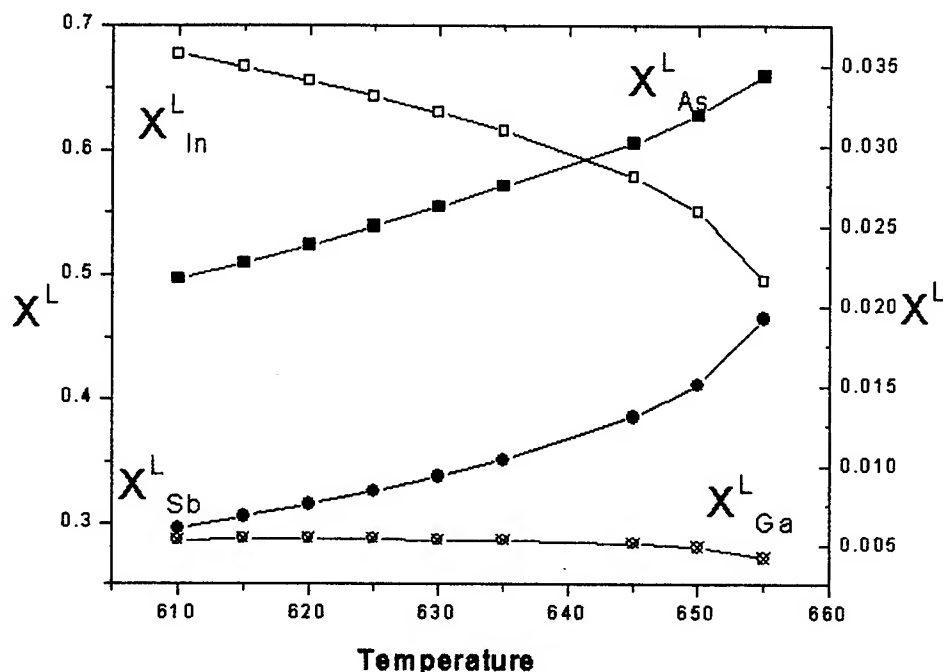


Figure 7. The atomic fractions X_L^{In} , X_L^{Ga} , X_L^{As} and X_L^{Sb} as a function of temperature with $x=0.92$ (indium content in solid) for the growth of lattice matched $In_xGa_{1-x}As_ySb_{1-y}$ on GaSb (100) substrates.

4. CONCLUSIONS

In this paper, we have studied the solidus-liquidus phase diagram of (100) oriented $In_xGa_{1-x}As_ySb_{1-y}$ quaternary alloy, which is lattice-matched to GaSb substrate. The plot of the phase diagram at different temperatures has its own characteristics. A new feasible growth region was found, where the crystal quality can be improved with a higher indium content in the alloy.

REFERENCES

1. A.E.Drakin, Peter G. Eliseev, B. N. Sverdlov, A. E. Bochkarev, L.M. Dolginov and L.V. Duzhinina, "InGaSbAs injection lasers", *Journal of Quantum Electronics* **23**, pp. 1089-1094, 1987.
2. H.K.Choi, G.W.Turner, M.K. Connors, S.Fox, C.Dauga and M.Dagenais, "High-power, high-temperature operation of GaInAsSb-AlGaAsSb ridge-waveguide lasers emitting at 1.9 μm ", *Photonics Technology Letters* **7**, pp. 1041-1043, 1995.
3. Yu Zhu Gao, XY Gong, Hirofumi Kan, M. Aoyama and T. Yamaguchi, "InAs_{1-y}Sb_y single crystal with cutoff wavelength of 8-12 μm growth by a new method", *Jpn. J. Appl. Phys.* **38**, pp. 1939-1940, 1999.
4. Xiu Ying Gong, Hirofumi Kan, Takamitsu Makino, Takefumi Iida, Yuzhu Gao, Mitsuru Aoyama, Masahi Kumagawa and Tomuo Yamaguchi, "Room-temperature Operation of InAsSb/InAsPSb photodetectors with a cut-off wavelength of 4.3 μm ", *Jpn.J.Appl.Phys.* **38**, pp. 685-686, 1999.
5. T.H. Chiu, J.L.Zyskind and W.T. Tsang, "Molecular beam epitaxial growth of InGaAsSb on (100) GaSb with emission wavelength in the 2 to 2.5 μm range", *J.Electron. Matter* **16**, pp. 57-61, 1987.
6. G.Gougnot, F.Delanoy, F.Pascal, F.Roumanille, A.Foucaran, P.Grosse, J.Bougnot, L.Gousskov, "Metal organic chemical vapor deposition (MOCVD) growth of GaInAsSb: first electrical and optical characterization of materials and devices", SPIE "Material and Technologies for Optical Communications", pp. 135-142, 1987.

7. M.B.Panish, M. Ilegems, "Phase equilibria in ternary III-V systems", *Progress in Solid State Chemistry* **7**, pp. 39-83, Pergamon Press, Oxford, 1972.
8. A.S. Jordan and M.Ilegems, "Solid-liquid equilibria for quaternary solid solutions involving compound semiconductors in the regular solution approximation", *J.Phys. Chem. Solids* **36**, pp 329, 1975.
9. J.Lazzari, E.Tournie, F.Pitard and A.Joullie, "Growth limitations by the miscibility gap in liquid phase epitaxy of $\text{Ga}_{1-x}\text{In}_x\text{As}_y\text{Sb}_{1-y}$ on GaSb", *Materials Science and Engineering* **9**, pp. 125-128, 1991.
10. E. Tournie, F. Pitard and A. Joullie, "High temperature liquid phase epitaxy of (100) oriented GaInAsSb near the miscibility gap boundary", *Journal of Crystal Growth* **104**, pp. 683-694, 1990.
11. E.Tournie, J.L.Lazzari, H.Mani, F. Pitard, C. Alibert, A. Joullie, "Growth by liquid phase epitaxy and characterization of GaInAsSb and InAsSbP alloys for mid-infrared application (2-3 μm)", SPIE Vol. 1361 Physical Concepts of Materials for Novel Optoelectronic Device Applications, pp. 641, 1990.
12. G.B.Stringfellow and P.E.Greene "Calculation of III-V ternary phase diagram: In-Ga-As and In-As-Sb", *J.Phys.Chem.Solids* **30**, pp. 1779-1791, 1969.
13. K.Levenberg, "A Method for the Solution of Certain Problems in Last Squares", *Quart. Appl.Math.* **2**, pp. 164-168, 1944.
14. Kentaro ONABE, "Unstable region in quaternary $\text{In}_{1-x}\text{Ga}_x\text{As}_{1-y}\text{Sb}_y$ calculated using strictly regular solution approximation", *Jpn. J. Appl.Phys.* **21**, pp. 323-325, 1982.

Fabrication of infrared LEDs/LDs at wavelength of 1.5 μm using LPE grown wafer

Dwi Bayuwati^a, Masbah Rotuanta Tagore Siregar^b and Tomi Budi Waluyo^a

^aResearch and Development Centre for Applied Physics,
Indonesia Institute of Sciences
Kawasan PUSPIPTEK, Serpong 15314 Tangerang Indonesia

^bResearch and Development Centre for Telecommunication,
Microelectronics and Informatics, Indonesia Institute of Sciences.
Komplek LIPI, Jl. Sangkuriang Bandung 40132 Indonesia

ABSTRACT

We describe our research on the fabrication of GaInAsP/InP Light Emitting Diodes (LEDs) / Laser Diodes (LDs) at wavelength of 1.5 μm using wafer grown by Liquid Phase Epitaxy (LPE) system. The source materials (In, InP, GaAs and InAs and doping of In-Te and In-Zn) are baked at temperature of 610 °C at the horizontal LPE system. The epitaxially layers are formed on (100) InP substrate in the graphite boat with the cooling rate of 0.7 °C/min. The wafers are characterized using Scanning Electron Microscope (SEM), Photoluminescence (PL) and X-Ray Diffraction (XRD) techniques. It is formed into LED chips by cleaving method after metallization, annealing and lapping processes. About 20-30 LED chips (100 μm x 300 μm) can be obtained from a (8 mm x 10 mm) wafer. Characterization has been conducted to examine the LED basics characteristics which showing the diode characteristics of the chips at its voltage – current (V-i) curve. Furthermore, electroluminescence process is conducted by giving an instantaneous current pulse (100-400 ns, 1 KHz) on the chip and detecting the output light using Ge detector; resulting a voltage – time (V-t) curve displayed at a digital storage oscilloscope. The spectrum of the LED chip was observed by using an optical spectrum analyzer, giving peak wavelength at $\lambda \sim 1.5 \mu\text{m}$ with spectral width between 90-105 nm. Future works in fabrication of GaInAsP/InP LD at this wavelength is still underway starting with preliminary experiment of photolithography and etching techniques of LPE grown wafers is conducted.

Keywords: LEDs/LDs chips, LPE system, GaInAsP/InP wafer.

1. INTRODUCTION

LED or LD is one of the main components for optical communication and photonic instruments. LEDs are commonly used as light source for short distance optical fiber communication networks and as display at various instrument systems. LDs are widely used for long distance optical fiber communication networks, sensors, optical instrumentation etc^{1,2}.

There are various materials can be used for LED and LD fabrication which emit wavelength from visible until infra red region. The alloy crystals based on GaAs and InP and its combination with neighboring elements such as Al, In, P, As and Sb are the most widely used. The $\text{Ga}_x\text{In}_{1-x}\text{As}_y\text{P}_{1-y}$ quaternary crystal can be grown with small lattice mismatch value at InP (100) substrate; and output wavelength can be varied from 1-1.67 μm ¹⁻⁴. This range of wavelength is popular for optical fiber communication system.

The LD or LED structure consists of several epitaxial layers with an active area in the middle part. Metal layers are added into the structure to give the contact area for the device. The most simple LD structures are the broad contact area and stripe double heterostructure. Other advanced structure are distributed feedback (DFB), buried heterostructure (BH), double channel planar buried heterostructure (DCPBH), surface emitting (SE) LDs and so on. The epitaxial layers can be grown using growing apparatus system such as LPE, metal oxide chemical vapour deposition (MOCVD) and molecular beam epitaxy (MBE). The simplest and lowest invested system for LED/LD fabrication is LPE system.

In this paper we describe research on the fabrication of infra red LEDs/LDs at wavelength of 1.5 μm using LPE grown wafer. The preliminary works has resulted in broad contact area LED chips emitting at 1.5 μm . The process consists of growing of GaInAsP/ InP epitaxial layers with LPE and its characterization, substrate lapping, electrode ohmic contact layers formation (metallization & annealing), cleaving process to form the chips, chip mounting and device characterization. The LED fabrication process still needs further steps such as bonding process to reduce heat excess and capsulization to protect the chips and form into convenient packages of device. For LD fabrication, we are conducting several experiments in photolithography and chemical etch to make channels/mesas for other laser structures such as stripe geometry, buried heterostructure etc.

2. THEORY

The basic structure of LEDs or LDs is a p-n junction. If forward bias current is applied, electrons in p semiconductor area move across the junction to the n type area, recombine with holes and generate spontaneous emission. Not every single electron participates in radiative recombination and the efficiency of the device is called as quantum efficiency.

The relationship between current and voltage ($i - V$) can be expressed as^{1,2}:

$$i = i_0 \left[\exp\left(\frac{eV}{kT}\right) - 1 \right] \dots\dots\dots(1)$$

where i_0 is total of diffusion currents and generation / recombination currents, e is electron charge, V is voltage, k is Boltzmann's constant and T is temperature. If the transition is from conduction band to valence band, the emitted wavelength is following the expression as follows¹⁻³:

$$\lambda_g = \frac{hc}{E_g} \dots\dots\dots(2)$$

where h is Planck's constant, c is light velocity and E_g is energy gap. The emitted radiation between the two bands is subject to heavy reabsorption and the quantum efficiency is very low.

Other structure which can reduce the possibility of the reabsorption is double heterostructure (DH)¹⁻⁴. In this structure the active layer is sandwiched between two layers of different materials and refractive index. By using this structure, one can obtain a waveguide structure which is more efficient and radiation can be confined to the active area. In a laser structure, the active layer can be made as thin as 0.1 μm resulting lower threshold current density. The expression for threshold current density for laser can be written as²:

$$(J)_{th} = (J_{eff})_o \frac{d}{\eta_{int}} + \frac{d}{\Gamma \beta \eta_{int}} \left[\alpha_s + \frac{\ln(1/R_1 R_2)}{2l} \right] \dots\dots\dots(3)$$

where J_{eff} is effective current density, d is depth of the active region, η_{int} is internal quantum efficiency, Γ is confinement factor, β is propagation constant in the medium, α_s is scattering loss coefficient, R_1 , R_2 are reflection coefficients and l is effective length of the active medium. The reduction of threshold current density is obtained by restricting the current along a junction plane in a narrow stripe.

There are various growth techniques of the double heterostructure layers. LPE is used because of its simple apparatus and ease of operation^{3,4}, although have several limitations such as in producing very thin/thick layers, a large number of stacked layers and a large substrate size. The apparatus in the growth of LED/LD crystal layers uses a horizontal furnace and a multiple-well growth boat. The multi-well horizontal growth boat is made of high purity graphite boat. The boat consists of a slider, a support slider and body containing multiple well. The complete LPE system consists of a chamber, vacuum pump and exhaust system, loading box, heater system, and control equipment. The chamber consists of a quartz tube, growth boat, s-type thermocouple and slider moving system. The source materials are put into the growth boat wells with composition according to the designed emission wavelength and baked at saturated temperature until mixed well. The temperature is then cooled down gradually at a certain cooling rate. The layers are formed on the substrate one by one by pulling the slider boat of the graphite boat at certain temperature.

The crystal epitaxial layers for the LED/LD consists of GaInAsP active layer, n and p type InP clad layers. GaInAsP cap layer can be added to protect the other layers and provide facility for ohmic contact layer formation. The epitaxial layers with the same crystal growth direction can be grown on the substrate when substrate comes into contact with the supersaturated solution in the graphite boat. There are four techniques for growing epitaxial layers by LPE⁴:

- The step cooling technique: the substrate comes into contact with the solution after the later is cooled by Δt lower than the saturation temperature. The substrate is hold in this condition for a certain of time period.
- The equilibrium-cooling technique: the substrate is in contact with the solution while the temperature is decreasing at a fixed cooling rate.
- The super cooling technique: this is a combination of both techniques above. The substrate comes into contact with the solution after the temperature is lowered by Δt and is cooled down at fixed cooling rate.
- The two phase solution technique: in this technique, the solution is sufficiently supersaturated and this condition is maintained during the growth. This technique is suitable for the GaInAsP/InP system.

The actual weight of each materials can be calculated from several equations which relate the lattice mismatch, the band energy, x and y composition in $Ga_xIn_{1-x}As_yP_{1-y}$, and atomic fraction of each elements⁴. The required steps in LPE growth are weighing, rinse and etch of the materials, preparation and crystal growth. The thickness of the layers depend on the growth time, saturation temperature, cooling rate and several constants of the materials⁴. For LD, the active layer is made thinner to get the low threshold current density.

The LED/LD fabrication consists of several steps: wafer growth, waveguide and resonator formation and electrode formation process. For simpler LED/LD, the last two steps can be conducted by lapping, metallization, annealing and cleaving process. Advanced structures need additional techniques such as electron beam, x-ray, photolithography and ion etch, microplasma, RF sputtering, chemical etch etc^{5,6}. Photolithography and chemical etch techniques are the simplest and easiest technique for LEDs/LDs chips fabrication.

3. EXPERIMENT

The schematic diagram of our research work on LED/LD chips fabrication is given in Figure 1. Firstly, the composition of the materials for epitaxial layers is designed to give peak emission at $\lambda \sim 1.5 \mu m^4$. The source materials are In, InP, GaAs and InAs, while dopants are In-Te and In-Zn. The GaInAsP/InP double heterostructure layers consists of GaInAs active layer sandwiched between n and p type InP clad, grown on InP (100) substrate using LPE system. Metal layers are added at the top and bottom of the layer respectively, namely, Au-Sn/Au for n-type layer and Au-Zn/Au for p-type layer. The schematic diagram of the GaInAsP/InP broad contact area - LED chip is given in Figure 2.

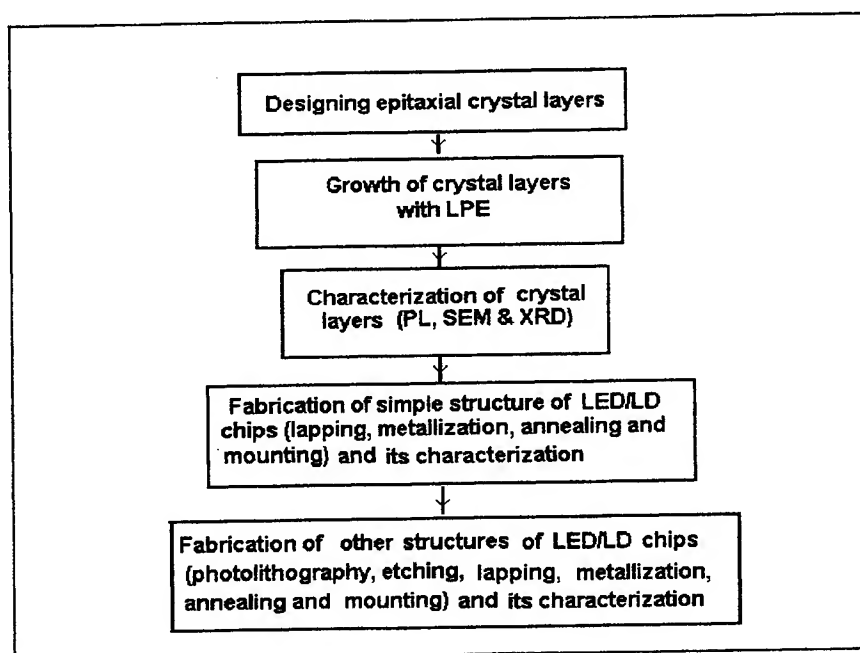


Figure 1. The schematic diagram of LED/LD chips fabrication.

To grow the double heterostructure layer for LED we use a LPE system which was bought in 1994 with several fixing work in various parts. The growth is conducted several times and continuously until we obtain good parameters such as growth temperature, cooling rate and also actual weight or material composition according to the required peak emission wavelength. We started to grow epitaxial layers to emit light at wavelength 1.17 μm followed by 1.3 μm and 1.5 μm .

As described before, the LPE uses a movable-horizontal furnace with 3-zone heating (left, middle and right). The quartz tube is 170 cm length and 55 mm diameter. The movable heater is needed when we need to cool down the chamber rapidly. The cooling is then continued with the help of an electric fan. One end of the tube is joined into a vacuum joint and connected to the gas tube. We use the nitrogen gas for cleaning the system and hydrogen for the growth process. A graphite boat is located inside the quartz tube. It has 10 wells for the solution. The slider boat moving is controlled by a simpler forward and backward moving controller. A s-type thermocouple is located under the graphite boat for monitoring the temperature during the growth process.

Other parts of the LPE system is a loading box, pump and exhaust system and gas flow system. The loading box is installed and filled with nitrogen gas all the time especially when we load or remove the materials from the graphite boat. It is equipped with rubber sealed and gloves to minimize all of the unwanted gases or powders flow into the reactor system. A bench for the boat place is also available in the box to fix the boat when we load or remove the materials.

The pump and exhaust system is built by ourselves, equipped with mechanic and diffusion pumps enable to produce vacuum level of about 10^{-5} torr. To clean the system, we do not only use the vacuum system but also flowing the hydrogen gas into the chamber for a period of time (about 1 hour). By this method, all the harmful gases and powders hopefully can be flushed out of the chamber. The end of the exhaust system is equipped with two glass tubes filled with silicon oil and water (called bubbler) to cut-off the backflow-gas.

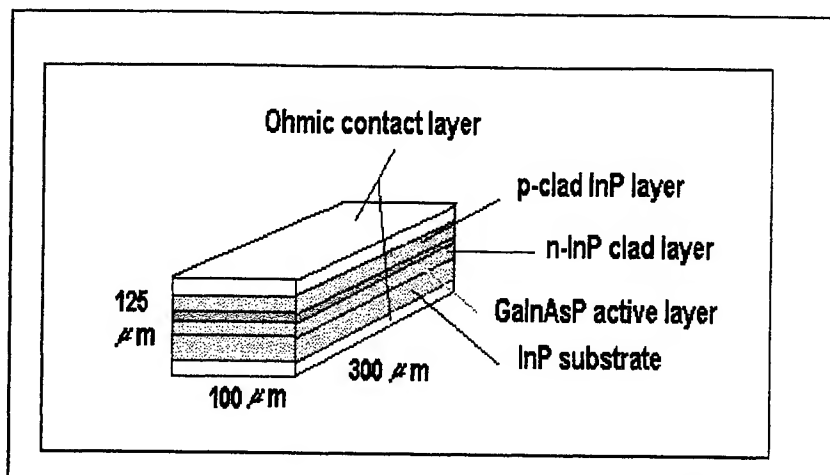


Figure 2. The GaInAsP/InP double hetero structure wafer for LED/LD.

Before growing process, all materials are cleaned and etched to remove all of the unwanted elements. The substrate is cleaned with chemical solution and etched with acid solution. The chemical and acid solution used for cleaning the materials is presented in Table 1.

Table 1. The cleaning and etch solution for GaInAsP/InP material system.

	In	GaAs	InAs-poly	InP Substrate	InP source	In-Te In-Zn
Ultra Sonic Cleaning	-	CH ₃ OH 10 min.	CH ₃ OH 10 min.	CH ₃ OH 10 min.	CH ₃ OH 10 min.	-
Cleaning	-	-	-	Pure water	-	-
Etchant	HNO ₃	Br+ CH ₃ OH 0.2%	Br+ CH ₃ OH 0.2%	H ₂ SO ₄ :H ₂ O:H ₂ O ₂ : 3:1:1	Br+ CH ₃ OH 0.2%	HNO ₃ + H ₂ O:
Time	80 sec.	120 sec.	120 sec.	40 sec.	120 sec.	20 sec.
Stop etch	H ₂ O CH ₃ OH	CH ₃ OH	CH ₃ OH	H ₂ O CH ₃ OH	CH ₃ OH	H ₂ O CH ₃ OH
Etchant	-	-	-	Br+ CH ₃ OH 0.2%	-	
Time	-	-	-	120 sec.	-	
Stop etch	-	-	-	CH ₃ OH	-	

After cleaning, substrate and materials are dried and loaded into the growth boat in LPE chamber. The chamber is then baked at temperature 610°C for one hour in hydrogen circumstances then the temperature is cooled down gradually with slope $0.7^{\circ}\text{C}/\text{min}$. The growing process starts at 592°C and layers are formed one by one on InP substrate by pulling the slider of the growth boat ^{3,4}.

The sample is then characterized with PL, SEM and XRD to examine the emission wavelength, flatness or thickness of layers and lattice mismatch between substrate and active layer. After characterization, good samples are processed to be simple LEDs or LDs chips (for example broad contact type) through lapping, metallization, annealing, cleaving and mounting process. For advanced structures (for example stripe geometry, distributed feedback, buried heterostructure and so on), other techniques, such as electron beam, x-ray, photolithography and ion etch, microplasma, RF sputtering, chemical etch etc. are needed. We use the simplest techniques namely photolithography and chemical etch to make channels or mesas structure on InP substrate. The fabrication of the micro structure pattern (stripe form) is conducted using photolithography system type BKJ 50 from Shanghai Institute of Optics and Fine Mechanics (SIOM), China. We use stripe mask with stripe width varies between $10\text{ }\mu\text{m}$ – $1\text{ }\mu\text{m}$ and distance between stripe $200\text{ }\mu\text{m}$ – $1\text{ }\mu\text{m}$. The best result of the pattern is obtained using exposure time 1 minute (because the ultra violet lamp is of low intensity) while developing and fixing time are 3 and 1 minute each. We etching the masked InP substrate using ($\text{HBr} + \text{K}_2\text{Cr}_2\text{O}_7 + \text{CH}_3\text{COOH}$) solution.

4. RESULTS

Several samples for LED and Ldcrystal layers have been grown using LPE system. The GaInAsP/InP grown wafers are characterized with PL, SEM and XRD technique. For PL measurement, sample is excited by using He-Ne laser at $\lambda \sim 632.8\text{ nm}$ with power 30 mW . Light reflected from the sample is launched into a length of optical fiber to be analyzed using ANDO AQ 6312B optical spectrum analyzer. The PL spectrum is presented in Figure 3. It shows dominant peaks at wavelength $\sim 0.9\text{ }\mu\text{m}$ (from clad layer) and $1.5\text{ }\mu\text{m}$ (from active layer). The SEM examination shows the relatively flat layers. From the XRD characterization, we obtain lattice mismatch between substrate and active layer is about 0.05% .

The next step is fabrication of broad contact GaInAsP/InP LED chips. The grown wafer is formed into the chips with lapping, metallization, annealing, cleaving and mounting process. Characterization is conducted to examine the diode characteristics of the chip by measuring the voltage – current (V-i) relationship while driving the chip with pulse current. If the V-i curve has shown a diode characteristic, the chip is then characterized on its emission spectrum using electroluminescence technique and observing the intensity or power versus wavelength relationship. In Figure 4 we present the V-i of one LED chip (which has shown a diode characteristics) compared to that of a resistor (straight line). Figure 5 is the emission spectrum of one LED chip, displayed at optical spectrum analyzer, shows peak at wavelength $\sim 1.5\text{ }\mu\text{m}$. The driving is instantaneous current pulse ($100\text{--}400\text{ ns}$, 1 KHz) and the detector is Germanium. From several LED chips we obtained spectral width between $90\text{--}105\text{ nm}$.

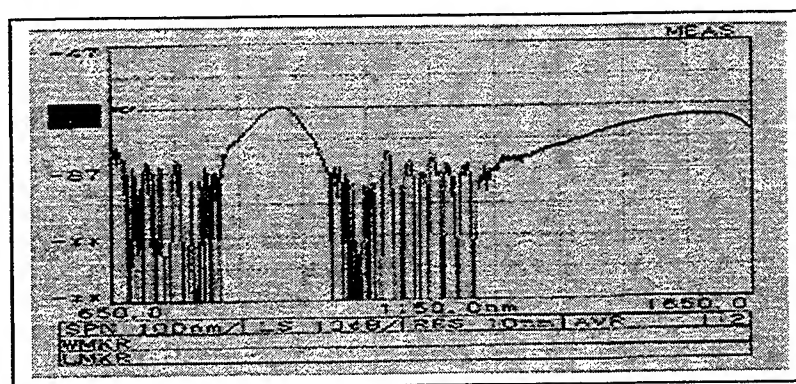


Figure 3. The photoluminescence spectrum of the GaInAsP/InP grown wafer.

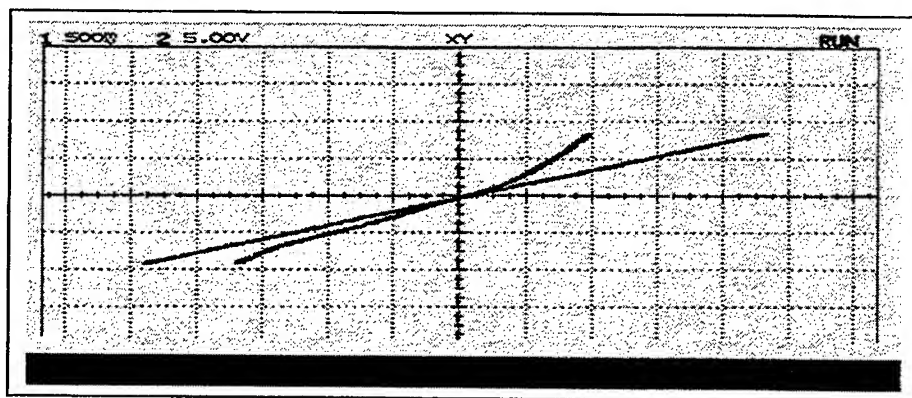


Figure 4. Voltage versus current of one LED chip compared to that of a resistor.

We are still under way in fabricating stripe geometry and buried heterostructure LDs. Besides working for optimizing the quality of the LPE grown wafer, we also conduct several experiments using photolithography and chemical etch to make channels or mesa structure for these lasers. One example of channels or mesas structure on InP substrate is shown in Figure 6. The etch solution is $(\text{HBr} + \text{K}_2\text{Cr}_2\text{O}_7 + \text{CH}_3\text{COOH})^{5,6}$.

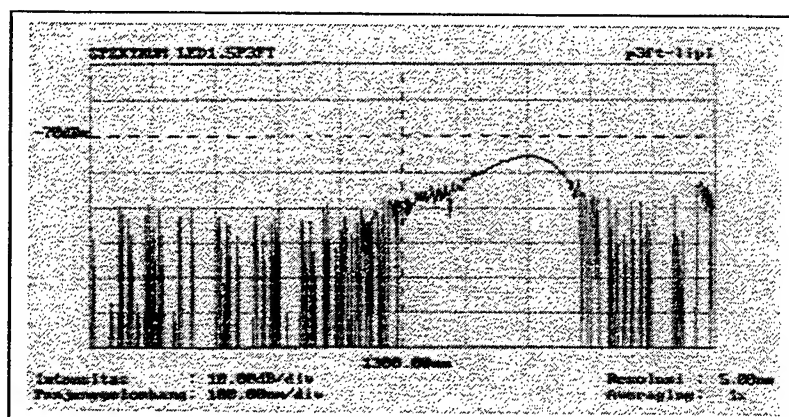


Figure 5. The emission spectrum of broad contact LED chip at $\lambda \sim 1.5 \mu\text{m}$.

CONCLUSIONS

Our research on the fabrication of GaInAsP/InP LEDs/LDs at wavelength of $1.5 \mu\text{m}$ using wafer grown by Liquid Phase Epitaxy /LPE system has been described. The wafer is characterized using SEM, PL and XRD techniques and formed into broad contact LED chips by cleaving method after lapping, metallization and annealing processes. About 20-30 LED chips ($100 \mu\text{m} \times 300 \mu\text{m}$) can be obtained from a ($8 \text{ mm} \times 10 \text{ mm}$) wafer. Characterization on the voltage – current (V-i) curve showing the diode characteristics of the chips. The spectrum of the LED chip is then obtained by using an optical spectrum analyzer, giving peak wavelength at $\lambda \sim 1.5 \mu\text{m}$ with spectral width between 90-105 nm. The LED chips still need addition process such as bonding process to reduce heat excess and packaging or capsulization to protect the chips and form into convenient packages of device. We also describe preliminary work of fabrication of GaInAsP/InP LDs at this wavelength using photolithography and etching techniques.

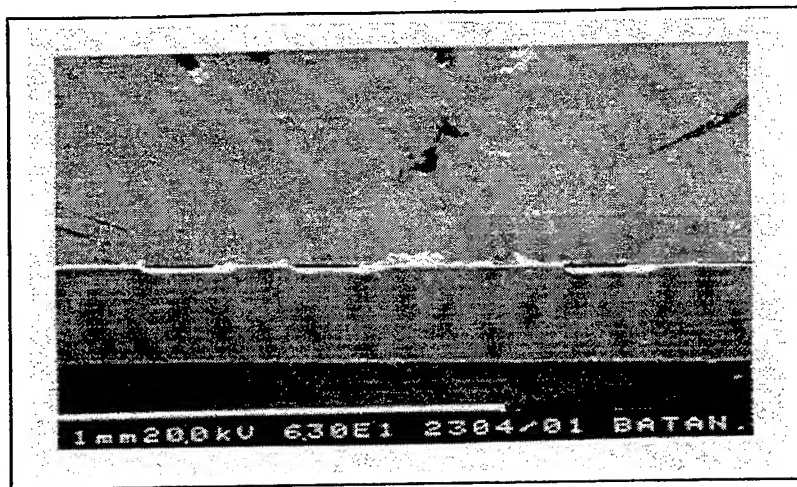


Figure 6. One example of channels or mesas structure on InP substrate.

ACKNOWLEDGMENTS

The authors would like to thank gratefully to Research and Development Center for Applied Physics; and to Research and Development Center for Microelectronics, Electronics Components, and Telecommunications, Indonesian Institute of Sciences (Puslitbang Fisika Terapan serta Puslitbang Telkoma – Lembaga Ilmu Pengetahuan Indonesia) for funding and facilitating the research work.

REFERENCES

1. John Senior, *Optical Fiber Communications, Principles and Practice*, Second edition, Prentice Hall International, United Kingdom, 1992.
2. John Gower, *Optical Communication Systems*, Prentice Hall International Series in Optoelectronics, series editor: P.J. Dean, 1984, Prentice Hall International Inc., London, 1984.
3. M.G. Astles, *Liquid Phase Epitaxial Growth of III-V Compound Semiconductor Materials and Their Device Applications*, Adam Hilger – IOP Publishing Ltd., England, 1990.
4. Iga, K. and Kinoshita, S., *Process Technology for Semiconductor Lasers*, Springer Verlag, Berlin, 1996.
5. Sadao Adachi, "Chemical Etching of InP and GaInAsP/InP", *J. Electrochem. Soc.: Solid State Science and Technology*, **130**, no. 9, March, 1982, pp. 609-613.
6. L.A. Coldren, K. Furuya, and B.I. Miller, "On the Formation of Planar-etched Facets in GaInAsP/InP Double Heterostructures", *J. Electrochem. Soc.: Solid State Science and Technology*, **130**, no. 9, Sept., pp. 1918-1925, 1983.

Development of a Laser Holographic Interference Lithography System

Oki Gunawan, Lui Whye Hoe, Boon Siew Ooi*, Yuen Chuen Chan, Yee Loy Lam, and Yan Zhou

Photonics Research Group, School of Electrical and Electronic Engineering,
Nanyang Technological University, Singapore 639798

ABSTRACT

Fabrication of periodic grating is very important for photonic devices such as Distributed Feedback (DFB) lasers, optical fiber Bragg grating based devices and optical couplers. Here, we report the development of holographic grating techniques utilizing a rotary mirror holder for grating period from 10 μm to 0.5 μm and Fresnel bimirrors for period greater than 1 μm . These holographic technique offers a wide range of tunability, good resolution, relatively simple apparatus, high uniformity and large-coverage of pattern area. A single line HeCd laser was used in these set up. The grating patterns have been successfully transfer onto GaAs substrate after dry etching with photoresist as mask. In addition, with the insertion of orthogonal Fresnel bimirror in the system, square grating patterns have been successfully obtained with grating period of $2 \mu\text{m} \times 2 \mu\text{m}$.

Keywords: Holography, lithography, interference, grating

1. INTRODUCTION

Diffraction gratings fabricated in waveguide structures are widely used as components for realising wavelength dispersion, conversion, modulation and control of guided wavefronts in optical integrated circuits¹. Such gratings are one type of the important elements in optical integrated circuits because they can be used as various passive components and in many applications. The formation of periodic corrugations is very important for integrated optic devices, such as distributed feedback (DFB) lasers, optical fibers and optical couplers. Normally, since the period of the corrugation required is in order of a micrometer or less, conventional photolithography could not be applied. Hence, the most widely used lithography techniques are laser holographic exposure and electron beam writing.

Holographic technique offer advantages such as relatively simple apparatus, maskless, good period controllability and relatively good uniformity in patterning that makes fabrication of large area of grating relatively easier. However it requires rearrangement of optical setup to control grating parameter, requires extra control on the quality of the laser beam, and less flexibility in fabricating modulated grating.

2. THEORY

When two coherent and monochromatic optical plane waves with same intensity, wavelength and polarization overlaps at certain region, a standing wave pattern will be formed. The resultant intensity distribution forms a set of straight and equally-spaced fringes of bright and dark lines². This pattern can be recorded on photographic plate as a fringe pattern. The regions of zero field intensity would leave the film unexposed while the regions of maximum intensity would leave the film maximally exposed. In the regions between these extremes the film will be partially exposed (Figure 1).

*Email: ebsooi@ntu.edu.sg, Tel: (65)-7904517, Fax: (65)-7912687

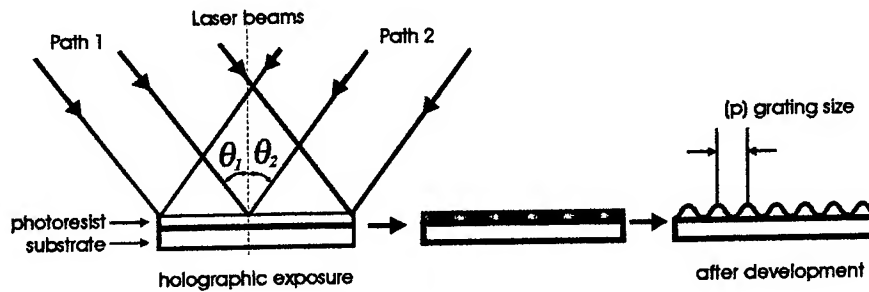


Figure 1. Grating patterning by two-beam interference

Using basic geometrical optics we can construct the Huygen's wavefront of the two incoming light paths, and the period of constructive interference can be determined as:

$$p = \frac{\lambda}{\sin \theta_1 + \sin \theta_2} \quad (1)$$

The resulting pattern appears as sinusoidal function on the recording surface. Therefore irregardless of the method used the grating size can be controlled by simply adjusting the incident angle.

Extending the idea, a pattern of dots grating can be created using four wave interference technique where four symmetric wavefront overlap and gives interference pattern on the sample as conceptualised in Figure 2. A set of two orthogonal Fresnel bimirrors can be used to create this four wave interference as shown schematically in Figure 5 (b) .

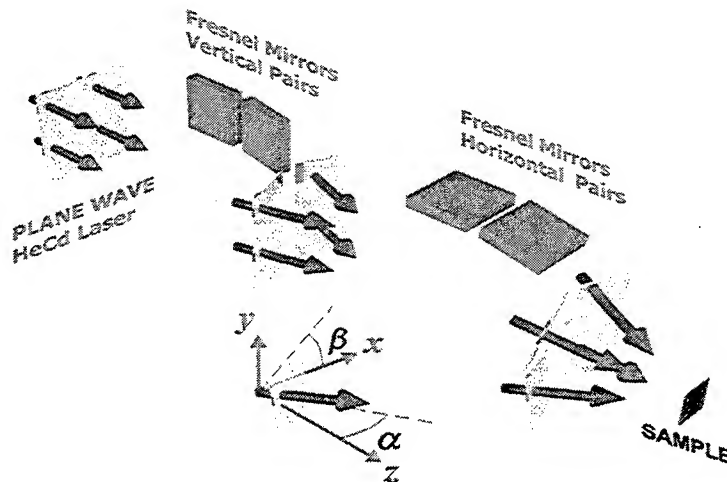


Figure 2. Illustration diagram of the principle of the wavefront division. The final wave front will be splitted into four with deflection angle of $\pm \alpha$ and $\pm \beta$

Assuming the incoming wave is a plane wave in the coordinate system as shown in Figure 2. The wavevector (\mathbf{k}) is at the direction of the propagation, normal to the wavefront. The electric field of the incoming wave can be expressed in phasor form as:

$$\xi = \xi_0 e^{i\mathbf{k} \cdot \mathbf{r}} \quad (2)$$

With two pairs of Fresnel bimirror the original beam will be deflected into two horizontal directions and two vertical directions. In terms of wavefront, it is splitted into four symmteric directions represented by four different wavevectors (\mathbf{k}_n):

$$\begin{aligned}
\mathbf{k}_1 &= k_0 [\sin(\beta)\hat{x} + \sin(\alpha)\hat{y} + \cos(\beta)\cos(\alpha)\hat{z}] \\
\mathbf{k}_2 &= k_0 [\sin(\beta)\hat{x} - \sin(\alpha)\hat{y} + \cos(\beta)\cos(\alpha)\hat{z}] \\
\mathbf{k}_3 &= k_0 [-\sin(\beta)\hat{x} + \sin(\alpha)\hat{y} + \cos(\beta)\cos(\alpha)\hat{z}] \\
\mathbf{k}_4 &= k_0 [-\sin(\beta)\hat{x} - \sin(\alpha)\hat{y} + \cos(\beta)\cos(\alpha)\hat{z}]
\end{aligned} \tag{3}$$

where k_0 is the magnitude of the original wavevector and the angle α and β are the deflection angle as shown in Figure 2.

At the sample, positioned in such a way that all of this four wavefront overlap, the intensity distribution on the x - y plane is given as :

$$I(x, y, z_S) = |\xi_1 + \xi_2 + \xi_3 + \xi_4|^2 = \xi_0 |e^{i\mathbf{k}_1 \cdot \mathbf{r}} + e^{i\mathbf{k}_2 \cdot \mathbf{r}} + e^{i\mathbf{k}_3 \cdot \mathbf{r}} + e^{i\mathbf{k}_4 \cdot \mathbf{r}}|^2 \tag{4}$$

where z_S is the arbitrary z -axis position of the sample. Figure 3 shows the numerical calculation of the intensity distribution. The contour plot shows a very good resemblance with the actual interference pattern obtained from the experiment (Figure 8).

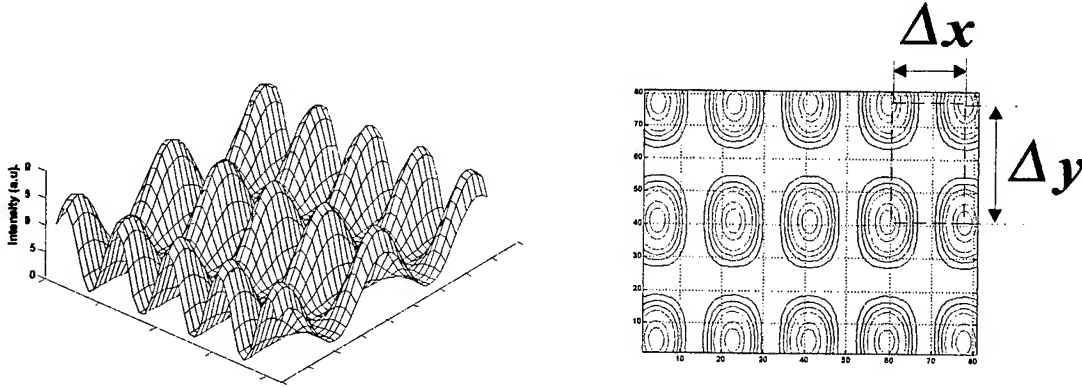


Figure 3. Computation result for the laser intensity distribution and the contour plot of the dots grating

Similar to two beam interference technique to create wire grating, the period of the dots grating are given as:

$$\Delta x = \frac{\lambda}{2 \sin \alpha} \tag{5}$$

and

$$\Delta y = \frac{\lambda}{2 \sin \beta} \tag{6}$$

where λ is the wavelength of the laser. By controlling the angle α and β independently, the aspect ratio of the array structure ($\Delta x / \Delta y$) can be adjusted thus giving additional flexibility to control the desired shape of the dots array.

3. THE EXPERIMENT

3.1 Sample Preparation

The sample, which can be a Si or GaAs sample, is coated by photoresist to facilitate pattern transfer. The photoresist used here is positive type. Some amount of thinner is added with ratio of TSMR-CR to thinner set at 1:2. The purpose of adding the thinner in the holographic preparation is to help spreading the resist to a thinner layer on the sample as well as make the resist more sensitive to light illumination. The recommended dilution of photoresist to make distributed feedback (DFB) laser and distributed-Bragg reflector laser (DBR) is 1:2. The spinning speed in the spinner is also adjusted to 4000 rpm, in order to obtain a thinner coat of photoresist.

Instead of exposing the samples to UV light in the mask aligner, the samples are placed in the holographic set-up. After exposing the samples to the laser beam, the samples were developed in NMD-3 solution for 30 seconds and in de-ionized water for a further 30 seconds before sending it for post baking. Good developing technique is important in getting a clear grating. As the photoresist were kept for a period of time after preparation, hence a longer developing time was needed than usual. Two beakers, one filled with NMD-3 and the other de-ionized water are prepared in advance. Once the exposure is done, the sample is brought to the work table and placed in NMD-3. The liquid in the beaker is twirled to ensure proper removal of the exposed photoresist. It is then removed and dipped in de-ionized water for a further 30 seconds. Post-baking is done on the hot plate at 110° degrees for 90 seconds. The samples are then ready to be observed under optical microscope to measure the grating. On the other hand we can also use He-Ne laser to get diffraction pattern from the sample where the grating period can be determined.

3.2 Optical Setup

The optical setups to create interference pattern are quite simple, some that have been constructed are:

1. Llyod's mirror (Figure 4.a)
2. Rotating Llyod's mirror (Figure 4.b)
3. Fresnel bimirror (Figure 5.a)
4. Double Fresnel bimirror (Figure 5.b)

Setup 1 to 3 gives wire gratings while setup 4 gives dots grating. The set-up consists of a He-Cd laser at 325 nm wavelength, an iris, plane mirrors, a spatial filter with interchangeable aperture and a screen for the sample to be mounted on. The laser beam passes through a 10 μ m pin hole that acts as spatial filter. The beam from this spatial filter will be diffracted. In the far field approximation the middle portion of the diffracted beam can be considered as plane wave whose wavefront will be splitted. The difference in all of these setups is basically the way they split and combine the wavefront to interfere on the sample.

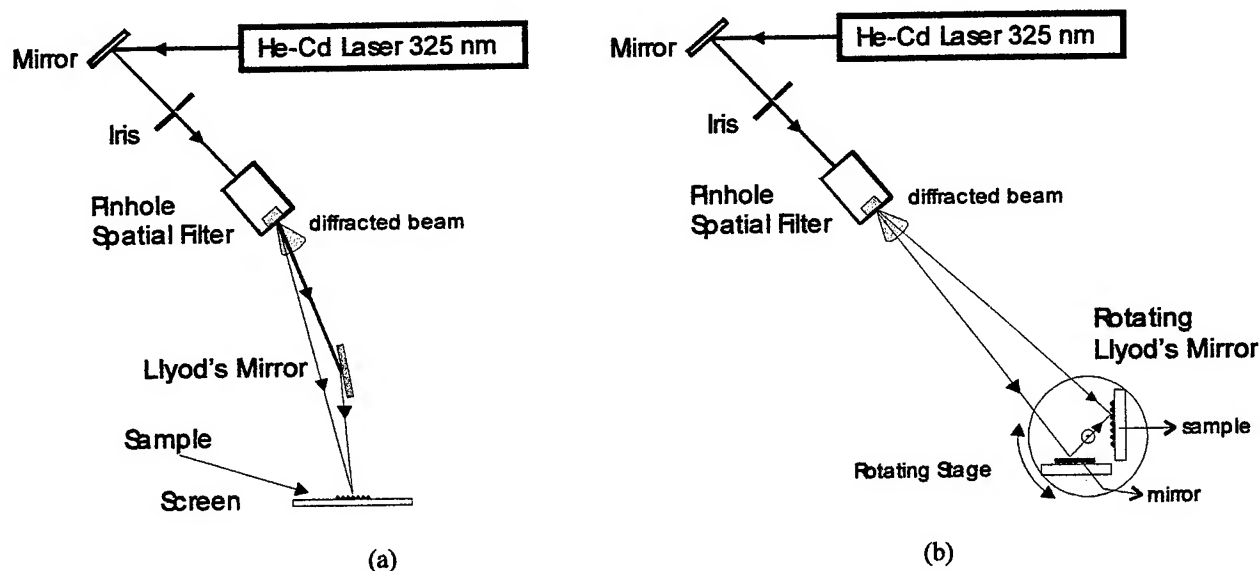


Figure 4. Optical configuration of (a) Llyod's Mirror (b) Rotating Llyod's Mirror

Problems arise when using a two-beam interference technique to obtain gratings. It becomes difficult to ensure that the optical path length differences and intensity ratio of the beams to be the constant throughout the experiment. Controlling and maintaining the parameters of the beams are important to achieve good quality of grating.

The Lloyd's mirror was the easiest to set up. The technique of obtaining an interference pattern is to place a white cardboard on a stand and using it to observe the pattern. Place the screen some distance in front of the pinhole such that the diffraction pattern from a circular pinhole can be observed. A mirror is slowly pushed parallel to the beam such that the edge of the mirror covers half of the Airy disk. A thin strip of diffraction pattern ought to be seen to the left of the original pattern from the circular aperture. Adjust the mirror slightly before securing it to the optical table. The screen can be moved about to obtain the desired grating size.

As there is limited space on the optical table, a mirror is used to reflect the beam to make use of the available space on the table. Minimal mirrors and equipment are used to reduce losses when the beam passed through these equipment. The rotating Lloyd's mirror has the advantage of flexibility in controlling the grating size. However both Llyods' mirror setup has limited fringe contrast ratio due to unequal intensity of the two incoming beam. Because only one of them undergoes mirror reflection. However high reflectivity mirror can alleviate this problem. The Fresnel bimirror setup has the advantage that all the incoming light experience equal amount of reflection resulting in better fringe contrast ratio.

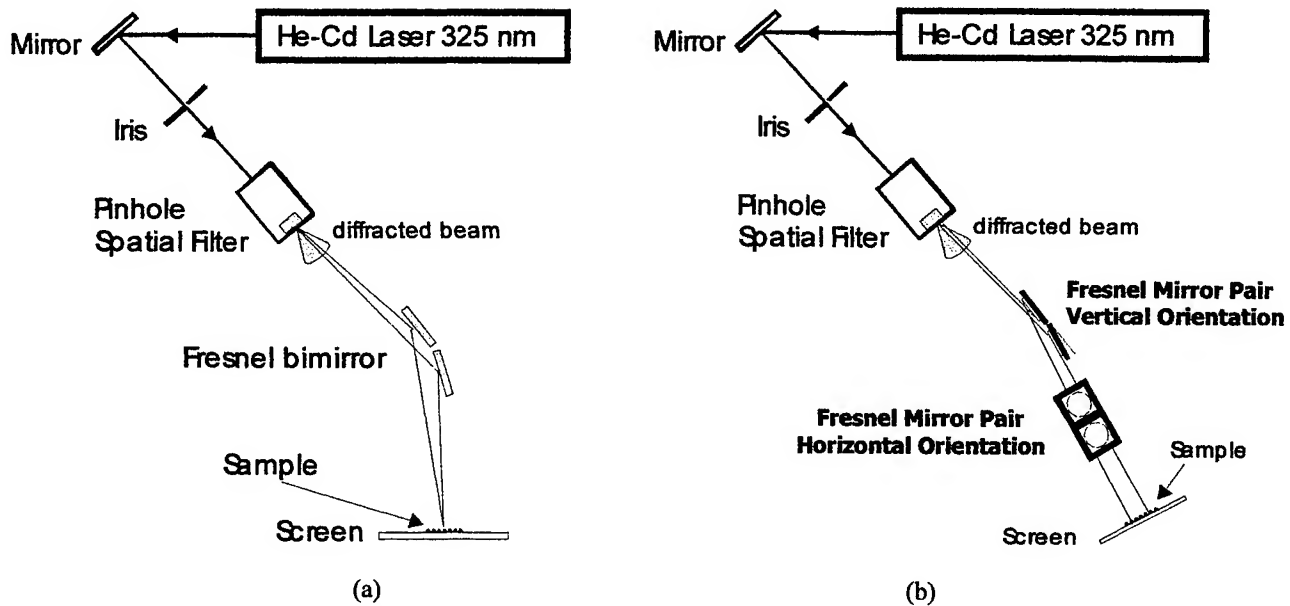


Figure 5. Configuration of (a) A Fresnel Bimirror (b) Double Fresnel Bimirror

To achieve four wave interference to create dots grating, double bimirror can be setup as shown in Figure 5 (b). The actual setup on the optical table is shown at Figure 6.

The dimensions of the grating that can be created are in order of $0.5 \mu\text{m}$ to more than $10 \mu\text{m}$. The theoretical limit of the minimum grating size is $\lambda/2$, however this can not be achieved since it requires the two beam to arrive at very wide angle. Even though it is still too big to create nanoscale structures, the technique to create interference pattern can be further developed using higher resolution lithography technique such as e-beam or ion beam to realise nanoscale structures⁵. In this case the appropriate beam optics have to be chosen.

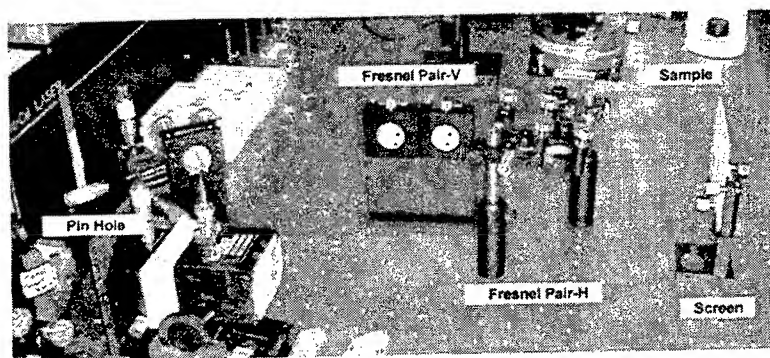


Figure 6. Experimental setup of the dots array holographic exposure

4. RESULTS AND DISCUSSION

The steps to set up the Fresnel bimirror are relatively similar to the Lloyd's mirror. However, the second mirror has to be placed slightly behind the first before adjusting the angle. A common error is that the second mirror is slightly ahead of the first mirror causing the reflection from the first mirror to be reflected again by the second. Hence adjusting the mirror and the distance of the screen will not obtain any interference pattern. Once the second mirror is in place, two strips of light could be seen on the screen. To get the required grating size, the angle of the mirror is adjusted to the required value. This angle can be measured using another visible laser beam technique. Once the angle has been measured, the screen is placed at a distance where the two strips of light overlaps to form grating.

The typical wire grating created is shown in Figure 7 and the dots grating is shown in Figure 8 :

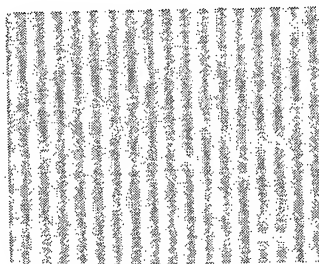


Figure 7. Wires grating created using Fresnel bimirror.

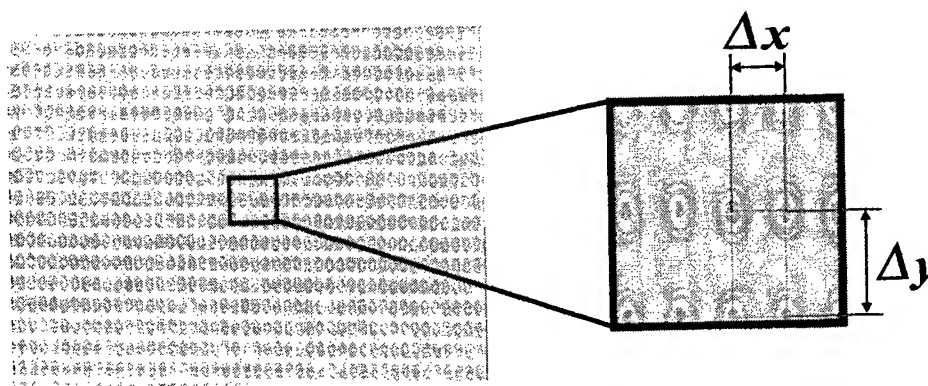


Figure 8. Dots grating created using double Fresnel bimirror.

The grating pattern in the Lloyd's mirror configuration after exposure were found to be of a lower quality when compared to Fresnel's double mirror in terms of clarity. This is because of low fringe due to unequal intensity of incoming laser beam. However the rotating Lloyd's mirror is capable of creating very small grating since it can enable the two beam to arrive at very wide angle. The Fresnel's bimirror was also easy to set-up and reliable however limited to only large grating size. Although getting the interference pattern was slightly more complex than Lloyd's Mirror, the technique was quickly picked up and subsequent adjustment of angles was swift and accurate.

Figure 9 shows the experimental result of grating fabricated where grating period size from $1.1 \mu\text{m}$ to $10.5 \mu\text{m}$ can be achieved. To achieve smaller grating sizes, the angle between the two Fresnel's mirrors can be further increased. Using the rotating Lloyd's mirror grating as small as $0.5 \mu\text{m}$ can be achieved. The measured grating size showed that it conformed to the theoretical curves (Eq. 1). Hence this method is reliable and can easily be reproduced to obtain a desired grating size.

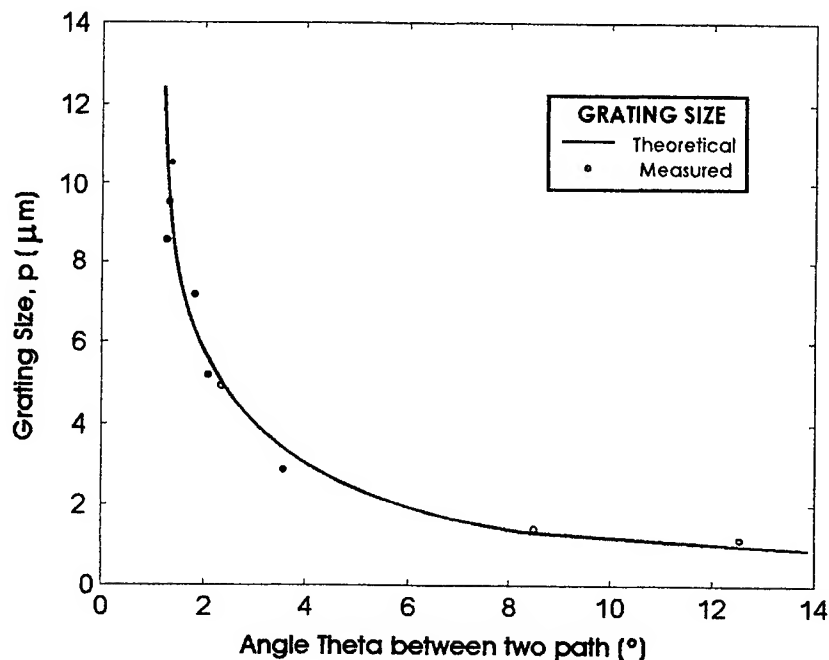


Figure 9. Plots of grating size p (μm) against θ ($^\circ$), the calculated angle between the path

Problems faced during the experiment include getting the correct ratio of photoresist to thinner. It was found that a ratio of 1:3 caused the resist to turn a darker shade of brown after post-baking which rendered them useless as the grating patterns cannot be observed under those conditions. A ratio of 1:2 will turn the resist sky blue after post-baking. This condition is extremely favorable to observe the gratings under the microscope. The contrast in colors between dark and light blue makes the grating patterns extremely clear. The different shade of blue is a result of the time difference during exposure to the UV laser beam.

5. CONCLUSION

In this paper few techniques of creating grating structure of wire and dots pattern have been presented. The techniques are simple and reliable, employing Lloyd's mirrors and Fresnel bimirrors. Lloyd's mirror setup offers a very simple technique to create wire grating. With rotating Lloyd's mirror a very small grating can be achieved added with the flexibility to control the grating size. However it has a drawback of less fringe contrast ratio. Fresnel bimirror offers another simple alternative to create grating. It has the advantage to be able to create dots grating by cascading another orthogonal pair of bimirror. Wire

grating with dimension of $0.5\text{ }\mu\text{m}$ to more than $10\text{ }\mu\text{m}$ and dots grating with dimension of $2\text{ }\mu\text{m} \times 2\text{ }\mu\text{m}$ have been successfully created using all of these techniques. These holographic techniques offer a wide range of tunability, good resolution, relatively simple apparatus, high uniformity and large-coverage of pattern area. The techniques can be developed further for relevant applications like for the fabrication of distributed feedback lasers, optical fiber Bragg grating based devices, optical couplers, and photonics crystal.

REFERENCES

1. Yariv, A. and M. Nakamura, "Periodic Structures for integrated Optics", *IEEE J. Quantum Electronics*, QE-13 (4), pp. 233, 1977.
2. Max Born and Emil Wolf, *Principle of Optics*, 6th edition, pp. 259, 1983
3. Feng-Lan Xu et al, "Development of Laser Holographic Interference System for Optical Grating Fabrication", *Masters Program Report*, School of EEE Nanyang Technological University, 1997
4. Robert Guenther, *Modern Optics*, John Wiley & Sons, 1990
5. K. Ogai, Y. Kimura, R. Shimizu, J. Fujita, S. Matsui, "Nanofabrication of grating and dot patterns by electron holographic lithography", *Appl. Phys. Lett.* **66** (12), pp. 1560-1562, 1995

Study on the electrodeposited polycrystalline GaAs films and their characteristics

Chunhui Yang*, Zhimei Zhang, Xu Wusheng, Aizhen Han

Department of Applied Chemistry, Harbin Institute of Technology, Harbin 150001, CHINA

ABSTRACT

The preparation of polycrystalline GaAs films by using electrodeposition technology is described. Influences of electrodeposition parameters on the quality of films were discussed, such as the current density, the relative concentration of ions, the value of pH of the electrolyte. On the basis of observing the micrographs, we have measured the chemical composition, microstructure and parameters of the energy band of the films. The results show that the composition of the films deposited is $\text{Ga}_{0.9946}\text{As}_{1.0054}$, and the direct gap nature of the deposited material, its band gap is 1.40eV.

Keywords: Electrodeposition, GaAs films, current density, absorption curve, XRD analysis, energy band parameters

1. INTRODUCTION

GaAs has a higher electron mobility and a wider band gap than Si, and it is favourable for fabricating microwave devices, monolithic microwave integrated circuits, optical fibers and solar cells, etc. The bulk crystals of GaAs have been grown successfully using various techniques, for example liquid encapsulated Czochralski and horizontal Bridgman methods. Further research work concentrates on preparing GaAs films, for example molecular beam epitaxy, chemical vapour deposition and metal organic chemical vapour deposition, are very complicated and expensive in terms of the power used, time involved and the actual cost. In contrast, the electrodeposition technique for preparing III-V and II-VI compound semiconductor films is inexpensive, time saving and less contaminating to the environment. For instance, AsSb^1 , MoSe_2^2 , $\text{GaAs}_{1-x}\text{Sb}_x^3$, CuIn^4 , and $\text{InAs}_{1-x}\text{Sb}_x^5$ films have been prepared successfully using this technique. Polycrystalline GaAs films approaching stoichiometry have been deposited on the SnO_2 coated glass substrates using this method and the composition and properties of films are analyzed in this work. Finally, the photoelectrochemical performance of the $\text{Ga}_{0.9946}\text{As}_{1.0054}$ /electrolyte junction is measured.

2. EXPERIMENTAL DETAILS

There are many technological parameters of co-electrodeposition for preparing GaAs films, such as the relative concentration of Ga and As ions in the electrolyte, the temperature, the pH of the electrolyte, the deposition time and the current density. Optimizing these parameters in order to obtain the right stoichiometry GaAs film is the key to this research, and we carried out the electrodeposition experiments using dilute HCl aqueous solution with an appropriate ratio of Ga and As_2O_3 as the cathod, and a Pt sheet (or a sheet of graphite) as the anode. The best technology parameters are shown in Table 1 and the dimensions of the electrodeposited film was 30mm × 20mm.

Table 1 Optimum technology parameters of electrodeposition GaAs films

Concentration of electrolyte			Current density $\text{mA} \cdot \text{cm}^{-2}$	pH	Temperature $^{\circ}\text{C}$	Time Min
$\text{C}_{\text{Ga}}^{3+}$ $\text{g} \cdot \text{l}^{-1}$	$\text{C}_{\text{AsO}}^{+}$ $\text{g} \cdot \text{l}^{-1}$	$\text{C}_{\text{Ga}}^{3+}/\text{C}_{\text{AsO}}^{+}$				
0.3088	0.0397	7.781	6.25	1.42	34	6.5

The stoichiometry of the deposited film is determined by an energy spectra analyzer attached to a scanning electron microscope (S-570-SEM). The X-ray diffraction (XRD) of the film is recorded using a model D/max-rB X-ray diffractometer from the optical absorption spectrum which is recorded with a spectrophotometer at room temperature.

The Mott-Schottky plot was measured with a three electrode cell and a model CG-1 HF capacitance voltage tester. The electrolyte had the composition 1M NaOH + 1M Na₂S + 1M S. Thereby the flat band potential of the film is calculated.

3.RESULTS AND DISCUSSION

The results of energy spectra analysis of the film show that the composition of the deposited films depends on the deposition parameters. The stoichiometry of the deposited film with the technological parameters listed in Table 1 is Ga_{0.9946}As_{1.0054}.

The effect of current intensity on the ratio of Ga to As of the deposits is shown in the Table 2. There was more Ga on the deposits when the current density was higher, while, there was more As when it was lower. The cathodic polarization was improved when the current density became higher, which was beneficial to the deposition of cations with lower electrode potential. The standard electrode potential of Ga is -0.529V, and that of As is 0.254V. The higher current density should be chosen, so that the ratio of Ga to As of the deposits was near to 1.

Table 2 Influences of the current density J on the atomic ratio of Ga, As of the deposited films

J mA · cm ⁻²	Ga:As	J mA · cm ⁻²	Ga:As
16.61	1.2008:0.7992	15.73	1.2001:0.7999
13.33	1.1437:0.8563	11.97	1.1125:0.8875
10.68	1.1073:0.8927	9.33	1.0987:0.9013
6.29	0.9688:1.0332	5.64	0.9624:1.0376
4.81	0.9327:1.0673	3.95	0.9219:1.0781
3.53	0.9324:1.0676	2.56	0.9233:1.0767

Notes: C_{Ga}³⁺/C_{AsO}⁺=6.4; Temperature =14°C; pH=1.42; Time=5min

The effect of the ratio of Ga³⁺ to AsO⁺ in the electrolyte on the quality of the deposits is shown in Table 3. It is well known that the deposits voltage of cations are as followed

$$\varphi = \varphi^0 + \frac{RT}{nF} \ln \alpha + \Delta\varphi \quad (1)$$

Where φ^0 , α , $\Delta\varphi$, R, F, n and T constitutes the standard potential, ionic activity, excess potential, gas constant, Faraday constant, electron numbers and temperature of the electrolyte. Usually, the more easily cation was deposited, the higher the composition of cation in the electrolyte was. In our experiments, the ratio of Ga³⁺ to AsO⁺ is near to 9. Thus, the deposition potential of Ga was equal to that of As. Ga and As were codeposited.

The XRD spectrum of the deposited film is shown in Fig.1, which shows a good correspondence with the standard values of GaAs powder. We can see that some intense peaks are present in the XRD spectrum, which are additional peaks owing to SnO and Sn. Fig.2 shows the optical absorption curve of the deposited film.

The absorption coefficient near the absorption edge can be written as

$$\alpha \approx K(E - E_g)^n \quad (2)$$

Where K is a constant, E is the photo energy, E_g is the band gap, n is a constant which equals 0.5 for GaAs. The comparison with the absorption curve of the intrinsic GaAs shows that the absorption edge shifts towards a longer wavelength and an exponential tail is generated. It is demonstrated that the presence of shallow impurity states, lattice microstrains, and a non-

uniform distribution of charged centers may cause this tail. Fig.3 shows a plot of α^2 vs. $h\nu$ which is a straight line. This indicates the direct band gap nature of the deposited material.

Table 3 Influences of the relative concentration of Ga^{3+} , AsO^+ on the atomic ration of the deposited films

Concentration of electrolyte			Ga:As
$C_{\text{Ga}^{3+}}$ $\text{g} \cdot \text{l}^{-1}$	C_{AsO^+} $\text{g} \cdot \text{l}^{-1}$	$C_{\text{Ga}^{3+}}/C_{\text{AsO}^+}$	
0.3088	0.0206	15	1.2088:0.7992
0.3088	0.0257	12	1.1852:0.8148
0.3088	0.0343	9	1.0206:0.9794
0.3088	0.0515	6	0.9668:1.0332
0.3088	0.1029	3	0.9270:1.0830
0.3088	0.3088	1	0.8218:1.1782
0.3088	0.9264	1/3	0.7878:1.2122
0.1544	0.9264	1/6	0.6790:1.3210
0.1544	1.3896	1/9	0.5803:1.4692
0.0772	0.9264	1/12	0.4382:1.5618
0.0772	1.1580	1/15	0.0342:1.9658

Notes: $J=6.29 \text{ mA} \cdot \text{cm}^{-2}$; Temperature = 14°C ; pH=1.42; Time=5 min

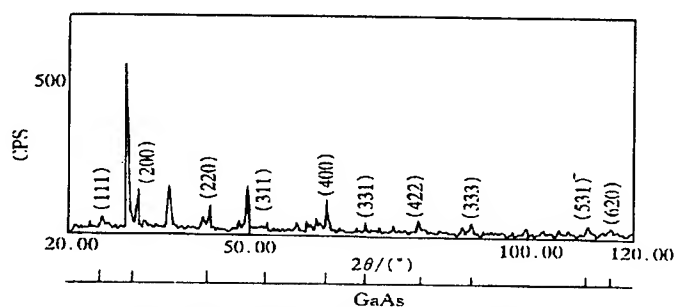


Fig. 1 XRD patterns of the $\text{Ga}_{0.9946}\text{As}_{1.0054}$ film

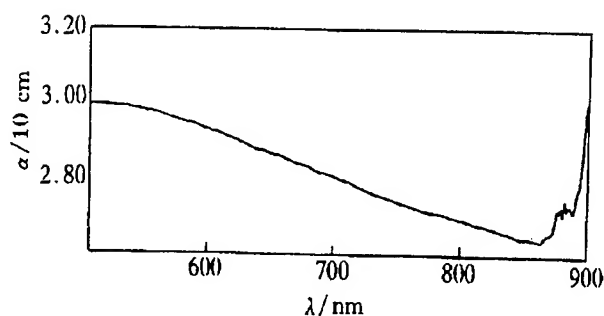


Fig. 2 Absorption curve of the $\text{Ga}_{0.9946}\text{As}_{1.0054}$ film

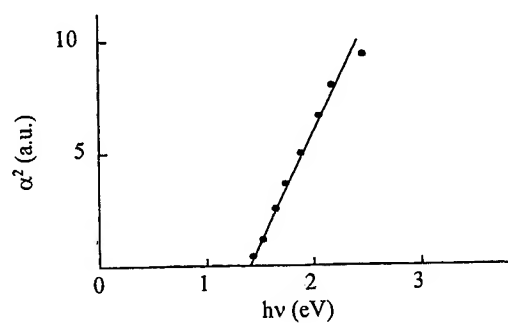


Fig. 3 α^2 plotted vs. $h\nu$, from the absorption spectral studies for determining the band gap of the $\text{Ga}_{0.9946}\text{As}_{1.0054}$ film

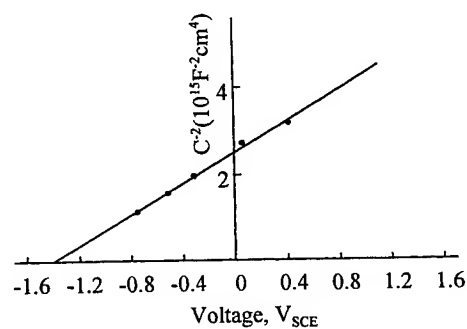


Fig.4 The Mott-Schottky plot for the $\text{Ga}_{0.9946}\text{As}_{1.0054}$ film.

Table 4 Parameters of the energy band of the deposited film.

Parameter	Value
Electrolyte	$\text{S}^{2-}/\text{S}_2^{2-}$
Flat band potential, $V_{fb}(V_{SCE})$	-1.4
Band bending, $V_b(V)$	0.65
Donor concentration, $N_d(\text{cm}^{-3})$	6.9×10^{15}
Density of states in the conduction band, $N_c(\text{cm}^{-3})$	4.7×10^{17}
Depletion width, $\omega(\mu\text{m})$	0.34
Valence band edge, $E_v^{(n)}(V_{SCE})$	-0.08
Conduction band edge, $E_c^{(n)}(V_{SCE})$	-1.51
Fermi level, E_f of semiconductor below the conduction band edge (v)	0.11
Redox Fermi level of the electrolyte $E_{F,redox}(V_{SCE})$	-0.75
Carrier type	n^-
Bond gap, $E_g(\text{eV})$	1.43

On the basis of the results of C-V measurements, a Mott-Schottky plot is obtained. Fig.4 indicates that the intercept on the axis gives the flat band potential V_{fb} and from the slope of the straight line the value of N_D can be calculated. The sign of the slope shows that the material is n- type. Knowing V_{fb} and N_D , the potentials near the interface can be calculated by using the well known equations². The results are given in Table 4.

Here it should be noted, however, that the above calculation is crude because the condition for applicability of Mott-Schottky plot are limited, i.e. the doping density should be uniform, the relative dielectric constant of the semiconductor ϵ_g should be frequency independent, and neither impurities nor surface states should be present.

4.CONCLUSION

Electrodeposition is simpler, lower cost and less contaminating method for preparing polycrystalline GaAs films. Optimizing the technological parameters is the key for obtaining high quality films. The deposited film material is measured by using energy spectra analysis, X-ray diffraction and spectrophotometry. The results show that the component of the films approaches the stoichiometry GaAs. On the basis of the results obtained from measuring the Mott-Schottky plot, the levers are calculated.

REFERENCES

1. M. M. Musiani, F. Paolucci, P. Cuerriero, "Electrodeposition of As-Sb alloys", *J. Electroanal. Chem.* **332**, pp. 113-116, 1992.
2. S. Chandra, S.N.Sahu, "Electrodeposited Semiconducting molybdenum selenide films: I. Preparatory technique and structural characterization", *J. Phys. D*, **17**, pp. 2115-2118, 1984.
3. P.Andreoli, S.Cattarin, M.Musiani, F. Paolucci, "Electrochemical approaches to GaAs_{1-x}Sb_x thin films", *J. Electroanal. Chem.* **385**, pp. 265-269, 1995.
4. J.Herrero, J.Orbeya. "Electrodeposition of Cu-In alloys for preparing CuInS₂ thin films", *Solar Energy Mater.* **20**, pp. 531-536, 1990.
5. G. Mengoli, M. M. Musiani, F. Paolucci. "Synthesis of InAs and InAs_{1-x}Sb_x from electrodeposited layers of indium arsenic and As-Sb alloys", *J. Electroanal. chem*, **332**, pp.199-203, 1992.

*Correspondence: Email: yangchh@fmail.hl.cninfo.net

Solute redistribution during the accelerated crucible rotation Bridgman growth of $\text{Hg}_{1-x}\text{Mn}_x\text{Te}$

Jie Wanqi, Li Yujie, Liu Xiaohua

State Key Laboratory of Solidification Processing
Northwestern Polytechnical University, Xi'an 710072, P. R. China

Abstract

In order to study the Mn macrosegregation in accelerated crucible rotation Bridgman (ACRT-B) growth of $\text{Hg}_{1-x}\text{Mn}_x\text{Te}$ crystal, a mathematics model was established for the evaluation of the solute (Mn) distribution in the growth direction based on quantitative analyses and several assumptions. The results reveal that in $\text{Hg}_{1-x}\text{Mn}_x\text{Te}$ crystal grown by ACRT-B method, Mn content is much higher than the average value in the initial region and reduces gradually to a lower value in the final region because of solute redistribution. Only a section of the crystal fit the required composition with the acceptable error. The crystal section with acceptable composition can be also obtained in $\text{Hg}_{1-x}\text{Mn}_x\text{Te}$ ingot grown from the melt with no stoichiometric compositions. The length of the section increases with decreasing in x_0 value. Meanwhile, it moves toward the initial region. To grow $\text{Hg}_{1-x}\text{Mn}_x\text{Te}$ crystal with a certain composition, such as $x=0.11$, it is preferable to use the melt with a lower average Mn content, so that the crystal with the acceptable composition will be longer and located in the early region where the crystalline quality is better. A 5mm-diameter $\text{Hg}_{0.89}\text{Mn}_{0.11}\text{Te}$ ingot was grown by ACRT-B method for the comparison. A single crystal is obtained in the early part of the ingot after the competitive growth of several grains in the initial region. However, the single crystal is blocked by several new grains, which were nucleated on the ampoule wall after about 1 cm. The composition distribution along the growth direction was analyzed by electron microprobe. The experimental data are essentially coincident with the calculation result in the main part of the ingot, but lower than it in the initial region and higher in the final region. These errors may stem from the approximation of homogeneous mixture in the liquid in the mathematical model, which is not true in the initial and final regions because the convection there is limited.

Keywords: HgMnTe , crystal growth, Bridgman method, ACRT, solute redistribution, segregation

1. Introduction

$\text{Hg}_{1-x}\text{Mn}_x\text{Te}$ is an important semimagnetic semiconductor as well as a new candidate for infrared detector material^[1-6], which has attracted much attention in the last decades. Even though several film epitaxy methods have been developed for film materials preparation, bulk crystal growth is still the most important way to get high quality single crystals which are more likely to be used in the industry. Among these crystal growth methods, such as Bridgman^[7-10], solid-state recrystallization^[11], zone melting^[12,13] and traveling heater methods^[12,14], vertical Bridgman technique is more often adopted because of its advantages over the other methods. Since the application of ACRT (accelerated crucible rotation technique) in Bridgman has successfully improved the crystal quality of $\text{Hg}_{1-x}\text{Cd}_x\text{Te}$ ^[15-17], we used ACRT with Bridgman (ACRT-B) for the crystal growth of $\text{Hg}_{1-x}\text{Mn}_x\text{Te}$. A theoretical model is presented in the paper to evaluate the solute redistribution during ACRT-B process. The calculated results are compared with experimental data obtained from a 5mm-diameter $\text{Hg}_{1-x}\text{Mn}_x\text{Te}$ ingot grown by this method.

2. Theoretical Model for the Solute (Mn) Distributions

As other ternary II-VI compounds, $\text{Hg}_{1-x}\text{Mn}_x\text{Te}$ can be treated as a pseudo-binary alloy of HgTe-MnTe , where homogeneous solid solution with Zinc-blende-type structure can be formed up to $x=0.36$. Composition segregation in the resulted crystal is determined by the solute redistribution during the growth process, which includes three items, i.e. solute partition at the solid/liquid interface, the solute transport in the solid and the solute transport in the liquid. The calculation of the solute distribution in the crystal depends on three assumptions, which will be discussed separately as follows.

(1) The real solute partition ratio at the solid/liquid interface can be evaluated by the Aziz model^[18] for stepwise growth, which is written as,

$$k_a = k_0 + (1 - k_0) \exp\left(-\frac{D_i}{R\delta}\right) \quad (1)$$

where R is the growth rate, and $R=0.97\text{mm/hr}$ in our experiment. D_i is the interface diffusion coefficient, which can be approximated by the diffusion coefficient in the liquid phase D_L . For the diffusion of Mn in $\text{Hg}_{1-x}\text{Mn}_x\text{Te}$ melt, D_L is of the order of $10^{-3}\text{mm}^2/\text{s}$. δ is the distance between the two neighbor layers of atoms, which is about 0.63nm ^[19]. By using these

parameters, it is found that $k_a - k_0 = (1 - k_0) \exp(-D_i/R\delta) \approx 0$. Therefore, the local equilibrium at the growth interface will be reached and the equilibrium solute partition ratio $k_0 = x_s/x_L$ can be safely used in the calculations.

(2) The solute transport in the solid is a pure diffusion control led process and can be evaluated by the diffusion parameter a ,

$$a = \frac{D_s \tau}{L^2} \quad (2)$$

where D_s is the diffusion coefficient in the solid, which is of the order of 10^{-6} mm²/s for the diffusion of Mn in the crystal. τ is the diffusion time and is about 1.5×10^5 s. L is the diffusion distance. Significant diffusion requires a to be close or larger than 1. This means that the diffusion distance L is about 0.4 mm in our experiment according to the above mentioned parameters. Comparing with the crystal length, this quantity can essentially be ignored. Therefore, the assumption of no diffusion in the solid can be adopted.

This conclusion also confirms that composition of the crystal will not change essentially after freezing.

(3) For the following two reasons, a homogeneous mixture in the liquid can be assumed:

First, the diffusion in the liquid is relatively fast compared with that in the solid. If we use similar evaluation method as that for the diffusion in the solid, the diffusion length in the liquid is of the order of 10 mm.

Secondly, ACRT forced convection promotes the mixture in the liquid. In this case, the efficient solute partition ratio k_e can be evaluated by Burton's model^[20]

$$k_e = \frac{k_0}{k_0 + (1 - k_0) \exp(-\frac{R}{D_L} \delta)} \quad (3)$$

The thickness of Ekman boundary layer can be also used for the adherent boundary in front of growth interface. It is evaluated that $k_e/k_0 \approx 1$.

Based on the above evaluations, the profile of solute (Mn) distribution during ACRT-B growth of Hg_{1-x}Mn_xTe is drawn as shown in fig.1. The solute balance requires that the solute accepted by the advancing interface in the time interval $d\tau$ (dark region 1) equals to that reduced in the bulk liquid (dark region 2). In the taper shaped initial region, the solute balance condition is written as follows,

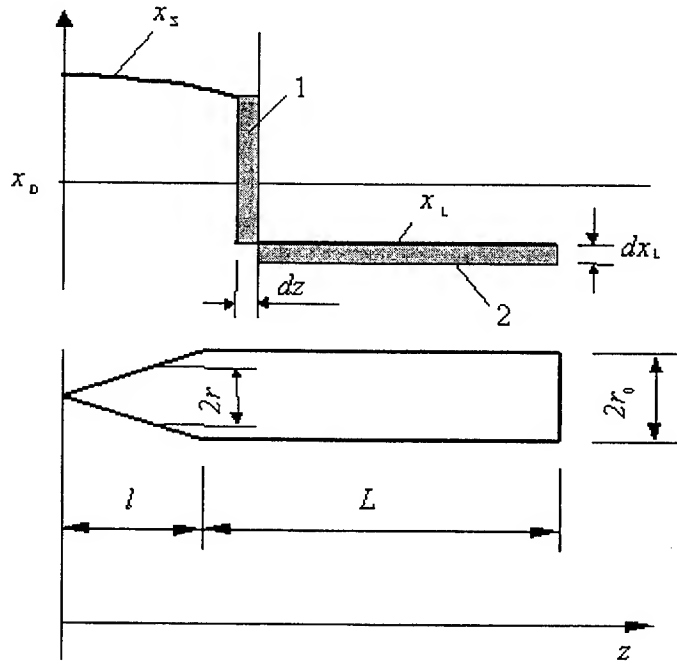


Fig.1 Sketch for the solute distribution along the growth direction and the main parameters for the mathematical model.

$$\left[\pi r_0^2 L + \frac{\pi}{3} \left(\frac{r_0}{l} \right)^2 (l^3 - z^3) \right] dx_L = x_L (1 - k_0) \pi r^2 dz \quad (4)$$

where $r = r_0 z/l$, x_L is the mole fraction of solute in the liquid.

At the initial condition of $x_L(z=0) = x_0$, the solution for equ.(4) is found to be

$$x_s = k_0 x_L = k_0 x_0 \left(1 - \frac{z^3}{3l^2 L + l^3} \right)^{k_0 - 1} \quad 0 < z < l \quad (5)$$

where x_s is the x value in the solid and x_0 is its average value.

The solute balance condition in the main part of the crystal will be

$$-(L+l-z)dx_L = (x_S - x_L)dz \quad (6)$$

where the boundary condition is

$$x_S(z=l) = k_0 x_0 \left(1 - \frac{l}{3L+l}\right)^{k_0-1} \quad (7)$$

and the solution for equ. (6) is deduced to be

$$x_S = k_0 x_0 \left(1 - \frac{l}{3L+l}\right)^{k_0-1} \left(1 + \frac{l-z}{L}\right)^{k_0-1} \quad l < z < L \quad (8)$$

3. Evaluation and discussions

The application of eqs. (5) and (8) for the calculation of the solute (Mn) distribution in the crystal requires the real value of k_0 , which has strong influence on the results. k_0 changes in the region of 2 to 3. We used k_0 value of 2.2, suggested by Kaniewski et al^[21] in the calculation. Suppose $L=5l$, and take the prospected 8~12mm infrared detector materials $\text{Hg}_{0.89}\text{Mn}_{0.11}\text{Te}$, i.e. $x_0=0.11$ as an example in the calculation. The calculated solute concentration (x value) distribution of an ACRT-B grown $\text{Hg}_{0.89}\text{Mn}_{0.11}\text{Te}$ along the growth direction is shown in fig.2. MnTe concentration (x value) in the initial part of the ingot is much higher than the average value and then reduces gradually to a very low value in the final region. The theoretical value at starting point is 0.242, which equal to $k_0 x_0$. If the acceptable concentration error for a certain application is Δx , only in the small section Δl of the ingot as shown in fig.2 can be used.

From the above evaluations, it can be judged that the crystal with acceptable concentration $x_0 \pm \Delta x$ can be obtained in the ingot grown from the melt with other compositions (no stoichiometric composition). Changing the original melt composition can change the position and the length of the crystal with acceptable composition in the ingot. Fig.3 shows the calculation results with four different arbitrary compositions. It is seen that a longer crystal section with acceptable solute concentration is obtained in the ingot with lower x_0 value rather than that with exactly stoichiometric one. And what is more, this section moves to the early part of the ingot, where the crystal has better quality.

The variation of the position and the length of the crystal section with acceptable concentration with the original concentration x_0 is shown in fig.4 according to the calculation. The results will be helpful for the selection of the original solute concentration.

4. Experiments

4.1 Crystal Growth

$\text{Hg}_{0.89}\text{Mn}_{0.11}\text{Te}$ compound is synthesized from 6 nines Hg and Te and 4 nines Mn in a carbon coated quartz ampoule with the diameter of 5mm. ACRT-B growth was performed in

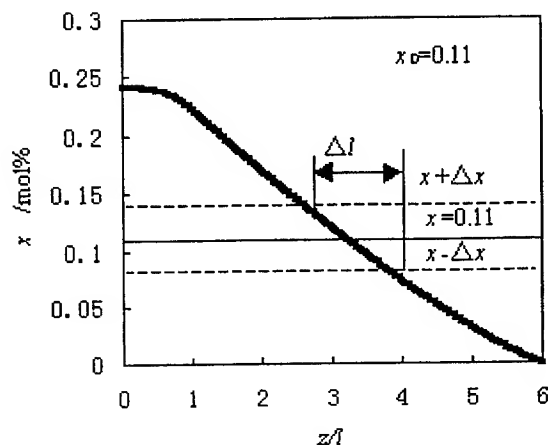


Fig.2 Calculated solute (x value) distribution in an ACRT-B grown $\text{Hg}_{1-x}\text{Mn}_x\text{Te}$ crystal from a $\text{Hg}_{0.89}\text{Mn}_{0.11}\text{Te}$ melt.

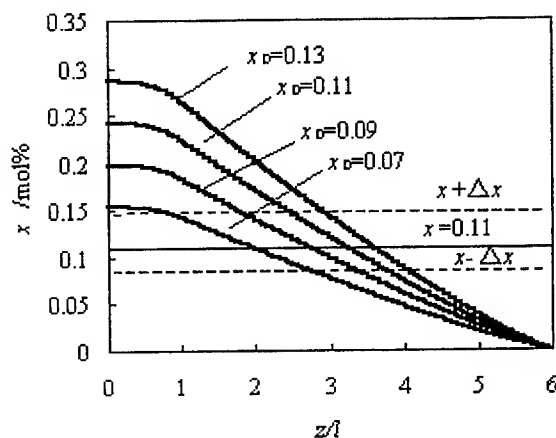


Fig.3 The comparison of the calculated solute distributions in $\text{Hg}_{1-x}\text{Mn}_x\text{Te}$ crystal ingots grown from the melt with different compositions.

the same ampoule. The temperature gradient of 13K/cm and the growth rate of 0.97mm/hr were adopted. The ACRT sequence used is shown in fig.5.

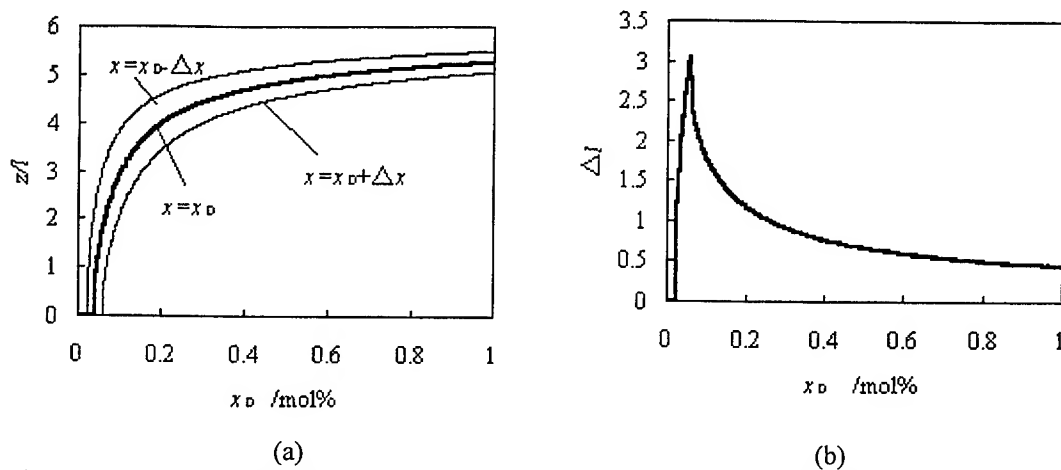


Fig.4 Dependence of the position (a) and the length (b) of the crystal section with acceptable composition in $\text{Hg}_{1-x}\text{Mn}_x\text{Te}$ ingot on the average composition.

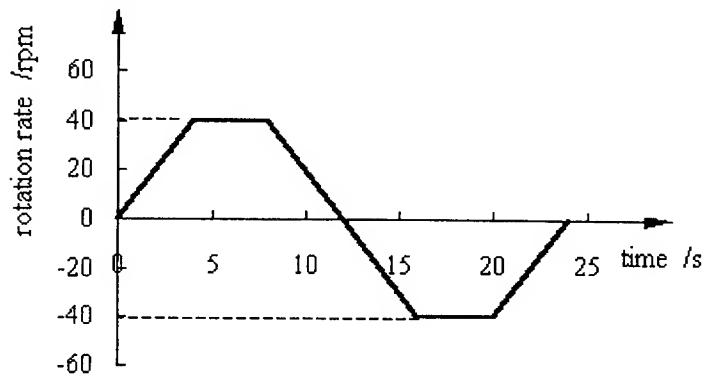


Fig.5 Crucible rotation sequence in ACRT-B growth process of $\text{Hg}_{1-x}\text{Mn}_x\text{Te}$ ingot.

4.2 Crystal Analysis and the Results

A relatively perfect $\text{Hg}_{0.89}\text{Mn}_{0.11}\text{Te}$ crystal was obtained which was cut into 5mm diameter and 1mm thick wafers perpendicular to the centerline for metallographic analysis and solute (Mn) distribution measurements. The grains in the crystal are sketched in fig.6. It is seen that several grains form at the beginning in the taper-shaped starting region. But, most of them are already eliminated through the competitive growth in the taper and about 12mm length of single crystal is obtained in the early part of the ingot. After that, several new grains nucleated near the ampoule wall block the single crystal, and the ingot changes to be the polycrystalline.

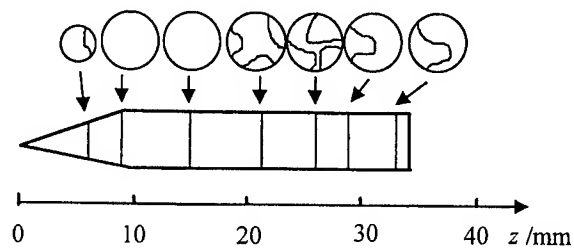


Fig.6 Grains on different sections.

Electron microprobe analysis was used to determine the composition at different sections. Since the ingot diameter is only 5mm, the composition variation on the transversal section is very limited. Mn content is only slightly higher near the ampoule wall than in the center. Similar positions close to the wafer ridge are chosen for the composition tests. The results are shown in table 1, where M_{Mn} , M_{Te} and M_{Hg} are mole fractions of Mn, Te, and Hg, respectively. It is seen that the sum of Hg and Mn contents is about 50mol% with some reasonable errors. From the measurement results, x values in $Hg_{1-x}Mn_xTe$ were also calculated. The Mn content in the initial region is much higher than the average value and reduces gradually to the relatively low values in the final region because of the solute redistribution during growth process.

Table 1 Composition measurement results

Distance from ingot tip /mm	Composition /mole %			$x = \frac{M_{Mn}}{M_{Mn} + M_{Hg}}$
	M_{Mn}	M_{Te}	M_{Hg}	
0	8.26	47.97	41.49	0.166
2	10.31	42.84	43.92	0.1901
6	8.41	50.91	40.68	0.1713
7.5	9.66	47.64	40.41	0.1929
10.1	11.05	51.98	36.97	0.2301
14.3	8.63	51.64	39.73	0.1785
18.5	6.43	50.21	43.37	0.1291
22.7	2.44	52.87	44.69	0.0518
26.9	2.60	52.34	45.06	0.0546
31.1	1.98	50.51	47.50	0.0404
33.9	2.51	52.76	44.73	0.0531
22.7	2.44	52.87	44.69	0.0518

4.3 Comparison of the mathematical model with the experimental results

The comparison of the calculation results with the experimental data is given in fig.7, which shows a relatively good agreement in the major part of the ingot. But larger errors occur in the initial region and the final region. The error may stem from the following reasons:

(1) From the pseudobinary-phase diagram presented by Delves et al [22], it is seen that k_0 is not constant but changes with x value.

(2) In the taper-shaped initial region, the influence of the convection is limited. This will prevent the solute transport. Poor Mn region formed in front of growth interface which results in a lower Mn content than that calculated based on the homogeneous mixture assumption, and therefore, a lower Mn crystal is grown in the initial region.

(3) In the final region, the normal ACRT induced flow does not exist. The solute transport becomes a diffusion-controlled process, which is much slower than that controlled by convection and a higher Mn content will be still kept there.

In spite of the errors described above, the model shown by equ.(6) and (8) is satisfactory to predict the solute redistribution evaluation in ACRT-B grown $Hg_{1-x}Mn_xTe$ crystal. Better results can be obtained if k_0 is better defined.

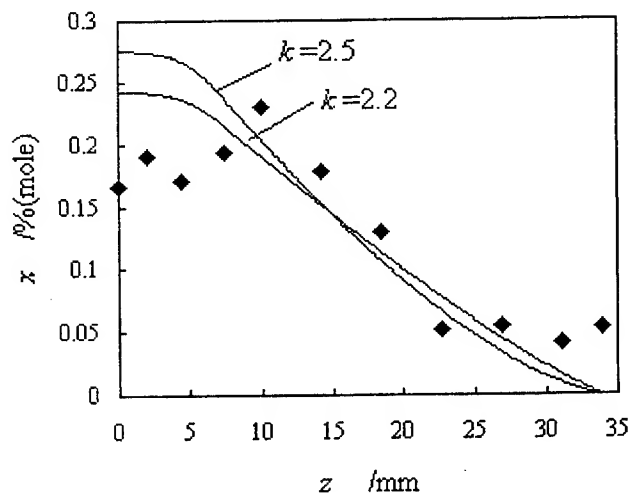


Fig.7 Comparison between evaluation results with the mathematical model and experimental data.

◆ — experimental data

5. Conclusions

(1) Based on some quantitative evaluations on the solute partition at growth interface, diffusion in the solid and the liquid, a mathematical model is deduced for the calculation of the solute redistribution during ACRT-B growth of $\text{Hg}_{1-x}\text{Mn}_x\text{Te}$ crystal. The results reveal that in $\text{Hg}_{1-x}\text{Mn}_x\text{Te}$ crystal grown by ACRT-B method, Mn content is much higher than the average value in the initial region and reduces gradually to a lower value in the final region because of solute redistribution. Only a section of the crystal fit the required composition with the acceptable error. The crystal section with acceptable composition can be also obtained in $\text{Hg}_{1-x}\text{Mn}_x\text{Te}$ ingot grown from the melt with no stoichiometric compositions. The length of the section with acceptable composition increases with decreasing in x_0 value until x_0 reaches a certain limit. Meanwhile, the region moves toward the initial region. To grown $\text{Hg}_{1-x}\text{Mn}_x\text{Te}$ crystal with a certain composition, such as $x=0.11$, it is preferable to use the melt with a lower average Cd content, so that the region with the acceptable composition will be longer and located in the early region of the ingot where the crystalline quality is better.

(2) Experimental measurement on Mn distribution (i.e. x values) along the growth direction in a 5mm-diameter $\text{Hg}_{0.89}\text{Mn}_{0.11}\text{Te}$ grown by ACRT-B method shows that Mn content is much higher than the average value in the initial region and decreases gradually to very low value in the final region. The measurement data are coincident with the calculation results by a mathematical model, except for some discrepancies in the initial and final regions of the grown ingot, where the assumption of homogeneous mixture in the liquid used is not true. Even though, the mathematical model essentially reflects the real solute redistribution process during ACRT-B growth.

References

- [1] S. Wong and P. Becla, J. Vac. Sci. Technol., 1986, A4:2019
- [2] P. Becla, P. A. Wolff, R. L. Aggarwall and S. Y. Yuen, J. Vac. Sci. Technol., 1985, A3:116
- [3] R. R. Galazka, J. Crystal Growth, 1985, 72:364
- [4] P. Becla, J. Vac. Sci. Technol., 1986, A4:2014
- [5] Detector Mini-Magazine, Photonics Spectra, 1988:94
- [6] J. K. Furdyna, J. Appl. Phys., 1988, 64:R29
- [7] J. K. Furdyna, J. Vac. Sci. Technol., 1982, 21:220
- [8] R. E. Kremer and M. R. Tamjidi, J. Crystal Growth, 1986, 75:415
- [9] R. E. Kremer, Y. Tang and F. G. Moore, J. Crystal Growth, 1988, 86:797
- [10] T. Piotrowski, O. De Melo, F. Leccabue, B. E. Watts, V. Sagredo, M. Chourio and J. Martin, Mater. Lett. 1990, 10:296
- [11] R. G. Mani, T. McNair, C. R. Lu and R. Grober, J. Crystal Growth, 1989, 97:617
- [12] W. Giriat and J. K. Furdyna, in Semiconductor and Semimetals, Vol.25, p.1, edited by R. K. Willardson and A. C. Beer, Academic Press, Boston (1988)
- [13] N. G. Garbuz, S. V. Kondrakov, S. A. Popov, E. V. Susov, A. V. Filatov, R. A. Chazieva and E. N. Chalina, Nieorg. Mat, 1990, 26:536
- [14] J. K. Furdyna, J. Appl. Phys. 1982, 53:7637
- [15] P. Capper, W. G. Coates, C. L. Jones, J. J. Gosney, C. K. Ard and I. Kenworthy, J. Crystal Growth, 1987, 83(1):69-76
- [16] P. Capper, J. C. Birce, C. L. Jones, W. G. Coates, J. J. G. Gosney, C. Ard and I. Kenworthy, J. Crystal Growth. 1988, 89:171-176
- [17] P. Capper, J. J. G. Gosney, C. L. Jones and I. Kenworthy, Journal of Electronic Materials, 1986, 15(6):361-170
- [18] M. J. Aziz, J. of Applied Physics. 1982, 53(2):1158~1168
- [19] Antoni Rogalski, New Ternary Alloys Systems for Infrared Detectors, Spie Optical Engineering Press, 1994, p.70
- [20] J. A. Burton, R. C. Prim, W. G. Slichter, J. of Chem. Phys. 1953, 21:1987~1996
- [21] J. Kaniewski, B. Witkoska and W. Girait, J. of Crystal Growth, 1982, 60:179
- [22] R. T. Delves and A. Franciosi, Phys. Chem. Solids, 1963, 24:549

Acknowledgement

The research is supported by the National Natural Science Foundation of P. R. China.

Simple theory of steam oxidation of AlAs

Marek Osiński^{*a}, Tengiz Svimonishvili^a, Gennady A. Smolyakov^a, Vladimir A. Smagley^a,
Paweł Maćkowiak^b, and Włodzimierz Nakwaski^{a,b}

^aCenter for High Technology Materials, University of New Mexico, 1313 Goddard SE
Albuquerque, New Mexico 87106, USA

^bInstitute of Physics, Technical University of Łódź, ul. Wólczńska 219, PL-93005 Łódź, Poland

ABSTRACT

Kinetics of AlAs steam oxidation process is investigated theoretically in cylindrically symmetric mesa structures. Under the assumption of a steady-state process, compact analytical formulae are obtained for time evolution of the oxidation front and for the oxidation rate. Values of main oxidation process parameters ($A = 3.92 \mu\text{m}$, $B = 1.48 \mu\text{m}^2/\text{min}$, and $\beta = 0.716$) are extracted from existing experimental data for $T = 350^\circ\text{C}$ and the layer thickness $d = 250 \text{ nm}$. The oxidation rate is found to first decrease from its initial value of B/A and remain almost constant for a large range of intermediate sizes of unoxidized region. When the unoxidized region becomes very small, a rapid increase in this rate up to the value of $B/[A(1-\beta)]$ is predicted. This renders the process control of fabricating miniature oxide apertures with diameters $< 2 \mu\text{m}$ extremely difficult. Comparison with 1D model of oxidation process in Cartesian geometry reveals significant differences in time evolution of the oxidation front. Understanding these differences is important for achieving a good control of the oxidation process in cylindrical structures.

Key words: Steam oxidation, reaction kinetics, AlAs, VCSELs

1. INTRODUCTION

Hydrolytic oxidation of AlAs, discovered serendipitously by Holonyak's group in early 90's [Dallesasse 1990a], [Dallesasse 1990b], has evolved into a rapidly developing enabling technology for a growing number of optoelectronic and electronic devices and structures. Application of the selective steam oxidation process of AlAs (or AlGaAs with high Al content) layers, transforming them into native-oxide Al_2O_3 layers, for current confinement and distributed-Bragg reflector layers in vertical-cavity surface-emitting lasers (VCSELs) has resulted in dramatic improvements in their performance [Choquette 1994], [Choquette 1997], [Deppe 1998]. Steam oxidation is also a promising technology for development of GaAs-on-insulator [Parikh 1997] and metal-oxide-semiconductor [Bond 1996] electronic devices, photonic crystals [Krauss 1999], magnetic memories [Wong 1999], etc.

A typical approach in oxide-confined VCSEL (OCSEL) fabrication is to create a few- μm -wide unoxidized aperture at the center of a much larger oxidized mesa [Huffaker 1994], [Jung 1997], [MacDougall 1998], [Yang 1998], which is a rather difficult task. To avoid ambiguities associated with a curvilinear oxidation front, possibly influenced by anisotropy of the process, the experimental studies of steam oxidation have largely focused on the process originating from either elongated stripe mesas [Ochiai 1996], [Blum 1997], [Yoshikawa 1998], [Pan 1998], or from a freshly cleaved edge of the Al(Ga)As layer [Kim 1996], [Naone 1997]. In either case, the sample geometry would produce a straight oxidation front, adequately described by a one-dimensional (1D), Cartesian model of oxidation kinetics in the layer plane. Consequently, nearly all theoretical considerations of the Al(Ga)As oxidation process have been limited to the 1D Cartesian case [Ochiai 1996], [Choquette 1997], [Naone 1997], [Pan 1998]. In this paper, we examine to what extent the predictions of 1D Cartesian analysis are applicable to cylindrically symmetric structures, and point out important differences in process kinetics arising from cylindrical geometry.

Reliable simulation of the oxidation process can be very helpful in achieving good controllability and high yield, necessary for commercialization of OCSELs. Yet, very little work seems to have been done towards development of oxidation process modeling tools. Apparently, there have been only two attempts to model AlAs oxidation kinetics in cylindrically symmetric mesa structures: an analytical model of [Koley 1997], and a semi-analytical model of [Alonzo 1998]. Unfortunately, as explained below, the paper of [Koley 1997] suffers from serious errors and inconsistencies in both analytical formulation as well as in calculated results. Most importantly, the final expression for time evolution of

the oxidation front, given in Eq. (16) of [Koley 1997], as well as process parameters, given in Table I of [Koley 1997], are incorrect. The same work does, however, contain experimental results that will be used in this paper to determine process parameters of steam oxidation.

2. ANALYTICAL MODEL OF OXIDATION KINETICS IN CYLINDRICAL STRUCTURES

Similarly to Cartesian models [Ochiai 1996], [Choquette 1997], [Naone 1997], [Pan 1998], our approach is based on a simple theory of thermal oxidation of silicon proposed by Deal and Grove [Deal 1965]. The oxidation is assumed to be mainly governed by the diffusion of O (or H₂O) through the oxidized AlAs (or AlGaAs) layer to the oxidation front, and by chemical reactions that form the oxide. The whole process is composed of three phases, illustrated in Fig. 1:

- transport of the oxidant from the external ambient across the interface with the oxidized layer:

$$F_1 = h(C^* - C_0) \quad (1)$$

- diffusion of the oxidant through the oxidized region towards the oxidation front:

$$F_2(r) = -D \frac{dC(r)}{dr} , \quad (2)$$

- chemical reactions during hydrolyzation and/or oxidation leading to formation of alumina:

$$F_3 = kC_i . \quad (3)$$

Here, F_1 , $F_2(r)$, and F_3 represent the corresponding oxidant flux densities per unit area and unit time, h is the gas-phase transport coefficient, C^* is the equilibrium concentration of the oxidant, C_0 is the oxidant concentration at $r = R_0$, r is the radial distance from the symmetry axis, R_0 is the outer radius of the mesa, D is the diffusion constant, $C(r)$ is the distribution of oxidant concentration in the bulk of the oxidized region, k is the oxidation reaction rate constant, $C_i \equiv C(R_i)$, and R_i is the inner radius of the oxidized region.

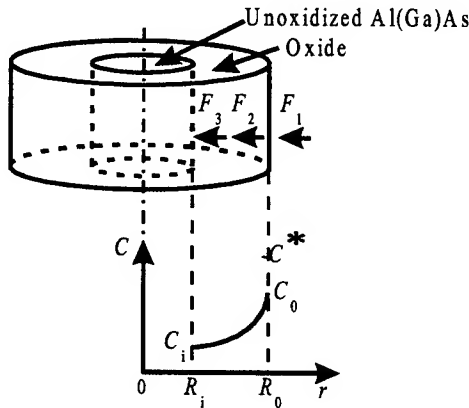


Fig. 1. Schematic illustration of the oxidation process of a cylindrical Al(Ga)As mesa.

Under steady-state process conditions, total fluxes of the oxidant can be assumed to be the same in all three phases:

$$\left(\int F_1 dS \right)_{R_0} = \left(\int F_2 dS \right)_{R_i} = \left(\int F_3 dS \right)_{R_i} , \quad (4)$$

where dS is the elementary surface and R_0 and R_i are the radii of the external surface of an oxidized layer and of the oxide/AlAs interface, respectively.

The usual assumption made in 1D Cartesian analysis is that the flux $F_2(x)$ of the oxidant particles per unit cross-sectional area and per unit time should be constant, *i.e.* independent of the distance x from the interface with the ambient. Instead, for cylindrical structures, a more proper formulation for a steady-state process is to require that the divergence of the flux $F_2(r)$ vanishes. This leads to the following condition for $F_2(r)$ in a layer of thickness d :

$$F_2(r) = G/(2\pi rd) , \quad (5)$$

where G is the total number of particles crossing any $r = \text{const}$ surface. Note that G is a function of both the outer radius of the mesa R_0 and the inner radius of the oxidized region R_i . Eq. (5) immediately implies that $C(r)$ should be of the form $a + b \ln r$, with constant a and b . In addition, time evolution of the oxidized region length ρ (measured from the outer perimeter) can be written in terms of the flux $F_2(r)$ as follows [Deal 1965]:

$$-d\rho/dt = F_2(r)/N_0 , \quad (6)$$

where $r = R_0 - \rho$, and N_0 is the density of oxidant particles incorporated into the oxidized material. The solution of this system of equations, describing the oxidation kinetics in a cylindrical mesa structure, can be written in a simple analytical form:

$$Bt = (R_0 - \rho)^2 \ln \left(1 - \frac{\rho}{R_0} \right) + \rho(A + R_0) - \frac{\rho^2}{2} \left(1 + \beta \frac{A}{R_0} \right) , \quad (7)$$

where t stands for the oxidation time, while the β , A , and B parameters are expressed as [Deal 1965], [Koley 1997]:

$$\beta = k/(k+h) , \quad (8)$$

$$A = 2D(1/h + 1/k) = 2D/(\beta h) , \quad (9)$$

$$B = 2DC^*/N_0 . \quad (10)$$

Note that in the limit of $R_0 \rightarrow \infty$, Eq. (7) reduces to the classical Deal and Grove solution valid for Cartesian geometry [Deal 1965] [cf. Eq. (18) in Section 3]. Hence, the parameters A and B are expected to play the same role as in the Cartesian case. Specifically, the parameter B describes the diffusive mechanism of oxidation, while the rate parameter B/A represents the reaction-limited process [Deal 1965], [Ochiai 1996]. The corresponding radial distribution of oxidant concentration $C(r)$ is given by:

$$C(r) = [C_0 \ln(r/R_i) + C_i \ln(R_0/r)] / \ln(R_0/R_i) \quad (11)$$

where C_i is expressed as:

$$C_i = C_0 D / [D + k R_i \ln(R_0/R_i)] . \quad (12)$$

Finally, the total number of oxidant particles G is given by:

$$G = 2\pi R_i k d C_0 D / [D + k R_i \ln(R_0/R_i)] \quad (13)$$

Note that, as expected, G becomes zero when the oxidation process is fully completed and the unoxidized window is closed.

3. RESULTS FOR OXIDATION OF BULK AIAs

Oxidation process parameters can be determined from reported measurements of AIAs oxidation in cylindrical geometry. Fig. 2 shows the experimental data of [Koley 1997] together with the theoretical curves obtained using Eq. (7) with a nonlinear least squares fitting procedure. The following values of parameters A , B , and β are found for the oxidation process performed at 350 °C on relatively thick ($d = 2500$ Å) AIAs layers:

$$A = 3.92 \mu\text{m} , \quad B = 1.48 \mu\text{m}^2/\text{min} , \quad \beta = 0.716 \quad (14)$$

It should be noted that these values differ considerably from those reported earlier in [Koley 1997] ($A = 5 \mu\text{m}$, $B = 6 \mu\text{m}^2/\text{min}$ and $\beta = 0.95$). As shown in Fig. 2, the values quoted by Koley *et al.* are in large disagreement with their experimental data. The discrepancy becomes even larger if the erroneous formula (16) of [Koley 1997] is used together with the values of process parameters quoted in that same paper. We also note that Eq. (16) of [Koley 1997] gives a wrong limit when $R_0 \rightarrow \infty$, different from that of [Deal 1965].

Fig. 3 shows radial profiles of the oxidant concentration $C(r)$ inside the oxide layer. In the calculations, approximate values of the process parameters $C^* = 3.0 \times 10^{19} \text{ cm}^{-3}$ and $N_0 = 4.5 \times 10^{22} \text{ cm}^{-3}$, found for wet silicon oxidation [Deal 1965], were used. Analogous values of these parameters for AlAs steam oxidation are currently unknown, but we do not expect them to be very different. The remaining process parameters deduced from these values and from the A , B , and β given in Eq. (14) are: $h \approx 791 \mu\text{m}/\text{min}$, $k \approx 1994 \mu\text{m}/\text{min}$, and $D \approx 1110 \mu\text{m}^2/\text{min}$. Note that the oxidant concentration $C(r)$ in Fig. 3 changes rather slowly far from the structure axis, but is reduced dramatically when approaching the center. Such a rapid decrease in the oxidant concentration makes the process control in this area extremely difficult.

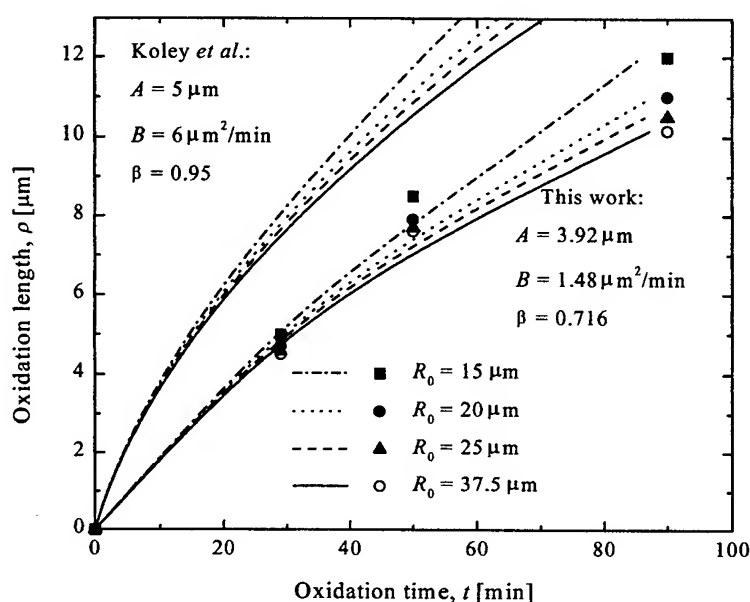


Fig. 2. Oxidation length ρ versus oxidation time t for steam oxidation of AlAs at 350 °C for cylindrical mesas of different radii R_0 . Experimental points are taken from [Koley 1997]. The oxidation process parameters listed under "This work" are found using the least-square method. Curves labeled as "Koley *et al.*", obtained using the formula and process parameters reported in [Koley 1997], clearly disagree with experimental data.

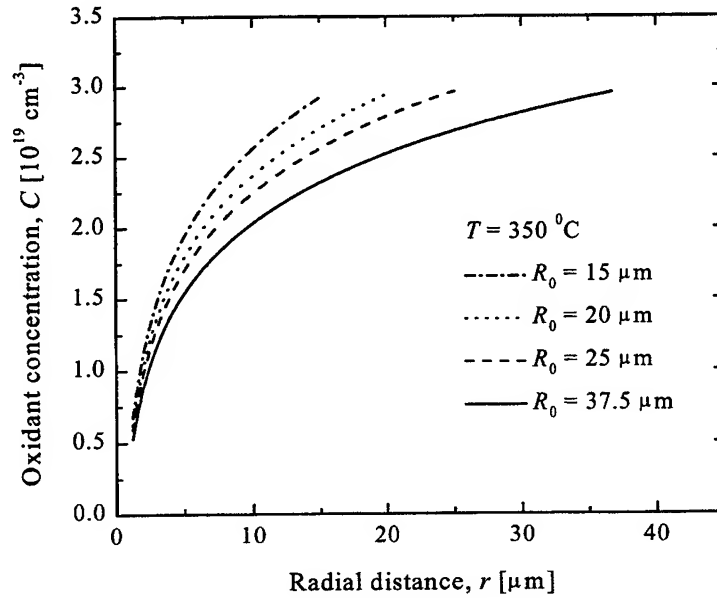


Fig. 3. Approximate radial profiles of the oxidant concentration C inside oxide layer during steam oxidation at 350 °C for various radii R_0 of the mesa. The inner radius R_i of the oxidized region is taken as 1 μm .

Fig. 4 reveals that the oxidant flux density $F_2(r)$ inside an oxide layer increases rapidly while approaching the symmetry axis (thus deviating considerably from the $F_2 = \text{const}$ assumption of [Koley 1997]). It is, however, nearly independent of the mesa radius R_0 , being for a given r practically the same for all cases considered.

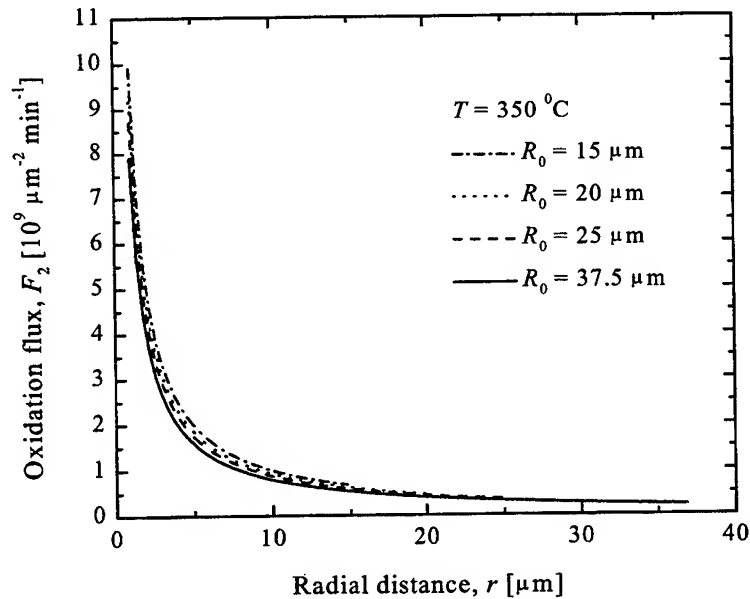


Fig. 4. Approximate radial profiles of the oxidant flux density $F_2(r)$ inside oxide layer during steam oxidation at 350 °C for various radii R_0 of the mesa.

4. OXIDATION RATE IN BULK AlAs

Differentiation of Eq. (7) gives the oxidation rate in the following form:

$$\frac{d\rho}{dt} = \frac{B}{A\left(1 - \beta \frac{\rho}{R_0}\right) - 2(R_0 - \rho) \ln\left(1 - \frac{\rho}{R_0}\right)} \quad (15)$$

Note that the initial rate of oxidation (at $\rho = 0$) is equal to B/A . The rate at the end of the oxidation process, when $\rho \rightarrow R_0$, is given by $B/[A(1 - \beta)]$ and can be considerably greater than the initial rate if β is close to 1. Between these extremes, the oxidation process slows down (provided $R_0 > \beta A/2$), to reach the minimum rate of

$$(d\rho/dt)_{\min} = B/[A(1 - \beta) + 2(R_0 - \rho_{cr})] , \quad (16)$$

where ρ_{cr} is the oxidation length at which the rate slows down to its minimum:

$$\rho_{cr} = R_0 \{1 - \exp[(\beta A/2R_0) - 1]\} . \quad (17)$$

When $R_0 \gg A$ (which is indeed the case in most practical applications), $\rho_{cr} \approx R_0(1 - e^{-1}) \approx 0.63 R_0$, and $(d\rho/dt)_{\min} \approx eB/(2R_0) \approx 1.36B/R_0$.

Eq. (7) should be compared to the solution of a 1D Cartesian problem [Deal 1965], [Ochiai 1996], [Choquette 1997], [Naone 1997], [Pan 1998]:

$$Bt = x^2 + Ax , \quad (18)$$

where x is the position of the oxidation front measured from the outer edge. In the initial stages of oxidation (when $\rho \ll R_0$), Eq. (7) reduces to Eq. (18), provided the outer radius of the mesa is sufficiently large, *i.e.* when $R_0 \gg A$. According to Eq. (18), the oxidation rate in Cartesian geometry is given by:

$$dx/dt = B/(2x + A) . \quad (19)$$

Thus, the Cartesian oxidation rate steadily decreases from its initial value of B/A . The initial rate is the same as in cylindrical geometry, which means the oxidation process in its initial stage is purely reaction limited, independent of geometry. However, as shown in Fig. 5, significant deviations between the cylindrical and Cartesian process kinetics develop after the oxidation front passes approximately half of the outer radius R_0 . The difference becomes dramatic in the last couple of μm before the complete closure of the oxide window.

The initial oxidation rate in Fig. 5 is equal to $0.378 \mu\text{m}/\text{min}$ and is independent of R_0 . It decreases gradually up to the critical point ρ_{cr} where it reaches a minimum. The minimal oxidation rates in Fig. 5 range from $0.112 \mu\text{m}/\text{min}$ for $R_0 = 15 \mu\text{m}$ to $0.047 \mu\text{m}/\text{min}$ for $R_0 = 37.5 \mu\text{m}$. Starting from ρ_{cr} , ranging from $8.94 \mu\text{m}$ to $23.18 \mu\text{m}$ for the above R_0 values, the rate change is reversed: it begins to increase, initially very slowly, but when approaching the center of the structure, this increase becomes extremely rapid. The final rate of $1.33 \mu\text{m}/\text{min}$ at the closure of the oxide window is reached almost instantaneously. The sudden increase in the oxidation rate in the last couple of μm before the complete closure poses a significant technological challenge and makes the control of oxidation process extremely difficult for small target diameters of oxide window ($\leq 4 \mu\text{m}$).

For relatively large oxidized mesas (or large R_0), the oxidation rate is practically constant for most part of the oxidation process (*c.f.* the curve for $R_0 = 37.5 \mu\text{m}$ in Fig. 5) and close to its minimal value [Eq. (16)]. This behavior is supported by numerous observations of nearly constant oxidation rates in Al(Ga)As/GaAs structures, reported in many publications [Burton 1994], [Nickel 1995], [Choquette 1995], [Geib 1997], [Weigl 1997], [Ashby 1997], [Feld 1998], [Reese 1998].

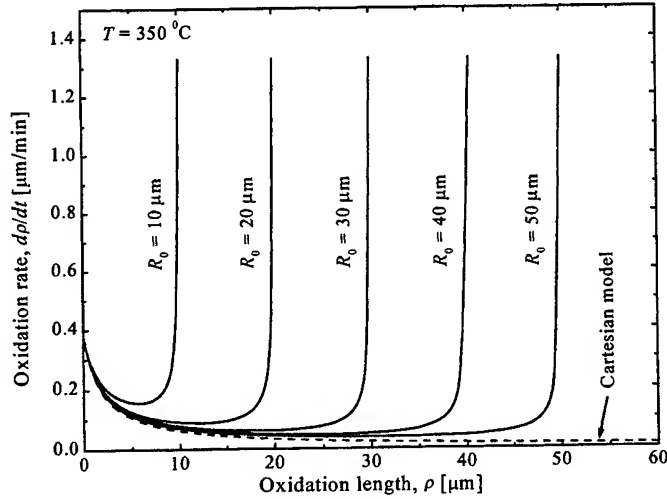


Fig. 5. Oxidation rate dp/dt versus oxidation length ρ for steam oxidation of AlAs at 350 °C for cylindrical mesas of various radii R_0 (solid lines). The values of parameters A , B , and β are listed in Eq. (14). Each curve ends when $\rho = R_0$, with the final rate equal to $B/[A(1 - \beta)]$. The broken line represents the 1D Cartesian solution obtained for the same values of A and B parameters.

As shown in Fig. 5, the oxidation rate at any value of ρ decreases with increasing outer radius R_0 and is always higher than the rate predicted by the 1D Cartesian model (broken line in Fig. 5). This behavior is consistent with similar observations reported in [Langenfelder 1997].

Based on Fig. 5, one might be tempted to presume that as long as the target inner radius R_i of the oxidized region is within the flat minimum part of the dp/dt curve, the 1D Cartesian model could well approximate the process. However, as shown in Fig. 6, this is not the case, as gross errors would be introduced in the predicted oxidation time even well before the onset of sudden acceleration of dp/dt in cylindrical structures. The 1D Cartesian model consistently underestimates the time required to reach a desired length of the oxidized region in a cylindrical structure.

The time t_c necessary to reach complete oxidation of a cylindrical structure is obtained from Eq. (7) by setting $\rho = R_0$:

$$t_c = R_0[(2 - \beta)A + R_0]/2B \quad (20)$$

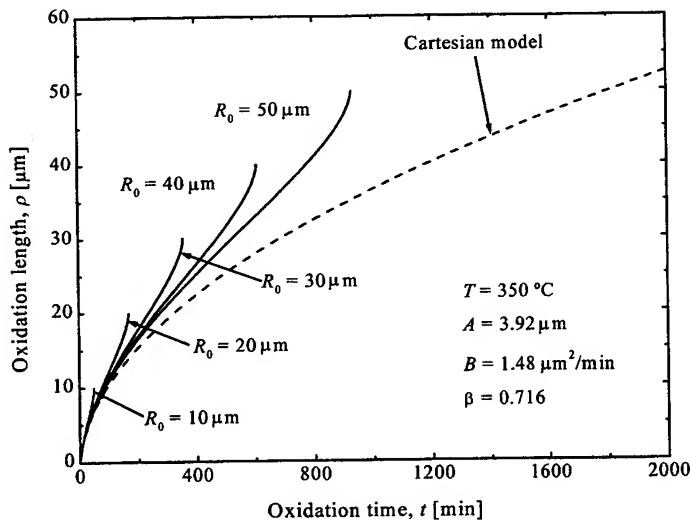


Fig. 6. Comparison of AlAs oxidation process kinetics at 350 °C in cylindrical structures of various radii R_0 (solid lines) and in the 1D Cartesian model (broken line).

The first term on the right-hand side of Eq. (20) is identical with the result of the 1D Cartesian model for the oxidation front to reach the depth R_0 , whereas the second term represents the reduction of t_c associated with cylindrical geometry. When $R_0 \gg A$, t_c is two times smaller than the Cartesian result. Consequently, any attempt to use the Cartesian model to predict the process time for structures with $R_i < R_0/2$ will result in large errors if R_0 exceeds A considerably (which is usually the case).

Recently, a much more complicated model of wet thermal oxidation in cylindrically symmetric AlAs structures has been proposed, in which the distribution of oxidant inside the oxidized region is expressed in terms of an infinite series of Bessel functions [Alonzo 1998]. In order to predict oxidation length vs. time curves, that model requires lengthy numerical calculations. The results shown in Fig. 6 using our analytical model are qualitatively very similar to those shown in [Alonzo 1998], and follow directly from Eq. (7).

5. OXIDATION PROCESS DEPENDENCE ON TEMPERATURE AND LAYER THICKNESS

5.1. Process Parameters

The steam oxidation process is known to be very sensitive to temperature [Ochiai 1996], [Naone 1997]. In addition, it has been demonstrated that the oxidation process rate strongly depends on the AlAs layer thickness d if it is smaller than 800 Å [Kim 1996], [Choquette 1997], [Naone 1997], [Langenfelter 1997], [Deppe 1998], [Yoshikawa 1998]. We expect the formulae derived in this paper to still apply at various temperatures and for thin layers, but with appropriately adjusted values of parameters A , B , and β . In general, all three of these parameters can be temperature and layer-thickness dependent. However, in view of the absence of experimental data for cylindrical geometry, we set the parameter β to be constant, and use the published data for Cartesian geometry to determine $A(d, T)$ and $B(d, T)$, noting that they should coincide with the parameters used for cylindrical geometry as long as we consider them to be independent of the mesa radius R_0 . We postulate the following form of the process parameters $A(d, T)$ and $B(d, T)$:

$$A(d, T) = A_\infty(d) \exp[-E_A(d)/(k_B T)] , \quad (21)$$

$$B(d, T) = B_\infty(d) \exp[-E_B(d)/(k_B T)] , \quad (22)$$

where k_B is Boltzmann's constant. Based on the experimental data of [Ochiai 1996], [Naone 1997], [Koley 1997], and [Alonzo 1998], the high-temperature limits $A_\infty(d)$ and $B_\infty(d)$ are postulated in the form:

$$A_\infty(d) = A_0 \exp[-d/d_{A0}] , \quad (23)$$

$$B_\infty(d) = B_0 \exp[-d/d_{B0}] . \quad (24)$$

We find that the following form of layer thickness dependence fits well the activation energies $E_A(d)$, $E_B(d)$:

$$E_A(d) = E_{Ab} + \varepsilon_{EA}/d , \quad (25)$$

$$E_B(d) = E_{Bb} + \varepsilon_{EB}/d , \quad (26)$$

where E_{Ab} and E_{Bb} represent the bulk limits of the activation energies E_A and E_B , respectively. The form of Eqs. (25) and (26) is consistent with the layer thickness dependence of the activation energy $E_{B/A}$ for the linear rate coefficient B/A , as shown in Fig. 3 of [Naone 1997]:

$$E_{B/A}(d) = E_{B/A,b} + \varepsilon_{EB/A}/d , \quad (27)$$

where

$$E_{B/A,b} = 1.55 \text{ eV}, \quad \text{and} \quad \varepsilon_{EB/A} = 3.96 \text{ eV}\cdot\text{nm}. \quad (28)$$

Using the data from Table 1 in [Naone 1997] and assuming they should follow the relationship (26), we can also obtain

$$E_{Bb} = 0.90 \text{ eV}, \quad \text{and} \quad \varepsilon_{EB} = 1.75 \text{ eV}\cdot\text{nm}. \quad (29)$$

Combining Eqs. (26)-(29), we can determine the parameters E_{Ab} and ε_{EA} using

$$E_A(d) = E_B(d) - E_{B/A}(d) . \quad (30)$$

The result is

$$E_{Ab} = -0.65 \text{ eV}, \quad \text{and} \quad \varepsilon_{AB} = -2.21 \text{ eV}\cdot\text{nm}. \quad (31)$$

The first three columns in Table 1 contain a list the $A_\infty(d)$, $B_\infty(d)$ parameters extracted from experimental data for samples of various thicknesses. $B_\infty(25 \text{ nm})$ and $B_\infty(25 \text{ nm})/A_\infty(25 \text{ nm})$ are taken from Table 1 of [Naone 1997].

Applying the least squares fitting method to experimental data of [Ochiai 1996] for $d = 45 \text{ nm}$ and $T = 440^\circ\text{C}$, we find $A = 64.67 \mu\text{m}$ and $B = 351.16 \mu\text{m}^2/\text{min}$. Eqs. (25), (26) together with (29) and (31) give $E_A(45 \text{ nm}) = -0.699 \text{ eV}$ and $E_B(45 \text{ nm}) = 0.939 \text{ eV}$. The corresponding values of $A_\infty(45 \text{ nm})$ and $B_\infty(45 \text{ nm})$ are then found from Eqs. (21) and (22).

Table 1. Experimental values of $A_\infty(d)$, $B_\infty(d)$ parameters and their best-fit counterparts satisfying Eqs. (23), (24)

Thickness, d [nm]	Parameters extracted from experimental data			Fitted parameters	
	$A_\infty(d)$ [$10^{-4} \mu\text{m}$]	$B_\infty(d)$ [$10^9 \mu\text{m}^2/\text{min}$]	Reference	$A_\infty(d)$ [$10^{-4} \mu\text{m}$]	$B_\infty(d)$ [$10^9 \mu\text{m}^2/\text{min}$]
25	10.45	2.3	[Naone 1997]	10.52	2.213
45	7.42	1.52	[Ochiai 1996]	7.345	1.519
100	2.36	0.37	[Alonzo 1998]	2.731	0.540
250	0.184	0.0320	[Koley 1997]	0.184	0.0322

The following reaction parameters have been reported in [Alonzo 1998] for $d = 100 \text{ nm}$ and $T = 425^\circ\text{C}$: $B = 89 \mu\text{m}^2/\text{min}$, $B/A = 5.3 \mu\text{m}/\text{min}$, corresponding to $A = 16.8 \mu\text{m}$. Eqs. (25), (26) together with (29) and (31) give $E_A(100 \text{ nm}) = -0.672 \text{ eV}$ and $E_B(100 \text{ nm}) = 0.918 \text{ eV}$. The corresponding values of $A_\infty(100 \text{ nm})$ and $B_\infty(100 \text{ nm})$ are again found from Eqs. (21) and (22).

The same procedure is also repeated for $d = 250 \text{ nm}$, using the values of A , B given in Eq. (14) for $T = 350^\circ\text{C}$. The corresponding activation energies are $E_A(250 \text{ nm}) = -0.659 \text{ eV}$ and $E_B(250 \text{ nm}) = 0.907 \text{ eV}$. Note that the negative value of E_A is consistent with the results of [Deal 1965], [Ochiai 1996], and [Naone 1997], but in sharp disagreement with [Koley 1997] who claimed that $E_A(250 \text{ nm}) = 0.2 \text{ eV}$.

We then find the remaining parameters A_0 , B_0 , d_{A0} , and d_{B0} by fitting Eqs. (23) and (24) to the data listed in columns 2 and 3 of Table 1. The best fit is obtained by choosing

$$A_0 = 1.65 \times 10^{-3} \mu\text{m} , \quad B_0 = 3.54 \times 10^9 \mu\text{m}^2/\text{min} , \quad (32)$$

$$d_{A0} = 55.6 \text{ nm} , \quad d_{B0} = 53.2 \text{ nm} . \quad (33)$$

The last two columns in Table 1 show the values of $A_\infty(d)$ and $B_\infty(d)$ calculated using Eqs. (23) and (24) with the parameters specified in Eqs. (32), (33).

5.2. Results

We now examine the temperature and layer thickness dependence of the oxidation process in cylindrically symmetric structures, using the parameters $A(d, T)$ and $B(d, T)$ as described in Section 5.1. In absence of any data that could be used to determine possible variation of β with d and T , we assume β to be constant [and equal to 0.716, as in Eq. (14)].

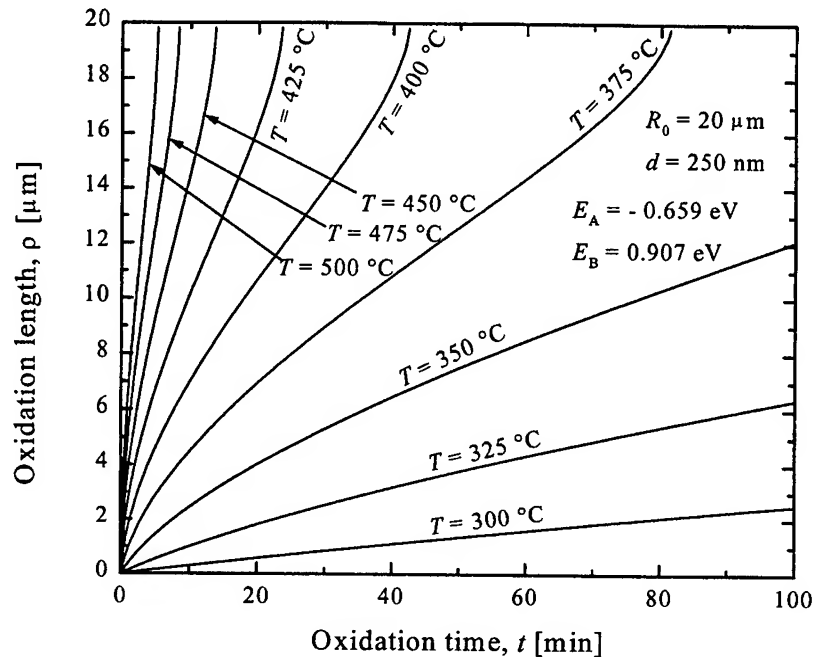


Fig. 7. Oxidation length ρ in a cylindrical mesa of radius $R_0 = 20 \mu\text{m}$ with the AlAs layer thickness $d = 250 \text{ nm}$ versus oxidation time t for steam oxidation of AlAs conducted at various temperatures.

Fig. 7 illustrates temperature sensitivity of the oxidation process in a thick (250 nm) sample. The initial slope of $\rho(t)$ curves is shown to increase rapidly with temperature, as described by the activation energy $E_{B/A}(250 \text{ nm}) = 1.566 \text{ eV}$. Between 350 and 467 °C, the initial reaction rate increases by a factor of 100. Therefore, higher oxidation temperatures result in a substantial reduction of the oxidation time necessary to produce an assumed oxide aperture, while simultaneously rendering the control of the oxidation process more difficult.

As shown in Fig. 8, the oxidation rate at temperatures lower than 350 °C remains almost constant throughout the entire process. At higher temperatures ($\geq 400 \text{ °C}$) the process is highly unstable, with much higher rates at the onset of the oxidation and at its very end (when the oxide aperture is less than $4 \mu\text{m}$ in diameter).

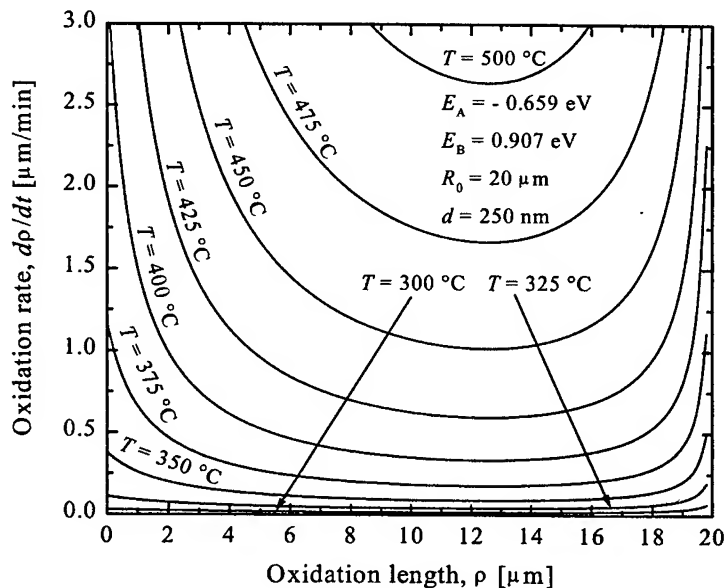


Fig. 8. Oxidation rate $d\rho/dt$ versus oxidation length ρ for the same cylindrical structure as in Fig. 7.

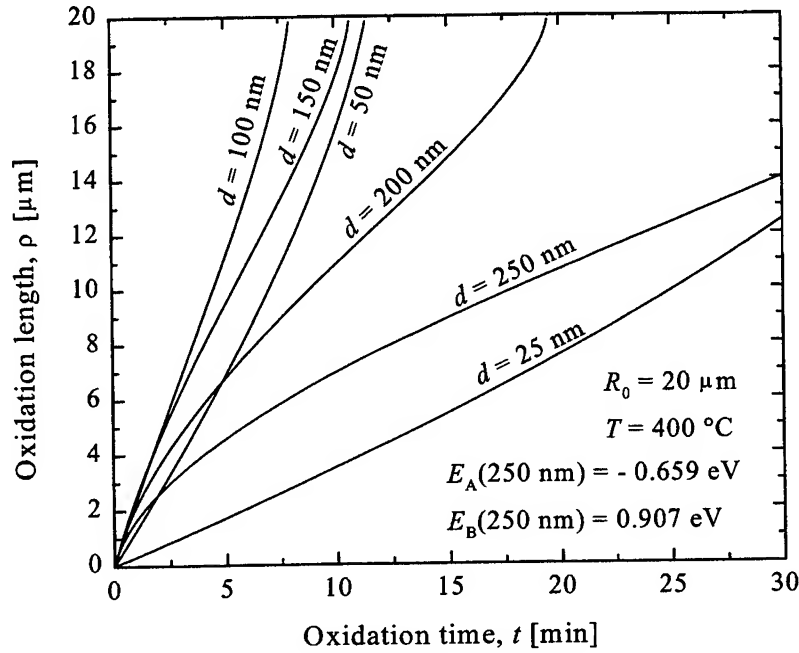


Fig. 9. Oxidation length ρ oxidation time t for cylindrical mesas of radius $R_0 = 20 \mu\text{m}$ and various AlAs layer thicknesses, steam oxidized at $T = 400^\circ\text{C}$.

Fig. 9 reveals a very interesting dependence of the oxidation process on the AlAs layer thickness d . In the range of thicknesses shown in Fig. 9, the initial oxidation rate B/A increases monotonically with increasing d . However, for d larger than 100 nm, the oxidation process becomes slower as the oxidation front moves further into the AlAs layer. It is possible to find the AlAs layer thickness d_c at which the complete oxidation time t_c , as given by Eq. (20), reaches a minimum. The resultant equation is transcendental, and for the parameters listed in Section 5.1 we obtain $d_c = 93.4 \text{ nm}$, consistent with the picture presented in Fig. 9.

The initial oxidation rate B/A also has a non-monotonic character, reaching a maximum at a thickness d_{max} larger than those shown in Fig. 9. Eqs. (21) - (26) give the following analytical result for d_{max} :

$$d_{\text{max}} = \{(\varepsilon_{\text{EB}} - \varepsilon_{\text{EA}})d_{\text{A0}}d_{\text{B0}}/[k_{\text{BT}}(d_{\text{A0}} - d_{\text{B0}})]\}^{1/2}. \quad (34)$$

Using the parameter values given in Section 5.1, we obtain $d_{\text{max}} = 290.1 \text{ nm}$ at $T = 400^\circ\text{C}$.

6. CONCLUSIONS

In this paper, we have presented compact analytical formulae describing the kinetics of the AlAs steam oxidation process in cylindrically symmetric mesa structures. The relations describing both the time necessary to obtain the oxide layer of an assumed length and the oxidation rate have been derived. Wet AlAs oxidation process parameters: $A = 3.92 \mu\text{m}$, $B = 1.48 \mu\text{m}^2/\text{min}$ and $\beta = 0.716$, have been found for the oxidation temperature of 350°C and the layer thickness $d = 250 \text{ nm}$. Approximate values for the remaining process parameters: $h \approx 791 \mu\text{m}/\text{min}$, $k \approx 1994 \mu\text{m}/\text{min}$, and $D \approx 1110 \mu\text{m}^2/\text{min}$ have been also deduced. Good agreement with available experimental data has been obtained. The oxidation rate is independent of the mesa radius and is equal to B/A at the beginning of the oxidation process, then it is steadily reduced to its minimal value achieved for oxide lengths equal to about 60% of the mesa radius. From that point, the oxidation rate is steadily accelerated and its rapid increase is obtained at the end of the process up to the maximum value of $B/A(1-\beta)$. Such an unstable behavior makes the control over the oxidation process extremely difficult in manufacturing microresonator VCSELs with very small oxide-aperture diameters. Additional difficulties may arise from strong dependence of the oxidation process on the layer thickness and ambient temperature. We show that significant differences exist between the predictions of the cylindrical model and those of widely used 1D Cartesian model. Our results can therefore be very important for achieving a good control of the oxidation process in cylindrically symmetric structures.

ACKNOWLEDGMENTS

The authors gratefully acknowledge helpful discussions with Olga Blum and Kent Choquette, both of Sandia National Laboratories. This work was supported by DARPA under the Optoelectronic Materials Center program, by CFD Research Corporation, by the US-Poland Maria Skłodowska-Curie Joint Fund, grant No MEN/NSF-98-336, and by the Polish State Committee for Scientific Research (KBN), grants No 8-T11B-018-12 and No 8-T11B-025-17.

REFERENCES

- [Alonzo 1998] A. C. Alonzo, X.-C. Cheng, and T. C. McGill, "Effect of cylindrical geometry on the wet thermal oxidation of AlAs", *J. Appl. Phys.*, vol. 84 (12), pp. 6901-6905, 15 Dec. 1998.
- [Ashby 1997] C. I. H. Ashby, J. P. Sullivan, K. D. Choquette, K. M. Geib, and H. Q. Hou, "Wet oxidation of AlGaAs: the role of hydrogen", *J. Appl. Phys.*, vol. 82 (6), pp. 3134-3136, 15 Sept. 1997.
- [Blum 1997] O. Blum, C. I. H. Ashby, and H. Q. Hou, "Barrier-layer-thickness control of selective wet oxidation of AlGaAs for embedded optical elements", *Appl. Phys. Lett.*, vol. 70 (21), pp. 2870-2872, 26 May 1997.
- [Bond 1996] A. E. Bond, C. K. Lin, M. H. MacDougall, P. D. Dapkus, K. Kaviani, O. Adamczyk, and R. Nottenburg, "Backgating reduction in MESFETs using an AlAs native-oxide buffer layer", *Electron. Lett.*, vol. 32, pp. 2271-2273, 21 Nov. 1996.
- [Burton 1994] R. S. Burton and T. E. Schlesinger, "Wet thermal oxidation of $\text{Al}_x\text{Ga}_{1-x}\text{As}$ compounds", *J. Appl. Phys.*, vol. 76 (9), pp. 5503-5507, 1 Nov. 1994.
- [Choquette 1994] K. D. Choquette, R. P. Schneider, Jr., K. L. Lear, and K. M. Geib, "Low threshold voltage vertical-cavity lasers fabricated by selective oxidation", *Electron. Lett.*, vol. 30 (24), pp. 2043-2044, 24 Nov. 1994.
- [Choquette 1995] K. D. Choquette, K. L. Lear, R. P. Schneider, Jr., K. M. Geib, J. J. Figiel, and R. Hull, "Fabrication and performance of selectively oxidized vertical-cavity lasers", *IEEE Photon. Technol. Lett.*, vol. 7 (11), pp. 1237-1239, Nov. 1995.
- [Choquette 1997] K. D. Choquette, K. M. Geib, C. I. H. Ashby, R. D. Twesten, O. Blum, H. Q. Hou, D. M. Follstaedt, B. E. Hammons, D. Mathes, and R. Hull, "Advances in selective wet oxidation of AlGaAs alloys", *IEEE J. Sel. Topics Quantum Electron.*, vol. 3 (3), pp. 916-926, June 1997.
- [Dallesasse 1990a] J. M. Dallesasse, P. Gavrilovic, N. Holonyak, Jr., R. W. Kaliski, D. W. Nam, E. J. Vesely, and R. D. Burnham, "Stability of AlAs in $\text{Al}_x\text{Ga}_{1-x}\text{As}$ -AlAs-GaAs quantum well heterostructures", *Appl. Phys. Lett.*, vol. 56 (24), pp. 2436-2438, 11 June 1990.
- [Dallesasse 1990b] J. M. Dallesasse, N. Holonyak, Jr., A. R. Sugg, T. A. Richard, and L. El-Zein, "Hydrolyzation oxidation of $\text{Al}_x\text{Ga}_{1-x}\text{As}$ -AlAs-GaAs quantum well heterostructures and superlattices", *Appl. Phys. Lett.*, vol. 57 (26), pp. 2844-2846, 24 Dec. 1990.
- [Deal 1965] B. E. Deal and A. S. Grove, "General relationship for the thermal oxidation of silicon", *J. Appl. Phys.*, vol. 36 (12), pp. 3770-3778, Dec. 1965.
- [Deppe 1998] D. G. Deppe and D. L. Huffaker, "Native oxide technology for III-V optoelectronic devices", in *Heterogeneous Integration: Systems on a Chip*, (A. Husain and M. Fallahi, Eds.), San Jose, CA, 26-27 Jan. 1998, *Proc. SPIE*, vol. CR70, pp. 141-183 (1998).
- [Feld 1998] S. A. Feld, J. P. Loehr, R. F. Sherriff, J. Wiemer, and R. Kaspi, "In situ optical monitoring of AlAs wet oxidation using a novel low-temperature low-pressure steam furnace design", *IEEE Photon. Technol. Lett.*, vol. 10 (2), pp. 197-199, Feb. 1998.
- [Geib 1997] K. Geib, K. M. Choquette, H. Q. Hou, and B. E. Hammons, "Fabrication issues of oxide-confined VCSELs", Vertical-Cavity Surface-Emitting Lasers (K. D. Choquette and D. G. Deppe, Eds.), San Jose, CA, 10-11 Feb. 1997, *Proc. SPIE*, Vol. 3003, pp. 69-74.
- [Huffaker 1994] D. L. Huffaker, D. G. Deppe, K. Kumar, and T. J. Rogers, "Native-oxide defined ring contact for low threshold vertical-cavity lasers", *Appl. Phys. Lett.*, vol. 65 (1), pp. 97-99, 4 July 1994.
- [Jung 1997] C. Jung, R. Jäger, M. Grabherr, P. Schnitzer, R. Michalzik, B. Weigl, S. Müller, and K. J. Ebeling, "4.8 mW single-mode oxide confined top-surface emitting vertical-cavity laser diodes", *Electron. Lett.*, vol. 33 (21), pp. 1790-1791, 9 Oct. 1997.
- [Kim 1996] J.-H. Kim, D. H. Lim, K. S. Kim, G. M. Yang, K. Y. Lim, and H. J. Lee, "Lateral wet oxidation of $\text{Al}_x\text{Ga}_{1-x}\text{As}$ -GaAs depending on its structures", *Appl. Phys. Lett.*, vol. 69 (22), pp. 3357-3359, 25 Nov. 1996.
- [Koley 1997] B. Koley, M. Dagenais, R. Jin, J. Pham, G. Simonis, G. McLane, and D. Stone, "Kinetics of growth of AlAs oxide in selectively oxidized vertical cavity surface emitting lasers", *J. Appl. Phys.*, vol. 82 (9), pp. 4586-4589, 1 Nov. 1997.

- [Krauss 1999] T. F. Krauss and R. M. De La Rue, "Photonic crystals in the optical regime - past, present and future", *Progress Quantum Electron.*, vol. 23 (2), pp. 51-96, 1999.
- [Langenfelder 1997] T. Langenfelder, S. Schröder, and H. Grothe, "Lateral oxidation of buried $\text{Al}_x\text{Ga}_{1-x}\text{As}$ layers in a wet ambient", *J. Appl. Phys.*, vol. 82 (7), pp. 3548-3551, 1 Oct. 1997.
- [MacDougal 1998] M. H. MacDougal, J. Geske, C. K. Lin, A. E. Bond, and P. D. Dapkus, "Low resistance intracavity-contacted oxide-aperture VCSELs", *IEEE Photon. Technol. Lett.*, vol. 10 (1), pp. 9-11, Jan. 1998.
- [Naone 1997] R. L. Naone and L. A. Coldren, "Surface energy model for the thickness dependence of the lateral oxidation of AlAs", *J. Appl. Phys.*, vol. 82, (5), pp. 2277-2280, 1 Sept. 1997.
- [Nickel 1995] H. Nickel, "A detailed experimental study of the wet oxidation kinetics of $\text{Al}_x\text{Ga}_{1-x}\text{As}$ layers", *J. Appl. Phys.*, vol. 78 (8), pp. 5201-5203, 15 Oct. 1995.
- [Ochiai 1996] M. Ochiai, G. E. Giudice, H. Temkin, J. W. Scott, T. M. Cockerill, "Kinetics of thermal oxidation of AlAs in water vapor", *Appl. Phys. Lett.*, vol. 68 (14), pp. 1898-1900, 1 April 1996.
- [Pan 1998] Z. Pan, Y. Zhang, Y. Du, and R. Wu, "Stability improvement of selective oxidation during the fabrication of InGaAs/GaAs vertical-cavity surface emitting laser", *Jpn. J. Appl. Phys. Pt. 1*, vol. 37 (6B), pp. 3673-3675, 30 June 1998.
- [Parikh 1997] P. A. Parikh, P. M. Chavarkar, and U. K. Mishra, "GaAs MESFETs on a truly insulating buffer layer: Demonstration of the GaAs on insulator technology", *IEEE Electron Dev. Lett.*, vol. 18 (3), pp. 111-113, March 1997.
- [Reese 1998] H. Reese, Y. J. Chiu, E. Hu, "Low-temperature-grown GaAs enhanced wet thermal oxidation of $\text{Al}_{0.98}\text{Ga}_{0.02}\text{As}$ ", *Appl. Phys. Lett.*, vol. 73 (18), pp. 2624-2626, 2 Nov. 1998.
- [Weigl 1997] B. Weigl, M. Grabherr, C. Jung, R. Jäger, G. Reiner, R. Michalzik, R. Sowada, and K. J. Ebeling, "High-performance oxide-confined GaAs VCSEL's", *IEEE J. Select. Topics Quantum Electron.*, vol. 3 (2), pp. 409-415, Apr. 1997.
- [Wong 1999] J. Wong, A. Scherer, M. Todorovic, and S. Schultz, "Fabrication and characterization of high aspect ratio perpendicular patterned information storage media in an $\text{Al}_2\text{O}_3/\text{GaAs}$ substrate", *J. Appl. Phys.*, vol. 85 (8/2B), pp. 5489-5491, 15 Apr. 1999.
- [Yang 1998] G. M. Yang, D. H. Lim, J. H. Kim, K. Y. Lim, H. J. Lee, "Selective oxidation of AlGaAs/GaAs structure and its application to vertical-cavity lasers", *Jpn. J. Appl. Phys. Pt. 1*, vol. 37 (3B), pp. 1391-1393, March 1998.
- [Yoshikawa 1998] T. Yoshikawa, H. Saito, H. Kosaka, Y. Sugimoto, and K. Kasahara, "Self-stopping selective-oxidation process of AlAs", *Appl. Phys. Lett.*, vol. 72 (18), pp. 2310-2312, 4 May 1998.

*Correspondence: Email: osinski@chtm.unm.edu; WWW: <http://www.chtm.unm.edu>; Telephone: (505) 272 7812; Fax: (505) 272 7801

Dual wavelength response in double barrier quantum well infrared photodetector

T.Osotchan and D.H.Zhang and W.Shi

School of Electrical and Electronic Engineering, Nanyang Technological University, Singapore

ABSTRACT

Quantum well infrared photodetector (QWIP) which exhibits the dual wavelength response in region of 3-5 and 8-12 μm was demonstrated in one stack of double barrier quantum well (DBQW) structures. These dual-band photoresponses originate from intersubband absorption between bound-to-quasibound and bound-to-continuum states, respectively. The symmetric DBQW consists of two subsequence barriers on both sides of the well i.e. inner thin high barrier and outer thick low barrier. The inner barrier was designed to be thin enough to allow photocarriers in quasibound-state tunnel through and also to make the continuum-state occurs at the top of the outer barrier. Due to photoresponse from the transitions between bound-to-quasi-bound and bound-to-continuous states, the desired wavelength regions were tailored by the barrier height of both inner and outer barriers while the sensitivities of each band were designed by thickness of the inner barrier. The optimum structure was proposed by 14-band $\vec{k}\cdot\vec{p}$ Hamiltonian including six p -like conduction band states. The absorption in TE and TM mode were separately derived and illustrated in each response wavelength for the optimum structure.

Keywords: Quantum well infrared photodetector (QWIP), dual wavelength response, and quasibound state

1. INTRODUCTION

Due to mature technology of GaAs and its epitaxy, quantum well infrared photodetector (QWIP) becomes significant alternative infrared photodetector rather than small band gap materials. Compatibility of its integration with amplifier and signal processing part makes more attractive than those for not well establish material. The development from the first observed intersubband absorption to demonstrated 128x128 array AlGaAs/GaAs QWIP has been progressed in very short period of time.¹

By conventional intersubband absorption in multiple quantum well (MQW) occurs when incident photon is absorbed by either electron or hole at ground state in conduction or valence band respectively and transits to higher energy level within the same band. The response wavelength of QWIP is determined by energy difference between these two transition energy levels and the shortest response wavelength is limited by barrier height or band offset. For n-type AlGaAs/GaAs MQW system the AlGaAs barrier material has a limit range of the aluminum content for direct band gap since when aluminum mole fraction greater than 45 percent it will becomes indirect band gap with conduction band minimum at X-point. The reported short wavelength by intersubband transition of bound-to-bound or even bound-to-continuum which can provide shorter wavelength has still not been in the shorter atmospheric window.

Instead of the implement the full barrier layer of indirect band which may results in the band mixing effect, a very thin barrier of indirect gap AlAs has been employed together with the thick direct gap barrier of AlGaAs . This structure is named as a double barrier quantum well (DBQW) since there are two barrier layers on both side quantum well i.e. thick outer barrier and very thin inner barrier. The DBQW of AlGaAs/AlAs/GaAs demonstrated the intersubband absorption at response wavelength of 2-6 μm .²⁻⁵ The thin inner AlAs barrier can rise the excited level to energy higher than the outer barrier height and the wavefunction in this excited state is no longer tightly bound in well but displace to over the region and become quasi-bound state.⁶

In additional to array photodetector and short wavelength detector development, there also has been attempted to develop the infrared detector in multiple wavelength response. This allows to fully utilize spectrum regions of low loss fiber optic and atmospheric windows in particular the region of 3-5 μm and 8-12 μm . A number of researches on multicolor detector have been reported by using two stacks of different structure parameter MQW.⁷⁻⁹

In order to implement dual wavelength QWIP of the well established AlGaAs/GaAs system in two atmospheric windows including the short wavelength region, two stacks of conventional MQW and DBQW have been demonstrated by a number of researches.^{10,11} However the dual wavelength with one stack of the DBQW was previously proposed

by utilized the intersubband transition of bound-to-quasibound and the transition between the bound state and extended continuum state.¹² Since the oscillation strength of these two transitions are determined by the thickness of the inner barrier, the thickness of the inner barrier is required to optimized for comparable absorption at two atmospheric windows.

Due to including of indirect band gap material in the $Al_{0.3}Ga_{0.7}As/AlAs/GaAs$ DBQW structure the calculation methods which include the full band effect were previously employed^{6,13} to investigate the band mixing both in electronic energy level and transport mechanism. Psuedopotential method¹³ is widely used in band calculation when entire band structure is required to be included. To apply psuedopotential method to heterostructure system the combination of bulk basic plane wavefunction at different wave vector can be treaded similar to a single band wavefunction and extended transfer matrix can be utilized with proper boundary condition apply on submatrix of interact multiband wavefunctions. The wave vectors in extended wavefunction include the real and imaginary value since the wave function may propagate when the state energy is greater than the potential and wavefunction may localize and/or terminate when the state energy is less than the potential. Since the method is base on the combination of plane wave then it is easy to implement to investigate the transport mechanism. Tight binding method⁶ was used to calculate the energy band of superlattice state since the calculation is required the fully periodic system. The wavefunction of the system is derived from the tightly interaction atomic layer wavefunction in periodic of superlattice. The wavefunction of above barrier state originated naturally from the superlattice state however the use of this extended state in MQW is needed to be verified. Although the semi-empirical psuedopotential and semi-empirical tight binding method can use band parameters derived from experimental values, these methods still cannot represent the significant parameters particularly effective mass which is sensitive to determine state in heterostructure. The $\vec{k} \cdot \vec{p}$ method directly defines effective mass by coefficient of \vec{k} term then $\vec{k} \cdot \vec{p}$ method widely uses to calculate quantum well eigen energy.

The above barrier state in $\vec{k} \cdot \vec{p}$ method can be evaluate by either transmission coefficient or insert heterostructure into the large infinite well. The conventional approach for $\vec{k} \cdot \vec{p}$ method cannot be employed because the above barrier state is not really tightly bound in the region. For the transmission approach the propagate wavefunction is assumed to incidence on one side of the heterostructure region and the amplitude of the transmission wavefunction on the other side is evaluated. The above barrier resonant state energy can be derived at the peak of the transmission as a function of incident energy. While for the wide infinite well model, the resonant energy state can be calculated by the bound state of the wide well state. The well is required to be sufficient wide to be able to provide continuum-like state at the heterostructure near resonant state. In this calculation the large infinite well was utilized to calculate the above outer barrier state of $Al_{0.3}Ga_{0.7}As/AlAs/GaAs$ DBQW structure by fourteen band $\vec{k} \cdot \vec{p}$ method. The optical matrix element was evaluated to demonstrate strength of two intersubband transitions for dual wavelength QWIP application.

2. CALCULATION DETAILS

Details of the calculating implementation of fourteen-band $\vec{k} \cdot \vec{p}$ model for large infinite quantum well states will be briefly reviewed and apply to $Al_{0.3}Ga_{0.7}As/AlAs/GaAs$ DBQW structures. In order to obtain more realistic electron curvature the seven bands were extended in the usual eight-band $\vec{k} \cdot \vec{p}$ model. The model for bulk lattice will firstly be mentioned and the extended envelop function will be derived for heterostructure. The particular solution in large infinite well will be given by expanding basic wavefunction into the harmonic of sinusindol function. The optical matrix for TE and TM absorption will also be given for any initial and final states.

2.1. Fourteen band $\vec{k} \cdot \vec{p}$ model

For an independence particle moving in a periodic potential $V(\vec{r})$ of bulk lattice, the bulk wavefunction can be written in term of Bloch function as

$$\psi_{n\vec{k}} = e^{i\vec{k} \cdot \vec{r}} u_{n\vec{k}}, \quad (1)$$

where $u_{n\vec{k}}$ is bulk Bloch function which has the periodicity of $V(\vec{r})$, and $\psi_{n\vec{k}}$ is the wavefunction of independence particle at band index n and wave vector \vec{k} . Here \vec{k} lies in the first Brillouin zone and the band index runs over a complete set of the bands. Substituting this wavefunction into one-particle Schrodinger equation with periodic bulk crystal potential $V(\vec{r})$ gives

$$\left[\frac{p^2}{2m} + \frac{\hbar}{m} \vec{k} \cdot \vec{p} + \frac{\hbar^2 k^2}{2m} + V(\vec{r}) \right] u_{n\vec{k}} = E_n(\vec{k}) u_{n\vec{k}}. \quad (2)$$

Here $E_n(\vec{k})$ is energy of particle at band index n and wave vector \vec{k} and $\vec{p} = -i\hbar\vec{\nabla}$. Expanding the finite \vec{k} Bloch wavefunction into the complete set of the Bloch function at $\vec{k} = \vec{k}_0$,

$$u_{n\vec{k}} = \sum_{n'} c_{nn'}(\vec{k}) u_{n'\vec{k}_0}. \quad (3)$$

By substituting this expanded Bloch function into the Schrodinger equation (Eq.(2)), permultiplying by $u_{m\vec{k}_0}$, integrating over unit cell and using orthonormality of the band edge Bloch functions, we can convert to a matrix eigen value equation

$$\sum_{n'} [(E_{n'}(\vec{k}_0) + \frac{\hbar^2(k^2 - k_0^2)}{2m})\delta_{mn'} + \hbar(\vec{k} - \vec{k}_0) \cdot \vec{P}_{mn'}] c_{nn'} - E_n(\vec{k}) c_{nn} = 0, \quad (4)$$

where

$$\vec{P}_{mn'} = \langle u_{m\vec{k}_0} | \frac{\vec{p}}{m} | u_{n'\vec{k}_0} \rangle. \quad (5)$$

The above equation is written eigen energy for point \vec{k} in term of value at point \vec{k}_0 . Although the equation is correct for any \vec{k} , it is usually treated the non-diagonal part of the Hamiltonian $\hbar(\vec{k} - \vec{k}_0) \cdot \vec{P}_{mn'}$ as a perturbation and utilized only when \vec{k} is near \vec{k}_0 . For our case only the band near conduction band minimum $\vec{k}_0 = 0$ or near Γ point was taken into consideration and the effects from the X and L point were neglected here as mentioned in previously calculation on their effects.¹²

The \vec{k}, \vec{p} model of eight bands including the double degeneracy of heavy hole (hh), light hole (lh), hole split off (so-h), and conduction electron (c) states has been extended by fourteen bands with additional double degeneracy bands of heavy-like electron (he), light-like electron (le) and electron split off (so-e) states. The wavefunction of conduction electron (u_c) can directly refer to conduction antibonding \bar{S} state while wavefunction of hh, lh, and so-h are written in combination of the valence bonding p states including X^v , Y^v , and Z^v . The six extended states of he, le and so-e are derived from conduction antibonding \bar{p} composing of X^c , Y^c and Z^c . These wavefunctions can be written in combination of the atomic wavefunction as relation below

$$u_{le} = \sqrt{\frac{1}{6}}(X^c + iY^c) \downarrow - \sqrt{\frac{2}{3}}Z^c \uparrow, \quad (6)$$

$$u_{he} = \sqrt{\frac{1}{2}}(X^c + iY^c) \uparrow, \quad (7)$$

$$u_{so-e} = \sqrt{\frac{1}{3}}(X^c + iY^c) \downarrow + \sqrt{\frac{1}{3}}Z^c \uparrow, \quad (8)$$

$$u_{lh} = \sqrt{\frac{1}{6}}(X^v + iY^v) \downarrow - \sqrt{\frac{2}{3}}Z^v \uparrow, \quad (9)$$

$$u_{hh} = \sqrt{\frac{1}{2}}(X^v + iY^v) \uparrow, \quad (10)$$

$$u_{so-h} = \sqrt{\frac{1}{3}}(X^v + iY^v) \downarrow + \sqrt{\frac{1}{3}}Z^v \uparrow, \quad (11)$$

$$u_c = iS \uparrow, \quad (12)$$

$$u_{\bar{le}} = \sqrt{\frac{1}{6}}(X^c - iY^c) \uparrow + \sqrt{\frac{2}{3}}Z^c \downarrow, \quad (13)$$

$$u_{\bar{he}} = -\sqrt{\frac{1}{2}}(X^c - iY^c) \downarrow, \quad (14)$$

$$u_{\bar{so-e}} = \sqrt{\frac{1}{3}}(X^c - iY^c) \uparrow - \sqrt{\frac{1}{3}}Z^c \downarrow, \quad (15)$$

$$u_{\bar{lh}} = \sqrt{\frac{1}{6}}(X^v - iY^v) \uparrow + \sqrt{\frac{2}{3}}Z^v \downarrow, \quad (16)$$

$$u_{\bar{hh}} = -\sqrt{\frac{1}{2}}(X^v - iY^v) \downarrow, \quad (17)$$

$$u_{so-h} = \sqrt{\frac{1}{3}}(X^v - iY^v) \uparrow - \sqrt{\frac{1}{3}}Z^v \downarrow, \quad (18)$$

$$u_{\bar{c}} = iS \downarrow. \quad (19)$$

The non-zero momentum matrix for tetrahedral symmetry are

$$P_0 = -\frac{i}{m} \langle S | p_x | X^v \rangle, \quad (20)$$

$$P_1 = -\frac{i}{m} \langle S | p_x | X^c \rangle, \quad (21)$$

$$Q = -\frac{i}{m} \langle X^v | p_y | Z^c \rangle. \quad (22)$$

According to semiempirical procedure, the momentum matrix parameters were derived from the experiment bulk values of the band gap energy, spin orbit splitting energy and effective mass.¹⁴ The momentum matrix Q is derived by effective mass of heavy hole while the momentum matrix of P_0 and P_1 were derived by effective mass of electron. The ratio of P_0 and P_1 was determined by the curvature of conduction band at high energy.

2.2. Heterostructure states

In applying the $\vec{k} \cdot \vec{p}$ model to a heterostructure system, basic wavefunctions of well and barrier layers are slowing change wavefunction along the growth direction (z) and assumed to be equal. Therefore the wave function of the heterostructure can be written as

$$\psi_{n\vec{k}_0}(\vec{r}) = e^{i\vec{k}_{\parallel} \cdot \vec{\rho}} \sum_{j=1}^{14} F_j(z) u_{j\vec{k}_0}(\vec{r}). \quad (23)$$

where $F_j(z)$ is an envelop function. The \vec{k}_{\parallel} and $\vec{\rho}$ are respectively wave vector and space vector parallel to the interface.

Since the envelop function depends only on the z direction and here only $\vec{k}_x = \vec{k}_y = 0$ is consider, the bulk Hamiltonian eigen value matrix in Eq. (4) can be written in the zero determinant

$$|H_{\pm}(k_z) - E_n I| = 0. \quad (24)$$

Here I is 7×7 identity matrix and H_+ and H_- are the 7×7 decoupling bulk Hamiltonians at $\vec{k}_x = \vec{k}_y = 0$ of wavefunction $\{u_{le}, u_{he}, u_{so-e}, u_{lh}, u_{hh}, u_{so-h}, u_c\}$ and $\{u_{\bar{l}e}, u_{\bar{h}e}, u_{\bar{so}-e}, u_{\bar{l}h}, u_{\bar{h}h}, u_{\bar{so}-h}, u_{\bar{c}}\}$, respectively.

By unitary similarity transformation the corresponding Hamiltonian of H_+ and H_- can be related by

$$H_- = U H_+ U^\dagger, \quad (25)$$

where

$$U = \begin{pmatrix} -1 & 0 & 0 & 0 & 0 & 0 & 0 \\ 0 & -1 & 0 & 0 & 0 & 0 & 0 \\ 0 & 0 & -1 & 0 & 0 & 0 & 0 \\ 0 & 0 & 0 & -1 & 0 & 0 & 0 \\ 0 & 0 & 0 & 0 & -1 & 0 & 0 \\ 0 & 0 & 0 & 0 & 0 & -1 & 0 \\ 0 & 0 & 0 & 0 & 0 & 0 & 1 \end{pmatrix}. \quad (26)$$

For heterostructure the Hamiltonian matrix in Eq. (4) has to be modified by substitute the vector k_z by operator $\hat{k}_z = -i \frac{d}{dz}$ and add the heterostructure potential on the diagonal elements. The heterostructure potential ($V_n(z)$) in flat band condition is defined by the band discontinuity of band index n . Therefore the two eigen value matrices of heterostructure are converted to

$$[H_{\pm}(-i \frac{d}{dz}) + V_n(z)] F_n^{\pm} = E_n^{\pm} F_n^{\pm}. \quad (27)$$

The envelop wavefunctions are defined by

$$F_n^+ = \{f_{le}, f_{he}, f_{so-e}, f_{lh}, f_{hh}, f_{so-h}, f_c\}, \quad (28)$$

and

$$F_n^- = \{f_{le}, f_{he}, f_{so-e}, f_{lh}, f_{hh}, f_{so-h}, f_e\}. \quad (29)$$

For heterostructure in wide infinite well the solution is valid only the wide of large well (L) is much wider than the concerned quantum well structure width (L_w) so that there is sufficient energy levels to represent the discrete level in the investigate structure. With infinite well the fixed boundary condition of wavefunction at the both end indicates the zero value of wavefunction at both end i.e. $f_n(0) = f_n(L) = 0$. Therefore in expanding the envelope function into sinusoidal function only sine term is valid and can be written as¹⁵

$$F_j(z) = \sum_{n=1}^N C_n^j \phi_n(z) = \sum_{n=1}^N C_n^j \sqrt{\frac{2}{L}} \sin\left(\frac{n\pi z}{L}\right), \quad (30)$$

where the infinite basis function has been truncated at N terms which should be large enough to ensure convergence. Substituting this wavefunction into the Eq. (27), premultiplying by $\sqrt{2/L} \sin(m\pi z/L)$ and integrating from 0 to L , gives the eigen equation

$$\sum_{jn} [H_{(im)(jn)} - E \delta_{(im)(jn)}] C_n^j = 0, \quad (31)$$

with $7N \times 7N$ Hamiltonian matrix

$$H_{(im)(jn)} = \frac{2}{L} \int_0^L \sin\left(\frac{m\pi z}{L}\right) H_{ij} \sin\left(\frac{n\pi z}{L}\right) dz. \quad (32)$$

Since the heterostructure wavefunction strongly depends on the boundary condition at the hetero-interfaces and no matching boundary condition is required in this entire expanded sinusoidal wavefunction, the interface terms including in the construction of Hamiltonian matrix has to be treated properly. The hermitian contains an effective-mass-like parameter $\gamma(z)$ which depends on position. The $\gamma(z)$ parameter is constant over the layer and abrupt change at the interface because it is defined by bulk material parameters including momentum coupling constants and band edge energies. The contribution of hetero-interface on the hamitian can be written into the form $\langle m | \hat{p}_z \gamma(z) \hat{p}_z | n \rangle$ which can be expressed by

$$\langle m | \hat{p}_z \gamma(z) \hat{p}_z | n \rangle = \langle m | -\hbar^2 \frac{d}{dz} \gamma(z) \frac{d}{dz} | n \rangle, \quad (33)$$

$$= -\hbar^2 \left[\sum_{L_i, L_{i+1}} \gamma_{L_i, L_{i+1}} \int_{L_i}^{L_{i+1}} \phi_m \frac{d^2}{dz^2} \phi_n dz + \sum_{L_i} (\gamma_{L_i, L_{i+1}} - \gamma_{L_{i-1}, L_i}) \phi_m(L_i) \frac{d}{dz} \phi_n(L_i) \right]. \quad (34)$$

The $\sum_{L_i, L_{i+1}}$ is summation of layer at distance L_i to L_{i+1} and summed over the entire wide well region $[0, L]$ while the \sum_{L_i} is summation of hetero-interface over the entire region. The interface contribution in the second summation term is not zero only if the difference of $\gamma(z)$, wavefunction and its first derivative are not zero.

In calculation the number of expansion term of 50 ($N = 50$ and given a 350×350 Hamiltonian matrix) is normally employed to achieve the reasonable accuracy of resulted wavefunction. By reducing the uncoupling states of 7×7 Hamiltonian matrix into the 3×3 matrix of $\{u_{he}, u_c, u_{hh}\}$, the size of the matrix required to be diagonalized can be reduced to 150×150 . However this reduced hermitian also depends on the energy therefore the value of eigen energy is needed to iterative to obtain the consistence result. The iteration with reduced Hamiltonian matrix may consume the computational time as long as that for diagonalise the large matrix.

2.3. TE and TM optical matrix element

In dipole approximation the optical matrix element which determines intersubband transition strength between subband m and n is written by

$$\langle \psi_m | \frac{\hat{\epsilon} \cdot \hat{P}}{m} | \psi_n \rangle = \sum_i \sum_j \langle F_{im} | F_{jn} \rangle \langle u_i | \frac{\hat{\epsilon} \cdot \hat{P}}{m} | u_j \rangle + \hat{z} \sum_j \langle F_{jm} | \frac{\hat{\epsilon}_z \cdot \hat{p}_z}{m} | F_{jm} \rangle, \quad (35)$$

where $\hat{\epsilon}$ is the photon polarization vector and z is growth direction. The slowly varying envelop function can be taken as a factor when integrated with the rapidly varying Bloch functions. By the Eq. (2) the momentum matrix can be written by the first derivative of Hamiltonian matrix respective to the wave vector

$$P_{ij} = \frac{1}{\hbar} \frac{\partial H}{\partial \vec{k}}. \quad (36)$$

By the above relations as well as the orthonormality of envelop function, the optical matrix can be written as

$$\langle \psi_m | \frac{\hat{\epsilon} \cdot \vec{p}}{m} | \psi_n \rangle = \int F_m^\dagger (\hat{\epsilon} \cdot \frac{1}{\hbar} \frac{\partial H}{\partial \vec{k}}) F_n dz. \quad (37)$$

The optical matrix was evaluated by including the fourteen components of envelop function and the full fourteen-band bulk $\vec{k} \cdot \vec{p}$ Hamiltonian. However the envelop function and Hamiltonian can be considered separately into two sets of seven band.

For TE absorption at $\vec{k}_{||} = 0$ the 14×14 hermitian matrix can be written into the 7×7 submatrix as

$$\frac{1}{\hbar} \frac{\partial H}{\partial k_x} = \begin{pmatrix} 0 & M_x \\ M_x^T & 0 \end{pmatrix}, \quad (38)$$

where 0 is a 7×7 zero matrix. Therefore for TE absorption the optical matrix element between states m and n can be separately expressed by

$$\langle \psi_m^+ | \frac{p_x}{m} | \psi_n^+ \rangle = 0, \quad (39)$$

$$\langle \psi_m^- | \frac{p_x}{m} | \psi_n^- \rangle = 0, \quad (40)$$

$$\langle \psi_m^+ | \frac{p_x}{m} | \psi_n^- \rangle = \int f_m^+ M_x f_n^- dz, \quad (41)$$

$$\langle \psi_m^- | \frac{p_x}{m} | \psi_n^+ \rangle = \int f_m^- M_x^T f_n^+ dz, \quad (42)$$

where the ψ_m^+ and f_m^+ are first seven wavefunctions and ψ_m^- and f_m^- are their correspond wavefunctions at opposite spin states.

To evaluate TM absorption at $\vec{k}_{||} = 0$ the Hamiltonian derivative can be defined by the 7×7 submatrix as

$$\frac{1}{\hbar} \frac{\partial H}{\partial k_z} = \begin{pmatrix} M_z^+ & 0 \\ 0 & M_z^- \end{pmatrix}, \quad (43)$$

where both diagonal submatrices can be related by unitary transform as $M_z^- = U M_z^+ U^\dagger$. Thus the TE matrix elements can be written separately by

$$\langle \psi_m^+ | \frac{p_z}{m} | \psi_n^+ \rangle = \int f_m^+ M_z^+ f_n^+ dz, \quad (44)$$

$$\langle \psi_m^- | \frac{p_z}{m} | \psi_n^- \rangle = \int f_m^- M_z^- f_n^- dz, \quad (45)$$

$$\langle \psi_m^+ | \frac{p_z}{m} | \psi_n^- \rangle = 0, \quad (46)$$

$$\langle \psi_m^- | \frac{p_z}{m} | \psi_n^+ \rangle = 0. \quad (47)$$

3. RESULTS AND DISCUSSION

The electron energy levels and the optical matrix elements of the (100) $Al_{0.3}Ga_{0.7}As/AlAs/GaAs$ DBQW structures were systematically evaluated by varying the structure dimensions including well width and barrier thickness. The response wavelength of the structure corresponds to the energy difference between the initial and final states. While here two types of final state will be consider in two types, continuum state above the outer barrier and quasi bound

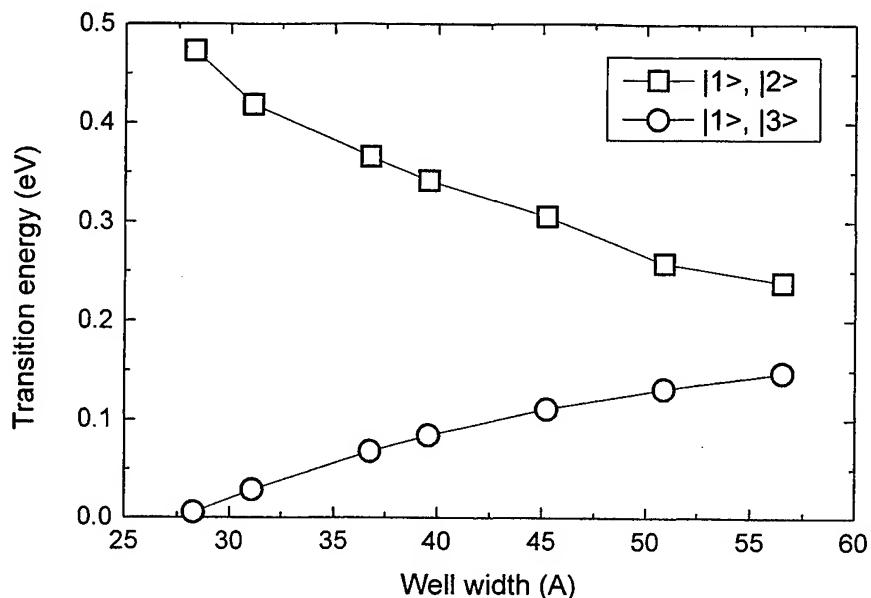


Figure 1. Transition energy as a function of well width for $Al_{0.3}Ga_{0.7}As/AlAs/GaAs$ DBQW structures with four monolayers of inner $AlAs$ barrier. Square and circle respectively represent the transition from bound ground state to excited quasi-bound and continuum states.

state occur between two thin inner barrier layers. The relative strength of absorption can be indicated by optical matrix elements which was determined both for TM and TE absorption.

The typical $Al_{0.3}Ga_{0.7}As/AlAs/GaAs$ DBQW structures consists of outer barrier of $Al_{0.3}Ga_{0.7}As$ layer with the fixed thickness of 300\AA , ultra-thin layer of $AlAs$ inner barrier with thickness varied from one to nine monolayers and the typical value of four monolayers was used with typical $GaAs$ well thickness of 45\AA . The discrete thickness is employed when the thickness of layer in quantum well structure becomes comparable to the distance between monoatomic layer. In calculation the single quantum well of $Al_{0.3}Ga_{0.7}As/AlAs/GaAs$ DBQW was used with the total length of about 650\AA since the thick outer barrier is required for the QWIP structure to achieve low dark current and it is also required for calculating the continuum and quasi-bound states in the wide infinite well approach. When the calculation involves hetero-structure with small thickness relative to the entire large well, more harmonic terms in sinusoidal expansion is necessary to implement to be able to represent fast changing in the narrow region.

The composition of alloy in three layers were maintained at the values of 0.3 aluminum mole fraction in outer barrier and using pure binary compounds of $AlAs$ and $GaAs$ for inner barrier and well layer due to the constrain during the growth for different alloy composition in case of limited number of the element source. With only one layer of ternary compound would be possible to growth with all single aluminum and gallium source without interrupting for source temperature difference requirement. The aluminum mole fraction of 0.3 was selected to obtained $AlGaAs$ material with direct band gap.

Material parameters used in the calculation were obtained from M.Levinshtein et.al..¹⁶ The most significant material parameters to determine the heterostructure states are band offset and effective mass. The valence band discontinuity of $0.46x$ where x is the aluminum mole fraction is used to determine the band offset for the entire range from $GaAs$ ($x=0$) to $AlAs$ ($x=1$). The conduction band discontinuity of $AlGaAs$ is not well defined since the conduction band minimum in $AlGaAs$ changes from the Γ point to X point when the aluminum content increase

to 45 percent. Therefore the conduction band offset was derived indirectly with the band gap relation of $1.424 + 1.155x + 0.37x^2$. The experimental value of effective mass was used in semi-empirical procedure to determine the interaction matrix element while an addition parameter from the fourteen band configuration was used to fit effective mass at high energy which is significant in this calculated since the energy levels of both continuum and quasi-bound states lie at relatively high energy. It has been pointed out that the use of the fourteen band $\vec{k} \cdot \vec{p}$ is required for energies about 50 meV above the conduction band edge of the bulk *GaAs*.¹⁷

The energy levels of the *Al_{0.3}Ga_{0.7}As/AlAs/GaAs* DBQW structures with four monolayers of inner *AlAs* barrier were calculated as a function of well width and the transition energy corresponding to the state energy difference are shown in Fig. 1. From the calculation there is one bound state below the thick outer barrier and its energy increases as the well decreases. If the well width extended decreases beyond the displayed range there will be no bound state below the low outer barrier. The first excited state is a quasi-bound state occurring between the inner thin barrier with energy higher than the outer barrier. Therefore electron in the first excited state is tightly bounded in the well and the calculated wavefunction showed spread part through thin inner barrier to the outer barrier. Since the electron potential barrier originating from band offset of the direct band gap of *AlAs* is very high, this excited quasi-bound state can be tailored at very high energy so that the response wavelength from the transition between the bound ground state and this excited states can be in the short wavelength of atmospheric window. The transition energy between these states ($|1 \rangle, |2 \rangle$) are shown in Fig. 1 with square symbol. From the figure the transition energy also increases as well width decreases therefore the excited state energy level is risen much more than the ground state and the response wavelength correspond to this transition enrage range is in the range of 2.5 to $5\mu\text{m}$.

In addition to the quasi-bound excited state there also the other excited state above the outer barrier and its calculated wavefunction spread through the thin inner barrier to the well region. Since the outer barrier is very thick compare to the other layer and remained at constant thickness, this continuum excited state level almost has a constant energy. However the transition energy between the ground and this excited state ($|1 \rangle, |3 \rangle$), represented by circle in Fig. 1, is decrease as well width decreases. This is due to the risen of ground bounded energy level and the ground bounded level become close to the outer barrier height at the narrow well width range showed in Fig. 1. At the typical well width this transition energy is equal to the response wavelength in the 8 to $12\mu\text{m}$. It should be reminded that these designed response wavelengths are satisfied for the QWIP structure which can be used in dual wavelength region of atmospheric window.

The optical matrix elements of the *Al_{0.3}Ga_{0.7}As/AlAs/GaAs* DBQW structures were also calculated as a function of the well width and for both transition in both for TM and TE photon absorption. Figure 2a showed the calculated optical matrix element in term of momentum matrix element with normalized by the electron mass in TM and TE absorption represented by square and circle, respectively. The optical matrix element of transition between ground bounded and excited quasi-bound states is higher than that for transition between ground bounded and excited continuous states, represented respectively by open and solid symbols in Fig. 2. For n-type conduction QWIP, the TM absorption is very much stronger than the TE absorption in which the intersubband occurs only if there is some component of incidence light parallel to the interface. Even the TE absorption cannot evaluated by single band calculation but it can be conducted in the multiband calculation when the interaction between band allowed. The optical matrix element of TE absorption for continuum and quasi-bound state transitions in Fig. 2 are about two orders less than that for TM absorption. As the well width varied, the optical matrix elements are slightly modified at narrow well width due to the risen of bounded state level. The absorption from the continuum state transition is weaker than that for quasi-bound state since only small part of wavefunction in continuum state spreads through the well region.

In order to demonstrate the transition strength of continuum state the thickness of inner barrier was varied to examine distribution of excited continuum state wavefunction through the well region. Figure 2b showed the optical momentum matrix element as a function of inner barrier thickness from one to nine monolayers. When inner barrier thickness reduced the absorption strength of the continuum state transition becomes stronger while absorption from the quasi-bound state transition becomes weaker. This is due to the wavefunction of continuum states in outer barrier can spread through thinner inner barrier to the well region more thus it exhibits stronger transition. While the wavefunction of quasi-bound state in well region also spreads out of the well region then the absorption from the transition between the ground state located in well to this state becomes weak. The variation of optical matrix elements are consistence both for TM and TE absorption as their curves are parallel shift.

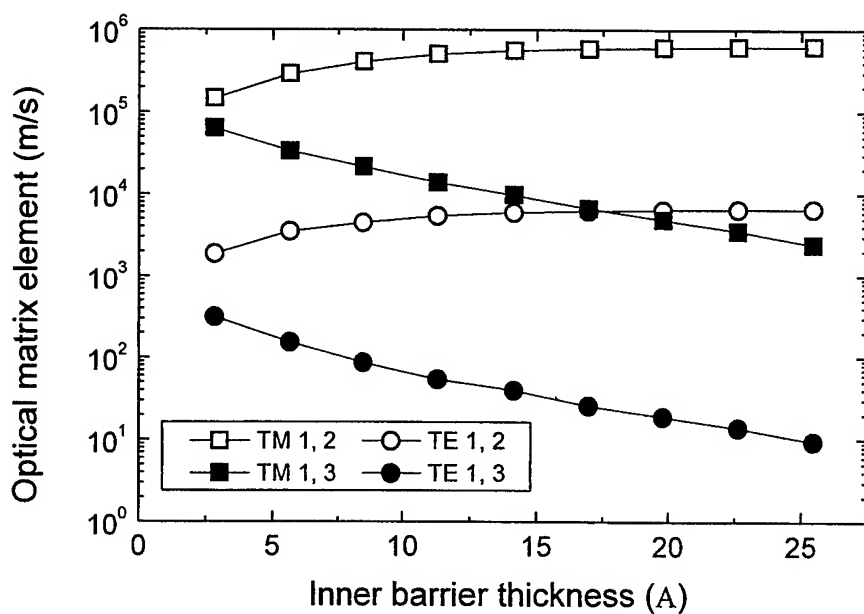
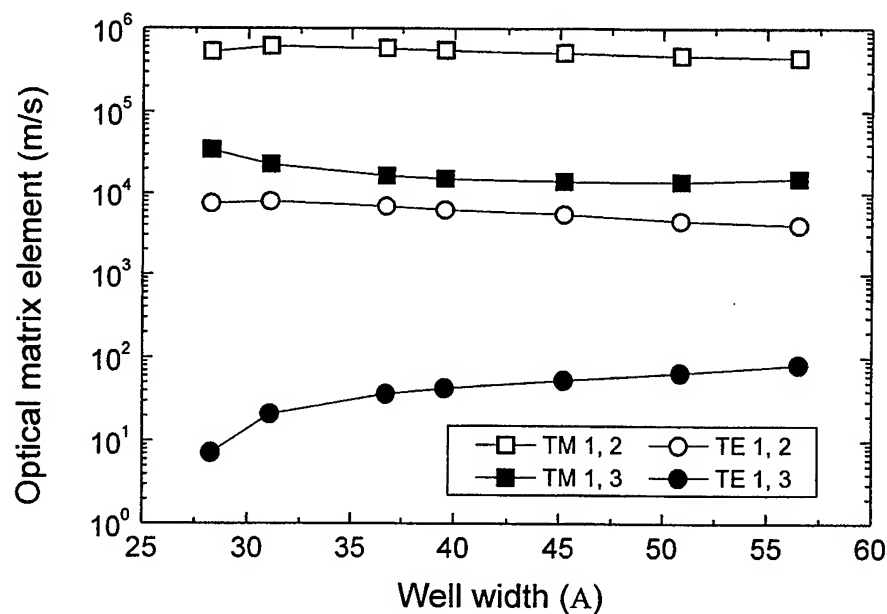


Figure 2. Optical matrix element as a function of a) well width with four monolayers of inner *AlAs* barrier and b) as a function of inner *AlAs* barrier thickness with 45 Å thick *GaAs* well for $Al_{0.3}Ga_{0.7}As/AlAs/GaAs$ DBQW structures. Open and solid symbols respectively represent the transition from bound ground state to excited quasi-bound and continuum states while square and circle represent TM and TE absorption, respectively.

4. CONCLUSION

The fourteen band $\vec{k}\cdot\vec{p}$ model was utilized to evaluate the absorption in (100) $Al_{0.3}Ga_{0.7}As/AlAs/GaAs$ DBQW structures by calculating transition energy and optical matrix element of the QWIP varied the structure dimension. With the fourteen band model allowing calculation at high energy the transition between bound ground state and two excited high energy levels of continuum and quasi-bound states can be calculated both for TM and TE absorption. The two response wavelengths for the transitions from ground bound to excited continuum and quasi-bound states can be tuned with in two atmospheric window by tailor the dimension structure while the modified strength of the absorption in each transition was demonstrated by varying the thickness of the inner barrier.

REFERENCES

1. B.F.Levine, "Quantum-well infrared photodetectors," *J. Appl. Phys.* **74**, pp. R1-R81, 1993.
2. E.C.Larkins, H.Schneider, S.Ehret, J.Fleibner, B.Dishler, P.Koidl, and J.D.Ralston, "Influences of MBE growth processes on photovoltaic 3-5 μm intersubband photodetectors," *IEEE Trans. Electron Dev.* **41**, pp. 511-518, 1994.
3. J.-J.Shi and E.M.Goldys, "Intersubband optical absorption in strained double barrier quantum well infrared photodetectors," *IEEE Trans. Electron Dev.* **46**, pp. 83-88, 1999.
4. T.Osotchan, V.W.L.Chin, T.L.Tansley, B.F.Usher, A.Clark, and R.J.Egan, "MBE and MOCVD growth of AlGaAs-AlAs-GaAs double barrier multiple quantum well infrared detector," *Materials Science Engineering B* **35**, pp. 176-179, 1995.
5. H.C.Liu, M.Buchanan, and Z.R.Wasilewski, "Short wavelength (1-4 μm) infrared detectors using intersubband transitions in GaAs-based quantum wells," *J. Appl. Phys.* **83**, pp. 6178-6181, 1998.
6. T.Osotchan, V.W.L.Chin, M.R.Vaughan, T.L.Tansley, and E.M.Goldys, "Electronic band structure of $Al_xGa_{1-x}As/Al_yGa_{1-y}As/GaAs$ double-barrier superlattices," *Phys. Rev. B* **50**, pp. 2409-2419, 1994-II.
7. J.C.Chiang, S.S.Li, and A.Singh, "A two-stack indirect-barrier/triple-coupled quantum well infrared detector for mid-wavelength and long-wavelength infrared dual band detection," *Appl. Phys. Lett.* **71**, pp. 3546-3548, 1997.
8. T.Mei, G.Karunasiri, and S.J.Chua, "Two-color infrared detection using intersubband transitions in multiple step quantum wells with superlattice barriers," *Appl. Phys. Lett.* **71**, pp. 2017-2019, 1997.
9. M.Z.Tidrow, K.K.Choi, A.J.DeAnni, W.H.Chang, and S.P.Svensson, "Grating coupled multicolor quantum well infrared photodetectors," *Appl. Phys. Lett.* **67**, pp. 1800-1802, 1995.
10. Y.Zhang, D.S.Jiang, J.B.Xia, L.Q.Cui, C.Y.Song, Z.Q.Zhou, and W.K.Ge, "A voltage-controlled tunable two-color infrared photodetector using GaAs/AlAs/GaAlAs and GaAs/GaAlAs stacked multiquantum wells," *Appl. Phys. Lett.* **68**, pp. 2114-2116, 1996.
11. Y.H.Wang, J.-C. ad S.S.Li, and P.Ho, "A GaAs/AlAs/AlGaAs and GaAs/AlGaAs stacked quantum well infrared photodetector for 3-5 and 8-14 μm detection," *J. Appl. Phys.* **76**, pp. 2538-2540, 1994.
12. T.Osotchan, V.W.L.Chin, and T.L.Tansley, "Transition in (001) AlGaAs/AlAs/GaAs double-barrier quantum structure for infrared photodetection," *J. Appl. Phys.* **80**, pp. 5342-5347, 1996.
13. T.Osotchan, V.W.L.Chin, and T.L.Tansley, "Transport mechanism of Γ - and X-band electrons in $Al_xGa_{1-x}As/AlAs/GaAs$ double-barrier quantum-well infrared photodetectors," *Phys. Rev. B* **54**, pp. 2059-2066, 1996-I.
14. M.E.Flatte, P.M.Young, L.-H.Peng, and H.Ehrenreich, "Generalized superlattice K.p theory and intersubband optical transitions," *Phys. Rev. B* **53**, pp. 1963-1978, 1996-II.
15. W.Batty and K.A.Shore, "Normal-incidence TE intersub-band transitions," *IEE Proc.-Optoelectron.* **145**, pp. 21-30, 1998.
16. M.Levinshtein, S.Rumyantsev, and M.Shur, *Handbook series on semiconductor parameters volume 2: ternary and quaternary A_3B_5 semiconductors*, World Scientific, Singapore, 1999.
17. L.H.Peng and C.G.Fonstad, "Multiband coupling effects on electron quantum well intersubband transitions," *J. Appl. Phys.* **77**, pp. 747-754, 1995.

Novel method for stabilization in harmonically mode-locked erbium-doped fiber laser with external optical modulation by laser diode

Van Hoi Pham^a, Duc Thinh Vu^a, Quoc Viet Tran^c,
Chun-Ju Yuon^b, Yun-Chun Chung^b

^a Institute of Materials Science, NCST of Vietnam
Hoang Quoc Viet Road, Cau giay Dist. Hanoi Vietnam

^b Department of Electrical Engineering, KAIST.
373-1 Kusong-dong, Yusong-gu, Taejon 305-701, Korea

^c Vietnam Post & Telecommunication Incorp.
18 Nguyen Du str. Hanoi Vietnam

ABSTRACT

A novel method to suppress noise in a high harmonically mode-locked erbium fiber laser with external optical modulator using DFB - laser diodes is presented. The DFB-diode laser played both roles as external-cavity modulator and as stabilizer. The driving frequency is of 2.5 GHz and the wavelength difference between DFB- diode laser emission and fiber laser dominant was adjusted in range of ± 2 nm. The fiber laser modulation frequencies can be tunable at 2.5; 5 and 10 GHz by the adjusting an external laser diode modulation rounding 2.5 GHz ± 66 KHz. A fiber laser so stabilized has enabled at 2.5 or 5 GHz remaining error free for more 4 hours with nearly transform-limited pulse width of 25-35 ps.

Key words: Erbium - doped Optical Fibers, Active-Modulated Er-doped Fiber ring laser, External fiber cavity modulation.

I. INTRODUCTION

Harmonically mode-locked fiber lasers are important light sources, because they can generate transform-limited pulses with large wavelength tunability and high - repetition rate suitable for many applications, such as high-speed optical switching, optical communications and wavelength-division-multiplexing. Passively mode-locked Erbium fiber lasers using NOLM or NALM can generate femtosecond pulses at Megahertz repetition rate [1]-[3]. Actively mode-locked, especially harmonically mode-locked, Erbium fiber ring lasers are suitable for producing transform-limited light pulses with adjustable multi-Gigahertz rate and variable pulse widths in picosecond range [4]-[5]. Fiber ring lasers have been actively mode-locked using a Mach-Zehnder modulator, a semiconductor multi-quantum-well (MQW) electro-absorption modulator, or a MQW semiconductor phase modulator. Meanwhile, wavelength tuning is achieved using a separate Fabry- Perot tunable etalon or a tunable fiber Bragg grating [6]. Typically, fiber ring lasers are sensitive to small environmental perturbations, such as thermal fluctuations and acoustic vibrations that affect the fiber cavity length. As a result, these lasers do not exhibit long-term stability without active stabilization. Several stabilization techniques have been reported [7]-[10]. One technique requires an active control of overall cavity length either by using a piezoelectric transducer or by fiber heating, another technique utilizes the nonlinear polarization rotation effect to suppress pulse-to-pulse intensity fluctuations. In this paper, we present the characteristics of harmonically mode-locked Er-doped fiber ring laser stabilized by external-cavity DFB-diode laser. The DFB-diode laser operated as active semiconductor modulator and the stabilization based on small carrier-

induced change in the refractive index. This fiber ring laser stabilized more 4 hours with repetition rates of 2.5 or 5 GHz and output pulse width of 25 - 35 ps.

II. EXPERIMENT AND RESULTS

Fig. 1 shows the schematic of the Erbium fiber ring laser. The total cavity length is 16.6 m, which corresponds to fundamental laser cavity frequency about 12 MHz. The standard single-mode fiber of 9 / 125 micron was used for majority of the laser cavity. A 12 - m long erbium-doped fiber was used as an active medium, which was pumped by a 980-nm diode laser, supplied a maximum pump power of 120 mW. A 1550-nm commercial DFB - diode laser (LD) was used as external modulator and stabilizer. The LD was biased around threshold and it was modulated by a RF signal of frequency range of 2.4-2.5 GHz. The threshold of the LD at 25⁰ C was of 17 mA. The bandpass filter is a wavelength tuning element and had been adjusted rounding laser diode emission wavelength in the range of +/- 2 nm. By adjusting the driving frequency to match the laser roundtrip frequency or one of

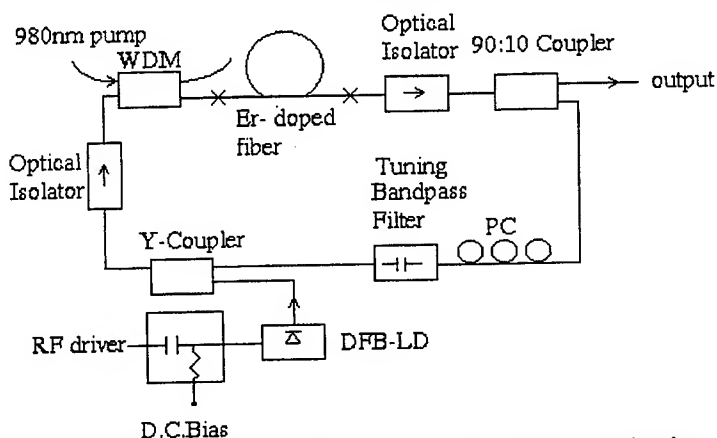


Fig.1. Experimental setup of the fiber ring mode-locked laser using the external optical modulation by DFB diode laser

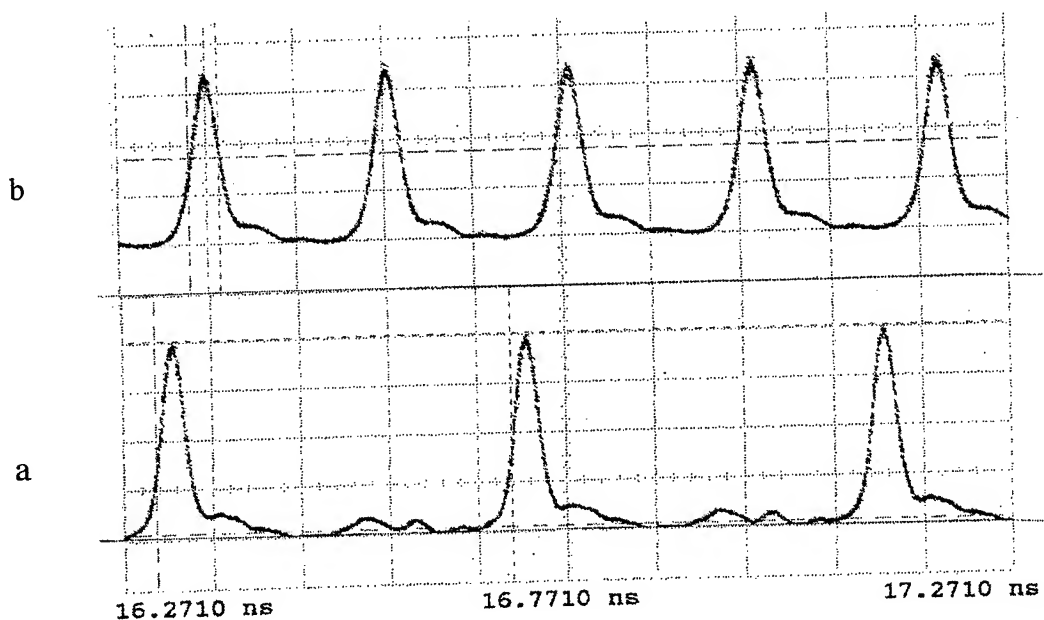


Fig.2: The pulse waveforms of mode-locked output at modulation frequency f_m of 2.48632 GHz (a) and of 2.41983 GHz (b). The repetition rates of signal output are equal or twice f_m .

its multiple, the fundamental or harmonic mode-locking was readily demonstrated. Fig.2 shows a mode-locked output pulse waveform, when the modulator was driven at 2.48632 GHz (2a) and 2.41983 GHz (2b). The LD semiconductor modulator was DC biased at 16.5 mA and the RF driving current was of ± 5 mA. The average output power was +5.2 dBm with a 980-nm pump power of 70 mW. As shown in Fig. 2a, a stable pulse train at a repetition rate as the same of the RF driving frequency (2.48632 GHz) and in Fig. 2b a repetition rate (4.840 GHz) twice that of the modulation frequency were achieved. In fact, the observation of output pulse repetition equal or twice the modulation frequency on the LD indirectly confirmed that the LD played the role of an intensity modulator and gain medium [11]. In case of gain medium, the repetition rate had to be equal to driving frequency. In our experiment, only small part of the fiber laser beam can be trip into DFB laser diode by the reflection, then we distinguished this effect as small gain medium. Furthermore, in the case of intensity modulation, when the driving frequency was detuned by a value of $\pm f_0 / n$ (n is positive integer) from one of the harmonics of the cavity fundamental frequency f_0 , an optical pulse train with repetition rate of about n times that of the driving frequency was generated by rational harmonic mode-locking. Around the 2.5 GHz driving frequency in our experiments, rational harmonic with n value up to 4 were demonstrated by properly detuning the modulation frequency, but the amplitude of the output pulses at 10 GHz -repetition rate was small. Fig. 3 demonstrates the longitudinal mode of the ring laser cavity and emission mode of LD, when the output power was mode - locked. Experiments show that the output power can be locked, when the difference between longitudinal modes of ring cavity and emission mode of LD is in the range of ± 2 nm rounding the LD modes. Fig. 4 shows the autocorrelation trace of the output pulses. Depending on the RF modulation power and the modulation frequency detuning from amplitude modulation frequency f_m (in our case $f_m = 2.48632$ GHz) we observed pulses with adjustable widths from 25 to 35 ps. The spectral width of the output pulses was 0.2 nm at -3 dB. The pulse trains at repetition rates of 2.4 and 4.8 GHz were stable for more 4 hours in comparison with internal electro-optic modulator stable of 2 hours at the same atmosphere condition. In addition, experiments shows that, when the modulation frequency was detuned on

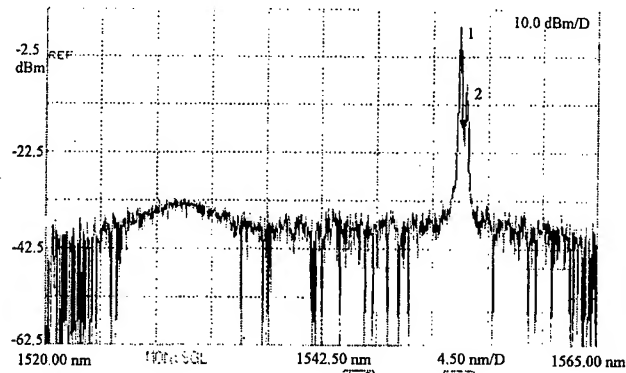


Fig. 3: Spectrum of the mode-locked laser (1) and LD emission (2). $\Delta\lambda = 0.4$ nm

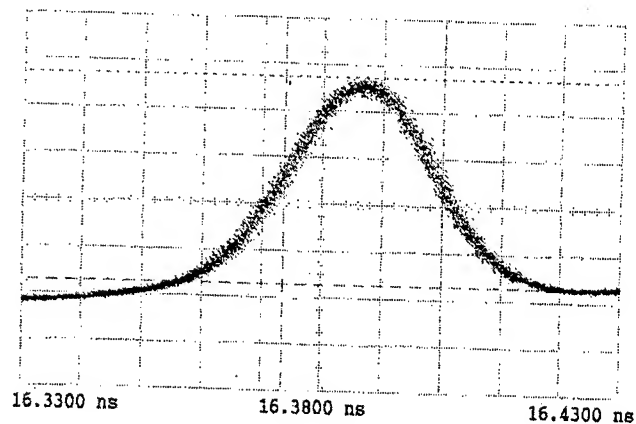


Fig.4: Autocorrelation trace of 4.840 GHz output pulses of the mode-locked ring laser by DFB diode laser

16.62 kHz the new mode locking may be established. From this fact, the thermal expansions of the cavity length and acoustic vibration introduce a negligible change in the positions of the laser ring cavity modes. Although this stabilization technique does not keep the absolute lasing wavelength constant, we obtained a center wavelength drift of a few hundredths of nanometer over several hours of stable operation. Qualitatively, this behavior is consistent with standard mode-locking theory and a more detailed analysis concerning ring laser stable by diode lasers is in progress.

III. CONCLUSION

The performance of an actively stabilized, harmonically mode-locked, erbium -doped fiber ring laser was demonstrated by using DFB-diode lasers as an intensity modulator and as a small gain medium. In this fiber ring laser the semiconductor modulator serves both as a mode-locker and as stabilizer. The laser output characteristics remain stable for long periods of time without any need for external adjustments. The fiber ring laser produces nearly transform-limited pulses (25-35 ps) at multi-gigahertz repetition rates.

ACKNOWLEDGMENT

The authors are grateful to Prof. Nguyen Van Hieu and Phan Hong Khoi for their helpful discussions and fruitful supports. This work was supported in part by Korean Science-Engineering Foundation (KOSEF) and Vietnam National Project KHCN-03-14.

REFERENCES

- [1] I.N. Duling III, " Subpicosecond all-fiber erbium laser," *Electron. Lett.*, vol.27, pp. 544-545, 1991.
- [2] V.J. Matsas, W.H. Loh and D.J. Richardson, " Self-starting, passively mode-locked Fabry-Perot fiber soliton laser using nonlinear polarization evaluation," *IEEE Photon.Technol. Lett.*, vol.5, pp.492-484, 1993.
- [3] K.Tamura, H.A. Haus and E.P. Ippen, " Self-starting additive pulse mode-locked erbium fiber ring laser," *Electron. Lett.*, vol.28, pp. 2226-2227, 1992.
- [4] A. Takada and H. Miyazawa, " 30 GHz picosecond pulse generation from actively mode-locked erbium-doped fiber laser," *Electron.Lett.*, vol.26, pp. 216-217, 1990.
- [5] X.Shan and D.M. Spirit, " Novel method to suppress noise in harmonically mode-locked erbium fiber lasers," *Electron.Lett.*, vol.29, pp. 979-981, 1993.
- [6] G.T.Harvey and L.F. Mollenauer, " Harmonically mode-locked fiber ring laser with an internal Fabry-Perot stabilizer for soliton transmission," *Opt. Lett.*, vol.18, pp.107-109, 1993.
- [7] J.S. Wey, J. Goldhar, D.W. Rush, M.W. Chbat, G.M. Carter and G.L. Burdge, "Performance characterization of harmonically mode-locked erbium fiber ring laser," *IEEE Photon. Technol. Lett.*, vol.7, No.2, pp. 152-154, 1995.
- [8] H.A. Haus, K.Tamura, L.E. Nelson and E.P. Ippen, " Stretched-pulse additive pulse mode-locking in fiber ring lasers: Theory and Experiment," *IEEE J. Quantum Electron.*, vol.31, No.3, pp. 591-598, 1995.
- [9] Liguao Luo and P.L. Chu, " Suppression of self - pulsing in an erbium -doped fiber laser," *Opt.Lett.*, vol.22, No.15, pp. 1174-1176, 1997.
- [10] C.R. Doerr, H.A. Haus, E.P. Ippen, M. Shirasaki and K. Tamura, " Additive-pulse limiting " *Opt. Lett.*, vol.19, No.1, pp. 31-33, 1994.
- [11] Charles X. Yu, Shu Namiki and H.A. Haus, " Noise of the Stretched pulse fiber laser: Part II - Experiments," *IEEE J. Quantum Electron.*, vol.33, No.5, pp. 660-668, 1997.

[12] Shenping Li and K.T. Chan, " Wavelength-Tunable actively Mode-locked fiber ring laser with a Fabry - Perot semiconductor modulator based on Carrier-induced refractive index change ," Tech. Dig. of OFC, TuB2/7, 1999.

Tunable long period fiber gratings for EDFA gain equalization

Kin Seng Chiang*, Zhihao Chen, and Malay K. Pandit

Optoelectronics Research Centre and Department of Electronic Engineering,
City University of Hong Kong, Hong Kong, China

ABSTRACT

We propose and use for the first time tunable long-period fiber gratings (LPFG) to facilitate the gain equalization of an erbium-doped fiber amplifier (EDFA). The ASE peak of an EDFA around the wavelength 1534 nm was equalized by 7.5 dB and the gain peak by 3 dB.

Keywords: Fiber amplifier, gain equalization, long-period gratings

1. INTRODUCTION

When a LPFG is used for EDFA gain equalization,^{1,2} the tolerance on the period of the grating, which determines the notch wavelengths in its transmission spectrum, is extremely tight. This is because it involves an accurate knowledge of the fiber parameters as well as the complex coupling dynamics among the core and the cladding modes.³ It is therefore important to incorporate a fine-tuning mechanism in the filter to relax the said tolerance. In this paper, we report an online tuning technique based on bending a LPFG.

Bending a LPFG shifts its transmission spectrum towards longer wavelengths with only 1-2 dB reduction in the notch depths. To compensate for the deterioration, the dips can be made strong during fabrication by using proper Excimer laser pulse energy and exposure time. This allows us to precisely align the LPFG notches with the EDFA gain spectrum peaks in an economic way. In our work, LPFG's with periods of approximately 160 micron, which corresponded to the 1534 nm peak of the EDFA, were tuned to demonstrate the effectiveness of this method.

The present method holds important promise for a range of gain flattening schemes including that involving dual wavelength pumping by 980 nm and 1480 nm light. It will also be applicable in gain-locked EDFAs.

2. EXPERIMENTAL

The configuration shown in Fig.1 was constructed to observe the performance of EDFA gain flattening. A pump source and an optical signal generator were coupled to a 6 m long erbium-doped fiber (EDF) (Lucent's HG 980), which was followed by two LPFG filters in cascade. The EDF was pumped with 15-70 mW of 980 nm light.

* Correspondence: E-mail: eeksc@cityu.edu.hk; Telephone: + (852) 2788 9605; Fax: + (852) 2788 7791

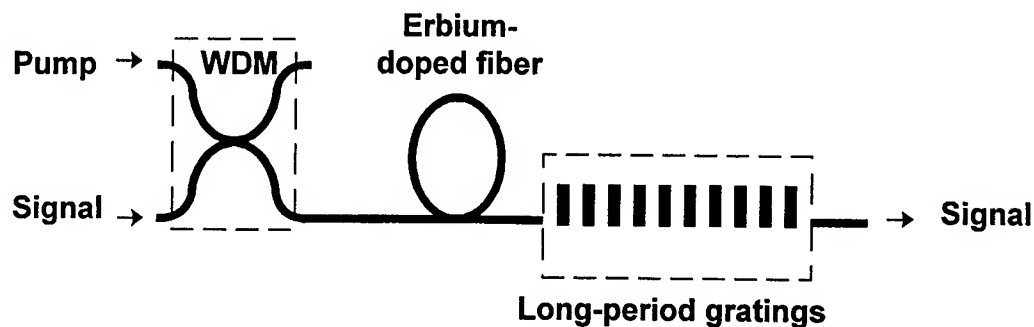


Fig. 1. Schematic of the experimental setup for EDFA gain equalisation.

The LPFGs had their notch wavelengths at 1526 and 1530 nm, without bending. The 1530 nm grating was bent during gain equalization. They were fabricated by exposing a section of a photosensitive fiber (QPS fiber) to 248 nm KrF excimer laser beam through an amplitude mask. The grating filters had a periodicity of $\Lambda = 160 \mu\text{m}$ and a typical length of 2.5 cm. We tailored the grating spectra by varying the exposure time and the length of the gratings.

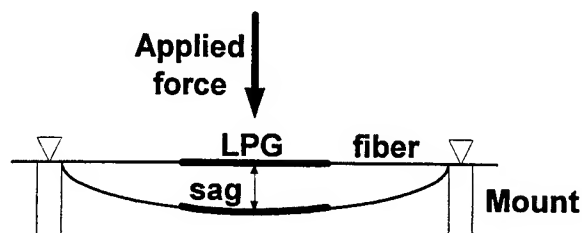


Fig. 2. Schematic of the setup for bending the LPFG.

The setup for bending the LPFG is shown in Fig.2. For each grating under test, a 7 cm section of the fiber with the LPFG in the center was epoxied on a polymer strip and clamped at the two ends. The fiber segment was bent by depressing (0.8 - 1.2 mm) it at the center in the lateral direction. The spectrum was measured using a broadband LED and an optical spectrum analyzer. As the LPFG was bent, the notch wavelength could be shifted to shorter or longer wavelengths, depending on whether the grating was compressed or stretched, as shown in Fig.3 and Fig.4, respectively. It can be seen from these figures that the shift is around 0.85 nm per mm sag and a maximum shift of about 5 nm is possible.

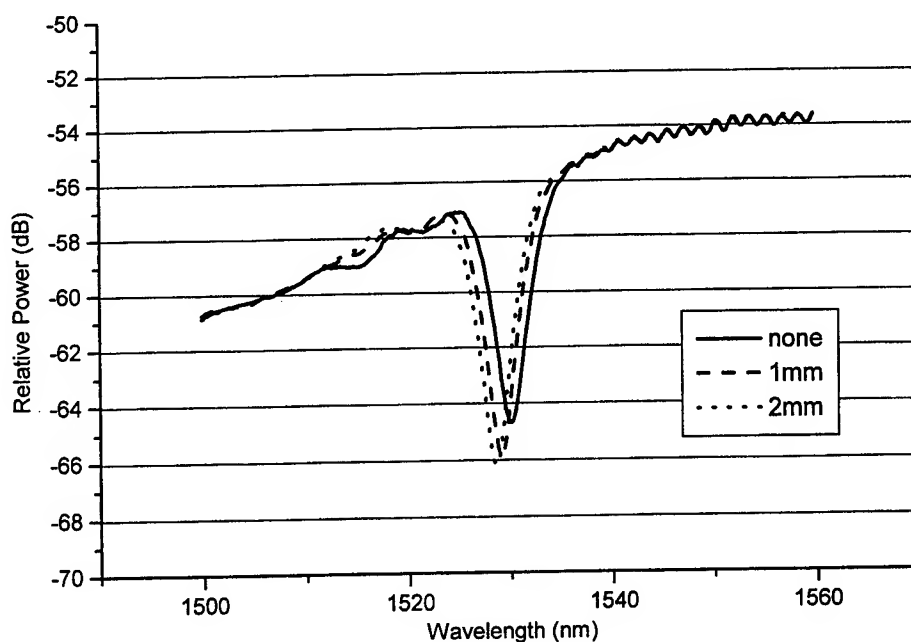


Fig. 3. The grating transmission spectra with different sags during bending (the LPFG was compressed).

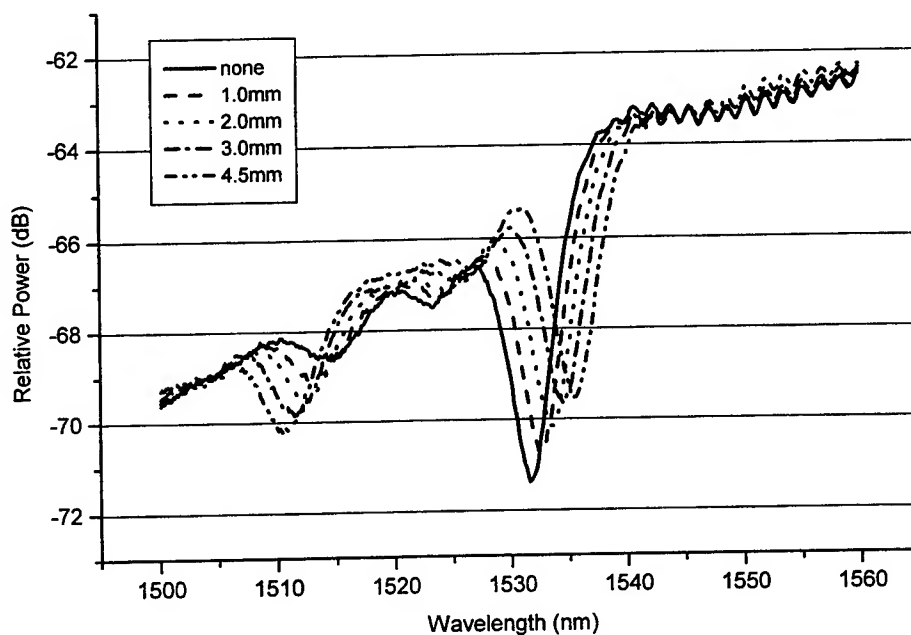


Fig. 4. The grating transmission spectra with different sags during bending (the LPFG was stretched).

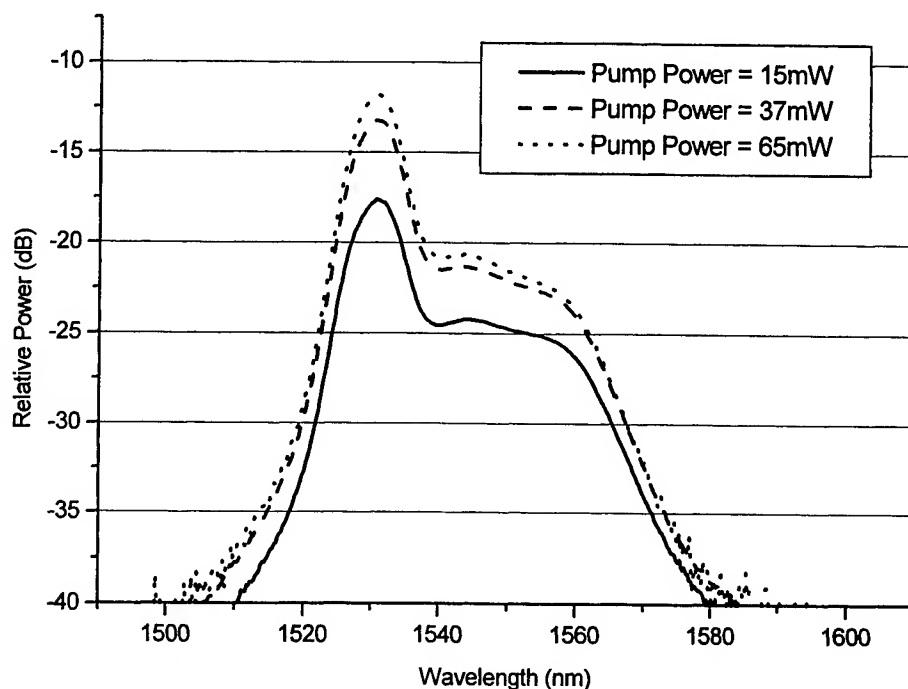


Fig. 5. Experimental unequalized ASE spectrum of HG 980 fiber.

The unequalized and equalized ASE spectra of the EDFA are shown in Fig.5 and Fig.6, respectively.

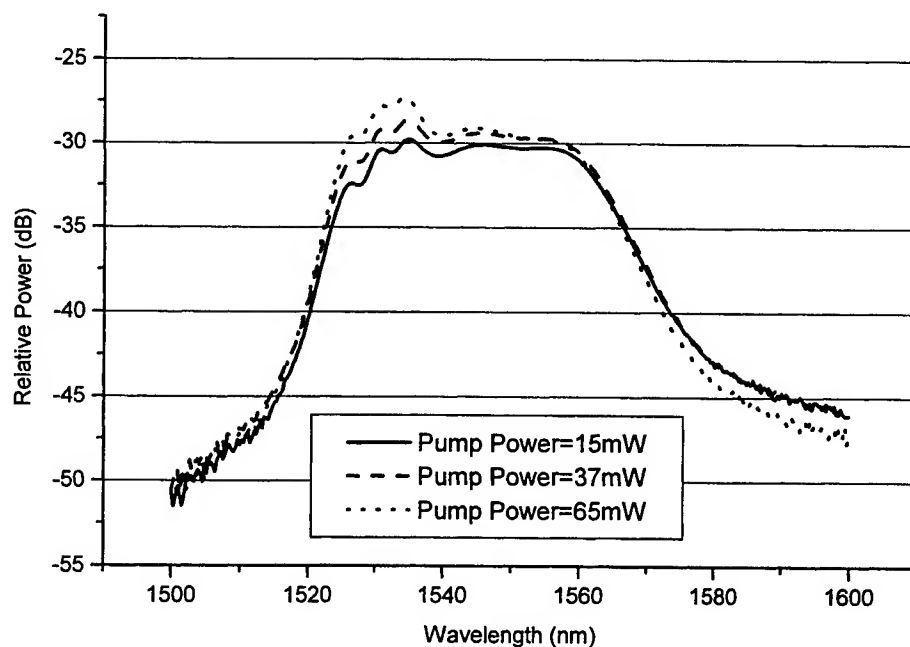


Fig. 6. Equalization of the ASE spectrum with two LPFGs.

As shown in Fig.6, the LPFG, designed for the center wavelength 1530nm, is bent until the optimum performance is reached. A spectral width of 34 nm (1526 to 1560 nm) is flattened by as much as 7.5 dB (from 10 dB:unequalized to 2.5 dB:equalized) at 37 mW pump power. This clearly demonstrates the usefulness of tuning a bent LPFG during equalization.

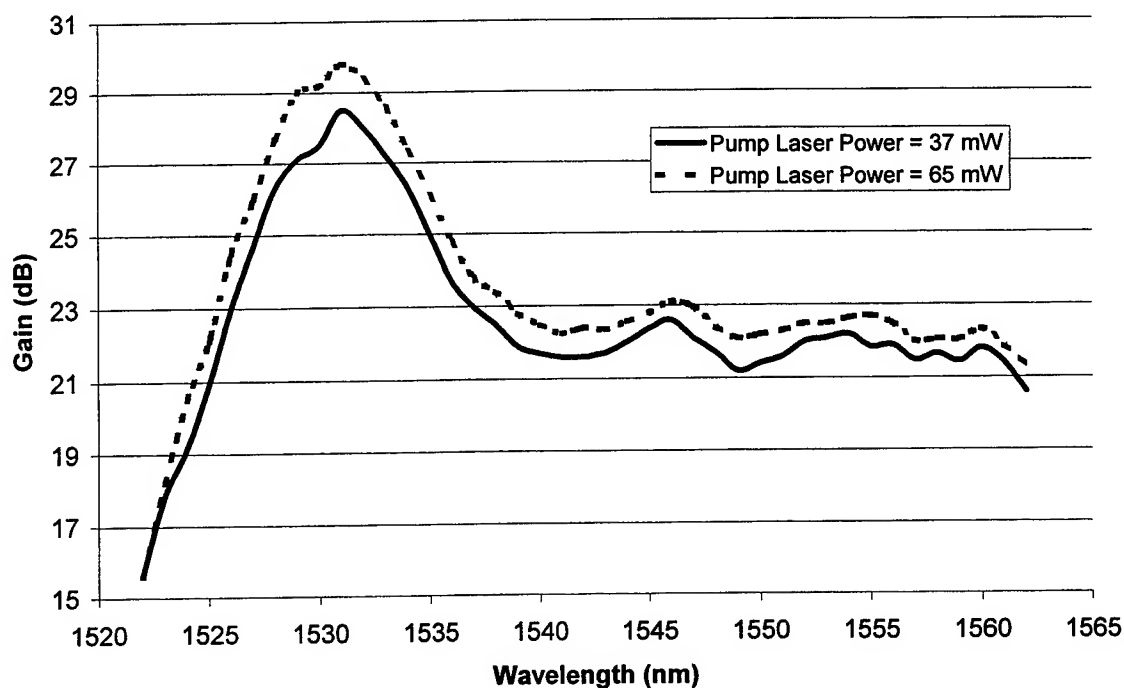


Fig. 7. Experimental unequalized gain spectrum of HG 980 fiber.

As also shown in Figs.7 & 8, the 1530 nm LPFG is bent until the optimum performance is reached. A spectral width of 31 nm (1526 to 1557 nm) is gain-flattened by 3 dB (from 7 dB:unequalized to 4 dB:equalized) at 37 mW pump power.

The step-by-step process of tuning a bent LPFG during equalization is demonstrated in Figs.9-11 for a range of pump powers. The best performance is reached at around 0.5 mm sag.

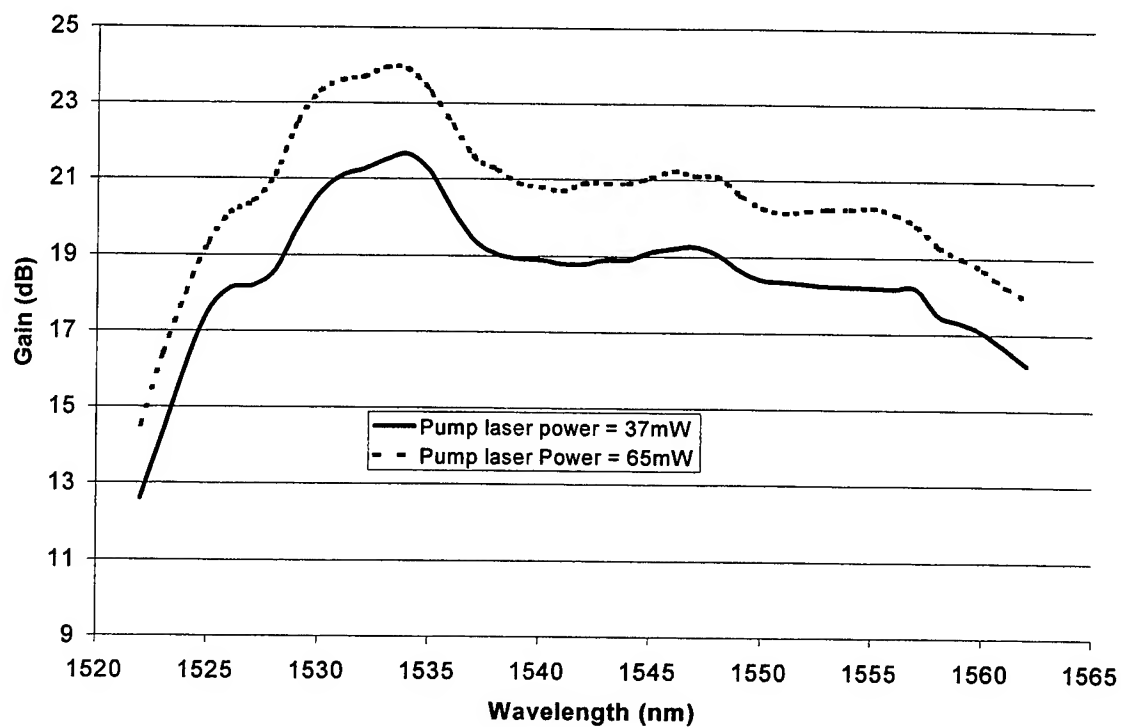


Fig. 8. Equalization of the gain spectrum with two LPFGs.

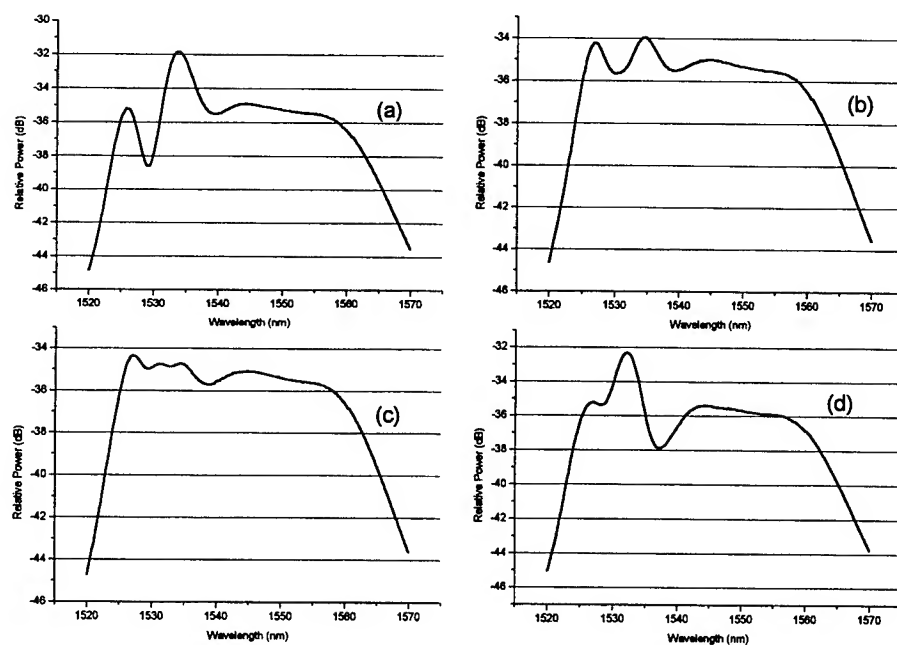


Fig. 9. Equalized ASE spectra with different sags of the bent LPFGs. Sag = (a) 0 mm; (b) 0.4 mm; (c) 0.5 mm; (d) 1 mm. Pump laser power = 15 mW.

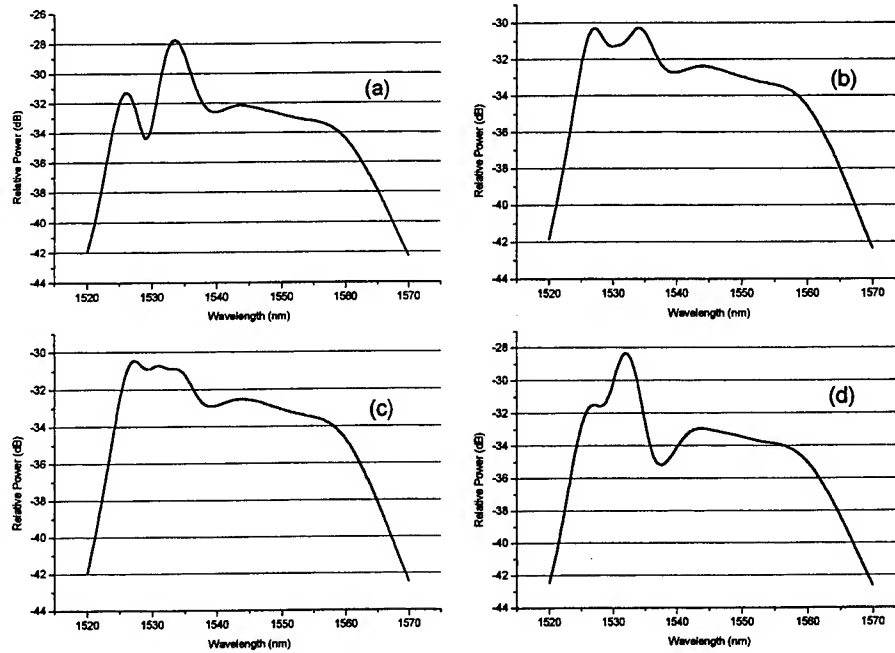


Fig. 10. Equalized ASE spectra with different sags of a bent LPFG. Sag = (a) 0 mm; (b) 0.4 mm; (c) 0.5 mm; (d) 1 mm. Pump laser power = 37 mW.

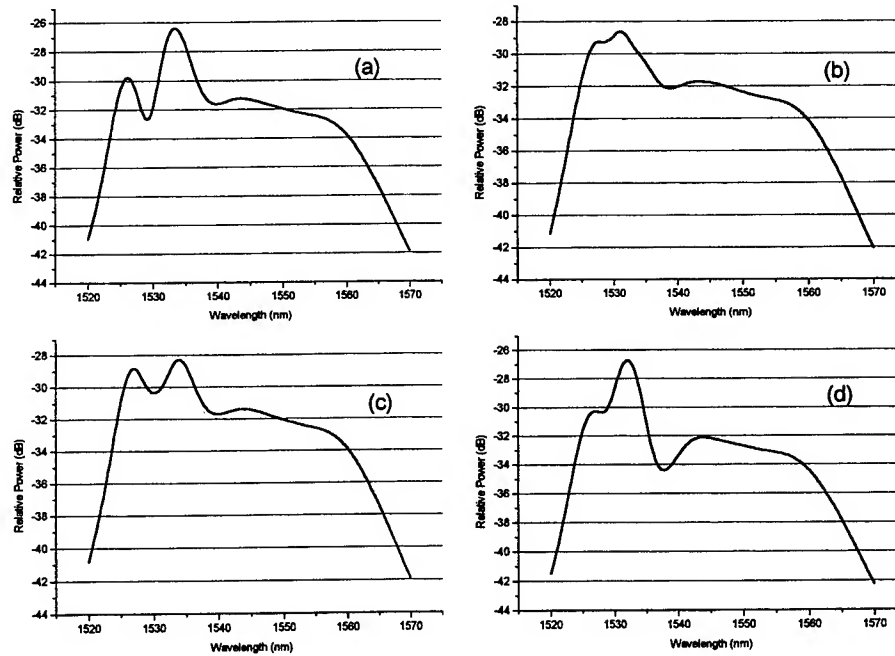


Fig. 11. Equalized ASE spectra with different sags of a bent LPFG. Sag = (a) 0 mm; (b) 0.4 mm; (c) 0.5 mm; (d) 1 mm. Pump laser power = 65 mW.

3. CONCLUSION

We have for the first time dynamically equalized the gain spectrum of an EDFA around the 1534 nm band by using bent LPFGs. The ASE peak of an EDFA around the wavelength 1534 nm was equalized by 7.5 dB and the gain peak by 3 dB.

4. ACKNOWLEDGMENTS

This research is supported by a City University small-scale research grant (no. 9030667) and a University Grants Committee (Hong Kong Government) research grant (no. 9040425). Contributions of S. P. Li and K. K. Cheung to the experimental side of this work are gratefully acknowledged.

5. REFERENCES

1. A. Vengsarkar, J. R. Pedrazzani, J. B. Judkins and P. J. Lemaire, N. S. Bergano and C. R. Davidson, "Long-period fiber-grating-based gain equalizers", *Opt. Lett.*, 21(5), pp.336-338, 1996.
2. P. F. Wysocki, J. B. Judkins, R. P. Espindola, M. Andrejco and A. M. Vengsarkar, "Broad-band erbium-doped fiber amplifier flattened beyond 40 nm using long-period grating filter", *IEEE Photon. Technol. Lett.*, 9(10), pp.1343-1345, 1997.
3. J. R. Qian, and H. F. Chen, "Gain flattening fiber filters using phase-shifted long period fibre gratings", *Electron. Lett.*, 34(11), pp.1132-1133, 1998.

Efficient white light-emitting organic/polymeric electroluminescent device

Jingsong Huang*, Kaixia Yang, Zhiyuan Xie, Chuannan Li, Yi Zhao, Shiyong Liu, Yue Wang^a,
Fang Wu^a, Yangqi Li^a, Jiacong Shen^a

National Lab of Integrated Optoelectronics, Jilin University, Changchun,
P. R. China, 130023

^aKey Lab of Supramolecular Structure and Spectroscopy, Jilin University, Changchun,
P. R. China, 130023

Tel: 86-0431-8922331-2935, Fax: 86-0431-8923939, Email: oed@mail.jlu.edu.cn

ABSTRACT

A white light-emitting organic/polymeric electroluminescent(EL) device with multilayer thin-film structure is demonstrated. The device structure of glass substrate/indium-tin oxide/poly(N-vinylcarbazole) (PVK)/phenylpyridine beryllium(BePP₂)/8-(quinolinolate)-aluminum (Alq) doped with 5,6,11,12-petraphenylnaphthacene/Alq/LiF/Al was employed. The turn-on voltage is as low as 2.9 V. Blue fluorescent BePP₂, yellow fluorescent rubrene, and green fluorescent Alq are used as three primary colors. The Commission Internationale de l'Eclairage (C.I.E) coordinates of the emitted light are (0.313, 0.356) at 10V, which is located in the white-light region. Bright white light, over 6800cd/m², was successfully obtained at about 17V, and the maximum efficiency reaches to 1.38lm/W at 8.5V.

Keywords: organic, electroluminescence, white-light, efficiency

1. INTRODUCTION

After the first report of a bright green light organic electroluminescent(EL) device by Tang and Van Slyke¹, organic EL devices have attracted great attention due to their potential application to the full-color flat-panel displays. There have been extensive studies on organic EL devices using low molecular-weight organic material^{1, 2}, polymer^{3, 4} and metal complexes⁵ with the aim of achieving the high brightness and efficiency, the multicolor emission and the improved stability. Among these organic or polymeric EL devices, the realization of efficient white ones is an absolutely necessary for a number of uses, such as an illumination light source and backlight for liquid crystal display as well as full color displays. Unfortunately, the production of white organic EL devices is difficult, since the single active materials, which emit white light, are quite rare. There have been several concepts presented⁶⁻¹⁷, which allow one to achieve white light emission. Blends of red, green and blue light-emitting polymers^{6, 7}, an exciplex in a bilayer device with two blue light-emitting polymers⁸ or chelate metal complexes⁹ alone can produce white light. Polymers doped with an appropriate combination of red, blue and green fluorescent dyes can also produce white light^{10, 11}. The AT&T researchers¹² describe a technique of a single microcavity layer of aluminum complex. The microcavity layer acts as a selective lens to steer out red, green and blue photons from the bottom

* Correspondence: email:oed@mail.jlu.edu.cn

of the device. J.Kido et al¹³ developed a multilayer device with three emitting layers, each layer emitting light in a different region of the visible spectrum to generate white light. Alternatively, Xie and Huang et al¹⁴ obtained the white light emission by confinement in organic multiheterostructures.

Among the organic multilayer structures to produce white light, triphenylamine derivative (TPD) is widely used as a hole-transporter or a hole-transporter and emitter.^{10, 13-15} However, TPD has poor thermal stability. In this approach, we used poly(N-vinylcarbazole) (PVK) as the hole-transporter, which is widely used as a polymer material^{3, 5} since it has good film-forming property and high thermal stability. Moreover, induction of PVK can effectively decrease the number of pinholes in thin-film, and suppress noisy leakage currents.

2. EXPERIMENT

Figure 1 shows the materials used in this experiment and the configuration of the organic/polymeric multilayer white EL device. Phenylpyridine beryllium (BePP₂)¹⁵ is synthesized in our laboratory and served as a blue light emitter, 8-(quinolinolate)-aluminum (Alq) doped with 5,6,11,12-petraphenyl naphthacene (rubrene) as a yellow light emitter, and undoped Alq as an electron-transporter. As we all known, the fluorescent yield of BePP₂, Alq and rubrene are all relatively high, which is of benefit to obtain the EL efficiency of device. PVK and rubrene are purchased from the Acros Organics, Alq from the Tokyo Kasei Kogyo Co. Ltd. All organic materials have been purified by a train sublimation method before use.

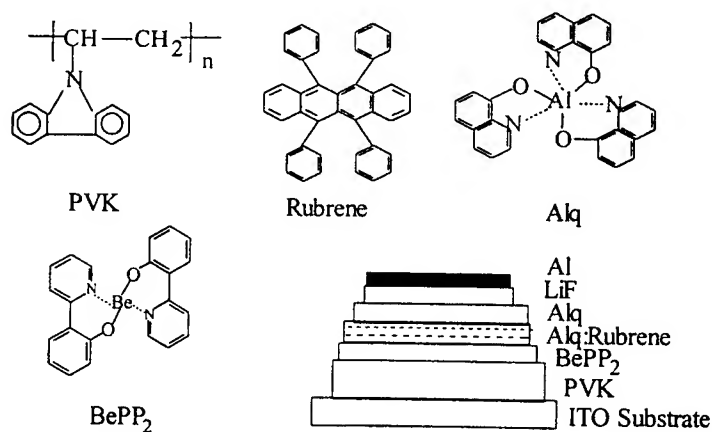


Fig. 1 The structure of the materials used and the configuration of the white EL device.

The solution of PVK in chloroform with 10mg/ml was prepared and spin-coated onto an indium-tin oxide (ITO) coated glass substrate. Thickness of PVK layer was about 200nm. Then, a 20nm-thick BePP₂, a 20nm-thick Alq doped with rubrene layer and a 20nm-thick undoped Alq layer were successively deposited onto the PVK layer. Rubrene doping level was controlled to about 5% (mol ratio). A 0.5nm-thick LiF and a 100nm-thick Al were successively deposited on the organic layer surface. The deposition rate was controlled by quartz oscillating thickness monitor to be 0.1nm/s for organic materials and metals. The luminance was measured with a 1980A Spectra pritchard photometer, and the emission spectra were measured with a RF-5301Pc Spectrofluorophotometer. All measurements were carried out at room temperature under ambient atmosphere.

3. RESULTS AND DISCUSSION

In Figure 2, the current-voltage curve and brightness-voltage curve of the white light EL device are depicted, respectively. Although there has thick hole-transporting layer in the device, luminescence starts at a low voltage such as 2.9V. Our previous studies showed that turn-on voltage could be effectively decreased by adding appropriate electron-transporting layers^{20, 21}. The maximum luminance of device is 6800cd/m² before the device degradation at 17V. The curve of device efficiency depend on voltage is shown in Figure 3. With the increase of driven voltage, the device efficiency sharply increases, and reaches to the maximum value of 1.38lm/W at 8.5V, then decreases gradually.

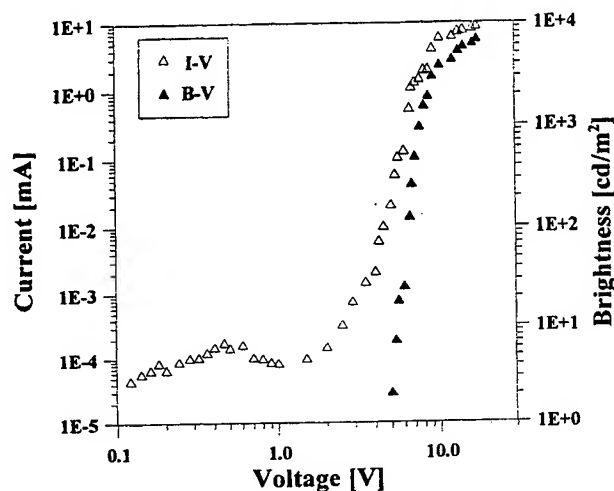


Fig. 2 The current-voltage and luminance-voltage characteristics of the white EL device.

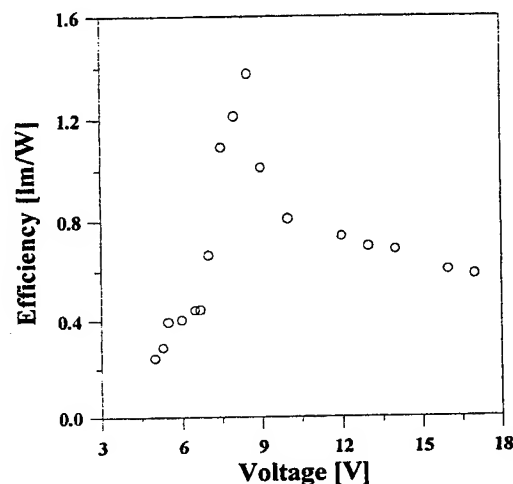


Fig.3 The efficiency-voltage curve of the white EL device.

In order to explain why our device with a common multilayer structure, ITO/PVK/BEPP₂/Alq:rubrene/Alq/LiF/Al (I-type), exhibited high EL properties, we employ the other devices with two kinds of structures, namely, ITO/PVK:BePP₂(10:1 wt %, 200nm)/Alq:rubrene(20nm)/Alq(20nm)/LiF(0.5nm)/Al(100nm) (II-type), ITO/TPD(50nm)/BePP₂(20nm)/Alq:rubrene(20nm)/Alq(20nm)/LiF(0.5nm)/Al(100nm) (III-type). Compared with the I-type device, the II-type device shows lower EL efficiency, which can be explained by the schematic diagram of the energy band of the I-type device (shown in Figure 4). The molecular ionization energy and the electron affinity of PVK, BePP₂, Alq and rubrene are (-2.32, -5.78eV), (-2.57, -5.73eV), (-2.91, -5.61eV) and (-3.59, -5.51eV), respectively. These values are all calculated by the cyclic voltammetry method and their absorption spectra. It is clearly seen from Figure 4 that the electron barrier of 0.59eV between PVK and Alq is divided into two gentle barriers of 0.25 and 0.34eV when we adopted the layered structure (PVK/BePP₂/Alq:rubrene/Alq) not the doped structure (PVK:BePP₂/Alq:rubrene/Alq). Obviously, the injection turns easier to happen for electrons from Alq layer to BePP₂ layer than to PVK layer under the same drive voltage, and the probability of exciton formation in BEPP₂ layer is increased. So, the EL efficiency of I-type device is enhanced. Compared with the III-type device, there is relatively small current flow in the I-type device at the same drive voltage, because the thick PVK layer induces relatively high resistance compared with TPD layer. However, the EL efficiency of the I-type device is larger than that of the III-type device. Therefore, the joule heat produced in I-type device is less, the influence on the fluorescent yield of the fluorescent dyes is less. It is general agreed that the fluorescent yield of organic dyes is decreased with

increasing the ambient temperature. We attributed inferior EL efficiency of the III-type device to the heat effect.

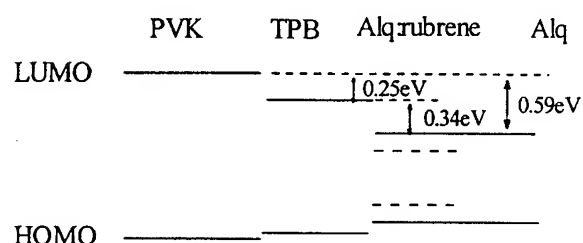


Fig. 4 The schematic energy band diagram of the organic/polymeric multilayer structure.

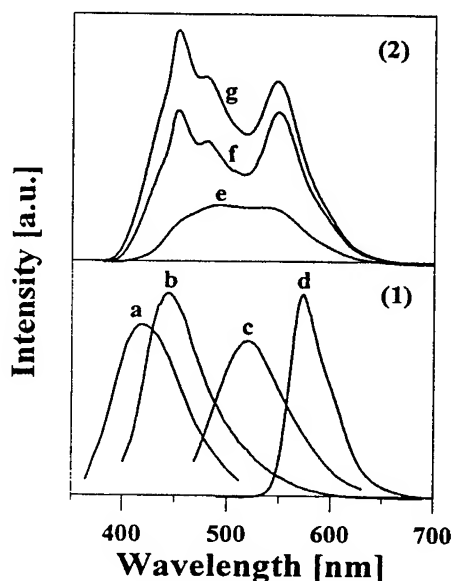


Fig. 5 (1) PL spectra of PVK(a), BEPP₂(b), Alq(c) and Alq:rubrene(d).

The excision peak for Alq:rubrene film is the maximum absorption wavelength of Alq(400nm).

(2) EL spectra of white EL device at different voltages. 5V(e), 9V(f), 16V(g).

Photoluminescence (PL) spectra of PVK, BePP₂, Alq and Alq doped with rubrene films and EL spectra of the typical white EL device at different voltages are depicted in Figure 5. The emission peaks of PL spectra are 412nm, 443nm, 520nm and 565nm, respectively. The PL peak of the Alq:rubrene film is the same as the PL peak of rubrene. In the EL spectra, two peaks at around 453nm and 547nm, corresponding to the emission from BePP₂ and rubrene respectively, are clearly seen after the driven voltage is larger than 5V. Since the highest occupied molecular orbital and lowest unoccupied molecular orbital of rubrene are located within the energy gap of Alq (shown in Figure 3) so that both electrons and holes are bound into the rubrene molecular. There exists energy transfer from Alq to rubrene in the doped layer. We can also see from this figure that there is a shoulder peak is around 478nm when the driven voltage is greater than 5V. We think it may be from the exciplex formation at the interface between BePP₂ layer and Alq:rubrene layer. The color of emitted light at the whole change region of voltage are all located into white region. The Commission Internationale de l'Eclairage (C.I.E) coordinates of the emitted light are (0.313, 0.356) at 10V, which is very near the equi-energy white point (0.333, 0.333).

Recently, the devices with thick organic layers have been reported^{20, 21}. The formation of thick organic layers is expected for making organic laser diode. The most promising structure for application is a waveguide type. The formation of thick carrier transport layers between electrodes and waveguiding emitter layer is expected to reduce the laser threshold and is unavoidable. We believed that the feasibility of thick layers would open up novel possibilities of organic EL devices.

4. CONCLUSION

In conclusion, we have fabricated a high brightness and efficiency white light organic EL device. PVK is served as a hole-transporter, BePP₂ and rubrene as the blue and yellow-light emitter respectively, Alq as a subsidiary green-light emitter and an electron-transporter. The turn-on voltage of our device is only about 2.9V. The maximum luminance and efficiency of the device reach to 6800cd/m² and 1.38lm/W. The optimum C.I.E of the emitted light are (0.313, 0.356) at 10V.

ACKNOWLEDGMENTS

The authors thank professor Z.Wang of the Changchun Institute of Physics, Chinese Academy of Sciences, for performing the luminance and C.I.E measurements. This study is supported by the National Natural Science Foundation of China under Grant No. 69637010, and the "863" Project under Grant No. 863-307-12-04(02).

REFERENCES

1. C.W.Tang, S.A.VanSlyke, "Organic electroluminescent diodes", *Appl.Phys.Lett.*, **51**, pp.913-515, 1987.
2. J.S.Huang, K.X.Yang, Z.Y.Xie, B.J.Chen, H.J.Jiang, S.Y.Liu, "Effect of well number on organic electroluminescent device characteristics", *Appl.Phys.Lett.*, **73**, pp.3348-3351, 1998.
3. J.Kido, K.Hongawa, K.Okyqama, K.Nagai, "Bright blue electroluminescent from poly(N-vinylcarbazole)", *Appl.Phys.Lett.*, **68**, pp.2627-2629, 1996.
4. J.S.Huang, H.F.Zhang, W.J.Tian, J.Y.Hou, Y.G.Ma, J.C.Shen, S.Y.Liu, "Violet-blue electroluminescent diodes utilizing conjugated polymer blends", *Synth.Met.*, **87**, pp.105-108, 1997.
5. J.Kido, K.Hongawa, K.Okuyama, K.Nagai, "White light-emitting organic electroluminescent device using the poly(N-vinylcarbazole) emitter layer doped with three fluorescent dyes", *Appl.Phys.Lett.*, **64**, pp.815-817, 1994.
6. M.Granstrom, O.Inganas, "White light emission from a polymer blend light emitting diode", *Appl.Phys.Lett.*, **68**, pp.147-149, 1996.
7. Y.Yang, Q.Pei, "Efficient blue-green and white light-emitting electroluminescent cells based on poly[9,9-bis(3,6-dioxaheptyl)-fluorene-2,7-diyl]", *J.Appl.Phys.*, **81**, pp.3294-3298, 1997.
8. C.L.Chao, S.A.Chen, "White light emission from exciplex in a bilayer device with two blue light-emitting polymers", *Appl.Phys.Lett.*, **73**, pp.426-428, 1998.
9. Y.Hamada, T.Sano, H.Fujii, Y.Nishio, "White-light-emitting material for organic electroluminescent devices", *Jpn.J.Appl.Phys.*, part 2, **35**, pp. L1330-L1341, 1996.
10. J.Kido, W.Ikeda, M.Kimura, K.Nagai, "White-light-emitting organic electroluminescent device using lanthanide complexes", *Jpn.J.Appl.Phys.*, part 2, **35**, pp. L394-L396, 1996.
11. S.Tasch, E.J.W.List, Q.Ekstrom, W.Graupner, G.Lersing, P.Schichting, U.Rohr, Y. Geerts, U.Scherf, K.Mullen, "Efficient white light-emitting diodes realized with new processable blends of conjugated polymers" *Appl.Phys.Lett.*, **71**, pp. 2883-2885, 1997.
12. A.Dodabalapur, L.J.Rotherg, T.M.Miller, E.W.Kwock, "Color variation with electroluminescent organic semiconductors in multimode resonant cavities", *Appl.Phys.Lett.*, **65**, pp.2308-2310, 1994.
13. J.Kido, M.Kimura, K.Nagai, "Multilayer white light-emitting organic electroluminescent device", *Science*, **267**,

pp.1332-1334, 1995.

14. Z.Y.Xie, J.S.Huang, C.N.Li, S.Y.Liu, Y.Wang, Y.Q.Li, J.C.Shen, "White light emission induced by confinement in organic multiheterostructures", *Appl.Phys.Lett.*, **74**, pp641-643, 1999.
15. M.Strukelj, R.H.Jordan, A.Dodabalapur, "Organic multilayer white light emitting diodes", *J.Am.Chem.Soc.*, **118**, pp.1213-1214, 1996.
16. R.H.Jordan, A.Dodabalapur, M.Strukelj, T.M.Miller, "White organic electroluminescent devices", *Appl.Phys.Lett.*, **68**, pp. 1192-1194, 1996.
17. M.Berggren, G.Gustafsson, O.Inganas, "White light from an electroluminescent diode made from poly[3(4-octylphenyl)-2,2'-bithiophene] and an oxadiazole derivative", *J.Appl.Phys.*, **76**, pp.7530-7534, 1994.
18. J.S.Huang, W.J.Tian, H.Y.An, S.H.Xue, B.J.Chen, J.Y.Hou, S.Y.Liu, J.C.Shen, "Structural analysis of polymer blue light emitting devices", *Semiconductor Optoelectronics*, **17**, pp.349-352, 1996.
19. W.J.Tian, J.S.Huang, F.Wu, C.Q.Sun, X.D.Liu, Y.G.Ma, S.Y.Liu, J.C.Shen, "Influence of the energy level matching on the performances of organic/polymeric electroluminescent devices", *Chin.Phys.Lett.*, **13**, pp. 790-793, 1996.
20. A.Yamamori, C.Adachi, T.Koyama, Y.Taniguchi, "Doped organic light emitting diodes having a 650-nm—thick hole transport layer", *Appl.Phys.Lett.*, **72**, pp. 2147-2149, 1998.
21. J.Blochitz, M.Pfeiffer, T.Fritz, K.Leo, "Low voltage organic light emitting diodes featuring doped phthalocyanine as hole transport material", *Appl.Phys.Lett.*, **73**, pp.729-731, 1998.

Applications of FFT and Digital Filtering in Reconstruction of Refractive Index Profile of Surface Channel Waveguides from Near-field Intensity Pattern

Hery Susanto^{*a}, Henri P. Uranus^{a,b}, Muljono^a, John E. Batubara^a

^aUniversity of Pelita Harapan, Lippo Karawaci, Tangerang 15811, Indonesia

^bUniversity of Indonesia, Jalan Salemba 4, Jakarta 10430, Indonesia

ABSTRACT

Refractive index profile of surface channel waveguides can be determined by analyzing the near-field intensity pattern. A mathematical model, the inverse Helmholtz equation, is derived in order to use these data to reconstruct the refractive index profile under consideration. In this work, the measured near-field intensities are preprocessed by means of gamma correction, background noise subtraction, Fast Fourier Transform (FFT), and low pass Finite Impulse Response (FIR) digital filter. Several types of FIR windows are chosen. The results are used to reconstruct the refractive index profile of the waveguide. The results show that the application of low pass FIR digital filter by using Hamming window reduces noises better than other windows. The application of this method in determination of refractive index profile of annealed proton exchange LiNbO₃ channel waveguides is demonstrated.

Keywords: refractive index profile, near-field, gamma correction, background noise subtraction, FIR digital filter, lithium niobate, annealed proton exchange

1. INTRODUCTION

The two step proton exchange and thermal annealing process used in the formation of optical waveguides in LiNbO₃ and LiTaO₃ has proven to be an attractive alternative to the Ti-indiffusion technique. The waveguides were formed by immersing LiNbO₃ substrates in molten benzoic acid. The proton exchanged waveguides exhibited a higher photorefractive damage threshold than Ti-indiffused waveguides. There was a steplike increase of the extraordinary index and a slight decrease in the ordinary index in exchanging H⁺ ions for Li⁺ ions using undiluted benzoic acid.¹

The refractive index is one of the most important properties of an optical waveguide. The propagation characteristics of the optical waveguide are determined by their refractive index profiles. Accurate knowledge of the refractive index profile is necessary in order to calculate and determine properties of an optical waveguide. The propagation characteristics and modal transverse field distributions are determined by their refractive index profiles. The refractive index profile is also required to calculate waveguide properties like insertion losses, cutoff wavelengths for propagating modes, and the intensity distributions of the modes themselves. The refractive index can be modified to minimize losses, give specific cutoff wavelength, and to optimize the mode profile, by changing the parameters used in the fabrication process. The more accurate refractive index measurement, the more precise will be the calculation of the waveguide properties.

Various methods have been proposed for determining the refractive index distribution, including reflectivity measurement², surface plasmon resonance³, incoherent light transmission⁴, prism coupling^{3,5}, the measurement of surface topography after chemical etching⁶, measurement of the mode indices through a prism coupler in conjunction with an evaluation using the WKB approximation^{7,8}, reflectivity measurement of angular polished substrates⁹, and the near-field analysis for single mode fiber reconstruction.¹⁰ Most of these methods have limited resolution, destructive one, and require the index enhanced region to be at or near the substrate surface, while others have initial conditions that are difficult to fulfil. Measurement of refractive index profile from mode intensity distribution is a non-destructive method that applicable for both surface and buried, planar, and non-planar waveguides.

The measured intensity distribution through near-field measurement has errors. Many factors cause these errors, such as noises, quantization error, defocussing, non-linearity of camera, etc. Noise from camera and image capture electronics must

* Correspondence: Department of Electrical Engineering, Faculty of Industrial Technology, University of Pelita Harapan, Lippo Karawaci 15811, Tangerang, Indonesia; Telephone: 62-21-5460901; Fax: 62-21-5460910.

be eliminated so that the intensity distribution can be presmoothed and reconstructed. In order to increase signal to noise ratio, some numerical data processing methods are necessary to presmooth and preprocess data which are a low pass filter, background noise subtraction, and gamma correction. Hence, the reconstruction of refractive index profile is impossible without eliminating the high frequency noise of the near-field image.¹²

In this work, the authors have used a method which estimate the refractive index from from near-field measurement by inverse Helmholtz equation algorithm. In this paper, this method using is demonstrated for a single mode surface channel waveguide. A low pass FIR digital filter was used to remove high spatial frequency noise while low frequency noise is reduced by back ground noise subtraction techniques.¹³ The non-linearity of camera is overcome by gamma correction.¹³ Those signal processing techniques and inverse Helmholtz algorithm are implemented using computer program coded in Delphi 2.0. These techniques will be demonstrated for determination of refractive index profile of channel waveguide fabricated using annealed proton exchange process on Z-cut Y-propagating LiNbO₃ substrate.

2. THEORY: THE INVERSE HELMHOLTZ EQUATION

For a weakly guiding waveguide, in which the peak refractive index change is small, the optical field distribution is given through the description of the transversal field as given by the scalar wave equation or the Helmholtz equation:

$$\nabla_t^2 E(x, y) + (n^2(x, y)k^2 - \beta^2)E(x, y) = 0 \quad (1)$$

where ∇_t is the transverse Nabla operator, $k=2\pi/\lambda$ is the free space wave number, $n(x, y)$ is the refractive index profile function, and β is the propagation constant. The refractive index profile can be obtained by rearranging Eq. (1) as¹⁴:

$$n(x, y)\frac{k}{\beta} = \left[1 - \frac{\nabla_t^2 E(x, y)}{E(x, y)} \right]^{\frac{1}{2}} \quad (2)$$

The term on the right hand of Eq. (2) can be expanded into Mac Laurin series for $(1-x)^{1/2}$ -form:

$$n(x, y)\frac{k}{\beta} = 1 - \frac{1}{2} \frac{\nabla_t^2 E(x, y)}{\beta^2 E(x, y)} - \frac{1}{4} \left[\frac{\nabla_t^2 E(x, y)}{\beta^2 E(x, y)} \right]^2 - \frac{3}{8} \left[\frac{\nabla_t^2 E(x, y)}{\beta^2 E(x, y)} \right]^3 - \dots \quad (3)$$

We can eliminate terms started from the third term of (3) on the right hand side because of their small values compared with the first two terms and obtain:

$$n(x, y) \cong \frac{\beta}{k} - \frac{1}{2} \frac{\nabla_t^2 E(x, y)}{\beta k E(x, y)} \quad (4)$$

and introduce the general two dimensional refractive index function for small $\Delta n(x, y)$:

$$n(x, y) = n_s + \Delta n(x, y) \quad (5)$$

where n_s = the refractive index of substrate and $\Delta n(x, y)$ = the refractive index change.

In weakly guiding waveguide, the effective refractive index ($n_{\text{eff}} = \beta/k$) is closed to the value of the refractive index of substrate. We can approximate $n_s \cong \beta/k$ and the propagation constant equals to $\beta \cong n_s k$. By comparing Eq. (4) and Eq. (5), we get the inverse two dimensional Helmholtz equation:

$$\Delta n(x, y) \cong -\frac{1}{2} \frac{\nabla_t^2 E(x, y)}{n_s k^2 E(x, y)} \quad (6)$$

Making the substitution for intensity, $I(x, y) \approx E^2(x, y)$, assumes that there is no phase variations across the measured wavefield. This approximation is quite valid since the mode field intensity is measured at the waveguide endface where the phase variation is negligible.

$$\Delta n(x, y) \cong -\frac{1}{2} \frac{\nabla_t^2 \sqrt{I(x, y)}}{n_s k^2 \sqrt{I(x, y)}} \quad (7)$$

In the case of a separable transverse electrical field, Eq. (7) can also be written as:

$$\Delta n(x, y) \cong -\frac{1}{2n_s k^2} \left[\frac{1}{\sqrt{I(x)}} \frac{\partial^2 \sqrt{I(x)}}{\partial x^2} + \frac{1}{\sqrt{I(y)}} \frac{\partial^2 \sqrt{I(y)}}{\partial y^2} \right] \quad (8)$$

The one dimensional inverse Helmholtz equation can be rewritten with respect to the depth coordinate x :

$$\Delta n(x) \cong -\frac{1}{2n_s k^2 \sqrt{I(x)}} \left[\frac{\partial^2 \sqrt{I(x)}}{\partial x^2} \right] \quad (9)$$

The term on the right hand of Eq. (9) has the second derivative of the intensity distribution function. It can be solved using a numerical method. In this work, we use *high accuracy numerical differentiation formula* for second derivative calculation¹⁵ at the data point x with step size, $\partial x = \Delta x = 1$ as follows:

$$\frac{\partial^2 \sqrt{I(x)}}{\partial x^2} \cong \frac{-\sqrt{I(x+2)} + 16\sqrt{I(x+1)} - 30\sqrt{I(x)} + 16\sqrt{I(x-1)} - \sqrt{I(x-2)}}{12} \quad (10)$$

3. EXPERIMENT: NEAR-FIELD MEASUREMENT

The near-field intensity of the end face of the waveguide measured using set-up shown in Fig. 1.

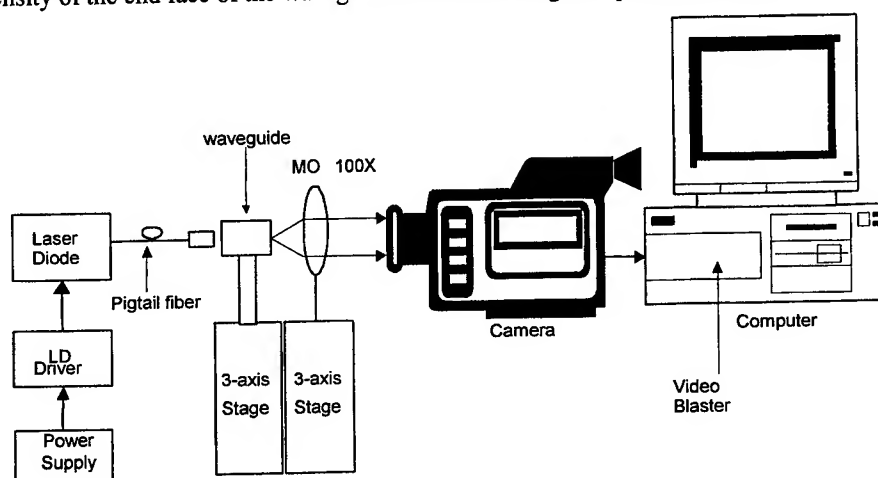


Figure 1. Near-field measurement setup.¹⁵

The single mode surface channel waveguide, that was fabricated using annealed proton exchange process on Z-cut Y-propagating LiNbO₃ substrate purchased from Crystal Technology, was mounted on the high precision translation 3-axis stage in order to achieve the best possible coupling between the fiber and the waveguide. Because of the measured waveguide is a passive component, the light is excited by a diode laser QLM3S813 ($\lambda = 1.3 \mu\text{m}$) from Lasertron, that is driven by a diode laser driver.

Previous authors have demonstrated the noise sensitivity of the inverse Helmholtz equation process.¹² Since the results depends on the second spatial derivative of the data, the original data must have as high signal to noise ratio (SNR) as possible. In order to maximize the SNR of the intensity distribution, the diode laser was fed in low operating current that is adjusted near the threshold current. The camera detector was exposed for as long as possible, without saturating the captured image.

The output of the diode laser with tight buffer single mode pigtail with core/cladding diameter of $8.3/125 \mu\text{m}$, was coupled to one end face of the waveguide through $1/4$ pitch micro rod lens with pitch length of 6.3 mm. The coupling between the pigtail fiber and rod lens was aligned by rod-lens-fiber holder/coupler from Newport. The output of near-field pattern was imaged with an infinity 100X microscope objective (MO) lens that focused on the waveguide output end face and mounted also on another 3-axis stage.

The focal plane of the lens was placed near the output end face of the waveguide so that the image of the near-field intensity pattern of the waveguide endface was located on the detector plane of a Vidicon (Micron Viewer 7290 from Electrophysics) camera with imaging lens detached. The camera was connected to Video Blaster SE100 frame grabber card from Creative installed in the computer.¹⁶ The scale of the image was measured by moving a certain amount of displacement of the aligned fiber-rod lens-waveguide and monitoring the number of pixel shift in the display.

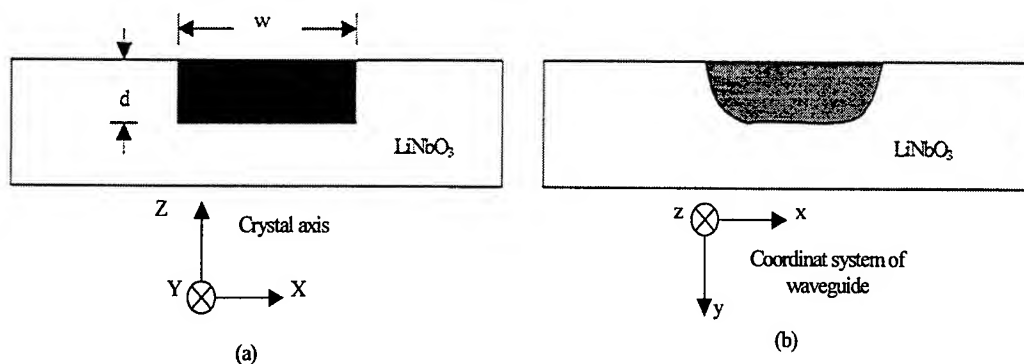


Figure 2. Channel waveguide cross section on Z-cut Y-propagating LiNbO_3 substrate
(a) *Proton Exchange* (b) *Annealed Proton Exchange*.¹

The substrate was proton exchanged for 90 min in a undiluted 10 ml melt of benzoic acid kept at 175°C . The sampled was annealed for 2 hours and kept at 360°C .¹ Captured near-field patterns were stored in the personal computer. Back ground noise subtraction and gamma correction was carried out by our own-made ScanDist program.¹⁵ The data exported by ScanDist were then further processed in spatial frequency domain by computer program coded in Delphi 2.0.

4. RESULTS AND DISCUSSION

Based on this measurement, authors observe the vertical scanning of waveguide sample to get the data of vertical intensity distribution. The spacings between vertical pixels elements of the digitized image were calculated from measured scale as $40/248 \mu\text{m}$ ($0.16129\mu\text{m}$). The vertical image shows asymetricity because the scanning path is started from cover (air), film, and substrates (LiNbO_3) perpendicularly through the substrate largest surface plane.

Authors will reconstruct the refractive index and analyze four types of data of intensity distributions from the same waveguides sample, i.e:

1. Intensity profile without background noise subtraction and gamma correction
2. Intensity profile with only background noise subtraction
3. Intensity profile with only gamma correction
4. Intensity profile with background noise subtraction and gamma correction

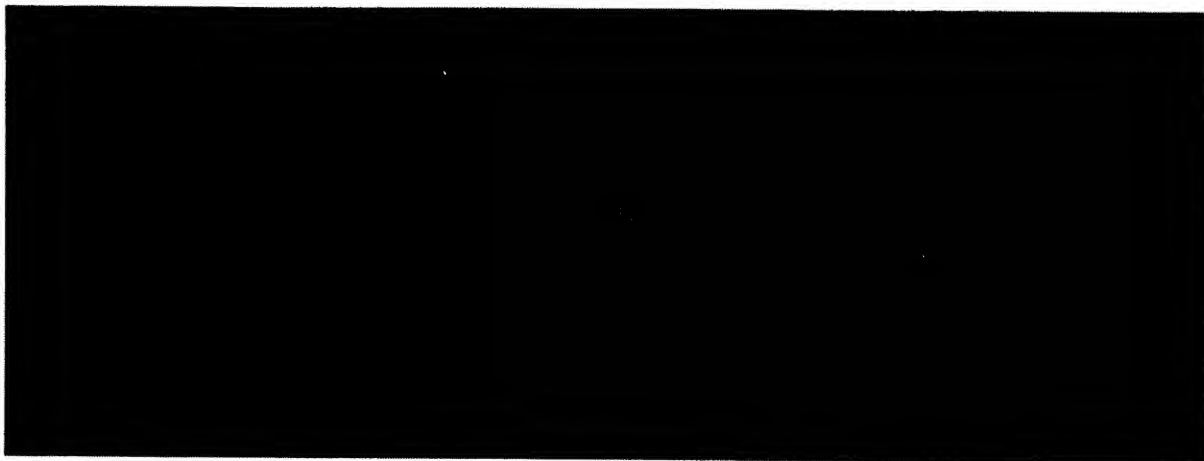


Figure 3. Near-field image of a surface channel waveguide after 2 hours of annealing at 360°C .

Point with highest intensity will be marked as the point $y=0$. The intensity data were all normalized to this peak intensity value.

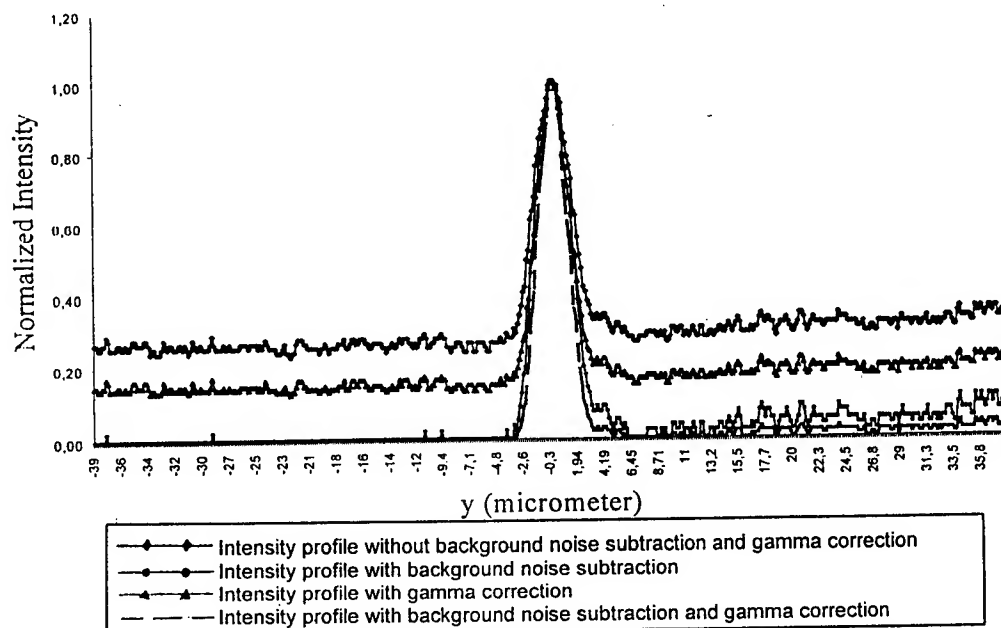


Figure 4. Intensity profiles of a surface channel waveguide without low pass FIR digital filtering.

A plot of a measured intensity profile without further filtering were shown in Fig. 4. Intensity profile without background noise subtraction and gamma correction shows background light that was captured by camera. The background light does not appear after applying background noise subtraction. Intensity profile with background noise subtraction and gamma correction was better and smoother because there was no background light and there was reduction in oscillation of adjacent pixels.

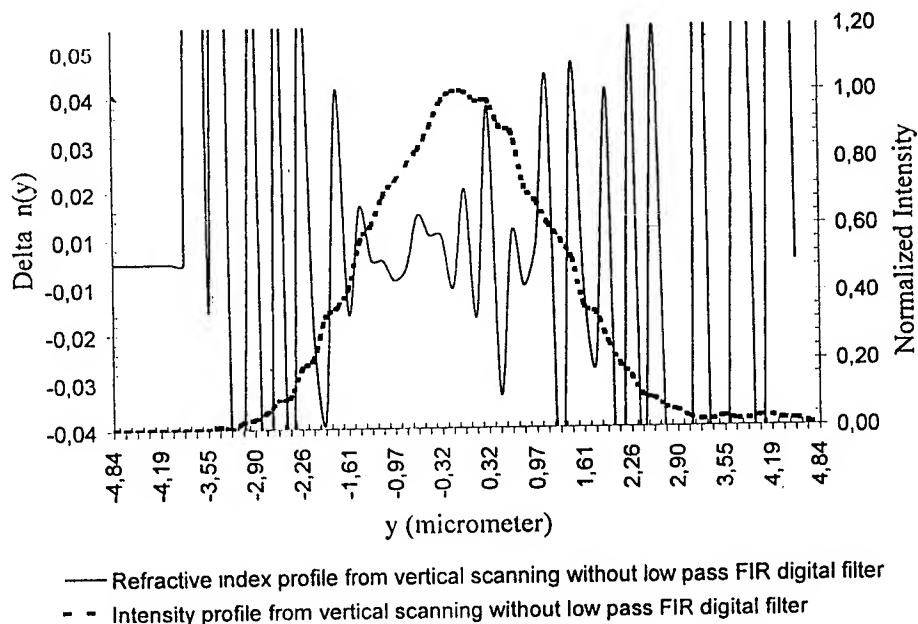


Figure 5. Refractive index reconstruction from near-field intensity processing with back ground noise subtraction and gamma correction using the inverse Helmholtz equation without low pass FIR digital filtering.

Inverse Helmholtz equation algorithm was applied to reconstruct its refractive index profile and the result were shown in Fig. 5. The reconstructed refractive index profile was oscillating and that was different from its actual refractive index profile. Obviously problems arise because high spatial frequency noise has not been removed by background noise subtraction and gamma correction preprocessing. Thus the refractive index profile reconstruction is impossible without filtering the high spatial frequency noise of the near-field image.¹²

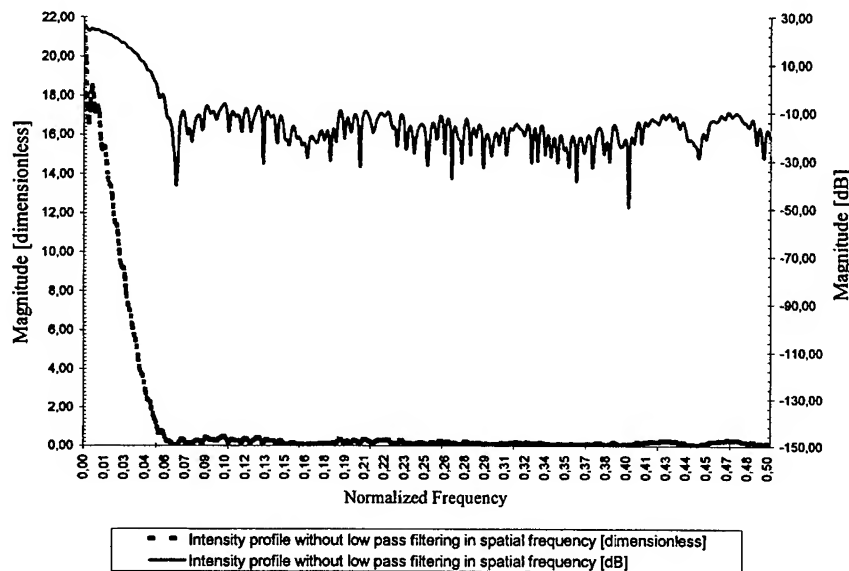


Figure 6. Intensity profile with back ground noise subtraction and gamma correction but without low pass FIR digital filtering in spatial frequency.

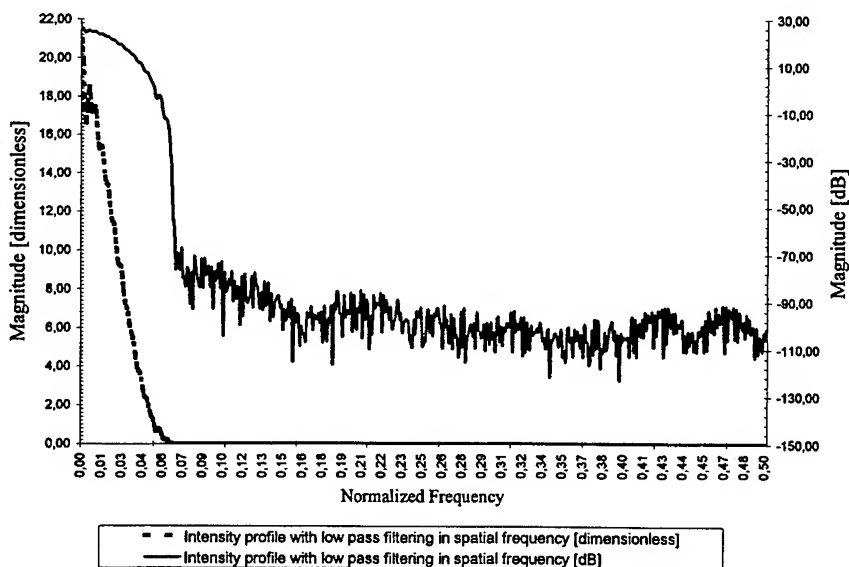


Figure 7. Intensity profile with back ground noise subtraction, gamma correction, and low pass FIR digital filtering in spatial frequency.

Authors will use the low pass FIR digital filter to remove this noise. The filter is selected because of its simplicity, stability, and linearity phase response. FIR is a realization from iteration of convolution integral in discrete form. Input parameter to the filter can be determined after transforming the discrete intensity data from spatial domain to spatial frequency. The transformation is efficiently carried out using FFT by implementing decimation in space algorithm.

Fig. 6 shows the intensity profile without low pass filtering which is transformed from spatial domain to spatial frequency. There were many ripples that represent the high frequency noises in the measured intensity profile. These ripples were not appeared after applying low pass FIR digital filter algorithm, as demonstrated in Fig. 7. The low pass filter removes spatial frequency components from the data in the spatial frequency that are higher than the cycle-period cutoff value. The reconstructed profile became progressively flatter, and smeared out.

In the low pass FIR digital filter algorithm, authors have to select the best window among rectangular window, Bartlett window, Hamming window, Hanning window, and Blackman window. By optimizing the input parameters of this algorithm, Hamming window and Hanning window show the best result for low pass filtering. The low pass FIR digital filtering using Hamming window is demonstrated in Fig. 7, with input parameters $N_c=75$, $N_r=70$, $K_c=-49.085$ dB, and $K_r=-30.472$ dB.

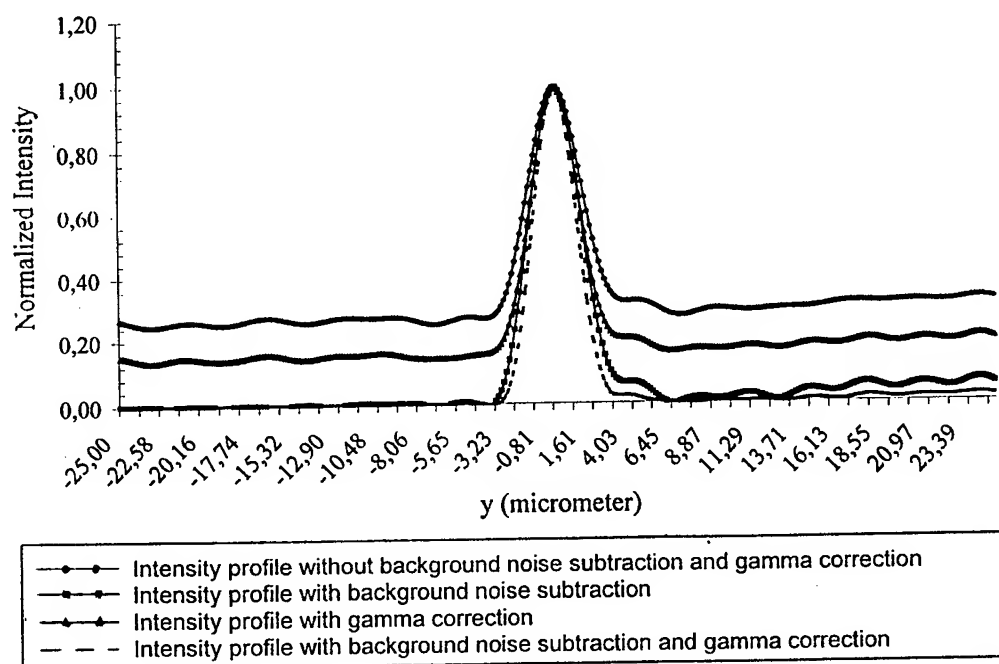


Figure 8. Intensity profiles of a surface channel waveguide with low pass FIR digital filtering.

After the high spatial frequency noises were removed, the filtered intensity profiles were smoother and the oscillation of adjacent pixels were reduced, as shown in Fig. 8. These changes made it possible to reconstruct the refractive index profiles using the inverse Helmholtz equation. Analytically, the second derivative calculation to the data in Eq. (10) will not be oscillated anymore, since the curve is progressively smoother.

Tabel 1. Comparison of maximum fluctuation change of adjacent pixels after low pass filtering

No.	Intensity profile of surface channel waveguide	Maximum fluctuation change (%)
1.	Without background noise subtraction and gamma correction	42.19
2.	With only background noise subtraction	42.69
3.	With only gamma correction	25.78
4.	With background noise subtraction and gamma correction	31.17

Tabel. 1 shows that low pass filter will reduce maximum fluctuation change of adjacent pixels, varied in the range 25.78% to 42.69%. Gamma correction (25.78%) reduced oscillations better than background noise subtraction (42.69%), and visually in Fig. 8, intensity profile with only gamma correction is smoother than intensity profile with only background noise subtraction.

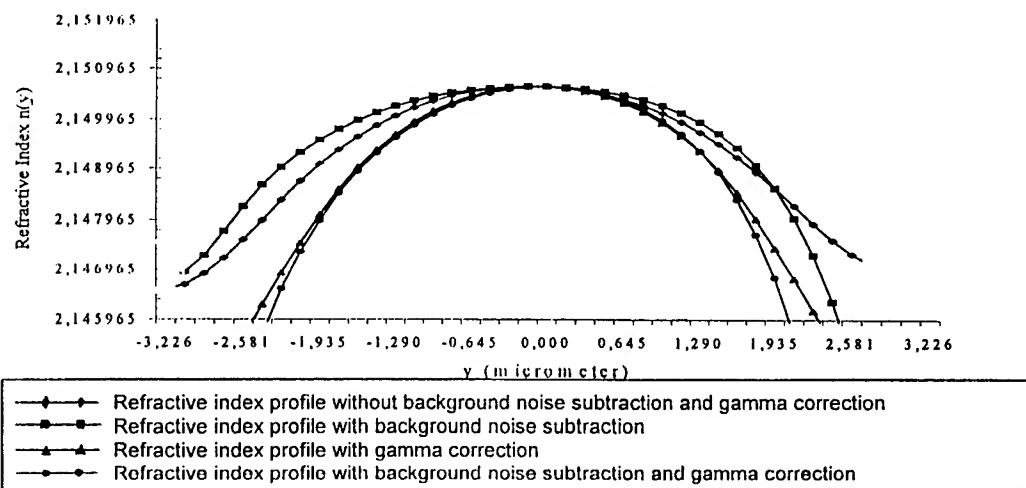


Figure 9. Refractive index reconstructed from near-field intensity processing with back ground noise subtraction, gamma correction, and low pass FIR digital filtering using the inverse Helmholtz equation.

A plot of a refractive index profile with low pass FIR digital filtering were shown in Fig. 4 for the same waveguide. The maximum refractive index values were nearly the same of $n_{\max}(y)=2.15061$ and $\Delta n_{\max}=0.004645$ or 0.216%. Refractive index profile with background subtraction and gamma correction was narrower than the other profiles. Gamma correction was better than background noise subtraction in reconstruction because refractive index profile with gamma correction was nearly the same with the refractive index profile with background noise subtraction and gamma correction.

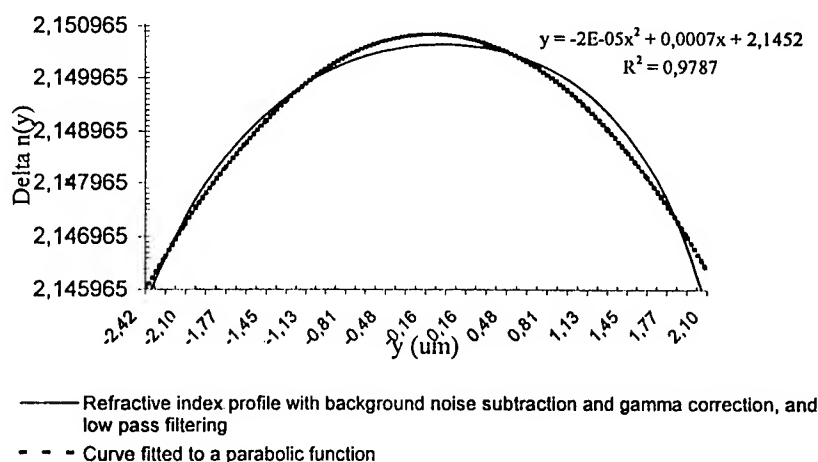


Figure 10. Curve fitting of reconstructed refractive index profile to a parabolic function

The reconstructed refractive index profile fit very well to a parabolic equation, as demonstrated in Fig. 10, but the method can be simply extended to other ones such as erf profiles and erfc profiles, which may occur under different diffusion circumstances. The coefficients were calculated using a Gauss-Newton algorithm. The approximation was carried out between the maximum value and as far as possible below the point of inflection. The result showed determinant value $R^2 = 0.9787$.

5. CONCLUSIONS

In this paper we have investigated the non-destructive refractive index reconstruction method for a single mode surface channel waveguide by processing near-field intensity pattern through inverse Helmholtz equation. We showed that the refractive index profile reconstruction is impossible without filtering the high spatial frequency noise of the near-field image. We found that a signal processing through low pass FIR digital filtering using window function by means of a Fast Fourier Transform can be used to remove high spatial frequency noise. The filtered intensity profiles were smoother and the oscillation of adjacent pixels were reduced. By optimizing the input parameter of this algorithm, Hamming window and Hanning window show the best result for low pass filtering. The reconstructed refractive index profile fit well to a parabolic function, as demonstrated in Fig. 10, but the method can simply extended to other ones.

ACKNOWLEDGMENTS

First author wishes to thank Mr. Danny Handoko, staff and students of the Electrical Engineering Department at the Pelita Harapan University for technical assistance and encouraging this paper. Second author would like to thank Dr. Indrajaya P. Januar of University of Indonesia for providing the waveguide sample.

REFERENCES

1. W. Charczenko, I.P. Januar, and A.R. Michelson, "Modelling of proton-exchanged and annealed waveguides and directional couplers", *J. Appl. Phys.*, Vol. 73, No. 7, pp. 3139-3148, 1993.
2. P.D. Townsend, "Optical effects of ion implantation", *Rep. Prog. Phys.*, Vol. 50, pp. 501-588, 1987.
3. Y. Dai, T. Okamoto, I. Yamaguchi, and M. Iwaki, "Optical characterization of ion-implanted glass surface layers with surface plasmon resonance method", *Japan J. Appl. Phys.*, Vol. 32, pp. L1269-L1272, 1993.
4. D. Gloge and E.A. Marcatili, "Multimode theory of graded core fibers", *Bell. Syst. Tech. J.*, Vol. 52, No. 9, pp. 1563-1578, 1973.
5. P.J. Chandler and F.L. Lama, "A new approach to the determination of planar waveguide profiles by means of a nonstationary mode index calculation", *Optica Acta*, Vol. 33, No. 2, pp. 127-143, 1986.
6. Q. Zhong and D. Inniss, "Characterization of the light guiding structure of optical fibers by atomic force microscopy", *J. Lightwave Technology*, Vol. 12, pp. 1517-1523, 1996.
7. J.M. White and P.F. Heidrich, "Optical waveguide refractive index profiles determined from measurement of mode indices: A simple analysis", *Appl. Opt.*, Vol. 15, pp. 151-155, 1978.
8. J. Noda, M. Minakata, S. Saito, and N. Uchida, "Precise determination of refractive index and thickness in the Ti-diffused LiNbO₃", *J. Opt. Soc. Amer.*, Vol. 68, pp. 1690-1693, 1978.
9. J. Steffen, A. Neyer, and E. Voges, "Direct measurement of refractive-index profiles of Ti: LiNbO₃ planar and stripe waveguides by reflectivity profiling", *GWO 1989 Tech. Dig. Ser.*, Vol. 4, pp. 121-124.
10. W. Freude and A. Sharma, "Refractive-index profile and modal dispersion prediction for a single-mode optical waveguide from its far-field radiation pattern", *J. Lightwave Technology*, Vol. LT-3, pp. 628-634, 1985.
11. Mark L. von Bibra and Ann Roberts, "Refractive index reconstruction of graded index buried channel waveguides from their mode intensities", *J. Lightwave Technology*, Vol. 15, pp. 1695-1699, 1997.
12. H. Susanto, "Rekonstruksi profil indeks bias pandu gelombang dengan pengolahan citra medan dekat", *Undergraduate Thesis*, Electrical Engineering Department, University of Pelita Harapan, 1999.
13. H.P. Uranus and I.P. Januar, "Pengukuran power ratio dari divais fotonik berkeluaran banyak melalui pengolahan citra medan dekat", *Proceeding of National Seminar on Optoelektronics*, Jakarta, Indonesia, August 27-28, 1997.
14. Jochen Helms, Joachim Schmidtchen, Bernd Schuppert, and Klaus Petermann, "Error analysis for refractive-index profile determination from near-field measurements", *J. Lightwave Technology*, Vol. 8, No. 5, pp. 625-633, May 1990.
15. S.C. Chapra and R.P. Canale, *Numerical Methods for Engineers*, 2nd ed. Singapore: Mc. Graw-Hill, 1990.
16. H.P. Uranus, I.P. Januar, and A. Ahmad, "Perangkat lunak untuk observasi and akuisisi data pengukuran pola medan dekat optik", *Proceeding of Jakarta Physics Seminar*, Puspiptek, Serpong, Indonesia, September 18, 1996.

A numerical study of beam propagation in multilayer planar waveguide with optically nonlinear medium

H. Harsoyono ^a, R.E. Siregar ^b, A. Soehiani ^a and M.O. Tjia ^a

^a Department of Physics, FMIPA - ITB,
Jln. Ganesha 10, Bandung 40132, Indonesia

^b Department of Physics, FMIPA - UNPAD,
Jln. Raya Jatinangor, Sumedang, Indonesia

Key words: nonlinear optical effect, IDRI, planar waveguide, all optical directional coupler, optical switch.

ABSTRACT

The extended coupled mode equation incorporating the intensity dependent refractive index (IDRI) nonlinear optical effect of the medium was applied to a basic study of beam propagation in a symmetrically configured five-layer planar structure composed of two optically coupled waveguides with identical optically nonlinear guiding media. The three cladding layers are constituted of linear optical materials of the same refractive index. The result of this study and the result of simulation employing an extended Finite-Difference Beam Propagation Method explicitly demonstrate the feasibility of developing an optical device serving both as an all optical directional coupler and optical switch using the basic multilayer planar structure considered in this study. Restricting ourselves to the lowest TE waveguide modes, the power transfer efficiency and coupling length L_c were determined and described as functions of the input light intensity and the waveguide parameters such as the waveguide separation and the refractive indices.

1. INTRODUCTION

The properties of wave propagation in a dielectric waveguide have been intensively studied for a long time, resulting in detailed understanding of the phenomena as well as a large number of practical devices ^{1,2}. One of the most widely adopted approaches for these studies is the Beam Propagation Method (BPM) which provides the practical numerical tool for modeling and simulation of electromagnetic wave propagation in homogenous as well as inhomogenous waveguide structures. One of its versions, the Finite Difference BPM (FD-BPM), has proved particularly adaptable for such studies in a variety of waveguide configurations, involving various combinations of guiding media and cladding materials, including nonlinear guiding media.

Wave propagation in optically nonlinear planar waveguide has also received considerable interest recently ^{2,3}, owing to its promising applications to optical devices employed in optical communication and optical computation. Many of these studies are also benefited by the proper use and extension of the Beam Propagation Method. Most of the studies undertaken so far have been confined however to single waveguide configuration ^{4,5,6,7}. A number of researches have also been addressed to the problem of mode coupling between the confined modes of two different and separate waveguides ^{8,9,10,11}. These investigations are either limited to eigen value solutions for the transversal field distributions, lacking the full description of its variation along the propagation path, or restricted to power coupling behavior along the propagation length without description of its field distribution. Further, even those studies concerned with device applications mainly addressed themselves to single function operation.

In this work, a study of wave coupling is carried out on the basis of extended coupled mode equation along with the simulations of the coupled-wave propagation by means of Menufast program ¹² which is an extended version of the

forward FD-BPM originally developed for solving the paraxial wave equation in optically linear media¹³. These extended equation and program incorporate the optically nonlinear effect of intensity dependent refractive index (IDRI) arising from the third order nonlinear optical effect, and they are applied to the study of scalar wave propagation in a symmetrical two-slab waveguide structure containing lossless Kerr guiding media. It will be shown that the result , extending that of a previous study¹, exhibits interesting mode coupling behaviour potentially useful for both directional coupling and optical switching operations, and may offer a simpler alternative design to those employing Stimulated raman Scattering¹⁴ and fiber grating^{15,16}.

2. THE COUPLED MODE EQUATIONS

We consider the coupling between two fundamental modes associated respectively with each of the parallel waveguides depicted in Fig.1. The five-layer planar structure shown in this figure is a symmetrical system in terms of geometrical as well as material configurations. The coupled wave propagation along the waveguide (z-axis) is governed by the following equation for the spatial part of the waveguide field

$$\left(\frac{\partial^2}{\partial x^2} + \frac{\partial^2}{\partial z^2} + \omega^2 \epsilon_c + \omega^2 \Delta \epsilon_1 + \omega^2 \Delta \epsilon_2 + 3\chi_{yyy}^{(3)} \omega^2 \epsilon_0 (|E_1(x,z)|^2 + |E_2(x,z)|^2) \right) E(x,z) = 0 \quad (1)$$

where $E_1(x,z)$ and $E_2(x,z)$ are the solution fields of respective waveguides correspondingly labeled in the figure. The constant $\omega^2 \mu \epsilon_c = k^2$ represents the free wave propagation constant (k) and ϵ_c = permittivity of the cladding material , while $\Delta \epsilon_1$ and $\Delta \epsilon_2$ denote the deviations of dielectric constant in the respective guiding media with respect to ϵ_c , and $\chi^{(3)}$ is the third order susceptibility parameter related to the Optical Kerr effect. To this equation one can write the general solution describing the coupled mode propagation of two guided waves in the form,

$$E_y(x,z) = A_1(z) E_1(x) \exp(-i\beta_1 z) + A_2(z) E_2(x) \exp(-i\beta_2 z), \quad (2)$$

The individual waveguide field $E_m(x,y)$ in eq.(2) satisfies the following eigen value equation

$$\left[\frac{d^2}{dx^2} + \omega^2 \mu \epsilon_c + \omega^2 \mu \Delta \epsilon_m - \beta_m^2 \right] E_m(x) = 0; \quad m = 1, 2 \quad (3)$$

with the appropriate boundary value conditions. For the corresponding electric field in the cladding, the associated eigen value equation is given by

$$\left[\frac{d^2}{dx^2} + \omega^2 \mu \epsilon_c - \beta_m^2 \right] E_m(x) = 0; \quad (4)$$

These eigen modes are supposed to satisfy also the orthonormality relation

$$\int E_m^* E_l dx = \frac{2\omega\mu}{|\beta_m|} \delta_{lm} \quad (5)$$

Substituting eq.(2) for $E_y(x,z)$ in eq.(1), and making use of eq.(3) as well as the assumption of slow variation of mode amplitudes over z , we obtain the follow equation

$$\begin{aligned}
& -2i \sum_m \beta_m \frac{dA_m(z)}{dz} E_m(x) \exp(-i\beta_m z) + \omega^2 \mu \sum_{m,n} \Delta \epsilon_m A_n(z) E_n(x) \exp(-i\beta_m z) + \\
& 3\omega^2 \mu \epsilon_0 \chi^{(3)} \left[\sum_m |A_m(z)|^2 A_m(z) |E_m(x)|^2 E_m(x) \exp(-i\beta_m z) + \right. \\
& \left. \sum_{m,n} |A_m(z)|^2 A_n(z) |E_m(x)|^2 E_n(x) \exp(-i\beta_n z) \right] = 0
\end{aligned} \quad (6)$$

where $m, n = 1, 2$, and the terms with $m = n$ are excluded in the double summations. Taking the scalar product of eq.(3) with $E_1^*(x)$ and $E_2^*(x)$ respectively, and introducing the notations $a_1(z) = A_1(z) \exp(i(\beta_1 + K_{11})z)$, $a_2(z) = A_2(z) \exp(i(\beta_2 + K_{22})z)$ we arrive finally at the couple-mode equations

$$da_1(z)/dz = -iK_{12} a_2(z) \exp(i\Delta\beta z) - i(Q_{11} |a_1(z)|^2 + Q_{12} |a_2(z)|^2) a_1(z) \quad (7)$$

$$da_2(z)/dz = -iK_{21} a_1(z) \exp(-i\Delta\beta z) - i(Q_{22} |a_2(z)|^2 + Q_{12} |a_1(z)|^2) a_2(z) \quad (8)$$

where $\Delta\beta = (\beta_1 + K_{11}) - (\beta_2 + K_{22})$, while K and Q are the coupling coefficients defined by

$$K_{11} = \omega/4 \int E_1^* \Delta \epsilon_2 E_1 dx \quad K_{22} = \omega/4 \int E_2^* \Delta \epsilon_1 E_2 dx \quad (9)$$

$$K_{12} = \omega/4 \int E_1^* \Delta \epsilon_1 E_2 dx \quad K_{21} = \omega/4 \int E_2^* \Delta \epsilon_2 E_1 dx \quad (10)$$

$$Q_{11} = \omega n_{2c} n_0 \epsilon_0 \int |E_1|^4 dx \quad Q_{22} = \omega n_{2c} n_0 \epsilon_0 \int |E_2|^4 dx \quad (11)$$

$$Q_{12} = \omega n_{2c} n_0 \epsilon_0 \int |E_1|^2 |E_2|^2 dx \quad (12)$$

In arriving at the expressions for Q_{mn} 's, we have made the approximation $3\chi^{(3)} \approx 4 n_{2c} n_0$ where n_{2c} and n_0 are related to the intensity dependent refractive index by the equation $n_{NL} = n_0 + 2 n_{2c} |E|^2$. The coupling coefficients can be readily evaluated by using eigen functions $E_1(x)$ and $E_2(x)$ for the two parallel nonlinear planar waveguides. For the special case of two identical waveguides with $\Delta \epsilon_1 = \Delta \epsilon_2 = \Delta \epsilon$ and the same guide widths ($t_1 = t_2 = t$), we have $K_{11} = K_{22} = K_1$, $K_{12} = K_{21} = K_2$, $Q_{11} = Q_{22} = Q_1$, $Q_{12} = Q_2$ and $\beta = \beta_1 = \beta_2$. The linear coupling coefficient K_2 is given explicitly by¹⁷

$$K_2 = \frac{2h^2 p e^{-ps}}{\hat{a} t(h^2 + p^2)} \left[\frac{2\pi}{\lambda} \right]^2 \frac{\Delta \epsilon}{\epsilon_0} \quad (13)$$

where s denotes the waveguide separation, while h and p are the eigen values associated with eigen functions in the waveguide and in the cladding respectively. These parameters are related to the propagation constant β in accordance with eqs.(3) and (4)

$$h = \left[\omega^2 \mu \epsilon_c + \omega^2 \mu \Delta \epsilon - \beta^2 \right]^{1/2} \quad (14)$$

$$p = \left[\beta^2 - \omega^2 \mu \epsilon_c \right]^{1/2} \quad (15)$$

In order to solve for $a_i(z)$ in eq. (7), one must calculate the coefficient K_1 , K_2 , Q_1 and Q_2 using the fundamental-mode solutions of the two guides within guide 1 as given by the expressions

$$E_1(x) = C \left[\cos(hx) - \frac{p}{h} \sin(hx) \right] \quad (16)$$

$$E_2(x) = C [\exp(-ps)] \exp[-h(x+t)] \quad (17)$$

The constant $C = 2h(\omega\mu)^{1/2} \{ [t + 2/p](h^2 + p^2) \}^{-1/2}$ is a normalization constant. The coupling coefficients Q_1 and Q_2 arise respectively from the nonlinear interaction of a mode with itself (self effect) and with a mode from the other waveguide. It is clear from eq.(7) and eq.(10) that propagation of a single mode guided wave in each waveguide is influenced by the linear coupling coefficient K_2 as well as the nonlinear coupling coefficients Q_1 and Q_2 .

3. A PRACTICAL SOLUTION AND ITS CHARACTERISTICS

The basic operation of most of the non-linear coupled mode devices can be formulated by equations (7) and (8). The solution fields of these equations generally involves the Jacobian elliptic integrals, and they are much more complicated than those of the linearly coupled cases. However in the special case of practical interest considered here, the total power P_t is initially launched into guide 1 at $z = 0$, namely $P_1(0) = P_t$ and $P_2(0) = 0$. In this case the power in guide 1 at an arbitrary point z along the guide can be simply expressed in terms of a Jacobian elliptic integral of the first kind given below¹

$$P_1(K_2 z) = P_1(0) [1 + \text{cn}(2K_2 z|m)]/2 \quad (18)$$

In this equation, $\text{cn}(u|m)$ represents a Jacobian elliptic integral, where $u = 2K_2 z$ and m is the modulus of the associated elliptic integral. In this case, m is given by $m = P_1(0)/P_c$, where P_c is the critical power defined by

$$P_c = 4K_2/(Q_1 - 2Q_2) \quad (19)$$

Based on eq.(18) and the well known properties of the Jacobian elliptic integral, one readily observes that a near perfect transfer of power from waveguide 1 to waveguide 2 can only take place for very low input power ($m \approx 0$), since $\text{cn}(u|m) = \cos u$ at this limit. On the other hand, an even (50/50) power distribution between the two waveguides can be attained for $m = 1$ after the light traverses a certain length, as governed by the corresponding expression $\text{cn}(u|1) = \text{sech } u$. For large enough values of m ($m \gg 1$), no significant power transfer takes place along the guide. It is clear then, that a variety of operational functions of the device can be effectively controlled by the incoming light intensity. However, the detailed performance of the device depends further on the material property and the waveguide structure as described below.

For simplicity, we shall only consider the effect of geometrical factors in the following discussion. It should be clear that the most crucial parameter determining the coupling characteristics is the critical power P_c given by eq.(19). Knowing this and the total input power will allow the description of $P_1(Z)$ in terms of the parameter m where $Z = K_2 z$. This critical power is calculated by using eq.(11) for Q_1 and eq.(12) for Q_2 , whereas the linear coupling coefficient K_2 can be found by eq.(13), with p and h given by eqs.(14) and (15). For this calculation, we restrict ourselves to the fundamental guided modes corresponding to three different guide widths $t = 2.500 \mu\text{m}$, $3.000 \mu\text{m}$, $3.500 \mu\text{m}$, for which we have $\beta/k_0 = 2.57530$, 2.57532 and 2.57534 respectively.

The resulted P_c is plotted in Fig.2 as a function of waveguide separation s for various t 's. It is seen that P_c generally decreases with increasing s , but increases with decreasing t for given $\Delta\epsilon$. This is consistent with our understanding of P_c as a measure of coupling strength between two guides. From this figure, one can determine the initial total power required to operate the nonlinear waveguide for a specific function. This information will be needed later for our wave propagation simulation program.

For the time being we shall illustrate in Fig.3 the different behaviors of $P_1(Z)/P_c$ as a function of $Z = K_2 z$ for various values of m . For a certain t and s , Fig.3 clearly shows that for low input power ($m < 1$), complete transfer of power between the guides will take place periodically, with longer period for larger value of m . As the value of m becomes equal to 1, one observes a sudden switch of behavior to one resembling the operation of 50/50 power divider or 3-dB directional coupler. When the input power is further increased well above $m = 1$, a major part of the initial power will be retained in the launching waveguide, with remaining fraction of the power oscillating in and out of the guide. A higher value of m leads to more rapid oscillation with smaller amplitude. From these intensity-induced variation of behavior one can readily envision various optical coupling and gating functions generated by this simple nonlinear planar structure. Changing the structural parameters t, s leads to different value of P_c as depicted in Fig.2. This simply means that the same

functions described above will be implemented by different total input power in compliance with the corresponding m values.

As a final note of this section, it is important to point out that departing from $m = 1$, the function of 50/50 power divider can still be realized, as long as the system is operated with the appropriate length. This together with the other m -dependent features should be properly taken into account in the design of a realistic device as will be illustrated in the following section.

4. SIMULATION OF BEAM PROPAGATION

In the following, a specific illustration will be given of the feasibility of operating the waveguide system as an “on-off” switch as well as a 3-dB divider. For this purpose, we have chosen the following reasonably realistic waveguide parameters; namely, $n_c = 2.575$, $n_{o1} = 2.580$, $t = 3.0 \mu\text{m}$, $s = 3.0 \mu\text{m}$ and $\lambda = 1.06 \mu\text{m}$. This choice of parameters leads to the critical power of $P_c = 4.1 \text{ (W/m)}$, and a linear coupling coefficient of $K_2 = 6.3 \text{ (1/cm)}$. As shown in Fig.4, at the high and low input powers, $P_1(0) = 7.874 \pm 0.025 \text{ (W/m)}$ and $P_1(0) = 2.849 \pm 0.062 \text{ (W/m)}$, for which $m = 1.927 \pm 0.025$ and $m = 0.695 \pm 0.015$ respectively, this waveguide is capable of functioning as an “on - off” switch with a 100% transfer of power from guide 1 to guide 2 occurring at $z = L_c = 2.500 \text{ mm}$ known as the coupling or transfer length. This transfer is estimated to take about 15 ps to complete, given an instantaneous response of The Kerr medium. For $P_1(0) = 4.098 \pm 0.002 \text{ (W/m)}$, which corresponds to $m = 0.999 \pm 0.001$, this waveguide operates effectively as a 3 dB power divider with the same length of the guide. All these optically control functions are realized by the waveguide of a fixed configuration. Thus, this result demonstrates the possibility of designing a planar waveguide configuration which could function either as an “on-off” switch or a 3 dB power divider, depending only on the input light intensity.

In order to substantiate the above illustration, a full description of the field evolution along the guide is given below as a result of applying the MenuFast simulation program developed previously by Hoekstra et.al.¹². The results are described in Figs. 5, 6 and 7 respectively for “low”, “high” and “medium” input powers respectively. Fig. 5 clearly shows that complete wave transfer from guide 1 to guide 2 occurs at the propagation distance $L_c = \pi/(2K_2) = 2.500 \text{ mm}$ as indicated in Fig.4. This corresponds to the familiar crossed state of a phase-matched coupler, and under phase-matched conditions, power transfer occurs periodically with z as already expected from Fig.3. In the case of high input power as shown in Fig.6, no significant wave transfer takes place from guide 1 to guide 2 as long as the value of m is well above 1. On the other hand, when input power $P_1(0) = P_c$, Fig.7 demonstrates the function of a 3 dB directional coupler in agreement with Fig.4, in which case the input power in guide 1 becomes evenly divided between the waveguides again at a distance of $L_{3dB} = 2.500 \text{ mm}$.¹⁸

5. CONCLUSION

The results of this study clearly demonstrate the feasibility of developing an optical device serving both as an all optical 3-dB coupler and optical switch employing a symmetrical multilayer planar structure with optically nonlinear guiding media. At low intensity, the light excited in one guide couples over to the other waveguide with a near 100% efficiency. At high intensity, the intensity enhanced nonlinear index detunes the waveguides, and the coupling is blocked. Working at a medium intensity, the same system functions as a 50/50 power divider. Our numerical simulation further indicates that the model system considered here exhibits a certain tolerance for variations in the input intensity, and thus implying the possibility of fulfilling a relatively robust performance of this system by developing a more suitable set of guide parameters.

ACKNOWLEDGEMENT

This work was partially supported by a research Project of *Hibah Tim Pascasarjana* (URGE) Directorate General of Higher Education, The Indonesian Ministry of Education and Culture, under the Contract No. 004/HTTP-II/URGE/1996. We wish to thank Dr.H.J.W.M. Hoekstra of Twente University Netherlands for allowing to use the Menufast program and valuable comments.

REFERENCES

1. Stephen M. Jensen, "The Nonlinear Coherent Coupler", *IEEE Journal of Quantum Electronics*, Vol. QE-18, NO. 10, pp. 1580 - 1583, October 1982.
2. T. Tamir, *Topics in Applied Physics - Integrated Optics*, Vol. 7, Springer-Verlag, Berlin Heidelberg, New York, Tokyo 1979.
3. Michael Cada, John D. Begin, "An Analysis of a Planar Optical Directional Coupler with Losses Kerr-like Coupling Medium", *IEEE Journal of Quantum Electronics*, Vol. 26, No. 2, pp. 361-371, February 1990.
4. Toshiyuki Sakakibara and Naomichi Okamoto, "Nonlinear TE Waves in a Dielectric Slab Waveguide with Two Optically Nonlinear Layers", *IEEE Journal of Quantum Electronics*, Vol. QE-23, No. 12, pp. 2084-2088, December 1987.
5. Weiping Huang, Chenglin Xu, Sai-Tak Chu, and Sujeet K. Chaudhuri, "The Finite-Difference Vector Beam Propagation Method: Analysis and Assessment", *Journal of Lightwave Technology*, Vol. 10, No. 3, pp. 295-305, March 1992.
6. Allan D. Boardman and P. Egan, "Optically Nonlinear Waves in Thin Films", *IEEE Journal of Quantum Electronics*, Vol. QE-22, No. 2, pp. 319-324, February 1986.
7. Li-Pen Yuan, "A Numerical Technique for Determination of the Propagation Characteristics of Nonlinear Planar Optical Waveguides", *IEEE Journal of Quantum Electronics*, Vol. 30, No. 1, pp. 134-138, January 1994.
8. Junji Yamauchi, Jun Shibayama, Minoru Sekiguchi, and Hisamatsu Nakano, "Finite-Difference Beam Propagation Method Based on The Generalized Douglas Scheme for a Nonuniform Grid", *IEEE Photonics Technology Letters*, Vol. 9, No. 1, pp. 67-69, January 1997.
9. M.D. Feit and J.A. Fleck, Jr., "Light Propagation in Graded-Index Optical Fibers", *App. Opt.*, Vol. 17, No. 24, pp. 3990-3998, 1978.
10. G.I. Stegeman, E.M. Wright, "All-Optical Waveguide Switching", *Optical and Quantum Electronics* 22, pp. 95-122, 1990.
11. Yaron Silberberg, George I. Stegeman, "Nonlinear coupling of waveguide modes", *Appl. Phys. Lett.* 50 (13), pp. 801-803, 30 March 1987.
12. H.J.W.M. Hoekstra, G.J.W. Krijnen, and L. Abelman, *Menufast: A Beam Propagation Method Programme*, Transducers and Materials Science, University of Twente - The Netherlands, 11 Sep. 1995.
13. H.J.W.M. Hoekstra, "Theory and Numerical Strategies of BPMs On Beam Propagation Methods for modelling in Integrated Optics", *Optical and Quantum Electronic*, Vol. 29, No. 2, pp. 157 - 171, February 1997.
14. A.N. Staradumov, Yu.O. Barmenkov, A. Martinez, and I. Torres, "Nonlinear Optical Switch Based on Stimulated Raman Scattering", *Optical Fiber Technology* 4, pp. 285-292, 1998.
15. C. Martin De Sterke, N.G. Raphael Broderick, Benyamin J. Eggleton, and M.J. Steel, "Nonlinear Optics in Fiber Gratings", *Optical Fiber Technology* 2, pp. 235-268, 1996.
16. Masaki Asobe, "Nonlinear Optical Properties of Chalcogenide Glass Fibers and Their Application to All-Optical Switching", *Optical Fiber Technology* 3, pp. 142-148, 1997.
17. Pochi Yeh, *Optical Waves in Layered Media*, p. 361, John Wiley & Sons, New York, 1988.
18. Wenjiang Nie, "Optical Nonlinearity: Phenomena, Applications, and Materials", *Adv. Mater.* 5, No. 7/8, pp. 520-545, 1993.

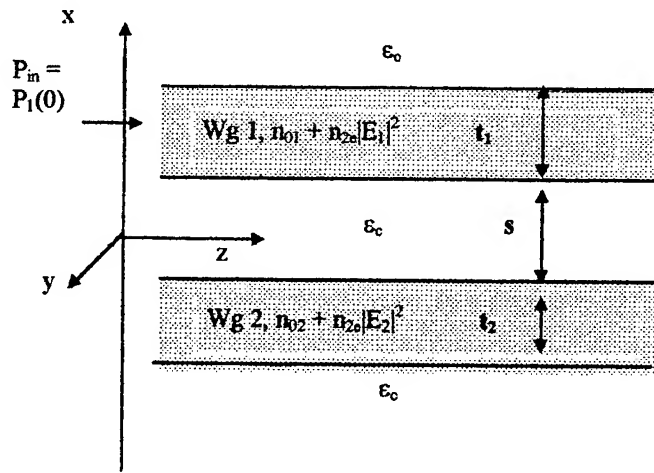


Figure 1: Structure of a symmetrical planar nonlinear directional coupler with its geometrical and material parameters.; $n_{01} = n_c \Delta n_1 = (\epsilon_c/\epsilon_0)^{1/2} + 0.5(\Delta\epsilon_1/\epsilon_0)$ and $n_{02} = n_c + \Delta n_2 = (\epsilon_c/\epsilon_0)^{1/2} + 0.5(\Delta\epsilon_2/\epsilon_0)$

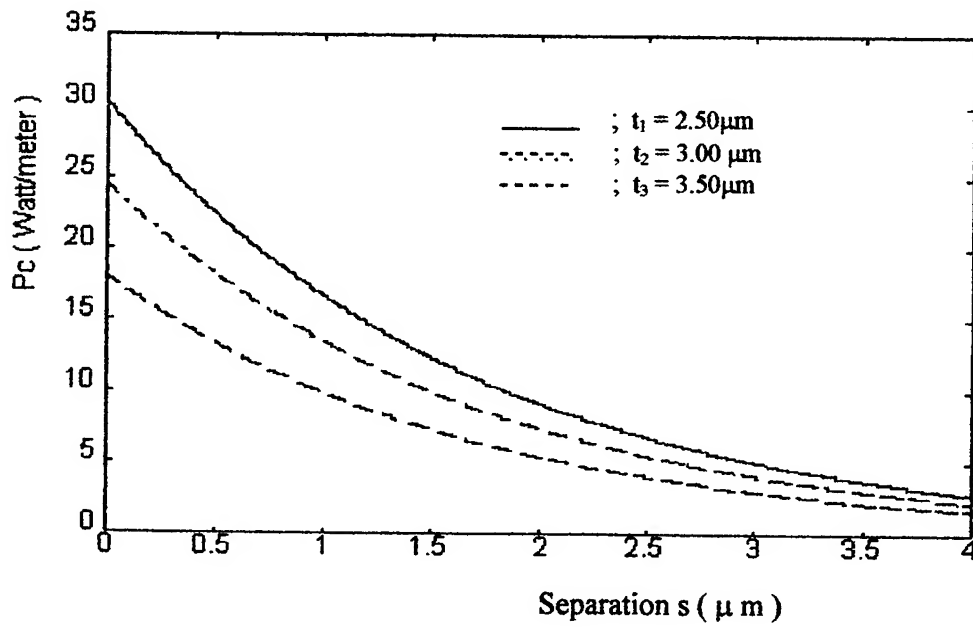


Figure 2: The value of critical power P_c as a function of the separation distances s for various guide widths t .

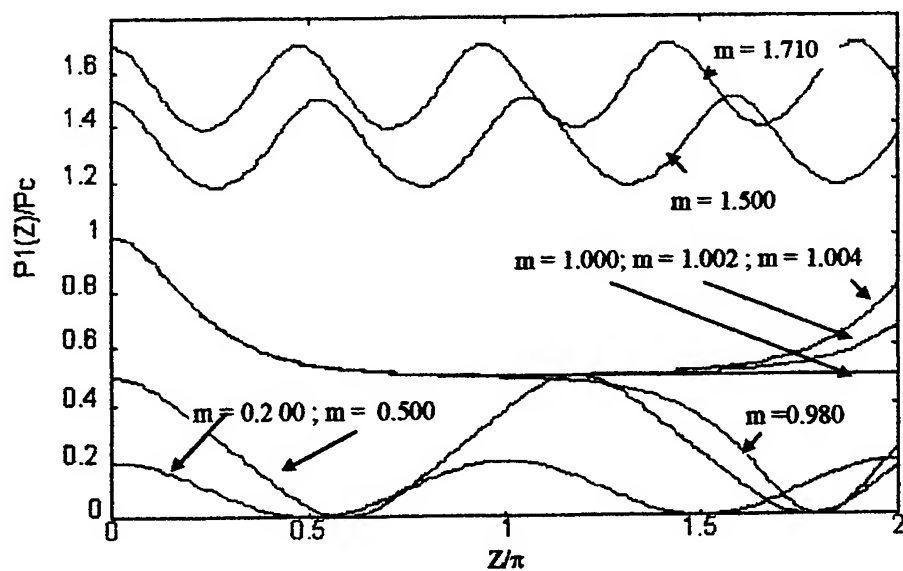


Figure 3: Power propagation as a function of Z/π in guide 1 nonlinear directional coupler for various m .

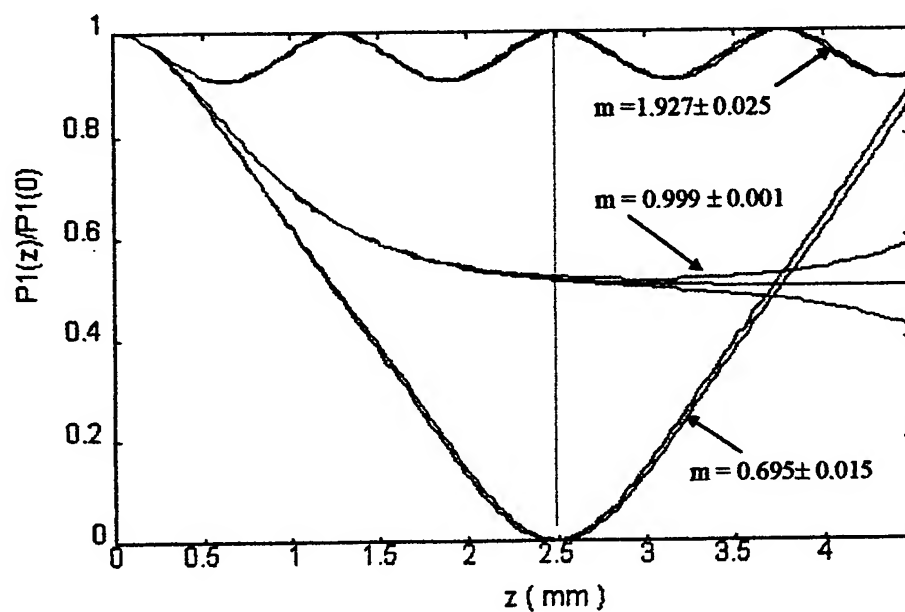


Figure 4: Power variation in guide 1 from the structure displaying functions an "on - off" switch and 3 - dB power divider at $z = 2.5$ mm and various m for $t = 3.0 \mu\text{m}$ and $s = 3.0 \mu\text{m}$ and corresponding m 's.

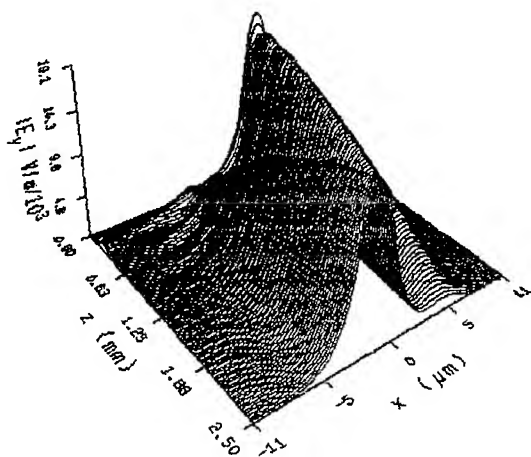


Figure 5 ; 3 - dimensional distribution of field in directional coupler, with $P_c = 4.100$ (W/m) and $P_1(0) = 2.800$ (W/m)

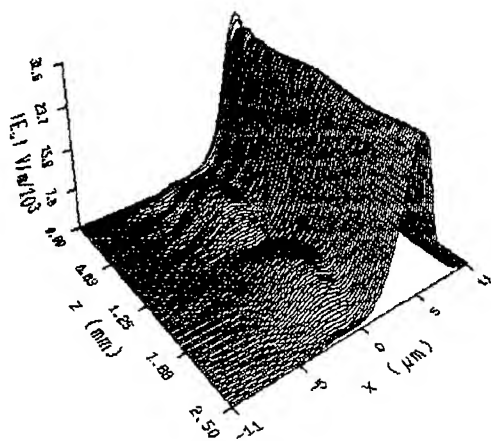


Figure 6 ; 3 - dimensional distribution of field in directional coupler, with $P_c = 4.100$ (W/m) and $P_1(0) = 7.899$ (W/m)

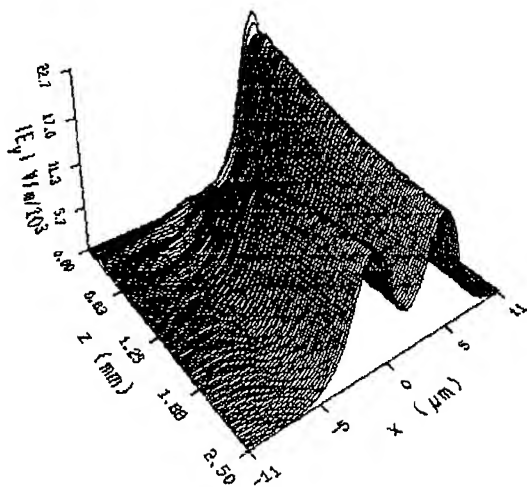


Figure 7 ; 3 - dimensional distribution of field in directional coupler, with $P_c = 4.100$ (W/m) and $P_1(0) = 4.100$ (W/m)

Mode theory and analysis of planar array waveguides

Hongbing LEI*, Haiyan OU, Qinqing YANG, Xiongwei HU, Qiming WANG

State Key Laboratory on Integrated Optoelectronics, Institute of Semiconductors

Chinese Academy of Sciences, Beijing 100083 China

ABSTRACT

Bloch modes can be excited in planar array due to its periodic lateral refractive index. The power coupled into each eigenmode of the array waveguides is calculated through the overlap integrals of the input field with the eigenmode fields of the coupled infinite array waveguides projected onto the x-axis. Low losses can be obtained if the transition from the array to the free propagation region is adiabatic. Due to the finite resolution of lithographic process the gap between the waveguides will stop abruptly, however, when the waveguides come into too close together. Calculation results show that losses will occur at this discontinuity, which are dependent on the ratio of the gap between the waveguides and grating pitch and on the confinement of field in the array waveguides. Tapered waveguides and low index contrast between the core and cladding layers can lower the transmitted losses.

Keywords: Array waveguides grating, Mode theory, Transmitted loss

1. INTRODUCTION

Wavelength division multiplex (WDM) technology is emerging in response to the rapid increase of bandwidth and capacity requirements in communication systems and networks^[1, 2]. In recent years, high performance and sophisticated photonic devices have been developed to meet WDM system requirements. The components based on phased-arrayed waveguide gratings (AWG) represent one of the key enabling technologies for WDM systems^[3-5]. The layout of array waveguides shown in figure 1 has a constant length difference ΔL between neighboring waveguides, which provides additional phase term in the grating equation. The grating equation takes the following form:

$$an_s \sin \theta_i + an_s \sin \theta_o + n_c \Delta L = m\lambda \quad (1)$$

where n_c is the effective refractive index of the array waveguides, n_s is the effective refractive index of free propagation region (FPR), a is the pitch of the grating, θ_i and θ_o are the input and output angles of light wave respectively, m is the diffraction orders and λ is the wavelength.

For properly designed AWG realized with low loss waveguides the total loss is dominated by the loss occurring at the junctions between the array waveguides and the FPR. Low loss can be obtained if the transition from the array to the FPR is adiabatic i.e. if the gap between the waveguides reduces linearly to zero. Due to the finite resolution of the lithographic process the gap between the waveguides will stop abruptly, however, when the waveguides come too close together. At this

*Correspondence: Tel: 86-10-62339511, Fax: 86-10-62322388, Email: lei hb@red.semi.ac.cn

discontinuity the field coming into the array at the input will show a modulation that is dependent on the width of the gap between the array waveguides and on the confinement of the field in the waveguides. Meanwhile at the input besides the fundamental mode, the m th mode ($m \neq 0$) will be excited and part of light wave will be reflected into the FPR.

A tapered waveguide usually be used at the input / output of AWG^[6-9]. The excited light wave passes through the tapered waveguide, and then come into the single mode waveguide, where the couple between waveguides is negligible.

Suppose the waveguide width changes very slowly in the tapered waveguides, so the couple between fundamental mode and m th modes of $m \neq 0$ is negligible, that means no loss takes place in the tapered waveguides. So only the losses at the interface

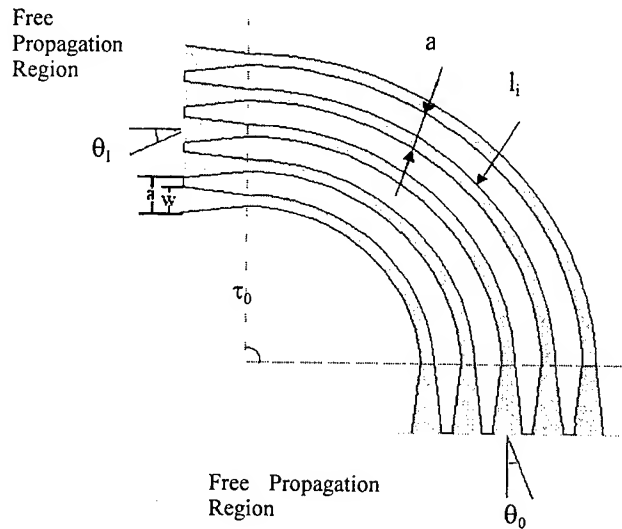


Figure 1. The layout of the array waveguide grating

of the FPR and the AWG have been considered.

The paper mainly discusses the mode distribution of the AWG and the transmission of light wave at the interface of the FPR and the AWG. The transmitted loss and the loss nonuniformity for different incident diffraction angles have been discussed.

2. PROPAGATION OF A BLOCH MODE IN THE AWG

The refractive index distribution of planar array waveguides is shown in Figure 2, where n_1 and n_2 are the refractive indexes of the core and cladding layers respectively, w is the core width and a is the grating pitch. A set of infinite of waveguides composes of the array waveguides.

The field distribution is modeled by solving the following wave equation:

$$\left(\frac{\partial^2}{\partial x^2} + \frac{\partial^2}{\partial z^2} + k^2 \right) \varphi = 0 \quad (2)$$

where φ is the wave function and k is the propagation constant in AWG, which can be derived from

$$k^2 = k_0^2 n^2(x),$$

where k_0 is the propagation constant in vacuum, and $n(x)$ is the refractive index. $n(x)$ changes periodically in the x direction, so k^2 is a periodic function of x , which means:

$$\begin{aligned} k^2(x) &= k_0^2 n^2(x) \\ &= k_0^2 n^2(x+na) \\ &= k^2(x+na) \end{aligned}$$

According to the Bloch theorem, the solution of the equation (2) is a Bloch mode written as:

$$\varphi(\sigma, x) = u(\sigma, x) e^{i\sigma x} e^{i\beta z}$$

where σ and β are the propagation constant in the x and z directions respectively, and $u(\sigma, x) = u(\sigma, x+na)$ is a periodic function of x .

Then in general we will see the mode:

$$\begin{aligned} \varphi(\sigma, x+na) &= u(\sigma, x+na) e^{i\sigma(x+na)} e^{i\beta z} \\ &= u(\sigma, x) e^{i\sigma x} e^{i\sigma na} e^{i\beta z} \\ &= e^{i\sigma na} \varphi(\sigma, x) \end{aligned}$$

In one period ($0 < x < a$), the core refractive index $k_1 = n_1 \cdot k_0$, and the cladding refractive index $k_2 = n_2 \cdot k_0$. With the propagation

$$\left(\frac{\partial^2}{\partial x^2} - \beta^2 + k^2 \right) \varphi = 0 \quad (3)$$

constant β in the z direction, the mode is given by the following wave function:

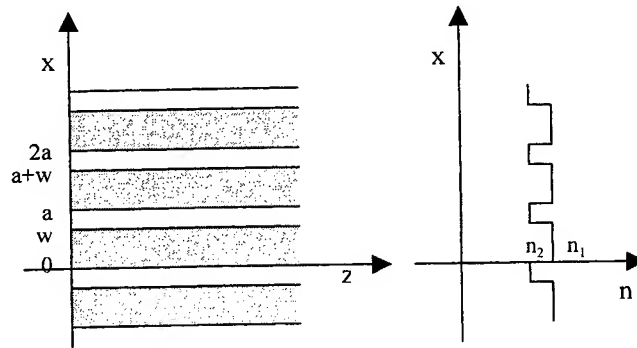


Figure 2. the refractive index distribution of array waveguide (core index n_1 , cladding index n_2)

Because the mode must transmit in the waveguides, β should satisfy the conditions:

$$\begin{aligned} \beta^2 &< k_1^2, \\ \beta^2 &> k_2^2, \end{aligned}$$

Therefore the solution for Eq. (3) is

$$\varphi(x) = \begin{cases} A \exp(ihx) + B \exp(-ihx) & 0 < x < w, n = n_1 \\ C \exp(q(x-w)) + D \exp(-q(x-w)) & w < x < a, n = n_2 \end{cases} \quad (4)$$

where q, h are the real and satisfy following conditions:

$$\begin{aligned} h^2 + \beta^2 &= n_1^2 k_0^2 \\ \beta^2 - q^2 &= n_2^2 k_0^2 \end{aligned}$$

Meanwhile, $\varphi(x)$ and its differentiation should satisfy the boundary conditions:

at $x=w$,

$$\begin{aligned} C + D &= A \exp(ihw) + B \exp(-ihw) \\ Cq - Dq &= ihA \exp(ihw) - ihB \exp(-ihw) \end{aligned}$$

at $x=a$,

$$\begin{aligned} \varphi_{x \rightarrow a^+} &= \varphi_{x \rightarrow 0^+} \cdot \exp(i\sigma a), & \varphi'_{x \rightarrow a^+} &= \varphi'_{x \rightarrow 0^+} \cdot \exp(i\sigma a) \\ (A + B) \exp(i\sigma a) &= C \exp(q(a-w)) + D \exp(-q(a-w)) \\ (ihA - ihB) \exp(i\sigma a) &= qC \exp(q(a-w)) - qD \exp(-q(a-w)) \end{aligned}$$

Solve the above equations, we will get the eigenvalues of β :

$$\beta_0 > \beta_1 > \beta_2 > \beta_3 \dots$$

corresponding eigen modes:

$$\varphi_0, \varphi_1, \varphi_2, \varphi_3 \dots$$

where φ_0 is the fundamental mode.

3. TRANSMISSION FROM THE FPR TO THE AWG

The refractive index changes at the interface of the FPR and the AWG, corresponding eigen mode is the Bloch modes in AWG:

$$(\varphi_0, \varphi_1, \varphi_2, \dots),$$

and the plane wave in FPR:

$$(\phi_0, \phi_1, \phi_2, \dots).$$

The incident plane wave can be written as $A_0 \phi_0(x) \exp(i\beta_0 z)$, the m th Bloch mode transmitted for $z > 0$ can be expressed in a similar way :

$$A_0 T_m \varphi_m(x) \exp(i\beta'_m z)$$

where T_m is the transmission coefficient of the m th mode. By requiring continuity of light field and its differentiation at

$z=0$, one obtains the two conditions:

$$(1 + R_0)\phi_0 = T_0\varphi_0 + \sum_{s \neq 0} (T_s - R_s)\varphi_s + \delta a \quad (6)$$

$$(1 - R_0)\beta_0\phi_0 = \beta'_0 T_0\varphi_0 + \sum_{s \neq 0} \beta'_s (T_s - R_s)\varphi_s + \delta b$$

where

$$\delta a = \sum_{s \neq 0} R_s (\varphi_s - \phi_s), \quad \delta b = -\sum_{s \neq 0} R_s (\beta'_s \varphi_s - \beta_s \phi_s)$$

and it will be assumed that ϕ, φ are normalized.

We solve the above equations by neglecting δa and δb , then multiplication by φ_m , followed by integration over a period, eliminates for $m=0$ all unknowns T_s, R_s except T_0, R_0 , and one obtains:

$$R_0 = \frac{\beta_0 - \beta'_0}{\beta_0 + \beta'_0}, \quad T_0 = \frac{2\beta_0}{\beta_0 + \beta'_0} \frac{(\phi_0, \varphi_0)}{(\varphi_0, \varphi_0)}$$

And for $m \neq 0$,

$$T_m = \frac{(1 - R_0)\beta_0 + (1 + R_0)\beta'_m}{2\beta'_m} \frac{(\phi_0, \varphi_m)}{(\varphi_m, \varphi_m)}$$

$$R_m = \frac{(1 - R_0)\beta_0 - (1 + R_0)\beta'_m}{2\beta'_m} \frac{(\phi_m, \varphi_m)}{(\varphi_m, \varphi_m)}$$

If the differences

$$\begin{cases} \delta u_m = \varphi_m - \phi_m \\ \delta \beta_s = \beta'_m - \beta_s \end{cases}$$

are small, or if $(\beta'_m - \beta_0)/\beta_0 \ll 1$, then $R_m \approx 0$.

These conditions apply to many optical waveguides it is in general satisfied when the refractive index variations are small and $a \gg \lambda$.

Eq. (60) then simplifies to the well-known expression

$$T_m \cong \frac{(\phi_0, \varphi_m)}{(\varphi_m, \varphi_m)} \quad (7)$$

4. TRANSMITTED POWER

For a certain σ value of lateral propagation constant, besides fundamental $\varphi_0(\sigma, r)$, other modes $\varphi_m(\sigma, r)$ ($m \neq 0$) also can be excited. The various modes are orthogonal, normalized and complete. For an incident light $\phi(\sigma, r)$, the excited mode in array waveguide must be $\varphi(\sigma, r)$. When the incident light is in the Brillouin zone of Ω of order $m=0$, ($-\pi < a\sigma < \pi$), the excited modes in array waveguide are dominated by the fundamental mode $\varphi_0(\sigma, r)$. Because the modes $\varphi_m(\sigma, r)$ ($m \neq 0$) in the input

of array waveguide will radiate out while coming into the separated single mode waveguides, we just consider the excitation

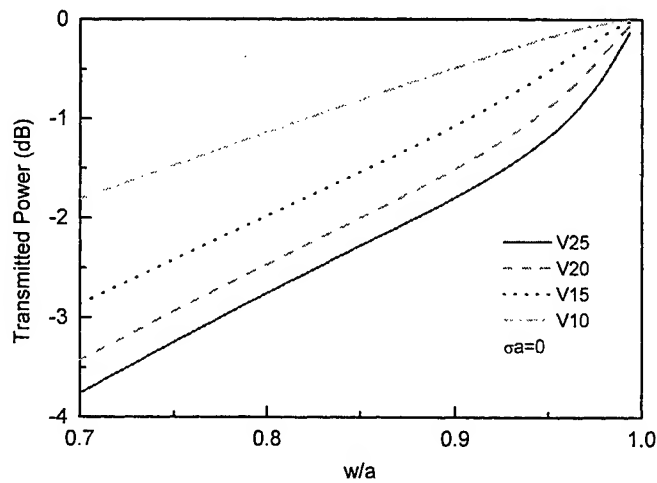


Figure 3. Transmitted power of central wavelength versus the ratio of the waveguides gap to the waveguides pitch. (V parameter: 10, 15, 20 and 25)

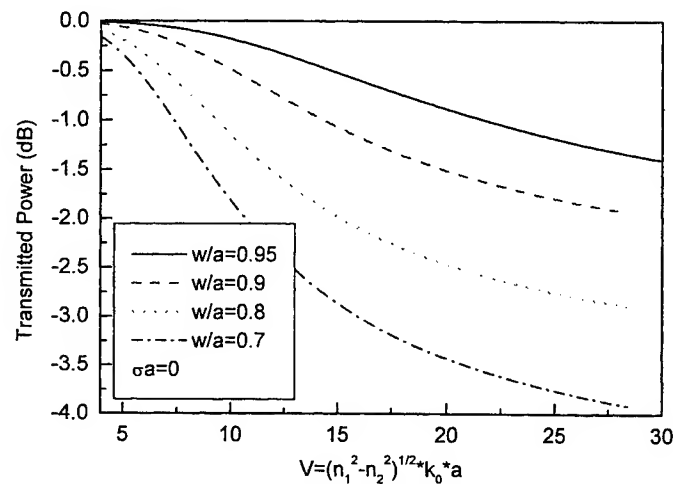


Figure 4. Transmitted power of central wavelength versus the lateral V parameter.

of fundamental mode $\phi_0(\sigma, r)$.

Just consider the fundamental mode and neglect other modes, from Eq (7), one can get the transmitted coefficient of a plane wave into array waveguide approximately written as:

$$T \cong \frac{(\phi_0, \phi_0)}{(\phi_0, \phi_0)}$$

And the transmitted power (in decibel):

$$TP = 20 \log_{10} |T|^2 \quad (8)$$

On the reciprocity grounds, this loss will occur at the output of the array waveguides, which has been considered in Eq. (8).

Central wavelength of AWG is determined by grating equation when both θ_i and θ_o equal to zero ($\sigma a = 0$), the corresponding transmitted power changes with the grating structure (lateral V parameter) and the relation of the gap between neighboring waveguides to the grating period, which is shown in figure 3.

Waveguide width at interface is a in the free propagation region side and w in the array waveguide side. This discontinuity results in the transmitted loss. Transmitted power increases with increase the w/a values. When w/a value rises up to 1, the change of refractive index can be considered as continuous, so the transmitted loss is close to zero dB. Increasing the waveguide core width at the interface (requiring better lithography) can decrease the transmitted loss.

The confinement of waveguide can be described using V parameters. Large value of V parameter means that more m -th modes can be excited in waveguide. As pointed before the m th modes ($m \neq 0$) will radiate out in the single mode waveguide. Thus the transmitted loss increases. The transmitted power versus V parameter for central wavelength is shown in figure 4.

Low transmitted loss can be obtained by reducing the confinement of waveguide, and by adopting low refractive index contrast waveguide. According to the couple theory the modes excited in the waveguide is dependent on the x direction propagation constant, meanwhile the transmitted efficiency T is related to the value of σa . The similar loss exist at the output because of the diffraction loss, which is shown in figure 5. For central wavelength the loss is the lowest, additional loss should be considered when $\sigma a \neq 0$, the σa dependence of transmitted loss reflect the nonuniformity of transmitted loss of different wavelength, which is an important performance of AWG device. From Figure 5 we can find that the nonuniformity of transmitted loss is not pronounced when the value of waveguide width at the interface is close to a . When w becomes

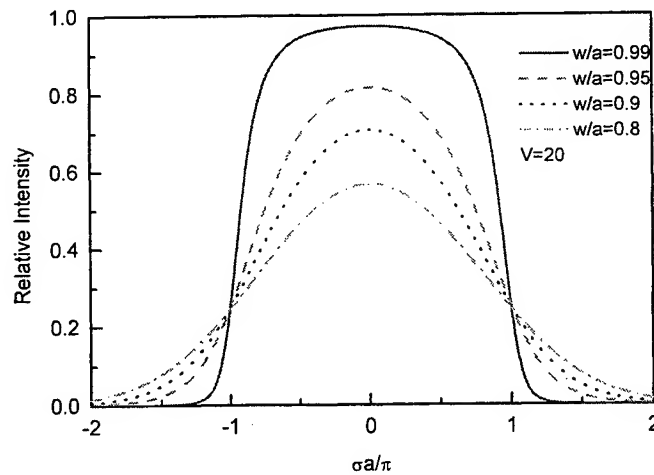


Figure 5. Nonuniformity of the transmitted power due to different incident angles.

small, however, more power will diffract into other Brillouin Zone, so the central wavelength loss become large, meanwhile the loss nonuniformity become pronounced. Because array waveguides are single mode waveguides, the core size and the

index contrast are determined by single mode waveguides conditions. e. g. when the index contrast is about 0.01 for silica based waveguide, the core width should be less than $5\mu\text{m}$. But the grating pitch a much wider than $5\mu\text{m}$ usually be selected.

So a tapered waveguide should be adopted in the input /output of AWG, to connect wider waveguide in the start of the AWG to collect power efficiently to the narrower width waveguide required by single mode waveguide. In tapered waveguide the width of waveguide decreases gradually to prevent the couple of fundamental mode to other modes.

5. CONCLUSION

The paper is concerned with the problem of designing a planar array waveguides with efficient transmitted power. Bloch modes can be excited in planar array due to its periodic lateral refraction index. Due to the finite resolution of lithographical process the gap between the waveguides will stop abruptly when the waveguides come into too close together. Calculation results show that losses will occur at this discontinuity, which are dependent on the ratio of the gap between the waveguides and grating pitch and on the confinement of field in the array waveguides. Tapered waveguides and low index contrast between the core and cladding layers can improve the performances of transmitted loss and loss nonuniformity of array waveguide grating.

ACKNOWLEDGEMENTS

The authors gratefully acknowledge the support of National Natural Science Foundation of China under grant 69896260, 69889701.

REFERENCES:

1. A. Brackett, A. S. Acampora, J. Sweitzer, G. Tangonan, M. T. Smith, W. Lennon, "A scalable multiwavelength multihop optical network: a proposal for research on all-optical networks", *J. Lightwave Technol*, vol. 11 no. 5/6, pp. 736-753, 1993.
2. S. Johansson, M. Lindblom, P. Granstrand, B. Lagerstrom, L. Thylen, "Optical cross-connect system in broad-band networks: system concept and demonstrators description", *J. Lightwave Technol*, vol. 11, no. 5/6, pp. 688-694, 1993.
3. J. B. D. Soole, K. Poguntke, A. Scherer, H. P. LeBlanc, C. Chang-Hasnain, J. R. Hayes, C. Caneau, R. Bhat and M. A. Koza, "Multistripe array grating integrated cavity (MAGIC) laser : a new semiconductor laser for WDM applications", *Electron. Lett.* Vol. 28, No. 19, pp. 1805-1807, 1992.
4. H. Li, W. Lin, Y. J. Chen and D. Stone, "8-channel switch using phased-array waveguide grating multi/demultiplexers", *CLEO' 96. Tech. Dig., CFG1* 1996
5. K. Okamoto, K. Takiguchi and Y. Ohmori, "16-channel optical add/drop multiplexer using silica based arrayed-waveguide gratings", *Electron. Lett.*, vol. 31, no. 9, pp. 723-724, 1995.
6. K. Okamoto, K. Moriwaki, and S. Suzuki, "Fabrication of 64×64 arrayed waveguide grating multiplexer on silicon". *Elec. Lett.* Vol. 31, no. 3. Pp. 184-186, 1995.
7. M. R. Amersfoort, C. R. DeBoer, F. P. G. M VanHam, M. K. Smit, P. Demeester, J. J. G. M. Van der Tol and A. Kuntze. "Phased-array wavelength demultiplexer with flattened wavelength response", *Elec. Lett.*, vol. 30. No. 4, pp. 300-302. 1994.
8. C. Dragone, "Optimum design of a planar array of tapered waveguides", *J. Opt. Soc. Am. A*, vol. 7, no. 11, pp2081-2093, 1990.

Energy approach to the propagation of light waves in anisotropic crystals

Sina Khorasani, Bizhan Rashidian *

Dept. of Electrical Engineering, Sharif University of Technology, P. O. Box 11365-9363, Tehran, Iran

ABSTRACT

In this article the relation between the directions of eigen-polarizations of light waves with the stored electrical energy in an anisotropic medium is discussed, and it is shown that each of two eigen-polarizations correspond to an extremum in the stored electrical energy. So for a given direction of a wave vector and a given magnitude of displacement electric field vector, there exist two extrema that result in the eigen-polarizations. It is shown that this conclusion also holds for plane waves in materials with anisotropic permeability tensor. An interesting effect is found that normal to the crystal axes, the distribution of energy in different directions is uniform. Therefore, for uniaxial crystals, only one of such plane directions could exist while for biaxial crystals, two such planes could be found, corresponding to the two optical axes.

Keywords: Light Propagation, , Anisotropic Crystal, Eigen-polarization, Biaxial Crystal, Uniaxial Crystal

1. INTRODUCTION

In a lossless, homogeneous, and time-independent anisotropic crystal without magnetic anisotropy (i.e., permeability tensor $[\mu] = \mu_0$, with μ_0 being the permeability of vacuum tensor), the time harmonic Maxwell's equations become¹

$$\nabla \times \mathbf{E} = -j\omega\mathbf{B} = -j\omega\mu_0\mathbf{H}, \text{ and} \quad (1a)$$

$$\nabla \times \mathbf{H} = j\omega\mathbf{D} = j\omega[\epsilon]\mathbf{E}, \quad (1b)$$

where $[\epsilon]$ is the Hermitian dielectric permittivity tensor, ω is the angular frequency, and \mathbf{E} and \mathbf{H} are phasors of electric and displacement magnetic field intensities. Notice that the optical activity may be included in the imaginary part of $[\epsilon]$ as an antisymmetric term, thus the above definition would be preserved. The plane wave solution of (1) may be obtained by formally inserting $\nabla = j\mathbf{k}$ and eliminating \mathbf{H} . Thus the following wave equation in terms of \mathbf{E} results:

$$\mathbf{k} \times (\mathbf{k} \times \mathbf{E}) + \omega^2 \mu_0 [\epsilon] \mathbf{E} = 0, \quad (2)$$

If the dielectric permittivity tensor $[\epsilon]$ is Hermitian, it can be diagonalized in the principal coordinate system, i.e.

$$[\epsilon] = \begin{bmatrix} \epsilon_x & 0 & 0 \\ 0 & \epsilon_y & 0 \\ 0 & 0 & \epsilon_z \end{bmatrix}, \quad (3)$$

and rewriting (2) the system of equations²

$$\begin{bmatrix} \omega^2 \mu_0 \epsilon_x - k_y^2 - k_z^2 & k_x k_y & k_x k_z \\ k_y k_x & \omega^2 \mu_0 \epsilon_y - k_x^2 - k_z^2 & k_y k_z \\ k_z k_x & k_z k_y & \omega^2 \mu_0 \epsilon_z - k_x^2 - k_y^2 \end{bmatrix} \begin{bmatrix} E_x \\ E_y \\ E_z \end{bmatrix} = \begin{bmatrix} 0 \\ 0 \\ 0 \end{bmatrix} \quad (4)$$

* Correspondence: Email: rashidia@ee.sharif.ac.ir; Telephone: +98-21-9182631; Fax: +98-21-6036008

results. In order for (4) to have non-trivial solutions, it is necessary that the determinant of the coefficients matrix be zero. Adopting the replacement $\mathbf{k} = (\omega/c)\mathbf{n}\mathbf{s}$, with \mathbf{s} and n being a unit vector parallel to the wave vector \mathbf{k} , and index of refraction, respectively, the direction of eigen-polarization electric field vectors would be²

$$\begin{bmatrix} \frac{s_x}{n^2 - \epsilon_x/\epsilon_0} \\ \frac{s_y}{n^2 - \epsilon_y/\epsilon_0} \\ \frac{s_z}{n^2 - \epsilon_z/\epsilon_0} \end{bmatrix}, \quad (5)$$

in which the index of refraction n may be obtained from this quadratic equation

$$\frac{s_x^2}{n^2 - \epsilon_x/\epsilon_0} + \frac{s_y^2}{n^2 - \epsilon_y/\epsilon_0} + \frac{s_z^2}{n^2 - \epsilon_z/\epsilon_0} = \frac{1}{n^2}. \quad (6)$$

Thus, for a given direction of propagation vector \mathbf{s} , two solutions for n and corresponding eigen-polarizations in general exist. In the case that these two solutions coincide, this direction is referred as the optical axis. Two optical axes are found in biaxial crystals, while uniaxial crystals have only one; this is the case that two of the diagonal terms in (3) are equal.

In the next section, it is shown that the above directions for eigen-polarization refer indeed to the extrema in stored electric energy $U_e = \mathbf{D} \cdot \mathbf{E}/2$. That is, for a prescribed direction of propagation \mathbf{s} , and a given magnitude of displacement electric field vector \mathbf{D} , the eigen-polarizations may be also found from extremizing the stored electric energy function U_e as a functional. When the system (4) is degenerate, i.e., \mathbf{s} is directed along one of crystal axes, the distribution of stored electric energy U_e would be independent of polarization. It will be discussed that this result justifies the general properties of the optical axis. As a result, for a uniaxial crystal only one such plane exist while for biaxial crystals, only one single direction could be found, which results from the intersection of the two planes normal to two optical axes. The distribution of stored magnetic energy $U_m = \mathbf{B} \cdot \mathbf{H}/2$ and total stored energy $U = U_e + U_m$ for non-magnetic materials are also investigated. It is concluded that they exhibit two extrema that coincide with that of stored electric energy U_e , if the direction of wave vector is along crystal axes.

2. MATHEMATICAL ARGUMENT

In this section the following theorem is considered:

Theorem: In a non-magnetic, homogeneous, and time-independent anisotropic crystal and in absence of loss, and for a given direction of propagation vector \mathbf{s} and displacement electric field vector \mathbf{D} , the eigen-polarizations of propagation correspond to the extrema of stored electrical energy.

Proof: The proof of the above statement is somewhat lengthy but straightforward. Considering the linearity of Maxwell's equations (1), the displacement electric field vector \mathbf{D} can be normalized as

$$|\mathbf{D}| = 1, \quad (7)$$

without loss of generality. Now consider the stored electric energy function

$$U_e = \frac{1}{2} \mathbf{D} \cdot \mathbf{E} = \frac{1}{2\epsilon_0} \sum_{i=1}^3 \sum_{j=1}^3 D_i \eta_{ij} D_j, \quad (8)$$

in which η_{ij} are elements of the impermeability tensor $[\eta] = \epsilon_0 [\epsilon]^{-1}$. Here, the stored electric energy U_e would be treated as the function to be extremized subject to the conditions:

$$\mathbf{s} \cdot \mathbf{D} = s_x D_x + s_y D_y + s_z D_z = \sum_{i=1}^3 s_i D_i = 0, \quad (9a)$$

and

$$\mathbf{D} \cdot \mathbf{D} = D_x^2 + D_y^2 + D_z^2 = \sum_{i=1}^3 D_i^2 = 1. \quad (9b)$$

The condition (9a) follows from (1b), while (9b) re-expresses the assumption (7).

To extremize (8) subject to constraints (9) the method of Lagrangian multipliers³ may be used. Hence, the modified definition of (8) satisfying (9) at its extrema is obtained as

$$U'_e = \frac{1}{2\epsilon_0} \sum_{i=1}^3 \sum_{j=1}^3 D_i \eta_{ij} D_j + \lambda_1 \sum_{i=1}^3 s_i D_i + \lambda_2 \left(\sum_{i=1}^3 D_i^2 - 1 \right), \quad (10)$$

where the Lagrangian multipliers λ_1 and λ_2 are some constants to be determined. Taking partial derivative of U'_e with respect to D_i and setting it to zero results in

$$\frac{\partial U'_e}{\partial D_i} = \frac{1}{\epsilon_0} \sum_{j=1}^3 \eta_{ij} D_j + \lambda_1 s_i + 2\lambda_2 D_i = 0, \quad i=1,2,3. \quad (11)$$

Multiplying both sides first by D_i , then by s_i , performing a summation on index i , and noting that by definition \mathbf{s} is a unit vector, results in

$$\frac{1}{\epsilon_0} \sum_{i=1}^3 \sum_{j=1}^3 D_i \eta_{ij} D_j + 2\lambda_2 = 0, \quad (12a)$$

and

$$\frac{1}{\epsilon_0} \sum_{i=1}^3 s_i \sum_{j=1}^3 \eta_{ij} D_j + \lambda_1 = 0. \quad (12b)$$

The equations (12) may be rewritten as

$$\lambda_2 = -U_e, \quad (13a)$$

and

$$\lambda_1 = -\mathbf{s} \cdot \mathbf{E}. \quad (13b)$$

Inserting (13) into (11) results in

$$\mathbf{D} = \epsilon_0 n^2 [\mathbf{E} - (\mathbf{E} \cdot \mathbf{s}) \mathbf{s}]. \quad (14)$$

Here, the relation

$$\varepsilon_0 n^2 = \mathbf{D} \cdot \mathbf{D} / \mathbf{D} \cdot \mathbf{E} \quad (15)$$

according to the definition of refractive index n is used. It may be easily shown that (14) is equivalent to the wave equation (2), if one inserts $\mathbf{k} = (\omega/c)\mathbf{n}\mathbf{s}$ in (2) and expands the cross products in terms of \mathbf{s} and \mathbf{E} . This completes the proof.

Now some deductions from the above theorem are presented.

COROLLARY 1: Since

$$U_e = \mathbf{D} \cdot \mathbf{D} / 2\varepsilon_0 n^2, \quad (16)$$

the extrema of stored electric energy coincide with extrema in refractive index n . This result justifies with the method of index ellipsoid² which is generally used for determining polarization directions. In this method, the major and minor radii of the ellipse formed from intersection of the plane normal to \mathbf{s} and index ellipsoid characterized by the equation

$$\frac{x^2}{n_x^2} + \frac{y^2}{n_y^2} + \frac{z^2}{n_z^2} = 1, \quad (17)$$

resolve the eigen-polarization directions. In addition, one of the extrema would be a minimum while the other would be a maximum.

This situation is illustrated in Figs. 1. Here, the stored electrical energy vs. polarization angle, normal to the wave vector \mathbf{k} is plotted for a typical permittivity tensor and an arbitrary direction. For the given wave vector $\mathbf{k} = 2\hat{x} - \hat{y} + 3\hat{z}$, and relative permittivities $\varepsilon'_x = 1$, $\varepsilon'_y = 4$, and $\varepsilon'_z = 9$ it may be shown that the propagation eigen-polarizations lie at the angles 13.92° and 92.22° . These values are in exact agreement with respectively the maximum and minimum of the stored electrical energy curve in Fig. 1(a). However, since the optical axes lie in x-z plane, the wave vector $\mathbf{k} = \hat{y}$ in Fig. 1(b) is normal to both optical axes. It could be seen that in this case the distribution of electrical energy is independent of polarizations.

In Figs. 2, a uniaxial crystal with relative permittivities $\varepsilon'_x = 1$, $\varepsilon'_y = 4$, and $\varepsilon'_z = 4$ is considered. This time, the optical axis lies in \hat{x} direction. In Fig. 2(a) the extrema are located at 90° and 11.25° , and similar to Fig. 1(a) exact matching between extrema and propagation directions may be found. As expected in Fig. 2(b), because the wave vector is normal to the optical axis, the energy distribution is uniform and therefore it is independent of polarization.

COROLLARY 2: Along the optical axes, the eigen-polarizations are degenerate and their refractive indices match together. This means that the two eigen-polarizations see the same index of refraction n ; this corresponds to a circular cross section of the index ellipsoid (17). According to (16), the distribution of energy would uniform, and propagation would be polarization-independent. For uniaxial crystals, only one circular cut of index ellipsoid may be produced normal to its optical axis. Therefore, only one of such planes with degenerate radial direction may be found.

COROLLARY 3: Because of duality theorem¹ between electric and magnetic fields in Maxwell's equations, it is readily deduced that the following statement holds: In an electrically isotropic, homogeneous, and time-independent magnetically anisotropic crystal and in absence of loss, and for a given direction of propagation vector \mathbf{s} and magnetic field vector \mathbf{B} , the eigen-polarizations of propagation correspond to the extrema of stored magnetic energy.

COROLLARY 4: According to the above theorem and Corollary 2, an extended version of the above theorem may be arranged for the case of permeability tensor being an anisotropic tensor, not a scalar one. However, it would be sufficient to replace μ_0 with $[\mu]$ in Maxwell's equations (1) as

$$\mathbf{k} \times \mathbf{E} = \omega \mathbf{B} = \omega [\mu] \mathbf{H}, \quad (18a)$$

and

$$\mathbf{k} \times \mathbf{H} = -\omega \mathbf{D} = -\omega [\varepsilon] \mathbf{E}. \quad (18b)$$

From (18) it could be written down that

$$\mathbf{B} \times (\mathbf{k} \times \mathbf{H}) = \mathbf{D} \times (\mathbf{k} \times \mathbf{E}). \quad (19)$$

After expanding both sides it can be written that

$$\mathbf{k}(\mathbf{B} \cdot \mathbf{H}) - \mathbf{H}(\mathbf{B} \cdot \mathbf{k}) = \mathbf{k}(\mathbf{D} \cdot \mathbf{E}) - \mathbf{E}(\mathbf{D} \cdot \mathbf{k}), \quad (20)$$

which by applying $\mathbf{s} \cdot \mathbf{D} = \mathbf{s} \cdot \mathbf{B} = 0$, it is concluded as a very general theorem for plane waves:

$$U_e = U_m = \frac{1}{2} U. \quad (21)$$

That is, the total stored energy is divided equally between electric and magnetic components for plane waves. Therefore, the theorem stated above is a very general result.

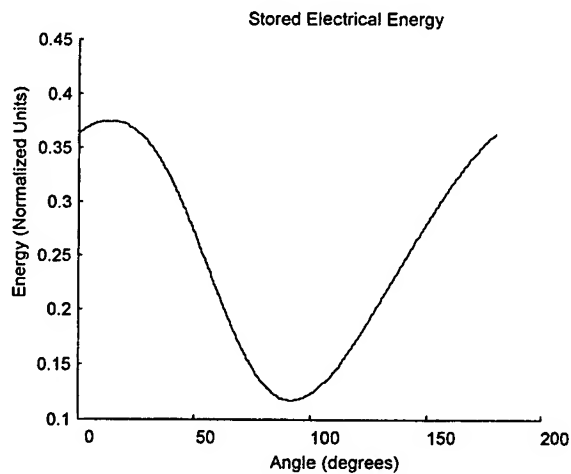
As a final remark it should be pointed out that if permittivity or permeability are not Hermitian, e.g. system has losses, the above theorem does not hold, because no principal coordinates can be found; in other words, permittivity or permeability tensors can not be diagonalized. In such cases \mathbf{B} and \mathbf{H} are not necessarily normal to the wave propagation vector \mathbf{k} .

3. CONCLUSIONS

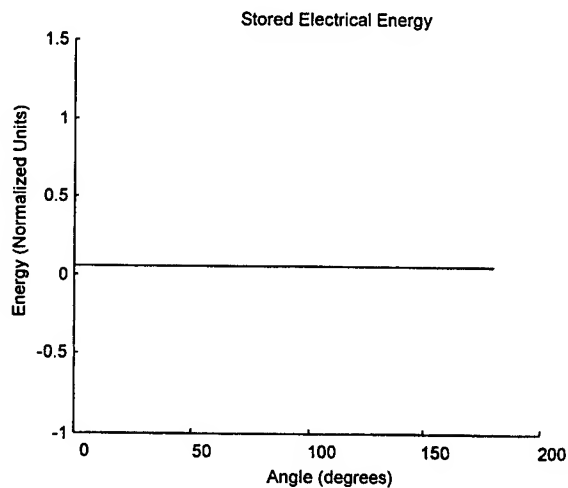
It has been mathematically shown that for a harmonic plane wave propagating in an anisotropic, homogeneous, and time-independent crystal, and in absence of losses and isotropic magnetic permeability, that the two propagation eigenpolarizations corresponds to extrema of stored electric energy. It has been discussed that one of these two extrema is a minimum while the other is a maximum. The equivalency of this approach to the method of index ellipsoid has been demonstrated. It has been shown that due to duality of Maxwell's equations between electric and magnetic fields that the same theorem hold for materials with isotropic permittivity and anisotropic permeability. Finally, it was shown as a very general result that for a plane wave, the total stored energy divides equally between electric and magnetic energies, and thus the theorem may be generalized for the case of anisotropic permittivity and anisotropic permeability.

REFERENCES

1. M. Born and E. Wolf, *Principles of Optics*, Pergamon Press, New York, 1965.
2. A. Yariv and P. Yeh, *Optical Waves in Crystals*, John Wiley & Sons, New York, 1984.
3. G. Arfken, *Mathematical Methods for Physicists*, 3rd ed., Academic Press, Orlando, 1985.

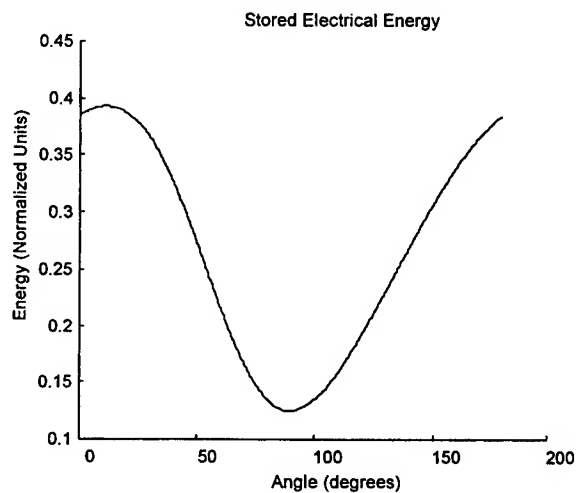


(a)

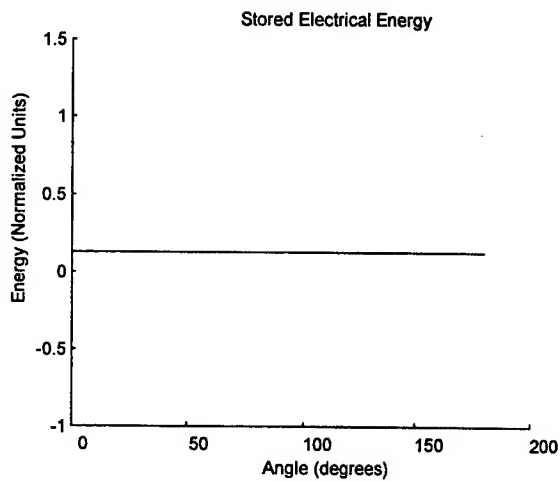


(b)

Fig. 1. Stored electrical energy plotted for a biaxial crystal ($\epsilon'_x = 1$, $\epsilon'_y = 4$, and $\epsilon'_z = 9$). (a) $\mathbf{k} = 2\hat{x} - \hat{y} + 3\hat{z}$, (b) $\mathbf{k} = \hat{y}$. In both cases the extrema of energy curve coincide with eigen-polarization angles.



(a)



(b)

Fig. 2. Stored electrical energy plotted for a uniaxial crystal ($\epsilon'_x = 1$, $\epsilon'_y = 4$, and $\epsilon'_z = 4$). (a) $\mathbf{k} = 2\hat{x} - \hat{y} + 3\hat{z}$, (b) $\mathbf{k} = \hat{y}$. In both cases the extrema of energy curve coincide with eigen-polarization angles.

Optical damage in Zn:Ga:LiNbO₃ waveguide substrates

Zhao Yequan*, Xu Wusheng, Zhang Hongxi, Xu Yuheng

Department of Applied Chemistry, Harbin Institute of Technology, Harbin, China, 150001

Wang Jiyang

Caystal Material National Laboratory, Shandong University, Jinan, China, 250100

ABSTRACT

Doping ZnO and Ga₂O₃ in LiNbO₃ crystal, the Zn:Ga:LiNbO₃ was grown by Czochralski method. The infrared transmission spectra and the photo damage resistance ability of the LiNbO₃ and Zn:Ga:LiNbO₃ crystal were measured. The proton exchange technology was used to make the LiNbO₃ and Zn:Ga:LiNbO₃ crystal waveguide substrates. The m-line method was taken to study the photo damage of waveguide substrate. We observed that the threshold of Zn:Ga:LiNbO₃ is above two magnitude higher than that of Mg:LiNbO₃. Zn:Ga:LiNbO₃ crystal is better performance than LiNbO₃ crystal.

Keywords: Zn:Ga:LiNbO₃ crystal, photo waveguide substrate, photo damage, proton exchange, integrated optics, refractive index, optical system, light-wave scatter, continuous laser, optical element

1. INTRODUCTION

The waveguide optics and thin film technology are the two basic components of integrated optics, which itself is composed of waveguide substrates and other optical elements. The optical wave of light circuit can be defined as a kind of surface wave transmission along two-dimension plane. The waveguide element must be in good conditions for a lon time. The refractive index of waveguide substrate made of LiNbO₃ crystal changes when it is rayed by the blue or green laser with higher density, and the wavelength of transmittance optical wave depletes, resulting the scattering of light¹⁻³. So the improvement of light damage resistance is very important. In this work, Zn:Ga: LiNbO₃ are grown by Czochralski method. The capability of light damage resistance of Zn:Ga: LiNbO₃ is two magnitudes higher than that of LiNbO₃. This shows that Zn:Ga: LiNbO₃ is an excellent material for waveguide substrates.

2. CRYSTAL GROWTH

Using siliconit as heater, Zn:Ga:LiNbO₃ crystal was grown by Czochralski method.

2.1 Raw Material

The quality of Nb₂O₅ and Li₂CO₃ is 99%. The quality of ZnO and Ga₂O₃ is spectra purity. The ratio of Li₂CO₃ to Nb₂O₅ is 48.6:51.4(mol ratio). The doped quantity of ZnO and Ga₂O₃ is 3.5mol% and 1.5mol% respectively. The weight of Nb₂O₅, Li₂CO₃, Fe₂O₃, and In₂O₃ was calculated and weighed by analytical balance. For the sake of keeping congruent raito, every component could not be lost during blending course. The raw materials were mixed in pulsator and shaken for twenty-two hours. Then the mixed symmetrical material was sintered and turned into Zn:Ga:LiNbO₃ polytropism.

2.2 Crystal Growth Technology

The parameters of Zn:Ga:LiNbO₃ crystal growth include the temperature gradient, the crystal growth rate, the crystal rotation rate and the crystal polarization.

2.2.1 Temperature Gradient

The temperature gradient comprises axial direction and radial direction temperature gradient. The unit differential temperature above and under the melt level denotes axial direction temperature gradient. Selecting proper temperature

Correspondence: Fax:86-0451-6221048

gradient required the condition as following: (1) to generate the advisable degree of supercooling in the center of the melt surface; (2) to keep invariable temperature during crystal growth in order to make crystal shape controlled easily; (3) to make the thermal stress crystal endured small to avoid crack; (4) not to produce the component supercooling. Because the temperature gradient is the impetus of crystal growth, one important factor to grow highquality crystals is to select the proper temperature gradient. The proper axial direction temperature gradient to grow In:Fe:LiNbO_3 crystal is 40°C above the melt surface and 15°C under the melt surface.

2.2.2 Crystal Growth Rate

The time that the crystal growth face increases unit thickness along the normal direction is called the crystal growth axial rate. It includes both the mechanical lifting rate and the melt surface descending rate. The crystal growth rate depends on the temperature gradient, the crystal diameter, the material purity, the dopant species and the dopant quantity. When the condition above-mentioned is ascertained, the crystal growth rate has a maximum. If the growth rate exceeds the maximum, the component supercooling and varieties of crystal defects will appear. To grow crystal with 20mm~30mm diameter, the growth rate should be 1~2mm/h.

2.2.3 Crystal Rotation rate

The crystal quality depends on the flat degree of the solid-melt interface. The rotation rate is one of most important factors that influent the flat degree of the solid-melt interface. When crystal rotation rate is high, the solid-melt interface can turn flat from convex. When crystal rotation rate is low, the trend that the solid-melt interface turns concave decreases. The proper rotation rate is selected and the flat solid-melt interface will be gained. In our experiment, the crystal rotation rate is 15rpm-20rpm.

2.2.4 Crystal Polarization

Zn:Ga:LiNbO_3 crystal is ferroelectrics. It has a ferroelectric transition point (Curie point) between 1150°C and 1210°C . During crystal from high temperature through Curie point to low temperature, the crystal will turn into ferroelectric phase from paraelectric phase. Zn:Ga:LiNbO_3 crystal is one dimension ferroelectrics. In some temperature, the self-polarization exists, which intensity changes with the outer electric field adding on. The self-polarization of as-grown crystal has different directions and the crystal is multidomain crystal. When electromagnetic wave pass multidomain crystal, it will be scattered at domainwall, which will make the device property poor. So as-grown crystal must be polarized artificially so that the Ps turn direction along the c-axial and the crystal becomes the single domain crystal. In our experiment, the polarization current density is $5\text{mA}/\text{cm}^2$ and the polarization temperature is 1200°C . After polarized, the HF and HNO_3 mixture liquid which ratio was 1:2 eroded the crystal piece. Using metallographical microscope to observe the piece, the Zn:Ga:LiNbO_3 crystal was polarized completely.

3. TRANSMISSION OF OH^{-1} VIBRATION OF CRSTAL⁴

The transmission spectra OH^{-1} vibration of pure LiNbO_3 and Zn:Ga:LiNbO_3 are shown in Fig.1 and Fig. 2 respectively. The absorption peak of LiNbO_3 is at 3485.869cm^{-1} ($2.87\ \mu\text{m}$), while that of Zn:Ga:LiNbO_3 is at 3535.864cm^{-1} ($2.83\ \mu\text{m}$). for Mg:LiNbO_3 , the transmittance peak of crystal shifts from $2.87\ \mu\text{m}$ to $2.83\ \mu\text{m}$ when the concentration of Mg is higher than the threshold, and the capability of light damage resistance of Mg:LiNbO_3 is higher two magnitudes than that of LiNbO_3 . The absorption peak of Zn:Ga:LiNbO_3 is at $2.83\ \mu\text{m}$, this indicates that the capability of light damage resistance of Zn:Ga:LiNbO_3 is higher two magnitudes than that of LiNbO_3 .

4. LIGHT DAMAGE RESISTANCE MEASUREMENT

the light resistance of Zn:Ga:LiNbO_3 and LiNbO_3 are measured by observing the transmission light spot. As Ar^+ light power, λ of 488.0nm , laser beam focus on the crystal crossing optical grating. The transmission light spot is a circle when there is no light damage in the crystal. The power density of laser is increased continuously to a certain value, then the transmission light spot begin to became longer along c axis, generating light depletion. The value of power density which begin to cause light damage is called the light damage resistance of crystal. The results of measurement indicates that the capability of light damage resistance of Zn:Ga:LiNbO_3 is higher two magnitudes than that of LiNbO_3 (Table 1).

5. LIGHT DAMAGE RESISTANCE OF WAVEGUIDE SUBSTRATES⁵⁻⁶

Usually, there are thin film and stripe waveguide substrates. The laser beam is focused because the waveguide substrates are very thin. Thus, the light damage of waveguide substrates is more sensitive than that of bulk crystal. Nowadays, waveguide substrates are made by proton-exchanged in Benzoic acid.

5.1 proton-exchanged for waveguide mechanism

In proton-exchanged for waveguide element method, dopants are diffused into substrates, occupying the vacancy and replacing the atoms of lattice. Thus, the refractive index increases by increasing the polarization or decreasing the volume of unit cell, and forming light waveguide. In the meantime, there exists outer diffusion. The atoms or molecules diffuse to the outer surface, forming vacancy on the surface of substrates. The refractive index increases by the replacement of bonds or the contraction of unit cell.

When proton-exchanged in Benzoic acid is used for waveguide, the speed of proton-exchange is very fast, and along with the depletion of surface lattice structure caused by too large concentration of dopants, resulting in the corrosion of crystal. LiCl is added into Benzoic acid to control the concentration of Li of compound and the speed of exchange, reducing corrosion.

The chemical equation of exchange of LiNbO₃ with the proton of Benzoic acid is as follows



The relationship between the concentration of H⁺ of Li_{1-x}H_xNbO₃ and Δn_e is a line only at smaller value of x. Δn_e is up to its maximum value when x is 0.3. In exchange process, the equation (1) direction is left if a certain dopant is added, which is beneficial to the increase of H⁺ or the decrease of Li⁺. The reaction speed is decreased.

The reaction when LiCl is added into the compound is as follows



It is obvious the exchange can be controlled because of the addition of LiCl. The diffusion coefficient sharply decreases with the increase of LiCl. It is convenient to make exchange layer with accuracy thickness.

5.2 proton-exchanged in Benzoic acid technology⁶

Benzoic acid sealed in quartz tube is placed in diffusion furnace to reduce the volatile. LiNbO₃ (or Zn:Ga:LiNbO₃) substrates is dipped into the melt of Benzoic acid of 200°C to inform waveguide. The advantage of proton-exchanged in Benzoic acid for waveguide is as follows: (1) The larger refractive index. The refractive index can be measured by the coupling of beams in waveguide substrates with He-Ne laser measurement system. Δn_e of waveguide substrates is larger than 0.06, which is obtained by dipping into the Benzoic acid melt of 200°C for 10 minutes, while Δn_e is 0.11 for 5 hours. (2) The smaller dissipation. The dissipation of waveguide substrates made by proton-exchanged in Benzoic acid is about 0.5dB/cm. (3) The little light scatter. The scatter angle is not more than 1.3mr at the peak of 40dB with the measurement system mentioned above.

5.3 light damage of waveguide substrate

Light damage of waveguide substrates is studied by m-line method. The refractive index changes because of the light damage, when laser beam coupled in prism crosses along the waveguide substrates, resulting in the scatter increase of light in the waveguide plane. Therefore, the light intensity distribution of m-line changes. The intensity of center peak of m-line decreases, and the scatter angle in plane broadens. When the light damage in waveguide substrates occurs, the intensity of m-line broadens or draws until it became a light line. The light damage threshold can be defined by measuring the change of center light spot with the light intensity.

The setup of m-line method is shown in Fig. 3. A is a light attenuator, B is a piece of glass, C is a crack, L is a fluori lens with focal distance of 250mm. The input terminal of waveguide substrates and TiO₂ prism system is placed at the focal point. The light transfers along the waveguide substrates, then outputs by TiO₂ prism. The center light spot of m-line is recorded by photoelectric multipliers H₂. In our experiment, we find that, at first, the intensity of center light spot of m-line increases with the increase of input light intensity, but, the intensity of output light suddenly begin to decrease when that of input light is up to a certain value(Fig. 4). And the center light spot of m-line gradually became a light line.

The light damage threshold is defined as the input light intensity I_{ngo} under which the transmission performance is completely damaged or the center light spot vanishes sharply, or as the corresponding energy density E_0 . The transmittance ratio of laser in the prism is as follows

$$\eta_{IN} = \frac{I_{IN} - I_R}{I_{IN}} \quad (4)$$

where I_{IN} is the total light intensity, I_R is the reflection intensity. The laser intensity usually shows gauss distribution. Only 80% percent of light intensity is coupled into waveguide substrates. And other factors, such as surface clean degree, are considered, the actual transmittance ratio $\eta_{in}' = \eta_{in} \times 70\%$. The input intensity of light $I_{ngo} = I_{IN} \times \eta_{in}'$. The results of light damage threshold are listed in Table 2. It shows that the capability of light damage resistance of Zn:Ga:LiNbO₃ is higher two magnitudes than that of LiNbO₃.

6. CONCLUSION

Doping ZnO and Ga₂O₃ in LiNbO₃ crystal, the Zn:Ga:LiNbO₃ was grown by Czochralski method. The infrared transmission spectra and the photo damage resistance ability of the LiNbO₃ and Zn:Ga:LiNbO₃ crystal were measured. The proton exchange technology was used to make the LiNbO₃ and Zn:Ga:LiNbO₃ crystal waveguide substrates. The m-line method was taken to study the photo damage of waveguide substrate. We observed that the threshold of Zn:Ga:LiNbO₃ is above two magnitude higher than that of Mg:LiNbO₃. Zn:Ga:LiNbO₃ crystal is better performance than LiNbO₃ crystal.

REFERENCES

1. Xu shiwen, Li Minhua, and Gao Yuankai, "Study of photo damage of waveguide substrate of doped LiNbO₃ by m-line method", *ACTA Photonica Sinica*, **23**, pp.179-183,1994.
2. F.S.Chen, J.T.Lamacchia, and D.B.Fraser, "Holographic storage in Lithium Niobate", *Appl. Phys. Lett.* **13**, pp.223-226, 1968.
3. J.B.Thaxter, "Electrisal control of holographic storage in Strontium Barium Niobate", *Appl. Phys. Lett.* **15**, pp.210-213, 1969.
4. Feng Xiqi, Ying Jifeng, and Wang Jinchang, "The OH⁻ absorption spectrum as a probe for defect structure of LiNbO₃ crystal", *ACTA Physics sinica*, **37**, pp.2062-2066, 1988.
5. Zuo Zhuang, Shao Zhongshu, and Chen Jun, "Study of the proton-exchanged LiTaO₃ Waveguide in Benzoic acid and its annealing property", *Chinese J. Laser*, **21**, pp. 517-521, 1994.
6. Li Minghua, Zhao Yequan, and Xu Yuheng, "Study of light damage of waveguide substrates of LN and Mg:LN by holographic method", *Chinese J. Laser*, **19**, pp. 566-569, 1992.

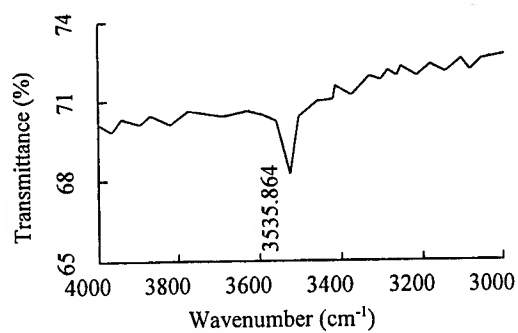


Fig. 1 The infrared transmission spectrum of LiNbO₃ crystal

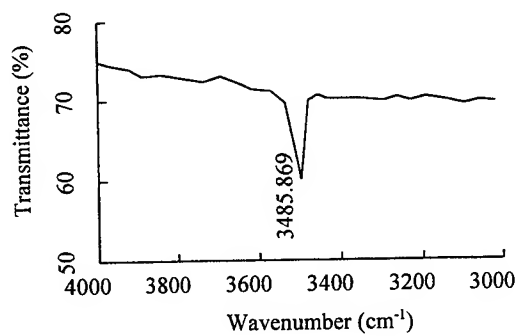


Fig. 2 The infrared transmission spectrum of Zn:Ga:LiNbO₃ crystal

Table 1 Photo damage resistance ability of crystals

Crystals	Photo damage resistance ability (W/cm ²)
LiNbO ₃	3.6×10^2
Zn:Ga:LiNbO ₃	6.5×10^4

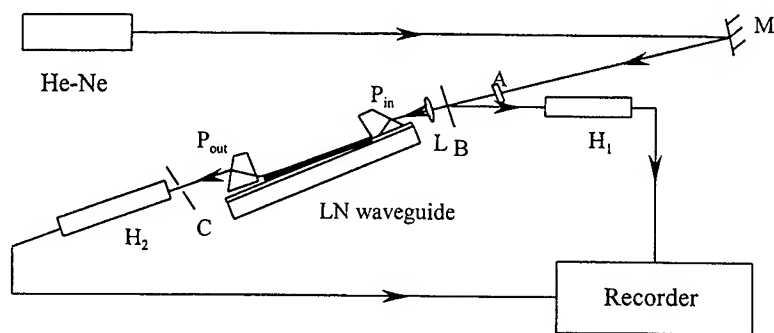


Fig.3 Experimental arrangement of m-line method: A's, light attenuator; B's, a piece of glass; C's, crack; L's, Fourier lens ($f=250\text{mm}$); H_1 and H_2 's, photoelectric multipliers; P_{in} and P_{out} 's, input prism and output prism.

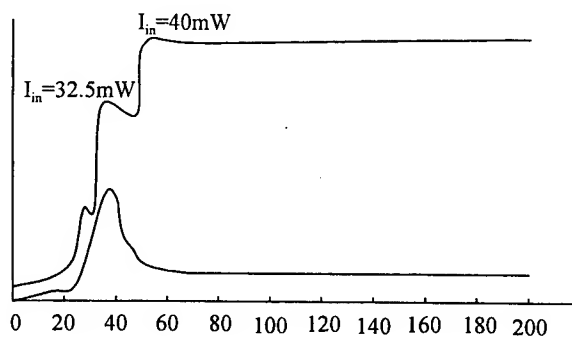


Fig. 4 Changes curve of I_{in} and I_{out} of PE:LiNbO₃ waveguide

Table 2 The photo damage threshold of LiNbO₃ and Zn:Ga:LiNbO₃ waveguide substrates

Waveguide	Transmission mode	Transmission direction	Illumination time	Illumination intensity (mW)	Damage threshold
PE:LiNbO ₃ (proton exchange)	TM ₀	Z cut and X transmission	30	20	2×10^4
PE:LiNbO ₃	TM ₀	Z cut and X transmission	10	30	3×10^4
PE:Zn:Ga:LiNbO ₃	TE ₀	Y cut and X transmission	10×60	15	3.5×10^6
PE:Zn:Ga:LiNbO ₃	TE ₀	Y cut and X transmission	20×60	20	4×10^6

A Novel U-groove channel for self-alignment of optical fibres with optical quality end-polished silicon rib waveguides using wet chemical micromachining techniques

N.Q. Ngo*, M.A. Rosa², D. Sweatman, S. Dimitrijevic, H.B. Harrison, and A. Titmarsh.

School of Microelectronic Engineering, Nathan, Queensland 4111, Griffith University, Australia.

²Xerox, Palo Alto Research Center, 3333 Coyote Hill Road, Palo Alto, CA 94304, USA.

ABSTRACT

This paper presents a new cost-effective fibre-to-waveguide coupling method for self-aligning optical fibres on silicon platforms, and for achieving optical quality end-polished silicon-on-insulator (SOI) single-mode rib waveguide devices using wet chemical micromachining techniques. Through accurate alignment to the $\langle 011 \rangle$ plane(s) of the (100) device layer of a SOI wafer, rib waveguide devices with self-alignment features are fabricated with the ends of each waveguide wet etched and concurrently polished providing an optical quality facet or fibre-to-waveguide interface. Eliminating the need to saw cut and then mechanically polish the waveguide device ends, the overall fabrication process is simplified and provides a fibre alignment capability at the ends of the waveguide devices with an alignment accuracy limited by fibre size tolerance. Experimental measurements were carried out to verify the optical quality of the waveguide facets formed using this new technique, which proved excess facet losses of practically unmeasurable quantities. Both simulation and experimental results were obtained to verify the single-mode nature of the rib waveguides.

Keywords: Optical Planar Waveguides, Fibre Pigtailling, Micromachining, Integrated Optics, Rib Waveguides, Silicon-On-Insulator Technology.

1. INTRODUCTION

Photonics technology is one of the enabling technologies in the 21st century, and will play key roles in the fastest growing industry of telecommunications. This is due to the fact that the market demand for high-speed cost-effective transport of large amount of information has created a need for the development of smaller, faster and economical optical fibre networks. These networks make use of integrated optical waveguide devices and circuits to perform such functions as switching, filtering, and signal processing. This market demand has generated a need to employ the well-developed low-cost microelectronics processing SOI technology to develop monolithically integrated optoelectronic devices and circuits on silicon platforms to provide greater functionality for the next generation of optical networks.

SOI optical waveguide technology has many unique advantages which include [1]-[4]:

- Silicon has low optical absorption at the important communications wavelengths of 1300 nm and 1550 nm.
- SOI substrates have no intrinsic stress, and hence waveguide birefringence is small.
- High quality SOI substrates are available at low and reducing cost due to recent thrust for using them for CMOS (complementary metal-oxide-semiconductors) integrated electronic circuits for low-power high-speed applications.
- SOI technology offers the potential for monolithic integration of optical and electronic functions all on the same silicon platform at a potentially low cost and high manufacturing yield to provide greater functionality for next-generation optical networks.
- The large refractive index difference between SiO_2 (~ 1.5) and Si waveguide (~ 3.5) permits: (a) The use of thin cladding layers ($< 1.0 \mu\text{m}$), making them compatible with VLSI (very large scale integration) technology and providing great

* Correspondence: Email: J.Ngo@me.gu.edu.au; WWW: <http://www.gu.edu.au/school/mee/home.html>; Tel: 617 3875 3652; Fax: 617 3875 5198.

advantage over the conventional silica-based waveguide technology, in which 10–20 μm thick cladding and cover layers are required due to the low index difference); (b) Light to be strongly guided within the waveguide structure; (c) Fabrication of very tight and compact waveguide bends with a small radius of curvature, permitting high-density integration of circuits; (d) Single-mode propagation in large cross-sectional waveguides with a mode size comparable to that of single-mode optical fibres to provide high coupling efficiency.

SOI optical waveguide technology is still in an early stage of development, however, it can be developed using the well-established low-cost microelectronics processing for silicon. Although integrated optical circuits using SOI technology have recently been demonstrated as directional couplers, star couplers, and multi/demultiplexers [1]–[4], the potential application advantages of SOI technology have not yet been well exploited to enhance existing or create new applications. The waveguide ends of these circuits [1]–[4] may not be of the highest quality because they had been saw cut and mechanically polished to achieve vertical facets, resulting in low coupling efficiency when coupled with optical fibres or integrated-optic devices. These conventional techniques are not cost-effective and not acceptable in a mass production environment. Currently, optical fibre alignment can be achieved on (100) Si wafers using V-grooves etched into the wafer's surface by either Potassium Hydroxide (KOH) or a mixture of Ethylene Diamine and Pyrocatechol (EDP), both of which are anisotropic wet chemical etchants [5], [6]. The $\langle 111 \rangle$ planes of bulk silicon act as etch stops when these and similar anisotropic etchants are used, creating V-shaped grooves with a sidewall angle of 54.74° to the wafer surface. Similar alignment dependent processing techniques are often applied to the fabrication of active and passive rib/ridge waveguide devices in order to achieve smooth sidewalls and hence minimize optical power losses [7], [8]. The 54.74° sidewall angle present along the length of a single-mode waveguide structure, although not greatly affecting its modal distribution, is also present at its ends. This results in significant power losses when coupled to a cleaved fibre positioned in a V-groove structure. Attempts to overcome this have resulted in: (1) a saw cut being made across the ends of the waveguide structure flattening the interface region [8], [9], and this can possibly introduce losses via a reduction in optical quality at the waveguide ends; and (2) the passive V-groove fibre alignment structure (Figure 1(a)) being kept separate from the optical device and aligned as a final step once the ends of the optical device have themselves been cut and mechanically polished to an optical quality [10]. A commonly used alternative to these two techniques is the formation of rib waveguide and associated waveguide facets via plasma etching techniques [11], [12]. Although in some cases allowing the integration of dry etched rib waveguide and wet etched V-groove on the same substrate, this process of waveguide formation still incurs additional power loss due to the inherent roughness in the dry etch process and more dominantly mask roughness that can be transferred through lithography to sidewall and facet areas of the waveguide [13].

This paper presents a unique method for fabricating via micromachining techniques and careful alignment to the $\langle 011 \rangle$ plane(s) of a (100) bonded and etched back silicon-on-insulator (BESOI) wafer, an interface that can be easily adapted to any rib waveguide structure. The proposed method provides a fibre-to-waveguide self-alignment capability with an accuracy limited by fibre size tolerance and also an optical quality chemical etching and simultaneous polishing of the associated waveguide end/facet. A series of passive rib waveguide structures similar to that shown schematically in Figure 1(b) were constructed and loss measurements were carried out to demonstrate the effectiveness and achievable optical quality of this new interface fabrication technique and to illustrate the enhanced simplicity in alignment it provides when compared to similar single-mode rib waveguide devices fabricated using the conventional saw cut and mechanical polish technique. The intensity mode profile of the rib waveguides were numerically simulated and experimentally measured to verify the single-mode nature of the fabricated rib waveguide structures.

2. RIB WAVEGUIDE FABRICATION

A series of single-mode SOI rib waveguide devices of different lengths with the new fibre-to-waveguide interface were fabricated on a (100) n-type BESOI wafer using a two mask lithography process in conjunction with an alignment to the $\langle 011 \rangle$ plane and wet chemical anisotropic etchant processing. To ensure the single-mode nature of the SOI rib waveguides fabricated using both the proposed method and conventional processing techniques respectively, all were designed such that their heights H and widths W conformed to the single-mode condition [14] (where as defined in Figure 2, r is the ratio of the thickness of the side and center regions of the rib structure):

$$\frac{W}{H} \leq 0.3 + \frac{r}{\sqrt{1-r^2}}, \quad r \leq 0.5 \quad (1)$$

The cross section of both sets of waveguide devices (as defined in Figure 2) were designed with the dimensions $H = 11\mu\text{m}$, $W = 9\mu\text{m}$ and $r = 0.5$ to satisfy Eq.(1), and more importantly to ensure an optimum coupling efficiency to a standard single-mode fibre with a mode field diameter of $10.5\mu\text{m}$. As an aid in confirming the single-mode nature of the rib waveguide devices, numerical simulation based on the Beam Propagation Method (BPM) of analysis was performed to calculate the mode field distribution using the physical attributes of both sets of fabricated devices. Figure 2 shows the simulation result (Fig. 2(a)) and experimental result (Fig. 2(b)) of the intensity mode profile of the silicon rib waveguide device, which is single-moded as expected.

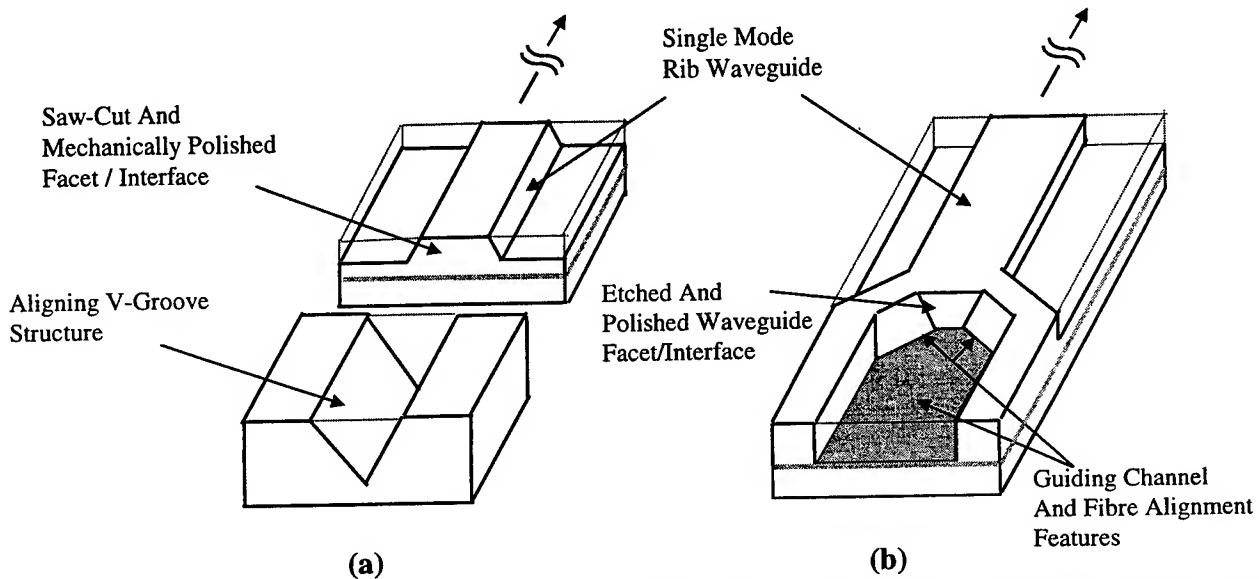


Figure 1 (a) Standard processing techniques call for segregation of the fabricated rib waveguide device and the alignment structure whilst also having to saw cut and mechanically polish each waveguide facet in order to achieve an optically smooth surface. (b) Fabrication of both fibre alignment features and optical quality waveguide facet polishing are completed concurrently and integrated on the same substrate. The combinational advantages of this processing technique greatly reduce the power loss through misalignment errors and surface roughness on the waveguide sidewalls or end facets.

A BESOI wafer, with a device layer thickness of $11\mu\text{m}$ and buried oxide (BOX) layer thickness of $2\mu\text{m}$, was cleaned and prepared for lithography using standard wafer preparation techniques [15]. Initial alignment to the $\langle 011 \rangle$ plane was achieved using alignment marks at an angle of 45° to the $\langle 100 \rangle$ plane. A solution consisting of Tetra-methyl Ammonium Hydroxide (TMAH) 50%, Isopropyl Alcohol (IPA) 30% and H_2O 20% at 40°C with an etch rate of $\approx 54.5 \text{ nm/min}$ was used to controllably etch along the $\langle 011 \rangle$ plane(s) of the Si device layer during device processing. Rather than using KOH or a solution of EDP, TMAH was chosen for its adequately high selectivity of Si over SiO_2 ($\approx 2000:1$), its relative ease of use and low toxicity [16], [7].

The SEM micrograph in Figure 3 shows a top view of one end of the fabricated waveguide device(s), indicating which areas were fabricated during each of the two lithography and etch stages. The first lithography and timed wet etch steps defined and formed the U-groove channels for fibre alignment, along with the optical quality waveguide facets. Upon a further wafer cleaning and a subsequent re-oxidation step, a second lithography process and timed wet etch were performed. This second set of process steps resulted in the formation of the waveguide structures and their alignment with the already fabricated U-groove channels.

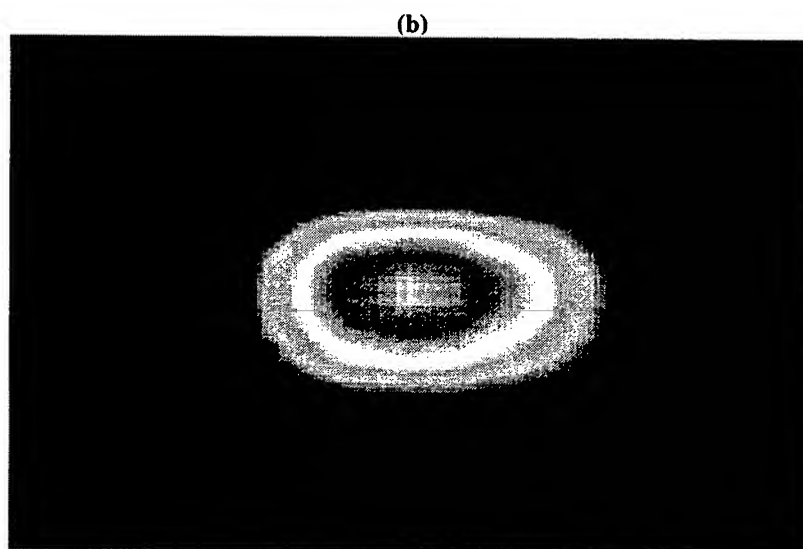
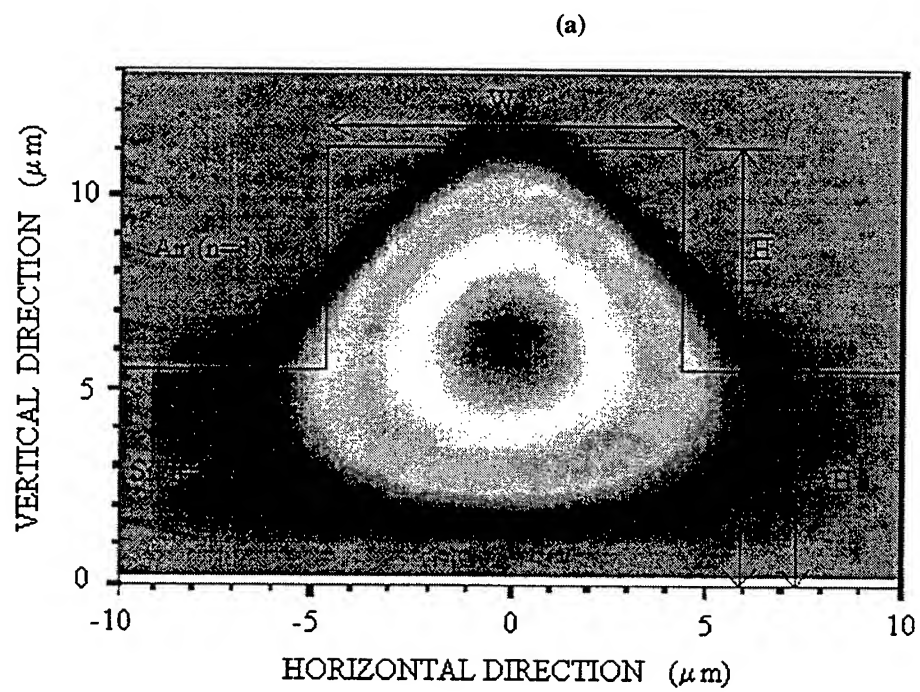


Figure 2 (a) A numerically simulated intensity mode distribution of a single-mode silicon rib waveguide. (b) An experimentally measured intensity mode distribution of a single-mode silicon rib waveguide.

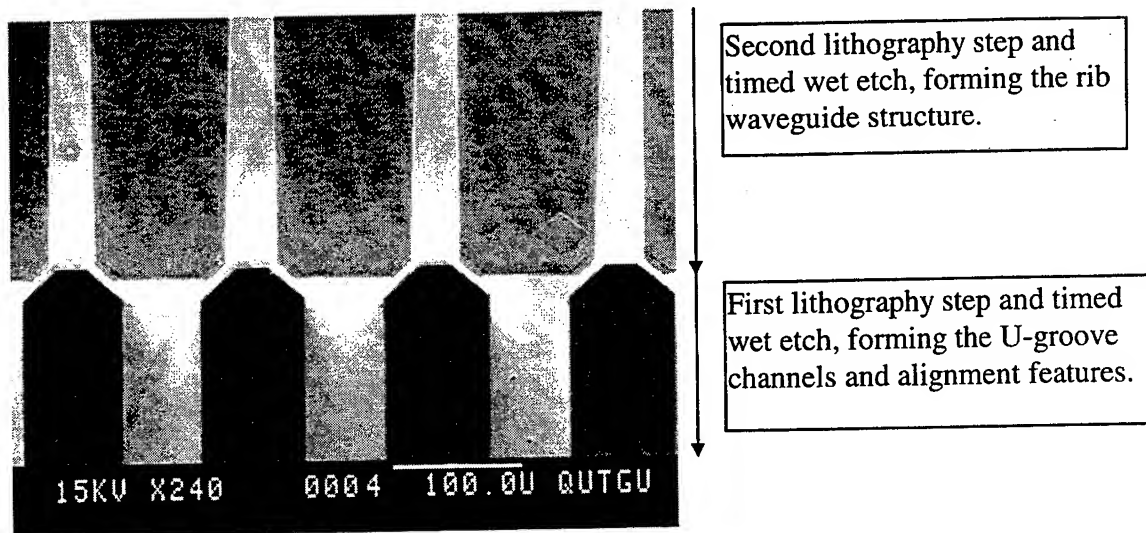


Figure 3 Top view of the fibre-to-waveguide interface region. Added are lines indicating the parts of the device formed at each lithography step.

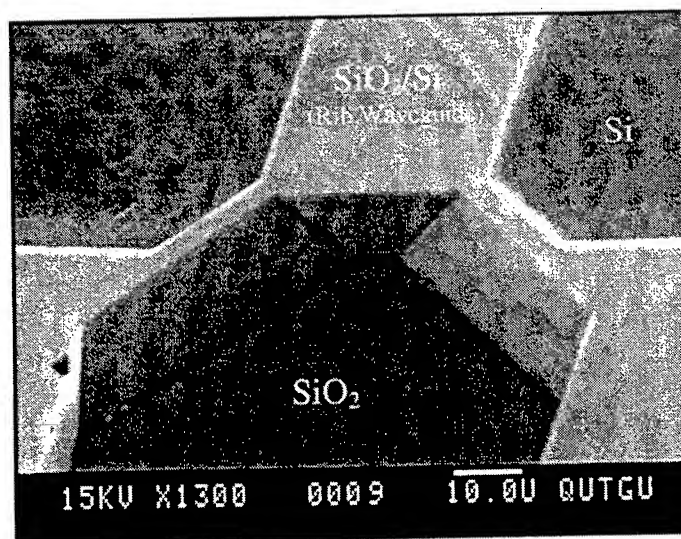


Figure 4 Entrance to rib waveguide structure showing the polished waveguide end and the alignment features at the end of the U-groove channel.

The SEM micrograph in Figure 4 identifies the various materials around the end of one of the silicon rib waveguide structures. It also shows a close up view of the waveguide facet and its associated fibre alignment features. Figures 3 and 4 demonstrate how precise alignment to the $\langle 011 \rangle$ plane(s) and fine control over the wet etch chemistry used can result in a well aligned structure with visually smooth and optically flat ends. It should however be noted that the angular dependence of the alignment step is quite large, with a misalignment $\geq \pm 1^\circ$ resulting in terraces forming along the etched sidewalls of the

<011> plane(s) [17]. Correct alignment is critical to ensure the waveguide facet and sidewalls are perfectly flat and maintain an optical quality smoothness. Unlike V-grooves, the U-grooves shown in Figure 3 have vertical sidewalls and taper at their ends due to the intersection with <111> planes. Given the precision of modern photolithography processes, the newly proposed technique enables reduction of the alignment errors to the level of fibre size tolerances. Hence, optically flat waveguide facets and a passive fibre alignment mechanism can be achieved concurrently during the fabrication of the waveguide devices themselves.

The waveguide devices shown are tailored for a single-mode fibre with a mode field diameter of $10.5\mu\text{m} \pm 0.5\mu\text{m}$. To help minimize any mode field mismatch between the coupling fibres and the rib waveguides, optical fibres of $\approx 10\mu\text{m}$ diameter were obtained through a process of timed isotropic wet chemical etching of the cladding of one end of a $125\mu\text{m}$ diameter single-mode fibre in a solution of concentrated Hydrofluoric Acid (HF 50%) with an experimentally determined etch rate of $\approx 1.78\mu\text{m} / \text{min}$ [cf.18]. Experimental tests have shown that retaining only a very small amount of cladding around the core of a single-mode fibre does not contribute to any significant power loss. Due to the unavailability of (110) oriented SOI wafers of the required dimensions, thinned $10\mu\text{m}$ fibres were used so as to facilitate experimental verification of the newly proposed concepts using (100) oriented BESOI wafers. Figure 5 shows an optical micrograph of a thinned ($\sim 10\mu\text{m}$) fibre in place at the end of one of the waveguide structures described in this section.

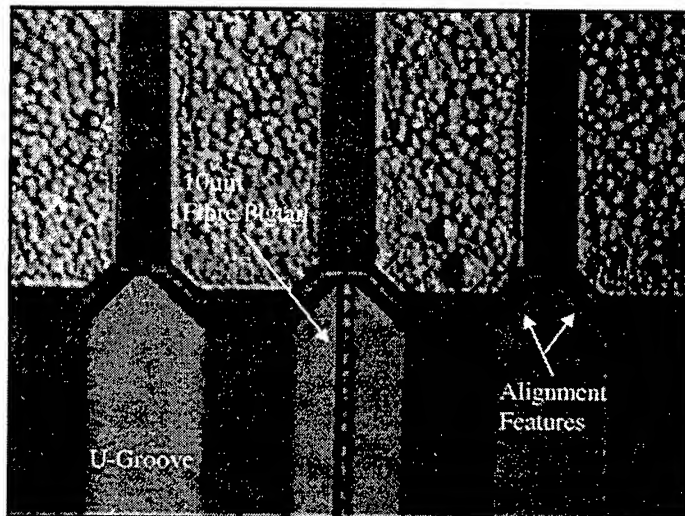


Figure 5 A $10\mu\text{m}$ fibre is aligned to and butted up against the end of a rib waveguide structure using the U-groove and self-alignment features provided. Particulates seen along the fibre are due to the cleanliness of the atmosphere in the room at the time this optical micrograph was taken.

Device fabrication using (110) oriented BESOI wafers would result in the fabrication of an optical quality waveguide end/facet and U-groove alignment feature of dimensions such that the thinning of the $125\mu\text{m}$ cladding is no longer required. Beginning the process with a (110) oriented SOI wafer, the first mask layer can be designed to match the thickness of the fibre which is to be coupled to the waveguide. In the first lithography process step the U-groove pattern is to be aligned to the <110> plane (similar alignment is required for subsequent waveguide patterning) so unlike fabrication using a (100) oriented substrate, the vertical etch rate becomes dominant over the lateral etch rate which in this case is impeded due to the <111> crystallography along the walls of the etched U-groove. Once the anisotropic wet etch step commences, etching continues vertically until the buried oxide layer is reached where an additional timed wet etch in buffered HF etchant is required to remove the underlying SiO_2 , before the anisotropic wet etching of the U-groove re-commences (etching is now at the depth of the handle wafer) and continues until the desired depth is reached. In this case the desired depth of the U-groove channel is determined by the diameter of the fibre used and ultimately by the duration of the wet etch process. As a result of these material and process changes, the angled <111> planes (as shown in both Figures 3 and 4) are now removed resulting in the perpendicular termination of the U-groove structure (ie., sidewalls) with the waveguide facet. As in previous experimental

discussions, this is a timed wet etch process and can be designed to give greater fibre-to-waveguide alignment, while at the same time maintain the functionality and facet quality demonstrated in this paper. It should also be noted that changes to the fabrication of the U-groove structure in the first lithography and wet etch processing steps in no way alters subsequent process steps in which the waveguide itself is defined and etched.

This example of the self-alignment of a fibre to a waveguide structure demonstrates the potential advantage and applicability of this method to self align active and passive waveguide devices on the same silicon platform (i.e. monolithic integration). An example of this may be in the alignment or coupling of active and passive devices used together with flip-chip bonding techniques where laser and photodiode devices are fabricated on a multi-layered substrate and later coupled to the active/passive optic waveguide circuitry which resides on a separate SOI substrate.

In order to compare this newly proposed fabrication method with existing techniques, a series of single-mode rib waveguides of varying lengths were fabricated on SOI substrates using conventional processing techniques including waveguide alignment along the $\langle 001 \rangle$ plane and subsequent sawing and mechanical polishing of the waveguide ends [8], [19]. Figure 6 shows an optical micrograph of one of the conventionally processed waveguide facets that has been saw cut and mechanically polished using $9\mu\text{m}$, $1\mu\text{m}$ and finally $0.3\mu\text{m}$ grade polymer sheets coated with aluminum oxide. The loss measurements for these and the previously introduced SOI rib waveguide devices fabricated using the proposed method are discussed in the following sections.

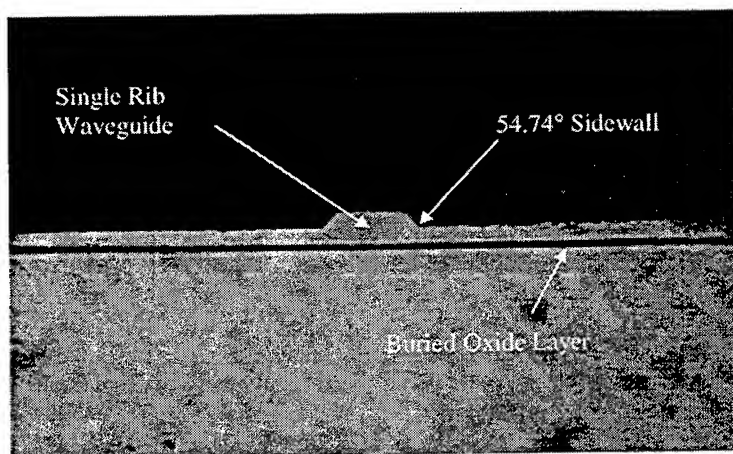


Figure 6 A conventionally processed waveguide facet showing its smooth mechanically polished surface, the sloping 54.74° sidewalls and the underlying $2\mu\text{m}$ buried oxide layer.

3. EXPERIMENTAL RESULTS AND DISCUSSION

3.1 Experimental Setup

The power loss measurements were taken using an experimental setup as shown in Figure 7. A 1300-nm laser diode with a fibre pigtail was used to launch the light into a length of single-mode fibre having a mode field diameter of $10.5\mu\text{m} \pm 0.5\mu\text{m}$ and a core diameter of $8.3\mu\text{m}$. Two xyz micro-positioners were used to manipulate the thinned ($\approx 10\mu\text{m}$ diameter) end sections of both the launch and receive fibres. With the sample position fixed between both positioners, the vertical, horizontal and angular position of the launch and receive fibres are adjusted until a maximum output power is achieved. This fine tuning is avoided almost entirely when taking power loss measurements for waveguide devices fabricated using the new fibre-to-waveguide interface. In these instances, once the send or receive fibre is placed resting in the alignment channel, the fibre can be advanced until making contact with an alignment plane located at both the left and right of the launch window (waveguide facet) where further advancement slides the fibre into the center of the optical quality waveguide facet. This precise alignment is dependent on the accuracy and control used during the fabrication of the device with which the interface

is to be used. However, we have found during experimentation that it is in stark contrast to the difficulty and time incurred whilst trying to align fibres to conventionally processed waveguide ends like the one shown in Figure 6.

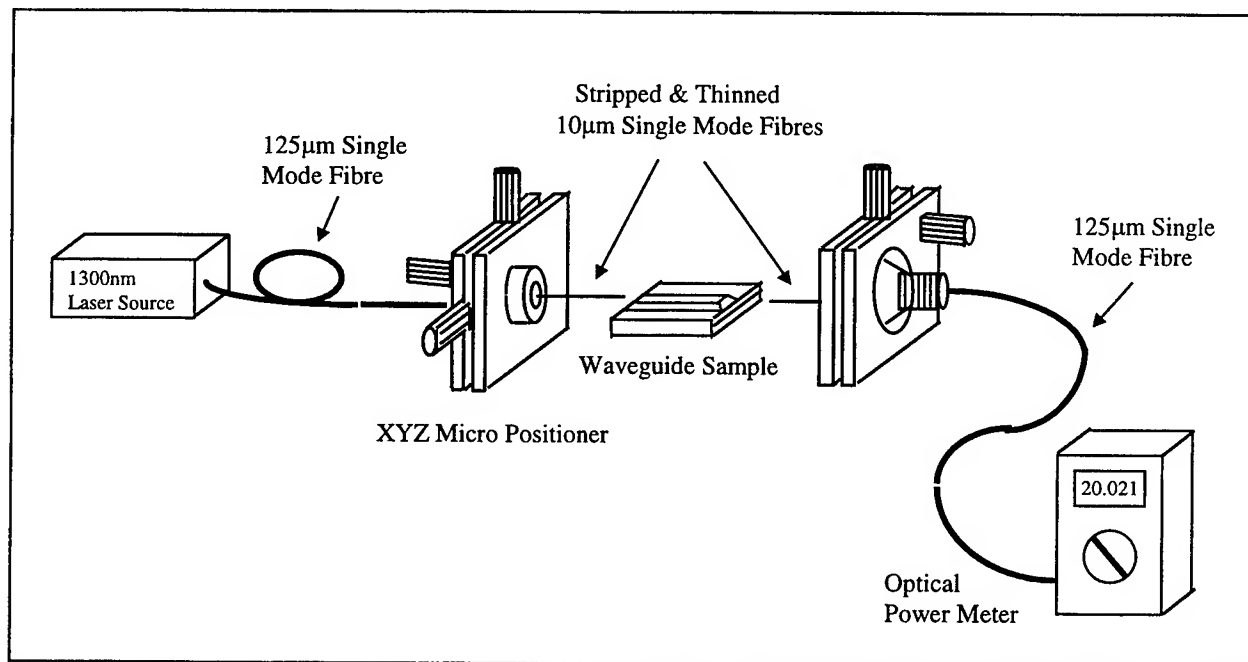


Figure 7 The experimental setup used to test the two sets of single-mode rib waveguides fabricated using both the conventional waveguide manufacturing technique and the newly presented micromachining based technique.

3.2 Measurement Results And Analysis

Each set of straight rib waveguide devices varied in length from 1mm to 5mm and from 10mm to 40mm for both sets of devices fabricated using the new and conventional processing techniques, respectively. Using measurement techniques described as per the experimental setup in Figure 7, the measured waveguide losses obtained for both sets of devices are shown in Figure 8. The slope of the line(s) passing through the points on the main graph of Figure 8 and its inset are identical and fixed at a value of 0.13 dB/cm (the waveguide loss) determined mathematically using the line of best fit through the measurement results shown on the main graph. By curve fitting this line to the points of the inset graph in Figure 8, the waveguide loss is assumed to be equal for all fabricated waveguide devices. Therefore, a more accurate quantitative comparison of the optical quality of the end facets for the waveguide devices fabricated using both new and old techniques can be made based solely on the loss measured due to facet roughness (assuming any measurement inaccuracy, mode field mismatch, etc to be shared). As can be seen from the graph(s) of Figure 8, both sets of measured results are reasonably consistent with each other and lie around this line. The line intercepts indicate power losses at the facets (power losses for "zero-length waveguide"). It can be seen from the insert-figure that our waveguide devices whose facets were fabricated using standard mechanical cut and polish techniques resulted in a measured power loss which was much higher than the theoretically calculated Fresnel Loss, which was found to be approximately 3.6 dB. As opposed to this result, the waveguide devices fabricated using the proposed technique whose facets were wet etched resulted in a much smaller loss, so much so, that the excess facet loss becomes practically unmeasurable. The results obtained indicate a superior quality of waveguide facet having been etched and polished concurrently using the proposed fabrication method. The greater loss shown for the waveguide facets processed using the conventional saw cut and mechanical polishing techniques, although possibly due to inconsistencies in fabrication, merely highlights the greater probability of the introduction of loss due to what appears to be a

lesser quality fabrication technique. Whether the added loss is introduced via inconsistencies in mechanical polishing or fibre-to-waveguide alignment is uncertain since both were painstakingly performed across a number of samples to verify the experimental results reported. What does remain clear however, is the fact that the proposed fabrication technique can remove many of the inaccuracies associated with fibre-to-waveguide alignment and polishing inconsistencies which lead to undue power loss at the fibre-to-waveguide interface.

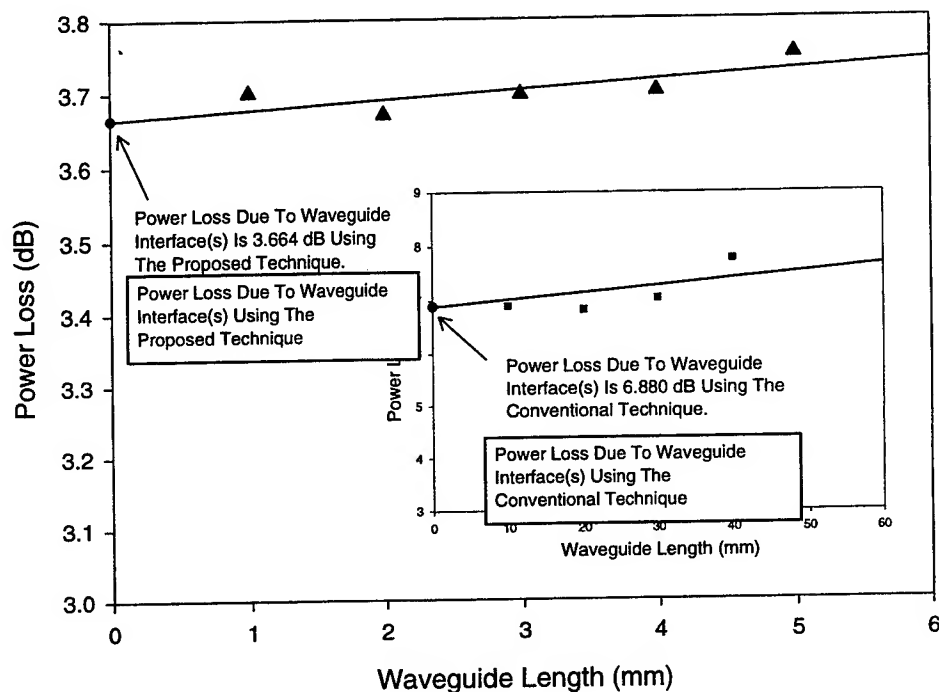


Figure 8 Experimentally determined waveguide loss measurements showing the quality of the waveguide facet when fabricated using the new design technique. The inset shows the waveguide loss measurements using the conventional saw-cut and mechanical polishing techniques.

4. CONCLUSION

This paper has introduced and discussed a unique method (which is equally applicable to the fabrication of an active device) by which a passive rib waveguide device can be fabricated with an integrated passive fibre alignment feature and optical quality waveguide facets, simply and automatically as part of the overall fabrication process. This method has been demonstrated by the fabrication and testing of a series of straight rib waveguide devices. When compared with similar devices fabricated using conventional techniques, loss measurements indicated that the optical quality of the waveguide facet produced as a result of the new wet etching process was of a higher quality and less prone to loss due to fabrication error. This new device processing technique is considered to be of great practical importance since it not only simplifies and makes more efficient a process that currently incurs an increase in production time and cost due to the added mechanical handling of the waveguide devices after their initial fabrication, but it also has been shown through experimental measurements to produce a higher optical quality waveguide facet.

ACKNOWLEDGMENTS

The authors would like to thank Prof B. Jalali and S. Yegnanarayanan of the University of California, Los Angeles, for their useful discussion. Also, thanks must go to Prof Mike Austin of RMIT for the time taken to discuss some of the issues covered in this paper.

REFERENCES

1. B. Jalali, P.D. Trinh, S. Yegnanarayanan and T. Coppinger, " Guided-wave optics in Silicon-on-Insulator technology", *IEEE Proc. Optoelectronics*, **143**, pp. 307-311, 1996.
2. H. Fujita, "Application of micromachining technology to optical devices and systems", *SPIE Conf*, **2880**, pp. 2-11, 1996.
3. S.J. Walker, "OPTICS & MEMS : An Overview Of Current Technology", *MOEMS '97*, Nagoya, Japan, pp. 179-185, 1997.
4. R. Soref, "Applications of Silicon-based optoelectronics", *Materials Research Society Bulletin*, April Issue, pp. 20-24, 1988.
5. C. Strandman and Y. Backlund, "Passive Alignment And Holding Of Devices Using Flexible Tongues Formed By Selective Etching", *Proc. Of MME '96*, Barcelona, Spain, pp. 113-116, 1996.
6. M. Guendouz, N. Pedrono, J. Charrier, P. Joubert and J. Le Rouzic, "Electrochemical Micromachining Of Silicon Platforms For Optical Fibre Alignment", *Electronics Letters*, **33**, pp. 1695-1696, 1997.
7. R-S. Cheng, T-J. Wang and W-S. Wang, "Wet Etched Ridge Waveguides in Y-cut Lithium Niobate", *J. of Lightwave Technology*, **15**, pp. 1880-1887, 1997.
8. T. Zinke, U. Fischer, et al., " Comparison Of Optical Waveguide Losses In Silicon-On-Insulator", *Electronics Letters*, **29**, pp. 2031-2032, 1993.
9. H. Ahlfeldt, J. Holm, S. Lindgren, L. Backlin, C. Vieider, S. Nilsson, T. Klinga, M. Nilsson, M. Svensson, L. Granlund, P. Laubert and B. Sundstrom, "Passive Alignment Of Laser Arrays To Single-Mode Fibres Using Microstructured Silicon Carriers", *MOEMS '97*, Nagoya, Japan, pp. 155-159, 1997.
10. C.A. Jones and K. Cooper, "Hybrid Integration Onto Silicon Motherboards With Planar silica Waveguides", *IEEE Proc. Optoelectronics*, **143**, pp. 316-321, 1996.
11. F. Shimokawa, "New Dry etching System Using High-Density Plasma Source For An Optical Microelectromechanical System", *MOEMS '97 : International Conference On Optical MEMS And Their applications*, Nara, Japan, Nov 18-21, pp. 74-79, 1997.
12. A.V. Churenkov, "Silicon Micromechanical Optical Waveguide For Sensing And Modulation", *Sensors And Actuators A*, **57**, pp. 21-27, 1996.
13. A. Harpin, "Integrated Optics In Silicon : Coming Of Age", *SPIE Conf : Silicon- Based Monolithic and Hybrid Optoelectronic Devices*, San Jose, California, 13 Feb, **3007**, pp. 128-135, 1997.
14. U. Fisher, et.al. "0.1 dB/cm Waveguide Losses In Single-Mode SOI Rib Waveguides", *IEEE Photonics Technology Letters*, **8**, pp. 647-648, 1996.
15. M.A. Rosa, S. Dimitrijevic and H.B. Harrison, "KOH Wet Etching Techniques For The Micromachining Of (100) SOI Wafers", *IEEE COMMAD Conf*, pp. 454-457, Dec, 1996.
16. Les M. Landsberger, S. Naseh, M. Kahrizi and M. Paranjape, "On Hillocks Generated During Anisotropic Etching Of Si In TMAH", *IEEE J.MEMS*, **5**, pp.106-116, 1996.
17. M. Vangbo and Y. Backlund, "Terracing Of (100) Si With One Mask And One Etching Step Using Misaligned V-Grooves", *J. Micromech and Microeng*, **6**, pp. 39-42, 1996.
18. H.M. Marchman, J.E. Griffith and R.W. Filas, "Fabrication Of Optical Fiber Probes For Nanometer-Scale Dimensional Metrology", *Rev. Sci. Instrum*, **65**, pp. 2538-2541, 1994.
19. P.D. Trinh, S. Yegnanarayanan, B. Jalali, "Optical Couplers In Silicon-On-Insulator Technology", *Conference On Lasers And Electro-Optics*, **9**, pp. 250-251, June 2-7, 1996.

Crossover photonic switching network with CMOS/SEED smart pixel device and 2D optical fiber bundle array

Fengguang Luo^{*a}, Mingcui Cao^a, Qiaoyan Hu^a, Anjun Wan^a, Jun Xu^a, Cong Deng^a, Deming Liu^b

^aNational Laboratory of Laser Technology, Huazhong University of Science & Technology,

1037 Luo Yu Road, Wuhan 430074 P. R. China

^bDept. of Optoelectronic Engineering, Huazhong University of Science & Technology,

1037 Luo Yu Road, Wuhan 430074 P. R. China

ABSTRACT

A 16×16 Crossover photonic switching network with hybrid integrated CMOS/SEED smart pixel device and 2D optical fiber bundle array I/O access device is reported in this paper. SEED array devices are used as light receivers and transmitters(modulators), while CMOS devices make efficient logical processing. 4×40 2D multilayer optical fiber bundle arrays are fabricated and are used as I/O access devices in the crossover photonic switching network. The center to center spacing between adjacent optical fibers in the same layer of the fiber array is 125 μ m, and the spacing between adjacent layers is 250 μ m. Displacing tolerance of the fiber bundle arrays is less than 4 μ m and the angular tilt error is less than 0.03 degree. It has the feature of high density, high precision, array permutation and easy to couple with 2D CMOS/SEED smart pixel device.

Keywords: Photonic switching; Crossover interconnection network; CMOS/SEED smart pixel devices; 2D optical fiber bundle array

1. INTRODUCTION

Optical interconnection networks are mainly divided into two kind of interconnection ones. One is single stage interconnection network, and the other is multistage interconnection network. In one hand, although single stage interconnection network (such as crossbar network) has the feature of simple construction, the numbers of the switching nodes needed in the interconnection network system are much higher.¹ On the other hand, multistage interconnection network (such as Omega network, crossover network, banyan network) use less numbers of the switching nodes, but the optical hardwares needed in the whole multistage interconnection network are increased greatly because of different interconnection stages.²⁻⁵ If one can find a recirculating method to realize different interconnection stages of multistage interconnection network by using a same single stage optical setup, the optical hardwares used in multistage optical interconnection network will be reduced greatly. In recent years, Owing to rapid evolution in optoelectronic devices and VLSI technologies,⁶⁻⁸ hybrid integrated smart pixel CMOS/SEED (silicon complementary metal oxide semiconductor/self-electro-optic-effect-device) is regarded as one of the extremely attractive optoelectronic device for optical communications, optical computing, photonic switching and information processing. It also supplies a possibility to construct multistage optical interconnection network with single stage circulating setup. In this paper, we propose a kind of optical circulating

*Correspondence: Email: lmccao@mail.hust.edu.cn; Telephone: +86 27 87544096; Fax: +86 27 87544096

implementation method for the optical crossover switching network with optoelectronic smart pixel devices and 2D optical fiber bundle array. A 16×16 crossover recirculating implementation setup has been constructed. SEED array devices are used as light receivers and transmitters(modulators), while CMOS devices make efficient logical processing. In order to couple with 2D light window array of the SEED device, 4×40 high density multilayer optical fiber bundle array has been fabricated in our experiment. This photonic switching network system has the features of high density, small size, simple architecture and easy to realize.

2. MULTISTAGE CROSSOVER INTERCONNECTION NETWORK

The optical crossover interconnection network is one of the main multistage regular interconnection networks. Schematic diagrams of the crossover network for $N=16$ (where N is the number of input/output channels) are shown in Fig. 1. Four interconnection stages are needed to construct 16×16 crossover network. In each stage of the crossover network, there are a number of switching nodes. Each of them has two possible fan-in and two possible fan-out lines, one corresponds to straight connection while the other to cross exchange connection. We define the address of the i -th node in layer j as K_i^j , where $i = 0, 1, 2, \dots, N-1$. At the input of the network, $j = 0$ while $j = 1, 2, 3$ and 4 , respectively, in the subsequent layers. The output of the i -th node in layer j is either in straight connection or cross exchange connection, which are denoted as K_{is}^j and K_{ic}^j ($i = 0, 1, 2, \dots, N-1$), respectively. The output channel K_{is}^j or K_{ic}^j of the current stage becomes the input channel K_i^{j+1} of the next stage. The interconnection of the crossover network can be described as follows.

In the first interconnection stage,

$$K_{is}^0 = K_i^1 \quad (i = 0, 1, 2, \dots, N-1), \quad (1)$$

$$K_{ic}^0 = K_{N-1-i}^1 \quad (i = 0, 1, 2, \dots, N-1), \quad (2)$$

In the second interconnection stage,

$$K_{is}^1 = K_i^2 \quad (i = 0, 1, 2, \dots, N-1), \quad (3)$$

$$K_{ic}^1 = \begin{cases} K_{N/2-1-i}^2 & (i < N/2) \\ K_{3N/2-1-i}^2 & (N/2 \leq i < N) \end{cases} \quad (4)$$

In the third interconnection stage,

$$K_{is}^2 = K_i^3 \quad (i = 0, 1, 2, \dots, N-1), \quad (5)$$

$$K_{ic}^2 = \begin{cases} K_{N/4-1-i}^3 & (i < N/4) \\ K_{3N/4-1-i}^3 & (N/4 \leq i < N/2) \\ K_{5N/4-1-i}^3 & (N/2 \leq i < 3N/4) \\ K_{7N/4-1-i}^3 & (3N/4 \leq i < N) \end{cases} \quad (6)$$

In the final interconnection stage,

$$K_{i8}^3 = K_i^4 \quad (i = 0, 1, 2, \dots, N-1), \quad (7)$$

$$K_{i8}^3 = \begin{cases} K_{i+N/8}^4 & (\text{for even } i) \\ K_{i-N/8}^4 & (\text{for odd } i) \end{cases} \quad (8)$$

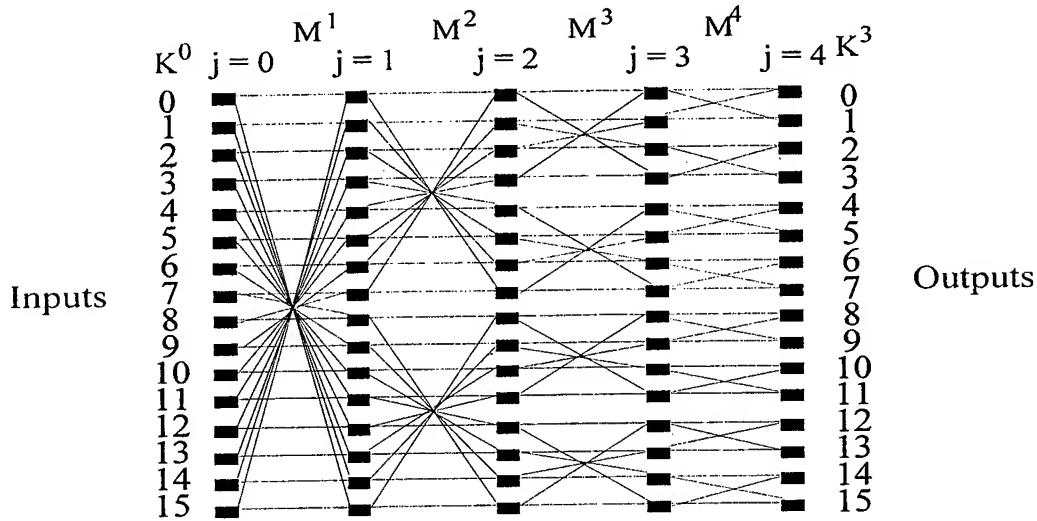


Fig. 1. Schematic diagrams of the four stage crossover network for $N=16$

3. RECIRCULATING IMPLEMENTATION OF CROSSOVER SWITCHING NETWORK

In order to implement optoelectronic recirculating crossover switching network, an optoelectronic switching network module has been constructed which is shown in Fig. 2. It consists of three main parts: one is the free-space optical interconnect network path; Second is the optoelectronic hybrid CMOS/SEED smart pixel array device; Third is 2D optical fiber bundle array I/O access device. The free-space optical interconnect path is composed of the polarization beamsplitter (PBS), the quarter waveplate (QWP), the imaging lenses (L), the binary phase grating (BPG), and the pumped quantum well semiconductor laser diode (PLD). A flip-chip assembled CMOS/SEED smart pixel array is used as the switching nodes. The SEED array is composed of a number of detectors (receivers) and modulators (transmitters) while the CMOS chip makes efficient logical processing. Input signal light beams are sent into the end of 2D input fiber bundle array, then travel through high-bandwidth free-space crossover interconnection network that is implemented by an optical imaging system to form 2D spot array on the windows of the receivers of the SEED array interface of OE-VLSI chip. Light beam from a semiconductor laser diode is first rectified and collimated, then split into 2D spot array by a binary phase grating splitter (BPG) which provides the necessary pumped light source for the modulators of the SEED array. After switched by the CMOS/SEED node array, the output signal beams will be sent into the end of 2D output fiber bundle array to implement the photonic switching. In order to implement the 16×16 crossover switching network in a recirculating

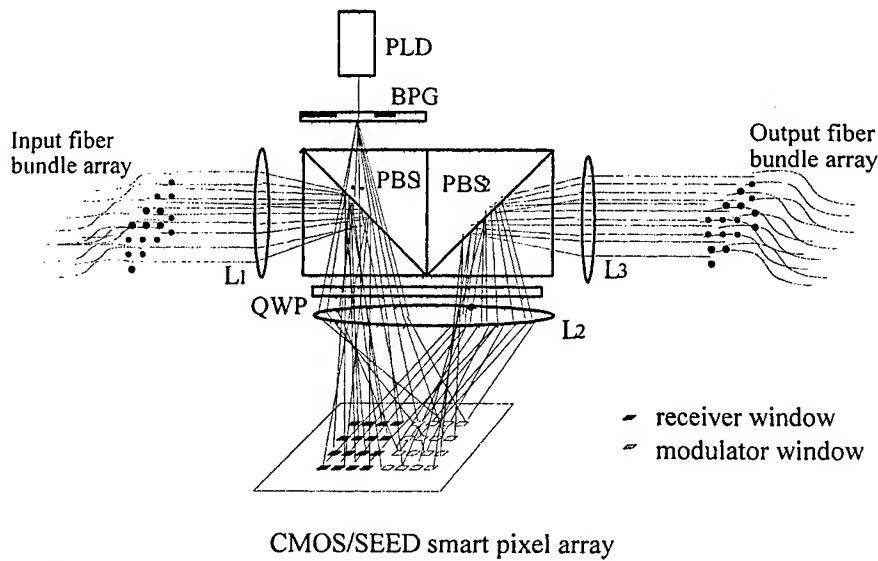


Fig. 2. The crossover optoelectronic switching network

method, a switching logic circuit of the CMOS/SEED smart pixel node array has been designed which is shown in Fig. 3. For a 16×16 channels crossover network, only the 1:5 selector has been used for four stage crossover interconnect network. The input optical signals pass through the free-space optical interconnect network and incident onto the windows of the receiver array on SEED array chip. The input optical signals are first converted to electrical signals through the O/E conversion function of the receivers of SEED pixel array, the converted signals are then fed into the 1:4 selectors of the CMOS logic circuit in a special arrangement. The 1:5 selector has five input ports and one output port, so it can choose one of the five input signals as the output one in a time. The input signals to the 1:5 selector of output channel 0' come from the input channels 0, 1, 3, 7, & 15 in all four interconnect stages; while those to the 1:5 selector of output channel 1' are from the input channels 0, 1, 2, 6, & 14. Similarly, in the last output channel, the input signals to the 1:5 selector come from the input channels 0, 8, 12, 14, & 15. The output electrical signals chosen by the 1:5 selectors are converted to optical signals again through the E/O conversion function of the modulators of the SEED pixel array. They are sent to the output channels of the stage. In each recirculating stage of the crossover network, only two of the five input channels are chosen by each 1:5 selector to perform straight or cross exchange connection according to the requirement of the corresponding interconnection. In the first stage, the output channel 0' selects input channel 0 when a straight connection is required. Otherwise, input channel 15 is chosen. The output channel 1' selects input channel 1 when a straight connection is required. Otherwise, input channel 14 is chosen. Similarly, output channel 15' selects input channel 15 or input channel 0 for straight or exchange connection, respectively. After all the interconnections required in the first stage of the crossover network have been performed, the output optical signals are fed back to the input channels of the recirculating setup. Similar operations are carried out in the subsequent stages until the fourth one. As a result, the whole multistage crossover interconnection switching network can be realized. In order to comparison, a switching logic circuit of the CMOS/SEED smart pixel node array for the single stage crossbar interconnection network is shown in Fig. 4. The 1:16 selector must be needed for 16×16 crossbar interconnect network in this constructure. The numbers of the logic gates in the crossbar switching network is

much larger than the numbers of the logic gates in the crossover switching network. Therefore, the optoelectronic recirculating crossover switching network based on the CMOS/SEED smart pixel array device has the advantages over the crossbar switching network.

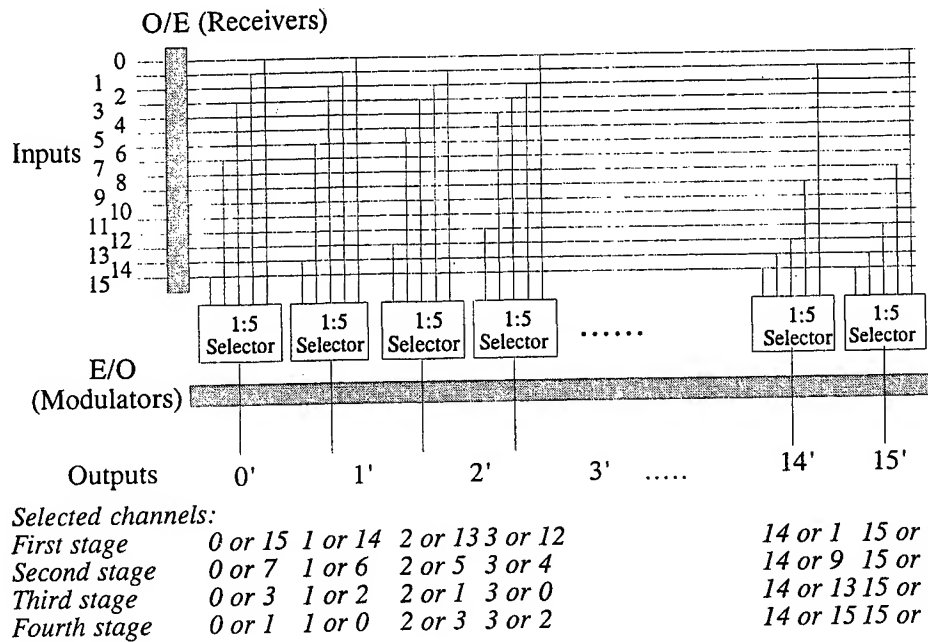


Fig. 3. Switching logic circuit of the CMOS/SEED smart pixel node array for the crossover network

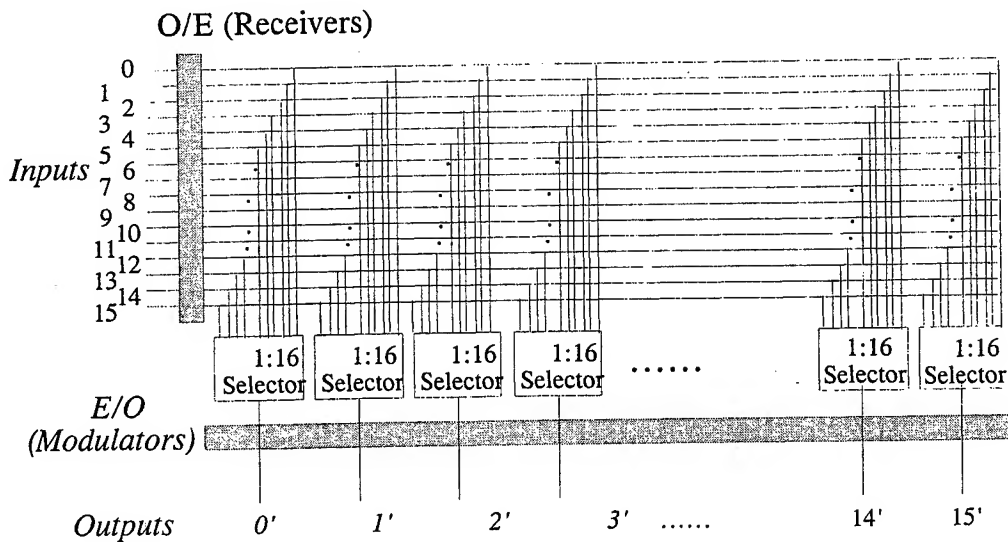


Fig. 4. Switching logic circuit of the CMOS/SEED smart pixel node array for the crossbar network

4. 4×40 MULTILAYER FIBER BUNDLE ARRAY I/O ACCESS DEVICE

As the demands for bandwidth increasing in photonic switching network, large amounts of input data are sent into the photonic switching network and are incidented to the windows of SEED array, then output modulated data signals after switching. As the permutation of light windows of the SEED array is regular, 2D optical fiber arrays are required for I/O access. In order to couple with 2D light window array of the SEED device, on the basis of 2×32 optical fiber bundle array, 4×40 high density multilayer optical fiber bundle array has also been fabricated in our experiment. a novel architecture and assembling technique for two dimensional optical fiber bundle array has been developed. High precision positional glass box is used for assembling optical fiber bundle array. A set of optical monitoring system is set up to control the precision in the process of the optical fiber array adjustment. The micrograph of the ends of 4×40 single-mode optical fiber bundle array are shown in Fig.5. The center to center spacing between adjacent fibers in a layer is $125\mu\text{m}$, and the spacing between two layers is $250\mu\text{m}$. In order to examine the precision of the 2D optical fiber bundle array, a computer-aided CCD image measurement system is used to test the fiber bundle array. The ends of the fiber array are imaged by a CCD image camera and the picture is shown on the screen of the monitor. The spacing between the optical fibers can be measured by shifting the scan line on the screen. Each pixel passed by the scan line has a certain size, so the spacing between optical fibers is confirmed according to the number of the pixels passed from the center of the end of one fiber to the center of the end of the other fiber by the scan line. The measurement results show that the displacement errors in a fiber layer and between two fiber layers are both less than $4\mu\text{m}$, and the angular tilt is less than 0.03 degree. In our

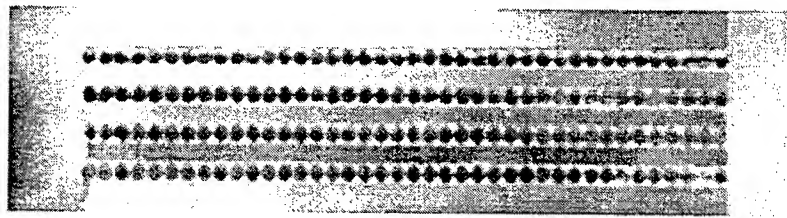


Fig. 5. Micrograph of the ends of 4×40 optical fiber bundle array

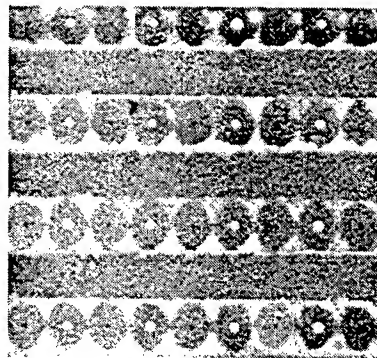


Fig. 6. Micrograph of 4×4 light spots from 2D fiber bundle array

experiment system, only 16 (4×4) data channels are needed. We can only choose 4×4 optical fiber array from 4×40 optical fiber bundle array as the I/O access of the CMOS/SEED smart pixel array. The micrograph of 4×4 light spots from 2D optical fiber bundle array is shown in Fig. 6.

5. CONCLUSIONS

A 16×16 optical recirculating implementation of CMOS/SEED optoelectronic integrated crossover switching network with 2D optical fiber bundle array is presented in this paper. The CMOS/SEED smart pixel arrays with O/E light windows are used as logical controlling switch nodes. High-precision 2D optical fiber bundle arrays are used as the I/O access devices. 4×40 high density multilayer optical fiber bundle array is fabricated. 16×16 optical crossover switching network is constructed using single stage recirculating setup.

ACKNOWLEDGMENTS

The authors gratefully acknowledge the supports by Chinese 863 High Technology Program, and the Science Research Fund provided by the Huazhong university of science & technology, P. R. China.

REFERENCES

1. Mingcui Cao, Qiaoyan Hu, Fengguang Luo, Anjun Wan, and Xu Jun, "A new system architecture of photonic switching model by using an optoelectronic VLSI switching chip," in *Optics in Computing '98*, Pierre Chavel, David A. B. Miller, Hugo Thienpont, Editors, Brugge, Belgium, Proceeding of SPIE Vol. 3490, pp. 84-90, 1998.
2. Mingcui Cao, Fengguang Luo, Hongpu Li, and Shouhu Wang, "Optical perfect-shuffle-exchange interconnection network using a liquid-crystal spatial light switch," *Appl. Opt.* **32**, pp. 6817-6819, 1992.
3. J. Jahns and M. J. Murococa, "Crossover networks and their optical implementation," *Appl. Opt.* **27**, pp. 3155-3160, 1988.
4. T. J. Cloonan, M. J. Herron, F. A. Tooley, G. W. Richards, F. B. McCormick, E. Kerbis, J. L. Brubaker, and A. L. Lentine, "An all-optical implementation of a 3-D crossover switching network," *IEEE Photonics Technology Letters*, **2**(6), pp. 438-440, 1990.
5. J. Jahns, "Optical implementation of the banyan networks," *Opt. Commun.* **76**, pp. 321-324, 1990.
6. A. L. Lentine and D. A. B. Miller, "Evolution of the SEED technology: bistable logic gates to optoelectronic smart pixels," *IEEE J. Quantum Electron.* **QE-29**(2), pp. 655-669, 1993.
7. F. B. McCormick, T. J. Cloonan, A. L. Lentine, J. M. Sasian, R. L. Morrison, M. G. Beckman, S. L. Walker, M. J. Wojcik, S. J. Hinterlong, R. J. Crisci, R. A. Novotny, and H. S. Hinton, "Five-stage free-space optical switching network with field-effect transistor self-electro-optic-effect-device smart-pixel arrays," *Appl. Opt.* **33**(8), pp. 1601-1618, 1994.
8. A. V. Krishnamoorthy, A. L. Lentine, K. W. Goossen, J. A. Walker, T. K. Woodward, J. E. Ford, G. F. Aplin, L. A. D'Asaro, S. P. Hui, B. Tseng, R. Leibenguth, D. Kossives, D. Dahringer, L. M. F. Chirovsky, and D. A. B. Miller, "3-D integration of MQW modulators over active submicron CMOS circuits: 375 Mb/s transimpedance receiver-transmitter circuit," *IEEE Photonics Technology Letters*, **7**(11), pp. 1288-1290, 1995.

Photo-, electro- and cathodoluminescence of porous silicon

L.S.Monastyrskii, I.B.Olenych,, V.P.Savchyn

Physical Department, Iv.Franko Lviv State University,

50 Dragomanov Str.,290005, Lviv, Ukraine

ABSTRACT

The research of spectroscopic properties of porous silicon has been done. Complex of photoluminescence , electroluminescence , cathodoluminescence , thermostimulated depolarisation current analyth methods have been applied to study of geterostructures and free layers of porous silicon. Lightemitting processes had tendency to decrease. The character of decay for all kinds of luminescence were different.

Keywords: porous silicon, luminescence, thermo stimulated depolarisation current.

1. INTRODUCTION

For the first time Canham [1] in Appl. Phys. Letters (1990) reported about exotic visible room-temperature photoluminescence of porous silicon. So it become the possiblyty to create light-emitting dicodes (LED) and lasers on the same substrate of Si. Porous silicon may be a new material for intergrated micro- and optoelectronics.

2.EXPERIMENTAL METHODS

Layers of porous silicon (PS) were obtained by electrochemical etching of n,p-types monocrystalline silicon in HF ethanolic solution. We used (111) Si substrates with thickness of about 400 μm . HF-ethanolic solution with 25% HF concentration was used as electrolyte. Specimens of n-type conductivity were irradiated by white light during electrochemical etching. Some specimens after anodization were etched in concentrated HF about 2.5 h for increasing the porosity [1].

Studies of surface and near surface region of por-Si were done by ellipsometry on wave length of He-Ne laser (633 nm). In the result of experiment we have obtained polarization angles ψ and Δ for different angles of incident light. Using measured values the inverse problem of ellipsometry - determination of refractive index n , absorbtion coefficient k , layers thickness d has been solved. It was nessesary to use two- or three-layers model and create computer programme for obtaining n , k , d values of por-Si layers. We also investigated the influence of technological conditions on optical constants of por-Si and porosity p of the material. The porosity was calculated on the base of n and k using Lorentz-Lorenc equation [2]. Error of calculations was about 10%.

The Thermo Stimulated Depolarisation Current (TSDC) investigation was made by formed thermoelectret state in the sample PS with area 1 cm^2 in vacuum cryostat. Polarisation was carried out in the electric field of the capacitor cell at the temperature between 450 and 480 K. The electric field was about $1\text{-}2 \cdot 10^4$ V/m. After switcing off the polarising electric field the TSD current has been measured with linear heating [3].

For identification of the nature of the defects wich are responsible for the electret state we have carried out the analysis of the energy distribution $g(E)$ of the involved in polarization defect. According phenomenological theory of TSD current for disordered dielectric by way of numerical solving of the Fredgolm integral equation wich is based on the Tikhonov's regularisation method we have calculated $g(E)$ [3].

The photoluminescence (PL) and electroluminescence (EL) in visible (400÷800 nm) spectrum range was studied by automatic equipment. Exciting of luminescence was obtained by nitrogen or argon lasers with wave length 337 and 488 nm, respectively.

PS EL was registered by us in electrochemical cell with 0.5M H_2SO_4 + 0.1M $\text{K}_2\text{S}_2\text{O}_8$ electrolyte in current injection regime. Initial PS layers were created on n-Si (100) substrates with resistivity 4.5 $\Omega\text{-cm}$ by anode etching in HF ethanol solution with current density 10 mA / cm^2 and white light irradiation during 30 seconds. Direct or pulsed current of various

duration and polarity in the current stabilization regime was applied between ohmic contact to the silicon substrate and platinum electrode [4,5].

Cathodoluminescence (CL) of PS we was studied in 300-700 nm spectrum range. The electron beam exiting had such parametres: $U=9$ KV, $\tau=2.5$ μ s, $I=100-200$ μ A, $S=0.1$ mm², $f=30-50$ Gz. The investigation were made at room and temperature of liquid nitrogen.

3.RESULTS AND DISCUSSION

PS optical properties were studied on the basis of ellipsometrical research. In the Fig.1 is shown the relation of refractive indexes of PS pre-surface areas to the degree of porosity which is in its turn determined by the parameters and duration of electrochemical etching of silicon.

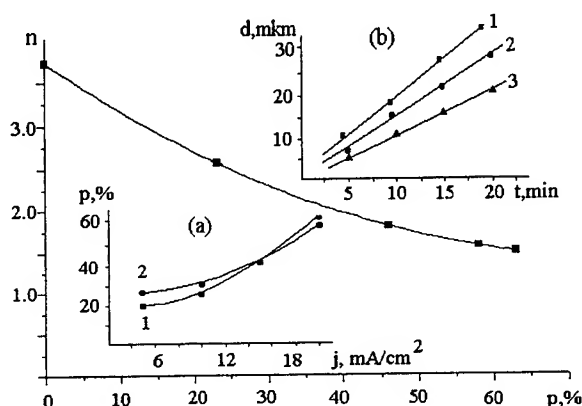


Fig.1. Refractive index dependence via porosity degree of PS:

Insert (a): PS porosity changes wiht increasing of electrochemical etching current density determined by gravimetric (1) and ellisometric (2) metods.

Insert (b): Time electrochemical etching dependence of porous layer thickness for different etching current density: 1-30 mA/cm², 2-20 mA/cm², 3-10 mA/cm².

Refractive index decreases 2 times with the increase in porosity from 0 to 80%.The porosity was calculated from Lorentz-Lorenc equation [2]:

$$\frac{\tilde{n}_{por}^2 - 1}{\tilde{n}_{por}^2 + 2} = \frac{\tilde{n}_{Si}^2 - 1}{\tilde{n}_{Si}^2 + 2} (1 - p') + \frac{n_0^2 - 1}{n_0^2 + 2} p',$$

were n_{Si} , n_{por} - refractive indexes of silicium and porous silicon, n_0 - refractive index of porous syrround, p' -porosity.

Thickness of porous silicon layer changed from 0.1 to 100 micrometers. Such a profound change of pre-surface areas can be atributted due to the change of the composition of porous silicon surface films with different porosity in the process of electrochemical etching.

The typical TSDC spectra of the porous Si-Si substrate structures in the temperature range between 200-450 K are presented on the Fig.3. Structures show quite clear maxima at the temperatures near 350-375 and 425-450 K. The TSDC spectra are not enough informative in indentification of the nature the defects wich are responsible for the electret state. That is why we have carried out the analysis of the energy distribution function $g(E)$ of the involved in polarization defects. The phenomenological theory TSD currents for disordered dielectrics with quasicontinuous energy distribution of the electrically active defects was used with this purpose. According to [3] the thermally stimulated discharge current $j(T)$ can be writtenes :

$$J(T) = \int g(E) \xi(E, T) dE,$$

where

$$\xi(E, T) = \omega \exp\left(-\frac{E}{kT}\right) - \frac{\omega}{\beta} \int_{T_0}^T \exp\left(-\frac{E}{kT'}\right) dT',$$

ω - is the frequency factor, E - is the activation energy, β - the rate of increase of temperature to the initial temperature. For our experimental results $j(T)$ is expressed by the Fredholm's integral equation, which has been solved for $g(E)$ by numerical integration which is based on the Tikhonov regularisation method.

For solving this equation we have used the method of the regularisation by Tikhonov. The left part of the equation numerical file.

So, after numerical calculation we must be introduced by having obtained energy activation distribution function for charged defects (ions) in porous silicon (Fig.2). There were distribution function of filled electron states in energy gap by energy and frequency factor. From these curves we have seen exiting of thermoelectret condition in PS which have made by redistribution of ions which are defect in PS. Obtained spectra were characterised not one date of activation energy but certain distribution.

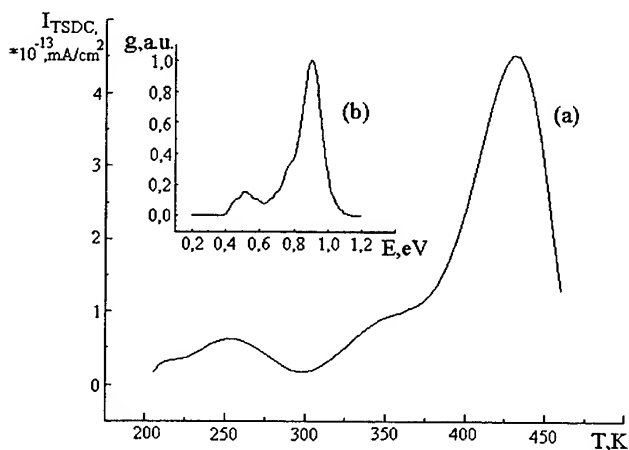


Fig.2. (a). The TSDC spectra of PS-Si heterostructure. Insert (b): The activation energy distribution functions of the defects in por-Si-Si heterostructure.

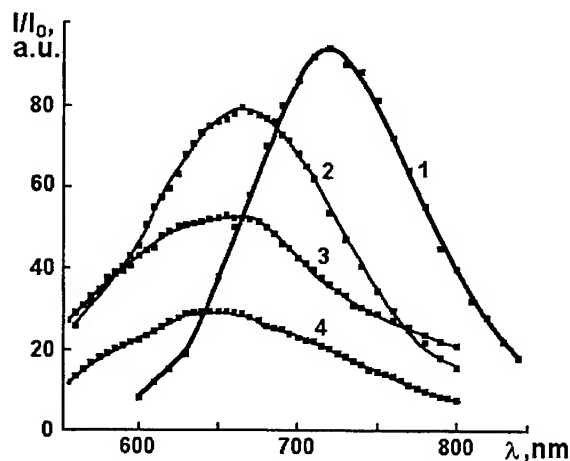


Fig.3. a) The photoluminescence spectra of por-Si under nitrogen (2, 3, 4) and argon (1) laser exciting at $T=293$ K: 1- $p=40\%$, 2- $p=40\%$, 3- $p=60\%$, 4- $p=44\%$ (1, 2- p -type Si, 3, 4- n -type Si).

The intensive photoluminescence (PL) (which was visible at daylight) in p- and n-types of por-Si took place under such conditions of exciting. PL properties of por-Si films were changed with electrochemical etching conditions, type and level of silicon substrates doping. It has been obtained after mathematical approximation of PL spectrum by Gauss curves that luminescence maximum of n-type porous Si specimens was at wavelength about 660 nm and intensity of peak depended on porosity values. In contrast the maximum of luminescence band of p-type was near λ equal to 667 nm. The intensity of light also depends on electrochemical etching conditions (Fig.3). Absolute value of PL intensity of p-type por-Si was higher than PL in n-type por-Si. PL intensity of n-type porous Si increased after additional chemical etching in pure HF, with the material porosity raise.

There have been studied the processes of polymetacrylic acid (PMA) polymer film precipitation from water solution on PS surface swing to the fact that chemical reactions on PS surface continue under atmospheric condition. Precipitation was conducted by placing PS samples into PMA water solution for 5-24 hours. There have been used PMA water solution with different molecular masses (10000-70000) and different ionization degrees (0-1.0). Real medium speed of precipitation was 0.8-1 $\mu\text{m}/\text{hour}$ for 5-10 μm PMA film thickness.

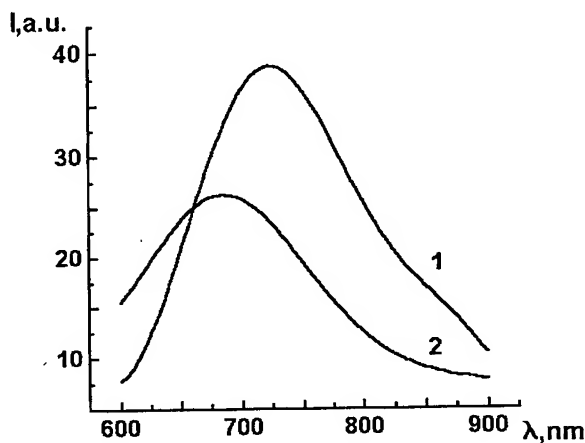


Fig.4. The photoluminescence spectra of PS with nature thin film coating (1) and with polymer film coating (2).

The obtained heterostructures of PS-PMA had photoluminescence properties. Photoluminescence spectrum of the PS was transformed owing to interaction between PMA and the PS surface. Photoluminescence curves had gaussian shape with one wide maximum at room temperature which was moved by 70-80 nm toward short wave band of the spectrum in connection with PS spectrum without polymer film. The maximum of luminescence was located at about 600-625 nm owing to the ionization degree. Luminescence in the maximum decreased 2-2.5 times with the increase in intensity (Fig.4).

EL with wide band in the interval of wave lengths of 500-900 nm was observed for various regimes under direct PS shift (Fig.5). Under inverse PS shift EL intensity approached zero. Integrated PS EL, which was registered by PEM-62 photoelectronic multiplier, decreased after switching on the injection direct current. That was especially characteristic for p-type PS samples, when the integrated intensity decreased twice during 1 minute. We have investigated the effect of the character of pulsed excitation regime on EL intensity and degradation (Fig.6).

For n-type samples EL PS intensity was by an order higher than for those of p-type, and it was stable during the time of measurements (30 minutes). EL was excited by periodic direct and inverse pulses of 1 and 0,2 seconds duration, respectively, and with -10 and +5 mA amplitude. A peculiar feature here is full reproduction of EL spectra after the fifth measurement. That is, in this excitation regime no irreversible changes were observed.

EL bandwidth did not change when EL was excited by short duration pulses (direct pulse of duration- 0,2 sec. and inverse - 0,05 sec.) with the previous values of current. Nevertheless, EL intensity in maximum increased by 25 % and it did not changed for 30 minutes during 5 consecutive measurements, but decreased exponentially by 3÷5 times as compared with the initial one. EL degradation was irreversible. EL restoration was possible only after electrochemical etching of the sample in HF (30 minutes), what is likely to have resulted in dissolution of the oxide film on PS surface. It should however be mentioned that the intensity of renewed EL was 5÷10 times less than the initial one, what may be explained by reduction of PS layer thickness. Spectral dependence of PS EL velocity decay was investigated by us in the inverse changes regime, that

is, in the regime of long duration pulses (direct pulse 1 sec., inverse pulse 0,2 sec.). EL decay velocity was different when the inverse pulse was sent with different wavelengths. Moreover, intensity decay within the same testing time was greater for EL short wavelength part of the spectrum. That is, in PS there are the groups of EL centres which are characterized by sharp decay kinetics short - wave length groups by faster kinetics and long wave length by slower kinetics.

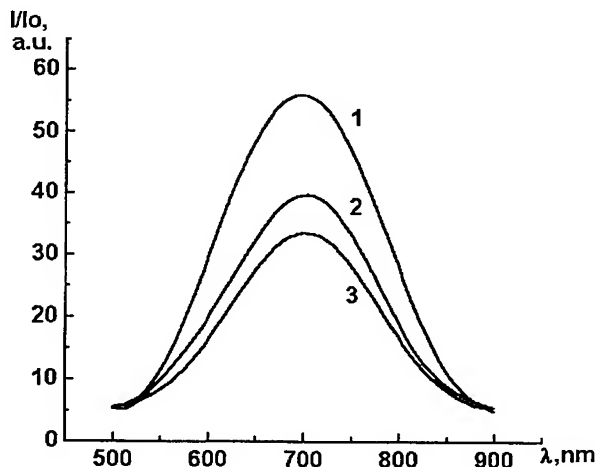


Fig.5. EL spectrum of PS in electrolyte contact:
(1) - initial time moment, (2) - after 5 min, (3) - after 10 min.

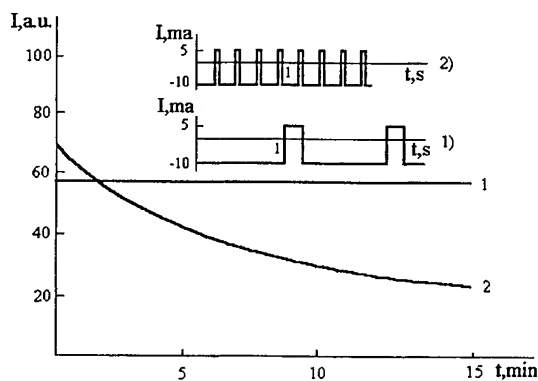


Fig.6. Time dependence of maximum EL intensity decay: 1-a)-type injection current;
2-b)-type injection current.

We also have investigated cathodoluminescence (CL) from PS. Two dominant CL bands with maximum in visible (at 550-570 nm) and ultraviolet (360-380 nm) regions were observed (Fig.7). The intensity of short wave band was in some times more, but decreasing velocity was strongly high comparatively with long wave one.

CL blue band confirm existing of dielectric coating on quantum wires surface ($\epsilon_g \approx 3.1$ eV). Long wave CL peak shift into short wave region comparatively with the same bands of PL and EL ($\epsilon_g \approx 2.4$ eV). This may be connected with different depth of exciting PL, EL, CL and absorption of radiation by porous silicon.

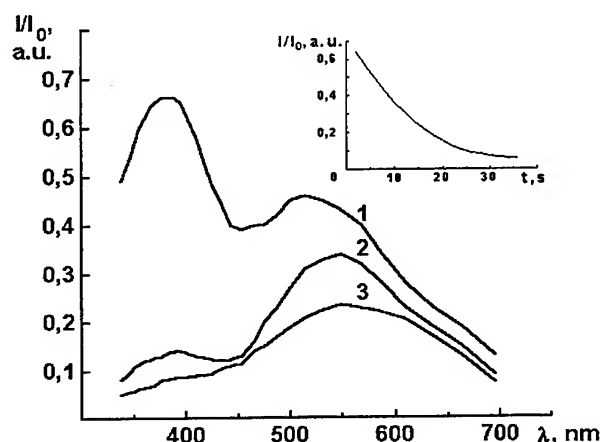


Fig.7.CL PS spectrum at 77 K (1,2) and 300 K (3) at initial time moment (1,3) and after 20 min.(2).
Insert - CL time intensity decay at λ_{max} .

Decreasing kinetics of this kinds of luminescence were different: PL was stable for investigation time (~ 1 h). Decreasing times for CL and EL were 15-20 min and 10-15 min. So the photo-, electro- and cathodoluminescence in porous silicon have strong the different nature.

CONCLUSIONS

All specimens have wide band of PL with maximum in range from 650 nm to 760 nm. Intensity of n-type por-Si specimens PL is by 5÷6 times lower than from p-type por-Si ones.

Thus, PS EL intensity has a tendency to decrease when passing through direct and pulsed injection current. These changes may be reversible or irreversible depending on the excitation conditions. The character of luminescence fatigue in both cases is different. PS EL spectral decay in the inverse changes regime is faster for the spectrum of short range part as compared with the long range part, what testifies to the existence in PS of different types of kinetic radiation centres. The possibility of precipitation of PMA film on PS surface have been applied to isolate PS from external and atmospheric influences. So from our investigations we have said that the surface of porous silicon is not homogenous with presence on it fragments Si or SiH_y and also thin dielectric coating of SiO_xC_y .

Besides SiOC clusters on the surface and SiH_y coatings play the significant roles in the light emission of porous silicon. The intensive PL, EL and CL of PS were observed all specimens have wide band of PL with maximum in the range from 650 nm to 750 nm. PS LE intensity has a tendency to decrease when passing direct and pulsed injection current through the electrochemical cell. This spectral decay is connect with depolarisation process in PS.

REFERENCES

1. L.T. Canham, *Appl.Phys.Lett*, Vol.57, p.1046,1990.
2. M. Born, E. Wolf, *Principles of optics*, Pergamon. Oxford, 1968.
3. I. A. Gorohovatskii, *The base of TSDC method*, Moscow, Nauka, 1981.
4. R. Collins, P. Fauchet, M. Tischler, *Porous Silicon: From Luminescence to LEDs*, Phys. Today, Vol.1, p.24,1997..
5. J.-E. Lim, W.-S. Chae, Y. Lee, K.-J. Kim, *Spectral Shifts of Electroluminescence from Porous n-Si under Cathodic Bias*, J. Electrochem. Soc., Vol. 144, p.647, 1997.

Radiative transitions in porous silicon

Bui Huy, Phi Hoa Binh, Dao Tran Cao*, Pham Van Hoi, and Vu Duc Thinh

Institute of Materials Science, NCST of Vietnam

ABSTRACT

Radiative transitions in porous silicon (PS) have been studied using a new variant of the time-resolved photoluminescence (TRPL) spectroscopic measurement, in which beside the pulsed light source the sample was irradiated additionally by a continuous light source. With this modification a certain photoluminescence (PL) region in the TRPL spectrum of PS may be quenched, the position and width of which depends strictly on the wavelength range and intensity of the continuous light source. Using different continuous light sources (blue, red-infrared, and monochromatic), the quenching of different PL regions has been observed experimentally. The results obtained are discussed with the model of recombination in the core and on the surface of nanocrystallinities. It seems that the selective quenching of PL in the TRPL spectrum is helpful to reveal the origin of the light emission for PS.

Keywords: Porous Si, Si nanocrystals, photoluminescence, time-resolved spectroscopy, radiative recombination

1. INTRODUCTION

Since the discovery of the strong visible photoluminescence (PL) of porous silicon (PS) in 1990¹, considerable studies of PS have been carried out from many different points of view, aimed at both understanding the fundamental of the mechanism of light emission^{2,3} and the possible applications⁴. In spite of all these activities, the origin of light emission for PS is still under debate. Two arguments, the quantum confinement effect and the effect of surface states seem to be in the first place, and it is more than likely that the eventual answer will be a combination of the two.

Among experimental methods commonly used for study the PL of PS, the measurement of the TRPL spectra can be considered as very powerful, because this method makes it possible to study in detail the two PL bands, in the red and blue spectral ranges. In this work we report a new variant of the TRPL measurement, in which an additional continuous light source (CLS) is used for irradiation the sample in combination with the pulsed light source (PLS) which is normally used for excitation in such kind of measurements. The new arrangement is advantageous from the point of view that it can result in the quenching of a certain PL region in the TRPL spectrum. In fact, in the TRPL spectroscopy the sequence of events is as follows: at first, with a short laser pulse from the PLS, we excite the electrons from the ground states (the valence band) to some upper energy states, after that we observe the light emitted from the radiative transitions of the excited electrons from the above mentioned upper states either to some lower states or back to the ground. Here two comments should be made. First, it is obvious that the light emission originated from a final state could be observed only if the excitation to this state took place, what in its turn is possible only if that final state was free (non-occupied). Second, it should be emphasized that only the excitation with the laser pulses from the PLS could result in the light collected in the TRPL spectrum, the light from all other mechanisms of excitation (if any) will be discarded due to non-synchronism. With these two remarks in mind we can now consider the case when the PS sample is illuminated additionally by a generally non-monochromatic CLS. In this circumstance the CLS will *continuously* excites the electrons from the ground states to a whole extent of adequate upper states so that this extent always is fully filled by electrons and no non-occupied states were left for the excitation by the laser pulses of the PLS. The ultimate result is that in the TRPL spectrum the PL region originated from this extent of final states is quenched. Thus, the CLS can be called the "quenching" light source by the role it plays in the TRPL measurements. However, in principle the quenching light source is not necessarily continuous, it is enough to choose its parameters (such as wavelength, modulation frequency, phase, etc.) adequate to the TRPL measurements. In general, our variant of the TRPL measurements presented here is only a particular case of the common concept of the combination of two light sources in optical spectroscopy, a famous application example of which is the pump-probe technique.

In this work, by using different CLS (blue, red-infrared, and monochromatic), the quenching of different PL regions has been observed experimentally. The results obtained are discussed with the model of recombination in the core and on the surface of nanocrystallinities.

* Corresponding author. Email: dtao@ims.ncst.ac.vn; Telephone: (84.4) 8358333 / Ext. 1138; Fax: (84.4) 8352483.

2. EXPERIMENTAL

The schematic diagram of the TRPL spectroscopic measurement performed in combination with continuous light illumination is presented in fig. 1. As shown, the TRPL measurements were carried out by the BOXCAR technique (BOXCAR BCI-280 with the time resolution of 220 ps). In our TRPL system the pulsed excitation light source is the 337.1 nm line with the duration of 5 ns from a pulsed 500 kW-power nitrogen laser and the spectrometer is a SPM-2 system. Two kinds of continuous light sources were used, a xenon lamp XBO-100 with different filters in order to have various desired spectral emission regions and a He-Ne laser with the emission line of 628 nm. The PS samples were prepared by the anode etching of *p*-type, 10 Ω cm silicon wafers with a HF:metanol (1:1) solution at the current density of 10 mAcm⁻² during 30 min. The anodization was carried out in the dark, at room temperature.

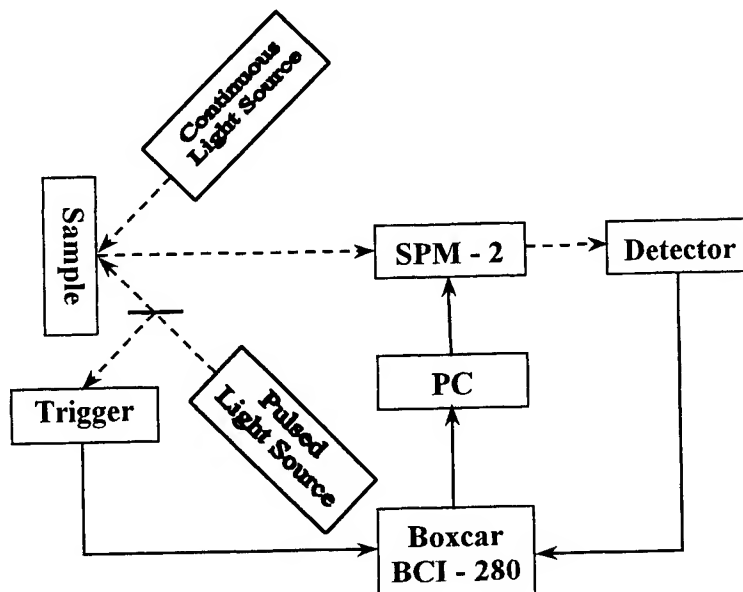


Fig. 1: Schematic of the TRPL spectroscopy measurement with additional sample illumination by a continuous light source.

3. RESULTS AND DISCUSSION

The TRPL spectra of a PS sample measured under two different conditions, with and without additional sample illumination by a blue CLS consisting of a xenon lamp XBO-100 and a BG-12 bandpass filter are presented in fig. 2. The same spectra obtained in the case of the red-infrared CLS consisting of a xenon lamp and a 530 nm longpass filter are presented in fig. 3. First of all, it can be seen that without the illumination by the CLS the TRPL spectrum of the PS-sample, as usual, consists of two zones, in the red-infrared and blue ranges. Our previous results concerning the gradual appearance of the blue PL zone in the conventional TRPL spectrum of PS when the delay time is reduced and especially the

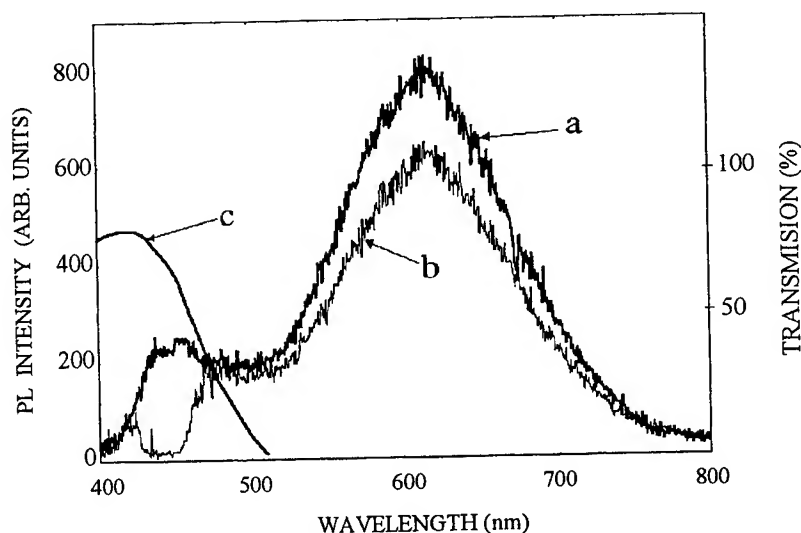


Fig. 2: Time-resolved PL spectra of a PS sample for two cases: without (curve a) and with (curve b) additional sample illumination by a continuous light source consisting of a xenon lamp XBO-100 and a bandpass filter BG-12. Curve c is the transmission spectrum of the bandpass filter BG-12.

existence of the discrete peaks in the blue PL zone⁵, as well as the results of other authors obtained by analyzing the time-resolved and static PL spectra of PS treated by the high temperature in different gas ambients^{6,7} have shown that the blue and the red-infrared zones of the PL spectrum of PS are possibly originated from the radiative recombination processes in the core (band-to-band recombination) and at the surface (surface state-to-band recombination) of PS nanocrystallites, respectively.

For the case with additional sample illumination by a blue CLS shown in fig. 2 (the curve b), the quenching of the PL in a region from 420 to 470 nm of the blue zone together with the decreasing of the PL intensity in a region from 530 to 720 nm of the red zone in the TRPL spectrum of the PS-sample can be noted. If we accept the above mentioned point of view that the blue PL zone is related to the band-to-band recombinations, whereas the red-infrared PL zone is related to the surface state-to-band recombinations, then the meaning of the stated experimental fact is that the carriers in the surfaces states partially have come from the core states. The physical picture can be as follows. In the normal TRPL measurement (without the CLS), if there were the electron trap surface states in the bandgap of the PS nanocrystals, then a part of the electrons after the excitation from the valence band to the conduction band by the laser pulses of the PLS will not go back to the valence band directly, but in two steps. The first step is to a electron trap level, and only after that will follow the second step - to the valence band. The overall result is that two kinds of light, the blue and the red, will be emitted. Different from fig. 2, fig. 3 shows that when the spectral range of the quenching radiation is from 530 to 1200 nm,

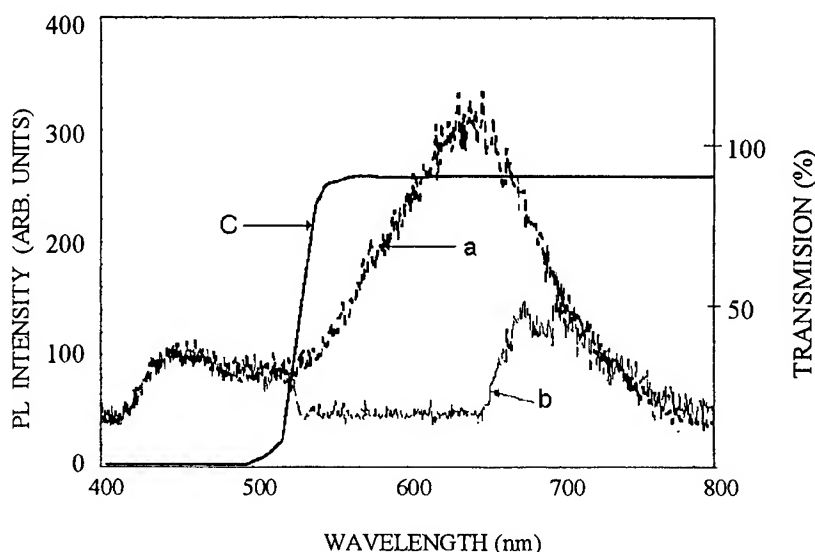


Fig. 3: Time-resolved PL spectra of a PS sample for two cases: without (curve a) and with (curve b) additional sample illumination by a continuous light source consisting of a xenon lamp XBO-100 and a 530 nm-longpass filter BG-12. Curve c is the transmission spectrum of the 530 nm-longpass filter.

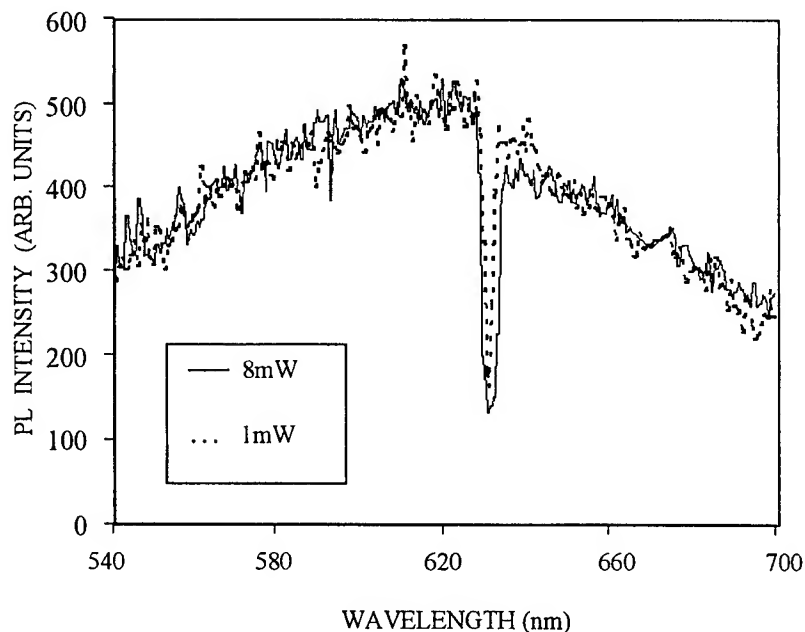


Fig. 4: Time-resolved PL spectra of a PS sample, which was additionally illuminated by a continuous He-Ne laser (628 nm emission) operating at different light emitting powers.

the spectral region where the PL is fully quenched is only in the range from 530 to 650 nm. The PL is partially quenched in the range from 650 to 720 nm and not quenched at all after 720 nm. In our opinion, this fact indicates that in all probability there are two types of radiative recombination processes which are responsible for the PL in the red-infrared zone, what is consistent with the point of view of Hill and Whalley⁸. The infrared PL zone (the photons with the wavelengths longer than 720 nm) perhaps is the result of recombination of a conduction band electron with a hole captured by a deep surface trap, whereas the red PL zone (the photons with the wavelengths shorter than 650 nm), in accordance with our above mentioned results, is due to recombination of a electron captured by a surface trap with a valence band hole.

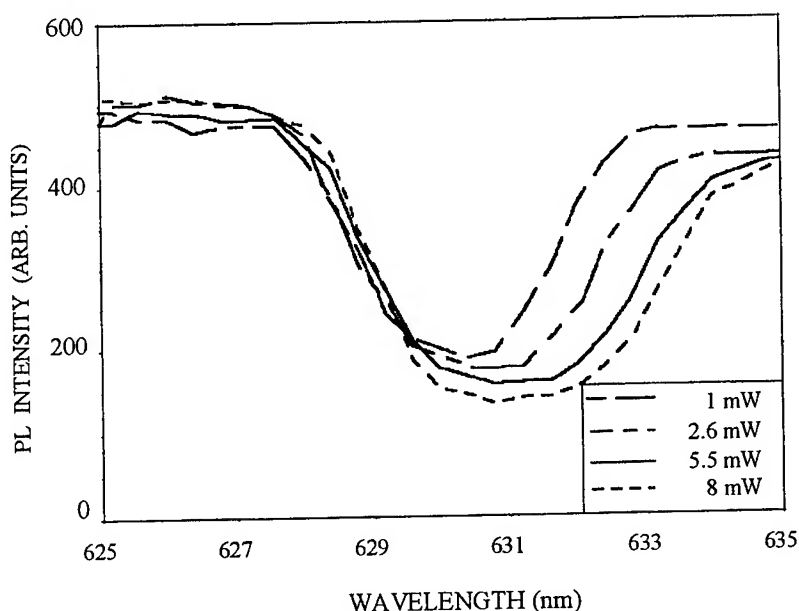


Fig. 5: Detailed dependence of the quenched PL spectral region shown in fig. 4 on the light emitting power of the continuous He-Ne laser.

Furthermore, the radiative transition processes in the red PL zone were studied in more details by using a He-Ne laser with the emission line of 628 nm as the quenching light source instead of the xenon lamp. The results illustrated in fig. 4 and 5 show that the PL spectral region close to the line 628 nm is fully quenched and, in addition, the width of the quenched region increases, shifting towards the long wavelength side when the intensity of laser is increased. This result is the evidence of the fact that the surface states which are responsible for the PL of PS in the red zone are not localized on a single level, but on a whole band of levels in the bandgap of the PS nanocrystals. To be more concrete, it seems probable that in our case the surface states which are related to the red PL are the states produced by the Si-H bonds on the surface of the PS nanocrystals. Our TRPL measurements which were performed on the same PS sample before and after the annealing in the vacuum at 420 °C are in favor of this viewpoint, since after the annealing only the blue PL zone remains while the red one disappears. Moreover, the Si-H bonds are also what other authors^{7,9,10} have proposed to explain the origin of the surface states of PS in many cases. In this circumstance the reason why the energy levels of the surface states corresponding to the red PL form a band in the bandgap of the PS nanocrystals lies in the number of hydrogen atoms participating in the Si-H bonds as well as the angle of these bonds.

4. CONCLUSIONS

In summary, in this work, for the first time the TRPL-spectra of PS which have been measured when the PS sample is irradiated additionally by a continuous light sources are presented. The role of the continuous light source is to quench a certain PL region in the TRPL spectrum. With different continuous light sources (blue, red-infrared, and monochromatic) the measured TRPL spectra showed different quenched PL regions, the study of which has led to the following preliminary conclusions: (1) A part of the carriers in the surface states (which are related to the red PL zone) is originated from the carriers in the core states (which are related to the blue PL zone); (2) The energy levels of the surface states which are responsible for the PL in the red zone form a band in the band gap of PS nanocrystals; (3) The mechanism of recombination corresponding to the infrared PL is different from those corresponding to the red PL.

ACKNOWLEDGMENTS

The authors would like to thank Prof. Vu Xuan Quang and MSc. Pham Van Binh for the help in PL measurements. This work is supported by the Vietnamese National Basic Research Program in Natural Science KT- 04.

REFERENCES

1. L.T. Canham, "Silicon quantum wire array fabrication by electrochemical and chemical dissolution of wafers," *Appl. Phys. Lett.* **57**, pp. 1046-1048, 1990.
2. Y. Kanemitsu, "Light emission from porous silicon and related materials," *Physics Reports* **263**, pp 1-91, 1995.
3. Xun Wang, "Luminescence behavior and mechanism of light-emitting porous silicon," *Modern Phys. Lett.* **B8**, pp. 69-92, 1994.
4. R. T. Collins, P. M. Fauchet and M. A. Tischler, "Porous silicon: from luminescence to LEDs," *Physics Today* **50**, pp. 24-31, 1997.
5. Bui Huy et al, "Time-resolved luminescence spectrum and radiation recombination process in surface and core of porous silicon," *Proc. of the 9th Int. Symp. on Electrets*, eds. Xia Zhongfu and Zhang Hongyan, pp. 668-672, IEEE Publication, 1996.
6. Qi Zhang, S. C. Bayliss, and D. A. Hutt, "Blue photoluminescence and local structure of Si nanostructures embedded in SiO₂ matrices" *Appl. Phys. Lett.* **66**, pp. 1977-1979, 1995.
7. F. Koch, in *Silicon-Based Optoelectronic Materials*, eds. M. A. Tischler, R. T. Collins, M. L. Thewalt, and G. Abstreiter, MRS Symposia Proceedings No. **298**, p. 319, Materials Research Society, Pittsburg, 1993.
8. N. A. Hill, and K. B. Whaley, "A theoretical study of light emission from nanoscale silicon," *Journal of Electronic Materials* **25**, pp. 269-285, 1996.
9. L. Tsybekov, Ju. V. Vandyshv, and P. M. Fauchet, "Blue emission in porous silicon: oxygen-related photoluminescence," *Phys. Rev.* **B49**, pp. 7821-7824, 1994.
10. S. M. Prokes, et al., "SiH excitation: an alternate mechanism for porous Si photoluminescence," *Phys. Rev.* **B45**, pp. 13788-13791, 1992.

Optoelectronic Properties of New Amorphous Silicon Photoreceptor

Jung-Chuan Chou*, Hsu-Ying Yang

Institute of Electronic and Information Engineering, National Yunlin University of Science and Technology, Touliu, Yunlin, Taiwan, 640, R.O.C.

ABSTRACT

A new highly sensitive photoreceptor in visible-spectrum region with high contrast voltage ratio has been developed for an electrophotographic device. The multilayered amorphous silicon photoreceptor has been prepared with PE-LPCVD and sputtering system. The structure of the photoreceptor consists of four part: (a) Al substrate, (b) a-WO₃ blocking layer, (c) a-Si:H(i) photogeneration and transport layer, (d) a-C:H surface protecting layer. In this study, the photoreceptor is exposed with different wavelength (451~720 nm) and illumination (0~40 Lux). Keithley 236 Semiconductor Parameter Analyzer is used to measure the current-voltage (I-V) curves of photoreceptor. In addition, Electrostatic Paper Analyzer (EPA-8100) is used to measure the photo-induced discharge curves (PIDC), which is used to simulate the processes of copying machines. According to the I-V curves and PID curves, we can investigate the transport of photocarrier in photoreceptor and the optoelectronic parameters (initial surface potential V_{so} , dark decay time t_d , photosensitivity $E_{1/2}$, residual potential V_r and contrast voltage ratio).

Keywords: photoreceptor, electrophotographic, photo-induced discharge curves, initial surface potential, dark decay time, photosensitivity, residual potential, contrast voltage ratio

1. INTRODUCTION

The electrophotographic process which was discovered by Carlson¹ is simple, rapid and economic. There are still many types of electrophotographic processes to be developed during this time, but all high-speed copying machines and laser line printers are operated under the process based on the Carlson's invention at present². The fundamental processes of duplicating images for copying machines are illustrated in Fig.1. The photoreceptor with sensitized material in copying machine is an important device for electrophotography. The characteristics of material will affect directly the quality of xerography³. Many sensitized materials for electrophotography have also been developed such as amorphous selenium (a-Se) and its alloy (a-As₂Se₃, a-Se:Te), ZnO, CdS and organic semiconductors (PVK-TNF)⁴⁻⁸. Since one of the most exciting works for amorphous silicon (a-Si) was reported by Spear and Lecomber⁹, increasing attention has been paid to the advances in photoelectronic device based on plasma-deposited hydrogenated amorphous silicon (a-Si:H) in recent years. Some advantages of a-Si:H¹⁰, e.g., an excellent photoconductivity, wide spectral photosensitivity, high absorption coefficient in the visible spectrum range, special homogeneity, rather high electric resistivity, the ability to control the electric properties by doping with some foreign elements and an inexpensive thin film with large area, are fascinating from a technological point of view. The use of a-Si:H as a photoreceptor has been reported by Shimizu *et. al.*¹¹ for the first time. However, the primary advantages of a-Si:H for electrophotography are the hardness of the surface, stability against temperature and non-toxicity, which has excellent properties without losing any merit of conventional materials.

On the other hand, an excellent photoreceptor should have some characteristics such as high initial surface potential (V_{so}), long dark decay time (t_d), superior photosensitivity ($E_{1/2}$), low residual potential (V_r), and high contrast voltage ratio. In this paper, to obtain superior optoelectronic properties, we deposit an hydrogenated amorphous carbon (a-C:H) film on amorphous silicon photoreceptor as the passivation layer. The hydrogenated amorphous carbon film has some advantages such as large thermal conductivity, chemical inertness, high electrical resistivity and break-down field and optical transparency¹²⁻¹⁴, which is suitable for the coating material in microelectronics. In this study, the charging and the photo-discharging behaviors of photoreceptor will be discussed. Furthermore, we will investigate the effects of photoreceptor with a-C:H passivation layer.

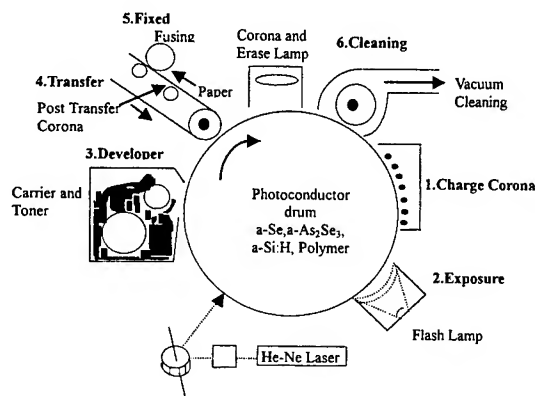


Fig. 1 Duplication steps of electrophotography

2. THEOREM

A photoreceptor must have three essential properties in order to accept charges from a corotron¹⁵. First, it must have a sufficient surface trap density to trap the ion charge. Then, it must have an effective blocking substrate electrode. Finally, it must have a low bulk dark decay. A photoreceptor must have a large surface trap density to be useful in xerography. A trap is a localized energy state that can hold a hole or an electron in a manner that prevent the hole or electron to be transported through the photoreceptor. An example is shown in Fig.2¹⁶. The trapping sites lie between the conduction and valence bands. Holes can be transported in the valence bands when the photoreceptor is charged with positive charges. Electrons can be transported in the conduction band. No charge transport is allowed in the forbidden energy gap between the conduction and valence band edge. The surface trap lies in the forbidden gap. A blocking substrate is one that does not allow charge to inject from the conductive substrate into the bulk of the photoreceptor. If charge did inject, the charges would drift through the bulk to the surface where they would neutralize the surface trapped charge, thereby reducing the surface potential.

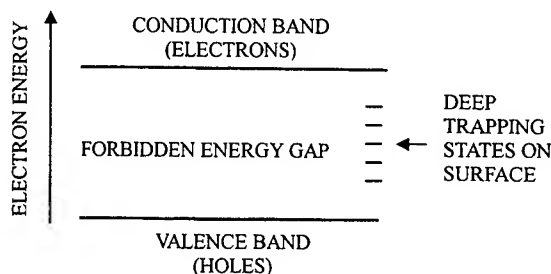


Fig. 2 Energy band diagram showing the location of deep trapping surface states required for corona charging

Fig. 3 shows that an example energy band diagram of a blocking contact for a positively charged photoreceptor, where E_i is the energetic difference between the Fermi level in the metal and the conduction band edge of the photoreceptor, E_p is the electric field in the photoreceptor, e is the charge of the electron, ϵ is the permittivity of the photoreceptor, and $\Delta\phi$ is the reduction in barrier height. The ideal xerographic photoreceptor is one that appears as a pure insulator in the dark and as an efficient photogenerator in the light. To appear as an insulator, the photoreceptor must not inject surface or substrate charge as described above. In addition, it must not thermally generate carriers in the bulk of the material. Thermal generation occurs when an energy state exists and closes the band edge in the forbidden gap. If the state is close enough and the temperature is large enough, a carrier can be emitted from the state into the band where it can be swept out under the influence of the charging field. This generation and sweep out process is defined as "bulk dark decay".

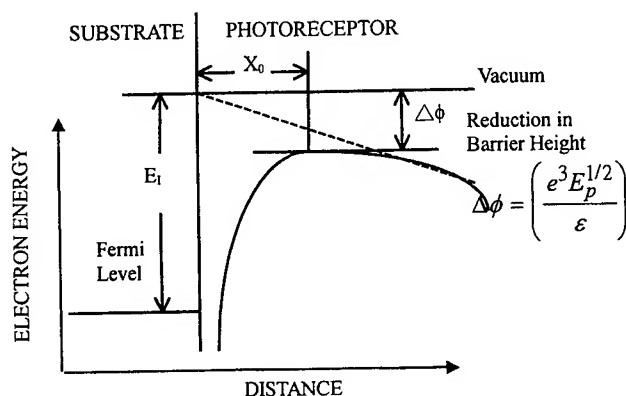


Fig. 3 Energy band diagram showing a blocking contact between the substrate and photoreceptor. The internal field in the photoreceptor lowers the energetic barrier.

The important optoelectronic characteristics of xerographic photoreceptor coatings are: (1) photosensitivity, (2) acceptance potential, (3) retentivity, (4) residual potential. Some of these characteristics are illustrated in Fig. 4, which is an typical photoinduced discharge curve.

(1) The photosensitivity is determined by the rate of decay of the surface potential when the photoreceptor is illuminated. The photosensitivity of a-Se photoreceptor is mostly in the blue-violet end of the spectrum, although some red sensitivity is produced by evaporating the selenium onto substrates held at elevated temperatures.

(2) The dark resistivity of a photoconductive film is a decreasing function of the electrical field applied across the film. Thus, when a photoreceptor is sensitized, the amount of charge on the photoreceptor will be accepted and held which is limited by the decreased resistance of the film as the electrical field builds up to high value. This decreased resistance allows a greater amount of current to flow through the film, and as sensitizing is continued, a point is reached where charges leak away as fast as they are supplied. The photoreceptor potential at this point is called the "acceptance potential" (see Fig. 4). This is an important characteristic of xerographic photoreceptor since it is the primary factor in determining the amount of voltage contrast obtainable.

(3) The length of time that an electrostatic latent image is retained on a photoreceptor is determined by the rate of decay of the electrical potential in the dark (see Fig. 4). This is a function of the effective dark resistivity of the

photoreceptor. When the period between exposure and development is long, the retentivity becomes an important factor. However, when exposure and development take place in rapid sequence, such as in automatic machines, a relatively rapid decay of the latent image can be tolerated. The coating material and the photoreceptor preparation method will determine its charge retentivity, which is usually measured as the time required for the photoreceptor potential to decay one-half its original value in the dark.

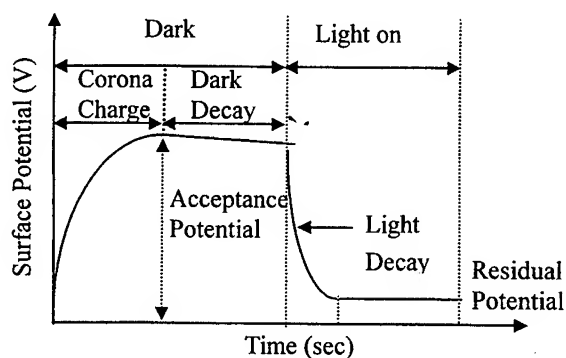


Fig. 4 Charging and discharging of xerographic photoreceptor.

(4) When a sensitized xerographic photoreceptor is exposed to light, the electrical potential undergoes an initial rapid decay, followed by a slow decay begins is called the residual potential. This potential may vary from near zero to as much as 20 or 30 percent of the acceptance potential. A low residual potential is a desirable characteristic of xerographic photoreceptor because of the greater voltage contrast obtainable.

3. EXPERIMENTAL

In this paper, we have prepared three kinds of samples to investigate. The structures are $Al/Al_2O_3/a-Si:H$, $Al/Al_2O_3/a-WO_3/a-Si:H$, and $Al/Al_2O_3/a-WO_3/a-Si:H/a-C:H$, respectively. The schematic structures of photoreceptors are respectively shown in Fig. 5. The substrates for the samples consisted of $2.5\text{cm} \times 2.5\text{cm}$ in

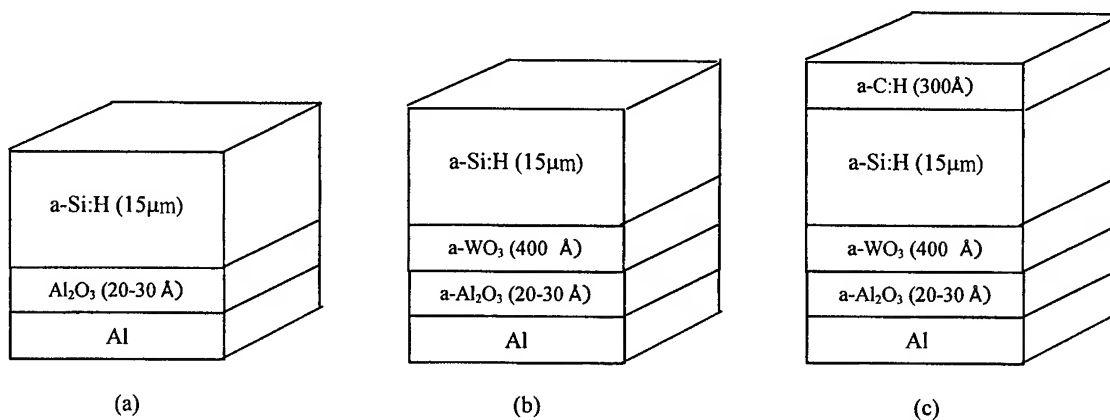


Fig. 5 Schematic structures of three kinds of a-Si:H photoreceptors

aluminum (Al) plates, 0.2cm thick, and polished on one face. The aluminum oxide (Al_2O_3) and tungsten trioxide (a-WO_3) were deposited on the polished Al substrates as the blocking layers by using the thermal oxidation (95-100°C; 20-30Å) and vacuum sputtering systems (R.F. power = 90W; 400Å), respectively. The a-Si thin film used in this study has been prepared by R.F. glow discharge of silane diluted by H_2 (10% SiH_4 in H_2). It is deposited on a conductive substrate (Al) by plasma-enhanced low pressure chemical vapor deposition (PE-LPCVD) system (Model: SAMCO PD-10). The reaction chamber of a capacitively coupled diode system is used for the preparation. Using the same method, a-C:H thin film is also prepared by R.F. glow discharge of methane diluted by H_2 (30% CH_4 in H_2), and it is deposited on the top of a-Si:H film to be the passivation layer of photoreceptor. All deposition conditions of the films are indicated in Table 1.

Table 1 Experimental preparation conditions of Al_2O_3 , a-WO_3 , a-Si:H and a-C:H films

Conditions	Al_2O_3	a-WO_3	a-Si:H	a-C:H
System	thermal oxidation	Sputtering	PE-LPCVD	PE-LPCVD
R.F. Frequency	—	13.56 MHz	13.56 MHz	13.56 MHz
Power	—	90W	30W	40W
Reaction Gas	—	O_2 (5% in Ar)	SiH_4 (10% in H_2)	CH_4 (30% in H_2)
Flow Rate	—	20 sccm	150 sccm	150 sccm
Pressure	—	30 mTorr	2 Torr	0.8 Torr
Substrate Temperature	95-100°C	30°C	150°C	30°C
Thickness	20-30Å	400Å	15μm	300Å

The photoinduced discharge curve (PIDC) could be measured under illumination with light of intensity 10 Lux by using Electrostatic Paper Analyzer (Model: EPA-8100), which is usually used to simulate the processes of copying machines. Figure 6 shows the schematic diagram of the EPA-8100 experimental apparatus. The sample was located in a holder on the rotatable plate of this apparatus and the a-Se surface was charged from a corotron. This corotron supplied with 7KV from a high-voltage dc power supply. The sample was then rotated to be underneath a measuring plate. With a fixed distance between the photoreceptor surface and the measuring plate, the potential was measured as a function of time with a electrometer connected to a time-chart recorder. The actual potential of the charged surface V was found by multiplying the measured voltage by the ratio $(C_1+C_2)/C_1$, where C_2 is the capacitance between the measuring plate and the a-Se surface and C_1 is the capacitance of the electrometer and leads. After recording the voltage for few second in the dark, the sample was moved away from the measuring plate and illuminated with a tungsten lamp. It was then moved back under the measuring plate to record the post-illumination voltage. All these results and experimental conditions are taken out by an X-Y plotter. The typical output of an X-Y plotter is shown in Fig. 4. As indicated in Fig. 4, the value of V just after charging is called the initial surface voltage V_{so} . According to PIDC, the optoelectronic parameters (initial surface potential (V_{so}), dark decay time (t_d), photosensitivity ($E_{1/2}$), residual potential (V_r) and contrast voltage ratio) could be obtained by calculation.

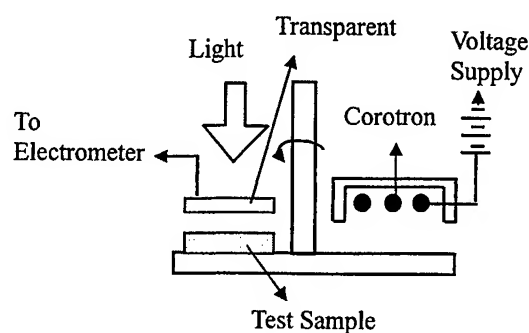


Fig. 6 Diagram of apparatus for measuring the xerographic properties by EPA-8100 system

4. RESULTS AND DISCUSSIONS

4.1 The Multilayered Design of Separated Functions

In our study, we fabricate the multilayered hydrogenated amorphous silicon photoreceptor by concept of separated functions¹⁷. It is consisted of blocking layer, photocarrier generation and transport layer (CGL/CTL), and passivation layer. They will affect the properties of photoreceptor. The aluminum (Al) is a conductive substrate, which is similar to the drum of copying machine. The Al_2O_3 and $a-WO_3$ films are blocking layers, and they are usually used to provide the injection of substrate carriers, which will decrease the initial surface potential when the photoreceptor is charging. The $a-Si:H$ film is used to be CGL/CTL. Many photocarriers will be generated and transported to surface once the photoreceptor is illuminated. They will be attracted by the electric field of surface potential to neutralize the charges of surface. The $a-C:H$ film is a passivation layer, and it has ability to maintain the retention of surface charges and resists the damages during duplicating xerography.

Table 2 shows the difference of optoelectronic properties of the three kinds of photoreceptors. The PID curves of the three kinds of samples are shown in Fig. 7. The results reveal that $Al/Al_2O_3/a-WO_3/a-Si:H/a-C:H$ photoreceptor has excellent optoelectronic properties for electrophotography ($V_{so} = 418V$ ($27.8 V/\mu m$), $t_d = 5$ Sec, contrast voltage ratio = 20.9 ($418V/20V$)).

Table 2 Optoelectronic parameters of three structures of photoreceptors for electrophotography.

Structures	$Al/Al_2O_3/a-Si:H$	$Al/Al_2O_3/a-WO_3/a-Si:H$	$Al/Al_2O_3/a-WO_3/a-Si:H/a-C:H$
Optoelectronic Parameters			
Charging Corona (Volts)	-7 K	-7 K	-7 K
Initial Surface Potential (V_{so} , Volts)	62 (4.1 V/ μm)	96 (6.4 V/ μm)	418 (27.8 V/ μm)
Dark Decay Time (t_d , Sec)	3	3.6	5
Photosensitivity ($E_{1/2}$, Lux·Sec)	1.6	2	4.8
Residual Potential (V_r , Volts)	9	12	20
Contrast Voltage Ratio	6.8 (62V / 9V)	8 (96V / 12V)	20.9 (418V / 20V)

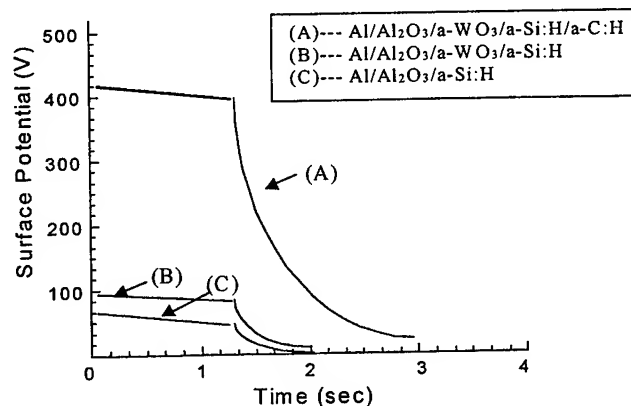


Fig. 7 PID curves of three structures of photoreceptors for electrophotography

4.2 Optoelectronic Characteristics

The intrinsic a-Si:H film is close to a *n*-type material which suits the transmission of electron rather than hole. Using this physical property, the photoreceptor surface is charged with negative charges and the positive carriers that inject from substrate would not easily drift to neutralize the surface charges. For *Al/Al₂O₃/a-Si:H* photoreceptor, the energy gap of *Al₂O₃* film is about 6~8 eV¹⁸, and it could regard as an insulator to be a blocking layer. Once *Al₂O₃* and a-Si:H films are deposited on the Al substrate, a metal-insulator-semiconductor (MIS) structure would be generated. At thermal equilibrium, there will be a potential barrier to be formed at the interface of *Al₂O₃* layer. However, the thickness of *Al₂O₃* film is too thin (20~30Å), and the tunneling effect would be generated. The initial surface potential is low because the injected carriers from substrate will tunnel the potential barrier into the bulk, and easily drift to neutralize the surface charges. Therefore, it is known that the optoelectronic characteristics are not so good in Table 2 and Fig. 7 ($V_{so} = 62V$ (4.1V/μm); $t_d = 3$ Sec; $E_{1/2} = 1.6$ Lux·Sec; $V_t = 9V$; contrast voltage ratio = 6.8 (62V/9V)).

To enhance the blocking ability of photoreceptor, we deposited a-WO₃ film on *Al₂O₃* film to form double blocking layer structure. For *Al/Al₂O₃/a-WO₃/a-Si:H* photoreceptor, the energy gap of a-WO₃ film is about 3.65 eV¹⁹. Once a-WO₃ film is deposited between *Al₂O₃* and a-Si:H film, it could regard as a MIS structure at *Al/Al₂O₃/a-WO₃*, and regard as a heterojunction between a-WO₃ and a-Si:H film. When the photoreceptor is charged with negative corona (-7KV), the injected carriers from substrate must overcome not only the barrier height at *Al₂O₃/a-WO₃* interface, but also the potential well at a-WO₃/a-Si:H interface. Hence, the initial surface potential of photoreceptor increases (96V) as shown in Table 2 and Fig.7. In the same situation, the substrate injected carriers could be effectively blocked by double blocking layer due to the barriers between *Al₂O₃/a-WO₃* and a-WO₃/a-Si:H interface. The surface charges would be retained and the dark decay time would be increased (3.6 sec).

In addition, Fig. 8 shows the I-V curves of two structure of photoreceptors. It is known that the dark conductivity (σ_{dark}) of *Al/Al₂O₃/a-Si:H* photoreceptor is $9.7 \times 10^{-11} \Omega^{-1} \cdot cm^{-1}$, and *Al/Al₂O₃/a-WO₃/a-Si:H* photoreceptor is $1.056 \times 10^{-13} \Omega^{-1} \cdot cm^{-1}$. It has suggested that the double blocking layer (*Al₂O₃/a-WO₃*) has better ability to block the substrate injected carriers in the dark than single blocking layer (*Al₂O₃*). Therefore, it is known that the optoelectronic characteristics are improved in Table 2 and Fig. 7 ($V_{so} = 96V$ (6.4V/μm); $t_d = 3.6$ Sec; $E_{1/2} = 2$

Lux·Sec; $V_r = 12V$;

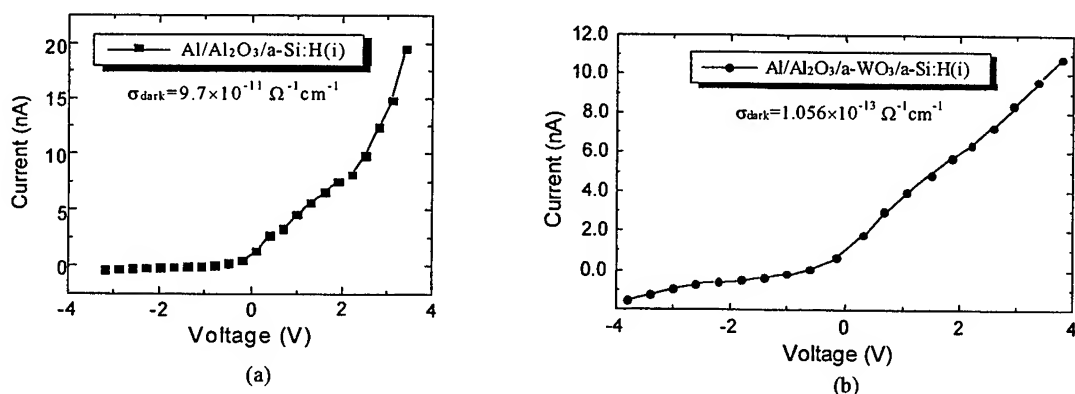


Fig. 8 I-V Curves of two structures of photoreceptors (a)Al/Al₂O₃/a-Si:H (b)Al/Al₂O₃/a-WO₃/a-Si:H

contrast voltage ratio = 8 (96V/12V)). When the photoreceptor is illuminated, the photo-induced carriers will be attracted by the carriers which retains in the potential well of a-WO₃/a-Si:H interface, and the photosensitivity becomes poor. On the other hand, under different illumination (10~40 Lux) and wavelength (498~720 nm) for Al/Al₂O₃/a-WO₃/a-Si:H photoreceptor, it is known that the photosensitivity of photoreceptor becomes better with illumination increase, and has excellent sensitivity at 690nm wavelength as shown in Fig. 9.

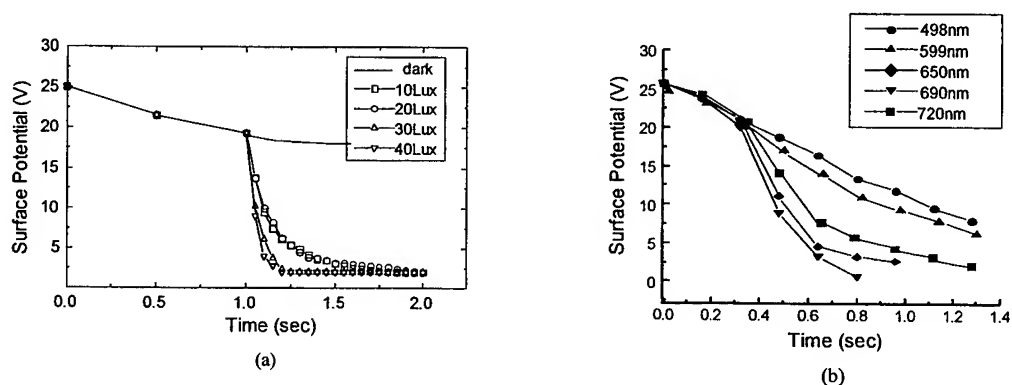


Fig. 9 Different illumination and wavelength for Al/Al₂O₃/a-WO₃/a-Si:H (3μm) photoreceptor.

Unfortunately, although the double blocking layer can improve the initial surface potential, however, it is still not enough to develop the latent image, and the contrast voltage ratio which will directly affects the resolution is too small. Therefore, the a-C:H film is deposited on the surface of a-Si:H photoreceptor by the concept of separated function to improve the initial surface potential and contrast voltage ratio. Table 2 and Fig. 7 shows the optoelectronic

characteristics of $Al/Al_2O_3/a-WO_3/a-Si:H/a-C:H$ photoreceptor ($V_{so} = 418V$ ($27.8V/\mu m$); $t_d = 5$ Sec; $E_{1/2} = 4.8$ Lux·Sec; $V_r = 20V$; contrast voltage ratio = 20.9 ($418V/20V$)). Because a-C:H film is a good insulator material, it could decrease the surface conductivity and enhance the initial surface potential ($418V$). In addition, a-C:H film could effectively block the surface charges which will drift or diffusion in the bulk, and increase the dark decay time (5 sec). When the photoreceptor is illuminated, the photo-induced carriers will not easily drift through a-C:H film to neutralize the surface charges, and increase the residual potential. Although it is not a good news for electrophotography, $Al/Al_2O_3/a-WO_3/a-Si:H/a-C:H$ photoreceptor still has excellent resolution because the contrast voltage ratio is improved ($8 \rightarrow 20.9$).

In duplicating xerography, there would be some ions to produce such as CO_3^- and O_3^- under charging negative corona. During repeating charging and discharging, these ions would be accumulated on the surface of a-Si:H photoreceptor. The physical absorption will affect the conductivity and decrease the initial surface potential. Because a-C:H films have chemical inertness, high electrical resistivity, breakdown field, optical transparency, mechanic stress and hardness, it is suitable for the protection layer in the photoreceptor. To compare the difference of $Al/Al_2O_3/a-WO_3/a-Si:H$ and $Al/Al_2O_3/a-WO_3/a-Si:H/a-C:H$, it is known that the decrease of the initial surface potential after duplicating xerography in Fig. 10, and a-C:H film has ability to maintain the retention of surface charges.

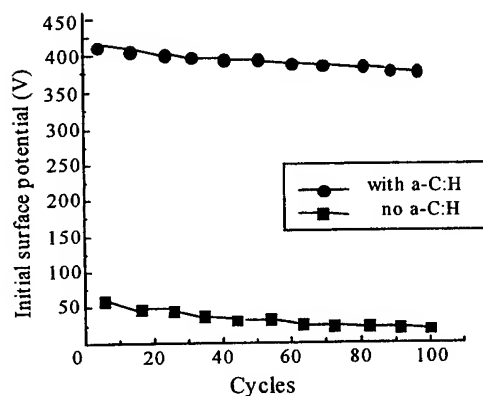


Fig. 10 Curves of the photoreceptor with and without a-C:H passivation layer for duplicating xerography.

5. CONCLUSIONS

In this study, we prepared three structures of photoreceptors by the concept of separated functions to investigate the optoelectronic characteristics. It is found that the photoreceptor with double blocking layer ($Al_2O_3/a-WO_3$) has higher initial surface potential (96V) than the photoreceptor with single blocking layer (Al_2O_3) (62V). In addition, the dark conductivity of double blocking layer structure ($1.056 \times 10^{-13} \Omega^{-1} \cdot cm^{-1}$) is smaller than single blocking layer structure ($9.7 \times 10^{-11} \Omega^{-1} \cdot cm^{-1}$). It indicates that double blocking layer has higher potential barrier between substrate and a-Si:H layer. That could effectively block the substrate injected carriers into a-Si:H layer to neutralize the surface charges in the dark, and increase the dark decay time to retain surface charges. On the other

hand, under different illumination (10~40 Lux) and wavelength (498~720 nm) for $Al/Al_2O_3/a-WO_3/a-Si:H$ photoreceptor, it is known that the photosensitivity of photoreceptor becomes better with illumination increase, and has excellent sensitivity at 690nm wavelength. Besides, because a-C:H film is a material with wide energy gap, a barrier is formed between bulk and surface once a-C:H film is deposited on the a-Si:H film. It could eliminate the surface effect that the surface charges drift or diffusion into the bulk to decrease the initial surface potential. Hence, $Al/Al_2O_3/a-WO_3/a-Si:H/a-C:H$ structure is the best photoreceptor for electrophotography which has excellent optoelectronic characteristics ($V_{so} = 418V$ (27.8V/ μm); $t_d = 5$ Sec; $E_{1/2} = 4.8$ Lux·Sec; $V_r = 20V$; contrast voltage ratio = 20.9 (418V/20V)).

ACKNOWLEDGMENTS

This work is supported by the National Science Council of the Republic of China under grant NSC88-2215-E-004-001.

REFERENCES

1. C. F. Carlson, U.S. Patent 222, 176 (Nov. 19, 1940).
2. Y. Nakayama, A. Sugimura, M. Nakano, and T. Kawamura, "A New a-Si:H Photoreceptor Drum: Preparation, Electrophotographic Properties and Application", *Photogr. Sci. and Eng.* **26**(4), pp.188-192, 1982.
3. S. Y. Yang and J. C. Chou, "Study on Photoelectric Properties of the A-Si:H Photoreceptor", *Proceedings of the 1997 Annual Conference of the Chinese Society for Materials Science*, Vol. F, pp.55-58, Tainan, Taiwan, 1997.
4. R. M. Schaffert, *Electrophotography*, Focal Press, New York, 1975.
5. R. A. C. M. van Swaaij, W. P. M. Willems, J. P. Lokker, J. Bezemer, and W. F. van der Weg, "Electrophotographic Discharge of CdS Explained by a Surface-Depletion Discharge Model", *J. Appl. Phys.* **77**(4), pp.1635-1639, 1995.
6. Y. Taniguchi, H. Yamamoto, S. Horigome, S. Saito, and E. Maruyama, "A Highly Sensitive Chalcogenide Photoconductor in a Near-infrared Wavelength Region", *J. Appl. Phys.* **52**(12), pp.7261-7269, 1981.
7. R. C. Chittick, J. H. Alexander, and H. F. Sterling, "The Preparation and Properties of Amorphous Silicon", *Journal of Electrochemistry Society Solid State Science* **116**(1), pp.77-79, 1969.
8. T. Fukude, S. Shirai, K. Saitoh, and K. Ogawa, "Fabrication Technology for a-Si:H Photosensitive Drum", *Optoelectronics-Device and Technologies* **4**(2), pp.273-280, 1989.
9. W. E. Spear and P. G. LeComber, "", *Solid State Commun.* **17**, pp.1193-, 1975.
10. I. Shimizu, T. Komatsu, D. Saito, and E. Inoue, "Electrophotographic Studies of Glow-Discharge Amorphous Silicon", *Philosophical Magazine B* **43**(6), pp.1079-1089, 1981.
11. M. Shimozuma, "Hydrogenated Amorphous Carbon Films Deposited by Low-Frequency Plasma Chemical Vapor Deposition at Room Temperature", *J. Appl. Phys.* **66**(1), pp.447-449, 1989.
12. E. Pascual, C. Serra, and E. Bertran, "Optical Absorption from Graphitic Clusters of Hydrogenated Amorphous Carbon Films", *J. Appl. Phys.* **70**, pp.5119-5121, 1991.
13. H. Yokoyama, M. Okamoto, T. Yamasaki, K. Takahiro, Y. Oskak, and T. Imura, "Optical and Mechanical Properties of Hard Hydrogenated Amorphous Carbon Films Deposited by Plasma CVD", *Japanese J. Appl.*

- Phys.* **29**, pp.2815-2819, 1990.
14. A. Bubenzer, B. Dischler, G. Brandt, and P. Koidl, "RF-Plasma Deposited Amorphous Hydrogenated Hard Carbon Film: Preparation, Properties, and Application", *J. Appl. Phys.* **54**, pp.4590-4595, 1983.
 15. M. E. Scharfe and F. W. Schmidlin, *Charged Pigment Xerography, Advances in Electronics and Electron Physics* **38**, Academic Press, New York, 1975.
 16. M. E. Scharfe, *Electrophotography Principles and Optimization* **38**, Research Studies Press, New York, 1984.
 17. S. Y. Yang, and J. C. Chou, "Study on the Fabrication and Optoelectronic Characteristics of the Hydrogenated Amorphous Silicon Photoreceptors", *Proceedings of the Optical and Photonics Symposium/Taiwan'97*, pp.105-108, Hsin-Chu, Taiwan, 1997.
 18. A. M. Doodman, "Photoemission of Holes and Electrons from Aluminum into Aluminum Oxide", *J. Appl. Phys.* **41**(5), pp.2176-2179, 1970.
 19. S. K. Deb, "Optical and Photoelectric Properties and Colour Centers in Thin Films of Tungsten Oxide", *Philosophical Magazine* **27**, pp.801-822, 1973.

*Correspondence: Tel.: 886-5-5342601 Ext.2500

Fax: 886-5-5312029, 5312063

Email: choujc@pine.yuntech.edu.tw

Temperature dependent luminescence characteristics of Sm^{3+} - doped silicate glass

Kalyandurg Annapurna*, Rabindra Nath Dwivedi and Srinvasa Buddhudu^a

Glass Technology Section, Central Glass & Ceramic Research Institute.
196, Raja S. C. Mullick Road, Calcutta 700 032, India

^a Department of Physics, Sri Venkateswara University, Tirupati 517 502, India.

ABSTRACT

We report the optical characterization of Sm^{3+} : $\text{SiO}_2+\text{Al}_2\text{O}_3+\text{Li}_2\text{O}+\text{Na}_2\text{O}+\text{MgO}$ glass from the measurements of optical absorption spectra (at 300 K), total luminescence spectra (10 K - 300 K) and fluorescence lifetimes (10 K - 300 K) of the prominent emission transitions of the Sm^{3+} ions. Besides the analysis of spectral properties, physical and nonlinearity characterizing property parameters have also been computed to understand the optical dispersive power of this glass. By the application of Judd-Ofelt parameters (Ω_λ) of the measured absorption spectrum, the radiative transition probability factors (A) and stimulated emission cross-section ($\sigma^{\text{E}}_{\text{p}}$) of the observed fluorescent levels have been analyzed. Both emission intensity and measured lifetimes of the prominent luminescent transition ($^4\text{G}_{5/2} \rightarrow ^6\text{H}_{7/2}$) concerning Sm^{3+} - glass are showing a descending trend with a rise in temperature having a N_2 - laser (337.1 nm) as the excitation source.

Key Words : Luminescence, Sm^{3+} - Glass, Silicate Glass

1. INTRODUCTION

The optical properties of rare earth ions in vitreous matrices have been widely investigated because of their basic interest and potential applications as lasers and phosphors. It is well known that the positions of the absorption and emission bands of these ions are not very sensitive to their environment and so they are more or less the same in different matrices. However, the probabilities for radiative and non-radiative transitions change with the host and so it is important to study the optical properties of rare-earth ions in different materials. Several papers have been published on the optical properties of 4f ions in different glasses¹⁻⁵, but only few of them have been concerned with Samarium^{6, 7}. Although the stimulated cross-sections for emissions in the visible region are at least one order of magnitude lower than that of the 1.06 μm emission of Nd^{3+} in Silicate glasses, the intensities of some of them are still large enough as to have some applications. The fluorescent level for these visible emissions is $^4\text{G}_{5/2}$ which is at about 7000 cm^{-1} above the next lower energy level. Since this is not a large energy gap, multiphonon relaxation from the $^4\text{G}_{5/2}$ level can be expected to be important in those cases in which high energy phonons are present in the host. In the present paper optical properties and temperature dependent luminescence characteristics of Sm^{3+} ions in a $\text{Li}_2\text{O}-\text{Al}_2\text{O}_3-\text{MgO}-\text{SiO}_2$ glass are reported. From the optical absorption spectrum, by the application of Judd-Ofelt theory, the transition probabilities and stimulated emission cross-sections of the observed fluorescent levels have been analysed and compared with the experimental

2. EXPERIMENTAL METHODS

Glasses doped with excess 5 wt% Sm_2O_3 and having following chemical composition (in mol %) were prepared by the conventional quenching technique by using the reagent grade chemicals:



* Correspondance: Email: anna@cscgcricri.re.nic.in; Telephone: +91-033-4733469; Fax: +91-033-4730957

Chemical batches of 40 - 50 g were thoroughly mixed, melted in a platinum crucible in the temperature range of 1250-1300°C in an electric furnace for 4 hr and finally poured onto a preheated cast iron mould. Glass block was then quickly transferred to an annealing furnace which was set at 450°C. It was thus annealed at this temperature for about 5 h and cooled slowly to the room temperature. Such a glass block was cut and polished according to the required dimensions for the measurement work. The density (d) of the glass was measured by using the Archimedes' Principle with distilled water as an immersion liquid. The refractive indices n_d , n_f and n_c at three different wavelengths $\lambda_d = 587.6$ nm, $\lambda_f = 486.1$ nm and $\lambda_c = 656.3$ nm respectively were measured on a Pulfrich refractometer. The linear thermal expansion coefficient (α) and the glass transformation temperature (T_g) for the Sm^{3+} - glass samples with dimension 50x10x5 mm were measured on a Orton automatic recording dilatometer.

Polished glass plates of dimension 20x20x1 mm were used for spectral studies. The room temperature optical absorption spectrum for Sm^{3+} (5 wt%) -doped Silicate glass was recorded on UV-VIS-NIR scanning spectrophotometer (Shimadzu model UV-3101 PC) in the wavelength range 300 - 1800 nm. The total luminescence spectra of Sm^{3+} ; Silicate glass at different temperatures (10 K - 300 K) were measured on a Spex -1401 Double Spectrometer with a PMT (Hamamatsu Model C-3350) and with a lockin amplifier of the model Sr-400 two channel gated photon counter by using a N_2 - laser (337.1 nm) as the source of excitation. The decay times of the fluorescence transitions of the Sm^{3+} - doped glass were measured by using a Tektronix TDS-420 four channel digital oscilloscope. The low temperature cryogenic system was a He-Unit from M/s. Displex Air Products fitted with a temperature controller of the model (9600-1 Silicon diode from scientific Inst. Inc., Tokyo.

3. RESULTS AND DISCUSSION

From the measured density (d), refractive index (n_d), a few other physical properties such as Sm^{3+} ion concentration (N), polaron radius (r_p), interionic distance (r_i) and field strength (F) have been computed by using the relevant formulae expressions already available in the literature^{8,9}. Table 1 lists out the physical property data along with glass transition temperature (T_g) and Coefficient of linear thermal expansion (α) of Sm^{3+} - doped Silicate glass. This Table also lists out the nonlinear properties of Sm^{3+} - doped Silicate glass evaluated through their refractive indices (n_d , n_f and n_c) measured at three different wavelengths by following the reports made earlier¹⁰⁻¹². The measured UV-Vis-NIR Optical absorption spectrum of Sm^{3+} - doped glass is shown in Fig. 1. The absorption spectrum has revealed fourteen electronic transitions and are assigned appropriately from their energies. Spectral oscillator strengths of certain well defined absorption bands have been measured for the application of the Judd-Ofelt theory^{13,14} to estimate the best fit intensity parameters (Ω_λ) and thereby calculating line strengths and the oscillator strengths theoretically¹⁵. The values obtained for the Judd-Ofelt

Table 1: Values of physical, nonlinearity and thermal properties of Sm^{3+} - doped Silicate Glass

Average Molecular Weight (\bar{M} , g)	51.530
Density (d , g/cm ³)	2.503
Refractive index at $\lambda = 587.6$ nm (n_d)	1.557
Mean dispersion	0.0098
Abbe number (v_d)	57
Nonlinear refractive index (n_2 , 10 ⁻¹³ esu)	1.567
Nonlinear refractive index Coeff. (γ 10 ¹⁶ cm ² /W)	4.208
Nonlinear susceptibility (χ^3 10 ¹⁵ cm ²)	6.482
Sm^{3+} - concentration ($N \times 10^{22}$ ions/cm ³)	2.16
Polaron radius (r_p , Å)	1.446
Interionic distance (r_i , Å)	3.558
Field strength ($F \times 10^{-16}$, cm ²)	1.434
Glass transition temperature (T_g , °C)	465
Coeff. of linear thermal expansion (α) (30-300°C) $\times 10^{-7}/^\circ\text{C}$	120

Table 2: Measured absorption band energies (ν cm^{-1}), line strengths (S_{ed} cm^2), oscillator strengths ($f_{\text{expt.}}$ & f_{cal}) along with Judd-Ofelt intensity (Ω_{λ} cm^2) parameters of Sm^{3+} - doped Silicate Glass.

Absorption transition from $^6\text{H}_{5/2}$	Energy (cm^{-1})	$S_{\text{ed}} (10^{20} \text{ cm}^2)$	$f (10^6)$	
			Expt.	Cal.
$^6\text{H}_{15/2}$	6508	0.007	0.787	0.607
$^6\text{F}_{3/2}$	6803	0.639	1.106	1.072
$^6\text{F}_{5/2}$	7310	0.812	1.482	1.464
$^6\text{F}_{7/2}$	8170	1.080	1.881	2.177
$^6\text{F}_{9/2}$	9311	0.609	1.803	1.407
$^6\text{F}_{11/2}$	10616	0.085	0.910	0.227
$^4\text{I}_{11/2}$	21186	0.018	2.541	0.094

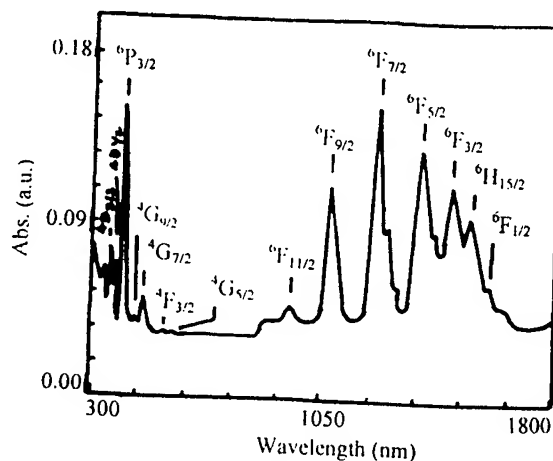


Fig. 1 : UV-Vis-NIR Absorption spectrum of Sm^{3+} - doped Silicate glass (300 K)

parameters for the -silicate glass are $\Omega_2 = 1.935 \times 10^{-20} \text{ cm}^2$, $\Omega_4 = 2.634 \times 10^{-20} \text{ cm}^2$, $\Omega_6 = 1.626 \times 10^{-20} \text{ cm}^2$. Both measured and calculated oscillator strengths for the recorded absorption bands of Sm^{3+} -silicate glass have been presented along with their respective energies and line strengths.

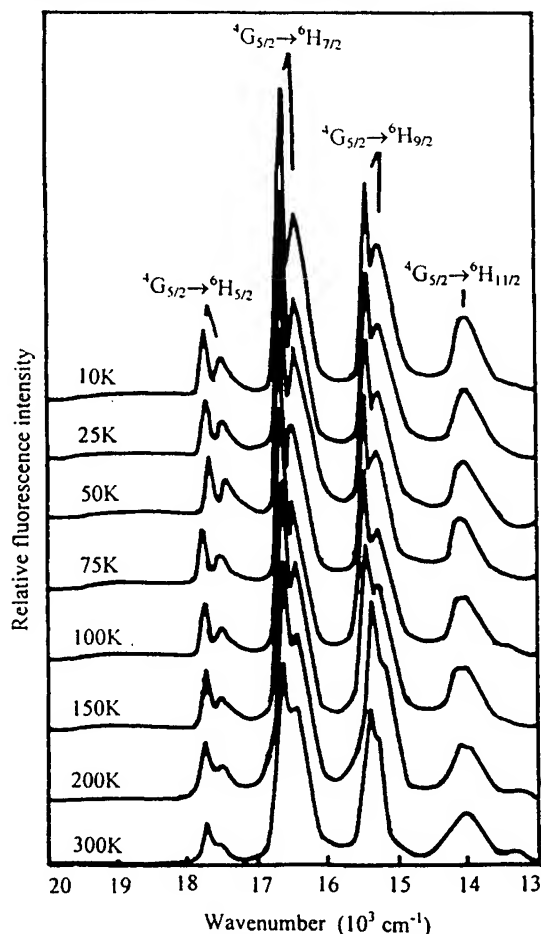


Fig.2 : Luminescence spectra of sm^{3+} -doped Silicate glass at different temperatures

Table 3: Transition energies (ν cm^{-1}) and evaluated Radiative transition probabilities (A s^{-1}) for the emission transitions of Sm^{3+} - doped Silicate Glass

Emission Transition	Energy(cm^{-1})	A (s^{-1})
$^4\text{G}_{5/2} \rightarrow ^6\text{F}_{9/2}$	8842	1
$^6\text{F}_{7/2}$	10022	2
$^6\text{F}_{5/2}$	10890	8
$^6\text{F}_{3/2}$	11394	1
$^6\text{H}_{13/2}$	12954	2
$^6\text{H}_{11/2}$	14367	18
$^6\text{H}_{9/2}$	15690	60
$^6\text{H}_{7/2}$	16896	65
$^6\text{H}_{5/2}$	17930	6

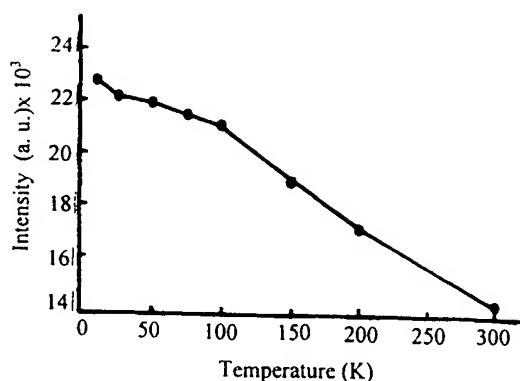


Fig. 3 : Temperature dependence of the Intensity for the emission transition $^4\text{G}_{5/2} \rightarrow ^6\text{H}_{7/2}$ of Sm^{3+} -doped Silicate glass with N_2 laser as excitation source

Photoluminescence of Sm^{3+} ions in silicate glass has been measured at different temperatures (10, 25, 50, 75, 100, 150, 200 and 300 K) and the spectra are shown in the Fig. 2. The spectra revealed four emission transitions $^4\text{G}_{5/2} \rightarrow ^6\text{H}_{5/2}$, $^6\text{H}_{7/2}$, $^6\text{H}_{9/2}$ and $^6\text{H}_{11/2}$. It is interesting to note from this figure that, in the low temperature emission spectra, the shoulders have become more prominent in some of the emission bands which can be attributed to the transitions to the different stark components of the final state¹⁶. With the best fit Judd-Ofelt intensity parameters, radiative properties such as transition probability (A), branching ratio (β_R) for the emission transitions of Sm^{3+} - silicate glass have been determined by using relevant expressions¹⁷. The results are given in Table 3. From this table it is noticed that, for emission transition $^4\text{G}_{5/2} \rightarrow ^6\text{H}_{7/2}$, the transition probability and branching ratios are higher, this is in confirmation with the maximum intensity observed in the measured luminescence spectra of Sm^{3+} -silicate glass at different temperatures. Intensity dependence of the emission level $^4\text{G}_{5/2} \rightarrow ^6\text{H}_{7/2}$ has been graphically represented in Fig. 3. Table 4 presents the emission transition energies (λ_p nm), effective half band widths ($\Delta\lambda_p$ nm) and stimulated emission cross-section (σ_p^E cm²) of the measured fluorescence transitions of the Sm^{3+} - silicate glass.

The fluorescence decay curves for all the observed emission transitions of the Sm^{3+} - silicate glass have been measured at room temperature which could only be fitted in double exponential and resulted in with short and long components (τ_1 , τ_2) of the decay times. hence the average lifetimes (τ) have been calculated form the relevant formula¹⁸. The computed value of average lifetimes of the measured emission transitions have been given in Table 4. Among the four emission transitions measured, the particular emission transition $^4\text{G}_{5/2} \rightarrow ^6\text{H}_{7/2}$ which is in electronic dipole in nature with $\Delta L = \pm 1$, $\Delta J = \pm 1$ and $\Delta S = \pm 1$ demonstrated brighter intensity for which lifetimes have been measured at different temperatures (10 - 300 K). The temperature dependence of the short and long components of fluorescence lifetimes for the Sm^{3+} - silicate glass have been depicted in Fig. 4. From this figure it is clear that there is a descending trend in the measured lifetimes (τ_1 , τ_2) with a rise in temperature. This indicates that, multiphonon relaxation of $^4\text{G}_{5/2}$ level plays an important role in the measured lifetimes.

Table 4: Peak wavelength (λ_p nm), effective half band width ($\Delta\lambda_p$ nm), Stimulated emission cross-section ($\sigma_p^E \times 10^{22}$ cm²) and average lifetimes (τ μ s) of the fluorescence transitions of Sm^{3+} -doped Silicate Glass

Parameter	Emission transition from $^4\text{G}_{5/2} \rightarrow$			
	$^6\text{H}_{5/2}$	$^6\text{H}_{7/2}$	$^6\text{H}_{9/2}$	$^6\text{H}_{11/2}$
λ_p	562.9	600.2	648.0	711.0
$\Delta\lambda_p$	3.3	4.3	5.5	18
σ_p^E	1.035	10.274	10.095	1.329
τ	1461.1	1419.3	1395.8	1380.3

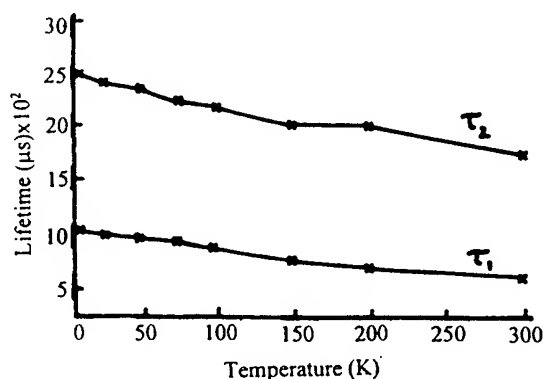


Fig. 4 : Temperature dependence of the lifetimes (τ_1 , τ_2) of double exponential fitting for the promising transition $^4\text{G}_{5/2} \rightarrow ^6\text{H}_{7/2}$ of the Sm^{3+} - Silicate glass

In conclusion, spectral characterization of Sm^{3+} - doped $\text{SiO}_2\text{-Al}_2\text{O}_3\text{-MgO-Li}_2\text{O-Na}_2\text{O}$ glass has been carried out by application of the Judd-Ofelt theory on the recorded absorption and fluorescence spectra. The measured fluorescence lifetimes as well as intensity of the prominent emission transition $^4\text{G}_{5/2} \rightarrow ^6\text{H}_{7/2}$ showed the temperature dependence which may be attributed to the multiphonon assisted non-radiative relaxation in the silicate host matrix under investigation.

ACKNOWLEDGMENTS

We express our grateful thanks to our Institute Director, for his kind co-operation and encouragement in the present work. Our thanks are due to BRNS, Department of Atomic Energy for its financial support.

REFERENCES

1. E. G. Behrens, R. C. Powell and D. H. Blackburn, *Appl. Opt.*, **29**, 1659, 1990.
2. R. Cases and M. A. Chamarro, *J. Solid State Chem.*, **90**, 313, 1991.
3. T. T. Basiev, A. Y. Dergachev, Y. V. Orlovskii and A. M. Prohkorov, *J. Lumin.*, **53**, 19, 1992.
4. M. M. Broer, A. J. Bruce and W. H. Grodkiewicz, *J. Lumin.*, **53**, 15, 1992.
5. J. Wang, W. S. Brocklesby, J. R. Uncoln, J. E. Towensend and D. N. Payne, *J. Non-Cryst. Solids*, **163**, 261, 1993.
6. R. Reisfeld, A. Bornstein and L. Boehm, *J. Solid State Chem.*, **14**, 14, 1975.
7. V. D. Rodriguez, I. R. Martin, R. Alcala and R. Cases, *J. Lumin.*, **54**, 231, 1992.
8. A. Shankar, A. Dasgupta, B. Basu and A. Paul, *J. Mater. Sci. Lett.*, **4**, 697, 1983.
9. M. M. Ahmed, E. A. Hogarth and M. N. Khan, *J. Mater. Sci.*, **19**, 4041, 1984.
10. A. J. Glass, *Laser Program Annual report*, Lawrence Livermore Labs, Report No. URCL-50021-72, 1975.
11. M. J. Weber, J. E. Lynch, D. H. Blackburn and D.J. Cronin, *IEEE J. Quantum Electron.*, **19**, 1600, 1983.
12. S. H. Kim, T. Yoko and S. Sakka, *J. Amer. Ceram. Soc.*, **76**, 865, 1993.
13. G. S. Ofelt, *J. Chem. Phys.* **37**, 511, 1962.
14. W. T. Carnall, P. R. Fields and K. Rajnak, *J. Chem. Phys.*, **49**, 4424, 1968. Bunzli and G. 15. F. Auzel, *Spectroscopy of Solid State Laser Type Materials*, B. DiBartolo (Ed.), Plenum Press, 1987.
16. M. Canalojo, R. Cases and R. Alcala, *Phys. Chem. Glasses*, **29**, 187, 1988.
17. M. A. Chamarro, R. Cases and R. Alcala, *Ann. De Phys.*, **16**, 227, 1991.
18. T. Fujii, K. Kodaira, O. Kawanchi, N. Tanaka, H. Yamashita, M. Anpo, *J. Phys. Chem. B* **101**, 10631, 1997.

Energy transfer luminescence in (Eu³⁺, Nd³⁺)-doped tellurite glass

Kalyandurg Annapurna[†], Rabindra Nath Dwivedi and Srinivasa Buddhudu^a

Glass Technology Section, Central Glass & Ceramic Research Institute
196, Raja S C Mullick Road, Calcutta - 700 032, India.

^a Department of Physics, Sri Venkateswara University Tirupati - 517 502, India.

ABSTRACT

Here, we bring out an infrared transmitting new optical glass based on TeO₂ added with AlF₃ and LiF, containing dual rare earth ions (Eu³⁺ & Nd³⁺) as the dopants with a purpose to examine their luminescence and also the decay times pertaining to a prominent transition of Eu³⁺ (⁵D₀ → ⁷F₂ at 615 nm) as a function of temperature both in the presence and absence of Nd³⁺ ions. The energy transfer rates (W_{tr}), critical distances (R₀) and transfer efficiencies (η_{tr}) have been evaluated based on the measured lifetime data of this glass.

Keywords : Energy transfer, Luminescence, Tellurite glass

1. INTRODUCTION

In the past several years, tellurium based glasses have been the subject of investigations with all greater interest as these are found to be the IR-transmitting (≈ 15 μm) materials for their use as the optical components in the forms of windows, prisms, laser glasses and also in the area of fibre optic communications¹⁻⁵. Earlier, some preliminary research works were carried out on optical spectra of Nd³⁺: TeO₂-B₂O₃-RiF (R=Li, Na, K) glasses⁶. It has been a well known fact that the TeO₂ chemical by itself does not form a glass, however it has been considered that with an addition of an intermediate (AlF₃) and a modifier (LiF), the very TeO₂ would form a good glass with high strength and transparency. The present paper aims in reporting yet another newly developed (Eu³⁺, Nd³⁺): TeO₂-AlF₃-LiF optical glass and to analyse its energy transfer from the donor (Eu³⁺) ion to the acceptor (Nd³⁺) ion by the measurement of the temperature dependent (10K -300K) luminescence spectra and also the lifetimes of a prominent emission transition (⁵D₀→⁷F₂) of Eu³⁺ ions.

2. EXPERIMENTAL

For the present work, three kinds of glasses such as (i) reference (host) glass (ii) Eu³⁺ - glass and (iii) (Eu³⁺+ Nd³⁺) - glass, have been developed and their compositions (in mol %) are given below :

- | | |
|---|--|
| i) Host Glass | : 79TeO ₂ + 6AlF ₃ + 15LiF |
| ii) Eu ³⁺ - Glass | : 78TeO ₂ + 6AlF ₃ + 15LiF |
| iii) (Eu ³⁺ + Nd ³⁺) - Glass | : 77TeO ₂ + 6AlF ₃ + 15LiF |

While making the Eu³⁺ and (Eu³⁺, Nd³⁺) - glasses, only the TeO₂ content was changed by keeping the contents of both the glass intermediate (AlF₃) and the modifier (LiF) in appropriate quantities fixed uniformly in all three glasses. The dopant ions

[†] Correspondance: Email: anna@cscgcricri.ernet.in; Telephone: +91-033-4733469; Fax: +91-033-4730957

concentrations were fixed at 1 mol % each. The Te-glasses have been prepared by using analar grade TeO_2 , AlF_3 , LiF and rare earth oxides (Eu_2O_3 & Nd_2O_3) of 99.99% purity. The batches of 50 g each thoroughly mixed were melted in platinum crucible first at 300°C for 10 min. and later at 700°C for 30 min. to ensure the homogeneity. The melt was then poured on to a steel plate and quenched with the other. The resulted glass samples were annealed at 300°C and then cooled slowly to room temperature. For the reference glass only the physical properties (d and n_d) were determined by adopting the conventional procedures and the thermal properties (T_g & T_m) were measured on a Shimadzu Diffraction Thermal Analysis (DTA) system. This instrument is sensitive for the ready evaluation of the thermal properties in the range of 300K to 1600K. The glass nature of the material studied was confirmed by an X-ray phase analysis (TUR M62 Diffractometer Cu K_α radiation with Ni filter). The infrared transmission ability was also measured and the glass infrared cut-off wavelength is found to $15\ \mu\text{m}$ from the spectral profile recorded on Shimadzu spectrophotometer. The physical and thermal property data for the host glass :

Density (d , g/cm^3)	: 4.380
Refractive Index (n_d)	: 1.695
Glass Transition Temperature (T_g , $^\circ\text{C}$)	: 385
Glass Softening Point (T_m , $^\circ\text{C}$)	: 540

The total luminescence spectra of Eu^{3+} and (Eu^{3+} , Nd^{3+}) : Tellurite glass at different temperatures (10 K - 300 K) were measured on a Spex -1401 Double Spectrometer with a PMT (Hamamatsu Model C-3350) and with a lockin amplifier of the model Sr-400 two channel gated photon counter by using a N_2 - laser (337.1 nm) as the source of excitation.

The decay times of the prominent fluorescence transition ($^5\text{D}_0 \rightarrow ^7\text{F}_2$) of the Eu^{3+} in both Eu^{3+} and (Eu^{3+} , Nd^{3+}) doped Tellurite glass were measured at different temperatures by using a Tektronix TDS-420 four channel digital oscilloscope. The low temperature cryogenic system was a He-Unit from M/s. Displex Air Products fitted with a temperature controller of the model (9600-1 Silicon diode from scientific Inst. Inc., Tokyo).

3. RESULTS AND DISCUSSION

Photoluminescence spectra measured at 300 K and 10 K for Eu^{3+} and (Eu^{3+} , Nd^{3+}) : TeO_2 - AlF_3 - LiF glasses are shown in Figs. 1 & 2 respectively. Fig. 1 reveals five emission transitions ($^5\text{D}_0 \rightarrow ^7\text{F}_{0,1,2,3,4}$) of Eu^{3+} doped glass and in Fig. 2 for (Eu^{3+} , Nd^{3+}) : glass only four emission transitions are observed excepting that of a forbidden transition ($^5\text{D}_0 \rightarrow ^7\text{F}_0$) which is suppressed due to the Nd^{3+} availability as the codopant with the Eu^{3+} ions in the glass matrix investigated. It is also interesting to notice that the more prominent transition ($^5\text{D}_0 \rightarrow ^7\text{F}_2$ at 615 nm) has got its fluorescence intensity significantly brightened at 10K compared at 300K as we see in Figs. 1 & 2. Comparison of these two profiles indicates that Eu^{3+} fluorescence efficiency has drastically been reduced particularly for the transition $^5\text{D}_0 \rightarrow ^7\text{F}_2$ and however, the magnetic dipole transition $^5\text{D}_0 \rightarrow ^7\text{F}_1$ remains unchanged due to codopant presence along with the Eu^{3+} in the glass. Thus, Fig. 3 presents a comparison of the relative fluorescence intensity of the prominent transition $^5\text{D}_0 \rightarrow ^7\text{F}_2$ for Eu^{3+} and (Eu^{3+} , Nd^{3+}) : glass at different temperatures. This decrease in the Eu^{3+} emission intensity with the presence of codopant may be attributed to the direct energy transfer from Eu^{3+} to Nd^{3+} ions. In support of the spectral features in Figs. 1 & 2 and a graphical representation in Fig. 3, the measured decay curves of the prominent transition ($^5\text{D}_0 \rightarrow ^7\text{F}_2$) at 300K and 10K show the lifetimes of this transition as follows :

Eu^{3+} : Glass	$\tau_{300\text{K}} = 252.65\ \mu\text{s}$
	$\tau_{10\text{K}} = 411.67\ \mu\text{s}$
(Eu^{3+} , Nd^{3+}): Glass	$\tau_{300\text{K}} = 209.50\ \mu\text{s}$
	$\tau_{10\text{K}} = 333.80\ \mu\text{s}$

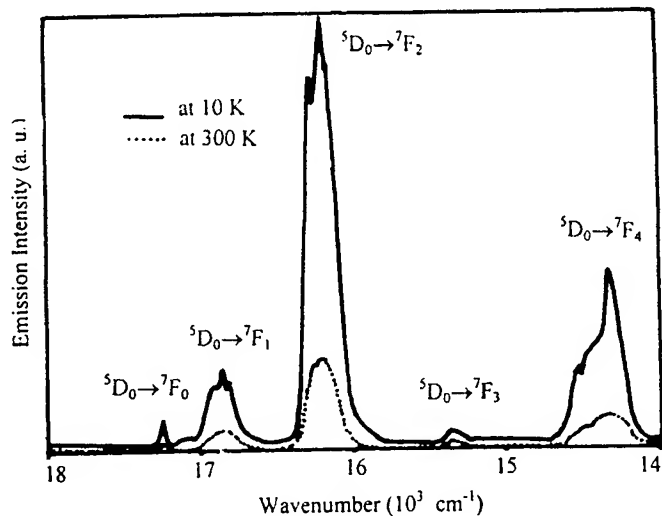


Fig. 1 : Luminescence Spectra of Eu^{3+} -doped Tellurite glass

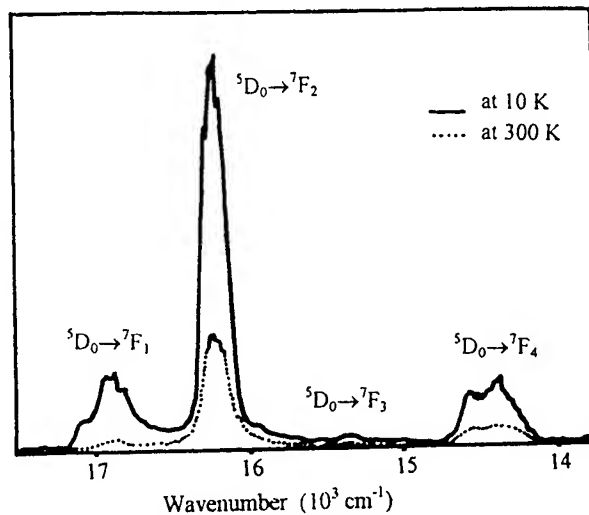


Fig. 2 : Luminescence spectra of $(\text{Eu}^{3+}, \text{Nd}^{3+})$ -doped Tellurite glass at different temperatures

The fluorescence intensity $I(t)$ has been approximated by taking the sum of the two exponential decay components as given below⁷:

$$I(t) = A_1 \exp(-t/\tau_1) + A_2 \exp(-t/\tau_2) \quad (1)$$

where τ_1 and τ_2 are the short and long decay components, where as A_1 and A_2 are computer fitting constants. By using the above equation, the average lifetime $\langle \tau \rangle$ or τ is evaluated as follows :

$$\tau = \frac{A_1 \tau_1^2 + A_2 \tau_2^2}{A_1 \tau_1 + A_2 \tau_2} \quad (2)$$

Due to the introduction of weight factors (A_1 and A_2), a reasonable estimation of average lifetime values in the case of complicated decay profile has been achieved⁸.

Temperature dependent decay times of $^5\text{D}_0 \rightarrow ^7\text{F}_2$ for both Eu^{3+} and $(\text{Eu}^{3+}, \text{Nd}^{3+})$: glasses are shown in Fig. 4 ; and the trends in this figure confirm the reduction in the decay times as the temperature increased. The energy transfer in rare earth ions doped glasses is considered to be the resonant energy transfer from donor to the acceptor energy levels. The energy transfer probability, W_{tr} is evaluated from the following expression

$$W_{tr} = (1/\tau_0 - 1/\tau) \quad (3)$$

where τ_0 is the lifetime of $^5\text{D}_0 \rightarrow ^7\text{F}_2$ of Eu^{3+} ions and τ is the lifetime of the same transition in the presence of Nd^{3+} ions.

For the electric dipole-dipole mechanism, the critical distance, R_0 is computed from

$$R_0 = [(9 W_{tr} \tau_0 C^2)/(16 \pi^2)]^{1/6} \quad (4)$$

This parameter is a measure of the energy transfer at which intrinsic emission probability of donor and energy transfer from

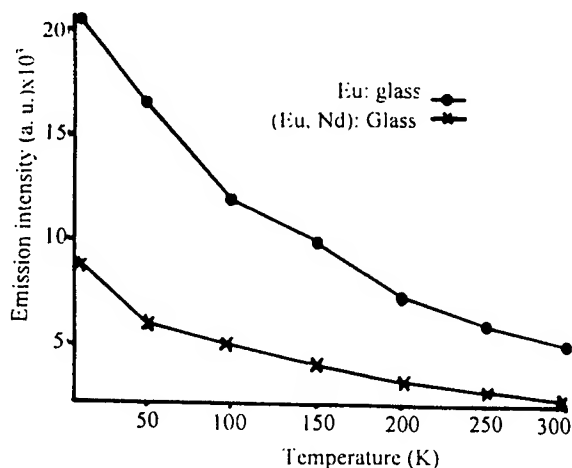


Fig. 3 : Comparison of Relative fluorescence intensity of the prominent emission transition ($^5D_0 \rightarrow ^7F_2$) of Eu^{3+} in Eu^{3+} and $(\text{Eu}^{3+}, \text{Nd}^{3+})$ -doped tellurite glass at different temperatures

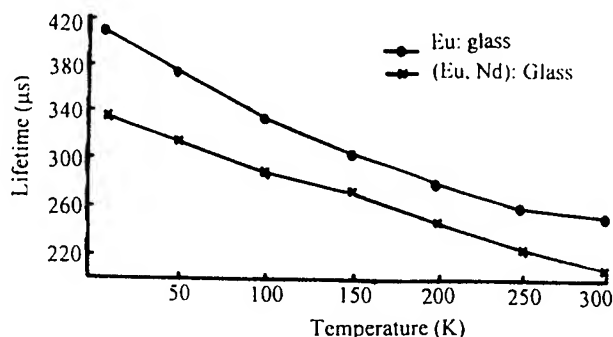


Fig. 4 : Comparison of lifetimes of the prominent emission transition ($^5D_0 \rightarrow ^7F_2$) of Eu^{3+} in Eu^{3+} and $(\text{Eu}^{3+}, \text{Nd}^{3+})$ -doped tellurite glass at different temperatures

donor to acceptor are coinciding to each other.

Another important energy transfer parameter namely energy transfer efficiency η_{tr} is calculated from

$$\eta_{tr} = (1 - \tau / \tau_0) \quad (5)$$

The data related to W_{tr} , R_0 and η_{tr} for $(\text{Eu}^{3+}, \text{Nd}^{3+})$: Tellurite glass investigated is presented in the following table as a function of temperature (10K -300K)

Temp.(K)	W_{tr} (s^{-1})	R_0 (nm)	η_{tr}
10	548.4	1.23	0.183
100	490.2	1.17	0.142
200	467.0	1.12	0.116
300	455.8	1.08	0.103

From this table it is clear that the energy transfer between the donor and acceptor at lower temperatures is larger than at room temperature.

In essence, it could be stated that, we have prepared IR-transmitting new optical glass based on TeO_2 , added with AlF_3 and LiF as glass network intermediates and modifier respectively and have studied energy transfer from Eu^{3+} ions to Nd^{3+} ions. Luminescence spectra and decay curves of donor ion (Eu^{3+}) showed pronounced changes on the addition of the acceptor (Nd^{3+}) to the glass matrix.

ACKNOWLEDGEMENTS

We are gratefully thankful to Dr. H. S. Maiti, Director of the CGCRI, Calcutta for his kind cooperation and encouragement in the present work.

REFERENCES

1. M. J. Weber, *J. Non-Cryst. Solids* **123**, 208, 1990.
2. J. S. Wang, E. M. Vogel, E. Snitzer, *Opt. Mater.* **3**, 187, 1994.
3. J. McDougall, D. B. Hollis, J. P. Payne, *Phys. Chem. Glasses* **37(6)**, 254, 1996.
4. T. Komatsu, K. Shioya, *J. Non-Cryst. Solids* **209(3)**, 305, 1997.
5. Y. Ohishi, A. Mori, M. Yamada, H. Ono, Y. Nishida, K. Oikawa, *Opt. Letters* **23(4)**, 274, 1998.
6. N. Sooraj Hussain, K. Annapurna, S. Buddhudu, *Phys. Chem. Glasses* **38**, 511997.
7. T. Fujii, K. Kodaira, O. Kawanchi, N. Tanaka, H. Yamashita, M. Anpo, *J. Phys. Chem. B* **101**, 10631, 1997.
8. Z. Assefa, R. G. Haire, N. A. Stump, *Mater. Res. Soc. Sym. Proc.* **459**, 471, 1997.

Temperature dependent luminescence in (Eu³⁺, Dy³⁺) doped tellurite glass

Kalyandurg Annapurna*, Rabindra Nath Dwivedi and Srinivasa Buddhudu^a

Glass Technology Section, Central Glass & Ceramic Research Institute
196, Raja S C Mullick Road, Calcutta - 700 032, India.

^a Department of Physics, Sri Venkateswara University, Tirupati - 517 502, India.

ABSTRACT

This short paper reports both the photoluminescence and the lifetime measurements of a prominent emission transition (⁵D₀→⁷F₂) of Eu³⁺ both in the presence and absence of the codopant rare earth ion (Dy³⁺) in an optical glass of the composition (79-x)TeO₂+6AlF₃+15LiF+xLn₂O₃ as a function of temperature down to 10K.

Keywords : Temperature Dependent Luminescence, Rare earth doped Glass, Tellurite Glass

1. INTRODUCTION

The important applications of the TeO₂ based glasses have earlier been reported¹⁻³. Keeping in mind their applications, our main objective is to examine the emission properties and also the energy transfer between Eu³⁺ and Dy³⁺ in the tellurite glass system.

2. EXPERIMENTAL

For the present work, three kinds of host glasses such as (i) reference (undoped) glass, (ii) Eu³⁺ - glass and (iii) (Eu³⁺+ Dy³⁺)-glass were prepared and their compositions (in mol %) are given below :

- i) undoped Glass : 79TeO₂ + 6AlF₃ + 15LiF
- ii) Eu³⁺ - Glass : 78TeO₂ + 6AlF₃ + 15LiF
- iii) (Eu³⁺, Dy³⁺) - Glass : 77TeO₂ + 6AlF₃ + 15LiF

In making the Eu³⁺ and (Eu³⁺, Dy³⁺) - glasses, only the TeO₂ content was changed while keeping the contents of both the glass intermediate (AlF₃) and the modifier (LiF) in appropriate fixed quantities uniformly in all three glasses reported here. The dopant ion concentrations were fixed at 1 mol % each. Only for the reference glass the physical properties, density and refractive index (d and n_d) were determined by adopting conventional procedures and the thermal properties (T_g & T_m) measured using a Shimadzu Diffraction thermal Analysis (DTA) system. This instrument is sensitive for the ready evaluation of thermal behaviour over the temperature range from the ambient up to 1600K. The amorphous state of the glass was confirmed by an X-ray phase analysis (TUR M62 Diffractometer Cu K_α radiation with Ni filter). The infrared transmission ability was also measured and the glass infrared cut-off wavelength found to be 15 μm from the spectral profile recorded on a Shimadzu spectrophotometer.

* Correspondance : Email: anna@cscgcri.ren.nic.in; Telephone: +91-033-4733469; Fax: +91-033-4730957

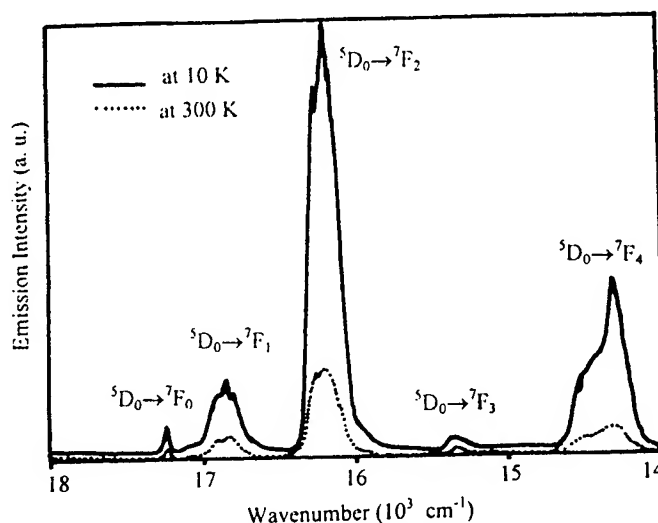


Fig. 1 : Luminescence Spectra of Eu^{3+} - doped Tellurite glass

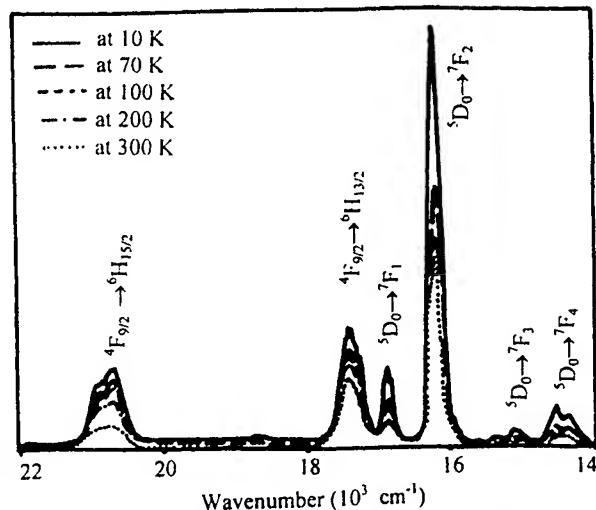


Fig. 2 : Luminescence spectra of $(\text{Eu}^{3+}, \text{Dy}^{3+})$ -doped Tellurite glass at different temperatures

The physical and thermal property data relating to the host glass is given below :

Density ($d, \text{g/cm}^3$)	: 4.380
Refractive Index (n_d)	: 1.695
Glass Transition Temperature ($T_g, ^\circ\text{C}$)	: 385
Glass Softening Point ($T_m, ^\circ\text{C}$)	: 540

The total luminescence spectra of Eu^{3+} and $(\text{Eu}^{3+}, \text{Dy}^{3+})$: Tellurite glasses at different temperatures (10 K - 300 K) were measured using a Spex -1401 Double Spectrometer with a PMT (Hamamatsu Model C-3350) and a lockin amplifier, model Sr-400, two channel gated photon counter by using a N_2 - laser (337.1 nm) as the source of excitation.

The decay times of the prominent fluorescence transition ($^5\text{D}_0 \rightarrow ^7\text{F}_2$) of the Eu^{3+} ion in both Eu^{3+} and $(\text{Eu}^{3+}, \text{Dy}^{3+})$ doped Tellurite glass were measured at different temperatures by using a Tektronix TDS-420 four channel digital oscilloscope. The low temperature cryogenic system was a He-Unit from M/s. Displex Air Products fitted with a temperature controller model (9600-1, with Silicon diode) from scientific Inst. Inc., Tokyo.

3. RESULTS AND DISCUSSION

The emission spectral features of Eu^{3+} glass are shown in Figs. 1 & 2 to demonstrate the significant influences due to the changes in temperature (300 - 10K) and also because of the presence of the codopant (Dy^{3+}) in the tellurite glass. Fig. 3 compares the fluorescence intensity variation of the stronger emission peak ($^5\text{D}_0 \rightarrow ^7\text{F}_2$) of Eu^{3+} with and without codopant (Dy^{3+}) availability in the glass matrix under report. The lifetimes of the stronger emission transition ($^5\text{D}_0 \rightarrow ^7\text{F}_2$) of Eu^{3+} at the red region (615 nm) have been measured for Eu^{3+} -glass without and with codopant (Dy^{3+}) present in the host glass matrix as a function of temperature. The temperature dependent decay times of transition ($^5\text{D}_0 \rightarrow ^7\text{F}_2$) of Eu^{3+} ion in Eu^{3+} and $(\text{Eu}^{3+}, \text{Dy}^{3+})$ doped tellurite glasses are shown in Fig. 4. By employing earlier reported relevant expressions^{4,5}, the energy transfer in the codoped tellurite

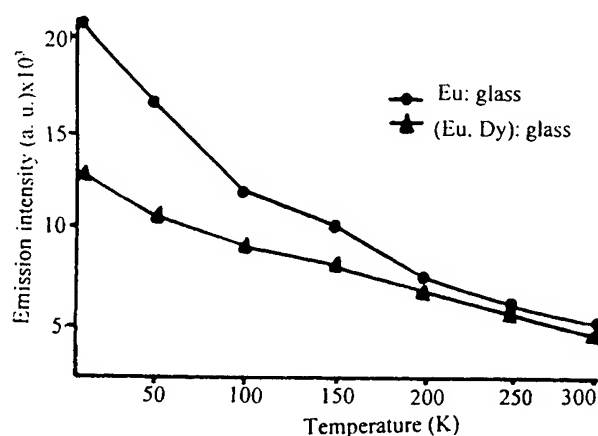


Fig. 3 : Comparison of Relative fluorescence intensity of the prominent emission transition (${}^3D_0 \rightarrow {}^7F_2$) of Eu^{3+} in Eu^{3+} and $(\text{Eu}^{3+}, \text{Dy}^{3+})$ -doped tellurite glass at different temperatures

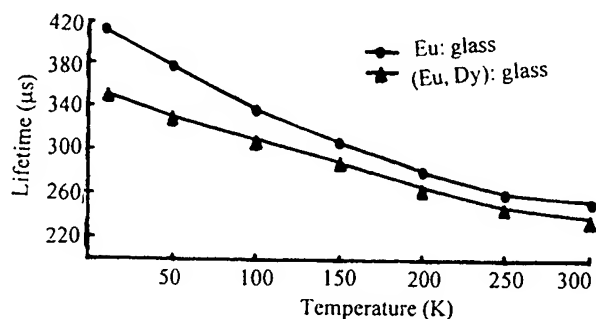


Fig. 4 : Comparison of lifetimes of the prominent emission transition (${}^3D_0 \rightarrow {}^7F_2$) of Eu^{3+} in Eu^{3+} and $(\text{Eu}^{3+}, \text{Dy}^{3+})$ -doped tellurite glass at different temperatures

glass was systematically understood by computing the necessary parametrisation concerning the (a) energy transfer probability, W_{tr} ; (b) critical distance, R_0 and (c) energy transfer efficiency factor, η_{tr} . The results are presented below to understand the trends in energy transfer as a function of temperature.

Temp.(K)	W_{tr} (s^{-1})	R_0 (nm)	η_{tr}
10	412.0	1.17	1.442
100	267.0	1.06	0.821
200	185.3	0.96	0.495
300	156.9	0.92	0.381

From the above data and also from the Fig. 3, it is clear that energy transfer in the codoped rare earth glass at lower temperature is quite significant.

Due to the addition of AlF_3 and LiF to the TeO_2 based glass composition, a good quality system having an extended IR-transmission up to $15 \mu\text{m}$ was successfully prepared. Further, by changing the temperature (10K-300K), the energy transfer mechanism from the donor Eu^{3+} to the acceptor (Dy^{3+}) in this glass was systematically understood.

ACKNOWLEDGEMENTS

We are grateful to Dr. H. S. Maiti, Director of CGCRI, Calcutta for his kind co-operation and encouragement in the present work.

REFERENCES

1. Z. Pan, K. Dyer, A. Loper and S. H. Morgan, *Synthesis and Application of Lanthanide Doped Materials*, B. G. Potter Jr., A. J. Bruce (Eds.), p. 55, The American Ceramic Society, Westerville, OH, 1996,.
2. Y. Himei, Y. Miura, T. Nanbe and A. Osaka, *J. Non-Cryst. Solids* **211(1-2)**, 64, 1997.
3. D. L. Sidebottom, M. A. Hruschka, B. G. Potter and R. K. Brow, *J. Non-Cryst. Solids* **222**, 282, 1997.
4. T. Fujii, K. Kodaira, O. Kawanchi, N. Tanaka, H. Yamashita, M. Anpo, *J. Phys. Chem. B* **101**, 10631, 1997.
5. Z. Assefa, R. G. Haire, N. A. Stump, *Mater. Res. Soc. Sym. Proc.* **459**, 471, 1997.

Comparison of Er-doped sol-gel glasses with various hosts

Q. Xiang, Y. Zhou, Y.L. Lam, B. S. Ooi, Y.C. Chan, and C.H. Kam

Photonics Research Group, School of Electrical and Electronic Engineering,
Nanyang Technological University, Nanyang Avenue, Singapore 639798

ABSTRACT

Using the sol-gel process, we prepared three groups of Er-doped glasses, namely, Er-doped $\text{SiO}_2\text{-AlO}_{1.5}$ (SAE) glass, Er-doped $\text{SiO}_2\text{-TiO}_2\text{-AlO}_{1.5}$ (STAE) glass, and Er-doped $\text{SiO}_2\text{-GeO}_2\text{-AlO}_{1.5}$ (SGAE) glass. Various erbium concentration and different host composition under the same processing condition have been studied in order to optimize the material composition to get the strongest fluorescence emission for each material system. It has been found that for SAE glass, the strongest fluorescence emission is obtained when the mole ratio of the three constituent oxides is $100\text{SiO}_2 : 20\text{AlO}_{1.5} : 2\text{ErO}_{1.5}$. For the STAE material system, the best composition ratio for the strongest fluorescence emission is $93\text{SiO}_2 : 7\text{TiO}_2 : 20\text{AlO}_{1.5} : 1\text{ErO}_{1.5}$, whereas the value for SGAE glass is $90\text{SiO}_2 : 10\text{GeO}_2 : 20\text{AlO}_{1.5} : 1\text{ErO}_{1.5}$. But the relative lifetimes were obtained with the recipe $100\text{SiO}_2 : 10\text{AlO}_{1.5} : 1\text{ErO}_{1.5}$ for SAE series, $90\text{SiO}_2 : 10\text{GeO}_2 : 10\text{AlO}_{1.5} : 1\text{ErO}_{1.5}$ for SGAE group and $93\text{SiO}_2 : 7\text{TiO}_2 : 20\text{AlO}_{1.5} : 1\text{ErO}_{1.5}$ for STAE group. Using these recipes, three 20-layer (up to $2.5\text{ }\mu\text{m}$) crack-free films have been deposited on silica-on-silicon (SOS) substrates with multiple spin-coating and rapid thermal annealing (RTA). Only the STAE film and the SGAE film are found to guide light. The experimental results show that STAE glasses have higher hydrophilicity than SGAE glasses and SGAE glasses has lower crystallization temperature than STAE glasses. The fact that these waveguiding films emit relatively strong fluorescence around the wavelength of $1.55\text{ }\mu\text{m}$ implies that such planar waveguides are potential candidates from which integrated optical waveguide amplifiers and lasers operating at the third optical fiber communication window can be fabricated.

Keywords: Sol-gel process, Silica-based glasses, Fluorescence intensity, Fluorescence lifetime

1. INTRODUCTION

Recently, research activity toward the sol-gel process in the synthesis of new materials has extensively been carried out, as it possesses many advantages. For examples, the processing temperature is relatively low, the material composition and final form are flexible, and the dopants can disperse in the host homogeneously.

The fluorescence behavior of a rare earth ion will generally be only slightly different in various glass hosts because the f-electronic shell in the rare earth is a well-shielded inner electronic shell. However, the glass network and modifier ions may still affect the spectroscopic properties of rare earth ions by the ligand field of their environment¹. For example, the line width and peak wavelength of absorption and fluorescence of a rare earth ion can be manipulated to a very limited extent by tailoring the host glass composition. In order to figure out the influence of glass composition on the fluorescence properties of typical sol-gel derived Er doped integrated optical waveguide glasses, we prepared Er-doped $\text{SiO}_2\text{-AlO}_{1.5}$ (SAE) glass, Er-doped $\text{SiO}_2\text{-TiO}_2\text{-AlO}_{1.5}$ (STAE) glass, and Er-doped $\text{SiO}_2\text{-GeO}_2\text{-AlO}_{1.5}$ (SGAE) glass. Here S stands for silica, A for aluminum, E for erbium, T for titanium and G for germanium and all the concentrations are expressed by atom ratios. The main purpose for choosing these glass modifiers (Ti or Ge) is to get different function materials. $\text{SiO}_2\text{-TiO}_2$ system offers the possibility to control the refractive index from 1.46 (the refractive index of pure SiO_2) to 2.2 (that of pure amorphous TiO_2). The large index value that could be provided means that a strong mode confinement optical waveguide can be fabricated on many solid substrates. Alumina co-doping has demonstrated the improvement in the homogenous distribution of rare earth ions in the host. Hence, the fluorescence intensity can be enhanced greatly²⁻³. $\text{SiO}_2\text{-GeO}_2$ glasses, prepared by the sol-gel process, have been found to be photosensitive⁴⁻⁵. This effect enables the photo-inscription of permanent refractive index gratings and therefore the possibility of achieving optical devices such as narrow band reflection filters, WDM devices and beam splitters, etc⁶⁻⁷. Er-doped germanosilicate glasses also offer the additional advantage of combining photosensitivity with light emission. Hence, with UV-writing to produce grating mirrors, a channel waveguide made from such a material system

Correspondence: Email: qxjiang@ntu.edu.sg; Tel: +65-7905461; Fax: +65-7904161

on a silicon chip has the potential of being made into a narrow linewidth solid state waveguide laser emitting at around 1.5 μ m, just as in the case of germanium doped fiber lasers. As a basic research, Er-doped SiO₂-AlO_{1.5} system was researched firstly. In this paper, we chose three samples from each group which have same material compositions except for the glass modifiers, their fluorescence emission intensity and lifetimes were compared. The difference of their refractive index and crystalline properties are also presented.

2. EXPERIMENT

Tetraethoxysilane [TEOS, Si(OC₂H₅)₄], aluminium nitrate [Al(NO₃)₃·9H₂O], and erbium nitrate [Er(NO₃)₃·5H₂O] were employed as precursors of SiO₂, Al₂O₃, Er₂O₃ respectively in three materials. TEOS was diluted in ethanol and water with HCl added as a catalyst. The mole ratio of the mixture TEOS/water/ethanol is 1:12:10. Water and ethanol are added in two steps in equal proportions in order to get a more miscible solution. In separate bakers, Al(NO₃)₃·9H₂O and Er(NO₃)₃·5H₂O were dissolved in de-ionized water and were added into the TEOS solution after 2 hours' hydrolyses at 60°C. The preparation of sol for the SiO₂-TiO₂ and SiO₂-GeO₂ systems must take into account the different hydrolysis rate of the alkoxide precursors for the two oxides. Therefore, for the STAE material system, tetrapropyl orthotitanate [TPOT, Ti((CH₃)₂CHO)₄] was initially mixed with acetylacetone [C₅H₈O₂] before it was added to the pre-hydrolyzed TEOS solution. The details of the preparation procedures have been described elsewhere⁸. For the SGAE material system, Germanium (IV) ethoxide [TEOG, Ge(OC₂H₅)₄], also needed to be mixed with 2-methoxyethanol (CH₃OCH₂CH₂OH or C₃H₈O₂) before it was added into the pre-hydrolyzed TEOS solution⁹. The end solutions were perfectly clear and were kept in a sealed bottle at room temperature for several days to obtain the necessary viscosity.

Table 1 Recipes of the SAE, SGAE and STAE material systems

Recipes for SAE material system	Recipes for STAE material system	Recipes for SGAE material system
1. 100SiO ₂ : 10AlO _{1.5} : 1.0ErO _{1.5}	1. 93SiO ₂ : 7TiO ₂ : 10AlO _{1.5} : 1.0ErO _{1.5}	1. 90SiO ₂ : 10GeO ₂ : 10AlO _{1.5} : 1.0ErO _{1.5}
2. 100SiO ₂ : 20AlO _{1.5} : 1.0ErO _{1.5}	2. 93SiO ₂ : 7TiO ₂ : 20AlO _{1.5} : 1.0ErO _{1.5}	2. 90SiO ₂ : 10GeO ₂ : 20AlO _{1.5} : 1.0ErO _{1.5}
3. 100SiO ₂ : 20AlO _{1.5} : 2.0ErO _{1.5}	3. 93SiO ₂ : 7TiO ₂ : 20AlO _{1.5} : 2.0ErO _{1.5}	3. 90SiO ₂ : 10GeO ₂ : 20AlO _{1.5} : 2.0ErO _{1.5}

Using the procedures stated above, a series of solutions with different constituent compositions for each material system were prepared and three from each material system were chosen to conduct the comparison with the details shown in Table 1. In our experiment, both powdered glass and thin film were prepared for each material group. But we could only compare the fluorescence intensity of the powdered glass because the coupling efficiency of the pump power is quite different for each planar waveguide no matter what kind of coupling methods are used. Because of this reason, for each kind of material group, we firstly optimised the material composition using the powdered glasses by comparing the fluorescence emission intensity and lifetime and then used the optimized composition to fabricate the planar waveguide.

In the case of powder, we poured the end solution into an uncovered dish after 2 to 3 weeks' aging, dried gels were obtained a few days later. The dried gels were heated in a furnace to 1000°C to remove water and the solvent, and to condense into a glass. The ramping up speed of temperature in the furnace was 1.5°C/min. The temperature was kept constant at 200°C for half an hour, at 600°C for an hour, and at 1000°C for 5 hours respectively. It was then allowed to cool down gradually to room temperature. For the case of thin films, single or multiple layer films were deposited on silicon-based substrates after the end solution had aged for two days by using spin-coating and rapid thermal annealing in rapid thermal processor (RTP). The spinner was adjusted to 3000rpm for 30s. In the RTP, the temperature ramped up to 1000°C in 30 seconds, stayed at this final temperature for 15 seconds, and then cooled down to room temperature in 30 seconds. The preparation flow chart is shown in Figure 1.

Fluorescence measurement was carried out on all powdered glasses at room temperature. The experimental apparatus used was described elsewhere¹⁰. Briefly, an Ar⁺ laser at 488nm mechanically chopped at 80Hz was used as the pump source. The fluorescence light emitted is collected by two lenses, analyzed with an ORIEL (model 77200) monochromator and detected with an ORIEL (model 71905) detector. A long pass filter was placed in front of the monochromator to remove the pump wavelength. The lifetime measurement set-up is shown in Figure 2. A 10Hz chopped Ar⁺ laser beam (488nm) was split by a beam splitter. One beam was directed to the sample, and another was directly monitored by detector 2 with its output serving as the trigger signal of a digital oscilloscope (Tektronix TDS 360). The fluorescence signal focused onto detector 1 was channelled to the same digital oscilloscope on which the fluorescence decay was recorded.

The refractive index of the thin films was measured by an ellipsometer (UVISELTM Spectroscopic Phase Modulated Ellipsometer). The X-ray diffraction (XRD) measurement is performed on a Rigaku system (RINT 2000) at glancing angle of 1°.

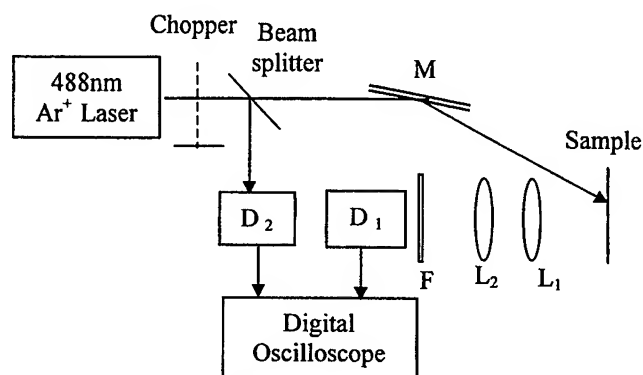
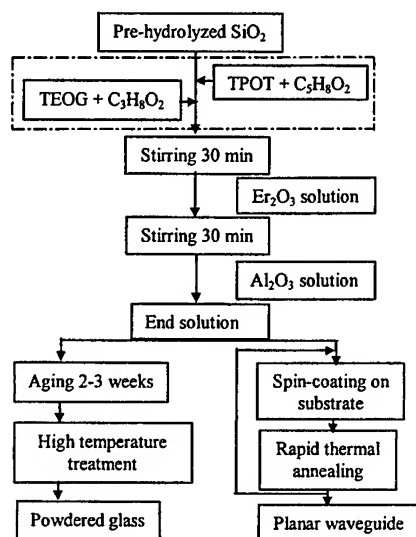


Fig. 1 Preparation procedures for powdered glasses and thin films Fig. 2 the setup for lifetime measurement of Er-doped glasses

3. RESULTS AND DISCUSSION

3.1 Fluorescence intensities and lifetimes of the powdered glasses

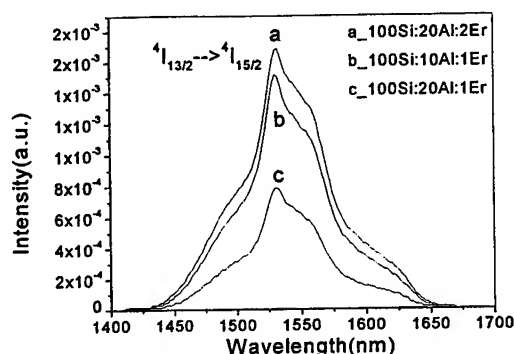
Figure 3 shows the fluorescence emission spectra of the 9 samples shown in Table I. Figure 3(a) is related to SAE material system, Figure 3(b) to SGAE material system and Figure 3(c) to STAE material system. As can be seen in Figure 3(a), for SAE material system, the fluorescence emission intensity of the 20Al:2Er sample is almost the same as that of the 10Al:1Er sample but the 20Al:2Er sample shows a little higher peak than the sample 10Al:1Er. Both of them have same Al/Er ratio of 10. This result implies that Al can disperse as high as 2 mole Er in SiO₂ host with the Al/Er ratio of 10. Meanwhile the fluorescence intensity of the sample with 10Al:1Er is much stronger than that of the sample with 20Al:1Er. This result tells us that too much Al³⁺ will lead to decrement of the fluorescence intensity instead of increment. However, for SGAE and STAE material systems as can be seen in Figure 3(b) and 3(c), the strongest fluorescence intensity results from the sample with 20Al:1Er instead of 20Al:2Er as shown in SAE material system. The only reason for this difference comes from the glass modifiers Ge and Ti. The experimental results show that these glass modifiers make Al³⁺ less efficient in dispersing the rare-earth ions in glass network and thus a higher Al/Er ratio is needed for an optimum fluorescence intensity. By comparing curve (b) and (c) in Figure 3(b) and 3(c), we can see that when the Al/Er ratio is maintained at 10 in these two glasses, the overall fluorescence intensity of the 20Al:2Er sample is stronger than that of the 10Al:1Er sample.

As we can expect, the peak wavelength and the spectrum width are fairly independent of the host modifiers. Since the erbium luminescence is duo to an intra-4f shell transition, to which the influence of the crystal field of the host lattice is weak.

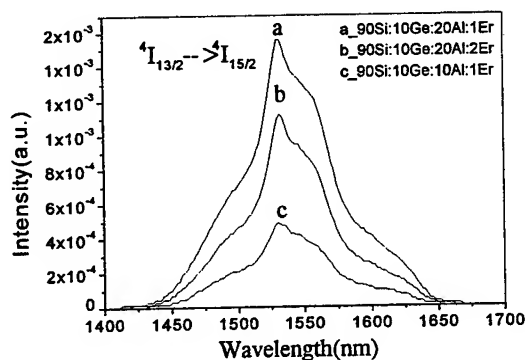
The ⁴I_{13/2} energy level lifetimes of Er³⁺ of the above 9 samples are shown in Table 2. For SAE material system, although the fluorescence emission intensity of the 10Al:1Er sample is not the strongest, its lifetime is much longer than the others. By comparing the fluorescence intensity and lifetime, we think that the recipe 100SiO₂:10AlO_{1.5}:1ErO_{1.5} is the best one in SAE series in terms of the overall fluorescence property.

For SGAE material system, the lifetime of the 10Al:1Er sample is much longer (3.15ms) than that of the 20Al:1Er sample (1.76ms) although its fluorescence intensity is weaker than the latter's. So it is difficult to say which one is better for general practical application. However, STAE material system shows different results as compared with SAE and SGAE material systems. The 20Al:1Er sample which has the strongest fluorescence intensity also shows the longest lifetime. Therefore, the

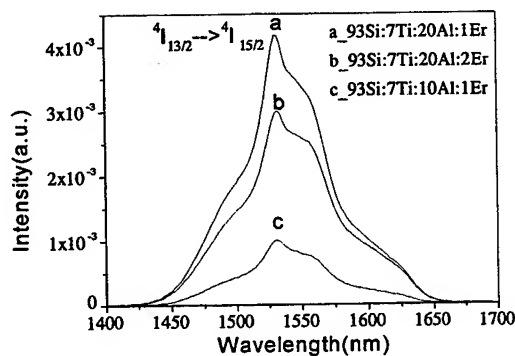
recipe $93\text{SiO}_2:7\text{TiO}_2:20\text{AlO}_{1.5}:1\text{ErO}_{1.5}$ has the obvious advantage in both fluorescence intensity and lifetime. However, with the same Al^{3+} and Er^{3+} content, STAE materials have a shorter lifetime than SAE and SGAE materials. Considering that all these samples thermally processed identically, we suspect that the difference comes from the hydroxyl (OH) impurities in the glasses that result from the incorporation of Ti. OH vibrational frequencies typically occur in the range of $2.77\text{--}3.57\mu\text{m}$, which is higher than other vibrational frequencies in the glass¹⁰. As a result, only two or three phonons are usually required for nonradiative deexcitation of most rare earth in glass laser transmission. Because the sol gel process is a wet chemical one, it will bring about the existence of a relatively large amount of OH quenchers in sol-gel glasses. The fact that Ti-containing glasses have, on average, a lower fluorescence lifetime than the two others implies that Ti has higher hydrophilicity than Germanium.



(a) the fluorescence spectra of SAE material system



(b) the fluorescence spectra of SAE material system



(c) the fluorescence spectra of SAE material system

Figure 3 the fluorescence spectra of SAE, SGAE and STAE material systems

Table 2 The lifetime of $^4\text{I}_{13/2}$ energy level of Er^{3+} in different host

Composition	$T_{1/e}$ Lifetime in SAE series (ms)	$T_{1/e}$ Lifetime in SGAE series (ms)	$T_{1/e}$ Lifetime in STAE series (ms)
10Al:1Er	3.55	3.12	1.19
20Al:1Er	1.81	1.76	1.97
20Al:2Er	1.51	1.54	0.86

3.2 The refractive index and crystallization properties of the thin films

For each kind of material system, a 1-layer film was deposited on silicon under the same preparation condition in order to measure their refractive index. The used recipes of the solutions were 100Si:20Al:1Er for SAE series, 90Si:10Ge:20Al:1Er for SGAE series, and 93Si:7Ti:20Al:1Er for STAE series. The films were annealed in RTP to 1000°C under O_2 atmosphere

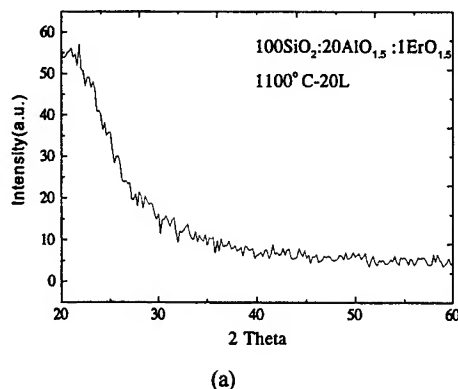
using the temperature program stated above. Their refractive index was measured by an ellipsometer at 6328nm. The results are 1.462 for SAE series, 1.474 for SGAE series, and 1.491 for STAE series. Based on these values, a 20-layer film was fabricated on silica-on-silicon (with a 2 μ m thermal grown silica of a refractive index of 1.460) for each material system. Light guiding experiments were conducted using the prism-coupling method together with a He-Ne (6328nm) light source. As expected, the SAE 20-layer film could not guide light, but both the SGAE and STAE 20-layer film could guide light.

The three material system films also showed different crystallization property. In this experiment, we again used the recipe of 100Si:20Al:1Er for SAE, 90Si:10Ge:20Al:1Er for SGAE, and 93Si:7Ti:20Al:1Er for STAE. Some 2-layer and 20-layer films were deposited on SOS under the same preparation condition as stated above. X-ray diffraction curves were measured of the films and the results are shown in Figure 4. From Figure 4(a), we know that the 20-layer SAE film annealed under 1100°C does not show any peaks that indicate crystallization. Meanwhile, Figure 4(c) shows that there is no peak on the XRD curve of the 2-layer STAE film annealed under 1100°C, but there exist one peak on the XRD curve of the 20-layer STAE film under the same annealing condition. We can thus conclude that this crystallization peak results from the multiple annealing in the rapid thermal processor. For SGAE system, as can be seen in Figure 4(b), the 2-layer film has shown a crystallization peak after 1050°C annealing. As annealing temperature increases, the peak becomes more obvious. By comparing the three cases, we can summarize that the annealing temperature can be as high as 1100°C for SAE system and the material will still be amorphous, but if low-scattering-loss multi-layer waveguides are to be fabricated, the annealing temperature should not be higher than 1100°C for STAE system, or higher than 1000°C for SGAE system.

Based on the above research, we can say that the SAE material system is more suitable as a bulk laser glass for solid state laser applications and SGAE and STAE material systems are more suitable for waveguide amplifier and laser applications. In addition, the potential photosensitivity of the SGAE system can perhaps find more applications in photonics circuits, although more experiments need to be conducted to assess the photosensitivity of the material.

4. CONCLUSION

We have prepared three kinds of Er-doped glasses, simply named as SAE, STAE, and SGAE by the sol-gel process. The fluorescence spectra and lifetimes of the powdered glasses with different constituent compositions for each system were studied and compared. The wavelength peak and bandwidth do not show any observable change among the three glass series as expected due to the intra-4f shell transition of erbium. However, even with the same processing procedures, all samples show different luminescence intensity and lifetime as a result of a different composition of the material. We believe that there are two reasons for the difference. One is the change in the efficiency of aluminum in dispersing the Er ion when different modifiers are co-doped together. The other is the difference in the hydrophilicity of the modifiers. Our experimental results have shown that in Ge or Ti co-doped glass, Ge or Ti modifier has more profound influence than aluminum on the materials' fluorescence property. Between Ge and Ti, the former has a lower hydrophilicity than the latter. We also investigated on the refractive index and crystallization properties of these materials and have found that while both Ge and Ti can significantly enhance the refractive index of the material, Ge co-doped films are easier to crystallize than Ti co-doped films.



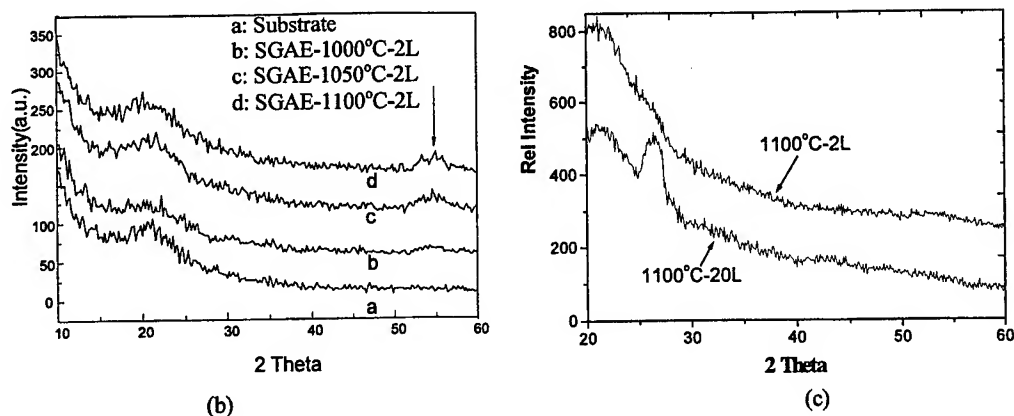


Fig. 4 XRD curves of the three material systems (a) SAE system, (b) SGAE system, (c) STAE system

REFERENCES

1. Jacobs, R. R., M. J. Weber, "Dependence of the $^4F_{3/2}$ to $^4I_{11/2}$ Induced Emission Cross Section for Nd^{3+} on Glass Composition." *IEEE J. Quantum Electronics*, (1976) Vol. QE-12, No.2, p102.
2. Aria, K., "Aluminium or phosphorus co-doping effects on the fluorescence and structural properties of neodymium-doped silica glass" *J. Appl. Phys.* 59(1986) 3430.
3. Y. Zhou, Y. L. Lam, S. S. Wang, H. L. Liu, C. H. Kam, and Y. C. Chan, "Fluorescence enhancement of Er^{3+} -doped sol-gel glass by aluminium codoping" *Appl. Phys. Lett.* 71(5) (1997) 587.
4. F. Wu, D. Machewirth, E. Snitzer and H. Sigel, *J. Mat. Res.* 9(1994) 2703.
5. W. Xu, S. Dai, L. M. Toth, G. D. Del Cul and J. R. Peterson, *J. Phys. Chem.* 99(1995) 4447.
6. S. Legaubin, E. Fertien, M. Douay, P. Bernage, P. Niay, H. Bayon and T. Georges, *Electron. Lett.* 27(1991) 1845.
7. T. Kitagawa, F. Bilodeau, B. Malo, St. Theriault, J. Alber, D. C. Johnson, K. O. Hill, K. Hattori and Y. Hibino, *Electron. Lett.* 30(1994) 131.
8. Q. Xiang, Y. Zhou, Y. L. Lam, Y. C. Chan and C. H. Kam, "Preparation and Characterization of Er-doped $SiO_2-TiO_2-Al_2O_3$ planar optical waveguide by Sol-gel Method", Photonics West '99, (3622-18)S4, 23 - 29 January 1999, San Jose, California, USA.
9. Q. Xiang, Y. Zhou, Y. L. Lam, Y. C. Chan, C. H. Kam, B. S. Ooi, H. X. Zhang, "Preparation and fluorescence properties of Sol-gel derived Er-doped $SiO_2-GeO_2-Al_2O_3$ Planar optical waveguides", Processings of CLEO/Pacific Rim'99, V4 p.1085-86, 30 Aug. - 3 Sep. 1999, Korea.
10. E. G. Bondarenko, E. I. Galant, S. G. Lunter, A. K. Przhnevskii, M. N. Tolstoi, *Sov. J. Opt. Technol.* 42 (1995) 283.

Preparation and properties of organically modified sol-gel silica/titania optical waveguides

Wenxiu Que*, Y. Zhou, Y. L. Lam, S. D. Cheng, Y. C. Chan, C. H. Kam, L. P. Zhao, S. Buddhudu

Photonics Research Group, School of Electrical & Electronic Engineering,
Nanyang Technological University, Nanyang Avenue, Singapore 639798, Singapore

ABSTRACT

Silica/titania optical waveguides have been prepared by the sol-gel technique using γ -Glycidoxypolytrimethoxysilane and tetrapropylorthotitanate as the starting materials. Scanning electron microscopy, atomic force microscopy, thermal gravimetric analysis, differential thermal analysis, and UV-Visible spectroscopy have been used to characterize the morphology, the optical and structural properties of the waveguide films. The waveguides are also characterized by measuring their refractive index, thickness, and propagation loss as a function of titanium content and thermal treatment. The obtained results show that after an annealing at 500°C or above, an inorganic silica/titania crack-free film could be obtained. The single layer spin-coated film has high transparency in the visible range and is more than 0.5 micron thick. The propagation loss of the waveguide films was also estimated by using the scattered-light measurement method and was found to be around 1.0 dB/cm at the wavelength of 632.8 nm.

Keywords: Sol-gel technique, Silica/titania, Optical waveguide, Optical properties

1. INTRODUCTION

The use of sol-gel process for the fabrication of optical waveguides has attracted greater attention, much of which has been focused on planar waveguides for use at visible wavelengths, where the requirements on performance and geometry are generally modest. Sol-gel integrated optics is also beginning to show potential photonics applications. For example, the sol-gel process makes use of low-cost materials and equipment, and is thus an interesting alternative for the fabrication of basic integrated optical circuits. With channel waveguides being the basic component of integrated optics, the development of its fabrication technology is hence essential to the realization of high-performance devices such as splitters, couplers, deflectors, and optical amplifiers.¹⁻³ Research on inorganic sol-gel derived materials has been carried out widely for a long time and such sol-gel materials as silica and titania have been investigated for optical applications.⁴ However, the heat treatment temperature is generally quite high (around 1000°C) and it is very difficult to produce a thick single layer of pure inorganic sol-gel film. The maximum thickness of a layer resulting from a single deposition is about 0.2 μm and thicker layers generally crack as a result of shrinkage at the drying stage. Of course, this limitation does not preclude the production of multilayer film in which each layer is spun on and dried before the next layer is deposited. But inhomogeneities, defects, and dusts, which will affect the optical properties of the final waveguide film, may be introduced between each layer. An attractive way to overcome these problems is to combine the properties of very different materials and produce molecular-scale composite materials via sol-gel processing. A typical example is the use of organically modified silane (ORMOSIL) precursors that can produce a relatively thick single coating layer.⁵⁻⁷ Another alternative developed recently is to incorporate organic molecules into the inorganic matrix using basically the same sol-gel technique.⁸⁻⁹ When organic groups are integrated in the glass, the shrinkage is low because the bulky organic components fill the pores between the inorganic oxide chains. In this work, we have investigated the preparation of sol-gel derived silica/titania optical waveguide films made from γ -Glycidoxypolytrimethoxysilane (GLYMO) and tetrapropylorthotitanate (TPOT). We have also studied the characteristics and properties of the waveguide films using scanning electron microscopy (SEM), atomic force microscopy (AFM), X-ray diffractometry (XRD), thermal gravimetric analysis (TGA), differential thermal analysis (DTA), and UV-visible spectroscopy (UV-VIS). The waveguides are also characterized by measuring their refractive index, thickness, and propagation loss as a function of titanium content and thermal treatment history.

* Correspondence: Email: ewxque@ntu.edu.sg; Telephone: (65)7905642; Fax: (65)7912687

2. EXPERIMENTS

One mole of GLYMO was mixed with 4 moles of ethanol and 4 moles of de-ionized water, and the solution was stirred for about 30 minutes. Tetrapropyl orthotitanate [$\text{Ti}(\text{OC}_3\text{H}_7)_4$] was added to acetylacetone [$\text{CH}_3\text{COCH}_2\text{COCH}_3$] at a molar ratio of 1:4 under a nitrogen environment and the solution was agitated for homogenization. The two solutions were then mixed with a ratio depending on the desired titanium content in the final sol-gel film. In our case, the studied molar ratio of GLYMO:Ti was 0.8: 0.2, 0.7: 0.3, 0.6: 0.4, and 0.5: 0.5. The final mixture was stirred for 30 h at room temperature. The experimental procedure is schematically shown in Fig. 1.

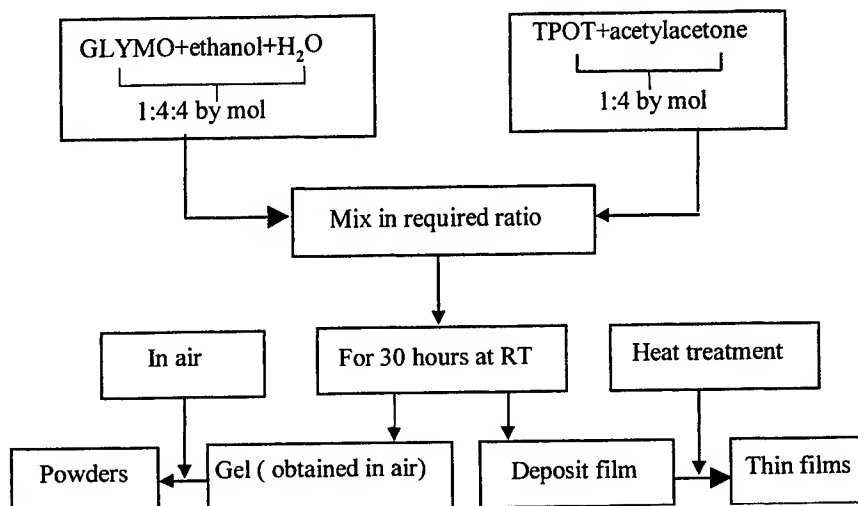


Figure 1 Flow chart of the synthesis of composite films and powders by a sol-gel process

It should be noted that cleaning of the substrate is important for proper adhesion of the films. All the substrates, including silicon (Si), silica on silicon, and microscope glass slides (Glass), were ultrasonically cleaned in acetone and ethanol respectively, rinsed with de-ionized water and dried with pure nitrogen. After one sol-gel layer was spun in a clean room environment (class 100) on the substrate at 4000 rpm for 35 seconds, the coated film was heated at 100, 200, 300, 400, 500°C or higher for about 10 minutes to study the properties of the films. It was found that a dense, stable and transparent silica/titania film could be obtained after a heat treatment at 500°C. A film thickness of more than 0.5 μm could be easily obtained by a single-coating process. When such a film was deposited on a glass slide or a silica-on-silicon substrate, light wave guiding was easily demonstrated. In the following sections, we will present our study on the structural and optical properties of the optical waveguide films.

3. CHARACTERIZATION OF FILMS

The sol-gel films were characterized using SEM, AFM, XRD, TGA, DTA, and UV-VIS spectroscopy. The morphology of the film was examined under a SEM (JSM-5600 LV) and an AFM (Digital Instruments, Nanoscope IIIa) using the tapping mode. XRD was carried out for the waveguide films using a Rigaku Rint 2000 Series X-ray diffractometer equipped with a thin film attachment unit. The X-ray radiation source used was Cu K α , operated at 40 kV, 35 mA and the scanning speed was 4°/min at a step of 0.02°. TGA and DTA were conducted using a Perkin Elmer 7 Series thermal analysis system for the material powders obtained from solutions at a heating rate 2°C/min. The UV-visible transmission spectra in the range of 250-800 nm were examined with a Perkin Elmer Lambda 16 UV/VIS Spectrometer for those films deposited on microscope glass slides. The thickness and refractive index of the films were measured with a Filmetric F-20 Thin-Film Measurement System. The propagation loss of the waveguide films with different titanium content was also estimated using the scattered-light measurement method and for the film with low titanium content the loss value was found to be around 1.0 dB/cm at the wavelength of 632.8 nm.

3.1 Results of XRD

XRD results of the waveguide films heated at different temperatures and with different titanium contents showed no crystalline phase and the films were thus all amorphous.

3.2 Results and discussion of SEM and AFM

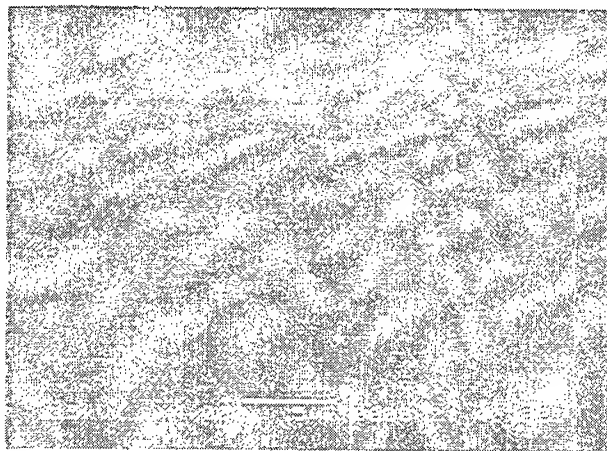


Figure 2 SEM micrograph of the film heated at 500°C

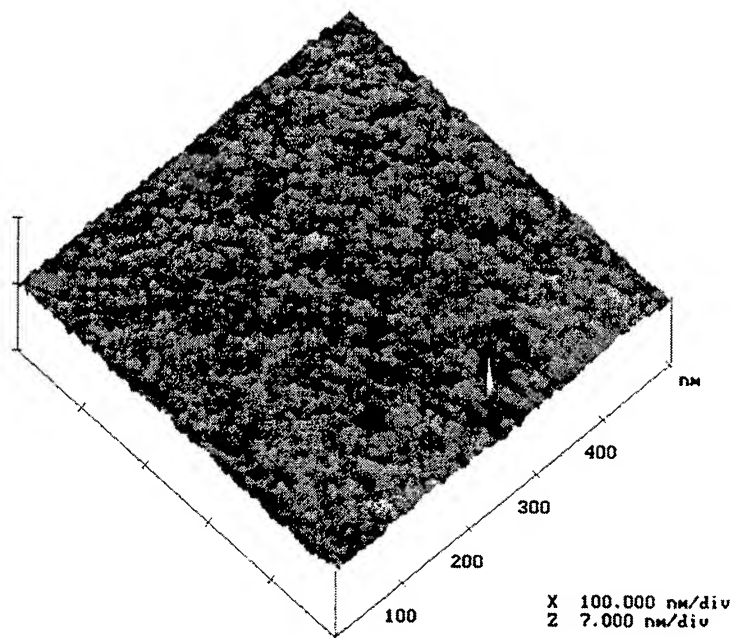


Figure 3 AFM image of the film heated at 500°C

Figure 2 shows the SEM micrograph of the waveguide film heat-treated at 500°C. The molar ratio of GLYMO:TiO₂ was fixed at 0.8:0.2 and the film was spin-coated on a pure Si substrate by a single coating process. It can be seen from surface appearance of the film in Fig.2 that the film is colorless, transparent, and crack-free. It is obvious that the film shows an amorphous structure and this confirms further the XRD result. In order to clearly examine the surface morphology of the waveguide film, an AFM image of the film was measured and is shown in Figure 3. It can be observed from Fig.3 that the film has a dense and uniform morphology and relatively small surface roughness. The root mean square (RMS) roughness of the film is about 0.2 nm. Obviously, it is sufficiently small for optical waveguide application. However, for the film

baked at 300°C and 400°C, some pores can be observed. We suspect that these pores are due to the incomplete combustion and decomposition of the organic compounds. To understand better about the heat treatment process, TGA and DTA were used to characterize the thermal properties of the material.

3.3 Results and discussion of TGA and DTA

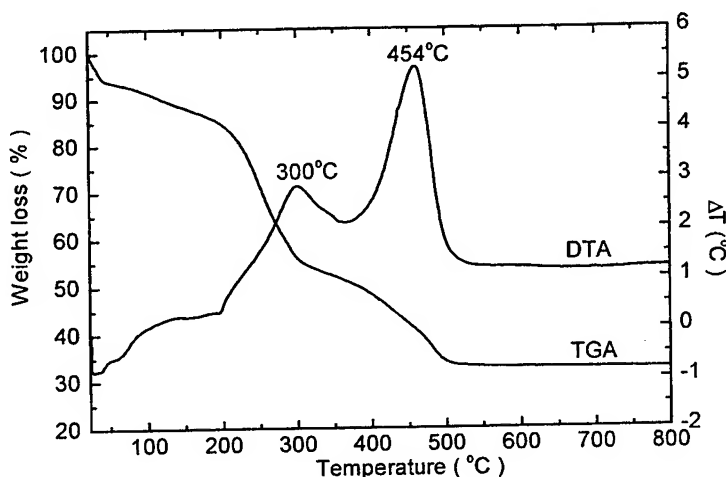


Figure 4 TGA/DTA curves of the gel obtained from the solution as used for Fig.2

The thermal analysis was done for the gel obtained by drying the coating solution poured into petri dishes at room temperature for about one week. Samples of 30-40mg crushed gel powder are put into an Au crucible for TGA or a Pt crucible for DTA, respectively. The heating rate was 2°C/min in air. The recorded temperature range was from room temperature to 800°C. Figure 4 shows the TGA/DTA curves of the gel powder. The exothermic peaks are observed at 300 and 454°C. The weight loss occurs at three stages, namely, below 200°C, between 200 and 310°C, and from 310 to 480°C. Evidently, the DTA curve corresponds to that of the TGA, i.e., the two exothermic peaks are just in the range of the significant weight loss. Below 200°C, the weight loss is considered to be due to the evaporation of water and the volatilization of the remnant of organic solvents. Between 200 and 310°C, the weight loss is attributed to the combustion of organic compounds. Between 310 and 480°C, the weight losses are probably ascribed to the further combustion of organic compounds. Therefore, the two exothermic peaks at 300 and 454°C are due to the burning of organic compounds. Evidently, these results can be used to explain the appearance of the pores in AFM results where the films were heated at 300 and 400°C. Since there is basically no further weight loss after 500°C, it can thus be inferred that a heat treatment at 500°C or above is able to produce a dense inorganic silica/titania waveguide film.

3.4 Results and discussion of UV-VIS transmittance spectra

Figure 5 shows the optical transmittance spectra of the films baked at different temperatures. The molar ratio of GLYMO:TiO₂ was fixed at 0.8:0.2 and the film was spin-coated on a microscope glass slide by a single coating process. It can be seen that the films baked at 100 and 200°C have high transmittance. However, the films baked at 300 and 400°C have a significantly larger absorption up to 600 nm, and noticeable discoloration is actually observed. However, the film baked at 500°C has a much higher transmittance than those baked at 300 and 400°C and no discoloration was observed. Based on the result obtained by TGA and AFM as mentioned before, we can explain this behavior as follows. The films baked at 300 and 400°C are porous due to the incomplete decomposition of the organic compounds. As a result, in addition to the absorption because of the remaining acetylacetate complex, a relatively large degree of scattering of light could also occur from the pores caused by the incomplete decomposition of the organic compounds. When the baking temperature was increased to 500°C, the organic compounds would be completely decomposed and a purely inorganic dense film was obtained. As a result, both absorption and scattering caused by the relatively large pores are substantially suppressed. It can thus be concluded that with our present recipe, a heat-treatment temperature of 500°C is required to attain a sol-gel silica/titania waveguide thin film with minimum macro-pores, low absorption, and high transparency in the visible range.

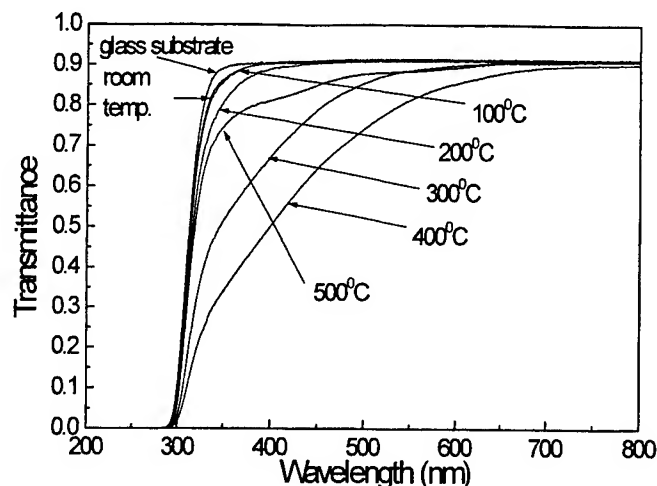


Figure 5 The optical transmittance spectra of the films baked at different temperatures for 10 minutes

4. OPTICAL PROPERTIES OF WAVEGUIDES

Figure 6 shows the change of the thickness and refractive index of the films with Ti molar fraction. The films were spun on Si substrates and baked at 500°C for 10 minutes. It is observed that the film becomes thinner and its refractive index increases as the Ti content rises. It can also be clearly seen that within the studied Ti content range, the refractive index of the film can be varied from 1.58 to 1.69 at the wavelength of 633 nm and the variation is basically proportional to the molar concentration of Ti. The dependence of the refractive index on the molar concentration of Ti can be obtained based on the experimental data in Figure 6 and a linear fitting. This linear dependence was found to be

$$n(X) = 1.51 + 0.36X, \quad (1)$$

where X is the Ti molar fraction. In fact, the above dependence of the refractive index on the Ti content is similar to that reported by Sorek and Weisfeld [9]. However, the increase rate with the Ti content in the refractive index of our films is higher as compared to Sorek and Weisfeld's films and we believe that this could be due to the different preparation processes of our precursors and films. As for the film thickness, Figure 6 shows that its dependence on Ti content is approximately linear.

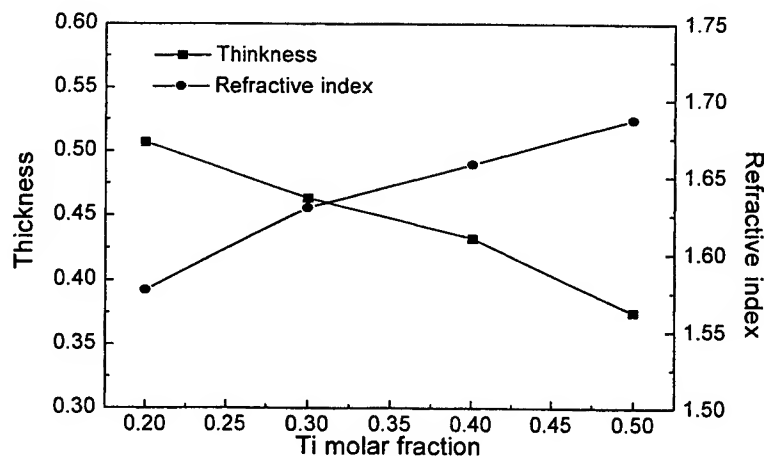


Figure 6 Dependence of the thickness and refractive index of the films baked at 500°C on Ti content

In order to further characterize the waveguide properties of the films, a four-layer-film with a molar ratio of GLYMO to $\text{TiO}_2 = 0.8:0.2$ was deposited on a silica-on-silicon substrate to enable optical waveguiding. The waveguide film is found to have a thickness of about 2.0 μm . The propagation loss of the planar waveguide was evaluated by the scattered-light method.¹⁰⁻¹¹ Figure 7 shows the scattered-light power as a function of propagation length. The scattered light power was measured at every 2 mm apart. A total of five or above separate points was taken. The mean loss is typically about 1.0 dB/cm at 633 nm. It is obvious that the loss of waveguide prepared using the present processing conditions is relatively high as compared to those reported previously for $\text{SiO}_2\text{-TiO}_2$ planar waveguide.⁶ In addition, it is noted that those films with a higher titanium content have a higher loss. In general, defects such as dust points can be observed in the waveguide film and these will certainly scatter light to a greater extent than a defect-free sol-gel medium. Obviously, the loss value is expected to improve if a dust/impurity-free situation can be ensured. It should be mentioned that since a precise loss measurement system was not available in our laboratory, the precise loss value of our waveguides could not be obtained.

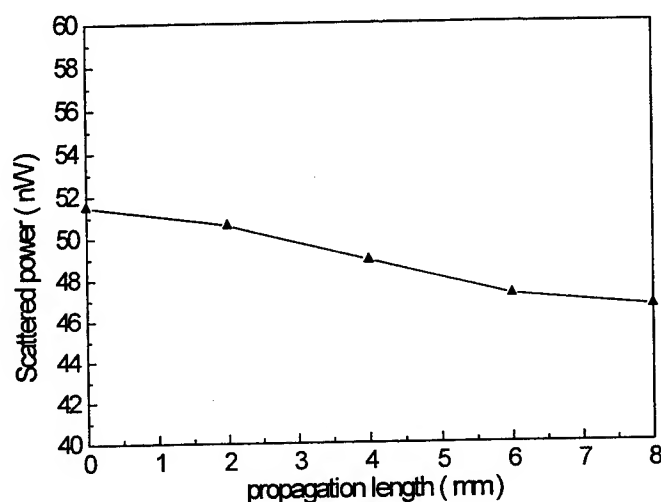


Figure 7 Scattered-light power as a function of propagation length

5. CONCLUSIONS

We have successfully prepared an inorganic silica-titania crack-free waveguide film by the sol-gel technique using GLYMO and TOPT as the starting materials. We have also studied the structure and the optical properties of the waveguiding films. The single layer spin-coated film has high transparency in the visible range and is more than 0.5 micron thick. The propagation loss of a four-layer waveguide film has also been estimated using the scattered-light measurement method and is found to be around 1.0 dB/cm at the wavelength of 632.8 nm. It has also been observed that the film becomes thinner and its refractive index increases as the Ti content rises. Within the studied Ti content range, the refractive index of the film can be varied from 1.58 to 1.69 at the wavelength of 633 nm.

REFERENCES

1. X. M. Du, T. Touam, L. Degachi, J. L. Guibault, M. P. Andrews, and S. I. Najafi, "Sol-gel waveguide fabrication parameters: an experimental investigation," *Opt. Eng.* **37**(4), pp. 1104-1104, 1998.
2. S. Holmes, R. R. A. Syms, Ming Li, and Mino Green, "Fabrication of buried channel waveguides on silicon substrates using spin-on glass," *Appl. Opt.* **32**(25), pp. 4916-4921, 1993.
3. Y. Li, J. Chisham, M. P. Andrews, S. I. Najafi, J. D. Mackenzie, and N. Peyghambarian, "Sol-gel integrated optical coupler by ultraviolet light imprinting," *Elect. Lett.* **31**(4), pp. 271-272, 1995.
4. M. Bahtal, J. Mugnier, L. Lou, and J. Seruhgetti, In *Sol-Gel Optics II*, J. D. Mackensie, ed., *Proc. Soc. Photo-Opt. Instrum. Eng.*, **1758**, pp. 173-179, 1992.
5. P. Innocenzi, G. Brusatin, A. Martucci, and K. Urabr, "Microstructural characterization of gold-doped silica-titania sol-gel films," *Thin Solid Films* **279**, pp. 23-28, 1996.

6. G. Brusatin, M. Guglielmi, P. Innocenzi, A. Martucci, G. Battaglin, S. Pelli, and G. Righini, "Microstructural and optical properties of sol-gel silica-titania waveguides," *J. Non-Cryst. Solids* **220**, pp. 202-209, 1997.
7. S. Motakef, J. M. Boulton, and D. R. Uhlmann, "Organic-inorganic optical materials," *Opt. Lett.* **19(15)**, pp. 1125-1127, 1994.
8. Y. Sorek, M. Zevin, R. Reisfeld, T. Hurvits, and S. Ruschin, "Zirconia and Zirconia-ORMOSIL planar waveguides prepared at room temperature," *Chem. Mater.* **9**, pp. 670-676, 1997.
9. Y. Sorek, R. Reisfeld, I. Finkelstein, and S. Ruschin, "Sol-gel glass waveguides prepared at low temperature," *Appl. Phys. Lett.* **63(24)**, pp. 3256-3258, 1993.
10. Y. Okamura, A. Miki, and S. Yamamoto, "Observation of wave propagation in integrated optical circuits," *Appl. Opt.* **25(19)**, pp. 3405-3408, 1986.
11. K. H. Haegele and R. Ulrich, "Pyroelectric loss measurement in $\text{LiNbO}_3\text{:Ti}$ guides," *Opt. Lett.* **4(2)**, pp. 60-62, 1979.

Dependence of cracking behavior of sol-gel films on symmetries of substrates

S.D. Cheng ^{a*}, Y. Zhou ^a, C.H. Kam ^a, W.X. Que ^a, Y.L. Lam ^a, Y.C. Chan ^a, and W.S. Gan ^b

^a Photonics Research Group, School of Electrical and Electronic Engineering
Nanyang Technological University, Nanyang Avenue, S639798, Singapore

^b Acoustical Technologies Singapore Pte. Ltd., 209-212 Innovation Center
Nanyang Avenue, S639798, Singapore

ABSTRACT

The cracking of sol-gel derived films on Si(100), Si(111), and glass substrates has been studied experimentally using optical microscopy, scanning electron microscopy and optical scattering method, as well as theoretically using the static method and the dynamic method. The experimental observations show that the primary cracking directions of the sol-gel derived film depend strongly on the symmetry of the substrate. As all the studied substrates have a uniform biaxial elastic modulus, the static method cannot explain such cracking behavior. However, the most probable directions of the primary cracks can be determined by considering the anisotropy of the longitudinal and the transversal elastic waves, and these directions are in good agreement with the experimental observations.

Keywords: Sol-gel film, Anisotropic crack, Optical scattering method, Biaxial Young's modulus, Elastic waves.

1. INTRODUCTION

One of the most common failures of films prepared by the sol-gel method, as well as by other techniques, is the cracking of the film during heat treatment ¹. In the heating-up and cooling-down processes, the sol-gel film becomes dense and because of the difference in the thermal expansion coefficients between the film and the substrate, a biaxial tensile stress will develop in the film ². When this stress reaches a critical point, cracks are generated. The directions of the crack are generally dependent on the substrate used other than the film itself. Some typical cracking behaviors and their dependence on the substrate have been observed by several authors, including thick silica-titania films on Si(100) ³, PLZT films on Si(111) ⁴, and LiNbO₃ films on MgO buffered GaAs(111) ⁵. However, there is presently very little satisfactory theoretical explanation for these phenomena.

In this paper, the cracking behavior of PbTiO₃ films on Si(100), Si(111) and glass are studied both experimentally and theoretically. The experimental studies are carried out using optical microscopy, scanning electron microscopy (SEM) and optical scattering method. The results show that the primary cracks of the film have a four-fold symmetry on Si(100), a six-fold symmetry on Si(111), and an isotropic symmetry on glass. Our theoretical study shows that the phenomena cannot be explained by the static mechanical biaxial stress model ¹. We have thus developed a dynamic model, which takes into account the propagation of elastic waves, and have introduced an anisotropic factor to explain the behavior. The dynamic analysis result reveals that the directions of the crack depend on the anisotropy of the acoustic velocities of the substrates and this result agrees very well with experimental observations.

2. EXPERIMENTS AND OBSERVATIONS

As has been reported in our previous paper ⁶, the solution for sol-gel PbTiO₃ is prepared by mixing lead acetic trihydrate (Pb(CH₃COO)₂•3H₂O) and tetrapropyl orthotitanate (TPOT) and the films are deposited by multiple spin coating. When the film thickness reaches about 600nm, cracks develop in the film and they can be observed with the naked eye as the samples are cooled down to room temperature.

These cracks are examined under an optical microscope and Fig.1(a) illustrates a typical crack pattern of a PbTiO₃ film on glass. The stress is tensile as can be identified by the mosaic- pattern, the scrolling of the film and the peeling-off of the film at the edges. Figures 1 (b), (c) and (d) show the microscopic images of cracks on Si(100), Si(111) and glass, respectively.

* Corresponding author, Tel: +65-7905461; Fax: +65-7933318; E-mail: P142977657@ntu.edu.sg.

As we can see, for films on Si(100) substrate (Fig. 1(b)), the cracks are formed in two orthogonal directions, which are perpendicular to the [010] and [001] directions of the substrate respectively. In the case of Si(111) substrate (Fig. 1(c)), the cracks are in three dominant directions which are perpendicular to the [110], [101], and [011] directions, respectively. For the glass substrate (Fig. 1(d)), the cracks are randomly oriented and no preferred directions can be identified. Bear in mind that for a large stress in one direction (say, x-axis), the cracks caused by the stress tend to be in the orthogonal direction (i.e., y-axis). Therefore, for Si(100), the largest stress appears in the [010] and [001] directions, while for Si(111), it is in the [110], [101], and [011] directions.

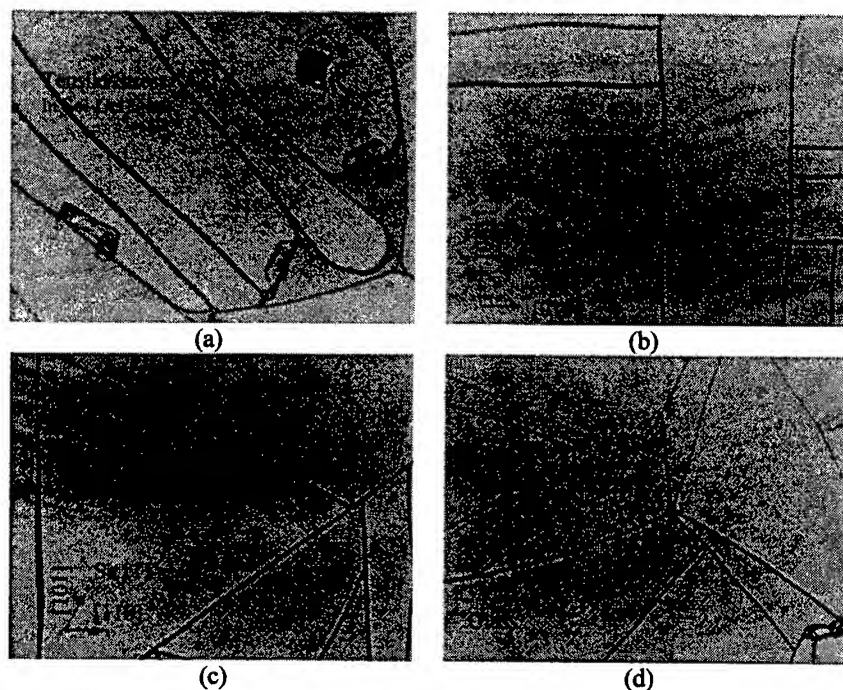


Fig. 1 Tensile stress in a sol-gel derived film causes the peeling of the film from a glass substrate (a) and, cracking of film on different substrates of (b) Si(100), (c) Si(111), and (d) glass.

The crack patterns are also examined under SEM and Fig. 2 shows the SEM image of a crack pattern on a Si(111) substrate. As can be seen, in addition to the primary crack, a secondary crack also occurs. The former is almost in a straight line whereas the latter lies in an irregular way. In fact, for all of the SEM examined samples, no preferred directions can be found for the secondary cracks and this implies that the formation of the secondary cracks is random rather than governed by the symmetry of the substrate. In this paper, we focus our study only on the primary cracks.

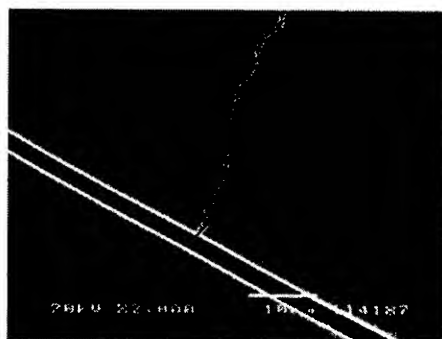


Fig. 2 The primary crack is in a straight line and secondary crack of the film has an irregular direction.

To further investigate the features of the crack patterns, an optical scattering method is employed and the experimental setup is shown in Fig. 3. A laser beam is directed onto the sample, and the scattered light pattern is captured on a screen. It is well

known that in the perpendicular direction of a crack, the intensity of the scattered light is strong and in the parallel direction of a crack, it is weak⁷. The scattered pattern can thus statistically reveal the crack directions.

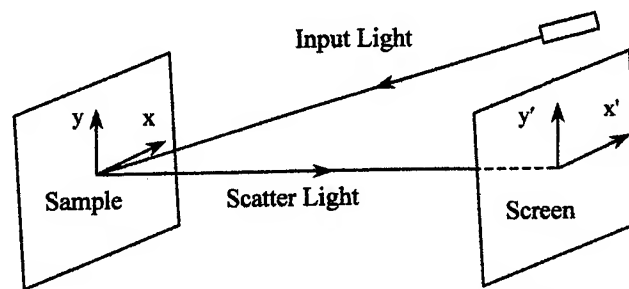


Fig. 3 Experimental setup of the optical scattering method.

The scattered patterns of the samples are shown in Fig. 4. From these images, we can clearly see the relation between the crack directions and the symmetries of the substrates. There is a four-fold symmetry for Si(100), a six-fold symmetry for Si(111), and an isotropic symmetry for glass substrate.

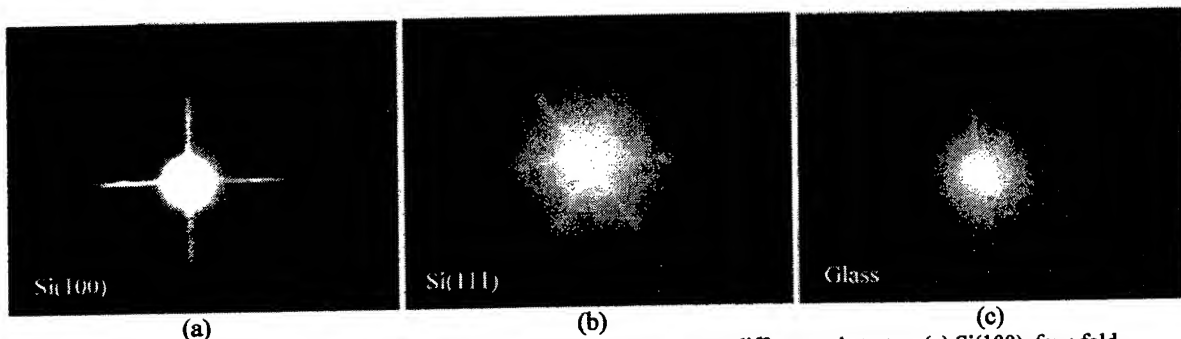


Fig. 4 The optical scattering results show different crack symmetry on different substrates, (a) Si(100), four-fold (b) Si(111), six-fold, and (c) glass, isotropic.

3. THEORETICAL CONSIDERATION

3.1 Static Model

It is well known that for a biaxial stress, the stress in the film will be balanced with the stress caused by the curvature of the substrate, and it can be expressed as¹,

$$\sigma_f = -\left(\frac{E}{1-\nu}\right)_s \frac{T_s^2}{6RT_f^2} = -E' \frac{T_s^2}{6RT_f^2}, \quad E' = \left(\frac{E}{1-\nu}\right)_s \quad (1)$$

where σ_f is the stress in the film, E is the Young's modulus, ν is Poisson ratio of the substrate, T_s and T_f are the thickness of the substrate and the film respectively, and R is the radius of curvature of the substrate. E' is known as the biaxial elastic modulus. In cubic crystals, both E and ν are anisotropic. The expressions for E and ν as given by Brantley are⁸,

$$\frac{1}{E} = S_{11} - (2S_{11} - S_{12} - \frac{1}{2}S_{44})(l_1^2 l_2^2 + l_2^2 l_3^2 + l_3^2 l_1^2) \quad (2)$$

$$\nu = -\frac{S_{12} + (S_{11} - S_{12} - \frac{1}{2}S_{44})(l_1^2 m_1^2 + l_2^2 m_2^2 + l_3^2 m_3^2)}{S_{11} - (2S_{11} - S_{12} - \frac{1}{2}S_{44})(l_1^2 l_2^2 + l_2^2 l_3^2 + l_3^2 l_1^2)}$$

where S_{ij} is the elastic compliance, l_i and m_i are the direction cosines of \mathbf{l} and \mathbf{m} respectively, with \mathbf{l} being the longitudinal stress axis direction vector and \mathbf{m} being the direction vector orthogonal to \mathbf{l} .

Considering that our crack formation is observed when the films are cooled down close to room temperature, we have used the parameters of silicon at room temperature for our calculation. However, the reasoning is still valid for other temperatures provided that the anisotropy η , as will be defined soon, is greater than one, although the relative values will be

different. At room temperature, the stiffness coefficients of silicon⁹ are $C_{11} = 1.657 \times 10^{11} \text{ N/m}^2$, $C_{22} = 0.639 \times 10^{11} \text{ N/m}^2$, and $C_{44} = 0.799 \times 10^{11} \text{ N/m}^2$, and thus the elastic compliance coefficients are $S_{11} = 0.768 \times 10^{-11} \text{ m}^2/\text{N}$, $S_{22} = -0.214 \times 10^{-11} \text{ m}^2/\text{N}$, and $S_{44} = 1.251 \times 10^{-11} \text{ m}^2/\text{N}$. The anisotropy is given by $\eta = 2C_{44}/(C_{11} - C_{22})$, and for silicon, $\eta = 1.57$. Since when $\eta = 1$, the media is considered isotropic, therefore, in the calculations for the glass substrate, we can only set $\eta = 1$.

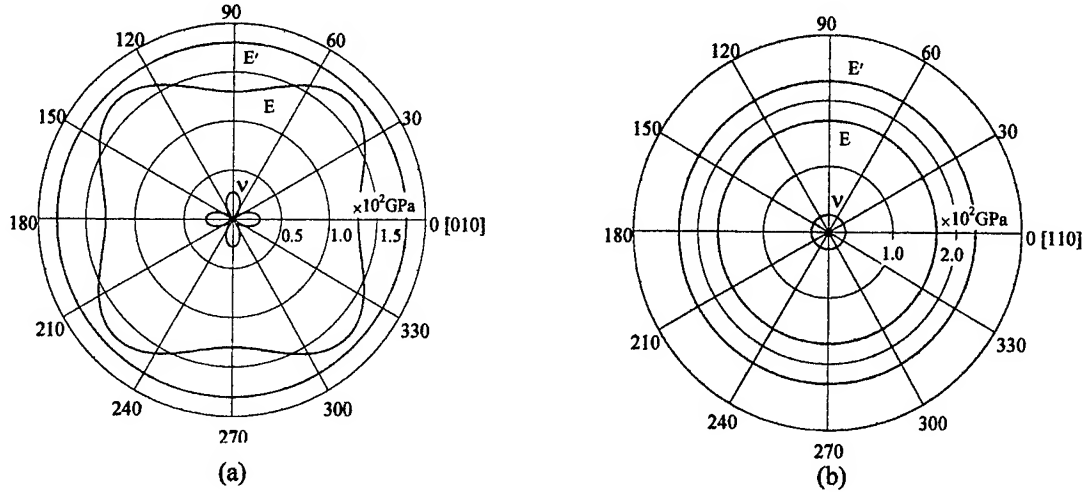


Fig. 5 Young's modulus, E , Poisson ratio, ν , and biaxial Young's modulus, E' , of (a) Si(100), and (b) Si(111).

By substituting the above values into Equations (2) and (1), E , ν , and E' values for all the directions in the substrate plane can be calculated and the results are shown Fig. 5. Figure 5(a) is for the case of Si(100) substrate. For this substrate, the angular axis starts from the [010] direction and, as can be seen, both E and ν vary with the polar angle. The smallest value for E appears in the [010] and [001] directions, but in these directions, ν has the largest value. The resultant E' is actually found to be isotropic in all directions with a value of 181 GPa. For Si(111) (Fig. 5(b)), the angular axis starts from the [110] direction, and E , ν and thus E' are all isotropic with the value of E' equal to 230 GPa. These calculated E' values are in good agreement with those given in Ref. [1]. For the case of glass substrate, it is well known that E , ν and E' are all isotropic in all directions and the calculated results are thus not shown here.

Referring to Equation (1), we can find that the stress in the film, σ_f , is dependent only on E' and it is thus isotropic for all the samples if the static model is used. Obviously, the static model cannot explain the direction-related-cracking behavior for cases of the Si(100) and Si(111) substrates.

3.2 Dynamic Model

Considering that the velocities of the elastic wave describe the dynamic property of a material, we suspect that the anisotropy of the elastic waves is the reason for the anisotropic cracking behavior because an elastic wave can help the dissipation of stress in the films in its vibrational direction. For a longitudinal elastic wave, the vibration is along the wave propagation direction; accordingly, longitudinal wave of high speed is favorable to the release of stress in the wave propagation direction. For a transversal elastic wave, the vibration is orthogonal to the wave propagation direction and therefore a fast propagating transversal wave is favorable to the release of film stress in its vibration direction.

Based on Cristoffel Equation¹⁰, the elastic wave velocities for different directions in the plane of a substrate can be calculated. Figure 6 shows the calculated results for the case of Si(100) and Si(111), where V_L is the velocity of the longitudinal wave and V_{T1} and V_{T2} are the velocities of the two transversal elastic waves. It should be pointed that for cubic crystals,

$$V_L^2 + V_{T1}^2 + V_{T2}^2 = \frac{C_{11} + 2C_{44}}{\rho} = C_0 \quad (3)$$

where ρ is the density of silicon which has a value of $\rho = 2328 \text{ kg/m}^3$. The above equation tells us that the summation of the squares of the velocities of longitudinal and transversal waves is a constant for all directions. For silicon, $C_0 = 1.40 \times 10^8 \text{ km}^2/\text{s}^2$.

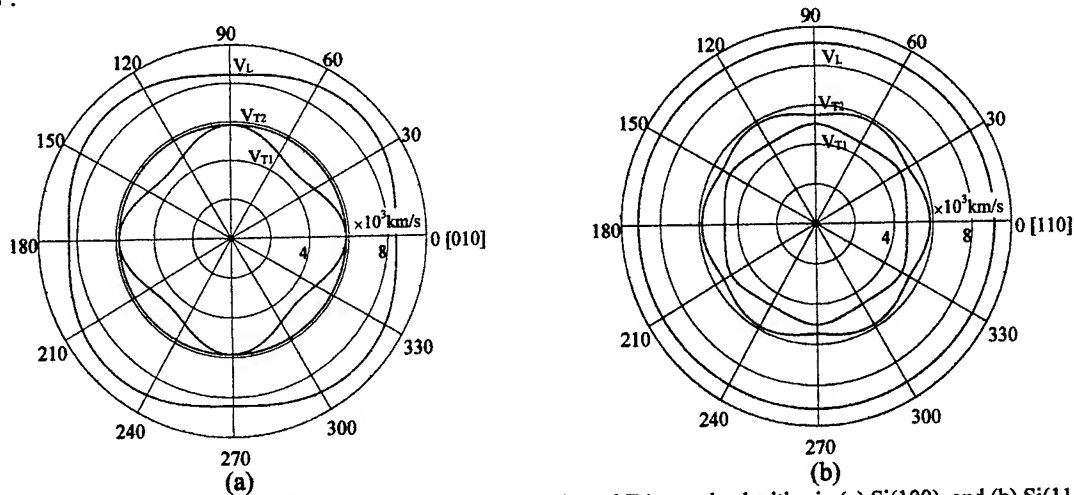


Fig. 6 Anisotropic longitudinal(L) and transversal (T_1 , and T_2) sound velocities in (a) Si(100), and (b) Si(111).

Comparing Figs. 1, 4 and 6, we can see that the cracks are always perpendicular to the directions with low V_L value and high V_{T1} and V_{T2} values. Based on these observations and with the help of Equation (3), we can define an anisotropic factor (A.F.),

$$\text{A.F.} = \frac{V_{T1}^2 + V_{T2}^2}{V_L^2} = \frac{C_0}{V_L^2} - 1 \quad (4)$$

The calculated anisotropic factors for Si(100), Si(111) and glass are shown in Fig. 7, where, the angular axis starts from the [010] direction, the [110] direction and an arbitrary direction for Si(100), Si(111) and glass, respectively. From this figure, it can be seen that the experimentally observed cracks in the films on different substrates are all perpendicular to the directions that have the highest anisotropic factor values. As mentioned before, for a large stress in one direction, the cracks caused by the stress tend to be in its orthogonal direction. The experimental observation thus implies that in a direction with highest A.F. value, the stress will be the largest.

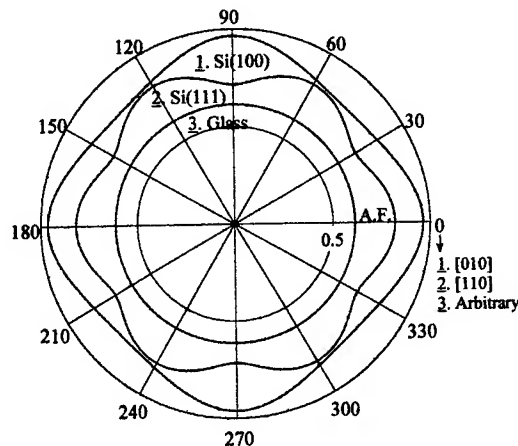


Fig. 7 Anisotropic factor for different substrates of Si(100), Si(111) and glass.

This is understandable because in a direction with low V_L value (i.e., high A.F.), the stress tends to dissipate slowly and the stress will thus be high in this direction. On the contrary, in a direction with high V_L (i.e., low A.F.), the stress in the film can dissipate fast and hence the stress will be low in that direction. As we can see from Fig.7, for Si(100), the largest stress

is in the [010] and [001] directions, while for Si(111), it is in the [110], [101], and [011] directions. For a glass substrate, the A.F. value is the same in all directions, and thus the stress is the same in all directions. These are all in good agreement with the experimental observations.

From Fig. 7, we can also see that, for Si(100), the maximum and minimum values of A.F. are 0.96 and 0.67 respectively and the relative difference is 26%; whereas for Si(111), the maximum and the minimum values of A.F. are 0.67 and 0.66 respectively and the relative difference is only 1.5%. It is thus expected that cracks are more deterministic on Si(100) than on Si(111). This is indeed the case as can be seen in Fig 4 (a) and (b), where the scattered light pattern of the film on Si(100) has a much sharper and stronger intensity distribution than that of the film on Si(111), although the films are prepared under the same condition.

Figure 8(a) shows an interesting sine-wave-like cracking phenomenon of a film at the edge of Si(100) substrate. It is confined by the thickness of the film (narrow part of the crack) and dominated by the cracking directions of [100] and [010] of Si(100) (wide part of the crack). The thickness of the film is shown in Fig. 8(b), which is obtained by a surface profiler.

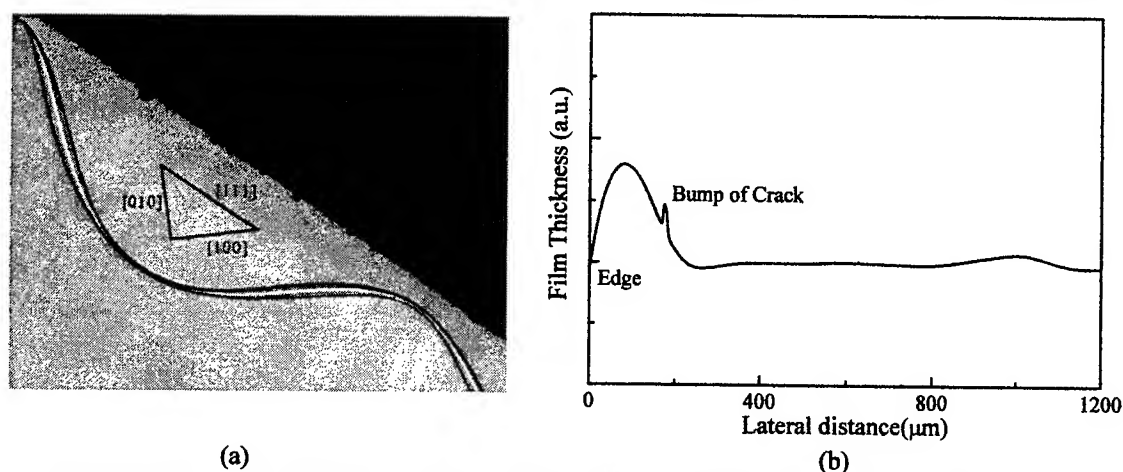


Fig. 8 The sine wave like cracking phenomenon of film at the edge of Si(100) substrate (a), and the relative thickness of the film obtained by a surface profiler (b).

4. CONCLUSION

The cracking behavior of sol-gel derived PbTiO_3 films on different substrates of Si(100), Si(111) and glass have been studied both experimentally and theoretically. The symmetrical dependence of the crack directions on the substrates is observed. Such cracking behavior cannot be explained using the static model but it can be explained with our dynamic model by considering the effect of anisotropic elastic waves in the substrate. The dynamic theoretical analysis agrees very well with the experimental observations. We believe that the model is also applicable to other substrates of cubic symmetry with an anisotropy of $\eta > 1$, such as GaAs, MgO and InP, etc.

ACKNOWLEDGEMENTS

Thanks are giving to Dr. Z. Sun, and Mr. J. Liu for their helpful discussions.

REFERENCES

1. D.L. Smith, *Thin Film Deposition, Principle and Practice*, McGraw-Hill, Inc., New York, 1995, pp. 185-197.
2. C.J. Brinker and G.W. Scherer, *Sol-Gel Science, the Physics and Chemistry of Sol-Gel Processing*, Academic Press, Inc., Boston, 1990.
3. R.R.A. Syms, A.S. Holmes, "Deposition of thick silica-titania sol-gel films on Si substrates", *J. Non-Cryst. Solids*, **170**, pp. 223-233, 1994.
4. P.F. Baude, C.Ye, T. Tamagawa, D.L. Polla, "Fabrication of sol-gel derived ferroelectric PLZT(9/65/35) optical waveguide", *Mat. Res. Soc. Symp. Proc.*, **243**, pp. 275-280, 1992.

5. D.K. Fork, J.J. Kingston, G.B. Anderson, E.J. Tarsa, and J.S. Speck, "Progress toward viable epitaxial oxide ferroelectric waveguide heterostructures on GaAs", *Mat. Res. Soc. Symp. Proc.*, **310**, pp. 113-118, 1993.
6. S.D. Cheng, C.H. Kam, Y. Zhou, Y.L. Lam, and Y.C. Chan, "Sol-gel derived nanocrystalline films of PbTiO_3 for optical waveguide applications", *Materials Research Society (MRS) Symposium*, April 13-17, San Francisco, USA, 1998.
7. J.C. Stover, *Optical Scattering, Measurement and Analysis*, McGraw-Hill, New York, 1990.
8. V. Swaminathan, and A.T. Macrander, *Materials Aspects of GaAs and InP Based Structures*, Prentice Hall, Englewood Cliffs, 1991.
9. G.W. Farnell, in: *Physical Acoustics, Principles and Methods*, W.P. Mason and R.N. Thurston ed., Vol. VI, Academic Press, New York, 1970.
10. J.F. Rosenbaum, *Bulk Acoustic Wave Theory and Devices*, Artech House, Boston, 1988.

Characteristics of sol-gel derived (Pb,Ca)TiO₃ pyroelectric thin films

Chih-Ming Wang, Ying-Chung Chen*, Yao-Te Huang and Ming-Cheng Kao

Department of Electrical Engineering, National Sun Yat-Sen University,

Kaohsiung, Taiwan, R.O.C.

ABSTRACT

Polycrystalline thin films of Ca-modified lead titanate (PCT) were deposited on Pt/SiO₂/Si substrates using a diol-based sol-gel process. Calcium acetylacetonate hydrate was adopted as a starting material instead of calcium acetate or calcium nitrate tetra-hydrate used in general. By changing the Ca content (5~35 mol%) and heating temperature (500~800 °C), the influences of various processing parameters on the characteristics of thin films are studied. With the increase of Ca content, the relative dielectric constant (ϵ_r) of PCT thin film increases from 43 up to 70 at the heating temperature of 700°C. It was found that the coercive field (E_c) and the remanent polarization (P_r) decreased, but the pyroelectric coefficient (γ) increased with an increase of Ca content. The results show that PCT thin film exhibits the largest figures of merit for the voltage responsivity and the specific detectivity at heating temperature of 700°C and Ca content of 25 mol%.

Keywords: sol-gel, PCT, thin film, relative dielectric constant, pyroelectric coefficient

1. INTRODUCTION

In recent years, ferroelectric thin films based on lead titanate composition have been used as piezoelectric transducers, memory devices and pyroelectric infrared (IR) detectors.¹⁻⁶ Several modifications of these materials have been researched with the purpose of obtaining improved properties and make them potentially useful in applications.⁷⁻¹⁰ For the ferroelectric characterization, thin films of calcium modified lead titanate, Pb_{1-x}Ca_xTiO₃ (abbreviated to PCT), have attracted some interest because the substitution of Ca²⁺ for Pb²⁺ reduces the c/a ratio of the parent PbTiO₃ unit cell and facilitates ferroelectric switching.¹¹⁻¹⁴ The sol-gel method is effective for preparing thin films and has several advantages, such as excellent control of stoichiometry, compositional modification with liquid mixed level homogeneity, nonvacuum and low processing temperature, film uniformity over large areas, and low cost of equipment. Until now the most widely used starting reagents for PCT syntheses have been Pb-acetate hydrate, Ti-tetra-isopropoxide and Ca-acetate (or Ca-nitrate tetrahydrate) in 2-methoxyethanol solvent. The mixed solutions are heated under reflux to initiate solvent exchange and molecular association reactions.^{9,12,15} However, some disadvantages of many of the available metal alkoxides in 2-methoxyethanol solvent for thin film applications are their extreme reactivity toward atmospheric moisture and the limited crack-free thickness of the film. In addition, handling the methoxyethanol, used as a solvent, is quite dangerous. In order to solve the problems mentioned above, we have investigated the use of diol route in place of methoxyethanol route, and successfully fabricated crack-free PbTiO₃ and (Pb,Lu)TiO₃ thin films.¹⁶ The handling and processing procedures are more straight forward than for most alkoxide sol-gel system that must be chemically modified to a acetylacetonate chelating groups.

In the present study, we adopt calcium acetylacetonate hydrate that is an acetylacetone derivative like Ti precursor instead of calcium acetate or calcium nitrate tetrahydrate, and the diol-based sol-gel process to obtain PCT thin films. The effects of Ca contents on the surface morphology and electrical properties of thin films are reported.

2. EXPERIMENTAL

The processing scheme for preparing PCT precursor sols is summarized in Fig. 1. Lead acetate trihydrate, Pb(CH₃COO)₂·3H₂O, titanium diisopropoxide bis(2,4-pentanedionate) (TIAA), Ti(OC₃H₇)₂(CH₃COCHCOCH₃)₂ and calcium acetylacetonate hydrate, Ca(CH₃COCHCOCH₃)₂·2H₂O, were used as source materials and 1,3-propanediol, HO(CH₂)₂OH, was used as solvent. The gravimetrically assayed Pb(CH₃COO)₂·3H₂O and Ca(CH₃COCHCOCH₃)₂·2H₂O reagents were mixed in propanediol in a 1:5 molar ratio of (Pb+Ca) to diol, to obtain various Pb_{1-x}Ca_xTiO₃ sol compositions. Films with

*Correspondence: Email: ycc@ee.nsysu.edu.tw

Ca contents of $x = 0.05, 0.15, 0.25$ and 0.35 are designated as PCT(5), PCT(15), PCT(25) and PLT(35), respectively. The solutions were refluxed at 140°C for 1 h in atmosphere and then cooled to 80°C . After adding TIAA, the solutions were further refluxed at 120°C for 1 h and 80°C for 10 h, then a stock solution of ~ 1 M concentration was obtained. The obtained solution is gold-like in color. Usually, sol composition of calcium content exceeded 25 mol%, the precipitation occurred in reflux reaction process. It was found that 2 ml water and 2.5 ml of acetic acid additions could be adopted to prevent precipitation. The modified solution was further reflux for 0.5 h to improve homogeneity of this solution. Inductively coupled plasma mass spectrometry (ICP-MS) was used to confirm that the deviation from stoichiometry was within about $\pm 1\%$.

The stock solutions were spin-coated on Pt(111)/SiO₂/Si(100) substrates at 3000 rpm for 30 s using a commercial spinner. These substrates were prepared by sputtering platinum onto oxidized ($0.1\ \mu\text{m}$ of SiO₂) silicon substrates. The precursor solutions were deposited onto the substrates via a syringe filter to avoid particulate contamination. The films were dried in air at 350°C for 0.5 h and coating/drying operations were repeated until the desired thickness was obtained. Films with four layers were fabricated, then fired in air at $500\text{--}800^{\circ}\text{C}$ for 1 h at a heating rate of $5^{\circ}\text{C}/\text{min}$ and cooled to room temperature.

The thermal decomposition characteristic of precursor gel was identified using differential thermal analysis (DTA) and thermogravimetric analysis (TGA). In this study, the gel was pre-dried at 100°C for 12 h and then analyzed using a heating rate of $10^{\circ}\text{C}/\text{min}$. The thickness of PCT film was measured to be about $1\ \mu\text{m}$ by a surface profiler. Crystal orientations and lattice parameters of the films were analyzed using a x-ray diffraction (XRD) with Cu-K α radiation. The microstructures of the PCT films were examined by a scanning electron microscopy (SEM). To determine the electrical characteristics of the thin films, 1 mm diameter of the Pt top electrodes were deposited on the surfaces of the fired films. In order to make contact with the Pt bottom electrode, a corner of the film was etched away using a 50 wt% solution of fluoroboric acid, HBF₄. The dielectric property was measured at room temperature by an impedance analyzer (HP-4194A). Current-voltage (I-V) characteristic was measured using a semiconductor parameter analyzer (HP-4145B). Measurements of the hysteresis loop and the pyroelectric current were carried out using a Sawyer-Tower circuit and a pA meter, respectively.

3. RESULTS AND DISCUSSION

The thermolysis behavior of PCT(5) gel that had been pre-dried at 100°C is shown in Fig. 2. TGA analysis indicated a major weight loss step between 100°C and 300°C , and a smaller weight loss in the range of $300\text{--}400^{\circ}\text{C}$, the final weight loss was completed at about 450°C . It can be seen that the gel exhibited approximately 40% weight loss in the temperature range of 100°C to 450°C due to the elimination of adsorbed water, solvent (b.p. of diol is 212°C) and the decomposition of organic by-products. DTA data indicated a series of exothermic peaks. The peaks at temperatures between 100°C and 400°C are associated with the former weight losses. The final peak which appears at about 450°C is associated with a weight loss, that is probably due to crystallization of (Pb,Ca)TiO₃.

X-ray patterns of PCT(5) films heated at temperatures from 500°C to 800°C for 1 h are shown in Fig. 3. The predominant phase is perovskite type PCT, but there was also evidence of a minor presence of pyrochlore phase in the film heated at 500°C . However, no pyrochlore phase was detected by XRD in films with firing temperature of above 600°C . Figure 3 also shows that the PCT(5) films exhibit randomly oriented polycrystalline. The result is consistent with that reported by Chewasatn *et al.*¹⁷ This phenomenon may be due to the difference in the thermal expansion between PCT thin film and silicon substrate during cooling through the Curie transition temperature. The phase evolution of other compositions was similar to that of PCT(5).

The variation of lattice constants as a function of Ca content is shown in Fig. 4. The a axis gradually increases, and the c axis obviously decreases with the increasing of Ca content. These changes of the lattice constants indicate that Ca atoms were dissolved in the crystal structure systematically. Figure 4 also shows the tetragonality (c/a) of the PCT films as a function of the film composition. The tetragonality decreased with an increase of Ca content, thus the crystal structure gradually transferred from tetragonal to cubic.

The evolution of surface microstructure of PCT(5) films deposited on Pt coated silicon substrates and heat-treated at temperatures from $500\text{--}800^{\circ}\text{C}$ is shown in Fig. 5. The film fired at 500°C for 1 h (Fig. 5a), exhibited no resolution of microstructural feature, by increasing the firing temperature to 600°C , the grains of $< 0.15\ \mu\text{m}$ in size could be identified (Fig. 5b). At a firing temperature of 700°C (Fig. 5c), the homogeneous microstructure consisting of uniform grain size about $0.3\ \mu\text{m}$ can be observed. When the firing temperature was raised to 800°C , the grains became irregular and larger in size ($\leq 0.5\ \mu\text{m}$). Figures 6(a)–6(d) show the typical microstructures of the films with $x \leq 0.35$ heated at 700°C for 1 h. With an increase of Ca content, the grain size was significantly reduced. The microstructure of PCT(35) film displayed

the coalescence of small grains. The porous microstructure with the grain size about 0.3 μm and a thickness of about 1 μm of the PCT(5) thin film heated at 700°C is shown in Fig. 7. The result indicated that the thickness of PCT thin film is consistent with that measured by a surface profiler.

Figure 8 shows the dependence of the relative dielectric constant, ϵ_r , on various Ca content measured at 10 kHz for the films heated at 700°C with $x = 0.05, 0.15, 0.25$ and 0.35 . It can be seen that ϵ_r increased with the increasing of Ca content. This trend might be due to the increased microstructure density as La content was increased (Fig. 6). For all films, the dielectric loss factor ($\tan\delta$) measured at 10 kHz was in the range of 0.0009 ~ 0.0013. Figure 9 shows the current density-electric field characteristics for the films with various Ca contents heated at 700°C for 1 h. It is obvious that the increasing Ca content suppressed the leakage current. Figures 10(a)-10(d) show the ferroelectric hysteresis loops of PCT films with $x \leq 0.35$ heated at 700°C for 1 h, and the corresponding results of the coercive field (E_c) and remanent polarization (P_r) are plotted in Fig. 11. The apparent values of E_c and P_r drastically decreased with the increase of La content from $E_c = 36 \text{ kV/cm}$ and $P_r = 2.0 \mu\text{C/cm}^2$ for $x = 0.05$ to $E_c = 9.6 \text{ kV/cm}$ and $P_r = 1.0 \mu\text{C/cm}^2$ for $x = 0.35$. This phenomenon is due to the decrease of tetragonality.

The pyroelectric coefficient (γ) as a function of Ca content is shown in Fig. 12. It increased from $2.2 \times 10^{-8} \text{ C/cm}^2\text{K}$ for $x = 0.05$ to $3.54 \times 10^{-8} \text{ C/cm}^2\text{K}$ for $x = 0.35$. However, the increasing rate of γ slows down as Ca content is in excess of $x = 0.25$. The averaged figures of merit $F_v (= \gamma / C_v \epsilon_r)$ for voltage responsivity R_v and $F_m (= \gamma / C_v (\epsilon_r \tan\delta)^{1/2})$ for specific detectivity D^* of PCT thin films with the same thickness as a function of Ca content are shown in Fig. 13, where C_v is volume specific heat ($= 3.2 \text{ J/cm}^3\text{K}$). Both F_v and F_m increased significantly with an increase in Ca content. However, F_v and F_m decreased when Ca content exceeded 25 %. It was found that the PCT(25) thin film exhibits a large F_v of $1.64 \times 10^{-10} \text{ Ccm/J}$ and F_m of $4.04 \times 10^{-8} \text{ Ccm/J}$. The characteristic evaluation of above results showed that $\text{Pb}_{1-x}\text{Ca}_x\text{TiO}_3$ thin film with $x = 0.25$ was the most suitable for the pyroelectric applications.

4. CONCLUSIONS

Polycrystalline $\text{Pb}_{1-x}\text{Ca}_x\text{TiO}_3$ thin films ($x = 0.05$ to 0.35) were fabricated on $\text{Pt/SiO}_2/\text{Si}$ (100) substrates by a diol-based sol-gel process. The 1 μm thickness can be achieved for four layers PCT thin film. The modified Ca source in this study plays an important role in PCT precursor sol. The films showed no preferred orientation, and the tetragonality decreased with the increase of Ca content. The addition of Ca restrained the growth of grains in the microstructure of PCT films. Generally, the dielectric constant increased and leakage current decreased with the increasing of Ca content of the films. The coercive field and remanent polarization of the films decreased with the increasing of Ca content. The pyroelectric coefficient increased with the increase of Ca content. The obtained PCT thin films exhibit high figures of merit, F_v and F_m , and show an excellent pyroelectric property which are suitable for the application of highly sensitive pyroelectric infrared devices.

ACKNOWLEDGEMENTS

This study was supported by the National Science Council, R.O.C. under contract no. NSC88-2216-E-151-006.

REFERENCES

1. H. D. Chen, K. R. Udayakumar, C. J. Gaskey, and L. E. Cross, "Electrical-properties maxima in thin-films of the lead zirconate lead titanate solid-solution system," *Appl. Phys. Lett.* **67**, pp. 3411-3413, 1995.
2. A. Yamada, C. Maeda, T. Umemura, F. Uckikawa, S. Wadaka, and T. Ishikawa, "Preparation and piezoelectric property of lead titanate thin-films for ghz-band resonators," *Jpn. J. Appl. Phys.* **36**, pp. 6073-6076, 1997.
3. R. Moazzami, C. Hu, and W. H. Shepherd, "Electrical characteristics of ferroelectric PZT thin-films for dram applications," *IEEE Trans. Electron Devices* **39**, pp. 2044-2049, 1992.
4. P. K. Larsen, R. Cuppens, and G. A. C. M. Spierings, "Ferroelectric Memories," *Ferroelectrics* **128**, pp. 265-292, 1992.
5. W. A. Geideman, "Progress in Ferroelectric Memory Technology," *IEEE Trans. Ultrason. Ferroelectr. Freq. Control* **38**, pp. 704-711, 1991.
6. J. J. Ho, Y. K. Fang, K. H. Wu, W. T. Hsieh, C. W. Chu, C. R. Huang, M. S. Ju, and C. P. Chang, "A high sensitivity lead-titanate (PbTiO_3) pyroelectric thin-film infrared sensor with temperature isolation improvement

- structure," IEEE Electron Device Lett. **19**, pp. 189-191, 1998.
7. M. Kohli, C. Wuethrich, K. Brooks, B. Willing, M. Forster, P. Muralt, N. Setter, and P. Ryser, "Pyroelectric thin-film sensor array," Sens. & Actuat. A **61**, pp. 147-153, 1997.
 8. D. S. Paik, A. V. Prasadara, and S. Komarneni, "Sol-Gel Fabrication of Samarium and Manganese Modified Lead Titanate Thin-Films and Ceramics," Mater. Lett. **32**, pp. 97-101, 1997.
 9. A. Kholkin, A. Seifert, and N. Setter, "Electromechanical properties of sol-gel derived ca-modified PbTiO₃ films," Appl. Phys. Lett. **72**, pp. 3374-3376, 1998.
 10. S. R. Shannigrahi, R. N. P. Choudhary, and H. N. Acharya, "Characterizations of sol-gel Grown (PbLaLi)(Zr_{0.6}Ti_{0.4})O₃," J. Appl. Phys. **85**, pp. 1713-1721, 1999.
 11. E. Yamaka, H. Watanabe, H. Kimura, H. Kanaya, and H. Ohkuma, "Structural, ferroelectric, and pyroelectric properties of highly c-axis oriented Pb_{1-x}Ca_xTiO₃ thin-film grown by radio-frequency magnetron sputtering," J. Vac. Sci. Technol. A **6**, pp. 2921-2928, 1988.
 12. A. Tsuzuki, H. Murakami, K. Kani, K. Watari, and Y. Torii, "Preparation and ferroelectric properties of sol-gel-derived (Pb,Ca)TiO₃ thin films," J. Mater. Sci. Lett. **10**, pp. 125-128, 1991.
 13. R. Sirera, M. L. Calzada, F. Carmana, and B. Jimenez, "Ferroelectric thin films of calcium modified lead titanate by sol-gel processing," J. Mater. Sci. Lett. **13**, pp. 1804-1805, 1994.
 14. M. L. Calzada, M. J. Martin P. Raos, J. Mendiola, R. Sirera, M. F. Dasilva, and J. C. Soares, "Effect of compositions and annealing conditions on the properties of sol-gel prepared calcium-modified lead titanate thin-films," J. Phys. & Chem. Solids **58**, pp. 1033-1039, 1997.
 15. J. J. Shyu, and K. L. Mo, "Characterization of sol-gel derived Ca-doped PbTiO₃ thin films," J. Mater. Sci. Lett. **15**, pp. 620-623, 1996.
 16. C. M. Wang, Y. C. Chen, M. S. Lee, J. W. Wu, and C. C. Chiou, "The properties of lead titanate thin films derived from a diol-based sol-gel process," Jpn. J. Appl. Phys. **37**, pp. 951-957, 1998.
 17. S. Chewasatn, and S. J. Milne, "Sol-gel synthesis and electrical characterization of (Pb,Ca)TiO₃ thin films," J. Mater. Sci. **32**, pp. 575-582, 1997.

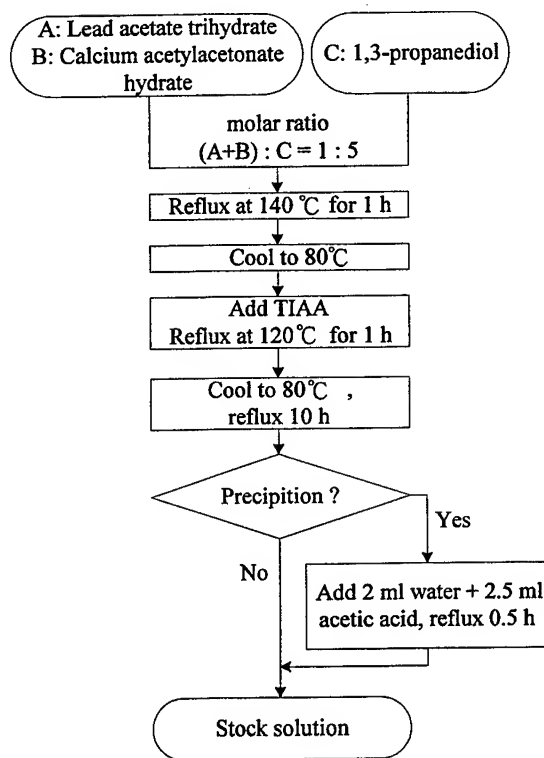


Fig. 1. Flow diagram of the synthesis process of PCT sol.

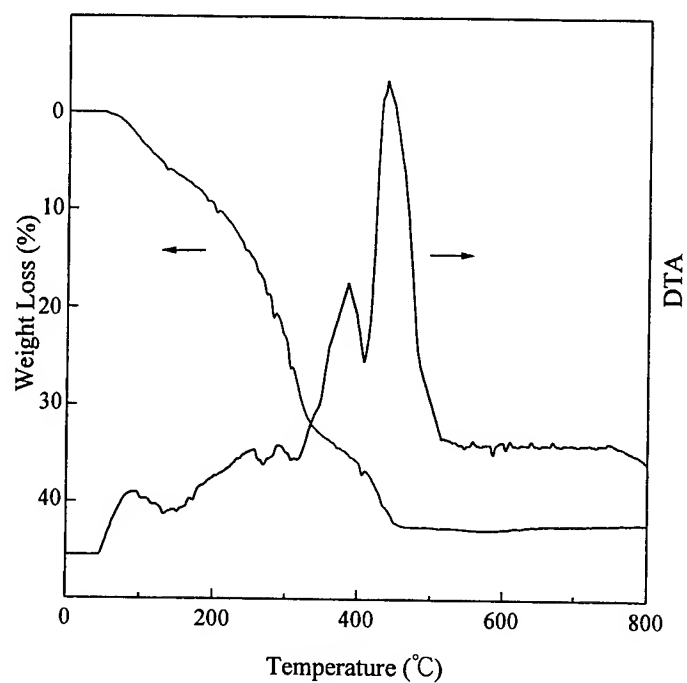


Fig. 2. Thermogravimetric analysis data (TGA) and the corresponding DTA data for gel of PCT(5).

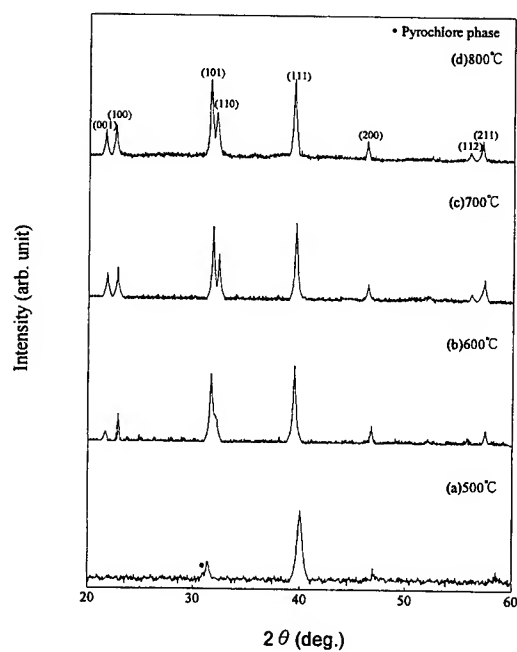


Fig. 3. XRD results as a function of firing temperature for PCT(5) films.

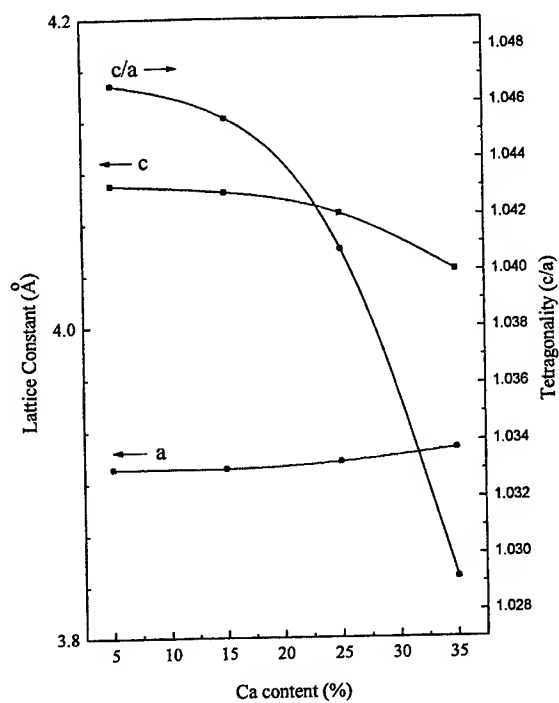


Fig. 4. Lattice constants and tetragonality for $\text{Pb}_{1-x}\text{Ca}_x\text{TiO}_3$ films.

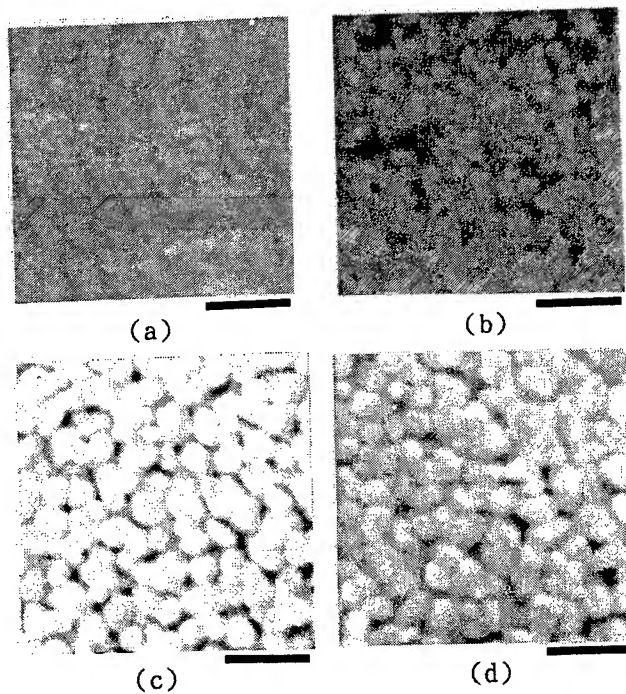


Fig. 5. Surface microstructures of PCT(5) films fired for 1h at different temperatures: (a) 500°C; (b) 600°C; (c) 700°C; (d) 800°C (bar = 0.5 μm).

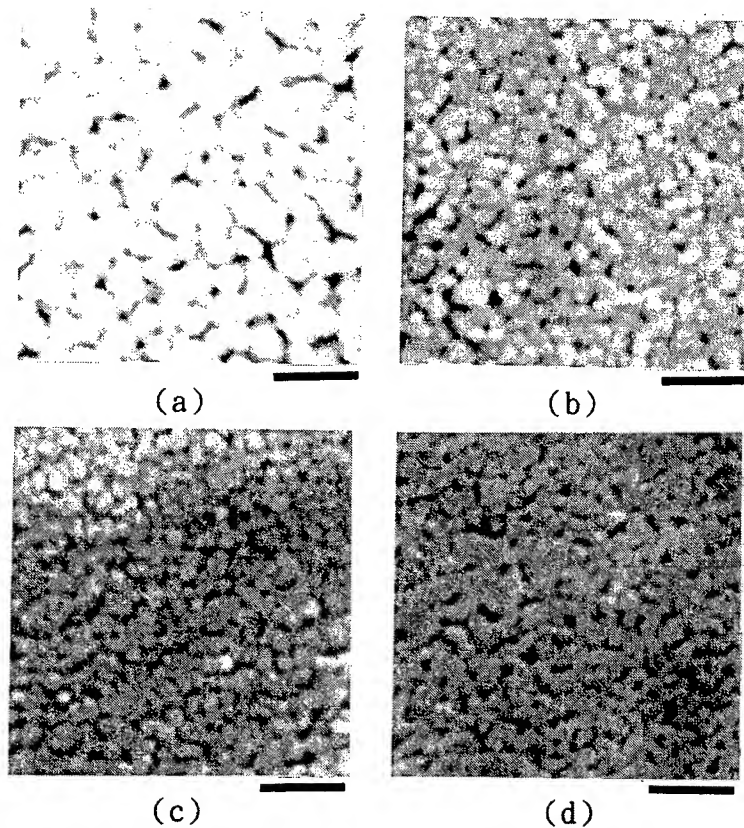


Fig. 6. Surface microstructures of the films with $x =$ (a) 0.05, (b) 0.15, (c) 0.25 and (d) 0.35, heated at 700°C for 1 h (bar = 0.5 μm).

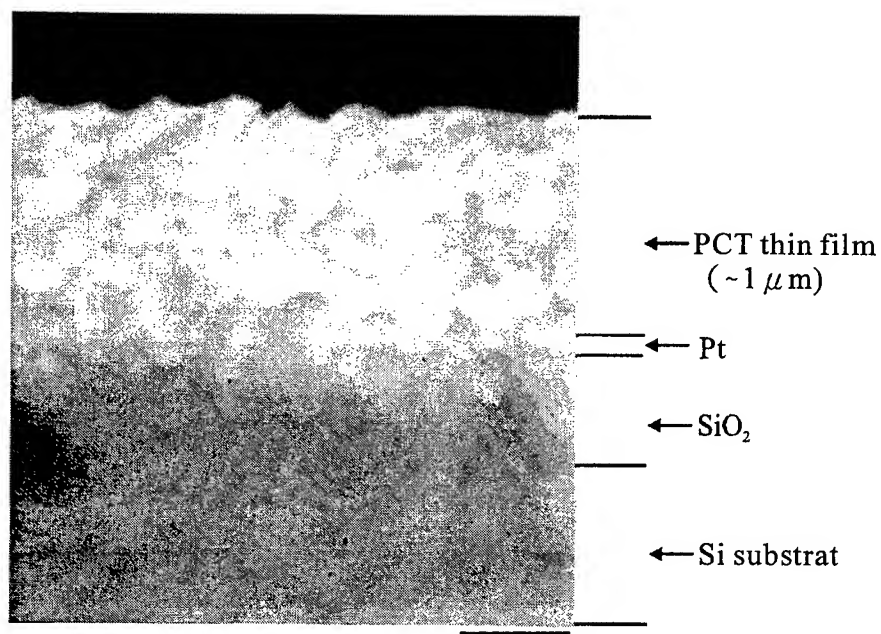


Fig. 7. Cross-sectional SEM micrograph of PCT(5) film heated at 700°C for 1 h (bar = 0.5 μm).

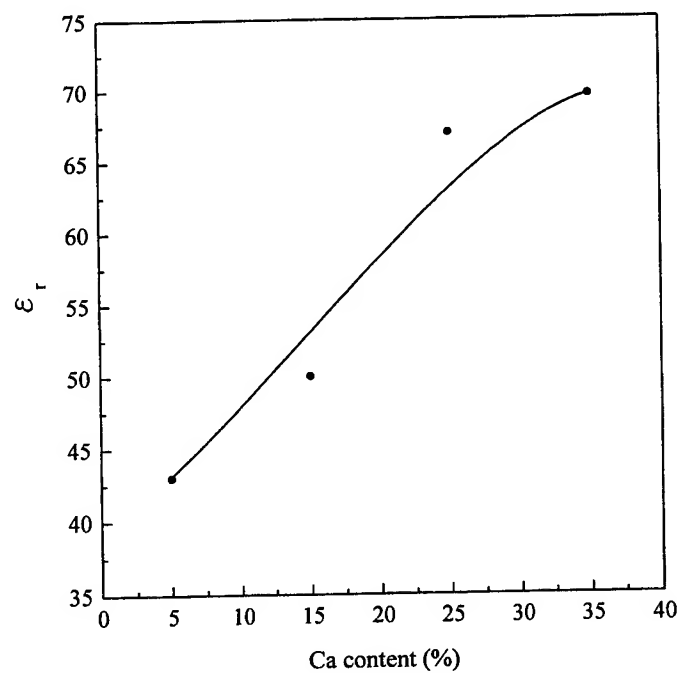


Fig. 8. Dependence of the relative dielectric constant on Ca content.

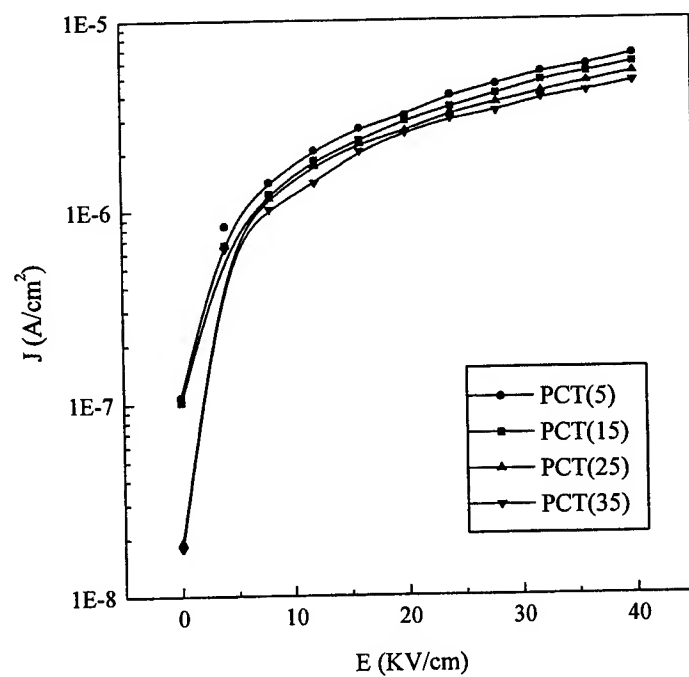


Fig. 9. Current density-electric field characteristics for PCT films heated at 700°C for 1 h.

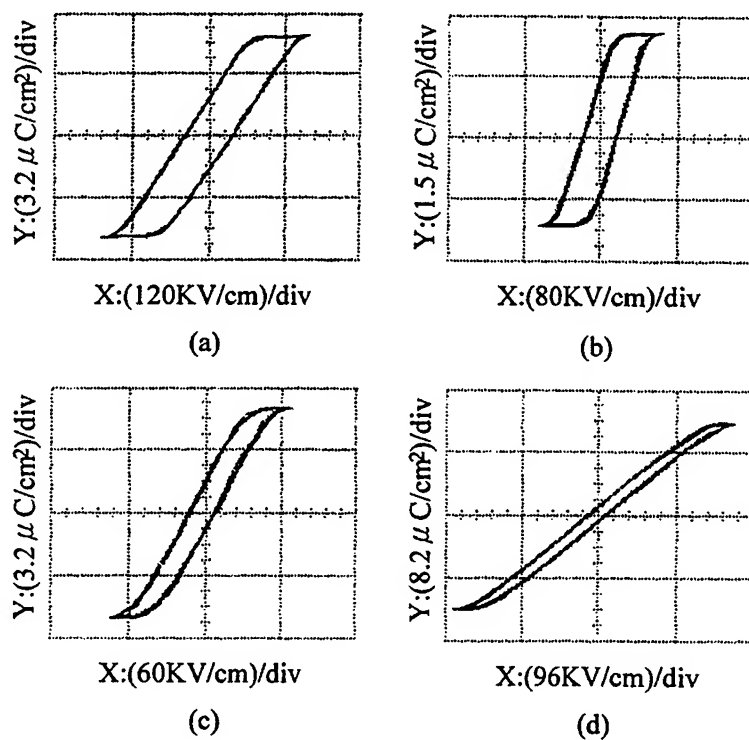


Fig. 10. P-E hysteresis loops of the PCT films with $x =$ (a) 0.05, (b) 0.15, (c) 0.25 and (d) 0.35 (X: electric field, Y: polarization).

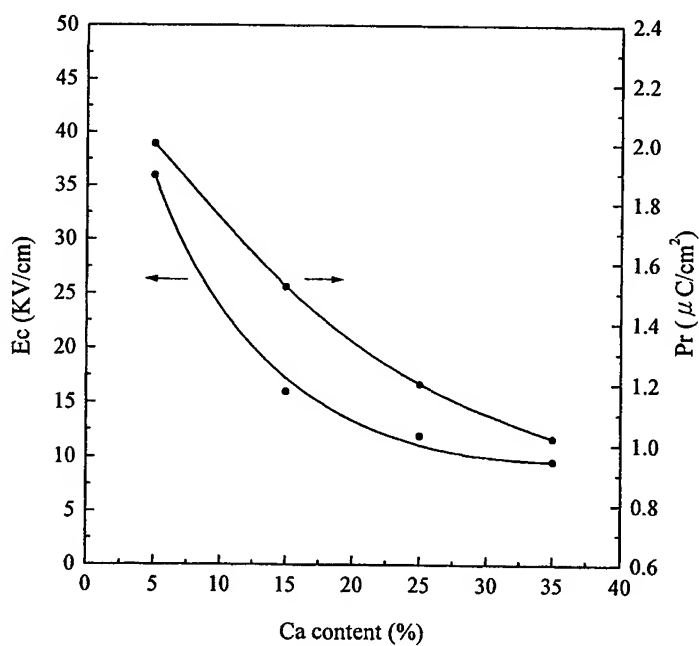


Fig. 11. Dependence of the coercive field and the remanent polarization on Ca content.

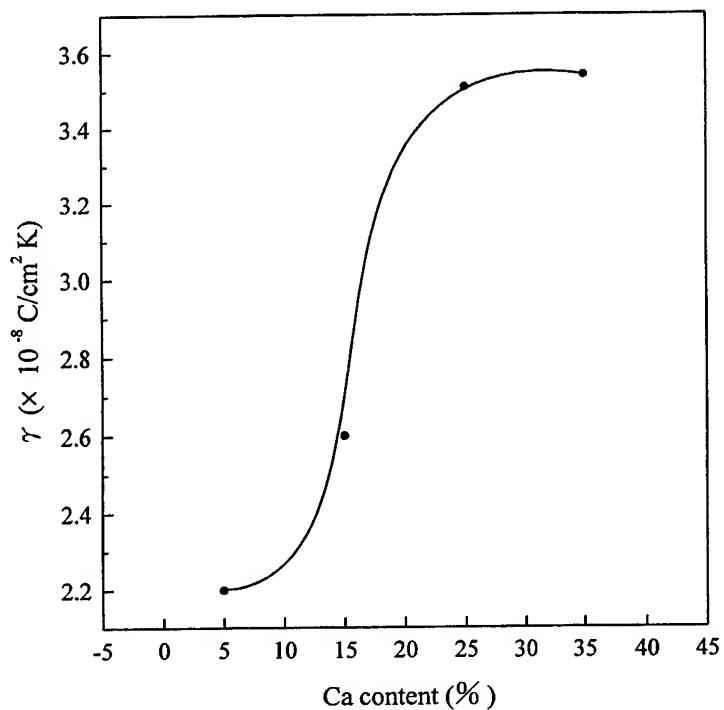


Fig. 12. The pyroelectric coefficients as a function of Ca content.

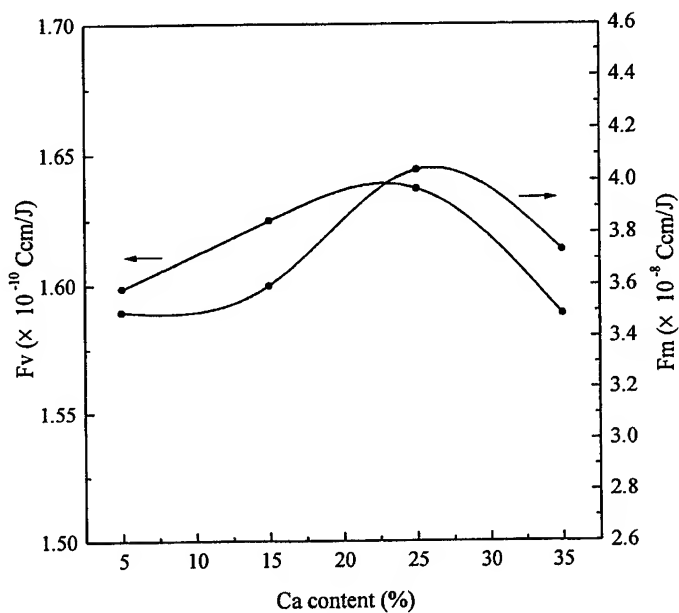


Fig. 13. Figures of merit (F_v) for voltage responsivity (R_v) and figures of merit (F_m) for specific detectivity (D^*) as a function of Ca content.

Fabrication of Planar Waveguides of Poly(N-vinylcarbazole)

Fitri Fitrilawati ^{a,b}, May On Tjia ^a, Jochen Ziegler ^c, Christoph Bubeck ^c

^a Department of Physics Institut Teknologi Bandung,
Jl. Ganesha no. 10 Bandung 40132, Indonesia

^b Department of Physics Universitas Padjadjaran,
Jl. Raya Jatinangor Sumedang 45363, Indonesia

^c Max-Planck-Institute for Polymer Research,
Ackermannweg 10, 55128 Mainz, Germany

ABSTRACT

Thin films of poly(N-vinylcarbazole) (PVK) were prepared by spincoating upon fused silica substrates. PVK was dissolved in dimethyl formamide (DMF) and processed at elevated temperatures. Thin films with the required thickness and low surface roughness were obtained by careful optimization of the preparation parameters, such as concentration, spinning speed and temperature of the spincoating process. The dispersion of refractive indices of PVK films was measured by reflectometry and by prism coupling at 633 nm and 1064 nm. The attenuation loss of slab waveguides was measured by monitoring the stray light of the guided mode with a diode array. The loss depends significantly on the relative ratio of surface roughness to thickness. As this ratio depends on preparation conditions, we succeeded in fabricating planar waveguides of PVK that had an attenuation loss of only 1 dB/cm at 633 nm.

Keywords: Poly(N-vinylcarbazole), PVK, spincoating, surface roughness, refractive index, integrated optics, waveguide, attenuation loss.

1. INTRODUCTION

Fabrication of photonic devices requires materials that can be processed to thin films with high structural and optical quality. We chose poly(N-vinylcarbazole) (PVK) as an example to study the influence of the preparation parameters of the spincoating process on the properties of slab waveguides. PVK has already found many applications because it is a well known photoconductor¹. Recently it has gained additional interest as photorefractive material and as a matrix for NLO dyes². It was further used in electroluminescence devices^{3,4} and for the preparation of planar waveguides⁵. PVK has a relatively high refractive index ($n_D = 1.68$), good optical transparency, and high thermal stability as well as processability. These favourable properties qualify PVK as promising material for the fabrication of waveguides that are highly demanded for integrated optical devices. Specific investigations aimed to optimize the preparation parameters of slab waveguides of PVK in order to minimize the attenuation loss have not been reported yet, to the best of our knowledge.

It is well known that the fabrication of waveguides faces stringent conditions imposed on the film quality. Foremost are purity, homogeneity, and surface smoothness of the film needed to obtain a low loss waveguide. Most of the works done on thin polymer film deposition have so far adopted the spincoating technique^{6,7}. The quality of films produced by this technique has been discussed recently^{8,9}. It is generally recognized that important factors such as solution concentration, viscosity, and spinning speed should be optimized in order to produce a good quality film.

We report experimental results of spincoating PVK upon fused silica substrates. It will be shown that employing the proper processing parameters involving the solution concentration, spinning speed, and coating temperature, optically transparent films of good quality can be fabricated that are really suitable for waveguide applications.

2. EXPERIMENT

Poly(N-vinylcarbazole) (PVK) was purchased from Aldrich Chem. (average $M_w = 1,100,000$, $T_g = 200$ °C) and used without purification. It was dissolved in dimethyl formamide (DMF) (Fluka Chem., $T_b = 153$ °C) and filtered by 0.5 or 5 μ m micropore filters prior to the spinning process. Fused silica substrates (35 mm x 25 mm x 1 mm) were cleaned for 15 min in an ultrasonic bath containing 1 % Hellmanex solution and then rinsed successively with Millipore water and ethanol. The

substrates were subsequently dried by blowing them with nitrogen gas immediately after being taken out from the ethanol solution. For the preparation of high quality PVK waveguides, the parameters of the spincoating process were systematically varied such as the concentration of the polymer solution by weight ($2\% \leq c_w \leq 10\%$), the spinning speed ($500 \text{ rpm} \leq \omega \leq 9000 \text{ rpm}$) and the coating temperature T which was adjusted by means of a fan with regulated heating power (room temperature $\leq T \leq 65^\circ\text{C}$). All films were prepared under a laminar flow hood which provided clean room conditions with less than 100 particles per cubic feet. The films were further annealed at 200°C for 14 hours in vacuum to remove residual solvent.

The films were characterized in terms of their thickness (d), surface roughness (R_a), and optical properties. The thickness and roughness were measured with a Tencor Instrument model α -step 200 profiler by scanning the depth profile on the film surface at $2000 \mu\text{m}$ scale range. The surface roughness was determined by graphical centerline criterion¹⁰. A reference point for thickness measurements was established by making a scratch on the film with a sharp needle. Each reported data point is an average of five measurements made at different positions on the same film. The transmission and reflection spectra were measured by spectrophotometer (Perkin Elmer model Lambda 9). The refractive index of the waveguide was measured by prism coupler. For this purpose, the TE polarized light from a He-Ne laser (633 nm) was coupled into the waveguide using a high index glass prism (LaSFN18, $n_p = 1.9077$). The film was pressed against the base plane of half-cut prism mounted on a precision rotary table. Our experimental set-up was already described previously¹¹. The coupling angle was adjusted until a guided mode was launched through the waveguide. The refractive indices were then calculated from the coupling angles following the method of Ulrich and Torge¹². The dispersion of the refractive index was evaluated from the transmission and reflection spectra as described recently¹³. The characterization of waveguide loss was performed by employing the same prism coupling set-up described above. The losses of the waveguide were measured by imaging the scattered light from the guided mode onto a diode array using a lens¹¹. The loss coefficient was determined from a semilogarithmic plot of the scattered intensity along the waveguide.

3. RESULTS AND DISCUSSION

The choice of the solvent is of crucial importance for the preparation of spincoat films with high quality. Various solvents have already been reported to be suitable for PVK, such as tetrahydrofuran³, 1,1,2-trichloroethane⁴ and chloroform⁵. We observed that low boiling point solvents such as chloroform and dichloroethane resulted in poor surface quality of the spincoated PVK films, exhibiting what is known as orange peel effect^{14,15}. We also found that PVK of high molecular weight dissolves in toluene at elevated temperatures only. We finally chose dimethyl formamide (DMF) because it dissolves PVK at room temperature quite well and has a moderate boiling point ($T_b = 153^\circ\text{C}$). Higher concentrations of PVK solutions could be readily prepared which provided the required flexibility for concentration variations. We optimized the coating temperature and spinning speed to produce films of desired quality as characterized by minimum surface roughness at a given thickness.

The results of film characterization demonstrate the crucial influence of processing parameters such as processing temperature, spinning speed and polymer concentration on the quality of film. Among these, the temperature effect on the quality of the film is quite remarkable. We observed that good optical transparency could be achieved only with a coating temperature in the order of $52 - 54^\circ\text{C}$. Films prepared below 50°C appeared opaque, while working at temperatures above 60°C led to poor surface quality of the films. The thickness and surface property of the film were also considerably affected by the spinning speed. Below 2000 rpm , the film showed unacceptable surface roughness, while spinning speeds above 4000 rpm led to thinner films. On the other hand, the solution concentration in the range considered mostly affected the film thickness only. Films with a good optical transparency and small surface roughness were obtained with coating temperature around 52°C , spinning speeds between 2000 rpm and 4000 rpm and solution concentrations c_w between 2% and 10% by weight. As an illustration, Fig. 1 shows the surface profiler traces of films fabricated at the optimal temperature (52°C) and at lower temperature. Films prepared at $T = 52^\circ\text{C}$, $\omega = 4000 \text{ rpm}$, and $c_w = 10\%$ weight concentration were quite smooth. In contrast, the film prepared at $T = 44^\circ\text{C}$, $\omega = 2000 \text{ rpm}$, and $c_w = 10\%$ was very rough. A square dip in the trace resulted from scratching the film using a sharp needle. It is used to evaluate the film thickness.

The absorption spectrum of the film is shown in Fig. 2. The dashed line represents the original measurement. It shows a significant tail to longer wavelengths ($\lambda > 400 \text{ nm}$). This apparent tail appears similar to the tail of the absorption spectrum reported by Allegrini et al.⁴. It is caused by reflection losses which can be properly corrected following the procedure reported previously¹³. The corrected intrinsic absorption spectrum (full line in Fig. 2) shows high optical transparency of the PVK films for $\lambda \geq 400 \text{ nm}$. Our PVK films possess also superior stability that we checked in the following way: After baking at 220°C for 24 hours the absorption spectrum remained practically unchanged with respect to

the one presented in Fig. 2. The same spectrum was also obtained after exposing a PVK film to ambient laboratory conditions for about 1 month.

The dispersion of the refractive index as measured by reflectometry is shown in Fig. 3. In order to avoid interference problems of the reflectometry measurement, very thin films are required for this measurement which were obtained at $c_w = 2\%$, $\omega = 2000$ rpm and $T = 52^\circ\text{C}$. The refractive indices obtained by reflectometry agree very well with the results from prism coupling as described below.

The effective refractive index (n_{eff}) of PVK waveguides was calculated from the coupling angle in the prism coupling set-up. The angle of incidence at the entrance face of the prism (θ_i) is related to n_{eff} according to the following equation

$$n_{\text{eff}} = n_p \sin \left[A + \sin^{-1} \left(\frac{\sin \theta_i}{n_p} \right) \right] \quad (1)$$

where n_p is the refractive index of the prism, A is the angle of the prism, and θ_i is the measured coupling angle of guided mode TE_i. The value of θ_i is an averaged result of several measurements performed at different lateral positions on the same waveguide. The values of n_{eff} for waveguides with varying thickness are plotted in Fig. 4. PVK waveguides with $d < 580$ nm can only support a single mode, while two modes can be excited in the waveguides at $600 \text{ nm} \leq d \leq 900$ nm, for example. The solid curves in the Fig. 4 are calculated by means of Snellius law and the following relations¹⁶

$$2kn_1d \cos \theta - 2\phi_{10} - 2\phi_{12} = 2m\pi \quad (2)$$

$$\tan \phi_{10} = \frac{(n_1^2 \sin^2 \theta - n_0^2)^{0.5}}{n_1 \cos \theta} \quad (3)$$

$$\tan \phi_{12} = \frac{(n_1^2 \sin^2 \theta - n_2^2)^{0.5}}{n_1 \cos \theta} \quad (4)$$

where n_1 , n_2 and n_0 are refractive indices of film, substrate, and air respectively, while m is the mode number. The data of TE₀ in Fig. 4 can be excellently fitted with the theoretical relation, while the fits for the higher modes are of lesser quality although they are still reasonably good. This is related to the fact that coupling angles for the higher modes are less well resolved in our experimental set-up.

We used Eqs. (1 - 4) for an independent determination of the refractive index of PVK films at wavelengths $\lambda = 633$ nm and 1064 nm following the evaluation procedure of Ulrich and Torge¹². The result is displayed in Fig. 3 along with the dispersion of n from reflectometry. The values of n are averages of several measurements from films supporting either one, two or three modes. We obtain $n(633\text{nm}) = 1.682 \pm 0.015$ and $n(1064 \text{ nm}) = 1.655 \pm 0.019$ for TE polarization. The agreement between the two kinds of measurement is very good.

The quality of PVK waveguides was characterized by the waveguide attenuation loss coefficient α_{gw} that we obtained from semilogarithmic plot of scattered intensity measured along the waveguide as shown in Fig. 5. The intensity of light propagated in the waveguide is generally expected to suffer from a loss along the distance transversed due to absorption and light scattering at the interfaces and within the film. The data of Fig. 5 show that film (a) has $R_a/d = 0.4\%$ and $\alpha_{\text{gw}} = 1$ dB/cm and film (b) has $R_a/d = 6.8\%$ and $\alpha_{\text{gw}} = 7.6$ dB/cm. This example demonstrates the key influence of R_a/d on α_{gw} . Our approach provides a solution to the problem how to fabricate better waveguides of PVK as compared to those reported previously⁵.

4. SUMMARY AND CONCLUSION

We have demonstrated high quality PVK waveguides which were prepared by the suitable choice of processing parameters consisting of a coating temperature in the order of 52 °C, weight concentration of 5 – 10 %, and spinning speed of 2000 – 4000 rpm. The PVK films possess excellent thermal stability and have good structural as well as optical properties suitable for waveguide applications. We achieved waveguide attenuation losses of 1 dB/cm at 633 nm, which is superior to previous reports. We conclude that PVK films, when properly processed, can be used as low loss waveguides in photonic devices.

ACKNOWLEDGEMENTS

This project was made possible by a grant of the German Academic Exchange Service (DAAD) to F. Fitrilawati to perform the experimental part of this work in Germany. We acknowledge considerable technical support given by A. Best, L. Horbach, G. Herrmann and W. Scholdei. Financial support was given by the Federal Ministry for Education and Research of Germany (OPTIMAS project, grant 03N1021B7), Hibah Tim Urge project no. 004/HHTP-II/URGE/1996 for supporting parts of analysis in the Institute of Technology Bandung, and the University of Padjadjaran for financial support for attending SPIE conference.

REFERENCES

1. M. Pope and C.E. Swenberg, *Electronic Process in Organic Crystals*, Clarendon Press, Oxford, pp. 701–707, 1982.
2. Y. Zhang, T. Wada, and H. Sasabe, "Carbazole photorefractive materials", *J. Mater. Chem.* **8**, pp 809-828, 1998.
3. D.D. Gebler, Y.Z. Wang, D.-K. Fu, T.M. Swager, A.J. Epstein, "Exciplex emission from bilayers of poly(vinylcarbazole) and pyridine based conjugated copolymers", *J. Chem. Phys.* **108**, pp 7842-7848, 1998.
4. M. Allegrini, A. Arena, M. Labardi, G. Martino, R. Girlanda, C. Pace, S. Patane, G. Saitta, S. Savasta, "Photoluminescence from a soluble semiconducting polymer in waveguide and microcavity configurations", *Appl. Surf. Sci.* **142**, pp 603-607, 1999.
5. F. Ghailane, G. Manivannan, E.J. Knystautas, R.A. Lessard, "Fabrication of poly(vinylcarbazole) waveguides by oxygen ion implantation", *J. Opt. Soc. Am. A-Opt. Image Sci.* **12**, pp 1683-1686, 1995.
6. J.T. Ives and W.M. Reichert, "Polymer thin film integrated optics: fabrication and characterization of polystyrene waveguide", *J. Appl. Polym. Sci.* **36**, pp 429-443, 1988.
7. W.R. Holland, "Fabrication and characterization of polymeric lightwave devices", *Polymers for Lightwave and Integrated Optics*, L.A. Hornak (Ed), 15, Marcel Dekker Inc., New York, pp 397-431, 1992.
8. C.B. Walsh, E. I. Franses, "Thickness and quality of spin-coated polymer films by two angle ellipsometry", *Thin Solid Films* **347**, pp 167 – 177, 1999.
9. R.A. Pethrick, K.E. Rankin, "Criteria for uniform thin film formation for polymeric materials", *J. Mater. Sci-Mater. El.* **10**, pp 141-144, 1999.
10. Manual of Tencor Instrument model alpha-step 200 profiler.
11. A. Mathy, H-U Simmrock, C. Bubeck, "Optical waveguiding in thin films of polyelectrolytes", *J. Phys. D: Appl. Phys.* **24**, pp 1003-1008, 1991.
12. R. Ulrich, R. Torge, "Measurement of thin film parameters with a prism coupler", *App. Opt.* **12**, pp 2901-2908, 1973.
13. A. Mathy, K. Ueberhofen, R. Schenk, H. Gregorius, R. Garay, K. Muellen, C. Bubeck, "Third-harmonic-generation spectroscopy of poly(p-phenylene): A comparison with oligomers and scaling laws for conjugated polymers", *Phys. Rev.* **B53**, pp 4367-4376, 1996.
14. B.T. Chen, "Investigation of the solvent-evaporation effect on spin coating of thin films", *Polym. Eng. Sci.* **23**, pp 399-403, 1983.
15. L.L. Spangler, J.M. Torkelson, J.S. Royal, "Influence of solvent and molecular weight on thickness and surface topography of spin-coated polymer films", *Polym. Eng. Sci.* **30**, pp 644-653, 1990.
16. P.K. Tien, "Light waves in thin films and integrated optics", *App. Opt.* **10**, pp 2295-2413, 1971.

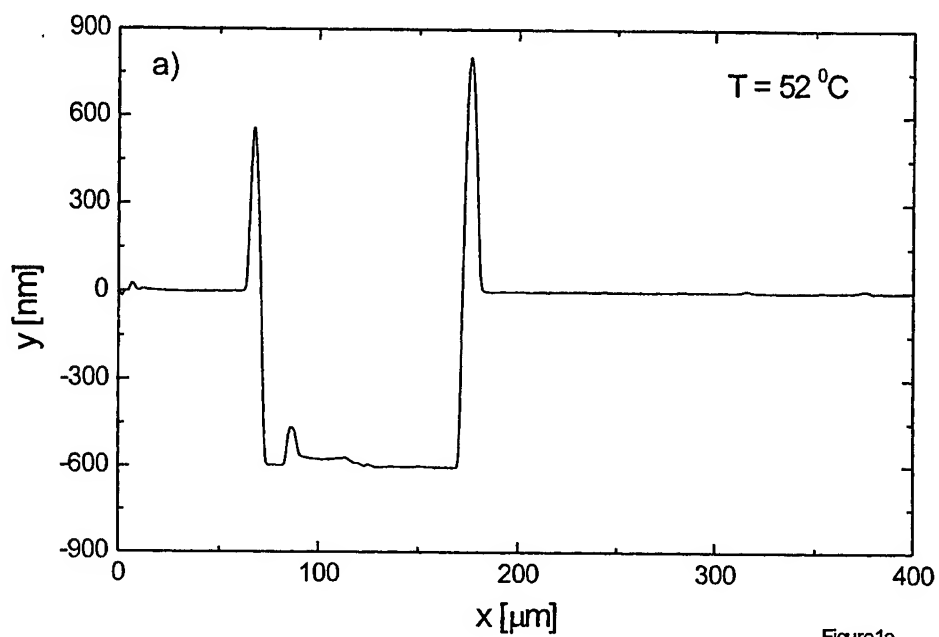


Figure1a

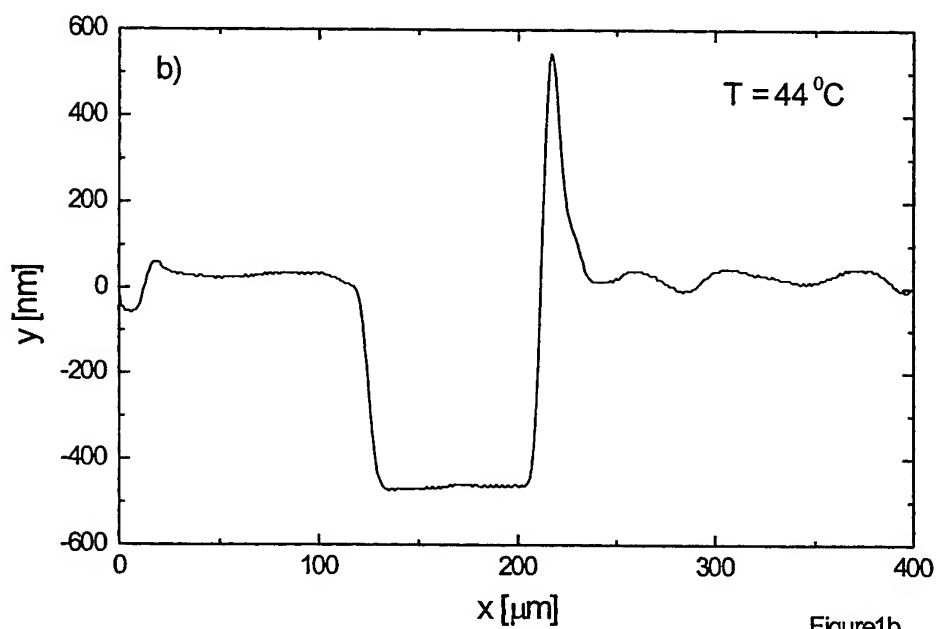


Figure1b

Figure 1. Step profiler traces of PVK films prepared from DMF solutions: (a) surface profile of a film prepared at $T = 52\text{ }^{\circ}\text{C}$, $\omega = 4000$ rpm, $c_w = 10\%$, (b) surface profile of a film prepared at less appropriate condition ($T = 44\text{ }^{\circ}\text{C}$, $\omega = 2000$ rpm, $c_w = 10\%$).

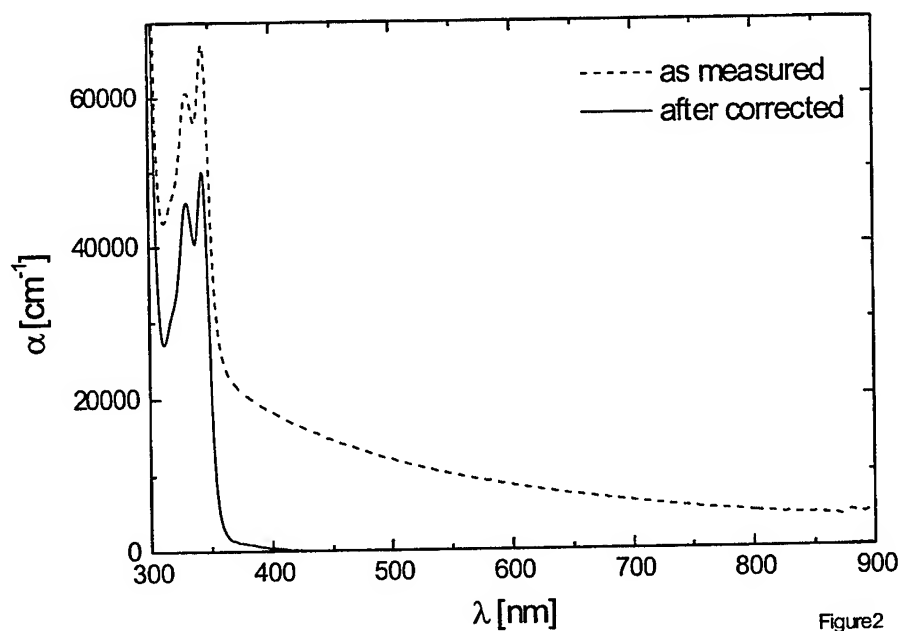


Figure2

Figure 2. The absorption spectra of PVK film prepared at $T = 52\text{ }^{\circ}\text{C}$ and $\omega = 2000\text{ rpm}$ before (dashed line) and after (solid line) subtraction of reflection losses.

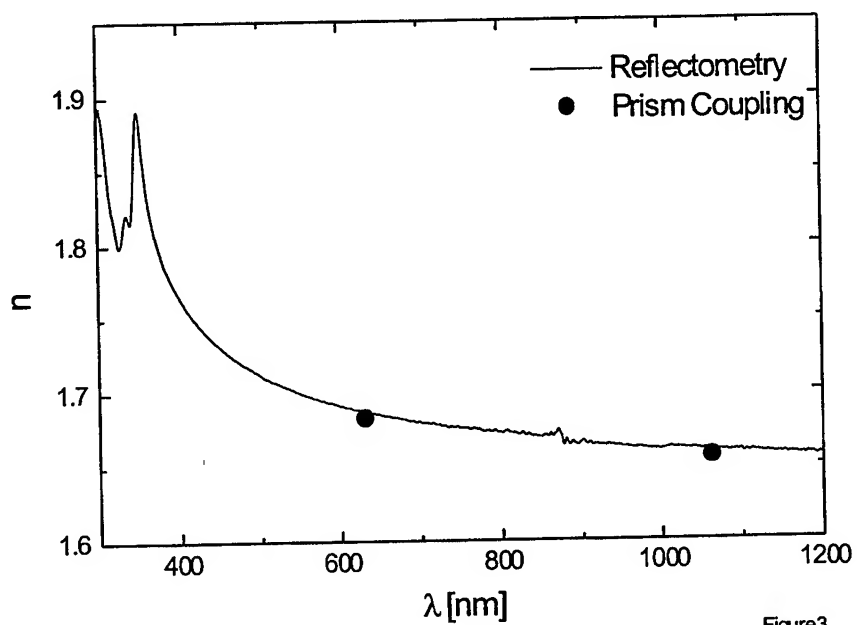


Figure3

Figure 3. Dispersion of the refractive index of a PVK film ($d = 54.5\text{ nm}$) measured by reflectometry and by prism coupling (data points at $\lambda = 633\text{ nm}$ and 1064 nm).

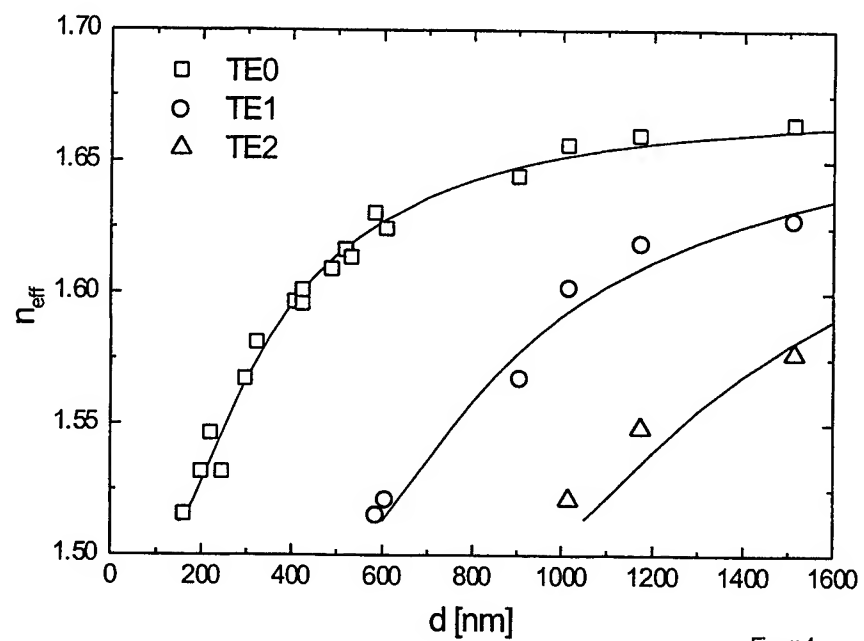


Figure4

Figure 4. Variation of waveguide effective indices as functions of film thickness for the guided modes of TE_n with $n = 0, 1, 2$ and the corresponding calculated curves ($\lambda = 633 \text{ nm}$).

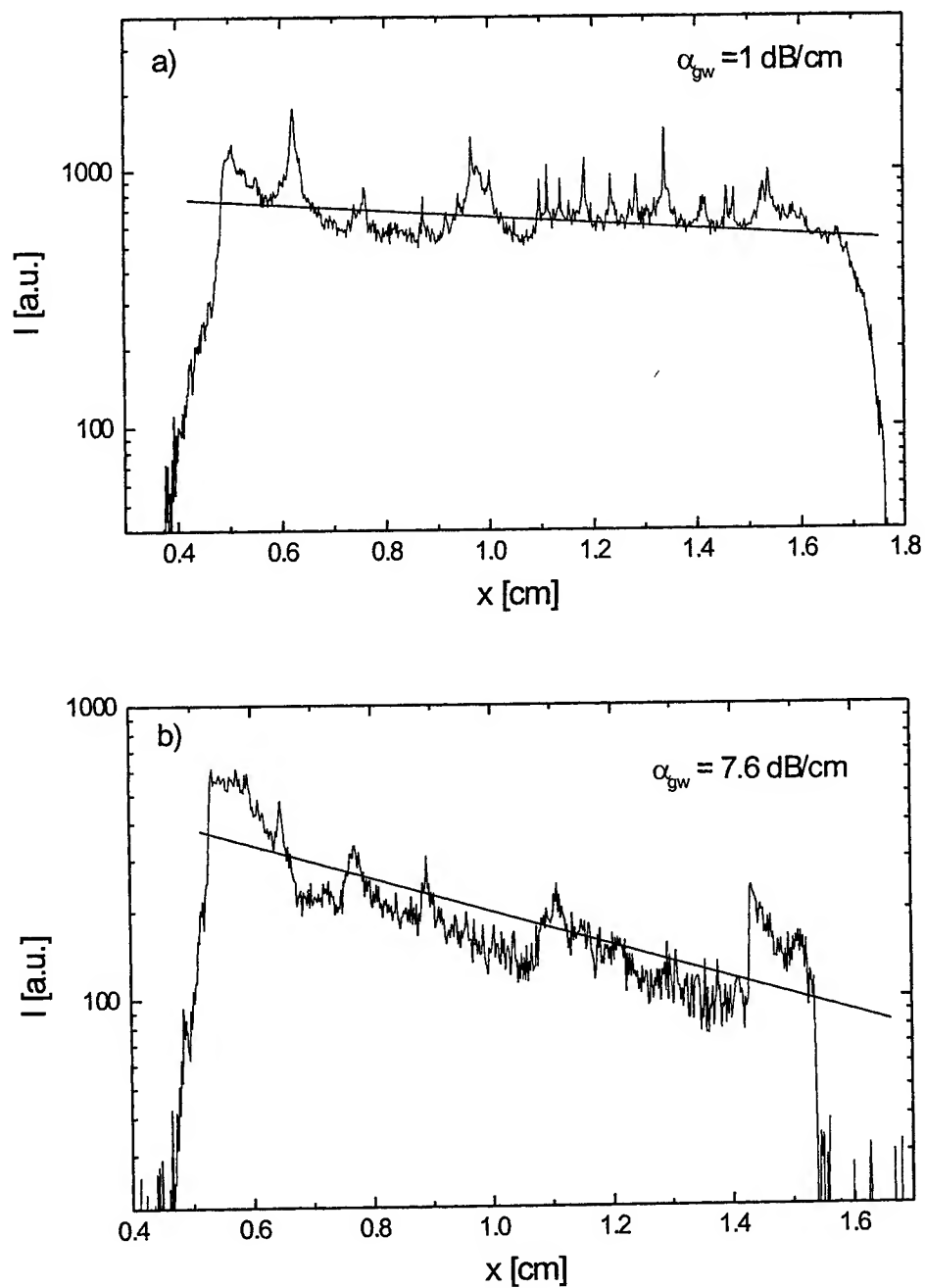


Figure 5. Scattered light intensity of waveguide modes in different thin films of PVK (TE0 mode, $\lambda = 633 \text{ nm}$) versus distance from coupling prism: (a) Film preparation at $T = 52 \text{ }^\circ\text{C}$, $\omega = 4000 \text{ rpm}$, $c_w = 10 \%$ resulted in $d = 585 \text{ nm}$ and $R_a = 2.6 \text{ nm}$, (b) Film preparation at $T = 44 \text{ }^\circ\text{C}$, $\omega = 2000 \text{ rpm}$, $c_w = 10 \%$ resulted in $d = 532 \text{ nm}$ and $R_a = 36 \text{ nm}$.

Electro-optical properties of an epoxy-based Polymer Dispersed Liquid Crystals

P. Mormile*, L. Petti*[^], M. Abbate[°], P. Musto[°], G. Ragosta[°] and W. J. Blau[^]

* IC-CNR, Dept. Of Optics, via Toiano 6, I-80072 Arco Felice (Naples), Italy

[°] IRTEMP-CNR, via Toiano 6, I-80072 Arco Felice (Naples), Italy

[^] Physics Department, Trinity College, Dublin 2, Ireland

ABSTRACT

Electro-optical properties of an epoxy-based Polymer Dispersed Liquid Crystal (PDLC) have been investigated. A morphological analysis has been performed by optical microscopy in order to estimate initially the average diameter of the liquid crystal microdroplets dispersed in the polymeric matrix. We present the observation of an electro-optical switching effect from an opaque to a transparent state occurring at a threshold value of the applied field in a PDLC. Optical responses of the composite film under the conditions of an externally applied ac electric field (90-250 V_{pp}) and a film thickness of 50 μ m, were determined using an Argon laser (wavelength 514 nm). The experimental results showed promising switching times with a rise time of 200 μ sec and a decay time of 2.2 msec and an exceptionally high contrast ratio up to 410. These results demonstrate the validity of employing this new PDLC in electro-optical devices.

Keywords: Polymer Dispersed Liquid Crystal, Electro-optical switching, Morphological analysis, Responses times measurements, contrast ratio.

1. INTRODUCTION

The scientific and technical development has been always supported by the research of new materials with innovative characteristics for the realization of advanced systems.

The fields of application are various and among these photonics and in general integrated optics are those which have utilized and exploited for the best the results of chemical engineering concerning innovative materials. Among the promising materials, those concerning microdroplets of liquid crystal (LC) distributed in polymeric matrices are certainly to be considered. In these materials, prepared in thin films, the droplets are spontaneously formed from a suitable oligomer/liquid crystal solution during polymerization of the matrix material.

We refer to those films as Polymer Dispersed Liquid Crystal films^{1,2}. They are potentially useful for electro-optical displays, variable transmission windows, color projectors, temperature sensors, colored films with electrically controllable optical density and other electro-optical devices. For each application the chemical and physical characteristics play a very relevant role³, so that it is necessary to evaluate preliminarily the specific properties of the prepared PDLC sample.

One of the most interesting attractions of such materials is their capability to switch the transmittivity from the low level (OFF state) to the high one (ON state), and viceversa, under the action of an applied electric field. This behavior is due to mismatching or matching of the refractive indices of the two components: liquid crystal and polymeric matrix.

In the field OFF-state, surface anchoring causes a non-uniform director field within the droplets, and the film scatters light due to the mismatching between the effective refractive index n_{eff} of the liquid crystal and the refractive index n_p of the polymer.^[4] In the field ON-state, the director is aligned along the field direction ($n_{eff} = n_o$) and for normal light incidence the film becomes transparent if the ordinary refractive index n_o of the liquid crystal is equal to n_p .^[5-6] The threshold voltage V_{th} and the response times τ_R and τ_D (rise and decay time) at which the PDLC switches from whiteness to transparency and the optical contrast between the white and transparent state is controlled by the size, shape,^[7-8] and anchoring energy of the liquid crystal domains, as well as the dielectric anisotropy and viscosity of the LC. While the latter properties depend on the selection of the liquid crystalline material, the former properties depend on the liquid crystal/monomer composition.

For normal display applications, high contrast and high ON-state clarity, low threshold voltages, and fast switching times are desirable⁹⁻¹³. In this communication we present experimental results on electro-optical properties of PDLC samples prepared in our laboratories, consisting of nematic liquid crystal (commercially known as E7) droplets in a epoxy resin binder.^[14-15] We measured the rise time and the decay time as a function of the applied electric field (square wave) and also the transmitted light vs the applied voltage. The experimental results demonstrate the validity of employing this new PDLC in electro-optical devices.

2. MATERIALS

The technique for obtaining our PDLC samples has been the polymerization-induced phase separation. The epoxy prepolymer used in this process is the diglycidyl ether of bisphenol A (DGEBA), commercially available under the trade name of Epikote 828. Methyl-5-norbornene-2,3-dicarboxylic anhydride (MNA) was used as hardener, and 2,4,6-tris(dimethylaminomethyl)-phenol (DMP-30) was employed as initiator. The LC component was a eutectic mixture of four liquid crystals, commercially available as E7. The weight ratio DGEBA/MNA/DMP-30 in the epoxy formulation was 0.53/0.46/0.01. In fig. 1A and 1B we report the chemical formulas of the two components of our PDLC.

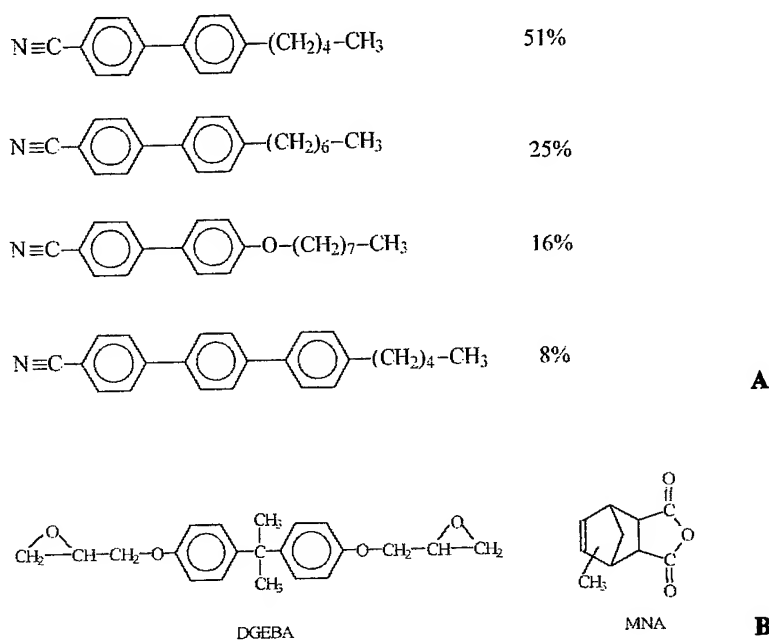


FIGURE 1: Chemical formulas of the liquid crystal E7 (A), and the bifunctional epoxy resin (DGEBA) + hardener (MNA).

The glass transition temperature of this mixture, as evaluated by Differential Scanning Calorimetry (DSC), is -65°C , while the nematic-isotropic transition occurs at 58°C .

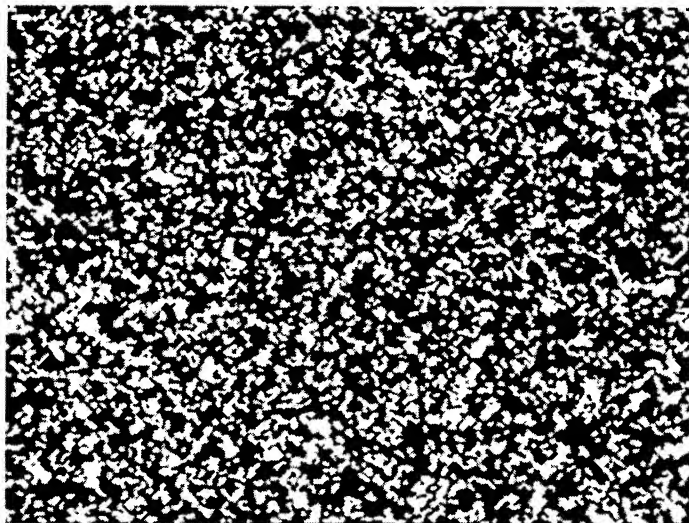
The epoxy-based PDLC was prepared by mixing the LC component (40% by weight) with the uncured epoxy matrix at 70°C , obtaining a complete homogenization of the mixture. The mixture was then sandwiched between two conductive film of ITO (Indium Tin Oxide) deposited on transparent substrates, spaced at $50\mu\text{m}$ by appropriate mylar spacers. The PDLC droplets were allowed to cure at 130°C reached with a heating rate of $2^{\circ}\text{C}/\text{min}$.

3. MORPHOLOGICAL ANALYSIS

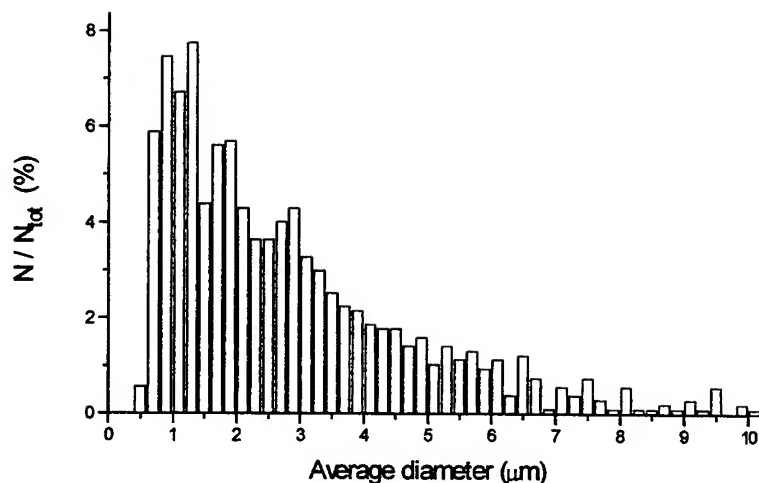
A preliminary investigation on the epoxy-based PDLC system, over the composition range 0 - 60 wt % of LC, was performed by optical microscopy.

Optical microscopy was employed to follow the mixing of the components and the phase separation before and after the curing process. Prior to curing all the investigated compositions appear to be featureless under cross-polarized light (completely dark field). After curing, no changes are observed up to the 30 wt % composition. However, starting from the

40 wt % mixture, a homogeneous distribution of birefringent LC droplets is clearly identifiable (see Figure 2A). Therefore, up to 30 wt % of LC the mixture is as a single phase, homogeneous system even after curing; the LC component remains molecularly dispersed into the epoxy matrix and acts as a plasticizer. At 40 wt % of LC and above a phase separation process takes place upon curing.



A



B

FIGURE 2: Optical micrograph at room temperature under polarised light of the 60/40 PDLC composition after curing; magnification 160x (A). Histogram of the particle size distribution inside the polymeric matrix. This distribution was evaluated by computerised image analysis from several SEM micrographs (B).

In Fig. 2B we report a histogram of the particle size distribution inside the polymeric matrix. This distribution was evaluated by an image analysis software from several SEM micrographs. In this case the particle size distribution is considerably narrower, with most of the domains ranging between 0.7 and 3 μm. The peak of the statistical distribution (exceeding 60 %) is located between 0.7 and 2 μm.

As reported in literature ^[16-17], the size of the LC droplets plays a fundamental role in determining the electro-optical response of a PDLC system. Increasing droplet diameter reduces the magnitude of surface effects compared with bulk effects, so that decay time is expected to increase and rise time to decrease.

3. EXPERIMENTAL RESULTS AND DISCUSSION

In order to evaluate the electro-optical properties of this type of PDLC we used the experimental arrangement shown in fig. 3.

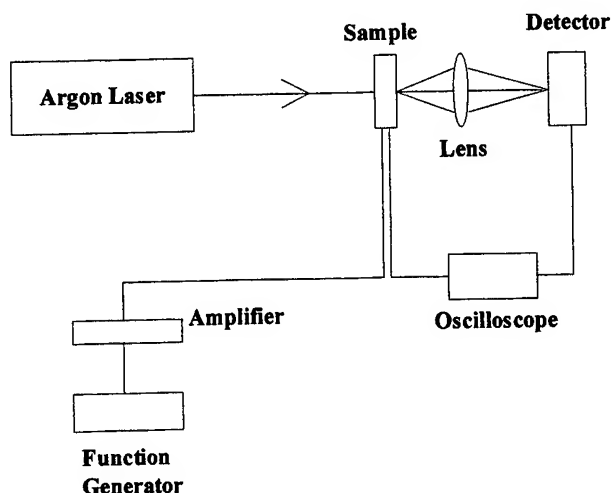


FIGURE 3: Experimental setup.

A light beam from a cw Argon laser ($\lambda=514$ nm) impinges normally on the sample sandwiched between the two conducting substrates, used for applying the electric field. The output light is focused on a photodiode placed in front of the sample to collect the total transmitted power. An electric field of known intensity and duration is provided by application of a voltage from a pulse generator and amplifier to the transparent conductive electrodes. The voltage signal and optical response are monitored on a storage oscilloscope.

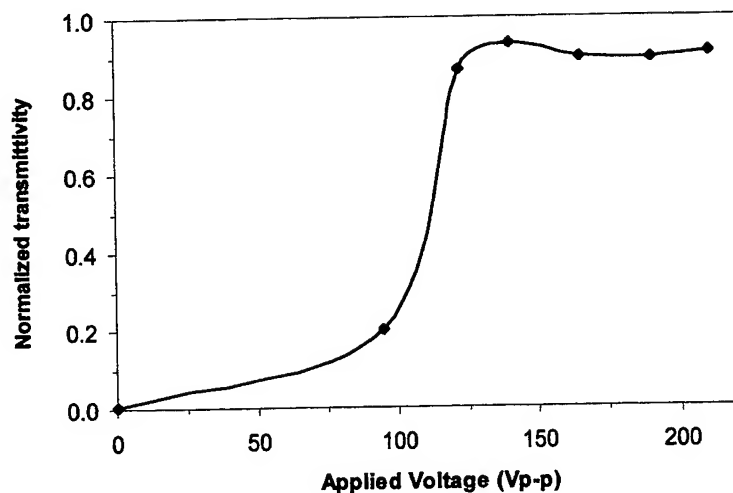


FIGURE 4: Normalized transmitted optical power as a function of applied voltage at a frequency of 50 Hz.

In order to analyze the electro-optical behavior of our device, we changed the polarization states, the amplitude and frequency of the electric field. In all the tested configurations a square wave applied voltage drove the field. As a first step, we sent a light beam into the sample at which a driving voltage up to $V_{pp} = 220$ V at different frequencies was applied. Over $\nu = 100$ Hz the optical signal was no more able to follow the driving field.

In figure 4 we show the transmitted signal as a function of the applied voltage at a frequency of 50 Hz. A low transmittance remains up to a threshold value of the voltage, corresponding to 90 Vpp, after which the transmitted signal increases drastically in the range 90-200 Vpp, where it reaches a value of 90% of the incident one. Around the threshold the optical behavior of PDLC sample is determinate by the refractive index variation of the LC component. When the applied voltage is lower than a threshold value (approximately 120 V), no distortion induced in the LC molecular director appears and the sample is in its OFF-state. It is worth noting that the OFF-state scattering is a function of refractive index differences: a) between a liquid crystal droplet and the polymer, b) between two adjacent droplets, and c) within a droplet of liquid crystal.

When the voltage is increased above the threshold, the reorientation of NLC molecules occurs: for positive dielectric anisotropy, the molecules are forced to be aligned parallel to the applied electric field direction and the refractive index seen by the incident light is n_o . In this case, there is a good index matching between the liquid crystal domains and the polymer matrix; this results in highly transmitted light, so that the sample is driven to the ON state.

Figure 5 shows the voltage dependence of the magnitude of rise time (τ_R) and decay time (τ_D). The increasing or decreasing behavior of the response times values is due to the different dynamic responses when the system passes from one state to the other one. In fact, in the field-ON condition, molecular reorientation occurs under the action of the electric field torque which competes with the elastic torque, main cause of the initial undistorted alignment. On the contrary, the OFF-ON switch is achieved when the electric field is turned off and the relaxation of the molecules back to the initial orientation is only due to the elastic restoring torque. The latter process is generally slower than the former. Rise time is usually defined as the time needed for the composite to reach 90% of the ON-state transmission when an alternating voltage of amplitude Vpp is applied. Similarly, decay time is the time needed for the composite in the ON-state to reach 10% of the OFF-state transmission when the voltage is set to zero. Rise time is mainly a function of electric field (V/d , d is the thickness of the film), viscosity, resistivities and dielectric anisotropy. Decay time depends on viscosity and elasticity of the LC, as well as on shape and size of the droplet.

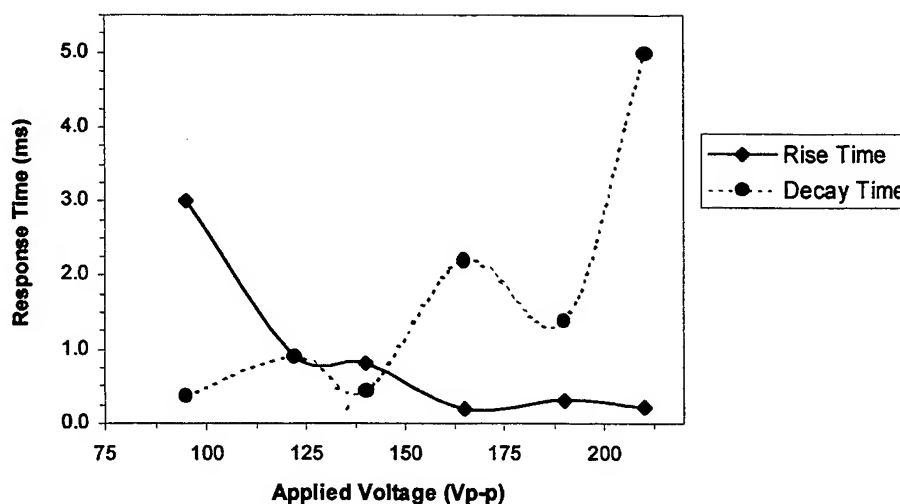


FIGURE 5: Response time as a function of applied voltage.

In order to evaluate the response times of our material when the square wave voltage is applied, we measured directly the rise time (τ_R) and the decay time (τ_D) on the traces shown at the oscilloscope, by varying the frequency and the voltage value. In fig. 6A we show a photo of traces at the oscilloscope of the driving signal (lower curve), at a frequency of 50 Hz and a voltage of 95 V_{p-p} (under the threshold voltage V_{th}), and of the output signal (upper curve), respectively. While the

modulated electric field is in the low state the sample is OFF. But when the electric field is in the high state, light is transmitted and the device is ON. We measured a rise time of 3 ms and a decay time of 0.37 ms which are expected under the threshold value of the applied voltage. The contrast ratio, T_{ON}/T_{OFF} (maximum transmission /minimum transmission) based on transmittance was of 100. It is worth noting that to get a true measure of the transmittivity in the ON-state it is necessary to use a small collection angle in the detecting optics. If large collection angles are used, the photodiode collects light, which is scattered out of the specular beam, thus leading to a false measure of ON-state clarity.

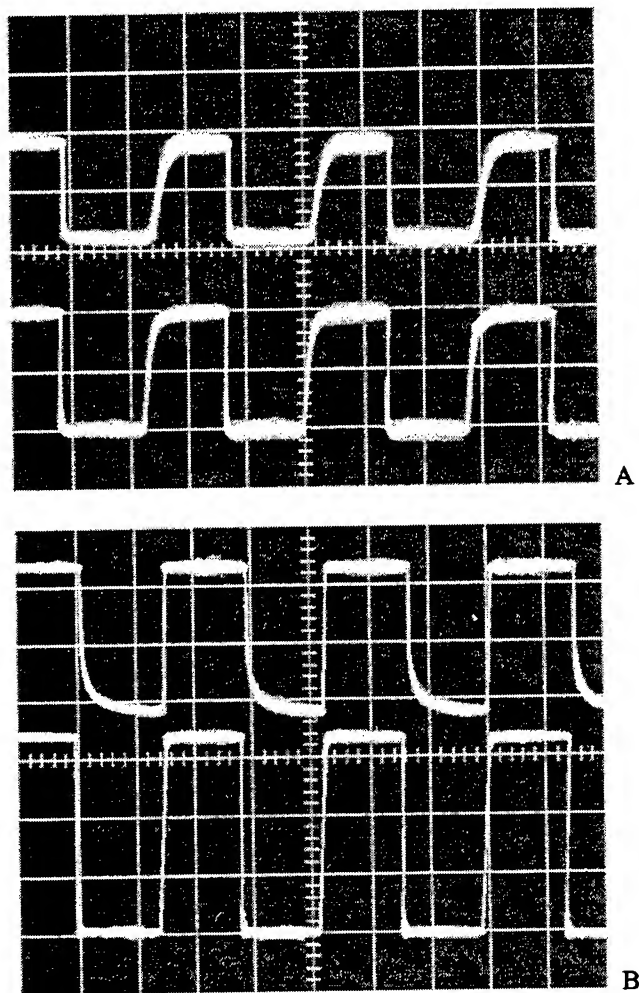


FIGURE 6: Optical response of our sample (upper traces): (A) $V_{pp} = 95V < V_{th}$ and (B) $V_{pp} = 165V > V_{th}$. In the lower traces is shown the driving voltage whose frequency is 50 Hz. The time scale is 10ms/cm; the output voltage scale is 5V/cm; the driving voltage scale is 50V/cm.

In figure 6B we report the traces shown at the oscilloscope of the driving signal (lower curve), at a frequency of 50 Hz and a voltage of 165 V_{pp} (above the threshold), and of the output signal (upper curve), respectively. The switching time was measured to be faster than in the previous case and, depending on the driving field values up to peak performances of $\tau_R = 200 \mu s$ and $\tau_D = 2.2 ms$ and an exceptionally high contrast ratio up to 410. In our case this very large contrast ratio is a result of a really small OFF-state transmittance (high OFF-state scattering efficiency). In the OFF-state, incident light is strongly scattered because the refractive index undergoes a large sudden change at each polymer-droplet interface. Multiple scattering occurs because the sample thickness ($\sim 50 \mu m$) is large compared with the diameters of the liquid crystal droplets ($\sim 1 \mu m$).

4. CONCLUSION

In this communication we presented experimental results on electro-optical properties of a new type of PDLC sample prepared by the authors. We analyzed the morphology of this type of material in order to estimate the distribution of the LC micridroplets and their size, shape and the average diameter. We estimated the rise time and the decay time as a function of the applied electric field, transmitted light vs voltage, and contrast ratio.

Contrast ratio is an important measure of the performance of an electro-optical display. The experimental results showed fast switching times with a rise time of 200 μ sec and a decay time of 2.2 msec and an exceptionally high contrast ratio up to 410. These performances are certainly appealing.

The results presented in this paper suggest that it is possible to achieve high ON-state clarity, high OFF-state opacity and fast time responses by choosing the liquid crystal, the polymer and the liquid crystal concentration carefully and by optimizing the curing conditions.

In view of such a high contrast ratio of our PDLC samples, applications in electro-optical switching appear promising.

ACKNOWLEDGEMENTS

The authors wish to thank Dr. C. E. Beitia for his help and Mr E. Casale for his technical assistance.

This work was supported by a grant from Regione Campania - Assessorato alla Ricerca entitled "Programma Operativo Plurifondo, Azione 5.4.2".

REFERENCES

1. R. A. Weiss and C. K. Ober, *Liquid Crystalline Polymers*, Ch. 32, p. 475, ACS Symposium Series 435 (1990).
2. Iam-Choon Khoo, Shin-Tron Wu, *Optics and nonlinear optics of liquid crystals*, Word Scientific Ed., Chap. 2 part 2 (1993).
3. R.L. Sutherland, V.P. Tondiglia, and L.V. Natarajan, "Electrically switchable volume gratings in polymer dispersed liquid crystals", *Appl. Phys. Lett.* **64**, 1074 (1994).
4. D.K. Yang, L.C. Chien, and J.W. Doane, "Cholesteric liquid crystal/polymer dispersion for haze-free light shutters", *Appl. Phys. Lett.* **60**, 3102 (1992).
5. S.C. Jain, R.S. Thakur, and S.T. Lakshmikummar, *J. Appl. Phys.* **73**, 1057 (1993).
6. J.B. Whitehead, Jr., S. Zumer, and J.W. Doane, "Light scattering from a dispersion of aligned nematic droplets", *J. Appl. Phys.* **73**, 1057 (1993).
7. H. S. Kitzerow and P.P. Crooker, "Polymer-Dispersed Cholesteric Liquid Crystals - Challenge For Research And Application" *Ferroelectrics* **122**, 183 (1991).
8. S.C. Jain and D.K. Rout, "Electro-optic response of polymer dispersed liquid-crystal films", *J. Appl. Phys.* **70**, 6988 (1991).
9. S. Zumer and J.W. Doane, *Phys. Rev. A*, **34**, 3373 (1986).
10. B.G. Wu, J.L. West, and J.W. Doane, *J. Appl. Phys.* **62**, 3925 (1987).
11. G.P. Montgomery, Jr. And N.A. Vaz, "Contrast ratios of PDLC films", *Appl. Opt.* **26**, 738 (1987).
12. P. Drzaic, "Polymer dispersed nematic liquid crystal for large area displays and light valves", *J. Appl. Phys.* **60**, 2142 (1986).
13. R. Yamaguchi and S. Sato, *Jpn. J. Appl. Phys.* **33**, 4007 (1994).
14. P.Mormile, L. Petti, M. Abbate, P. Musto, G. Ragosta, P. Villano, "Temperature switch and thermally induced optical bistability in a PDLC", *Optics Communications* **147**, 269 (1998).
15. P. Mormile, E. Casale, L. Petti, M. Abbate, P. Musto, G. Ragosta, *Advances in Materials and Processing Technologies*, ed. by M. Andritschky, Vol.1, pp. 249,253 (1997).
16. G. Chidichimo, G. Arabia, A. Golemme and J. W. Doane, "Electrooptic properties of polymer dispersed liquid crystals", *Liq. Cryst.* **5**, 1443 (1989).
17. Sung-Chang Peng, Jiunn-Wen Yu and Sung-Nung Lee, "Effect of droplet size on the dielectric properties of PDLC film", *Journal of Polymer Science - Polymer Physics*, Vol. 35, 1373 (1997).

Crystal growth and morphology investigation with 3D luminance of photonic organic DAST thin film

Tien-Jey Sheu^a, Yui Whei Chen-Yang^{a*}, Song-Shiang Lin^a, Fu-Yuan Tsai^b, Yuan-Kuang Tu^b,

^aDept. of Chemistry, Chung Yuan Christian University, Chung-Li, Taiwan 320 ROC

^bChunghwa Telecom Lab., P.O.Box 6-25, Yang-Mei, Taiwan 326 ROC
stj@ms.chttl.com.tw

ABSTRACT

A nearly perfect single crystal DAST thin film has been grown in this study. The polarized optic microscopy photograph demonstrated an ordered morphology for the surface of this thin film. The FTIR spectrum showed that the intensities of the characteristic absorption bands for the single crystal thin film were different from that for the crystalline thin film. With 3D luminance image analysis, it was found that the intensity of a guided laser light passing through the single crystal thin film along its a-axis is a little bit stronger than that guided along a standard 8.5/125 μm silica optic fiber. The diameter of the guided light and the space between the two guided lights estimated were about 25 μm and 65 μm , respectively. This study indicates that only the single crystal thin film can be used as a waveguide without further process and is a promising candidate for electro-optic modulators and other active optical devices.

Keywords: Organic nonlinear optics, DAST crystal, Optical waveguide, 3D luminance image, Microscopic FTIR

1. INTRODUCTION

The need of organic compounds with large second-order hyperpolarizabilities, β , for use in high performance modulators and other nonlinear optical (NLO) devices has led in recent years to an intense worldwide effort in materials synthesis and engineering. Most of the NLO organic film research to date has been focused on polymers which required external electric field poling to achieve the necessary structure asymmetry to exhibit significant nonlinear susceptibilities, $\chi^{(2)}$.

An alternative, potentially advantageous approach is to use small organic molecules with a large, built-in β due to the lack of inversion symmetry in the crystal lattice. These noncentro-symmetric materials, such as the organic salts, can exhibit a significant β and also have good thermal stability. An archetype salt is 4'-dimethylamino-N-methyl-4-stilbazolium tosylate (DAST)^{1,2}. Until recently, it was not possible to grow ordered thin films of DAST with large EO coefficients.

A new method for the growth of thin films of complex organic compounds, called Organic Vapor Phase Deposition (OVPD) has been recently developed by PD-LD, Inc. in cooperation with the ATC/POEM (Advanced Technology Center/Princeton Opto-Electronic Materials) of Princeton University. This method was successfully used to deposit thin films of chemically pure DAST, a material with optical nonlinear properties among the best ever reported. On the basis of these results, S. Ban and Stephen R. Forrest, are developing a prototype fiber optic modulator, based on thin films of DAST deposited by OVPD on a silicon optical bench configured for efficient coupling to optical fibers. This addresses for the first time the integration of waveguides of highly nonlinear organic materials with silicon optical benches, which might be populated with standard fiber optic components, such as laser diodes, detectors, optical fibers, etc. Thus, this study represents an important step toward the fully integrated optoelectronic integrated circuits (OEIC), where different materials will be combined for the optimal performance of various functions, such as light generation, light guiding, light modulating and light detection. Since DAST-based devices have superior performance and lower prices than the competing products typically employing LiNbO_3 , the markets for high performance fiber optic modulators will grow rapidly. Some review papers on the growth of high quality nonlinear optical crystal DAST had been published³⁻⁷.

There are still some technical difficulties to be solved, including controlling the single crystal growth, the crystallographic orientation of thin film crystal, and the growth speed of thin film, etc. Also, the fabrication process of the organic NLO

* Further author information: (Send correspondence to)

E-mail: yuiwhei@mbbox.cycu.edu.tw

Department of Chemistry, Chung Yuan Christian University, Chung-Li, Taiwan 320

waveguides needs to be developed to produce efficient devices suitable for integrated optics and fiber optical communications. For example, to make the organic optical modulator to be practical, it should exhibit a large extinction ratio and a low switching voltage less than 100 volts.

In this report the characteristics of a single crystal DAST thin film with high optical quality needed for practical modulation application obtained are studied. The propagation of a laser beam on this thin film in alternative directions is also demonstrated to study its waveguide property.

2. EXPERIMENTAL

2.1 Preparation of DAST Thin Film

DAST was synthesized by the condensation of 4-methyl-N-methyl pyridinium tosylate, which was prepared from 4-picoline and methyl toluenesulphonate, and 4-N, N-dimethylamino-benzaldehyde in the presence of piperidine. DAST was then purified by recrystallization from methyl alcohol solvent. Solvent concentration control technique was used to grow the DAST thin film. For growing sharp-faceted crystals a crystal growth facility was designed. The facility consists of the thermal reaction vessels with temperature control. The vessels was carefully cleaned and dried, then filled with the DAST powder dissolved in methanol, which has been treated before use. The crystal growth was carried out under dry nitrogen. With proper condition the crystals with high quality and $3 \times 3 \times 1 \text{ mm}^3$ of size could be routinely grown and the crystal as large as $5 \times 5 \times 1 \text{ mm}^3$ with small defects was also obtained.

2.2 Characterization

The microscopic FTIR spectrum of DAST thin film was measured using Bruker IFS-48 model. The numerical aperture (NA) of the lens 0.75 was used, and the instrument was equipped with a liquid nitrogen cooled MCT (HgCdTe) detector and a polarizer constructed of an aluminum wire grid on a KRS-5 substrate. Spectra were taken by counting 32 scans at a resolution of 4 cm^{-1} . The scan range is from 400 cm^{-1} to 4000 cm^{-1} . The thermal transition behavior of the DAST thin film was determined by a differential scanning calorimeter (Seiko II DSC) and a thermogravimetric analyzer (TGA). The morphology was investigated by a polarize optical microscopy with digital analysis of the thin film lattice pattern by the 3-D luminance image analysis. The image obtained (by using fiber-optic video geometry) was compared with that of the diameter of a standard fiber to measure the thickness of the DAST thin film.

3. RESULTS AND DISCUSSION

There are different approaches to prepare the films or bulk crystals of organic salts. These include the solution-based techniques, the organic vapor phase deposition techniques, and the melt-based techniques. The solution growth with spontaneous nucleation method has been successfully used to grow the ordered thin film of DAST crystals. Several variables were found to affect the morphology of the crystal grown.

In this study 3 types of DAST crystal in different morphology have been grown. In an open system the orange needle-like DAST crystals were obtained. As shown in Fig.1 the surface of the crystal is quite clean and flat. By comparison with an $8.5/125 \mu\text{m}$ optical fiber it is found that the diameter of the crystal is about $120 \mu\text{m}$. The flatness of the surface and the size reveals that the crystals of this type may manufactured to a useful waveguide by a patented technique⁸.

The polycrystalline DAST thin film, which was formed by many crystalline platelets, was prepared in a closed system, while, with a proper condition, an ordered single crystal thin film was obtained in a saturated solution. Both types of the thin films appeared bright green, metallic luster in reflection and red color in transmission. The results of DSC measurements showed a sharp melting endothermic at 258°C implying high crystallinity. The TGA curves, on the other hand, reveal that the films were thermal stables up to 313°C in both types.

As known, an ordered morphology of the surface of crystal is important for optic applications. Although the surface of the polycrystalline thin film looked flat and shiny as the single crystal thin film, as shown in Fig.2, the optical microscopy exhibits that the surface of the polycrystalline type is actually quite rough and a thin layer orientation is not observed. Usually, surface polish is used to modify it. However, an attempt to polish the film was not successful because it was too small and

not hard enough.

As mentioned in the experimental section, the single crystal thin film prepared in this study was as big as $5 \times 5 \times 1 \text{ mm}^3$, which looked quite ordered on the surface and expected to be useful as a waveguide without further process. The morphology of this thin film was investigated by the combination of FTIR spectroscopy, optical microscopy and image of 3D luminance.

It is known that the intensity of an absorption band in a Fourier transform infrared spectrum is related to the orientation and the average conformation of the corresponding molecules in the sample. Therefore, it may be used to distinguish the crystalline samples with different morphology. Fig.3a and 3b represent the spectrum of the single crystal thin film and that of the polycrystalline thin film, respectively. As can be seen the characteristic absorption bands are similar in both spectra, while the intensities of the bands are different as expected. The higher intensity at 3500 cm^{-1} for the polycrystalline thin film implies that more water was adsorbed on the surface because there are more free volume on the rough surface than the densely packed single crystal. The absorption band at 3040 cm^{-1} is ascribed to the C-H stretching vibration of the methylene units. It is found that the intensity for the ordered single crystal thin film is lower than that for the disordered one. As reported by Pan³ one of the overtones of the C-H stretching vibration at $\nu=3000 \pm 300 \text{ cm}^{-1}$, $\lambda=3.3 \pm 0.3 \mu\text{m}$, is at $\nu=7200 \text{ cm}^{-1}$, $\lambda=1.4 \mu\text{m}$, named B-band. If B-band is too strong when the material is used as a communication window, the transmission loss in $1.3\text{--}1.5 \mu\text{m}$ will be influenced. Since the intensity of the absorption at 3040 cm^{-1} for the single crystal thin film is lower its overtone will be lower correspondingly, we may predict that the single crystal thin film obtained in this study can be a candidate for use as a communication window.

The optical microscopy of the surface of the single crystal thin film is shown in Fig.4a with an $8.5/125 \mu\text{m}$ standard optical fiber in the shadow area as reference. It confirms that the thin film has a perfect ordered surface with small defect. For estimation of the dimension of the lattice the optical microscopy of the standard optical fiber with a laser light passing through its core is shown in Fig.4b. It can be seen that the space between the dark lines along a-axis is about the same dimension as the optical fiber implying that the crystal thin film may be used as a laser light guide. In fact, when a 655 nm laser light was introduced to pass through this thin film, the light was guided along the a-axis direction as expected.

In order to measure the optical transmission intensity of the thin film its 3D-luminance image analysis was carried out. As shown in Fig.5 a quite smooth pattern for the polycrystalline thin film is observed, revealing that the intensities of the lights scattered from the surface of the polycrystalline are similar. This may be ascribed to the isotropy of the scattered lights caused by the roughness of the surface as observed in Fig.2. Therefore, when a laser light passed through the polycrystalline thin film no waveguide was observed in all directions.

On the other hand, an anisotropic pattern was obtained for the intensity profile of 3D luminance image of the single crystal thin film indicating an ordered surface. When a laser light with 655 nm illuminated the single crystal thin film in different directions, the wave guide property was clearly observed along the a-axis direction which is the same direction as that of the pattern lines seen in Fig.3a. This indicates that the laser light may be guided along the gap between the molecular planes of the ions along a-axis direction, which is related to the crystal packing of the thin film. Fig.6 shows the intensity profile of the 3D luminance along the b-axis direction observed in the single crystal thin film illuminated by the laser light (upper curve). The profile for the standard $8.5/125 \mu\text{m}$ optical fiber illuminated by the same laser light (lower curve) is exhibited as a reference. It is found that the intensities of the two guided lights in the thin film are about the same and higher than the intensity of the light of fiber core. By comparing to the diameter of the fiber core ($8.5 \mu\text{m}$), the diameters of the two guided lights and the space between them are about $25 \mu\text{m}$ and $65 \mu\text{m}$, respectively. It reveals that the diameter is wide enough for this crystal to confine a broadband optical fiber with $8.5 \mu\text{m}$ core to transmit high-speed signal and modulate the signal with the state of the art side polished fiber (SPF) technique.

4. CONCLUSION

3 types of DAST crystal in different morphology have been grown in this study. The morphology of each type was investigated by the optic microscopy. By the combination of the results of FTIR spectroscopy, optic microscopy and 3D luminance image analysis, it was found that only the type of single crystal thin film showed an ordered surface and exhibited waveguide property when a laser light with 655 nm wavelength passed through the surface along a-axis. This result indicates that only the single crystal thin film can be used as a waveguide without further process and is a promising candidate for electro-optic modulators and other active optical devices.

References

- 1..S.R.Forrest, P.E.Burrows, A. Stroustrup; D.Strickland ; V.S.Ban "Intense second harmonic generation and long-range structural ordering in thin films of an organic salt grown by organic vapor phase deposition" *Applied Physics Letters* v68 p 1326-1328 1996
- 2.Adachi,H.;Takahashi,Y.;Yabuzaki,J.;Mori,Y.;Sasaki,T."Growth of high quality nonlinear optical crystal 4-dimethylamono-N-methyl-stilbazolium tosylate (DAST)" *J. Cryst. Growth* vol.198 p568 1999
- 3.F. Pan, M. S. Wong, C. Bosshard, and P. Gunter, "Growth and Characterization of the Organic Salt Nonlinear Optical crystal: 4-N,Ndimethylainino-4N'-methyl-stilbazolium Tosylate (DAST)," *Adv. Mater.* vol. 1, pp. 591-594, 1996
- 4.Guang S. He, Raffaella Signorini, Paras N. Prasad, "Longitudinally Two-Photon Pumped Leaky Waveguide Dye Film Laser," *IEEE J. Quantum Electron.*, vol. 34, pp.7-13, 1998.
- 5.Peter Gunter "Optical frequency conversion in inorganic and organic materials" *International Phoronic Conference IPC'98* meeting invited paper, at Taiwan, NTU p FS3-B1
6. J.Xu; A.Mahadevan; L Zhou; M Thakur."Single pass thin film electro-optic modulator based on DAST" *Polymer preprints* vol 39 p1017 1997
7. Pan, F.; McCallion, K.; Chiappetta, M "Waveguide fabrication and high speed intensity modulation in organic crystal 4-N,N-dimethylamino-4 prime -N prime -methylstilbazolium tosylate (DAST)" *Polymer Preprints American Chemical Society Proceedings Meeting of the 1997 Boston* p 1018-1019 1997
- 8.US patent.5094553

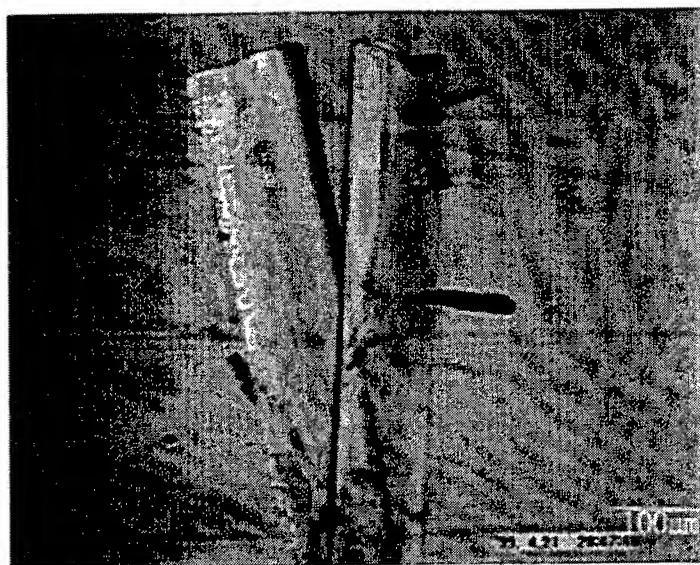


Fig.1. The optical microscopy photograph of the needle-like DAST crystal

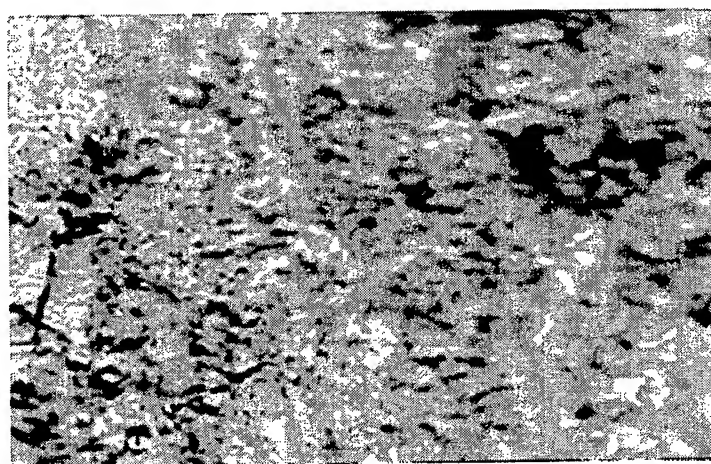


Fig.2. The optical microscopy photograph of surface of the polycrystalline DAST thin film

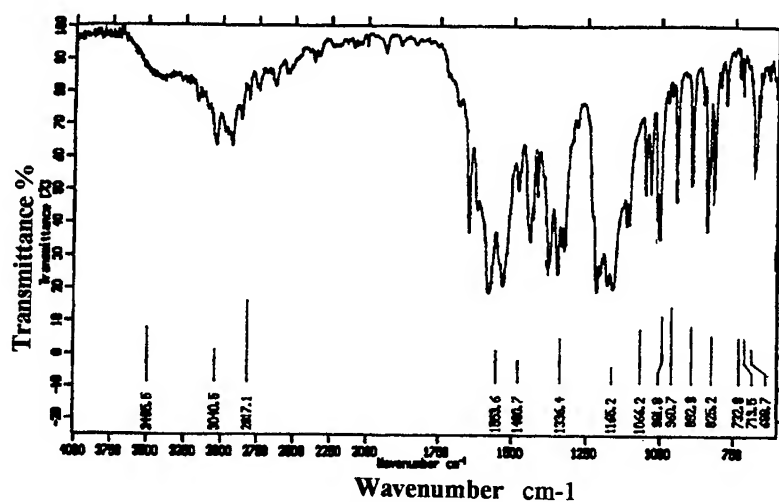


Fig.3a The FTIR spectrum of the single crystal DAST thin film

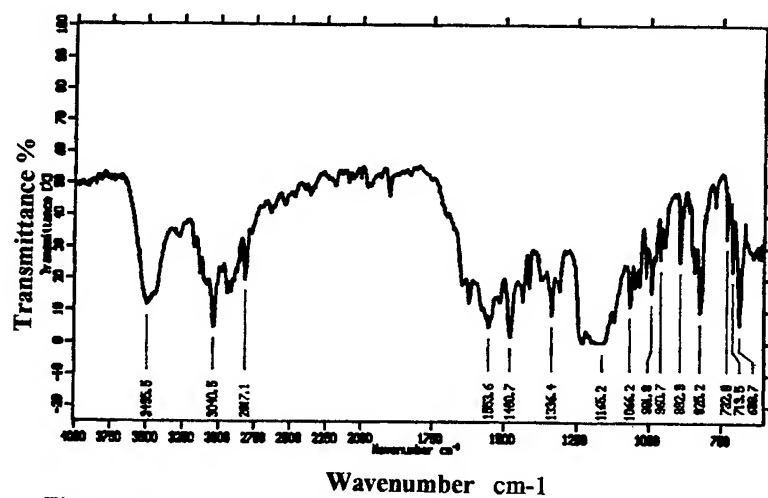


Fig.3b The FTIR spectrum of the polycrystalline DAST thin film

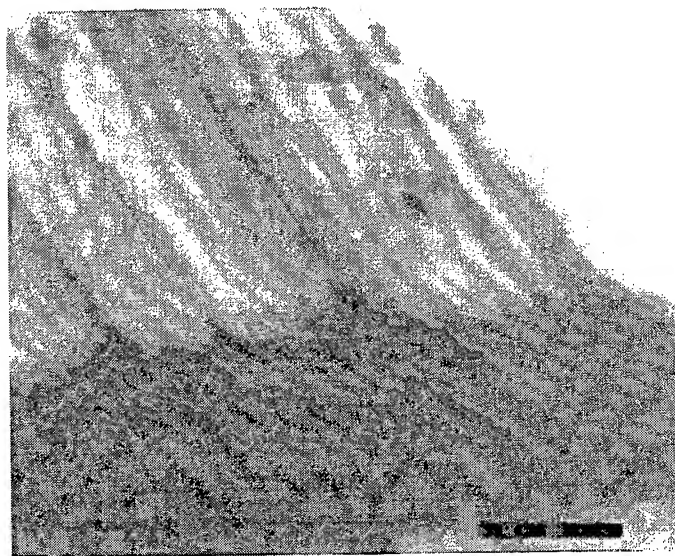


Fig 4a The optical microscopy photograph of the single crystal DAST thin film. The shadow area is a standard single mode 8.5/125 μ m silica optical fiber as a reference.

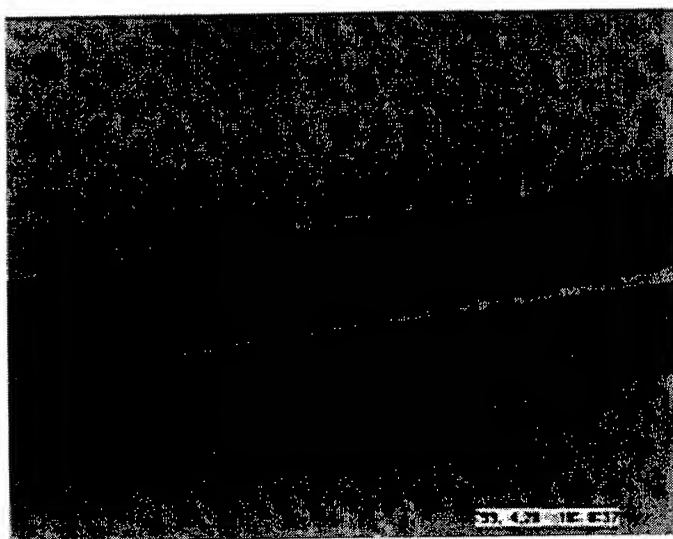


Fig 4b The optical microscopy of an single mode 8.5/125 μ m standard optical fiber with a laser light pass through the fiber core. The photo is with transmitted mode and scale with magnification of 100X.

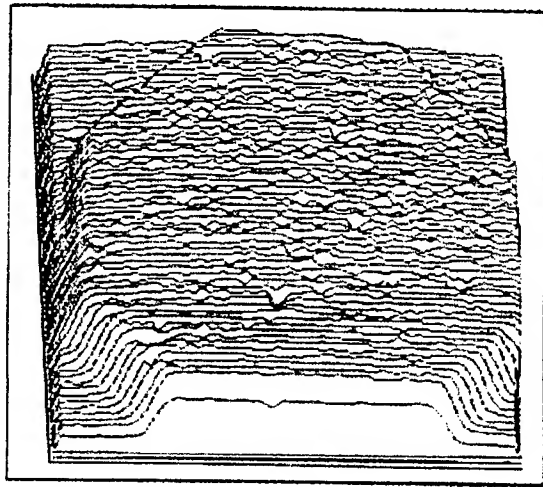


Fig.5. The intensity profile of 3D luminance image of polycrystalline DAST thin film .in transmission mode with magnification of 50x

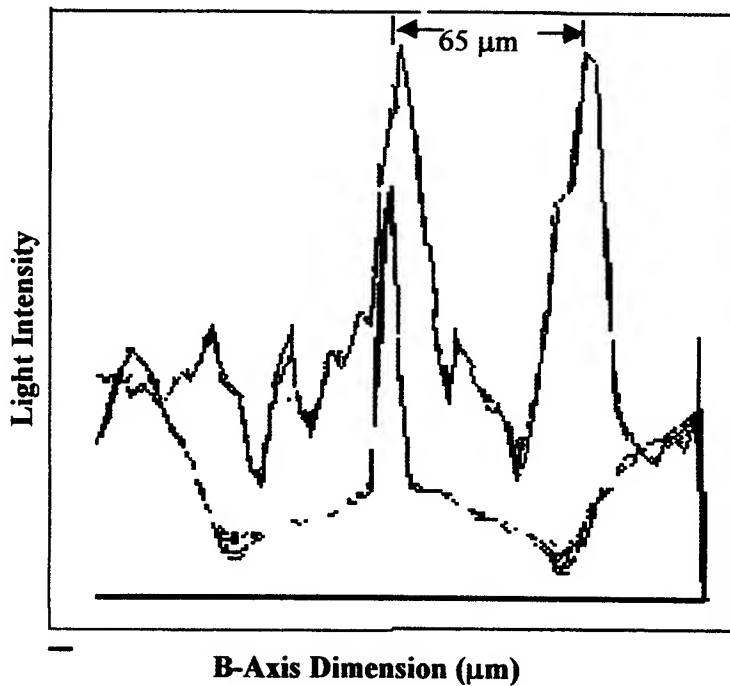


Fig.6. The cross section between the two guided lights of the intensity profile of the 3D luminance image of the single crystal DAST thin film illuminated by a 655 nm laser light along the a-axis direction (upper curve) and that of a standard 8.5/125 μm optical fiber (lower curve).

Optical Refractive Synchronization - Line Width Coherency Analysis And Measurement

James R. Palmer

SilkRoad, Inc.
9707 Waples St.
San Diego, Ca. 92121
U.S.A.

Abstract

The direction of this paper is to describe the various analytical tools and measurement techniques used at SilkRoad to evaluate the transmission - laser cavity control and optical beam train going into the electrooptical modulator and subsequently into the optical transmission fiber. The measurement values for the line width and the coherent length of the laser beam, and the subsequent Laguerre orders that are generated in the electrooptical modulator, are critical to the operation of the SilkRoad *Optical Refractive Synchronization* transmission technique.

We begin the paper with the various analytical techniques that are used to calculate the line width and the coherency length. Following the analytical model, we describe the various measurement techniques and the subsequent data that results from our experiments.

Line width

The line width can be measured either in terms of wavelength ($\Delta\lambda$) or in terms of frequency (Δf). These are related by the expression;

so that, ^{(1),(2),(3),(4)}

$$\Delta f \approx \frac{c}{\lambda^2} \Delta\lambda$$

in like fashion, we can find the value as a function of wavelength such that,

$$\Delta\lambda \approx \frac{\Delta f \lambda^2}{c}$$

where;

c = Speed of light in a vacuum, ⁽⁵⁾ $\approx 3(10^8) \frac{\text{meters}}{\text{second}}$

Δf = Delta frequency, $\frac{\text{cycles}}{\text{second}}$

$\Delta\lambda$ = Delta wavelength, meters

λ = Wavelength of the laser, meters

In like fashion, we need to evaluate the coherency length of the SilkRoad *Optical Refractive Synchronization* technique. In order to obtain the basic coherency length we would use the following;

$$L_w = \frac{c}{\Delta f 2 \pi N} \quad (2)$$

However, because of the techniques used in the *Optical Refractive Synchronization* (6),(7),(8),(9) Technique, we would have,

$$L_w = \frac{4 * N_o * N}{(N_o + N)^2} * \frac{c}{\Delta f 2 \pi N} * L_p^1 \left(\frac{2 * \rho^2}{W(z)} \right) \quad (3)$$

where;

N_o = Real part of the index of refraction of the Optical Modulator
 N = Real part of the index of refraction of the optical fiber.

$$L_p^1 \left(\frac{2 * \rho^2}{W(z)} \right) = \text{Laguerre order} \quad (10)$$

As Gåsvik⁽¹¹⁾ has pointed out, “. . .the gain profile of even nominally monochromatic lasers normally span several longitudinal modes, each with slightly different wavelengths. The basic idea of line width narrowing is to insert into the laser cavity optical elements, which restricts oscillations to a range of wavelengths so narrow that it includes only a single mode.” One of the major reasons for trying to maintain the narrow line width

is suggested by R. Ramaswami and K. N. Sivaarajan⁽¹⁾ who state, “Chromatic dispersion arises for two reasons. The first is the refractive index of silica, the material used to make optical fiber, is frequency dependent. Thus different frequency components travel at different speeds in silica.” The fewer the number of frequencies, the less number of different speeds that need to be contended with. Additionally, the second means of dispersion is the waveguide dispersion. “. . . if the wavelength changes, the power distribution changes, causing the effective index or propagation constant of the mode to change.”⁽¹⁾

The essence, then, of the problem is to insure as narrow a line width as possible starting at the laser cavity. In so doing one is able to minimize both components of chromatic dispersion. In *Optical Refractive Synchronization* we achieve this through the use of the orders of the Laguerre so that the laser beam is not subject to the same type of

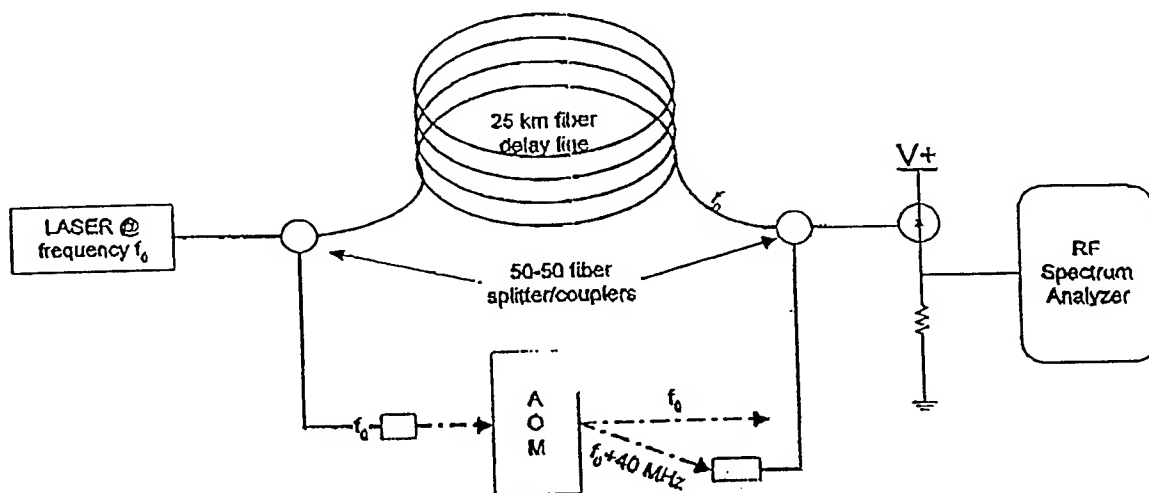
chromatic dispersion suggested by R. Ramaswami and K. N. Sivaarajan⁽¹⁾.

The next part of the problem is to insure that the laser beam comports to the requirements of a TEM₀₀ mode to provide a Hermitian Gauss beam, in the z axis, through the lenticular optical beam train leading to the optical modulator and subsequently into the transmission fiber.

To accurately measure the line width of a laser requires a setup which has greater resolution than is available with optical spectrum analyzers, wavemeters or other grating based instrumentation. At 1.55 μ , a change of 10GHz in frequency roughly equates to a wavelength change of 1 Å (Angstrom). An Optical Spectrum analyzer will resolve down to 0.5 Å, and high quality wave meters down to \approx 0.1 Å. To measure wavelength differences

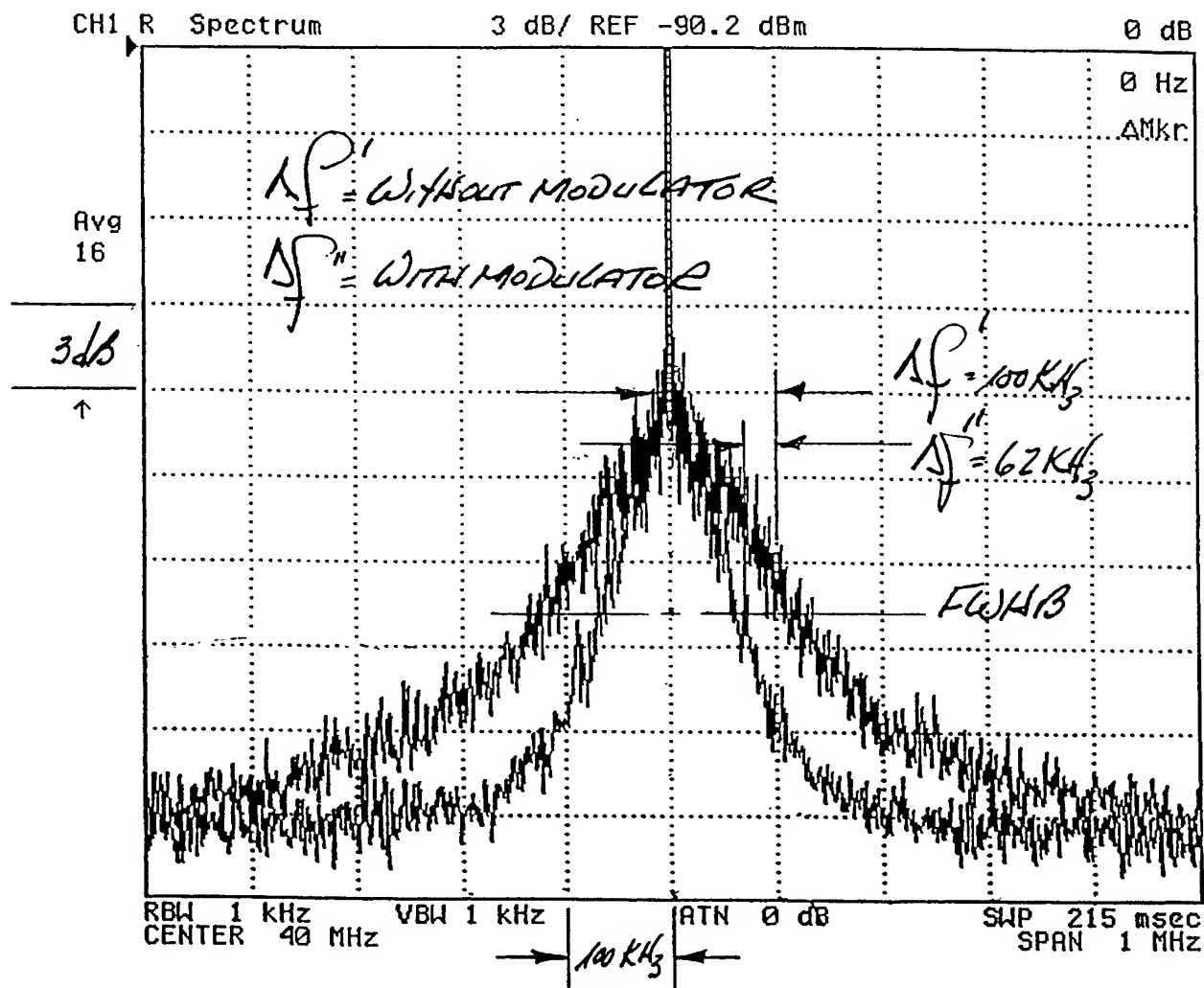
on the order of 1 KHz we need the ability to resolve a wavelength delta of $8(10^{-8}) \text{ \AA}$. To perform the measurement to the necessary resolution we use a homodyne technique shown in Figure 1.0.⁽¹²⁾ The output for the measurement is shown in Figures 2.0 and 3.0. The standard Gaussian technique for evaluating a Gaussian beam is used to determine the FWHB of the Gaussian beam and thereby determine the line width which is half of the FWHB.⁽¹³⁾ D. Derickson⁽¹⁴⁾ provides a complete set of techniques for self-heterodyne evaluation of line width that are valuable in understanding the measurement values. We should go on to say that the beam geometry for the Far Field Fourier Transform follows the work of Palmer.^{(15),(16),(17)}

1. A 50-50 splitter/coupler splits the laser's light into two fiber paths.
2. One path goes through 25 km of fiber. This delay line decorrelates the two paths.
3. The other fiber path goes through an acousto-optic modulator (AOM). It is free space at this point.
4. The AOM deflects some of the light, and frequency shifts the deflected beam by 40 MHz.
5. The frequency shifted light is coupled into a fiber, and is combined in another 50-50 coupler with the light from the delay line. The zero order (undeflected) light from the AOM is not used.
6. The combined signals go to a high frequency photodiode, which responds to the heterodyne signal of the two frequencies.
7. This signal goes into an RF spectrum analyzer, which will show a feature at 40 MHz.
8. The laser's linewidth is the FWHM of the heterodyne signal.



- Optical frequency @ 1550 nm is 192 THz.
- $\Delta f = 10 \text{ GHz} \rightarrow \Delta \lambda \approx 0.08 \text{ nm}$, $\Delta f = 1 \text{ GHz} \rightarrow \Delta \lambda \approx 0.008 \text{ nm}$, $\Delta f = 1 \text{ MHz} \rightarrow \Delta \lambda \approx 0.000008 \text{ nm}$
- The 25 km fiber line is sufficient to decorrelate sources with linewidths down to 4 kHz
- The AOM is driven using a crystal controlled oscillator with a linewidth on the order of 1 Hz, too small to affect our measurement

FIGURE 1.0

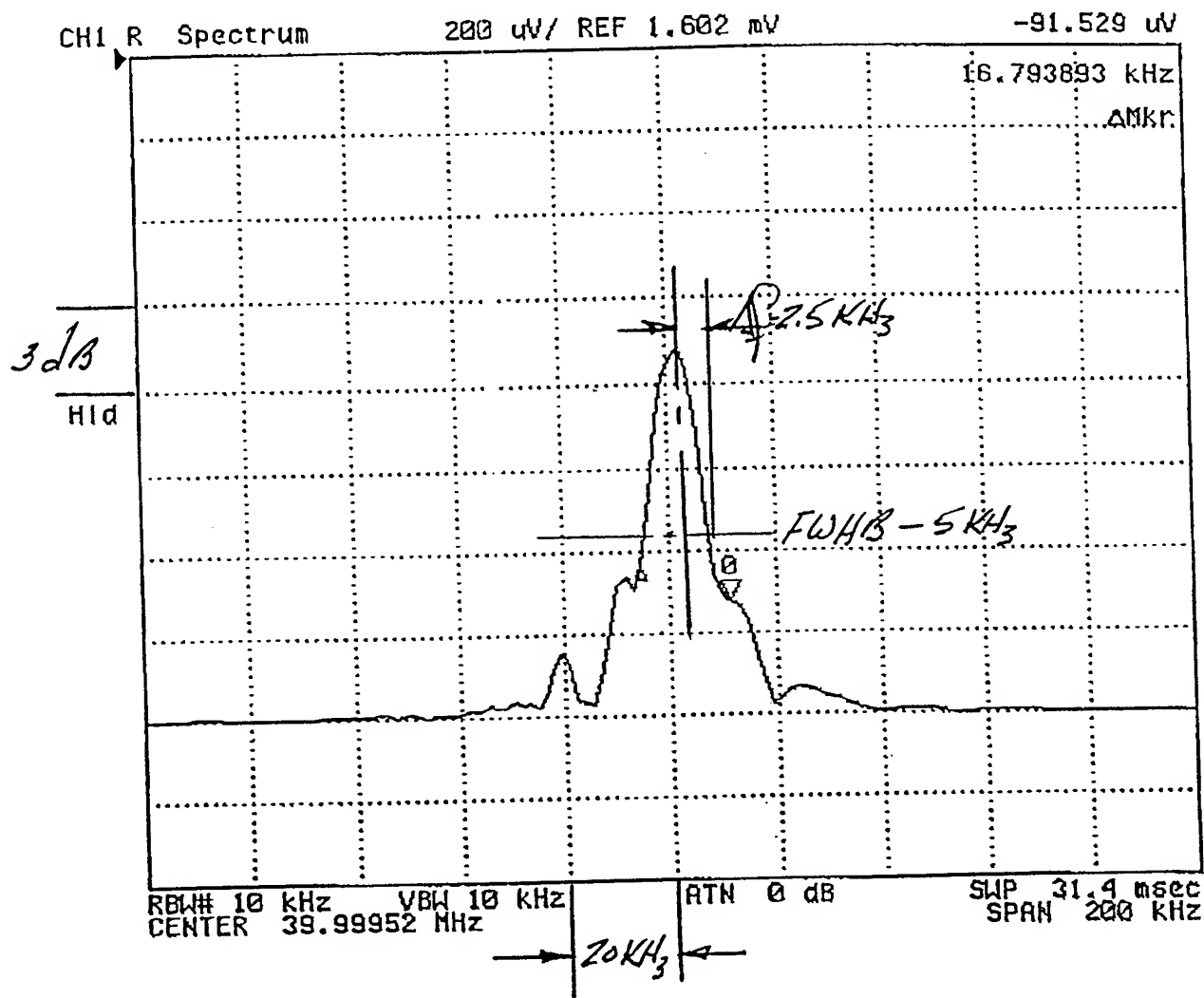


$$\omega \Delta f' = 2.01(10^{-7}) \text{ nm OR } 8.01(10^{-6}) \text{ \AA}$$

$$\omega \Delta f'' = 4.965(10^{-7}) \text{ nm OR } 4.965(10^{-6}) \text{ \AA}$$

LUCENT DFB LASERS

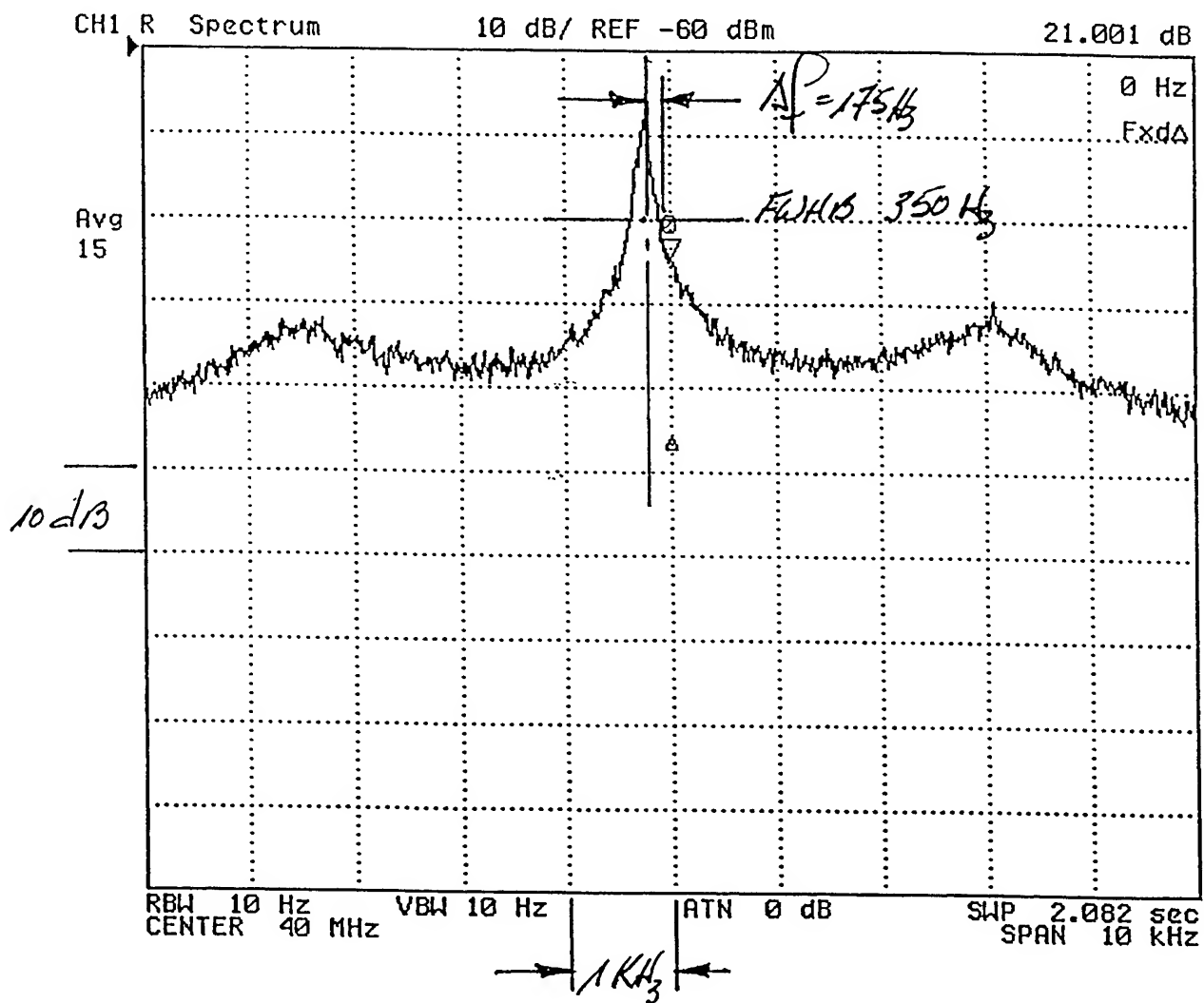
FIGURE 2.0



$$\Delta \nu = 2.002 (10^8) \text{ Hz. or } 2.002 (10^7) \text{ \AA}$$

LASER POWER T-2000 LASER

FIGURE 3.0



$$\Delta \lambda_f = 1.401 (10^{-9}) \text{ nm OR } 1.401 (10^{-8}) \text{ \AA}$$

LASER POWER T-2000 LASER

FIGURE 4.0

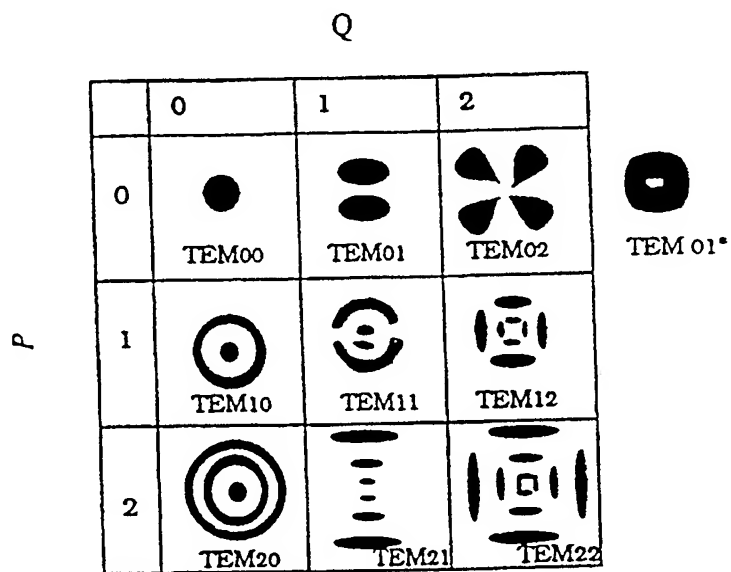


FIGURE 5.0

At this point we need to evaluate the coherency length as a function of the various line widths shown in the figures. In order to do this we will employ Eq. (3) to see how far the various orders of the Laguerre will travel. Then,

$$L_{co} = \frac{4*N_o*N}{(N_o + N)^2} * \frac{c}{\Delta f 2 \pi N} * L_p^1 \left(\frac{2*\rho^2}{W(z)} \right)$$

where;

N_o = Real part of the index of refraction of the Optical Modulator

N = Real part of the index of refraction of the optical fiber.

$L_p^1 \left(\frac{2*\rho^2}{W(z)} \right)$ = Laguerre order (10)

For Lithium Niobate, depending upon the doping function of the Modulator, the real part of the optical index will be ⁽⁹⁾, 2.2151 @ 1.55μ and the k , the imaginary part of the optical index, will be $5.07(10^{-6})$. Then, for the unit under onsideration,

$$W^2(z) = \left\{ R_o^2 \left\{ 1.0 + \left(\frac{\lambda \left(\frac{c \tau}{N_o} \right)^2}{2} \right) \right\} \right\}$$

$$R_o = 1.22 * N.A. * \lambda \quad [9],[15]$$

$$\rho = \sqrt{2 * \left\{ 1.22 N.A. \lambda (2*p + Q + 1.0) \right\}^2} * 0.1743533 \quad [9],[15]$$

p = Radial zero fields of the Transverse modes of the laser.

Q = Angular zero fields of the Transverse modes of the laser. ^{[9],[15]}

note: see Figure 5.0 for different TEM beam shapes.

τ = Time, seconds

We will take a select two problems so that τ will equal 10^{-20} and

10^{-15} seconds from the diffraction limited Airy disc wherein the beam waist is at the smallest value and progressing down the z axis with a Hermetian Gauss beam profile with a TEM₀₀ outcoupled laser beam profile.
then,

$$N.A. = 0.12$$

$$\rho = 1.33999(10^{-7}) \text{ and } \rho^2 = 1.7956(10^{-14})$$

$$R_o = 2.2692(10^{-7})$$

so that,

$$\text{for } \tau = 10^{-20}$$

$$W^2(z) = \left\{ R_o^2 \left\{ 1.0 + \left(\frac{\lambda \left(\frac{c \tau}{N_o} \right)^2}{2} \right) \right\} \right\}$$

and

$$W^2(z) = 5.149268(10^{-14})$$

and

$$\left(\frac{2^* \rho^2}{2}\right) = 0.6974194$$

$$\frac{W(z)}{(\varphi)} = 0.6974194$$

for $\tau = 10^{-15}$

$$W^2(z) = \left\{ R_0^2 \left\{ 1.0 + \left(\frac{\lambda \left(\frac{c \tau}{N_0} \right)^2}{2} \right) \right\} \right\}$$

$$\pi R_0$$

and

$$W^2(z) = 1.382036(10^{-13})$$

and

$$\left(\frac{2^* \rho^2}{2}\right) = 0.25985$$

$$\frac{W(z)}{(\varphi)} = 0.25985$$

For the second order of the Laguerre, we have, for $\tau = 10^{-20}$

$$L_p^2 \left(\frac{2^* \rho^2}{2} \right) = \frac{2 - 4(\varphi) + 1(\varphi)^2}{2!}$$

$$\frac{W(z)}{(\varphi)} = -0.1011$$

order (3)

$$L_p^3 \left(\frac{2^* \rho^2}{2} \right) = \frac{6 - 18(\varphi) + 9(\varphi)^2 - 1(\varphi)^3}{3!}$$

$$\frac{W(z)}{(\varphi)} = -0.4192$$

order (4)

$$L_p^4 \left(\frac{2^* \rho^2}{2} \right) = \frac{24 - 96(\varphi) + 72(\varphi)^2 - 16(\varphi)^3 + 1(\varphi)^4}{4!}$$

$$\frac{W(z)}{(\varphi)} = -1.3123$$

order (5)

$$L_p^5 \left(\frac{2^* \rho^2}{2} \right) = \frac{120 - 600(\varphi) + 600(\varphi)^2 - 200(\varphi)^3 + 25(\varphi)^4 + 1(\varphi)^5}{5!}$$

$$\frac{W(z)}{(\varphi)} = -4.58066$$

order (6)

$$L_p^6 \left(\frac{2^* \rho^2}{W^2(z)} \right) = \frac{720 - 4320(\varphi) + 5400(\varphi)^2 - 2400(\varphi)^3 + 450(\varphi)^4 - 36(\varphi)^5 + 1(\varphi)^6}{6!}$$

$$=-18.0866$$

order (7)

$$L_p^7 \left(\frac{2^* \rho^2}{W^2(z)} \right) = (5040 - 3.528(10^4)(\varphi) + 5.9292(10^4)(\varphi)^2 - 2.94(10^4)(\varphi)^3 +$$

$$7350(\varphi)^4 - 882(\varphi)^5 + 49(\varphi)^6 - 1(\varphi)^7) * \frac{1.0}{7!}$$

$$=-78.543$$

order (8)

$$L_p^8 \left(\frac{2^* \rho^2}{W^2(z)} \right) = (4.032(10^4) - 3.2256(10^5)(\varphi) + 5.6448(10^5)(\varphi)^2 - 3.7632(10^5)(\varphi)^3$$

$$+ 1.1176(10^5)(\varphi)^5 - 18.816(10^4)(\varphi)^5 + 1568(\varphi)^6 - 64(\varphi)^7 +$$

$$1(\varphi)^8) * \frac{1.0}{8!}$$

$$=-356.75$$

order (9)

$$L_p^9 \left(\frac{2^* \rho^2}{W^2(z)} \right) = (3.629(10^5) - 3.226(10^6)(\varphi) + 6.532(10^6)(\varphi)^2 - 5.0803(10^6)(\varphi)^3$$

$$+ 1.9051(10^6)(\varphi)^5 - 3.8102(10^5)(\varphi)^5 + 4.2336(10^5)(\varphi)^6 - 2592(\varphi)^7$$

$$+ 81(\varphi)^8 - 1(\varphi)^9) * \frac{1.0}{9!}$$

$$=-1525.02$$

order (10)

$$L_p^{10} \left(\frac{2^* \rho^2}{W^2(z)} \right) = (3.629(10^6) - 36.288(10^6)(\varphi) + 81.648(10^6)(\varphi)^2 - 72.258(10^6)(\varphi)^3$$

$$+ 31.752(10^6)(\varphi)^5 - 7.6205(10^6)(\varphi)^5 + 1.0584(10^6)(\varphi)^6$$

$$- 8.64(10^4)(\varphi)^7 + 4050(\varphi)^8 - 100(\varphi)^9 + 1(\varphi)^{10}) * \frac{1.0}{10!}$$

$$=-3922.656$$

order (11)

$$L_p^{11} \left(\frac{2^* \rho^2}{W(z)} \right) = (39.917(10^6) - 439.085(10^6)(\varphi) + 1.098(10^9)(\varphi)^2 - 1.098(10^9)(\varphi)^3 \\ + 548.856(10^6)(\varphi)^5 - 153.68(10^6)(\varphi)^5 + 25.613(10^6)(\varphi)^6 \\ - 2.614(10^6)(\varphi)^7 + 1.634(10^5)(\varphi)^8 - 6050(\varphi)^9 + 121(\varphi)^{10} - 1(\varphi)^{11}) * \frac{1.0}{11!} \\ = +37612.235$$

We see, then, that the electric field energy is quite low at the low order of the Laguerre. Additionally, one should note that the orders are counter clockwise up to the 11th order before they begin to become positive in seminal inception. We can then look at the equation for the coherency length for each order of the Laguerre for a fiber having a value of N of 1.448 @ 1.55μ, and taking the value of Δf from Figure 2.0 of 8.01(10⁻⁷) naometers, i.e. 62KHz, and looking at the strength of the orders at (10⁻²⁰) seconds, then,

$$L_{co} = \frac{4 * N_o * N}{(N_o + N)^2} * \frac{c}{\Delta f 2 \pi N} * L_p^1 \left(\frac{2^* \rho^2}{W(z)} \right) \\ L_{co} = 1.898705 * 531.8401 \text{ meters} * L_p^1 \left(\frac{2^* \rho^2}{W(z)} \right)$$

for order 2	$L_{co} = 102.09 \text{ meters}$
for order 3	$L_{co} = 423.31 \text{ meters}$
for order 4	$L_{co} = 1,325.17 \text{ meters}$
for order 5	$L_{co} = 4,625.585 \text{ meters}$
for order 6	$L_{co} = 18,263.98 \text{ meters or } 18.264 \text{ Kilometers}$
for order 7	$L_{co} = 79,313.31 \text{ meters or } 79.3 \text{ Kilometers}$
for order 8	$L_{co} = 3.6025(10^5) \text{ meters or } 360 \text{ Kilometers}$
for order 9	$L_{co} = 1.53996(10^6) \text{ meters or } 1540 \text{ Kilometers}$

The values would change slightly for the longer number of seconds removed from the center of the beam waist. However, the major change is the point where the Laguerre order change from counter clockwise to clockwise at inception. The key element to this problem, of course, is to be able to have a sensor that is capable of sensing these higher orders for the longer distances because of the incipient extinction coefficient associated with the attenuation in the fiber materials.

Conclusion

The foregoing paper has described both the analytical models and experimental test setup with some corresponding measurements to reflect the line width and coherency of lasers presently in use in the SilkRoad *Optical Refractive Synchronization* technique. The thrust of this data is to demonstrate that with the higher order of the Laguerre, the narrow line of the laser coupled with the coherent technique used to place the information onto the E field of the Laguerre's, the beam quality and energy levels will allow for the coherent signals to go significant distances before there is a need to either amplify or regenerate the transmitted signals.

References

1. R. Ramaswami and K. N. Sivaarajan, *Optical Networks: A Practical Perspective*, Morgan, Kaufmann Publishers, Inc., San Francisco, CA., 1998.
2. S. Beeti, G. deMarchis and E. Iannone, *Coherent Optical Communications Systems*, John Wiley and Sons, Inc., New York, NY, 1995.
3. M. Ohtsu, ed., *Frequency Control Of Semiconductor Lasers*, John Wiley and Sons, Inc., New York, NY, 1996.
4. M. J. N. Sibley, *Optical Communications*, McGraw-Hill Book Co., New York, NY, 1990.
5. D. E. Gray, *American Institute Of Physics Handbook*, 3rd. ed., McGraw-Hill Book Co., 1972.
6. J. Gowar, *Optical Communication Systems*, 2nd., ed., Prentice Hall, N.Y., N.Y., 1993.
7. W. H. A. Fincham, *Optics*, 5th ed., Hatton Press, Ltd., London, England, 1949.
8. L. Allen, M. W. Beijersbergen, R. J. C. Spreeuw and J. P. Woerdman, "Orbital Angular Momentum Of Light And The Transformation Of Laguerre-Gaussian Laser Modes," *Physical Review "A"*, Vol. 45, NO. 11, June 1992.
9. J. R. Palmer, *Optical Refractive Synchronization Coherent Information In A Waveguide*, Optical Systems Design And Production Technical University Of Berlin, Germany--26-29 May 1999.
10. R. A. Beth, "Mechanical Detection And Measurement Of The Angular Momentum Of Light," *Physical Review*, Vol. 50, July 15, 1936.
11. K. J. Gåsvik, *Optical Metrology*, 2nd. ed., John Wiley and Sons, Inc., New York, NY, 1995.

12. Personal communication with Laser Power Optics.
13. G. F. Marshall, ed., *Laser Beam Scanning*, Marcel Dekker, Inc., New York, NY, 1985.
14. D. Derickson, ed., *Fiber Optic Test And Measurement*, Prentice Hall, Upper Saddle River, NJ, 1998.
15. J. R. Palmer, W. M., Steen and S. Martellucci, , "Analytical Model For Aberrated Diffraction In High Power CW Laser Beam Trains: Laser Cavity To Work Piece," *Laser Applications For Mechanical Industry*, Series E: Applied Sciences - Vol. 238, NATO ASI Series, Kluwer Academic Publishers, London, England, (1992).
16. J. R. Palmer, "Analytical Model For Transient Strehl Ratio Distribution In Soft X-Ray Optical Systems," *Proc. International Conference On Soft X-Ray Optics And Technology*, SPIE No 733, Berlin, Germany, 1986.
17. J. R. Palmer, *High Power Laser Optics*; 2nd ed., Pro Se Publishing Co., San Diego, CA, 1995.

Correspondence: Email: james.palmer@silkroadcorp.com; <http://www.silkroadcorp.com>;
Telephone: 858-457-6767; Fax: 858-457-6757

Analyses of Stark effect modulation with Doppler broadening at 10.784 μ m

Dayong Zhu^{*a}, Zuowen Wan^b, Zhuoxun Zhang^a

^aDepartment of Opto-electronic Technology,
University of Electronic Science and Technology of China

^b Southwest Institute of Technical Physics

ABSTRACT

The Stark effect modulations with Doppler broadening have been analyzed by semiclassical theory. The absorption coefficient and modulating depth of Stark effect system have been derived by density matrix method. Modulation characteristics between R(18) line of the isotopic $^{13}\text{CO}_2$ laser at 10.784 μ m and asQ(6,6) transition of NH_3 molecular have been researched. When modulating frequency is 1MHz, modulating depth reaches 33%. An isotopic $^{13}\text{CO}_2$ laser, which outputs 4W and has 25 lines of spectrum, was fabricated. Instability of laser intensity is less than 1%.

Keywords: Laser modulation, Stark effect, Doppler broadening, isotopic $^{13}\text{CO}_2$ laser, Paschen breakdown, modulating depth, frequency response

1. INTRODUCTION

The molecular Stark effect in the infrared field was used to research the level structure of the molecular in the early time. It is used to research modulation of laser ¹, frequency stability ² of laser and optical bistability ³ in recent years. Some Stark devices find their latent applications such as free space communication ⁴ and laser radar⁵. Theory of Stark effect modulation with homogeneous broadening was reported ¹ in the past. The Stark effect modulation with Doppler broadening has been analyzed using semiclassical theory in the paper and corresponding experimental results in the wavelength of 10.784 μ m has been given.

2. THEORETICAL ANALYSES

Stark effect modulation of NH_3 molecular will be discussed in the paper. When no voltage is applied to the Stark cell, the transition frequency of NH_3 molecular is $\omega_{ab}(0) = (\omega_a + \omega_b)/\eta$. When the voltage V is applied to the cell, frequency shift $\Delta\omega = RV$ is produced due to Stark effect, where R is constant relative to level structure. The voltage applied to the cell is $V = V_b - V_m \cos(\nu t)$, where V_b is the bias voltage and $V_m \cos(\nu t)$ is AC modulation voltages.

Because width of homogeneous broadening is in the order of 0.75MHz/Pa ⁶ and the pressure of NH_3 molecular in the cell is low (40Pa), the homogeneous broadening is 30MHz and just 1/3 of width of Doppler broadening (84MHz). Therefore Doppler broadening is dominant. It is difficult to analyze the system of Stark effect modulation in the form of total broadening. For simplify, we only consider the modulation with Doppler broadening. The absorption coefficient is

* Correspondence: Email: dyzhu@uestc.edu.cn; Telephone: (028)3203369; Fax: 3334131

expressed by electric susceptibility

$$\alpha(\omega, t) = (\omega/c) \text{Im} \chi \quad (1)$$

and polarization is

$$P(z, t) = \text{Re}[\epsilon_0 \chi E(z, t)] \quad (2)$$

where χ is electric susceptibility.

The polarization is given by the element of density matrix, that is

$$P(z, t) = \Re \int dv D \rho_{ab}(z, v, t) + \text{c.c} \quad (3)$$

where D is the molecular dipole moment, \Re is matrix element which is relative to Einstein coefficient A_{ab} . From the equation of motion of density matrix, we have

$$\rho_{ab}(z, v, t) = -(i\omega_{ab} + \gamma) \rho_{ab}(z, v, t) + i\hbar^{-1} F(z, t)_{ab} [\rho_{aa}(z, v, t) - \rho_{bb}(z, v, t)] \quad (4)$$

where γ is absorption coefficient of small signal. Using the transformation $T = t - t'$ and considering the interaction of radiation field ,

$$F(z, t)_{ab} = -\frac{1}{2} DE(z, t) e^{-i(\omega t + \phi - kt)} e^{i(\omega - kv)t} \quad (5)$$

equation (4) can be rewritten as

$$\begin{aligned} \rho_{ab}(z, v, t) &= -[DE(z, t)/2\hbar] [\rho_{aa}(z, v, t) - \rho_{bb}(z, v, t)] i \int_0^\infty dt' \exp[-i \int_{t-T}^{t'} (\omega_{ab} - \omega) dt' - \gamma T - ikvt] e^{-i(\omega t + \phi - kz)} \\ &= -[DE(z, t)/2\hbar] f(v, t) [\rho_{aa}(z, v, t) - \rho_{bb}(z, v, t)] e^{-i(\omega t + \phi - kz)} \end{aligned} \quad (6)$$

where

$$f(v, t) = i \int_0^\infty dt' \exp[-i \int_{t-T}^{t'} (\omega_{ab} - \omega) dt' - \gamma T - ikvt] \quad (7)$$

$\rho_{aa}(z, v, t) - \rho_{bb}(z, v, t)$ is the population inversion in the equation (6), and is negative in the case of absorption . Because the velocity distribution of the molecular is Maxwell-Boltzman distribution, the molecular numbers N between v and $v+dv$ is

$$N(v)dv = (N/u) \sqrt{\pi} \exp(-v^2/u^2) dv \quad (8)$$

where N is density of molecular, u is the most probable velocity :

$$u = \sqrt{2K_r T / M} \quad (9)$$

where T is gaseous temperature, M is the molecular mass, K_r is the Boltzman constant.

If the gaseous absorption is not saturated by the incident light, we have

$$\rho_{aa}(z, \nu, t) - \rho_{bb}(z, \nu, t) = -N(\nu)N \quad (10)$$

Substituting it into equation 6, we obtain

$$\rho_{ab}(z, \nu, t) = [E(z, t)N(\nu)f(\nu, t)]ND/\hbar \quad (11)$$

We will discuss two kinds of modulation according to its frequency in the following.

1) low-frequency modulation. In this case, $\nu \ll \gamma$ (ν is frequency of the modulation, γ is the absorption coefficient of small signal. In the case of Doppler broadening, γ is equal to Doppler broadening $\Delta\omega_D$). From equation 11, we obtain

$$\rho_{ab}(z, \nu, t) = ND/\hbar [E(z, t) - iN(\nu)/\gamma + i(\omega_{ab} - \omega + k\nu)] \quad (12)$$

where $k = \omega/c$. Substituting equation (12) into equation (3), we have absorption coefficient,

$$\alpha(\omega, t) = ND^2\omega \sqrt{\pi}/c\epsilon_0\hbar k u \cdot \exp[-(\omega_{ab} - \omega)^2/(ku)^2] \quad (13)$$

Setting $\alpha_0 = 2ND\omega/c\epsilon_0\hbar k u$ and $\Delta\omega_D = ku\sqrt{\ln 2}$, we obtain the absorption coefficient

$$\alpha(\omega, t) = \alpha_0 \exp[-4\ln 2 (\omega_{ab} - \omega)^2 / \Delta\omega_D^2] \quad (14)$$

From equation (14), the absorption coefficient of Stark modulation with Doppler broadening is Gaussian line shape. Defining modulation depth as the ratio of AC peak-to-peak value and DC value, modulation depth per length is

$$[MD/L] \approx (\Delta\alpha)_1 + (\Delta\alpha)_2 \quad (15)$$

where

$$(\Delta\alpha)_1 = [\alpha(\omega, t)_{\max}] - [\alpha(\omega)_{dc}]$$

$$(\Delta\alpha)_2 = [\alpha(\omega)_{dc}] - [\alpha(\omega, t)_{\min}]$$

Substituting equation (14) into equation (15), we obtain the following equation :

$$[MD/L] = 16\ln 2 \sqrt{\pi} \cdot \omega' | \omega_{ab} - \omega | \exp[-4\ln 2 (\omega_{ab} - \omega)^2 / \Delta\omega_D^2] \quad (16)$$

2) high-frequency modulation. In this case, $\nu > \gamma$, the absorption coefficient is Bessel function:

$$\alpha(\omega, t) = (4\alpha_0/\sqrt{\pi}) J_0(\omega'/\nu) J_1(\omega'/\nu) \cos(\nu t + \Phi_s) \exp(-\varpi^2/k^2 u^2) \int_0^{\varpi/k\nu} e^{x^2} dx \quad (17)$$

where $\varpi = \omega_{ab} - \omega$. Substituting it into equation (15), we obtain the equation (18) of modulation depth per length.

$$[MD/L] = 8\alpha_0/\sqrt{\pi} \cdot J_0(\omega'/\nu) J_1(\omega'/\nu) \exp(-\varpi^2/k^2 u^2) \int_0^{\varpi/k\nu} e^{x^2} dx \quad (18)$$

In the case of high-frequency modulation, ω'/ν is very small, Bessel function $J_1(\omega'/\nu) \approx \omega'/\nu$, and $J_0(\omega'/\nu) \approx 1$, then equation (18) is rewritten as

$$[MD/L] = 8\alpha_0/\sqrt{\pi} \cdot (\omega'/\nu) \exp(-\omega^2/k^2 u^2) \int_0^{\omega/k\nu} e^{x^2} dx \quad (19)$$

In conclusion, in the case of low-frequency modulation (equation 6), modulation depth is independent of modulating frequency, and the maximum Stark shift ω' is in proportion to amplitude of modulation signal V_m , thus $[MD/L]$ is in proportion to V_m . In the case of high-frequency modulation (equation 19), modulation depth decreases with increasing modulation frequency. These results will be proven by later experimental results.

3. EXPERIMENTS AND DISCUSSION

The experimental setup is shown in Fig. 1. The light source is an isotopic $^{13}\text{CO}_2$ laser, which uses invar with small thermal expanding as compartment to support mirrors and grating. The laser can oscillate in different lines by tuning the grating. Discharge tube of the laser is 60cm long and diameter is 8mm. Two ends of the tube are sealed by ZnSe windows with Brewster angle. Ratios of gaseous mixtures of the laser are $^{13}\text{CO}_2: ^{16}\text{N}_2:\text{Xe}:\text{He}=3.6:3.6:1:10$. The total gaseous pressure is 2426Pa. The laser outputs single mode, linearly polarized beam. The maximum output power is about 4W. Additionally, we take some measures such as controlling of temperature and pressure of cooling water. The instability of laser intensity is less than 1%.

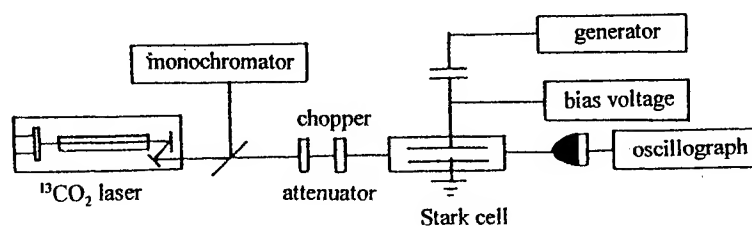


Figure 1. Experimental arrangement

Table 1. Comparison of $^{13}\text{CO}_2^{16}$ with $^{12}\text{CO}_2^{16}$ energy level relative to ground state (00⁰0)

Energy Level	$^{13}\text{CO}_2^{16}$ (cm ⁻¹)	$^{12}\text{CO}_2^{16}$ (cm ⁻¹)
00 ⁰ 1	2283. 5	2349. 3
00 ⁰ 1	1370. 1	1387. 8
02 ⁰ 0	1265. 8	1285. 4
01 ¹ 0	632. 9	667. 3
00 ⁰ 1-00 ⁰ 1	913. 3	960. 9
00 ⁰ 1-02 ⁰ 0	917. 7	963. 9

Comparing isotopic $^{13}\text{CO}_2$ laser with common $^{12}\text{CO}_2$ laser, energy of all levels is some low. Energy gaps relative to ground

state are listed in Tab.1. Energy level 00^01 and 10^00 are very close. Fermi resonance between two levels forms $[10^00, 02^00]$ I band and $[10^00, 02^00]$ II band. Transitions between upper energy level 00^01 and $[10^00, 02^00]$ I band form band of $10.9\mu\text{m}$ (common $^{12}\text{CO}_2^{16}$ transitions are band of $10.4\mu\text{m}$). Transitions between energy level 00^01 and $[10^00, 02^00]$ band II form band of $9.8\mu\text{m}$ (common $^{12}\text{CO}_2^{16}$ transitions are band of $9.4\mu\text{m}$). According to rules of transitions $\Delta J = \pm 1$, two bands have 60 branches respectively. However it is difficult to observe all spectrums in general ways. We observe 13 lines of P branch and 12 lines of R branch in $[10^00, 02^00]$ I band with high gain.

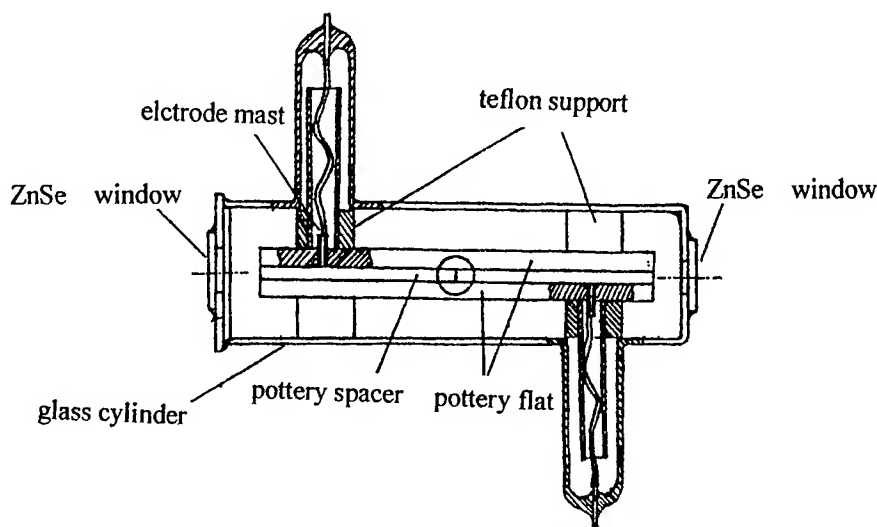


Figure 2. Stark cell configuration

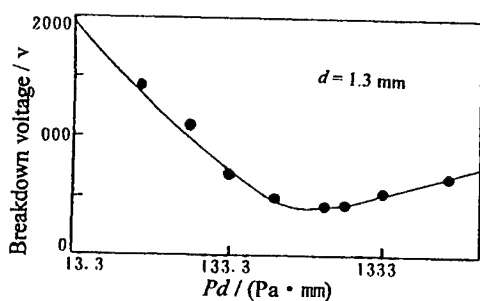


Figure 3. (a) Paschen curve of NH_3 Stark cell

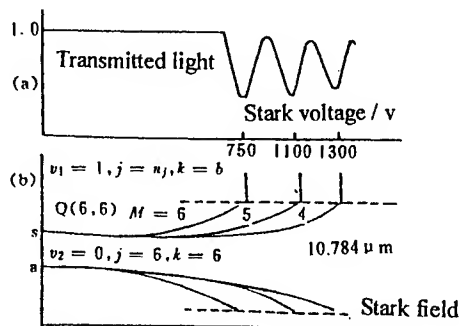


Figure 4. NH_3 Stark absorption spectrum (b) Relevant Energy levels of a $Q(6,6)$ for the interaction of $R(18) ^{13}\text{CO}_2$ laser

The Stark cell is the key element. Inside it there is a pair of plates terminated by a matching load, as shown in Fig.2. It is 10cm long and has a 1.2mm plate separation. One of the most important parameters of the cell is Paschen breakdown voltage which depends mainly on pd value (multiplier of pressure p and separation distance d) and is also relative to gaseous characteristic, electrode material and electrode planeness. Besides discharge between two plates, there exist long-

distance discharges caused by electrode margins and electrode down-leads. Due to very low breakdown voltages which are much lower than working voltage, long-distance discharge must be avoided. We take a lot of measures such as polish of ceramic plates, golden deposition of plates and shield of electrode down-leads, so that breakdown voltage is only depend on pd values. Pressure of gas in the cell is very low. It works in the vicinity of $pd=48\text{Pa}\cdot\text{mm}$ in the left branch of Paschen curves. Paschen curve of NH_3 Stark cell is shown in Fig.3.

In order to detect signals of high frequency, HgCdTe detector cooled by liquid nitrogen (77k) is chosen and output signals are displayed and tested in an oscilloscope.

What we are interested in is the interaction between the transition $Q(6,6)$ of NH_3 molecular and R(18) line of isotopic $^{13}\text{CO}_2$ laser at $10.784\text{ }\mu\text{m}$. Energy levels of NH_3 molecular are shown in Fig.4b. The Stark field is dependent on polarization of laser. When Stark field is parallel to polarization, the maximum absorption coefficient is obtained and Fig.4a shows such results.

Tuning the angle of grating, the laser can run at R(18) line and output at $10.784\text{ }\mu\text{m}$. The laser beam is chopped. When no voltages is applied to Stark cell, NH_3 molecules don't absorb laser light at all and the absorption coefficient is zero, then the transmission through the Stark cell is 1. When an electric field is applied to a cell containing NH_3 molecular, the Stark effect acts to mix and split the two lower states into 7 components each, designed by $|M|=6,5,\dots,0$. As the electric field increase to $6.5\text{--}9.8\text{ kV/cm}$, successive $|M|$ sublevels of the two state are brought into resonance with the $^{13}\text{CO}_2$ laser frequency, then an absorption line appears in the voltage-dependent transmission spectrum, shown in Fig.4a. The absorption coefficient of the first peak is very large. Its value is

$$\alpha_0 = \ln[I_{\text{out}}(0)/I_{\text{out}}(V_0)]/L \quad (20)$$

where L is plate length, $I_{\text{out}}(0)$ is intensity in the case of no Stark field, $I_{\text{out}}(V_0)$ is the intensity in the case of resonant absorption. From equ.20, we obtain

$$\alpha_0 = 6.8 \times 10^{-3} \text{ cm}^{-1} \text{ Pa}^{-1}$$

After removing the chopper, we can measure the modulating depth by applying the AC modulation signals and DC bias voltages. The depth of modulation is defined as

$$MD = \frac{I_{\text{max}} - I_{\text{min}}}{I_{\text{max}} + I_{\text{min}}} \times 100\% \quad (21)$$

where I_{max} and I_{min} is the maximum and minimum value of modulating signals. The relation between depth of modulation and peak-peak voltages of modulation signal is shown in Fig.5, when frequency of modulation is 20 kHz , pressure of the gas is 30 Pa , the bias voltage is 740 V . As shown in Fig.5, depth of modulation is in proportion to voltage of modulation. This is because Stark shift of the lower states varies with the electric field and splitting of the excited state is neglected. Experimental results correspond to theoretical analyses. Frequency response curve of modulation system is shown in Fig.6. The depth of modulation can reach 50% and is independent of modulating frequency in the case of low frequencies. When modulating frequency is large than 200 kHz , modulation depth begin to decrease. At 1 MHz modulating frequency, modulation depth is 33% . When modulation frequency reaches 10 MHz , modulation depth decrease to 4.8% . Theoretical

analyses also give corresponding results. However frequency response is much lower than that of theoretical analyses, this is because load doesn't match well in the system. If load matching is improved, better experimental results are expected. Modulation waveforms are shown in Fig.7 when modulation frequency $f=2\text{MHz}$.

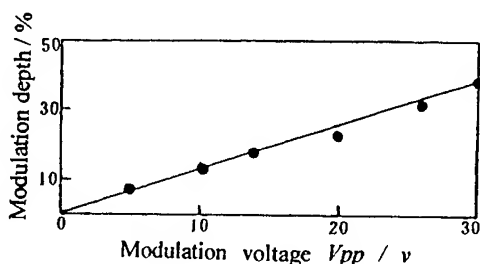


Figure 5. variation of modulation depth with modulation voltage
($v_b=740\text{V}$, $p=30\text{pa}$, $f=20\text{kHz}$)

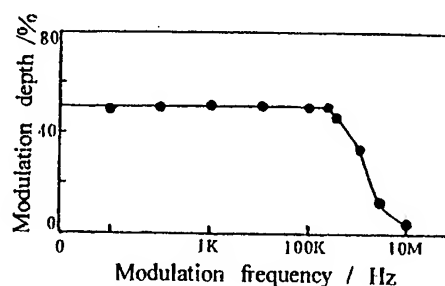


Figure 6. Frequency response curve of Stark modulation
($v_{pp}=20\text{V}$, $v_b=740\text{V}$, $p=30\text{pa}$)

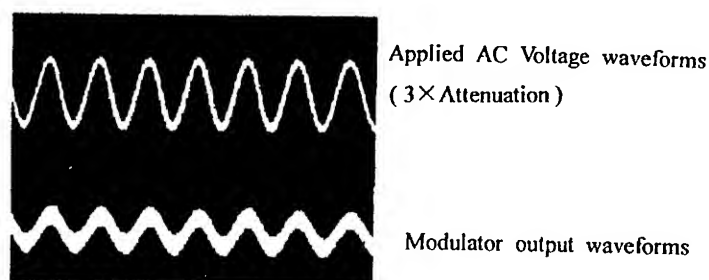


Figure 7. Stark effect modulation waveform at 2MHz ($v_b=740\text{V}$, $p=30\text{pa}$, $v_{pp}=20\text{V}$)

4. CONCLUSION

The Stark effect modulations with Doppler broadening have been analyzed theoretically. The absorption coefficient and modulating depth of Stark effect system have been derived. The absorption coefficient is Gaussian-shape distribution. Modulation characteristics between R(18) line of the isotopic $^{13}\text{CO}_2$ laser at $10.784\text{ }\mu\text{m}$ and asQ(6,6) transition of NH_3 molecular have been researched. Theoretical results coincide with experimental results. In order to improve modulating depth and modulating bandwidth, it is important to improve further load matching and circuit shields. $^{13}\text{CO}_2$ laser is a light source which has very good transmission characteristic of atmosphere⁹ and can find many applications in laser radar¹⁰ and is also used as frequency reference¹¹ in the $11\text{-}\mu\text{m}$ wavelength region, so research on C^{13}O_2 ¹⁶ laser and its modulation is important in this field.

5.ACKNOWLEDGMENT

The authors wish to thank associate Prof. Naiqun Ye for her help.

REFERENCES

1. P.C Claspy and Yoh-han Pao, "Basic characteristics of high-frequency Stark-effect modulation of CO₂ laser" ,*IEEE J.Quantum Electron.*,**QE-7**,PP. 512-519,1971.
2. S.A Rackley and R.J Butcher, "Stabilization of carbon dioxide lasers using the Stark effect" , *J.Phys*, **16**.pp.505~516, 1983.
3. David m and M.B Klein, "Observation of mirrorless optical bistability and optical limiting using stark tunable gases" , *IEEE J.Quantum Electron.*, **QE-15**,PP. 1979.
4. Dayong Zhu,Zuowen Wan,Xuecai Yu,Naique Ye, "Bistable optical devices for the isotopic C¹³O₂¹⁶ laser communication" ,*Proc.SPIE 1635*,pp.144-151, 1992.
5. Dayong Zhu, Xuecai Yu, Naique Ye, Zuowen Wan, "Research on frequency stabilization and offset frequency locking for coherent CO₂ laser rader", *Proc.SPIE 1633*,pp.330-336,1992.
6. D.M.pepper,M.B.Klein, " Tunable optical filters, modulators, and limiters using Stark-induced birefringence and dischromatism", *Appl.Phys.Lett.*,**48**,pp.567-569, 1986.
7. koichi shimoda, *Introduction to laser physics*, springe-Verlag, New York, Tokyo, London,1986.
8. C.K.Asawa and T.K.Plant, wideband modulation of the ¹³CO₂¹⁶ laser R(18)line at 10.784 μ m with an N¹⁴H₃ Stark cell" ,*Apli.Phys.Lett.*,**30**,pp.96-98,1977
9. R.C.Hayney, "comparison of techniques for long-range laser ranging", *proc.SPIE*, **783**.pp.91-100,1987.
10. R.K.Ackerman,"Laser radar discriminates against decoy targets" ,*Signal*,1990,**6**.pp.41-42
11. Che-hung chou,K.R.Zink,A.G.Maki,and Jow-Tsong Shy,"New CO₂ lasers in the 11-μm wavelength region: new hot bands", *IEEE J.Quantum Electron.*, vol.**QE-15**,PP.343-345 1995.

Theoretical comparison of 0.78% tensile strained InGaAs/InAlGaAs and InGaAs/InGaAsP quantum-well lasers emitting at 1.55 μm

Hong Khai Khoo^a, Soo Jin Chua^b

Department of Electrical Engineering, National University of Singapore

ABSTRACT

0.78% tensile strained InGaAs/InAlGaAs and InGaAs/InGaAsP QW lasers emitting at 1.55 μm are studied theoretically. Independent of material system, large band discontinuity (large barrier band gap) results in a large number of subbands and high density of states, which gives rise to lower optical gain and T_0 . Besides, the 3 dB bandwidth is increased and is more resilient to high temperature. InGaAs/InAlGaAs QW lasers (0.78% strained, barrier band gap = 1.12 eV) can achieve threshold of 572 Acm^{-2} , T_0 of 45K and 3 dB bandwidth of 38 GHz at gain of 100 cm^{-1} . InGaAs/InGaAsP QW lasers (0.78% strained, barrier band gap = 1.2 eV) can only achieve 22 GHz. This suggests that the low conduction band offset ratio limits the bandwidth of InGaAs/InGaAsP QW lasers. InGaAs/InAlGaAs laser, on the other hand, could be designed to give low threshold, large bandwidth and high T_0 .

Key words: InAlGaAs, InGaAsP, tensile strain.

1. INTRODUCTION

Quantum well lasers emitting at 1.55 μm draw considerable attention because of the superior interest for large capacity optical communication system. Low threshold current and high optical gain are the most appreciated properties. In this respect, strained QW lasers have received special interest since 1986, for it was predicted theoretically to improve the performance of QW lasers¹⁻³. To date, enhanced performance and reliable strained layer QW lasers have been reported with the wells grown under compressive as well as tensile strain for InGaAs(P)/InP and InAlGaAs/InP telecommunication lasers. The dramatic impact of the use of strained-layer QW's is best illustrated by the fact that they are already used in advanced commercial visible, near infrared, and telecommunication lasers.

Introduction of strain into QW lasers has been shown to lead to reduction in threshold current density. Reduction in threshold current density were observed for both compressive as well as tensile strained InGaAsP SQW lasers, with a minimum as low as 92 Acm^{-2} for 1.1 cm cavity length 1.6% tensile strained InGaAs/InGaAsP SQW laser⁴⁻⁵. For compressive strained SQW lasers, minimum threshold current density around $140\text{-}160 \text{ Acm}^{-2}$ were observed for devices ranging from 4.5 to 3.5 mm in cavity length and employing ternary InGaAs⁶⁻⁷ and quaternary InGaAsP⁸.

On the other hand, experimental results using MOCVD growth, by Kasukawa *et al.*⁹, obtained very low threshold current densities on InAlGaAs based lasers: 640 Acm^{-2} for lattice matched for QW lasers; 400 Acm^{-2} for 1% compressive strained three QW lasers; and 200 Acm^{-2} for single 1% tensile strained QW lasers.

These promising experimental results described above have prompted the authors to focus their study on the strained QW lasers. Further, theoretical study on tensile strained QW lasers has revealed the superiority of these lasers over the compressive strained QW laser¹⁰. Experimental results as described above also showed that the lowest threshold current is achieved at 1.6% of tensile strain. In this respect, **the authors focused their study on tensile strained QW lasers.**

Besides, literature¹¹⁻¹⁶ has shown that the band discontinuity affects the optical gain, threshold current and temperature sensitivity of QW lasers. Ref. [11] has shown that the large conduction band discontinuity of InAlGaAs lasers lead to lower laser thresholds, higher output intensities, and higher T_0 . Ref. [9] also showed that InAlGaAs based lasers could achieve threshold current density comparable to InGaAsP based lasers. In this respect, InAlGaAs and InGaAsP which differs

^a Email: HongKhai@techsemi.com.sg

^b Email: elechj@nus.edu.sg

in conduction band offset ratio, prompted the authors to study **tensile strained InGaAs/InAlGaAs and InGaAs/InGaAsP QW lasers** to investigate the role of band discontinuity and conduction band offset ratio in the optical gain, threshold current, modulation response and temperature sensitivity.

2. THEORY

2.1 Band Structure

In order to understand the optical properties of semiconductor, such as absorption or gain due to electronic transitions in the presence of an incident optical wave, the electronic structure, including the energy band and wave function, has to be known. In this work, the conduction band is assumed decoupled from the valence band. It is further assumed that the conduction subbands are parabolic. On the other hand, the valence band is described by 4x4 Luttinger-Kohn Hamiltonian¹⁷. The wave function satisfies the Hamiltonian equation

$$\begin{bmatrix} P+Q-V(z) & \tilde{R} \\ \tilde{R}^+ & P-Q-V(z) \end{bmatrix} \begin{bmatrix} F^{(1)}(k_t, z) \\ F^{(2)}(k_t, z) \end{bmatrix} = E(k_t) \begin{bmatrix} F^{(1)}(k_t, z) \\ F^{(2)}(k_t, z) \end{bmatrix} \quad (1)$$

$$\begin{aligned} P &= \frac{\hbar^2 \gamma_1}{2m_0} (k_t^2 - \frac{\partial^2}{\partial z^2}) \\ Q &= \frac{\hbar^2 \gamma_2}{2m_0} (k_t^2 + 2 \frac{\partial^2}{\partial z^2}) \\ \tilde{R} &= \frac{\hbar^2 \sqrt{3}}{2m_0} \gamma k_t^2 - \frac{\hbar^2 \gamma_3}{2m_0} 2\sqrt{3} k_t \frac{\partial}{\partial z} \\ \tilde{R}^+ &= \frac{\hbar^2 \sqrt{3}}{2m_0} \gamma k_t^2 + \frac{\hbar^2 \gamma_3}{2m_0} 2\sqrt{3} k_t \frac{\partial}{\partial z} \\ \gamma &= \frac{\gamma_2 + \gamma_3}{2} \end{aligned} \quad (2)$$

where P, Q, and \tilde{R} are all differential operators. k_t , γ_1 , γ_2 and γ_3 are transverse wave vector and Luttinger mass parameters respectively. These wave functions $F^{(1)}$ and $F^{(2)}$ depend on the magnitude of the wave vector k_t and position z , and are independent of the direction of the wave vector:

When a crystal is under a uniform deformation, it may preserve the periodic property such that the Bloch theorem may still be applicable. The modulating part of the Bloch function remains periodic, with a period equal to that of the new elementary cell, since the elementary cell is also deformed. Bir and Pikus¹⁸⁻¹⁹ have derived the Hamiltonian for strained-layer superlattices. They showed that eq. (1) has to be modified as follows:

$$\begin{aligned} P &\rightarrow P + P_\epsilon \\ Q &\rightarrow Q + Q_\epsilon \\ R &\rightarrow R + R_\epsilon \\ S &\rightarrow S + S_\epsilon \end{aligned} \quad (3)$$

where

$$\begin{aligned}
P_\varepsilon &= -a_v(\varepsilon_{xx} + \varepsilon_{yy} + \varepsilon_{zz}) \\
Q_\varepsilon &= -\frac{b}{2}(\varepsilon_{xx} + \varepsilon_{yy} - 2\varepsilon_{zz}) \\
R_\varepsilon &= \frac{\sqrt{3}}{2}b(\varepsilon_{xx} - \varepsilon_{yy}) - id\varepsilon_{xy} \\
S_\varepsilon &= -d(\varepsilon_{xz} - i\varepsilon_{yz})
\end{aligned} \tag{4}$$

where a_v , b , and d are the Pikus-Bir deformation potentials. For the special case of biaxial strain, namely,

$$\begin{aligned}
\varepsilon_{xx} &= \varepsilon_{yy} \neq \varepsilon_{zz} \\
\varepsilon_{xy} &= \varepsilon_{yz} = \varepsilon_{zx} = 0
\end{aligned} \tag{5}$$

Thus, $R_\varepsilon = S_\varepsilon = 0$, which essentially covers two of the most important strained systems: (1) a strained-layer semiconductor pseudomorphically grown on a (001)-oriented substrate and (2) a bulk semiconductor under an external uniaxial stress along the z direction. For the case of the lattice-mismatched strain,

$$\begin{aligned}
\varepsilon_{xx} &= \varepsilon_{yy} = \frac{a_0 - a}{a} \\
\varepsilon_{zz} &= -\frac{2C_{12}}{C_{11}}\varepsilon_{xx}
\end{aligned} \tag{6}$$

where a_0 and a are the lattice constants of the substrate and the layer material, and C_{11} and C_{12} are the elastic stiffness constants. Eq. (6) can be derived by using the fact that in the plane of the heterojunction, the layered material is strained such that the lattice constant along the plane of the layer is equal to a_0 .

2.2 Optical Gain, Radiative Current and Auger Current

The general material gain can be obtained:

$$G(\hbar\omega) = \int g(E_{eh})L(\hbar\omega - E_{eh})dE_{eh} \tag{7}$$

where

$$g(E_{eh}) = C_0 |M_T(E_{eh})|^2 \rho_r(E_{eh})|_{E_{eh}=\hbar\omega} (f_c - f_v) \tag{8}$$

$$C_0 = \frac{\pi q^2 \hbar}{n_r \varepsilon_0 c m_0^2} \frac{1}{\hbar\omega} \tag{9}$$

$$L(\hbar\omega - E_{eh}) = \frac{1}{\pi} \frac{\hbar/\tau_{in}}{(\hbar/\tau_{in})^2 + (\hbar\omega - E_{eh})^2} \tag{10}$$

where n_r and ε_0 are refractive index and dielectric permittivity respectively. ρ_r is the reduced density of states; f_c and f_v are conduction and valence band Fermi function. Note that M_T is the transition matrix element. $L(\hbar\omega - E_{eh})$ is a normalized Lorentzian lineshape function, and τ_{in} is the intraband relaxation time, or simply the lifetime of each state and is about 0.1 ps²⁰⁻²² in bulk material. In addition, to account for photon not confined within the active region, eq. (7) has to be multiplied by the optical confinement factor Γ :

The spontaneous emission rate is given by:

$$R_{sp}(\hbar\omega) = \frac{4n\pi q^2}{\epsilon_0 \hbar^2 c^3 m_0^2} \hbar\omega \int |\overline{M}_T(E_{eh})|^2 \rho_r(E_{eh}) f_c(1-f_v) L(\hbar\omega - E_{eh}) dE_{eh} \quad (11)$$

$$|\overline{M}_T(E_{eh})|^2 = \frac{1}{3} \sum_{\text{all three polarization}} |M_T(E_{eh})|^2 \quad (12)$$

It has been pointed out that Auger recombination²³⁻²⁵ is the leading carrier loss in InGaAs quantum well lasers. The Auger recombination rate, R_{Auger} , is characterized by the non-radiative Auger recombination constant, C (cm⁴s⁻¹). Assuming CHHS process is the dominant process, the Auger recombination rate is given by:

$$R_{Auger} = CP^2N \quad (13)$$

where P and N are sheet carrier density of hole and electron in the well respectively. The Auger recombination constant C is given in literature [26].

2.3 Modulation Response

In this section, the authors assumed transport model presented in Ref. [27,28] to study the modulation response of InAlGaAs and InGaAsP QW lasers. Rate equations are used here to describe the carrier density dynamics in the quantum well and the SCH layer, and the photon density dynamics in the laser cavity for SQW laser. The MQW laser will be discussed later. The rate equations for the carrier density in the quantum wells (P_w) and the SCH layer (P_{SCH}) and the photon density in the cavity (S) are written as:

$$\frac{dP_{SCH}}{dt} = \frac{I}{qV_{SCH}} - \frac{P_{SCH}}{\tau_s} - \frac{P_{SCH}}{\tau_{n,SCH}} + \frac{P_w(V_w/V_{SCH})}{\tau_e} \quad (14)$$

$$\frac{dP_w}{dt} = \frac{P_{SCH}(V_{SCH}/V_w)}{\tau_s} - \frac{P_w}{\tau_n} - \frac{P_w}{\tau_e} - \frac{P_w}{\tau_{nr}} - \frac{v_g GS}{1 + \epsilon S} \quad (15)$$

$$\frac{dS}{dt} = \frac{\Gamma v_g GS}{1 + \epsilon S} - \frac{S}{\tau_p} \quad (16)$$

where τ_s is the transport time across SCH, τ_e is the escape time from the QW by thermionic emission, τ_n is the spontaneous time in QW, $\tau_{n,SCH}$ is the spontaneous time in SCH, τ_{nr} is the Auger recombination time, τ_p is the photon lifetime, Γ is the optical confinement factor, G is the gain of the laser, v_g is the mode velocity, ϵ is the gain compression factor, V_w is the volume of the quantum well, and V_{SCH} is the volume of the SCH.

In principle, τ_s would have to include the finite capture time of the quantum well. However, it has been neglected because it is < 1 ps²⁹⁻³⁰ for holes, which contribute most to the magnitude of τ_s . The spontaneous emission feedback term in eq. (16) has been neglected because it does not have a significant effect on the modulation response.

The small signal solution of the rate equations is given by adding a small sinusoidal signal to the corresponding steady state components. The modulation response, $|M(\omega)|$, is given by:

$$|M(\omega)| = \left(\frac{\Gamma v_g g_0 S_0}{qV_w} \right) \frac{1}{A_0 + jA_1\omega - A_2\omega^2 - jA_3\omega^3} \quad (17)$$

$$A_0 = \frac{v_g g_0 S_0}{\tau_p} \left(1 + \frac{\tau_s}{\tau_{n,SCH}} \right) \left(1 + \frac{\epsilon}{v_g g_0 \tau_n} + \frac{\epsilon}{v_g g_0 \tau_{nr}} \right) \quad (18)$$

$$A_1 = \nu_g g_0 S_0 \left(1 + \frac{\tau_s}{\tau_p} + \frac{\tau_s}{\tau_{n,SCH}} \right) + \frac{\varepsilon S_0}{\tau_p} \left(1 + \frac{\tau_s}{\tau_e} + \frac{\tau_s}{\tau_n} + \frac{\tau_s}{\tau_{nr}} + \frac{\tau_s}{\tau_{n,SCH}} \right) + (1 + \varepsilon S_0) \left(\frac{1}{\tau_n} + \frac{1}{\tau_{nr}} \right) \left(1 + \frac{\tau_s}{\tau_{n,SCH}} \right) + \frac{\tau_s}{\tau_{n,SCH}} \frac{1}{\tau_e} (1 + \varepsilon S_0) \quad (19)$$

$$A_2 = (1 + \varepsilon S_0) \left(1 + \frac{\tau_s}{\tau_e} + \frac{\tau_s}{\tau_n} + \frac{\tau_s}{\tau_{nr}} + \frac{\tau_s}{\tau_{n,SCH}} \right) + \nu_g g_0 S_0 \tau_s + \frac{\varepsilon S_0 \tau_s}{\tau_p} \quad (20)$$

$$A_3 = (1 + \varepsilon S_0) \tau_s \quad (21)$$

where S_0 and g_0 is the photon density and differential gain at steady state respectively. The steady state solution to the photon density equation gives the basic gain loss relationship in the laser cavity:

$$\frac{\Gamma \nu_g G_0}{1 + \varepsilon S_0} = \frac{1}{\tau_p} \quad (22)$$

where G_0 is the gain at steady state. Note that, Auger recombination and spontaneous emission has been included in eq. (14) and (15), which is absent in Ref. [27].

Ref. [27] proposed a rate-equation model for MQW laser taking into account carrier transport across the SCH. The model is an extension of the rate equations described above. Each well of the MQW laser is described by a rate equation given by eq. (15). In addition, a coupling term is introduced into the rate equation to model the transport of carriers across the barrier region. The transport mechanisms across the barrier are tunneling and thermionic emission. In this work, the authors followed the model described in Ref. [27] to study the modulation response of MQW lasers. In contrast to Ref. [27], the authors assumed that the carrier density of each well is equal (as described in Ref. [27], the carrier density of each well may be different). This follows from the assumption that carriers transport across the barrier instantaneously. Thus, the MQW region can be regarded as a large "single quantum well". In this respect, only one rate equation is needed to describe the dynamics of this "single quantum well", i.e. the rate equations described above can be used to approximate the modulation response of MQW. However, P_W and G have to be interpreted at the total carrier density in the "single quantum well" and total gain contributed from each quantum well in the "single quantum well".

3. QUANTUM WELL STRUCTURE

In this work, the InGaAs/InAlGaAs/InP and InGaAs/InGaAsP/InP multiple quantum wells lasers will be investigated. The lasers consists of four tensile strained InGaAs quantum wells, each with well width L_z , separated by lattice-matched (to InP) InAlGaAs (or InGaAsP) barriers, each with barrier width $L_b = 10$ nm. The separate confinement layer is also lattice-matched (to InP) InAlGaAs (or InGaAsP) with thickness of 215 nm at each side. The In composition of the wells is chosen to give the required tensile strain. The well width is then adjusted to give 1.55 μm emission.

The authors considered five 0.78% tensile strained QW lasers, i.e. the well material is 0.78% tensile strained and given by $\text{In}_{0.42}\text{Ga}_{0.58}\text{As}$. These lasers are labeled as QW Laser 1 – 5 as tabulated in Table 1.

Lasers	Barrier material	Barrier bandgap (eV)	Well width (nm)
QW Laser 1	$\text{In}_{0.52}\text{Al}_{0.144}\text{Ga}_{0.336}\text{As}$	0.866	14
QW Laser 2	$\text{In}_{0.52}\text{Al}_{0.264}\text{Ga}_{0.216}\text{As}$	1.12	16
QW Laser 3	$\text{In}_{0.52}\text{Al}_{0.312}\text{Ga}_{0.168}\text{As}$	1.21	17
QW Laser 4	$\text{In}_{0.723}\text{Ga}_{0.277}\text{As}_{0.6}\text{P}_{0.4}$	0.94	15
QW Laser 5	$\text{In}_{0.909}\text{Ga}_{0.091}\text{As}_{0.2}\text{P}_{0.8}$	1.2	17

Table 1 Barrier materials of tensile strained (0.78%) $\text{In}_{0.42}\text{Ga}_{0.58}\text{As}$ quantum well lasers.

4. THEORETICAL CALCULATION OF VALENCE BAND STRUCTURE, OPTICAL GAIN AND THRESHOLD

4.1 Valence Band Structure

The valence band structure of QW Laser 1, QW Laser 2, QW Laser 3 and QW Laser 4, are shown in Fig. 1 to Fig. 4, respectively. It is clear that interaction between LH and HH produces band non-parabolicity. As described in literature³¹⁻³⁵, light hole – heavy hole crossing would increase the in-plane hole effective mass. For certain tensile strain, and quantum well width, the band structure even becomes indirect. The resulting heavy hole mass increases both the threshold current and the nonradiative losses such that it prevents up to 2 mm cavity length 0.3, 0.6 and 0.9% tensile strained InGaAs SQW lasers from lasing at room temperature. So far, low threshold current lasers with strains in the quantum wells ranging from 0 to 1% tension have not been reported in agreement with our observations. However, by choosing a wider QW width (14nm – 20nm), the authors showed that the first light hole subband lies above the heavy hole subbands, as presented by Fig. 1 – Fig. 4., no band crossing is observed. Thus, the authors predicted the emission of QW lasers with tensile strain less than 0.9%.

4.2 Optical Gain and Threshold Current

The optical gain given in eq. (7) show that at a given optical frequency, the optical gain increases with the joint density of the electron and hole states that are separated by the photon energy. It also increases with the difference between the occupation probabilities of electrons in the conduction band and holes in the valence band that are separated by the photon energy ($f_c - f_v$). Thus, the greater the occupation of the electrons and holes at the band edges, the larger the material gain will be. The occupation probability ($f_c - f_v$) is set by Fermi functions for electrons and holes and increases as the quasi-Fermi levels rise farther above the electron or hole energies. Hence, for a given carrier concentration, it is desirable to force the quasi-Fermi levels for the electron and hole distributions as far into the bands as possible. For a given carrier concentration, the position of the quasi-Fermi level is set by the density of states. Thus, low density of states is desirable, i.e. low effective mass is favourable.

Another way to affect the position of the quasi-Fermi levels is the separation between the energy subbands in the QW. The ideal subband configuration for a QW laser would consist of a single subband with a low effective. This is possible for the conduction band QW, but the valence band effective mass is so large that it is not possible to have a single valence subband level. For the valence band, it is important to obtain as large a separation as possible between the lowest energy subband and the higher energy subbands.

Fig. 5 shows the optical gain and current density (radiative J_{rad} and Auger current) of QW Laser 1, QW Laser 2 and QW Laser 3. It is clear that QW Laser 1 achieve lowest total current density for a given optical gain. This is due to lesser number of subbands in the quantum wells, leading to lower carrier density and radiative current. Fig. 6 compares the optical gain of QW Laser 1 (InAlGaAs) and QW Laser 4 (InGaAsP). As can be seen, QW Laser 4 performs better than QW Laser 1. Table 2 and Table 3 tabulate the temperature sensitivity of the above laser for a given threshold gain of 30 and 100 cm^{-1} respectively. The results shows that lasers structure with small number of subbands (QW Laser 1 and QW Laser 4) can lead to low threshold and temperature sensitivity. Besides, the T_0 of QW Laser 4 is lower than QW Laser 1. This justifies that structure with larger conduction band offset ratio has higher T_0 .

Laser	Threshold current density (Acm^{-2})	Temperature sensitivity T_0 (K)
QW Laser 1	314	115
QW Laser 2	362	52
QW Laser 3	511	37
QW Laser 4	264	71

Table 2 Threshold current density and temperature sensitivity of QW Laser 1, QW Laser 2, QW Laser 3 and QW Laser 4. The threshold gain is 30 cm^{-1} .

Laser	Threshold current density (Acm^{-2})	Temperature sensitivity T_0 (K)
QW Laser 1	439	97
QW Laser 2	572	45
QW Laser 3	848	32
QW Laser 4	364	60

Table 3 Threshold current density and temperature sensitivity of QW Laser 1, QW Laser 2, QW Laser 3 and QW Laser 4. The threshold gain is 100 cm^{-1} .

5. THEORETICAL CALCULATION OF MODULATION BANDWIDTH

In this section, the modulation response of InAlGaAs and InGaAsP QW lasers is studied. The 3 dB bandwidth of the above lasers at different temperature (290K and 350K) is studied and compared.

5.1 3 dB Bandwidth of InAlGaAs QW Lasers

Fig. 7 shows the 3 dB bandwidth of QW Laser 1 at threshold gain of 100 cm^{-1} . The figure shows that the maximum modulation bandwidth achieved is no more than 15 GHz. In addition, the bandwidth is severely degraded at high temperature (350K). A reduction of 40% - 50% is expected, as shown in the figure.

Fig. 8 shows the 3 dB bandwidth of QW Laser 2 at threshold gain of 100 cm^{-1} . The maximum bandwidth achieved is 38 GHz, which is more than 2 time that of QW Laser 1. Besides, at high temperature (350K), a reduction of 20% - 30% of bandwidth is predicted as compared to 40% - 50% of QW Laser 1. Comparing Fig. 7 and Fig. 8, it is concluded that large band discontinuity of QW Laser 2 (resulting from barrier band gap) leads its modulation bandwidth to be more resilient to high temperature.

5.2 3 dB Bandwidth of InGaAsP QW Lasers

Fig. 9 shows the 3 dB bandwidth of QW Laser 4 at threshold gain of 100 cm^{-1} . The maximum bandwidth achieved is 19 GHz. As shown, the bandwidth is severely degraded at high temperature, i.e. 40% - 50% of reduction is predicted. Similarly, the degradation of bandwidth at high temperature is attributed to small band discontinuity of the QW, i.e. the barrier band gap of QW Laser 4 is small. Fig. 10 shows the 3 dB bandwidth of QW Laser 5 at threshold gain of 100 cm^{-1} . As can be seen, the maximum bandwidth can be achieved is 22 GHz at 290K. Although its band discontinuity is larger than QW Laser 2, the maximum modulation bandwidth is smaller. Comparing QW Laser 2 and QW Laser 5, the authors attributed the smaller modulation bandwidth of QW Laser 5 to the conduction band offset ratio of InGaAs/InGaAsP system.

6. CONCLUSION

In summary, the authors observed that large band discontinuity results in large number of subbands, which in turn gives rise to large density of states. This would reduce the occupation probability of the laser and result in lower optical gain. Besides, it also leads to lower T_0 . Further, it gives rise to high modulation bandwidth and more resilient to high temperature. These characteristics are observed in QW Laser 2, QW Laser 3 and QW Laser 5. In the case of small band discontinuity, small number of subbands results, thus, lower density of states. As a consequence, the occupation probability of the laser is improved as can be seen in QW Laser 1 and QW Laser 5. Besides, in higher T_0 is observed. The modulation bandwidth of QW Laser 1 and QW Laser 5 is largely limited and is vulnerable to high temperature operation. Finally, the conduction band offset ratio also plays an important role. Modulation bandwidth of InGaAsP system is limited by its small conduction band offset ratio, i.e. the modulation of QW Laser 5 is smaller than that of QW Laser 2.

To conclude, the authors observed that InGaAsP laser is limited by its intrinsic characteristic: small conduction band offset ratio. On the other hand, InAlGaAs laser, due to its large conduction band offset ratio, could be designed to give low threshold, large bandwidth and low temperature sensitivity.

REFERENCE

1. A. R. Adams, *Electron. Lett.* **22**, 249-250 (1986).
2. E. Yablonovitch, and E. O. Kane, *J. Lightwave Technol.* **LT-4**, 504-506 (1986).
3. E. Yablonovitch, and E. O. Kane, *J. Lightwave Technol.* **6**, 1292-1299 (1988).
4. P. J. A. Thijs, J. J. M. Binsma, L. F. Tiemeijer, and T. van Dongen, *Tech. Dig. ECOC/IOOC*, Paris, France, vol. **2**, 31-38 (1991).
5. P. J. A. Thijs, J. J. M. Binsma, L. F. Tiemeijer, and T. van Dongen, *Electron. Lett.* **28**, 829-830 (1992).
6. P. J. A. Thijs, J. J. M. Binsma, P. I. Kuindersma, L. F. Tiemeijer, and T. van Dongen, *IEEE J. Quantum Electron.* **QE-27**, 1426-1439 (1991).
7. P. J. A. Thijs, J. J. M. Binsma, L. F. Tiemeijer, P. I. Kuindersma, and T. van Dongen, *J. Microelectron. Eng.* **18**, 57-74 (1992).
8. J. S. Osinski, Y. Zou, P. Grodzinski, A. Mathur, and P. D. Dapkus, *IEEE Photon. Technol. Lett.* **4**, 10-13 (1992).
9. A. Kasukawa, R. Bath, C. Caneau, N.C. Zah, M. A. Koza, and T. P. Lee, *Jpn. J. Appl. Phys.* **31**, 1365 (1992).
10. S. Seki, T. Yamanaka, W. Lui, Y. Yoshikuni, and K. Yokoyama, *IEEE J. Quantum Electron.* **QE-30**, 500 (1994).
11. O. Issanchou, J. Barrau, E. Idiart-Alhor, and M. Quillec, *J. Appl. Phys.* **78**, 3925 (1995).
12. R. Nagarajan, T. Kamiya, and A. Kurobe, *IEEE J. Quantum Electron.* **QE-25**, 1161 (1989).
13. M. Nido, K. Naniwae, J. Shimizu, S. Murata, and A. Suzuki, *IEEE J. Quantum Electron.* **QE-29**, 885 (1993).
14. P. A. Chen, C. Y. Chang, and C. Yang, *J. Appl. Phys.* **76**, 85 (1994).
15. A. Heinamaki, and J. Tulkki, *J. Appl. Phys.* **81**, 3268 (1997).
16. H. Ishikawa, and I. Suemune, *IEEE Photonics Tech. Lett.* **6**, 344 (1994).
17. S. L. Chuang, "Efficient band-structure calculation of strained quantum wells," *Phys. Rev. B*, **43**, 9649-9661 (1991).
18. G. E. Pikus and G. L. Bir, "Effects of deformation on the hole energy spectrum of germanium and silicon," *Sov. Phys.-Solid State* **1**, 1502-1517 (1960).
19. G. E. Pikus and G. L. Bir, *Symmetry and Strain-Induced Effects in Semiconductor*, Wiley, New York, 1974.
20. M. Yamada, H. Isiguro and H. Nagato, *Japan. J. Appl. Phys.* **19**, 135 (1980).
21. M. Yamada and H. Isiguro, *Japan. J. Appl. Phys.* **20**, 1279 (1981).
22. M. Asada, A. Kameyama and Y. Suematsu, *IEEE J. Quantum Electron.* **QE-20**, 745 (1984).
23. G. Fuchs, C. Schiedel, A. Hangleiter, V. Harle, and F. Scholz, *Appl. Phys. Lett.* **62**, 396 (1993).
24. A. Haug, *J. Phys. C* **16**, 4159 (1983).
25. S. Hausser, G. Fuchs, A. Hangleiter, K. Streubel, and W. T. Tsang, , *Appl. Phys. Lett.* **56**, 913 (1990).
26. M. C. Wang, K. Kash, C. E. Zah, R. Bhat, and S. L. Chuang, *Appl. Phys. Lett.* **62**, 166 (1993).
27. R. Nagarajan, T. Fukushima, S. W. Corzine, and J. E. Bowers, *Appl. Phys. Lett.* **59**, 1835 (1991).
28. R. Nagarajan, M. Ishikawa, T. Fukushima, R. S. Geels, and J. E. Bowers, *IEEE J. Quantum Electron.* **QE-28**, 1990 (1992).
29. S. Morin, B. Deveaud, F. Clerot, K. Fujiwara, and K. Mitsunaga, *IEEE J. Quantum Electron.* **QE-27**, 1669 (1991).
30. B. Deveaud, F. Clearot, A. Regency, K. Fujiwara, K. Mitsunaga, and J. Ohta, *Appl. Phys. Lett.* **55**, 2646 (1989).
31. M. P. C. M. Krijin, G. W. 't Hooft, M. J. B. Boermans, P. J. A. Thijs, T. van Dongen, J. J. M. Binsma, and L. F. Tiemeijer, *Appl. Phys. Lett.* **61**, 1772-1774 (1992).
32. E. P. O'Reilly, G. Jones, A. Ghiti, and A. R. Adams, *Electron. Lett.* **27**, 1417-1419 (1991).
33. M. P. Houn, and Y. C. Chang, *J. Appl. Phys.* **65**, 3092-3097 (1989).
34. S. Corzine, and L. A. Coldren, *Appl. Phys. Lett.* **59**, 588-590 (1991).
35. M. Nido, K. Naniwae, J. Shimizu, S. Murata, and A. Suzuki, *IEEE J. Quantum Electron.* **QE-29**, 885-895 (1993).

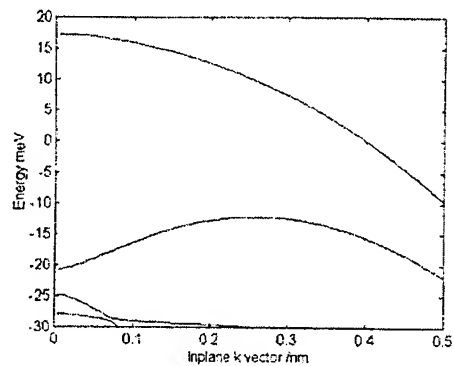


Fig. 1 Valence band structure of QW Laser 1

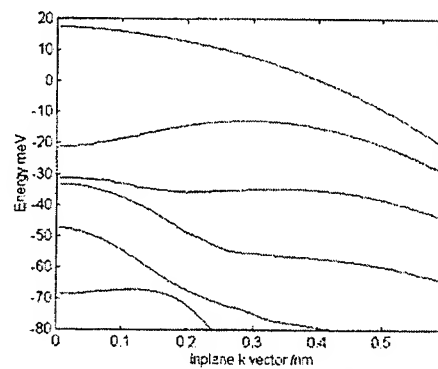


Fig. 2 Valence band structure of QW Laser 2

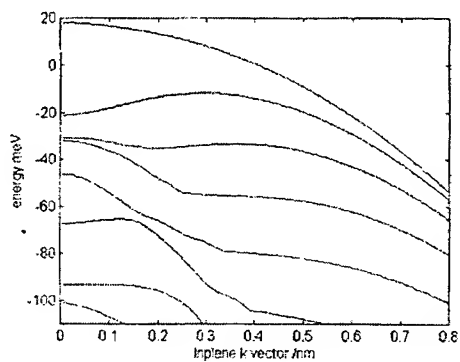


Fig. 3 Valence band structure of QW Laser 3

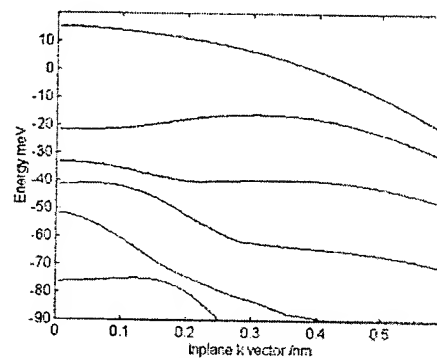


Fig. 4 Valence band structure of QW Laser 4

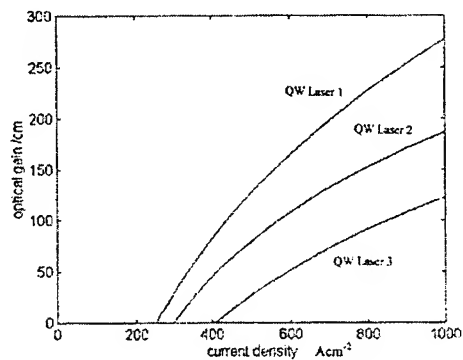


Fig. 5 Optical gain and current density of QW Laser 1, 2, and 3

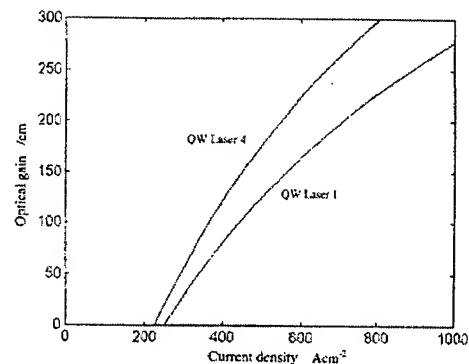


Fig. 6 Optical gain and current density of QW Laser 1 and 4

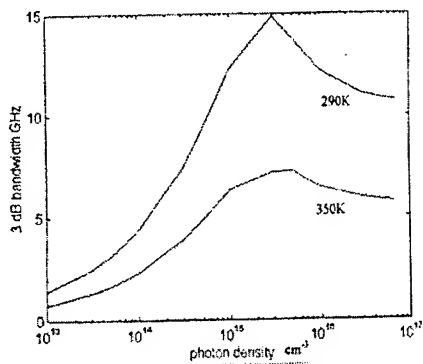


Fig. 7 3 dB bandwidth of QW Laser 1 at optical gain of 100 cm^{-1}

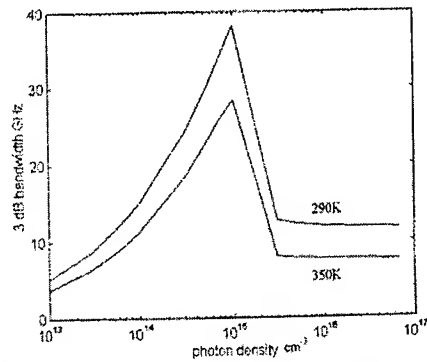


Fig. 8 3 dB bandwidth of QW Laser 2 at optical gain of 100 cm^{-1}

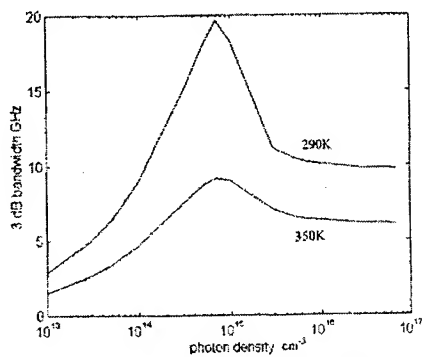


Fig. 9 3 dB bandwidth of QW Laser 4 at optical gain of 100 cm^{-1}

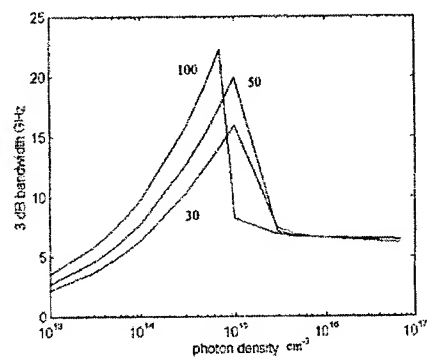


Fig. 10 3 dB bandwidth of QW Laser 5 at optical gain of 30, 50 and 100 cm^{-1}

IMAGING THE NEAR-FIELD INTENSITY GRADIENTS OF A LOW POWER SEMICONDUCTOR LASER

Nien Hua Lu

Department of Electronic Engineering, Sze-hai Institute of Technology and Commerce,
Tuchen, Taipei County, Taiwan, 236

Din Ping Tsai

Department of Physics, National Taiwan University, Taipei, Taiwan, 10617

Wei Chih Lin, Hung Ji Huang

Department of Physics, National Chung Cheng University, Chia Yi, Taiwan 621

ABSTRACT

A newly developed inverted tapping-mode tuning-fork near-field scanning optical microscope is used to study the local near-field radiation properties of a strained AlGaInP/Ga_{0.4}In_{0.6}P low power visible multiquantum-well laser diode. With this novel technique, we can easily image the local near-field optical intensity gradients. In the intensity ratio image there are remarkable contrasts among the various regions on the laser diode facet. The anomalous phenomenon manifests the different origins of the near-field optical waves from various regions on the laser diode facet. We believe that this method should be very important for further understanding the optical radiation properties in the near-field region.

Keywords: near-field optics, semiconductor laser, near-field scanning optical microscopy, near-field optical intensity gradients.

1. INTRODUCTION

Semiconductor lasers have become indispensable commercial components to our everyday life. For example, they are widely used in various applications ranging from the light sources for optical information processing systems such as bar-code readers, high-speed laser printers, and compact disk players to the transmitters in optical fiber communication systems. Accordingly, characterization and further understanding of the performance of various semiconductor lasers turn out to be an important task. Because

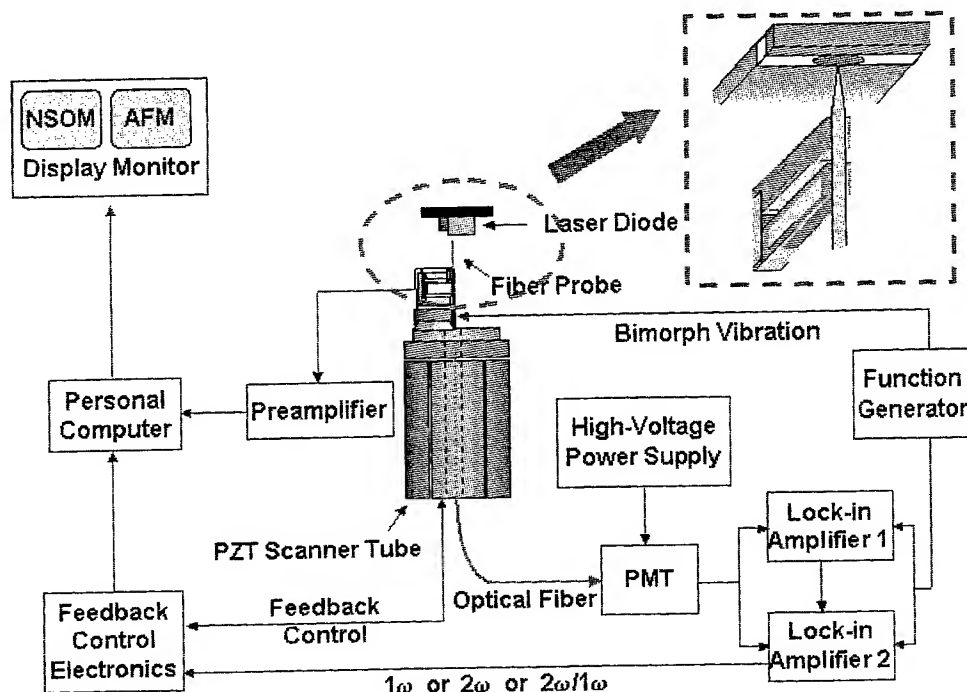


FIG. 1. A schematic of the experimental setup for measuring the local near-field intensity gradient of the facet of a laser diode is shown. An inverted TMTF-SNOM system and two external lock-in amplifiers were used to simultaneously provide images of both the topography and the optical signals of 1ω , 2ω , and their ratio.

of the superior spatial resolution of scanning near-field optical microscopy (SNOM), and the ease of implementation of local spectroscopy, recently SNOM has played an important role in near-field optical imaging and spectroscopy study of the diagnostics of semiconductor lasers.¹⁻⁵ Lately we have applied both collection and excitation modes of SNOM to study a strained AlGaInP/Ga_{0.4}In_{0.6}P low power visible multiquantum-well laser diode (MQWLD).⁶ Results show both the near-field optical beam induced current and spectroscopy of the near-field electroluminescence can be studied at the same region in nanometer scale, and are the complementary methods. The location of defect, and the energy range of defect level were able to be found by the excitation mode SNOM using pump sources of different wavelengths. In this paper, we intend to use another novel method, tapping-mode tuning fork SNOM⁷⁻⁹, to study the near-field intensity gradients of semiconductor lasers.

2. EXPERIMENTAL

2.1 Tapping-mode tuning-fork scanning near-field optical microscope

A recently developed tapping-mode tuning-fork near-field scanning optical microscope (TMTF-SNOM)⁷⁻⁹ was used in the measurements of the local near-field radiation property of semiconductor lasers. A schematic of the experimental setup is shown in Fig. 1. An inverted TMTF-SNOM was used to probe the near-field intensity at the region of active layers of the samples in collection mode. Light coupled to the tapered fiber tip operated in the near-field was detected by a photomultiplier tube whose signal was fed to two external lock-in amplifiers which acquired signals at the tapping frequency ω , at 2ω and provided their ratio $(I(2\omega)/I(\omega))$. The feedback control of the near-field optical fiber probe was provided by an internal lock-in amplifier of a commercial electronic control unit of an atomic force microscope (AFM), which is described elsewhere⁷⁻⁹. The feedback control of the probe height is a non-optical method, and has all the advantages of the tapping-mode including high spatial resolution, high sensitivity, and excellent stability. Images of the topographic and near-field optical signals are acquired simultaneously.

2.2 Imaging of the near-field optical intensity gradients

An important capability of the TMTF-SNOM is the imaging of the near-field intensity gradients. For an optical intensity I in near field consists of two terms, a propagating term (I_p) and an evanescent term (I_e)

$$I = I_p + I_e = I_s + I_o \exp(-2qz), \quad (1)$$

where I_s is the constant propagating intensity, I_o is the intensity at the surface of the sample, z is the probe height above the sample surface, and q is the decay coefficient. Instead of operating a near-field microscope in the conventional constant height (constant z) mode, z is modulated in TMTF-SNOM: $z = z_0 + A \cos \omega t$. For a small amplitude (A), we can expand the evanescent intensity in the following manner:

$$I = I_s + I_o \exp(-2qz_0) [1 + q^2 A^2 - 2qA \cos(\omega t) + q^2 A^2 \cos(2\omega t) - \dots], \quad (2)$$

and the measurement of the intensity at both the modulation frequency (ω) and at twice that frequency (2ω),

$$I(2\omega)/I(\omega) = I_o \exp(-2qz_0) \cdot q^2 A^2 / I_o \exp(-2qz_0) \cdot (-2qA) = -Aq/2, \quad (3)$$

will provide the q for the known tapping amplitude A . Here q represents the local optical property. The imaging of this ratio $I(2\omega)/I(\omega)$ gives the image of the local near-field intensity gradients^{8,9} because of

$$\frac{dI}{dZ} = 0 - 2qI_o \exp(-2qZ) = -2q[I - I_s]. \quad (4)$$

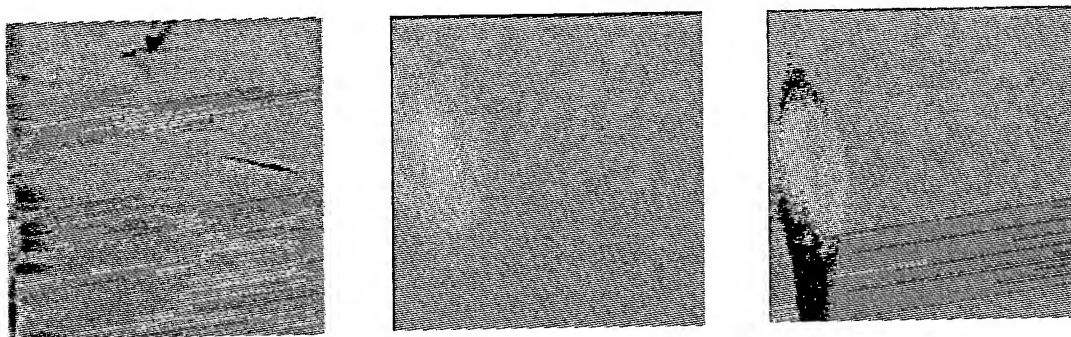


FIG. 2. A $10\ \mu\text{m} \times 10\ \mu\text{m}$ scan of AFM and SNOM images on the facet of a strained AlGaInP/Ga_{0.4}In_{0.6}P low power visible multiquantum-well laser diode. (a) AFM image on the laser diode facet. (b) Simultaneously measured near-field emission image of the laser diode (acquired at ω , the ordinary SNOM image). (c) is the SNOM image of the ratio R of the optical signals acquired at frequencies 2ω to ω . Remarkable contrasts are seen around the active region.

3. RESULTS AND DISCUSSIONS

Shown in Figs. 2(a) and (b) are the simultaneously measured surface morphology and near-field intensity output distribution on the facet of a strained AlGaInP/GaInP MQWLD operating at a current of 23 mA. The epitaxial structure of the MQWLD has been described elsewhere.⁶ Shown in the left of the topographic micrograph is the protruding metal contact on top of the cap layer and the dielectric film. Correlation between the topographic structure and the optical intensity output of the LD can thus be obtained easily. As expected, the emission is generated from one elliptical spot just below the p electrode in the positive-intrinsic-negative junction.

In Fig. 2(c) we display the ratio of the evanescent intensity detected at 2ω to that detected at ω : $R = I(2\omega)/I(\omega)$, which is proportional to the local near-field intensity gradient by a factor of $A/4$. Obviously, there is a distinct contrast in the intensity ratio image. Comparing with the active region, the $p\text{-(Al}_{0.7}\text{Ga}_{0.3})_{0.5}\text{In}_{0.5}\text{P}$ cladding layer just beside the active region shows a brighter contrast. On the other hand, the two wings beside the active region in the lateral direction appear to be darker. Variations of the refraction indexes of the epitaxial layers and the dielectric can not account for such an anomalous phenomenon. For the present, we suggest the near-field optical waves from the active region and the two side wings consist of both the evanescent and propagating components; however, only near-field propagation wave exists in the $p\text{-(Al}_{0.7}\text{Ga}_{0.3})_{0.5}\text{In}_{0.5}\text{P}$ cladding layer just beside the active region. A detailed systematic study is required to further understand the intrinsic properties of the near-field optical intensity gradients.

4. SUMMARY

In summary, we have applied the newly developed inverted tapping-mode tuning-fork near-field scanning optical microscope to study the local near-field radiation properties of a strained AlGaInP/Ga_{0.4}In_{0.6}P low power visible multi-quantum-well laser diode. With this novel technique, we can easily image the local near-field optical intensity gradients. The remarkable contrasts in the intensity ratio image manifest the different origins of the near-field optical waves from various regions on the laser diode facet. We suggest that the near-field optical waves from the active region and the two side wings consist of both the evanescent and propagating components; however, only near-field propagation wave exists in the $p\text{-(Al}_{0.7}\text{Ga}_{0.3})_{0.5}\text{In}_{0.5}\text{P}$ cladding layer just beside the active region.

REFERENCES

1. S. K. Buratto, J. W. P. Hsu, E. Betzig, J. K. Trautman, R. B. Bylisma, C. C. Bahr, and M. J. Cardillo, Appl. Phys. Lett. **65**, 2654 (1994); S. K. Buratto, J. W. P. Hsu, J. K. Trautman, E. Betzig, R. B. Bylisma, C. C. Bahr, and M. J. Cardillo, J. Appl. Phys. **76**, 7720 (1994).
2. A. Richter, J. W. Tomm, Ch. Lienau, and J. Luft, Appl. Phys. Lett. **69**, 3981 (1996).
3. J. Kim, D. E. Pride, J. T. Boyd, and H. E. Jackson, Appl. Phys. Lett. **72**, 3112 (1998).
4. U. Ben-Ami, R. Nagar, N. Ben-Ami, J. Scheuer, M. Orenstein, G. Eisenstein, A. Lewis, E. Kapon, F. Reinhardt, P. Ils, and A. Gustafsson, Appl. Phys. Lett. **73**, 1619 (1998).
5. D. K. Young, M. P. Mack, A. C. Abare, M. Hansen, L. A. Coldren, S. P. Denbaars, E. L. Hu, and D. D. Awschalom, Appl. Phys. Lett. **74**, 2349 (1999).
6. N. H. Lu, D. P. Tsai, C. S. Chang, and T. T. Tsong, Appl. Phys. Lett. **74**, 2746 (1999).
7. D. P. Tsai, Y. Y. Lu, Appl. Phys. Lett. **73**, 2724 (1998).
8. C. W. Yang, D. P. Tsai, Scanning **21**, 74 (1999).
9. D. P. Tsai, C. W. Yang, S. Z. Lo, H. E. Jackson, Appl. Phys. Lett. **75**, 1039 (1999).

Influence of pulse reversal on the characteristics of CdSe films

Murali K R and Swaminathan V

Electrochemical Materials Science Division
Central Electrochemical Research Institute
Karaikudi – 630 001, India.

ABSTRACT

This paper embodies the first report on the pulse reversal deposition of CdSe thin films. The as-deposited and heat treated films were characterised by XRD, optical absorption spectroscopy and electrical properties. The polycrystalline deposits of CdSe obtained indicated a hexagonal structure after heat treatment at 550°C. From the optical absorption studies the bandgap was found to be 1.70 eV and absorption co-efficient of 10^4cm^{-1} were obtained. At an illumination of 80 mWcm^{-2} conversion efficiencies of 5.56% and 6.74% were obtained for the photoelectrodes without and with pulse reversal.

Keywords: Semiconductor, Thin films, Pulse reversal, Photoelectrochemical cell.

1.INTRODUCTION

CdSe thin films have been used as photoanodes in photoelectrochemical(PEC) cells to give high power conversion efficiency. MIS type solid state solar cells and PEC cells based on CdSe are being actively investigated. Several methods like vacuum evaporation, screen printing, spray pyrolysis, chemical bath deposition, electrodeposition etc have been employed for the preparation of CdSe films. We report here results on pulse plated CdSe films with and without pulse reversal.

Pulse plating technique has distinct advantage compared to conventional electrodeposition namely, better adhesion, crackfree and hard deposits and fine grained films with more uniformity and lower porosity. In pulse reversal, the main purpose of inverting the voltage/current from cathodic to anodic during a small fraction of the total period is to remove species preferentially from areas that tend to overplate during the cathodic part of the cycle¹⁻⁶. Changes in deposit structure, mainly grain size can also be achieved, because of forced nucleation at each new cathodic pulse. It is clear that adsorption, desorption as well as recrystallization takes place. The main purpose of carrying out pulse reversal plating⁷ is to obtain better film thickness with good adherent films which in turn will yield higher grain size due to better nucleation sites and hence high conversion efficiencies⁸ for photoelectrochemical cells fabricated using these films.

2.EXPERIMENTAL

CdSe films used in this work were deposited on titanium or SnO₂ substrate at room temperature. The deposition bath consisted of 0.5M CdSO₄ and 10⁻³ to 10⁻² M of SeO₂. To improve conductivity 10% d.H₂SO₄ was added to make pH~2⁹. The films were deposited at a potential of -900 mV vs SCE for one hour by varying the duty cycle from 50 % to 6% for pulse plating. Films were deposited using pulse reversal during the off period by varying the reversal time in the range 30–90 ms and maintaining the on time and off time as 1 s and 10 s respectively. The thickness of the films was estimated by gravimetric method. The films were characterized by x-ray diffraction studies using model JEOL JDX-8030 and CuK α radiation. Optical absorption studies were carried out for the films deposited on conducting substrates with a Hitachi UV-VIS-NIR spectrophotometer. Conductivity of the films was measured by using two probe technique.

The PEC cell consisted of the photoanode as working electrode, graphite as counter electrode and SCE as reference electrode with 1M alkaline polysulphide as the electrolyte. The light source was an Oriel 250 W tungsten halogen lamp. The photon flux reaching the electrode surface was measured by a CEL suryamapi. After heat treatment the electrodes were photoetched by shorting the photoelectrode and the counter electrode in 10% HCl for different durations in the range of 5s to 40s under an illumination of 80 mWcm⁻².

3.RESULT AND DISCUSSION

The as deposited films with and without reversal exhibit cubic structure. After heat treatment, the diffractogram of the films indicate polycrystalline nature with prominent peaks corresponding to (100),(101),(002) reflections of the hexagonal CdSe phase. The intensity of the peak(100) is found to increase with increase of the reversal time(Fig.1)

Optical absorption studies indicated a bandgap of 1.71 eV for the films annealed at 550°C irrespective of the dutycycle and pulse reversal. Absorption co-efficient of 10⁴cm⁻¹ was obtained for the films without and with pulse reversal. The linearity of the ($\alpha h\nu$)² vs $h\nu$ plot (Fig.2) indicate the direct bandgap nature of the films.

The PEC parameters for the electrodes made using the pulse plated films deposited without and with pulse reversal are indicated in Table.1. Both V_{oc} and J_{sc} are found to increase upto 60 ms pulse reversal, beyond which they decrease due to decrease in thickness of the film. Hence a photoetching time of 30s was maintained. After photoetching the electrodes the PEC parameters are found to increase. The efficiency of the photoetched electrodes is found to increase its value for the electrodes deposited with 60ms pulse reversal, the efficiency of the photoetched electrodes deposited with 90ms pulse reversal decrease due to a reduction in the output parameters, this can be attributed to the reduction in thickness of these films, as the reversal time of 90ms is high enough to remove a few monolayers of the deposited film. To check the reproducibility about 25 films were prepared under each condition.

Quantum efficiency(ϕ) was evaluated from the spectral response measurements by employing the following expression

$$\phi = \frac{1240 J_{sc}}{\lambda P} \quad (1)$$

Where J_{sc} is current density expressed in A cm⁻², λ the wavelength expressed in nm, P is the radiant power absorbed in the photoactive region, expressed in Wcm⁻²¹⁰. The variation of quantum efficiency was studied in the wavelength range 500-800 nm. A peak quantum efficiency of 0.56 and 0.80 was obtained for the electrodes without and with reversal at 1.70 eV, agreeing with the bandgap of the material.

CONCLUSION

The results of the present investigation indicate that efficient photoelectrodes could be prepared by introducing pulse reversal during the off time.

REFERENCES

1. N Ibl, J C Puippe, *J. Appl. Electrochem.*, **10**(1980)725.
2. D L Rehrig, H Leidsheiser, M R Notis, *Plat. Surf. Finish.*, **64**(1977)40.
3. K I Popov, M D Maksimoric, B M Ocokoljic, B J Lazarevic, *Surf. Technol.*, **11**(1980) 99.
4. J Lam, A Kaike, I Ohno, S Narayuma, *Kinzoku Hyomen Gijutusu.*, **34**(1983)428.
5. K R Murali, V Subramanian, N Rangarajan, A S Lakshmanan S K Rangarajan, *J. Elec. Anal. Chem.*, **303**(1991) 261.
6. G Devaraj, K I Vasu, N Seshadri, *Bull of Electrochem.*, **5**(1989a)333.
7. A Barnes, J A Lochlet, *AESF 3rd International pulse plating symposium*, Washington, Oct 28-29(1986)173-184.
8. C Lanza, H Hovel, *IEEE Trans. Electron Devices*, **ED.**, **27**(1980)2085.
9. V Subramanian, K R Murali, N Rangarajan, A S Lakshmanan, *Bull Mat Sci.*, **17**(1994) 1049.
10. J Sequi, S Hot Chandri, D Baddau, R M Leblance., *J. Phys. Chem*, **95**(1991)8807.

Table -1

Before photoetching

Duty Cycle %	V _{oc} mV	J _{sc} mA/cm ⁻²	ff	η %	R _{sh} KΩ	R _s Ω
1:10	350	9.31	0.37	5.65	4.15	105
1:10:30	351	10.0	0.37	5.62	3.78	160
1:10:60	360	16.54	0.38	6.74	4.20	98
1:10:90	340	11.35	0.38	5.34	4.05	130
After photoetching for 30s						
1:10	377	13.56	0.44	5.22	4.96	92
1:10:30	375	13.21	0.36	5.08	4.89	105
1:10:60	396	22.35	0.40	6.88	8.68	88
1:10:90	372	9.620	0.33	5.71	3.68	115

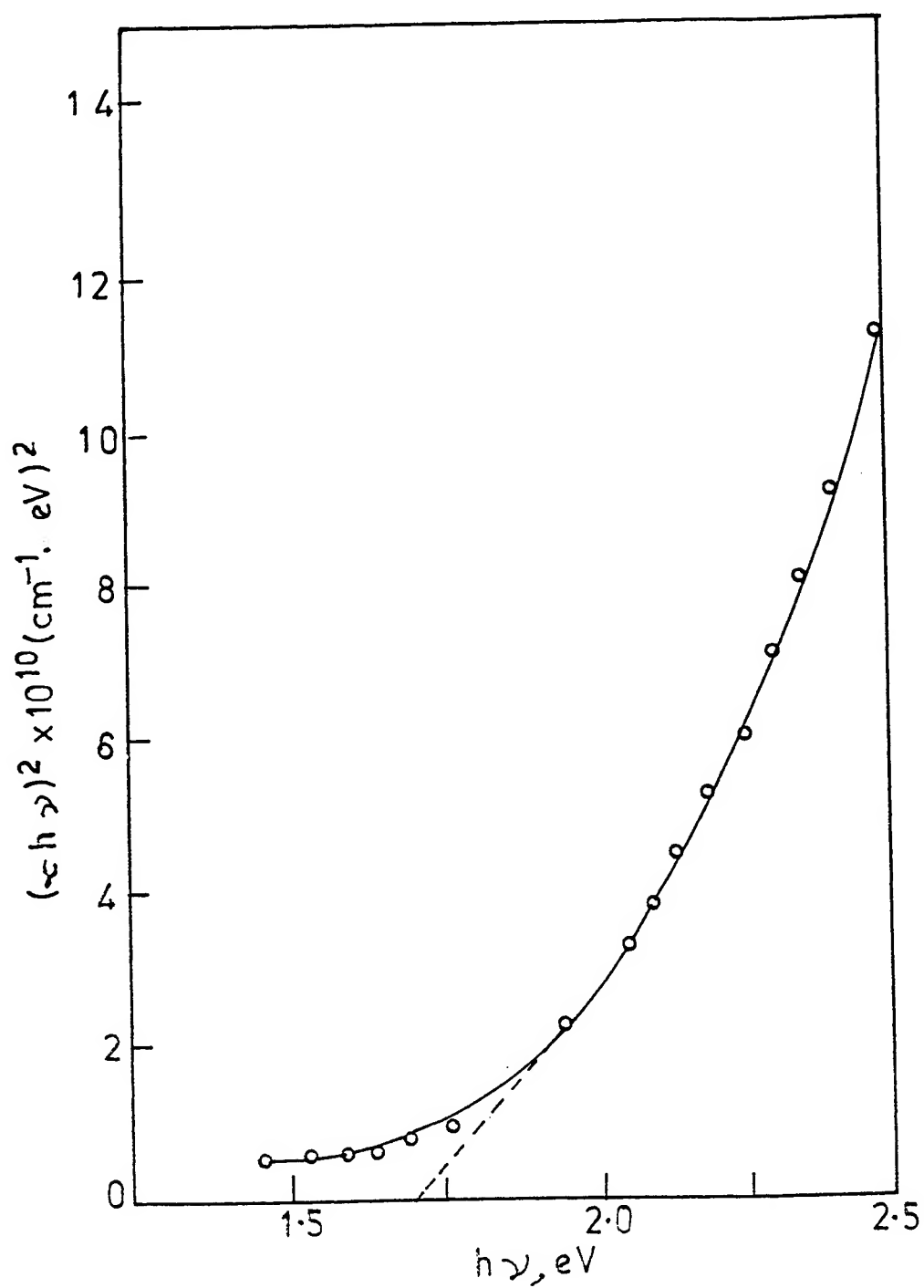


Fig-2 : $(\alpha h\nu)^2$ vs $h\nu$ curve for CdSe films heat treated at 550°C.

Additional Paper from Session 7

Fiber Distributed-Feedback Lasers and Dispersion Compensators

M. N. Zervas, M. Ibsen, M.K. Durkin, L. Chao*, M. J. Cole**, R. I. Laming***
and D.N. Payne

Optoelectronics Research Centre, University of Southampton,
Southampton SO17 1BJ, United Kingdom.

*Nanyang Technological Univ., Singapore,

**Qtera Corp., USA,

***Kymata Ltd., United Kingdom.

Abstract: Fibre Bragg Gratings (FBGs) are high-performance versatile devices that have had a major impact on different areas of optical fibre technology. Their unique filtering and dispersion properties allow them to be used in DFB and DBR fibre lasers, wavelength-stabilised semiconductor lasers, gain-flattened EDFAs, Raman amplifiers and lasers, dispersion-compensators and add/drop multiplexers. We report some of the latest advances in the area of grating fabrication, fibre grating dispersion-compensators and all-fibre DFB lasers and address how our improved dispersion-compensating gratings have a performance close to that theoretically predicted.

I. Introduction

UV-written Fibre Bragg Gratings (FBG's) [1,2] are proving to be one of the most important emerging technologies and are finding an increasing number of diverse applications throughout the field of Optical Fibre Technology. FBG's are simple versatile devices exhibiting extremely-low polarisation sensitivity and insertion loss, easily controllable characteristics, wavelength stability and longevity. Their unique reflection and dispersion characteristics permit their use in, for example, distributed-feedback (DFB) and distributed- Bragg-reflector (DBR) fibre lasers, gain-flattened EDFA's, Raman amplifiers and lasers, dispersion-compensators, add/drop multiplexers and semiconductor lasers stabilizers [3]. Passive and active FBG-based devices have also revitalised the fibre sensor field and have found extensive use as pressure and temperature sensors and in sensor arrays [4].

To be able to manufacture the above highlighted FBG devices, a number of different interferometric [2] and phase-mask based [5] grating fabrication techniques have been demonstrated, resulting in a range of high-quality fibre grating components. Recently, a number of groups have reported different versatile methods that combine phase masks with controlled fibre movement to give long gratings with fully adjustable spectral and phase characteristics [6-9].

In this paper, we report on Bragg grating devices made using the "continuous Bragg grating fabrication technique" pioneered and developed at Southampton University. We concentrate on some of the results coming from our fabrication approach and review the most recent progress in the areas of chirped-grating dispersion compensators and advanced grating devices, including fibre-DFB lasers and laser arrays. We also discuss its capability to manufacture extremely high-quality uniform apodised gratings and Bragg grating structures with very complex refractive index modulation profiles.

II. Chirped Fibre Bragg Grating Dispersion Compensators

The initial drive for the development of a very flexible grating fabrication technique was fueled by the urgent need for truly broadband fibre Bragg grating dispersion-compensators. The principle of a chirped FBG is a simple one. It reflects different incoming wavelengths at different positions along its length and therefore provides differential time delay between the various spectral components which constitute an input pulse. This enables pulse compression and chirped FBGs have indeed been proposed [10] and successfully demonstrated to be capable of providing efficient dispersion compensation over wide bandwidths ($>10\text{nm}$) at bit rates of 10Gb/s [11-13], 20Gb/s [14] and even 40Gb/s [15].

The Southampton grating manufacturing technique, is based on a moving fibre/stationary phase mask "stroboscopic" fabrication method, which provides accurate control over the apodisation and chirp profile along the length of the grating. Using this technique, we have demonstrated high quality meter-long continuously chirped apodised FBGs suitable for linear as well as higher-order dispersion compensation [16]. Figure 1(a) shows the reflection and time-delay spectra of a 1m-long linearly-chirped grating exhibiting a bandwidth of $\sim 5\text{nm}$ and linear dispersion of $\sim 2000\text{ps/nm}$. The peak-to-peak time delay ripple in this case is less than $\sim 40\text{ps}$. Figure 1(b) shows the reflection and time delay spectra of a 1m-long parabolically-chirped grating exhibiting a bandwidth of $\sim 10\text{nm}$ and an average dispersion of $\sim 1000\text{ps/nm}$. In addition to linear dispersion, the latter grating shows $\sim 12\text{ps/nm}^2$ 3rd-order dispersion.

The full control versatility provided by the fabrication method also enables the continuous writing of single Moiré-type linearly-chirped gratings with multiple identical broadband dispersion-compensating channels [17]. Recently, high quality super-linear dispersion-compensators have been demonstrated [18] using a newly-developed inverse-scattering exact design method [19].

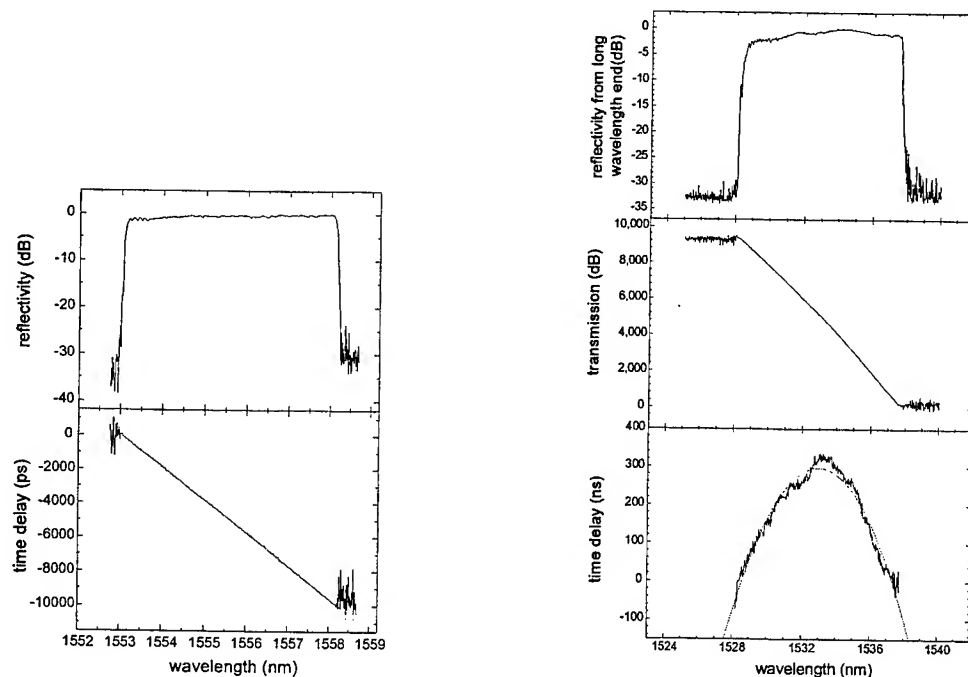


Figure 1: 1m long chirped grating dispersion compensators, (a) linearly-chirped FBG for 2nd order DC, (b) parabolically-chirped FBG for combined 2nd and 3rd order DC.

The precise control over all the relevant grating manufacturing parameters provided by our grating fabrication technique enables us to make gratings with system performance approaching that predicted theoretically [20-21], namely robust dispersion compensation over large bandwidths.

III. High-quality apodised and super-structured Bragg gratings

The excellent control over phase errors and exact phase-shift positions provided by the “continuous grating writing technique” has also resulted in the demonstration of a number of advanced high-quality gratings, including sinc-sampled square-envelope multiple-peak (4-16) reflectors [22] and strong reflectors with sidelobe suppression in excess of 45dB. Figure 2(a) shows the experimental reflection spectrum of such a strong apodised grating, written using a Blackman-apodisation profile. Figure 2(b) shows the measured response of a similar grating written through a silicone-rubber fibre coating [23]. In this case an increased level of the sidelobes can be seen. These are due to phase errors [24] that are induced by the thick coating ($\sim 60\mu\text{m}$), which could be minimised by the use of either thinner or higher-quality coatings. Despite these increased sidelobe levels, ~ 25 dB sidelobe suppression is still comparable to many commercially-available Bragg gratings written with the protective coating/jacket removed.

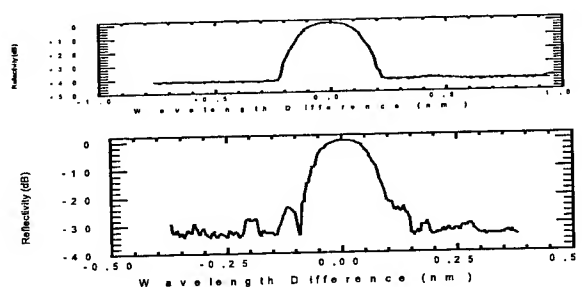


Figure 2: Blackman-apodised FBG reflectors written, (a) without fibre coating, (b) through coating.

The ability to write not just high-quality uniform gratings, but also chirped grating dispersion compensators through the fibre coating, is a high priority. Despite the good results presented in Fig. 2b the quality of the coatings is currently not up to the very demanding and strict control needed for dispersion compensating gratings, but work is in progress.

IV. Fibre DFB Lasers and Laser Arrays

Fibre-DFB lasers [25] are ideal sources for high bit-rate telecommunications systems and, being based on FBG technology, they can provide low insertion loss, high output power and excellent wavelength accuracy and stability. Fibre-DFB lasers can now be designed to provide single-polarisation, single-sided, high power CW output ($\sim 20\text{mW}$) with high signal-to-noise-ratio (SNR) [26]. These characteristics therefore make them strong rivals to their semiconductor counterparts. Recently, in a $4 \times 10\text{Gbit/s}$ WDM transmission experiment, we demonstrated that fibre-DFB lasers can successfully replace semiconductor lasers without any deterioration in system performance [27].

We have also demonstrated for the first time 8 and 16 channel (100GHz and 50GHz spacing) all-fibre laser WDM transmitter modules with integrated pump redundancy [28]. The employment of a pump redundancy scheme safeguards against the failure of one or more pump diodes. We show that with 8×8 -pump redundancy circuitry, the power reduction to each of 8 WDM channels resulting from the failure of 1 out of 8 pumps is just 2 dB. All WDM channels remain in operation despite the drop of as many as 7 out of 8 pump-diodes.

Figure 3 shows the schematic of an 8-channel transmitter module. This module consists of 8 pump diodes, a pump redundancy unit and 8 asymmetric all-fibre DFB lasers of length 5 cm, with isolators on the output end [26]. The role of the pump redundancy module is to split the power from each pump equally between all DFB fibre lasers. Therefore, with all pumps operating, each laser still receives the pump power corresponding to that provided by one dedicated pump diode. The particular module is made up of 12 couplers (50:50 @ 980nm) spliced appropriately together. The total insertion loss for each pump diode in this 8 channel module is ~1dB.

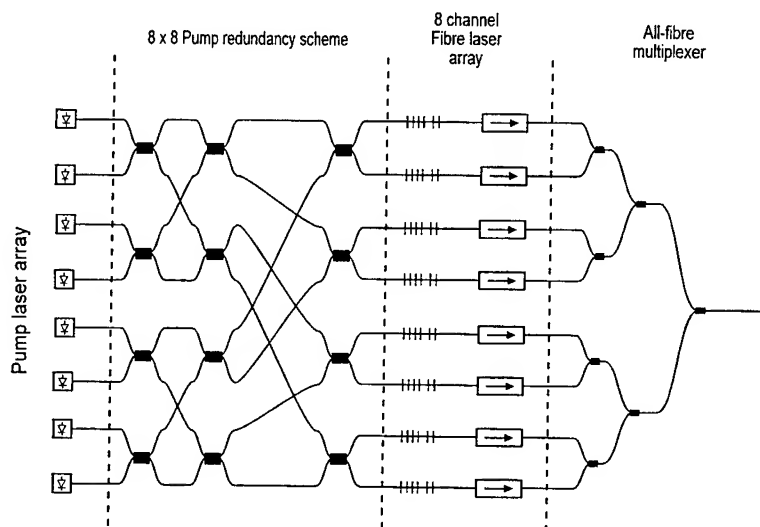


Figure 3: 8-channel fibre-DFB laser WDM transmitter module with 8x8 pump redundancy scheme.

The eight fibre-DFB lasers were separated in frequency by 100GHz and were fabricated using our grating writing technique [7] with CW 244nm UV light. They are 5 cm long and the lasers operate in a single-polarisation mode with a purity of >40 dB and with a single-sided output power ratio of ~50:1 [26]. The slope efficiency of the lasers is ~25% and, using the pump redundancy scheme with ~50mW (17dBm) power from each pump diodes, results in CW output powers of ~7 dBm \pm 0.25 dBm, from all the lasers. The outputs of the 8 lasers are combined by an all-fibre multiplexer, consisting of seven 1550 nm 3-dB splitters with a total insertion loss of ~10 dB. Noise measurements of the lasers show RIN < -160 dB/Hz ($f > 10$ MHz) and RIN < -165 dB/Hz for frequencies larger than 30 MHz, indicating very quiet sources with performance well suited for high speed communication systems.

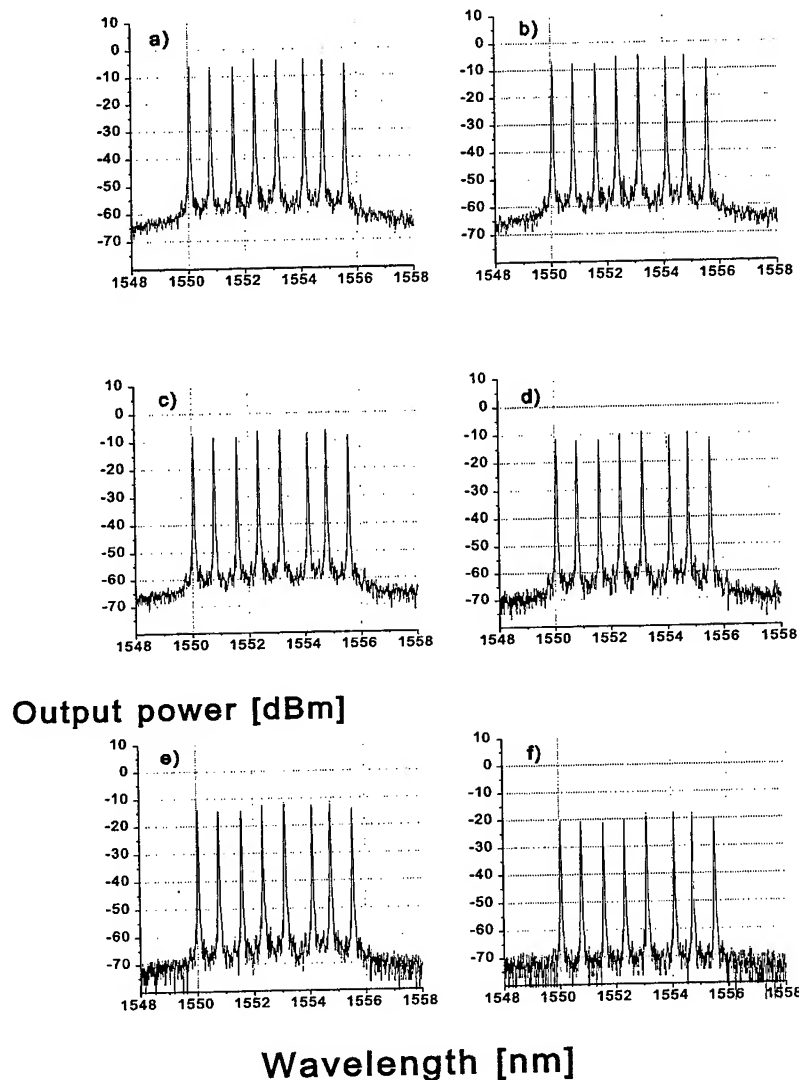


Figure 4: Output spectra of the 8-channel, 100GHz spacing WDM transmitter unit with (a) 8 pumps, (b) 7pumps, (c) 6 pumps, (d) 4 pumps, (e) 3 pumps, and (f) only 1 pump live.

Figure 4(a) shows the output spectrum of the multiplexed 8-channel, 100GHz spaced WDM transmitter with all 8 pump diodes operating (0.02 nm res.). Note that the SNR between the channels is in excess of 50dB and that the channel powers are equal to within 2.0 dB. The displayed channel output power fluctuation is due to small differences in the splitting ratios and differential losses of the 1550nm 3dB-coupler fibre-multiplexer and can be avoided with improved designs. The power stability of the lasers when operated in this configuration is $\sim 0.05\text{dBm}$ and the wavelength stability is stable to within 0.1pm (measured with a wave-meter with 0.1pm resolution). To demonstrate the benefit of the redundancy scheme and test its effect on the output power and wavelength stability of the eight fibre-DFB lasers, the pump diodes were turned off gradually and their spectra monitored (see Figures 2(b)-(f)). As expected, the output power of all channels drops uniformly and all channels survive even in the extreme case when only one pump is alive (Figure 2(f)). It should be also noticed that the SNR is unaffected by the pump

failures, as is the RIN. Owing to the reduced pump power, the lasing wavelength of the fibre-DFB lasers shows a slight blue shift (~ 500 MHz/pump failure). This shift is of thermal origin and is due to the strong pump absorption in the Er/Yb-doped fibre used for the lasers. The use of the pump redundancy scheme not only protects against sudden pump failures, but also averages out diode power fluctuations.

The extension of this scheme to provide 16 DFB fibre laser transmitter module, with 50GHz channel spacing and only 8 pumps, has also been demonstrated [26]. This pump redundancy scheme has been realised by splitting the 8 outputs from the previous 8-channel scheme, with an additional set of 3-dB couplers at the output. The module showed similar behaviour against pump failures.

V. Conclusions

We have reviewed the various uses of FBG devices as high-performance dispersion-compensators and fibre-DFB laser and laser arrays. It is shown that grating technology offers unique design and manufacturing flexibility and can provide a wide range of high-performance all-fibre passive and active devices.

Acknowledgements

The authors greatly acknowledge L. Reekie for useful discussions on the experiments related to writing gratings through the fibre coating, R. Feced, S. -u. Alam and A. B. Grudinin for help in testing and packaging of the fibre-DFB lasers, together with H. S. Kim and D. J. Richardson for collaborative measurements on the noise performance of the lasers. This work was in part supported by Pirelli Cavi SpA, Italy.

References

- [1] K. O. Hill, Y. Fujii, D. C. Johnson and B. S. Kawasaki, "Photosensitivity in optical fibre waveguides: application to reflection filter fabrication", *Appl. Phys. Lett.*, **32**, (10), pp. 647-9 (1978).
- [2] G. Meltz, W. W. Morey, and W. H. Glen, "Formation of Bragg gratings in optical fibres by a transverse holographic method", *Opt. Lett.*, **14**, pp. 823-5 (1989).
- [3] C. R. Giles, "Lightwave applications of fibre Bragg gratings", *J. Lightwave Technol.*, **15**, (8), pp. 1391-1404 (1997).
- [4] A. D. Kersey, M. A. Davis, H. J. Patrick, M. LeBlanc, K. P. Koo, C. G. Askins, M. A. Putnam and E. J. Friebele, "Fiber Grating Sensors", *J. Lightwave Technol.*, **15**, (8), pp. 1442-63 (1997).
- [5] B. Malo, S. Theriault, D. C. Johnson, F. Bilodeau, J. Albert and K. O. Hill, "Apodised in-fibre Bragg grating reflectors photo-imprinted using a phase mask", *Electron. Lett.*, **31**, (3), pp. 223-225 (1995).
- [6] A. Asseh, H. Storøy, B. E. Sahlgren, S. Sangren and R. A. H. Stubbe, "A writing technique for long fiber gratings with complex reflectivity profiles", *J. Lightwave Technol.*, **15**, (8), pp. 1419-1423 (1997).
- [7] M. J. Cole, W. H. Loh, R. I. Laming, M. N. Zervas and S. Barcelos, "Moving fibre/phase mask-scanning beam technique for enhanced flexibility in producing fibre gratings with uniform phase mask", *Electron. Lett.*, **31**, (17), pp. 1488-1489 (1995).
- [8] R. I. Laming, W. H. Loh, M. J. Cole, M. N. Zervas, K. E. Ennser and V. Gusmeroli, "Fiber gratings for dispersion compensation", in proceedings to *OFC '97*, pp. 234-235, Dallas, USA, 1997.
- [9] J. F. Brennan III and D. L. LaBrake, "Realisation of >10m-long chirped fibre Bragg gratings", in proceedings to *BGPP '99*, pp. 35-37, Stuart (Florida), USA, (1999).
- [10] F. Ouellette, "Dispersion cancellation using linearly chirped Bragg grating filters in optical waveguides", *Opt. Lett.*, **12**, (10), pp. 847-849 (1987).

- [11] D. Garthe, W. S. Lee, R. E. Epworth, T. Brichenno and C. P. Chew, "Practical dispersion equalizer based on fibre gratings with a bitrate product of 1.6Tb/s km, in proceedings to *ECOC'94*, 4, post-deadline papers, pp. 11-14, 1994.
- [12] R. I. Laming, N. Robinson, P. L. Scrivener, M. N. Zervas, S. Barcelos, L. Reekie and J. A. Tucknott, "A dispersion tunable grating in a 10Gbit/s 100-220km step-index fibre link", *IEEE Photon. Technol. Lett.*, 8, (3), pp. 428-430, (1996).
- [13] W. H. Loh, R. I. Laming, N. Robinson, A. Cavaciuti, F. Vaninetti, C. J. Anderson, M. N. Zervas and M. J. Cole, "Dispersion compensation over distances in excess of 500km for 10Gbit/s systems using chirped fibre gratings", *IEEE Photon. Technol. Lett.*, 8, (7), pp. 944-946 (1996).
- [14] B.J.Eggleston, J.A. Rogers, P.S. Westbrook and T.A. Strasser: "Electrically tunable power efficient dispersion compensating fiber Bragg gratings for dynamic operation in nonlinear lightwave systems", in proceedings to *OFC'99*, post-deadline paper PD27, San Diego, USA, 1999.
- [15] L. Dong, M. J. Cole, A. D. Ellis, M. Durkin, M. Ibsen, V. Gusmeroli and R. I. Laming, "40Gbit/s 1.55 μ m transmission over 109km of non-dispersion-shifted fibre with long continuously chirped fibre gratings", in proceedings to *OFC '97*, Post-deadline paper PD-6, Dallas, USA, 1997.
- [16] M. Ibsen, M.K. Durkin, K. Ennser, M.J. Cole and R.I. Laming: "Long continuously chirped fibre Bragg gratings for compensation of linear- and 3rd-order dispersion", in proceedings to *ECOC'97*, 2, pp. 49-52, Edinburgh, UK, 1997.
- [17] M. Ibsen, M.K. Durkin and R.I. Laming: "Chirped Moiré fibre gratings operating on two-wavelength channels for use as dual-channel dispersion compensators", *IEEE Photon. Technol. Lett.*, 10, (1), pp. 84-86, (1998).
- [18] M. Durkin, R. Feced, C. Ramirez and M. N. Zervas, "Advanced fiber Bragg gratings for high performance dispersion compensation in DWDM systems", submitted to *OFC'2000*, Baltimore, USA, 2000.
- [19] R. Feced, M. N. Zervas and M. A. Muriel: "An efficient inverse scattering algorithm for the design of nonuniform fiber Bragg gratings", *IEEE J. Quantum Electron.*, 35, (8), pp. 1105-1115, (1999).
- [20] K. Ennser, M. Ibsen, M. K. Durkin, R.I. Laming: "Influence of non-ideal chirped fibre grating characteristics on dispersion cancellation", *IEEE Photon. Technol. Lett.*, 10, (10), 1998.
- [21] K. Ennser, M.N. Zervas and R.I. Laming: "Optimization of apodized linearly chirped fiber gratings for optical communication", *IEEE J. Quantum Electron.*, 34, (5), pp. 770-778, (1998).
- [22] M. Ibsen, M.K. Durkin, M.J. Cole and R.I. Laming: "Sinc-sampled fibre Bragg gratings for identical multiple wavelength operation", *IEEE Photon. Technol. Lett.*, 10, (6), pp. 842-844, 1998.
- [23] L. Chao, L. Reekie and M. Ibsen: "Grating writing through the fibre coating using a 244 nm CW- and 248 nm excimer laser", in proceedings to *OFC'99*, paper ThD5, pp. 62-63, San Diego, USA, 1999.
- [24] F. Ouellette: "The effect of profile noise on the spectral response of fiber gratings", in proceedings to *BGPP'97*, paper BMG13, Williamsburg, USA, 1997.
- [25] J.T. Kringlebotn, J.-L. Archambault, L. Reekie and D.N. Payne: 'Er³⁺:Yb³⁺-co-doped fibre distributed-feedback laser', *Optics Lett.*, 19, (24), pp. 2101-2103, 1994.
- [26] M. Ibsen, E. Rønnekleiv, G.J. Cowle, M.O. Berendt, O. Haderl, M.N. Zervas and R.I. Laming: 'Robust high power (>20 mW) all-fibre DFB lasers with unidirectional and truly single polarisation outputs', in proceedings to *CLEO '99*, paper CWE4, pp. 245-246, Baltimore, USA, 1999.
- [27] M. Ibsen, A. Fu, H. Geiger and R.I. Laming: 'Fibre DFB lasers in a 4x10 Gbit/s link with a single sinc-sampled fibre grating dispersion compensator', in proceedings to *ECOC '98*, post-deadline papers, 3, pp. 109-111, Madrid, Spain, 1998.
- [28] M. Ibsen, S.-u. Alam, M.N. Zervas, A.B. Grudinin and D.N. Payne: "All-fibre DFB laser WDM-transmitters with integrated pump redundancy", in proceedings to *ECOC'99*, 1, pp. 74-75, Nice, France, 1999.

Author Index

- Abbate, Mario, 705
 Ang, Tze Wei, 360
 Annapurna, Kalyandurg, 653, 658, 663
 Bärwolff, A., 56
 Batubara, John E., 319, 334, 576
 Bayuwati, Dwi, 507
 Bergh, Arpad A., 2
 Bidnyk, Sergiy, 72
 Blau, Werner J., 705
 Brandenburg, Wolfgang, 65
 Bubeck, Christoph, 697
 Buddhudu, Srinivasa, 459, 653, 658, 663, 673
 Bui, Huy, 637
 Campbell, Kevin T., 133
 Cao, Mingcui, 624
 Chan, Wai Kin, 223
 Chan, Yuen Chuen, 184, 199, 207, 231, 265, 412, 417, 425, 433, 438, 446, 453, 459, 499, 515, 667, 673, 680
 Chandramohan, Rathnam, 107
 Chao, Lu, 762
 Chen, Ying-Chung, 687
 Chen, Yu Wen, 199
 Chen, Zhihao, 562
 Cheng, Shide D., 425, 446, 466, 673, 680
 Chia, C. K., 385
 Chiang, Kin Seng, 369, 562
 Chichibu, Shigefusa F., 98
 Chockalingam, Mary Juliana, 474
 Chou, Jung-Chuan, 642
 Chua, Soo Jin, 155, 191, 741
 Chung, Yun-Chun, 557
 Cole, M. J., 762
 Coppée, Daniël, 281
 Dai, Enguang, 403
 Dao, Tran Cao, 637
 David, John P. R., 163, 385
 Day, Gordon W., 308
 Deguchi, Takahiro, 98
 DenBaars, Steven P., 98
 Deng, Cong, 624
 Deppe, Dennis G., 12
 Dimitrijević, Sima, 614
 Duan, Zhengcheng, 494
 Durkin, M. K., 762
 Dwivedi, Rabindra Nath, 653, 658, 663
 Ebeling, Karl Joachim, 116, 273
 Eliseev, Peter G., 86
 Evans, Alan G. R., 352, 360
 Fitrilawati, Fitri, 697
 Gaff, Keith W., 342
 Gan, Woon Siong, 466, 680
 Grabherr, Martin, 116
 Graham, Luke A., 12
 Grey, R., 163, 385
 Gunawan, Oki, 184, 515
 Han, Aizhen, 523
 Han, X. Q., 425, 466
 Harrison, H. Barry, 614
 Harsoyono, H., 585
 Hayduk, Michael J., 290
 Hoe, Lui Whye, 515
 Hoerhold, Hans-Heinrich, 237
 Hou, Sijian, 223
 Hu, Qiaoyan, 624
 Hu, Xiao, 484
 Hu, Xiongwei, 594
 Huang, Dexiu, 494
 Huang, Hung Ji, 751
 Huang, H., 12
 Huang, Jingsong, 231, 570
 Huang, Y. H., 191
 Huang, Yao-Te, 687
 Huda, Md. Quamrul, 328
 Huffaker, Diana L., 12
 Ibsen, Morten, 762
 Imai, Masaaki M., 328
 Islam, Mohammed Nazrul, 328
 Jackson, Howard E., 313
 Jäger, Roland, 116, 273
 Jandeleit, Jürgen, 65
 Janos, Mark, 380
 Jayachandran, M., 474
 Jha, Animesh, 298
 Jiang, Hongjing, 231
 Jie, Wanqi, 528
 Josey, Mike R., 352, 360
 Jung, Christian, 116
 Kam, Chan Hin, 425, 433, 446, 453, 459, 466, 667, 673, 680
 Kao, Ming-Cheng, 687
 Khoo, E. A., 163
 Khoo, Hong Khai, 741
 Khorasani, Sina, 395, 602
 Kicherer, Max, 116, 273
 King, Roger, 116
 Kobayashi, Kohroh, 46
 Koch, Stephan W., 24
 Koike, Yasuhiro, 214, 250
 Kuijk, Maarten, 281
 Kwan, Chung Ho, 369
 Ladouceur, François J., 342

- Lam, Yee Loy, 184, 207, 231, 265, 412, 417, 425, 433, 438, 446, 453, 459, 466, 499, 515, 667, 673, 680
- Laming, Richard I., 762
- Lee, Jinhyun, 86
- Lee, Liang Pao, 155
- Lei, Hongbing, 594
- Li, Chuannan, 570
- Li, E. Herbert, 172
- Li, G., 191
- Li, Heping, 446
- Li, Yangqi, 570
- Li, Yujie, 528
- Liaw, Chin Yi, 412
- Liebegott, Heike, 237
- Lim, Hwi Siong, 207
- Lin, Song-Shiang, 712
- Lin, Wei Chih, 751
- Liu, Deming, 494, 624
- Liu, Jian, 412, 417, 446
- Liu, Shiyong, 570
- Liu, Xiaohua, 528
- Loosen, Peter, 65
- Lorenzen, Dirk, 56
- Love, John D., 342
- Lu, Nien Hua, 751
- Luo, Fengguang, 624
- Luther-Davies, Barry, 237
- Maćkowiak, Paweł, 534
- Mahalingam, T., 107
- Mao, Xiang-jun, 499
- Marsh, John H., 191
- Mederer, Felix, 116, 273
- Meier, Torsten, 24
- Miller, Michael, 116
- Monastyrskii, Liubomyr S., 631
- Morita, Makoto, 459
- Mormile, Pasquale, 705
- Mukai, Takashi, 98
- Muljono, 319, 334, 576
- Müller, Ralf, 56
- Murali, K. R., 756
- Musto, Pellegrino, 705
- Nafataly, M., 298
- Nakai, Rikuro, 98
- Nakamura, Shuji, 98
- Nakwaski, Włodzimierz, 534
- Namavar, Fereydoon, 352
- Naritomi, Masaki, 273
- Ng, Geok Ing, 199
- Ng, Po King, 223
- Ng, Seng Lee, 184, 459
- Ngo, Nam Quoe, 614
- Nojeh, Alireza, 395
- Nomura, Tadakazu, 328
- Olenych, Igor B., 631
- Ong, Teik Kooi, 207
- Ooi, Boon Siew, 184, 199, 207, 231, 265, 417, 425, 433, 438, 459, 515, 667
- Osiński, Marek, 86, 143, 534
- Osotchan, T., 547
- Ostlender, Andreas, 65
- Ou, Haiyan, 594
- Pabla, Arbinder S., 163
- Palmer, James R., 720
- Pandit, Malay K., 562
- Payne, David N., 762
- Petti, Lucia, 705
- Pham, Van Hoi, 557, 637
- Phi, Hoa Binh, 637
- Pillai, A. Sivathanu, 36
- Pita, K., 466
- Plimmer, S. A., 385
- Poole, Simon B., 380
- Poprawe, Reinhart, 65
- Que, Wenxiu, 417, 446, 459, 466, 673, 680
- Ragosta, Giuseppe, 705
- Rashidian, Bizhan, 395, 602
- Reed, Graham T., 352, 360
- Rees, G. J., 163, 385
- Robertson, Alexander, 133
- Rosa, Michel A., 614
- Routley, Paul R., 352, 360
- Saher Helmy, A., 191
- Sakai, Shiro, 86
- Samoc, Anna, 237
- Samoc, Marek, 237
- Sanjeeviraja, C., 474
- Savchyn, Volodymyr P., 631
- Schmidt, Theodore J., 72
- Schnitzer, Peter, 116, 273
- Setoguchi, Akiko, 98
- Shen, Jiacong, 570
- Shen, S., 298
- Sheu, Tien-Jey, 712
- Shi, W., 547
- Shi, Xu, 425, 466
- Shikanai, Amane, 98
- Siregar, Masbah Rotuanta Tagore, 507
- Siregar, Rustam E., 585
- Smagley, Vladimir A., 86, 534
- Smith, Ben, 380
- Smolyakov, Gennady A., 143, 534
- Soehiani, Agoes, 585
- Song, Jin-Joo, 72
- Sota, Takayuki, 98
- Stockmann, Regina, 237
- Subramanian, B., 474
- Sugahara, Tomoya, 86
- Sun, Z., 425, 466
- Supit, Andrew, 334
- Susanto, Hery, 576
- Svimonishvili, Tengiz, 534
- Swaminathan, V., 756

Sweatman, Denis R., 614
 Tagaya, Akihiro, 214
 Tan, C. L., 199
 Tan, Gu, 412, 417
 Teng, Jing H., 191
 Thai, Serey, 290
 Titmarsh, Andrew, 614
 Tjia, May On, 585, 697
 Tomm, Jens W., 56
 Tran, Quoc Viet, 557
 Tsai, Din Ping, 313, 751
 Tsai, Fu-Yuan, 712
 Tu, Yuan-Kuang, 712
 Unold, Heiko J., 273
 Uranus, Henri P., 319, 334, 576
 Vonsovici, Adrian, 352, 360
 Vounckx, Roger A., 281
 Vu, Duc Thinh, 557, 637
 Wada, Kazumi, 98
 Waluyo, Tomi Budi, 507
 Wan, Anjun, 624
 Wan, Zuowen, 733
 Wang, Chao, 265
 Wang, Chih-Ming, 687
 Wang, Guangming, 484
 Wang, Jiyang, 608
 Wang, Qiming, 594
 Wang, Yue, 570
 Wee, Terence C. L., 438
 Wetzel, Steven J., 133
 Wiedenmann, Dieter, 116
 Wiedmann, Nicolas, 65
 Wong, Chi Tak, 223
 Wong, Terence K. S., 459, 484
 Woodhead, J., 163
 Wu, Deming, 403
 Wu, Fang, 570
 Xiang, Qing, 433, 453, 667
 Xie, Zhiyuan, 570
 Xu, Anshi, 403
 Xu, Jun, 624
 Xu, Wenchao, 494
 Xu, Wusheng, 523, 608
 Xu, Yuheng, 608
 Yang, Chi Wen, 313
 Yang, Chunhui, 523
 Yang, Hsu Ying, 642
 Yang, Kaixia, 570
 Yang, Qinqing, 594
 Yoon, Soon Fatt, 425
 Yoshida, Ryouta, 273
 Yu, M. B., 425
 Yu, Sze Chit, 223
 Yui Whei, Chen-Yang, 712
 Yulianto, Hendik R., 319
 Zervas, Michael N., 762
 Yuon, Chun-Ju, 557
 Zhang, D. H., 547
 Zhang, Hong Xi, 425, 459, 466
 Zhang, Hongxi, 608
 Zhang, Z. H., 191
 Zhang, Zhimei, 523
 Zhang, Zhouxun, 733
 Zhao, Li Ping, 673
 Zhao, Yequan, 608
 Zhao, Yi, 570
 Zhou, Yan, 184, 207, 231, 412, 417, 425, 433, 438, 446, 453, 459, 466, 515, 667, 673, 680
 Zhu, Dayong, 733
 Ziegler, Jochen, 697